

Total Synthesis of Clickable Natural Product Derivatives and Manufacturing of Conjugates for Target-Specific Application of Potential Drugs

Inaugural Dissertation

Submitted to the

Faculty of Mathematics and Natural Sciences

of the Heinrich Heine University Düsseldorf

by

Tim Moritz Weber

October, 2025

Institute of Bioorganic Chemistry,

Heinrich Heine University Düsseldorf

Printed with permission of the Faculty of Mathematics and Natural Sciences

of the Heinrich Heine University Düsseldorf

Examiners:

1. Examiner: Prof. Dr. Jörg Pietruszka

2. Examiner: Prof. Dr. Julia Frunzke

3. Examiner: Prof. Dr. Uli Kazmaier

Oral examination date: 17.04.2026

In memory of my beloved grandparents

Your lives were a blessing,
your memory a treasure.
You are loved beyond words
and missed beyond measure.

Goodbyes are not forever,
are not the true end;
it simply means I'll miss you,
until we meet again.

Danke. Für alles.

Publications

Parts of this dissertation were previously submitted or published in scientific journals, uploaded as preprints, or were presented at international conferences. Own contributions are highlighted in bold.

Preprints

Weber, T. M., Guadarrama-Gonzalez, R., MacKenzie, C. R., & Pietruszka, J. Hoisted by Their Own Petard: Defeating Immunity Protein–Mediated Bacteriocin Resistance. *BioRxiv* preprint. https://www.biorxiv.org/content/10.1101/2025.10.23.684137v1.

Journal Publications

Weber, T. M., & Pietruszka, J. Functionalized in Triplicate: A Ring-by-Ring Approach to Tailored Prodiginine Derivatives for Site-Specific Conjugation Through Click Chemistry. *Chem. Eur. J.* **2025**, 31(*43*):e202502066.

Weber, T. M., Özdüzenciler, P., Tamgüney, G., & Pietruszka, J. Utilization of a Branched Late-Stage Clickable Biotinylated Chassis on the Example of a Pittsburgh B Analogue. *Org. Lett*. **2024**, 26(*31*), 6771–6775.

Weber, T. M., Leyens, A., Berning, L., Stork, B., & Pietruszka, J. New Prodigiosin Derivatives – Chemoenzymatic Synthesis and Physiological Evaluation. *Catal. Sci. Technol.* **2023**, 13(*21*), 6165–6184.

Weber, T. M. & Pietruszka, J. Synthesis of a Water-Soluble Tridentate (Dimethylamino)ethyl Cu(I)/Cu(II)-Ligand. *Synthesis* **2023**, 55(*14*), 2128–2133.

Kossmann, D. F., Huang, M., Weihmann, R., Xiao, X., Gätgens, F., **Weber, T. M.**, Brass, H. U. C., Bitzenhofer, N. L., Ibrahim, S., Bangert, K., Rehling, L., Mueller, C., Tiso, T., Blank, L. M., Drepper, T., Jaeger, K.-E., Grundler, F. M. W., Pietruszka, J., Schleker, A. S. S., & Loeschcke, A. Production of tailored hydroxylated prodiginine showing combinatorial activity with rhamnolipids against plant-parasitic nematodes. *Front. Microbiol.* **2023**, *14*:1151882.

Habash, S. S., Brass, H. U., Klein, A. S., Klebl, D. P., **Weber, T. M.**, Classen, T., Pietruszka, J., Grundler, F. M. W., & Schleker, A. S. S. Novel prodiginine derivatives demonstrate bioactivities on plants, nematodes, and fungi. *Front. Plant Sci.* **2020**, *11*:579807.

Conferences and Poster Contributions

Weber, T. M., & Pietruszka, J., Total Synthesis of Azide-Functionalised Prodiginines for Conjugation via Copper-Catalysed Azide-Alkyne Cycloaddition, presented at the 22nd European Symposium on Organic Chemistry (ESOC 2023) in Ghent (Belgium). (Poster)

Weber, T. M., MacKenzie, C. R. & Pietruszka, J., Pyocin S2 Conjugates for the Treatment of PyoS2-Resistant MDR Clinical Isolates of *Pseudomonas aeruginosa*, presented at the 9th Symposium on Antimicrobial Resistance in Animals and the Environment (ARAE 2023) in Tours (France). (Poster)

Table of Contents

Abbreviations ..... **XI**
Abstract ..... **XV**

I Introduction **19**

II The Novel Cu(I)/Cu(II) Ligand TDETA – A Precious Accelerator of CuAAC Reactions in the Preparation of Biologically Relevant Conjugates **23**
II.1 State of the Knowledge **23**
II.1.1 Click Chemistry 24
II.1.1.1 Azide-Alkyne Cycloadditions 24
II.1.1.2 CuAAC Reactions in the Spotlight of Application 26
II.1.1.2.1 Antibody-Drug Conjugates 27
II.1.1.2.2 Click-Tools in DNA and RNA Research 32
II.1.1.2.3 Click-Tools in Glycochemistry 34
II.1.1.3 Copper-Stabilising Ligands and Mechanistic Considerations in CuAAC Reactions 36
II.1.1.3.1 Nitrogen-Containing Polydentate Copper-Ligands in CuAAC 38
II.1.1.3.2 The Synthesis of the Superior Cu(I)/Cu(II)-Ligand DTEA Underlies the Chemical Weapons Convention 42
II.2 Aims **45**
II.3 Results and Discussion **47**
II.3.1 Synthesis of TDETA as Legal Alternative for DTEA 47
II.3.1.1 Preparation of Suitable Substrates for the Evaluation of CuAAC Ligands 48
II.3.1.2 Ligand Screening for CuAAC under Mild Cu(II) Catalysis 49
II.3.1.3 Ligand Screening for CuAAC Under Reducing Cu(I) Conditions 52
II.3.1.4 Validation of TDETA in Preparative Organic Chemistry 53
II.3.1.5 Stress Test of TDETA under Aqueous Conditions 54
II.3.2 TDETA-Assisted CuAAC Gives Rise to Biotinylated Conjugates of Bioactive Molecules 57
II.3.2.1 Biotinylated Cholesterol for the Screening of Cholesterol-Binding Peptide Libraries via Phage Display 58
II.3.3 CuAAC as a Tool for Rapid Structural Diversification on the Example of Biotinylated Pittsburgh B 60
II.3.3.1 The Biotinylated Pittsburgh B Analogue CAP-1 Binds Amyloid Fibrils Associated with Neurodegenerative Diseases 60
II.3.3.2 An Alternate Biotin-Bis-PEG-Azide Design Enables Late-Stage Functionalisation and Probe Diversification 62
II.3.3.3 Two Independent Routes Lead to the *N*-Methylated PiB Probe 65
II.3.3.4 TDETA-Assisted Click Chemistry Renders the Clicked Amyloid Capture Molecule cCAP-1 66
II.3.3.5 cCAP-1 Binds α-Syn Fibrils *In Vitro* 67
II.4 Summary Chapter II – The Novel Cu(I)/Cu(II) Ligand TDETA **71**
II.5 Outook Chapter II **75**
II.5.1 Synthesis of Polymer-Supported TDETA for Improved Recycling 75
II.5.2 Biocompatibility and *In Vivo* Application of TDETA **II-44** 76
II.5.3 In-Depth Biochemical Characterisation of cCAP-1 **II-73** and α-Syn Binding 77
II.5.4 Preparation of Libraries and High-Throughput Screening With the Biotinylated Bis-Azide **II-79** Chassis 78

III Chemoenzymatic and Total Synthesis of Prodigiosin Alkaloids as Potent Antitumoral Agents Suitable for Target-Specific Application **78**
III.1 State of the Knowledge **81**
III.1.1 Prodigiosin – A Tripyrrolic Bacterial Secondary Metabolite with a Long-Standing History 81

III.1.1.1 Structural Diversity of Natural Derivatives from the Prodiginine Family ... 82
III.1.1.2 Biosynthesis of Prodigiosin ... 84
III.1.1.2.1 Biosynthesis of MBC ... 84
III.1.1.2.2 Biosynthesis of MAP ... 85
III.1.1.2.3 Prodigiosin Ligases ... 86
III.1.1.3 Substrate Promiscuity of Prodiginine Ligating Enzymes ... 87
III.1.1.3.1 Monopyrrole Promiscuity ... 87
III.1.1.3.2 Bipyrrole Promiscuity ... 88
III.1.1.4 A-Ring Modifications of Prodiginine-Related Natural Products and Non-Natural Derivatives ... 89
III.1.1.5 Biological Activities ... 90
III.1.1.5.1 Cytotoxicity and Antibiotic Effects ... 90
III.1.1.5.2 Autophagy Modulation ... 92
III.1.1.5.3 Immunosuppressive Activity ... 93
III.1.1.5.4 Antimalarial Activity ... 94
III.1.1.6 Selected Total Syntheses of the Prodiginine Scaffold ... 94
III.1.1.6.1 Biomimetic Syntheses of Prodigiosin ... 95
III.1.1.6.2 Non-Biomimetic Synthesis of Prodigiosin ... 96
III.1.1.7 Targeting Approaches for Site-Specific Prodiginine Applications ... 97
III.1.1.7.1 Non-Covalent Targeting Approaches ... 97
III.1.1.7.2 Covalent Targeting Approaches ... 99
III.2 Aims ... 103
III.3 Results and Discussion ... 105
III.3.1 Total Synthesis of Clickable Prodiginine Azides for Targeted Applications ... 105
III.3.1.1 Prodigiosin A-Ring Azide ... 106
III.3.1.1.1 Alkylated C-Ring Precursor ... 106
III.3.1.1.2 C-Ring Alkylated Dipyrromethene ... 107
III.3.1.1.3 A-Ring Azide Precursor ... 107
III.3.1.1.4 Ligand Screening for Suzuki-Miyaura Cross-Coupling Reactions ... 112
III.3.1.1.5 Biaryl Coupling Towards Prodigiosin A-Ring Azide and its Clickable *F*-BODIPY ... 114
III.3.1.2 Prodigiosin B-Ring Azide ... 117
III.3.1.2.1 B-Ring Azide Precursor and B-Ring Azide Dipyrromethene ... 117
III.3.1.2.2 Alkylated A-Ring Precursor ... 118
III.3.1.2.3 Biaryl Coupling Towards Prodigiosin B-Ring Azide ... 119
III.3.1.3 Prodigiosin C-Ring Azide ... 119
III.3.1.4 Click Conjugates of Functionalised Prodiginines ... 122
III.3.1.4.1 Synthesis of a Bifunctional Alkyne-Maleimide Linker ... 122
III.3.1.4.2 CuAAC Click Functionalisation of Prodiginine Azides Requires Homo-Dimeric Zinc Complexes ... 123
III.3.1.4.3 Trastuzumab-Prodigiosin Conjugates – The First Antibody-Drug Conjugates of Prodigiosin ... 125
III.3.2 Chemoenzymatic Synthesis of Novel A-Ring Alkylated Prodigiosin Derivatives ... 131
III.3.2.1 Synthesis of C-Ring Monopyrrole Precursors ... 131
III.3.2.2 Synthesis of 5'-Alkylated MBC Precursors ... 132
III.3.2.3 Chemical Synthesis of A-Ring Alkylated Prodiginines ... 134
III.3.2.4 Influence of Prodigiosin A-Ring Alkylation on Absorption and Molar Extinction Coefficients ... 134
III.3.2.5 Prodigiosin Ligase Substrate Scope for A-Ring Alkylated MBC ... 137
III.3.2.6 Anticancer Activity of Prodigiosin Azides and A-Ring Alkylated Prodiginines ... 141
III.4 Summary Chapter III – Chemoenzymatic and Total Synthesis of Prodigiosin Alkaloids ... 147
III.5 Outlook Chapter III ... 153
III.5.1 Link Between pK_a and Cytotoxicity of Prodiginines ... 153
III.5.2 Extended Substrate Scope of Prodiginine Ligases and Proposed Synthesis of Alternative MBC Analogues ... 154

III.5.3 Target Fishing with Biotinylated Prodiginines 157
III.5.4 Prodiginine Conjugates with Cleavable Linkers and in Conjunction with Small-Molecule Carriers 157

IV Conjugates of the Bacterial Protein Toxin Pyocin S2 Target Multidrug-Resistant Clinical Isolates of *Pseudomonas aeruginosa* 163
IV.1 State of the Knowledge 163
IV.1.1 Antibiotics 163
IV.1.1.1 β-Lactam Antibiotics and Their Mode of Action 165
IV.1.1.2 Antibiotic Resistance 167
IV.1.1.2.1 Mechanisms Without Drug Inactivation 168
IV.1.1.2.2 β-Lactamases – A Group of β-Lactam Hydrolysing Enzymes 169
IV.1.1.2.3 Carbapenemases 171
IV.1.2 *Pseudomonas aeruginosa* – An Opportunistic Human Pathogen 172
IV.1.2.1 Virulence Factors and Pathogenicity 172
IV.1.2.2 Biofilms and Quorum Sensing Shape Cell-to-Cell Interaction 173
IV.1.2.3 Surface Exposed Virulence Factors 174
IV.1.2.4 Secretion Systems and Their Secreted Exoenzymes 175
IV.1.2.5 Siderophores – Metal Chelators for Trace Metal Acquisition 176
IV.1.2.5.1 Exploitation of Siderophore Uptake Mechanisms for the Channelling of Drugs into the Bacterial Cell 177
IV.1.3 Research on Alternatives for Common Antibiotics Against *Pseudomonas aeruginosa* 178
IV.1.3.1 Bacteriocins – Narrow-Spectrum Antimicrobial Peptides as Extension to Antibiotics? 178
IV.1.3.1.1 Pyocins – The Bacteriocins of *Pseudomonas aeruginosa* 178
IV.1.3.1.2 S-Type Pyocins 181
IV.1.3.1.2.1 S-Type Pyocins Share Conserved Mechanisms of Translocation 182
IV.1.3.1.2.2 Bacterial LPS Acts as Secondary Receptor of S-Type Pyocins 185
IV.1.3.1.2.3 Pyocin S2 Binds its Immunity Protein S2 with Ultra-High-Affinity 186
IV.2 Aims 189
IV.3 Results and Discussion 191
IV.3.1 Pyocin S2 Conjugates – Structural Conditions and Rational Protein Design 191
IV.3.1.1 A Few Residues Mediate Ultra-High-Affinity Binding Between PyoS2 and ImS2 191
IV.3.1.2 Selection of Sites for PyoS2 Labelling 194
IV.3.1.3 Design of DNase-Inactive PyoS2 Mutants 196
IV.3.1.4 Rational Design of a PyoS2 Mutant with Deficiency for Interaction with ImS2 197
IV.3.2 Purification of PyoS2 and DNase Knock-Outs 198
IV.3.3 Validation of wild-type PyoS2 and DNase Knock-Outs 200
IV.3.4 Conjugation of PyoS2 to Small Molecule Fluorophore Labels 202
IV.3.4.1 Expression and Purification of PyoS2 Cysteine Mutants for Labelling 202
IV.3.4.2 Maleimide Labelling of PyoS2 Cysteine Mutants with Non-Toxic Fluorophores 205
IV.3.5 Labelling at the PyoS2/ImS2 Interface Impairs Association of the Inhibitory Complex *In Vitro* 207
IV.3.6 PyoS2 ID Mutants are Highly Deficient in ImS2 Binding but Show Strongly Impaired DNase Activity 213
IV.3.7 Long-Term Exposure of DNA to PyoS2 Variants Discloses Hidden Aspects of Mutagenesis and Labelling *In Vitro* 218
IV.3.8 Impaired Binding of ImS2 to the PyoS2 DNase Overrules PyoS2-Resistance of *Pseudomonas aeruginosa* PAO1 221
IV.3.9 PAO1 is Killed by Single Dose Treatment with PyoS2 Y640C Conjugate in Liquid Media 227
IV.3.10 Characterisation of PyoS2-Related Genetic Determinants in a Strain Collection of MDRs CRPsA 230
IV.3.10.1 Identification of FpvA-Subtypes and PyoS2-Producers by Multiplex PCR 231
IV.3.11 PyoS2 Y640C and PyoS2 ID Variants are Suitable to Obliterate MDR CRPsA 235
IV.3.12 Whole-Genome Sequencing Reveals Commonalities and Differences in OM Composition 239
IV.3.12.1 Sequencing, Genome Assemblies, and Their Alignment 239
IV.3.12.2 The OM Composition Impacts the Cytotoxicity of PyoS2 and Labelled Derivatives Thereof 240

IV.3.12.2.1 Mutations in the Glycosyltransferase WbpZ and in the ATPase Subunit Wzt Show No Impact on PyoS2 Sensitivity 241
IV.3.12.2.2 Mutations in the *gmd* Locus Impair CPA Biosynthesis and Cause Secondary PyoS2 Resistance 243
IV.3.12.2.3 The O-Serotype Determines the Sensitivity to PyoS2 244
IV.3.13 Utilisation of PyoS2 Conjugates to Traverse Potential Drugs Across the Bacterial Membrane 252
IV.3.13.1 Design and Preparation of PyoS2-Prodigiosin Conjugates 253
IV.3.13.2 PyoS2-Prodigiosin Conjugates Enter the Bacterial Cytoplasm, But Only Display DNase Activity 256
IV.4 Summary Chapter IV – Conjugates of Pyocin S2 Target MDR Isolates of *P. aeruginosa* 263
IV.5 Outlook Chapter IV 267
IV.5.1 Characterisation of O-Serotypes and Isolation of LPS to Verify Malfunctions in OSA and CPA Biosynthesis and Overcome Secondary Pyocin Resistance 267
IV.5.2 Transfer of Impaired Toxin/Immunity Association to Other Pyocins and Bacteriocins of Gram-Negative Bacteria 268
IV.5.3 Investigation on the Restoration of Catalytic DNase Activity of PyoS2 Y640C Through Maleimide-Functionalisation 271
IV.5.4 Stopped-Flow Fluorescence Measurements to Analyse DNase/Immunity Dissociation Constants 273
IV.5.5 PyoS2 Conjugates in Eukaryotic Infection Models and Their Application in Antibiotic Formulations 273
IV.5.6 Development of S-Type Pyocin Targeting Novel Outer Membrane Receptors 274
IV.5.7 Pyocins as Trojan Horse for Targeted Delivery of Antimicrobial Drugs into Multidrug-Resistant *Pseudomonas aeruginosa* 276

V Materials and Methods 279
V.1 Ethical Compliance Statement 279
V.2 Software 279
V.3 Chemical Methods 280
V.3.1 General Information 280
V.3.1.1 Naming of Compounds 280
V.3.1.2 Fine Chemicals, Solvents, and Reagent Handling 280
V.3.1.3 Analytical and Preparative Chromatography 281
V.3.2 Analytical Methods 281
V.3.2.1 Quantitative and Non-Quantitative Nuclear Magnetic Resonance Spectroscopy (qNMR and NMR) 281
V.3.2.2 Fourier-Transform Infrared Spectroscopy (FT-IR) 282
V.3.2.3 High-Resolution Mass Spectrometry (HRMS) 282
V.3.2.4 Melting points 282
V.3.2.5 Optical Rotation 282
V.3.2.6 Coupled Gas Chromatography-Mass Spectrometry (GC-MS) 282
V.3.2.7 Coupled Liquid Chromatography-Mass Spectrometry (LC-MS) 283
V.3.2.8 Quantification of Prodiginines from LC Chromatograms 283
V.3.2.9 Experimental Determination of Molar Extinction Coefficients 284
V.3.2.10 Approximation of Molar Extinction Coefficients 284
V.3.3 Other Methods 284
V.3.3.1 General Procedure for the TLC-Based CuAAC Screening for Ligand Comparison 284
V.3.3.2 Fluorometric Analysis of Tripodal Tetradentate Cu-ligands 285
V.3.4 Synthetic Procedures 286
(2-Chloroethyl)dimethylamine hydrochloride (**II-39·HCl**) 286
2-Azido-*N*,*N*-dimethylethan-1-amine (**II-43**) 286
2-(4-((Bis((1-(2-(dimethylamino)ethyl)-1*H*-1,2,3-triazol-4-yl)methyl)amino)methyl)-1*H*-1,2,3-triazol-1-yl)-*N*,*N*-dimethylethan-1-amine (**II-44**, TDETA) 287
2-(Azidomethyl)pyridine (**II-46**) 287
1-Azidooctane (**II-48**) 287
(4-Azidophenyl)methanol (**II-50**) 288

General Preparative Procedure for Preparative CuAAC Reactions to Access Products **II-57a–g** 288
2-((4-Phenyl-1*H*-1,2,3-triazol-1-yl)methyl)pyridine (**II-57a**) 288
1-(1-Benzyl-1*H*-1,2,3-triazol-4-yl)cyclohexan-1-ol (**II-57b**) 289
(4-(4-(Hydroxymethyl)-1*H*-1,2,3-triazol-1-yl)phenyl)methanol (**II-57c**) 289
Recycling of the Cu-ligand TDETA **II-44** 290
1-Benzyl-4-butyl-1*H*-1,2,3-triazole (**II-57d**) 290
1-Octyl-4-phenyl-1*H*-1,2,3-triazole (**II-57e**) 290
4-Butyl-1-octyl-1*H*-1,2,3-triazole (**II-57f**) 291
1-Benzyl-4-phenyl-1*H*-1,2,3-triazole (**II-57g**) 291
(3*S*,8*S*,9*S*,10*R*,13*R*,14*S*,17*R*)-10,13-Dimethyl-17-((*R*)-6-methylheptan-2-yl)-2,3,4,7,8,9,10,11,12,13,14,15,16,17-tetradecahydro-1*H*-cyclopenta[*a*]phenanthren-3-yl (2-(2-(2-(2-(4-(15-oxo-19-((3a*S*,4*S*,6a*R*)-2-oxohexahydro-1*H*-thieno[3,4-*d*]imidazol-4-yl)-2,5,8,11-tetraoxa-14-azanonadecyl)-1*H*-1,2,3-triazol-1-yl)ethoxy)ethoxy)ethoxy)ethyl)carbamate (**II-67**) 292
2,5-Dioxopyrrolidin-1-yl 5-((3a*S*,4*S*,6a*R*)-2-oxohexahydro-1*H*-thieno[3,4-*d*]imidazol-4-yl)pentanoate (**II-63**) 292
2-(4-(Dimethylamino)phenyl)benzo[*d*]thiazol-6-ol (**II-71**) 293
2-(4-(Dimethylamino)phenyl)benzo[*d*]thiazol-6-ol (**II-71**) 293
N,*N*-Bis(2-(2-(4-((2-(2-((2-(4-(dimethylamino)phenyl)benzo[*d*]thiazol-6-yl)oxy)ethoxy)ethoxy)methyl)-1*H*-1,2,3-triazol-1-yl)ethoxy)ethyl)-5-((3a*S*,4*S*,6a*R*)-2-oxohexahydro-1*H*-thieno[3,4-*d*]imidazol-4-yl)pentanamide (**II-73**, cCAP-1) 294
2,2'-((Azanediylbis(ethane-2,1-diyl))bis(oxy))bis(ethan-1-ol) (**II-74**) 295
N,*N*-Bis(2-(2-hydroxyethoxy)ethyl)-5-((3a*S*,4*S*,6a*R*)-2-oxohexahydro-1*H*-thieno[3,4-*d*]imidazol-4-yl)pentanamide (**II-77**) 295
N,*N*-Bis(2-(2-iodoethoxy)ethyl)-5-((3a*S*,4*S*,6a*R*)-2-oxohexahydro-1*H*-thieno[3,4-*d*]imidazol-4-yl)pentanamide (**II-78**) 296
N,*N*-Bis(2-(2-azidoethoxy)ethyl)-5-((3a*S*,4*S*,6a*R*)-2-oxohexahydro-1*H*-thieno[3,4-*d*]imidazol-4-yl)pentanamide (**II-79**) 296
2-Amino-5-methoxybenzenethiol (**II-88**) 297
4-(6-Methoxybenzo[*d*]thiazol-2-yl)-*N*,*N*-dimethylaniline (**II-90**) 297
3-(2-(2-Bromoethoxy)ethoxy)prop-1-yne (**II-92**) 297
N,*N*-Dimethyl-4-(6-(2-(2-(prop-2-yn-1-yloxy)ethoxy)ethoxy)benzo[*d*]thiazol-2-yl)aniline (**II-93**) 298
(*Z*)-4'-Methoxy-5'-((5-methyl-4-propyl-1*H*-pyrrol-2-yl)methylene)-1*H*,5'*H*-[2,2'-bipyrrol]-1'-ium chloride (**III-1aa·HCl**) 298
(*Z*)-4'-Methoxy-5'-((5-methyl-4-pentyl-1*H*-pyrrol-2-yl)methylene)-1*H*,5'*H*-[2,2'-bipyrrol]-1'-ium chloride (**III-1ab·HCl**, prodigiosin·HCl) 299
General Procedure for the Synthesis of 5-Alkylated Prodiginines **III-1ba–gb** 300
(*Z*)-4'-Methoxy-5-methyl-5'-((5-methyl-4-propyl-1*H*-pyrrol-2-yl)methylene)-1*H*,5'*H*-[2,2'-bipyrrol]-1'-ium chloride (**III-1ba·HCl**) 300
(*Z*)-4'-Methoxy-5-methyl-5'-((5-methyl-4-pentyl-1*H*-pyrrol-2-yl)methylene)-1*H*,5'*H*-[2,2'-bipyrrol]-1'-ium chloride (**III-1bb·HCl**) 300
(*Z*)-4'-Methoxy-5-methyl-5'-((5-methyl-4-heptyl-1*H*-pyrrol-2-yl)methylene)-1*H*,5'*H*-[2,2'-bipyrrol]-1'-ium chloride (**III-1bc·HCl**) 301
(*Z*)-5-Ethyl-4'-methoxy-5'-((5-methyl-4-pentyl-1*H*-pyrrol-2-yl)methylene)-1*H*,5'*H*-[2,2'-bipyrrol]-1'-ium chloride (**III-1cb·HCl**) 301
(*Z*)-4'-Methoxy-5-propyl-5'-((5-methyl-4-pentyl-1*H*-pyrrol-2-yl)methylene)-1*H*,5'*H*-[2,2'-bipyrrol]-1'-ium chloride (**III-1db·HCl**) 301
(*Z*)-5-Butyl-4'-methoxy-5'-((5-methyl-4-pentyl-1*H*-pyrrol-2-yl)methylene)-1*H*,5'*H*-[2,2'-bipyrrol]-1'-ium chloride (**III-1eb·HCl**) 302
(*Z*)-4'-Methoxy-5-pentyl-5'-((5-methyl-4-pentyl-1*H*-pyrrol-2-yl)methylene)-1*H*,5'*H*-[2,2'-bipyrrol]-1'-ium chloride (**III-1fb·HCl**) 302
(*Z*)-5-Hexyl-4'-methoxy-5'-((5-methyl-4-pentyl-1*H*-pyrrol-2-yl)methylene)-1*H*,5'*H*-[2,2'-bipyrrol]-1'-ium chloride (**III-1gb·HCl**) 303
(*Z*)-4'-Methoxy-5'-((5-methyl-4-propyl-1*H*-pyrrol-2-yl)methylene)-5-pentyl-1*H*,5'*H*-[2,2'-bipyrrol]-1'-ium chloride (**III-1fa·HCl**) 303
4-Methoxy-1*H*,1'*H*-[2,2'-bipyrrole]-5-carbaldehyde (**III-14a**, MBC) 304
General Procedure for the Synthesis of 5'-*n*-Alkylated MBC Derivatives **III-14b–g** 304
4-Methoxy-5'-methyl-1*H*,1'*H*-[2,2'-bipyrrole]-5-carbaldehyde (**III-14b**) 305

5'-Ethyl-4-methoxy-1*H*,1'*H*-[2,2'-bipyrrole]-5-carbaldehyde (**III-14c**) 305
4-Methoxy-5'-propyl-1*H*,1'*H*-[2,2'-bipyrrole]-5-carbaldehyde (**III-14d**) 305
5'-Butyl-4-methoxy-1*H*,1'*H*-[2,2'-bipyrrole]-5-carbaldehyde (**III-14e**) 306
4-Methoxy-5'-pentyl-1*H*,1'*H*-[2,2'-bipyrrole]-5-carbaldehyde (**III-14f**) 306
5'-Hexyl-4-methoxy-1*H*,1'*H*-[2,2'-bipyrrole]-5-carbaldehyde (**III-14g**) 306
General Procedure for the Synthesis of 3-Alkyl-2-Methyl-1*H*-Pyrroles **III-15a–c** 307
2-Methyl-3-propyl-1*H*-pyrrole (**III-15a**) 307
2-Methyl-3-pentyl-1*H*-pyrrole (**III-15b**) 307
3-Heptyl-2-methyl-1*H*-pyrrole (**III-15c**) 307
(*Z*)-*N*-[(5-Bromo-3-methoxy-2H-pyrrol-2-ylidene)methyl]-*N*-ethylethanamine (**III-75**) 308
(*Z*)-5-(5-Azidopentyl)-4'-methoxy-5'-((5-methyl-4-propyl-1*H*-pyrrol-2-yl)methylene)-1*H*,5'*H*-[2,2'-bipyrrol]-1'-ium chloride (**III-89·HCl**) 308
(*Z*)-4'-(4-Azidobutoxy)-5'-((5-methyl-4-propyl-1*H*-pyrrol-2-yl)methylene)-5-pentyl-1*H*,5'*H*-[2,2'-bipyrrol]-1'-ium chloride (**III-90·HCl**) 309
(*Z*)-5'-((4-(4-Azidobutyl)-5-methyl-1*H*-pyrrol-2-yl)methylene)-4'-methoxy-5-pentyl-1*H*,5'*H*-[2,2'-bipyrrol]-1'-ium chloride (**III-91·HCl**) 309
General Procedure for the Synthesis of (*E*/*Z*)-Oximes **III-93a–c** 310
(*E*/*Z*)-Hexan-2-one oxime (**III-93a**) 310
(*E*/*Z*)-Octan-2-one oxime (**III-93b**) 310
(*E*/*Z*)-Decan-2-one oxime (**III-93c**) 311
5-Methyl-4-propyl-1*H*-pyrrole-2-carbaldehyde (**III-94**) 311
(*Z*)-4-Methoxy-5-((5-methyl-4-propyl-1*H*-pyrrol-2-yl)methylene)-1,5-dihydro-2*H*-pyrrol-2-one (**III-95**) 312
(*Z*)-4-Methoxy-5-((5-methyl-4-propyl-2*H*-pyrrol-2-ylidene)methyl)-1*H*-pyrrol-2-yl trifluoromethanesulfonate (**III-96**) 312
2-(Pent-4-en-1-yl)-1*H*-pyrrole (**III-97**) 312
1-(1*H*-Pyrrol-2-yl)pent-4-en-1-one (**III-100**) 313
5-(1*H*-Pyrrol-2-yl)pentan-1-ol (**III-101**) 313
5-Chloro-1-(1*H*-pyrrol-2-yl)pentan-1-one (**III-103**) 314
2-(5-Chloropentyl)-1*H*-pyrrole (**III-104**) 314
(1*H*-Pyrrol-2-yl)pentan-1-one (**III-105f**) 315
2-Pentyl-1*H*-pyrrole (**III-106f**) 315
Ethyl 5-oxo-5-(1*H*-pyrrol-2-yl)pentanoate (**III-109**) 315
5-(1*H*-Pyrrol-2-yl)pentyl 4-methylbenzenesulfonate (**III-111**) 316
tert-Butyl 2-(5-(tosyloxy)pentyl)-1*H*-pyrrole-1-carboxylate (**III-112**) 316
tert-Butyl 2-(5-azidopentyl)-1*H*-pyrrole-1-carboxylate (**III-113**) 317
(5-(5-Azidopentyl)-1-(*tert*-butoxycarbonyl)-1*H*-pyrrol-2-yl)boronic acid (**III-114**) 317
3-(5-(5-Azidopentyl)-1*H*-pyrrol-2-yl)-5,5-difluoro-1-methoxy-7-methyl-8-propyl-5*H*-5λ^4,6λ^4-dipyrrolo[1,2-*c*:2',1'-*f*][1,3,2]diazaborinine (**III-125**) 318
tert-Butyl 4-hydroxy-2-oxo-2,5-dihydro-1*H*-pyrrole-1-carboxylate (**III-126**) 319
N-Boc-Glycine (**III-128**) 319
tert-Butyl 2-oxo-4-(tosyloxy)-2,5-dihydro-1*H*-pyrrole-1-carboxylate (**III-130**) 319
tert-Butyl 4-(hex-5-en-1-yloxy)-2-oxo-2,5-dihydro-1*H*-pyrrole-1-carboxylate (**III-131**) 320
4-Azidobutan-1-ol (**III-132**) 320
tert-Butyl 4-(4-azidobutoxy)-2-oxo-2,5-dihydro-1*H*-pyrrole-1-carboxylate (**III-134**) 320
4-(4-Azidobutoxy)-1,5-dihydro-2*H*-pyrrol-2-one (**III-135**) 321
(*Z*)-4-(4-Azidobutoxy)-5-((5-methyl-4-propyl-1*H*-pyrrol-2-yl)methylene)-1,5-dihydro-2*H*-pyrrol-2-one (**III-136**) 321
(*Z*)-4-(4-Azidobutoxy)-5-((5-methyl-4-propyl-2*H*-pyrrol-2-ylidene)methyl)-1*H*-pyrrol-2-yl trifluoromethanesulfonate (**III-137**) 322
1-*tert*-Butyloxycarbonyl 2-pentyl-1*H*-pyrrole (**III-139f**) 322
General Procedure for the Synthesis of Boc-Protected Pyrroles **III-139b–e** and **III-139g** 322
1-*tert*-Butyloxycarbonyl 2-methyl-1*H*-pyrrole (**III-139b**) 323
1-*tert*-Butyloxycarbonyl 2-ethyl-1*H*-pyrrole (**III-139c**) 323
1-*tert*-Butyloxycarbonyl 2-propyl-1*H*-pyrrole (**III-139d**) 324
1-*tert*-Butyloxycarbonyl 2-butyl-1*H*-pyrrole (**III-139e**) 324
1-*tert*-Butyloxycarbonyl 2-hexyl-1*H*-pyrrole (**III-139g**) 324
(1-(*tert*-Butoxycarbonyl)-5-pentyl-1*H*-pyrrol-2-yl)boronic acid (**III-140f**) 324

General Procedure for the Synthesis of Pyrrole-2-boronic Acids **III-140b–e** and **III-140g** 325
NMR data of crude boronic acids **III-140b–e** and **III-140g**: 326
(1-(*tert*-Butoxycarbonyl)-5-methyl-1*H*-pyrrol-2-yl)boronic acid (**III-140b**) 326
(1-(*tert*-Butoxycarbonyl)-5-ethyl-1*H*-pyrrol-2-yl)boronic acid (**III-140c**) 326
(1-(*tert*-Butoxycarbonyl)-5-propyl-1*H*-pyrrol-2-yl)boronic acid (**III-140d**) 326
(1-(*tert*-Butoxycarbonyl)-5-butyl-1*H*-pyrrol-2-yl)boronic acid (**III-140e**) 326
(1-(*tert*-Butoxycarbonyl)-5-hexyl-1*H*-pyrrol-2-yl)boronic acid (**III-140g**) 326
N-Methoxy-*N*-methylhex-5-enamide (**III-142**) 326
Hept-6-en-2-one (**III-143**) 327
(*E*/*Z*)-Hept-6-en-2-one oxime (**III-144**) 327
3-(But-3-en-1-yl)-2-methyl-1*H*-pyrrole (**III-145**) 328
4-(2-Methyl-1*H*-pyrrol-3-yl)butan-1-ol (**III-146**) 328
4-(2-Methyl-1*H*-pyrrol-3-yl)butan-1-ol (**III-146**) 328
Methyl 4-chloro-4-oxobutanoate (**III-148**) 329
4-Methoxy-4-oxobutanoic acid (**III-150**) 329
Ethyl 4-(4-methoxy-4-oxobutanoyl)-5-methyl-1*H*-pyrrole-2-carboxylate (**III-151**) 329
Ethyl 4-(4-hydroxybutyl)-5-methyl-1*H*-pyrrole-2-carboxylate (**III-152**) 330
3-(4-Azidobutyl)-2-methyl-1*H*-pyrrole (**III-155**) 330
4-(4-Azidobutyl)-5-methyl-1*H*-pyrrole-2-carbaldehyde (**III-156**) 331
(*Z*)-5-((4-(4-Azidobutyl)-5-methyl-1*H*-pyrrol-2-yl)methylene)-4-methoxy-1,5-dihydro-2*H*-pyrrol-2-one (**III-157**) 331
(*Z*)-5-((4-(4-Azidobutyl)-5-methyl-2*H*-pyrrol-2-ylidene)methyl)-4-methoxy-1*H*-pyrrol-2-yl trifluoromethanesulfonate (**III-158**) 332
Bifunctional Alkyne-Maleimide Linker 332
N-(2-(2,5-Dioxo-2,5-dihydro-1*H*-pyrrol-1-yl)ethyl)hex-5-ynamide (**III-159**) 332
Methyl 2,5-dioxo-2,5-dihydro-1*H*-pyrrole-1-carboxylate (**III-161**) 333
tert-Butyl (2-(2,5-dioxo-2,5-dihydro-1*H*-pyrrol-1-yl)ethyl)carbamate (**III-164**) 333
2-(2,5-Dioxo-2,5-dihydro-1*H*-pyrrol-1-yl)ethan-1-aminium 2,2,2-trifluoroacetate (**III-165**) 334
Homo-Dimeric Zinc Complexes of Prodigiosin Azides 334
Prodigiosin A-Ring Azide Zinc Complex (**III-166**) 334
Prodigiosin B-Ring Azide Zinc Complex (**III-167**) 334
Prodigiosin C-Ring Azide Zinc Complex (**III-168**) 335
(*Z*)-5-(5-(4-(4-((2-(2,5-Dioxo-2,5-dihydro-1*H*-pyrrol-1-yl)ethyl)amino)-4-oxobutyl)-1*H*-1,2,3-triazol-1-yl)pentyl)-4'-methoxy-5'-((5-methyl-4-propyl-1*H*-pyrrol-2-yl)methylene)-1*H*,5'*H*-[2,2'-bipyrrol]-1'-ium chloride (**III-169·HCl**) 336
(*Z*)-4'-(4-(4-(4-((2-(2,5-Dioxo-2,5-dihydro-1*H*-pyrrol-1-yl)ethyl)amino)-4-oxobutyl)-1*H*-1,2,3-triazol-1-yl)butoxy)-5'-((5-methyl-4-propyl-1*H*-pyrrol-2-yl)methylene)-5-pentyl-1*H*,5'*H*-[2,2'-bipyrrol]-1'-ium chloride (**III-170·HCl**) 336
(*Z*)-5'-((4-(4-(4-(4-((2-(2,5-Dioxo-2,5-dihydro-1*H*-pyrrol-1-yl)ethyl)amino)-4-oxobutyl)-1*H*-1,2,3-triazol-1-yl)butyl)-5-methyl-1*H*-pyrrol-2-yl)methylene)-4'-methoxy-5-pentyl-1*H*,5'*H*-[2,2'-bipyrrol]-1'-ium chloride (**III-171·HCl**) 337
(*Z*)-5'-((5-Methyl-4-propyl-1*H*-pyrrol-2-yl)methylene)-4'-(4-(4-(15-oxo-19-((3a*S*,4*S*,6a*R*)-2-oxohexahydro-1*H*-thieno[3,4-*d*]imidazol-4-yl)-2,5,8,11-tetraoxa-14-azanonadecyl)-1*H*-1,2,3-triazol-1-yl)butoxy)-5-pentyl-1*H*,5'*H*-[2,2'-bipyrrol]-1'-ium chloride (**III-172·HCl**) 338
tert-Butyl 5'-formyl-4'-methoxy-1*H*,1'*H*-[2,2'-bipyrrole]-1-carboxylate (**III-174**, Boc-MBC) 339

V.4 Microbiological Methods 341

V.4.1 Sterilisation 341
V.4.2 Bacterial Cultivation Media 341
V.4.3 Antibiotics and Media Supplements 341
V.4.4 Bacterial Strains 341
V.4.5 Bacterial Precultures 342
V.4.6 Preparation of Chemically Competent Cells 342
V.4.7 Heat-Shock Transformation of Chemically Competent Cells 342
V.4.8 Cryo-Preservation of Bacterial Strains 342
V.4.9 Heterologous Protein Synthesis 342
V.4.9.1 Protein Synthesis of PyoS2 Mutants and ImS2 343
V.4.9.2 Protein Synthesis of Prodiginine Ligases 343

V.4.10 Plate Killing Assay ... 343
V.4.11 Liquid Growth Inhibition Assay ... 343
V.4.12 Isolation and Identification of *P. aeruginosa* Strains from Human Patients ... 344
V.4.13 Characterisation of ESBL and Carbapenemase Genes ... 344
V.5 Molecular Biology Methods ... 346
V.5.1 DNA Oligonucleotides ... 346
V.5.2 Plasmids ... 348
V.5.3 Molecular Cloning Methods ... 349
V.5.3.1 Restriction-Ligation (RL) Cloning ... 349
V.5.3.2 Quick-Change (QC) Cloning ... 350
V.5.3.3 Round-the-Horn (RTH) Cloning ... 351
V.5.4 DNA Quantification ... 352
V.5.5 Agarose Gel Electrophoresis ... 352
V.5.6 DNA Isolation from Agarose Gels ... 353
V.5.7 Isolation of Plasmid DNA ... 353
V.5.8 Sequencing of Plasmid DNA ... 354
V.5.9 Isolation of Genomic DNA of *P. aeruginosa* ... 354
V.5.10 Whole-Genome Sequencing and Genome Assembly ... 354
V.5.10.1 Genome Mining for Serotypes, and Defects in LPS Biogenesis, Resistance Genes, and Virulence Factors ... 357
V.6 Biochemical Methods ... 359
V.6.1 Protein Purification of PyoS2 Variants and ImS2 ... 359
V.6.1.1 Cell Lysis ... 359
V.6.1.2 Immobilised Nickel Affinity Chromatography ... 359
V.6.1.3 Ion Exchange Chromatography (IEX) ... 359
V.6.1.4 Size Exclusion Chromatography (SEC) ... 360
V.6.2 Maleimide Labelling of PyoS2 Cysteine Mutants ... 360
V.6.3 Determination of Maleimide Labelling Efficiency ... 360
V.6.4 Protein Quantification ... 360
V.6.4.1 UV-Based Protein Quantification ... 360
V.6.4.2 Pierce 660 nm Protein Quantification ... 361
V.6.5 Sodium Dodecyl Sulfate Polyacrylamide Gel Electrophoresis (SDS-PAGE) ... 361
V.7 Special Methods ... 362
V.7.1 Multiplex PCR for Detection of *fpvAI–III* and *pyoS2_imS2* ... 362
V.7.2 Plasmid Nicking Assay ... 362
V.7.3 Densitometric Analysis of DNase Activity ... 363
V.7.3.1 Stretched Exponential Decay (Kohlrausch–Williams–Watts Function) ... 363
V.7.3.2 Linear Regression ... 364
V.7.3.3 Pearson Correlation Analysis ... 365
V.7.3.4 Permutation Analysis ... 365
V.7.4 Electrospray Ionisation Mass Spectrometry (ESI-MS) of Proteins ... 366
V.7.5 Analytical *In Vitro* Biocatalysis with Prodiginine Ligating Enzymes ... 366
V.7.6 Labelling and Purification of Trastuzumab-Prodigiosin ADCs ... 367
V.7.7 Cellular Binding Assays of Trastuzumab-Prodigiosin ADCs ... 367
V.7.8 Cellular Viability Assays with Trastuzumab-Prodigiosin ADCs ... 367

VI References ... 369

VII Table of Compounds ... 403

VIII Declaration of Originality ... 411

IX Supporting Information ... 413

IX.1 Identification and Prevention Strategies of Grease Contaminations 413
IX.2 Substrate Promiscuity of Prodiginine Ligase – Unprocessed Raw Data 416
IX.3 Absorption Properties of A-Ring Alkylated Prodiginines 417
IX.4 IC_{50} Values of Synthetic Prodiginines Against Urothelial Cancer Cell Lines 418
IX.5 Dose-Response Plots for Cell Viability Screening of Urothelial Carcinoma Cell Lines RT-112 and RT-112res with Prodiginine Azides III-89, III-90, III-91, and the Alkylated Derivative III-1fa 419
IX.6 Activation of PyoS2 DNase Activity in the Presence of Divalent Metal Ions 420
IX.7 Mass Spectrometry Data of Purified PyoS2 Variants and AlF-Conjugates 420
IX.8 Statistical Analysis of DNase Activity of PyoS2 and its Mutants and Conjugates 421
IX.8.1 Exponential Fitting and Half-Life Determination 421
IX.8.2 Linear Fitting and Half-Life Determination 424
IX.8.3 Permutation Analysis 426
IX.8.4 Fit Parameters 430
IX.9 *P. aeruginosa* Strain Collection 433
IX.10 FpvA Siderovars and *pyoS2* Genotypes of MDR *P. aeruginosa* Isolates 435
IX.11 Antibiotic Susceptibility of CRPsA Isolates with *fpvAI* Genotype 436
IX.12 Genetic Determinants of CRPsA Isolates with *fpvAI* Genotype 437
IX.13 Mass Spectrometry Data of PyoS2-Prodigiosin Conjugates 438
IX.14 SDS Gels of PyoS2-Prodigiosin Conjugates 439
IX.15 Absorption Spectra of Prodiginine Maleimides 439
IX.16 Extinction Coefficients of Prodigiosin Maleimides 440
IX.17 NMR Spectra 441
IX.18 LC-MS Chromatograms and Spectra – Negative Controls 556

X Acknowledgements 567

Abbreviations

A	Adenylation domain
Aβ	Amyloid β (amyloid beta)
A. baumannii	*Acinetobacter baumannii*
ACP	Acyl carrier protein
AD	Alzheimer's Disease
ADC	Antibody-Drug conjugate
ADP	Adenosine diphosphate
ADPRC	Adenosine diphosphate-ribosylcyclase
AlF	AlphaFluor
AGE	Agarose gel electrophoresis
Alox	Aluminium oxide
AMI	Amikacin
Amp	Ampicillin
α-syn	α-Synuclein
ATP	Adenosine triphosphate
ATPB	ATP-Binding domain
AZT	Aztreonam
9-BBN	9-Borabicyclo(3.3.1)nonane
BHL	*N*-Butyryl-L-homoserine lactone
Bim	Benzimidazole
Boc	*tert*-Butyloxycarbonyl
BODIPY	Boron dipyrromethene
Bp	Boiling point
BSA	Bovine serum albumin
CAM	Cerium ammonium molybdate
CAP-1	Capture molecule for amyloid precipitation
CAZ	Ceftazidime
cCAP-1	Clicked capture molecule for amyloid precipitation
CDI	*N*,*N*'-Carbonyldiimidazole
cDNA	Copy DNA
CIP	Ciprofloxacin
CoA	Coenzyme A
CP	Cytoplasm
CPA	Common polysaccharide antigen
CPM	Cefepime
CRPsA	Carbapenem-resistant *P. aeruginosa*
CSA	Chondroitin sulfate A
CSF	Cerebrospinal fluid
CuAAC	Copper-catalysed azide-alkyne cycloaddition
CV	Column volume
CWC	Chemical Weapons Convention
Da	Dalton
DABCO	1,4-Diazabicyclo[2.2.2]octane
DBU	1,8-Diazabicyclo(5.4.0)undec-7-ene
1,2-DCE	1,2-Dichloroethane
DCVC	Dry column vacuum chromatography
DEAD	Diethyl azodicarboxylate
DEF	Diethylformamide
DH	Dehydrogenase
DIBAL-H	Diisobutyl aluminium hydride
DIPEA	Diisopropylethylamine
DLB	Dementia with Lewy bodies
DMAP	4-(Dimethylamino)pyridine
DMB	3,4-Dimethoxybenzyl
DMF	Dimethylformamide
DMSO	Dimethyl sulfoxide
DNA	Deoxy ribonucleic acid
dppf	1,1'-Bis(diphenylphosphanyl)ferrocene
DPS	2,2'-Dipyridyl disulfide
DSC	Disuccinimidyl carbonate
DTEA	Tris(2-(4-(dimethylaminomethyl)-1*H*-1,2,3-triazol-1-yl)ethyl)amine
DTT	Dithiothreitol
EC	Enzyme Commission
E. coli	*Escherichia coli*
EDC	1-Ethyl-3-(3-dimethylaminopropyl)carbodiimide
EDTA	Ethylenediaminetetraacetic acid
ELISA	Enzyme-linked immunosorbent assay
Eq.	Equivalents
ER	Estrogen receptor
ESBL	Extended-spectrum β-lactamase
EtOAc	Ethyl acetate
EV	Empty vector
FAD	Flavin adenine dinucleotide
FMN	Flavin mononucleotide
FT-IR	Fourier-transform infrared spectroscopy
FRα	Folate receptor alpha
FRET	Förster resonance energy transfer
Fuc	Fucose
GalNAz	*N*-Azidoacetylgalactosamine
GC	Gas chromatography
Gdn HCl	Guanidinium hydrochloride
GDP	Guanosine diphosphate
GEN	Gentamicin
GlcNAc	*N*-Acetylglucosamine
Glyme	Dimethoxyethane
HATU	1-[Bis(dimethylamino)methylene]-1*H*-1,2,3-triazolo[4,5-*b*]pyridinium 3-oxide hexafluorophosphate
HER2	Human epidermal growth factor receptor 2
HDL	High density lipoprotein
HN3	2-Chloro-*N*,*N*-dimethylethan-1-amine
HMTETA	1,1,4,7,10,10-Hexamethyltriethylenetetramine
HRMS	High resolution mass spectrometry
HRP	Horseradish peroxidase
IC_{50}	Half-maximal inhibitory concentration
IEDDA	Inverse electron demand Diels-Alder
IM	Inner membrane
ImS2	Immunity protein S2
IPE	Immunity protein exosite
IPM	Imipenem
IPTG	Isopropyl-β-D-thiogalactopyranoside
IQS	Integrating quorum sensing signal

IUPAC	International Union of Pure and Applied Chemistry
Kan	Kanamycin
Kbp/bp	(Kilo)Basepairs
kDa/Da	(Kilo)Dalton
KDO	3-Deoxy-D-manno-octulosonic acid
K. pneumoniae	*Klebsiella pneumoniae*
KP_i	Inorganic potassium phosphate buffer
KS	Ketosynthase
LB	Lysogeny broth
LC	Liquid chromatography
LD_{50}	Half-maximal lethal dose
LDL	Low density lipoprotein
LHRH	Luteinising hormone-releasing hormone
LiTMP	Lithium 2,2,6,6-tetramethylpiperidide
LPS	Lipopolysaccharide
Man	Mannose
ManNAz	*N*-Azidoacetylmannosamine
MAP	2-Methyl-3-amylpyrrole
MBC	4-Methoxy-2,2′-bipyrrol-5-carbaldehyde
MBL	Metallo-β-lactamase
***m*DAPA**	*meso*-Diaminopimelic acid
MDR	Multidrug resistance
MEM	Meropenem
MIC	Minimal inhibitory concentration
MIDA	*N*-Methyliminodiacetic acid
MMAE	Monomethyl auristatin E
MMH	Monomethylhydrazine
Mp	Melting point
MS	Mass spectrometry
MSA	Multiple System Atrophy
MTBE	Methyl *tert*-butyl ether
MTT	3-(4,5-Dimethylthiazol-2-yl)-2,5-diphenyltetrazolium bromide
MTTPI	Methyltriphenylphosphonium iodide
MW	Microwave
MWCO	Molecular weight cut-off
NAD	Nicotinamide adenine dinucleotide
NAG	*N*-Acetylglucosamine
NAM	*N*-Acetylmuramic acid
Neu5Ac2en	*N*-Acetyl-2,3-dehydro-2-deoxyneuraminic acid
NGS	Next-generation sequencing
NHC	*N*-Heterocyclic carbene
NHS	*N*-Hydroxy succinimide
NMM	*N*-Methyl morpholine
NMR	Nuclear magnetic resonance
NRPS	Non-ribosomal peptide synthetase
NTA	Nitrilotriacetic acid
NTD	N-Terminal domain
OAS	α-Oxamine synthase
OD	Optical density
OdDHL	*N*-(3-Oxododecanoyl)-L-homoserine lactone
OM	Outer membrane
OMP	Outer membrane protein
OMT	*O*-Methyl transferase
o/n	Overnight
OPCW	Organization for the Prohibition of Chemical Weapons
OSA	O-Specific antigen
P. aeruginosa	*Pseudomonas aeruginosa*
PAGE	Polyacrylamide gel electrophoresis
PCB	Propylene cross-bridged
PCP	Peptidyl carrier protein
PCR	Polymerase chain reaction
PD	Parkinson's Disease
PDB	Protein database
PE	Petroleum ether
PEG	Polyethylene glycol
PET	Positron emission tomography
PG	Peptidoglycan
PGT	Peptidoglycan glycosyltransferase
PiB	Pittsburgh Compound B
PIP	Piperacillin
PKS	Polyketide synthase
PLP	Pyridoxal phosphate
PMDETA	*N*,*N*′,*N*′,*N*″,*N*′′-Pentamethyldiethylenetriamine
PMSF	Phenylmethanesulfonyl fluoride
ppm	Parts per million
PPT	Piperacillin/Tazobactam
PPTase	Phosphopantetheinyl transferase
P. putida	*Pseudomonas putida*
PQS	*Pseudomonas* quinolone signal
PR	Progesterone receptor
P. rubra	*Pseudoalteromonas rubra*
Py	Pyridine
PyBOP	Benzotriazol-1-yloxytripyrrolidinophosphonium hexafluorophosphate
PyoS2	Pyocin S2
QC	Quick-Change
QS	Quorum sensing
R_f	Retention factor
RL	Restriction-Ligation
RNA	Ribonucleic acid
ROS	Reactive oxygen species
RPM	Revolutions per minute
RT	Room temperature
RTH	Round-the-Horn
RuPhos	2-Dicyclohexylphosphino-2′,6′-diisopropoxybiphenyl
S. aureus	*Staphylococcus aureus*
SAM	*S*-Adenosyl methionine
SAR	Structure-activity relationship
SDS	Sodium dodecyl sulfate
SEC	Size exclusion chromatography
SiaNAz	*N*-Azidoacetylsialic acid
S. marcescens	*Serratia marcescens*
SNP	Single nucleotide polymorphism
SPAAC	Strain-promoted azide-alkyne cycloaddition
SPhos	Dicyclohexyl(2′,6′-dimethoxy[1,1′-biphenyl]-2-yl)phosphane

ssDNA	Single-stranded DNA
TAE	Tris-acetate-EDTA
TB	Terrific broth
TBDT	TonB-dependent transporter
TBTA	Tris(benzyltriazolylmethyl)amine
TDETA	Tris dimethylethyl triazolyl amine
TDP	Thiamine diphosphate
TdT	Terminal deoxynucleotidyl transferase
TEA	Triethylamine
TFA	Trifluoroacetic acid
TFE	2,2,2-Trifluoroethanol
THF	Tetrahydrofuran
THPTA	Tris(3-hydroxypropyltriazolylmethyl)amine
TLC	Thin-layer chromatography
TMB	3,3',5,5'-Tetramethylbenzidine
TMP	2,2,6,6-Tetramethylpiperidine
TOB	Tobramycin
TPMA	Tris(2-pyridylmethyl)amine
TPY	Terpyridine
t_R	Retention time
Tris	Tris(hydroxymethyl)aminomethane
Trz	Triazole
Ts	Tosyl
UDP	Uridine diphosphate
WGS	Whole-Genome Sequencing
WHO	World Health Organization
WW	World War

Abstract

The last century has brought immense scientific and technological progress, providing solutions for many major health challenges. Nonetheless, as some diseases have been eradicated or brought under control, new and complex problems have emerged, requiring immediate attention and action. The increasing age of the global population, combined with the rise of chronic diseases, cancer, and multidrug-resistant infections, presents mounting challenges for modern medicine. These trends place unprecedented pressure on healthcare systems and highlight the limitations of existing therapeutic strategies, which often suffer from poor selectivity, insufficient cellular delivery, and incompatibility with complex biological environments. Addressing these issues requires new approaches that enable precise diagnostics, molecular targeting, robust delivery mechanisms, and biocompatible chemical tools.

In response to these challenges, this thesis explores three complementary areas at the interface of chemistry and biology: bioorthogonal chemistry, functionalisation of natural products through chemical synthesis, and protein engineering. The research presented in this work encompasses the development of a safe and efficient copper ligand for click chemistry, the structural modification and conjugation of natural products for targeted therapeutic applications, and the engineering of antibacterial proteins as vehicles to target multidrug-resistant strains of the opportunistic human pathogen *Pseudomonas aeruginosa*. Collectively, the studies comprised in this PhD thesis illustrate how fundamental advances in chemical biology can be translated into strategic innovations in drug conjugation and targeted delivery, paving the way for more precise, efficient, and adaptable treatment options where conventional therapies have reached their limits.

Chapter II: A Regulatory-Safe and High-Performance CuAAC Ligand for Bioorthogonal Chemistry

Click chemistry, particularly the copper-catalysed azide-alkyne cycloaddition (CuAAC), has revolutionised bioconjugation strategies. Since catalytic copper-species, showing high sensitivity to oxidation and aggregation, are essentially involved in the cycloaddition reaction, stabilising ligands are used to accelerate the reaction rate and improve the oxidative stability of copper. However, the most widely used Cu(I) ligands – **t**ris((1-**b**enzyl-4-**t**riazolyl)methyl)**a**mine (TBTA) and **t**ris(3-**h**ydroxy**p**ropyl**t**riazolylmethyl)**a**mine (THPTA) – are limited by weak metal binding, solvent sensitivity, and varying catalytic performance with aliphatic and aromatic alkynes and azides. Additionally, the powerful ligand tris(2-(4-(**d**imethylaminomethyl)-1-**t**riazolyl)**e**thyl)**a**mine) (DTEA), while more effective, suffers from regulatory restrictions due to its synthesis involving the chemical weapon precursor HN3, whose usage is regulated by the Chemical Weapons Convention (CWC). The general problem addressed in this work is the need for a high-performing, non-restricted CuAAC ligand suitable for biological and synthetic applications.

Here, the synthesis and characterisation of a novel tripodal copper-ligand, **t**ris **d**imethyl**e**thyl **t**riazolyl **a**mine (TDETA), is reported. TDETA retains the favourable catalytic and solubility profile of DTEA but is synthesised via a legally permissible route, avoiding the use of highly toxic and legally restricted HN3. TDETA is prepared in 91% overall yield over three steps, exhibits excellent aqueous and organic solubility, and outperforms commercial ligands in CuAAC efficiency under diverse reaction conditions. TDETA's utility is further demonstrated through its successful application in CuAAC-catalysed bioconjugations of cholesterol and benzothiazole derivatives to biotin. The thereby generated conjugates are affinity probes for the enrichment of bioactive peptides interacting with arteriosclerotic cholesterol plaques, as well as structure-specific pull-down of amyloidogenic proteins such as α-synuclein – tools intended to support the discovery of diagnostic markers and therapeutic targets in cardiovascular and neurodegenerative diseases.

Altogether, the introduced copper-ligand TDETA is, unlike commercially available ligands intended for the acceleration of CuAAC reactions, a “one fits all” solution without preferences for certain compound classes. It offers not only regulatory safety but also superior solvent compatibility and catalytic properties. These advantages mark a significant advancement in the toolkit for modular bioorthogonal synthesis, supporting broader use of CuAAC in drug discovery and chemical biology in both academic and industrial settings.

Chapter III: Functionalisation of Prodiginines for Bioorthogonal Conjugation and Targeted Cancer Therapy

Prodiginines are a versatile family of tripyrrole alkaloids known for their potent bioactivity across antimicrobial and antitumoral domains. Decades of research on prodiginines have already provided valuable insights on how chemical functionalisation modulates the physicochemical characteristics and drug properties of these cytotoxic compounds. Nonetheless, the translation of prodiginines to therapeutics is still a challenge due to poor target specificity. The challenge addressed in this chapter is to create modular prodiginine derivatives suitable for targeted delivery to cells of interest via bioorthogonal conjugation.

In order to address the inherent lack of target specificity in prodiginines, their coupling to target-specific drug vehicles or vectors is a promising strategy. Therefore, one part of this thesis was the development of organic total syntheses, enabling the installation of azide functionalities at prodigiosin’s A-, B-, and C-ring positions, and the subsequent bioconjugation of these prodiginines to small-molecule or protein carriers via bioorthogonal CuAAC or strain-promoted azide-alkyne cycloaddition (SPAAC) click chemistry. While previous studies had reported on C-ring azidation, this work first introduces access to the more synthetically challenging A- and B-ring azides, thereby significantly expanding the chemical space of prodiginine derivatisation for streamlined applications. Building on scalable multigram intermediates, novel routes to azide-substituted pyrrole precursors were devised in this work, achieving complex functionalised natural product derivatives. Maleimide-alkyne conjugation allowed for the generation of prodiginine-biomolecule conjugates, including the first antibody-drug conjugates (ADCs) of this compound class with the therapeutic monoclonal antibody trastuzumab.

To complement synthetic strategies, the substrate promiscuity of prodiginine biosynthetic enzymes was also investigated to enable chemoenzymatic access to structurally modified derivatives. While the ability of prodiginine ligases, which catalyse the final condensation reaction in prodigiosin biosynthesis, to accept diverse monopyrrole precursors (C-ring analogues) is well documented, their tolerance for A-ring modified bipyrrole (MBC) substrates has not been systematically explored.
Here, a series of 5’-alkylated MBC derivatives was synthesised to probe the enzymatic acceptance of A-ring-substituted bipyrroles. All tested prodiginine ligases exhibited previously unreported tolerance for these modified substrates, expanding the enzymatically synthesised spectrum of derivatives for this compound class. To further correlate A-ring alkylation with cytotoxicity of the prodiginine scaffold, a systematic evaluation of cytotoxicity in cisplatin-sensitive and -resistant urothelial bladder cancer cell lines was conducted. Notably, the generated derivatives with methyl substitution at the A-ring exhibited drastically enhanced cytotoxicity, not only compared to the parent compound prodigiosin, but also outperforming obatoclax mesylate – a former Phase II clinical candidate that shows strong autophagy modulation.

These findings provide the first comprehensive structure-activity relationship study for A-ring substitution in prodiginines and identify a chemically accessible site for targeted optimisation, supporting the design of more effective prodiginine-based therapeutics. Combined with the synthetic functionalisation of prodigiosin with reactive azides, this work redefines prodiginines as tunable pharmacophores and establishes modular strategies for

conjugation and delivery to potential target sites. Clarifying the structural determinants of activity and enabling protein-conjugation opens new avenues for prodiginine-based therapeutics.

Chapter IV: Pyocin S2 as a Trojan Horse for Targeted Delivery of Small-Molecule Cargo into Multidrug-Resistant *Pseudomonas aeruginosa*

Antimicrobial resistance (AMR) is a rapidly escalating global threat, with the World Health Organization (WHO) projecting up to 10 million AMR-related deaths annually by 2050. Among the most concerning contributors to this crisis is the Gram-negative bacterium *Pseudomonas aeruginosa*, an opportunistic human pathogen classified by the WHO as a critical priority organism. Infections with *P. aeruginosa* strains that are resistant to antibiotics of last-resort (e.g. carbapenems) present a major challenge for therapeutic intervention due to the bacterium's impermeable outer membrane and extensive mechanisms of drug resistance and immune evasion. Natural narrow-spectrum antimicrobial peptides and proteins called bacteriocins offer an intriguing yet underexploited solution for this problem of limited bacterial susceptibility to antibiotic treatment. One challenge for bacteriocin treatment is the widespread expression of cognate immunity proteins, conferring innate resistance to the pyocin-producing strains via the formation of ultra-high-affinity complexes between toxin and immunity protein. The challenge addressed in this chapter is to explore the application potential of bacteriocins from Gram-negative bacteria for the targeted treatment of bacterial pathogens. With a specific focus on the S-type pyocin S2 (PyoS2), a DNase-type pyocin produced by *P. aeruginosa* PAO1 and hijacking the conserved TonB machinery for cellular uptake via the FpvAI ferripyoverdine siderophore transporter, this work aims to advance our current knowledge on bacteriocin immunity and its implications for the development of bacteriocin therapeutics as future antimicrobials in the antimicrobial crisis.

In this work, it was shown for the first time that the ultra-high-affinity binding between PyoS2 and its cognate immunity protein ImS2 can be disrupted through a single-point mutation (Y640C) at the PyoS2/ImS2 interface of PyoS2's DNase domain (immunity protein exosite). The uncovered effect was further drastically enhanced by introducing bulky fluorophores at the interface, increasing the structural mismatch between the exosite of PyoS2 and the immunity protein. This modification overcomes natural immunity protein-mediated resistance to wild-type PyoS2 in *P. aeruginosa* strains and enhances the therapeutic applicability of PyoS2, positioning it as a promising alternative to conventional antibiotics. Furthermore, by leveraging its specific TonB-dependent uptake mechanism, PyoS2 was repurposed as a narrow-spectrum delivery vector for intracellular transport of fluorophores, enabling the targeted translocation of additional effector molecules into *P. aeruginosa* cells.
The efficiency and therapeutic relevance of overcoming immunity-dependent resistance to PyoS2 through engineering of PyoS2's immunity protein exosite (IPE) were further assessed by studying a collection of multidrug-resistant clinical isolates of *P. aeruginosa*, isolated at the University Hospital in Düsseldorf. Fluorophore-labelled pyocins demonstrated effective intracellular delivery and retained antimicrobial activity exerted by DNA degradation in a panel of 15 highly virulent isolates expressing the FpvAI transporter, the primary receptor exploited by PyoS2 for cellular binding and membrane translocation. Among these, eight strains expressed the immunity protein ImS2 and showed ImS2-dependent resistance to wild-type PyoS2. Strikingly, all eight ImS2-positive strains became susceptible to killing upon treatment with the engineered extended-spectrum PyoS2 Y640C-fluorophore conjugates, demonstrating that resistance mediated by cognate immunity proteins can be fully abolished through rational engineering of the PyoS2/ImS2 interface. Of the remaining seven ImS2-negative strains, four exhibited persistent resistance to both wild-type and all engineered PyoS2 variants. Whole-Genome Sequencing revealed that the resistance in these strains was attributed to nonsense and frame-shift mutations in the *wzt*, *gmd*, *wbpZ*, and *wbpL* loci, causing defects in the biosynthesis of the common polysaccharide antigen

(CPA), the secondary receptor essential for effective pyocin translocation. Notably, this study also provides the first evidence that S-type pyocin susceptibility is serotype-dependent. Here, the extent of bacterial killing, as reflected by minimal inhibitory concentrations, clustered according to O-serotype, suggesting that outer membrane architecture critically influences pyocin activity.
Lastly, conjugation of maleimide-functionalised prodiginines (from Chapter III) to PyoS2 cysteine mutants enabled the successful transport of small-molecule drug conjugates into the cytoplasm of *P. aeruginosa*. This establishes PyoS2 as a viable Trojan Horse vector for intracellular delivery of small-molecule drugs across the otherwise impermeable bacterial envelope – a critical step forward for future therapeutic strategies aimed at overcoming the formidable membrane barrier that limits the efficacy of many conventional antibiotics.

The innovative approach of interface engineering presented in this thesis, aiming to eliminate immunity protein-mediated resistance to DNase pyocins, holds great potential for combating infections caused by Gram-negative pathogens, such as the difficult-to-treat pathogen *P. aeruginosa*. Moreover, the conserved topology of the toxin/antitoxin binding interface suggests that the uncovered mechanism of corrupted immunity protein binding can be applied to a vast number of other bacteriocins from the HNH DNase family. Additionally, this work establishes PyoS2 as a modular transporter for target-selective Trojan Horse strategies via the conserved TonB-dependent uptake mechanism, demonstrating how engineered bacteriocins from Gram-negative bacteria can be repurposed as delivery platforms, especially against WHO-prioritised MDR pathogens. Collectively, this work launches advanced strategies that might challenge the general concept of innate bacterial immunity to bacteriocins through the expression of cognate immunity proteins, thereby providing highly selective antimicrobial agents with extended spectrum as novel therapeutic solutions against Gram-negative pathogens amidst the global antimicrobial resistance crisis.

Conclusion

Together, the presented studies define an integrated framework for advancing chemical and biological tools towards therapeutic relevance. From the design of a regulatory-safe CuAAC ligand to the modular derivatisation of prodiginines and the engineering of bacteriocin-based delivery vectors, this thesis provides novel strategies to overcome limitations in synthesis, selectivity, and cellular uptake of potential drugs into pathogenic bacteria. The findings have broad implications across drug development, antimicrobial resistance, and synthetic biology. Most notably, they suggest that next-generation chemotherapeutic approaches may not arise solely from new targets or scaffolds, but from better control over the vectors, conjugates, and transport systems that deliver them.

I Introduction

Since time immemorial, humanity has strived for technological progress, driven by the continuous improvement of established processes or the discovery of novel materials and substances. In this pursuit, nature serves a vital role as a source of innovation in engineering and chemistry, offering inspiration for design, functional principles and mechanisms, as well as for the development of modern drugs. The inspiration for these drugs is often found in an astonishingly vast array of biological molecules that emerged from millions of years of evolution and natural selection. The study of these molecules has already significantly advanced technological and medical progress over the past century. While these contributions often go unnoticed in daily life, they have a profound impact on our lives and the prosperity of both industrialised and emerging economies. Everyday examples of nature-inspired products include enzymes as biocatalysts in detergents, antibiotics for treating bacterial infections, and the production of human insulin using microorganisms for diabetes management. These examples highlight only a fraction of how insights drawn from nature have led to transformative applications with profound societal and scientific impact.

Despite an unimaginable abundance of structurally unique biomolecules in nature, their isolation from natural sources often yields only limited quantities of these molecules. However, unconfined availability and low costs are usually required for a broader application of these molecules in biotechnology or as therapeutics. Moreover, the unique biomolecular structures are typically optimised for specific cellular functions under defined natural conditions, which rarely align with the requirements for technological or medical applications. Consequently, there is significant interest in developing efficient and resource-friendly chemical and biotechnological synthesis methods to make these fractionally low-abundant biomolecules available in large quantities. By providing sufficient quantities of these compounds, these synthetic approaches also allow an in-depth characterisation of the target molecules and their structural optimisation through functionalisation. The latter process is a cornerstone of industrial and academic drug development, as extensive structure-activity relationship studies are essential to explore the mechanisms of new drug candidates, improve their targeting, and fully realise their therapeutic potential.

Numerous examples of engineered biomolecules provide excellent illustrations of the importance of structural optimisation for the purpose of application, but enzymes as biocatalysts and antibiotics as antimicrobial agents are probably familiar to almost everyone. Although Alexander Fleming discovered β-lactam antibiotics in 1928 with penicillin (**I-1**, benzyl penicillin, penicillin G),[1] it quickly became evident that it was effective only against Gram-positive infections (e.g. Streptococci or Pneumococci) and had little effect on Gram-negative bacteria.[2] Through semi-synthetic modification of the β-lactam core structure, the spectrum of antimicrobial activity was significantly broadened, enabling novel penicillin derivatives [e.g. amoxicillin (**I-2**)] to target Gram-negative bacteria as well (Figure I.1A).[3] Besides its limited antimicrobial spectrum, penicillin G (**I-1**) is acid-labile and poorly soluble in water. Hence, it had to be administered by intravenous or intramuscular injection to avoid disintegration in the acidic human stomach during oral administration. The improved β-lactam antibiotic amoxicillin (**I-2**) is an acid-stable derivative with better solubility in water, allowing for convenient oral uptake of the drug. Another example of structural optimisation outlines hydrolytically active enzymes, such as lipases and proteases. These industrially important enzymes are added to detergents to degrade fat and protein residues on clothing. Through laboratory-directed evolutionary processes, naturally occurring hydrolases, such as the bacterial protease subtilisin E (Figure I.1B), have been optimised to remain effective at harsh conditions needed for laundry washing. Hence, these enzymes were improved to withstand high washing temperatures, basic pH, and surfactants. To date, approximately 50% of the amino acids of subtilisin E have been substituted via protein engineering to enhance its performance in detergents.[4]

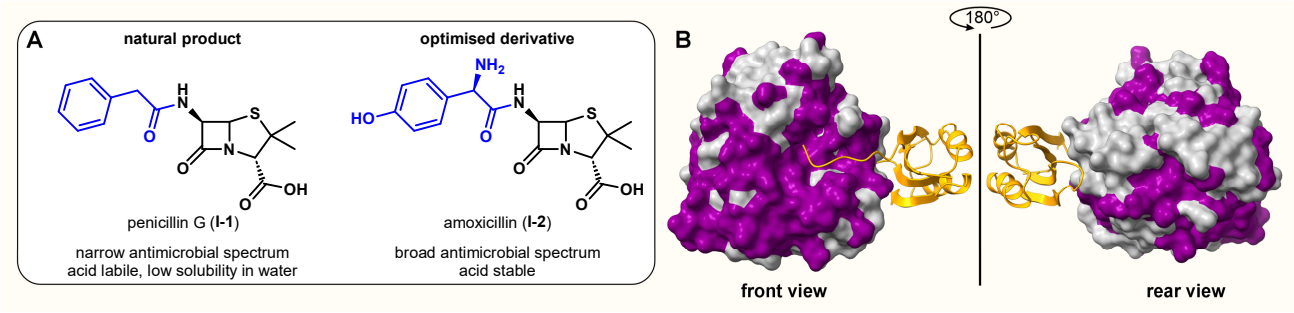


Figure I.1. A. Chemical structure of the natural antibiotic penicillin G (**I-1**) and the improved β-lactam derivative amoxicillin (**I-2**). **B**. Crystal structure of the industrially important bacterial protease subtilisin E (PDB 1SCJ, grey) in complex with the subtilisin propeptide (orange). The residues engineered to improve subtilisin stability against temperature, pH, and surfactants are highlighted in purple.

These selected examples underscore the transformative potential of biomolecules when optimised for specific applications. However, the challenges of the 21st century demand not only the optimisation of existing molecules but also the discovery of novel bioactive (lead) compounds and enzymes capable of addressing urgent global issues. The World Health Organization (WHO), as a representative of global health policy, identifies the most pressing issues for humanity in the coming decades as '*climate change and air pollution*', '*prevention of non-communicable diseases*' (e.g. diabetes, cancer, Alzheimer's disease), '*combating drug resistance*', and '*prevention of global pandemics*'.[5, 6] These challenges pose significant threats to global prosperity, and neglecting them could result in immense healthcare costs and millions of deaths. Thus, the objectives are clear: amidst a global demographic shift towards ageing populations and the associated rise in age-related diseases, there is an urgent need for novel therapies, selective drug targeting mechanisms, and diagnostic tools for early detection of these diseases. Simultaneously, established therapies must be re-evaluated, and alternative active substances sought, as the increasing prevalence of resistance (e.g. antimicrobial resistance or resistance to chemotherapeutics) could lead to a resurgence of infections and diseases previously considered manageable. The wealth of natural diversity continues to inspire innovative solutions for these urgent problems, whether for combating antimicrobial resistance, developing sustainable industrial processes, or advancing medical therapies. Harnessing this potential requires an interdisciplinary approach that combines insights from chemistry, biology, biotechnology, and medicine to identify promising lead compounds and optimise them for maximum impact.

The challenges formulated by the WHO for the coming decades form both the foundation and the framework of this work. It aims to harness nature's resources to generate novel bioactive agents that exhibit anticancer and antimicrobial activities, or are known to specifically interact with pathological markers of neurodegenerative diseases. While simultaneously advancing methods to enable the efficient synthesis, structural optimisation, and application of these compounds, this work will operate at the interface between organic chemistry, biochemistry, and microbiology.

Chapter II

The Novel Cu(I)/Cu(II) Ligand TDETA
–
A Precious Accelerator of CuAAC Reactions in the Preparation of Biologically Relevant Conjugates

Parts of this chapter were published in the following peer-reviewed articles:

Synthesis of a Water-Soluble Tridentate (Dimethylamino)ethyl Cu(I)/Cu(II)-Ligand

Authors:
T. M. Weber & J. Pietruszka.

Journal:
Synthesis **2023**, 55(*14*), 2128–2133.

Own Contributions:
Project idea and conceptualisation; Experimental work and data evaluation; Writing and editing of the manuscript; Revision.

Utilization of a Branched Late-Stage Clickable Biotinylated Chassis on the Example of a Pittsburgh B Analog

Authors:
T.M. Weber, P. Özdüzenciler, G. Tamgüney & J. Pietruszka.

Journal:
Org. Lett. **2024**, 26(*31*), 6771–6775.

Own Contributions:
Project idea and conceptualisation; Experimental work; Writing and editing of the manuscript; Revision.

Contributions of Others:
Testing of α-syn binding (*Pelin Özdüzenciler*, *Gültekin Tamgüney*, IBI-7, FZ Jülich); Synthesis of **II-74**, **II-92**, and scale-up of **II-63** (*Alexandra Leyens*, IBOC, FZ Jülich).

II The Novel Cu(I)/Cu(II) Ligand TDETA – A Precious Accelerator of CuAAC Reactions in the Preparation of Biologically Relevant Conjugates

II.1 State of the Knowledge

Drug development is an essential branch of modern medicinal research, driving significant advancements in life expectancy around the globe in the last century.[7] While nature plays a vital role in finding novel structural motifs and bioactive scaffolds,[8] rational drug development from lead structures has evolved into a multidisciplinary research field committed to improving the drug properties of pharmacophores.[9] In the initial drug discovery process, namely the identification of bioactive lead structures, rapid structural diversification and simple readout of association and dissociation kinetics between potential targets and the molecular probe or drug are key objectives. Especially in the context of large compound libraries requiring screening of thousands of molecules, these criteria significantly impact the time consumption and the cost of these studies. Emphasising that the expenses in drug development from scratch to market can lie in the billion-dollar range for a single drug, cost minimisation is an essential objective in process development and streamlining.[10] While several factors may be considered for cost and risk minimisation, such as waste reduction, rationalising the synthetic route by using cheaper or safer precursors and reagents and reducing the total reaction steps, time is yet a substantial obstacle.[11] Although shortening the time scale of drug and process development may reduce the cost of the overall development and manufacturing process, the SARS-CoV-2 (COVID) pandemic from 2020–2023 and the rapid development of RNA-based vaccines illustrated the need for quick adjustments to unforeseen circumstances from another perspective and highlight the advantages of rapid structural diversification. Among all known synthetic transformations, only a handful of reactions meet the three key requirements of bioorthogonality, which are needed in this regard and are defined as prerequisites for expanding these reactions to living systems. Firstly, reactions must be highly reliable, providing excellent yields under mild conditions and ensuring high regio- and stereoselectivity. Generally, broad solvent compatibility, a wide pH range, fast kinetics at room temperature, and robustness in the presence of other (macro)molecules are essential cornerstones of bioorthogonal reactions.[12, 13] Secondly, the reactive species should not interfere with natural metabolites and their functional groups at the cellular site of action, which is why biologically uncommon reactive motifs are needed to prevent undesired side reactions and enable fully bioorthogonal chemistry.[14] And lastly, rapid diversification of probes and carrier molecules requires interchangeable, modular building blocks that can be easily substituted in a single reaction (Figure II.1).[15] The chemistry meeting all these requirements is gathered under the term “click chemistry”.

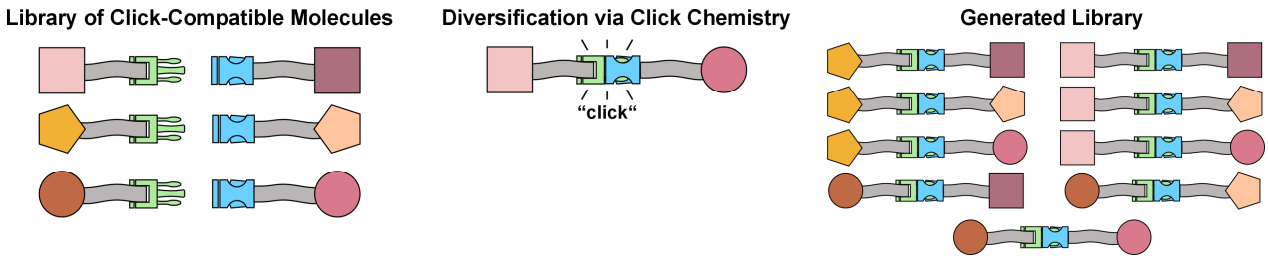
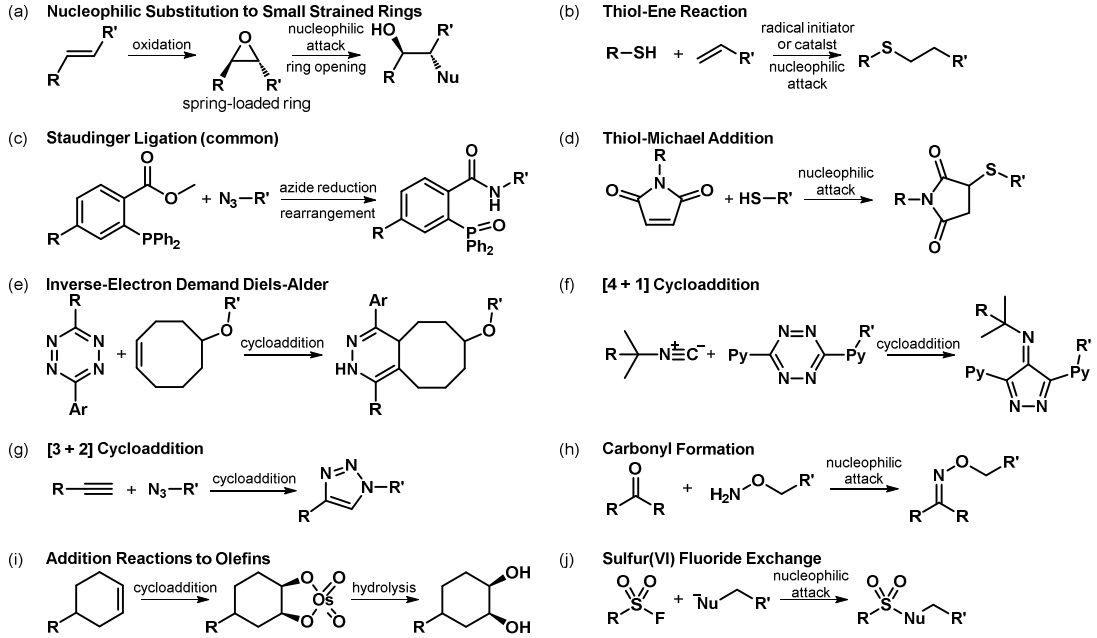


Figure II.1. Schematic illustration of joining molecules or building blocks via “click chemistry”. Coloured squares, circles, and pentagons represent arbitrary molecules, functionalised with reactive groups (represented by the two sides of the plug buckle). Appropriate reaction conditions enable the covalent reaction between the interchangeable molecules and allow the generation of large libraries from a small set of reactive molecules according to a modular principle. A library of 10 x 10 reactive molecules can generate a library of up to 100 compounds by just one reaction type.

II.1.1 Click Chemistry

The term click chemistry was first introduced in 2001 by Barry Sharpless, Hartmut Kolb, and M. G. Finn and describes the fast and modular approach to discover new molecules (cf. Figure II.1).[12, 13] Although the selection of suitable reactions following the definition of click chemistry is rather sparse, they provide a huge potential in chemical, biological, and medical contexts. Within the past 23 years, the following reactions were defined as click reactions (Scheme II.1):[16]

(a) nucleophilic substitution to small strained rings (e.g. epoxides, aziridines, and cyclic sulfates),
(b) thiol-ene reaction,
(c) Staudinger ligation (common or traceless variant),
(d) thiol-Michael addition,
(e) Diels-Alder (DA) reactions and inverse electron demand Diels-Alder (IEDDA) reactions,
(f) [4 + 1] cycloadditions between isonitriles and tetrazines,
(g) [3 + 2] cycloadditions (CuAAC, SPAAC),
(h) carbonyl-chemistry-like formation of ureas,
(i) addition reactions to carbon-carbon double bonds (e.g. dihydroxylation) or alkynes (e.g. thiol-yne),
(j) sulfur(VI) fluoride exchange (SuFEx).

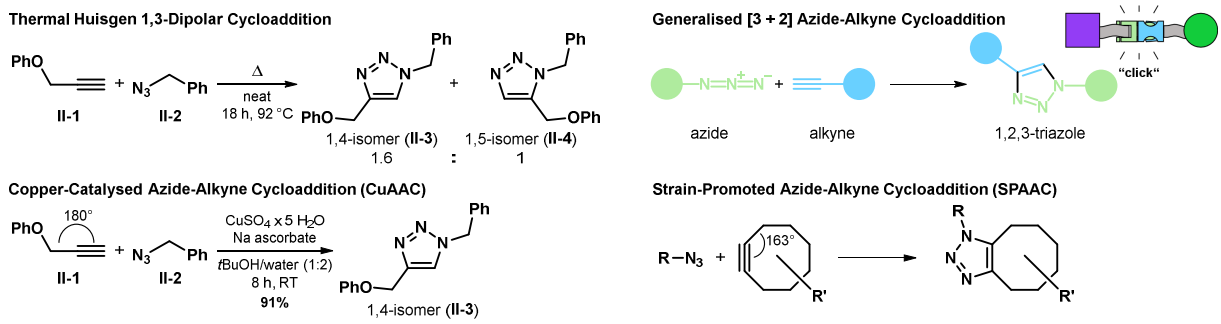


Scheme II.1. Generalised overview of reactions classified as “click reactions” with generalised examples.[16]

II.1.1.1 Azide-Alkyne Cycloadditions

Cycloadditions are fundamental to click chemistry, with the [3 + 2] cycloaddition between azides and alkynes being particularly significant. In 1961, Rolf Huisgen reported on the formation of substituted 4,5-dihydro-1,2,3-triazoles, promoted by the thermal induction of a 1,3-dipolar cycloaddition between organic azides and alkenes.[17, 18] Even if the applied reaction conditions of the original thermal cycloaddition are incompatible with delicate cellular metabolites, the newly discovered reaction type should have a tremendous impact on synthetic biology and biological chemistry 40 years later. While the impact of Huisgen’s finding on later generations of scientists was not foreseeable at that time, the Huisgen [3 + 2] cycloaddition between azides and olefins or alkynes was

later defined as the mother of all click reactions and was used to develop broadly applied reaction types and tools (*vide infra*).[15] The thermal Huisgen cycloaddition proceeds at elevated temperatures and gives rise to two reaction products: a 1,4-adduct and a 1,5-adduct.[19, 20] In the light of bioorthogonal chemistry, harsh reaction conditions (e.g. high temperatures) and the formation of two regioisomers are undesirable, rendering them incompatible with applications in living systems and limiting their utility for functionalising heat-sensitive cellular components like proteins and RNA.[21] In 2002, Rostovtsev *et al*. and Tornøe *et al*. from the groups of Sharpless and Meldal, respectively, independently discovered a copper-catalysed Huisgen reaction, selectively forming a single isomer at room temperature.[22-24] This finding cleared the bioincompatible obstacles of the thermal Huisgen reaction. A direct comparison between the thermal and the Cu-catalysed cycloaddition between phenyl propargyl ether (**II-1**) and benzyl azide (**II-2**) selectively provided the 1,4-isomer in a yield of 91% in the Cu-catalysed azide-alkyne cycloaddition (CuAAC) using 1 mol% of a copper(II) source and 5 mol% sodium ascorbate as reducing agent (Scheme II.2). In contrast, the thermal reaction at 92 °C resulted in a 1.6:1 ratio between both regioisomers, **II-3** and **II-4**, favouring the sterically less hindered 1,4-isomer.[23, 24] Although the fastest reaction kinetics in CuAAC are observable with Cu(I) salts, the reaction can be conducted with Cu(II) salts or copper turnings as well.[23-25] And yet, the heavy metal copper is cytotoxic to both bacterial and mammalian cells, limiting the use of CuAAC primarily to cell surface chemistry or scenarios where cell viability is not critical for the intended analysis.



Scheme II.2. Triazoles as versatile products in click chemistry. Substituted 1,2,3-triazoles can be generated via thermal Huisgen 1,3-dipolar cycloaddition, copper-catalysed azide-alkyne cycloaddition (CuAAC) or strain-promoted azide-alkyne cycloaddition (SPAAC).

The copper-induced cytotoxicity to sensitive biological materials motivated biological chemists to strive for a catalyst-free and fully biocompatible variation of the [3 + 2] azide-alkyne cycloaddition. This need was finally fulfilled by the discovery of strain-promoted azide-alkyne cycloadditions (SPAAC) between arbitrary azides and cyclooctynes (Scheme II.2).[21] While the exploration of the vastly exothermic reaction between phenyl azides and the strained cyclic alkyne by Wittig and Krebs dates back to 1961,[26] it took a further 43 years to translate this observation into practically and biologically expedient application. Cyclooctyne, the smallest possible cyclic alkyne, exhibits strong bond deformation of 163° compared to a bond angle of 180° in aliphatic alkynes.[27] This ring tension bears 18 kcal/mol of energy,[28] which is abruptly released upon reaction between the strained alkyne and the azide. In 2004, Bertozzi and co-workers adopted this knowledge and developed a biocompatible click reaction, based on this relaxation of the strained cyclooctyne ring.[21] Their proof-of-principle study used the cellular uptake of azide-labelled and peracetylated *N*-azidoacetylmannosamine (ManNAz) by Jurkat cells.[29] Intracellular conversion of ManNAz to *N*-azidoacetylsialic acid (SiaNAz) and the incorporation within the cell's surface-displayed glycoproteins was further used to conjugate the azide-modified glycoproteins to biotinylated cyclooctyne via SPAAC. Lastly, the high-affinity binding of the biotin moiety to a fluorescent conjugate of avidin-

fluorescein (avidin-FITC) was employed to quantify the SPAAC labelling efficiency in flow cytometry experiments.[21, 30]

Even though both reactions, CuAAC and SPAAC, utilise the same kind of [3 + 2] azide-alkyne cycloaddition, a contrasting juxtaposition reveals prevalent and elementary differences, shaping and defining their preferred application area. Particularly, CuAAC reactions are known for their high efficiency and rapid reaction rates (10–100 M^{-1} s^{-1}).[16] The copper catalyst significantly accelerates the cycloaddition, allowing the reaction to proceed quickly at room temperature or even lower temperatures, especially in the presence of Cu-stabilising and rate-accelerating ligands.[31-36] Click products obtained from the copper-catalysed process are generally recovered in high yields and with high regioselectivity, since only the 1,4-isomer of the triazole product is exclusively formed.[16, 37] The CuAAC reaction can be performed in a variety of solvents, including water, which is advantageous for biological applications. Nonetheless, complications may occur in strong donor solvents capable of interacting with copper salts, as this copper binding reduces the available catalyst for the CuAAC reaction between alkyne and azide.[16, 34] The broad solvent tolerance of CuAAC is accompanied by a high tolerance towards a wide range of functional groups, making it a versatile approach for the conjugation of different substrates and complex molecules.[37] However, as copper is essential for the reaction, copper-complexing (bio)molecules, such as siderophores or Cu-binding proteins, can inhibit the reaction.[38] The primary drawback of CuAAC is the use of copper, which is cytotoxic to living organisms and can harm sensitive biological systems through oxidative damage to proteins and other biomolecules.[16, 38, 39] This limits its application in live-cell labelling and *in vivo* studies. Furthermore, excess copper and reducing agent must be removed from the final product, which can be challenging and time-consuming.[16]

In comparison to CuAAC reaction, SPAAC reactions are often slower (10^{-2}–1 M^{-1} s^{-1}),[16] limiting the utilisation if fast reaction rates are needed. Moreover, the strain-promoted click reaction always produces two isomers, resulting from the possible addition of the azide to both sides of the alkyne. Since functionalisation of the cyclooctyne carbon scaffold generates an asymmetric electrophile, this burden cannot be ruled out. In SPAAC, the solvent compatibility is not as broad as CuAAC, which can be explained by the hydrophobic structure of the cyclooctyne and an overall reduced solubility in aqueous solvents. The greatest strength of the strain-promoted AAC reaction is its independence from a toxic catalyst.[21, 40, 41] Instead, it easily proceeds with azides and strained alkynes. This independence from a toxic metal catalyst avoids copper-associated toxicity effects on living cells as seen in CuAAC. Moreover, the absence of additional toxic catalysts simplifies the reaction process and drastically increases the biocompatibility of SPAAC. Lastly, reaction efficiency and reactant availability can be a drawback of SPAAC in some instances, as the synthesis of strained alkynes (e.g. dibenzocyclooctyne) can be complex and costly, and alkynes with reduced strain-promotion decrease the overall efficiency and yield.[40, 42]

Independent of the employed reaction setup, azide-alkyne cycloadditions have become extremely popular and useful in chemistry and chemical biology due to broad functional group tolerance and the properties of the non-natural and non-hydrolysable 1,2,3-triazole heterocycle.

II.1.1.2 CuAAC Reactions in the Spotlight of Application

Modifying biological entities and cellular components with non-natural molecules (labels) is a challenging task. However, the diverse toolbox of click chemistry reactions provides powerful methods to introduce non-natural post-translational protein modifications, to label RNA and DNA, or to target lipids, glycopolymers, or other cellular components *in vitro*, *in vivo*, or *ex vivo*. The following paragraph provides a brief overview of significant copper-catalysed azide-alkyne cycloaddition reactions, which have significantly contributed to the advancement of

modern tools and technologies, such as targeted drug delivery, cellular imaging, and probing distinct 5'-RNA modifications.

II.1.1.2.1 Antibody-Drug Conjugates

Antibody-drug conjugates (ADCs) are one of the most promising strategies to tackle cancerous tissue and solid tumours.[43, 44] Their principle of action is based on the covalent labelling of monoclonal antibodies with potent anticancer drugs via an intermediate linker subunit.[45] The high target selectivity of antibodies is leveraged to deliver conjugated drugs specifically to target cells, significantly reducing associated off-target effects commonly seen with traditional chemotherapeutics. Their non-invasive nature has also contributed to their growing success in recent clinical trials. To date, 15 ADCs have been approved by international agencies to market, and hundreds are under investigation in clinical and preclinical trials.[46] The innovative strength of ADCs lies in the idea that the utilised antibodies and their target-binding epitopes are selected to specifically bind antigens exclusively presented or at least overrepresented on cancer cells. Hence, the delivery of conjugated drugs is predefined for these antigen-presenting cancer cells. If other cells do not present the antigen on their surface, the ADC does not show any binding or response. As the binding of the antibody's epitope to antigens unique to cancer cells defines the selectivity and effectiveness of ADCs, these antigens should be permanently presented on the cell surface for a maximum response in target recognition and local drug release. So far, IgG1-type immunoglobulins are the most prevalent antibodies for the design of ADCs, based on their favourable balance of serum half-life (approx. 21 days) and their moderate to strong immune activation.[47, 48]

The mode of action of ADCs is subdivided into five sequential steps (Figure II.2). After intravenous administration of the ADCs, the ADCs diffuse through the blood vessels until they reach a target site and bind to the antigen on the cell surface. Internalisation of the conjugated antibody by receptor-mediated endocytosis is followed by transforming the membrane vesicle from an early endosome into a late endosome and the fusion with lysosomes. These lysosomes are acidic protease-containing cellular compartments, which are required for local and intracellular detachment of drugs from the ADC through acid-labile linkers or by protease-assisted degradation of the antibody. The mechanistically diverse mechanisms for drug release are crucial to fully unleash the cytotoxic and inhibitory potential of the antibody-conjugated drug payloads. Once released from the protein carrier, the traditionally used drugs diffuse from the fused lysosome into the cytoplasm and the nucleus, where they bind their cellular targets. At the target site, the drug payloads can, for instance, either disrupt the integrity of the cytoskeleton by inhibiting microtubule polymerisation in the cytoplasm or they tackle nucleic acid integrity by strong binding to DNA, which can cause cell cycle arrest, inhibition of DNA replication, or may induce DNA damage.[46] However, modern drug payloads of ADCs currently under investigation in clinical trials exhibit a broadened spectrum of cytotoxic activities, focusing not only on the cytoskeleton or DNA as primary targets. Since cancer cells have been shown to exploit diverse mechanisms to escape the cytotoxic influence of common ADC drugs, a broadened array of addressable cellular targets minimises the risk of escape by co-targeting or overcoming the devised resistance mechanisms.[49, 50]

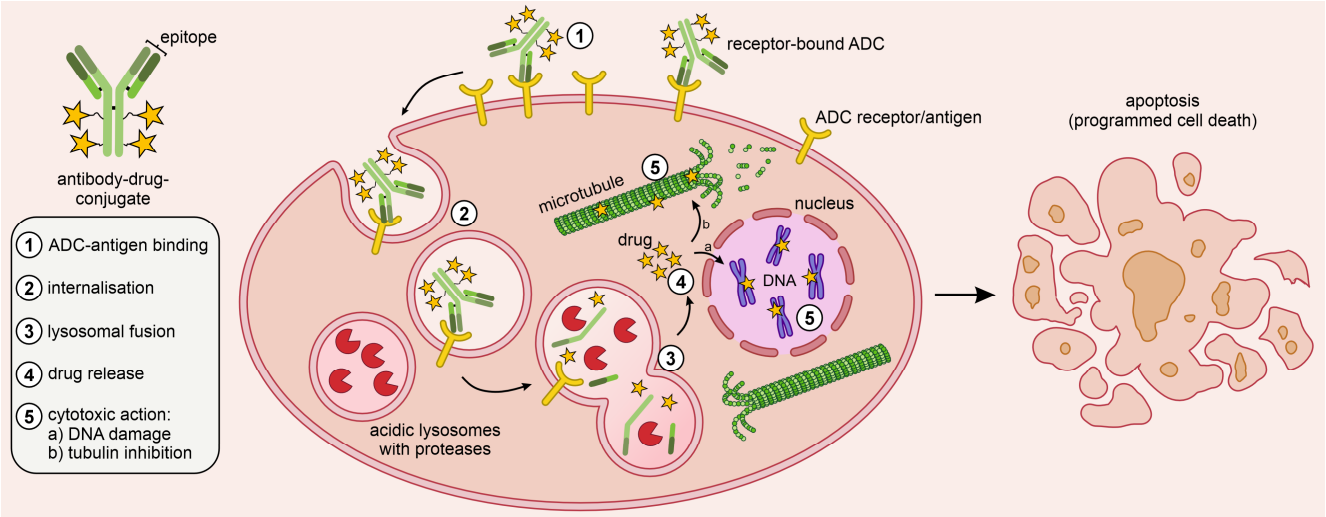
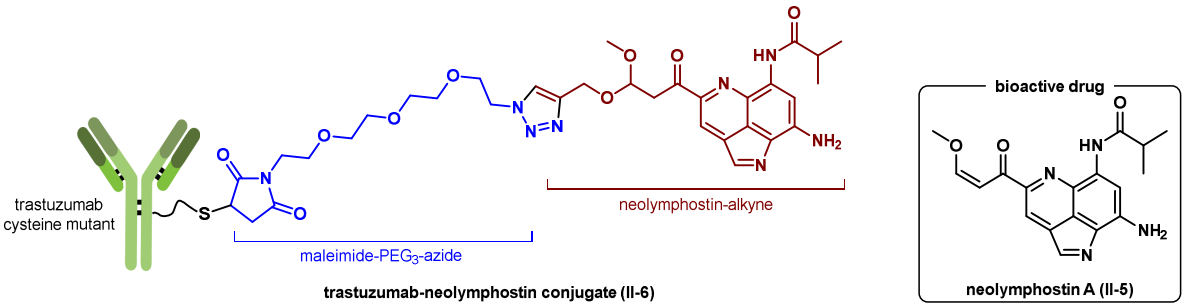


Figure II.2. Working principle of antibody-drug conjugates (ADCs) for specific targeting of cancer cells and the induction of apoptosis. The figure design was adapted from Riccardi *et al*.[46]

Antibodies are natural proteins, built from the 20 canonical amino acids. Consequently, their functionalisation can be attempted by utilising reactive groups appertaining to these amino acids (thiols, amines, phenolic alcohols, etc.) or by introducing non-canonical amino acids into the primary protein structure. Thiol-Michael reactions between reactive thiol groups of cysteine residues from the protein scaffold and functionalised maleimides are the most popular click chemistry reaction types to functionalise the antibodies, and the relatively low abundance of natural cysteine residues in antibodies allows labelling at more defined sites. The nucleophilic amine-harbouring side chain of lysine is a suitable modification site as well, but the high abundance of lysines in antibodies and other natural proteins would result in random labelling rather than site-specific labelling.[47, 51] Besides thiol-maleimide chemistry, [3 + 2] cycloadditions between azides and alkynes are also employed for antibody functionalisation to generate novel ADCs.[52] This would require azide- or alkyne-functionalised antibodies; however, as these functional groups are not natively present among the canonical amino acids, they can be introduced either via non-canonical amino acids during protein biosynthesis or through site-specific labelling of canonical amino acids with azide- or alkyne-functionalised linkers (e.g. alkyne-maleimides).

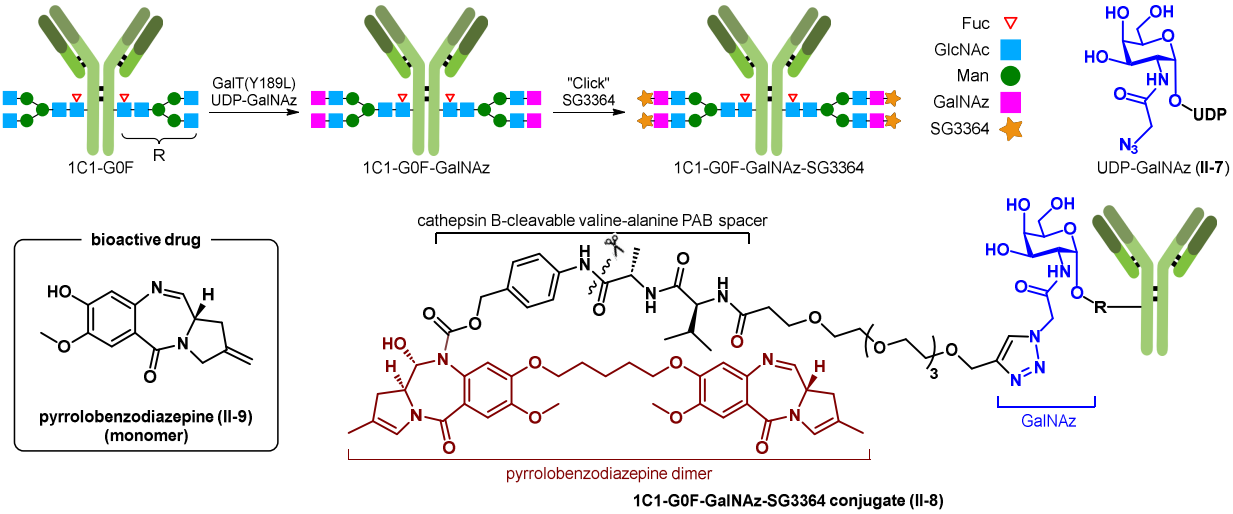
Zhou *et al*. coupled neolymphostin A **II-5**, a potent inhibitor of several regulatory phosphoinositide-3-kinase related kinases,[53, 54] to the cysteine mutant A114C of the antibody trastuzumab.[55] These kinases are essential regulatory elements in the motility, proliferation, and growth of eukaryotic cells. They have implications in DNA damage detection and repair, in protein biosynthesis, and are involved in cancer-related pathways.[55, 56] Trastuzumab, in turn, is a monoclonal antibody targeting the signal transduction of HER2 receptor-positive cancer cells by binding to the HER2 (human epidermal growth factor receptor 2) receptor tyrosine-protein kinase displayed on the outer membrane of those cells (e.g. HER2-positive breast cancer cell lines BT474, N87, and MDA-MB-361-DYT2).[57] Particularly, the systematic analysis of breast cancer cell lines revealed overexpression of the HER2 antigen in 20–30% of the malignant tissue compared to healthy tissue, making trastuzumab an ideal candidate for targeted cell-specific drug delivery.[58] To couple the neolymphostin payload with the trastuzumab antibody, Zhou *et al.* used an azide- or alkyne-functionalised neolymphostin derivative and employed the CuAAC reaction to couple the drug with a cleavable and non-cleavable alkyne- or azide-functionalised PEG-maleimide. The thiol-reactive maleimide was finally used to couple the maleimide-functionalised drug to the cysteine mutant of trastuzumab **II-6** (Scheme II.3).[55] By coupling the potent drug to the HER2-targeting trastuzumab antibody, the systemic toxicity against HER2-negative cells was selectively decreased compared to unconjugated neolymphostin (IC_{50} >750 nM

vs. 139 nM). Moreover, some of the tested conjugates were as potent as the drug alone when administered to HER2-positive cell lines *in vitro*,[55] highlighting the promise of this conjugation strategy of improved drug delivery without compromising the drug's effectiveness.



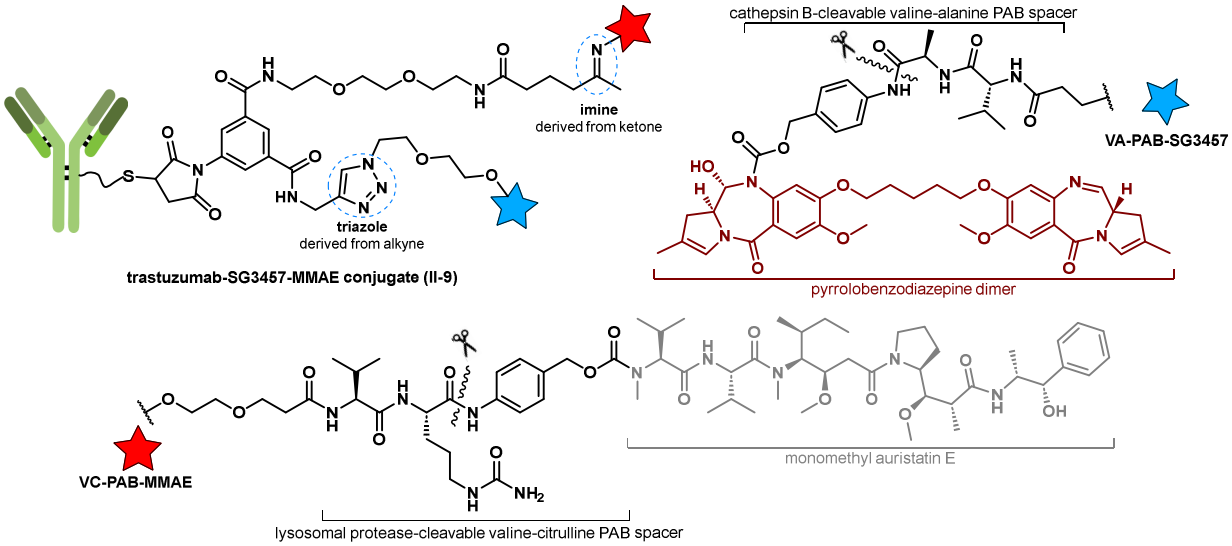
Scheme II.3. Structure of the maleimide-functionalised antibody trastuzumab-A114C, conjugated to a neolymphostin payload via CuAAC.[55]

Thompson *et al*. employed a distinct strategy to apply click chemistry on ADCs by combining biocatalysis and chemical biology in a chemoenzymatic approach. As site-specific labelling of antibodies remains challenging, a conserved glycosylation site in the CH2 domain of the heavy chain is an expedient target for modification.[59] However, glycosylation of monoclonal antibodies from eukaryotic expression hosts tends to be inhomogeneous (variations in saccharide constitution and polysaccharide branching),[60] why the glycosylation must typically be reshaped to a homogeneous appearance before conjugation may be considered.[61] Instead, the careful selection of an anti-EphA2 antibody (1C1) and its expression in a Chinese Hamster Ovary CHO-LEC8 host system enabled homogenous glycosylation with a branched sugar polymer. Subsequent overnight incubation of the glycosylated 1C1 antibody with galactose-1-phosphate uridylyltransferase (GalT Y189L) with UDP-activated azide-substituted galactosamine (**II-7**, UDP-GalNAz, uridine diphosphate-*N*-azidoacetylgalactosamine) yielded anti-EphA2 antibodies with four azide-sites available for CuAAC (Scheme II.4). *In vitro* labelling of these azide-doped antibodies with the alkyne-functionalised dimeric pyrrolobenzodiazepine (PBD) SG3364 warheads provided the 1C1-G0F-GalNAz-SG3364 conjugate **II-8** in an excellent antibody-drug-ratio (ADR) of 3.84.[61] PBDs (**II-9**) are engineered natural products, capable of forming cytotoxic DNA interstrand cross-links in the minor groove of DNA in a sequence-selective fashion.[62] The glycoengineered ADC derivatives with a cathepsin B-cleavable valine-alanine spacer, including a decarboxylation-driven self-immolative 4-aminobenzylcarbamate (PAB) unit for a traceless on-site drug release, displayed potent *in vitro* killing activity against the EphA2-positive PC3 prostate cancer cell line with an IC_{50} of 1.54 ng/mL, whereas the negative control immunoglobulin IgG-control-SG3364 did not (IC_{50} >1000 ng/mL).[61, 63]



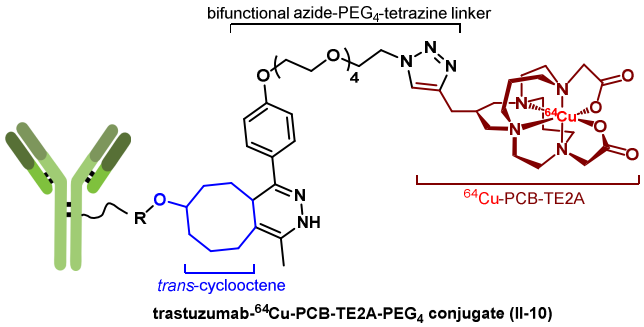
Scheme II.4. Structure of a glycoengineered ADC with the PBD dimer warhead SG3364.[61] Although the antibody is equipped with four reactive azides to attach up to four payloads, only one warhead is shown on full scale for clarification. Abbreviations: Fuc – fucose; GalNAz – *N*-azidoacetylgalactosamine; GlcNAc – *N*-acetylglucosamine; Man – mannose; PAB – *para*-aminobenzylcarbamate; UDP – uridine diphosphate.

The co-delivery of warheads within a single ADC offers an alternative to administering two independent ADCs that target the same antigen but carry different payloads. Besides improving the loading ratio of antibodies with the desired drug, Kumar *et al*. conjugated one antibody with two separate drugs to obtain a mixed ADC **II-9**.[64] Their study focused on the tubulin polymerisation inhibitor monomethyl auristatin E (MMAE) and the DNA minor groove cross-linking agent PBD.[62, 65] Essential for their bifunctionalisation approach was distinct chemistry for installing either warheads. A branched and bifunctional maleimide linker was exploited to decorate the cysteine mutant of the antibodies with a CuAAC-reactive alkyne and an amine-reactive ketone at the same time. While the CuAAC reaction was used to click a PBD-azide (SG3457) with the alkyne unit of the linker, the Schiff-base formation between an aminooxy-functionalised MMAE derivative and the ketone moiety of the linker was employed to generate a covalent oxime linkage (Scheme II.5). Both spacers, a cathepsin B-cleavable alanine-valine PAB spacer and a lysosomal protease-cleavable valine-citrulline PAB spacer, were designed to promote a traceless drug-release in the target cell. After labelling of the trastuzumab and NIP228 antibodies, especially the trastuzumab conjugates exhibited highly potent killing activity. Compared to unlabelled trastuzumab, single MMAE labelling already increased the cytotoxic potential. However, single SG3457 labelling and dual SG3457-MMAE labelling of trastuzumab in particular boosted the cytotoxicity even more. As the PBD warhead SG3457 is far more potent than MMAE, the single-labelled trastuzumab-SG3457 and the dual-labelled trastuzumab-SG3457-MMAE **II-9** ADCs displayed similar IC_{50} values against the HER2-expressing MDA-MB-453 breast cancer cell line.[64]



Scheme II.5. Structure of a trastuzumab ADC with mixed PBD-MMAE warheads.[64] Abbreviations: MMAE – monomethyl auristatin E; PAB – *para*-aminobenzylcarbamate; VA – valine-alanine; VC – valine-citrulline.

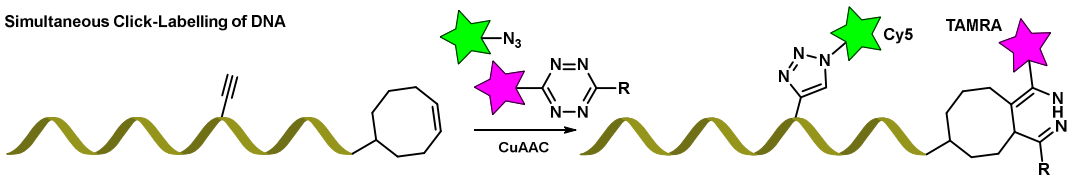
In the last example of CuAAC-related antibody chemistry, a cross-bridged bifunctional chelator was used for specific conjugation to antibodies in the context of immuno-PET (positron emission tomography) imaging. Lee *et al*. used a PCB-TE2A-tetrazine (propylene cross-bridged), cognate to the common DOTA, NOTA, and TETA chelators, which are frequently used in ^{64}Cu radiolabelling of antibodies.[66, 67] ^{64}Cu is a positron-emitting isotope of the transition metal copper. The copper radionuclides are currently under extensive investigation for PET imaging due to their beneficial half-life (12.7 h), good availability and well-established chelation chemistry. Tight chelation of the radionuclide and inertness towards decomplexation are essential properties, as PET imaging requires the toxic metal to be injected into the human body.[68] To generate the antibody-conjugable ^{64}Cu-radionuclides, the PCB-TE2A alkyne was conjugated to maleimide-, tetrazine-, amine-, carboxylic acid-, or oxaziridine-functionalised azide linkers via CuAAC and loaded with ^{64}Cu. In the selected example, a free amine on the trastuzumab antibody was labelled with a bifunctional NHS-*trans*-cyclooctene linker and subsequent click functionalisation of the linker with the ^{64}Cu-PCB-TE2A-tetrazine in an inverse electron demand Diels-Alder reaction provided the ^{64}Cu-labelled antibody **II-10** (Scheme II.6). As mentioned earlier, trastuzumab targets the HER2 receptor, which is overexpressed in 20–30% of the HER2-positive cancer cell lines.[57, 58] Moreover, the expression is known to be inhomogeneous, and the small amount of tumour might be insufficient for the reliable determination of HER2 receptor expression levels by biopsy.[69, 70] Immuno-PET imaging might therefore be a non-invasive method to assess HER2 expression in the whole body in real-time.[69] Utilisation of the ultra-stable ^{64}Cu-TE2A-trastuzumab conjugate showed selective binding and internalisation into HER2-positive cell lines, as the conjugate titre was ten times higher in HER2-positive cell lines NIH3T6.7 and SKOV3 than in HER2-negative CT26 cells. Furthermore, immuno-PET imaging on NIH3T6.7-infected nude mice showed an overall low background signal for the ^{64}Cu-TE2A-trastuzumab ADC with PEG units and high accumulation in cancerous tissue,[69] underlining the clinical potential of the presented conjugate for tumour visualisation.



Scheme II.6. Structure of a ^{64}Cu-doped trastuzumab-^{64}Cu-PCB-TE2A-PEG$_4$ ADC for selective visualisation of HER2-overexpressing cancer cells in PET imaging.[69] Abbreviation: PCB – propylene cross-bridged.

II.1.1.2.2 Click-Tools in DNA and RNA Research

The field of DNA and RNA research is a rapidly progressing field, and novel methods emerge frequently to study the role and fate of nucleic acids, their spatial localisation within a cell, covalent modifications, their sequence, or the effects of three-dimensional folds on metabolic processes. To investigate the fold of DNA species via FRET spectroscopy (Förster resonance energy transfer),[71] the group of Andres Jäschke developed a method for simultaneous co-labelling of DNA with two fluorophores via bioorthogonal CuAAC and inverse electron demand Diels-Alder reactions.[72] Alkyne and *trans*-cyclooctene electrophiles were introduced into DNA oligonucleotides through solid-phase synthesis and these modified oligonucleotides were subsequently merged with the DNA sequence of interest by polymerase chain reaction (PCR). Click labelling reactions with the fluorophores Cy5 azide and TAMRA tetrazine generated dual-labelled DNA species (Scheme II.7), suitable for FRET spectroscopy. Even though this proof-of-concept study for dual labelling of DNA was conducted *in vitro*, this approach could be transferred for use in living organisms through *in situ* hybridisation of clickable single-stranded DNA (ssDNA) probes with nucleic acids *in vivo*. Thereby, studying the cellular localisation of DNA species or other nucleic acid-related properties would become accessible.

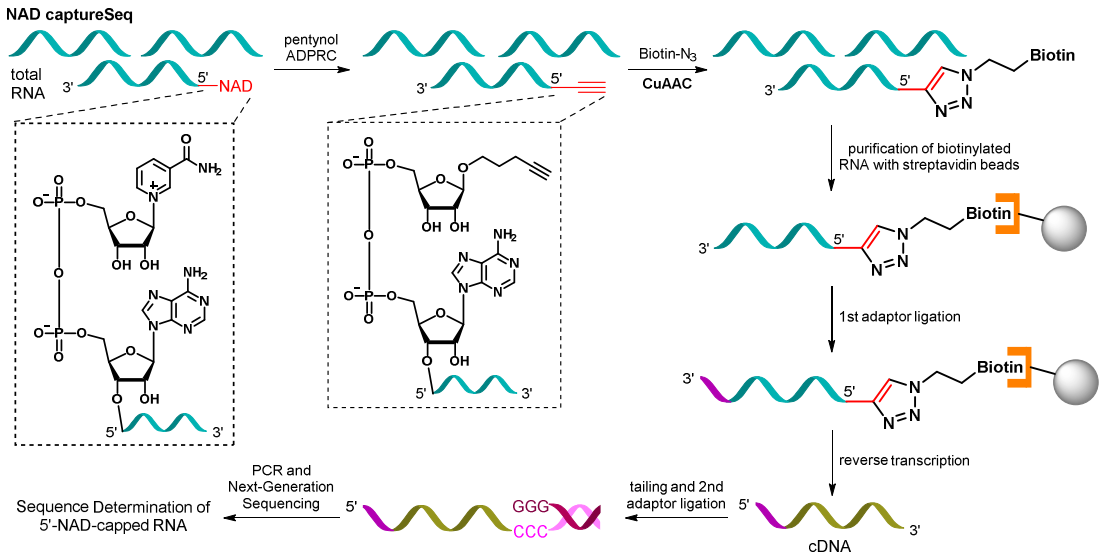


Scheme II.7. Click labelling of DNA oligonucleotides via bioorthogonal CuAAC and IEDDA reactions with the reactive fluorophore derivatives TAMRA tetrazine and Cy5 azide.[72]

The application of click chemistry holds significant potential to contribute to the evolution of other technologies, such as those in the area of Next-Generation Sequencing (NGS). Adhering to this, Miura *et al*. devised a strategy called “terminal deoxynucleotidyl transferase-assisted, copper-catalysed azide-alkyne cycloaddition-mediated ssDNA ligation” (TCS ligation) to generate libraries of ssDNA for NGS. This involves triazole formation with adaptor DNA, based on the CuAAC reaction. Isolated ssDNA of *Saccharomyces cerevisiae* was terminally tagged at the 3’-end with single azide-containing nucleotide analogues in a chemoenzymatic fashion, catalysed by the terminal deoxynucleotidyl transferase (TdT).[73] This semi-synthetic DNA species was then subjected to CuAAC ligation to 5’-ethynylated adaptor sequences,[74] which are crucial players in the NGS workflow. These adaptors are short oligonucleotides with known sequence, which are fused with the DNA molecules of interest at the 3’- and 5’-ends. Their known sequence allows barcoding and hybridisation of the isolated DNA to complementary linkers on the NGS flow cell’s surface and serves as a binding site for primers to PCR-amplify the DNA fragments

of unknown sequence.[75] By using the TCS ligation strategy with CuAAC as a synthetic step for the *in vitro* fusion of isolated ssDNA with 3'-azide functionalisation and the 5'-ethynylated oligonucleotides, the first standard method for adaptor tagging of ssDNA was presented for NGS library preparation.[74]

Although NGS is a powerful technology to uncover the sequence-encoded mysteries of nucleic acids, some properties remain concealed in this workflow. Here, the inclusion of click chemistry may eliminate certain limitations or expand the current capabilities of NGS to develop novel tools for nucleic acid research. The last decades have shown that cells use a sequence-independent regulatory mechanism (epigenetics), playing a fundamental regulatory role in determining the stability, fate, and function of DNA and RNA. On the example of RNA, more than 170 covalent modifications of coding and non-coding RNA species are well-known to shape the epitranscriptome of prokaryotes, eukaryotes, and viruses and contribute to RNA stability, fine-tuning of gene expression, and splicing by altering the overall RNA structure, its affinity to other interaction partners or by increasing the hydrolytic stability.[76-78] However, selective enrichment or a targeted analysis of certain modifications remains a challenging task. Recently, Chen *et al*. showed that terminal 5'-end NAD-capping is a highly abundant post-transcriptional modification of bacterial RNA.[79] The redox cofactor nicotinamide adenine dinucleotide (NAD^+; here referred to as NAD) is well-known to participate in catabolic processes, such as glycolysis or the citric acid cycle, and is an essential energy storage and hydride acceptor.[80-82] Nevertheless, its appearance as a covalent RNA modification remained unknown until Chen *et al*. discovered NAD-capped RNA in untargeted LC-MS studies in 2009. Shortly after this discovery, Cahová *et al*. developed NAD captureSeq (Scheme II.8), a chemoenzymatic procedure for the targeted enrichment and NGS sequencing of NAD-capped RNAs.[83] The cutting point of this workflow is the initial transglycosylation of NAD's nicotinamide moiety with the aliphatic alkyne alcohol 4-pentyn-1-ol, catalysed by the adenosine diphosphate-ribosylcyclase from *Aplysia californica*.[84] This introduction of the alkyne functionality into capped RNA enables highly selective CuAAC reactions on capped RNA species with azide-substituted biotin for the streptavidin-mediated enrichment of biotinylated click products of capped RNA. Following the 3'-fusion of RNA adaptor sequences, reverse transcription, and 5'-adaptor ligation, the identity of NAD-capped RNAs was revealed via NGS, marking the first steps towards uncovering the biological role of NAD-capped RNAs.[83]



Scheme II.8. Selective enrichment and sequencing strategy for 5'-NAD-capped RNA from total RNA samples via NAD captureSeq.[83] Abbreviations: PCR – polymerase chain reaction; cDNA – copy DNA; ADPRC – adenosine diphosphate-ribosylcyclase; NAD – nicotinamide adenine dinucleotide.

II.1.1.2.3 Click-Tools in Glycochemistry

Glycans are complex polysaccharides that are presented on proteins, lipids, and cell surfaces, playing crucial roles in cell adhesion, the virulence of bacterial pathogens, and antibody binding to invasive cells and organisms.[85-87] Furthermore, cells naturally utilise glycans to increase the solubility of certain hydrophobic cellular components or for a site-specific delivery of metabolites.[88, 89] The most prominent glycopolymer in the bacterial kingdom is present in the outer membrane (OM) of Gram-negative bacteria, called lipopolysaccharide (LPS). LPS is a chimera of the membrane-anchoring glycolipid lipid A and three layers of polysaccharides (inner core, outer core, O-antigen).[90] Both lipid A and the O-antigen are bacterial virulence factors and can significantly contribute to the pathogenicity of bacteria, such as *Pseudomonas aeruginosa*.[91, 92] Moreover, LPS renders the OM asymmetric and forms a dense layer of very polar polysaccharides. This makes the OM of some bacteria difficult to pass for hydrophobic molecules, which can serve as solvents, drugs, or agents of bacterial competition and threaten the integrity of the bacterial membrane.[93] Thus, the OM is often referred to as “the first line of defence” when it comes to self-protection of prokaryotes. Its mode of operation is vital to understand in order to target bacterial pathogens effectively. However, the complex variety of natural sugar monomers and dimers, along with the natural diversity of possible linkages between these carbohydrate units and the inhomogeneity of these glycopolymers, make LPS and glycans in general extremely challenging to study.[94] To investigate the dynamics of LPS, Vauzeilles and co-workers exploited the natural promiscuity of enzymes from intracellular glycan biogenesis and introduced a non-natural azide-labelled sugar into the inner core structure of LPS from the model organism *Escherichia coli* (Figure II.3). The sugar 3-deoxy-D-manno-octulosonic acid (KDO) is a unique and essential sugar, only present in the LPS core of Gram-negative bacteria.[95] For this reason, chemically synthesised 8-azido-3,8-dideoxy-D-manno-octulosonic acid (KDO-N_3) was fed to *E. coli* during the growth phase to incorporate the unnatural analogue into the LPS inner core. In a subsequent *in vitro* labelling step, the versatile CuAAC reaction was used to couple the incorporated KDO-azide with an alkyne-substituted AlexaFluor488 fluorophore that was utilised to visualise the bacterial OM in fluorescence microscopy.[96, 97] While this example on labelling techniques may enable future strategies for direct delivery of antimicrobial agents and prodrugs or for the extraction and characterisation of polysaccharides,[96, 97] it also impressively proves the versatility of CuAAC in bioorthogonal chemistry again.

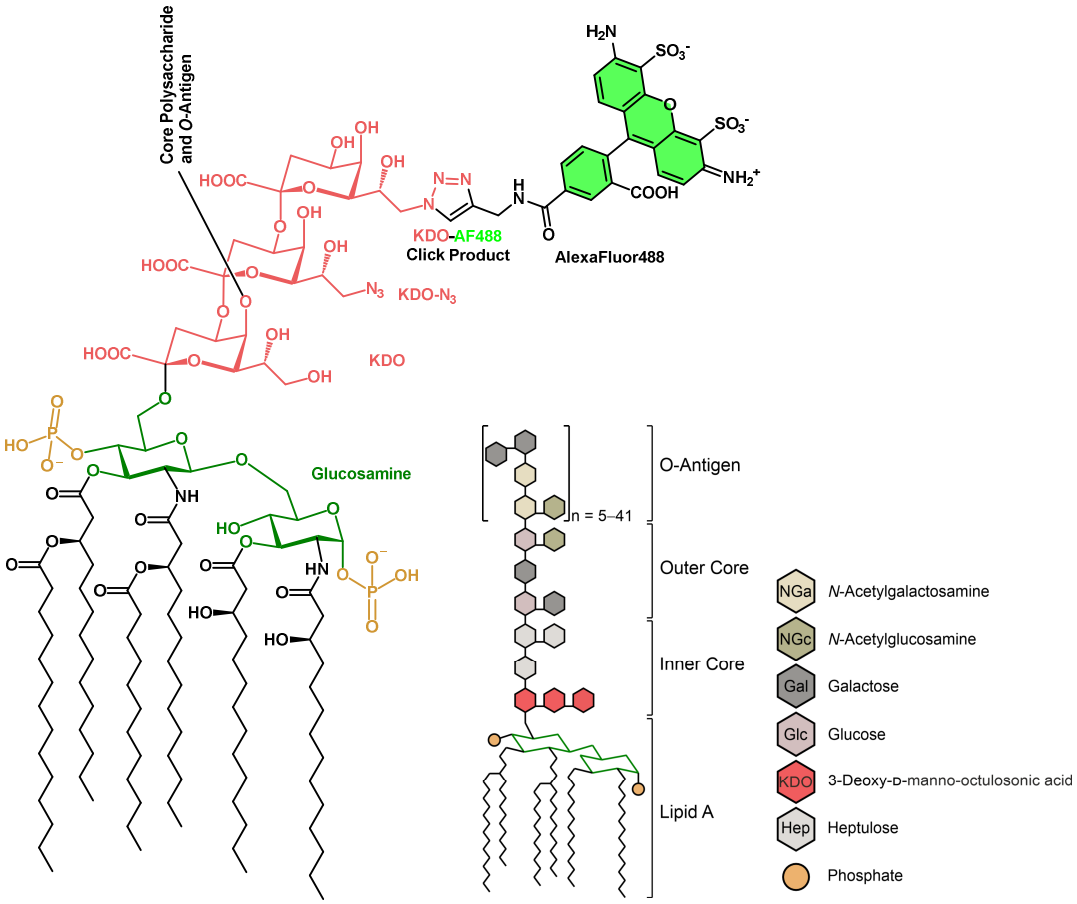
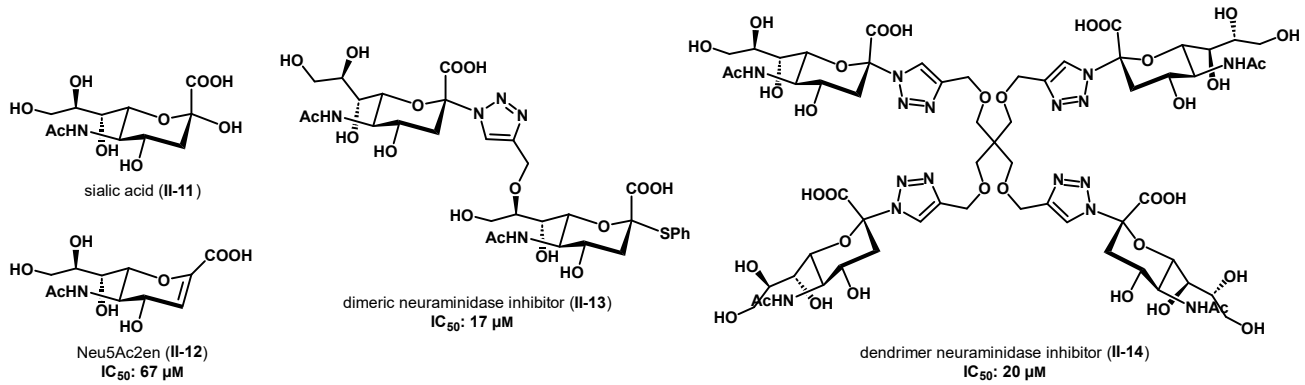


Figure II.3. Detailed structure of the bacterial outer membrane lipopolysaccharide (LPS) (Lipid A and inner core) of *E. coli* for bioorthogonal fluorescence labelling of KDO-azide via CuAAC and a schematic view of LPS,[96, 97] including Lipid A, inner and outer core, and the O-antigen (oxygens omitted for clarity). LPS consists of three KDO units. To highlight the AlexaFluor488-labelling of KDO-azide, natural KDO, KDO-azide, and the clicked KDO-AlexaFluor488 conjugate are shown from bottom to top.

The long list of glycoconjugates, leveraging the principle of CuAAC, was augmented by Linhardt's group by synthesising non-hydrolysable sialic acid-based neuraminidase inhibitors. Neuraminidases are viral enzymes capable of cleaving *O*-glycosidic bonds on sialic acid oligosaccharides. As sialic acid **II-11** and sialic acid polysaccharides are prevalent in glycans on eukaryotic and prokaryotic cell surfaces, neuraminidases are believed to remodel glycan architecture, facilitating the viral entry and the release of new infectious virions after replication within the host cell.[98-100] Although neuraminidase inhibition is an effective approach to suppress the release of virions from the host cell, only two competitive neuraminidase inhibitors are approved and available for therapeutic purposes.[101] The limited therapeutic options have favoured the development of resistance to these two inhibitors, urging the need to develop new inhibitors. Consequently, Linhardt's group targeted the synthesis of non-hydrolysable *N*-glycosides of sialic acid and 1,2,3-triazole as potential competitive inhibitors of neuraminidases and compared these derivatives to the commercial neuraminidase inhibitor *N*-acetyl-2,3-dehydro-2-deoxyneuraminic acid (**II-12**, Neu5Ac2en). Since mutations in the neuraminidase active site of influenza viruses have been shown to confer resistance to Neu5Ac2en and derivatives thereof,[102] the click strategy is a new approach to circumvent the existing viral mechanism of drug escape. The realisation of several dimeric and a dendrimer of non-hydrolysable triazole-harbouring neuraminidase inhibitors, exemplified by compounds **II-13** and **II-14**, culminated in an up to 3.9-fold increase of inhibitory potential against neuraminidase from *Clostridium perfringens* on low micromolar concentration scale in comparison to Neu5Ac2en (Scheme II.9). Finally, this study

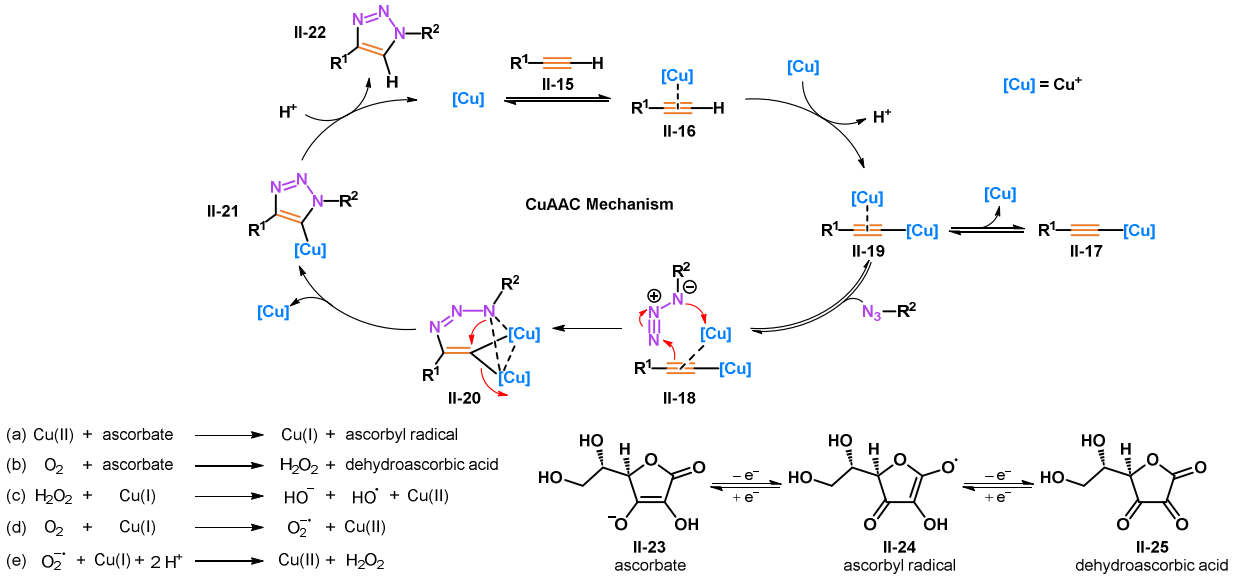
proved the utility of CuAAC in the preparation of sialic acid-like disaccharides and dendrimers in the spotlight of application.[101]



Scheme II.9. CuAAC- and sialic acid-based inhibitors of neuraminidase.[101]

II.1.1.3 Copper-Stabilising Ligands and Mechanistic Considerations in CuAAC Reactions

The catalysed azide-alkyne cycloaddition is essentially accelerated by the transition metal copper.[22-24] However, copper-catalysed reactions are rather challenging to investigate mechanistically in detail,[103] as copper ions can disproportionate in solution and complexes of the transition metal tend to aggregate.[104, 105] Nonetheless, significant progress has been made in understanding the mechanism of the CuAAC reaction over the past 20 years, leading to a consensus within the scientific community on the essential steps and milestones of the reaction (Scheme II.10). In the first place of the catalytic cycle proposed by Worrell *et al.*,[103] the copper(I) species coordinates to the π-bond of alkyne **II-15** under activation of the π-system by the formation of a Cu-π-complex **II-16**. Under the influence of a base, the activated terminal acetylene proton with a decreased pK_a value of 9.8 is deprotonated and substituted by another Cu species to generate a Cu-coordinated Cu-acetylide **II-17** in solution.[16] Certain σ-bonded copper-acetylide species are stable and isolable, as Nolte *et al.* showed through the synthesis of NHC (*N*-heterocyclic carbene)-stabilised Cu-phenyl acetylide.[106] The addition of electron-rich benzyl azide to the Cu-acetylide **II-17** in polar aprotic solvents left both reactants unconverted. Additional supplementation of exogenous copper in the form of $Cu(PPh_3)_2NO_3$, however, rapidly led to the formation of copper triazolide **II-18**, as the Cu-coordinated Cu-acetylide **II-19** was available instead. This observation led to the hypothesis that a dinuclear Cu-intermediate is present and involved in the catalytic cycle of the CuAAC reaction.[103] Based on a stoichiometric crossover experiment with $^{63/65}Cu$ labelling, the role of the two distinct copper nuclides from the coordinative organic azide/Cu-acetylide complex **II-18** was evaluated. Surprisingly, both copper nuclides were interchangeable and suggested unexpected migration of Cu nuclides within the cycloaddition complex **II-18**. Thus, the concerted cycloaddition of azide and σ-bonded Cu-acetylide yields a dinuclear intermediate **II-20**, which collapses under the loss of one Cu centre into the stable copper triazolide **II-21**. Reprotonation of the copper triazolide **II-21** forms the five-membered 1,2,3-triazole **II-22** heterocycle and the released copper species is available for a new round of catalysis.



Scheme II.10. Catalytic cycle of the copper-catalysed azide-alkyne cycloaddition.[16, 37] Besides the catalytic cycle of a generic CuAAC reaction, the generation of ROS by ascorbate-assisted Cu(II) reduction in the presence of molecular oxygen is highlighted. Stabilising Cu-ligands are omitted in the suggested catalytic cycle of Worrell *et al.*[103] for simplification of the scheme. The oxidation state of Cu(I) remains unchanged throughout the catalytic cycle. Colour code: Copper species (blue), alkyne/acetylene (orange), organic azide (purple).

Despite its role in CuAAC as an essential catalyst, copper is a potent cytotoxin that causes oxidative stress in living cells by generating reactive oxygen species (ROS).[107] These molecules, high in redox potential, may undergo undesired reactions with lipids, nucleic acids, or protein side chains.[39, 108, 109] Moreover, the sensing of ROS by cells induces specific costly countermeasures to eliminate the threatening species in order to retain cell viability.[110] In the context of CuAAC and the utilisation of sodium ascorbate **II-23** as reducing agent for inexpensive Cu(II) sources, sodium ascorbate firstly reduces Cu(II) to Cu(I) (Scheme II.10). The single electron transfer first generates the ascorbyl radical **II-24** until a second electron transfer generates dehydroascorbic acid **II-25**, which spontaneously hydrolyses in the presence of stoichiometric amounts of water.[111] In fact, the reduction of two Cu(II) nuclides requires only a single equivalent of sodium ascorbate. However, preparative setups under oxidative conditions typically use an excess of ascorbate to avoid oxygen-related oxidation of Cu(I) back to less reactive Cu(II) species and the concurrent release of the superoxide radical anion as highly reactive ROS.[108, 109] Although ascorbate was initially used with the intention to eliminate the negative influence of oxygen from the reaction, molecular oxygen can react with ascorbate under the formation of hydrogen peroxide, a highly reactive ROS.[112] The hydrogen peroxide, in turn, can oxidise Cu(I) to Cu(II), releasing the hydroxide anion and the hydroxyl radical into the reaction. The hydroxyl radical is the most reactive and toxic ROS, as no endogenous enzyme or antioxidant metabolite is known for its detoxification.[110] Lastly, the superoxide radical anion is capable of oxidising Cu(I) in the presence of protons to Cu(II) and the ROS hydrogen peroxide.[108] The generation of ROS and their high reactivity have implications for both live organisms and for *in vitro* CuAAC reactions when performed with biological materials, such as isolated proteins or peptides.[39]

One approach to avoid the Cu-related generation of ROS in CuAAC cycloadditions is the utilisation of ring-strain-activated alkynes in a strain-promoted SPAAC cycloaddition. While this copper-free reaction eliminates the ROS-related oxidative damage to biological conjugates in an oxidative atmosphere, SPAAC is notably slower than the copper-catalysed counterpart. Even the fastest reported SPAAC reaction involving (aza)dibenzocyclooctyne was with an observable rate constant k_{obs} of approximately 1 M^{-1} cm^{-1} tremendously slower than Cu(I)-catalysed

reactions with k_{obs} 10–100 M^{-1} cm^{-1}.[34, 40] In consequence, SPAAC is up to 100 times slower than CuAAC,[113, 114] which contradicts the idea of fast and thorough labelling of potentially transient metabolites via bioorthogonal click chemistry. Furthermore, cyclooctynes may react with surface-accessible cysteine residues of proteins in a thiol-yne reaction,[115, 116] which limits the biorthogonality of SPAAC to some extent.

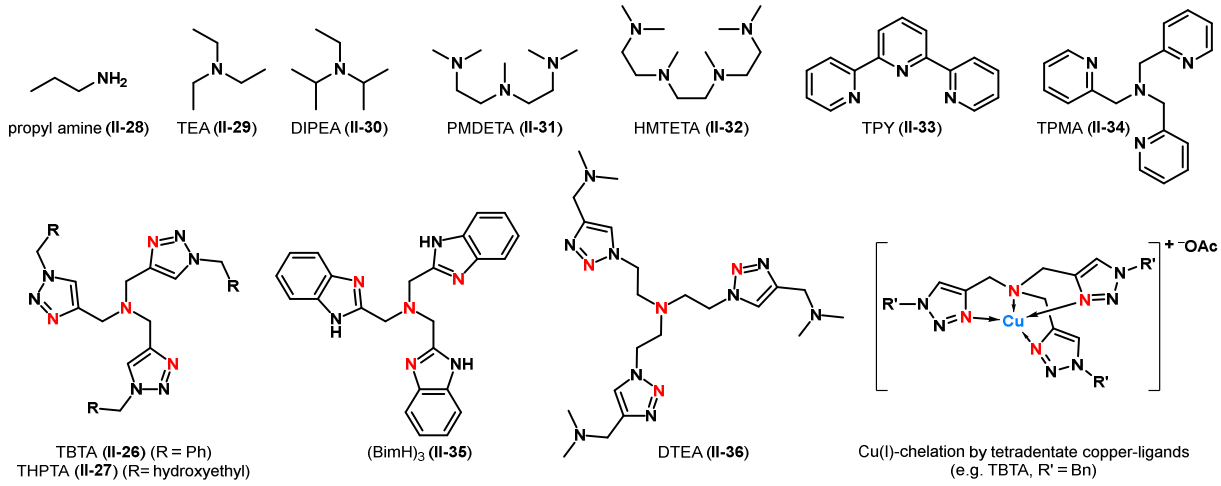
Since the CuAAC reaction is the most popular bioorthogonal click reaction, numerous attempts were made to minimise copper disproportionation, radical formation, and oxidative damage caused by ROS. While the Cu(II) reduction with sodium ascorbate in oxygen-containing environments favours the formation of highly reactive radicals and ROS, a photocatalytic Cu(II) reduction at 405 nm with the Irgacure 819 photoinitiator mostly suppressed oxidative side reactions and inactivation of the catalytic copper species.[117] However, the most common strategy to retain the fast reaction kinetics of CuAAC is the application of copper-chelating ligands. These ligands stabilise the Cu(I) oxidation state and shield the inorganic catalyst from the oxidative environment by tight complexation.[25] This shielding prevents the reaction of Cu(I) with an excess of reducing agent or with atmospheric oxygen, thereby avoiding the generation of highly reactive ROS.[118, 119] Furthermore, the CuAAC benefits from Cu-ligand interactions in several key aspects of the reaction parameters, as ligands can promote catalyst solubility in a wide range of reaction solvents, accelerate reaction rates, prevent the formation of unreactive polynuclear Cu(I) acetylides, and facilitate the formation of the initial Cu-acetylide **II-17** by acting as a base.[25, 37, 120]

Among all ligands available nowadays, TBTA [**II-26**, tris(benzyltriazolylmethyl)amine] was the first ligand ever applied for rate acceleration in a bioorthogonal CuAAC reaction for dye-labelling of the azide-modified capsid of cowpea mosaic virus.[121] This study by Wang *et al*. concurrently established CuAAC click chemistry as a tool in chemical biology. It was hypothesised that the ligand-occupied coordination sites of copper block the interaction of oxidising species with the catalytic metal centre and thus prevent the formation of ROS.[120] Furthermore, it was assumed that the strongly basic and sterically encumbered tertiary amine coordinates permanently to the Cu ion, while the tripodal triazole arms intermittently associate and dissociate from the metal centre to uncover coordination sites for the formation of intermediate species of the CuAAC catalytic cycle, such as the initial Cu-acetylide.[122] A holistic study on nitrogen-containing polydentate Cu-ligands from 2004 employed cyclic voltammetry measurements to show that chelation of Cu(I) by these ligands influences the redox potential of the metal. The work of Chan *et al*., conducted with the alternative water-soluble THPTA [**II-27**, tris(3-hydroxypropyltriazolylmethyl)amine] ligand, revealed an increase of 300 mV in redox potential of the Cu(I)/Cu(II) pair, enhancing the oxidative stability of the reactive Cu(I) centre by ligation with the polydentate nitrogen ligand.[122] Over the past 20 years, several ligands and ligand classes have been developed, aiming for improvements in Cu-coordination. These altered Cu-binding affinities exert influence on rate acceleration, solvent compatibility, and biocompatibility of the CuAAC reaction for applications in a biological or medical context. For this purpose, heteroatoms with strong chelation potential (such as sulfur, oxygen, phosphorus, nitrogen, carbene NHCs) have been used to devise auxiliary ligands. However, the following section will exclusively focus on the largest group of (poly)dentate ligands – the nitrogen ligands.

II.1.1.3.1 Nitrogen-Containing Polydentate Copper-Ligands in CuAAC

Nitrogen-containing ligands are the largest group of ligands used for Cu-chelation. The smallest ligands with sparse contributions in rate acceleration of the CuAAC are monodentate alkylamines, such as *n*-propyl amine (**II-28**), TEA (**II-29**), and DIPEA (**II-30**) (Scheme II.11). These sp^3-hybridised Lewis-basic amines are mostly added to the reaction for their basicity to promote the initial deprotonation of the CH-acidic acetylene and the following Cu-acetylide formation.[16, 123-125] However, their single coordination site for cuprous Cu(I) or cupric Cu(II) ions neither shields the bound copper efficiently from oxidants, nor do the respective Cu-complexes substantially

accelerate the CuAAC reaction. Significant improvements in rate acceleration are observable with polydentate ligands instead. For example, the dipodal tridentate ligand *N*,*N*,*N*',*N*'',*N*''-pentamethyldiethylenetriamine (**II-31**, PMDETA) rendered a 230-fold acceleration of a CuAAC reaction with CuBr as copper source and the click substrates propargyl ether and diazido-terminated (poly)styrene. The same reaction performed with the tripodal tetradentate ligand 1,1,4,7,10,10-hexamethyltriethylenetetramine (**II-32**, HMTETA) was up to more than four times slower than the PMDETA-assisted reaction (Scheme II.11).[126] This was attributed to the saturated Cu-coordination sites in HMTETA **II-32** and the lack of attachment sites for the alkyne to initiate the acetylene insertion in the first step of the catalytic cycle (cf. Scheme II.10).[16] Besides aliphatic polydentate ligands, polydentate pyridines were studied in the context of copper complexation to evaluate their application potential as stabilising ligands in CuAAC reactions. Although polypyridines, such as TPY (**II-33**, terpyridine) and TPMA [**II-34**, tris(2-pyridylmethyl)amine], are excellent chelators for transition metals and find broad application in catalysis and supramolecular chemistry,[127] they only contribute to a relatively low extent in CuAAC rate acceleration or have even adverse inhibitory effects.[126] Pyridines are recognised to be weaker bases than aliphatic amines, which causes an overall slower formation of the Cu-acetylene π-complex for *N*-heterocyclic pyridine ligands.[16] Moreover, the Cu-coordination of aliphatic amine ligands is more labile than for pyridine ligands. This circumstance explains the enhanced rate acceleration with PMDETA **II-31**, as only labile ligand groups allow transient dissociation from the metal centre to expose free coordination sites for the association of terminal alkynes and to promote competitive azide binding in the cycloaddition complex.[120, 128]



Scheme II.11. Structural comparison of CuAAC Cu(I)/Cu(II)-ligands. For the tripodal ligands TBTA (**II-26**), THPTA (**II-27**), $(BimH)_3$ (**II-35**), and the non-commercially available ligand DTEA (**II-36**), the Cu-chelating nitrogens are highlighted. The right-hand side scheme in the bottom line visualises the stabilisation of Cu-ions [here: Cu(I)] by tripodal tetradentate ligands through the formation of three *N*-Cu-*N*-coordinative five-membered [TBTA, THPTA, $(BimH)_3$] or six-membered [DTEA] chelates.

Taking the benefits of tripodal tri- and tetradentate polyamine ligands as inspiration and the structure of the tris-triazolyl gold standard ligand TBTA **II-26** as the basis for further ligand developments, several groups of ligands were introduced as auxiliary ligands for CuAAC reactions in miscellaneous applications. Most of these ligands share a common tris(arylmethyl)amine core to enable and modulate copper binding throughout the catalytic CuAAC cycle. This group of tris(arylmethyl)amine ligands is then further subdivided into tris(triazolylmethyl)amine (e.g. TBTA and THPTA) or tris(heteroarylmethyl)amine [e.g. $(BimH)_3$ (**II-35**), tris(benzimidazolylmethyl)amine] ligands,[32, 118, 119, 122, 129-133] both facilitating tetradentate Cu-complexation in five-membered chelates. In addition to these large groups, only a minor group of tripodal ligands relies on the cognate tris(triazolylethyl)amine core [e.g. DTEA (**II-36**)] (Scheme II.11),[25, 134-136] which is most likely owing to legal intricacies in the precursor synthesis

of the tertiary amine core (*vide infra*).[137] The group of benzimidazolyl chelators with their flagship ligand $(BimH)_3$ were shown to be the most competitive group of ligands and superior to TBTA, based on the apparent rate acceleration in CuAAC reactions.[32-34] Ligand fine-tuning, performed by additional attachment of ester or acid substituents in favourable positions on the heteroaryl scaffold of these ligands can even speed up the reaction, by facilitating the final proteolysis of the Cu-triazolide **II-21**.[32] A minor fraction of tris-triazolyl ligands exploits an asymmetric substitution of the arms to modulate several reaction parameters at a time. For instance, the two asymmetric ligands BTTAA and BTTES harbour two *tert*-butyl substituents and one acid substituent, increasing solubility and reaction kinetics in water and, most importantly, improving the biocompatibility through a minimised formation of copper-related ROS.[129-131]

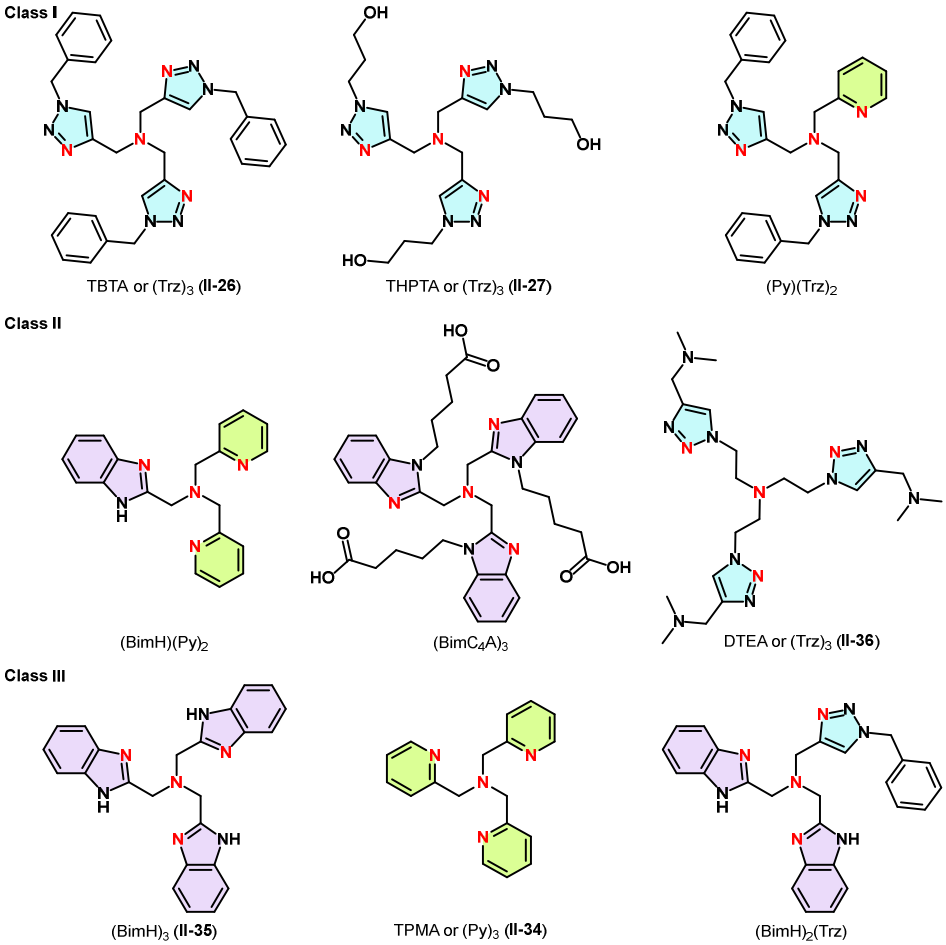
A comprehensive analysis by Presolski *et al.* from 2010 on rate acceleration under consideration of catalyst loading, the Cu(I)-to-ligand ratio, and reaction solvents suggested that nitrogen ligands can be classified into three distinct groups/types (Scheme II.12). This classification of CuAAC ligands correlates with relative copper affinities and is determined by the number and the copper affinity of metal-binding heterocycles [triazoles (Trz) << pyridines (Py) < benzimidazoles (Bim)].[32, 34]

Class I ligands do not contain any benzimidazolyl moiety and are relatively weak binders of copper. Hence, they compete with strong donor solvents, namely those that can bind and interact with Cu(I) (DMSO, DMF, acetonitrile). High concentrations of DMSO or other donor solvents can negate the rate acceleration of class I ligands. However, this inhibitory effect is not observed when using large ligand/Cu ratios >>1 in weakly coordinating solvents, such as water. The most prominent and broadly applied examples of class I ligands are TBTA **II-26** and THPTA **II-27**.[34]

Class II ligands typically contain two or more pyridyl or benzimidazolyl groups and their basicity drives strong copper coordination. Furthermore, these ligands exhibit peak activity at substoichiometric Cu/ligand ratios of 0.5 or stoichiometric copper loading at a ratio of 1. Utilisation of ligand in excess, however, drastically decreases the activity and has an inhibitory character.[34]

Class III ligands form strong complexes and are mostly uniformly equipped with benzimidazolyl [e.g. $(BimH)_3$ **II-35**] or pyridyl [e.g. TPMA/$(Py)_3$ **II-34**] residues or contain at least two of the strong chelating benzimidazole substituents. Although a high portion of very strong Cu-binding Bim or Py side arms can effectively shield the reactive metal from dissolved oxygen, their strong affinity towards Cu ions exerts an inhibitory effect on CuAAC catalysis. Consequently, class III Cu/ligand complexes are relatively inactive across a broad range of Cu/ligand ratios.[34]

The following scheme gives an overview of representative class I, class II, and class III ligands (Scheme II.12), based on their constitution (Trz, Py, and Bim side arms) and experimental evidence.



Scheme II.12. Representative CuAAC ligands from classes I, II, and III (classification according to Presolski *et al.* based on experimental evidence). Triazole (Trz) moieties are highlighted in blue, pyridine (Py) moieties in green, and benzimidazole (Bim) moieties in purple.

The only odd and outstanding example of a $(Trz)_3$ ligand classified in group II is DTEA (**II-36**, tris(2-(4-(dimethylaminomethyl)-1*H*-1,2,3-triazol-1-yl)ethyl)amine). In 2011, Michaels and Zhu invented a set of novel symmetrical tris(triazolylethyl)amine-based tetradentate Cu-ligands for a $Cu(OAc)_2$-accelerated click reaction and compared these to commercially available ligands, such as TBTA **II-26** or the water-soluble derivative THPTA **II-27**. Most CuAAC applications rely on the use of Cu(I) as a reactive species, which can be generated under reducing conditions from stable Cu(II) salts, e.g. $Cu(SO)_4$ and $Cu(OAc)_2$, or from their respective hydrates. However, substrates prone to reduction can be coupled under Cu(II) catalysis, assisted by stabilising and activating ligands. The best-performing ligand evaluated by Michaels and Zhu, namely DTEA **II-36**, was active and soluble in water and most organic solvents and outcompeted the mentioned commercial ligands TBTA **II-26** and THPTA **II-27** for a broad spectrum of aromatic and aliphatic azides and alkynes in a Cu(II)-catalysed click reaction.[25] While most nitrogen-containing ligands exclusively harbour nitrogen nuclei in their heterocyclic side arms (Trz, Py, and Bim), the ligand DTEA **II-36** comes with three additional dimethylaminomethyl moieties (Scheme II.12). The additional basicity displayed by these tertiary amines on DTEA contributes in the formation of the Cu-acetylide **II-17** by deprotonation of the acidic alkyne **II-15** and the protonated form of the amine side arms furthermore aids the proteolysis of the Cu-triazolide **II-21** (cf. Scheme II.10). Therefore, DTEA **II-36** not only shields and protects copper ions from oxidising agents and improves the solubility of Cu species, but also speeds up two essential steps of the catalytic CuAAC cycle. As the Lewis-basic amine side arms are expedient to coordinate copper as well and compete with triazolyl moieties in Cu-binding, the additional basicity is the rational

explanation for why DTEA **II-36** can form inhibitory complexes with Cu when used in excess and is therefore categorised as a class II ligand.

II.1.1.3.2 The Synthesis of the Superior Cu(I)/Cu(II)-Ligand DTEA Underlies the Chemical Weapons Convention

Other than the commercial ligands TBTA **II-26** and THPTA **II-26**, the class II Cu-ligand DTEA **II-36** is based on a tris(triazolylethyl)amine core. Owing to the core extension from methyl (TBTA and THPTA) to ethyl (DTEA), Michaels and Zhu introduced an alternative synthetic route to access the novel ligand DTEA **II-36** and similarly substituted ligands, comprising the substitution of tris(2-chloroethyl)amine **II-37** with sodium azide. In the next step, a click reaction with an arbitrary alkyne was used to generate ligands with tunable solubility and catalytic properties.[25] However, the preparation and use of tris(2-chloroethyl)amine **II-37**, which is also known as nitrogen mustard HN3, has severe drawbacks due to its highly toxic and hazardous blister effects (cf. Table II.1), making it a controlled substance from Schedule 1 under the Chemical Weapons Convention (CWC) (*vide infra*).[138, 139]

The origin of the CWC dates back to World War I and II (WWI and WWII) and the Iran-Iraq conflict from 1980, where sulfur-containing mustard gas and other highly cytotoxic chemicals were used as chemical warfare agents.[140-142] Although the Geneva protocol from 1925 was signed to regulate the use of chemical weapons between the 65 ratifying states, it did not govern the production and storage of these weapons or precursors for their production. Thus, the CWC was signed in 1997 to augment the Geneva protocol to set unambiguous rules associated with this group of chemicals between the 193 signatory states.[139] The CWC is a multilateral disarmament and arms control treaty that regulates the production, storage, disposal, and related obligations to control chemical weapons or precursors, which can be used to produce such weapons. In this regard, the CWC allows contracting states to use scheduled chemicals only for the purposes given in Article II No. 9.[139, 143] Those can be specified as follows:

"Purposes not prohibited under this convention" means:

(a) Industrial, agricultural, research, medical, pharmaceutical or other peaceful purposes;

(b) Protective purposes, namely those purposes directly related to protection against toxic chemicals and to protection against chemical weapons;

(c) Military purposes not connected with the use of chemical weapons and not dependent on the use of the toxic properties of chemicals as a method of warfare;

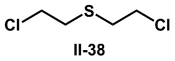
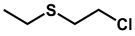
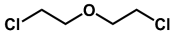
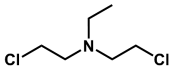
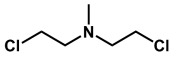
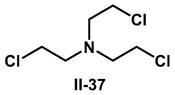
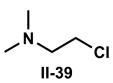
(d) Law enforcement, including domestic riot control purposes.

Facilities that produce, process, consume, dispose, store, or handle scheduled chemicals are subject to regular reporting and inspection obligations. In general, only Schedule 1 chemicals underlie strict restraints regarding permitted actions and purposes, mentioned in Article II, No. 9. Contractual states are not allowed to hold more than 1 ton of Schedule 1 chemicals. Production facilities with quantities >100 g are subject to reporting and inspection obligations (for further information, see CWC appendix, Part VI). Other than Schedule 1 chemicals, Schedule 2 chemicals are not subject to strict obligations according to the CWC. Thus, plant sites are subject to reporting obligations for producing or handling 1 ton per year and inspection obligations for >10 tons per year. However, the state parties are not limited to the production of quantities. Declarations and reports are submitted on an annual basis (CWC appendix, Part VII, A No. 3).

The DTEA precursor and nitrogen mustard HN3 **II-37** ranges in the same magnitude of toxicity as sulfur mustard **II-38**, leading to severe large-area skin burns, lasting destruction of cell tissue,[144] inhibition of cell replication by

DNA double-strand breaks,[145] and compromised lung function or collapse of the respiratory tract due to destruction of the bronchi.[146] All mustards have these so-called blister effects in common, which can be attributed to a 2-chloroethyl group, which is both responsible for their high reactivity and constitutes their ability to alkylate nucleic acid bases, such as *N*7-guanine in DNA and RNA.[147] Consequently, these mustards pose an extremely high risk of mutagenicity to genomic information. To prevent these toxic reagents from being used for the preparation of chemical weapons, the Organisation for the Prohibition of Chemical Weapons (OPCW) strictly controls the production, storage, processing, and disposal of certain oxygen, sulfur, and nitrogen mustards.[139] The cytotoxicity of most mustards ranges in the same order of magnitude as for the well-known poison potassium cyanide (LD_{50} of 5 mg/kg, oral, rats).[148] For example, oral administration of sulfur mustard gas **II-38** to male rats as model organisms resulted in a median lethal dose (LD_{50}) of 2.4 mg/kg (Table II.1).[149] When HN3 **II-37** was dispensed to rats, a slightly increased LD_{50} of 5 mg/kg was reported, proving that Schedule 1 mustards feature an overall very low LD_{50} for mammals.[150] Despite its synthetic benefits as a highly reactive chlorinated precursor, the synthesis of HN3 **II-37** as a Schedule 1 chemical (Schedule 1A06) is strictly prohibited on an industrial scale by the CWC and its synthesis and application are limited to research purposes (*vide supra*).[138] Hence, replacement of Schedule 1 chemicals, such as HN3 **II-37**, by Schedule 2 (e.g. nitrogen half-mustard **II-39**), Schedule 3, or unscheduled chemicals is desired from a synthetic point of view to allow safe application on laboratory scale and to overcome legal synthetic restrictions on industrial scale.

Table II.1. Toxicity data (median lethal dose; LD_{50}) of sulfur, oxygen, and nitrogen mustards, as well as half-mustards for oral administration on male rats.

Name	CWC Annex Schedule	Structure	LD_{50}[a] (mg/kg)	Reference
Sulfur Mustards				
Mustard gas (**II-38**, HD, sulfur mustard)	Schedule 1 (1A04)	 **II-38**	2.4	[149, 150]
2-Chloroethyl ethyl sulphide (CEES, sulfur half-mustard)	not scheduled		252	[150]
Oxygen Mustards				
Bis(2-chloroethyl) ether (BCEE, oxygen mustard)	not scheduled		75	[151]
Nitrogen Mustards				
2-Chloro-*N*-(2-chloroethyl)-*N*-ethylethan-1-amine (HN1, nitrogen mustard)	Schedule 1 (1A06)		2.5	[152]
2-Chloro-*N*-(2-chloroethyl)-*N*-methylethan-1-amine (HN2, nitrogen mustard)	Schedule 1 (1A06)		10	[152]
Tris(2-chloroethyl)amine (**II-37**, HN3, nitrogen mustard)	Schedule 1 (1A06)	 **II-37**	5	[152]
2-Chloro-*N*,*N*-dimethylethan-1-amine (**II-39**, nitrogen half-mustard)	Schedule 2 (2B10)	 **II-39**	238	[153]

[a] Half-maximal lethal dose (LD_{50}) for oral administration on rats.

II.2 Aims

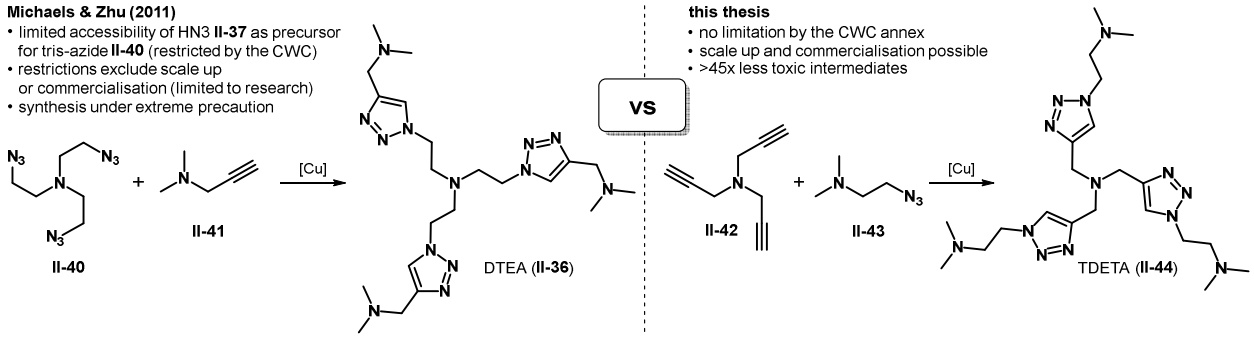
Click chemistry emerged around 20 years ago and with the development of the copper-catalysed azide-alkyne cycloaddition (CuAAC) reaction and subsequent advancements, CuAAC has become a “workhorse” in the field of modular bioorthogonal chemistry. Nitrogen-containing ligands coordinate Cu(I) and Cu(II) ions and cause a significant reaction rate acceleration in CuAAC reactions, by increasing Cu solubility, preventing Cu oxidation and ROS-generating side reactions, and by promoting the formation of intermediate species of the CuAAC catalytic cycle. Commercially available gold standard ligands, such as TBTA **II-26** and THPTA **II-27**, were specifically designed for applications in organic or aqueous solvents, respectively. However, both ligands are weak Cu binders and lack steadfastness in strong donor solvents. The alternative ligand DTEA **II-36** tolerates a broad variety of solvents, including aqueous and organic media. Nonetheless, its synthesis is tightly regulated by the Chemical Weapons Convention (CWC), as it relies on the highly toxic blister agent and nitrogen mustard HN3 **II-37**. Hence, DTEA **II-36** can only be synthesised under strict safety precautions, and its application is limited to academic research.

Chapter II aims to leverage the physico-chemical and catalytic advantages of the basic triazolyl CuAAC ligand DTEA **II-36** while developing a legal and chemically distinct alternative not restricted by the Chemical Weapons Convention (CWC). Thus, the ultimate goal of this chapter is to devise a CuAAC ligand that is safe to handle and free from regulatory restrictions, enabling efficient and streamlined syntheses of valuable biotinylated biological conjugates. By optimising the synthetic route towards this novel CuAAC ligand, the risk associated with the highly toxic DTEA precursor and nitrogen mustard HN3 **II-37** will be avoided while harnessing the versatility and bioorthogonality of the CuAAC click reaction.

II.3 Results and Discussion

II.3.1 Synthesis of TDETA as Legal Alternative for DTEA

The positive effects of DTEA **II-36** as Cu-chelating amine ligand on CuAAC acceleration, combined with the limitations imposed by the CWC on large-scale preparation of this superior ligand, drove our interest to develop a strategy that maximises these benefits while circumventing the use of toxic nitrogen mustard HN3 **II-37**. The original synthesis of DTEA **II-36** published by Michaels and Zhu was introduced with tris(2-azidoethyl)amine (**II-40**) and *N*,*N*-dimethylpropargylamine (**II-41**) for the final CuAAC-catalysed click reaction (Scheme II.13). To fulfil our formulated synthetic aim of circumventing the use of HN3 **II-37**, we selected tripropargylamine (**II-42**) and 2-azido-*N*,*N*-dimethylethan-1-amine (**II-43**) as respective substitutes (Scheme II.13), and thereby contemplating an inversion of alkyne and azide moieties in comparison to the original click reaction leading to DTEA **II-36**.

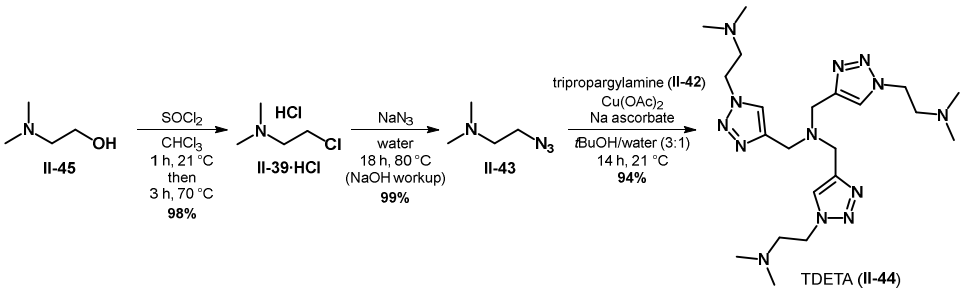


Scheme II.13. Comparison of direct precursors for the copper-ligand DTEA **II-36**, which is based on the nitrogen mustard HN3 **II-37**, and the novel ligand TDETA **II-44** that allows large-scale synthesis and safe handling of reagents.

Similar to the preparation of DTEA, the reactive azide **II-42** is synthesised from a mustard-like precursor, but instead of HN3 we intended to use the half-mustard 2-chloro-*N*,*N*-dimethylethan-1-amine **II-39**. The toxicity of the half-mustard **II-39** is more than 45-fold reduced compared to HN3 **II-37**, and more importantly, it is not classified as a Schedule 1 chemical in the CWC annex (cf. Table II.1).[150, 153] Furthermore, tripropargylamine **II-42** serves as a common and safe-to-handle precursor for the commercially available ligands TBTA **II-26** and THPTA **II-27** and is therefore an industrially improved precursor. The devised tris-functionalised triazole ligand, emerging from the click reaction between tripropargylamine (**II-42**) and 2-azido-*N*,*N*-dimethylethan-1-amine **II-43**, will be named TDETA[1] **II-44**.

The chemical synthesis of the novel tripodal ligand TDETA commenced with the transformation of inexpensive 2-(*N*,*N*-dimethylamino)-ethanol (**II-45**) into the corresponding hydrochloride of (2-chloroethyl)dimethylamine (**II-39·HCl**) (Scheme II.14). By reacting the aminoethanol **II-45** with thionyl chloride, the desired (chloroethyl)amine **II-39·HCl** was synthesised in a yield of 98%. The half-mustard (chloroethyl)amine **II-39·HCl** is listed in the CWC annex as a Schedule 2 chemical (Schedule 2B10) by the OPCW. Other than Schedule 1 chemicals (e.g. HN3 **II-37**) and their precursors, synthesis and application on ton scale is permitted under tight safety precautions and data monitoring (cf. Chapter II.1.1.3.2). Actually, (2-chloroethyl)dimethylamine hydrochloride (**II-39·HCl**) is amongst the most traded scheduled chemicals and used for the synthesis of agricultural chemicals, numerous medicinal drugs (e.g. Diltiazem, Doxylamine, Chlorphenoxamine HCl) or special purpose chemicals that find

[1] TDETA is a non-IUPAC conform nomenclature and is the acronym for **t**ris **d**imethyl**e**thyl **t**riazolyl **a**mine [IUPAC name: 2-(4-((bis((1-(2-(dimethylamino)ethyl)-1*H*-1,2,3-triazol-4-yl)methyl)amino)methyl)-1*H*-1,2,3-triazol-1-yl)-*N*,*N*-dimethyl-ethan-1-amine].



Scheme II.14. Synthesis of the Cu(I)/Cu(II)-ligand TDETA **II-44** as a safe and legal alternative to DTEA **II-36**.

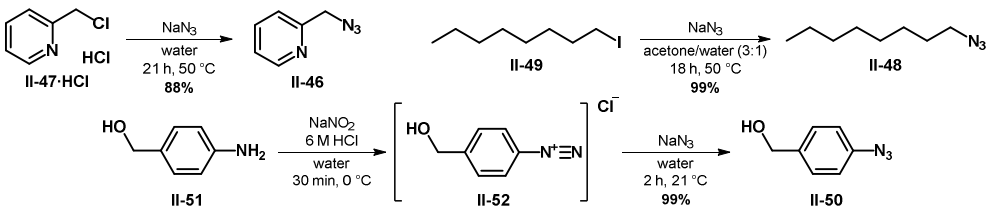
application as surfactants, surface disinfectants, and flocculants.[154] In the following step, sodium azide was utilised to substitute the halide and form 2-azido-*N*,*N*-dimethylethan-1-amine (**II-43**) after neutralisation of the HCl salt with aqueous NaOH. The very volatile azide was obtained in a yield of 99%. Previous reported syntheses under similar reaction conditions with Et_2O extraction led to significantly lower yields, providing 56%[155], 60%[156] or 81% of the desired azide.[157] Substitution of volatile Et_2O by less volatile EtOAc for extraction yielded even less product (40%[158]), caused by the prolonged time under high vacuum needed to thoroughly remove the solvent. Hence, the cited works emphasise that those conditions are required for high yields, which reduce the exposure of azide **II-43** to low pressures or high vacuum for a prolonged time. This prerequisite was addressed by co-evaporating volatile Et_2O, the low-boiling extraction solvent, through repeated additions of *n*-pentane, which minimised the needed exposure to low pressures and allowed for the predominant removal of solvent at pressures >800 mbar. It is also worth mentioning that (2-chloroethyl)dimethylamine (**II-39**) should be used in its hydrochloride form for the synthesis of azide **II-43**, and deprotonation of the HCl salt with KOH or NaOH should proceed after azide substitution, as performed in the route mentioned above. When the nitrogen of half-mustard **II-39** is protonated, its nucleophilicity is substantially lower than in the free base, depleting the risk of an undesired intramolecular nucleophilic attack of the terminal chlorine atom and the subsequent formation of *N*,*N*-dimethylaziridin-1-ium chloride at elevated temperatures. This intramolecular cyclisation is the cause for the high cytotoxicity of (nitrogen) mustards and the cytotoxic alkylation of nucleic acids *in vivo*.[159] Azide **II-43** is also considered a potential replacement for the commonly used but environmentally hazardous monomethylhydrazine (MMH) as rocket fuel and spaceship propellant,[160] highlighting the relevance of its precursor (2-chloroethyl)dimethylamine (**II-39**) as an important building block in industrial chemistry.

With the azide **II-43** in hand, the synthetic effort was directed toward completing the final step of TDETA assembly. Lastly, a self-accelerated and copper-catalysed click reaction between azide **II-43** and tripropargylamine (**II-42**) furnished the desired amine-ligand TDETA **II-44**. The strongly exothermic reaction provided TDETA **II-44** as a convenient white amorphous powder in an excellent yield of 94% after column chromatography (Scheme II.14), resulting in a combined yield of 86% over three synthetic steps.

II.3.1.1 Preparation of Suitable Substrates for the Evaluation of CuAAC Ligands

To elicit prospects and assess catalytic properties of the new (dimethylamino)ethyl-substituted ligand TDETA **II-44**, TDETA was compared to its cognate ligand DTEA **II-36** and other ligands from the literature.[25] However, as the synthesis of DTEA underlies the CWC and includes the highly toxic nitrogen mustard HN3 **II-37**, we opted to choose the identical sets of organic azides and alkynes as employed by Michaels and Zhu in their characterisation of DTEA. Using the original literature conditions and substrates makes it possible to draw direct comparisons without the need to perform the hazardous synthesis of DTEA on our own. From the set of desired organic azides and alkynes, only the alkynes were fully available from commercial sources. For the azides instead,

only benzyl azide was available from suppliers. Thus, we first concentrated on the preparation of organic azides (Scheme II.15, cf. Table II.2). 2-(Azidomethyl)pyridine (**II-46**) was synthesised according to a modified protocol from Ogden *et al*.,[161] namely azide substitution of 2-(chloromethyl)pyridine hydrochloride (**II-47·HCl**) in water at 50 °C. Simple basic extraction with 1 M NaOH for deprotonation of the hydrochloride yielded 88% of the organic azide **II-46** without further purification. Similarly, the preparation of 1-azidooctane (**II-48**) was attempted from the corresponding iodide **II-49** according to Gannarapu *et al*.[162] However, the lipophilic character of the aliphatic halide required acetone as a co-solvent to prevent the formation of a two-phase system with iodooctane **II-49** and the reaction solvent water. As before, extractive workup provided the aliphatic azide **II-48** in a yield of 99% without the need for further processing. In contrast to the two previous halide substitution reactions, (4-azidophenyl)methanol (**II-50**) was accessed via diazotisation of 4-aminobenzyl alcohol (**II-51**). Therefore, the aminobenzyl alcohol **II-51** was converted with nitrous acid (generated from $NaNO_3$ and 6 M HCl) into the corresponding intermediate diazonium salt **II-52** and the addition of sodium azide finally gave rise to the desired (4-azidophenyl)methanol (**II-50**), formed through an acyclic zwitterionic intermediate, in an excellent yield of 99%.[163, 164]



Scheme II.15. Synthesis scheme for the preparation of organic azides **II-46**, **II-48**, and **II-50** as substrates for benchmarking Cu-ligands.

II.3.1.2 Ligand Screening for CuAAC under Mild Cu(II) Catalysis

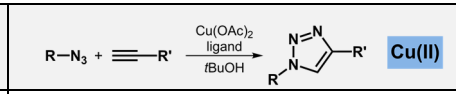
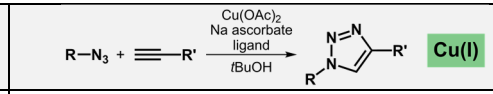
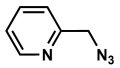
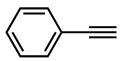
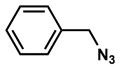
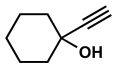
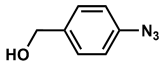
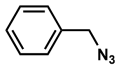
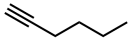
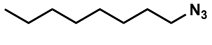
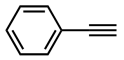
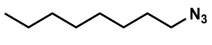
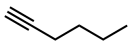
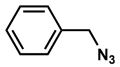
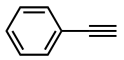
The (dimethylamino)ethyl-substituted Cu-ligand DTEA **II-36** was shown to be a superior ligand for Cu(II) in organic solvents. Since DTEA outperformed the commercially available ligands TBTA **II-26** and THPTA **II-27** in accelerating the CuAAC reaction with a representative selection of aromatic and aliphatic azides and alkynes,[25] we desired to compare the new ligand TDETA **II-44**, the cognate DTEA **II-36** and those ligands from the literature. Even though Cu(I) is the more potent and widely used as a catalyst in CuAAC, the milder Cu(II) source $Cu(OAc)_2$ was employed in *t*BuOH to draw an immediate comparison between our data and literature records (Table II.2). The time-resolved experiment was TLC-based (thin-layer chromatography), allowing for the detection the time point of complete azide consumption during the course of the reaction.

The first example between the basic pyridine derivative 2-(azidomethyl)pyridine (**II-46**, pyridyl azide) and phenylacetylene (**II-53**) showed complete conversion after 60 min in the absence of any stabilising ligand (Table II.2, entry 1, column 1). Only DTEA significantly accelerated the reaction, reducing the reaction time to 2.5 min. When TBTA was used instead, a 4-fold increase was observed in comparison to the non-catalysed reaction, leading to a shortened reaction time of 15 min. With the water-soluble ligands THPTA and TDETA, only a minor impact on reaction rates was observable, as THPTA rendered complete conversion after 40 min and TDETA after 50 min. TLC analysis showed that the ligand-free reaction with Cu(II) exhibited a faster initiation, as evidenced by the early consumption of starting material. In contrast, reactions with the rate-accelerating ligands THPTA and TDETA started more slowly but accelerated in the later stages, ultimately reaching completion before the ligand-free reaction. Based on these results, it was concluded that the pyridyl azide **II-46**, which is capable of forming a five-membered Cu(II) complex,[165] competes with other ligands for copper(II) ions. The reaction rate

acceleration is thus not only affected by the affinity of the triazole ligands to Cu(II), but also by the affinity of the reaction substrate pyridyl azide **II-46** to Cu(II). Only when the azide is consumed over time do the copper ions become available for the triazole ligand to a greater extent, and the reaction is accelerated in the desired manner.

Except for the aforementioned combination of pyridyl azide **II-46** and phenylacetylene (**II-53**), the application of TDETA was related to an enhanced reaction rate greater than that of the commercial ligands TBTA and THPTA. When reacting electron-rich azides with non-aromatic alkynes, the (dimethylamino)ethyl ligands TDETA **II-44** and DTEA **II-36** had comparable impacts on the acceleration of CuAAC reactions. Benzyl azide (**II-2**) and 1-ethynyl-1-cyclohexanol (**II-54**) were converted within 10 min with TDETA and 15 min with DTEA, while THPTA and TBTA indicated full conversion after 30 or 20 min, respectively, compared to 60 min reaction time in the absence of any ligand (Table II.2, entry 2, column 1). 1-Azido-4-(hydroxylmethyl)-benzene (**II-50**) and the aliphatic propargyl alcohol (**II-55**) were not converted to the triazolyl product in the absence of any ligand. While THPTA rendered complete conversion after 60 min, TBTA, TDETA, and DTEA allowed thorough consumption of azide after 20, 15 and 5 min (Table II.2, entry 3, column 1). The Cu(II)-catalysed click reaction between benzyl azide (**II-2**) and 1-hexyne (**II-56**) is an apt example of how Cu-ligands can affect the outcome of the click reaction. While the presence of the water-soluble THPTA had no effect on the reaction and left the educts unconverted after 60 min, the addition of TBTA facilitated a conversion of 74% within the same period. Seemingly, THPTA facilitates the conversion of a broad variety of aliphatic and aromatic azides under non-reducing conditions, but aliphatic alkynes are not converted. However, the dimethylamino-substituted ligands DTEA and TDETA demonstrated notable acceleration. The reaction between benzyl azide (**II-2**) and 1-hexyne (**II-56**) showed full conversion with DTEA within 60 min and our novel ligand TDETA was able to reduce the reaction time further to 20 min (Table II.2, entry 4, column 1). Even the more demanding electron-poor aliphatic octyl azide (**II-48**) was converted with phenylacetylene (**II-53**) by less reactive Cu(II) species in less than 30 min with our Ligand TDETA, while TBTA and THPTA aided complete conversion after 35 and 50 min, respectively (Table II.2, entry 5, column 1). No conversion was observed for the non-ligated Cu(II) instead. However, the combination of aliphatic octyl azide (**II-48**) and aliphatic 1-hexyne (**II-56**) was neither converted with the help of TDETA nor any other ligand under the milder Cu(II) catalysis (Table II.2, entry 6, column 1). This may be attributed to the high redox potential of the Cu(II) catalyst in combination with the relatively unreactive aliphatic azides and alkynes. To circumvent this limitation of Cu(II)-catalysed CuAAC reactions, more reactive Cu(I) species are typically used as the catalytically active transition metal. In conclusion, the new ligand TDETA **II-44** outperforms the commercial ligands TBTA and THPTA under Cu(II)-promoted catalysis for a wide variety of aliphatic and aromatic substrates and is on par with the HN3-based ligand DTEA **II-36**, emphasising the versatility of the ligand and the assets of the safe-to-perform synthesis under the circumvention of nitrogen mustard HN3.

Table II.2. Comparison of Cu-stabilising ligands in Cu(II)-accelerated CuAAC[a] and a Cu(I)-accelerated CuAAC[a][b] reaction with sodium ascorbate as reducing agent.

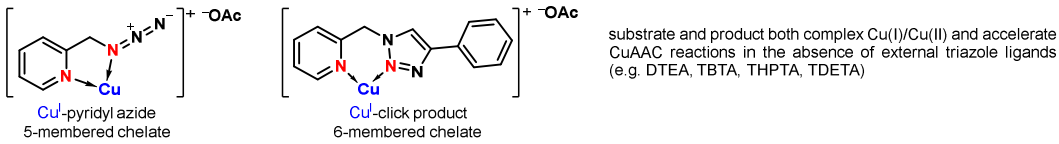
					 Cu(II)			 Cu(I)		
Entry	**Azide**	**Alkyne**	**Product**	**Ligand**	**Reaction time [min][c]**	**Conversion [%][d]**	**Reference**	**Reaction time [min][c]**	**Conversion [%][d]**	**Reference**
1	 II-46	 II-53	**II-57a**	none	60	100	this work	5	100	this work
				TBTA	15	100	this work	<2.5	100	this work
				THPTA	40	100	this work	n.d.	n.d.	-
				DTEA	2.5	100	[25]	n.d.a.	n.d.a.	-
				TDETA	50	100	this work	5	100	this work
2	 II-2	 II-54	**II-57b**	none	60	100	[25]	40	100	this work
				TBTA	20	100	[25]	7.5	100	this work
				THPTA	30	100	[25]	n.d.	n.d.	-
				DTEA	15	100	[25]	n.d.a.	n.d.a.	-
				TDETA	10	100	this work	7.5	100	this work
3	 II-50	 II-55	**II-57c**	none	60	0	[25]	60	4	this work
				TBTA	20	100	[25]	7.5	100	this work
				THPTA	60	100	[25]	n.d.	n.d.	-
				DTEA	5	100	[25]	n.d.a.	n.d.a.	-
				TDETA	15	100	this work	10	100	this work
4	 II-2	 II-56	**II-57d**	none	60	0	[25]	60	49	this work
				TBTA	60	74	[25]	35	100	this work
				THPTA	60	0	[25]	n.d.	n.d.	-
				DTEA	60	100	[25]	n.d.a.	n.d.a.	-
				TDETA	20	100	this work	20	100	this work
5	 II-48	 II-53	**II-57e**	none	60	0	this work	60	26	this work
				TBTA	35	100	this work	<2.5	100	this work
				THPTA	50	100	this work	n.d.	n.d.	-
				DTEA	60	100	[25]	n.d.a.	n.d.a.	-
				TDETA	30	100	this work	<2.5	100	this work
6	 II-48	 II-56	**II-57f**	none	60	0	this work	45	100	this work
				TBTA	60	0	this work	7.5	100	this work
				THPTA	60	0	this work	n.d.	n.d.	-
				DTEA	n.d.a.	n.d.a.	[25]	n.d.a.	n.d.a.	-
				TDETA	60	0	this work	7.5	100	this work
7	 II-2	 II-53	**II-57g**	none	25	100	this work	60	46	this work
				TBTA	5	100	this work	5	100	this work
				THPTA	7.5	100	this work	n.d.	n.d.	-
				DTEA	n.d.a.	n.d.a.	[25]	n.d.a.	n.d.a.	-
				TDETA	5	100	this work	5	100	this work

[a] Conditions: azide (0.20 mmol), alkyne (1.05 eq.), *t*BuOH (0.5 mL), $Cu(OAc)_2$ (25 µL, 0.4 M in H_2O, 5 mol%), ligand (5 mol%). [b] Additional sodium ascorbate (10 µL, 2 M in H_2O). [c] Reaction times were determined by monitoring the complete consumption of the azide through TLC via UV exposure or azide stain.[166] [d] Conversions towards the triazole products **II-57a–g** were deduced from ^{1}H NMR spectra of the crude products. n.d.a.: No data available from DTEA reference,[25] n.d.: not determined.

II.3.1.3 Ligand Screening for CuAAC Under Reducing Cu(I) Conditions

The introduced ligand TDETA **II-44** was highlighted as a competitive alternative to DTEA **II-36** and the commercially available ligands TBTA and THPTA under mild Cu(II) catalysis (cf. Table II.2). Therefore, it poses great potential to enable the coupling of delicate substrates prone to reduction in the presence of reducing agents. However, the most common copper sources are typically Cu(I) species, which have been reduced by an excess of sodium ascorbate *in situ* from a Cu(II) source, such as $CuSO_4$ or $Cu(OAc)_2$. This prompted us to further investigate and compare the ligand TDETA **II-44** to the widely distributed and applied ligand TBTA. In adaptation to our previous investigation with catalytic Cu(II) species (cf. Table II.2, column 1), the reaction parameters were kept constant, except for the addition of 10 mol% aqueous sodium ascorbate. Since performance data for DTEA with Cu(I) are not available, the following section solely focuses on the comparison between TDETA and the most frequently used ligand TBTA (Table II.2, column 2), using the same azides and alkynes as described for the Cu(II)-catalysed CuAAC reactions.

Cu(I) catalysis of the click reaction between pyridyl azide (**II-46**) and phenylacetylene (**II-53**) rendered full consumption of the azide in less than 5 min for the non-ligated copper (Table II.2, entry 1, column 2). Comparing this outcome to the Cu(II)-catalysed non-ligated reaction with a conversion within 60 min, impressively underlines that Cu(I) is the more potent catalyst for CuAAC reactions. The addition of TDETA did not improve the reaction acceleration (5 min), however, the reaction had finished within 2.5 min with TBTA. As already pointed out for the Cu(II)-catalysed reaction (cf. Table II.2, entry 1, column 1), the Cu-binding properties of pyridyl azide (**II-46**) allow for complexation of free copper in a five-membered ring that stabilises Cu(I)/Cu(II). Consequently, this substrate- and product-mediated Cu-binding accounts for the exceptional acceleration without additional ligand in comparison to all other ligand-free control reactions (Scheme II.16).



Scheme II.16. Pyridyl azide **II-46** and its click products are able to complex catalytic Cu(I) and Cu(II) species, superseding the need for external ligands.

For the reaction between benzyl azide (**II-2**) and 1-ethynyl-1-cyclohexanol (**II-54**), the reaction time of 20 min (TBTA) and 10 min (TDETA) for the Cu(II)-catalysed reaction was decreased to 7.5 min for both ligands, when the more reactive Cu(I) was used instead. In contrast, the ligand-free reaction was finished after 40 min (Table II.2, entry 2, column 2). A comparable rate acceleration was obtained for the reaction between 1-azido-4-(hydroxylmethyl)-benzene (**II-50**) and propargyl alcohol (**II-55**) (Table II.2, entry 2, column 2). Here, TBTA was slightly superior to TDETA, characterised by an increased acceleration with completion of the reaction after 7.5 min in comparison to 10 min, respectively. Without supplementation of stabilising ligands, only 4% conversion was achieved for the same reaction after 60 min, giving a comparable result to the reaction with Cu(II) species (cf. Table II.2, entry 3, column 1 and 2). The reactions between benzyl azide (**II-2**) and the less reactive aliphatic 1-hexyne (**II-56**) (Table II.2, entry 4, column 2) or the aromatic phenylacetylene (**II-53**) (Table II.2, entry 7, column 2) exhibited slow progress in the absence of ligands, too, culminating in respective conversions of 49% or 46% when the Cu(I)-promoted click reactions were allowed to react for 60 min. With the application of Cu-stabilising triazole ligands, the reaction times were drastically decreased. While the reaction between benzyl azide (**II-2**) and 1-hexyne (**II-56**) showed completion with TBTA after 35 min, TDETA **II-44** reduced the reaction time

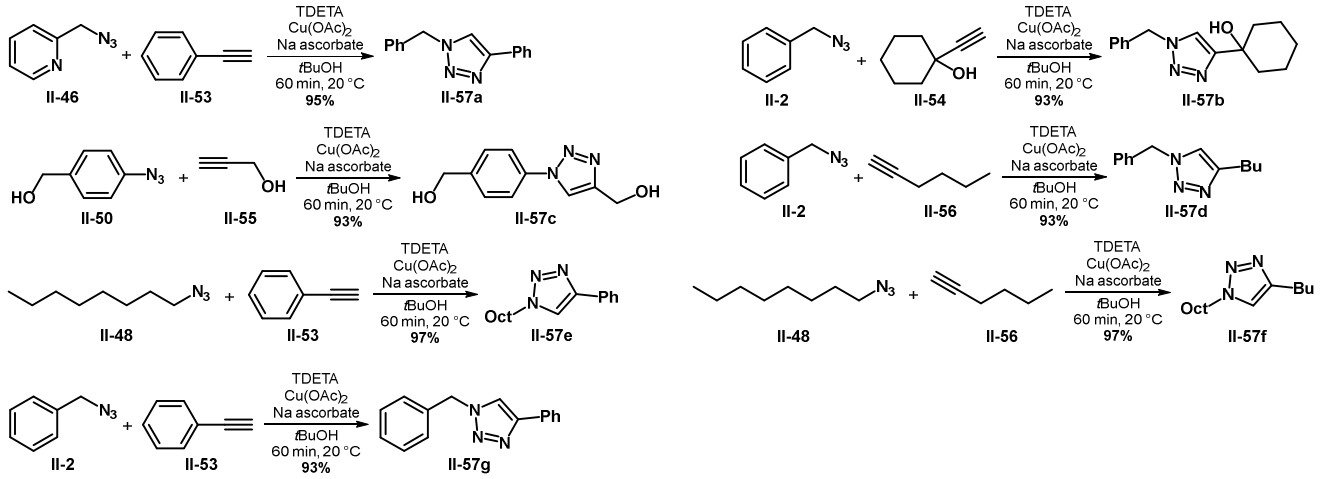
down to 20 min (Table II.2, entry 4, column 2). Replacement of the alkyne from hexyne **II-56** to the more reactive phenylacetylene (**II-53**) facilitated complete conversion with TBTA and TDETA **II-44** after 5 min and provided the corresponding triazole (Table II.2, entry 7, column 2). Moving from the electron-rich azides to the electron-poor 1-azidooctane (**II-48**) and its Cu(I)-catalysed click reaction with phenylacetylene (**II-53**) showed full azide consumption within 2.5 min when TBTA and TDETA **II-44** were used as ligands (Table II.2, entry 5, column 2). The ligand-free control, however, merely provided 26% conversion after 60 min of reaction time. The coupling reaction between two electron-deficient aliphatic azides and alkynes previously failed by means of Cu(II) catalysis. On the example of 1-azidooctane (**II-48**) and 1-hexyne (**II-56**), it was shown that even rate-accelerating ligands are not capable of activating the copper to overcome the activation energy barrier to form the corresponding triazole product. By applying TBTA and TDETA **II-44** in the Cu(I)-catalysed click reaction of 1-azidooctane (**II-48**) and 1-hexyne (**II-56**), fast formation of the desired triazole was observed in less than 7.5 min (Table II.2, entry 6, column 2). However, the ligand-free reaction also yielded complete conversion after 45 min.

Taken together, even utilising the more reactive system of Cu(I) and sodium ascorbate does not facilitate the formation of all click products **II-57a**–**g** without the use of Cu-stabilising ligands. Both tested ligands, namely the purchasable TBTA and our novel ligand TDETA **II-44**, showed minor differences in rate acceleration for a broad range of aliphatic and aromatic azides and alkynes and disclose their potential as CuAAC ligands. Summarising the data from Table II.2 with results of Cu(I)- and Cu(II)-catalysed CuAAC reactions, the basic ligands TDETA and DTEA operated with similar acceleration under Cu(II) catalysis, whereas TBTA was accompanied by broad applicability, albeit with an overall slower reaction rate. THPTA, as a commercial water-soluble alternative, revealed the narrowest scope of accepted azide/alkyne pairs, did not accept aliphatic alkynes, and showed the least acceleration in organic solvent, here represented by the protic polar solvent *t*BuOH. For this reason, TDETA **II-44** in combination with Cu(II) might be of special interest for organic syntheses with molecules prone to reduction in the presence of reducing agents, such as sodium ascorbate. Utilisation of the latter reagent for *in situ* generation of Cu(I) species promoted the click reaction in the same order of magnitude when using either TBTA or TDETA **II-44** as ligands, even though TBTA is poorly soluble in *t*BuOH. Hence, the array of tested substrates and the overall broad acceptance of aliphatic and aromatic azides and alkynes in Cu(I)- and Cu(II)-catalysed CuAAC reactions qualify TDETA as a superior ligand to the commercial alternative THPTA and as equally versatile to DTEA and the gold-standard ligand TBTA. Since the presented preparative synthesis of TDETA is not subject to the legal restrictions and obligations of the CWC, and its synthetic intermediates are safe to handle, TDETA is a competitive CuAAC ligand compared to commercially available tripodal triazole ligands.

II.3.1.4 Validation of TDETA in Preparative Organic Chemistry

Besides comparative kinetic investigations on TDETA **II-44** and other Cu-ligands on a small scale, we set out to synthesise all click products from Table II.2 in preparative yields to evaluate the preparative utility of TDETA **II-44** in chemical applications. Therefore, azides (1.00 eq.) and alkynes (1.05 eq.) were allowed to react in *t*BuOH in the presence of 5 mol% TDETA and $Cu(OAc)_2$ under reducing conditions with sodium ascorbate. Subsequently, the reaction products were directly purified by column chromatography without a prior aqueous extraction. It is worth mentioning that the exceptionally high water affinity of TDETA **II-44** favours its migration into the aqueous phase during aqueous workup. Hence, the aqueous extraction of the Cu-TDETA-complex in TDETA-assisted reactions practically supersedes the chromatographic removal of copper salts and ligand in reactions with complete substrate conversion. TBTA instead remains in the organic phase and must be removed by chromatographic means. All performed reactions provided the corresponding click products **II-57a**–**g** on a scale of up to 728 µmol or 180 mg in excellent yields of 93–97% (Scheme II.17), underlining the broad substrate scope

of TDETA **II-44** and its tolerance towards aliphatic and aromatic combinations of organic azides and alkynes. Consequently, TDETA **II-44** is not only applicable in small-scale CuAAC click reactions but also useful in preparative reactions (up to 180 mg isolated). Additionally, TDETA **II-44** was feasible for recovery in a click reaction on a scale of 4 mmol azide in a yield of 80%, greatly enhancing the precious ligand's economic value.



Scheme II.17. Preparative synthesis of 1,2,3-triazoles **II-57a–g** via Cu(I)-catalysed click chemistry under the assistance of the novel Cu-ligand TDETA **II-44**.

II.3.1.5 Stress Test of TDETA under Aqueous Conditions

Owing to the fact that all screening reactions so far were exclusively carried out in the protic polar solvent *t*BuOH for comparability to literature data, a broader evaluation of suitable solvents for TDETA **II-44** solvation was desired. It was found that the novel ligand is merely insoluble in aliphatic hydrocarbons and ethers, such as *n*-heptane, Et_2O, and MTBE, respectively, rendering these solvents ineligible for solvation of TDETA (<0.5 mg/mL) or as reaction solvents in TDETA-assisted CuAAC reactions. However, TDETA holds excellent solubility properties in many standard laboratory solvents, such as CH_2Cl_2, acetone, DMSO, DMF, alcohols (MeOH, EtOH, *i*PrOH, *t*BuOH), acetonitrile, 1,4-dioxane, THF, pyridine, water (>250 mg/mL), EtOAc and toluene (60 mg/mL). In contrast, the commercial ligand TBTA, for instance, is only soluble in DMSO, DMF, CH_2Cl_2, and THF, but is insoluble in alcohols or water. The other commercial ligand, THPTA, instead is well-soluble in DMSO, DMF, MeOH, and water. Although TBTA and THPTA possess excellent solubility in a wide range of organic solvents or water, respectively, they exhibit far less broad solvent promiscuity than the new ligand TDETA. A significant benefit of TDETA is its affinity for water. Hence, TDETA and copper are readily removed simultaneously by aqueous extraction from any water-immiscible solvent and do not require purification by chromatographic means. The outstanding solubility of TDETA in water and aqueous buffer solutions suggests biological application, e.g. for *in vivo* cell labelling or preparation of biological conjugates, such as RNA, proteins, small molecules, by means of CuAAC. Although CuAAC reactions in organic solvents often do not necessarily require ligands (cf. Table II.2), those approaches in aqueous biological environments typically fail without additional ligands. This is owing to the fact that many cellular metabolites, but also buffer substances (e.g. Tris, HEPES), chelate copper and might hamper the *in situ* availability of Cu(I) or Cu(II) species needed for catalysis. As the catalytic activity of ligands in aqueous CuAAC reactions is a crucial prerequisite for their application in complex biological systems, we aimed to benchmark the performance of TDETA in an aqueous reaction setup. Free copper, TDETA, THPTA, and the broadly applied TBTA were evaluated for their ability to accelerate the CuAAC click reaction between propargyl alcohol (**II-55**) and 3-azido-7-hydroxycoumarin (**II-58**) in phosphate buffer (KP_i) at neutral pH (Figure II.4A). The emerging

coumarin click product **II-59** exhibits strong fluorescence at 477 nm, which facilitates continuous reaction monitoring via fluorescence measurements.[118]

During the initial comparison of all ligands at a copper loading of 50 µM and a Cu:ligand ratio of 1:5, it was noted that the commercially available hydrophobic ligand TBTA displayed no acceleration of the dipolar cycloaddition between propargyl alcohol (**II-55**) and azide **II-58** (Figure II.4C). Instead, the monitored fluorescence increase was comparable to the ligand-free reaction with $CuSO_4$. This observation can be attributed to the insolubility of the TBTA ligand in aqueous solutions and the lack of availability of the Cu-stabilising ligand. There are two possible explanations related to TBTA solubility, explaining the absence of reaction rate acceleration of the CuAAC reaction in the presence of the TBTA ligand. On the one hand, the essential copper can be trapped in an insoluble complex with the ligand, resulting in a phase transfer-limited heterogeneous catalyst. On the other hand, the copper may remain non-ligated in the aqueous media under constant exposure to the oxidising atmosphere. In contrast, the addition of the alternative water-soluble ligands TDETA and THPTA to the reaction resulted in a significant acceleration of the reaction and led to conversions >90% after 60 min in direct competition with TBTA and non-ligated copper at Cu:ligand ratios of 1:5. Summarising the current results, the addition of TBTA to the CuAAC reaction between propargyl alcohol (**II-55**) and the coumarin azide **II-58** had no beneficial effect on reaction acceleration in aqueous buffer and performed as the non-ligated Cu(I) species. When the ligand was used in a 5:1 ratio with the Cu(I) species, the water-soluble ligands THPTA and our new ligand TDETA significantly accelerated the reaction rate, with a superior performance in rate acceleration and conversion for the commercially available THPTA.

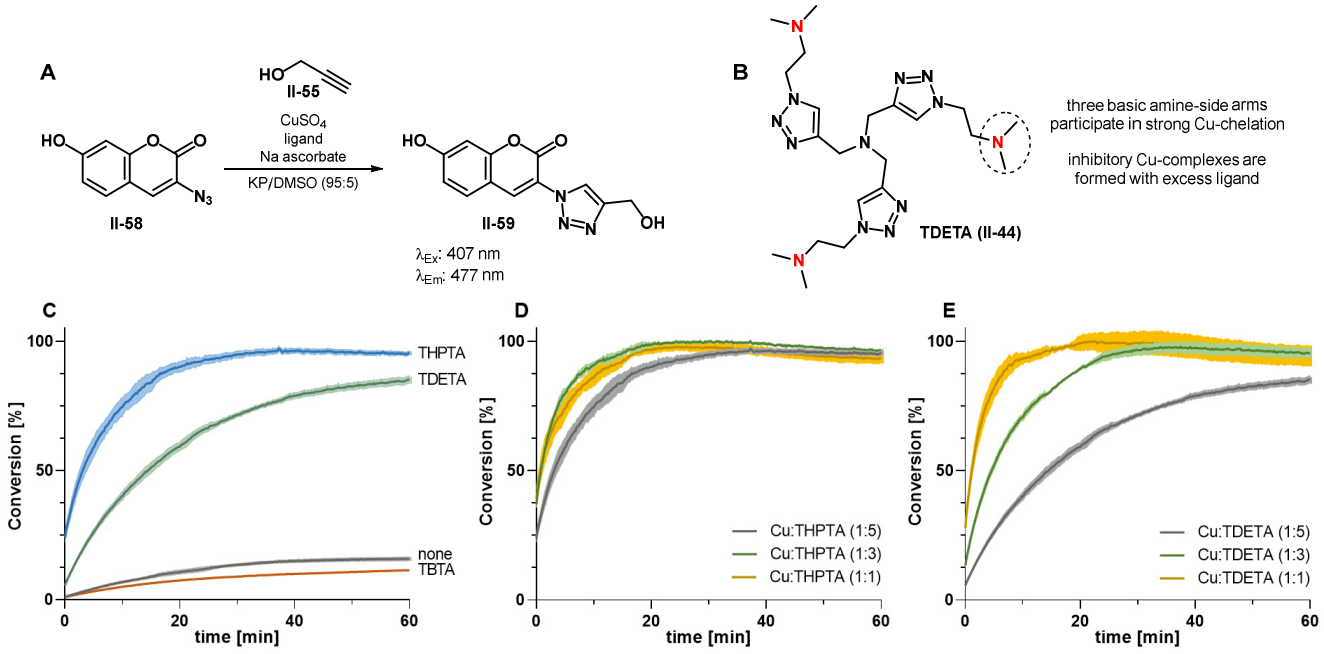


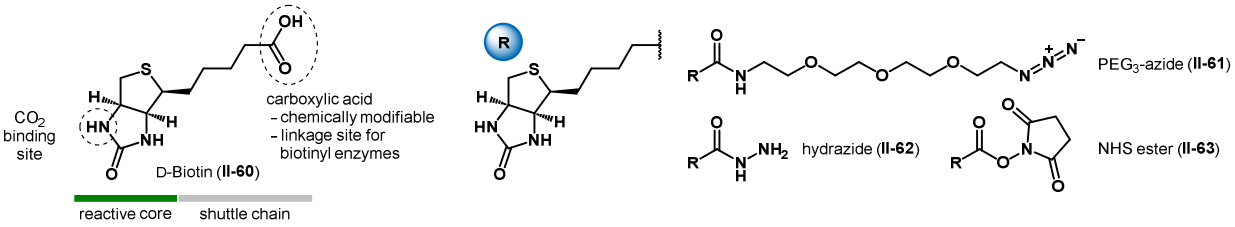
Figure II.4. Fluorometric analysis of aqueous CuAAC click reactions. **A**. Fluorometric assay for comparison of Cu-stabilising ligands. Formation of the 1,2,3-triazole ring in click product **II-59** causes fluorescence enhancement at 477 nm. **B**. Structure of the novel CuAAC ligand TDETA **II-44**. **C**. Fluorometric assay for comparison of CuAAC accelerating ligands TBTA, THPTA, and TDETA in aqueous buffer. The fluorescence trace at 477 nm for visualising the emerging click product **II-59** is shown for each condition (n=4). Conversion with 50 µM Cu(I) loading and Cu-ligands TBTA, THPTA, and TDETA in a Cu:ligand ratio of 1:5. **D**. Conversion with 50 µM Cu(I) loading and THPTA in Cu:ligand ratios of 1:5, 1:3, and 1:1. **E**. Conversion with 50 µM Cu(I) loading and TDETA in Cu:ligand ratios of 1:5, 1:3, and 1:1.

For an estimation of the importance of Cu:ligand ratios for the best-performing ligands THPTA and TDETA, the impact of decreased ligand availability under constant copper loading of 50 µM was further evaluated (Figure II.4D and Figure II.4E). In this context, Cu:ligand ratios of 1:5, 1:3, and 1:1 were selected for the comparative analysis of reaction rates and conversion upon decreased ligand availability. Complete conversion was obtained with THPTA for Cu:ligand ratios of 1:3 and 1:1 after approximately 20 min (Figure II.4D). For the Cu:ligand ratio of 1:5, the highest conversion was observed after 40 min reaction time. THPTA demonstrated a maximum rate of 9.3% conversion/min during the linear reaction onset at an optimum Cu:ligand ratio of 1:3 within the first five minutes of the reaction. For the new ligand TDETA, an excess of free ligand negatively affected the maximum conversion and rate acceleration of the click reaction (Figure II.4E). At a Cu:TDETA ratio of 1:5, a maximum conversion of 90% was reached after 60 min, but when the ligand availability was decreased to 1:3 or 1:1, a significant gain in reaction acceleration was obtained. Hence, TDETA forms inhibitory complexes when the ligand is used in excess or, in other words, at Cu:ligand ratios <1. At an economic Cu:ligand ratio of 1:1, the TDETA-promoted reaction featured the fastest reaction acceleration at a rate of 12.5% conversion/min during the linear reaction onset and was according to that even faster than the best-performing THPTA-assisted reaction with the previously mentioned 9.3% conversion/min at a Cu:THPTA ratio of 1:3. Based on this apparent dependency of rate acceleration from the Cu:ligand ratio, the basic amine-substituted ligand TDETA can be specified as a strong chelating class II ligand (cf. Figure II.4B). According to Presolski *et al*., class II ligands are typically characterised by amine- or pyridine-containing arms, which display strong chelating nature and result in formation of inhibitory complexes when the ligand is used in excess in aqueous solutions.[34] These complexes limit access of the alkyne to the metal centre and slow down the formation of CuAAC-initiating copper-acetylide species. The commercial alternatives TBTA and THPTA are not known for strong ligand excess inhibition and are thus recognised as class I ligands. From the presented results of this fluorescence kinetics experiment, we conclude that TDETA is an improved class II ligand for CuAAC reactions under aqueous conditions that performs best at an economic Cu:ligand ratio of 1:1.

The disclosed data presented in the previous chapters underline the advantages of the novel ligand TDETA **II-44**. As chemical synthesis of the symmetric ligand exclusively employs the safe-to-handle Schedule 2 chemical 2-(chloroethyl)-dimethylamine (**II-39**), the synthesis of TDETA **II-44** is legal on an industrial scale and suitable for commercialisation. Therefore, compared to the original dimethylaminomethyl-substituted tetradentate Cu-ligand DTEA **II-36**, which requires the OPCW Schedule 1 nitrogen mustard HN3 **II-37** as key precursor, handling, safety, and scalability of the synthetic procedure were improved. Furthermore, the outstanding solubility of TDETA in most organic solvents and aqueous solutions, in addition to a wide spectrum of accepted substrates, suggests broad applicability in organic chemistry and applied biochemistry, such as preparative organic synthesis or labelling of samples for bioimaging of live-cell materials, respectively. It is assumed that the basic amine side arms of TDETA can fine-tune the proteolysis of the Cu-triazolide **II-21** in a broad pH range and thereby drastically accelerate the reaction rate, similar to acid-substituted side arms of $(BimC_4A)_3$ (cf. Scheme II.12). Concurrently, the novel class II ligand TDETA supersedes the use of unsymmetrical ligands that have been purposely designed for improved solubility and rate acceleration in water, such as BTTAA and BTTES.[129-131] Thus, while commercial ligands TBTA and THPTA showed clear preferences for organic solvents or aqueous solutions, respectively, TDETA is a “one fits all” solution for organic and aqueous media that is most active at an economic and equimolar 1:1 loading of copper and ligand.

II.3.2 TDETA-Assisted CuAAC Gives Rise to Biotinylated Conjugates of Bioactive Molecules

D-Biotin (**II-60**, Vitamin B7) is an essential vitamin and growth-promoting nutrient, produced by bacteria, plants, and fungi (Scheme II.18).[167] In metabolism, biotin acts in different roles, e.g. as a covalently bound cofactor in biotin-dependent carboxylase enzymes involved in the biosynthesis of the fatty acid, amino acid, or cholesterol precursors,[168] as a post-translational modification of histones to regulate chromatin stability and DNA expression,[169] or as a mediator of protein-protein interactions between the biotinylated biotin carboxyl carrier protein and other subunits of carboxylase complexes.[170] It is evident that there are reams of proteins in nature that interact with D-biotin (**II-60**) for different purposes. One of these proteins is streptavidin, a relatively small (15 kDa) tetrameric protein from the actinobacterium *Streptomyces avidinii.* The streptavidin tetramer binds up to four molecules of D-biotin (**II-60**) with a remarkable ultra-high-affinity of 10^{-15} M (K_D).[171, 172] It was hypothesised that streptavidin functions as a protein used for bacterial competition,[173, 174] withholding the essential vitamin D-biotin (**II-60**) from competitors in the ecological niche. As D-biotin is crucial to maintain prokaryotic and eukaryotic cells viable, biotin depletion can cause cellular stress or cell death.[168, 175] A special characteristic of the biotin-streptavidin interaction is the striking stability across a broad range of conditions (pH 2–13, organic solvents, detergents, temperature, chaotropic salts).[172, 176, 177] Because of that, the extraordinarily stable interaction is the most stable non-covalent interaction found in nature.[178] These key features make the biotin-streptavidin interaction particularly appealing for generating or studying biological conjugates. Moreover, the small-molecule biotin can be subjected to chemical functionalisation on the terminal carboxylic acid moiety, by which a molecule of interest can be "biotinylated" in a process, which is referred to as "biotinylation". This functionalisation allows selective binding of these biotinylated molecules of interest to avidin or streptavidin-coated surfaces or to chimeric strept(avidin)-fusion proteins.[178-181] In the search of irreversible and specific linkages between (macro)molecules, the high-affinity- and highly selective binding of D-biotin to avidin or streptavidin has become one of the most exploited tools in chemistry, biology, and biophysics and is the basis for numerous applications in drug development,[182, 183] biophysical research,[180, 184] the study of protein-protein interactions,[185, 186] biochemical pull-down strategies for interaction studies between biomolecules or their purification and selective enrichment.[83, 181, 187-190] The practical significance of terminally functionalised and activated biotins with flexible polyethylene glycol (PEG) linkers for this purpose is emphasised by the vast number of, mostly linear and single-substituted, commercial substances (e.g. biotin-PEG_3-azide **II-61**, -PEG_4-alkyne, -PEG_4-NHS ester, -PEG_2-maleimide, etc.) (cf. Scheme II.18).



Scheme II.18. Chemical structure of D-biotin (**II-60**) and its reactive sites. The amine in the 1-position of the heterocyclic biotin core serves as the reactive site for carboxylation, enabling the carboxylation of fatty acid precursors, such as acetyl-CoA. The terminal carboxylic acid on the valeric acid shuttle chain is chemically tractable for biotinylation of molecules of interest, which can be used for streptavidin-mediated pull-downs. Furthermore, the carboxylic acid reacts with the amine side chain of lysine residues within biotin-dependent enzymes to form a covalent amide bond and attach the prosthetic biotin group to these enzymes. Examples of chemically functionalised biotin derivatives (biotin-PEG_3-azide **II-61**, biotin-hydrazide **II-62**, and biotin-NHS ester **II-63**) are displayed on the right-hand side.[191-193]

A yet underrepresented group are biotins with bis- or tris-substituted multi-arm linkers, displaying multiple units of targetable functional groups. Especially in the field of bioorthogonal click chemistry, symmetrical and unsymmetrical functionalisation with non-natural substituents, such as organic azides, terminal alkynes, and cyclooctynes, can be used for studies *in vivo* without interfering with the cell's metabolites.[194, 195] Thus, reliable chemical access to reactive and structurally diverse biotinylated chassis is quite essential to study the architecture,[196] cellular localisation,[190] or interaction partners of molecules in an isolated or cellular context.[197]

II.3.2.1 Biotinylated Cholesterol for the Screening of Cholesterol-Binding Peptide Libraries via Phage Display

Cholesterol **II-64** is a steroid hormone produced by all eukaryotes.[198] In humans, the waxy substance is produced in the liver and is required for the production of certain steroids and hormones,[199] to insulate nerves,[200] and to modulate membrane fluidity.[201] Apart from being synthesised by the own organism, cholesterol **II-64** is taken up in the diet through animal products. However, this additional supplementation is unnecessary, as the body already produces sufficient steroid levels.[202] Although cholesterol is a relatively small molecule, it circulates in large lipoprotein particles through the body. These lipoprotein particles are commonly subdivided into two simplifying categories (although more exist): the healthy or "good" high-density lipoprotein (HDL) and the unhealthy or "bad" low-density lipoprotein (LDL).[202] Both LDL and HDL lipoprotein particles contain mixtures of proteins and several lipids in varying ratios (cholesterol, phospholipids, and triglycerides).[203] This is because of their behaviour and role in cholesterol metabolism. While both lipoprotein particles circulate through the blood system to transport the water-insoluble cholesterol **II-64**, HDL adsorbs discharged fats and cholesterol from cells and clears the blood serum from cholesterol to transport it back to the liver for recycling or excretion.[204, 205] LDL, in contrast, transports cholesterol from the liver to the cells and membranes and is considered the leading risk factor associated with heart diseases.[206] When cholesterol or LDL levels in the blood plasma are high for a long time, hypercholesterolemia may develop and provoke cholesterol aggregation. These cholesterol deposits can form in the arteries, causing macroscopic cholesterol plaques and hardening, thickening, and blocking of arteries, contributing to atherosclerosis. Atherosclerosis is the pathological process underlying heart attacks, strokes, vulnerable plaques, and other cardiovascular diseases.[202] This presents a major challenge to the global healthcare system. In the US, approximately 43% of the population is suffering from total blood cholesterol of >200 mg/dL (103.3 Mio.) or >240 mg/dL (41.3 Mio.). A level above 200 mg/dL is generally considered a threshold for a high or an extremely high risk of heart disease.[202] Drugs that block cholesterol synthesis, such as statins (e.g. Atorvastatin), are widely prescribed in the US, illustrating the high demand for treatments addressing elevated cholesterol levels.[207, 208] Although statins are generally considered safe for patients of all ages, they may cause side effects such as muscle pain, sleep problems, dizziness, and digestive issues, among others.[209] For the aforementioned reasons, the search for potential drug candidates to erode these sclerotic plaques in patients at risk creates desire among researchers and pharma companies, as a promising drug candidate could be a door opener to a billion-dollar market. Besides small-molecule drugs, such as statins, peptide-based drugs have experienced a revival of interest these days.[210] Especially all-D-peptides, exclusively built from D-amino acids, are ultrastable and may possess an exceptionally long half-life in the human body,[211, 212] owing to the absence of proteases within the eukaryotic proteome that are able to cleave DD-peptide bonds. One strategy to find novel molecules on a peptide basis is the so-called phage display.[213] In this approach, viruses of bacteria (bacteriophages) are engineered to display fusion proteins of their own proteins with peptides from a randomly or rationally designed DNA library on the viral capsid. The protein-peptide fusions on the viral surface are then used to probe for interactions between an immobilised molecule of interest, such as proteins or nucleic acids, and the peptides from the library. If one of the peptides binds to the target of interest with a high enough affinity, the

corresponding phage remains bound to the surface-immobilised molecule and can be recovered to subsequently elucidate the peptide sequence via phage propagation and DNA sequencing (Figure II.5). Engineered phages, displaying variations of peptides on their capsid surfaces, can also be used to bind immobilised cholesterol, facilitating the screening of cholesterol-binding phages and peptides. In the search for a peptide-based molecule capable of interacting with cholesterol (plaques) and potentially dissolving unhealthy arterial cholesterol deposits in the long term, phage display presents a strategic approach to uncover a bioactive lead peptide as a needle in a haystack. By identifying promising peptide candidates or protein compositions for further evaluation and sequence evolution, this approach facilitates the analysis of cholesterol plaque dissociation kinetics in the presence of the evolved peptides.

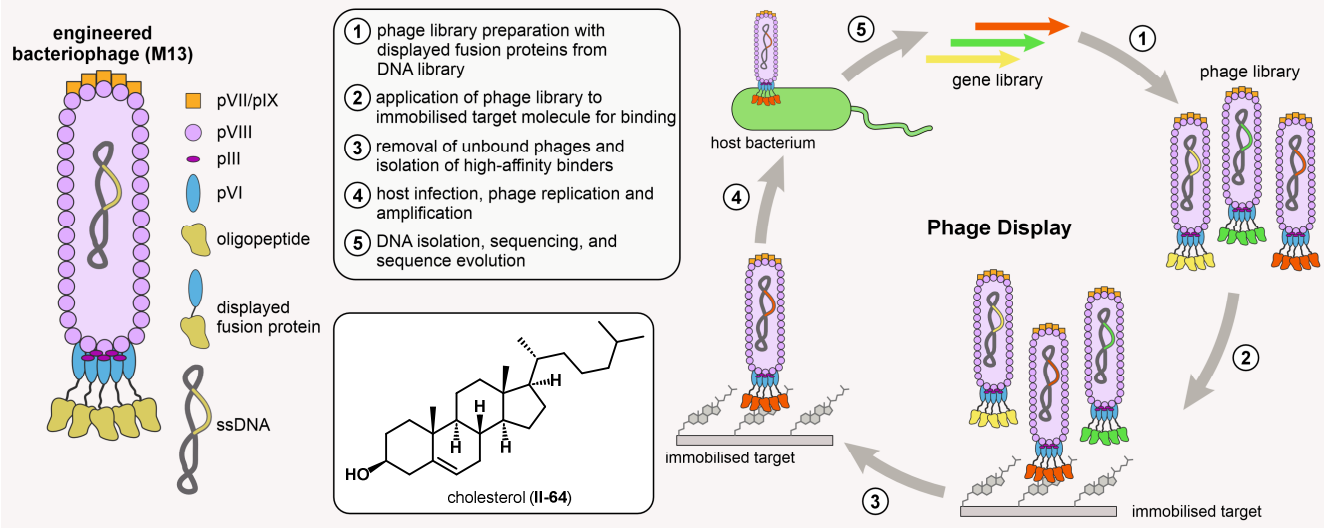
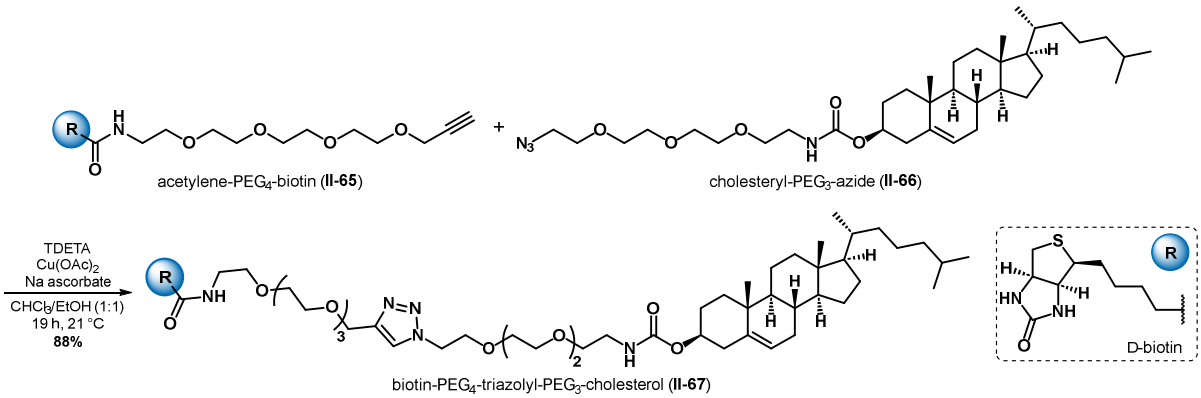


Figure II.5. Working principle of phage display for the identification of peptides or proteins capable of interacting with molecules of interest. Left: Schematic representation of the *E. coli* bacteriophage M13. The single-stranded phage DNA is surrounded by structural proteins, abbreviated as p and a sequential number. These structural proteins are fused to oligopeptides or whole proteins, which are then displayed on the viral surface. Right: The workflow of phage display with an immobilised target (here: cholesterol **II-64**). Figure design inspired by Jaroszewicz *et al.*[213]

To immobilise cholesterol for phage-display-based interaction studies, its functionalisation with biotin enables high-affinity binding to commercially available streptavidin-coated surfaces, presenting cholesterol to a mixed population of engineered bacteriophages. In this context, our previously introduced tetradentate copper ligand TDETA **II-44** (cf. Chapter II.3.1) was employed to synthesise a biotinylated cholesterol via CuAAC from commercially available acetylene-PEG$_4$-biotin (**II-65**) and cholesteryl-PEG$_3$-azide (**II-66**) (Scheme II.19). This biotinylated cholesterol derivative **II-67** was designated to be used in phage display in collaboration with Prof. Dieter Willbold's group at IBI-7, Forschungszentrum Jülich. The probe was designed with flexible PEG units on both sides of the triazole heterocycle, allowing for free rotation of the immobilised cholesterol on the solid support without rotational constraints and enhancing its solubility in aqueous media.[214]



Scheme II.19. Synthesis of the biotinylated cholesterol derivative **II-67** via click chemistry in a TDETA-assisted CuAAC reaction for phage display applications.

Small-scale CuAAC reactions with excess alkyne **II-65** (R_f 0.36) or azide **II-66** (R_f 0.90) quickly revealed the experimental need to use cholesteryl-PEG_3-azide **II-66** in excess, as the biotinylated alkyne **II-65** and the click product **II-67** (R_f 0.40) exhibit virtually identical retention times in chromatography. While an excess of alkyne **II-65** hampers product purification due to residual unreacted biotinylated alkyne in the mixture, utilisation of an excess of cholesteryl azide **II-66** allowed excellent separation of unreacted azide **II-66** from the click product **II-67** and a straightforward purification by chromatography on silica. The single-step CuAAC click reaction finally provided click product **II-67** in a very good yield of 88% for further application. Currently, the biotinylated cholesterol **II-67** is under investigation to identify potential binding peptides via phage display and thereby find novel peptide-based therapeutics to dissolve arterial cholesterol deposits, responsible for atherosclerosis. However, preliminary peptide binding or sequence data are not available so far.

II.3.3 CuAAC as a Tool for Rapid Structural Diversification on the Example of Biotinylated Pittsburgh B

II.3.3.1 The Biotinylated Pittsburgh B Analogue CAP-1 Binds Amyloid Fibrils Associated with Neurodegenerative Diseases

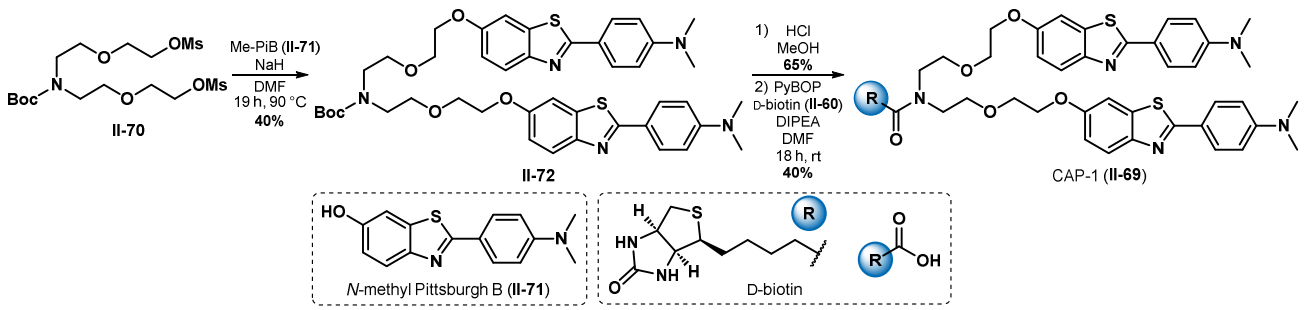
In today's society, facing the trend of ageing populations, the spotlight of modern medicine is turned on age-related diseases, which demand costly and labour-intensive care for relatives and the healthcare system. Alzheimer's disease (AD) is an example of diseases associated with ageing, which caused 121,404 deaths in 2017 in the United States. Between 2000 and 2017, deaths related to AD increased by 145%, making it the sixth leading cause of death in the US. Approximately 1.7% (5.8 Mio) of the current US population is diagnosed with Alzheimer's dementia.[215] AD and other progressive yet incurable neurodegenerative disorders, such as Parkinson's disease (PD), are characterised by pathological misfolding and aggregation of proteins into highly structured amyloid fibrils, effectuating debilitation of the ageing population by causing dementia and motor impairment.[216-218] The spontaneous aggregation of proteins into toxic fibrils [amyloid beta (Aβ) and protein tau in AD;[216] α-synuclein (α-syn) in PD, dementia with Lewy bodies (DLB), and multiple system atrophy (MSA)[219, 220] requires means that allow diagnosis of these neurodegenerative disorders. However, overlapping neuropathological features between these diseases, as known for DLB,[220] can further complicate diagnosis in low-symptom early stages of the etiopathology.

The accurate and early diagnosis of these neurodegenerative diseases remains a challenge. Still, it is yet important because it has a tremendous impact on the selection of individuals for clinical trials and the choice of

therapeutic interventions.[221] Detection and quantification of amyloid fibrils in nervous tissue and body fluids, such as brain, cerebrospinal fluid (CSF), and blood, can provide essential diagnostic information about the specific type and severity of the disease. Additionally, amyloid fibrils serve as valuable biomarkers for tracking disease progression and assessing the efficacy of therapeutic interventions targeting amyloids.[222]

Since all mentioned neurodegenerative diseases are based on the formation of highly ordered amyloid fibrils, compounds capable of specifically binding to amyloid fibrils are required to enable their detection, quantification, and characterisation. The development of such compounds supports both the advancement of diagnostic tools and the creation of effective treatments. Although effective medication for late-stage dementia is a desirable goal to prolong the lives of patients, the development of early warning models is essential to detect and suppress the onset of all kinds of dementia before the perceptible cognitive decline begins. Benzothiazole-containing probes emerged in the late 90s as potent molecules to selectively bind and detect biomarkers of progressive neurogenerative diseases, such as Aβ aggregates.[223] In 2004, Klunk *et al*. introduced the benzothiazole Pittsburgh Compound B (PiB, **II-68**) as a novel amyloid-imaging PET tracer to visualise amyloid plaques in AD brain tissue.[224] Furthermore, PiB was shown to bind Lewy body-derived α-syn fibrils,[225] which are pathogenic hallmarks in other synucleinopathies (e.g. PD and MSA), too.[226] However, PET brain imaging as a diagnostic tool is expensive and not ubiquitously available. Although amyloid fibrils in neurodegenerative diseases are often associated with specific organs, such as AD plaques in brain tissue, amyloid fibrils are present in numerous body fluids. Blood, stool, CSF, and other biofluids are further sources of amyloid fibrils, and hence, they can be used as a cheaper and more readily accessible fibril pool for diagnostic purposes. It is worth mentioning that fibril titres in these body fluids can be relatively low. Thus, methods for the selective enrichment of amyloid fibrils from these sources are being developed as a universal way to diagnose amyloid diseases and monitor their progression and the effectiveness of therapeutic interventions.[227-230]

A recent innovation in molecular benzothiazole probes was the synthesis of the bis-functionalised biotinylated capture molecule for amyloid precipitation (CAP-1, **II-69**, Scheme II.20),[187] which addresses the need for diagnostic tools for the detection of developing neurodegenerative diseases and protein fibrils. CAP-1-mediated detection of protein fibrils profits from the high-affinity interaction of biotin with streptavidin. This interaction is utilised to selectively precipitate amyloid fibrils from highly complex biofluids by streptavidin-coated magnetic beads and employs a rarely used bifurcated amide linker. This linker enables the display of two molecular probes akin to PiB **II-68** per biotin unit and thereby increases the strength of interaction with the amyloid fibrils.[30, 187] Rodrigues *et al.* synthesised CAP-1 **II-69** in a three-step protocol (Scheme II.20, omitting several reaction steps and yields) to generate the probe.[187]

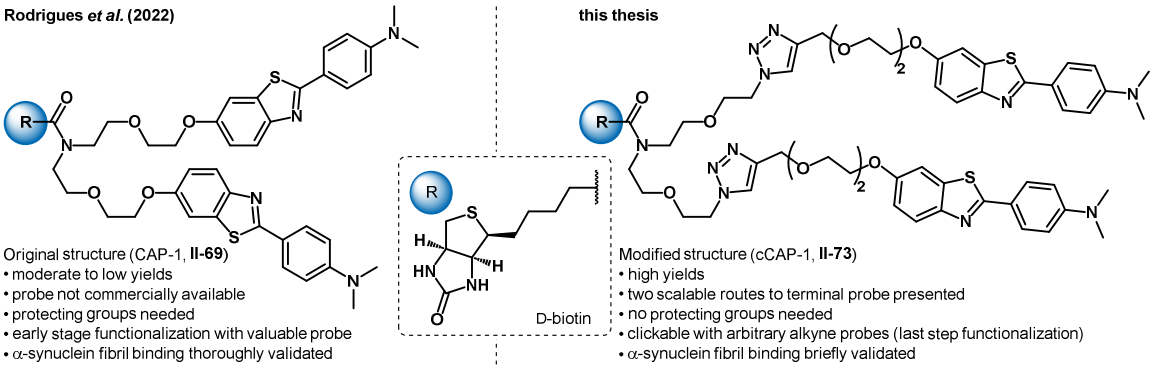


Scheme II.20. Synthesis scheme of CAP-1 **II-69** – the capture molecule of amyloid precipitation by Rodrigues *et al*.[187] The synthesis procedure and yields for the Boc-protected mesylate **II-70** (minimum three steps) and the non-commercially available *N*-methyl Pittsburgh B probe **II-71** are not provided in the original publication.

In the first step, the *N*-Boc-protected and mesylated PEG-linker **II-70** (requires a minimum of three synthetic steps) was functionalised with *N*-methyl Pittsburgh B (**II-71**, Me-PiB) to provide the bis-functionalised phenolic ether **II-72** in a yield of 40%. After deprotection of the Boc-protecting group under acidic conditions with hydrochloric acid in MeOH with a yield of 65%, PyBOP-mediated amide coupling with plain D-biotin enabled the isolation of the capture molecule **II-69** in a yield of 40%. Although this three-step synthetic procedure was essential to get a hand on the CAP-1 probe to study the interaction with amyloid fibrils and its potential as an anchor for amyloid precipitation, a closer look uncovers several drawbacks in the reported synthesis. Firstly, the *N*-methylated probe **II-71**, derived from the benzothiazole family and akin to Pittsburgh Compound B **II-68**, is not commercially available, and moreover, Pittsburgh Compound B is very pricy (CAS 566169-93-5, 985 USD or 1025 EUR per gram at BLDpharm). As the probe is attached to the Boc-protected linker in an early stage of the synthesis with a low yield of 40%, followed by deprotection (65% yield) and amide coupling with D-biotin in 40% yield, the yield over three consecutive steps that include the valuable benzothiazole probe is only 10%. Adhering to this, the late-stage attachment of biotin to the probe-decorated linker does not allow for a simple probe exchange. Instead, a three-step procedure is required to synthesise every additional target molecule. Although the bifurcated biotin anchor is a highly appealing structural motif for diagnostic and biochemical tools, the early-stage probe attachment would prohibit a streamlined preparation of large biotinylated compound libraries for high-throughput screenings and preclude bioorthogonal application through the high prevalence of amines and carboxylic acids in natural biomolecules. However, large biotinylated compound libraries with high structural diversity are of interest in the untargeted screening of potential interaction partners for pharmacologically relevant biological targets.

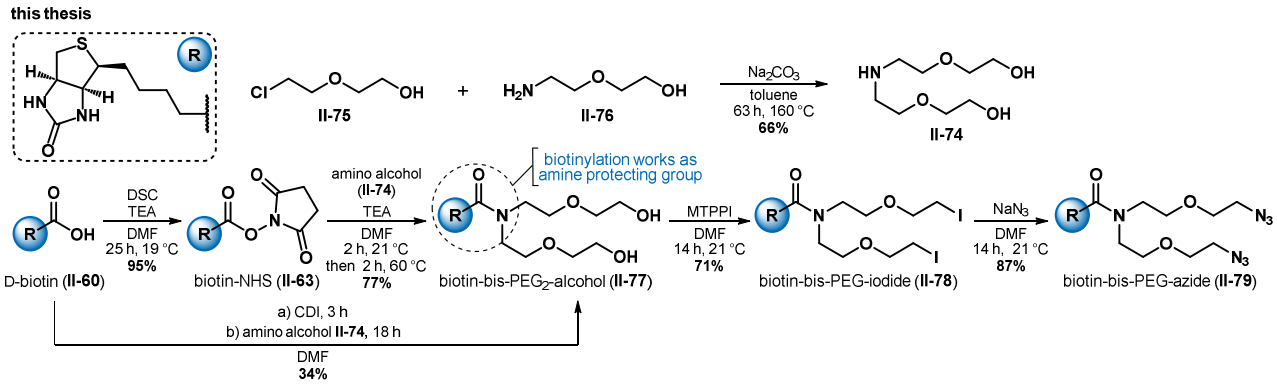
II.3.3.2 An Alternate Biotin-Bis-PEG-Azide Design Enables Late-Stage Functionalisation and Probe Diversification

Inspired by the design of CAP-1 **II-69**, we intended to overcome three critical limitations and cost drivers of the synthetic route presented by Rodrigues *et al*.:[187] the overall low and uneconomic yield of 10% over the reported synthetic transformations, the limited access towards very expensive and non-commercially available *N*-methylated PiB **II-71**, and the non-bioorthogonally compatible linker architecture. Hence, we aimed to redesign the original CAP-1 structure while retaining the same benzothiazole probe and the multi-arm Y-shaped biotin (Scheme II.21). The latter is utilised to exploit the highly selective biotin-streptavidin interaction for immobilisation on streptavidin-functionalised surfaces. In contrast to the synthesis of CAP-1 **II-69**, an approach was chosen that provides a symmetrical and ubiquitously usable bifurcated biotin-bis-PEG-azide, derived from a protecting-group-free synthesis. By independent transformations on the biotin and the benzothiazole moiety, both functional units are mergeable in a reliable and commutable last-step copper-catalysed click reaction and give rise to the clicked capture molecules for amyloid precipitation cCAP-1 (**II-73**). The primary benefit of the intermediate biotin-bis-PEG-azide chassis is its compatibility with bioorthogonal applications and a rapid structural diversification with arbitrary alkynes via CuAAC or SPAAC.



Scheme II.21. Same but different: a Y-shaped biotin anchor for benzothiazole-based structure-specific precipitation of amyloid fibrils. Both molecules comprise the D-biotin moiety for binding to streptavidin and display two benzothiazole probes for the selective binding of amyloid fibrils. However, CAP-1 **II-69** and cCAP-1 **II-73** fundamentally differ in their linker architecture and the type of chemistry employed.

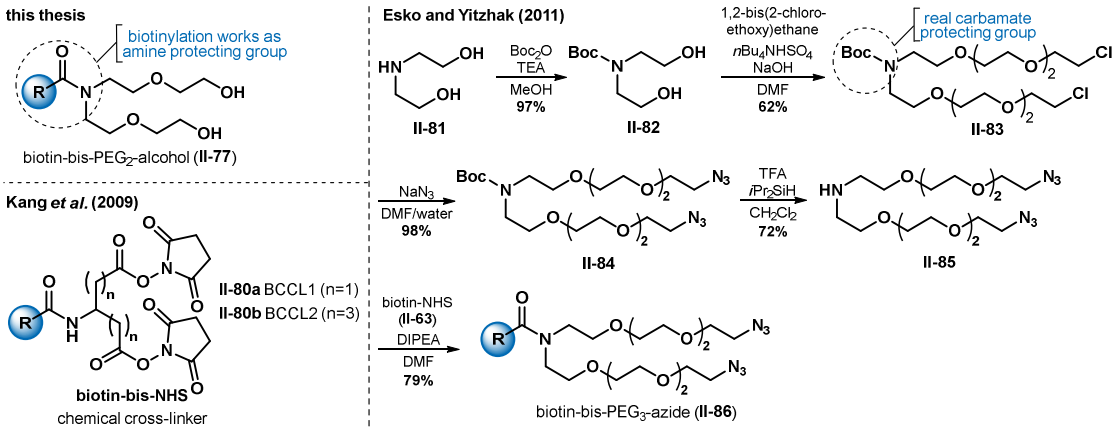
Starting with the synthesis of a symmetric bifurcated PEG-based linker, amino alcohol **II-74** was prepared in a one-step procedure by reacting 2-(2-chloroethoxy)ethanol **II-75** with an excess of 2-(2-aminoethoxy)ethanol **II-76** in the presence of anhydrous sodium carbonate in refluxing toluene (Scheme II.22).[231] Distillation of the residue gave the amino alcohol **II-74** in 66% yield, ready for coupling with biotin. Cheap and ubiquitously available D-biotin (**II-60**) was first activated due to the inherently low carbonyl activity of the terminal acid. Therefore, its carboxylic acid functionality was transformed into the *N*-hydroxy succinimide (NHS) ester **II-63** for activation. The reaction with disuccinimidyl carbonate (DSC) in dimethylformamide (DMF) provided the NHS-activated biotin **II-63** in a yield of 95% without the need for chromatographic purification.[192] By performing the amide coupling between biotin and the linker at an early stage, the formation of the tertiary amine as a hinge between both functional units reduces the inherent nucleophilicity of the linker nitrogen, redundantising the need for an additional protecting group strategy, as employed by Rodrigues *et al.* (cf. Scheme II.20).[187] The reaction between the unprotected amino alcohol **II-74** and NHS-biotin **II-63** was then carried out in DMF, using triethylamine (TEA) as base, yielding 77% of the bis-hydroxy-functionalised biotin **II-77** under formation of an amide bond. The resulting product represented a very sticky oil, which was only soluble in DMSO, MeOH, or DMF, very much limiting the solvent options for further transformations. A direct approach from D-biotin **II-60** to bis-hydroxy-biotin **II-77** with *in situ* activation of biotin using *N,N'*-carbonyldiimidazole (CDI) only led to product formation in 34% isolated yield.



Scheme II.22. Protecting-group-free synthesis of the Y-shaped bis-azide-functionalised biotin-bis-PEG-azide linker **II-79** from D-biotin (**II-60**).

As the terminal hydroxy groups of bis-hydroxy-functionalised biotin **II-77** cannot be transformed directly into the corresponding azide, activation via intermediate alkyl halide or (pseudo)halide was necessary. Typical transformations to the alkyl bromide (Appel reaction) with CBr_4 and PPh_3 in CH_2Cl_2 or alkyl mesylate with mesyl chloride in pyridine failed or produced several side products. While searching for alternative halogenating reagents, we stumbled across the rather uncommon reagent methyltriphenoxyphosphonium iodide (MTPPI). The iodinating reagent can be easily prepared on a gram scale by the reaction of triphenyl phosphite and methyl iodide under solvent-free conditions and has been extensively used in the 1960s and 1970s in the halogenation of nucleosides.[232, 233] Conversion of bis-hydroxy-biotin **II-77** with MTPPI in DMF provided the desired bis-iodide-biotin **II-78** in a good yield of 71% as colourless oil. Lastly, simple halide substitution with sodium azide in DMF gave access to the clickable Y-shaped bis-azide-biotin **II-79** (biotin-bis-PEG-azide) as colourless glass in 87% yield.

The apparent advantage of this presented protecting-group-free synthesis route towards bis-azide-biotin **II-79** is easy access to all three biotin derivatives with the branched linker architecture (biotin-bis-PEG_2-alcohol **II-77**, -PEG-iodide **II-78**, and -PEG-azide **II-79**). Their synthetically interesting functional groups can be used for further functional group interconversions (oxidation of hydroxy groups to aldehydes or acids, reduction of azides to amines), etherifications, esterifications, substitutions, and click chemistry. Some of these synthetically useful functional groups may be used to install click-reactive functional groups (e.g. azide, alkynes, tetrazines) for bioorthogonal click chemistry. Other reactive species (e.g. biotin-bis-PEG-aldehyde derived from oxidation of biotin-bis-PEG_2-alcohol **II-77**) may enable molecular spatiomics by concurrently facilitating biotinylation and randomised, sequence-independent proximity-based cross-linking of low-abundance interacting proteins. This approach offers an alternative to enzyme- and proximity-dependent biotinylation techniques like BioID and related tools.[234, 235] The commercial availability of monoclonal and polyclonal anti-biotin antibodies, coupled with fluorophores or enzymes to facilitate detection of antibody binding, would then allow protein-independent detection of cross-linked proteins, mediated through the biotin moiety and the biotin-recognising epitope of the antibody. Moreover, bis-functionalised biotin could be used to study enriched and trypsin-digested cross-linked proteins, whose cross-link is based on protein-protein interactions. Such a study was previously published by Kang *et al*., making use of the biotinylated bis-NHS cross-linkers BCCL1 **II-80a** and BCCL2 **II-80b** for the coupled mass-spectrometric analysis of cross-linked HIV-1 CA capsid protein (cf. Scheme II.23).[236]



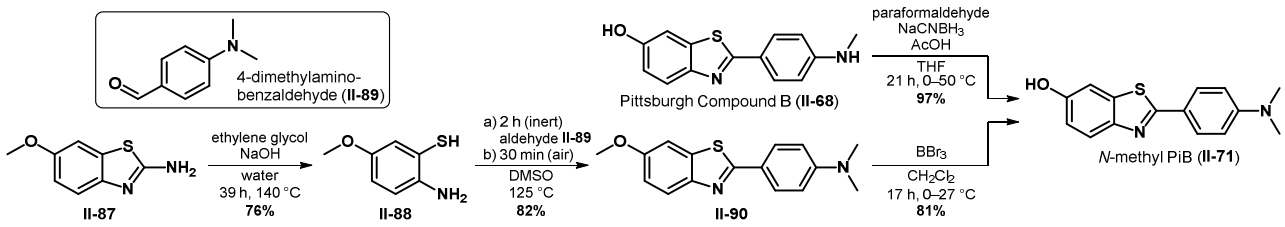
Scheme II.23. Protecting-group-free synthesis of the Y-shaped bis-azide-functionalised biotin-bis-PEG-azide linker **II-79** in comparison to the patented synthesis of biotin-bis-PEG_3-azide **II-86** by Esko and Yitzhak.[237, 238] The biotin-bis-NHS chemical protein cross-linking reagents BCCL1 **II-80a** and BCCL2 **II-80b** by Kang *et al*. are depicted on the right side of the scheme.[236]

To date, one other biotinylated bis-PEG-azide has been published in a patent by Esko and Yitzhak (cf. Scheme II.23).[237, 238] However, their presented route follows a fundamentally different strategy by starting from bis-(hydroxyethyl)amine **II-81** and proceeding with an *N*-Boc-protection to generate a tertiary amine. Thereby, the inherent nucleophilicity of the nitrogen is reduced to avoid the generation of side products in the subsequent substitution reaction. Next, the *N*-Boc-protected bis-(hydroxyethyl)amine **II-82** is then elongated with additional PEG-units through the reaction with 1,2-bis(2-chloroethoxy)ethane to give bis-chloride **II-83**. A simple azide substitution gives rise to the protected bis-azide **II-84**, followed by an acid-catalysed deprotection step. Lastly, the unprotected bis-azide **II-85** is coupled with the biotin-NHS ester to yield the desired biotin-bis-PEG_3-azide **II-86**. The direct comparison between the patented work and the synthetic route devised in this thesis reveals that our novel coupling strategy includes the same logical arguments, namely, the *N*-protection before nucleophilic substitution reactions can be performed on the linker side arms. However, the innovative early-stage amide-coupling between linker **II-74** and NHS-biotin **II-63** has the same effect as a protecting group. Still, it supersedes the use of additional "real" carbamate protecting groups that need to be removed later on (cf. Scheme II.23). Furthermore, the early-stage biotinylation gives access to a functional group prosperity of biotinylated species, which are not provided in the synthesis with last-stage biotinylation by Esko and Yitzhak.

And lastly, the biotin unit of the novel biotin-bis-PEG-azide chassis **II-79** features two azide moieties rather than terminal alkynes or cyclooctynes, allowing click chemistry with alkyne-functionalised probes to extend beyond copper-catalysed CuAAC and to include copper-free SPAAC. This versatility is particularly advantageous for applying bioorthogonal click chemistry in copper-sensitive living cell systems (*vide supra*).

II.3.3.3 Two Independent Routes Lead to the *N*-Methylated PiB Probe

With the terminal *N*-methyl PiB **II-71** (Me-PiB) probe of CAP-1 **II-69** not commercially available, we sought individual and reliable approaches, giving rise to the probe in good yields and with minimal purification effort. Firstly, commercially available PiB **II-68** was *N*-methylated in an Eschweiler-Clarke reaction using a modified procedure based on published works by Kaur *et al.* and Reed *et al*., which were initially developed for the *N*-methylation of substituted benzothiazoles or anilines, respectively (Scheme II.24).[239, 240] To synthesise Me-PiB **II-71**, PiB **II-68** was reacted with sodium cyanoborohydride and paraformaldehyde in a mixture of THF and glacial acetic acid, yielding 97% after simple extraction and washing of the solid and practically insoluble product. Although this procedure is simple to perform and the product is obtainable in excellent yields, the very high cost of PiB **II-68** (*vide supra*) is a significant disadvantage of this short route.



Scheme II.24. Synthesis of *N*-methyl PiB **II-71** from commercial Pittsburgh B (**II-68**) and from 6-methoxybenzothiazol-2-ylamine (**II-87**).

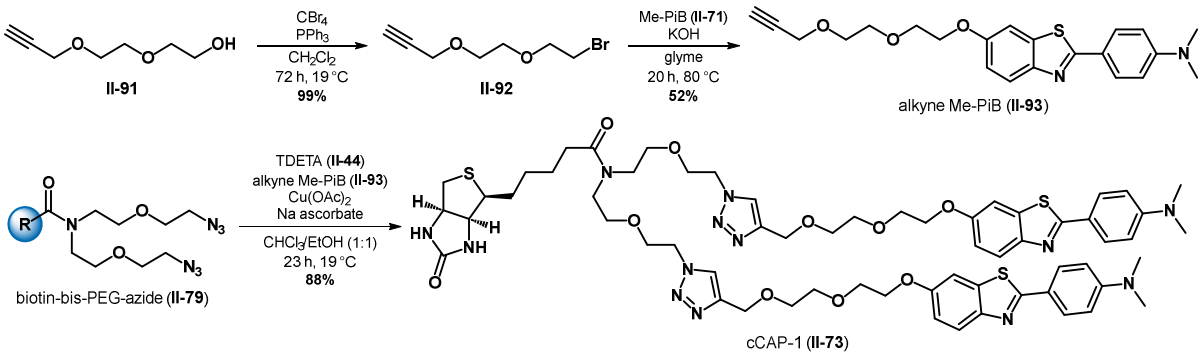
Next, we aimed to devise a synthesis route of Me-PiB **II-71** from inexpensive and available sources to offer alternative routes to the valuable probe. We selected 6-methoxybenzothiazol-2-ylamine (**II-87**, CAS 1747-60-0, 149 USD or 160 EUR per 500 grams at TCI) as staring material and subjected the benzothiazole to basic ring

opening with NaOH in aqueous solution at 140 °C (Scheme II.24). Although the obtained yields varied between 60 and 90%, careful handling under inert atmosphere including utilisation of degassed solvent was a prerequisite for a reliable outcome of the reaction, as otherwise the oxygen-induced competing disulfide formation took place (evidenced by the formation product with black colour instead of bright-yellow colour). Based on aminothiol **II-88**, the benzothiazole scaffold was built in an optimised two-step procedure, involving a condensation of 2-amino-5-methoxybenzenethiol (**II-88**) and 4-(dimethylamino)benzaldehyde (**II-89**), followed by an intramolecular cyclisation and oxidation reaction. The best results in terms of yield and purity were achieved when aminothiol **II-88** and aldehyde **II-89** were first reacted under an inert atmosphere at 125 °C in DMSO to form the dihydrobenzo[*d*]thiazole structure. Subsequent brief oxidation under air at 125 °C furnished the oxidised benzothiazole **II-90** in 82% yield. In contrast, direct exposure to air increased the formation of undesired side products. Overall, the reactive aldehyde **II-89** proved to be the superior coupling partner for aminothiol **II-88**, as yields dropped significantly to 35% when the aldehyde was substituted by the less reactive corresponding 4-(dimethylamino)benzoic acid, as demonstrated in the synthesis reported by Huang *et al*.[241] Final demethylation of the methoxy group with boron tribromide yielded 81% of *N*-methyl PiB **II-71** as an amorphous solid in gram quantities without the need for chromatographic purification in any of the presented synthesis steps (Scheme II.24).

II.3.3.4 TDETA-Assisted Click Chemistry Renders the Clicked Amyloid Capture Molecule cCAP-1

With the clickable biotinylated bis-azide chassis and the *N*-methylated PiB in hand, the effort was directed to installing a suitable alkyne tail on the PiB probe, enabling the conjunction of biotin-bis-azide and alkynylated Me-PiB moieties via CuAAC click chemistry. For this functionalisation, a bifunctional PEG-based alkyne bromide linker was chosen, enabling coupling to the phenolic alcohol of Me-PiB **II-71** in a nucleophilic substitution reaction.

To synthesise the alkyne-bromide linker, the diethylene glycol acetylene precursor **II-91** of the linker was first brominated in quantitative yield in an Appel reaction by substitution of the terminal hydroxy group (Scheme II.25). In the following step, the *N*-methylated PiB **II-71** was *O*-functionalised with the described brominated alkyne linker **II-92**, similar to the PiB-functionalisation of Diner *et al*.[242] Etherification of the phenolic hydroxy group proved to be rather challenging, as evidenced in the coupling reaction with the more readily available dummy substrate PiB **II-68** and alkyne bromide **II-92**. Many solvent/base combinations (e.g. K_2CO_3/MeCN, K_2CO_3/DMF, Cs_2CO_3/DMF, DIPEA/glyme, Cs_2CO_3/MeCN, K_2CO_3/acetone) either resulted in no conversion, low conversion, or undesired side products. The best solution found for this challenging coupling was a heterogeneous reaction system of KOH in



Scheme II.25. Alkyne-functionalisation of *N*-methyl PiB **II-71** and late-stage functionalisation of biotin-bis-PEG-azide **II-79** via CuAAC to form the clicked amyloid capture molecule cCAP-1 (**II-73**).

dry glyme at 80 °C, which was the only solvent/base combination suitable for rendering near-full conversion. Hence, the optimised glyme/KOH system was finally applied in the etherification of Me-PiB **II-71** with alkyne bromide **II-92** to present the alkyne Me-PiB **II-93** in a moderate yield of 52%. Since near-full conversion was observed in a TLC-based reaction control for the former reaction, it remains unclear whether the loss of product is due to the reaction conditions, workup conditions, or chromatographic purification on silica. Nevertheless, this procedure was the most practical among all tested to minimise the purification effort. It is hypothesised that significant amounts of the very polar product remain bound to the column, even with elution in polar alcoholic solvents. Thus, future studies should invest in optimising product purification to maximise the yield of the valuable alkyne-functionalised Me-PiB probe. Exploiting our novel and versatile Cu(I)/Cu(II) ligand TDETA **II-44** (cf. Chapter II.3.1),[137] the modified clicked capture molecule for amyloid precipitation cCAP-1 **II-73** was synthesised in a very good yield of 88% by combining the bis-azide-functionalised biotin **II-79** and the alkyne Me-PiB **II-93** building blocks in a copper-catalysed azide-alkyne cycloaddition (CuAAC) under reducing conditions (Scheme II.25).

II.3.3.5 cCAP-1 Binds α-Syn Fibrils *In Vitro*

Fluorescence enhancement upon binding of amyloid fibrils is a common feature of benzothiazoles (e.g. Thioflavin T and CAP-1 **II-69**) and can be utilised for imaging purposes of fibril-containing aggregates or their quantification.[187, 223, 224, 242-244] Hence, the novel biotinylated dual-payload benzothiazole probe cCAP-1 **II-73** was characterised for the intrinsic fluorescence in the presence or absence of α-syn fibrils. Upon binding of *in vitro* generated α-syn fibrils, a 2.8-fold increase of absorption at 380 nm and a 2.9-fold fluorescence enhancement at 434 nm (λ_{ex}= 365 nm) were observed for cCAP-1 **II-73**. Furthermore, the excitation and emission maxima of cCAP-1 **II-73** at 380 nm and 433.5 nm were slightly shifted in the presence of α-syn fibrils to 379 nm and 431 nm, respectively, giving a Stokes shift of 52 nm (Figure II.6A). Consequently, the intrinsic fluorescence and fluorescence enhancement of the clicked benzothiazole probe cCAP-1 **II-73** can be used to quantify or visualise α-syn fibrils *in vitro*. However, as this preliminary study was conducted on purified α-syn fibrils originating from heterologous expression, further analyses will be needed to validate the influence of matrix effects in complex mixtures, e.g. stool, blood plasma, tissue homogenates, *in vivo* or *ex vivo*. As these specimens from the human body vary significantly in their viscosity, protein, sugar, lipid, and cell composition, a cross-validation with externally spiked α-syn fibrils to samples of healthy human individuals will be needed to estimate the influence of these matrix effects on the intensity of the fluorescence signal and possible background interference, and to assess the reliability of cCAP-1 **II-73** for α-syn quantification in human patients. Analysis of the latter samples would be the ultimate goal to translate cCAP-1 **II-73** into a diagnostic tool to enrich and quantify low-abundant α-syn fibrils in the early stage of the disease, allowing for therapeutic interventions to reduce the progression of related synucleinopathies before the cognitive decline begins. Adhering to the fluorescence enhancement upon α-syn fibril binding, cCAP-1 **II-73** showed a linear increase of fluorescence in a range from 0–200 nM probe concentration in PBS buffer in the presence of a stationary concentration of 10 µM α-syn fibrils (Figure II.6B), proving comparable fluorescence and solubility properties to the original CAP-1 **II-69** structure.[187]

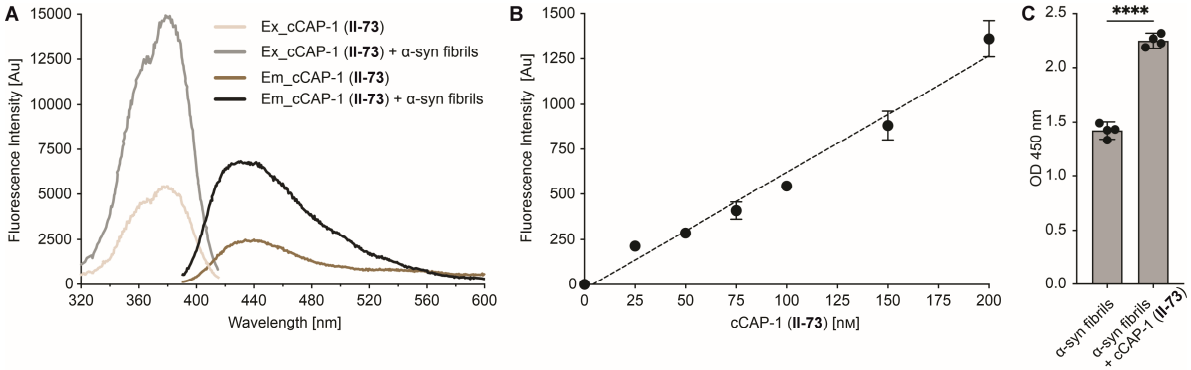


Figure II.6. Spectral validation of cCAP-1 (**II-73**) and its streptavidin-binding for enrichment of α-syn fibrils. **A**. Fluorescence excitation (Ex) and emission (Em) spectra of cCAP-1 **II-73** (20 µM) in the absence or presence of α-syn fibrils (10 µM monomer equivalent) in PBS buffer. Emission spectra were recorded after excitation at 365 nm. **B**. Fluorescence measurement of cCAP-1 **II-73** (0–200 nM) binding to α-syn fibrils (10 µM monomer equivalent) in PBS buffer (n=3). A linear regression fit was applied with an R^2 of 0.978. **C**. Binding of α-syn fibrils (0.34 µM monomer equivalent) to streptavidin-coated 96-well polystyrene plates in the absence or presence of 10 µM cCAP-1 **II-73**. Binding was quantified via an indirect ELISA assay (n=4). **** indicates significant difference (P < 0.0001). Data and figures were provided by G. Tamgüney (IBI-7, Forschungszentrum Jülich).

As the highly specific and affine interplay between streptavidin and biotin or functional biotin moieties is a key prerequisite in several pull-down strategies aiming for purification or quantification of target molecules,[30, 178, 187, 245, 246] the interaction of streptavidin-coated magnetic beads was used for structure-specific precipitation of α-syn fibrils from biofluids by the biotinylated dual probe CAP-1 **II-69**.[187] Attempts to reproduce these data to validate our cCAP-1 **II-73** were met with failure, as pronounced unspecific binding of α-syn fibrils to the beads occurred independent of the presence of cCAP-1 **II-73**. However, it should be mentioned that quantification of α-syn fibrils with the literature compound CAP-1 **II-69** was based on the intrinsic fluorescence enhancement upon binding of amyloid fibrils, while cCAP-1 **II-73** quantification was attempted with an indirect, thus antibody-dependent, ELISA assay (enzyme-linked immunosorbent assay). This indirect ELISA assay is based on primary binding of α-syn by the mouse monoclonal anti-α-synuclein Syn211 antibody and secondary binding of the primary antibody by the anti-mouse horseradish peroxidase (HRP)-linked secondary antibody, followed by a subsequent colour reaction induced by HRP-oxidation of the substrate 3,3',5,5'-tetramethylbenzidine (TMB). Consequently, the ELISA assay quantifies α-syn fibrils independent of binding the biotinylated probe, while the fluorescence assay quantifies only α-syn fibrils that interact with the *N*-methylated PiB probe. This discrepancy might be the reason for the overshadowing background signal of cCAP-1-independent α-syn fibril binding to the magnetic beads. Instead, cCAP-1 binding to α-syn fibrils was evaluated using streptavidin-coated polystyrene plates. These plates were pre-incubated with cCAP-1 **II-73** and purified α-syn fibrils to selectively accumulate α-syn fibrils by biotin-streptavidin-interaction between the plate surface and biotinylated cCAP-1 on one side and selective binding of α-syn fibrils by the cCAP-1 **II-73** benzothiazole probe on the other side. The binding of α-syn fibrils to the streptavidin-coated surface was validated by the previously mentioned colorimetric ELISA assay. While the antibody-mediated detection of fibrils demonstrated a high background of α-syn fibrils binding to the surface in the absence of any cCAP-1 **II-73**, a 58% increase of α-syn accumulation was observed when the selective α-syn-binding cCAP-1 probe was present (Figure II.6C). Nevertheless, unspecific binding of α-syn fibrils to the matrix is again an undesired side effect that limits the detection range of the assay and also partially blocks the available surface for selective interaction between cCAP-1 and streptavidin. In this regard, further optimisation of the assay system is needed to increase the sensitivity and selectivity of the employed method for reliable and highly sensitive detection of α-syn fibrils from human samples and the application of cCAP-1 in synucleinopathy diagnosis. For

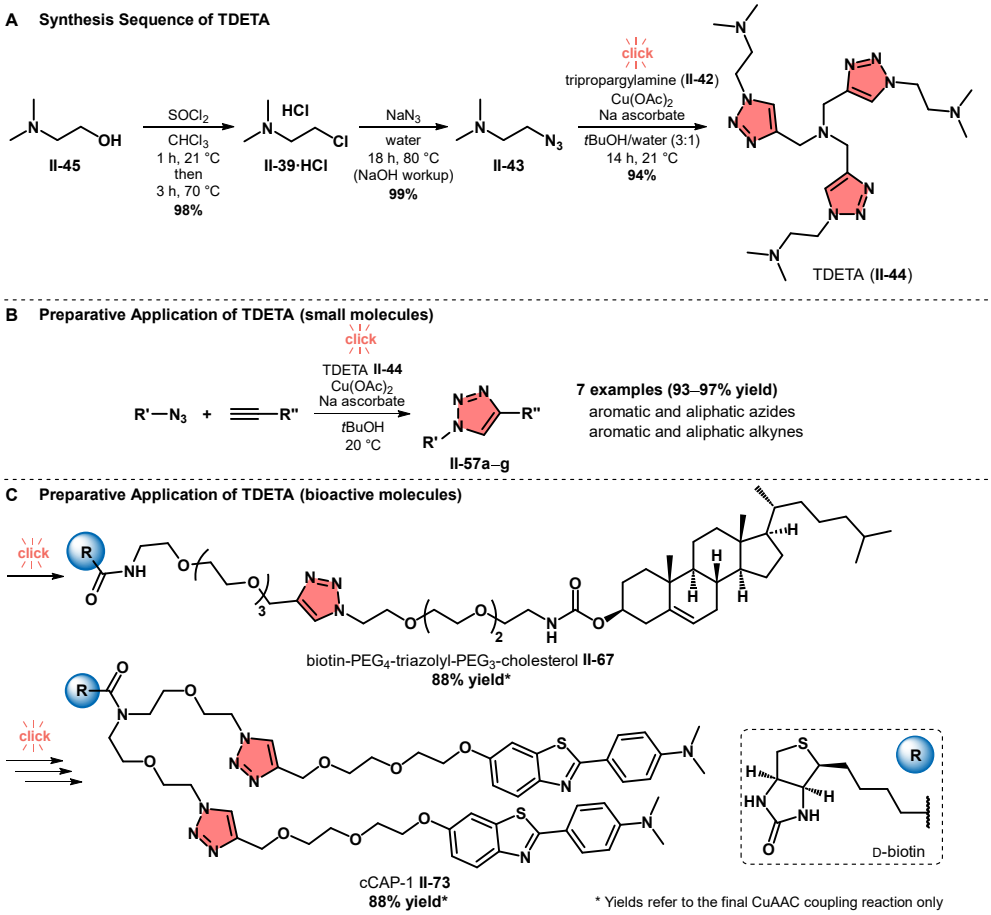
this future optimisation process, it is highly recommended to dismiss the ELISA-based approach and adapt the published methodology of highly sensitive fluorescence enhancement upon selective binding of α-syn fibrils by Rodrigues *et al*., thereby enabling benchmarking of our novel compound cCAP-1 **II-73** with a streamlined synthesis against the thoroughly validated literature compound CAP-1 **II-69**.[187] This will be of great importance to develop cCAP-1 **II-73** as a budget-friendly diagnostic tool, since the synthesis of CAP-1 **II-69** following the low-yielding literature procedure is very time-consuming and poorly documented, as noted earlier in the introduction (cf. Chapter II.3.3.1).

In conclusion, the new tetradentate class II copper-ligand TDETA **II-44** was successfully applied to generate biotinylated conjugates of cholesterol **II-67** and an analogue **II-73** of the amyloid-binding benzothiazole probe Pittsburgh Compound B in very good yields via CuAAC click chemistry. While the biotinylated cholesterol **II-67** will be used in a phage display to find novel peptide-based molecules that might help to counter atherosclerotic plaques, the benzothiazole probe cCAP-1 **II-73** will be of great importance to diagnose undetected neurodegenerative diseases, such as AD and PD, in early stages. Throughout the synthesis of cCAP-1, we devised a reliable and high-yielding synthesis of the branched biotin-bis-PEG-azide chassis **II-79** suitable for late-stage functionalisation and rapid library preparation with arbitrary alkyne probes via (bioorthogonal) click chemistry (CuAAC and SPACC). Building on the example of and inspired by the previously reported molecule CAP-1, we showcased the potential of the novel chassis by providing cCAP-1 **II-73** with dual probe loading as a synthetically more tractable and economical alternative for detecting amyloid fibrils from synucleinopathies, exemplified on α-synuclein. Furthermore, two independent routes leading to the non-commercially available Me-PiB **II-71** probe were presented, either starting from commercially available but yet expensive PiB **II-68**, or from inexpensive and available 6-methoxybenzothiazol-2-ylamine (**II-87**). To fully understand the amyloid- and streptavidin-binding properties of biotinylated cCAP-1 in complex biofluids, a detailed biochemical characterisation of cCAP-1 is required. This should be done in comparison to the well-characterised CAP-1 and with a focus on detecting amyloid fibrils through Me-PiB fluorescence enhancement or preparatively isolating amyloid fibrils via specific interactions between the biotin moiety of the probe and streptavidin-functionalised surfaces. This could be auxiliary in the purification, analysis, and quantification of amyloid fibrils from tissues and liquid biopsies of individuals at risk, while also contributing to an understanding of the mechanisms of amyloidogenesis and the development of predictive models for the early diagnosis of neurodegenerative diseases.

II.4 Summary Chapter II – The Novel Cu(I)/Cu(II) Ligand TDETA

In this work, the triazole-based tripodal Cu-ligand TDETA (**II-44**) was introduced as a versatile alternative to the previously reported ligand DTEA (**II-36**) (cf. Chapter II.3.1). The advantageous properties of the amine-substituted DTEA ligand, including broad solubility in aqueous and organic solvents, strong Cu(I)/Cu(II) binding, and excellent acceleration of both Cu(I)- and Cu(II)-catalysed CuAAC reactions, were successfully transferred to the novel ligand TDETA. Unlike precursors for DTEA synthesis, those precursors needed for the synthesis of TDETA are not restricted by the CWC, making this newly developed ligand an attractive option with significant potential for broad applications in synthetic chemistry and synthetic biology in academia and industry. The ligand TDETA was synthesised in a three-step process starting from ethanolamine (**II-45**) and relying solely on inexpensive components and reagents. The devised synthetic approach combines straightforwardness with an excellent overall yield of 91% over three consecutive synthesis steps (Scheme II.26), making TDETA a competitive ligand to commercially available alternatives, such as TBTA **II-26** and THPTA **II-27**, and a safe-to-synthesise alternative to the ligand DTEA (cf. Chapter II.3.1).

In the final step of the three-step synthesis of TDETA, an auto-catalysed and exothermic CuAAC reaction between tripropargylamine (**II-42**) and 2-azido-*N*,*N*-dimethylethan-1-amine (**II-43**) was employed to generate the novel tripodal ligand. First, aqueous extraction of the crude reaction product, containing the ligand TDETA, was considered for workup to remove soluble residues of the catalytic copper species. However, the high water-solubility of TDETA posed a challenge, as the very polar and hydrophilic ligand TDETA in complex with Cu-ions

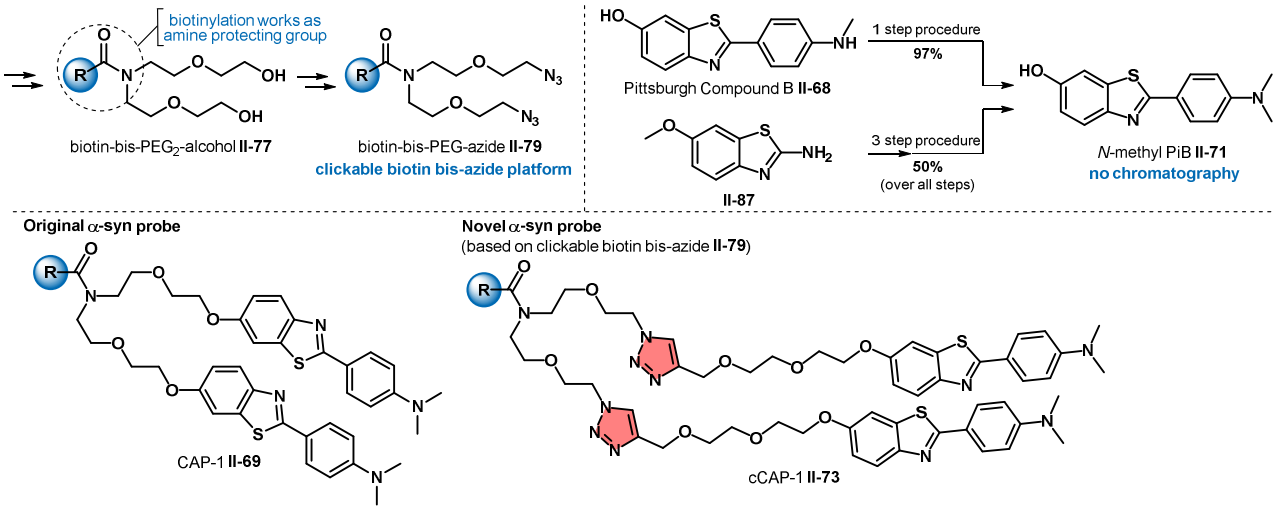


Scheme II.26. Presented synthesis scheme of the novel CuAAC ligand TDETA (**A**) and examples of its application in preparative organic synthesis of bioactive and small molecules (**B**–**C**). The triazole moiety formed in the CuAAC reaction between azide and alkyne is highlighted in orange.

remained in the aqueous phase, necessitating chromatographic purification without extractive removal of copper. Hence, chromatography on silica under strong basic conditions was used to remove catalytic copper and minor by-products from the desired tripodal reaction product TDETA. Nonetheless, the high water solubility of the ligand offers a practical advantage from another perspective: the positively charged TDETA-Cu(I) complex can be efficiently removed from preparative organic CuAAC reactions using aqueous extraction.
The broad functional group acceptance and versatility of TDETA as a rate-accelerating ligand in CuAAC click chemistry were demonstrated through various preparative examples involving aromatic and aliphatic azides and alkynes (cf. Chapter II.3.1.2 and Chapter II.3.1.3). In organic solvents (e.g. *t*BuOH), TDETA exhibited comparable performance to TBTA, the standard ligand for CuAAC reactions in organic solvents. Furthermore, TDETA outperformed the water-soluble ligand THPTA in terms of rate-acceleration of the CuAAC reaction in aqueous systems. The strong coordination of copper ions by the basic (dimethyl)amine groups qualify TDETA as a type II ligand, which functions optimally in a stoichiometric $[TDETA\text{-}Cu]^+$ complex (Figure II.4). Conversely, an excess of TDETA led to gradual inhibition of the CuAAC reaction due to competition for copper ions, reducing the availability of copper required for forming the initial copper-acetylide complex (cf. Chapter II.3.1.5). Taken together, the presented findings indicate that TDETA is a universally applicable ligand with high performance in both organic and aqueous systems, emphasising its broad utility for the acceleration of CuAAC reactions in diverse environments.

Beyond the characterisation of TDETA **II-44** and its ability to accelerate CuAAC reactions with a representative structural variety of substrates, the copper ligand was also employed in preparative syntheses of the respective products **II-57a**–**g**, achieving excellent yields ranging from 93% to 97% across seven selected reactions (cf. Chapter II.3.1.4). Furthermore, TDETA was utilised for the CuAAC synthesis of highly complex molecules with potential bioactive properties. For example, a biotinylated cholesterol derivative **II-67** was synthesised in a one-step reaction from commercially available biotin-PEG_4-alkyne (**II-65**) and cholesterol-PEG_3-azide (**II-66**) for use in phage display (cf. Chapter II.3.2.1). Similarly, TDETA facilitated the synthesis of maleimide-functionalised prodiginines, enabling targeted delivery of the cytotoxic tripyrrole scaffold via thiol-functionalised carriers such as antibodies or small molecules (cf. Chapter III.3.1).

Another example exploiting the benefits of TDETA for the preparative synthesis of valuable bioactive molecules was its utilisation in the synthesis of the α-synuclein and Aβ probe cCAP-1 **II-73** (Scheme II.26 and II.27) (cf. Chapter II.3.3). cCAP-1 represents an advancement of the well-characterised benzothiazole-based probe CAP-1 **II-69**, a molecular probe for detecting Alzheimer's disease and other neurodegenerative diseases. The original synthesis of CAP-1 involved poorly reproducible synthetic transformations and provided only moderate to low yields, despite the high cost of the synthetic precursor Pittsburgh Compound B (**II-68**). By redesigning the probe and adopting an alternative approach involving the introduction of reactive azides into a bis-functionalised biotin chassis **II-79**, cCAP-1 was synthesised efficiently via a protecting-group-free route using CuAAC (cf. Chapter II.3.3). The azide-functionalised biotin chassis introduced in this study offers the potential of versatile structural diversification through late-stage functionalisation with terminal alkynes (CuAAC-compatible) or cycloalkynes (SPAAC-compatible). This enables the reliable and straightforward generation of entire compound libraries, which – upon biotinylation – facilitate the structure-specific precipitation of probe interaction partners via the specific interaction between the biotin moiety and the protein streptavidin. Additionally, two independent synthetic routes were established for the *N*-methylated Pittsburgh B probe: a one-step Eschweiler-Clarke reaction for the *N*-methylation of commercially available PiB and a multistep sequence starting from 6-methoxybenzo[*d*]thiazol-2-amine (**II-87**). And lastly, selective binding of the benzothiazole probe cCAP-1 to *in vitro*-generated α-syn fibrils was validated and confirmed in a coupled ELISA assay (cf. Chapter II.3.3.5).



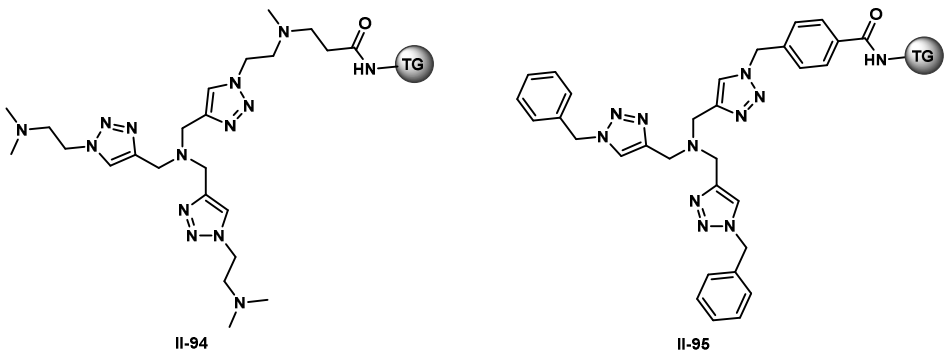
Scheme II.27. The streamlined synthesis towards the clickable biotin bis-azide **II-79** and the *N*-methylated benzothiazole probe **II-71** facilitate access to the clicked α-syn probe cCAP-1 **II-73**. The triazole moiety formed in the CuAAC reaction between azide and alkyne is highlighted in orange.

II.5 Outook Chapter II

This work made significant progress in developing a universally active and versatile copper-ligand for CuAAC-type click reactions, as the introduced ligand TDETA **II-44** showed strong reaction rate-acceleration in both aqueous and organic solvents. Since the presented preparative synthesis of TDETA is, other than the route towards the cognate ligand DTEA **II-36**, not subject to the legal restrictions and obligations of the Chemical Weapons Convention, and its synthetic intermediates are safe to handle, TDETA is a competitive CuAAC ligand compared to commercially available tripodal triazole ligands like TBTA and THPTA. While solid-supported variants of TDETA have the potential to overcome current limitations in ligand recycling and may help to make the utilisation of rate-accelerating and stabilising ligands more sustainable, the presented bis-azide biotin chassis could be adjuvant in generating large biotinylated compound libraries via CuAAC and SPAAC click chemistry for high-throughput screenings of potential drugs and other bioactive molecules. The following chapter highlights open research questions and future perspectives of CuAAC click reactions and how the designed molecules presented in Chapter II can assist in broadening the applicability of click chemistry in drug design and screening.

II.5.1 Synthesis of Polymer-Supported TDETA for Improved Recycling

Organic catalysts and ligands are precious goods, as they can become cost drivers in multikilogram synthesis. Consequently, cheap and efficient recoverability of these molecules is a desired property for large-scale applications in an industrial setup. In a scale-up CuAAC reaction with 5 mol% (201 µmol) loading of TDETA **II-44**, we could already show that the precious ligand can be recovered in a yield of 80%. However, the recovery process is based on chromatographic isolation and is hence a tedious and resource-intensive process. To minimise the effort of ligand recovery and attract a broad and straightforward application of TDETA-assisted CuAAC reactions on a large scale, developing a polymer-supported variant of TDETA **II-94** could be an alternative strategy. A similar polymer-supported ligand of TBTA (TentaGel TBTA **II-95**) is readily available on a commercial basis and reduces the recovery process to simple filtration (Scheme II.28).[247]



II-94
Proposed polymer-supported TDETA
TG-TDETA

II-95
Polymer-supported TBTA
TG-TBTA

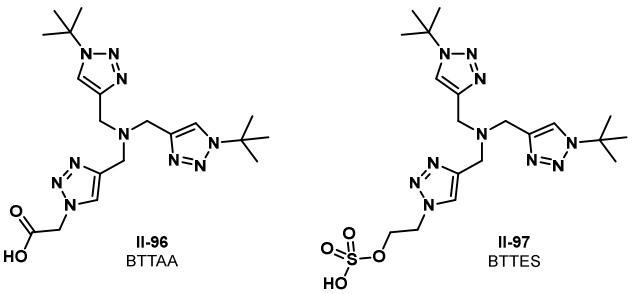
Scheme II.28. Structures of proposed polymer-supported TDETA **II-94** and the commercially available TBTA **II-95** equivalent.[247] Abbreviation: TG – TentaGel.

Although conjugation of TDETA **II-44** to the TentaGel matrix (PEG-coated polystyrene) might interfere with the ubiquitous solubility of the Cu-ligand in aqueous and organic solvents, the polymer-supported variant **II-95** of water-insoluble TBTA **II-26** has been shown to surprisingly catalyse CuAAC reactions in water, alcoholic solvents, CH_2Cl_2, and THF in a highly efficient manner with conversions >97%. Moreover, the TG-TBTA **II-95** maintained stable performance over ten consecutive cycles of catalysis and recycling.[247] The available stability and performance data on TG-TBTA **II-95** strongly support the potential for translating this polymer-support approach

to TDETA **II-44** as well, indicating prospects for improved recyclability while retaining catalytic efficiency. Hence, we infer that the polymer-supported TDETA **II-94** alternative would be highly appealing for large-scale industrial processes where large quantities of ligand are needed and recycling could help to minimise downstream processing, overall production costs, and the ecological footprint of the TDETA-catalysed CuAAC reactions.

II.5.2 Biocompatibility and *In Vivo* Application of TDETA II-44

Click reactions have been recognised as a strong driving force for widely applicable *in vivo* functionalisations of biomolecules, for instance, post-translational modification of proteins with non-natural amino acids or cell-surface labelling of bioengineered lipids and glycans, among others.[121, 248] The poor solubility of TBTA **II-26** in water initially motivated the development of the water-soluble ligand THPTA **II-27**, allowing for a broader application of CuAAC reactions in biological systems. As our novel ligand TDETA **II-44** poses exceptional solubility in various organic solvents and aqueous systems, its applicability in live-cell systems is a self-evident thought. Our current application proved its utility in organic synthesis and its compatibility with biologically relevant molecules (PiB probe, cholesterol). Next, experimental proof of compatibility with living cells or biopolymers (proteins, nucleic acids) might be considered to validate the biocompatibility of TDETA. As the copper catalyst used in CuAAC reactions generates ROS species, which are toxic to living cells, dedicated ligands have been developed in the past to increase the biocompatibility of the CuAAC reaction and mitigate the damage to living cells in the presence of copper. In this context, the group of Peng Wu developed two bis-*tert*-butyl ligands, namely BTTAA **II-96** and BTTES **II-97** (Scheme II.29), with a third tunable functional group for improved solubility and catalytic tuning in aqueous systems.[129-131] Moreover, the ligands are capable of shielding live cells from ROS and copper-mediated cytotoxicity that occurs through the reaction of copper with oxygen.[52] Both weak class I ligands outperformed TBTA **II-26** and THPTA **II-27** in a CuAAC labelling reaction of surface-exposed glycans in eukaryotic zebra fish cells and in the post-translational *in vitro* labelling of proteins. While THPTA **II-27** showed at least minor formation of fluorescent conjugates, TBTA **II-26** did not render any conversion at all. Furthermore, Li *et al*. extended the application of BTTAA **II-96** and other bis-*tert*-butyl ligands to in-cell labelling of alkynylated proteins,[249] emphasising the great potential of click reactions and the necessity of highly reactive and biocompatible copper-ligands. While TBTA, THPTA, BTTAA, and BTTES are all weak copper binders and categorised as class I ligands, our novel ligand TDETA is a stronger copper binder and class II ligand. Hence, TDETA is less likely to compete with cell surface-exposed proteins and glycopolymers for binding of copper ions, potentially leading to increased catalytic efficiency. Moreover, the symmetric design of TDETA simplifies its chemical synthesis, while synthetic routes leading to asymmetrical ligands, such as BTTAA and BTTES, suffer from lower yields and require additional synthetic steps. Together with the excellent solubility of TDETA in aqueous solutions, the novel Cu-ligand might be a competitive candidate for *in vivo* labelling of biomolecules through CuAAC click chemistry.



Scheme II.29. Biocompatible bis-*tert*-butyl copper-ligands BTTAA **II-96** and BTTES **II-97**.[129-131]

Based on the data availability for BTTAA, BTTES, and the commercially available ligands TBTA and THPTA, labelling of cell surface-exposed glycans would be an ideal starting point to validate the biocompatibility of TDETA **II-44** and to monitor cell viability in the presence of the Cu-TDETA complex. Although the incorporation of azido-sugars into natural glycans is catalysed by promiscuous glycosyltransferases in eukaryotes and prokaryotes,[96, 97, 129-131] bacteria are easier to cultivate and therefore a more accessible model for initial studies on this matter. To evaluate TDETA's biocompatibility, the application of an established system for fluorescent labelling of the bacterial LPS with alkynylated AlF488 via CuAAC could be suggested, facilitated by an incorporated azide-harbouring analogue of the essential LPS inner core sugar KDO (cf. Figure II.3).[96, 97] Thereby, the overall fluorescence count would be a simple readout for the performance of various ligands, such as TBTA **II-26**, THPTA **II-27**, BTTAA **II-96**, BTTES **II-97**, and TDETA **II-44**, in complex biological environments of living cells. Follow-up experiments should further evaluate the membrane permeability and cytotoxicity of all ligands to comprehensively assess their suitability for in-cell CuAAC reactions in living systems.

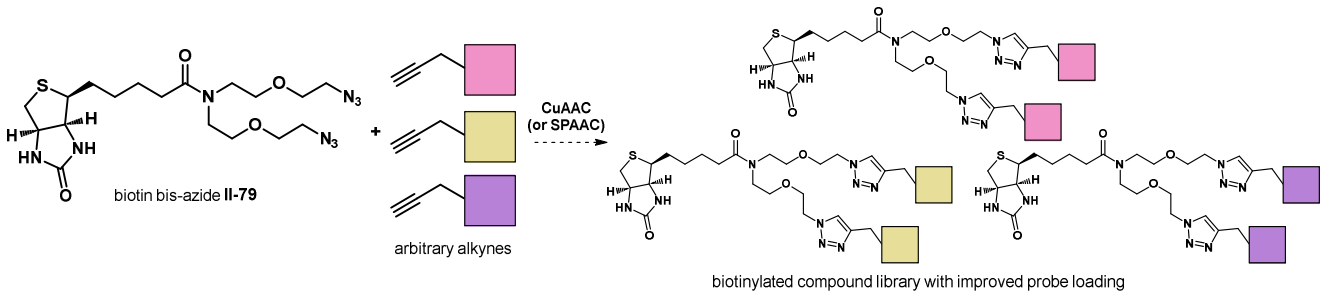
II.5.3 In-Depth Biochemical Characterisation of cCAP-1 II-73 and α-Syn Binding

The clicked capture molecule for amyloid precipitation (cCAP-1, **II-73**) was developed as an easier to synthesise and derivatise alternative to the previously reported biotinylated PiB probe CAP-1 **II-69** (cf. Scheme II.21). These probes from the family of benzothiazoles are able to intercalate into highly structured protein fibrils of α-syn, Aβ, and other proteins that have been associated with and are biomarkers of progressive neurodegenerative diseases, such Alzheimer's disease and Parkinson's disease.[223] As fibril binding of benzothiazoles is associated with a characteristic fluorescence enhancement of the probe, biotinylated benzothiazoles are currently being developed for structure-specific precipitation of fibrils from ubiquitously available biofluids (stool, blood, urine, etc.) and their quantification for early-stage detection of progressive neurodegenerative diseases with no cure.[187, 224, 244, 250] Thereby, these engineered molecules offer an inexpensive and less invasive tool in comparison to PET scans of human brains and tissue biopsies, respectively, to enrich low-abundant fibrils in early stages of the disease and moreover, develop early warning models to identify patients at risk even before the cognitive decline begins.

In the original publication of Rodrigues *et al*., the authors focused on an in-depth validation of CAP-1 **II-69** regarding its biological and biophysical properties and its limitations in α-syn fibril quantifications from liquid biopsies of human patients.[187] However, the applied synthesis route to access CAP-1 **II-69** was not fully reported on the one hand and highly inefficient on the other hand. Therefore, our reported route towards cCAP-1 **II-73** focused on the establishment of a modular and resource-efficient approach to gain hands-on bis-functionalised biotinylated probes in general through an intermediate biotinylated bis-azide chassis and the exploitation of click chemistry. Although we provided initial evidence for fluorescence enhancement upon α-syn fibril binding and selective binding of the biotin moiety to streptavidin, an in-depth characterisation of cCAP-1 **II-73** and a contrasting juxtaposition to CAP-1 **II-69** will be needed. These analyses should not only include an *in vitro* point-to-point analysis of fluorescence enhancement upon fibril binding, protein fibril selectivity (α-syn fibrils vs. Aβ amyloid fibrils), and biotin binding to streptavidin-functionalised surfaces, but should also include genuine human samples to distinguish fibril quantification in different biofluids and interference of possible matrix effects. This holistic characterisation of cCAP-1 **II-73** will allow us to fully outline the prospects of the alternative probe design and its value in developing easy-to-synthesise, highly modular, and broadly applicable diagnostic tools for neurodegenerative diseases in a rapidly ageing society.

II.5.4 Preparation of Libraries and High-Throughput Screening With the Biotinylated Bis-Azide II-79 Chassis

The bis-azide functionalised biotin chassis **II-79** offers a robust bioorthogonal platform for rapid functionalisation based on CuAAC and SPAAC click reactions. Furthermore, the universal nature of the azide-alkyne click reaction facilitates a simple probe exchange and structural diversification in the probe design and evaluation process. This ability may be a handy attribute in preparing large compound libraries for high-throughput screenings in the making of novel diagnostic tools or active agents (Scheme II.30), as it supersedes the development of lengthy syntheses for every individual probe and additional protecting group strategies. While commercially available biotinylated azides rely on a single azide “arm” and allow for only one probe attachment per biotin, the branched design of our reported bis-azide **II-79** doubles the probe/biotin ratio. This higher probe loading could enhance the binding of weak-interacting target molecules and thereby increase the overall sensitivity of the screening. Consequently, we hypothesise that a library of branched probes with increased assay sensitivity could uncover novel lead structures for further probe/drug optimisation via consecutive rounds of structural adaptations and binding analysis.



Scheme II.30. Scheme for the preparation of biotinylated compound libraries based on the biotin bis-azide chassis **II-79**. Libraries can either be generated via copper-catalysed click reactions with arbitrary alkynes (CuAAC shown) or in a strain-promoted fashion with cyclooctynes (SPAAC not shown).

Chapter II.5.4

Chemoenzymatic and Total Synthesis of Prodigiosin Alkaloids as Potent Antitumoral Agents Suitable for Target-Specific Application

Parts of this chapter were published in the following peer-reviewed articles:

New Prodigiosin Derivatives – Chemoenzymatic Synthesis and Physiological Evaluation Against Cisplatin-Resistant Cancer Cells.

Authors:
T. M. Weber, A. Leyens, L. Berning, B. Stork & J. Pietruszka.

Journal:
Catal. Sci. Technol. **2023**, 13(*21*), 6165–6184.

Own Contributions:
Project idea and conceptualisation; Experimental work and data evaluation; Writing and editing of the manuscript; Revision.

Contributions of Others:
Validation of anticancer activity on cisplatin-resistant cell lines (*Lena Berning, Björn Stork,* Institute of Molecular Medicine I, HHU Düsseldorf); final concendation of prodiginines **III-14d–g** (*Alexandra Leyens*, IBOC, FZ Jülich); chemical synthesis of 2-alkylated pyrroles **III-139c–g** (*Vera Ophoven*, IBOC, HHU Düsseldorf); Heterologeous expression of prodigiosin ligases (*Bea Paschold*, IBOC, HHU Düsseldorf); HPLC-MS measurements of reaction extracts and analytical standards (*Birgit Henßen*, IBOC, HHU Düsseldorf).

Functionalized in Triplicate: A Ring-by-Ring Approach to Tailored Prodiginine Derivatives for Site-Specific Conjugation Through Click Chemistry

Authors:
T.M. Weber & J. Pietruszka.

Journal:
Chem. Eur. J. **2025**, 31(*43*):e202502066.

Own Contributions:
Project idea and conceptualisation; Experimental work and data analysis; Writing and editing of the manuscript; Revision; Funding acquisition.

Other's contributions to this chapter not included in the above publications comprise the coupling of prodiginines **III-169**, **III-170**, and **III-171** to the trastuzumab-NEJ4 monoclonal antibody and cancer cell line binding studies (*Peter Bitsch*, *Harald Kolmar*, Applied Biochemistry, TU Darmstadt).

III Chemoenzymatic and Total Synthesis of Prodigiosin Alkaloids as Potent Antitumoral Agents Suitable for Target-Specific Application

III.1 State of the Knowledge

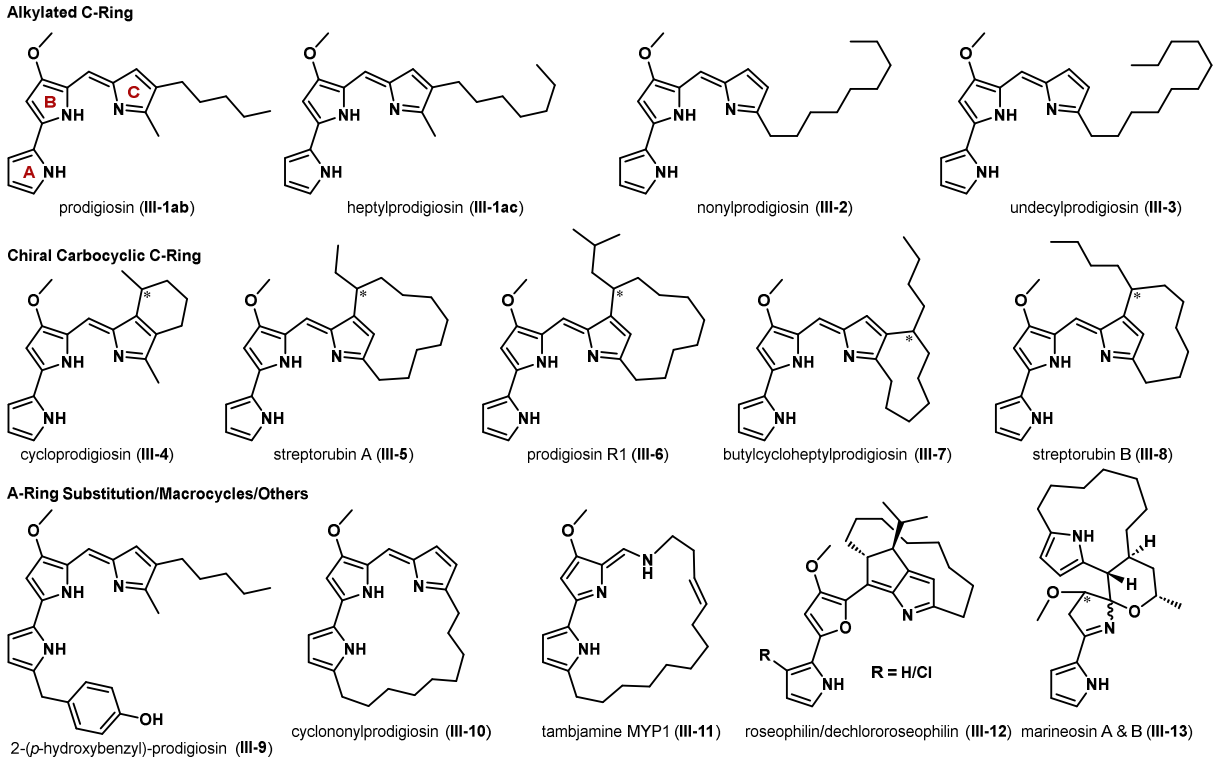
Natural products are, in a broad sense, all molecules produced by living matter that span from small molecules, which are built from only a few atoms, to highly complex polymeric molecules. To distinguish their diverging functions in cellular processes, these molecules are divided into two omnipresent groups – the so-called primary and secondary metabolites. However, despite their segregation into distinct groups, the boundary between primary and secondary metabolites is not well-defined and often blurred.[251] While primary metabolites are those molecules needed to establish and maintain essential cellular processes like DNA replication, protein biosynthesis, and energy metabolism, cell signalling, and cell differentiation, secondary metabolites are mostly non-essential molecules, which may play central roles in yet essential processes, for instance, in cell defence against competing species (e.g. antibiotics) or intraspecies communication (e.g. pheromones).[252, 253] Regardless, these two selected examples of antibiotics and pheromones as secondary metabolites just represent a tiny portion of the actual structural and functional opulence found within the class of bioactive secondary metabolites. Bioactivity in the context of secondary metabolites refers to the ability of these compounds to interact with biological systems and elicit a specific physiological or biochemical effect. The functions exploited by these bioactive secondary metabolites – or, in a narrower sense, natural products – are of particular interest for pharmaceutical applications, and their structures serve as an inspirational source in drug development to find new bioactive molecules and rationally improve their properties in various aspects.[254] To date, approximately 400,000 molecules from eukaryotes, prokaryotes, and archaea have been identified as secondary metabolites and have been fully characterised. Very recently, up to 67 million natural product-like molecules were identified through recurrent neural network training.[255] However, estimations forecast up to 100 million species on our planet, suggesting that the plethora of so far unknown natural products might be even significantly larger.[256] Although these natural products remain to be explored and their unknown metabolic roles and biological activities to be characterised, we can assume that some will find their way into pharmacological applications. In this regard, the field of bioorganic chemistry is devoted to finding purely chemical or chemoenzymatic modalities to make these fractionally low-abundant natural compounds accessible in large amounts and to prospect for synthetic routes to enable their structural derivatisation and pharmacological characterisation.[257]

III.1.1 Prodigiosin – A Tripyrrolic Bacterial Secondary Metabolite with a Long-Standing History

Prodigiosin (**III-1ab**) is a deep red coloured natural pigment of bacterial origin and it is the prototype compound and eponym for the generic family term of prodiginine or prodigiosin alkaloids (Scheme III.1). Although the younger chemical history of prodigiosin began to flourish in the first half of the 20th century, the pigment has been connected to several religious historical events throughout the centuries for more than 2000 years.[258, 259] Particularly, most historical blood miracles in which bread allegedly “bled” are inevitably connected with the natural product prodigiosin and can be traced back to contaminations with red prodiginine-producing bacteria. A famous example is the "Miracle of Bolsena" of 1263, in which a doubting priest saw blood on the sacramental bread (“host”) during mass, which was later recognised as a miracle and became the reason for the Corpus Christi festival and the construction of a cathedral in Orvieto. Lastly, the scientific cause of these miracles was only discovered in 1819 by Bartolomeo Bizio.[258, 259] Nevertheless, this is only one of many examples where prodigiosin has been connected to miracles and was misleadingly or deliberately interpreted as blood.

III.1.1.1 Structural Diversity of Natural Derivatives from the Prodiginine Family

Prodigiosin (**III-1ab**) was once identified due to its striking colourful appearance,[258, 259] being responsible for the characteristic red colouration of the bacterium *Serratia marcescens*, but nowadays its derivatives and their cytotoxic properties have raised scientific and clinical attention.[260-262] The family of natural prodiginines belongs to the class of secondary metabolites and shares a hydrophobic tripyrrole scaffold. Common for all prodiginines of natural and non-natural provenance is a congeneric conjugated scaffold of A-, B-, and C-ring pyrroles and decorations on the ring systems. Moreover, the B- and C-ring form a pyrrolylpyrromethene chromophore with a characteristic azafulvene element. During the last 70 years, the family of prodiginines has been first under investigation for structural elucidation, but then more and more has become of interest for the development of total synthesis strategies and for its manifold biological activities.[258, 259, 263-273] Owing to these efforts, the family of known chiral and achiral prodiginines of natural (Scheme III.1) and synthetic origin has steadily grown over the past decades.



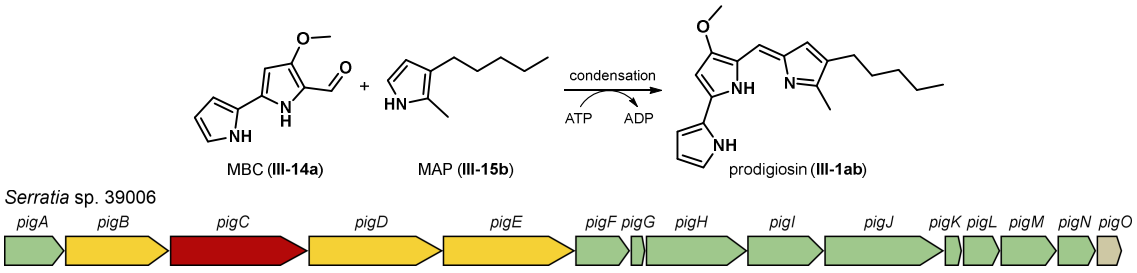
Scheme III.1. Structural diversity of natural prodiginines and related secondary metabolites from the tambjamine, roseophilin, and marineosin families. The structural information was gathered from the reviews of Williamson *et al.* and Hu *et al.*[274, 275] The molecule numbers of prodigiosin and heptylprodigiosin were endowed with additional letters for consistent denomination of A-ring alkylated prodiginines in the course of this thesis. The first letter **a** refers to no alkyl substitution in the 5-position[2] of the A-ring, while the second letter refers to the C-ring alkyl substitution [**a** = propyl (not shown), **b** = pentyl, **c** = heptyl].

Prodiginines and structurally related natural products are produced by a diverse group of Gram-positive and Gram-negative bacteria, which colonise soil, freshwater, and marine habitats. These bacteria belong to the phyla of Pseudomonadota [*Serratia*, *Pseudoalteromonas*, *Hahella*, (*Pseudo*)*Vibrio*] or Actinomycetota (*Streptomyces*,

[2] The atomic numbering according to IUPAC nomenclature assigns the number 5' to the nitrogen-adjacent secondary carbon of the A-ring in the free base of prodigiosin (**III-1ab**). However, this changes to 5 when using the corresponding HCl salt. To preclude confusion through a mixed nomenclature for A-ring alkylated prodiginines, the nitrogen-adjacent carbon will be exclusively denoted as 5-position.

Actinomadura, and *Saccharopolyspora*). Considering the wide distribution among the genus of bacteria, a rather surprisingly small number of prodiginines with an equally small structural diversity has been identified. The classification for these compounds is based upon the type of substitution, which is found on the C-ring. The first group of compounds includes prodigiosin (**III-1ab**), heptylprodigiosin (**III-1ac**), nonylprodigiosin (**III-2**), and undecylprodigiosin (**III-3**) and shares the feature of an *n*-alkylated C-ring. The second group uses the *n*-alkylated prodiginines for an enzyme-catalysed C-ring internal cyclisation reaction, providing chiral carbocycles with ring sizes of six [cycloprodigiosin (**III-4**)], twelve [streptorubin A (**III-5**) and prodigiosin R1 (**III-6**)], nine [butylcycloheptylprodigiosin (**III-7**)], or ten [streptorubin B (**III-8**)] carbons. Furthermore, some examples do not fit into these two predominant groups. Thus, the third group is a basin for all compounds, which cannot be classified according to the previously introduced categorisation system. Examples for representatives of this group are the A-ring modified 2-(*p*-hydroxybenzyl)prodigiosin (**III-9**), the macrocyclic cyclononylprodigiosin (**III-10**) and tambjamine MYP1 (**III-11**), or the B-ring derivatives roseophilin (**III-12**) and marineosin A and B spiroaminals (**III-13**).

At first glance, a high degree of structural homology between most prodiginines can be recognised. The tripyrrole pigments owe this fact to the underlying modular biosynthesis, which is largely conserved between the prodiginine-producing organisms in its essential steps. Briefly, the prodiginine scaffold is formed in the last step of a convergent route through the condensation reaction of a variable monopyrrole precursor and a unique bipyrrole precursor. On the example of prodigiosin, the bipyrrole precursor 4-methoxy-2,2′-bipyrrol-5-carbaldehyde (**III-14a**, MBC) and the monopyrrole precursor 2-methyl-3-*n*-amyl-1*H*-pyrrole (**III-15b**, MAP) are consolidated in a condensation reaction by the so-called prodigiosin ligase PigC (Enzyme Commission number EC 6.4) under consumption of adenosine triphosphate (ATP) to form the pyrrolylpyrromethene C-C bond between B- and C-ring (Scheme III.2). The MBC constitutes the latter A- and B-ring of the natural product, whereas the monopyrrole building block forms the C-ring. Other *n*-alkylated prodigiosin derivatives are obtained by modifications in the MAP biosynthesis that lead to a substitution of the C-ring monopyrrole MAP by 2-methyl-3-heptyl-1*H*-pyrrole, 2-nonylpyrrole, or 2-undecylpyrrole for the condensation reaction with MBC **III-14a**, and provide the derivatives **III-1ac**, **III-2**, and **III-3**, respectively.



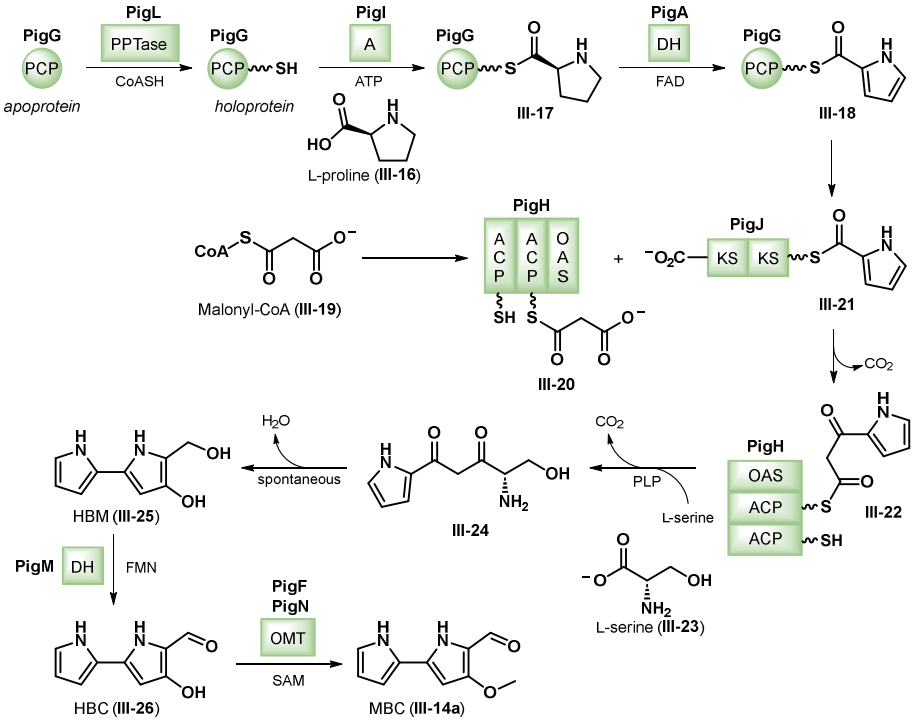
Scheme III.2. Top: Condensation reaction of the MBC **III-14a** and MAP **III-15a** building blocks in the last step of prodigiosin biosynthesis in *S. marcescens*. The molecule numbers of MBC, MAP, and prodigiosin were endowed with additional letters for consistent denomination of A-ring alkylated MBC derivatives and prodiginines in the course of this thesis. The letter **a** of unsubstituted MBC refers to no alkyl substitution in the 5'-position of the future A-ring, while the letter **b** of MAP refers to the 3-alkyl substitution [**a** = propyl (not shown), **b** = pentyl, **c** = heptyl (not shown)]. Bottom: Prodigiosin biosynthesis gene cluster (*pig*) from *Serratia* sp. 39006.[276] The colours correspond to the involvement in MBC biosynthesis (green), MAP biosynthesis (yellow), MBC and MAP condensation (red), and regulatory functions (beige).

III.1.1.2 Biosynthesis of Prodigiosin

With an increasing number of prodiginines and related natural products isolated and characterised from natural sources, the quantity of known bacterial gene clusters involved in their biosynthesis has constantly risen. To date, numerous clusters among diverse bacterial species, such as *pig* (*Serratia marcescens*, prodigiosin **III-1ab**),[276] *red* (*Streptomyces coelicolor*, undecylprodigiosin **III-3** and streptorubin B **III-13**),[277] *trea* (*Pseudoalteromonas citrea*, tambjamine MYP1 **III-11**),[278] and *mar* (marine *Streptomyces* sp., marineosin A) have been identified by genome mining and analyses of mutant strains paired with sequence homology analyses allowed the assignment of particular functions to the involved genes and enzymes (cf. Scheme III.2).[279-283] Despite the structural diversity of prodiginine-related natural products, their biosynthesis resorts to clustered genes, encoding enzymes with high similarity to other natural product synthases. Using the *pig* gene cluster from *S. marcescens* for the biosynthesis of prodigiosin (**III-1ab**) as a representative example, the assembly employs a convergent route with two key precursors, namely MBC **III-14a** and MAP **III-15b**.[276, 284-286] Enzymes from this cluster share homology to adenylation domains and peptidyl carrier proteins from non-ribosomal peptide synthetases (NRPS) of type II and to acyl carrier proteins and ketosynthase domains of polyketide synthases (PKS).[275, 277, 287] The current state of knowledge regarding the biosynthesis of MBC **III-14a** and MAP **III-15b** will be unravelled in the following paragraphs.

III.1.1.2.1 Biosynthesis of MBC

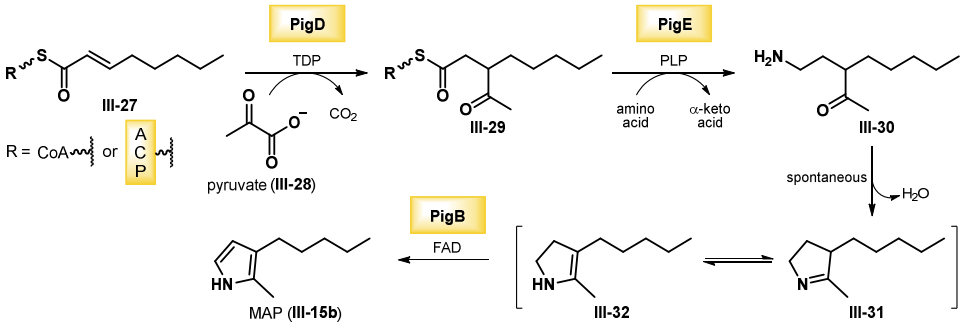
The biosynthesis of the highly conserved prodigiosin precursor MBC **III-14a** includes ten of the 15 genes from the *pig* cluster of *Serratia* species (cf. Scheme III.2).[274, 275] The biosynthesis commences with the transfer of the peptidyl carrier protein (PCP) PigG from the apoform into its active holoform through incorporation of the phosphopantetheinyl moiety (Scheme III.3). This activation is catalysed by PigL, a phosphopantetheinyl transferase (PPTase). Subsequently, the natural amino acid L-proline (**III-16**) is transferred onto the PCP in an ATP-catalysed process, which is mediated by the standalone NRPS adenylation domain PigI.[277] The thereby generated activated prolyl thioester **III-17** is then oxidised in a four-electron oxidation by the FAD-dependent dehydrogenase PigA to give the corresponding pyrrole-2-carboxyl thioester **III-18**. This pyrrole moiety constitutes the future unsubstituted A-ring of prodigiosin (**III-1ab**) and its synthesis was interestingly found to be identical to the first steps of undecylprodigiosin and pyoluteorin biosynthesis. In the following sequence, the B-ring is stepwise built through chain elongation, similarly to polyketide biosynthesis. The chain elongation is initiated by malonate **III-19**, which is activated through the corresponding coenzyme A (CoA) thioester **III-20**. After its transfer onto the acyl carrier protein (ACP) domain of PigH, the malonyl thioester and the PigJ ketosynthase-bound thioester moiety of pyrrole carboxylate **III-21** react in a Claisen condensation with subsequent decarboxylation to give the β-keto thioester **III-22**, which remains bound to the ACP of PigH. Assisted by the predicted C-terminal pyridoxal phosphate (PLP)-dependent α-oxamine synthase (OAS) domain of PigH, L-serine (**III-23**) is added to the β-keto thioester **III-22** via decarboxylative condensation and the resulting α,γ-dioxamine **III-24** is finally released from PigH. The next steps in forming the B-ring pyrrole are assumed to be spontaneous and thus enzyme-independent and include cyclisation, dehydration, and tautomerisation of α,γ-dioxamine **III-24**. As a result, the MBC precursor 4-hydroxyl-2,2′-bipyrrole-5-methanol (HBM, **III-25**) is obtained. While the 4-hydroxy group remains untouched, the 5-methanol hydroxy group is oxidised by the FMN-dependent dehydrogenase PigM to the direct MBC precursor 4-hydroxyl-2,2′-bipyrrole-5-carbaldehyde (HBC, **III-26**). In a final step, the remaining hydroxy group is *O*-methylated by the *S*-adenosyl methionine (SAM)-dependent *O*-methyl transferase (OMT) PigN/PigF to produce MBC **III-14a**.



Scheme III.3. Biosynthesis of the prodigiosin bipyrrole precursor MBC (**III-14a**) in *S. marcescens* encoded within the *pig* gene cluster. The figure was adapted from Hu *et al*.[274] Abbreviations: A – adenylation domain; ACP – acyl carrier protein; ATP – adenosine triphosphate; CoA – coenzyme A; DH – dehydrogenase; FAD – flavin adenine dinucleotide; FMN – flavin mononucleotide; KS – ketosynthase; OAS – α-oxamine synthase; OMT – *O*-methyltransferase; PCP – peptidyl carrier protein; PLP – pyridoxal phosphate; PPTase – phosphopantetheinyl transferase; SAM – *S*-adenosyl methionine.

III.1.1.2.2 Biosynthesis of MAP

The biosynthesis of the monopyrrole precursor MAP **III-15b** involves only three of the 15 genes encoded within the *pig* gene cluster of *Serratia* (cf. Scheme III.2).[274, 275, 283] In the first step of the biosynthesis, the thiamine diphosphate (TDP)-dependent enzyme PigD catalyses the decarboxylative condensation reaction of the 2-octenoyl-ACP or -CoA thioester **III-27** with pyruvate (**III-28**), providing the 1,4-dicarbonyl thioester **III-29** (Scheme III.4). PigD utilises the carbene cofactor TDP for a sequential Umpolung of the electrophilic keto carbonyl carbon and decarboxylation of pyruvate (**III-28**) to generate a nucleophilic species that reacts with the unsaturated 2-octenoyl thioester **III-27** in an enzymatic Stetter reaction.[288, 289]



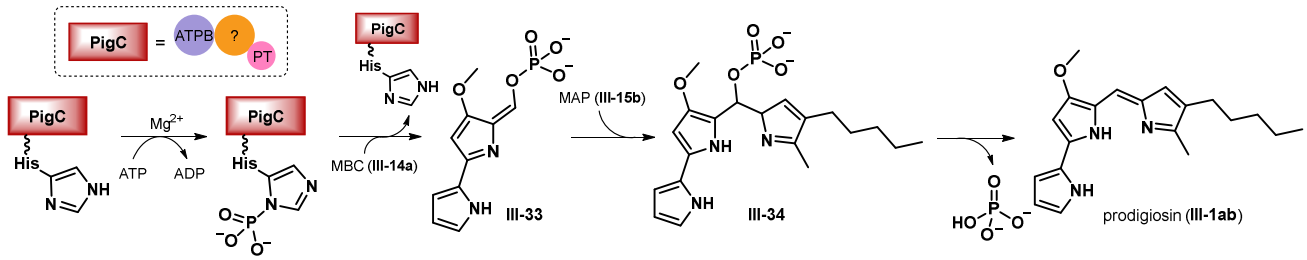
Scheme III.4. Biosynthesis of the prodigiosin monopyrrole precursor MAP (**III-15b**) in *S. marcescens* from the *pig* gene cluster. The figure was modified from Hu *et al*.[274] Abbreviations: ACP – acyl carrier protein; CoA – coenzyme A; FAD – flavin adenine dinucleotide; PLP – pyridoxal phosphate; TDP – thiamine diphosphate.

Recent results have suggested that PigE is a bifunctional enzyme, harbouring thioester reductase and PLP-dependent transaminase activity. While the reductase domain catalyses the conversion of the thioester functionality into the corresponding aldehyde, which triggers the release from the CoA or ACP carrier, the transaminase domain is responsible for the transamination of the aldehyde moiety into the primary amine to yield γ-ketoamine **III-30**.[290] Mediated by the high nucleophilicity of the amine, the intramolecular cyclisation reaction occurs spontaneously under the elimination of water to give the imine 3,4-dihydro-2*H*-pyrrole **III-31** species, which tautomerises to the enamine 2,3-dihydro-1*H*-pyrrole **III-32** form. In the last step of the MAP biosynthesis, the FAD-dependent enzyme PigB oxidises the enamine **III-32** in a two-electron oxidation to the monopyrrole precursor MAP **III-15b**.

The enzymes responsible for the C-C-bond-forming condensation reaction of monopyrroles and MBC belong to the class of ligases (EC 6.4). Here, the enzymes PigC, RedH, TreaP, and MarH from the aforementioned gene clusters take on the role of ligases in the corresponding pathways. Unfortunately, crystallisation attempts of these enzymes have not led to fruitful insights into structure-based mechanistic peculiarities so far. And yet, approximations to the structure were achieved through homology modelling and docking studies,[291, 292] while kinetic studies elucidated mechanistic intricacies.[293]

III.1.1.2.3 Prodigiosin Ligases

As noted in the previous paragraph, the class of prodigiosin ligases (EC 6.4) is responsible for the C-C-bond-forming condensation reaction between monopyrroles and the bipyrrole MBC **III-14a**. The first identified representative of these condensing enzymes was PigC, encoded within the *pig* gene cluster of *Serratia* species. Although no structural information has been obtained from classical methods, such as X-ray crystallography, NMR, or cryogenic electron microscopy, the group of condensing enzymes shows domain architecture and homologies to other enzyme families.[274, 275, 283, 286, 293-295] All condensing enzymes consist of a total of three domains (Scheme III.5), of which one domain is responsible for ATP-binding (ATPB domain). This C-terminal ATPB domain shares a high degree of similarity to the ATPB domain of phosphoenolpyruvate (PEP) synthases. A second domain is located at the N-terminus and is a homologue of the pyruvate phosphate dikinase (PPDK) enzymes. Consequently, this N-terminal domain is most likely involved in transferring phosphate groups from the cosubstrate ATP to the enzyme and subsequently transferring phosphate to the small-molecule substrate MBC **III-14a** or its structural analogues for their activation. Hence, phosphotransferase (PT) activity was assigned to this N-terminal domain of prodigiosin ligases. The last domain is located between the ATPB and the PT domain and does not show sequence homology to any known family of enzymes.



Scheme III.5. Final step of prodigiosin biosynthesis through the ATP-catalysed condensation reaction of MAP (**III-15b**) and MBC (**III-14a**) by the prodigiosin ligase PigC from *S. marcescens* encoded within the *pig* gene cluster. PigC consists of three domains, of which two domains share sequence homology to an ATP-binding domain (ATPB) and a phosphotransferase domain (PT). The figure was modified from Hu *et al.*[274] Abbreviations: ADP – adenosine diphosphate; ATP – adenosine triphosphate.

Even though the lack of structural information limits our current understanding of peculiarities in substrate binding, activation, and substrate promiscuity, the described domain homologies to other enzymes allow a mechanistic forecast of the ligation reaction between MAP **III-15b** and MBC **III-14a** for the representative enzyme PigC from *Serratia* species (Scheme III.5). It was hypothesised that the reaction is initiated by an ATP-dependent phosphorylation of a histidine side chain of PigC, while ADP is released from the enzyme. Upon binding of MBC **III-14a**, the phosphate residue is transferred onto the aldehyde moiety of the bipyrrole precursor. The monopyrrole **III-15b** then attacks the activated carbonyl **III-33**, which collapses under elimination of the phosphate group from intermediate **III-34** into the conjugated tripyrrole scaffold of prodigiosin **III-1ab**. Recent studies of Picott *et al*. with PigC and the homologue TamQ from *Pseudoalteromonas tunicata* suggested a Uni Uni Bi Uni ping-pong reaction mechanism for these enzymes that implies sequential binding and release of the involved components rather than concurrent binding at the active site.[293]

III.1.1.3 Substrate Promiscuity of Prodiginine Ligating Enzymes

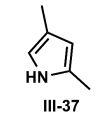
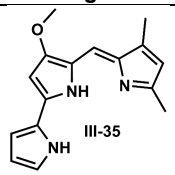
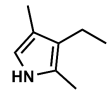
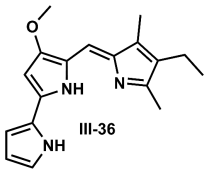
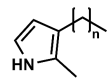
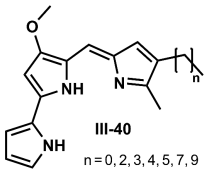
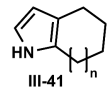
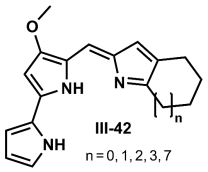
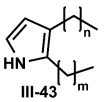
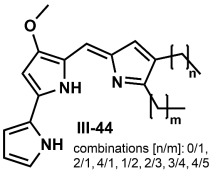
III.1.1.3.1 Monopyrrole Promiscuity

Throughout the years, several PigC homologues from other biosynthesis clusters were identified as prodiginine or tambjamine ligases to which the ATP-dependent ligation mechanism applies (cf. Scheme III.5). In addition to PigC from *Serratia* species, RedH (*Streptomyces coelicolor*),[294] MarH (*Streptomyces* sp. CNQ-617),[279] McpH (*Streptomyces longisporusruber*),[296] RphH (*Streptomyces griseoviridis*),[297] HapC (*Hahella chejuensis*),[298] TamQ (*P. tunicata*),[299] and TreaP (*Pseudoalteromonas citrea*) have been annotated.[295] As early as 1970, before the biosynthesis of prodigiosin was understood to involve clustered genes or specific functions were attributed to the *pig* genes within this cluster, Hearn *et al*. demonstrated that the *Serratia marcescens* mutant strain 9-3-3 could produce prodigiosin analogues **III-35** and **III-36** with 2,4-dimethyl- or 2,4-dimethyl-3-ethyl substitutions on the C-ring pyrrole following supplementation with the corresponding monopyrroles **III-37** and **III-38** (Table III.1).[300] Since the researchers were able to detect accumulation of MBC **III-14a** in this strain, it was concluded that a defect in MAP biosynthesis is likely. The concurrent absence of the natural prodigiosin monopyrrole precursor MAP in strain 9-3-3 and the conversion of MBC and supplemented non-natural monopyrroles into non-natural prodiginines suggested a certain promiscuity of the involved enzymes, of which we now know that it is only one enzyme, namely the prodigiosin ligase PigC. At the time, this was the first experimental proof of a broadened substrate scope for this family of ligating enzymes.

These results motivated Klein *et al*. in 2017 to characterise the monopyrrole substrate scope of PigC in detail.[301] PigC seemingly prefers pyrroles **III-39** with a medium alkyl chain length in the 3-position, as the highest product **III-40** titres were achieved for propyl, butyl, and pentyl substitution. Furthermore, the methyl group in the 2-position of the pyrrole is essential, as prodiginine yields drop significantly with ethyl substituents and no product is formed with propyl chain substituents or longer.[301] Shortly afterwards, the researchers demonstrated that the cyclic monopyrrole derivatives **III-41** are accepted as substrates by PigC, too, giving access to carbocyclic C-ring-derivatised prodiginines **III-42**.[302] The high interest in prodiginines as pharmacologically active scaffolds and previous efforts of their sustainable microbial mutasynthesis from renewable sources motivated Brass *et al.* to search for novel homologues of PigC with a distinct substrate scope. In 2019, the researchers identified two novel condensing enzymes from marine organisms by sequence homology to PigC, belonging to tambjamine biosynthesis pathways.[295] The two identified enzymes, namely TamQ and TreaP (*vide supra*), interestingly showed a clear preference for pyrrole substrates with long aliphatic side chains in the 3-position and broadly accepted pyrroles **III-43** with longer alkyl substitution in the 2-position that led to novel prodiginines **III-44**. From an evolutionary perspective, these differences to the substrate scope of PigC might result from the fact that TreaP

and TamQ evolved to accept long-chain aliphatic amines, which are used as a condensation partner for MBC **III-14a** in tambjamine biosynthesis (cf. tambjamine MYP1 **III-1**, Scheme III.1).

Table III.1. Incomplete selection of non-natural monopyrrole derivatives known to be accepted by PigC or other condensing enzymes *in vivo* (mutasynthesis) or *in vitro*. The monopyrroles are coupled with MBC **III-14a**.

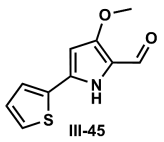
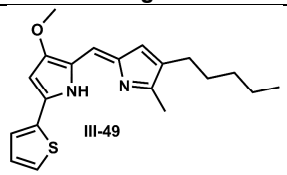
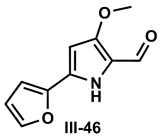
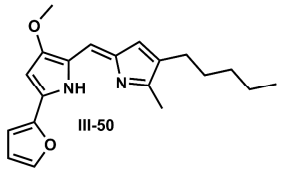
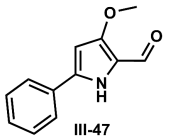
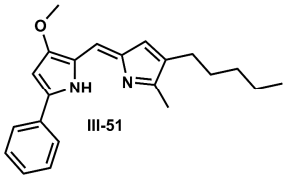
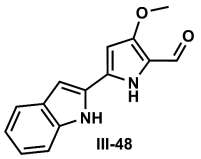
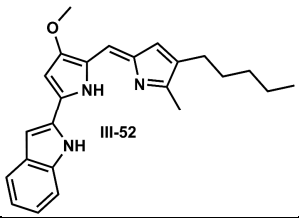
Monopyrrole Derivative	Strain (Enzyme)	Prodiginine	Reference
 **III-37**	*S. marcescens* 9-3-3 (PigC)	 **III-35**	[300]
 **III-38**	*S. marcescens* 9-3-3 (PigC)	 **III-36**	[300]
 **III-39** n = 0, 2, 3, 4, 5, 7, 9	*Pseudomonas putida* KT2440 pig-r2 Δ*pigD* (PigC) PigC/TamQ/TreaP (*in vitro*)	 **III-40** n = 0, 2, 3, 4, 5, 7, 9	[295, 301]
 **III-41** n = 0, 1, 2, 3, 7	*P. putida* KT2440 pig-r2 Δ*pigD* (PigC)	 **III-42** n = 0, 1, 2, 3, 7	[302]
 **III-43** combinations [n/m]: 0/1, 2/1, 4/1, 1/2, 2/3, 3/4, 4/5	PigC/TamQ/TreaP (*in vitro*)	 **III-44** combinations [n/m]: 0/1, 2/1, 4/1, 1/2, 2/3, 3/4, 4/5	[295]

III.1.1.3.2 Bipyrrole Promiscuity

Promiscuity of prodiginine ligating enzymes, exemplified by PigC from *S. marcescens*, is well-known for monopyrroles with cyclic and acyclic aliphatic side chains and the C-ring moiety of prodiginines.[295, 301, 302] Contemporaneously, little evidence has yet been provided in the context of MBC derivatives being suitable substrates for prodiginine ligating enzymes. Haynes *et al*. attempted an investigation of a RedH-catalysed condensation of a dechlororoseophilin-inspired MBC analogue in combination with 2-undecylpyrrole, but did not observe any product formation. Since their study was conducted as a feeding experiment with the mutant strain *S. coelicolor* W39, limited phase transfer across the bacterial membrane or a lack of eligibility as RedH substrate were deduced as potential causes for missing product formation.[294] Chawrai *et al.* were the first to demonstrate the enzymatic conversion of aryl-substituted derivatives of MBC (e.g. thienyl- **III-45**, furyl- **III-46**, phenyl- **III-47**, indoyl- **III-48**) by PigC, leading to novel A-ring-substituted prodiginine analogues **III-49**, **III-50**, **III-51**, and **III-52**, respectively (Table III.2).[286] However, since then, no biocatalytic studies with substituted MBC derivatives have been performed beyond that. Nevertheless, great potential lies dormant in A-ring derivatised prodiginines, as showcased by the chemically synthesised former clinical trial candidate obatoclax mesylate, whose A-ring pyrrole

is substituted by an indole moiety (*vide infra*).[260-262, 303] In summary, the largely unexplored promiscuity of prodiginine ligating enzymes for derivatives of its biaryl substrate MBC highlights the untapped potential of prodiginine ligases for advancing their biocatalytic applications in prodiginine chemistry and the discovery of novel prodiginine derivatives with A- and B-ring modifications.

Table III.2. Non-natural MBC derivatives known to be enzyme-convertible by the prodiginine ligase PigC.

MBC Derivative	Strain (Enzyme)	Prodiginine	Reference
 III-45	*Serratia* sp. 39006 Δ*pigH57* (PigC)	 III-49	[286]
 III-46	*Serratia* sp. 39006 Δ*pigH57* (PigC)	 III-50	[286]
 III-47	*Serratia* sp. 39006 Δ*pigH57* (PigC)	 III-51	[286]
 III-48	*Serratia* sp. 39006 Δ*pigH57* (PigC)	 III-52	[286]

III.1.1.4 A-Ring Modifications of Prodiginine-Related Natural Products and Non-Natural Derivatives

The known natural prodiginine and connatural tambjamine derivatives featuring aliphatic substitutions on the A-ring consistently belong to the class of macrocycles, except the oddly protruding 2-(*p*-hydroxybenzyl)prodigiosin (**III-9**) from the marine bacterium *Pseudoalteromonas rubra* (Scheme III.1).[304] The formation of macrocyclic prodiginines is specifically attributed to the late-stage oxidative carbocyclisation of long alkyl chains on the prodiginine C-ring, including a carbon-centred radical intermediate.[305, 306] Because of this enzymatic cyclisation reaction, either formation of C-to-A-ring (a, cyclononylprodigiosin **III-10** and tambjamine MYP1 **III-11**) or C-to-B-ring (b, marineosin A and B **III-15**) bridging macrocycles is observed. Moreover, the formation of C-ring internal chiral cycles (c, cycloprodigiosin **III-4**, streptorubin A **III-5**, streptorubin B **III-8**, prodigiosin R1 **III-6**) can be catalysed by cyclases. Prominent examples for those cyclase enzymes are the RedG homologue MarG involved in marineosin biosynthesis (b) or the Rieske oxygenase RedG in the biosynthesis of streptorubin B (c).[306] For the C-to-A-ring bridged carbomacrocycle cyclononylprodigiosin (**III-10**), the biosynthetic *non* gene cluster with the RedG-homologue NonG has been assigned (a).[307] However, the upstream condensation of bipyrrole and monopyrrole exclusively relies on the usage of unsubstituted MBC **III-14a** as a bipyrrole condensation partner, meaning that no naturally occurring A-ring-substituted MBC derivatives have been found to date. In the case of

A-ring-modified 2-(*p*-hydroxybenzyl)prodigiosin (**III-9**), no proposal on its biosynthesis and the involved genes, based on experimental evidence, has been published.[308] Another well-known example of a prodigiosin-related natural product is roseophilin (**III-12**) from *S. griseoviridis*, which shows 3-chlorination of the A-ring, substitution of the B-ring pyrrolyl moiety by a furyl heterocycle and a chiral macrocyclic C-ring. Although the chlorination pattern implies utilisation of a chlorinated MBC analogue, comparable to the biosynthesis of pyoluteorin,[309] an adequate precursor and identification of the responsible halogenating enzyme remain missing. A late-stage halogenation of dechlororoseophilin could be plausible, too. Indeed, the experimental lack of proof of substituted A-ring MBC derivatives from natural sources is not surprising, as the A-ring is biosynthetically built from the amino acid L-proline (**III-16**) (cf. Scheme III.3). Within the prodigiosin *pig* biosynthesis cluster of *Serratia* species, the early steps of transformation include PigI-catalysed activation of L-proline (**III-16**) as PCP-prolyl thioester **III-17** and the subsequent four-electron oxidation of the pyrrolidine core by the dehydrogenase PigA to give the pyrrole-2-carboxyl thioester **III-18**.[274, 276, 277] In other words, a prerequisite for natural A-ring variation on MBC derivatives would be the acceptance of alternative canonic amino acids by PigI during the initial steps in the biosynthesis or functionalisation of the A-ring pyrrole in successive steps. Nevertheless, no evidence has been provided for the existence of this type of A-ring-substituted MBC to date.

Even though the broad accessibility of A-ring-substituted prodiginines by biosynthetic methods is not given from today's perspective, those derivatives can be assessed by means of chemical synthesis. Some studies previously denoted positive effects on prodiginine-related cytotoxicity for chemically synthesised prodiginines with A-ring substitution.[310, 311] These results provide substantial evidence of value to further analyse synthetic prodiginines with derivatisation of the A-ring and the consequences for cytotoxicity and sustainable options of their microbial manufacturing with prodiginine ligases.

III.1.1.5 Biological Activities

Natural and non-natural prodiginines exhibit numerous biological activities, which is why the pyrrole alkaloids gained high attention in applied and pharmaceutical research. Besides antimicrobial activity against both Gram-positive and Gram-negative bacteria, antiprotozoal/antimalarial, antitumoral, and antifungal activities were described for this class of compounds. The following paragraphs will summarise the fundamental mechanisms that lead to cytotoxicity against these morphologically and genetically diverse organisms and diseases *in vivo* and *in vitro.*

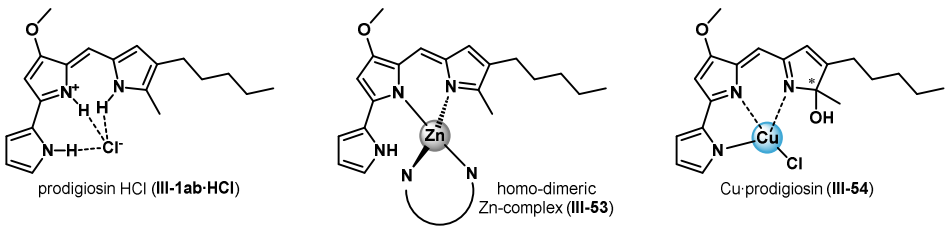
III.1.1.5.1 Cytotoxicity and Antibiotic Effects

The basic tripyrrole scaffold of the prodiginine family possesses a very high affinity to Lewis-acidic cations, such as H^+, Cu^+, Cu^{2+}, Zn^{2+}, and Co^{2+}, and forms a very tight lipophilic complex with the corresponding counter ions.[258, 259, 312] Especially, the hydrochloride complexes of several natural and non-natural prodiginines were shown to diffuse across biological membranes in an untargeted manner, facilitated by passive diffusion. Through this mechanism, H^+ and Cl^- ions are symported across the membrane along with the prodiginine, leading to uncoupling or depletion of ion gradients along the membrane.[313-316] These ion gradients are particularly essential for energy harvesting through molecular motor proteins located within the membrane (e.g. ATP synthase) or the proton motive force (PMF).[317] Furthermore, liposomal antiport was found for Cl^- and bicarbonate in the presence of prodigiosin (**III-1ab**).[318] Based on this ability to cross biological membranes, prodiginines can modulate the pH of single cells or cellular compartments, are eligible to remain within these membranes, or interact with the outer membrane of mitochondria to uncouple the F_0F_1-ATPase activity. This uncoupling of the mammalian F_0F_1-

ATPase, which generates ATP from ADP and inorganic phosphate along an ion gradient at the membrane, lastly induces programmed cell death due to a lack of energy in the form of ATP.[319]

The extraordinarily high cytotoxicity of prodigiosin is also owing to DNA damage, mediated by the tripyrrole alkaloid. In 1999, Melvin *et al.* demonstrated DNA binding of prodiginines by intercalation in the DNA minor groove at AT sites, where prodigiosin occupies 2 bp. Briefly after this first proof of interaction between prodigiosin and DNA, Melvin *et al*. were furthermore able to detect prodigiosin-mediated oxidative DNA cleavage (dsDNA and ssDNA breaks) in the presence of the redox-active transition metal Cu^{2+} and oxygen. In accordance with the higher cytotoxicity of prodiginines, the cognate tambjamine E, in contrast, could only induce ssDNA breaks.[320] A metal-induced oxidation of the electron-rich pyrrolylpyrromethene moiety to the respective π-radical cation is the initial trigger for the generation of oxidative stress. The subsequent activation of molecular oxygen and the formation of the ROS species H_2O_2, acting as a DNA-damaging agent, lead to the observed oxidative DNA strand cleavage.[321, 322] Besides oxidative DNA cleavage, prodigiosin inhibits DNA topoisomerase I and topoisomerase II, which are both key enzymes in DNA repair, replication, transcription, and chromosome segregation during mitosis.[323]

Interestingly, the coordination of Cu^{2+} ions differs significantly from the coordination mechanism of Zn^{2+} ions, which also explains the exceptional role of DNA strand scission with the transition metal copper (Scheme III.6). Upon crystallisation, Park *et al*. observed a tetracoordinated Zn ion, complexed by two twisted prodigiosin molecules. In this non-oxidised homo-dimeric complex **III-53**, only the nitrogen atoms of the pyrrolylpyrromethene chromophore are involved in metal binding. For copper complexation, only one molecule of prodigiosin is needed. Tetracoordinated copper binding involves coordination of the transition metal between all three nitrogen atoms of the pyrrole alkaloid and the counter ion Cl^- in the remaining coordination site (Scheme III.6). This observation is also in accordance with the facts that roseophilin **III-12** (weaker coordinating B-ring furyl) is not able to perform Cu-catalysed strand scission and that a displacement of the pyrrole A-ring with other arenes abolishes dsDNA scission mediated by prodigiosin.[321, 322] As the reported crystal structure of Cu·prodigiosin **III-54** contains an oxidised C-ring, resulting from nucleophilic attack of H_2O or MeOH in the C1 position of the C-ring, this position might play a vital role in generating the DNA-damaging ROS species H_2O_2.[322] Together, the ability of the pyrrole alkaloid to cause DNA damage is based on this metal chelation, which subsequently activates the cellular DNA damage repair machinery, promotes cell cycle arrest, and induces apoptosis.[258, 259]



Scheme III.6. Complexes of prodigiosin **III-1ab** with Lewis acids.[322] The prodigiosin hydrochloride **III-1ab·HCl** forms a tight lipophilic complex and can pass biological membranes via passive diffusion to uncouple ion gradients along lipid bilayers. Homo-dimeric Zn complexes of prodigiosin **III-53** show tetracoordinated Zn ions, trapped between two twisted prodigiosin molecules. The tetracoordinated Cu-prodigiosin complex **III-54** induces oxidative stress and causes DNA damage through dsDNA breaks.

III.1.1.5.2 Autophagy Modulation

In the past, prodiginines were shown to act as autophagy modulators. The process of autophagy describes a mammalian principle by which cellular components can be recycled by breaking down biological polymers into reusable small molecules. This recycling, for example, includes the disposal of damaged cell organelles, aggregated or misfolded proteins, or other toxic intermediates of the cell's metabolism. Whilst this process is of less therapeutic importance when there is an adequate supply of nutrients, it plays an even more important role when there is a nutrient deficiency. In fast-proliferating cancer cell lines, impaired autophagy results in limited availability of primary metabolites and nutrients, leading to starvation, a shortening in energy supply, and, lastly, cell death.[324, 325]

When the cellular machinery recognises damaged cell organelles, they are labelled with the small protein ubiquitin. This protein serves as a marker to flag cellular components or organelles for degradation via autophagy. A so-called phagophore consisting of proteins and lipids is recruited to the flagged components (Figure III.1A).[325] Concomitantly, the small and soluble cytosolic protein LC3-I is fused with phosphatidylethanolamine from the phagophore membrane to give the membrane-associated conjugate LC3-II.[326] Phagophore growth ultimately leads to the encapsulation of cytosolic proteins and ubiquitinylated components within autophagosomes.[325] These autophagosomes protect the cytosolic components from the ubiquitinylated cargo and allow modulation of the microenvironment to facilitate the degradation process. Acidic lysosomes, which carry lysosomal hydrolases, are recruited to the autophagosome and fuse to form autolysosomes. Through the membrane fusion of acidic lysosomes and autophagosomes, the pH in autolysosomes drops significantly, activating the acidic hydrolases and promoting the degradation of components encapsulated within the autolysosomal lumen.[325] Furthermore, the membrane-anchored LC3-II fusion is degraded inside the autolysosomes into soluble LC3-I and phosphatidylethanolamine. Thus, the LC3-II turnover within autolysosomes is a reliable marker for autophagy

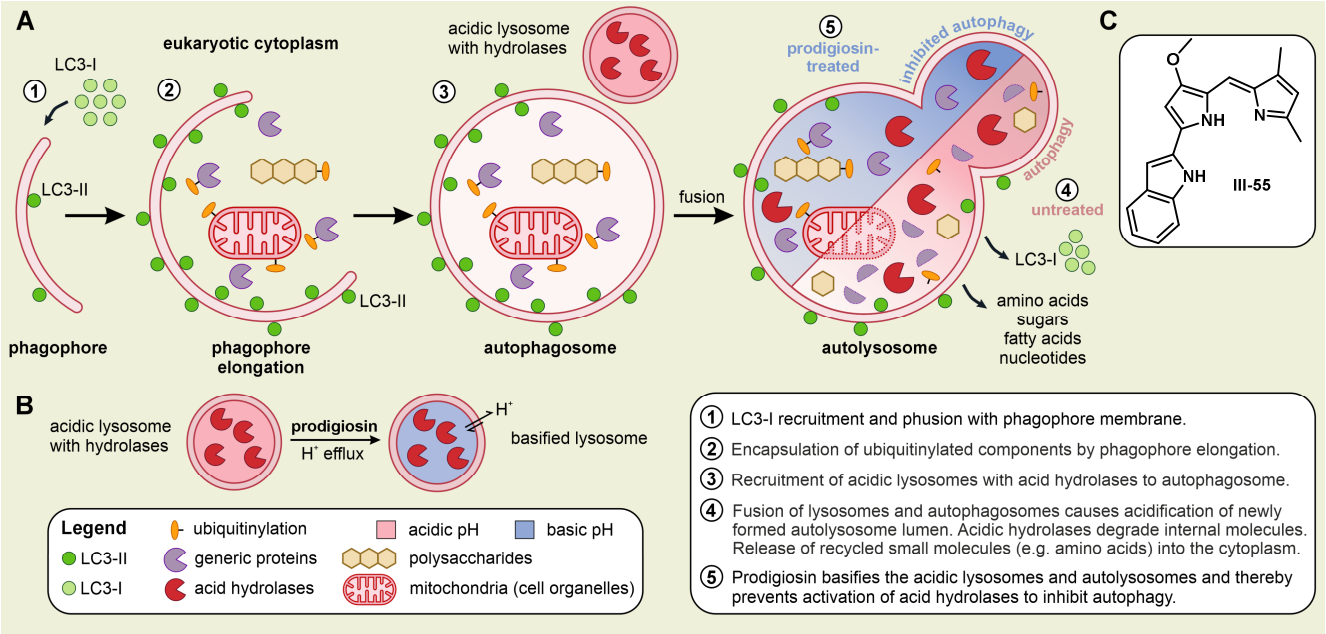


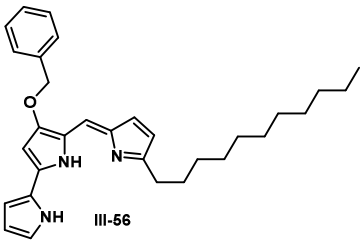
Figure III.1. A. The mechanism of autophagy for the degradation and recycling of misfolded and aggregated proteins, damaged organelles, or toxic intermediates in mammalian cells and its inhibition by prodigiosin. **B**. The HCl symporter prodigiosin promotes proton efflux from the acidic lysosomes, resulting in the basification of lysosomes and autolysosomes and thereby preventing the activation of acid hydrolases. **C**. Structure of the autophagy modulator and apoptosis inducer obatoclax (**III-55**). Figure design inspired by Petibone *et al*.[324]

activity.[326] Finally, recycled primary metabolites, such as amino acids, fatty acids, and nucleotides, are secreted into the cytoplasm.[325] The ability of prodigiosin (**III-1ab**) and related derivatives to passively diffuse across biological membranes, combined with their high proton affinity, enables the symport of H^+/Cl^- in a lipophilic complex. In combination with the uncoupling of vacuolar-type ATPase (V-ATPase) or mitochondrial-type ATPase (F-ATPase) activity, prodiginines basify lysosomes and autolysosomes and thereby lead to inhibition of the final step of autophagy (Figure III.1A and III.1B).[327-330]

The non-natural prodiginine derivative obatoclax (**III-55**, GX15-070MS, Figure III.1C) is descended from a SAR study (structure-activity relationship) of the Gemin X Pharmaceuticals company and was the only derivative which was tested in multiple clinical phase I and phase II trials for the treatment of leukemia, lymphoma, myelofibrosis, and mastocytosis.[260-262, 303, 331] However, phase III trials were halted before they had started due to financial business decisions.[332] Although autophagy modulation of prodiginines is a favourable property of obatoclax, the A-ring derivative is moreover an inhibitor of Bcl-2. Bcl-2 (B cell lymphoma 2) is a family of antiapoptotic proteins with repressor activity on apoptosis, the programmed cell death of mammalian cells. Upon release from Bcl-2 proteins and endogenous proteins that contain a conserved BH3 domain, Bax and Bak proteins (both belong to the Bcl-2 family) release apoptogenic molecules (e.g. cytochrome c) by permeabilisation of the mitochondrial membrane. As obatoclax binds to the BH3 domain of Bcl-2 proteins, the mimic inhibits the antiapoptotic activity of Bcl-2 family members and facilitates the release of these proapoptotic proteins into the cytoplasm. Consequently, apoptosis is induced in cancer cells, inhibiting their growth and, lastly, inhibiting the growth of the tumour.[333]

III.1.1.5.3 Immunosuppressive Activity

Pyrrole alkaloids of the prodiginine family share the ability to suppress the mammalian immune response.[258, 259] This immunosuppressive activity is already observable at non-toxic low nanomolar concentrations, which is an essential prerequisite of immunosuppressants, securing other metabolic functions or tissues from being harmed. In a mouse model, the prodigiosin derivative undecylprodigiosin **III-3** induced strong immunosuppression at a dose of 1.5 mg/kg, while cytotoxic activity was not observed at concentrations lower than 4 mg/kg.[334] The FDA-approved clinical immunosuppressants cyclosporin and FK506 inhibit the calmodulin-dependent protein phosphatase calcineurins and arrest the proliferation of T cells in the early G1 phase of the cell cycle.[335] In comparison, the mode of action displayed by prodiginines resorts to an inhibited blastogenesis of T cells and suppression of the T cell-dependent antibody response. But importantly, this activity is displayed *in vivo* without damaging the lymphoid organs.[258, 259, 310, 336, 337] As cyclosporin and FK506 (tacrolimus) utilise other basic mechanisms to effect immunosuppressive activity, concurrent treatment with prodiginines results in synergistic and cumulative effects.[338, 339] Seemingly, prodiginines can inhibit the cytoplasmic tyrosine kinase Jak3 (Janus kinase 3), which is part of the interleukin-2 (IL-2) signal transduction chain.[336, 340] IL-2 is a T cell growth factor secreted by activated T cells and dendritic cells. Upon binding to the IL-2 receptor CD25 and further recruitment of CD122 and the common cytokine receptor γ-chain (γ_c), the transcription of target genes involved in immune response is activated through the Janus kinase signal transducer and activator of transcription pathway (STAT), among others.[341] The non-natural prodiginine PNU156804 **III-56** (Scheme III.7), cognate to undecylprodigiosin **III-3**, was explicitly designed for immunosuppression and exhibits a 3-fold increase of activity in comparison to undecylprodigiosin **III-3**.[258, 259, 310, 342, 343] Besides inhibition of Jak3 kinase activity, activation of Jak3 substrates STAT5a and STAT5b, and extracellular regulated kinase 1 (Erk1) and Erk2 (p44/p42) was observed for PNU156804 **III-56**, too.[338, 339]



III-56

Scheme III.7. Structure of the immunosuppressant PNU156804 **III-56** developed by Mortellaro *et al*.[343] The non-natural prodigiosin analogue inhibits the cytoplasmic tyrosine kinase Jak3, which is involved in the transcriptional activation of target genes required for the immune response of T cells.

III.1.1.5.4 Antimalarial Activity

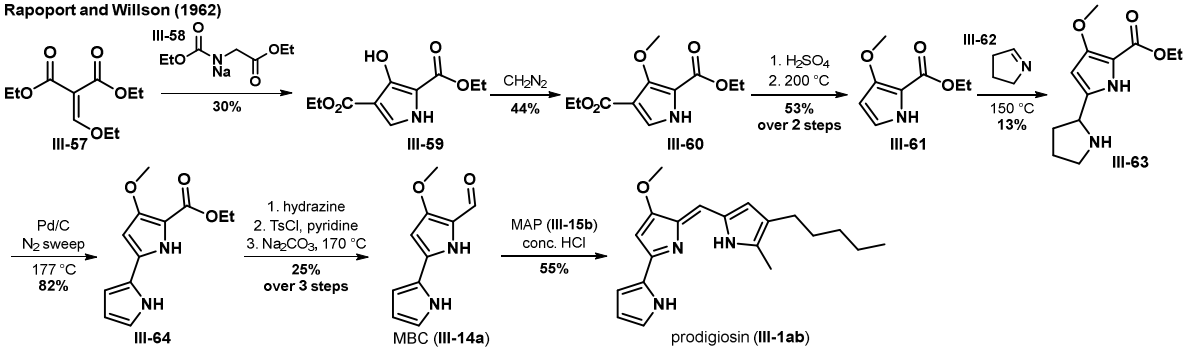
Malaria is a tropical disease caused by parasites spread to humans by female *Anopheles* mosquitoes. With over 500 million cases and 1 million deaths per year, malaria is a life-threatening disease. Most malaria cases worldwide can be attributed to infections with the protozoan parasite *Plasmodium falciparum*. As the parasite undergoes constant morphological transitions during its life cycle, medication remains extremely challenging.[344] A major success in malaria prevention and eradication was achieved in the US between 1947 and 1951 by combinatorial reduction of the *Anopheles* vector by dichlorodiphenyltrichloroethane-containing insecticide sprays and preventive treatment with the antimalarial drug chloroquine. However, other malaria eradication programs failed due to funding gaps and a lack of political will in poor countries on the African continent, where most cases are still reported. Concurrently, resistance to the few antimalarial drugs, such as chloroquine, artemisinin, and quinoline analogues, emerged, aggravating the need for alternative drugs and medications. In this context, prodigiosin **III-1ab** was shown to exhibit antiprotozoal activity against the malaria parasites from the *Plasmodium* family.[345] Although the underlying mechanism remains to be elucidated, numerous SAR studies have confirmed the antimalarial activity of the prodiginine scaffold and analysed the effects of miscellaneous natural and non-natural substitution patterns.[346-348] Substitutions of the pyrrolyl A-ring with other aromatic or aliphatic substituents led to a notable decrease (IC_{50} 5–50 µM) *in vitro* in antimalarial activity against *P. falciparum* in comparison to prodigiosin **III-1ab** (IC_{50} 11 nM).[346, 348] Furthermore, the antimalarial activity was tunable through the attachment of aliphatic and aromatic substitutions on the C-ring within a very broad range of inhibitory activity against *P. falciparum* (IC_{50} 1 nM to >25 µM).[346] A glance at natural prodiginines revealed precedence of cyclic prodiginines, such as metacycloprodigiosin or the streptorubins A **III-5** and B **III-8**, over the aliphatic prodiginines undecylprodigiosin **III-3** and prodigiosin **III-1ab** itself.[345, 349] Interestingly, the *in vitro* antiprotozoal activity against *Plasmodium* is readily obtained on low nanomolar concentration scales for many prodiginines, which is far below their cytotoxic activity against mammalian carcinoma cell lines.[346, 349]

III.1.1.6 Selected Total Syntheses of the Prodiginine Scaffold

To build the tripyrrole core of prodigiosin by means of organic total synthesis from scratch, two unlike approaches have been employed within the last 70 years. On the one hand, biomimetic syntheses utilise building blocks from the prodigiosin biosynthesis (cf. Scheme III.2) and resort to the A+B-ring biaryl MBC **III-14a** or cognate derivatives for a condensation reaction with C-ring monopyrroles. On the other hand, many syntheses employ non-biomimetic strategies to form the B+C-ring pyrrolylpyrromethene chromophore first, before the A-ring pyrrole is attached in the late synthesis stage. While the biomimetic approach is superior for chemoenzymatic and mutasynthetic strategies or organic syntheses aiming to modulate the C-ring substitution, the non-biomimetic approach is very useful for a late-stage chemical modulation of the A-ring. Both approaches will be briefly showcased in the following paragraphs on selected examples.

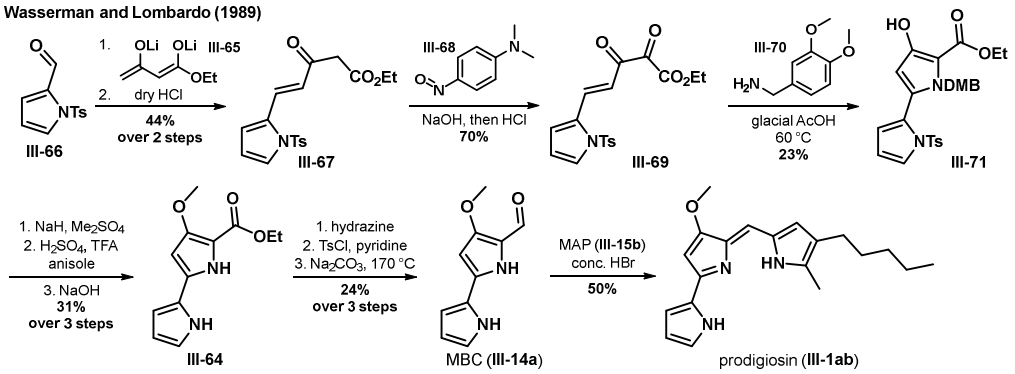
III.1.1.6.1 Biomimetic Syntheses of Prodigiosin

Although prodigiosin (**III-1ab**) was first isolated and reported in 1929,[350] it took more than 30 years to determine and verify its structure by total synthesis and spectral analysis. In 1962, Rapoport and Willson were the first to finally synthesise prodigiosin in a biomimetic synthesis, which also provided the natural prodigiosin precursor MBC **III-14a** as a synthetic intermediate (Scheme III.8). Starting from 1,3-dicarbonyl **III-57** and sodium glycinate **III-58**, a domino reaction sequence with conjugate addition and subsequent Dieckmann condensation provided the hydroxy pyrrole **III-59**. A diazomethane-promoted *O*-methylation provided intermediate **III-60**, which was then converted to the methoxy pyrrole carboxylate **III-61** in an acid-catalysed decarboxylation reaction. Via electrophilic aromatic substitution with 3,4-dihydro-2*H*-pyrrole **III-62**, the saturated MBC precursor **III-63** was obtained in a poor yield of only 13% and dehydrogenated on palladium on coal at high temperature to the corresponding MBC carboxylate **III-64**. A three-step McFayden-Stevens reduction of MBC carboxylate **III-64** yielded the corresponding aldehyde MBC **III-14a**, which was finally condensed with MAP **III-15b** under HCl catalysis to prodigiosin (**III-1ab**).[264, 274]



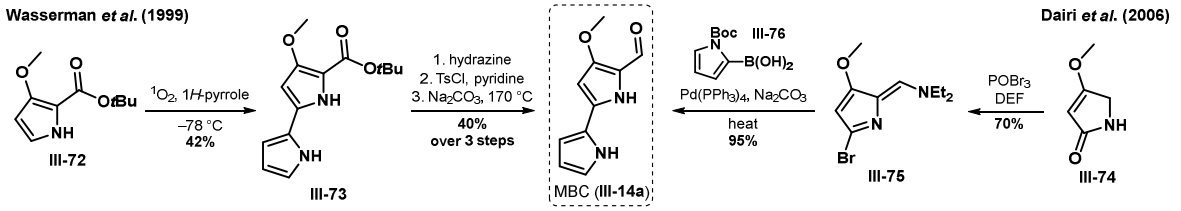
Scheme III.8. First biomimetic synthesis of prodigiosin by Rapoport and Willson.[264] Abbreviations: Ts – tosyl.

More than 30 years later, Wasserman and Lombardo presented an alternative strategy to access MBC **III-14a** and prodigiosin **III-1ab** (Scheme III.9). Their synthetic development coincides with the concurrent evolution of vicinal tricarbonyl chemistry, which was a suitable tool to build pyrroles. The dilithium salt of ethyl acetoacetate **III-65** was reacted with *N*-tosylated pyrrole aldehyde **III-66** to form the unsaturated condensation product **III-67**. After dehydration of β-keto ester **III-67** and oxidation with nitrosoaniline **III-68**, the unsaturated tricarbonyl **III-69** was isolated. A condensation reaction with 3,4-benzylamine **III-70** allowed the isolation of bipyrrole intermediate **III-71** with a tosyl protecting group on the future A-ring and a dimethoxybenzyl (DMB) protecting group on the future B-ring. A subsequent reaction sequence involving *O*-methylation, DMB deprotection, and tosyl deprotection provided MBC carboxylate **III-64**, which was finally reduced to MBC **III-14a** in a McFayden-Stevens reduction.[266, 274]



Scheme III.9. Biomimetic synthesis of prodigiosin by Wasserman and Lombardo.[266] Abbreviations: Ts – tosyl; DMB – 3,4-dimethoxybenzyl; TFA – trifluoroacetic acid.

As all disclosed routes towards MBC **III-14a** were lengthy so far, Wasserman *et al*. succeeded in 1999 with a two-step route towards the bipyrrole prodigiosin precursor (Scheme III.10). According to the researchers, pyrrole ester **III-72** was able to react with singlet oxygen at very low temperature and upon the addition of excess 1*H*-pyrrole, the desired MBC carboxylate **III-73** was obtained. Unfortunately, this reaction only proceeded on a small scale and still employed a low-yielding McFayden-Stevens reduction to reach the desired MBC building block **III-14a**, thereby restricting the total yield and scalability even further.[274, 351] A real game changer in the large-scale preparation of prodiginines or their biosynthetic precursors from biomimetic routes was the presented novelty by Dairi *et al*. from 2006 (Scheme III.10). Inspired by the approach of D'Alessio and Rossi, which employs a Vilsmeier-Haack formylation of pyrroles for the preparation of the pyrrolylpyrromethene chromophore and a Suzuki-Miyaura cross-coupling between a (pseudo)halogenated B-ring and an A-ring boronic acid (*vide infra*),[352] a reliable two-step protocol was developed to provide MBC **III-14a** in large quantities.[353] In their synthesis, tetramic acid **III-74** was transformed in a Vilsmeier-Haack haloformylation into bromoenamine **III-75**. A Pd-catalysed Suzuki-Miyaura cross-coupling reaction between *N*-Boc-protected 1*H*-pyrrole-2-boronic acid **III-76** and bromoenamine **III-75** with $Pd(PPh_3)_4$ under basic reaction conditions furnished MBC **III-14a** in a yield of 67% over two reaction steps.[274, 353] The practical utility of this approach was finally confirmed by Gemin X Pharmaceuticals, which developed and prepared the Bcl inhibitor obatoclax **III-55** on a multikilogram scale for the application in clinical trials.[331]

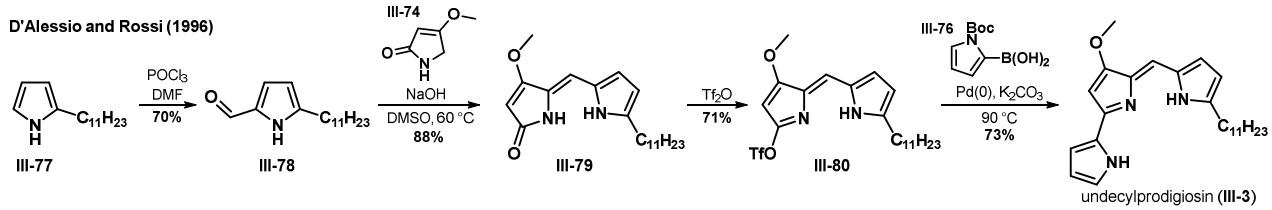


Scheme III.10. Streamlined biomimetic syntheses of the A+B-ring prodigiosin precursor MBC **III-14a**.[351, 353] Abbreviations: Ts – tosyl; DEF – diethylformamide.

III.1.1.6.2 Non-Biomimetic Synthesis of Prodigiosin

In 1996, D'Alessio and Rossi devised a synthetic route towards the prodigiosin analogue undecylprodigiosin **III-3** from actinomycetes. Although the presented synthesis works in a modular fashion as the biomimetic approaches (*vide supra*), the blatant difference lies in the independence from the A+B-ring bipyrrole precursor of the natural biosynthesis, namely MBC **III-14a** (Scheme III.11). Driven by the lacking scalability of the known biomimetic syntheses by this time, both researchers searched for an alternative method to produce sufficient amounts of lead

compounds for biomedical screenings.[274] Starting from undecylpyrrole **III-77**, the pyrrole was formylated in the 5-position under Vilsmeier-Haack conditions. A subsequent condensation reaction between aldehyde **III-78** and tetramic acid **III-74** under basic conditions provided the dipyrrinone **III-79**, which was then triflated with triflic anhydride to give the conjugated triflate **III-80**. A final Pd-catalysed cross-coupling reaction with *N*-Boc-protected pyrrole-2-boronic acid **III-76** under Suzuki-Miyaura conditions furnished undecylprodigiosin **III-3** in a good yield of 73% or 32% over four steps.[352] The inherent advantage of this route is the late-stage cross-coupling between triflate **III-80** and an aryl boronic acid, which allows a modular substitution of the A-ring pyrrole by any other aryl boronic acid. Consequently, D'Alessio *et al*. utilised this approach to generate a library of undecylprodigiosin analogues with numerous A-ring substitutions for SAR screenings.[310] Furthermore, Fürstner and co-workers adapted this route for the synthesis of A-ring-substituted cyclononylprodigiosin **III-10** or in the making of the *ortho*-bridged streptorubin B isomer butylcycloheptylprodigiosin **III-7**.[263, 271, 272]



Scheme III.11. Non-biomimetic route towards undecylprodigiosin **III-3** via the B+C-ring pyrrolylpyrromethene intermediate **III-79** and late-stage Pd-catalysed Suzuki-Miyaura cross-coupling according to D'Alessio and Rossi.[352]

III.1.1.7 Targeting Approaches for Site-Specific Prodiginine Applications

The lack of selectivity underlying the biological activities of prodigiosin and its derivatives is a limiting factor for applying these bioactive molecules as therapeutic agents. Concurrently, a selective targeting mechanism is required to minimise collateral damage to healthy cell types. Hence, applying target-selective drug vectors offers expedient opportunities to address the lack of target selectivity of prodiginine alkaloids. Although the literature examining target-selective vectors for site-selective delivery of prodiginines is insufficiently comprehensive, the few published examples will be discussed to reflect the exploited strategies for selective targeting and their consequences for future studies. In general, there are two unlike ideas to transport the alkaloid scaffold to or into cells: non-covalent and covalent methods. The non-covalent methods include the coating of solid particles or the encapsulation of prodiginines into macromolecular structures, such as vesicles, micelles, and microsphere particles. These methods profit from the fact that readily available prodiginines from natural sources or mutasynthesis can be used to load the carriers without the need for structural modification on the alkaloid scaffold. In contrast to this, the covalent attachment of prodigiosin to carrier molecules requires adjustments to the chemical structure of prodiginines to enable their covalent coupling to the carrier molecule and a profound strategy to implement these structural changes by means of chemical synthesis.

III.1.1.7.1 Non-Covalent Targeting Approaches

Dozie-Nwachukwu *et al*. used chitosan, a linear glycopolymer resulting from the alkaline deacetylation of the natural biopolymer chitin, to encapsulate prodigiosin. The researchers isolated the alkaloid from *S. marcescens* and were able to temporarily store it in a microporous material formed by adding the cross-linking reagent glutaraldehyde to a water-in-oil emulsion containing chitosan, prodigiosin, and Tween 20. Upon slow particle erosion, the encapsulated drug is then continuously released from the particles for up to 12 days. With prodigiosin encapsulation yields of up to 55%, the chitosan microspheres were finally subjected to *in vitro* testing on the breast

cancer cell line MDA-MB-231. Here, the prodigiosin-chitosan microspheres showed a significant dose-dependent decrease in cell viability of the malignant transformed cell line after treatment with encapsulated prodigiosin.[354] Nguyen *et al*. recently performed similar experiments but employed a single emulsion solvent evaporation method for encapsulation instead to prepare the chitosan microparticles, leading to a more homogenous size distribution and a smaller average size of the microporous matrix.[355] Although these encapsulated prodigiosin nanoparticles showed reasonable anticancer activity, a significant drawback remains their untargeted delivery mechanism, as these nanoparticles do not specifically accumulate in malignant cancerous tissue. Based on this challenge, Zhao *et al*. developed an alternative delivery approach, utilising the strategy of biomimetic peptides. Therefore, the terminal amino groups of commercially available poly-L-lysine dendrigrafts were first covalently linked with PEG3500-maleimide linkers before prodigiosin was loaded into the dendrigraft's lumens.[356] The maleimide functionalisation of the surface was further used to couple a synthetic placental chondroitin sulfate(CSA)-binding peptide (plCSA-BP) from the malarial protein VAR2CSA. VAR2CSA is a cysteine-rich protein antigen displayed on the surface of *P. falciparum*-infected red blood cells. This protein antigen specifically binds to chondroitin sulfate A, an acidic mucopolysaccharide used as a post-translational modification of cell surface proteins, among others. During pregnancy, placental malaria is accompanied by a sequestration of VAR2CSA-exposing blood cells in the placenta by binding of VAR2CSA to a specific type of CSA on the trophoblast, a specific type of cell forming the outer layer of a blastocyst, which is needed to provide nutrients to the embryo.[356, 357] Interestingly, VAR2CSA was also shown to bind 90% of tumours, which is why VAR2CSA has become a protein of interest in attempting targeted delivery of molecules to cancer cells. With prodigiosin dendrigrafts, covered with a 28 amino acid peptide mimicking the CSA binding site of VAR2CSA, Zhao *et al*. were able to specifically reduce the size and weight of JEG3 choriocarcinomas in a live model with mice by approximately 80% through targeted delivery to the tumour site. Exposure to freely diffusible prodigiosin, however, only caused a decline in tumour weight by approximately 30%. Moreover, the application of these prodigiosin-poly-L-lysine dendrigrafts for targeted delivery and slow release of the alkaloid led to a survival rate among treated mice of >70% after 16 days, while all other control groups (including free prodigiosin and saline) showed a survival rate of less than 20%.[356]

Although drugs encapsulated in porous materials enable a steady release of the drug from the matrix over time, their reliable and steady release depends on the erosion of the matrix. Therefore, no drug is released into the surrounding environment if the particles remain intact. This limitation can be countered by surface impregnation of solid particles with the desired drug in coatings. The first experiences with non-covalent prodiginine coatings were made in 2014. By using gold nanoparticles covered with undecylprodigiosin **III-3**, it was possible to overcome the observed loss of potency of free undecylprodigiosin over time in an *in vitro* model with mammalian cell lines. This inactivation of the bioactive alkaloid is a cause of pH alterations and oxidation processes. Gold nanoparticles can exert a beneficial influence on small molecules by increasing their overall stability (pH, redox, temperature, etc.), their solubility in aqueous media, or even reducing their drug efflux from target cells.[358] Moreover, gold nanoparticles are useful tools for the selective targeting of tumour cells and cancer treatment via photothermal treatment. Photothermal therapy is closely related to photodynamic therapy and uses a photothermal agent to convert the energy of light into local heat to kill target cells.[359] Photodynamic therapy instead uses a photosensitiser to harvest the energy of light and to produce toxic ROS species. The photothermal agent responds at longer wavelengths than photosensitisers and uses less energetic light to minimise off-target damage to non-cancerogenic cells.[359] Gold nanoparticles possess an intrinsically high light absorption, are compatible with other therapeutic solutions (e.g. chemotherapy), and localised surface plasmon resonance on the gold surface strongly enhances local heat generation, thereby multiplying the effect of the therapy. Hence, these desirable attributes of gold nanoparticles and their exploitation for coating with undecylprodigiosin would enable a dual treatment of cancer via photothermal therapy on the one hand and the anticancer activity of prodiginines on the other hand.

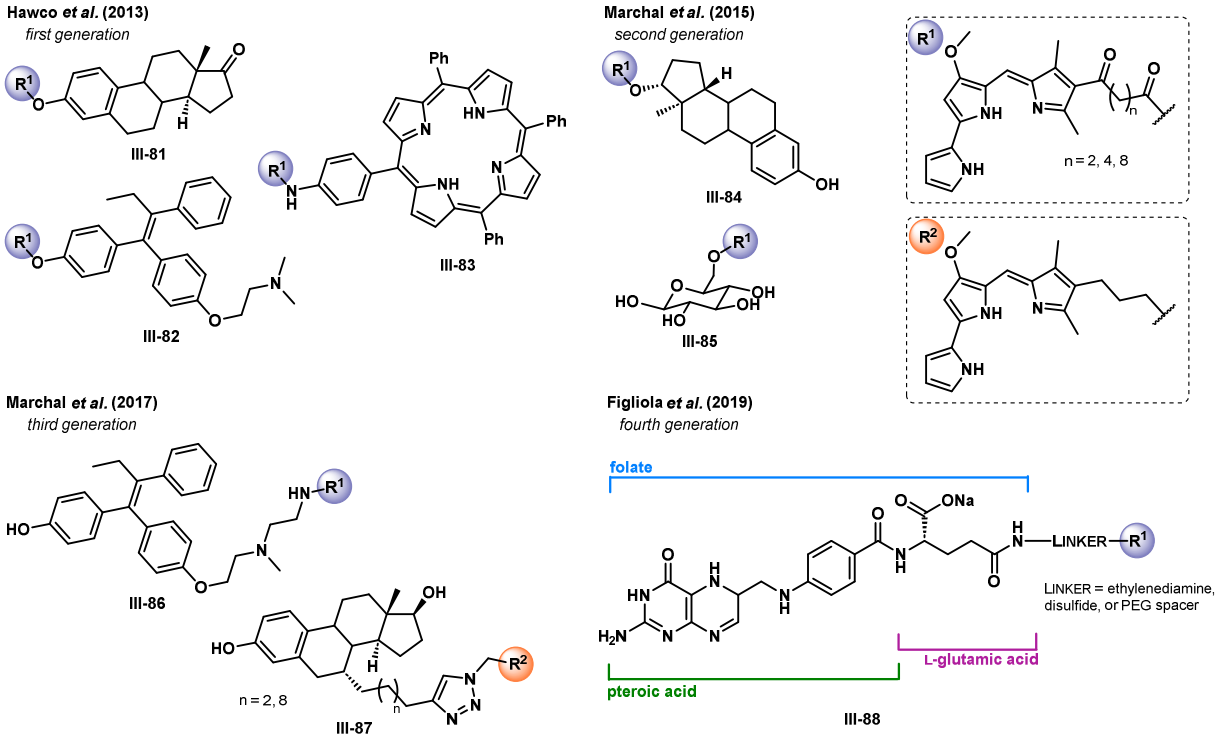
The authors of the same study additionally performed in-depth analyses to uncover cytotoxicity mechanisms of undecylprodigiosin-coated gold nanoparticles and monitor mitochondrial apoptotic pathway proteins in a colon cancer model. Thereby, a switch from undecylprodigiosin-triggered apoptosis signals from mitochondrial-dependent to mitochondrial-independent signalling was revealed, raising new and yet unanswered questions about the underlying mechanism of cytotoxicity for these coated nanoparticles.[358] The same strategy of nanoparticle coating was later employed to coat biosynthetically derived gold nanoparticles from plant leaf extracts of the African peach *Nauclea latifolia* with prodigiosin isolated from bacterial production or to co-synthesise prodigiosin and gold nanoparticles in *S. marcescens in vivo* and *ex vivo*.[360, 361] Dozie-Nwachukwu devised this tool to improve the drug targeting of cancerous tissues, which was impossible with their previously published chitosan microparticle approach. By simultaneously labelling the non-covalently prodigiosin-coated gold nanoparticles with a covalently bound peptide hormone that controls the production of sex hormones, called luteinising hormone-releasing hormone (LHRH), the researchers could selectively address LHRH-positive breast cancer cells. As the LHRH receptor is overexpressed in the triple-negative breast cancer cell line MDA-MB-231, but not in healthy breast cells, the adhesion of LHRH-coated particles to the breast cancer cells was five times greater than for the healthy cells.[360] Besides gold, other elements and materials, such as silver, selenium, and zinc oxide, are being tested as suitable nanoparticle carrier materials for drugs and drug coatings. Just recently, prodigiosin-coated selenium nanoparticles have also provided experimental evidence of being a promising immunosuppressant for treating the chronic autoimmune inflammatory disease Ulcerative colitis, reducing local colon inflammation and restoring colonic antioxidant capacity in a mouse model.[362]

III.1.1.7.2 Covalent Targeting Approaches

Although covalent modifications on the prodiginine scaffold beyond alkylations are scarce, the group of Alison Thompson invented and advanced the field of true, hence covalent, prodigiosin conjugates.[3] Covalent modifications open up a whole new range of post-translational protein modifications, labelling of nucleic acids, or other cellular components *in vivo* and *in vitro* that can be used for drug trafficking or other site-specific applications. A general approach of targeted drug delivery to cancer cells makes use of designated receptors that are known to be significantly overexpressed on the surface of specific cancer types. For example, porphyrins were shown to accumulate in cancer cells to a greater extent than in healthy cells.[363] Moreover, many breast cancer cell lines overexpress the estrogen receptor (ER) on their cell surface, regulating cell proliferation, transcriptional signalling, and cell differentiation through estrogen hormones. The small molecule estrone is one of such steroid hormones and is a natural ligand of this receptor.[364] Therefore, estrone conjugates are believed to enter ER-positive cancer cells preferentially over healthy cells, given the elevated expression level of the ER in cancer cells. Lastly, tamoxifen is a clinically approved drug and is used as a selective modulator of the ER. Competitive binding of tamoxifen to the ER produces a nuclear complex, leading to decreased DNA replication and estrogen signalling.[365, 366] Consequently, it was hypothesised that the tamoxifen subunit of tamoxifen conjugates can render both the facilitated cell entry through the estrogen receptor and a modulation of metabolic activity within the target cell. Based on these fundamentals in cancer metabolism, Hawco *et al*. launched a series of C-ring modified prodiginine conjugates with a non-natural substitution pattern on the alkaloid scaffold in 2013. These prodiginines were conjugated via esterification of the alkaloid's C-ring to produce prodiginine conjugates of estrone **III-81**, 4-hydroxytamoxifen **III-82**, and porphyrin **III-83** (Scheme III.12). All three molecules readily possess

[3] The authors Ayatollahi *et al*. of the publication 'Prodigiosin-Conjugated Aptamer for Attachment to the Surface of Brain Cancer Cells Mediated by Glutamate Receptor', published in *Colloids Interface Sci. Commun.* **2018**, *24*, 45–48, state the preparation of prodigiosin-conjugated DNA aptamers. However, neither chemical structures, nor synthetic procedures for DNA coupling or chemical synthesis or manipulation of prodiginine derivatives are provided, why this publication is not discussed within covalent prodigiosin applications.

affinity towards cancerous tissues and are predestined to facilitate the selective import of prodiginine conjugates into cancer cells.[367] The first generation of conjugates solely focused on ester-linked conjugates, which may undergo intracellular hydrolysis upon enzymatic digestion with hydrolases. The prodiginine-porphyrin conjugates **III-83** did not exhibit biological activity. For the prodiginine-estrone conjugates **III-81** targeting the ER, a surprisingly higher growth inhibition of ER-negative cell line MDA-MB-231 (IC_{50} 0.3 µM) than of the ER-positive cell line MCF-7 (IC_{50} 1.9 µM) was observed. Even more surprising was the astonishing observation that prodiginine-tamoxifen conjugates **III-82** (IC_{50} 30–50 nM) showed even higher growth inhibition of the ER-negative cell line than tamoxifen itself.[367]



Scheme III.12. Four generations of small-molecule conjugates of C-ring-appended prodiginines with estrogen hormones, 4-hydroxytamoxifen, porphyrin, glucose, and folate to address target-specific delivery and uptake of prodiginines in cancerous cells.[367-370]

The second generation of prodiginine conjugates did not implement novelties from the site of conjugation chemistry, but mainly focused on altering target specificity by selecting alternative small-molecule carriers for conjugation. Hence, the second conjugate generation comprised alternative steroid hormone conjugates **III-84** and a prodiginine-glucose conjugate **III-85**, including sophisticated protecting group strategies for their preparation. To target ER-positive cancer cell lines, the estrone carrier from the first generation was substituted by the estradiol E_2 hormone conjugate **III-84** with a propanolic chain in the 11β-position ($E_{2\text{-}11}$).[370] In the first two generations, the researchers noted that the ester linkage was quite delicate towards hydrolysis and that shorter alkyl chains on the C-ring were beneficial in terms of antitumoral activity. Therefore, the third generation addressed these issues by introducing a novel, more stable coupling chemistry into the prodiginine scaffold, enabling the coupling of prodiginines to the previously evaluated and biologically active carriers estradiol and 4-hydroxytamoxifen. While 4-hydroxytamoxifen was appended to prodigiosin by amide coupling to provide the prodigiosin-4-hydroxytamoxifen conjugate **III-86**, estradiol was functionalised with a terminal alkyne for coupling through CuAAC with an azide-functionalised prodiginine alkaloid to give the clicked prodigiosin-estradiol conjugate **III-87**. Although the functional group stability was significantly increased by substituting the ester linkage

with triazole or amide moieties, antitumoral activities against breast cancer cell lines only ranged in micromolar concentration spheres.[369] Nevertheless, the azide-bearing prodiginines are highly valuable tools, as their functional group facilitates a bioorthogonal application of these prodiginines via click chemistry, which has not been possible so far. The fourth and most recent generation of prodiginine conjugates **III-88** was released in 2019, exploiting the essential vitamin folic acid (vitamin B9) as a carrier molecule. The rationale behind choosing folate as a carrier molecule was again the elevated folate uptake into cancer cells. Folic acid is the natural precursor of the coenzyme tetrahydrofolate and plays a central role in C_1 metabolism. The folate receptor alpha (FRα) regulates cellular uptake of folate in all eukaryotic cells. Approximately 50% of triple-negative breast cancer lines show strong overexpression of the receptor.[368] Triple-negative cell lines owe their name to a lack of expression of the estrogen and progesterone receptors (ER and PR) and exhibit low expression of the HER2 receptor. This is why triple-negative cell types respond to a smaller extent to growth-controlling external cellular signals. Consequently, triple-negative breast cancer cells grow extraordinarily fast and are extremely difficult to combat by therapeutic interventions with common chemotherapeutic drugs, targeting the ER or the PR (e.g. tamoxifen and mifepristone, respectively). Therefore, the alternative targeting of FRα with chemotherapeutic conjugates becomes a promising approach to cure triple-negative breast cancer, as there is no standardised therapy available so far.[371]

The inhibition of cell proliferation was mainly observed at micromolar concentrations for the four conjugate generations, indicating a relatively low inhibitory activity of most synthesised conjugates. Nevertheless, these first examples of prodiginine conjugates provide indispensable proof of principle that the targeted delivery of prodiginines by covalent conjugates is possible, opening up a new field of prodiginine-appended macromolecular and small-molecule conjugates. As the studies of Thompson's group mainly focused on C-ring conjugated prodiginines, it remains unanswered which influence A- or B-ring attachments exert on the uptake and cytotoxic activity of the corresponding conjugates. Concurrently, a lack of chemical methods to introduce these modifications is most likely the reason why only C-ring derivatives have been studied so far. Thus, the conjugation on the other rings of the tripyrrole alkaloid may provide new perspectives for modulating the delivery and bioactivity of conjugated prodiginines, thereby increasing their therapeutic potential and enabling the development of novel therapeutic solutions.

III.2 Aims

More than 90 years ago, the deep purple tripyrrole pigment prodigiosin was isolated for the first time from bacterial sources. Since its structure was solved in the 1960s, novel methods and total synthesis approaches led to the elucidation of the biosynthesis pathway and, more recently, the identification and synthesis of numerous natural prodiginines and even more non-natural derivatives. Metaphorically speaking, the scaffold of the prodiginine family is a jack of all trades, as antimicrobial, antitumoral, antifungal, antiprotozoal, and antimalarial activities were attributed to the pyrrole alkaloid. Although several studies have aimed to improve certain properties of the cytotoxic scaffold, a lack of target specificity is a steady companion of the mostly untargeted modes of action. Hence, this lack of target specificity hinders a comprehensive exploitation of prodiginines' pharmacologically promising biological activities. To address this limitation, novel delivery strategies and structural optimisation of the cytotoxic scaffold may help to advance the chances of a therapeutic application of prodiginines in the future.

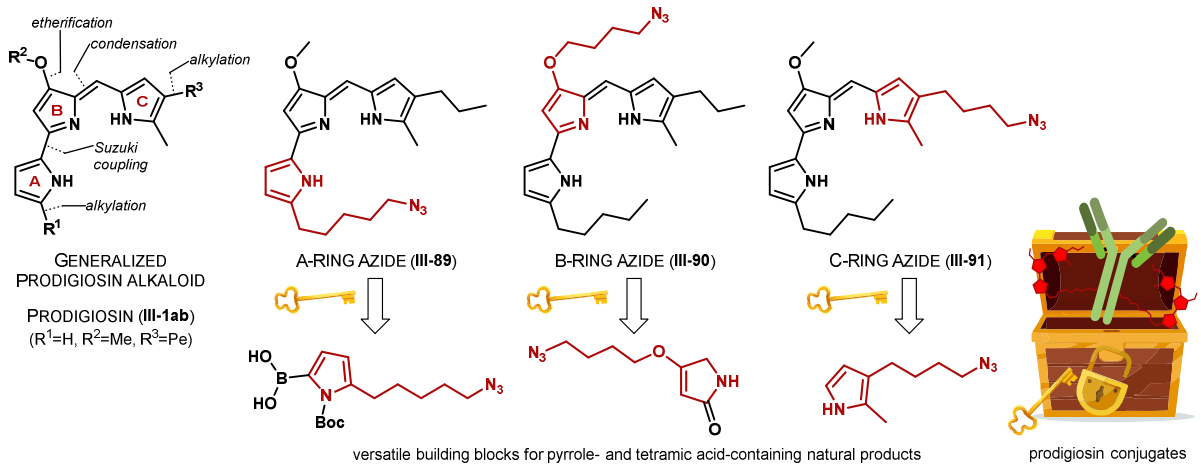
Chapter II.5.4 aims to take up the inherent obstacle of the lacking target specificity of prodiginines and consequently enhance their applicability as potential drugs. In this regard, key building blocks shall be identified and synthetic strategies shall be devised to functionalise the prodiginine scaffold with organic azides on the A-, B-, and C-ring by means of total synthesis. This functionalisation allows for bioorthogonal click functionalisation of the natural product derivatives with terminal alkynes via CuAAC or cyclooctynes via SPAAC (cf. Chapter II.1.1.1), which can be used to couple prodiginines to vectors for specific drug transport or cellular uptake. This expedient technology shall be finally used to prepare bioconjugable maleimide-functionalised prodiginines to tap the new resources of antibody-prodigiosin conjugates and validate their cytotoxic potential in cancer cell lines. Moreover, Chapter II.5.4 aims to expand our knowledge about the substrate specificity of prodiginine ligases from the biosynthetic pathways of prodigiosin or tambjamine synthesis. Previous studies deduced extended substrate promiscuity of these enzymes for the monopyrrole building block. Still, no investigation systematically examined promiscuity for functionalised analogues of the bipyrrole building block MBC to date. Consequently, this chapter attempts to bridge this knowledge gap by utilising 5'-*n*-alkylated MBC derivatives to probe the substrate promiscuity of prodiginine ligases for the bipyrrole building block, thereby enabling access to A-ring alkylated prodiginines through enzyme catalysis. Lastly, this chapter aims to systematically infer the consequences of these non-natural azide and A-ring alkyl substitutions on antitumoral activities of these prodiginine derivatives against cisplatin-resistant and -sensitive urothelial bladder cancer cell lines to advise suitable and advantageous positions for future structure manipulation and targeted drug delivery approaches.

III.3 Results and Discussion

III.3.1 Total Synthesis of Clickable Prodiginine Azides for Targeted Applications

Prodiginines are a functionally diverse class of tripyrrole alkaloids with a surprisingly low structural diversity. A multitude of biological activities have been assigned to the basic prodiginine scaffold, which can form tight lipophilic complexes with H^+/Cl^- ions and perform DNA double-strand scission in a complex with copper salts. While prodigiosin and its derivatives are recognised for their immunosuppressive, antimicrobial, antitumoral, antiprotozoal, and antimalarial activities (*vide supra*), their untargeted mode of action and broad range of biological effects concurrently coincide with undesirable side effects. This significant lack of target specificity and selectivity limits their potential as viable drugs or drug candidates.[258, 259, 369] Nevertheless, the striking number of non-natural derivatives of prodigiosin that have been synthesised by chemical means to unravel the underlying modes of action and to study structure-activity relationships for the family of cytotoxic tripyrrole alkaloids illustrates the high scientific and commercial interest in transferring the bioactive scaffold into drug development.[258-262, 274, 303, 331]

To circumvent undesired off-target effects of the natural product, this thesis aims to identify suitable means to selectively deliver prodiginines to distinct target sites. Inspiration for this was found in the field of conjugate chemistry, which is eligible to produce covalent conjugates of probes or warheads with vector molecules for transportation to the cellular target (e.g. ADCs). These targets can appear in numerous forms and can be either a defined cell type or a specialised cellular compartment. Conjugates of potential drugs and bioactive vector molecules provide expedient opportunities for target-specific delivery of active agents.[372, 373] So far, antibodies,[374, 375] proteins and peptides,[373, 376] lipids,[377, 378] and biological polymers just represent a small fraction of carrier molecules,[379-381] which have been functionalised to co-transport pharmacophores to fulfil their function as drug or regulatory element at a specific target site and circumnavigate off-target effects.[375, 382, 383] Since 2013, the first covalent C-ring conjugates of prodigiosin with porphyrin, estrone, and 4-hydroxytamoxifen emerged from chemical synthesis in Thompson's group to target estrogen receptor-positive breast cancer and provide a strategy to overcome the lack of specificity.[367, 370] The ester linkage was later augmented to amide, ether, and click chemistry, giving rise to additional conjugation options on the estradiol scaffold (cf. Scheme III.12).[369] Especially the bioorthogonal azide-substituted prodiginines have great potential as payloads in covalent conjugates, as they could be coupled fairly easily *in vitro* or even *in vivo* with any alkyne in an SPAAC or CuAAC azide-alkyne cycloaddition ("click chemistry").[41, 384, 385] In this regard, the fast-growing field of reliable and modular CuAAC chemistry was chosen as a synthetic bridge between the alkaloid scaffold and a potential linker or drug delivery vector to functionalise the natural product derivatives by means of organic total synthesis. Adhering to the approach of Hawco *et al.*,[367] the emphasis of the following paragraphs will be placed on the first comprehensive and systematic click-compatible azide-functionalisation of all three pyrrole moieties of prodigiosin, namely the A- **III-89**, B- **III-90**, and C-ring **III-91**, to streamline the *in vitro* preparation of biological (protein) conjugates thereof (Scheme III.13).

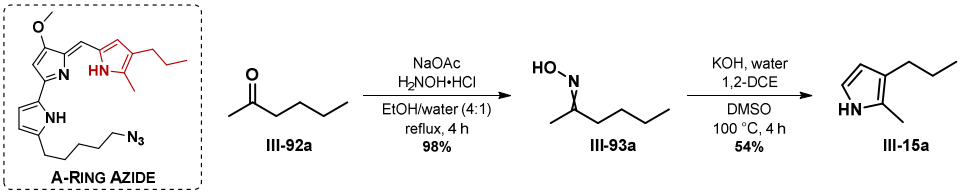


Scheme III.13. The retrosynthetic analysis of the prodiginine scaffold (shown as free base) uncovers essential synthons for transferring organic azides into the natural product family. Those appear to be key intermediates to unlock the treasure chest of prodigiosin conjugates (in the scheme exemplified by antibody-prodigiosin conjugates). The consistently long aliphatic chain on the A-ring was designed for a proof-of-principle and to only distinguish between effects originating from differences in the attachment site of the azide (A-, B-, or C-ring), rather than attachment site in combination with greatly varying alkyl chain patterns within a single ring [e.g. no A-ring substitution vs. azido-pentyl substitution (A-ring azide)].

III.3.1.1 Prodigiosin A-Ring Azide

III.3.1.1.1 Alkylated C-Ring Precursor

Although natural A-ring derivatives of prodigiosin have been rarely found, two distinct examples have been described, bearing substitutions in the 5-position, namely cyclononylprodigiosin **III-10** and 2-(*p*-hydroxybenzyl)prodigiosin **III-9** (cf. Scheme III.1).[386, 387] Based on these natural prototypes, the synthesis of prodigiosin A-ring azide **III-89** (Scheme III.13) was attempted by an adapted non-biomimetic route of D'Alessio and Rossi (cf. Scheme III.11),[310] which includes the cross-coupling of an azide-substituted pyrrole boronic acid key precursor (cf. Scheme III.13) with an alkylated azafulvene triflate as a central step to introduce the organic azide. The first steps en route to the prodigiosin A-ring azide and conjugates thereof adapt a short sequence previously reported by Weber *et al*. to provide the alkylated monopyrrole precursor of the future C-ring.[388] In detail, hexan-2-one (**III-92a**) was converted on a multigram scale with hydroxylamine hydrochloride and sodium acetate to the corresponding *E*/*Z* mixture of oxime **III-93a** in quantitative yield. As the stereogenic information of the oxime is annihilated in the synthesis of the planar *N*-heterocycle **III-15a**, the *E*/*Z* mixture was used straightaway for the follow-up Trofimov pyrrole synthesis. This reaction allows the preparation of 1*H*-pyrroles from the cyclisation of reaction adducts between oximes and the electrophile 1,2-dichloroethane (1,2-DCE) under superbasic conditions with degassed DMSO/KOH. By this means, the monopyrrole **III-15a** was synthesised in a yield of 54% (Scheme III.14).[388-390]

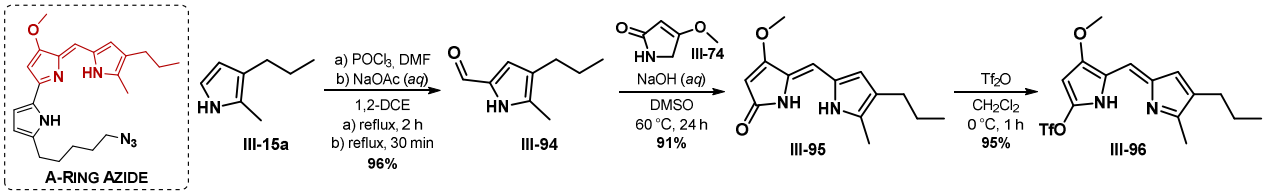


Scheme III.14. Synthesis of the alkylated monopyrrole **III-15a** from hexan-2-one (**III-92a**) as precursor for the prodigiosin A-ring azide **III-89**. Abbreviations: 1,2-DCE – 1,2-dichloroethane.

The rather short monopyrrole **III-15a** was selected on purpose, as soluble prodigiosin derivatives with short-chain substitution on the C-ring were shown to bear the highest inhibitory effects against sensitive Gram-negative bacteria and induce cytotoxicity in eukaryotic cells by causing pronounced accumulation of autophagosomes.[301, 391]

III.3.1.1.2 C-Ring Alkylated Dipyrromethene

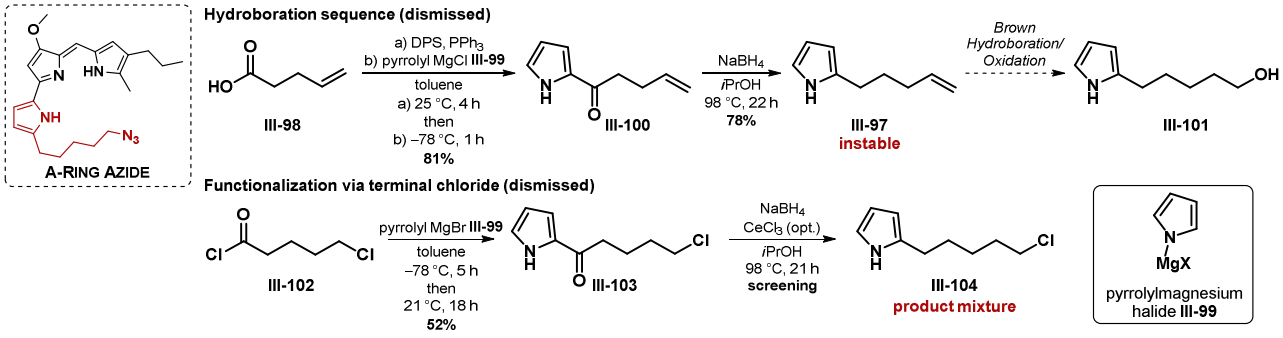
With the short-chain monopyrrole precursor **III-15a** in hand, the prodiginine synthesis was further advanced by building the dipyrromethene building block that represents the future B- and C-ring (Scheme III.15). First, pyrrole **III-15a** was transformed into a carbaldehyde electrophile for subsequent condensation reaction. Therefore, pyrrole **III-15a** was subjected to a Vilsmeier-Haack formylation according to a procedure of Fürstner *et al.*[263] With phosphoryl chloride and DMF in 1,2-dichloroethane (1,2-DCE), the 2-formylated pyrrole **III-94** was furnished in an excellent yield of 96% (Scheme III.15). Condensation of pyrrole **III-94** with the commercially available tetramic acid **III-74** in DMSO with aqueous NaOH at 60 °C in 91% yield, followed by triflation of dipyrrinone **III-95** with triflic anhydride gave access to the triflated azafulvene **III-96** in a yield of 95%.[263] In the latter synthesis, using freshly opened Tf_2O was found to be essential for complete conversion, eliminating the need for purification beyond extractive workup to obtain the pure alkyl triflate **III-96**.



Scheme III.15. Synthesis of the C-ring alkylated triflate **III-96** as precursor of the prodigiosin A-ring azide **III-89**.

III.3.1.1.3 A-Ring Azide Precursor

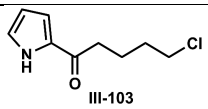
Equipped with the alkylated B+C-ring precursor **III-96** of the prodiginine A-ring azide target compound, the effort was turned towards the preparation of the A-ring carrying pyrrolic azide. Introduction of the azide-moiety into the future A-ring was first desired via an intermediate hydroxyl-group through functionalisation of the terminal alkene pyrrole **III-97** in a Brown hydroboration-oxidation sequence. The first step in the synthesis of alkene pyrrole **III-97** was the acylation of 1*H*-pyrrole with activated 4-pentenoic acid **III-98** (Scheme III.16). The latter was first transformed *in situ* into the thioester by the reaction with 2,2'-dipyridyl disulfide (DPS) and PPh_3 in toluene at ambient temperature.[263] Pyrrolylmagnesium chloride **III-99** was then allowed to react with the thioester at –78 °C, giving 81% of the acylated alkene pyrrole **III-100**. Although the reaction conditions rendered complete conversion, the side product triphenylphosphine oxide was hard to remove by chromatography on a large scale, accounting for the reduced yield. The subsequent reduction with $NaBH_4$ in *i*PrOH provided the instable alkene pyrrole **III-97**.[263, 392, 393] Despite the fact that a Brown hydroboration-oxidation sequence with 9-BBN and $NaOH/H_2O_2$ could have been feasible to transform the terminal double bond into a terminal hydroxy group to give pyrrole **III-101**,[394, 395] alternative measures were sought to circumvent the instable alkene intermediate **III-97**. Alternatively, the synthesis of a readily functionalised *n*-chlorinated pyrrole was attempted in the next step, to avoid the instable alkene pyrrole. Furthermore, the described formation of triphenylphosphine oxide in the acylation reaction with acid **III-98** was a severe disadvantage in the previous route, complicating product purification and worsening atom economics of the reaction.



Scheme III.16. Synthesis of terminally functionalised 2-alkylated pyrroles as precursors of the prodigiosin A-ring azide **III-89**. Both routes were dismissed due to a lack of stability (alkene pyrrole **III-97**) or non-separable reduction products emerging from the $NaBH_4$-reduction of chlorinated acyl pyrrole **III-103**. Abbreviation: DPS – 2,2'-dipyridyl disulfide.

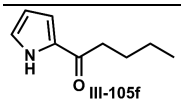
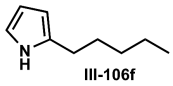
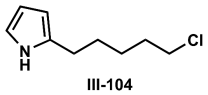
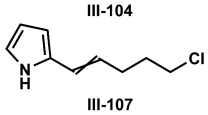
In order to introduce the chlorination into the pyrrole moiety, a chlorinated acid chloride was used for the 2-acylation of 1*H*-pyrrole (Scheme III.15). Starting from commercially available 5-chloro-pentanoic acid chloride (**III-102**), the use of PPh_3 and the consequent generation of $O{=}PPh_3$ was avoided, since the reactive acid chloride does not require PPh_3-assisted carbonyl activation as necessary for the relatively unreactive carboxylic acid **III-98**. 2-Acylation of 1*H*-pyrrole after deprotonation with pyrrolylmagnesium bromide (**III-99**) allowed isolation of the chlorinated acyl pyrrole **III-103** in a yield of 52%. However, isolation of the acyl pyrrole was rather difficult, as chromatographic separation of the two product isomers, presumably 2- and 3-acylated pyrrole, via TLC and preparative chromatography on silica was not possible in conventional two-component eluents (PE/EtOAc, *n*-pentane/CH_2Cl_2, *n*-pentane/MTBE, *n*-pentane/Et_2O). Tedious optimisation of purification conditions revealed that the addition of 5–10% CH_2Cl_2 to a mixture of *n*-pentane/MTBE is essential, as only this adjustment leads to separation of the isomers and long enough retention on the column for polar interaction with the stationary phase. The following reduction of chlorinated acyl pyrrole **III-103** to chlorinated alkyl pyrrole **III-104** with $NaBH_4$ as reducing agent and with optional supplementation of $CeCl_3$, known as Lewis acid from Lyche-type reductions, only resulted in product mixtures of numerous reduction and elimination products. Coupled gas chromatography-mass spectrometry (GC-MS) analyses revealed four main products of the attempted reduction, namely acyl pyrrole **III-105f** (*m/z* 151.10), the fully reduced alkyl pyrrole **III-106f** (*m/z* 137.12), terminally chlorinated alkyl pyrrole **III-104** (*m/z* 171.08), and the terminally chlorinated elimination product **III-107** (*m/z* 169.07, both *E*/*Z* isomers detected) (Table III.3). A brief screening for suitable solvents and additives only led a maximum of 40% (product ratios determined by GC-MS) of the chlorinated target **III-104** in an inseparable mixture of other side products (Table III.3). Concludingly, this route was dismissed owing to an unreasonable and uneconomic need for tedious product purification.

Table III.3. Screening for the $NaBH_4/CeCl_3$ reduction of chlorinated acyl pyrrole **III-103**.



III-103

[a] solvent → **complex product mixture**

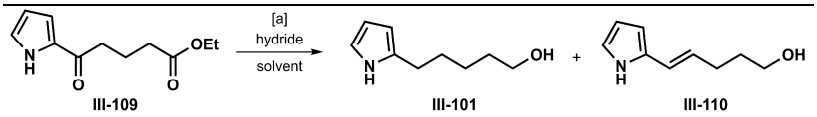
Reagents[b]	$NaBH_4$ (2.8) $CeCl_3$ (1.1)	$NaBH_4$ (1.5) $CeCl_3$ (1.1) NaOH (1.5)	$NaBH_4$ (1.5) $CeCl_3$ (1.1)	$NaBH_4$ (1.5)		
Solvent/ Products	*i*PrOH	*i*PrOH	THF/*i*PrOH (2:1)	*i*PrOH	retention time [min][c]	*m/z*[d]
 **III-105f**	33	44	2	43	8.32	151.10
 **III-106f**	3	1	0	2	7.01	137.12
 **III-104**	40	15	8	30	9.55	171.08
 **III-107**	24	40	90	25	9.74 + 9.98	169.07

[a] Conditions: Chlorinated acyl pyrrole **III-103** (50.0 mg, 269 µmol) was dissolved in 3 mL dry solvent. At 0 °C, $NaBH_4$ (and optional $CeCl_3$) were added. Solutions were refluxed under an inert atmosphere at 98 °C for 21 h, quenched with water and extracted with MTBE. Area% from GC-MS measurements of reaction extracts in MTBE; [b] Equivalents are indicated in parentheses. [c] Retention time on the GC-MS. The starting material elutes at 10.28 min with an m/z ratio of 185.06. [d] Observed mass/charge ratio (*m/z*) of the detected molecule peaks.

After the first two approaches via alkene pyrrole **III-97** or the chlorinated pyrrole **III-103** were accompanied by instable intermediates, a third attempt ultimately aimed for a practicable shortcut to circumvent the delicate alkene and pyrrole chloride. The idea to solve the instability and reactivity towards undesired side reactions was based on an ester-functionalised acid chloride, which already harboured a terminal hydroxy group in another oxidation state (Scheme III.17). Acylation of a pyrrole with a terminal ester would then allow for a one step reduction of the pyrrolic acyl group and the ethyl ester at the same time, reducing the synthesis of hydroxypentyl-functionalised pyrrole **III-101** by one step in comparison to the synthesis from acid **III-98** and avoiding the instable alkene intermediate **III-97**.

Starting with the acylation of 1*H*-pyrrole with ethyl glutaryl chloride (**III-108**) with $AlCl_3$ yielded 72% of the 2-functionalised acyl pyrrole **III-109**,[393] which was then subjected to hydride reduction. Several metal hydrides in ethereal solvents (THF, glyme, or 1,4-dioxane) or *i*PrOH as an alcoholic solvent were screened for their suitability to facilitate the concomitant reduction of ketone and ester to give access to terminally hydroxylated pyrrole **III-101** (Table III.4). Initially used $LiAlH_4$ (2.2 eq.) in THF (Table III.4, entry 1) left the starting material unconverted, while increased amounts of $LiAlH_4$ (5.0 eq.) rendered complete conversion after 4 h (Table III.4, entry 2). GC-MS analysis revealed two reaction products: the fully reduced pyrrole **III-101** (*m/z* 153.12) and the undesired elimination product **III-110** (*m/z* 151.10) in a ratio of 70:30 (Table III.4, entry 2). Utilisation of less reactive borohydrides, such as $LiBH_4$ and $NaBH_4$ (Table III.4, entry 3 and 4) in *i*PrOH, either led to 18% conversion towards the ethyl ester elimination product **AcO-III-110** (*m/z* 193.11) or near-full conversion with exclusive formation of elimination product **III-110** with severe side products, respectively. Performing the reaction with $LiAlH_4$ in the high-boiling-point solvent 1,4-dioxane provided a favourable ratio of 89:11 (Table III.4, entry 5), however, severe formation of unknown side products occurred as well, which would impede product purification. No conversion was obtained with diisobutyl aluminium hydride (DIBAL-H) in THF (Table III.4, entry 9).

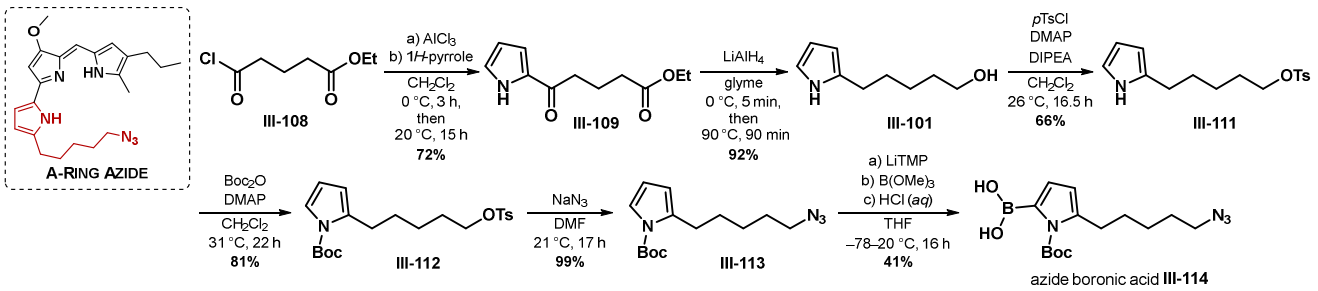
Table III.4. Screening of suitable metal hydrides for the attempted one-step reduction of 2-acylated pyrrole ester **III-109** to the corresponding 2-alkylated hydroxypentyl pyrrole **III-101** in ethereal and alcoholic solvents.



Entry	Metal hydride (eq.)	Solvent	Temp. [°C]	Time [h]	Ratio[b] (**III-101**:**III-110**)
1[c]	$LiAlH_4$ (2.2)	THF	80	12	no conversion
2[c]	$LiAlH_4$ (5.0)	THF	85	4	70:30
3	$LiBH_4$ (3.0)	*i*PrOH	98	3	0:0[f]
4	$NaBH_4$ (3.0)	*i*PrOH	98	4	0:100[g]
5[c]	$LiAlH_4$ (5.0)	1,4-dioxane	120	3	89:11[g]
6[c],[e]	$LiAlH_4$ (5.0)	THF	98	3	30:70
7[c]	$LiAlH_4$ (5.0)	THF	98	2	52:48
8[c]	$LiAlH_4$ (5.0)	glyme	90	2	92:8
9[c]	DIBAL-H (5.0)	THF	85	1	no conversion
10[d]	$LiAlH_4$ (5.0)	glyme	80	1	67:33
11[d]	$LiAlH_4$ (5.0)	glyme	100	1	42:58

[a] Conditions: Pyrrole **III-109** (100 mg, 478 µmol, 1.00 eq., 0.25 M in ethereal or alcoholic solvent). The reactants were heated after the addition of the metal hydride at the specified temperature under an inert atmosphere. Complete conversion was typically achieved unless stated otherwise; [b] Determined via GC-MS after Fieser workup and extraction with MTBE;[396] [c] $LiAlH_4$ addition at 0 °C and stirring for 15 min at 0 °C before heating; [d] Heated to 70 °C before $LiAlH_4$ addition; [e] $LiAlH_4$ suspension in THF added over 30 min via syringe pump while refluxing the pyrrole in THF; [f] 18% Conversion with the ethyl esters of **III-101** and **III-110** in a 0:100 ratio; [g] With additional side products.

The best results were achieved with glyme at 80 °C in the presence of $LiAlH_4$ (5.0 eq.), which gave smooth conversion and a favourable ratio of 92:8 between the desired product **III-101** and the elimination product **III-110** (Table III.4, entry 8). For all $LiAlH_4$-containing reactions so far (Table III.4, entry 1, 2, 5–8), the hydride was fed at 0 °C and stirring at 0 °C continued for 15 min until gas development had ceased before the solvent was refluxed. To investigate the effect of direct heating, the reaction solution was already heated at 70 °C before $LiAlH_4$ was supplemented (Table III.4, entry 10 and 11). Through this experiment, it was found that the initial cooling of the reaction is crucial for obtaining a high amount of the target molecule **III-101**, as initial heating to 70 °C resulted in unfavourable ratios of 67:33 (at 80 °C reaction temperature) or 42:58 (at 100 °C reaction temperature). In conclusion, the reduction of pyrrole **III-109** with $LiAlH_4$ (5.0 eq.) in glyme, according to entry 8, gave the best results to attempt a scale-up reaction and to bypass the instable alkene derivative **III-97**.

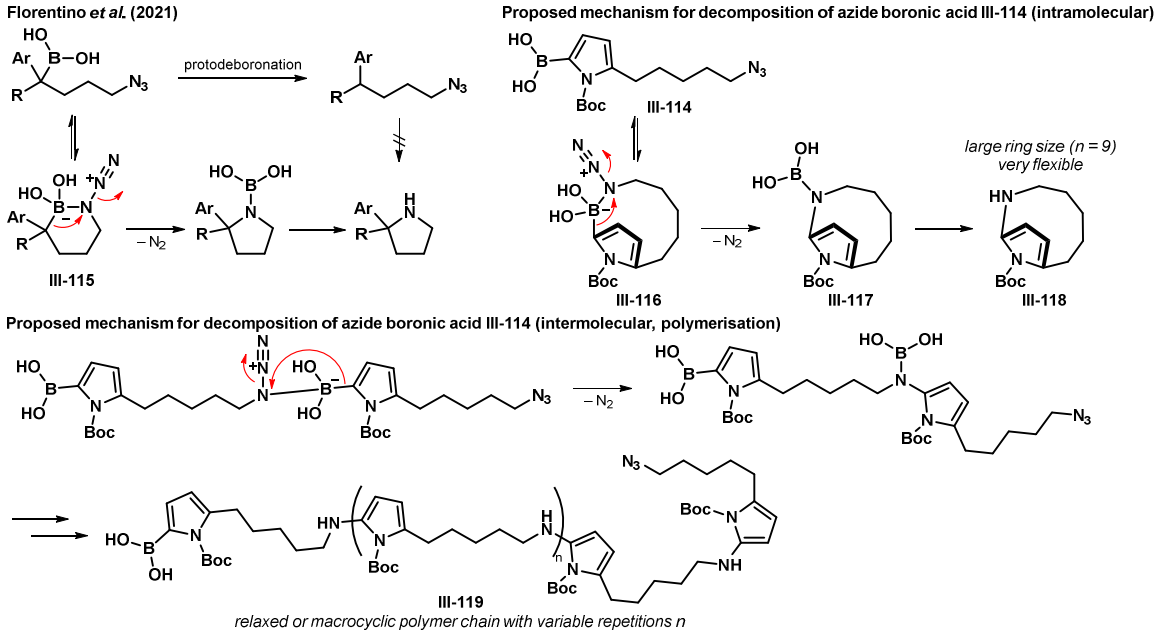


Scheme III.17. Synthesis sequence to access the very delicate prodigiosin A-ring azide precursor **III-114**.

After optimising the reduction on a small scale, the large-scale reduction of pyrrole ester **III-109** was performed on a 20 g scale and behaved as anticipated through the aforementioned systematic screening approach. Despite the use of large amounts of highly reactive $LiAlH_4$ (18.4 g) and the expected formation of vast amounts of hydrogen gas and insoluble lithium salts, quenching according to the Fieser protocol allowed easy removal of floating lithium salts.[396] The hydroxylated pyrrole **III-101** was obtained as a very sticky and polar oil in an excellent yield of 92% after chromatography using dry column vacuum chromatography (DCVC) (Scheme III.17).[397] *O*-Tosylation of the hydroxypentyl pyrrole **III-101** with *p*TsCl, diisopropyl ethylamine (DIPEA), and catalytic 4-(dimethylamino)pyridine (DMAP) gave 66% yield of the activated alcohol **III-111**. Boc-protection of tosylate **III-111** with Boc_2O and DMAP in CH_2Cl_2 and the subsequent tosyl substitution with NaN_3 in DMF furnished the *N*-protected tosylate **III-112** and organic azide **III-113** in a yield of 81% and 99%, respectively. An alternative attempt to permutate the order of events, namely starting with the Boc-protection of pyrrole **III-101** and then performing the tosylation reaction, was promptly dismissed after discovering numerous and hardly separable side products in the first protection step.

Lastly, the azide boronic acid **III-114** was synthesised by sequential *ortho*-metalation of pyrrole **III-113** with lithium 2,2,6,6-tetramethylpiperidide (LiTMP) at –78 °C, quenching of the reactive species with $B(OMe)_3$, and boronic ester hydrolysis with diluted aqueous HCl and isolated as an extremely delicate yellow solid in a yield of 41%.[263, 398, 399] First and foremost, the isolation of pure azide boronic acid **III-114** was the encountered bottleneck of attempts to acquire the A-ring azide precursors. Although pyrrole-2-boronic acids are generally stated to precipitate upon slow solvent removal after methyl ester hydrolysis with diluted HCl and extractive workup with Et_2O,[263, 398] impure boronic acids were isolated as oily residue in multiple attempts. Finally, repeating the washing step with dilute HCl after isolation of the oil was found to be effective in enabling precipitation of the delicate pyrrole boronic acid at first. It was hypothesised that residual boric acid impurities, which stem from hydrolysis of excess $B(OMe)_3$, and incomplete protonation of the boronic acid functional group, might hamper precipitation in the first step. Furthermore, the typically used solvent Et_2O is not ideal for precipitating pyrrole-2-boronic acid, as boronic acids are considerably soluble in ethereal solvents. Substituting Et_2O with even less polar hydrocarbon solvents (*n*-pentane, *n*-heptane, PE) led to immediate decomposition. Instead, stabiliser-free (BHT stabiliser removed by rotary evaporation) iPr_2O was the most suitable compromise between a less polar ether than diethyl ether but a more polar solvent than hydrocarbon solvents. Although pyrrole-2-boronic acids are highly reactive in transmetalation and common intermediates in prodigiosin chemistry,[263, 348, 353, 388, 400] their synthesis and isolation (this holds in particular true for the 2-heteroaryl boronic acids,[401-403] “2-pyridyl problem”) pose a significant challenge due to their inherent lability.[263, 404]

As far as is known, the presented synthesis of azide boronic acid **III-114** is the first successful preparation and isolation of an azide-substituted heteroaryl-2-boronic acid and one of the rarely met examples of azide-containing boronic acid derivatives.[405-408] This is justified by the fact that boronic acid **III-114** exhibited extreme delicacy in handling and stability. It readily decomposed at –20 °C under an argon atmosphere within less than three days and instantly decomposed when exposed to high vacuum. A potential mechanistic explanation for the inherent instability of the azide boronic acid **III-114** was recently published by Florentino *et al*., reporting on the synthesis of 2-alkyl-2-methylpyrrolidines via an intramolecular carboborylation of alkyl azides (Scheme III.18).[409, 410] The coordination of the flexible terminal azide to the strongly positively polarised boron atom of the boronic acid functional group of heteroaryl intermediate **III-115** might trigger an intramolecular rearrangement, resulting in the proposed carboborylation reaction and the release of molecular nitrogen (Scheme III.18).



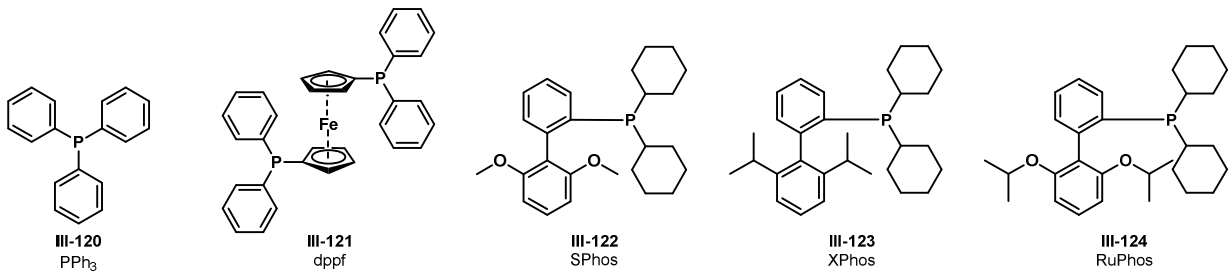
Scheme III.18. Proposed decomposition mechanism of azide-substituted boronic acids leading to the formation of pyrrolidines according to Florentino *et al*. and an adapted intramolecular or intermolecular reaction for *N*-Boc protected azide boronic acid **III-114**.[409, 410]

However, the carboborylation reaction was only observed for five-membered pyrrolidines, but not for the six-membered piperidines, pointing to tight restrictions regarding the ring size.[409, 410] Hypothetically, the very close distance of the sterically demanding hydrophobic aryl substituent in the six-membered intermediate **III-115** to the strongly polarised borate functional group may cause such a strong repulsion of both groups that a collapse of the transient azaborinane is forced and further promoted by the loss of nitrogen gas as an entropic driving force. Projecting this decomposition mechanism to azide boronic acid **III-114** would result in an intramolecular coordination of the terminal azide at the boron centre **III-116**, followed by a 1,2-migration of the tertiary substituent with the loss of molecular nitrogen to form the nine-membered *N*-boroazonane **III-117**. After protodeboronation, the very flexible *N*-Boc-protected pyrrole **III-118** with azonane handle is obtained. However, as this mechanism of boronic acid decomposition was only observed for 1,4-azidoboronic acids by Florentino *et al*., it becomes less likely for the long-distance coordination in azide boronic acid **III-114**. Instead, it is assumed that the extension of an intra- to an intermolecular reaction would clarify the rapid degradation upon compression of the solid under vacuum, facilitated by the shift of the equilibrium through the removal of nitrogen gas under reduced pressure. As this mechanism would result in relaxed polymers of variable chain length or macrocyclic polymers with negligible ring tension **III-119**, the polymerisation might overcome the tight restrictions of ring size, which were observed for the intermolecular reaction by Florentino *et al.*

III.3.1.1.4 Ligand Screening for Suzuki-Miyaura Cross-Coupling Reactions

With access to the azide-substituted prodiginine A-ring precursor **III-114** and the alkyl triflate **III-96**, their coupling was left as the missing link to the prodiginine A-ring azide **III-89**. Modern synthetic routes that aim to build the tripyrrole scaffold of prodigiosin typically utilise a Palladium-catalysed Suzuki-Miyaura cross-coupling to merge boronic acid derivatives of the A-ring pyrrole with brominated or triflated precursors of the B-ring pyrrole (cf. Scheme III.11).[263, 269, 271, 411-415] For this purpose, tetrakis(triphenylphosphine)palladium(0) with the triphenylphosphine ligand **III-120** was shown to be an appropriate catalyst for cross-coupling of pyrrole-2-boronic acids,[416] before first applied by Fürstner *et al.* in the total synthesis of nonylprodigiosin **III-2**.[263] Since then, the

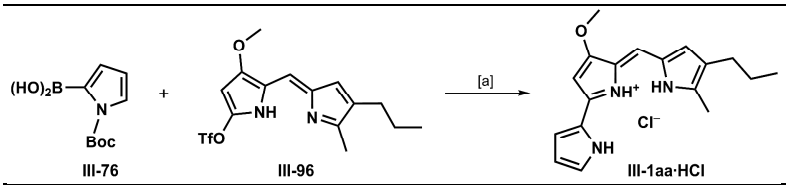
precatalyst has been used throughout numerous synthetic contributions related to prodigiosin, tambjamine, or marineosin chemistry.[310, 346, 369, 399, 400, 411] However, the commercially available tetra-substituted Pd(0) precatalyst requires elevated temperatures (>80 °C for OTf and Br) to shed the gratuitous triphenylphosphine ligands and leverage the oxidative addition of $Pd(PPh_3)_2$ into the carbon-halide bond (reactivity I > OTf ≈ Br >> Cl) in the first step of the catalytic cycle.[417-419] As organic azides and pyrrole-2-boronic acids in particular are known to be extremely delicate,[263, 404, 420-423] a screening of Pd-ligands that would allow coupling at a decreased temperature of 60 °C in reasonable yields was conducted. Temperatures of 60–70 °C are often encountered in the synthesis of organic azides from alkyl halides, which is why the organic azides are considered stable at this temperature. However, higher temperatures may lead to thermal disintegration and the irreversible release of nitrogen gas.[421, 422] Moreover, boronic acids are known to undergo irreversible protodeboronation in aqueous solutions, and the rate of protodeboronation is highly temperature-dependent, too.[424, 425] To avoid the use of reactive yet instable boronic acids, MIDA boronates are air-stable boronic acid derivatives that are known to increase the overall yield of Suzuki-Miyaura cross-couplings with unstable boronic acids. By allowing a slow release of boronic acid under mild basic conditions,[420] the rate of competing decomposition reactions is drastically decreased.[426] However, the preparation of MIDA boronates requires the free pyrrole-2-boronic acids and temperatures >70 °C when using the dehydrated MIDA anhydride.[426] As MIDA boronate protection is concomitant with a significant loss of yield even for the most stable unsubstituted *N*-Boc-pyrrole-2-boronic acid (**III-76**),[420] the MIDA protection to increase the stability of the utilised boronic acids was not pursued. Instead, the more reactive and accessible free pyrrole-2-boronic acids were chosen for the cross-coupling reaction. For the intended screening of Pd-ligands, triflate **III-96** with connatural alkyl substitution to prodigiosin and commercially available *N*-Boc-pyrrole-2-boronic acid (**III-76**) were selected as stable dummy substrates and heated at 60 °C in the presence of unactivated $Pd(OAc)_2$ (5 mol%) and a slight excess of ligand (6 mol%). Besides the tetrakis(triphenylphosphine)palladium precatalyst, the common dppf ligand **III-121** and ligands from the Buchwald group (SPhos **III-122**,[427-429] XPhos **III-123**,[427-429] and RuPhos **III-124**[427]) for the screening with K_3PO_4 as inorganic base in a solvent system of degassed *n*BuOH/water (4:1) (for ligand structures see Scheme III.19).



Scheme III.19. Structures of the phosphine-based Pd-ligands for Suzuki-Miyaura cross-coupling screening reactions.

With the standard $Pd(PPh_3)_4$ precatalyst (Table III.5, entry 1), a yield of 55% was achieved for the synthesis of the prodigiosin analogue **III-1aa** and was used as a reference to benchmark the other phosphine ligands. With the ferrocene ligand dppf **III-121** the yield dropped to 35% (Table III.5, entry 2) and utilisation of the Buchwald ligand XPhos **III-123** only led to an isolated yield of 18% (Table III.5, entry 3). RuPhos **III-124** instead could increase the yield to 76% (Table III.5, entry 4) and with SPhos **III-122** the yield rose even further to 84% (Table III.5, entry 5), being a significant improvement compared to $Pd(PPh_3)_4$. A further decrease in reaction temperature from 60 °C to 40 °C caused the yield in the SPhos-promoted coupling to drop to 60% (Table III.5, entry 6), proving the need for elevated temperatures of ≥60 °C to obtain good conversions and yields >80% for the coupling of aliphatic triflate **III-96** and unsubstituted pyrrole-2-boronic acid **III-76**.

Table III.5. Ligand screening for the Suzuki-Miyaura coupling between boronic acid **III-76** and triflate **III-96** under mild reaction conditions.



Entry	Ligand	Temp. [°C]	Yield[b]
1	$Pd(PPh_3)_4$[c] **III-120**	60	55
2	dppf[d] **III-121**	60	35
3	XPhos **III-123**	60	18
4	RuPhos **III-124**	60	76
5	SPhos **III-122**	60	84
6	SPhos **III-122**	40	60

[a] Conditions: Triflate **III-96** (50.0 mg, 132 µmol, 1.00 eq.), *N*-Boc-pyrrole-2-boronic acid (**III-76**, 2.00 eq.), ligand (see Table III.5, 0.06 eq.), $Pd(OAc)_2$ (0.05 eq.), and K_3PO_4 (2.00 eq.) in degassed *n*BuOH/water (4:1, 910 µL). Reactions were stirred under an inert atmosphere at 60 °C (40 °C for entry 6) for 18 h; [b] yields of isolated products; [c] tetrakis(triphenylphosphine)palladium(0) (0.05 eq.) was used to replace $Pd(OAc)_2$ and additional ligand supplementation; [d] 1,1'-bis(diphenylphosphanyl)ferrocene.

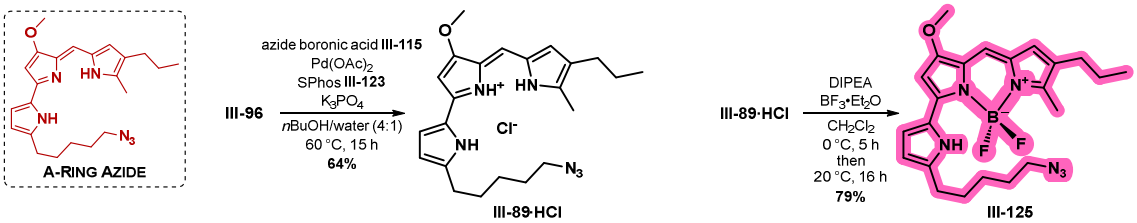
Based on the optimised conditions for the Suzuki-Miyaura cross-coupling reaction of pyrrole-2-boronic acids and pyrrolic triflates at 60 °C, the best performing catalyst system with $Pd(OAc)_2$ and a slight excess of SPhos **III-122** with K_3PO_4 as inorganic base in a solvent system of *n*BuOH/water was employed for further Suzuki-Miyaura cross-coupling reactions without further investigations on catalyst loading or the Pd:ligand ratio. After purification of prodiginine **III-1aa·HCl** from the screening reactions, recurring contaminations with persistent and non-removable *H*-grease were additionally noted. These contaminations were particularly noticeable in small-scale reactions with low amounts of the prodiginine product, and they could neither be removed by washing the product with *n*-pentane nor by chromatography. After screening standard laboratory equipment for the origin of *H*-grease, the cotton wool for filtration purposes was found to be the dominant source of *H*-grease. Nonetheless, many other daily expendable laboratory goods (unprocessed solvents, foldable septa, gloves, etc.) were also found to contribute to this problem (Table IX.1, Figure IX.1 and IX.2, Supporting Information). For this reason, a laboratory practice strategy and custom glassware were developed to eliminate any traces of *H*-grease beforehand and avoid contamination of the precious prodiginines during chemical synthesis and purification (cf. Chapter IX.1, Supporting Information).

III.3.1.1.5 Biaryl Coupling Towards Prodigiosin A-Ring Azide and its Clickable *F*-BODIPY

After having established reliable and high-yielding reaction conditions for the aryl-coupling between alkyl triflates and pyrrole-2-boronic acids, the method was applied for the final cross-coupling reaction in the synthesis of the prodiginine A-ring azide **III-89**. Despite the labile nature of azide-substituted boronic acid **III-114**, the Suzuki-Miyaura cross-coupling with alkyl triflate **III-96** and the Pd/SPhos catalyst system yielded 64% of the prodigiosin A-ring azide **III-89·HCl** (Scheme III.20). Summarising the presented route towards the first A-ring azide-substituted prodiginine **III-89·HCl**, the tripyrrole alkaloid was synthesised over 12 steps in 4.0% yield (79% per step on average).

Moreover, the prodigiosin A-ring azide **III-89·HCl** was used to synthesise the first clickable and fluorescent azide-containing prodigiosin *F*-BODIPY. The photosensitive and fluorescent aryl- and alkyl-azide-harbouring

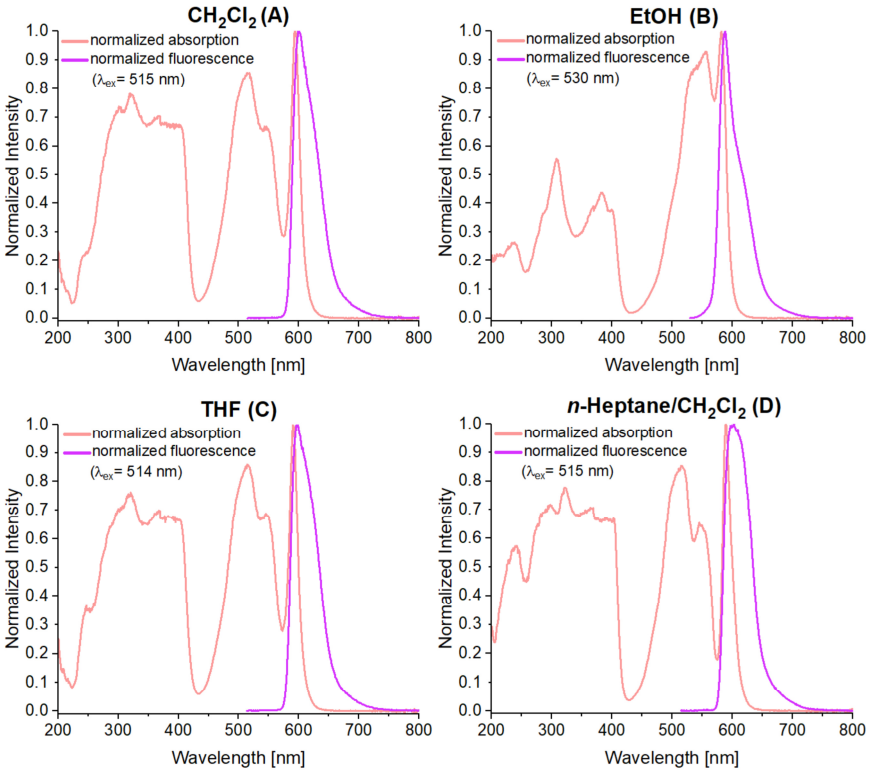
F-BODIPYs have been proven beneficial in various imaging applications and have been widely acknowledged for their remarkable properties, including large absorption coefficients, sharp fluorescence emission, small Stokes shift, low photobleaching, and high quantum yields.[430-433] Traditional BODIPYs are metalloid-dye complexes, built from the B+C-ring pyrrolylpyrromethene chromophore of the prodigiosin scaffold and boron difluoride. In these complexes, the BF_2 is trapped between the central nitrogen atoms of the chromophore, which can carry additional substitution at the bridging *meso*-position. These "original" BODIPYs exhibit absorption and emission at wavelengths between 470 nm and 530 nm.[434] This limited range of spectral activity constricts their potential applications, which is why extended BODIPYs for longer wavelengths are needed.[433] To achieve this goal, the synthesis of fused BODIPYs with expanded chromophores, achieved through additional aryl-, vinyl-, and styryl-substituents in the 3-position[4] of the fluorophore, has proved to be a useful lever to tune the spectral properties. In 2012, Zhang *et al*. introduced a pyrrole moiety to the BODIPY core via oxidative nucleophilic substitution, providing an extended pyrrole chromophore that resembles the three pyrrole-containing scaffold of prodiginines.[433] The intriguing similarity between these two classes of nitrogen-containing heterocycles, namely BODIPYs and prodiginines, inspired us to attempt the synthesis of the first reported prodigiosin-like *F*-BODIPY with clickable organic azide-functionalisation. In consequence, BODIPY A-ring azide was synthesised from the HCl salt of the prodigiosin A-ring azide **III-89·HCl** by deprotonation with DIPEA in CH_2Cl_2 and slow addition of BF_3 etherate at 0 °C.[430] After purification by column chromatography, the *F*-BODIPY A-ring azide **III-125** was provided as a deep purple solid in a yield of 79% (Scheme III.20).



Scheme III.20. Final cross-coupling reaction towards prodigiosin A-ring azide **III-89** and synthesis of the clickable bright-red fluorescent *F*-BODIPY **III-125**.

When the purple powder of *F*-BODIPY A-ring azide **III-125** was dissolved in organic solvents, bright-red fluorescent solutions were obtained under irradiation with sunlight (cf. Figure III.2). With a shift in the absorption maximum from 535 nm for the hydrochloride of prodigiosin **III-1ab·HCl** to up to 594 nm (CH_2Cl_2) for *F*-BODIPY **III-125**, a significant redshift of Δ59 nm was obtained. Concurrently, a sharp fluorescence emission signal was detected between 588–603 nm in the selected solvents (Figure III.2A–E). In the apolar solvent *n*-heptane (incl. 1% CH_2Cl_2 for solubility), the most considerable Stokes shift of 14 nm was provided. However, the Stokes shift was generally quite small, ranging from 5 nm to 14 nm. Complete absorption and fluorescence emission spectra in CH_2Cl_2, EtOH, THF, and *n*-heptane/CH_2Cl_2 (99:1) are presented in Figure III.2 (fluorescence quantum yields were not determined).

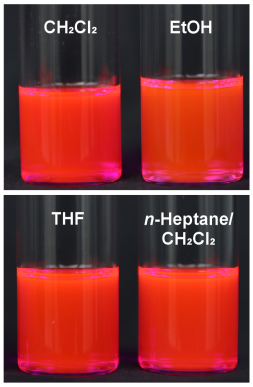
[4] The IUPAC BODIPY numbering does not match the IUPAC numbering of the 2,2'-dipyrromethene. While the *meso*-position (atom 8) in BODIPY nomenclature refers to atom number 5 in dipyrromethene, the BODIPY atom number 3 is equivalent to the 1-position in 2,2'-dipyrromethene.



E

Solvent	$\lambda_{max,ex}$ [nm]	$\lambda_{max,em}$ [nm]	Stokes shift
EtOH	582	588	6
CH_2Cl_2	594	599	5
THF	590	599	9
hept/CH_2Cl	589	603	14

F



F-BODIPY **III-125** in organic solvents

Figure III.2. Normalised absorption and fluorescence spectra of the bright-red fluorescent *F*-BODIPY A-ring azide **III-125** in various organic solvents. **A**–**D**. The BODIPY was dissolved in CH_2Cl_2 (**A**), EtOH (**B**), THF (**C**), and *n*-heptane/CH_2Cl_2 (99:1, **D**) to 80 µM and absorption spectra (orange) were measured in a range from 200–800 nm. Fluorescence emission (pink) was measured after excitation at 514 nm (THF), 515 nm (CH_2Cl_2 and *n*-heptane/CH_2Cl_2), and 530 nm (EtOH). All spectra were corrected for the solvent background signal. **E**. Summary of spectral properties of *F*-BODIPY **III-125** in solvents **A**–**D**, including the wavelengths of maximum absorption ($\lambda_{max,ex}$) and fluorescence emission ($\lambda_{max,em}$) and the corresponding Stokes shift. **F**. Red fluorescence of an 80 µM solution of *F*-BODIPY **III-125** in various organic solvents under exposure to sunlight.

As suggested by the plethora of BODIPY-related literature, BODIPY pigments are a fascinating and rapidly evolving field of organic dyes and fluorophores with various applications, especially in molecular imaging. The newly developed clickable prodigiosin-like *F*-BODIPY A-ring azide **III-125** represents a novel family of molecules whose properties can be exploited for tailored applications. In 2016, Vodyanova *et al*. used BODIPYs as biosensors of protein surface polarity on the example of bovine serum albumin.[435] Moreover, BODIPYs have been readily applied in photodynamic therapy.[436] Photodynamic therapy describes a medical treatment in which a non-toxic photosensitiser is activated by high-energy light of a distinct wavelength to induce photochemical or photophysical reactions that cause the formation of either highly reactive radicals or ROS species. The local formation of these potent cytotoxic species then causes cytotoxic damage to surrounding organelles or cells and thereby induces apoptosis.[437] The site-specific application of lasers already allows for minimising damage to surrounding healthy cells. However, by combining the well-established method of photodynamic therapy with conjugates of the clickable BODIPY **III-125** with target-selective binders, such as antibodies, it might be possible to enable a target-specific delivery of these BODIPY-photosensitisers to the desired cell type or facilitate their enrichment in specific tissues. This site-specificity update in photodynamic therapy would help to multiply the cytotoxic damage exerted on the targeted cells. But in molecular imaging, the classical domain of BODIPY application, the novel clickable prodigiosin-like *F*-BODIPY **III-125** might also find application. The researchers around Paulus *et al*. were able to develop an azide-modified bimodal fluorescence/PET probe through $^{18}F/^{19}F$ exchange to site-specifically label alkyne-harbouring synthetic peptides, e.g. the mammalian neurohormone

bombesin. The labelled bombesin was used to validate the performance of the ^{18}F-BODIPY-bombesin tracer for PET imaging of a bombesin receptor-positive prostate cancer model.[432]

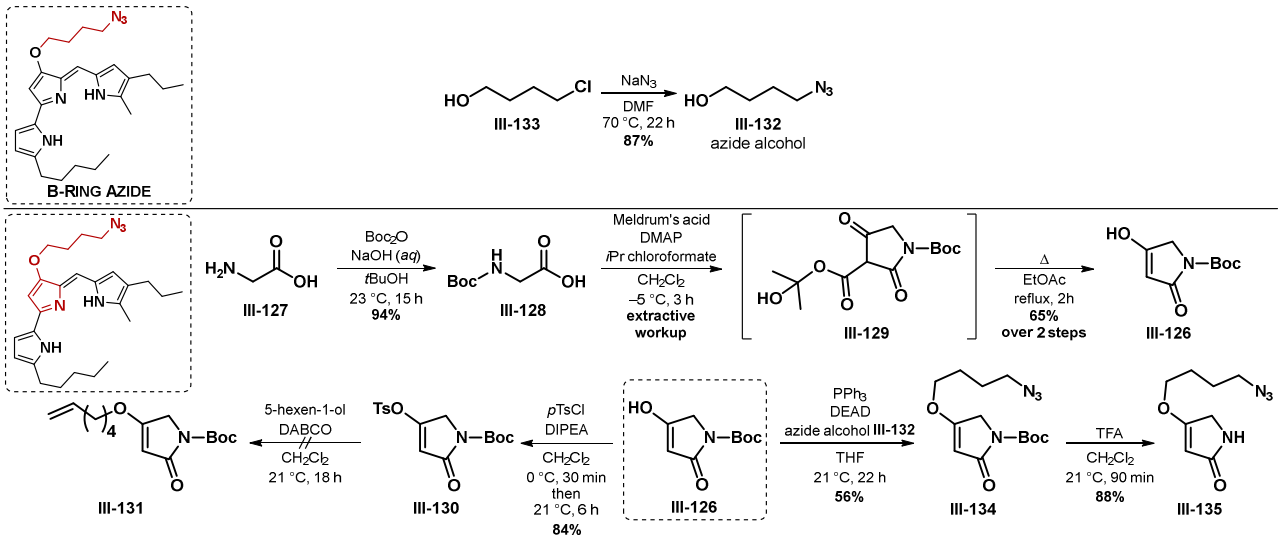
Summarising the insights gained during the synthesis of *F*-BODIPY **III-125**, the azide-substituted prodigiosin-like BODIPYs are more complicated to synthesise than most other BODIPYs due to a multitude of additional synthetic steps. Nonetheless, their unique spectral properties and their potential fields of application could lead to interesting examples of use in the future.

III.3.1.2 Prodigiosin B-Ring Azide

III.3.1.2.1 B-Ring Azide Precursor and B-Ring Azide Dipyrromethene

Prodigiosin and its naturally occurring analogues carry an *O*-methyl substituent in the 4'-position of the B-ring (cf. Scheme III.1). However, synthetic chemistry made B-ring derivatives of prodigiosin accessible, carrying *O*-aryl functionalisation in the 4'-position,[310, 314] as well as 4'-alkyl, 3',4'-alkyl or even no substitution in either of the two positions.[265, 310, 315, 411, 438] Structure-activity relationship (SAR) studies revealed that the 4'-alkoxy group of prodigiosin is yet crucial for maintaining the anticancer and immunosuppressive activity of the alkaloid.[265, 310, 439, 440] Therefore, suitable options were investigated to introduce *O*-alkyl substitution, allowing for terminal azide incorporation, mimicking the natural substitution of alkaloids from the prodigiosin family. In analogy to the unprotected B-ring tetramic acid precursor **III-74** for the *O*-methyl substitution pattern of prodigiosin, the *N*-Boc-protected tetramic acid **III-126** was initially used for further functionalisation (Scheme III.21).

To synthesise the *N*-Boc-protected tetramic acid **III-126** at first, the amino acid glycine (**III-127**) was *N*-Boc protected using Boc-anhydride and NaOH as a base in a mixture of *t*BuOH and water. After recovering the protected amino acid in a yield of 94% from aqueous workup, *N*-Boc-glycine (**III-128**) was subsequently converted in a batch reaction to a mixed anhydride with isopropyl chloroformate. DMAP as a base and catalyst was applied to deprotonate Meldrum's acid to attack the anhydride on the sterically less hindered glycine flank. Intramolecular attack of the nitrogen and opening of the 6-membered ring yielded the *C*-acylated tetramic acid intermediate **III-129** in the keto form. Heating in EtOAc triggered the concerted elimination of acetone and decarboxylation to culminate in the stable Boc-protected tetramic acid **III-126** in the enol form.[441-444] Based on the literature, *O*-functionalisation of tetramic acid **III-126** was first attempted via *O*-tosylation of enol **III-126** and subsequent etherification under DABCO [1,4-diazabicyclo(2.2.2)octane]-catalysis with an aliphatic alcohol (Scheme III.21).

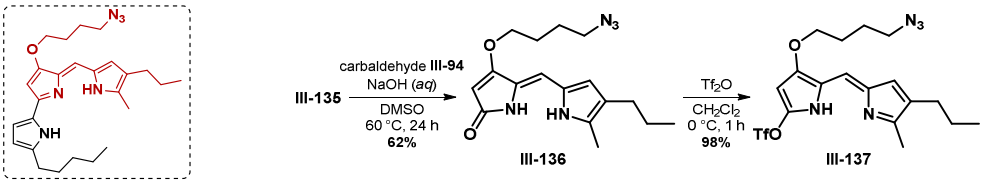


Scheme III.21. Synthesis of the azide-functionalised tetramic acid **III-135** as B-ring precursor.

However, no reaction was observed between tosylate **III-130** and the aliphatic alcohol towards the *O*-alkylated intermediate **III-131**, which was attributed to the lack of nucleophilicity of the aliphatic alcohol. As this employed etherification protocol was initially developed for electron-rich aromatic thiophenols as nucleophiles and already negatively affected by electron-withdrawing substituents on the thiophenol nucleophile,[445] this outcome was not surprising for less reactive aliphatic alcohols.

After the failure of the DABCO-catalysed route, a procedure for the direct *O*-alkylation of tetronic acid developed by Fort *et al*. was adapted instead.[441, 442] The etherification of enol **III-126** with the azide alcohol **III-132**, which had been synthesised in a one-step conversion from 4-chloro-1-butanol (**III-133**),[446] was accomplished through Mitsunobu displacement with the strong dehydrating reagent diethyl azodicarboxylate (DEAD) and PPh_3 in THF.[447] Even though the azide-functionalised Boc-protected tetramic acid **III-134** was difficult to purify from other reaction side products, it was isolated on a multigram scale in a yield of 56%. Standard deprotection with trifluoroacetic acid (TFA) in CH_2Cl_2 provided the free base of azide-functionalised *O*-alkylated tetramic acid **III-135** in reasonable yield as a direct B-ring precursor for the introduction of the azide moiety into the tripyrrole structure.

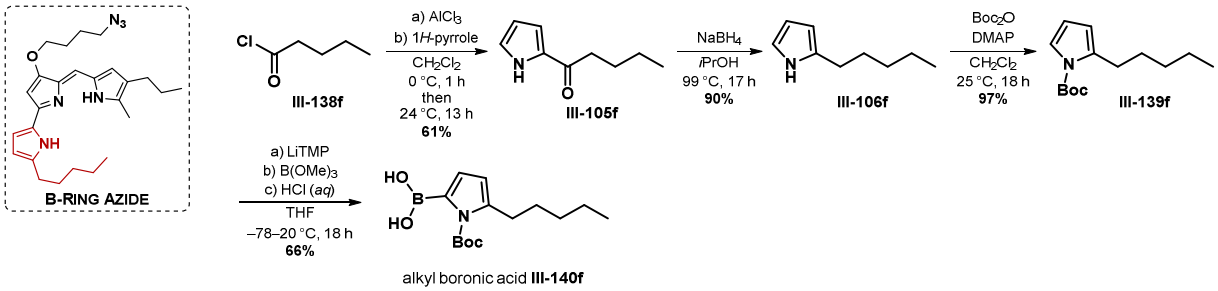
The synthesis towards the prodigiosin B-ring azide **III-90** proceeded via the previously introduced condensation reaction between tetramic acid derivative **III-135** and the carbaldehyde **III-94** in moderate yield. In the following, triflation of dipyrrinone **III-136** with triflic anhydride in CH_2Cl_2 in a near-quantitative yield of 98% was used to generate triflate **III-137** with azide substitution on the future B-ring (Scheme III.22).



Scheme III.22. Synthesis of the triflate **III-137** with B-ring azide substitution.

III.3.1.2.2 Alkylated A-Ring Precursor

With the triflate **III-137** with an azide substitution in the future B-ring at hand, the corresponding A-ring alkyl-functionalisation was introduced in analogy to the previously introduced A-ring azide via intermediate alkyl boronic acid. For the synthesis of this alkylated pyrrole-2-boronic acid, 1*H*-pyrrole was first acylated with pentanoyl chloride **III-138f** and $AlCl_3$ as Lewis acid, and the acylation product **III-105f** was subsequently reduced with $NaBH_4$ in *i*PrOH.[392, 393] Afterwards, *N*-Boc-protection of the alkylated pyrrole **III-106f** with Boc_2O and catalytic DMAP was used to mask the nucleophilic nitrogen, followed by utilisation of the Boc-protected 2-alkyl pyrrole **III-139f** to generate the desired alkylated pyrrole-2-boronic acid **III-140f** (Scheme III.23).[263]

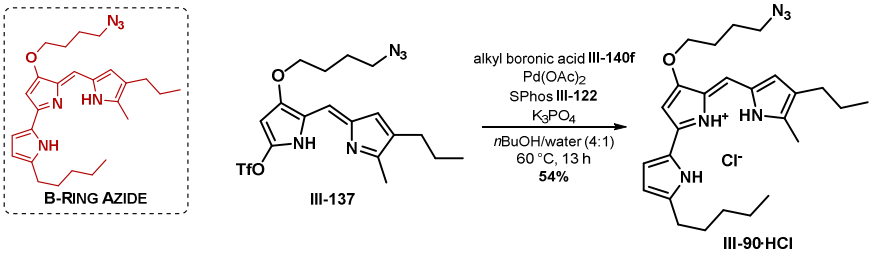


Scheme III.23. Synthesis of alkyl boronic acid **III-140f** as alkylated A-ring precursor.

Following the procedure for the preparation of azide boronic acid **III-114**, the alkylated boronic acid **III-140f** was isolated as a light-yellow solid in a good yield of 66%. However, in contrast to the very delicate azide boronic acid **III-114**, the alkylated derivative **III-140f** showed increased stability and did not readily decompose under high vacuum. Furthermore, the boronic acid was stable for a prolonged time at –20 °C under an argon atmosphere.

III.3.1.2.3 Biaryl Coupling Towards Prodigiosin B-Ring Azide

After having accessed the alkylated pyrrole-2-boronic acid **III-140f** and the azide-functionalised triflate **III-137**, the effort was directed to merge both intermediates in the final Suzuki-Miyaura cross-coupling reaction. Under the previously optimised reaction conditions, using $Pd(OAc)_2$ and the phosphine ligand SPhos in combination with a decreased reaction temperature of 60 °C, the prodigiosin B-ring azide **III-90·HCl** was isolated in a yield of 54% (Scheme III.24). Summarising the presented route towards the first B-ring azide-substituted prodiginine **III-90·HCl**, the tripyrrole alkaloid was synthesised over 12 steps in 3.2% yield (78% per step on average).



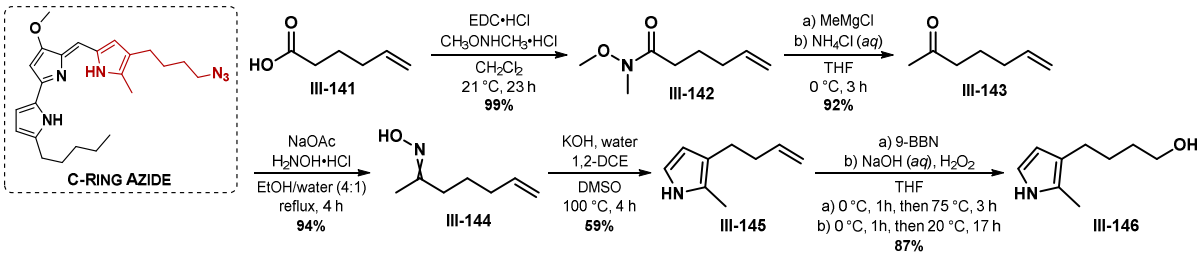
Scheme III.24. Suzuki-Miyaura cross-coupling between triflate **III-137** and alkyl boronic acid **III-140f** to provide the prodigiosin B-ring azide **III-90·HCl**.

III.3.1.3 Prodigiosin C-Ring Azide

To date, only two clickable azide-functionalised prodigiosin derivatives have been generated by introducing non-natural substitution patterns into the C-ring.[369] However, a substitution pattern resembling the 5-methyl-4-pentyl substitution of the natural product prodigiosin (**III-1ab**) is a desirable feature when comparing potential biological activities of the prodigiosin azides and their conjugates to the parent compound without introducing too many variables at the same time. These variables, for example, include changing conjugation sites (A-, B-, and C-ring) or the chemical substitution pattern on the pyrrole rings of the prodiginines. Hence, this work aimed to synthesise a clickable prodigiosin C-ring azide with a connatural substitution to the 5-methyl-4-pentyl pattern of the natural product prodigiosin (**III-1ab**).

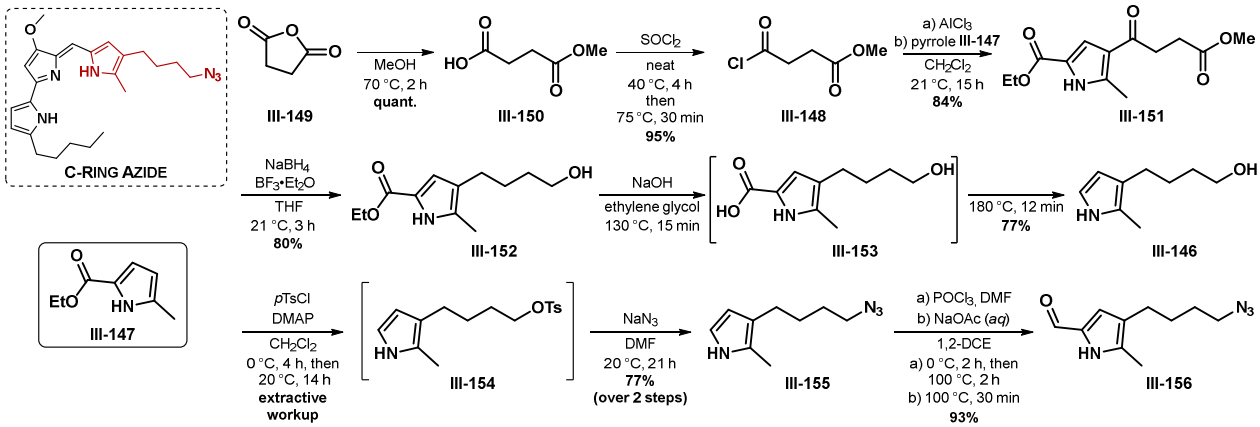
In the first place, the synthetic route of Scheme III.16 was adapted to introduce a reactive terminal double bond for further functionalisation of the future C-ring monopyrrole. Unfortunately, the limited commercial availability of alkene-functionalised ketones as starting materials for the designated Trofimov route necessitated the synthesis to start from 5-hexenoic acid (**III-141**) (Scheme III.25). Activation of the carboxylic acid with the HCl salt of 1-ethyl-3-(3-dimethylaminopropyl)carbodiimide (EDC) allowed conversion of acid **III-141** to the corresponding Weinreb amide **III-142**, which could be reduced with methylmagnesium chloride to release 6-hepten-2-one (**III-143**) upon acidic workup with aqueous ammonium chloride.[301] The subsequent reaction with hydroxylamine in the presence of sodium acetate as base rendered the *E*/*Z* mixture of oxime **III-144** in high yield.[390] This route benefits from complete conversion and water solubility of all reagents and side products so far, making purification other than aqueous extraction dispensable. In fact, the volatility of ketone **III-143** and oxime **III-144** entails the observed product loss during the workup procedure. Next, subjection of oxime **III-144** to Trofimov conditions allowed

isolation of the alkene pyrrole **III-145** in a good yield of 59% but required tedious purification effort,[389] including distillation and column chromatography to isolate the desired product in reasonable purity. The *anti*-Markovnikov alcohol **III-146** was lastly obtained in 87% by a Brown hydroboration-oxidation involving the *syn*-addition of 9-borabicyclo(3.3.1)nonane (9-BBN) to the alkene and the subsequent oxidation of the intermediate borane with NaOH and hydrogen peroxide.[394, 395]



Scheme III.25. Initial route towards the hydroxylated pyrrole **III-146** from alkene pyrrole **III-145** via hydroboration. Abbreviations: 9-BBN – 9-borabicyclo(3.3.1)nonane; EDC·HCl – 1-ethyl-3-(3-dimethylaminopropyl)carbodiimide.

Although the presented approach with the intermediate alkene pyrrole **III-145** provided access to the hydroxy-functionalised pyrrole **III-146**, a more practicable method was sought to circumvent the resource-demanding purification of alkene pyrrole **III-145**. To do so, a concept for the functionalisation of an existing pyrrole scaffold was developed, rather than forming the heterocycle *de novo* through synthesis. In this context, the methyl-substituted pyrrole ester **III-147**, which readily carries the desired methyl group in the nitrogen-adjacent 5-position, was selected as an appropriate starting material for further functionalisation. Pyrrole ester **III-147** is available from commercial suppliers in large quantities. It can be functionalised regioselectively by Lewis acid-catalysed acylation in the 4-position with commercially available monomethyl succinyl chloride **III-148** (here synthesised in two steps from succinic anhydride **III-149**), as the ester sterically hinders the adjacent 3-position (Scheme III.26).[387] Monomethyl succinyl chloride was prepared by a short synthesis sequence, involving ring opening of succinic anhydride (**III-149**) through the reaction with anhydrous methanol in quantitative yield, followed by the conversion of the carboxylic acid monomethyl ester **III-150** with thionyl chloride into the volatile acid chloride **III-148** (Scheme III.26).[448]



Scheme III.26. Synthesis scheme of C-ring azide precursor **III-156**.

Regioselective acylation of pyrrole ester **III-147** with $AlCl_3$ as Lewis acid in CH_2Cl_2 with acid chloride **III-148** yielded 84% of the desired acylation product **III-151**. Concurrent reduction of the acyl moiety and the terminal methyl ester of pyrrole **III-151** with $NaBH_4$ and BF_3 etherate in THF provided the pyrrole **III-152** with the terminal alcohol in a yield of 80%,[449] but leaving the ethyl ester directly attached to the pyrrole core unaffected. For the following saponification-decarboxylation reaction, serious effort was invested to forestall the competing polymerisation of pyrrole **III-152**, which was observed under literature reaction conditions, namely heating the ester **III-152** with NaOH in ethylene glycol at 160 °C for 1 h.[387] Time-resolved TLC analyses on small-scale reactions revealed complete ester hydrolysis at 130 °C after 10 min towards acid **III-153** (no decarboxylation) and its thorough decarboxylation at 170 °C after 8 min. Despite complete conversion, further heating at 170 °C only caused rapid degradation of the desired reaction product **III-146**. Since all optimisations were conducted on a small scale, the intrinsic obstacle of a preparative reaction would need to account for slower heat transfer in large reaction vessels. Thus, the reaction time was prolonged to 15 min at 130 °C for ester hydrolysis, followed by the decarboxylation step at 180 °C internal temperature for 12 min. Based on this streamlined procedure, the hydroxy-functionalised pyrrole **III-146** was obtained in an improved yield of 77%, compared to only 41% under literature conditions (*vide supra*). The presented reaction sequence was performed on a multigram scale, providing 49% of the pyrrole alcohol **III-146** over three steps. In comparison to the route that involves the alkene pyrrole **III-145**, the alternative route via diester **III-151** is favoured and generally more scalable for three reasons:

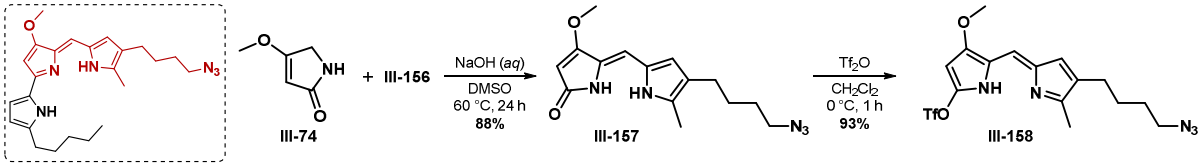
a) Chloride **III-158** and the pyrrole **III-147** are both commercially available and considerably cheaper than the 5-hexenoic acid (**III-141**) as starting material for the hydroboration route (Scheme III.25).

b) Target diversification can be easily accomplished by using differently substituted acid chlorides to functionalise pyrrole **III-147** in the first place, as previously performed in the work of Kancharla *et al*.[387]

c) The time-consuming purification of alkene pyrrole **III-145** in the hydroboration route is a clear disadvantage when performing the reaction on a large scale and aiming for an analytically pure (NMR) compound.

With satisfactory access to the hydroxy-functionalised pyrrole intermediate **III-146**, the synthetic effort was directed to gaining hands on the azide-functionalised C-ring precursor without using an additional protecting group strategy that would increase the number of synthetic transformations and increase the overall cost of the synthesis.

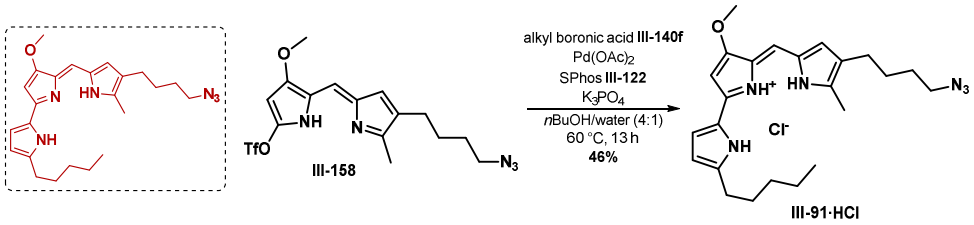
In adaptation of the previously used reaction sequence for the introduction of the azide moiety into A-ring of prodiginine **III-89·HCl** via *O*-tosylation and azide substitution (cf. Scheme III.17), the transformation of the terminal hydroxy group of pyrrole **III-146** into a tosylate leaving group was attempted with tosyl chloride (Scheme III.27). A base screening in CH_2Cl_2 with pyridine, DMAP, or 1,8-diazabicyclo(5.4.0)undec-7-ene (DBU) suggested only pyridine and DMAP as suitable bases for efficient conversion of pyrrole **III-146** into tosylate **III-154**. Still, only DMAP was able to render complete conversion. Nevertheless, every single attempt at product isolation, either by aqueous workup or column chromatography, led to thickening and allegedly polymerisation upon thorough solvent removal or contact with silica. Spiking the diluted CH_2Cl_2 reaction extract with the high-boiling-point solvent DMF and further removal of CH_2Cl_2 under reduced pressure addressed this problem without causing considerable decomposition. The solution of tosylate **III-154** in DMF was then supplemented with NaN_3 and the organic azide **III-155** was isolated in 77% over two consecutive steps. A Vilsmeier-Haack formylation finally provided the azide-functionalised carbaldehyde **III-156** in an excellent yield of 93%.[263] Similar to the previously described condensation between the monomeric B- and C-ring precursors, the dipyrrinone intermediate was built by joining



Scheme III.27. Synthesis of the azide-functionalised triflate **III-158** as precursor of the prodigiosin C-ring azide **III-91**.

the tetramic acid **III-74** with the azide-loaded carbaldehyde **III-156** (Scheme III.27). The condensation reaction and the follow-up triflation reaction both proceeded smoothly, omitting the need for chromatographic purification, and yielded 88% of the dipyrrinone intermediate **III-157** and 93% of the triflate **III-158** with azide-modification on the future C-ring.

Lastly, alkyl boronic acid **III-140f** was cross-coupled with triflate **III-158** under the optimised reaction conditions using SPhos/Pd(OAc)$_2$ in a yield of 46%, providing a moderate yield in comparison to the cross-coupling reaction towards A-ring and B-ring azides **III-89·HCl** (64%) and **III-90·HCl** (54%). Ultimately, the prodigiosin C-ring azide **III-91·HCl** was synthesised in a yield of 4.6% over 15 consecutive steps (83% per step on average) (Scheme III.28).



Scheme III.28. Suzuki-Miyaura cross-coupling reaction providing the prodigiosin C-ring azide **III-91·HCl**.

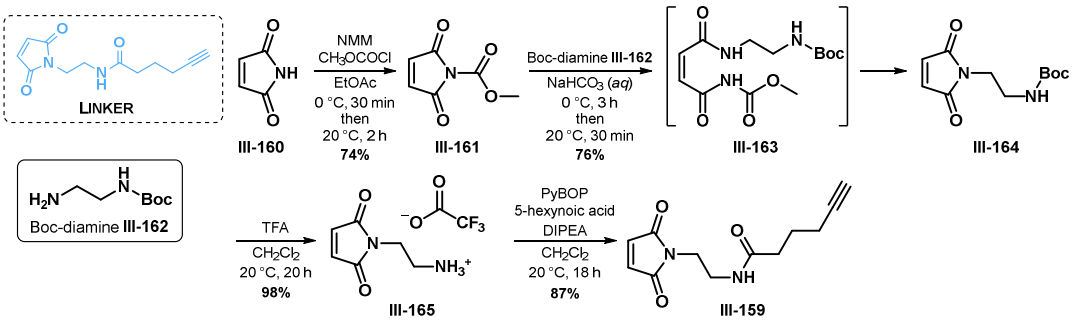
III.3.1.4 Click Conjugates of Functionalised Prodiginines

After accomplishing the primary aim of synthesising the azide-functionalised A-, B-, and C-ring derivatives **III-89·HCl**, **III-90·HCl**, and **III-91·HCl** of prodigiosin, the next aim was to prepare biological protein- and small-molecule conjugates thereof. Reliable and well-established thiol-maleimide chemistry, based on the thiol-Michael addition, was appointed as the foundation for protein conjugation.[450, 451] The bifunctional and commercially available alkyne-maleimide linker **III-159** was chosen as a suitable means to connect the prodigiosin azides through copper-catalysed click chemistry with the alkyne moiety of the linker. In contrast, the surface accessible thiol group of a cysteine residue within a protein was designated to react with the maleimide subunit of the linker.

III.3.1.4.1 Synthesis of a Bifunctional Alkyne-Maleimide Linker

In the first step of the synthesis of linker **III-159**, maleimide (**III-160**) was transformed into the *N*-protected carbamate **III-161** by reacting with *N*-methyl morpholine (NMM) and methyl chloroformate in EtOAc (Scheme III.29).[452] Nucleophilic attack of the *N*-protected carbamate **III-161** at the heterocyclic carbonyl group by *N*-Boc-ethylenediamine (**III-162**) allowed a transient ring opening under mild basic conditions in aqueous $NaHCO_3$ solution. The acyclic reaction intermediate **III-163** then underwent an intramolecular attack of the unprotected diamine nitrogen to the carbonyl group adjacent to the carbamate to form a stable five-membered carbamate **III-164** again and release methyl carbamate from the acyclic intermediate **III-163**.[453] Standard deprotection of the Boc-protecting group with TFA in CH_2Cl_2 provided the TFA salt **III-165** in 98% yield by simple filtration. Finally, the unprotected maleimide amine **III-165** was joined with 5-hexynoic acid in a PyBOP-mediated

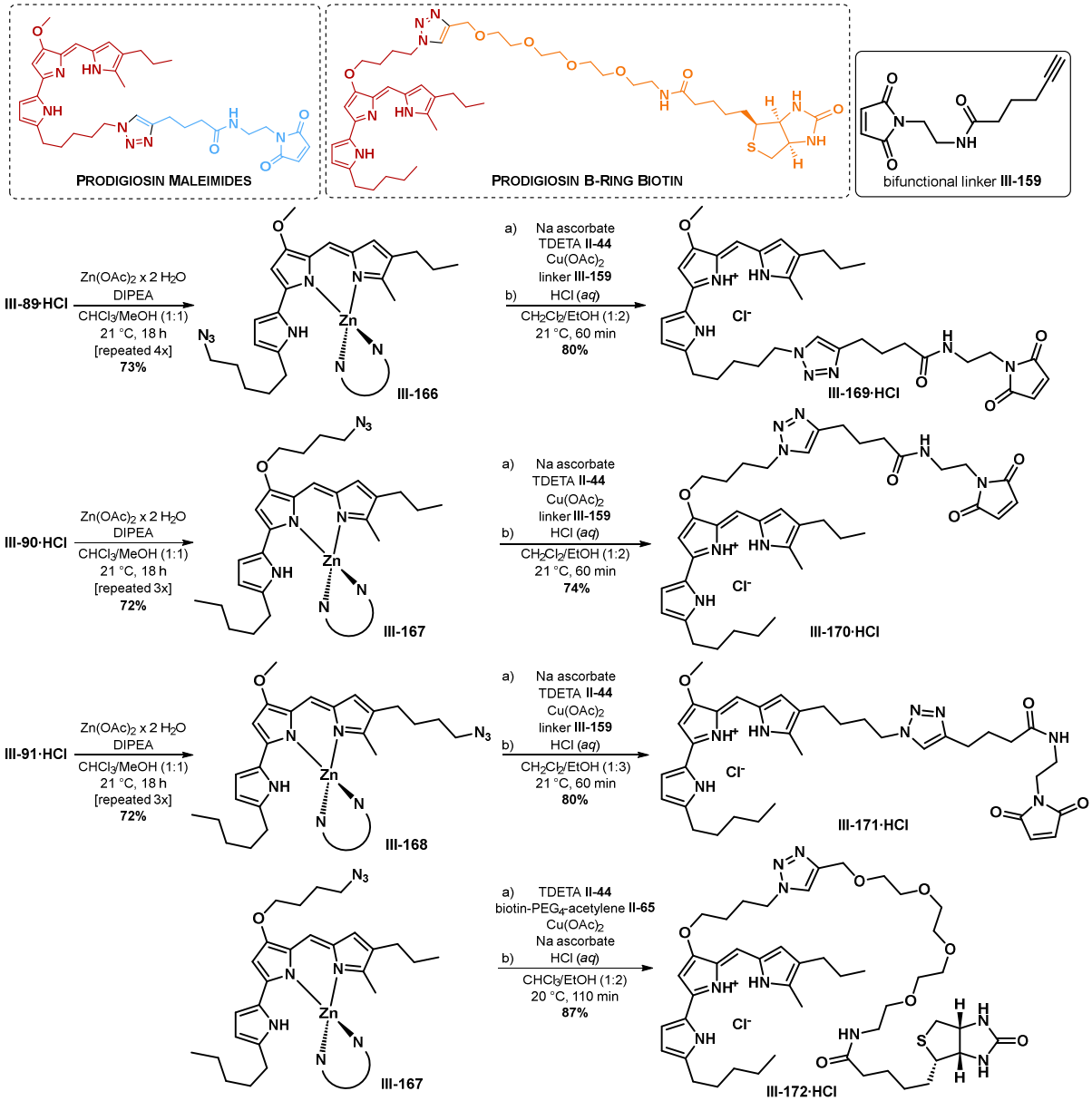
(benzotriazol-1-yloxytripyrrolidinophosphonium hexafluorophosphate) amide coupling reaction in an adapted procedure, originally used with the coupling reagent HATU {1-[bis(dimethylamino)methylene]-1*H*-1,2,3-triazolo[4,5-*b*]pyridinium 3-oxide hexafluorophosphate}.[452, 454] The bifunctional linker **III-159** was synthesised on a gram scale in a yield of 48% over four consecutive steps (84% per step on average) and was used for further maleimide functionalisation of the prodiginine azides **III-89·HCl**, **III-90·HCl**, and **III-91·HCl**.



Scheme III.29. Synthesis scheme of the commercially available bifunctional alkyne-maleimide linker **III-159** for click-functionalisation of prodigiosin azides and conjugation with cysteine-harbouring proteins via thiol-Michael addition. Abbreviations: DIPEA – diisopropylethylamine; NMM – *N*-methyl morpholine; PyBOP – benzotriazol-1-yloxytripyrrolidinophosphonium hexafluorophosphate; TFA – trifluoroacetic acid.

III.3.1.4.2 CuAAC Click Functionalisation of Prodiginine Azides Requires Homo-Dimeric Zinc Complexes

Metal-chelating heterocycles, such as prodigiosin, compete with the alkyne in complexation of Cu(I) and Cu(II) species when taking part in copper-catalysed azide-alkyne cycloadditions (CuAAC), as observed in self-accelerated chelation-assisted click reactions of *N*-heterocycles (cf. Chapter II.3.1.2 and II.3.1.3). For this reason, they must be protected prior to performing the click reaction.[455] Moreover, decomposition of unprotected azide-functionalised prodigiosin derivatives through copper-complexation in the dipyrrin structure was noted earlier by Marchal *et al*.[369] Hence, the strong metal-chelation of the tripyrrole scaffold was exploited to prepare homo-dimeric zinc complexes of A- **III-166**, B- **III-167**, and C-ring **III-168** prodigiosin azides by adding $Zn(OAc)_2$ and DIPEA to a solution of prodigiosin azides in $CHCl_3$/MeOH (Scheme III.30).[369] Although the reactions typically provided high conversions, the isolated yields after chromatography on silica were rather low (<40%). Hence, the process was repeated up to four times per compound to finally yield the homo-dimeric zinc complexes **III-166**, **III-167**, and **III-168** in reproducible yields between 72% and 73%. Subsequently, the homo-dimeric prodigiosin zinc complexes **III-166**, **III-167**, and **III-168** were functionalised with the thiol-reactive alkyne-maleimide linker **III-159** in a CuAAC click reaction. For this purpose, the Cu-ligand TDETA **II-44**, which was developed in this work (cf. Scheme II.14), was employed to catalyse the click reactions. The excellent solubility of the novel Cu(I)/Cu(II) ligand TDETA **II-44** in numerous protic and aprotic solvents proved to be beneficial in the copper-catalysed click reaction between the very polar bifunctional linker **III-159** and the rather apolar azide-functionalised zinc complexes.[137] In the presence of TDETA and under reducing conditions with sodium ascorbate, the Cu(I) species efficiently promoted the click reactions to complete conversion within 60 min. As the Zn complexes **III-166** and **III-167** of the A- and B-ring azide were rather insoluble in MeOH, but the linker needs polar solvents for good solvation, a solvent ratio of CH_2Cl_2/EtOH (1:2) was determined as optimal to allow the reaction to proceed to complete conversion. In contrast, the high solubility of the C-ring Zn complex **III-168** in MeOH allowed for an increase in the portion of polar protic alcoholic solvent to 1:3, which favoured the complete conversion of the



Scheme III.30. Click functionalisation of prodigiosin derivatives to generate protein-conjugable prodiginine-maleimide or prodiginine-biotin conjugates. Preparation and CuAAC-functionalisation of homo-dimeric prodigiosin zinc complexes **III-166**, **III-167**, and **III-168** with the bifunctional alkyne-maleimide linker **III-159** uncover the maleimide-decorated A-, B-, and C-ring prodiginines **III-169**, **III-170**, and **III-171**, respectively. Moreover, the D-biotin motif is introduced for high-affinity binding of avidin/streptavidin to be used in pull-down assays and target fishing approaches of prodigiosin binding partners, exemplified by B-ring functionalisation.

prodigiosin C-ring Zn complex **III-168** in the CuAAC reaction. After hydrolysis of the maleimide-functionalised zinc complexes **III-169**, **III-170**, and **III-171** with aqueous 1 M HCl during extractive workup and subsequent chromatographic purification, the maleimide-functionalised and protein-conjugable click products were isolated in very good yields of 80%, 74%, and 80%, respectively (Scheme III.30, top). In general, the obtained yields between 74–80% for the CuAAC reaction of prodigiosin azides are rated as a significant improvement in comparison to yields obtained in the literature with the common commercial ligand TBTA (46–58%), used in the preparation of estradiol- and tamoxifen-prodiginine conjugates via CuAAC.[369]

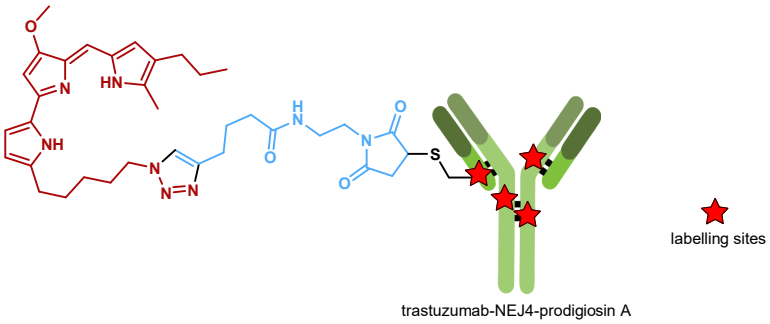
The high cytotoxicity of prodigiosin derivatives against several malignant eukaryotic cell lines and bacteria is owing to the physico-chemical properties of the tripyrrole scaffold (Chapter III.1.1.5). Although several cellular targets have been identified in the last decades, it remains vague whether prodigiosin can additionally interact with other cellular structures (e.g. enzymes), and thereby act as inhibitor of regulatory metabolic processes other than those already known (cf. Chapter III.1.1.5.2 and III.1.1.5.3). To approach this question in the long term and to identify potential interaction partners of prodiginines, biotinylation of the tripyrrole alkaloid was introduced to facilitate their application in pull-down assays. The structurally unique D-biotin moiety allows for high-affinity binding to the proteins avidin and streptavidin (cf. Chapter II.3.2),[30] whose tight interaction is commonly used for pull-down and target fishing approaches with streptavidin-coated surfaces, such as agarose or magnetic beads.[178, 187, 456] Hence, a biotin-prodigiosin conjugate can be used to elucidate so far unknown interaction partners and targets of prodigiosin.[457] For this reason, the biotinylated prodigiosin derivative **III-172** was generated in a single-step CuAAC reaction from the prodigiosin B-ring azide zinc complex **III-167** and the commercially available biotin-PEG_4-acetylene (Scheme III.30, bottom). The established CuAAC conditions with the novel ligand TDETA in combination with $Cu(OAc)_2$ under reducing conditions facilitated the isolation of a B-ring-attached prodigiosin-biotin conjugate **III-172**. While target fishing with this biotinylated prodiginine probe remains to be performed, the chemical synthesis of this conjugate readily proves that prodiginine conjugates of any alkyne coupling partner can be generated with the novel prodigiosin azides **III-89**, **III-90**, **III-91** via CuAAC click chemistry with the new copper-ligand TDETA **II-44**.

III.3.1.4.3 Trastuzumab-Prodigiosin Conjugates – The First Antibody-Drug Conjugates of Prodigiosin

The untargeted mechanism of prodigiosin causes cytotoxic damage to both healthy cells and cancer cells. Hence, the prodiginine derivatives **III-169·HCl**, **III-170·HCl**, and **III-171·HCl** with a cysteine-conjugable maleimide moiety are suitable for an attempted site-specific delivery of the alkaloid through covalent prodigiosin conjugates to reduce undesirable off-target effects. Adhering to the growing success of ADCs and their high target specificity conferred by the conjugated antibody, it was decided to test the cytotoxic potential and the selective delivery of the newly generated prodigiosin maleimides **III-169·HCl**, **III-170·HCl**, and **III-171·HCl** in ADCs with the therapeutic monoclonal antibody trastuzumab. This particular antibody targets the signal transduction of target cells by binding to the HER2 receptor tyrosine-protein kinase displayed on the outer membrane of HER2 receptor-positive cancer cells.[57] Notably, the HER2 receptor was shown to be overexpressed in 20–30% of the malignant tissue compared to healthy tissue, making trastuzumab an ideal candidate for targeted cell-specific drug delivery.[58]

The ADCs between a trastuzumab-NEJ4 antibody and the A-, B-, and C-ring maleimide-functionalised prodiginines **III-169·HCl**, **III-170·HCl**, and **III-171·HCl** were prepared in cooperation with the group of Prof. Harald Kolmar from the Technical University Darmstadt (Germany). The selected trastuzumab-NEJ4 antibody carries four cysteine mutations that are eligible for maleimide labelling via thiol-Michael addition. After reduction of potential disulfide bonds on the antibody's surface and removal of excess reducing reagent, the free thiols were labelled by the addition of excess prodigiosin maleimides (Scheme III.31). The residual unlabelled antibodies were separated from the labelled conjugates by hydrophobic interaction chromatography. However, the antibody-drug ratio of prodigiosin-labelled trastuzumab ADCs, representing the average number of prodiginines bound to the four available labelling sites, was not determined. Similar to the behaviour of prodiginines during preparative chromatography on silica gel, the prodigiosin-labelled trastuzumab antibodies did not show a defined elution profile, unlike the unlabelled antibody. Instead, they produced a broad smear, likely caused by a continuous

equilibrium between their protonated and deprotonated forms at physiological pH (cf. Scheme III.36, elution profiles not shown).



Scheme III.31. Schematic representation of trastuzumab-prodigiosin conjugates. The A-, B-, and C-ring prodigiosin maleimides are used for covalent labelling of reduced cysteine residues in the trastuzumab-NEJ4 monoclonal antibody, here exemplified by the prodigiosin A-ring maleimide. The trastuzumab-NEJ4 variant is equipped with a total of four labelling sites.

After prodiginine-labelling of the antibody carrier, the trastuzumab-prodigiosin conjugates were further evaluated for cytotoxic activity and their potential for site-specific delivery of the prodigiosin payload. Since the trastuzumab antibody targets the HER2 receptor, the two human cell lines SK-BR-3 (HER2 receptor-positive) and A431 (HER2 receptor-negative) were selected for the *in vitro* experiment. Both cell lines are malignant transformants and emerged from different types of carcinomas. While the HER2 receptor-negative and epidermal growth factor receptor (EGFR)-positive cell line A431 shows epithelial morphology and was isolated from an epidermoid carcinoma, the HER2 receptor-positive SK-BR-3 was isolated from a breast adenocarcinoma.[458] Therefore, A431 was used as a negative control, and SK-BR-3 was used as a positive control for the HER2 receptor-targeting trastuzumab conjugates. Validation of the conjugates took place at two levels, namely by evaluating their cellular binding to the SK-BR-3 and A431 cell lines and by monitoring the viability of these cell lines in the presence of prodigiosin-labelled ADCs. Firstly, binding of the HER2 receptor by the trastuzumab epitope was evaluated at a concentration of 10 nM (Figure III.3A). As expected, the trastuzumab-prodigiosin conjugates exhibited highly selective binding of HER2 receptor-positive SK-BR-3, whereas the conjugates did not show binding towards A431 owing to the absence of the outer membrane receptor. Secondly, the binding affinity of trastuzumab-prodigiosin conjugates was determined by treating HER2 receptor-positive SK-BR-3 cells with varying concentrations of trastuzumab-prodigiosin conjugates in a range of approximately 0.1–10 nM (Figure III.3B). For all ADCs, a concordant dissociation constant (K_D) of 0.6–0.8 nM was observed, proving high-affinity binding of the trastuzumab epitope to the cellular target. Lastly, SK-BR-3 and A431 cells were subjected to cell viability screening after treatment with the trastuzumab-prodigiosin conjugates in a concentration range of approximately 0.1–10 nM. As the working principle of ADCs relies on the internalisation of receptor-bound conjugates, their fusion with acidic lysosomes, and proteolytic degradation to release the cytotoxic payload (cf. Figure III.1), cytotoxic activity can only be displayed when the released drug is toxic on its own. Furthermore, the intracellular concentration of the potential drug must be high enough to cause intracellular cytotoxicity and provoke a cellular response that leads to cell death. Lastly, the A-, B-, and C-ring conjugates of trastuzumab and prodigiosin did not show cytotoxic activity in a cell viability screening, neither against the negative control A431, nor the HER2 receptor-positive cell line SK-BR-3 (Figure III.3C).

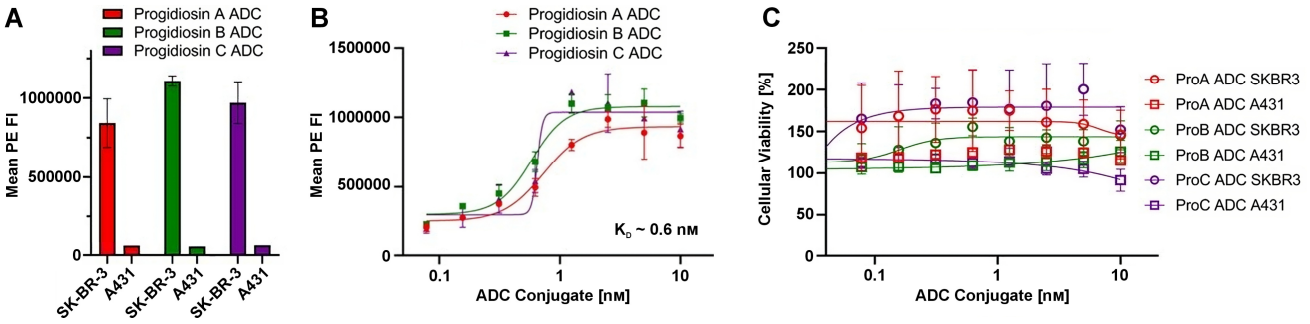


Figure III.3. Validation of cellular binding of trastuzumab-prodigiosin conjugates to the HER2 receptor on A431 and SK-BR-3 cell lines and cell viability screening. **A**. Cellular binding to HER2 receptor-negative A431 (negative control) and HER2 receptor-positive SK-BR-3 cell lines at a concentration of 10 nM conjugate (n=3). The binding of the trastuzumab conjugate was monitored via fluorescence of an R-phycoerythrin (PE)-conjugated Goat anti-Human IgG Fc secondary antibody. **B**. Cellular binding to HER2 receptor-positive SK-BR-3 at a variable conjugate concentration of 0.05–10 nM for the determination of dissociation constants (K_D) (n=3). The binding of the trastuzumab conjugate was monitored via fluorescence of an R-phycoerythrin (PE)-conjugated Goat anti-Human IgG Fc secondary antibody. **C**. MTT cell viability assay with A431 and SK-BR-3 and variable conjugate concentrations between approximately 0.1–10 nM (n=3). Data and graphs were provided by Peter Bitsch (TU Darmstadt, Germany). Prodigiosin A, B, and C ADC refer to conjugates of trastuzumab-NEJ4 with prodigiosin maleimides **III-169**, **III-170**, and **III-171**, respectively.

Considering the successful cellular binding of trastuzumab-prodigiosin conjugates, this in turn can only mean that the lacking cytotoxicity can be ascribed to the prodigiosin payload itself. From several SAR studies, it is already known that substitutions on the tripyrrolic scaffold can have severe effects on cytotoxicity.[310, 411, 459] All these SAR studies have been performed on freely diffusible prodiginines. However, the free diffusion of the proton-affine tripyrrole alkaloid prodigiosin across biological membranes is an important prerequisite for the alkaloid to act as an ionophore by symporting H^+/Cl^- and to uncouple proton gradients along membranes. The exploited maleimide linker **III-159**, which has been used in this given study to covalently connect the prodiginines with the trastuzumab-NEJ4 antibody, is unlikely to be cleavable under physiological conditions. Upon proteolytic digestion of the antibody-drug conjugates within the cells, it is assumed that both the linker and fragments of the protein (peptides) remain attached to the alkaloid core of the prodiginine payloads. This would not only have a significant impact on the size of the prodigiosin effector molecule but also severely impact the hydrophobicity of the prodigiosin-peptide remains. Although the overall solubility of the drug might increase due to polar peptide fragments from the trastuzumab antibody, the increased polarity might negatively affect the binding of the drug to its intracellular targets. Furthermore, a change in polarity could even cause an undesired binding to other cellular compartments, such as proteins or membrane lipids. Indeed, cleavable linkers (e.g. via enzymatic cleavage or through pH shift) are a useful tool to overcome a loss of biological activity upon conjugation.[460] Other drug-release mechanisms, for example, exploit the exclusive acidic extracellular environment of tumour cells. The abnormal metabolism creates this acidic environment (pH 6.5–7), which is not present in normal cells, and ultimately enables the target-specific cleavage of drug-loaded nanocarriers/nanoparticles in response to the acidic pH.[461] Admittedly, pH-responsive linkers, such as maleic acid amides, might fail in the context of prodigiosin conjugates. The reason for this lies in the preparation of the prodigiosin-linker conjugates through CuAAC. Since Marchal *et al*. observed oxidative degradation of the unprotected prodiginine scaffold upon addition of copper salts,[369] the click reaction is performed with *N*-protected homo-dimeric zinc complexes instead (cf. Scheme III.30). However, these complexes are stable towards neutral and basic pH and only disintegrate at low pH (e.g. 1 M aqueous HCl). This treatment during preparative workup would also harm an acid-sensitive linker and would cause a loss of the conjugable linker before an attempted preparation of the antibody conjugate. This fact is particularly emphasised by the small window of pH shift that acid-cleavable linkers aim for. While remaining intact in the bloodstream at

pH 7.4, these linkers are desired to be cleaved in acidic intracellular compartments, such as endosomes (pH 5.5–6.2) and lysosomes (pH 4.5–5.0) for site-specific release of the drug. Therefore, enzymatically cleavable linker technology appears to be more suitable for future structural modifications of prodigiosin conjugates. Hence, protease-cleavable linkers seem to be the most promising alternatives for antibody-prodiginine conjugates to facilitate the traceless intracellular release of the prodigiosin payload from the antibody and its fragments. A prominent example of ADC payloads that exploits the chemistry of a cleavable peptide linker is MMAE, an inhibitor of tubulin polymerisation and cell division in eukaryotes (cf. Chapter II.1.1.2.1 and Scheme II.5). Due to its high cytotoxicity and unselective targeting mechanism, MMAE cannot be used as a drug on its own. However, ADCs with non-cleavable MMAE payloads lose their cytotoxic potential as a consequence of covalent attachment and a missing drug release mechanism. Only in conjunction with a cathepsin B-cleavable valine-alanine linker, including a decarboxylation-driven self-immolative 4-aminobenzylcarbamate (PAB) unit for a traceless on-site drug release, antibody-MMAE conjugates show exceptional and selective killing activity against cancer cell lines.[462]

Another important consideration is the intracellular concentration of the toxin that is available to inhibit or damage cellular processes and targets. Although the utilised trastuzumab-prodiginine ADC concentration of ≤10 nM in our experiment for *in vivo* cell viability screenings is judged rather high for ADCs in general, the inhibitory concentrations for (soluble) prodiginines vary greatly, depending on the observed cytotoxic effect and the type of cell line. Most reported IC_{50} values for prodiginines against human cancer cell lines range from low nanomolar concentrations to low micromolar concentrations.[411, 463, 464] But even one of the lowest reported IC_{50} values for prodigiosin (**III-1ab**) against cisplatin-resistant urothelial bladder cancer cell line RT-112res is with 41 nM far beyond the tested concentration range (≤ 10 nM) of trastuzumab-prodigiosin conjugates in our experiment.[463] Although a single antibody is equipped with up to four equivalents of prodigiosin in the novel trastuzumab-prodiginine ADCs (cf. Scheme III.31), a 10 nM antibody concentration would result in a 40 nM drug concentration upon thorough intracellular release of the payload from the conjugate. However, as the excessively modified linker conjugates of A-, B-, and C-ring modified prodigiosin are likely to display lower inhibitory potential than the parent compound prodigiosin **III-1ab**, a significantly higher concentration range will be needed to evaluate cytotoxic phenotypes that emerge from treatment with trastuzumab-prodigiosin conjugates. This hypothesis is underlined by recent findings from Marchal *et al*. regarding anticancer properties of small-molecule conjugates with prodigiosin and estradiol **III-87** or 4-hydroxytamoxifen **III-86** (Scheme III.12).[369] The C-ring conjugated prodiginines reported in this study displayed moderate cytotoxicity against nine of the 60 screened cancer cell types from the National Cancer Institute (NCI-60). However, this moderate cytotoxic activity was only observed at a concentration of 1–10 µM,[367, 369] which is 100–1000 times higher than the highest tested concentration of trastuzumab-prodigiosin conjugates in our experiments.

In conclusion, the first holistic set of clickable prodiginines with A-, B-, and C-ring modifications was generated by chemical synthesis. Through maleimide functionalisation with a bifunctional alkyne maleimide linker, the prodiginines were further modified by CuAAC to generate bioconjugable derivatives of the three prodiginine species. Here, the novel tripodal copper-ligand TDETA provided very good and reproducible yields and once more proved its versatility in accelerating the CuAAC with chemically diverse substrates. Protein labelling via thiol-Michael addition with cysteine residues was exemplified on the HER2 receptor targeting antibody trastuzumab-NEJ4 and the generated trastuzumab-prodigiosin conjugates were further validated as potential antibody-drug conjugates for the selective targeting of HER2 receptor-positive breast cancer cells. On one site, selective binding of the conjugates to the HER2 receptor-positive cancer cell line SK-BR-3 was shown. Nevertheless, the prodigiosin payloads did not display cytotoxic activity, which is assumed to result from the non-cleavable linker

architecture that reduces the bioactivity of the prodiginines. Moreover, the absence of cytotoxic activity might be related to a low intracellular concentration of the toxin that is below the threshold needed to display biological activity. Finally, the ability to selectively deliver prodiginines to cancer cells via their conjugation with the trastuzumab antibody sets the starting point for further optimisations. Therefore, future work should focus on refining the prodigiosin payload by exploring alternative linker designs, with the overall goal of improving intracellular release and bioactivity.

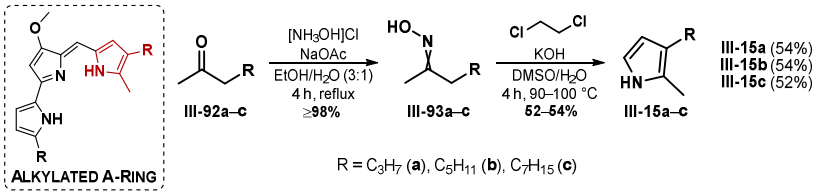
III.3.2 Chemoenzymatic Synthesis of Novel A-Ring Alkylated Prodigiosin Derivatives

Prodiginine ligases exploit the bipyrrole MBC **III-14a** and derivatives of 1*H*-monopyrroles as substrates for their ATP-catalysed reaction mechanism to synthesise prodigiosin **III-1ab** or cognate derivatives thereof (cf. Scheme III.1).[465, 466] So far, some of the annotated ligases from prodiginine or prodiginine-like biosynthesis clusters have been shown to accept a broad range of substituted 1*H*-monopyrroles in *in vitro* biocatalysis studies and in *in vivo* mutasynthesis experiments. The promiscuity of these condensing enzymes, exemplified by PigC from *S. marcescens*, is well-known for monopyrroles with cyclic and acyclic aliphatic side chains and the C-ring moiety of prodiginines.[295, 301, 302] Contemporaneously, little evidence has been presented regarding MBC derivatives being suitable substrates, yet. Chawrai *et al.* were the first to demonstrate that PigC could accept aryl-substituted A-ring derivatives of MBC (e.g. thienyl-, furyl-, phenyl-) (cf. Table III.2).[286] However, since then, no studies have further explored other MBC substitution patterns or enzymes. Even though broad accessibility of A-ring-substituted prodiginines by microbial biosynthesis or biocatalytic methods is not given from a today's perspective, those derivatives can be assessed by means of total synthesis. Melvin *et al*. attributed an adverse effect on the ability of the Cu^{II}·prodigiosin complex to cleave dsDNA when the A-ring of prodigiosin was either substituted with electron-withdrawing substituents in the 5-position or replaced by aryl residues other than pyrrolyl.[311] Similar effects were observed by D'Alessio *et al*. with a focus on cytotoxicity in extensive SAR studies.[310] At the same time, both studies denoted positive effects on DNA cleavage and cytotoxicity, respectively, by adding electron-donating alkyl substitutions in the 5-position of the A-ring.[310, 311] Hence, both works provide substantial evidence of value to further analyse the consequences of A-ring-associated alkylations on cytotoxicity displayed by the corresponding prodiginine derivatives.

Consequently, this chapter aims to expand the knowledge about the acceptance of A-ring *n*-alkylated MBC derivatives by the prodigiosin ligases PigC, TreaP, and TamQ to probe the substrate scope of the investigated enzymes experimentally. Therefore, a biomimetic synthesis procedure of alkylated MBC derivatives will be devised to use these building blocks as potential substrates for the enzymatic and chemical condensation reactions with different alkylated monopyrroles. Finally, this work will systematically infer the effects of prodigiosin A-ring alkylation on the anticancer activity of the chemically synthesised prodiginines.

III.3.2.1 Synthesis of C-Ring Monopyrrole Precursors

The chemical synthesis of the prodigiosin monopyrroles, serving as precursors for the chemical biomimetic condensation reaction, was approached using the previously introduced Trofimov reaction, which allows conversion of oximes to 2,3-dialkylated 1*H*-pyrroles.[301, 389] Starting from commercially available ketones, namely hexan-2-one (**III-92a**), octan-2-one (**III-92b**), and decan-2-one (**III-92c**), the respective oximes **III-93a**–**c** were synthesised in yields of ≥98% by refluxing the ketones with hydroxylamine hydrochloride and sodium acetate in EtOH/H_2O (4:1) (Scheme III.32).

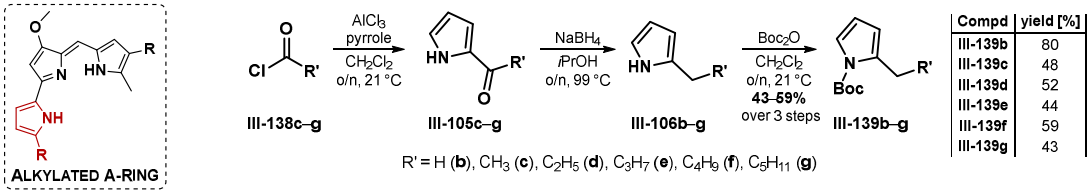


Scheme III.32. Synthesis of the 2,3-alkylated 1*H*-monopyrroles **III-15a**–**c** as biosynthetic precursors of the prodigiosin C-ring. The letters **a–c** refer to the alkylation pattern in the 3-position of the monopyrrole or the alkyl chain of ketone and oxime intermediates (**a** = propyl, **b** = pentyl, **c** = heptyl).

As conversions were near quantitative, no further purification was needed after aqueous extraction and removal of traces of acetic acid under slightly basic conditions. The obtained *E*/*Z* mixtures typically contained 73–76% of sterically less hindered *E*-oxime and could be used straightaway for the subsequent Trofimov reaction. The latter allows cyclisation of alkylated oximes in the presence of the electrophile 1,2-dichloroethane under superbasic reaction conditions that can be obtained by mixing DMSO, ground potassium hydroxide, and a small amount of H_2O.[389] The high reactivity of 1*H*-pyrroles originates from the electron-rich aromatic system, which is furthermore prone to oxygen-dependent oxidation and sensitive to light exposure. Consequently, in addition to inert reaction conditions, the utilisation of thoroughly degassed (and thus oxygen-free) and dried DMSO was identified as a key requirement for a reliable outcome of the reaction. By using degassed solvent, reaction temperatures of 90–100 °C over an extended period of 4 h resulted in a minimal amount of polymerisation during the reaction and yielded 52–54% of pyrroles **III-15a**–**c** (Scheme III.32) after chromatographic separation from typical side products, such as *N*-vinylated monopyrroles

III.3.2.2 Synthesis of 5'-Alkylated MBC Precursors

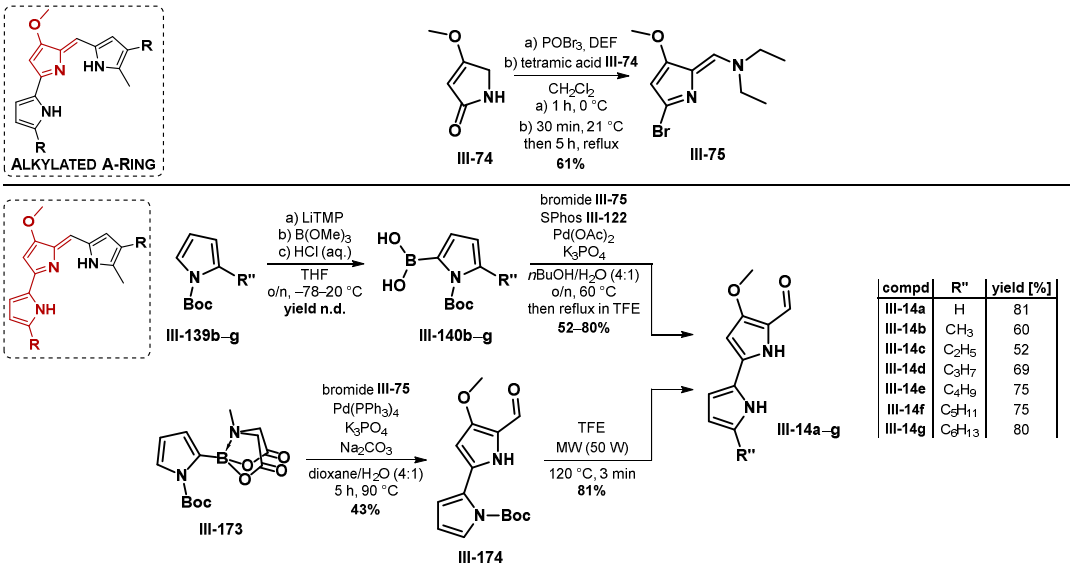
The bipyrrole MBC is the natural precursor of prodigiosin and an inevitable element in the biomimetic chemical synthesis of prodiginines. Hence, the use of such synthetic schemes that enable access to 5'-functionalised MBC derivatives is apparently essential for the chemoenzymatic approach followed in this work. The first biomimetic two-step sequence for gaining access to the natural prodigiosin and tambjamine precursor 4-methoxy-2,2'-bipyrrole-5-carboxaldehyde (**III-14a**, MBC) was devised by Dairi *et al*. (cf. Scheme III.10).[353] The reported route, which is also the synthetic foundation for this work, profits from a final Pd-catalysed Suzuki-Miyaura coupling between a brominated carbaldehyde precursor and a Boc-protected pyrrole-2-boronic acid to form the aryl-aryl axis. Based on this strategy, an adapted route was developed in this work to make 5'-*n*-alkylated derivatives of MBC as biomimetic precursors for enzyme-assisted or chemical synthesis accessible. Although other positions for MBC alkylation might be of interest as well in terms of cytotoxicity and the enzyme's substrate promiscuity, this work solely focuses on the 5'-position for this fundamental proof-of-principle study. The devised synthetic route for 5'-alkylation is predicated on the Vilsmeier-Haack haloformylation of 4-methoxy-3-pyrrolin-2-one (**III-74**) to give bromide **III-75**, followed by a Pd-catalysed cross-coupling of bromide **III-75** with 5-*n*-alkylated *N*-Boc-protected pyrrole-2-boronic acids. The foundation for the desired boronic acids were 2-alkylated *N*-Boc-protected 1*H*-pyrroles, which were afforded by a consecutive Friedel-Crafts acylation of 1*H*-pyrrole with acyl chlorides **III-138c**–**g** under the use of anhydrous $AlCl_3$ as a Lewis acid.[393] Although 3-acylation was regularly observed in minor quantities as a competing side reaction, the higher nucleophilicity of the nitrogen-adjacent 2-position yielded predominantly the 2-acylated pyrroles. Reduction of these product mixtures with sodium borohydride in *i*PrOH, mainly containing the 2-acylation products **III-105c**–**g**, and final *N*-protection of the alkyl pyrroles **III-106b**–**g** with Boc-anhydride yielded the target compounds **III-139b**–**g** (Scheme III.33) after a final chromatographic purification.[263] In this reaction sequence, the purification effort was reduced due to the utilisation of crude reaction products and exclusive purification of the Boc-protected products **III-139b**–**g** by flash column chromatography. By this means, the *N*-Boc-2-alkylated pyrroles were synthesised in yields of 43–59% over three steps.



Compd	yield [%]
III-139b	80
III-139c	48
III-139d	52
III-139e	44
III-139f	59
III-139g	43

Scheme III.33. Synthesis of the 2-alkylated 1*H*-pyrroles as precursors for the alkylated MBC derivatives.

Since boronic acids are more reactive than their related boronic acid pinacol or MIDA esters,[467] this work aimed for the synthesis of free pyrrole-2-boronic acids from *N*-Boc-2-alkylated pyrroles for the cross-coupling reaction with bromide **III-75**. Admittedly, 2-substituted boronic acids of *N*-heterocycles, such as pyrroles or pyridines, are delicate and lacking storage stability (cf. azide boronic acid **III-114**).[420] Thus, utilisation of crude boronic acids from pyrrole borylation reactions was considered more reliable than isolation of pure boronic acids. By using the crude reaction products, it was possible to minimise the number of steps involved in downstream processing and reduce the exposure of the delicate boronic acids to oxidative atmosphere, heat, and moisture. Indeed, the crude products of the borylation sequence, which comprises deprotonation and *ortho*-metalation of pyrroles **III-139b**–**g** with LiTMP, borylation with trimethyl borate, and lastly deprotection of the methyl ester with aqueous hydrochloric acid, were ideal starting materials.



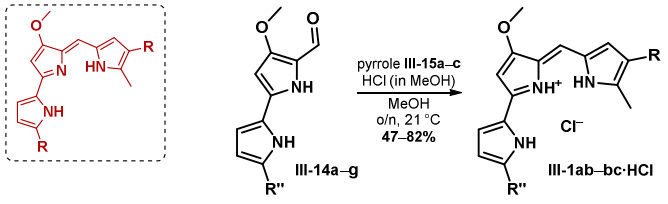
Scheme III.34. Synthesis of the unsubstituted MBC **III-14a** and its 5'-alkylated derivatives **III-14b–g**. Abbreviations: DEF – diethylformamide; MW – microwave.

The following Suzuki-Miyaura cross-coupling reaction was conducted under the optimised SPhos-assisted conditions in degassed *n*BuOH/H_2O (4:1) and with anhydrous tripotassium phosphate as a base (cf. Chapter III.3.1.1.4) to facilitate the C-C coupling between pyrrole-2-boronic acids **III-139b**–**g** and bromide **III-75** under mild reaction conditions (Scheme III.34). The reactions typically gave mixtures of Boc-protected and deprotected carbaldehydes. Full deprotection of the crude reaction product was achieved by refluxing in 2,2,2-trifluoroethanol (TFE), yielding the desired products after filtration. The overall low solubility of alkylated MBC derivatives in organic solvents, including TFE, prohibited microwave-assisted Boc-deprotection due to the boiling retardation and spillage. Resulting from this sequence, the 5'-*n*-alkylated MBC derivatives **III-14b**–**g** were obtained in good to yields between 52–80% (Scheme III.34). The unsubstituted biomimetic MBC precursor **III-14a** instead was synthesised according to the published literature procedure with a Suzuki-Miyaura cross-coupling reaction of bromide **III-75** and *N*-Boc-pyrrole-2-boronic acid MIDA ester **III-173** with $Pd(PPh_3)_4$ as precatalyst, followed by microwave-assisted deprotection of the Boc-protected intermediate **III-174** with TFE as solvent.[353] Apparently, the $Pd(PPh_3)_4$-catalysed two-step sequence towards unsubstituted MBC **III-14a** from MIDA boronate **III-173** provided only 36% of the bipyrrole, while yields of alkylated MBC derivatives from SPhos/$Pd(OAc)_2$-catalysed reactions ranged from 52–81%. It is assumed that these differences stem from the higher reactivity of free boronic

acids compared to the protected MIDA boronate. As no coherent trend in the reaction yield can be deduced from the chain length of alkylated MBC derivatives, varying purity and yield of the crude boronic acids as substrates for the cross-coupling reaction are most likely responsible for fluctuations in yields. Nevertheless, SPhos **III-122** seems to be a more fitting ligand for the coupling of pyrrole-2-boronic acids and pyrrole bromides, such as bromide **III-75**, or pyrrole triflates (cf. Chapter III.3.1.1.4), providing higher yields than the PPh_3 ligand **III-120** from the $Pd(PPh_3)_4$ precatalyst under milder reaction conditions. Hence, the utilisation of optimised conditions with SPhos precatalysts or free SPhos **III-122** in combination with $Pd(OAc)_2$ is suggested to substitute the standard conditions with $Pd(PPh_3)_4$ and to achieve higher yields of the precious prodigiosin precursor.

III.3.2.3 Chemical Synthesis of A-Ring Alkylated Prodiginines

Although the alkylated MBC **III-14b**–**g** derivatives were primarily synthesised for systematic characterisation of the substrate scope of prodigiosin ligases, they were also eligible for chemical synthesis of A-ring 5-alkylated prodiginines. Therefore, alkylated MBC carbaldehydes **III-14a**–**g** and pyrroles **III-15a**–**c** were subjected to a condensation reaction under acid catalysis according to Rapoport and Willson.[264] The addition of hydrochloric acid in MeOH initiated the coupling reaction and allowed the isolation of the corresponding prodiginines **III-1ba**-**bc** in yields of 47–82% after chromatographic purification (Scheme III.35). The hydrochlorides of prodigiosin (**III-1ab·HCl**) and the novel alkylated derivatives **III-1ba**–**bc·HCl** thereof were used as synthetic references for enzymatic condensation reactions, prodiginine quantification, cytotoxicity screening, and were accessible in purities of up to 99.9% (quantitative NMR).



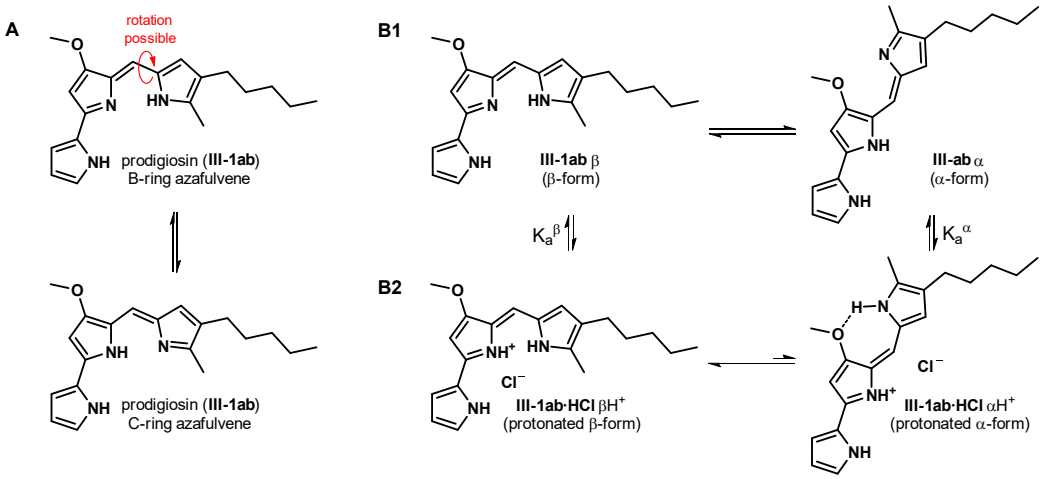
compd	R	R''	yield [%]	purity [%][a]
III-1ab·HCl	C_5H_{11}	H	68	n.d.
III-1bb·HCl	C_5H_{11}	CH_3	82	89.5
III-1cb·HCl	C_5H_{11}	C_2H_5	80	94.6
III-1db·HCl	C_5H_{11}	C_3H_7	58	99.5
III-1eb·HCl	C_5H_{11}	C_4H_9	73	99.8
III-1fb·HCl	C_5H_{11}	C_5H_{11}	47	99.9
III-1gb·HCl	C_5H_{11}	C_6H_{13}	48	99.3
III-1ba·HCl	C_3H_7	CH_3	66	95.7
III-1bc·HCl	C_7H_{15}	CH_3	80	87.3

R = C_3H_7 (**a**), C_5H_{11} (**b**), C_7H_{15} (**c**)
R'' = H (**a**), CH_3 (**b**), C_2H_5 (**c**), C_3H_7 (**d**), C_4H_9 (**e**), C_5H_{11} (**f**), C_6H_{13} (**g**)

Scheme III.35. Final biomimetic coupling reaction of 5'-alkylated MBC derivatives and monopyrroles to gain access to A-ring alkylated prodigiosin derivatives. [a] Determined by qNMR with triphenylmethane as secondary standard.

III.3.2.4 Influence of Prodigiosin A-Ring Alkylation on Absorption and Molar Extinction Coefficients

Prodiginines are well-known to display strong and characteristic light absorption, greatly varying with pH and solvent composition.[468] Hence, consistent conditions are crucial when analysing the spectral properties of prodiginines to ensure unconfined comparability of the collected data. To fulfil this prerequisite, extinction coefficients and absorption spectra of prodiginines are typically recorded in acidified ethanol in which the purple pigment prodigiosin **III-1ab** is uniformly protonated and exhibits a defined absorption maximum at 535 nm.[468, 469] The respective extinction coefficients at the wavelength of maximum absorption can then be used in turn for the quantification of prodiginines. The molecular cause for the strong effect of pH changes on the spectral properties of the prodiginine scaffold is the basic alkaloid scaffold and its high proton affinity. When hydrochloric acid or any other Brønsted acid is added, the basic prodiginine scaffold traps the Lewis-acidic proton between the three heterocyclic nitrogen atoms of the pyrrolic cores and prohibits rotation of the C-ring pyrrole along the azafulvene axis. The very tight and lipophilic HCl complex formed through this trapping mechanism is known as the β-form of prodigiosin and is the more stable rotamer compared to the twisted α-form (Scheme III.36).[342]



Scheme III.36. Interconvertible rotamers of prodigiosin. The tripyrrolic azafulvene of prodigiosin allows equilibria between two tautomers (B-ring and C-ring azafulvene, **A**) and four interconvertible rotamers (**B**), of which two rotamers describe the deprotonated (**B1**) and two others the protonated state (**B2**). When protonated, the equilibrium is fully shifted towards the more stable β-form in which the small Lewis-acidic proton is tightly trapped between the Lewis-basic nitrogen atoms. This circumstance is exploited for the quantification of prodigiosin through absorption spectroscopy. Interconversion between the protonated and deprotonated forms is described by acid dissociation constants K_a as indicated within the scheme. Rate constants for the interconversion of α- and β-forms are not explicitly mentioned. Figure inspired by Rizzo *et al*. and Melvin *et al*.[342, 400]

As both forms display different absorption properties, the addition of HCl completely shifts the equilibrium towards the β-form, allowing for the reliable quantification of protonated prodiginines from complex mixtures by absorption spectroscopy.[342]

By adding a 5-*n*-alkyl substitution to the prodiginine A-ring, the absorption maximum in acidified EtOH was shifted from 535 nm for the prodigiosin parent compound to 545–547 nm for the alkylated derivatives, resulting in a noticeable colour change from pink to purple in solution. With a constant pentyl substitution on the C-ring, variation in A-ring substitution greatly enhanced the molar extinction coefficient with increasing chain length, based on the inductive electron-donating effect of the attached alkyl substituents (Figure III.4A).

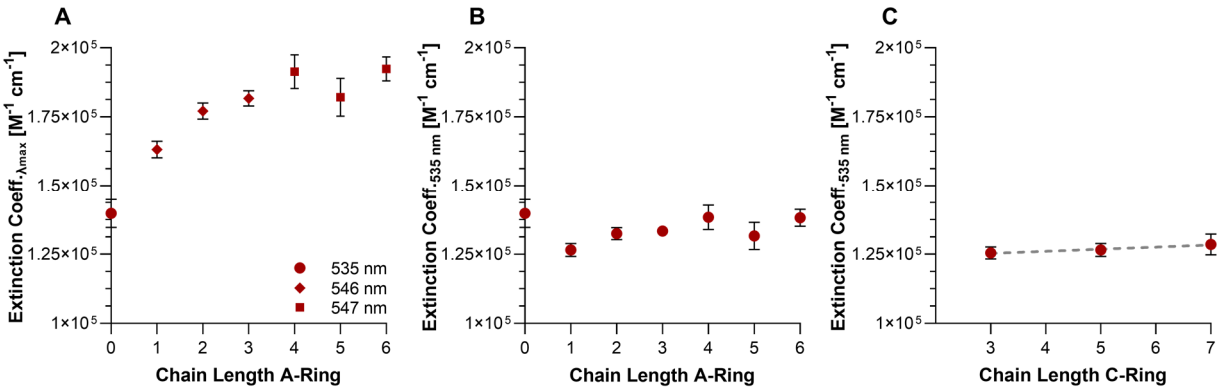
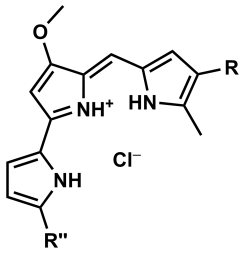


Figure III.4. Molar extinction coefficients of chemically synthesised prodiginines **III-1ab**–**III-1gb·HCl** in acidic ethanol (n=3). **A**. Molar extinction coefficients at the wavelength of maximum absorption in relation to the A-ring substitution with constant pentyl substitution on the C-ring. Varying symbols indicate the determined absorption maximum. **B**. Molar extinction coefficients in relation to the A-ring substitution at 535 nm with constant pentyl substitution on the C-ring. **C**. Molar extinction coefficients of the methyl-substituted A-ring derivatives **III-1ba·HCl**, **III-1bb·HCl**, and **III-1bc·HCl** at 535 nm in dependence on C-ring substitution. Linear regression (R^2=0.970) was applied to determine the slope and allow approximation of extinction coefficients for prodiginines, which had not been synthesised by chemical means.

For prodigiosin (**III-1ab·HCl**), a molar extinction coefficient of 139,800 M^{-1} cm^{-1} (535 nm) has been reported in the literature.[469] The A-ring methyl-derivative (**III-1bb·HCl**), however, exhibited an extinction coefficient of 163,233 M^{-1} cm^{-1} (546 nm), followed by the ethyl and propyl derivative with 177,092 M^{-1} cm^{-1} (**III-1cb·HCl**, 546 nm) and 181,692 M^{-1} cm^{-1} (**III-1db·HCl**, 546 nm), respectively (Table III.6). From butyl to hexyl substitutions **III-1eb**–**gb·HCl**, no significant increase of absorption was observed and the molar extinction coefficients seemed to reach a plateau around 190,000 M^{-1} cm^{-1} at 547 nm (Figure III.4A). Interestingly, molar extinction coefficients at 535 nm ranged from 126,508 M^{-1} cm^{-1} to 138,200 M^{-1} cm^{-1} for all tested derivatives, showing less chain length-dependent impact on extinction coefficients and solely fluctuations in the magnitude of standard deviations (Figure III.4B), making 535 nm an ideal wavelength for UV-Vis-based quantification of these prodiginines.

With a uniform methyl substitution on the A-ring and variation in C-ring chain length, a linear correlation between the alkyl chain length and the experimental molar extinction coefficients was observable at 535 nm for the three prodiginines **III-1ba·HCl**, **III-1bb·HCl**, and **III-1bc·HCl** (Figure III.4C, for equation V.5 see experimental section). Hence, it was assumed that the slope of the applied regression curve for the linear correlation of C-ring chain length and extinction coefficients would behave similarly with increasing chain length on the A-ring. By assuming the transferability of this linear correlation to other prodiginines with altered chain length on the A-ring, it was possible to approximate molar extinction coefficients for every A-ring alkyl substitution in combination with C-ring-substituted propyl and heptyl pyrroles (Table III.6).

Table III.6. Experimentally determined (ε) and mathematically approximated molar extinction coefficients (ε*) of A-ring alkylated prodiginines.



Experimentally Determined Molar Extinction Coefficients (ε)[a]					
Prodiginine	**Substitution A-Ring (R'')**	**Substitution C-Ring (R)**	**ε_{535} [M^{-1} cm^{-1}]**	**$\varepsilon_{\lambda max}$ [M^{-1} cm^{-1}]**	**λ_{max} [nm]**
III-1bb·HCl	methyl	pentyl	126508 ± 2380	163533 ± 3040	546
III-1cb·HCl	ethyl	pentyl	132425 ± 2211	177092 ± 2960	546
III-1db·HCl	propyl	pentyl	133375 ± 1200	181692 ± 2797	546
III-1eb·HCl	butyl	pentyl	138350 ± 4432	191400 ± 6105	547
III-1fb·HCl	pentyl	pentyl	131608 ± 4950	182125 ± 6805	547
III-1gb·HCl	hexyl	pentyl	138200 ± 3071	192358 ± 4337	547
III-1ba·HCl	methyl	propyl	125450 ± 2176	160358 ± 2707	545
III-1bc·HCl	methyl	heptyl	128500 ± 3815	166267 ± 48048	545
Approximated Molar Extinction Coefficients (ε*)[b]					
Prodiginine	**Substitution A-Ring (R'')**	**Substitution C-Ring (R)**	**ε^*_{535} [M^{-1} cm^{-1}]**		
III-1aa·HCl	H	propyl	138275		
III-1ac·HCl	H	heptyl	141325		
III-1ba·HCl	ethyl	propyl	130900		
III-1bc·HCl	ethyl	heptyl	133950		
III-1ca·HCl	propyl	propyl	131850		
III-1cc·HCl	propyl	heptyl	134900		
III-1ea·HCl	butyl	propyl	136825		
III-1ec·HCl	butyl	heptyl	139875		
III-1fa·HCl	pentyl	propyl	130083		
III-1fc·HCl	pentyl	heptyl	133133		
III-1ga·HCl	hexyl	propyl	136675		
III-1gc·HCl	hexyl	heptyl	139725		

[a] Experimentally determined extinction coefficients of chemically synthesised prodiginines **III-1bb–bc** at 535 nm and at the respective absorption maximum in acidic ethanol with standard errors are given (n=3).

[b] Approximated molar extinction coefficients at 535 nm in acidic ethanol for not synthesised prodiginines are summarised. *The calculation is based on the equation $\varepsilon^*_{535}(n) = 762.5\ M^{-1}\ cm^{-1} \cdot n + 123007\ M^{-1}\ cm^{-1}$, with n = A-ring chain length.

The experimental basis for this approximation was the experimental coefficients for the pentyl-substituted prodiginines with varying A-ring substituents and the slope of linear regression for the methyl-substituted prodiginines with a uniform A-ring and a variable C-ring alkylation. With the approximated extinction coefficients (Table III.6), it was possible to quantify even enzymatically produced prodiginines, whose references had not been synthesised by chemical means.

III.3.2.5 Prodigiosin Ligase Substrate Scope for A-Ring Alkylated MBC

Although structural information on prodigiosin ligases is a scarce good, mechanistic information has been deduced from kinetic experiments or from amino acid sequence homologies to well-characterised protein families.[274, 283, 291-293] The limited structural knowledge of prodiginine ligases, such as PigC or its recently discovered homologues TreaP and TamQ from *Pseudoalteromonadaceae*,[295] has prompted experimental probing of the enzymes' catalytic pockets. Substrate promiscuity of prodigiosin ligases has been demonstrated not only for linear alkylated prodigiosin C-ring monopyrrole precursors but also for carbocyclic derivatives, paving the way for the exploration of sustainable microbial mutasynthesis for prodigiosin production and derivatisation.[301, 302] However, little is known about the promiscuity of these enzymes regarding the structural diversity of the MBC building block. Chawrai *et al.* showed that prodigiosin derivatives with alternative aromatic A-rings are accepted by the ligase PigC from *S. marcescens*. Enzymatic activity was still present when the A-ring pyrrole moiety was either substituted by 2-phenyl-, 2-thienyl-, 2-furyl-, or 2-indolyl-residues. No activity was seen for naphthyl and biphenyl substitution instead,[286] indicating reduced acceptance of bipyrrole substrates with increasing steric demand of the aromatic A-ring. Furthermore, SAR studies from the past have not denoted adverse effects on Cu-mediated DNA hydrolysis, which stems from an electron-donating 5-ethyl substitution on the prodigiosin A-ring, while an electron-withdrawing acetylation had a severe negative impact on nuclease activity.[311] The limited knowledge on an extended substrate scope of prodiginine ligases for the bipyrrole precursor MBC prompted us to systematically investigate 5'-*n*-alkylated MBC derivatives in-depth. Based on previous SAR studies, the prodiginine reaction products with an alkylation in the 5-position of the A-ring might exhibit interesting properties related to the cytotoxicity of the tripyrrole alkaloid.

In our experiment, the three ligases PigC, TreaP, and TamQ were tested for their substrate acceptance of A-ring-substituted alkyl derivatives **III-14b**–**g** of MBC and MBC **III-14a** itself, as well as in a combination with monopyrroles with a varying chain length. Unusual for this experimental setup in comparison to earlier studies on prodiginine ligases is the two-dimensional testing, varying MBC derivatives and monopyrroles at the same time (Figure III.5). Previous studies reported that purification of membrane-associated PigC in a soluble and active form poses a major challenge,[293] why the most common setup for these biocatalytic conversions towards prodiginines exploits cell lysates after prior enzyme expression of prodiginine ligases.[295, 301, 391] Hence, *E. coli* cell lysate after expression of the corresponding prodigiosin ligase genes *pigC*, *tamQ*, and *treaP* from a pET28a(+) expression vector was used in this work rather than purified enzymes. Additionally, the cell lysate of *E. coli* harbouring the pET28a(+) empty vector was used as a negative control. To compare the enzymes and their substrate conversion with each other, the extracted prodiginines were quantified through LC-MS measurements with the corresponding extinction coefficients, which had been determined experimentally or by approximation (*vide supra*). It is emphasised that the quantification of these extracted prodiginines was normalised to the amount of cells, not to the amount of enzyme used in the experiment. Thus, differences in expression levels for the analysed ligases might have an additional impact on absolute prodiginine titres but should not affect the relative acceptance of A-ring-substituted MBC derivatives for each individual enzyme (Figure III.6).

Firstly, it was validated whether prodiginines can be formed from cellular metabolites in the presence of condensing enzymes. Therefore, enzyme-containing lysates were supplemented with ATP, but monopyrroles **III-15a**–**c** or MBC **III-14a** were not added to the reactions. LC-MS analyses with monitoring at 535 nm, at which wavelength prodigiosin exhibits its characteristic absorption, revealed no absorption at 535 nm and confirmed that no condensation reaction took place (Chapter IX.18, Figure IX.15–IX.18, Supporting Information). Hence, it was shown that all four components, namely ligating enzymes, ATP, monopyrroles, and MBC, are needed for biocatalytic prodigiosin synthesis *in vitro*. Secondly, it was investigated whether a background condensation reaction between ATP, monopyrroles, and MBC derivatives is readily catalysed in a catalyst-free environment. The absence of the characteristic prodiginine absorption at 535 nm in coupled LC-MS analyses again revealed that no spontaneous background reaction takes place (Chapter IX.18, Figure IX.19–IX.24, Supporting Information). Hence, the prodiginine ligating enzymes are needed for the condensation reaction to be catalysed.

After confirming the need for all four reaction components (ligase, ATP, MBC, and pyrrole) being present for successful biocatalytic *in vitro* synthesis of prodiginines, the focus was directed to characterising the substrate promiscuity of the prodiginine ligating enzymes PigC, TreaP, and TamQ for the 5'-alkylated MBC derivatives **III-14a**–**g** and the monopyrroles **III-15a**–**c**. The best characterised and most prominent prodiginine ligase PigC, originating from *S. marcescens*, showed high acceptance of methyl-substituted and unsubstituted MBC (**III-14b** and **III-14a**) in combination with the short-chain monopyrrole **III-15a**. In this context, the natural precursor MBC **III-14a** turned out to be the favoured bipyrrole, yielding 25.9 mg/L versus 16.7 mg/L for methyl-MBC **III-14b** in the reaction extracts (Figure III.5 for graphical representation of the substrate scope, Figure III.6 for quantification). Other MBC derivatives were not converted to the related prodiginines in noteworthy amounts. In contrast, the ligase TamQ, which is naturally involved in tambjamine biosynthesis, converted all shorter derivatives of MBC, including butyl-MBC **III-14e**, but not pentyl- and hexyl-MBC **III-14g** and **III-14g**. Here, the obtained product titres of prodiginines derived from short-chain MBC derivatives **III-14a**, **III-14b**, and **III-14c** were rather similar, ranging from 10–12 mg/L. The acceptance of MBC derivatives for the ligase TreaP was limited to C0–C3-substituted MBC **III-14a**–**d** and resulted in considerably lower titres (<3.6 mg/L) than for PigC or TamQ. However, TreaP showed the highest relative product concentrations for the ethyl-substituted MBC **III-14c**. With an increasing chain length of the monopyrrole precursor, all enzymes appeared to possess greater substrate promiscuity and conversions. For both, the medium- and long-chain monopyrroles **III-15b** and **III-15c**, respectively, the MBC substrate spectrum for PigC was expanded to propyl-MBC **III-14d** but also to higher prodiginine titres. In combination with the medium-chain monopyrrole precursor MAP **III-15b**, unsubstituted MBC **III-14a** was converted best of all tested MBC derivatives with a titre of 25.7 mg/L. However, with the long-chain monopyrrole precursor **III-15c**, the non-natural methyl-MBC derivative **III-14b** was identified as the best-performing MBC substrate for condensation, providing the related product in a titre of 32.8 mg/L. Supported by previous findings regarding the enzymes TamQ and TreaP,[295] both biocatalysts preferentially converted long-chain monopyrroles to the corresponding prodiginines, with TamQ in total exhibiting the broadest acceptance of 5'-alkyl-substituted MBC derivatives. Even though MBC **III-14a** is the common prodiginine and tambjamine precursor in nature for all three enzymes under investigation, TreaP and TamQ shared a similar trend of MBC derivative promiscuity for the medium-chain monopyrrole **III-15b**, showing the highest product titres for ethyl-MBC **III-14c** with 5.1 mg/L and 16.8 mg/L, respectively. The long-chain monopyrrole **III-15c** was best accepted in combination with methyl-MBC **III-14b** by PigC, providing the highest prodiginine product titre of 32.8 mg/L in this experiment.

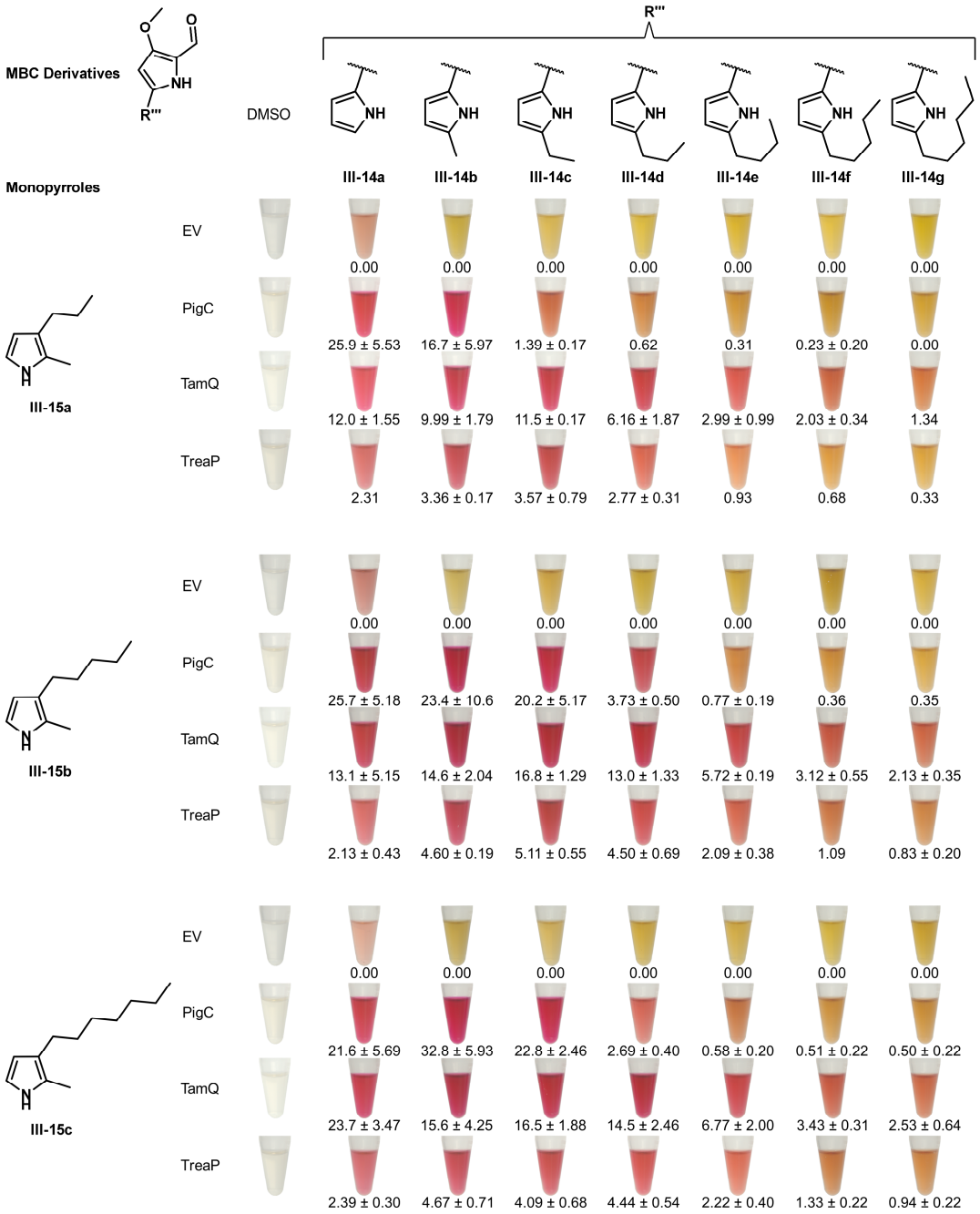


Figure III.5. Visual representation of the two-dimensional substrate spectrum of the prodiginine ligases PigC, TamQ, and TreaP for combinations of 2,3-alkylated monopyrroles **III-15a**–**c**, unsubstituted MBC **III-14a**, and 5'-*n*-alkylated MBC derivatives **III-14b**–**g**. Cell lysates of *E. coli* BL21 with corresponding ligases in KP_i buffer were treated with pyrroles (1 mM), MBC (1 mM), and ATP (1.25 mM) and incubated at 30 °C for 4 h. Cell lysate of *E. coli* BL21 pET28a(+) was used as a negative control. A red colouration of the solutions indicates the formation of products. Photographic records were employed to document the organic extracts in acidic ethanol. Product titres (mg/L) were determined by LC-MS measurements, based on experimental and approximated molar extinction coefficients, and the product titre mean values and respective standard errors of triplicate samples are given below the corresponding tubes. Abbreviations: EV – empty vector. LC-MS traces of negative controls can be found in the Supporting Information (Chapter IX.18) and LC-MS traces of all other reactions shown in this figure can be found in the Supporting Information of the publication Weber *et al.*, *Catal. Sci. Technol.* **2023**, *13*, 6165–6184, DOI 10.1039/D3CY00913K.

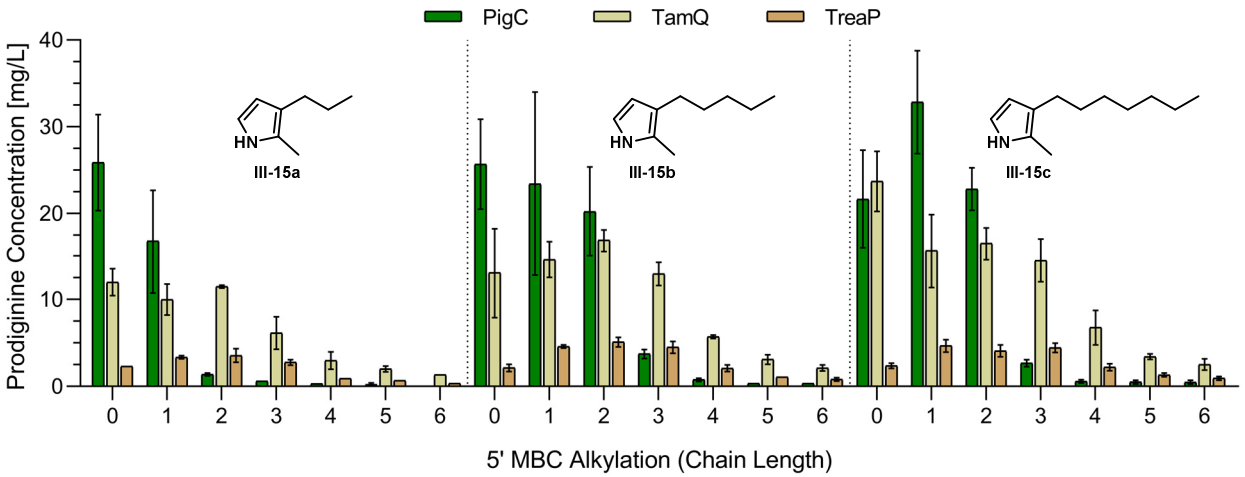


Figure III.6. Quantification of prodiginines from *in vitro* reactions with the prodiginine ligases PigC, TamQ, and TreaP with varying chain lengths on the A- and C-ring. Methanolic extracts of biocatalytic reactions between monopyrroles **III-15a**–**c** and 5'-*n*-alkyl MBC derivatives **III-14a**–**g** were subjected to coupled LC-MS measurements and the amount of substance quantified from the corresponding UV absorption at 535 nm and the prodiginine extinction coefficients (n=3). The chain length of alkylated MBC is depicted on the x-axis of the bar diagram. The used monopyrrole is shown in the diagram. Since all values for the empty vector control were zero, the data is not shown, but the plotted raw data can be found in the Supporting Information (Figure IX.4).

Among the group of tested prodiginine ligase enzymes, PigC was, in fact, the least promiscuous enzyme, as demonstrated by tight restraints in terms of tolerating alkyl substitution on the MBC part. In contrast, TamQ was identified as the most profitable catalyst for substitutions on the monopyrrole and the A-ring of MBC. It is hypothesised that multiple reasons contribute to the observed acceptance pattern of combinations for monopyrroles and MBC. As the monopyrrole serves as nucleophile in the proposed mechanism (devised for PigC), reviewed by Hu *et al.*,[274] it is hypothesised that shorter chain length may result in higher degrees of freedom and flexibility of side chains and less tight binding of the pyrrole core within the enzyme's active site pocket, potentially leading to depleted reaction rates. In addition, short-chain pyrroles are lacking additional activation, which is contributed by the electron-donating effect of alkyl chains. For the alkyl chain variation on MBC derivatives, steric reasons are assumed as the principal force behind the lack of conversion with an increased number of methylene groups within the alkyl chain. Electronic contributions are judged rather implausible, as the condensation chemistry between monopyrrole and MBC is taking place at the distal part of the MBC derivatives, namely the carbaldehyde. Moreover, the disclosed data may also shed light on a potential explanation for the biosynthesis of the only non-macrocyclic A-ring-substituted prodigiosin derivative, which has been found in nature, namely 2-(*p*-hydroxybenzyl)prodigiosin (**III-9**) from *P. rubra*.[304] Although the biosynthesis pathway of this compound has not been elucidated yet, the broad substrate tolerance for 5'-alkylated MBC derivatives of TamQ and TreaP, which both originate from other strains of the *Pseudoalteromonadaceae* family, might hint towards a coupling reaction between a 5-(*p*-hydroxylated) MBC analogue and the monopyrrole MAP **III-15b**. However, this putative precursor of the biosynthesis has not been reported so far, which is why this option remains speculative.

Given the experimental evidence that the condensing enzymes PigC, TreaP, and TamQ accept not only a wide variety of substituted monopyrroles but also alkylated MBC derivatives *in vitro*, the transfer of this knowledge into a sustainable *in vivo* mutasynthesis approach will be a challenging task. The current mutasynthesis strain *P. putida* KT2440 pig-r2 Δ*pigD* carries an incomplete prodigiosin biosynthesis *pig* gene cluster from *S. marcescens*, incapable of generating the monopyrrole precursor MAP but functional in MBC biosynthesis.[301]

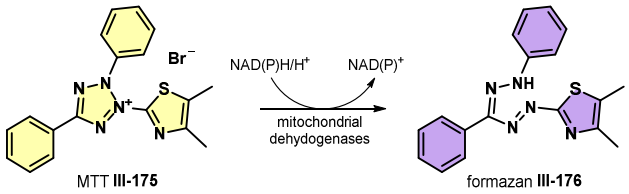
Supplementation with chemically synthesised derivatives of the C-ring monopyrrole enables sustainable and environmentally friendly synthesis of prodigiosin C-ring derivatives, as no chemical synthesis of the expensive MBC bipyrrole precursor is needed. However, free diffusion of the externally added monopyrrole across the bacterial membrane is a prerequisite for an intracellular condensation of MBC and monopyrrole to generate prodiginines. Equivalent safe-to-handle *P. putida* strains, either having the capability of synthesising MBC derivatives on their own or lacking a functional enzymatic cascade to synthesise the natural precursor MBC, have neither been generated nor reported so far. Furthermore, MBC is by far less water-soluble than the monopyrroles and unhindered membrane diffusion of externally spiked MBC derivatives is likely to be prohibited. Equivalent experimentation with the mutants BMJ816 (MBC-deficient, Δ*pigE*) and AMJ817 (MAP-deficient, *ΔpigMN*) of the opportunistic human pathogen *S. marcescens* suggested membrane diffusion of both precursors, MBC and MAP.[470] Although this result is a motivating glimmer of hope, the pathogeny of *S. marcescens* does not allow industrial use on large scale. Moreover, the Gram-negative bacterium *P. putida* exhibits a very low permeability membrane similar to *Pseudomonas aeruginosa*, which is up to 100 times less permeable than the membrane of *E. coli*.[471] This decreased membrane permeability is also the reason why *P. putida* is such a well-fitting strain for the mutasynthesis of the highly cytotoxic prodigiosin scaffold, and why *Pseudomonas aeruginosa* is resistant to treatment with prodigiosin.[469, 472] Therefore, it remains unclear whether the broadened substrate scope of prodigiosin ligases has any practical use other than probing the prodiginine ligases' active site experimentally. In fact, the last step condensation reaction between MBC derivatives and substituted monopyrroles can be catalysed by the inexpensive bulk chemical hydrochloric acid on a large scale in recyclable organic solvent. As the chemical synthesis is neither restricted to active site geometry nor to enzyme promiscuity, but also omits the need for enzyme preparation and complicated product separation from bacterial cells and metabolites, chemical preparation of A-ring-substituted prodiginines is the most practical approach so far.

III.3.2.6 Anticancer Activity of Prodigiosin Azides and A-Ring Alkylated Prodiginines

To assess the impact of substitution patterns on anticancer properties of chemically synthesised prodigiosin azides (cf. Chapter III.3.1) and A-ring alkylated prodiginines (cf. Chapter III.3.2), the urothelial carcinoma cell lines RT-112 (cisplatin-sensitive) and RT-112res (cisplatin-resistant) were selected for a small SAR study in cooperation with the Institute of Molecular Medicine I (HHU Düsseldorf).[473-475] Cisplatin-based therapy is the standard of care for this kind of carcinoma; however, miscellaneous mechanisms are involved in emerging resistance to cisplatin, such as autophagy and apoptosis.[473, 476-479] For this reason, alternative highly potent chemotherapeutics will be needed to treat these cell lines, which have developed resistance mechanisms against this treatment for urothelial cancer. For the compound class of the prodiginine family, several immunomodulating effects have been reported on a micromolar to nanomolar concentration scale.[480] Since the discovery of anticancer activity of prodigiosin and prodigiosin-like pigments, dozens of its derivatives have been tested in numerous studies against more than 60 human cell lines with an average IC_{50} value of 2.1 µg/mL.[481] However, as untargeted passive membrane diffusion and an associated uncoupling of membrane potentials are apparently the main contributions to the observed high cytotoxicity, no derivatives have been developed and pushed beyond an aborted phase II clinical trial.[260-262, 303] While the systematic evaluation of A-ring alkylation of prodiginines **III-1ba**–**gb·HCl** might help to understand the influence of particular substitutions on cytotoxicity, the clickable prodigiosin azides **III-89·HCl**, **III-90·HCl**, and **III-91·HCl** have the potential to overcome the untargeted mode of action for the tripyrrole pigments by the preparation of biological conjugates for cell-specific delivery and drug import.

In this regard, cell viability of the cell lines RT-112 and RT-112res was determined for dilution series of prodiginine derivatives through the colorimetric MTT [3-(4,5-dimethylthiazol-2-yl)-2,5-diphenyltetrazolium bromide] assay.[482]

The working principle of the assay makes use of enzyme-coupled formation of a purple dye, which reflects the cell's metabolic activity. Particularly, eukaryotic mitochondrial dehydrogenases can reduce the soluble and membrane-permeable yellow tetrazolium MTT salt **III-175** under the formation of the insoluble purple formazan pigment **III-176** (Scheme III.37). The latter can be solubilised with polar protic or aprotic solvents, such as EtOH or DMSO, respectively, and is detectable at a distinctive wavelength of 590 nm. While dead cells or cells with a low metabolic turnover produce no to little amount of the formazan pigment, high metabolic activity leads to pronounced accumulation of the coloured reporter pigment. Thus, the dye concentration reflects the number of living cells or the fitness of a defined number of cells within an ensemble of cells and can be used to evaluate cytotoxicity parameters of toxic cellular metabolites or (small-molecule) drugs against eukaryotic cell lines.[483]



Scheme III.37. Conversion of MTT **III-175** to the purple dye formazan **III-176** by mitochondrial dehydrogenases to report on the viability of eukaryotic cells.

Hence, azide-harbouring prodigiosin derivatives with azide substitution in the A-, B-, or C-ring and 5-*n*-alkylated prodiginines with substitutions on the A-ring were analysed for their anticancer activity on RT-112 cell lines via the MTT assay. Prodigiosin (**III-1ab·HCl**) has been shown to display cytotoxic activity at nanomolar concentrations against both cisplatin-sensitive and resistant cell lines and was thus judged as a potential drug candidate for the treatment of cisplatin-resistant urothelial carcinomas.[463] Prodigiosin (**III-1ab·HCl**) and the former phase II clinical candidate obatoclax mesylate **III-55·Mes** were selected as both positive controls and benchmark compounds.[260-262, 303] To assess the impact of substitutions on prodiginine derivatives, the two RT-112 cell lines were subjected to cell viability monitoring after 24 h and 72 h exposure to prodiginines and the formazan concentration was determined by spectroscopic measurements. Cell viability, displayed by absorption of the formed formazan, was plotted against the prodigiosin concentration for each data point and a dose-response fit applied to provide the IC_{50} value as a quantifiable parameter of cytotoxicity for every tested compound (data and dose-response fits in the Supporting Information, Chapter IX.4 and IX.5). In this connection, the half-maximal inhibitory concentration (IC_{50}) represents the concentration of the cytotoxic agent, at which exactly 50% of the treated cells survive. For the lead compound prodigiosin (**III-1ab·HCl**), an IC_{50} of 675 nM and 157 nM were traced after 24 h and were further reduced to 73.8 nM and 41.1 nM after 72 h for RT-112 and RT-112res, respectively (Figure III.7). In contrast, obatoclax mesylate **III-55·Mes** exhibited relatively low cytotoxic activity in RT-112 cells after 24 h of incubation. With 3.33 µM against RT-112 and 184 nM against RT-112res after 24 h, obatoclax was acting similarly to the least cytotoxic long-chain derivatives **III-1eb**–**gb·HCl**. With increased incubation time of 72 h, improved cytotoxicity with IC_{50} values of 172 nM (RT-112) and 36.0 nM (RT-112res) was achieved. Thus, obatoclax proved to be significantly less effective against RT-112 than prodigiosin (**III-1ab·HCl**) and showed similar efficacy against RT-112res.

In the following, prodiginines that originated from chemical synthesis were investigated for their cytotoxic effects against the RT-112 cell lines. First, the focus was set to those prodiginines with an altered A-ring alkyl substitution but a constant pentyl substitution on the C-ring. The addition of a single electron-donating methyl group in prodiginine **III-1bb·HCl** resulted in a substantial increase in cytotoxicity against both cell lines. With a final IC_{50} of 26.4 nM for RT-112 and 18.8 nM for RT-112res after 72 h, an up to 2.8-fold increase in cytotoxicity was observed. However, IC_{50} values after 24 h initially resembled the cytotoxicity of prodigiosin (**III-1ab·HCl**) itself. Interestingly,

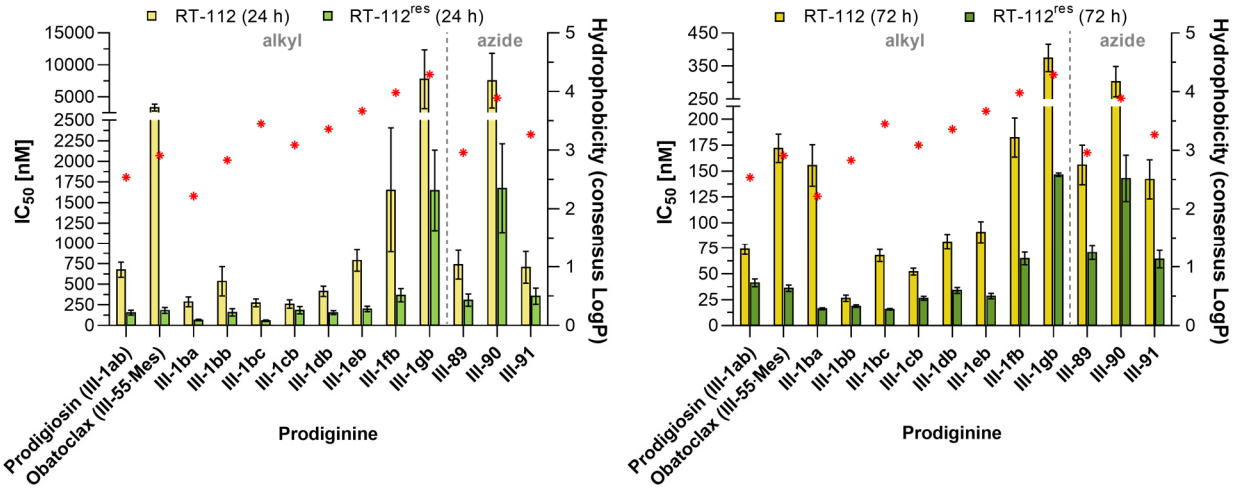


Figure III.7. Cell viability of urothelial cancer cell lines RT-112 (cisplatin-sensitive) and RT-112res (cisplatin-resistant) in the presence of prodigiosin (**III-1ab·HCl**), obatoclax mesylate (**III-55·Mes**), and chemically synthesised A-ring alkylated prodiginines (**III-1ba**–**gb·HCl**) and the prodigiosin A-, B-, and C-ring azides (**III-89·HCl**, **III-90·HCl**, and **III-91·HCl**) after 24 h (left) and 72 h (right). Cell survival was analysed using the MTT assay (n=3). Error bars represent the 95% confidence interval. Plotted raw data and dose-response fits for the determination of IC_{50} values can be found in the Supporting Information. The data for this plot were generated and provided by Lena Berning (Institute of Molecular Medicine I, Heinrich Heine University Düsseldorf). Predicted hydrophobicity/lipophilicity data (consensus LogP), provided by the SwissADME web tool, are indicated as red asterisks and plotted on the second y-axis.

further chain elongation on the A-ring of prodiginines **III-1cb**–**gb·HCl** led to a constant loss of biological activity with each step of elongation. Especially the transition from pentyl to hexyl substitution on the A-ring displayed a turning point in cytotoxicity and was accompanied by a significant loss of biological activity, independent of the cell line and time point of analysis. Aside from the effect of A-ring substitution with an invariable C-ring substitution pattern of compounds **III-1bb**–**gb·HCl**, the most cytotoxic methyl-substituted prodiginine **III-1bb·HCl** was chosen as a starting point for scrutinising which effect a substitution in the 4-position of the C-ring chain towards longer or shorter alkyl residues might have. All analysed prodiginines (**III-1ba·HCl**, **III-1bb·HCl**, and **III-1bc·HCl**) with methyl substitution on the A-ring appeared to have unspoiled high cytotoxicity against the cisplatin-resistant subtype RT-112res after 72 h when the C-ring was modulated. With IC_{50} values ranging between 15.7 nM (**III-1bc·HCl**) and 18.8 nM (**III-1bb·HCl**), the impact was rather negligible. Nonetheless, the tested derivatives were shown to act differently after 24 h, as prodiginine **III-1bb·HCl** with a C5-chain on the C-ring revealed lower inhibitory concentrations against both cell lines than observed for derivatives **III-1ba·HCl** and **III-1bc·HCl**. Summarising the presented data of anticancer activity for the 5-alkylated prodiginines, an additional methyl group in the 5-position of the A-ring boosted the cytotoxicity against both cisplatin-sensitive and resistant urothelial carcinoma cell lines. In addition to this increased performance, prodiginine **III-1bb·HCl** was found to display the highest cytotoxicity against both cell lines after 72 h (RT-112: 26.4 nM, RT-112res: 18.8 nM). Concurrently, prodiginines **III-1ba·HCl** and **III-1bc·HCl** were outstandingly fast in unleashing their cytotoxic potential, having substantial improvements of toxicity after 24 h in comparison to derivative **III-1bb·HCl**, the parent compound prodigiosin (**III-1ab·HCl**) and the former phase II clinical candidate obatoclax mesylate. The tripyrrole core structure of prodigiosin (**III-1ab·HCl**) and its substituted clinical relative obatoclax is well-known to inhibit the cellular process of autophagy,[301, 463, 484, 485] which is essential to recycle or degrade cell organelles or anomalous proteins (misfolded, aggregated, or damaged).[463] At the same time, prodigiosin (**III-1ab·HCl**) was shown to induce apoptosis, an ensemble of signalling pathways of programmed cell death.[464, 486, 487] In the past, the mechanistic cause for autophagy inhibition and induction of apoptosis in prodigiosin-treated cancer cell lines was

attributed to the capability of H^+/Cl^- symport across the membranes of lysosomes or other eukaryotic cell compartments and the cell cycle arrest.[328-330, 488]

The ion pair of protonated prodigiosin and the chloride counter ion is lipophilic and tight enough to diffuse across the membrane.[258, 259] However, this proton affinity is likely influenced by the electron density of the aromatic system, which can be modulated through the introduction of electron-donating or electron-withdrawing substituents into the prodiginine scaffold. Hence, a possible explanation for the increased cytotoxicity of prodiginines with short-chain electron-donating alkyl substituents on the A-ring could be a tighter bond between the B-ring nitrogen atom and the proton from the hydrochloride complex, increasing the pK_a value and facilitating the trespass of the charged prodiginine·H^+/Cl^- complex through the membrane. Although longer alkyl chains show even stronger electron donation, they also result in a more lipophilic character for the resulting prodiginine (cf. Figure III.7), raising the risk of functioning as a membrane anchor and attaching derivatives to the membrane. This would impede their diffusion across the membrane and thereby reduce the cytotoxic potential. In fact, the presented results regarding increased prodiginine cytotoxicity for short alkyl A-ring substitutions and a decrease in cytotoxicity with increasing chain length are in agreement with earlier studies on alkyl substitution on the C-ring, where short-chain propyl substitution was characterised by drastically stronger autophagy inhibition than for the long-chain octyl variant.[301]

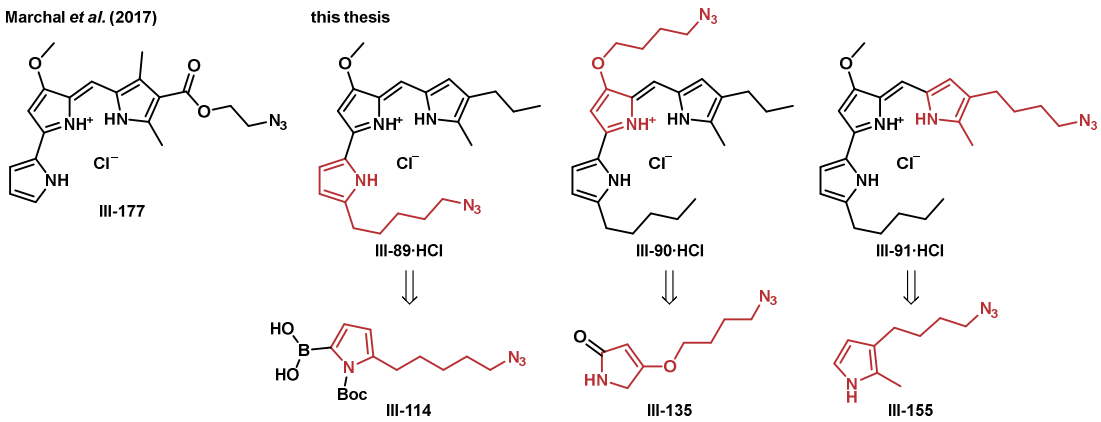
Shifting the focus from the alkyl to the azide-substituted prodiginines **III-89·HCl**, **III-90·HCl**, and **III-91·HCl**, having azide substituents on the A-, B-, or C-ring of the prodigiosin scaffold, a similar trend was observed, resembling the diminished cytotoxicity of prodiginines with a long alkyl chain on the A-ring. After 24 hours of incubation, the IC_{50} values of A-ring and C-ring azide **III-89·HCl** and **III-91·HCl** against cisplatin-sensitive RT-112 cells were 736 nM and 703 nM, respectively, comparable to that of prodigiosin **III-1ab·HCl** (675 nM). In contrast, the B-ring azide **III-90·HCl** was significantly less toxic, with an IC_{50} of 7.52 µM. After 72 hours of incubation, all derivatives showed lower IC_{50} values, indicating increased cytotoxicity. The A-ring and C-ring azides **III-89·HCl** and **III-91·HCl** displayed IC_{50} values of 156 nM and 142 nM, respectively, being approximately half as toxic as prodigiosin **III-1ab·HCl** (74 nM), while the B-ring azide **III-90·HCl** was four times less toxic (303 nM) than the parent natural product. As seen before, the cisplatin-resistant cell line RT-112^{res} showed increased receptiveness and sensitivity to prodigiosin treatment compared to the cisplatin-sensitive urothelial cancer cell line RT-112. Although after 24 h all prodigiosin azides showed a gain in cytotoxicity against RT-112^{res} compared to RT-112, the parent compound prodigiosin was, with an IC_{50} value of 157 nM, the most toxic alkaloid among the tested prodigiosin azides. Cytotoxicity of the prodigiosin A-ring and C-ring azide **III-89·HCl** and **III-91·HCl** was reduced to 308 nM and 353 nM, respectively, meaning a 2-fold decrease compared to prodigiosin. The B-ring azide **III-90·HCl** was again 10-fold less toxic (1.68 µM) than the benchmark compound prodigiosin. Prolonged incubation time of 72 h culminated in IC_{50} values of 41 nM for prodigiosin and slightly elevated values for A-ring (70 nM) and C-ring (64 nM). Nevertheless, the prodigiosin B-ring azide **III-90·HCl** was the least toxic derivative (143 nM) in the ensemble of tested azides. Respecting the data from the systematic analysis of alkyl substitutions on the A-ring, it is inferred that the loss of activity of all three organic azides **III-89·HCl**, **III-90·HCl**, and **III-91·HCl** can be attributed to the consistent pentyl or azido-pentyl substitution on the A-ring, which has been proven to negatively impact the cytotoxicity against both bladder cancer cell lines. Moreover, the B-ring methoxy group of prodigiosin is known to be essential for anticancer activity.[265, 310] The displacement of the latter with longer alkoxy substituents led to a significant decrease in anticancer activity and cytotoxicity in comparison to undecylprodigiosin (ethoxy: 1.82-fold, propoxy: 3.04-fold, butoxy: 14.3-fold),[310] which can be confirmed from the results of this work. Concurrently, the datasets for prodigiosin azides guide the future design of prodigiosin azides, if these are specifically developed and designed as anticancer agents for target-specific delivery to cancerous tissue, as attempted by our

trastuzumab-prodigiosin conjugates (cf. Chapter III.3.1.4.3). Firstly, the presented data of this study suggest that the B-ring should remain unmodified and the methoxy group of prodigiosin retained. Secondly, the A- and C-ring azide attachment also showed a negative impact on cytotoxicity, but far less drastic than for the B-ring azide. Hence, both positions for azide substitution proved to be disadvantageous for evolving the prodiginines towards better antitumoral activity. Nonetheless, since the study on A-ring alkylated prodiginines attests a drastic drop in cytotoxicity with elongated substitution on the A-ring, future modifications for the attachment of drug carrier molecules should concentrate on the C-ring. Prodigiosin C-ring azide modifications were previously connected to moderate cytotoxicity in estrogen conjugates, targeting estrogen receptor-positive breast cancer cell lines.[369] Combining these findings with the study on alkylated A-ring substitutions, the introduction of a small methyl substitution in the 5-position of the A-ring might be an effective adjusting screw to gain an extra increase in cytotoxicity compared to A-ring unsubstituted derivatives.

Finally, the presented data on anticancer activity of A-ring alkylated prodiginines and prodigiosin azides can also be used to shed light on the lacking cytotoxicity of the previously described and tested trastuzumab antibody-drug conjugates with prodigiosin warheads (cf. Chapter III.3.1.4.3). The antitumoral activities against cisplatin-sensitive and -resistant cell lines were determined for the soluble prodigiosin azides **III-89·HCl**, **III-90·HCl**, and **III-91·HCl** in the described experiment (cf. Figure III.7). However, to generate ADCs between these azide-functionalised prodiginines and the monoclonal antibody trastuzumab, the three alkaloids were further modified with the bifunctional maleimide linker **III-159**. Based on the made observations regarding the negative influence of long-chain alkyl and azide modifications on anticancer activity of the alkaloid scaffold, the attachment of the non-cleavable maleimide linker is very likely to reduce the IC_{50} values and the antitumoral potency in comparison to prodigiosin even further. Since the trastuzumab-prodigiosin conjugates were only tested to a maximum concentration of 10 nM over an incubation period of 72 h, even thorough release of the four prodiginine warheads from a single conjugate molecule would result in a maximal intracellular drug concentration of 40 nM. As this concentration lies far below the IC_{50} value of 141 nM for the most toxic soluble prodigiosin C-ring azide **III-91·HCl** against cell line RT-112 after 72 h, the prodiginine concentrations at which the alkaloid becomes toxic are never reached for the prodigiosin-functionalised ADCs. Hence, it becomes quite apparent why no killing activity was observed for the trastuzumab-prodigiosin antibody-drug conjugates. Besides optimisations of linker architecture and the installation of a cleavable linker design, future improvements on the alkaloid scaffold must address the tuning of anticancer activity to subnanomolar concentrations to transform the multipotent family of prodiginines into useful warheads for future (antibody-)drug conjugates.

III.4 Summary Chapter II.5.4 – Chemoenzymatic and Total Synthesis of Prodigiosin Alkaloids

A significant portion of this work involved functionalisation of the highly potent cytotoxic tripyrrole scaffold of prodiginines through chemical synthesis. With the formulated objective of introducing reactive organic azides into the prodiginine scaffold, enabling further functionalisation via copper-click chemistry and a potential long-term application as conjugable drug candidates, the incorporation of aliphatic azides into all three rings (A-, B-, and C-ring) of the natural product was set as a synthetic goal. Conjugation of prodiginines to suitable carrier molecules, facilitating selective delivery and cellular uptake of these conjugates, was considered a promising strategy for enhancing the target selectivity of prodiginines, whose natural mechanism of action via passive membrane diffusion allows minimal differentiation between various cell types and is the major cause for a lack of target selectivity. Based on the work of Marchal and Figliola,[369] whose synthetic sequence permits azide functionalisation exclusively on the prodigiosin C-ring with a non-natural substitution pattern (cf. prodiginine **III-177**), this thesis identified azide-functionalised key intermediates via retrosynthetic analyses for the A-, B-, and C-ring azide-incorporation into the prodiginine scaffold for the first time. This retrosynthetic analysis provided three essential synthons, namely the azide-substituted pyrrole-2-boronic acid **III-114** (A-ring azide), the *O*-alkylated tetramic acid derivative **III-135** (B-ring azide), and the substituted 1*H*-pyrrole **III-155** (C-ring azide) (Scheme III.38).

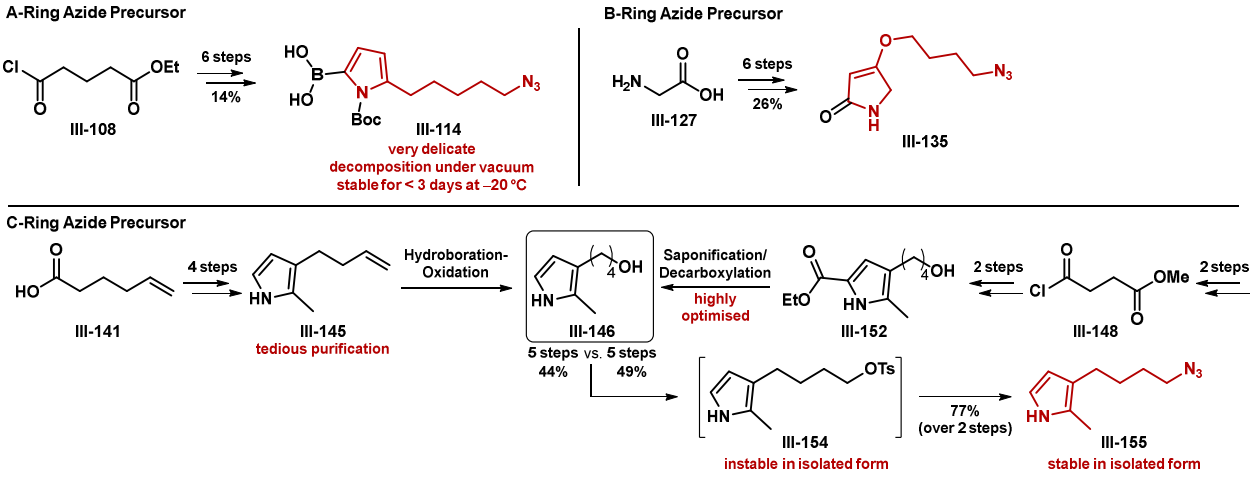


Scheme III.38. Targeted azide-functionalised prodiginines in this work and their corresponding azide-containing synthons identified via retrosynthetic analyses.

Among the key transformations for introducing the azide moiety into the prodiginine scaffold, the Suzuki-Miyaura cross-coupling reaction was found to be ideal to equip the A-ring of prodiginine **III-89** with the organic azide. Consequently, the Boc-protected, azide-functionalised pyrrole-2-boronic acid **III-114** was identified as the immediate reactive precursor. This precursor was synthesised through a six-step process starting from the ethyl ester of acid chloride **III-108** (Scheme III.39, cf. Chapter III.3.1.1). Optimisation of the reaction parameters for the one-step reduction of the acyl group and ethyl ester in the 2-acylated pyrrole **III-109** identified glyme and $LiAlH_4$ as the optimal solvent-reductant pair, maximising the yield of formed alcohol **III-101** due to minimised formation of the undesired elimination side product **III-110**. Subsequent synthetic transformations, involving *O*-tosylation, Boc-protection, and azide substitution, yielded the respective intermediates **III-111**, **III-112**, and **III-113** on a multigram scale with good to excellent yields. All intermediates **III-111**, **III-112**, and **III-113** are synthetically appealing, as they allow for a general 2-functionalisation of pyrroles and their further derivatisation through SN_2 reactions with other reactive nucleophiles. The azide-functionalised pyrrole-2-boronic acid **III-114** as azide-harbouring A-ring synthon proved inherently unstable, decomposing within less than three days at –20 °C or immediately under vacuum. This instability was attributed to a potential polymerisation reaction of the boronic

acids with nitrogen release, observed exclusively in azide-functionalised but not alkylated boronic acids. Ultimately, with boronic acid **III-114** an azide-functionalised boronic acid derived from the inherently unstable pyrrole-2-boronic acids was synthesised, isolated, and fully characterised for the first time (cf. Chapter III.3.1.1.3).

The B-ring of prodiginines originating from chemical syntheses is typically not derived from 1*H*-pyrroles. Instead, the B-ring is built from related non-aromatic tetramic acids (Scheme III.39, cf. Chapter III.3.1.2). The *N*-Boc-protected tetramic acid **III-126**, as a synthon for the introduction of the azide motif into the prodiginine B-ring, was synthesised via a three-step sequence from the inexpensive amino acid glycine with an overall yield of 61%. Subsequent *O*-alkylation of tetramic acid **III-126** with 4-azido-1-butanol **III-132** via a Mitsunobu reaction using DEAD as the coupling reagent proved effective. Following enol ether **III-134** formation, Boc-deprotection with TFA yielded the azide-functionalised tetramic acid **III-135** in six steps with an overall yield of 26% (cf. Chapter III.3.1.2.1).

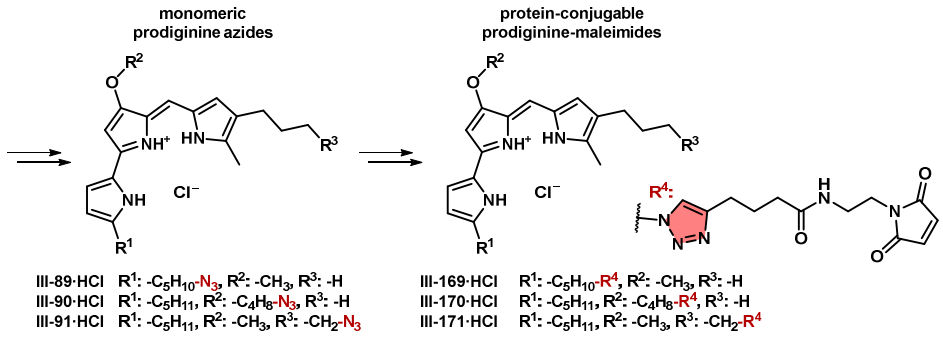


Scheme III.39. Reaction schemes, summarising the synthesis of azide-functionalised A-, B-, and C-ring precursors of azide-harbouring prodiginines.

For synthesising the precursor of the C-ring azide (cf. Chapter III.3.1.3), two routes converging at the terminal alcohol **III-146** were explored (Scheme III.39). A sequence involving a Trofimov pyrrole synthesis and hydroboration/oxidation of alkene **III-145** to terminal alcohol **III-146** revealed that the laborious purification of alkene **III-145** was a limiting factor for yield, resource efficiency, and reaction upscaling. An alternative approach devised in this work to access the hydroxylated pyrrole **III-146** involved the selective acylation of commercially available ethyl 5-methyl-1*H*-pyrrole-2-carboxylate (**III-147**) with the methyl ester of acid chloride **III-148** at the sterically less hindered 4-position of the pyrrole. While the acid chloride was prepared in two steps from succinic anhydride in this study, the route could be shortened using commercially available acylating reagents. Similar to the one-step $LiAlH_4$ reduction of pyrrole **III-109** under reflux conditions, reduction using $NaBH_4$ and boron trifluoride etherate achieved one-step reduction of the acyl group and aliphatic ester. This reaction approach has significant advantages over the more reactive $LiAlH_4$, as $NaBH_4/BF_3{\cdot}Et_2O$ operates at room temperature, offering a milder alternative to highly reactive aluminium hydrides. Due to the diminished reducing power of the formed diborane, the conjugated carbonyl at the 2-position of the heteroaromatic ring remained intact, necessitating further saponification and decarboxylation to yield alcohol **III-146** as a precursor to azide **III-155**. Avoiding competing polymerisation reactions during decarboxylation at temperatures of 180 °C was crucial, as these drastically reduced isolated yields. By reducing the exposure of pyrrole to oxygen and temperatures above 130 °C, the reaction sequence was optimised to achieve yields of up to 77%. Subsequent tosylation yielded an unstable

intermediate **III-154** that could not be isolated in pure form. Instead, in situ reaction with sodium azide provided the desired azide-functionalised C-ring precursor **III-155** in an overall yield of 38% over seven steps.

In line with modern syntheses for constructing the tripyrrole prodiginine scaffold, the synthesis of prodiginine azides was achieved through a central palladium-catalysed Suzuki-Miyaura cross-coupling reaction. The widely used $Pd(PPh_3)_4$ precatalyst was excluded due to the relatively high temperatures (100–110 °C) required for its activation, which are incompatible with the thermal instability of organic azides. To address this limitation, a ligand screening was conducted using Buchwald ligands SPhos **III-122**, XPhos **III-123**, RuPhos **III-124**, as well as dppf **III-121** and $Pd(PPh_3)_4$ (cf. Chapter III.3.1.1.4). This screening revealed that the highest yields under mild reaction conditions (60 °C) were obtained with SPhos **III-122**. For instance, the Pd/SPhos-catalysed reaction between Boc-pyrrole-2-boronic acid (**III-76**) and the aromatic triflate **III-96** produced the alkylated prodiginine **III-1aa·HCl** with an excellent yield of 84%. Under these optimised conditions, azide-functionalised prodiginines were isolated with yields ranging from 46% to 64% (Scheme III.40). Overall, three azide-functionalised prodiginines **III-89·HCl**, **III-90·HCl**, and **III-91·HCl** were synthesised through 12–15 steps with overall yields of up to 4.6%. In summary, this work provides the first systematic library of prodiginines with incorporated azide moiety in all three rings of the tripyrrolic core, eligible for coupling to terminal or strained alkynes via CuAAC or SPAAC, respectively. Furthermore, exemplary CuAAC reactions between the prodiginine azides and a bifunctional alkyne-maleimide linker **III-159** were exploited to introduce a bioconjugable and cysteine-reactive maleimide group into the corresponding prodiginines (cf. Chapter III.3.1.4.2). The copper ligand TDETA **II-44**, introduced in Chapter II, was successfully employed in this step, yielding excellent and reproducible results with yields between 74% and 80% for the maleimide-functionalised prodiginines **III-169**, **III-170**, and **III-171**. The A-, B-, and C-ring functionalised set of prodiginines presented in this chapter is not only the first holistic ensemble of prodiginine azides but also the first ensemble of protein-conjugable prodiginines ever synthesised.

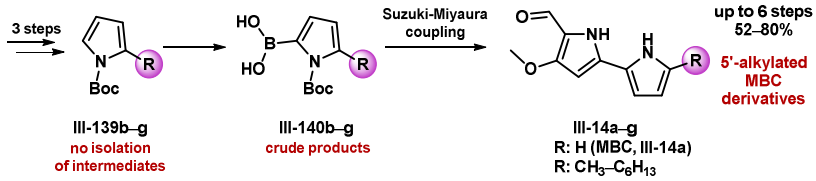


Scheme III.40. Synthesised bioconjugable prodiginine-maleimides with A-, B-, and C-ring attached thiol-reactive maleimides. The triazole moiety formed in the CuAAC reaction between azide and alkyne is highlighted in orange.

The maleimide approach to site-selective protein modification using prodiginines, by exploiting the thiol-Michael reaction between cysteine-containing proteins and novel prodiginine maleimides, was ultimately employed to generate antibody-prodiginine conjugates to attempt selective delivery of prodiginines to HER2-positive cancer cells and increase their target specificity (cf. Chapter III.3.1.4.3). By using the tetra-cysteine mutant NEJ4 of the HER2-targeting trastuzumab antibody in conjunction with the maleimide-functionalised prodiginines **III-169**, **III-170**, and **III-171**, three trastuzumab-prodigiosin ADCs were generated. When applied to the human cancer cell lines SK-BR-3 (HER2-positive) and A431 (HER2-negative), evidence was obtained for antibody binding to the HER2 receptor within the investigated concentration range (<10 nM). However, the investigated ADCs did not exhibit indications of prodiginine-mediated cytotoxicity. Nonetheless, the trastuzumab-prodiginine ADCs are the

first ever synthesised protein conjugates and ADCs of prodigiosin and most importantly showcase the straightforward applicability of the maleimide chemistry to conjugate prodiginines to any kind of protein covalently.

In the second part of this chapter, focusing on the natural product class of prodiginines, the previously optimised synthetic route for the SPhos-assisted heteroaryl coupling of A-ring-functionalised prodiginines was utilised to prepare new linearly 5'-alkylated MBC **III-14b–g** and prodigiosin **III-1ba–gb** derivatives (Chapter III.3.2). The alkylated MBC derivatives **III-14b–g** exhibit high structural similarity to the natural prodigiosin bipyrrole precursor MBC **III-14a** and are thus potential biomimetics of the natural building block in the final enzyme-catalysed condensation step of prodigiosin biosynthesis (Scheme III.41). Although representatives of these enzymes (PigC, TreaP, and TamQ) have been extensively studied with regard to their substrate promiscuity for the monopyrrole building block, there is only limited data available concerning the substrate promiscuity of the bipyrrole precursor MBC and structural analogues thereof.



Scheme III.41. Synthesis route of 5'-*n*-alkylated MBC derivatives as potential substrates for prodiginine ligases.

To address this knowledge gap and determine the spectrum of enzyme-convertible MBC mimetics, we first set out to access 5'-*n*-alkylated MBC derivatives through organic synthesis. Therefore, *n*-alkylated pyrrole-2-boronic acids **III-140b–g** were synthesised first, followed by oxidative Suzuki-Miyaura cross-coupling reactions with bromo enamine **III-75** (cf. Chapter III.3.2.2).

The alkylated boronic acids were synthesised in a preparative multi-step sequence. By using crude reaction products of sequence intermediates, we were able to reduce the practical effort of intermediate isolation and purification. Moreover, using crude boronic acids for the subsequent Suzuki-Miyaura cross-coupling also avoids the need to isolate the rather instable boronic acids. Under optimised conditions for the Suzuki-Miyaura reaction for the coupling of bromoenamine **III-75** and free pyrrole-2-boronic acids **III-140b–g** using a dual system of $Pd(OAc)_2$ and the ligand SPhos, mixtures of Boc-protected and deprotected MBC derivatives were obtained as reaction products. While the unsubstituted Boc-protected MBC **III-174** could be deprotected in a microwave-assisted reaction with trifluoroethanol, the *n*-alkylated derivatives of MBC exhibited very poor solubility in the fluorinated alcoholic solvent. Consequently, microwave irradiation not only led to low conversions but also caused significant boiling retardation during the reaction. Both factors severely negatively impacted the scalability of the deprotection reaction. For the *n*-alkylated MBC derivatives **III-14b–g**, these issues were circumvented by refluxing the intermediates in trifluoroethanol, allowing the mixtures of Boc-protected and partially deprotected heterocycles to be converted into fully deprotected bipyrrole building blocks **III-14b–g**. Due to their low solubility, a simple filtration and washing step was sufficient to isolate the desired products in reasonable purity. Using this scalable method, a total of six novel *n*-alkylated MBC derivatives were obtained in up to six steps, with good yields ranging from 52% to 80% for the final cross-coupling step. Therefore, the alkylated MBC building blocks are suitable not only for the chemical prodiginine synthesis, but also as potential biomimetic substrates for prodiginine ligases PigC, TreaP, and TamQ.

With the alkylated MBC derivatives **III-14b–g** in hand, the novel bipyrroles were subsequently employed for the experimental evaluation of the substrate scope of the bacterial prodiginine ligases (Figure III.8A, cf. Chapter III.3.2.5). The performed experiments demonstrated that these biocatalysts exhibit a previously unreported substrate scope with broad acceptance of alkylated bipyrroles **III-14b–g**. In particular, short-chain MBC derivatives were in some cases even more effectively converted than the natural MBC building block **III-14a** itself. Consistent with previous studies on the substrate spectrum for substituted 1*H*-monopyrroles, PigC showed a preference for short-chain MBC substitutions on the A-ring (–H and $-CH_3$), while the two enzymes TreaP and TamQ from tambjamine biosynthesis clusters achieved excellent conversions with medium-chain ethyl and propyl substitutions (–H to $-C_3H_7$). Although a lack of crystal structures of prodiginine ligases impedes in-depth investigations and computational analyses attempting to explain the observed substrate scope on a structural level, the new findings presented in this work suggest a highly promiscuous behaviour of these enzymes for both building blocks of the ATP-catalysed condensation reaction to prodigiosin, namely the monopyrrole and the bipyrrole precursor.

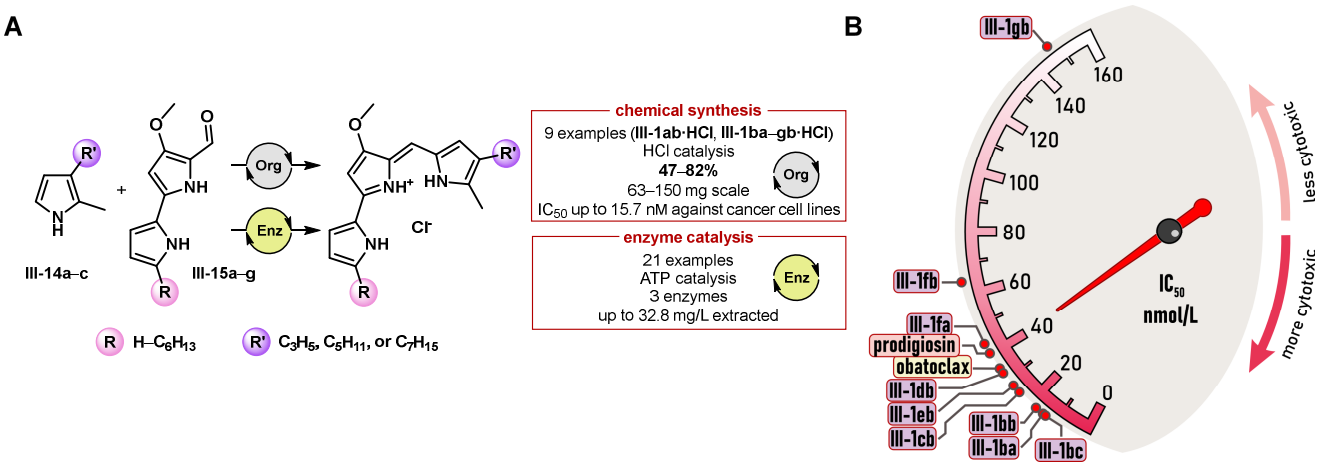


Figure III.8. A. Chemoenzymatic synthesis of A-ring-alkylated prodiginines from novel 5'-alkylated MBC analogues via HCl-catalysis or catalysed by bacterial prodiginine ligases. **B**. IC_{50} values (nanomolar) against the cisplatin-resistant urothelial cancer cell line RT-112res after a 72 h incubation period. Lower IC_{50} values (dark red gradient) represent higher cytotoxicity of the corresponding compounds.

In contrast to the biocatalytic production of A-ring-alkylated prodiginines defining the explored broadened substrate scope of prodiginine ligases, the preparative HCl-catalysed chemical synthesis yielded eight new prodiginines **III-1ab–gb·HCl** with alkylation at the 5-position of the prodiginine A-ring in yields ranging from 47–82% (cf. Chapter III.3.2.3). Based on the high cytotoxicity of prodigiosin **III-1ab** against malignant tumour cell lines, the cytotoxic potential of the novel 5-akylated prodiginines was assessed by cell viability screenings with cisplatin-sensitive and -resistant urothelial cancer cell lines RT-112 and RT-112res, respectively (cf. Chapter III.3.2.6). The novel prodiginines **III-1bb·HCl** and **III-1cb·HCl** with short methyl and ethyl chains in the 5-position of the A-ring demonstrated enhanced cytotoxicity against both cell lines compared to the natural product prodigiosin **III-1ab·HCl** and the former clinical candidate obatoclax mesylate **III-55·Mes** (Figure III.8B). The most potent inhibitory effect after 72 hours of incubation was observed for the methyl-substituted derivative **III-1bb·HCl**, whose cytotoxicity at low nanomolar concentrations (26.4 nM for RT-112 and 18.8 nM for RT-112res) represents a more than 2.8-fold increase in cytotoxic effect compared to prodigiosin **III-1ab·HCl**. In contrast, extending the alkyl chain beyond butyl negatively impacted cytotoxicity, likely resulting from impaired membrane diffusion of the charged HCl-complex due to altered membrane partitioning. While long-chain alkyl substitutions universally reduce cytotoxicity, A-ring derivatives with short-chain alkyl substitutions are promising lead structures for

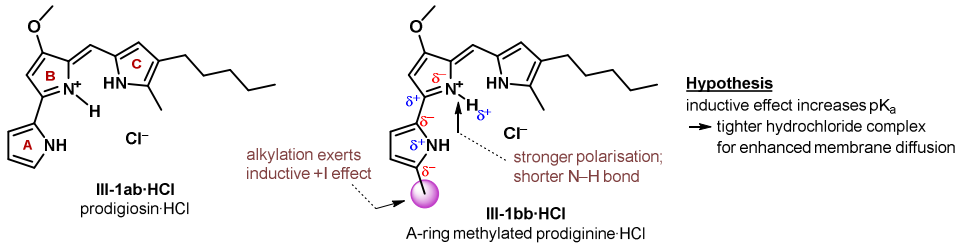
optimising pharmacologically relevant parameters in the future. Together, the presented cytotoxicity data of A-ring-alkylated prodiginines against urothelial cancer cell lines highlight the strong influence of A-ring substitutions on anticancer activity of prodiginines and particularly demonstrate the high potential of short alkyl-substituted derivatives as anti-tumour agents for carcinomas, which have developed resistance to the standard cisplatin-based therapy.

III.5 Outlook Chapter II.5.4

The findings presented in Chapter II.5.4 of this work have laid a strong foundation in advancing prodiginine alkaloids for target-specific applications of the bioactive scaffold based on conjugate chemistry. By devising synthetic strategies for introducing reactive azide moieties into prodigiosin's A-, B-, and C-ring, the first complete set of prodiginine azides was accessed by total synthesis. Functionalisation with a dual-reactive alkyne-maleimide linker in a CuAAC reaction finally rendered maleimide-functionalised prodiginines, suitable for the labelling of cysteine-carrying proteins or other thiol-modified molecules. This methodology lastly enabled the first synthesis of prodiginine-labelled proteins, including conjugates with the therapeutic monoclonal antibody trastuzumab and the antimicrobial protein pyocin S2. Together with improved anticancer activity of A-ring alkylated prodiginines with short alkyl substituents, the presented data set a direction for future optimisation of the bioactive prodiginine core. By combining short alkyl substituents on the A-ring with cleavable linker design and conjugation to drug carrier molecules for selective cellular uptake, we might overcome the lack of target selectivity of prodiginines. Modified prodiginines with optimised targeting strategies and improved biocompatibility may represent promising candidates for the future treatment of cisplatin-resistant cancer cell lines. The following chapter highlights open research questions and future perspectives of bioactive and conjugable prodiginines and their application as target-selective drugs.

III.5.1 Link Between pK_a and Cytotoxicity of Prodiginines

The systematic investigation of aliphatic substituent effects of the prodigiosin A-ring on the cytotoxicity against cisplatin-resistant and -sensitive bladder cancer cell lines had revealed a significant increase in cytotoxicity (up to 2.8-fold after 72 h) for small alkyl substituents (e.g. -methyl **III-1bb**, -ethyl **III-1cb**) in the 5-position of the A-ring in comparison to A-ring unfunctionalised prodigiosin (**III-1ab**). Longer alkyl chains instead (e.g. -pentyl **III-1fb**, -hexyl **III-1gb**) had converse effects and resulted in drastically decreased cytotoxicity. A common feature shared by all A-ring alkylated prodiginines is the basic tripyrrolic scaffold with high proton affinity. When protonated, the basicity of prodiginine alkaloids is responsible for forming tight lipophilic complexes with chloride counter ions that are tight enough to penetrate and diffuse across biological membranes.[258, 259] It was earlier hypothesised in this thesis that the increased cytotoxic activity of alkylated prodiginines with short substitution might be linked to the electron-donating effect of the substituents and their putative impact on the pK_a of the prodiginine scaffold. In the conjugated pyrrolic system, the higher electron density on the A-ring would donate additional negative charge to the protonated B-ring nitrogen and stabilise the positive charge in the protonated prodiginine-HCl complex. Consequently, the nitrogen becomes more basic and the N–H bond becomes tighter (Scheme III.43). Hence, the pK_a value of the nitrogen increases and the trespass of the charged complex through the membrane is facilitated. Besides impacting the basicity of the alkaloid scaffold, longer alkyl substituents on the A-ring also increase the lipophilicity of the natural product. Therefore, it is hypothesised that decreased cytotoxic values of those prodiginine derivatives with long aliphatic chains on the A-ring (e.g. **III-1fb** and **III-1gb**) may be explained by an increased risk of undesired anchoring of these prodiginines in the hydrophobic cell membrane, causing a less efficient passive diffusion across the membrane and reduced depletion of the proton gradient in comparison to prodigiosin **III-1ab**.

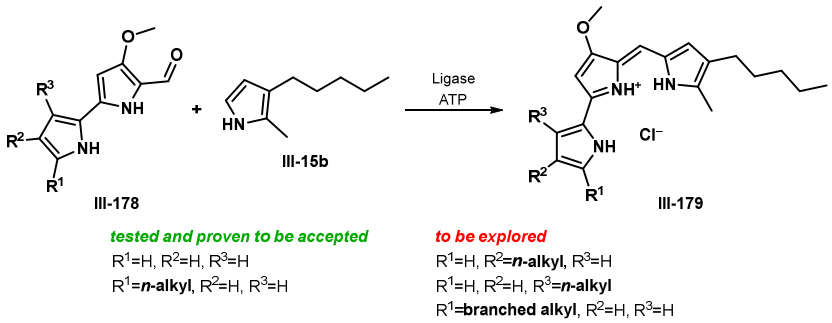


Scheme III.43. Electron-donating (inductive, +I) effect of prodigiosin A-ring alkyl substituents and their hypothetical impact on pK_a and the membrane diffusion of prodiginine-HCl complexes.

Previous studies, investigating the influence of alternative A-ring substituents (e.g. furyl, thiophenyl, nitrophenyl, among others) on prodiginine cytotoxicity against the HL-60 leukemia cancer cell line, did not show a clear correlation between cytotoxicity and pK_a of the analysed prodiginines.[400] However, instead of systematically investigating one type of A-ring substitution on the pyrrole moiety (e.g. alkyl), the study focused on substituting the whole A-ring pyrrole with other heteroaromatic moieties. Therefore, additional factors like electron distribution, membrane partitioning of respective prodiginines, and the overall ring size of the A-ring might interfere with the cytotoxic properties independent of the corresponding pK_a values. To disentangle superimposing effects, an independent analysis of pK_a values via UV-Vis titration according to Melvin *et al*. and an analysis of the N–H bond length through crystallographic analysis of prodigiosin (**III-1ab**) and the A-ring alkylated analogues **III-1ba–gb** should be performed in future studies.[400] To furthermore evaluate the second hypothesis regarding an incremental partitioning of prodiginines with long aliphatic substituents in the membrane, partitioning experiments with the prodiginine alkaloids in water/*n*-octanol or water/L-α-phosphatidylcholine dimyristoyl membrane vesicles should be performed in compliance with Gobas *et al*.[489] A systematic investigation of electron-donating aliphatic substituents at the 5-position of the prodiginine A-ring and their combined effects on cytotoxicity, pK_a, and lipophilicity may enable the formulation of clear design principles for future A-ring modifications to optimise the tripyrrolic core of the lead compound prodigiosin **III-1ab** and enhance cytotoxic potency of prodiginine alkaloids for therapeutic applications.

III.5.2 Extended Substrate Scope of Prodiginine Ligases and Proposed Synthesis of Alternative MBC Analogues

In this work, we demonstrated that the prodiginine ligases PigC, TreaP, and TamQ exhibit broad substrate tolerance towards 5'-*n*-alkylated MBC derivatives **III-14a–g**, thereby expanding and refining our current understanding of their substrate scope. Although the presented results have answered some questions regarding the acceptance of non-natural derivatives of the MBC building block, they also open up new directions and research questions for future investigations. For instance, can these prodiginine ligases also convert MBC derivatives with branched alkylation patterns and are 3'- and 4'-alkylated MBC derivatives **III-178** also viable substrates for these enzymes (Scheme III.44)? And if so, how would such structural substitutions influence the anticancer activity of the corresponding prodiginines **III-179**?



Scheme III.44. Comprehensive A-ring alkylation of the MBC building block and its eligibility for prodiginine biocatalysis. The tested prodigiosin ligases are PigC from *S. marcescens*, TamQ from *P. tunicata*, and TreaP from *P. citrea*. Branched alkyl substituents can be *iso*-Pr, *tert*-Bu, *sec*-Bu, for example.

In our proof-of-concept study on the promiscuity of prodiginine ligases for MBC precursor derivatives, we focused exclusively on 5'-alkylated MBC derivatives for a clear reason: their synthetic precursors – 2-alkylated, unprotected monopyrroles like the Boc-protected 2-methyl pyrrole **III-139b** (Scheme III.45A) – are relatively easy to synthesise. Moreover, borylation at the 5-position to form boronic acid **III-140b** is highly regioselective, as the position next to the nitrogen is both nucleophilic and acidic, resulting in minimal formation of undesired regioisomers. This regioselectivity of the borylation reaction is an essential prerequisite for gaining access to pure 5'-alkylated MBC species, as the regioisomers of the inherently delicate pyrrole boronic acids are not chromatographically stable and thereby not separable by means of chromatography.

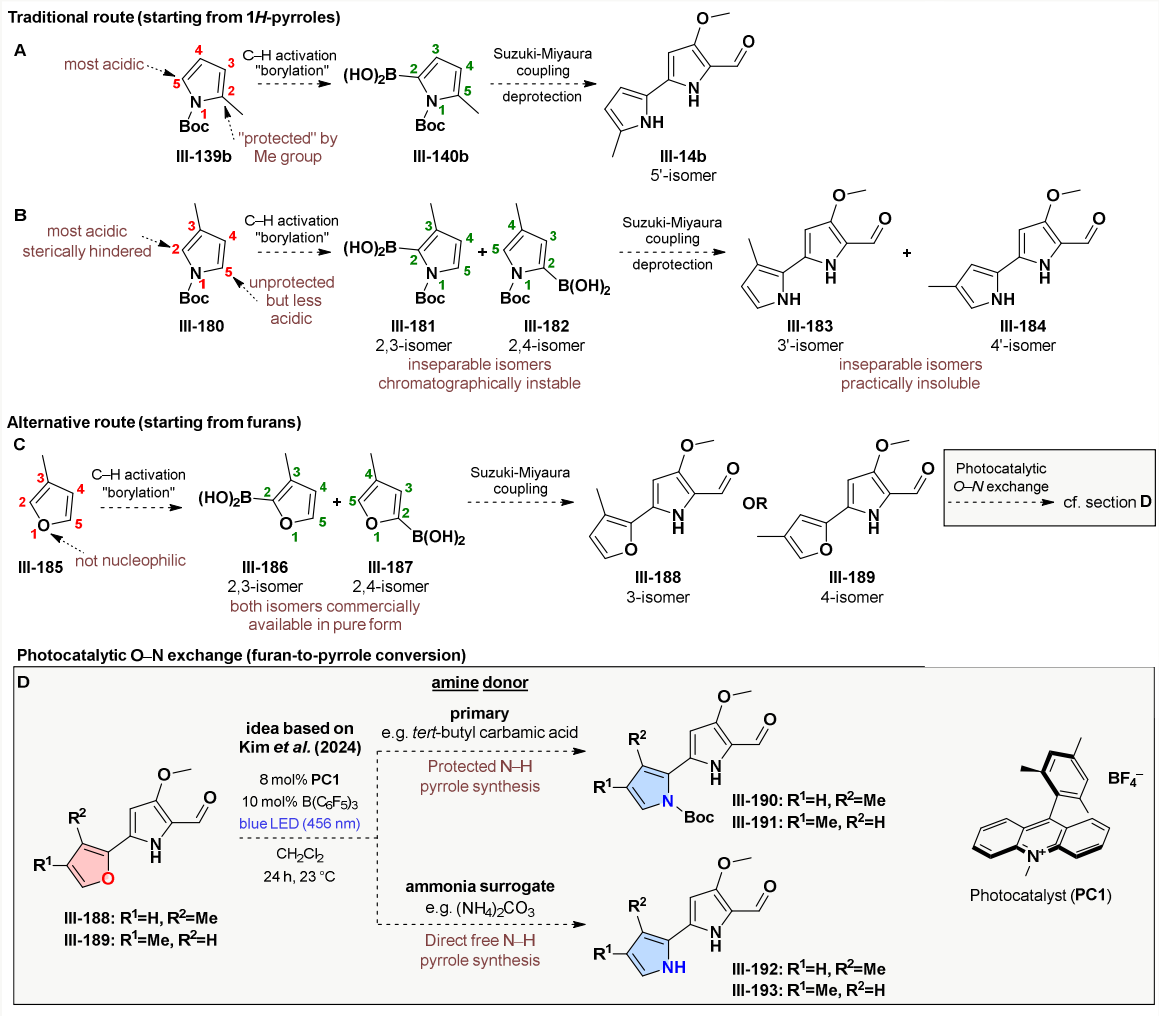
When turning the spotlight on 3-alkylated 1*H*-pyrroles **III-180** as synthetic precursors of currently unexplored 4'-alkylated MBC derivatives, many synthetic routes starting with a 3-alkylation of 1*H*-pyrrole suffer from low yields caused by the competing 2-alkylation, often requiring additional protecting group strategies to suppress this undesired side reaction. As the subsequent generation of boronic acids via the *ortho*-metalation and borylation sequence predominantly happens in the nitrogen-adjacent positions, inseparable 2,3- and 2,4-substituted regioisomers **III-181** and **III-182** are expected to be formed (Scheme III.45B). Furthermore, since the corresponding MBC derivatives are merely soluble in any organic solvent, the generated isomers **III-183** and **III-184** are likely to be inseparable, as 2-substituted boronic acids of pyrroles and pyridines are inherently instable and thus not stable towards chromatography.[402, 403]

With pyrroles and pyrrole-boronic acids being important building blocks in chemistry, several synthetic strategies have been deployed to substitute these delicate moieties in early steps of the synthesis sequence with more stable five-membered heterocycles, such as furans or thiophenes, improving the overall process and storage stability of intermediates. Both heteroarenes are considered eligible pyrrole substitutes, as they are less electron-rich than pyrroles yet exhibit similar reactivity. Furans, such as the methylated derivative **III-185**, are similarly reactive to pyrroles, but the central oxygen atom renders them less nucleophilic and prone to polymerisation, which is why furan-2-boronic acids possess drastically increased stability in comparison to pyrrole-2-boronic acids. Therefore, furan-2-boronic acids can be exploited to circumvent separability issues of pyrrole-2-boronic acid regioisomers. Although the borylation sequence starting from alkylated furans is identical in comparison to pyrroles, the 2,3- and 2,4-boronic acid isomers **III-186** and **III-187**, respectively, are commercially available in pure form (Scheme III.45C). This hints towards a higher stability of the furan-2-boronic acids **III-186** and **III-187** that allows their separation via chromatography or recrystallisation. By using these pure boronic acids, the Suzuki-Miyaura cross-coupling reaction would only provide one biaryl isomer **III-188** or **III-189**, depending on the utilised boronic acid isomers **III-186** or **III-187**. Nonetheless, furan-substituted MBC derivatives **III-188** and **III-189** as prodiginine precursors are only of limited interest, as prodiginines with A-ring furan substitution show drastically diminished cytotoxic activities in comparison to prodigiosin (e.g. antimalaria IC_{50}: >2920 nM vs. <8.0 nM,

respectively).[346] Consequently, synthetic procedures allowing for a late-stage furan-to-pyrrole exchange will be needed.

Just very recently, the group of Yoonsu Park reported on a photocatalytic furan-to-pyrrole conversion using blue light and photocatalysts.[490] Their work was predicated on early studies that could show furan-to-pyrrole exchange under extreme energy input (>450 °C, Hg lamp),[491, 492] and impressively highlights the capability of photochemistry. By combining the photocatalyst **PC1** and amine donors (numerous primary amines and ammonia surrogates), the authors exploited the three-step catalytic cycle of photoinduced electron transfer, radical C–N coupling and ring opening, and equilibrium and ring closure to generate a wide variety of unprotected and *N*-substituted pyrroles from their corresponding furans.

This versatile and efficient approach of photocatalytic O–N exchange could be used to convert the furan-containing biaryls **III-188** and **III-189** with methyl substitution in the 3- and 4-position into Boc-protected **III-190** and **III-191** or free MBC derivatives **III-192** and **III-193**, respectively (Scheme III.45D). While the exchange with *tert*-butyl carbamic acid as a primary amine donor would lead to the Boc-protected MBC analogues, ammonia surrogates, such as ammonium carbonate, would facilitate a direct free N–H pyrrole synthesis without the need for an additional deprotection step.



Scheme III.45. Challenges in preparing 3'- and 4'-alkylated MBC derivatives and an alternative synthesis route using furans in conjunction with a photocatalytic furan-to-pyrrole exchange. **A**. 5'-Alkylated MBC from 2-alkylated pyrroles. **B**. Inseparable 3'- and 4'-alkylated MBC derivatives from 3-alkylated pyrroles. **C**. Furan-containing MBC analogues from alkylated furans. **D**. Photocatalytic furan-to-pyrrole exchange to convert furan-containing MBC analogues into bipyrroles.[490]

Although the limited availability of commercially available alkylated furan-2-boronic acids would only allow the synthesis of 3'- and 4'-methyl MBC in the first place (Scheme III.45C), these building blocks would be sufficient to validate the acceptance of these substitution patterns as putative substrates of the prodiginine ligases. Furthermore, these novel alkylated bipyrrole building blocks can be used to chemically synthesise novel A-ring prodiginine derivatives and to evaluate the substitution effect on anticancer activity of these alkaloids. Thereby, we could devise future strategies to optimise the tripyrrole scaffold and maximise the cytotoxicity gain through chemical synthesis, advancing prodiginines to future therapeutics against cancer cell lines that have developed resistance against cisplatin treatment.

III.5.3 Target Fishing with Biotinylated Prodiginines

The cytotoxic activity of prodiginines involves different mechanisms and cellular targets, including lipid bilayer depolarisation,[329, 330, 488] DNA cleavage in complex with copper ions,[320] and inhibition of antiapoptotic proteins, ultimately leading to programmed cell death.[327, 485] Recently, the eukaryotic Golgi stacking protein GRASP55 was identified as a novel protein target of prodiginine alkaloids.[493] Although scientific endeavours aiming to identify all cellular targets of prodiginines have lasted for more than 30 years, it is very likely that even more unknown targets exist in eukaryotic and prokaryotic cells and organisms.

The azide-functionalised prodiginines **III-89·HCl**, **III-90·HCl**, and **III-91·HCl** or the readily biotinylated conjugate **III-172·HCl** can be used to identify all the targets of prodigiosin via structure-specific accumulation. For example, the biotinylated prodigiosin conjugate **III-172·HCl** can be used to capture covalent and non-covalent interaction partners of prodigiosin (e.g. proteins) by their co-enrichment with the probe on streptavidin-coated magnetic beads. Similarly, specific enrichment of prodiginines would be possible by clicking the novel prodiginine azides to alkynylated ligands (or surfaces) that facilitate the selective pull-down of prodiginines and their potential interaction partners in the target cell. Downstream analysis through coupled LC-MS analysis would then reveal putative binding partners and cellular targets of prodiginine alkaloids that may have remained unexplored in previous studies and experimental approaches, augmenting our understanding of prodigiosin's cytotoxic mechanisms and allowing for target-selective optimisation of its cytotoxic scaffold.

III.5.4 Prodiginine Conjugates with Cleavable Linkers and in Conjunction with Small-Molecule Carriers

The major mechanism contributing to the high cytotoxicity of prodiginines is their ability to passively diffuse across biological membranes and thereby deplete membrane potentials. However, biological membranes are essential to all living organisms, including eukaryotic cells and bacteria. Hence, despite the specific interaction of prodiginines with intracellular targets, such as Bcl-2 in eukaryotic cells, the passive uptake mechanism is responsible for the lack of target specificity of prodiginines, which cannot distinguish between cell types and different membranes. To address the lacking target specificity of prodiginines, owing to their unspecific diffusion across biological membranes, we were aiming to expand the group of conjugable prodiginines by organic synthesis, finally allowing for coupling of prodiginines to specificity-mediating vectors for highly selective cellular uptake.

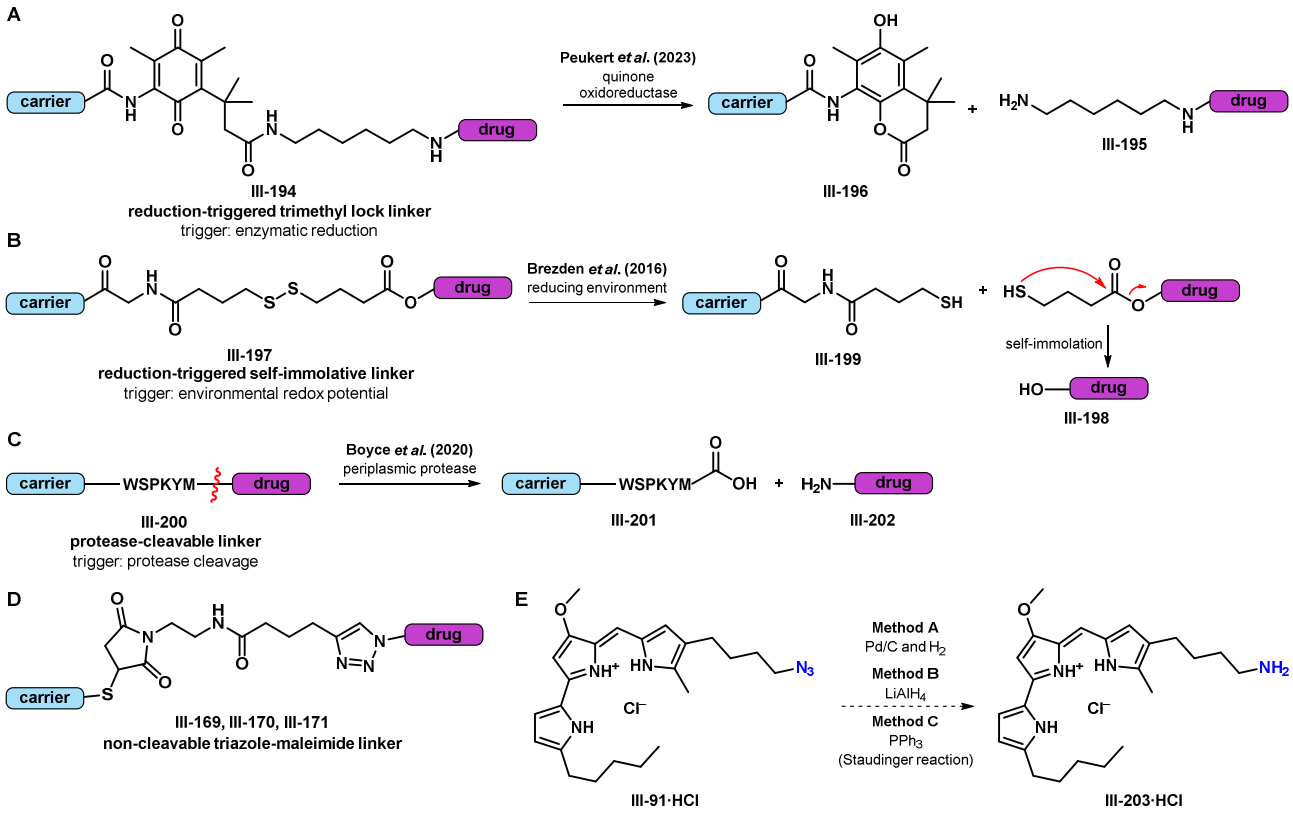
In addition to the previously presented C-ring conjugable derivatives with a clickable azide moiety,[369] we introduced equivalent azide-functionalisation in the A- and B-ring for the first time. Furthermore, the application of the CuAAC reaction provided us with prodiginine conjugates, carrying a reactive maleimide group, which was further used to install prodiginines on the *P. aeruginosa*-specific antimicrobial protein PyoS2 as a putative drug vector for selective import into the opportunistic human bacterial pathogen *P. aeruginosa*. Firstly, it was

successfully shown that PyoS2 and its conserved import mechanism via the Ton-pathway are suitable for importing the small molecule prodigiosin into *P. aeruginosa*. In fact, this co-transport and cellular uptake of prodigiosin is a remarkable achievement, as numerous drug efflux pumps render the membrane of *P. aeruginosa* highly impermeable for hydrophobic drugs and confer prodigiosin-resistance to the Gram-negative pathogen.

Secondly, although cellular import of the PyoS2-prodiginine conjugates into the target cells was proved, no apparent cytotoxicity of the attached prodiginine payloads was detected. This loss of cytotoxic potential of the tripyrrole alkaloid prodigiosin was hypothesised to be connected to a non-cleavable linker and a missing release mechanism of the drug from the PyoS2 protein carrier, inactivating the drug's cytotoxic activity. As the major obstacle of selective drug delivery, namely cellular import, has already been overcome by conjugation to PyoS2, future studies should address the design of suitable cleavable linkers and cleavable prodiginine conjugates, combined with a comprehensive evaluation of drug release efficiency and cytotoxic activities. The following paragraph will merely focus on ideas for drug release mechanisms for prokaryotic applications.

Many examples of cleavable linkers for applications in prokaryotic models emerge in the rapidly advancing field of siderophore-drug conjugates.[494] Siderophores are chelators of trace metals to sequester essential and growth-limiting nutrients from the environment. Their importance for bacterial metabolism led to the evolution of the Ton-pathway, which is needed for active uptake of metal-loaded siderophores and also hijacked by many antimicrobial peptides from the group of S-type pyocins for translocation into the target cell. The importance of Ton-mediated transport for bacterial viability makes this pathway and siderophores promising targets for specific drug delivery.
Numerous recent studies readily highlight the potential of siderophore-drug conjugates in conjunction with cleavable linkers for site-specific cargo release. For example, Peukert *et al*. applied a trimethyl lock linker **III-194** to couple rifamycin and ciprofloxacin antibiotics – RNA polymerase and DNA gyrase inhibitors, respectively – with siderophore carriers (Scheme III.46A). The trimethyl lock linkers require enzymatic activity for drug release, based on a cascade of enzymatic reduction of the quinone and spontaneous intramolecular lactone formation, triggering release of the conjugated drug. In the cited study of Peukert *et al*., two bacterial enzymes from the cytoplasmic compartment with quinone oxidoreductase activity were tested for conjugate cleavage, namely QOR2 from *E. coli* and diaphorase from *Clostridium kluyveri*. Both enzymes showed almost complete reduction of the quinone moiety after 24 h, leading to efficient cytoplasmic release of the rifamycin and ciprofloxacin payloads **III-195** from the tetramethylchroman-2-one **III-196** carrier.[495]
Although cytoplasmic delivery is favourable for many antimicrobials, most published siderophore-drug conjugates are predicated on cleavable linkers that undergo cleavage in the periplasmic space. From this large group of conjugates, two further linker candidates are presented, either using the spontaneous reduction of a redox-sensitive disulfide bond in the bacterial periplasm (Scheme III.46B, Brezden *et al*.) or active protease cleavage of a peptide linker (Scheme III.46C, Boyce *et al.*) to release the conjugated drug payloads.
Brezden *et al.* exploited conjugate **III-197** with a self-immolative disulfide linker for the coupling of the glycoside antibiotic kanamycin **III-198** and a cell-penetrating peptide **III-199** (Scheme III.46B), enabling cellular uptake and periplasmic release of the kanamycin antibiotic.[496] Passive diffusion across the inner membrane then leads to inhibition of protein biosynthesis by binding to the 30S ribosome subunit. Thereby, the installed self-immolation of the disulfide linker not only eliminates the risk of recurring disulfide formation but also minimises extraneous structural modifications to the drug that may influence its physicochemical or pharmacological properties, including diffusion, target affinity, and polarity.
In the last representative example highlighting the potential of cleavable linkers in siderophore-drug conjugates, Boyce *et al*. employed the rich pool of more than 20 periplasmic proteases to cleave antibiotic-siderophore conjugates **III-200** with a protease-cleavable linker and release antibiotics **III-201** from the peptide-functionalised

siderophore **III-202** (Scheme III.46C). Siderophore conjugates with daptomycin payload exhibited broadened antibacterial activity against pathogenic *Acinetobacter* species and certain *E. coli* strains, while unconjugated daptomycin was only active against the Gram-positive *S. aureus*.[497] Other cleavable linkers commonly used in the field of siderophore-drug conjugates include β-lactam linkers and (acyloxy)alkyl ester linkers (both not shown).[497]



Scheme III.46. Suitable linkers for cleavable drug conjugates in a prokaryotic model. **A**–**C**.[495-497] Three recent examples of cleavable linkers that require enzymatic activity or a change in the environmental redox potential. Drugs and carriers are simplified. **D**. Non-cleavable triazole-maleimide linker used in this work. **E**. One-step adaptation to reduce prodiginine azides to the corresponding amines for their coupling to the trimethyl lock or peptide linker from examples in section **A**.

A brief comparison of the cleavable linkers mentioned above with the non-cleavable triazole-maleimide linker used in this work to conjugate prodiginines to PyoS2 (Scheme III.46D) reveals that none of the cited works have used a triazole unit. The unique structural element of the 1,2,3-triazole is not only stable towards enzymatic digestion, but also its azide and alkyne precursors are relatively inert and thus ideal for bioorthogonal chemistry. Concurrently, the usage of a linker means an introduction of a relatively large structural subunit to the drug that may severely change the environment of the drug and might thereby render the payload inactive or useless. Prodiginines are known to be relatively sensitive to structural modifications and the attachment of artificial functional groups,[346, 411] which is why linker cleavage strategies would be required to preserve the native properties of the prodiginine scaffold upon cellular uptake. To explore this strategy of intracellular prodiginine release in the future, a renunciation of the azide group to install a terminal amine instead could be considered. Amines itself are widespread functional groups and are a fundamental part for the installation of the cleavable trimethyl lock or the protease-sensitive linkers (Scheme III.46A). With the organic azide of A-, B-, and C-ring modified prodiginines **III-89·HCl**, **III-90·HCl**, **III-91·HCl** in hand, the corresponding prodigiosin amines can be generated in a simple one-step reduction, exemplified by the C-ring amine **III-203** (Scheme III.46E). Three

methods, including a catalytic hydrogenation with Pd on carbon, lithium aluminium hydride reduction, and a Staudinger reaction with triphenylphosphine could be performed in order to facilitate coupling of prodiginines to cleavable linkers and generate cleavable prodiginines conjugates. However, including the results of anticancer activity of A-ring alkylated prodiginines (cf. Chapter III.3.2.6), where the 5-methyl substitution was shown to drastically boost the anticancer activity in comparison to non-functionalised prodigiosin, the long aliphatic pentyl-chain appendage on the A-ring of prodiginine C-ring azide **III-91·HCl** should be truncated prior to further conjugation approaches.

Taken together, the improved cytotoxicity of A-ring methyl-substituted prodiginines and the proven active import of PyoS2-prodiginine conjugates into cells of the human pathogen *P. aeruginosa* bear great potential for future optimisation of prodiginine conjugates. While the exploitation of carrier molecules can improve site-selective delivery of prodiginine alkaloids and overcome the lack of target specificity of the lipophilic small-molecule drug, the installation of cleavable linkers may be useful for local drug release at the desired target site and facilitate recovery of cytotoxic activity, which was mostly lost upon conjugation to the large hydrophilic carrier protein PyoS2.

Chapter IV

Conjugates of the Bacterial Protein Toxin Pyocin S2 Target Multidrug-Resistant Clinical Isolates of *Pseudomonas aeruginosa*

Parts of this chapter were published in the following peer-reviewed articles or uploaded as a preprint:

Functionalized in Triplicate: A Ring-by-Ring Approach to Tailored Prodiginine Derivatives for Site-Specific Conjugation Through Click Chemistry

Authors:
T.M. Weber & J. Pietruszka.

Journal:
Chem. Eur. J. **2025**, 31(*43*):e202502066.

Own Contributions:
Project idea and conceptualisation; Experimental work and data analysis; Writing and editing of the manuscript; Revision; Funding acquisition.

Contributions of Others:
LC-MS measurements of isolated and labelled proteins (*Beatrix Santiago-Schübel*, ZEA-3, FZ Jülich).

Hoisted by Their Own Petard: Defeating Immunity Protein–Mediated Bacteriocin Resistance

Authors:
T. M. Weber, R. Guadarrama-Gonzalez, C. R. MacKenzie & J. Pietruszka.

Journal:
BioRxiv preprint **2025**, https://www.biorxiv.org/content/10.1101/2025.10.23.684137v1.

Own Contributions:
Project idea, project conceptualisation, and project administration; Experimental work and data evaluation; Visualisation; Conceptualisation, writing, and editing of the manuscript; Revision; Funding acquisition.

Contributions of Others:
Isolation and antibiotic susceptibility testing of clinical *Pseudomonas aeruginosa* strains (*Raquel Guadarrama-Gonzalez*, *Colin Rae MacKenzie*, Institute of Medical Microbiology and Hospital Hygiene, UKD Düsseldorf). LC-MS measurements of isolated and labelled proteins (*Beatrix Santiago-Schübel*, ZEA-3, FZ Jülich).

IV Conjugates of the Bacterial Protein Toxin Pyocin S2 Target Multidrug-Resistant Clinical Isolates of *Pseudomonas aeruginosa*

IV.1 State of the Knowledge

With the ground-breaking discovery of penicillin in 1928 by Alexander Fleming,[1] the administration of antibiotics became a reliable and affordable medical approach of treatment for fighting invisible and previously unconquerable bacterial infections. Within the past 96 years, antibiotics have saved hundreds of millions of lives around the globe.[498-500] However, the decreasing number of newly discovered antibiotics and cellular bacterial targets in combination with the simultaneous and excessive use of antibiotics in hospitals and stock farming have forced antibiotic resistance to spread among bacterial species,[501] causing 4.95 million deaths associated with antimicrobial resistance per year.[502, 503] In fact, antibiotic resistance is a natural phenomenon that results from the co-evolution of antibiotic-producing fungi and bacteria with antibiotic-susceptible bacteria. However, the emergence of antibiotic resistance and the bacterial acquisition of antibiotic resistance genes is accelerated by anthropogenic selection pressures, such as the misuse of antibiotics in livestock farming, the extensive prescription of antibiotics to human patients, or inadequate wastewater management in antibiotic production plants.[504-508]

One of the pathogens with high clinical relevance is the Gram-negative bacterium *Pseudomonas aeruginosa*, which acts as an opportunistic nosocomial human pathogen and causes severe wound infections in burn victims and lung infections in cystic fibrosis patients. Hence, the demand for effective antimicrobial agents to treat these infections is globally high. However, *P. aeruginosa* synergises multiple resistance mechanisms to protect itself from environmental toxins, antibiotics, and from recognition by the human immune system.[509-511] Its multidrug resistance (MDR) is conferred by Resistance-Nodulation-Division (RND) efflux pumps, antibiotic hydrolysing enzymes, alterations in membrane composition, deletion of outer membrane porins, and the formation of biofilms, among others. Altogether, these factors make infections with *P. aeruginosa* extremely difficult to treat.[512-517] Especially the frequent occurrence of carbapenem-resistant strains of *P. aeruginosa* is of great concern, as carbapenems are considered broad-spectrum β-lactam last-resort antibiotics that exhibit the broadest activity of known antibiotics against Gram-positive and Gram-negative species.[518, 519] The escalating antimicrobial resistance underscores the urgency for scientific innovation and collaboration to identify and develop alternatives to conventional antibiotics. Failure to address this challenge risks ushering in a post-antibiotic era with profound consequences for global health.[520]

IV.1.1 Antibiotics

The common term antibiotics is borrowed from the Greek language and is assembled from the words *anti* (engl.: against) and *bios* (engl.: life). By definition, antibiotics are substances with antimicrobial activity that lead to inhibition of bacterial growth (bacteriostatic) or their irreversible killing (bacteriolytic and bactericidal).[521] Natural antibiotics are produced for intraspecies competition between microorganisms. The very first example of these molecules to be discovered was penicillin, an antibiotic produced by the mould *Penicillium*.[522] After the end of WWII, the acquired knowledge on where to find these antimicrobial agents and the limited activity spectrum of penicillin encouraged researchers to mine for further antimicrobials and bioactive structures. This mining marked the beginning of the *golden age of antibiotics,* in which appreciable amounts of new classes of antibiotics were discovered from the rich pool of bacterial and fungal secondary metabolites.[523] Between 1945 and 1979, 22 novel classes of molecules with antibacterial properties were identified (Figure IV.1).

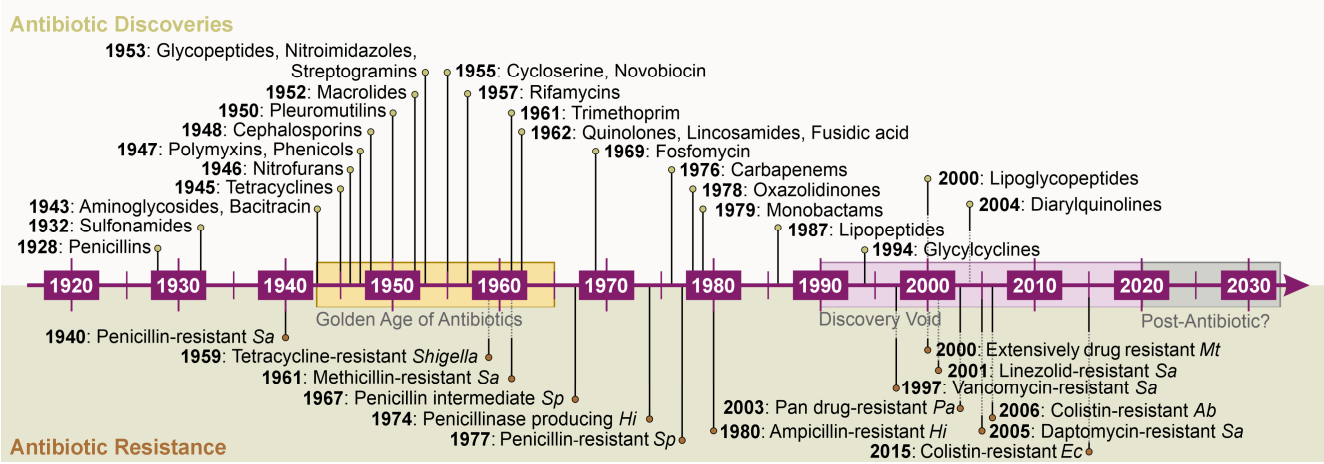


Figure IV.1. Timeline of antibiotic discoveries and emerging resistances. The years between the 1940s and the 1960s are named the golden age of antibiotics due to the cumulative discovery of novel classes of antibiotics. Since the 1990s, no new antibiotic classes with essential novelties have been discovered, but threatening resistances against last-resort antibiotics (e.g. carbapenems, colistin) have been sighted in (multidrug-resistant) pathogenic bacteria. The lack of discovery may prelude a post-antibiotic era. Abbreviations: *Ab* – *Acinetobacter baumannii*; *Ec* – *Escherichia coli*; *Hi* – *Haemophilus influenzae*; *Mt* – *Mycobacterium tuberculosis*; *Pa* – *P. aeruginosa*; *Sa* – *Staphylococcus aureus*; *Sp* – *Streptococcus pneumoniae*.

However, the heyday of antibiotic discovery was followed by a long-standing lean period.[524] Although a handful of new antibiotics were approved by the US Food and Drug Administration (FDA) between 1980 and 2020, most of these antibiotics belonged to already known classes of antibiotics and addressed well-known bacterial targets. Consequently, not only is the discovery of new classes of antibiotics progressing slowly, but also the development of new non-natural classes of antibiotics. In total, only three new classes were developed by semi-synthesis of existing classes (glycylcyclines in 1994 and lipoglycopeptides in the 2000s) or total synthesis (diarylquinolines in 2004).[525-527] Concurrently, antibiotic resistance can be observed to an increasing degree and its development or dissemination within or among bacterial species is accelerated by the therapeutic use of antibiotics in an unnecessary excess.[528] Although our knowledge about bacterial resistance to antibiotics is nearly as old as our knowledge of antimicrobials, an alarming development commenced with the beginning of this millennium (Figure IV.1). Continuous surveillance of antibiotic-resistant clinical isolates and bacteria from environmental sources revealed an accumulation of antibiotic resistance in difficult-to-treat pathogens.[524] Especially those resistances against so-called last-resort antibiotics are a growing concern in hospitals. Antibiotics rated as last-resort antimicrobials by the WHO are held back from the public to only treat serious and life-threatening infections with multidrug-resistant bacteria with acquired resistance to all other common antibiotics (Figure IV.1).[529] Hence, last-resort antibiotics are, so to speak, the life insurance of mankind and essential drugs in hospitals. Nevertheless, nosocomial pathogens managed to evolve resistance mechanisms to evade the influence of last-resort antimicrobials. The first last-resort antibiotic resistance was demonstrated in 1997 in Japan with the isolation and identification of a clone of the opportunistic human pathogen and Gram-positive bacterium *Staphylococcus aureus*, showing reduced susceptibility to vancomycin (glycopeptide) treatment.[530] In 2000, extensively drug-resistant strains of *Mycobacterium tuberculosis*, the causative agent of tuberculosis, were first reported.[531] Linezolid (oxazolidinone)-resistant strains of *S. aureus* followed in 2001.[532] In 2003, numerous *P. aeruginosa* strains in Taiwan were found to be non-susceptible to any known antibiotic (pan-resistance).[533] Lastly, resistance genes against daptomycin (lipopeptide) in *S. aureus* and colistin (polymyxin) in *Acinetobacter baumannii* were found in 2005 and 2006,[534-536] completed by the transferable plasmid-encoded colistin-resistance gene *mcr-1* in *E. coli* isolates from animals and humans in 2015.[537] The growing number of pathogens with prevalent MDR

against precious last-resort antibiotics and the declining number of antibiotic approvals reinforce the urgent need for new and effective alternatives to common antibiotics.

The known classes of antibiotics target evolutionarily conserved metabolic pathways or cellular machineries of the bacterial metabolism (Figure IV.2), as shown by the slower rate of evolution of the involved genes in comparison to the genome average.[538] But only because a compound shows biological activity against bacteria, it is not necessarily suited to be used as an antibiotic for treating or preventing bacterial infections in humans or animals. A second but very important prerequisite for a compound to be used as an antibiotic is its ability to selectively target unique bacterial cellular structures, which are fundamentally different from those of eukaryotic selectively target unique bacterial cellular structures, which are fundamentally different from those of eukaryotic cells. Just as an example, peptidoglycan (PG) is a structural component of the bacterial cell envelope and is not present in eukaryotic cells. Therefore, PG biosynthesis is a popular and very effective target for non-natural and natural antibiotics (e.g. penicillins).[539] As Gram-positive and Gram-negative bacteria differ in cell morphology and particularly membrane composition, certain antibiotics are exclusively active against Gram-positive bacteria and inactive against Gram-negative bacteria and *vice versa*.[540] Depending on their antimicrobial spectrum, antibiotics are thus classified as narrow-spectrum or broad-spectrum antibiotics.[541]

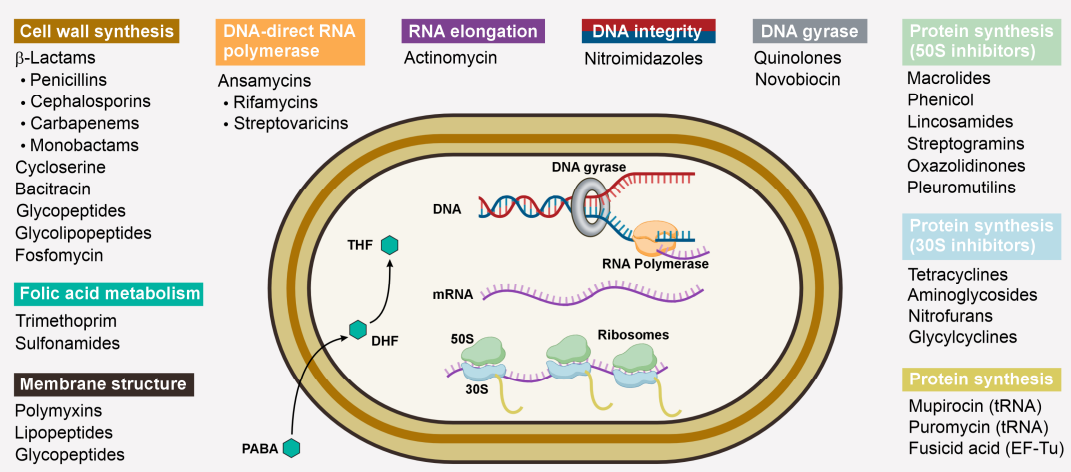
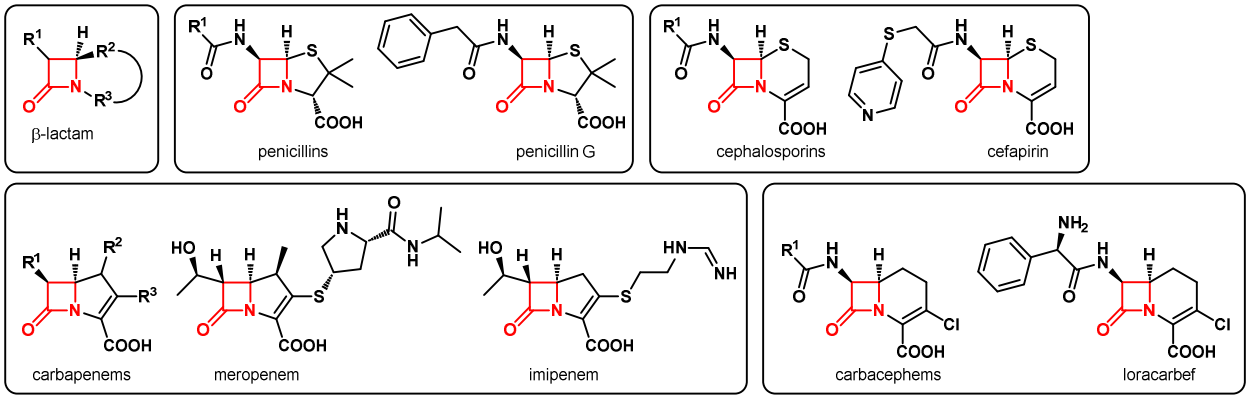


Figure IV.2. Cellular targets for different classes of antibiotics. A schematic (Gram-negative) bacterium is depicted with essential cellular targets for common classes of antibiotics. The colour of headings corresponds to the colour of the cellular components. Abbreviations: DHF – dihydrofolate; EF-Tu – elongation factor Tu; PABA – *p*-aminobenzoic acid; THF – tetrahydrofolate.

IV.1.1.1 β-Lactam Antibiotics and Their Mode of Action

β-Lactam antibiotics, or briefly β-lactams, are those antibiotics containing a substituted β-lactam ring (2-azetidinone) (Scheme IV.1). As the first described antibiotic, penicillin G, belongs to this broad group with bactericidal activity, it is probably the most familiar group of antibiotics, and it also accounts for 65% of antibiotic prescriptions in the US.[542] At the beginning of antibiotic therapy, β-lactams from the penicillin family were predominantly exploited to treat infections with Gram-positive bacteria. With further semi-synthetic modification and the discovery of other β-lactam families, the antibiotic spectrum was substantially broadened. Nowadays, broad-spectrum β-lactams are in use to treat both Gram-positive and Gram-negative infections.[542] Especially the last-resort antibiotics from the carbapenem family have the broadest activity spectrum and often retain antimicrobial activity, even if resistance to other β-lactams is developed.



Scheme IV.1. Selected β-lactam antibiotics with the common β-lactam motif that inhibit the bacterial cell wall biosynthesis by binding to D-alanyl-D-alanine transpeptidases. Depending on their substitutions on the residues R^1, R^2, and R^3, the lactams are grouped into several classes. These include penicillins, cephalosporins, carbacephems, and carbapenems, among others. Five actual examples are shown.

For this reason, these precious carbapenem antibiotics (e.g. imipenem and meropenem) are reserved for the treatment of severe infections with multidrug-resistant human pathogens, such as ESKAPE(E) strains (*Enterococcus faecium*, *S. aureus*, *Klebsiella pneumoniae*, *A. baumannii*, *P. aeruginosa*, and *Enterobacter* spp.), uropathogenic *E. coli*, etc. (*vide infra*).[524, 529, 543] The mode of action of β-lactams is actually independent of their chemical substitution and causes an inhibition of the bacterial cell wall synthesis and its modulation.[539, 542] The bacterial cell wall consists of an inner lipid bilayer and a densely cross-linked network of glycans, called peptidoglycan (Figure IV.3).

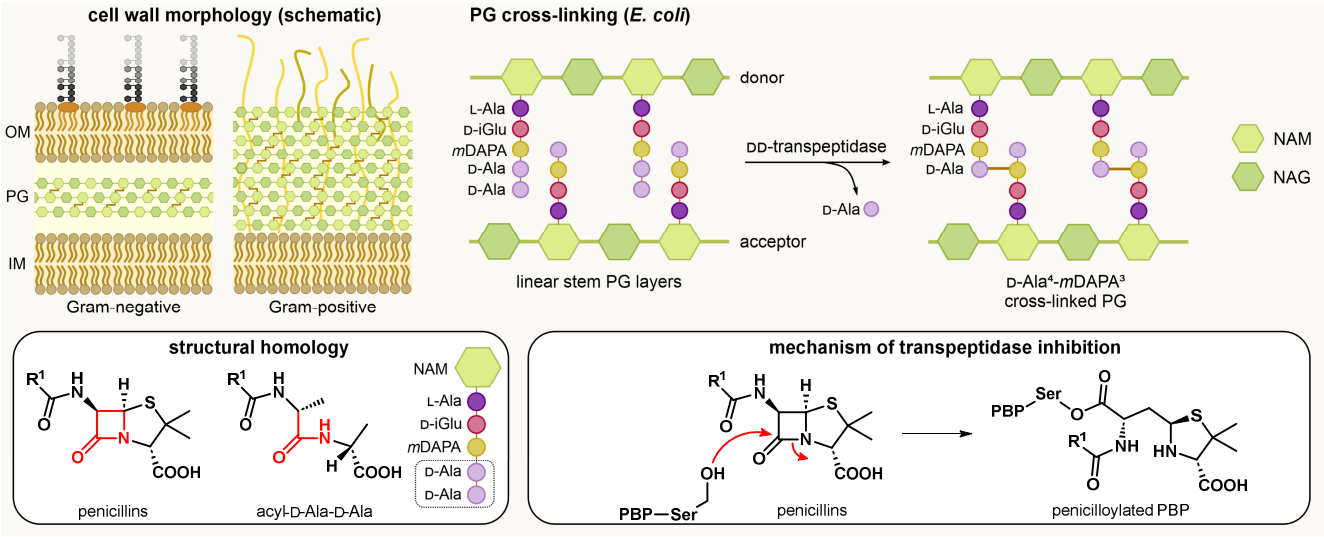


Figure IV.3. Cellular target structure and mode of action for β-lactam antibiotics. β-Lactams inhibit the biosynthesis of peptidoglycan within the bacterial cell wall. Inhibition is achieved by covalent and irreversible binding of the catalytically active serine residue in the active site of the penicillin-binding enzyme DD-transpeptidase. On the example of *E. coli*, this enzyme catalyses the cross-linking of peptidoglycan layers by introducing a D-ala^4-*m*DAPA^3 crosslink between two linear peptide stems of *N*-acetylmuramic acid donor and acceptor sugars. Abbreviations: D-iGlu – D-isoglutamic acid; IM – inner membrane; *m*DAPA – *meso*-diaminopimelic acid; NAG – *N*-acetylglucosamine; NAM – *N*-acetylmuramic acid; OM – outer membrane; PBP – penicillin-binding protein; PG – peptidoglycan. Figure design inspired by Aliashkevich *et al*.[544]

In Gram-positive bacteria, cells are surrounded by a thick layer of PG, which is directly exposed to the environment and which is why these bacteria are more susceptible to β-lactam antibiotics by nature. In Gram-negative bacteria, the PG is very thin and additionally encapsulated by a second lipid bilayer and therefore less accessible.[539] The cross-linking of PG layers is achieved by enzymatic transpeptidation of penta-peptides, which are appended to the PG sugars.[545] The so-called DD-transpeptidase catalyses the peptide bond formation between the linear donor and acceptor stem to covalently cross-link two adjacent PG layers. Antibiotics from the β-lactam family mimic the D-alanyl-D-alanine termini of the penta-peptide extension and competitively bind to the active site of the penicillin-binding protein (PBP) DD-transpeptidase enzyme.[546] At the active site, a catalytically active serine residue attacks the β-lactam moiety and remains covalently acylated. As this penicilloylation is irreversible, the modification renders the serine residue inaccessible for transpeptidation of PG layers.[547] As a result, cells are no longer able to reorganise or fasten the PG layers, both of which are essential processes in cell growth and cell division. Although PG cross-linking is vital for all bacteria, nature has created several variants of peptide cross-linkers that differ in their constitution and cross-linking pattern.[548-550] Thus, transpeptidases from different bacteria may exhibit varying affinities towards the same β-lactam, providing one of many reasons for limited success against one species while others might be effectively killed.

IV.1.1.2 Antibiotic Resistance

Antibiotic resistance describes a state where bacteria do not respond to antibiotic treatment anymore and continue to proliferate unharmed. This resistance can occur through independent mechanisms, namely alteration of the antibiotic target by mutation, drug inactivation, alteration of metabolic pathways, reduced drug accumulation, or ribosome splitting.[551, 552] Although resistances against antibiotics bear evolutionary benefit for the resistant strains and natural resistance genes and mechanisms for their dissemination have developed millions of years ago through the coevolution of microbes in competitive ecological niches, the current rate of resistance dissemination among bacteria is highly concerning, owing to anthropogenic overuse of antimicrobials.[553] Genes conferring resistance to antibiotics were observed for all known antibiotics so far (cf. Figure IV.1), but antimicrobial resistance to last-resort antibiotics is most alarming for the world community and public healthcare. The worrisome development in the area of resistant bacteria and the dismal prospects of 10 million deaths per year in 2050 by resistant bacteria prompted the WHO in 2017 to publish a priority list of pathogens for which new antibiotics or promising alternatives are urgently needed, where carbapenem-resistant *P. aeruginosa*, *A. baumannii*, and *Enterobacteriaceae* were the top tier listed pathogens and categorised in the highest priority class “critical”.[554, 555] In response to recent reports of decreased prevalence of MDR *P. aeruginosa* in the global resistance profile, carbapenem-resistant *P. aeruginosa* was shifted from critical to high priority in an updated risk assessment from 2024.[556] Consequently, the accumulation of antimicrobial resistance in human pathogens urges the need to understand the mechanisms and dissemination strategies of antimicrobial resistance, and to prospect for novel antibiotics and potent alternatives to treat these pathogens.

So far, antibiotic prescriptions for regular non-nosocomial infections have mostly reverted to broad-spectrum antibiotics. Two recent randomised clinical studies investigating the prescription of extended-spectrum antimicrobials to non-critically ill patients with pneumonia or urinary tract infections highlighted that most patients do not need these valuable broad-spectrum antimicrobials.[557, 558] Indeed, broad-spectrum antibiotics are a very effective means to empirically treat infections, as an in-depth characterisation of the invading bacterial species is skipped.[559] Especially in life-threatening infections with *P. aeruginosa*, the rapid administration of antibiotics to critically ill patients has been shown to correlate with a significantly increased rate of survival.[560] Even though this empirical approach saves time and effort, the exposure of the microbiome or pathogenic microbes to broad-

spectrum antibiotics, unfortunately, adds additional selection pressure to the involved bacteria, forcing the emergence and dissemination of genetic factors that contribute to antibiotic resistance.[561] Furthermore, it may harm the healthy microbiome and privilege 'unhealthy' bacteria or bacterial pathogens that are more resilient to antibiotic treatment.[528, 561] Thus, narrow-spectrum antibiotics are one partial strategy to reduce the risk of antibiotic escape and an accumulation of antibiotic resistance mechanisms, but also require an elaborate strain typing and a characterisation of its genetics. Nevertheless, novel intracellular targets for future antibiotics are additionally needed,[562-564] as antimicrobial resistance is often developed against the mode of action, rather than single antibiotics (e.g. β-lactam hydrolases, *vide infra*).

The resistance of bacteria against antibiotics can either be newly acquired and result from mutations or can be based on the acquisition of resistance genes through horizontal gene transfer. In environmental and hospital habitats, the horizontal transfer of genes (conjugation, transduction, and transformation) is the most efficient mechanism to shuttle genetic elements between bacterial species and equip recipient strains with virulence factors or antibiotic resistance genes.[565] While bacteriophage-mediated transduction and transformation of "free" floating DNA play important roles in the genetic engineering of strains in laboratory settings, they have been evaluated as less important mechanisms of horizontal gene transfer in the environment than conjugation. Conjugation describes the transfer of DNA and genes via pili or adhesins and requires tight cell-to-cell contact to occur. To facilitate the exchange of antibiotic resistance genes, they are often located on conjugative broad-host range plasmids or on mobile genetic elements within the bacterial chromosome to enable rapid spreading within microbial communities.[553, 566] As the mechanism of conjugation, in particular, is not restricted to intraspecies exchange of genes, the interspecies horizontal gene transfer between pathogens in a hospital environment dramatically accelerates the dissemination of antimicrobial resistance genes and worsens the current antimicrobial crisis. On the example of β-lactam antibiotics, different mechanisms of antibiotic resistance and enzyme classes that are able to confer antibiotic resistance will be shortly introduced in this section.

IV.1.1.2.1 Mechanisms Without Drug Inactivation

Although β-lactams are the most commonly prescribed group of antibiotics, bacteria have evolved ingenious ways to avoid impairment of their cell wall biosynthesis. The first contact point between drug and cell is the cell wall, a permeability barrier that shields the microbes from environmental stress. However, some bacteria are capable of synthesising biofilms, a dense polymeric matrix of bacterial communities encapsulated in exopolysaccharides, lipids, proteins, and nucleic acids. These biofilms pose challenges to antimicrobial treatment, as their surface is often inert and prevents exogenous molecules like drugs from reaching the cell membrane. For *P. aeruginosa*, it was shown that all three biofilm exopolysaccharides confer high resistance to antibiotics from the polymyxin and aminoglycoside families.[567, 568] The relatively small β-lactams (<400 Da) can reach the PG of Gram-positive bacteria without any problem, as these bacteria lack the second membrane. For Gram-negative bacteria, the asymmetric outer membrane with densely packed LPS on the outer surface poses the first obstacle. In order to bypass this first line of defence, unspecific porins with size exclusion for molecules >600 Da are hijacked, or more hydrophobic antibiotics can also diffuse through the lipid bilayer.[569] To hinder antibiotics from entering, specific Gram-negative bacteria use drug efflux pumps to actively repel these molecules from the membrane. While pathogenic strains of *E. coli* and *K. pneumoniae* predominantly utilise AcrAB-TolC RND pumps to increase their antibiotic tolerance, *P. aeruginosa* exploits Mex RND drug efflux pumps.[570] The most widespread pump is MexAB-OprM, which confers resistance to several antibiotics, including β-lactams, fluoroquinolones, tetracyclines, chloramphenicol, and macrolides. Additionally, MexXY-OprM and MexCD-OprJ play vital roles in antimicrobial resistance.[571-573] Although the tripartite membrane-spanning RND pumps are the most important

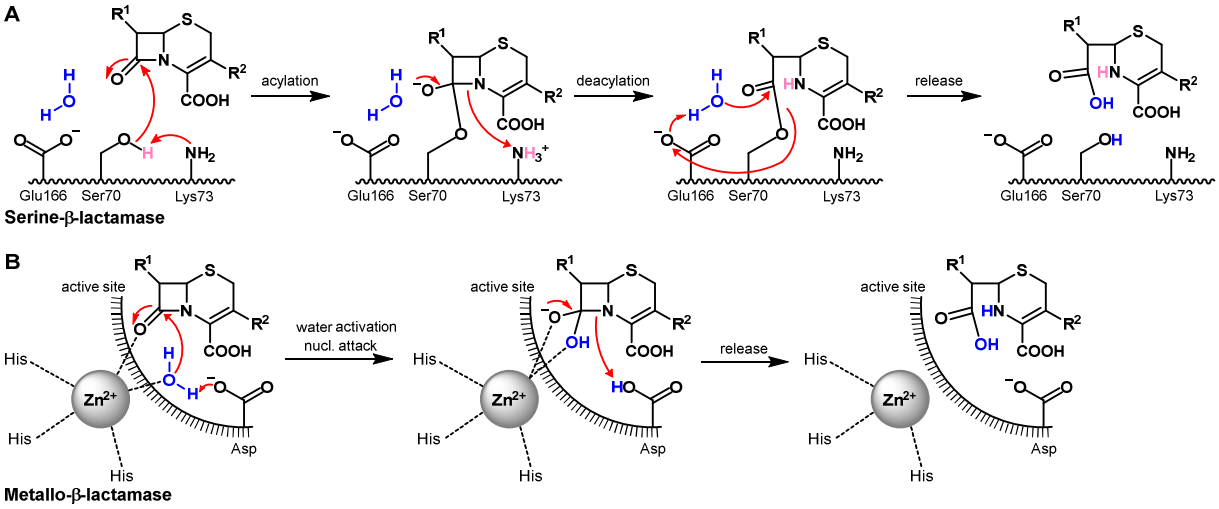
group of efflux pumps, several others have been identified to contribute to drug resistance in bacteria by active transport (ATP-binding cassette transporter superfamily, major facilitator superfamily, small multidrug resistance family, and multidrug and toxic compound extrusion family).[574]

Another strategy to escape from PG-targeting antibiotics is pathway engineering of PG biosynthesis. Since β-lactams target the DD-transpeptidase, evolution has created alternative enzymes for PG crosslinking that lead to alternative 3→3 cross-linked PG phenotypes. To date, DL-transpeptidases and DD-carboxypeptidases have been identified as alternative enzymes needed to catalyse the unconventional crosslinking. However, as these enzymes do not recognise the D-alanyl-D-alanine moiety from the pentapeptide, these proteins are inherently resistant to β-lactam antibiotics that mimic the D-alanyl-D-alanine-containing pentapeptide.[548, 549] Nowadays, it is widely accepted that LD-transpeptidases are closely associated with stress adaptations to β-lactam antibiotics, toxin delivery, and membrane stability and therefore play an important role in drug resistance.[544]

Another very efficient microbial strategy to evade the influence of β-lactam antibiotics is the alteration of PBP targets. The semi-synthetic penicillin derivative methicillin was once used as a narrow-spectrum antibiotic to treat infections of *S. aureus*. However, methicillin-resistant *S. aureus* (MRSA) emerged briefly after the market launch of methicillin in 1960 and quickly spread across Europe, causing the first MRSA epidemic.[575] MRSA produces an alternative transpeptidase enzyme, called PBP2a. PBP2a is encoded by the gene *mecA* on the mobile genetic element SCC*mec* (Staphylococcal Chromosomal Cassette *mec*) and shows low affinity to β-lactam antibiotics. The high transferability of the mobile genetic element harbouring PBP2a via horizontal gene transfer, in combination with significantly reduced lactam affinity and *mecA* overexpression, confers high resistance to β-lactam antibiotics and explains the rapid dissemination of MRSA in the 1960s.[576, 577]

IV.1.1.2.2 β-Lactamases – A Group of β-Lactam Hydrolysing Enzymes

Besides non-enzymatic principles that confer antibiotic resistance to bacteria, these microorganisms have developed specialised enzyme catalysts for the permanent inactivation of antibiotics. β-Lactam antibiotics are inactivated by so-called β-lactamases, which possess hydrolase activities and are the predominant resistance determinant against β-lactams in Gram-negative bacteria.[578] However, as β-lactams are an indispensable tool to treat microbial infections, β-lactamases and the horizontal gene transfer of β-lactamase genes pose a serious threat to the global population and its prosperity.[555, 579] To date, more than 2,800 individual β-lactamase genes have been identified from bacterial genomes or metagenome analyses.[578] Although the β-lactamases have been assigned to sequence- or substrate-dependent classes, all types of β-lactamases have one thing in common: the aptitude to hydrolyse the mechanistically important β-lactam ring (Scheme IV.2). While most resistance enzymes from the group of β-lactamases resort to a central catalytic serine residue for the nucleophilic attack on the β-lactam motif and the formation of an acyl enzyme, a smaller group of enzymes exploits a metal-catalysed mechanism. Consequently, these enzymes are either classified as serine- or metallo-β-lactamases (MBLs).



Scheme IV.2. Generalised mechanism of serine and metallo-β-lactamases (MBLs). All β-lactamases possess β-lactam hydrolysing activity and cleave the C-N bond of the β-lactam moiety through nucleophilic addition of water to the carbonyl. **A**. Mechanism of serine β-lactamases on the example of a generic cephalosporin. **B**. Mechanism of metallo-β-lactamases on the example of a generic cephalosporin. Adapted from He *et al*.[580]

β-Lactamases originate from the co-evolution of bacteria in proximity to β-lactam-producing fungi and bacteria, long before humans harnessed antibiotics to treat antimicrobial infections.[581] With the discovery of penicillin in 1929,[1] penicillin-resistant bacteria were observed shortly after. The first β-lactamase enzyme was finally identified in England in 1940 from a penicillin-resistant *Bacillus coli* (*E. coli*).[582] In the following years and decades, the discovery of novel classes of natural β-lactam antibiotics (cephalosporins, monobactams, and carbapenems) was always accompanied by the subsequent identification of appropriate β-lactamase enzymes. While the first penicillinases and cephalosporinases were still found in chromosomal loci, an increasing threat was perceived from transferable β-lactamase genes (*bla* genes), encoded within mobile broad-host range plasmids or other mobile genetic elements, such as replicative transposons or integrons.[578, 583] As mobile genetic elements can be easily transferred between microbes via horizontal gene transfer with only little species barriers, these have become not only the most prevalent cause of β-lactam resistance in Gram-negative bacteria, but also the leading cause of accumulated β-lactam resistance in difficult-to-treat pathogens, accelerated by the overuse of synthetic antibiotics.

The majority of modern age β-lactam antibiotics descend from natural antibiotics, but have been modified by semi-synthesis to increase their antimicrobial spectrum, hydrolytic stability, or their tolerability for human patients. Local epidemics with cephalosporin-resistant bacteria and limited activity against Gram-negative bacteria have driven the development of novel cephalosporins with expanded activity spectra against human pathogens. For example, the third-generation cephalosporin cefotaxime shows broad activity against *Neisseria* species and *Enterobacteriaceae*, while ceftazidime is much valued for its activity against *Pseudomonas* species.[584] The first epidemics of *Enterobacteriaceae* against ceftazidime and cefotaxime were documented in the late 1980s and have been traced back to novel variants of the very common TEM and SHV class A β-lactamases.[585] Owing to their hydrolytic activity against the precious third-generation cephalosporin antibiotics, these enzymes with an extended substrate spectrum were named ‘Extended Spectrum β-Lactamases’ (ESBLs).[586] Driven by the constant threat of microbial escape from working antibiotics through newly acquired resistance genes or mutational adaptations of established β-lactamases, the latest β-lactam antibiotics were introduced in 1976 and 1979,[587, 588] namely carbapenems and monobactams (cf. Scheme IV.1). Literally just in time to provide expedient alternatives to the third generation cephalosporins that would become ineffective against ESBLs just a few years

later and cause selection of ESBL-producing isolates in hospitals. Native carbapenems have been isolated from soil-borne actinomycetes and their analogues, such as imipenem and meropenem, have predominantly been used to treat infections with ESBL-producing pathogens, e.g. cephalosporin-resistant nosocomial *K. pneumoniae*.[587, 589] However, their very broad antimicrobial spectrum of these last-resort antibiotics against aerobic and anaerobic Gram-positive and -negative bacteria, including the opportunistic human pathogen *P. aeruginosa*, has forced a predictable selection of carbapenem-resistant strains in healthcare centres.[589-591]

IV.1.1.2.3 Carbapenemases

The phenomenon of carbapenem-resistance is a growing problem in hospitals around the globe, as carbapenems are classified as last-resort antibiotics for the treatment of severe infections and multidrug-resistant bacteria that have developed resistance to all other common antibiotics.[554, 555] Phenotypic selection of carbapenem-resistant bacteria has led to the identification of numerous resistance mechanisms, including the overproduction of class C cephalosporinases in conjunction with porin deficiency, target alteration by changes in the transpeptidase structure, and the synthesis of carbapenemase enzymes. Although all these mechanisms render serious pathogens, e.g. *Acinetobacter* species,[592] *Enterobacteriaceae*,[593] and *Pseudomonadaceae*,[591] resistant to carbapenem β-lactam antibiotics, chromosomal and plasmid encoded carbapenemases with β-lactamase activity are the dominant driver of resistance.[578]

Carbapenemases can be found among three of the four β-lactamase classes (A, B, and D).[578] Unfortunately, their substrate spectrum is not limited to carbapenem β-lactams, but also includes cephalosporins and penicillins (cf. Scheme IV.1). Moreover, serine carbapenemases from class A and D can hydrolyse monocyclic β-lactams from the monobactam family, while MBLs are not.[591] Hence, the implication of carbapenemases for clinicians is of great importance, as these enzymes take most available β-lactam antibiotics out of the portfolio of treatment options for nosocomial infections. And even worse, the majority of transferable carbapenemase genes are co-located with other resistance factors, increasing the risk of manifesting resistance to other classes of antibiotics as well. The biggest threat comes from transferable class B MBLs. The first of its kind was found in 1988 in Japan on a conjugable plasmid of a carbapenem-resistant *P. aeruginosa* (CRPsA) isolate, resistant to imipenem. The identified enzyme IMP-1 was shown to possess imipenemase activity that enables the hydrolysis of carbapenems.[594] Augmented prescriptions and administrations of carbapenems in severe nosocomial infections with ESBL-producing pathogens promoted the evolution and the widespread of additional metallo-β-lactamases with carbapenemase activity and have led to foreseeable outbreaks of carbapenem-resistant strains in hospitals across Europe, Asia, and America.[595-600] Mobile *bla* genes encoding carbapenemase MBLs are usually organised in gene cassettes within class 1 integrons and their transfer is facilitated by plasmids or, to a minor extent, by transposons.[595] The current contingent of transferable MBLs includes more than ten unique carbapenemase families (VIM, GIM, NDM, IMP, among others) and some contain even more than 60 subtypes,[594, 601-610] often distinguished just by single amino acid exchanges.[611] While some of the mobile MBLs have mostly been geographically restricted to local outbreaks (e.g. GIM in Germany) and have not significantly spread across continental borders,[600] especially the Verona integron-encoded MBL (VIM), New Delhi MBL (NDM), and IMP MBL of β-lactamase subgroup 3a are the most prevalent carbapenemases with a worldwide geographical distribution.[595, 600] In particular, VIM-type MBLs have become endemic in healthcare centres in Europe, Korea, and in countries on the American continents.[595, 612] But also carbapenemases with minor dissemination, such as the locally concentrated German imipenemase (GIM), have reached an endemic status, emphasised by a long-term outbreak of GIM-1 producing *P. aeruginosa* and *Enterobacteriaceae* over a period of more than 10 years in the University Hospital in Düsseldorf.[600] Worldwide resistance surveillance data accentuate the clinical

importance of carbapenemase MBLs in *P. aeruginosa* and the frequently encountered co-transfer of mobile resistance factors that help to evade antibiotic treatment through the development of pan-resistance.[591, 595, 612, 613] Hence, the increasingly fast spread of carbapenemase genes and their pronounced accumulation in opportunistic human ESKAPE(E) pathogens, such as *P. aeruginosa*, *A. baumannii*, *S. marcescens* and *K. pneumoniae*, urge the scientific community to not only develop novel classes of β-lactam antibiotics and β-lactamase inhibitors, but also to prospect for innovative novel antibiotic mechanisms to avert a post-antibiotic era.

IV.1.2 *Pseudomonas aeruginosa* – An Opportunistic Human Pathogen

Pseudomonas aeruginosa is a Gram-negative bacterium from the family of *Pseudomonadaceae* and it belongs to the group of ESKAPE(E) pathogens. It colonises soil, water, and plant habitats but also plays a central role as an opportunistic human pathogen in nosocomial infections.[573, 614, 615] Its nutritional requirements are relatively low, as *P. aeruginosa* can utilise a wide range of organic compounds and sources for energy and carbon metabolism, thereby allowing the bacterium to survive in various environments.[615] The clinical relevance of *P. aeruginosa* lies dormant in its opportunistic lifestyle, meaning that the bacterium mainly causes infections in individuals with an already compromised immune system. These include infections of the respiratory tract of patients with cystic fibrosis, wound infections of burn victims, infections of the urinary tract, bloodstream infections (bacteraemia), or of patients currently undergoing chemotherapy.[560] To promote the infection of humans and animals, *P. aeruginosa* has acquired a sweeping repertoire of host defence mechanisms to conceal itself from the immune system, to wiretap host cell resources, to circumvent extinction by manmade antibiotics, and to damage host tissue.[573, 615, 616] But in addition, the Gram-negative pathogen is able to rapidly adjust its metabolism and introduce beneficial mutations to adapt to challenging conditions and environments.[573] Moreover, it possesses the ability to adhere to wet surfaces and survive harsh disinfection processes.[615, 617] Taken together, these mechanisms make *P. aeruginosa* extremely difficult to treat and explain why the pathogen is a rapidly growing concern in hospitals worldwide.[560] This concern is underlined by epidemiology studies, which revealed that *P. aeruginosa* accounts for 7.1–7.3% of all healthcare-associated infections with increasing prevalence. As *P. aeruginosa* is a major cause of nosocomial pneumonia, the induced healthcare-associated pneumonia and ventilator-associated pneumonia stress the healthcare system and bind significant capacities for their treatment. In intensive care units, an elevated content of 16.2% were healthcare-associated infections with *P. aeruginosa* and 23% of intensive care patients showed intensive care-acquired infections caused by *P. aeruginosa*. On the example of *P. aeruginosa*-induced bloodstream infections, the mortality rate was estimated to be 43.2–58.8% of which 16.7–28% was caused by multidrug-resistant strains. However, the exceptionally high mortality rate is also observable for burn victims with wound infections, after transplantations, and for patients with pneumonia. Collectively, these epidemiology studies all emphasise the need for effective and selective approaches for the treatment of long-lasting and persistent *P. aeruginosa* infections.[618]

IV.1.2.1 Virulence Factors and Pathogenicity

So-called pathogens are microorganisms that are able to cause diseases. Therefore, pathogenicity refers to the qualitative potential to do so. Virulence instead describes the extent of damage that is caused by this microorganism to the host, making it a quantitative description.[619] *P. aeruginosa* produces and secretes various virulence factors that enhance its virulence and help to establish, maintain, and spread an infection in the host environment. The known virulence factors of *P. aeruginosa* include proteins, polysaccharides, lipopolysaccharides, siderophores, and others that are either surface-exposed, secreted, or involved in cell-to-cell

interaction.[615] In this regard, the most important virulence factors of *P. aeruginosa* will be briefly introduced in this section (Figure IV.4).

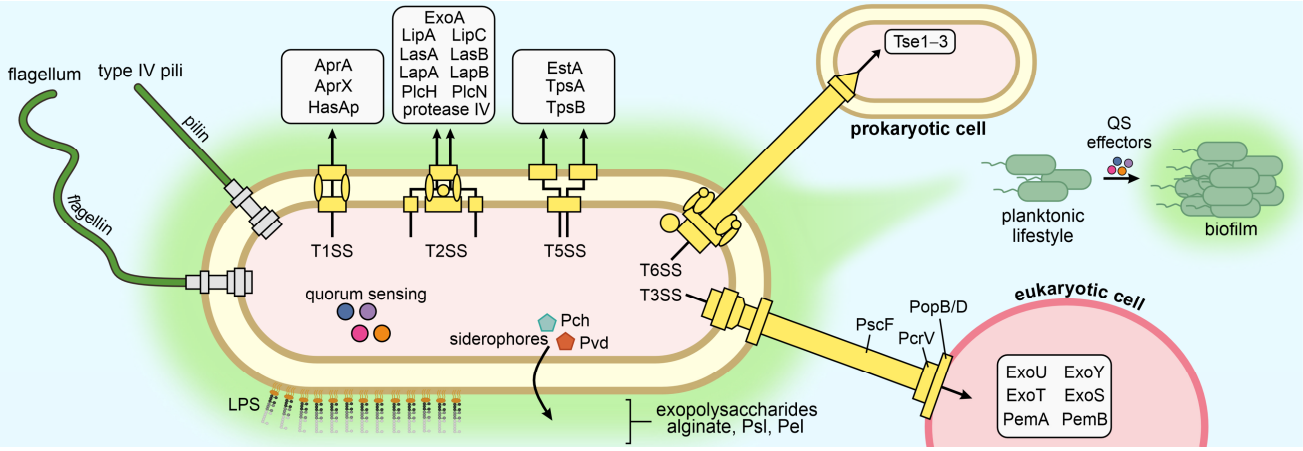


Figure IV.4. The most important virulence factors of pathogenic *P. aeruginosa* strains and their secretion pathways. Abbreviations: LPS – lipopolysaccharide; Pch – pyochelin; Pvd – pyoverdine; QS – quorum sensing; TXSS – type X secretion system. Figure adapted from Liao *et al*.[615]

IV.1.2.2 Biofilms and Quorum Sensing Shape Cell-to-Cell Interaction

Biofilms are living bacterial communities, encapsulated in an inert matrix of exopolysaccharides, lipids, proteins, and nucleic acids that protect the community from drugs or other external stress factors. In clinics, biofilms impede thorough disinfection and allow bacteria to stick to surfaces and medical devices, such as catheters or implants.[568] As many strains of the ubiquitous bacterium *P. aeruginosa* produce biofilms that allow colonisation of eukaryotic tissues and long-term persistence in the human body, it is important to study biofilm formation to understand the dynamics of *P. aeruginosa* infections and intraspecies communication. So far, three exopolysaccharides have been found to be important constituents of *P. aeruginosa* biofilms, namely Psl, Pel, and alginate.[568, 620, 621] Psl is a neutral oligosaccharide that functions as an adhesive, which attaches free-floating planktonic cells to other cells and to surfaces. As a structural component of biofilms, Psl also fulfils a protective role against antimicrobials and phagocytosis. The cationic polymer Pel is an important contributor to the structural stability of the biofilm and also helps to attach nonmucoid cells to non-biofilm surfaces. The polymer protects the bacterial community from antimicrobial agents and phagocytosis, thereby preventing an effective treatment or immune response to persistent *P. aeruginosa* infections. Lastly, the acetylated polymer alginate is a negatively charged component found in biofilms of mucoid *P. aeruginosa* strains in cystic fibrosis, where it is closely associated with the transformation of acute into chronic infections. Furthermore, alginate was found to be important for the maturation of the biofilm and its protection from antibiotics and the host immune system. As all three polysaccharides help to establish and maintain persistent infections with *P. aeruginosa*, Psl, Pel, and alginate are considered virulence factors.[615] The DNA that is an important constituent of biofilms originates from the lysis of cells, for example, induced by bacteriolytic antibiotics, lytic phages, or antimicrobial peptides (F- or R-type pyocins), and is therefore classified as environmental DNA (eDNA).[568, 622] The negatively charged eDNA is less significant for transcription, but it is yet important as an energy source, for acidification of biofilms, and as a cation scavenger (Mg^{2+} and Ca^{2+}).[622, 623] The scavenging of divalent cations from the surface of host cells was hypothesised to help activation of the *P. aeruginosa* T6SS (type 6 secretion system) for membrane penetration and the release of virulence factors into competing species.[623] Moreover, it was shown that DNA-associated

acidification of biofilms hinders antimicrobial agents from penetrating the peripheral biofilm layer, rendering the bacteria more resistant to abiotic stress and aminoglycoside antibiotics.[622]

The biofilm formation and dynamic processes within the bacterial community are orchestrated by a sophisticated cell-to-cell communication system called quorum sensing (QS).[568, 615, 624] These feedback circuits utilise self-secreted signalling molecules to probe how many bacteria are within the community and regulate gene expression in relation to population density. As these signalling molecules possess autoinducer properties and their concentration is dependent on the population size, pathogenic bacteria use this communication system to synchronise the production of virulence factors and synergise to antagonise the host's immune response in an infection. Furthermore, QS is used to regulate biofilm formation and the associated motility of planktonic bacteria. To date, four hierarchically organised QS systems have been identified in *P. aeruginosa* (*las*, *rhl*, *iqs*, and *pqs*), all showing significant importance in the transcriptional regulation of numerous virulence-related genes. For example, the *las* QS system positively regulates the virulence factors ExoA, LasA, LasB, and Apr (cf. Figure IV.4), while the *rhl* QS activates the expression of LasB, superoxide dismutase, rhamnolipids, the pigment pyocyanin, and biofilm-related genes.[568, 615]

IV.1.2.3 Surface Exposed Virulence Factors

The bacterial OM component and antigen LPS is a major constituent of the membrane and present in all strains of *P. aeruginosa* (cf. Figure IV.4). It is not only auxiliary in cell adhesion to host tissue, but also triggers a strong immune response when extracted from the cell surface by eukaryotic LPS-binding proteins and is recognised by the host immune system.[615] LPS was found to mainly activate two intracellular signalling cascades, namely the Toll-like receptor 4 (TLR4) and the cystic fibrosis transmembrane conductance regulator (CFTR) pathway. Both cascades culminate in the release of proinflammatory cytokines and chemokines, whose expression is controlled by rapid translocation of the mammalian nuclear transcription factor NF-κB into the nucleus, and may cause septic shock when overstimulated and overactivated.[615, 625] Furthermore, several glycopolysaccharide modifications of LPS, called O-specific antigens (OSA), have been shown to protect the bacteria from phagocytosis.[626]

Besides the polysaccharide LPS, *P. aeruginosa* is further equipped with two protein complex appendages that are involved in bacterial movement (cf. Figure IV.4). The flagellum is a motorised tail-like multi-protein complex protruding from the bacterial pole and its portion outside the cell is mainly constituted by the protein filament flagellin from FliC monomers. The protein FliD forms a cap and seals the flagellin filament. Bacterial flagella are essentially involved in chemotaxis and movement, but also play an important role in virulence through immune activation via TLR5.[615] Flagella-deficient strains showed similar dissemination and tissue colonisation to wild-type strains. Still, they were not developing lethal bloodstream infections in a mouse model, as infections with these non-motile mutants remained localised in the infected tissue.[627] Toutain *et al*. could also show that these flagellar stators contribute to polar surface attachment to abiotic surfaces and biofilms.[628] The second type of cell-surface protein complex is the type IV pilus. Pili are fimbriae, hair-like appendages, protruding from the cell surface. Similar to the flagellum, the type IV pilus is a motorised multi-protein complex with pilin proteins (predominantly PilA) on the environmentally exposed portion of the complex. In the past, type IV pili were shown to be important in twitching and smarming motility, helping to disseminate and colonise host tissues in an acute murine infection model with virulent *P. aeruginosa* strains.[629] Furthermore, it is associated with biofilm formation and functions as a primer to attach to surfaces for colonisation.[615] Another very important role of type IV pili is associated with the conjugative transfer of DNA from cell to cell or the uptake of environmental DNA. Carter *et al*. could link this type IV pilus-mediated uptake to the acquisition of the pathogenicity island PAPI-1 (*vide infra*) through a conjugative mechanism.[630]

IV.1.2.4 Secretion Systems and Their Secreted Exoenzymes

Pseudomonas aeruginosa uses certain membrane-spanning protein complexes to secret exoenzyme virulence factors or other effector molecules into the environment or directly into host cells (cf. Figure IV.4). These complexes are termed secretion systems, of which *P. aeruginosa* produces at least five different kinds. The type 1 secretion system (T1SS) resorts to ABC transporter architecture to couple ATP hydrolysis in the cytoplasm to active secretion of virulence factors.[615] With AprA and AprX, two alkaline proteases are secreted via T1SS. Both proteins are involved in the degradation of host complement proteins and cytokines and thereby modulate the immune response.[631] Furthermore, the virulence factor HasAp is secreted via T1SS. This protein is essentially involved in iron acquisition in a host environment with low levels of free iron to sustain functional iron homeostasis during infection. HasAp possesses high binding affinity towards the eukaryotic heme and is thus classified as a hemophore.[632] Heme, in turn, is the most abundant form of eukaryotic iron and is found as a prosthetic group in the protein hemoglobin within erythrocytes.[633] Considering the role of the secreted virulence factors, T1SS contributes to the early inflammation process in the onset of the infection.

The T2SS is needed to secrete major extracellular virulence factors with hydrolytic activity that are, for example, required to impair the membrane integrity of target cells. Currently, two T2SS have been identified in *P. aeruginosa*, showing secretion of numerous highly potent virulence factors. The alkaline phosphatases LapA and LapB are required under phosphate-limiting conditions. Other substrates are the lipases LipA and C, elastases LasA and LasB, exotoxin A (ExoA), protease IV, and hemolytic (PlcH) and non-hemolytic (PlcN) phospholipase C, which are all major virulence factors of the opportunistic human pathogen.[615] Exotoxin A inhibits the eukaryotic translation elongation factor 2 (EF-2), an essential protein factor in protein biosynthesis. Inactivation of EF-2 through ExoA-catalysed ADP-ribosylation leads to an arrest of the host protein biosynthesis.[634] The extracellular protease IV was demonstrated to degrade numerous biologically relevant protein components of the host immune system, for example, complement proteins, immunoglobulins (e.g. antibodies), and fibrinogen.[635] Hemolytic phospholipase C (PlcH) is a direct link to the HspAp effector of the corresponding T1SS. As the iron-containing heme-prosthetic group is protected by the cell wall of erythrocytes from the hemophore HspAp, the hemolytic PlcH with hydrolytic activity against the phospholipids and sphingomyelins disintegrates the eukaryotic membrane and releases its constituents from erythrocytes or other epithelial cells.[636]

The most invasive secretion system is the T3SS. In contrast to T1SS, T2SS, T4SS, and T5SS, the T3SS is not only a two-membrane-spanning complex but a three-membrane-spanning complex that also penetrates the host cell membrane. Thereby, the virulence factors secreted by T3SS are directly injected into the host cell through a needle complex. Virulent effectors secreted by the T3SS are ExoU, ExoS, ExoY, and ExoU, among others.[615] These exotoxins are highly virulent, destructive to the host cell, and subvert the host's immune response. Moreover, ExoU with a phospholipase A2 activity causes severe damage to the cell membrane and is considered the most toxic virulence factor of the secreted T3SS effectors. Both ExoS and ExoT share ADP-ribosyltransferase and GTPase-activating protein activity. Their ADP-ribosyltransferase activity leads to modification of host proteins and a repurposing of their innate cellular functions. Furthermore, the GTPase-activating activity interferes with cellular GTPases and leads to their inactivation. By doing so, ExoS and ExoT disrupt the cytoskeleton and show major effects on associated processes like phagocytosis and cell adhesion. Lastly, ExoY is the least studied exotoxin with adenylate cyclase activity. By modulating the intracellular levels of cyclic AMP, ExoY disrupts cellular signalling pathways in the target cells and modulates its immune response.[637]

The T5SS utilises autotransporters and two-partner secretion systems for the display of effector molecules.[615] One of its substrates is the autotransporter EstA, which is important for the production of rhamnolipids. As the

absence of EstA was connected to reduced rhamnolipid production, impaired swarming and twitching motility, and negatively affected biofilm formation, the role of EstA is linked to diverse virulence mechanisms.[638] Two other effectors secreted via the T5SS are the two-partner secretion systems TpsA and TpsB. While TpsB is the OM β-barrels of this transporter, TpsA is the transported passenger domain, equivalent to the transporter and passenger domains of chimeric autotransporters. The two-partner secretion system is mostly involved in the secretion of very large virulence exoproteins (100–500 kDa), for example, adhesins and cytolysins.[639]

The T6SS is the last secretion system and, similarly to T3SS, it is invasive to host cells by penetration of their membranes. Three hemolysin coregulated secretion islands (H1–3) have been found so far, each showing significant differences from the other two and targeting other aspects of the bacterial interaction with its host.[640] Other than T3SS, T6SS penetrates the cell wall of prokaryotes in addition to mammalian cells to release its effectors with phospholipase D activity. To do so, the H1-T6SS effectors Tse1–3 display bacteriolytic activity as they degrade the PG cell wall.[615] In contrast to this prokaryote-specific mode of action, the respective H2 and H3 effectors PldA and PldB utilise a dual mode with activity against prokaryotic and eukaryotic cells (trans-kingdom effector). PldB in particular exhibited strong activation of the PI3K/Akt pathway, leading to intracellular invasion of the host cell with the microbial intruder via bacterial endocytosis.[615, 640]

IV.1.2.5 Siderophores – Metal Chelators for Trace Metal Acquisition

Especially in the context of eukaryotic infections, the availability of free iron for microbes is intrinsically very low, as metabolically accessible iron is complexed in the eukaryotic proteins transferrin and ferritin or transported in red blood cells through heme.[641, 642] However, iron homeostasis is yet essential for survival of the bacterial perpetrator, as iron ions and ion cofactors are essentially involved in respiration (Fe^{2+}-heme-containing cytochrome), DNA replication and repair (Fe-S-clusters in DNA helicase), oxidative stress protection (Fe-superoxide dismutase), and the Krebs cycle (Fe-S-clusters in aconitase, succinate dehydrogenase, and fumarase).[643-646] For this reason, *P. aeruginosa* produces and secretes two major classes of siderophores to sequester the growth-limiting metal iron from its environment.[647] These siderophores are potent virulence factors and metal chelators that bind iron in its Fe^{3+} form with high affinity before they are transported back into the cell.[646] The cellular import of ferric siderophores is realised via conserved import machineries and specific cell-surface receptors that enable intracellular enzymatic reduction of Fe^{3+} to Fe^{2+} upon import. The two iron siderophore classes of *P. aeruginosa* comprise the extended group of fluorescent and high-affinity pyoverdine (Pvd) siderophores and the small molecule and secondary siderophore with lesser binding affinity and binding promiscuity called pyochelin (Pch).[646, 648] The third metallophore called pseudopaline is actually less involved in iron acquisition and acts as a narrow-spectrum ion chelator that primarily complexes zinc, nickel, and cobalt ions.[649, 650] Besides its role as a virulence factor, which enables *P. aeruginosa* to sequester iron in a hostile host environment, Pvd is also involved as a signalling molecule in the production of other virulence factors. Upon recognition of Pvd-Fe^{3+} (ferripyoverdine) at its outer membrane receptor, the alternative extracytoplasmic σ-factor PvdS is activated. PvdS directs the RNA polymerase to genes needed for iron acquisition but is also a key regulator in the expression of *toxA* and *prpL*, the genes encoding *P. aeruginosa*'s EF-2 inhibitor ExoA and the extracellular protease PrpL. Thus, the siderophore Pvd is a direct link between iron acquisition, quorum sensing, and the virulence displayed by pathogenic strains of *P. aeruginosa*.[651, 652]

To date, more than 100 pyoverdines have been identified from different fluorescent Pseudomonads.[653] All pyoverdines have a fluorescent dihydroxyquinoline chromophore core in common, which is further decorated with α-ketoacids from the Krebs cycle and unique linear or cyclic 6–14 amino acid peptides. The peptide composition and architecture are strain specific and dictate the siderophore receptor, which is needed for the uptake of the

Pvd-Fe^{3+} (ferripyoverdine) complexes into the bacterial cell. Within strains belonging to the species *P. aeruginosa*, three distinct classes of Pvd siderophores have been found, namely class I, II, and III, but every strain exclusively produces only one class.[647] These classes are inevitably linked with the β-barrel outer membrane siderophore transporters that are recruited for their uptake. The model strain PAO1 produces Pvd I and utilises the ferripyoverdine type I receptor FpvAI for its uptake. Similarly, class II pyoverdines are taken up via FpvAII and class III pyoverdines through FpvAIII, while Pch exploits the FptA receptor.[647, 654] Although another FpvB transporter has been linked with Pvd I uptake, this protein has been shown to be less effective than FpvA-type β-barrels.[647] All β-barrel siderophore transporters require a conserved machinery for the active import of iron-loaded siderophores from the external environment into the periplasm. This machinery is the membrane-spanning energy-transducing Ton machinery with its central protein TonB1 that harvests energy from the proton motive force (PMF) at the inner membrane and converts this ion potential into force and protein motion for energisation of the ATP-free periplasm and the outer membrane (*vide infra*).[642, 655, 656] All β-barrel outer membrane proteins (OMPs) involved in siderophore import are TonB-dependent transporters (TBDTs) that share a common TonB box in the *N*-terminal plug domain. The TonB box is a loosely conserved sequence of all TonB-dependent proteins with a high conservation of a β-strand formation potential allowing for the interaction with the periplasmic portion of TonB1 via a temporally formed interprotein β-sheet that is needed for a stroke-motion that induces conformational changes in the transporters (*vide infra*).

IV.1.2.5.1 Exploitation of Siderophore Uptake Mechanisms for the Channelling of Drugs into the Bacterial Cell

Bacterial siderophores are considered public goods, as some strains produce these iron chelators and others do not. As long as strains express the proteins needed for siderophore uptake, they can profit from the secretion of siderophores within the bacterial community. Similarly, siderophores can be used as microbial weapons to withhold iron from co-cultivating eukaryotic or microbial competitors that lack iron uptake mechanisms.[657] Furthermore, *P. aeruginosa* uses xenosiderophores for the acquisition of iron from its environment. The Pseudomonads are not able to produce these xenosiderophores themselves but have developed transporters for their uptake from the environment. Examples for xenosiderophores used by *P. aeruginosa* are enterobactin and ferrichrome siderophores, among others.[658-660] Although the role of xenosiderophores in microbial signalling and community dynamics during infections is still unexplored, the expression of xenosiderophore uptake systems also increases the repertoire of addressable targets for “Trojan Horse Strategies” to combat antimicrobial resistance. The Trojan Horse Strategy refers to the channelling of drug conjugates into the cell and circumvention of drug repulsion by efflux pumps, by utilising nature’s own recognition patterns.[658] The precious and essential character of siderophores for bacteria to counter iron limitation makes their import mechanism a promising target for drug import. This is why the essentiality of siderophores for iron homeostasis during infections has not gone unnoticed by nature and researchers, too. Naturally, antimicrobial peptides of bacterial origin (bacteriocin) are known to hijack siderophore transporters in the outer membrane by mimicking the binding mode of siderophores (*vide infra*).[661, 662] Moreover, nature has developed covalent conjugates of siderophores and antibiotics, so-called sideromycins. These sideromycins apply the Trojan Horse Strategy to channel unnoticed into the bacterial cell. By exploiting the selective and, more importantly, active uptake via siderophore transporters, the drug trafficking is more efficient than by using unspecific diffusion through outer membrane porins. The first identified and characterised representatives from this group are albomycins, a group of sideromycins from *Streptomyces*. Albomycin δ_2 utilises a ferrichrome siderophore and the thioribosyl pyrimidine antibiotic SB-217452, which inhibits the seryl-tRNA-synthetase of the target cell upon peptidase-cleavage from the siderophore carrier.[663] Researchers have already tried to emulate this Trojan Horse Strategy to make covalent conjugates of the

P. aeruginosa siderophores Pvd or Pch. Back in 1998, Kinzel *et al*. developed covalent conjugates of Pvd I and Pvd II with the β-lactam antibiotic ampicillin to which *P. aeruginosa* is inherently resistant (MIC >100 μM). The conjugates showed promising biological activity at minimal inhibitory concentrations between 0.024–0.39 μM and indicated utilisation of the corresponding FpvA-type receptors for directed uptake of the siderophore conjugates.[664, 665] For the small-molecule siderophore Pch, numerous conjugates have been synthesised with hydrolysable and non-hydrolysable linkers. For example, Pch conjugates with the antibiotics *N*-desmethyl-ofloxacin, ciprofloxacin, and norfloxacin reduced the growth of *P. aeruginosa* but were still less active than the free antibiotics. This observation of no biological activity or reduced activity compared to the free antibiotics has been common for all reported Pch conjugates, even though specific transport via the FptA receptor was shown.[658, 666] Just recently, another protein involved in siderophore uptake was identified as a novel bacterial target for antimicrobial agents, namely TonB. Peukert *et al*. developed artificial NECAM- and DOTAM-based siderophores and coupled these with peptides that resemble the TonB box. Upon TonB-mediated import of the peptide-NECAM/DOTAM conjugates through the PfeA and PirA receptors, TonB1 is inhibited by competitive binding of the peptide portion and cell suicide is induced at 0.1–0.5 μM conjugate concentrations.[667] Although none of the siderophore conjugates showing biological activity against *P. aeruginosa* have made it into application so far, the immense number of TBDTs and siderophores makes the Trojan Horse Strategy an appealing target for drug delivery at the present time.

IV.1.3 Research on Alternatives for Common Antibiotics Against *Pseudomonas aeruginosa*

IV.1.3.1 Bacteriocins – Narrow-Spectrum Antimicrobial Peptides as Extension to Antibiotics?

A long-known and often discussed alternative to common β-lactam, sulfonamide, or aminoglycoside antibiotics are so-called bacteriocins.[668] Bacteriocins are antimicrobial peptides and proteins produced by Gram-positive and Gram-negative species of all kinds for the purpose of intraspecies competition.[669-671] Depending on their size and constitution, they can be synthesised via the ribosomal protein synthesis machinery or by non-ribosomal peptide synthesis. Other than most typical antibiotics, bacteriocins are highly target-specific and are considered as narrow-spectrum antibiotics, killing closely related species from the same genus (colicins from *E. coli* kill *E. coli*, pyocins from *P. aeruginosa* kill *P. aeruginosa*, klebicins from *K. pneumoniae* kill *K. pneumoniae,* etc.).[541, 672-674] Interestingly, bacteriocins of Gram-positive species readily find broad application in food industries for preservation (e.g. nisin or enterocins),[675, 676] while bacteriocins of Gram-negative organisms lack proof of applicability so far.[677] Nevertheless, their narrow antimicrobial spectrum in conjunction with their distinct cytotoxic mechanism from common antibiotics makes these proteins and peptides interesting candidates to fight the globally growing concern of antimicrobial resistance to common antibiotics.

IV.1.3.1.1 Pyocins – The Bacteriocins of *Pseudomonas aeruginosa*

In 1954, François Jacob observed the production of an inducible compound upon treatment with ultraviolet light in *P. aeruginosa*. This compound was able to adsorb to the cell surface of sensitive strains of *P. aeruginosa* and induced their killing. Consequently, this finding marks the hour of birth for the antimicrobial peptides named pyocins[5], by analogy with antimicrobial peptides from *E. coli*, named colicins.[661, 678] The genome-encoded pyocin-type bacteriocins of *P. aeruginosa* are narrow-spectrum antibacterial proteins, which can be subdivided into different groups (R-, F-, L-, M-, and S-type) with varying architecture, size, and modes of action.[661, 679-681] R-Type

[5] Between 1870 and 1940 several binomial names were used for the same bacterium. *Pseudomonas aeruginosa* was introduced by Schröter in 1872 and is nowadays the predominant binomial name. The name *Pseudomonas pyocyanea* that was introduced by Zopf in 1884 was used contemporaneously and explains the denotation of pyocins rather than aeruginocins.

and F-type bacteriocins (tailocins) resemble the tail of bacteriophages and appear as microscopic particles. Both types of pyocins are protease- and nuclease-resistant but differ in their morphology. While R-type pyocins are rod-like contractile polymeric structures with a contractile sheath, the F-type pyocins appear as contorted non-contractile rod-like structures (Figure IV.5).

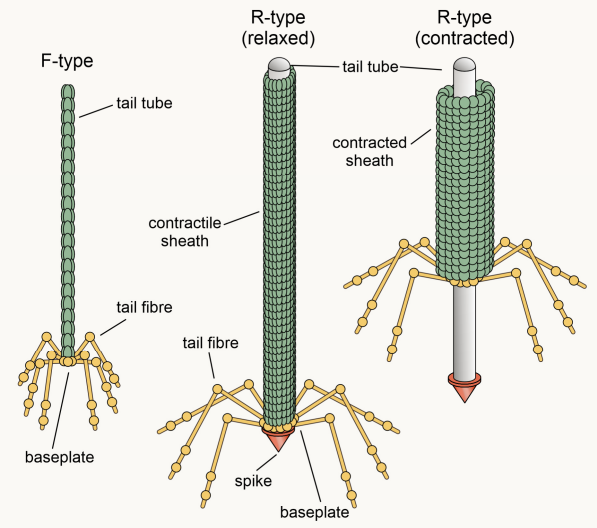


Figure IV.5. Macromolecular assemblies of F- and R-type pyocins (tailocins). Comparison of non-contractile rod-like F-type pyocins and the contractile rod-like R-type pyocins, both resembling the tail of bacteriophages. Figure design inspired by Michel-Briand *et al*.[661]

Although these types of pyocins resemble phages and their mechanism of cell entry, bacteriocins in general are only made of proteins and do not replicate within target cells. However, it is believed that R- and F-type pyocins originate from defective phages or phage tail structures and have evolved to become protein-based bacteriocins.[682] The outer membrane constituent LPS was shown to be the primary receptor for R-type pyocins,[683] with one L-rhamnose and two D-glucose residues of the outer core being essentially involved in the binding of pyocin R1, R2, and R5.[684] However, it is still unclear whether LPS remains the only receptor necessary for initial cell binding for R-type pyocin adsorption. Susceptibility studies with strains of *P. aeruginosa* with known O-serotypes recently suggested involvement of LPS in the binding of F-type pyocins, as some O-serotypes rendered bacterial killing while others did not. But admittedly, it remains unclear whether this is due to true binding of F-type pyocins to LPS or caused by denser packing of the LPS that renders the surface less accessible for pyocin entry into the cell.[685] Uratani and Hoshino were able to elucidate the mode of action of R-type pyocins on the example of pyocin R1. Upon binding to the sensitive receptor cell, pyocin R1 inserts into the cytoplasmic membrane and causes the formation of pores that puncture the membrane and cause an efflux of cellular ingredients. This permeabilisation is accompanied by a horrendous depolarisation of the membrane of >90 mV.[686] A comparative study between R-type pyocins was moreover able to identify an immediate arrest of protein and nucleic acid biosynthesis as primary targets for the toxic phage tail-like proteins.[687, 688] The mode of killing action for F-type pyocins remains mostly undetermined and killing specificity determinants remain to be elucidated,[685] but it is widely accepted that F-type bacteriocins dissipate membrane potentials as well. As these bacteriocins lack a contractile sheath and a single particle is enough to kill a bacterium, it was assumed that these hollow protein particles spontaneously integrate into the inner membrane to form pores that allow the uncontrolled efflux of ions.[675, 689]

The third class of bacteriocins from *P. aeruginosa* are L-type pyocins. L-Type bacteriocins are lectin-like proteins of medium size (approx. 30 kDa), harbouring two tandem monocot mannose-binding domains and lacking an apparent killing domain. Therefore, the lack of a killing domain obliterates the need for the co-expression of protective immunity protein.[690] As lectins are sugar-binding proteins, L-type pyocins of class A and B are characterised by a high binding affinity towards D-rhamnose, a sugar constituent of the common polysaccharide antigen (CPA).[690, 691] The CPA is similar to the O-specific antigen (OSA), an alternative cap for the LPS of Pseudomonads, and is built from repetitive D-rhamnose units. Thence, the cell surface-exposed CPA is an important structural motif for the binding of antibodies and other cell-targeting agents. While many other bacteria produce the OSA and display it on their cell surface, CPA is a structurally unique homopolymer and is only present in *P. aeruginosa*.[692] Two lectin-binding motifs in the C-terminal tandem of lectin L1 from *P. aeruginosa* were shown to bind the CPA for initial adsorption to the target cell,[693] but binding was not affected by the specific O-serotype of the targeted strains.[680] However, deletion of the C-terminal domain (CTD) did not fully lead to the abolishment of L-type pyocin killing activity, indicating a second cellular target different from LPS.[694] Ghequire *et al*. were able to identify this secondary cellular receptor of pyocin L1, the essential β-barrel assembly machinery (BAM) in the outer membrane. The BAM complex, composed of lipoproteins BamB, BamC, BamD, BamE, and the central outer membrane β-barrel insertase BamA, is an essential machinery of Gram-negative bacteria to integrate and fold newly synthesised OMPs into the outer membrane. Bactericidal activity of pyocin L1 involves binding of its N-terminal mannose-binding domain to the polymorphic external loop L6 of BamA, as frequent mutations in loop L6 lead to resistance to pyocin L1 and protect producing strains from bactericidal activity of L-type bacteriocins.[695] Although the central question about a detailed mode of bacterial killing for L-type pyocins remains unanswered, induction of cell envelope stress and morphological changes induced by an inhibition of BamA-mediated OMP insertion into the outer membrane have been suggested by studies with homologous lectin-like bacteriocins from *Bacteroidales* species.[696]

The fourth class of bacteriocins from *P. aeruginosa* are M-type pyocins that are typically encoded within the ExoU island A.[679] Their name originates from sequence and structural homology to the C-terminal cytotoxic domain of colicin M, a bacteriocin from *E. coli*, which inhibits the biosynthesis of PG and the OSA and thereby induces cell lysis.[679, 697] In detail, M-type pyocins are not able to hydrolyse PG and act more like β-lactam antibiotics that inhibit the biosynthesis of PG by interfering with essential steps of its synthesis. And yet, the modes of action of β-lactams and M-type bacteriocins are essentially different. While β-lactams inhibit the DD-transpeptidase for PG crosslinking (cf. Figure IV.3), M-type bacteriocins degrade the PG precursor lipid II by enzymatic hydrolysis. Lipid II is the cell wall/PG precursor of Gram-negative bacteria, which consists of a phosphorylated NAG-NAM-(pentapeptide) disaccharide with a bactoprenol hydrocarbon chain that anchors the lipid II building block in the bacterial inner membrane (Figure IV.6). ColM family bacteriocins exhibit hydrolytic activity and cleave off the phosphate ester adjacent to the bactoprenol alcohol. By reducing the availability of lipid II for PG biogenesis during cell division, the M-type pyocin-treated cells are no longer able to reproduce and consequently die.[698] M-Type pyocins are far less widespread among the genus of Pseudomonads than other pyocins and show a modular domain organisation, similar to other colicins and S-type pyocins. Their N-terminal domains (NTDs) are needed for receptor binding and translocation across the outer membrane and their C-terminal killing domain harbours the cytotoxic potential. Similar to most S-type pyocins, M-type pyocins hijack TonB-dependent β-barrel proteins for their entry into the cell. On the example of pyocin M4, the TonB-dependent heme receptor HxuC was shown to be the OM receptor that is needed to display cytotoxic activity.[681] Other M-type pyocins (M1 and M2) require the ferrichrome xenosiderophore transporter FiuA for the uptake of the bacteriocin.[699] As M-type pyocins are highly potent toxins, PyoM-producing cells protect themselves by the co-expression of immunity proteins that bind and neutralise the toxin. Although pyocin M4 is secreted, the membrane topology of its immunity protein PmiC

implies permanent residence in the bacterial membrane. Similar modes of action are also known from the pore-forming pyocin S5 and its immunity protein. but are generally less common among S-type pyocins or other colicin M homologues from the ColM family.[681]

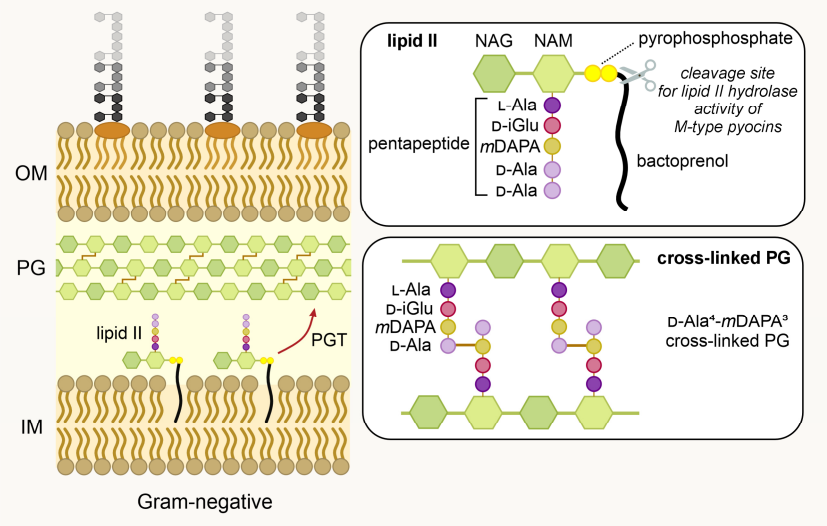


Figure IV.6. Inhibition of cell wall biosynthesis by M-type pyocins. The hydrolytic activity the C-terminal cytotoxic domain of M-type pyocins cleaves the PG precursor lipid II and releases the disaccharide-pentapeptide from the bactoprenol membrane anchor. In an intact PG biosynthesis, the disaccharide NAG-NAM-pentapeptide is transferred from the bactoprenol donor to the PG chain via peptidoglycan glycosyltransferases (PGTs). Without the bactoprenol donor chain (e.g. caused by hydrolytic activity of the ColM family), PGTs do not catalyse the transfer of NAG-NAM-pentapeptide onto the nascent polymer of PG. For a direct comparison of lipid II and the final cross-linked PG, both structures are shown in the figure, although the ColM family does not degrade cross-linked PG. Abbreviations: IM – inner membrane; OM – outer membrane; PG – peptidoglycan; PGT – peptidoglycan glycosyltransferase.

IV.1.3.1.2 S-Type Pyocins

S-Type pyocins (PyoS) are the fifth and last class of currently described bacteriocins from *P. aeruginosa* and represent the best studied class of pyocins from mechanistical and structural perspectives. The soluble and protease-susceptible S-type pyocins share similar modular domain organisation and high structural congruency, even though sequence similarity on the amino acid sequence level can be quite low.[661, 669] The toxic multi-domain proteins are segmented into three domains, harbouring receptor-binding and translocation potential in the three N-terminal domains and killing activity in the cytotoxic CTD. To protect themselves from the cytotoxic pyocin activity, PyoS-producing strains co-express certain immunity proteins that bind the respective cytotoxic domain with ultra-high-affinity and confer resistance to the producing cell.[700, 701] Various types of killing activity have been described so far, of which most rely on nuclease activity (DNase, tRNase, rRNase) that causes a breakdown of nucleic acid metabolism within the target cell. Furthermore, PyoS5 and PyoSX2 have been shown to exploit pore-forming activity in the inner membrane to deplete the PMF or inhibit protein biosynthesis, respectively. To date, 17 S-type pyocins have been experimentally validated or predicted from genome analysis of *P. aeruginosa* isolates, of which most are utilising the conserved TonB-mediated translocation across the outer membrane, similar to group B colicins (Table IV.1).[669, 702-711]

Table IV.1. Experimentally validated and predicted S-type pyocins, their outer membrane (OM) receptors, and the pathway of translocation.

Pyocin	Killing Activity	OM Receptor	Translocation pathway	Reference
PyoS1	DNase (HNH)	unknown	TonB1-dependent	[712]
PyoS2	DNase (HNH)	FpvAI	TonB1-dependent	[712-714]
PyoS3	DNase	FpvAII	TonB1-dependent	[708, 715]
PyoS4	tRNase	FpvAI	TonB1-dependent	[705, 716]
PyoS5	pore-forming	FptA	TonB1-dependent	[717-719]
PyoS6	rRNase	unknown	unknown	[709]
PyoS7*	rRNase	FpvAI†	TonB1-dependent	[669]
PyoS8	DNase (HNH)	unknown	unknown	[710]
PyoS9**	DNase (HNH)	unknown	unknown	[669]
PyoS10***	DNase	unknown	unknown	[669]
PyoAP41	DNase (HNH)	unknown	Tol-dependent	[720]
PyoG	nuclease	Hur	TonB1-dependent	[706]
PyoSX1	DNase (HNH)	CrtA	TonB1-dependent	[707]
PyoSX2	inhibition of protein synthesis	CrtA	TonB1-dependent	[707]
PyoS11/PyoSD2	tRNase	FpvAI	TonB1-dependent	[711]
PyoS12/PyoSD3	tRNase	FpvAII‡	TonB1-dependent	[711]
PyoS13/PyoSD1	tRNase	unknown	TonB1-dependent	[711]

* Predicted from *P. aeruginosa* BWHPSA018; not experimentally validated. † As the first 464 amino acids are identical to PyoS2 from *P. aeruginosa* PAO1, FpvAI must be the OM receptor protein of PyoS7.

** Predicted from *P. aeruginosa* BL04.

*** Predicted from *P. aeruginosa* PABL056.

‡ The high sequence homology between the N-terminal domains of PyoSD3 and PyoS3 suggests translocation via the FpvAII siderophore receptor. However, experimental proof is missing.

IV.1.3.1.2.1 S-Type Pyocins Share Conserved Mechanisms of Translocation

All experimentally validated S-type pyocins, except pyocin AP41, utilise TonB-dependent OM transporters for their translocation across the bacterial OM into the periplasm (cf. Table IV.1, Figure IV.7). The two N-terminal domains, consisting of tandemly repeated kinked three-helix bundles, do not exhibit intrinsic catalytic activities but are yet essential for species- and porin-selective hijacking of specific outer membrane proteins and recruitment of energy-transducing protein complexes (Ton or Tol),[712, 721-723] which are highly conserved but only occur in Gram-negative bacteria. The Ton machinery of Gram-negative bacteria is composed of three protein components: ExbB, ExbD, and TonB. Although the involved proteins have been known for many years, the underlying mechanism and stoichiometry that allow harnessing the PMF across the inner membrane into energy-coupled transport are still not fully resolved and have been mostly gathered from studies with the TonB homologue from *E. coli*.[656, 724] All three proteins of the Ton complex contain transmembrane domains and permanently reside in the inner membrane. Only TonB exhibits a membrane-spanning C-terminal extension that reaches deep into the periplasm and is needed for the PMF-dependent interaction with other proteins at or in the OM.[656] Recent cryo-electron microscopy studies with ExbB/ExbD homologues from *Pseudomonas savastanoi* suggested that the transmembrane helix of two ExbD proteins is surrounded by transmembrane helices of five ExbB proteins. As all Ton homologues show a conserved aspartate residue in the transmembrane helix of ExbD, it was assumed that repeated protonation/deprotonation of this particular residue drives a rotational movement of ExbB proteins around the two ExbD units.[656, 724] Since the PMF is generated through a high proton concentration in the periplasm and a low proton concentration in the cytoplasm, the motor movement is unidirectional and the proton flux is always directed inwards towards the cytoplasm. How this motor movement is connected to pull movements and structural changes of TonB is the matter of current research, but it was assumed that TonB is associated with

ExbB and rotates with the motor, thereby causing movement of the C-terminal TonB domain, which interacts with TBDTs and bacteriocins.[656]

Pyocin S2 with its HNH nuclease-fold DNase domain is the only S-type pyocin of which a truncated protein variant has been co-crystallised with its primary TonB-dependent porin receptor, namely FpvAI (PDB 5ODW).[662] Interestingly, FpvAI functions in this context as a primary receptor and translocator for the uptake of PyoS2 into the cell (Figure IV.7), while other bacteriocins use certain OMPs as primary receptors and other OMPs as translocators.[662, 725] The ferripyoverdine type I receptor FpvAI is a β-barrel OMP made of 22 anti-parallel β-strands and exhibits a plug domain on the periplasmic side of the barrel that seals the porin. For active transport of the ferric siderophore, binding of the siderophore ligand induces structural changes in FpvAI, which uncover the TonB box within the plug domain.

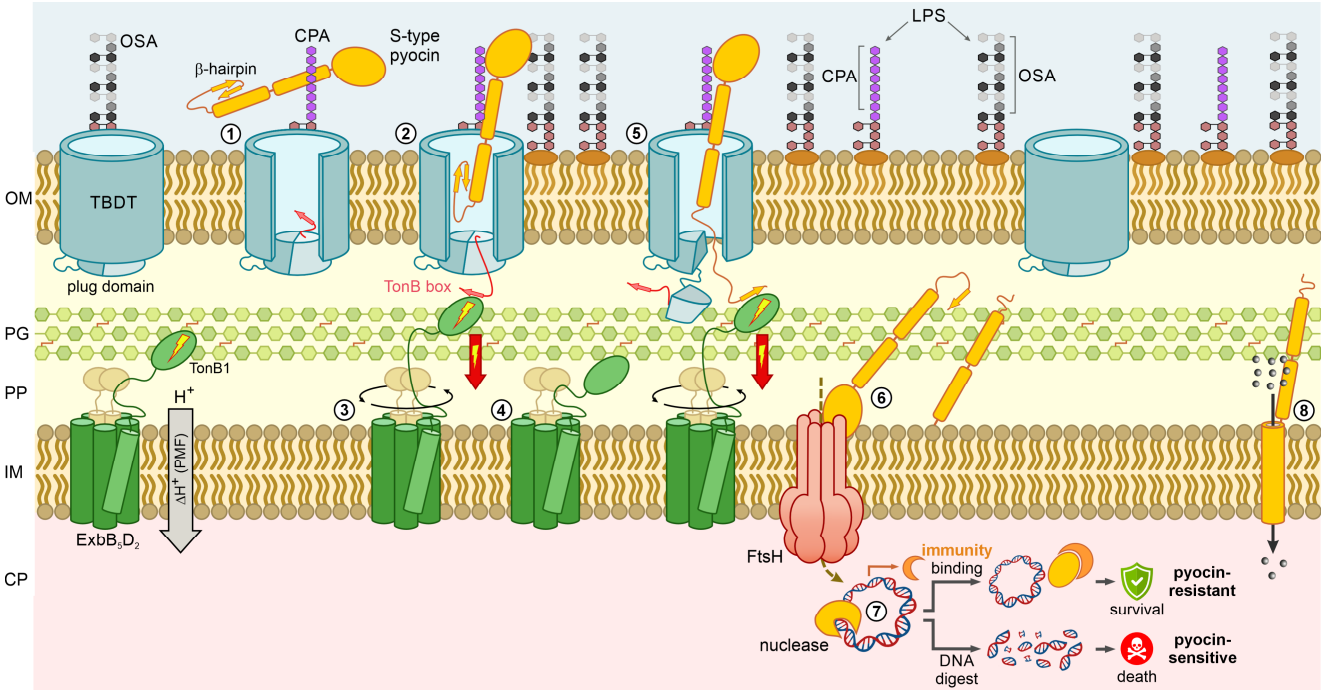


Figure IV.7. Import mechanism of Ton-dependent S-type pyocins into susceptible cells of *P. aeruginosa*. Most pyocins are imported via the conserved TonB-dependent pathway that exploits TBDTs as OM receptors and translocators across the OM and the PMF-dependent Ton machinery in the IM for active import. **1**. The flexible N-terminus of S-type pyocins is folded in a β-hairpin and docked to the bundle of helix I and V of the bacterial toxin. The TBDT is plugged on the periplasmic side through a plug domain that contains a force-resistant (blue) and force-labile (light blue) subdomain. The TonB box within the plug domain is buried in the lumen of the TBDT. **2**. Pyocin binding to the primary TBDT receptor and the CPA antigen induces conformational changes in the plug domain, uncovering the TonB box. **3**. The periplasmic portion of TonB1 from the Ton machinery is recruited and interacts with the TonB box of the TBDT through β-augmentation. Movement of the Ton motor removes the force-labile subdomain of the TBDT plug. **4**. Discharged TonB1 is recharged for subsequent motor movement. **5**. The flexible N-terminus of the S-type pyocin enters the periplasm and its TonB box aligns with the periplasmic portion of TonB1 through β-augmentation. Movement of the Ton motor drags the pyocin through the pore of the TBDT for translocation of the toxin into the target cell's periplasm. **6**. For nuclease pyocins, the IM AAA^+ protease FtsH cleaves the C-terminal cytotoxic domain from the helical receptor binding and translocation domain in an unknown mechanism. Only the nuclease domain is guided into the cytoplasm. **7**. The nuclease domain (DNase, tRNase, or rRNase) displays cytotoxic activity by hydrolytic cleavage of intracellular nucleic acids. Cognate immunity proteins can neutralise the toxin. **8**. The pore-forming PyoS5 can form pores in the inner membrane, causing a breakdown of the PMF through proton flux along the concentration gradient from the periplasmic space into the cytoplasm. Abbreviations: CP – cytoplasm; IM – inner membrane; LPS – lipopolysaccharide; OM – outer membrane; PG – peptidoglycan; PMF – proton motive force; PP – periplasm; TBDT – TonB-dependent transporter.

The TonB box is a short peptide sequence of 5–10 amino acids with relatively low conservation on a sequence level but very high conservation of the secondary structure.[656] This TonB box inherent structure is immanent for all TBDTs and TonB itself and mediates the interaction between TBDTs that allows for coupling of physical protein movement to the PMF. Once the TonB box is uncovered, the periplasmic CTD of *P. aeruginosa* TonB1 is recruited to the transporter to first remove force-labile portions of the FpvAI plug domain by a force-dependent motion and, in a second step, to import the FpvAI-bound ligand. White *et al*. could show that a proline-rich region (residues 35–45) on the unstructured N-terminus of PyoS2 mimics the structure and the binding mode of the ferripyoverdine siderophore to FpvAI and thereby induces the same structural changes in the FpvAI plug domain. However, PyoS2 binds FpvAI with an extraordinary affinity of 240 pM, which outcompetes binding of the native ferripyoverdine ligand. Removal of the force-labile subdomains within the FpvAI plug domain allows the N-terminal portion of PyoS2 to partially thread into the FpvAI lumen but does not allow complete transit. The N-terminal portion of PyoS2 contains the putative TonB box (^{11}MVITH^{15}) and is usually located in the first of two β-strands that fold into an anti-parallel β-hairpin and burrow into a helical bundle of helix I and V of PyoS2, which is surmised to stabilise the highly flexible N-terminus and promote availability for TonB1 recruitment.[662] From structural analyses with other TBDTs, it is known that the central β-sheet from the periplasmic CTD of TonB interacts with the TonB box of these proteins in a process called β-augmentation. β-Augmentation refers to the attachment of the TonB box β-strand to the β-sheet of TonB1, resulting in a stable mixed 4-stranded β-sheet with a parallel interprotein β-sheet between TonB1 and the TonB-dependent receptor.[642] Therefore, it is very likely that the N-terminal β-hairpin extends into the periplasm through the opened FpvAI pore and allows the interaction with the Ton machinery via the described interprotein interaction for translocation. A direct comparison of the unplugged FpvAI pore diameter (ca. 13 Å) and the diameter of the DNase domain of PyoS2 reveals that folded PyoS2 cannot pass the pore, even with active TonB-mediated transport. Therefore, it was hypothesised that PyoS2 undergoes partial unfolding while it is dragged by the Ton complex through the pore of FpvAI into the periplasmic space.[662, 674, 719] However, as the CTD of PyoS2 displays DNase activity, it can only unleash its cytotoxic power after refolding and translocation into the DNA-containing cytoplasm of the target cell.

In fact, PyoS2 is only one of hundreds of nuclease bacteriocins found in the bacterial kingdom, but their import mechanisms are still not fully understood. Especially the traverse of the inner membrane is an enigma. Although nuclease bacteriocins may share an overall low sequence conservation, a bioinformatic pipeline analysis of 3094 annotated and predicted nuclease bacteriocins identified a DPY sequence (D-X_4-FP-X_8-Y) between the middle and the C-terminal cytotoxic domain that is common to all nuclease bacteriocins.[726] However, the DPY sequence is the only unrestrictedly conserved motif among all nuclease bacteriocins. Together with the fact that the DPY motif lies directly upstream of the CTD, the only domain which is translocated into the periplasm of the target cell, this implies involvement of the DPY motif in the translocation of the CTD across the inner membrane. In 2007, it was shown that membrane translocation of nuclease colicins across the inner membrane is independent of the Sec and Tat translocon and involves the bacterial AAA$^+$ ATPase and protease FtsH instead.[727] From all five ATP-dependent AAA$^+$ proteases in *E. coli*, FtsH is the only essential protease and is structurally unique due to its anchoring in the cytoplasmic membrane.[728] In pathogenic strains of *P. aeruginosa*, FtsH is not only crucial in lipid metabolism through involvement in LPS maturation or degradation of misfolded inner membrane proteins or soluble σ-factors, but also for bacterial virulence, the formation of biofilms, or the production of secondary metabolites.[729] Although the involvement of FtsH in nuclease bacteriocin processing and translocation has been proven undoubtedly, it remains unclear how processing is mechanistically realised. Walker *et al*. suggested a charge-dependent partitioning of nuclease bacteriocins into the inner membrane, mediated by a net positive charge of the C-terminal nuclease domain.[727] The membrane penetration might facilitate entry of the C-terminal killing domain of bacteriocins into the axial cytoplasmic substrate channel of FtsH, enabling protein translocation

through an unfolding/translocation module into the FtsH degradation chamber and its controlled degradation through the FtsH M41 peptidase domain.[729] Afterwards, refolding of the nuclease domain in the cytoplasm of the target cell would be required to fulfil its cytotoxic activity. Once translocated all the way through the bacterial cell wall, the HNH endonuclease domain of PyoS2 rapidly degrades chromosomal and plasmid DNA, inducing the cellular DNA damage sensing SOS response and lastly causing cell death.[730, 731] The biggest portion of eight S-type pyocins exhibits DNase activity, of which six (S1, S2, S8, S9, AP41, SX1) share the conserved HNH DNase fold. Other mechanisms of cytotoxic activities displayed in the cytoplasm of target cells are tRNase activity (S4, S11, S12), rRNase activity (S6, S7) and inhibition of the protein biosynthesis (SX2) (cf. Table IV.1). The exclusive appearance of Ton- or Tol-related protein import, the high strain and sequence specificity of TonB boxes and TBDTs, and the intrinsic killing activity make these bacterial toxins interesting narrow-spectrum candidates as alternatives to common antibiotics and to fight multidrug-resistant clinical strains of *P. aeruginosa* against which other therapeutics have already failed.

IV.1.3.1.2.2 Bacterial LPS Acts as Secondary Receptor of S-Type Pyocins

S-Type pyocins are segregated into multiple domains, which serve distinct functions in cell adsorption, translocation, and cytotoxicity (Figure IV.8). While the domain with inherent cytotoxic activity is located at the C-terminus of the protein, the N-terminus is composed of two tandemly repeated N-terminal kinked three-helix bundle domains. All nuclease pyocins, which require import into the bacterial cytoplasm to unleash cytotoxic activity, additionally comprise a fourth domain. This fourth domain lies between the second kinked three-helix bundle domain and the C-terminal nuclease domain and is required for FtsH processing at the IM. Compared to many colicins, S-type pyocins display a quite distinct and unique fold, which can be attributed to the OM membrane organisation of *P. aeruginosa*.

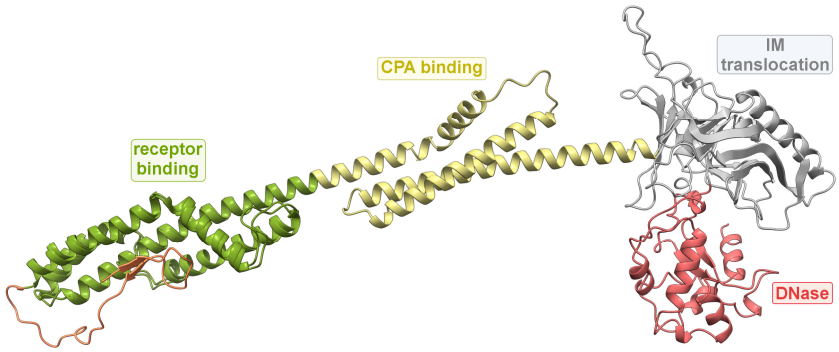


Figure IV.8. Cartoon model of full-length PyoS2 (74 kDa) representing the multi-domain organisation of S-type pyocins. The PyoS2 AlphaFold model (AF-A0A485ENN0-F1-model_v4) is aligned with the NTD of PyoS2 from the crystal structure of the PyoS2/FpvAI complex (PDB 5ODW). The AlphaFold model is the only available full-length model of PyoS2, however, the flexible N-terminus is missing. Therefore, the NTD of PyoS2 was aligned with an RMSD of 1.26 Å to visualise the docking of the TonB box-containing β-hairpin (salmon pink) to helix I and V of the NTD (olive green). The PyoS2 receptor-binding domain (residues 50–195, mint green),[662] the CPA-binding domain (residues 196–320, light khaki),[719] the inner membrane translocation domain (residues 320–556, grey),[732] and the C-terminal HNH DNase domain (residues 557–689, forest green) of the AlphaFold model are explicitly depicted.[701]

Particularly, the second kinked three-helix bundle domain is structurally conserved among S-type pyocins, as this latter inactive domain is instead responsible for recognition and binding of a secondary pyocin receptor on the cell surface. Although the cell surface displayed OMPs were previously introduced as primary cell surface receptors

and translocators, another structure on the cell surface of *P. aeruginosa* plays an important role in tight cellular binding of pyocins; the glycosylated LPS on the cell surface functions as a secondary receptor of many tailocins and S-, L-, and M-type pyocins to enhance their cellular adsorption and facilitate the cellular entry through the translocator.[687, 693, 711, 719] As bacterial LPS is an inhomogeneous mixture of lipopolysaccharides carrying branched polysaccharides with varying architecture and constitution (CPA and OSA[6]), McCaughey *et al*. were able to identify the D-rhamnose-containing CPA of *P. aeruginosa* as the secondary receptor of PyoSD2 and PyoSD3. PyoSD2 and SD3 are structural homologues of the N-terminus of PyoS2 and S3, respectively, and utilise a tRNase cytotoxic domain with homology to colicin D.[711] Similarly, PyoS5-susceptible *P. aeruginosa* PAO1 was becoming resistant when lacking a functional copy of *rmd*,[719] a reductase essential for the biosynthesis of GDP-D-rhamnose as a nucleotide sugar precursor of the CPA in *P. aeruginosa*.[692] Additional *in vitro* isothermal titration calorimetry binding studies with full-length PyoS5 and isolated mixtures of CPA and OSA proved binding of CPA with nanomolar affinities, but no binding for the OSA isolated from the PAO1 *Δrmd* mutant (serotype O5).[719] As the D-rhamnose-containing cell surface glycopolymer CPA is a unique trait only present in *P. aeruginosa*, the CPA-binding domain of S-type pyocins is similarly a structurally unique feature of bacteriocins from *P. aeruginosa* and not present in any other class of bacteriocins (colicin, klebicins, etc.). In combination with the strain-specific TonB box consensus sequence and the exclusive appearance of certain TBDTs in the OM of *P. aeruginosa*, these three bacteriocin-interacting cellular constituents are the molecular explanation for the narrow-spectrum activity of S-type pyocins against *P. aeruginosa*, while other γ-proteobacteria (e.g. *E. coli*) are left unharmed.

IV.1.3.1.2.3 Pyocin S2 Binds its Immunity Protein S2 with Ultra-High-Affinity

S-type pyocins from *P. aeruginosa* either display cytotoxic activity in the cytoplasm or the inner membrane, which is why pyocin-producing strains must protect themselves from these highly potent toxins through the co-expression of designated immunity proteins. Particularly, nuclease pyocins form very tight ultra-high-affinity complexes between the C-terminal cytotoxic nuclease domain and their cognate immunity protein. The structurally and mechanistically related pair of HNH DNase bacteriocin colicin E9 and its cognate immunity protein ImE9 from *E. coli* exhibited diffusion-controlled association and dissociation constant (K_D) of 10^{-17} M (or 10^{-2} fM). This femtomolar binding affinity is, metaphorically speaking, the life insurance for bacteriocin producers to not get killed by their own toxin.[733] Furthermore, partial cross-protection against ColE9 nuclease activity was observed for ImE2 and ImE8 *in vivo*, while *in vitro* stopped-flow measurements confirmed non-cognate cross-binding activity of these immunity proteins in a micromolar to femtomolar range.[734] These cognate and non-cognate binding modes of nuclease bacteriocins also confer resistance to these strains when they are challenged with bacteriocins from other bacteriocin-producing strains in their environment, as long as the binding affinity is high enough. Joshi and Grinter *et al.* attempted to deduce general requirements for the ultra-high-affinity binding from the high-resolution crystal structures of the nuclease pyocins AP41 and S2 and their cognate immunity proteins. Both pyocins possess the characteristic zinc-finger-like HNH nuclease fold of the cytotoxic domain with a mixed α/β fold (ββα-metal) known from other nuclease bacteriocins. Their immunity proteins share a similar fold as well, consisting of a four-helix bundle.[701] Previously reported crystal structures of ColE7 and ColE9 in a complex with DNA exhibited contact with the minor groove of double-stranded DNA, mediated by the concave DNase active site right next to the three-histidine-chelated metal cofactor.[735, 736] The metal cofactor, which is typically Mg^{2+}, Zn^{2+}, or Ni^{2+}, is required for the correct folding of the DNase domain and fixation of the negatively charged backbone of DNA at the active site to display nonspecific hydrolytic activity.[736] Interestingly, the pyocin immunity

[6] 20 Different serotypes owing to independent O-specific antigens have been identified in *P. aeruginosa*. The structurally diverse glycopolymers differ in their sugar constitution, their linkage and branching, whereas the only one type of CPA has been found. Further information can be found in the review of Lam *et al*., *Front. Microbiol*. **2011**, 2:118.

proteins ImAP41 and ImS2 do not inhibit bacteriocin interaction with DNA by competitive binding at the active site but through binding to the IPE adjacent to the active site, suggesting conformational changes within the nuclease domain upon binding of the immunity protein that lower the overall affinity to DNA.

The IPE within PyoS2 is built by helix V, loop 4, and β-strand 3 and interacts with helix II and III of its immunity protein ImS2 through several direct polar contacts and interfacial water-mediated intermolecular interactions (Figure IV.9). A remarkably low sequence conservation of 37% can be found in the hypervariable exosite between DNase bacteriocins, but a very high degree of structural conformity is conserved in the backbone (RMSD 0.56 Å). The central part of the IPE is free from any secondary structure and resembles a loop, whose conformation is fixed in the hydrophobic core of the protein by conserved residues. Furthermore, the structure of ImS2 in complex with the PyoS2 DNase domain reveals that helix II of ImS2 functions as a binding hotspot by creating the most specificity-determining contacts.[701] Low fits between helix II of ImS2 and the IPE of other nuclease pyocins are the main determinant of low binding affinity in non-cognate interactions. In contrast, helix III of ImS2 interacts with the exosite of PyoS2 via specific polar contacts that are the energy hotspot of DNase-immunity high-affinity-binding.[701]

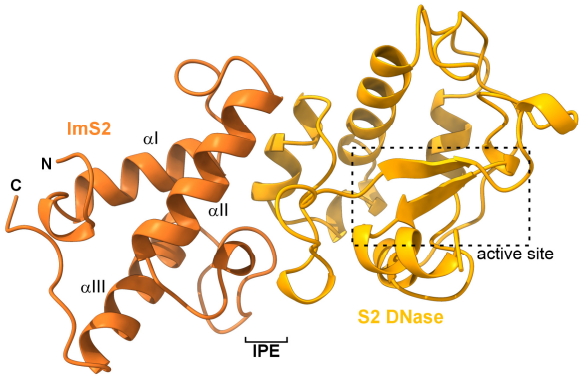


Figure IV.9. Crystal structure of the cognate complex of PyoS2 and ImS2 (PDB 4QKO, 1.8 Å resolution). The immunity protein binds PyoS2 with ultra-high affinity at the immunity protein exosite (IPE) within the HNH DNase. The RMSD between the crystallised DNase and the predicted DNase domain (cf. Figure IV.8) is 0.69 Å, showing a high structural congruency between the two models.

In summary, immunity proteins are of particular importance for bacteriocin producers to protect themselves from the cytotoxic activity of the bacteriocin during protein biosynthesis. However, they may also protect from bacteriocin-producing competitors by cognate or less efficient non-cognate neutralisation of the bacteriocins after cellular uptake via membrane translocation. Simultaneously, the widespread distribution of cognate immunity proteins limits the natural antibacterial spectrum of bacteriocins and thereby also their therapeutic benefit as alternatives to common antibiotics.

IV.2 Aims

The Gram-negative bacterium *Pseudomonas aeruginosa* is an opportunistic human pathogen responsible for severe infections of the respiratory tract and burn wounds, causing pneumonia, bloodstream infections, and sepsis. With a high mortality rate in immunocompromised patients, intensive care unit-associated and intensive care unit-acquired infections require high time and monetary investments to cure these patients. However, a growing number of therapies against *P. aeruginosa* have failed in recent years. Particularly, its ability to produce numerous highly toxic virulence factors, biofilms, and enzymes (ESBLs, MBLs, carbapenemases) that confer resistance to common antibiotics and last-resort β-lactam antibiotics, such as imipenem and meropenem, makes *P. aeruginosa* extremely difficult to treat. Collectively, these traits underscore the fact that combating multidrug-resistant *P. aeruginosa* is one of the greatest challenges of modern medicine. For this reason, new antibiotics or alternative treatment strategies are urgently needed to combat infections caused by carbapenemase-producing strains of *P. aeruginosa* and to avoid worsening of the antimicrobial crisis in order to avert a post-antibiotic era.

Bacteriocins are narrow-spectrum antimicrobial proteins produced by bacteria like *P. aeruginosa* for microbial competition, making them promising candidates to tackle multidrug-resistant Pseudomonads. While bacteriocins from Gram-positive bacteria are readily applied biotechnologically as food preservatives (e.g. nisin), no biotechnological or medical applications of bacteriocins from Gram-negative bacteria have been reported to date. One reason for this is a conserved toxin-antitoxin relationship, which is common to all S-type pyocins and most other bacteriocins from Gram-negative bacteria, vastly limiting the antimicrobial spectrum of natural bacteriocins among bacteriocin-producing strains and thereby reducing their impact as potential therapeutics.

In this chapter, the potential of bacteriocins from Gram-negative bacteria is explored by developing a novel therapeutic approach to challenge *P. aeruginosa*. The class of soluble and protease-sensitive S-type pyocins from *P. aeruginosa* exploits a conserved uptake machinery of outer membrane β-barrel proteins, energy transducing complexes (Ton or Tol), and inner membrane proteases to hijack the target cell's integrity. In this context, pyocin S2, its cognate immunity protein S2, the ferripyoverdine transporter FpvAI, and the periplasmic portion of the TonB1 protein are the only examples of a structurally well-characterised ensemble of proteins being involved in the membrane translocation of pyocins. Chapter IV aims to fathom the application potential of the conserved and unique mechanism of pyocin translocation across the impermeable membrane of *P. aeruginosa* to pilot potential drugs across the membrane through covalent pyocin S2 conjugates in a Trojan Horse Strategy. As the C-terminal killing domain of pyocin S2 is transported into the cytoplasm to disrupt DNA metabolism, cysteine residues shall be introduced into the CTD of pyocin S2 for covalent labelling with maleimide-functionalised probes and potential warheads and their co-transport into the bacterial cytoplasm. Labelling sites shall be introduced in several positions of the killing domain to investigate the effect of the labelling site on PyoS2's antimicrobial activity, its DNase activity, and its interaction with the immunity protein ImS2. Labelling shall be performed with non-toxic AlphaFluor fluorophores to review whether covalent labelling can weaken the high-affinity interaction between pyocin S2 and its cognate immunity protein when introduced at their binding interface. Furthermore, the chemically synthesised maleimide-functionalised A-, B-, and C-ring prodiginines **III-89·HCl**, **III-90·HCl**, and **III-91·HCl** from Chapter II.5.4 shall be used to investigate targeted delivery of prodiginines to overcome the inherent prodigiosin-resistance of *P. aeruginosa* and the lacking target specificity of prodiginines. And lastly, a strain collection of 113 multidrug-resistant clinical isolates of *P. aeruginosa* from the University Hospital Düsseldorf shall be characterised and experimentally validated for sensitivity and resistance to wild-type pyocin S2 and its covalent conjugates with AlphaFluor fluorophores and prodiginine alkaloids. Hereby, this thesis aims to assess the application potential of pyocins as representatives of bacteriocins from Gram-negative bacteria in complementing the clinical repertoire to treat infections caused by nosocomial multidrug-resistant pathogens.

IV.3 Results and Discussion

The narrow-spectrum antimicrobial proteins from the group of soluble S-type pyocins are the structurally and functionally best-studied class of bacteriocins from the opportunistic human pathogen *P. aeruginosa*. They bear clinical potential to expand the available treatment repertoire for multidrug-resistant *P. aeruginosa* strains, including those with accumulated resistance to last-resort carbapenem β-lactam antibiotics. Even though fundamental research has shed light on the matter of cell adsorption, membrane translocation, and cytotoxic activity for S-type pyocins, little effort was made to translate this knowledge into clinical application to exploit the potential of pyocins in combating *P. aeruginosa* infections. In this chapter, the DNase pyocin S2 (PyoS2) and its application against clinical isolates of *P. aeruginosa* are explored. Furthermore, the conserved Ton machinery is examined for its eligibility to co-transport potential drugs along with PyoS2 into the bacterial cell, facilitating their passage across the otherwise impermeable membrane barrier of Pseudomonads.

IV.3.1 Pyocin S2 Conjugates – Structural Conditions and Rational Protein Design

To harness the potent cytotoxic activities of pyocins for therapeutic applications and to exploit their conserved mechanism of import to specifically co-transport potential drugs, a sophisticated understanding of the structure-function relationship of those toxins is obligatory. Hence, the 74 kDa HNH DNase bacteriocin PyoS2 was selected for this study, as it is the currently best-studied S-type pyocin. Moreover, crystallographic datasets are readily available, highlighting the cognate interaction with ImS2 or the binding to the primary receptor, the TBDT siderophore transporter FpvAI.

IV.3.1.1 A Few Residues Mediate Ultra-High-Affinity Binding Between PyoS2 and ImS2

The DNase nuclease domain of PyoS2 forms a stoichiometric neutralising complex with the cognate 10 kDa immunity protein ImS2. Other than full-length PyoS2, the DNase/ImS2 complex has already been crystallised at 1.8 Å resolution (PDB-REDO 4QKO) (cf. Figure IV.9),[701] showing a high congruency for the DNase domain between the AlphaFold model and the crystal structure (RMSD 0.69 Å). Although HNH DNase bacteriocins and their cognate immunity proteins associate with femtomolar affinity,[733] the strong binding can be broken down into a handful of interacting amino acids. Additionally, a comparison of HNH DNase domains from multiple species also reveals that the sequence portion representing the IPE harbours the least sequence conservation, as this portion of the DNase domain mediates high-affinity binding to their sequentially unique cognate immunity proteins (Figure IV.10A). Accordingly, it was hypothesised that knowledge of those residues required for neutralising complex formation and mediating binding selectivity can be used to engineer bacteriocins that evade neutralisation of DNase activity through immunity protein binding. This would be an essential requirement to overcome the natural limitations of bacteriocins, caused by the widespread distribution of immunity proteins among the bacterial kingdom.

Based on molecular interface analyses of the PyoS2/ImS2 crystal complex with PDBePISA,[737] we identified nine amino acids within the IPE of PyoS2 that show attraction to ImS2 via hydrogen bonding or salt bridges (Table IV.2). From the identified residues R605, R608 (positioned in helix III), N626, A631 (helix V), D635, Y640 (loop 4), E643, N646 (3_{10} helix), and K652 (loop 5) (Figure IV.10B), D635 and Y640 are located in the large unstructured region of loop 4, which is devoid of any secondary structure. Additionally, both residues are enclosing a stabilising network of four interstitial water molecules that is found at the interface of PyoS2/ImS2 and is present within all four asymmetric units of the crystal unit cell (Figure IV.10C). This network with well-defined spherical electron density in the 2Fo-Fc density map (Figure IV.10D) is adjuvant in intraprotein stabilisation within both, the DNase and ImS2, and mediating interprotein contacts within the PyoS2/ImS2 complex. For example, the water

network enhances the binding of the PyoS2/ImS2 complex by fixing the distorted orientation of ImS2 loop 1, which is required for hydrogen bond formation between the ImS2 residues N23 and K25 with the DNase loop 4 residue D635. The aspartic acid residue D635 also interacts with K652 through the extended water network, stabilising the orientation of the ε-amino group at the interface. Additionally, the interface is stabilised by strong polar interactions and salt bridges between Y640 and K652 with the ImS2 residues H34 and E31 (Figure IV.10C), respectively, both located in the energy binding hotspot helix II of ImS2.

Table IV.2. Polar interaction of amino acid residues at the interface between PyoS2 and ImS2. Interactions and distances have been collected from the PDB-REDO structure 4QKO using PDBePISA.[737] Distances were measured between heteroatoms, omitting interjacent hydrogen atoms. Atom names refer to the corresponding PDB file. The given interactions were used for the semi-rational protein design of PyoS2 ID ("*ImS2 interactions-deficient*").

PyoS2			**ImS2**			
Hydrogen bonds						
Residue	**Position**	**Atom name**	**Residue**	**Position**	**Atom name**	**Distance [Å]**
N626	SC	ND2	Y21	SC	OH	3.78
	SC	ND2	L54	BB	O	2.89
	SC	ND2	D63	SC	OD1	3.22
	SC	ND2	D63	SC	OD2	3.22
A631	BB	O	N23	SC	ND2	3.13
D635	SC	OD2	N23	SC	OD1	3.31
	SC	OD2	K25	SC	NZ	2.75
Y640	SC	OH	H34	SC	ND1	2.75
	BB	O	Y56	SC	OH	2.64
E643	SC	OE1	K42	SC	NZ	3.26
	SC	OE2	K42	SC	NZ	2.96
	SC	OE2	S51	BB	N	2.88
	SC	OE2	S51	SC	OG	3.20
	BB	N	D52	SC	OD1	2.78
Q646	SC	NE2	S51	SC	OG	2.82
	SC	OE1	K42	SC	NZ	3.34
K652	SC	NZ	E31	SC	OE2	2.66
Salt bridges						
Residue	**Position**	**Atom name**	**Residue**	**Position**	**Atom name**	**Distance [Å]**
R605	SC	NH2	E32	SC	OE1	3.51
	SC	NH1	E32	SC	OE2	3.98
	SC	NH2	E32	SC	OE2	2.98
R608	SC	NH1	E31	SC	OE1	2.92
	SC	NH2	E31	SC	OE1	3.62
	SC	NH1	E31	SC	OE2	3.47
	SC	NH1	E31	SC	OE1	2.65
D635	SC	OD2	K25	SC	NZ	2.75
E643	SC	OE1	K42	SC	NZ	3.26
	SC	OE2	K42	SC	NZ	2.96
K652	SC	NZ	E31	SC	OE2	2.66

Abbreviations: BB – backbone; SC – side chain.

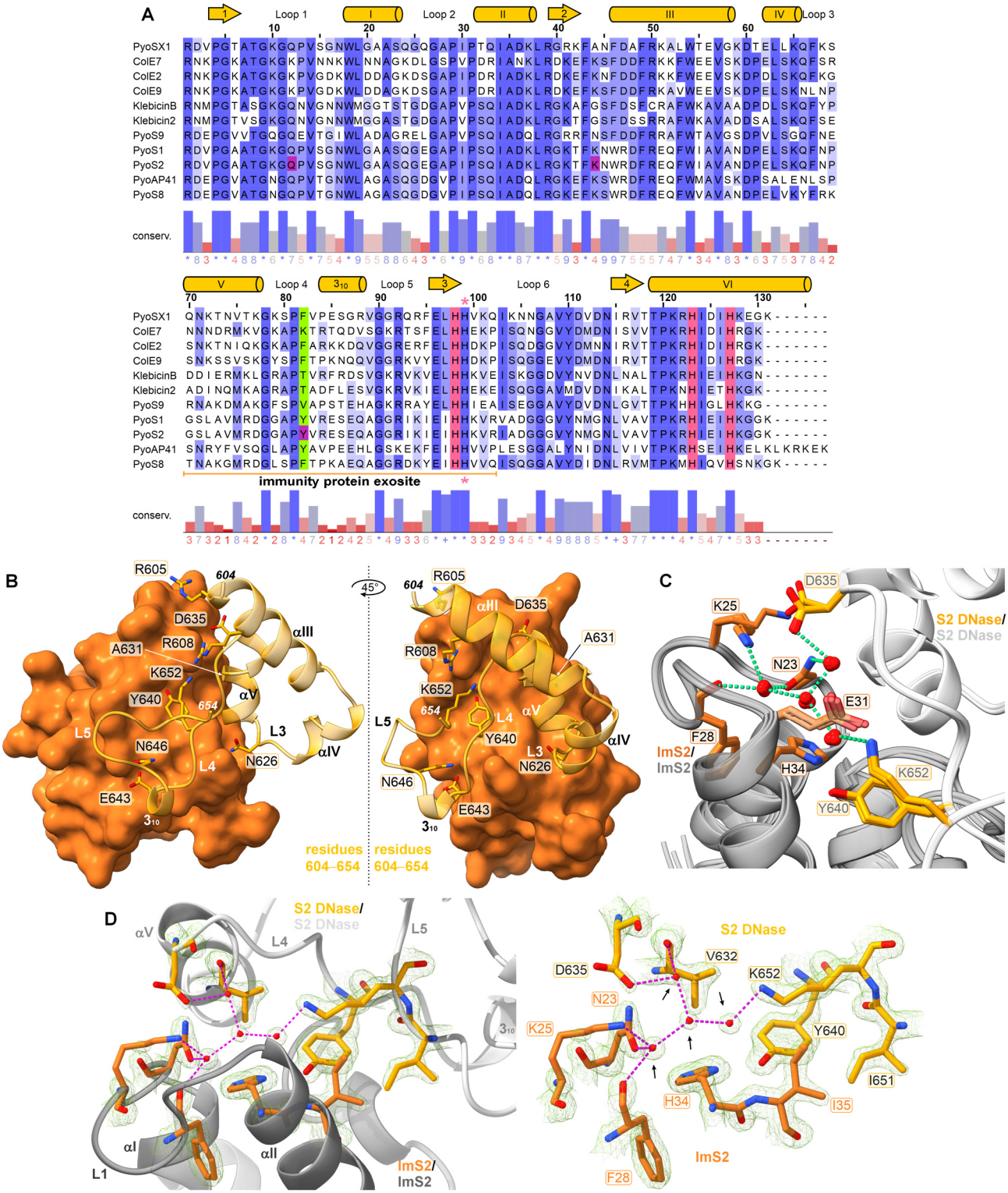


Figure IV.10. Sequential analysis and structural topology of the IPE. **A**. Multiple sequence alignment of nuclease domain amino acid sequences of HNH DNase bacteriocins. Positions equivalent to Y640 in PyoS2 are highlighted in green. Conserved histidine residues required for DNase activity are highlighted in pink (metal complexation) or marked with a pink asterisk (general base). **B**. Involved PyoS2 IPE residues in ultra-high-affinity binding to ImS2. **C**. Display of interstitial waters at the PyoS2/ImS2 interface, conserved within all four asymmetric units of the crystal unit cell (PDB-REDO 4QKO). **D**. Network of conserved interstitial waters at the PyoS2 IPE. The crystal structure is aligned with the 2Fo-Fc electron density map (green mesh) at 0.6σ in a range from –0.836 – 5.16. The left figure shows the interacting residues (PyoS2 DNase in yellow, ImS2 in orange) and the protein backbones (PyoS2 DNase in white, ImS2 in grey), the right figure exclusively depicts the involved amino acids and waters (red spheres, highlighted by black arrows).

Due to the involvement of the DNase residue Y640 in stabilising the interstitial water network and its exposed positioning at the IPE, which facilitates direct interaction with ImS2, it is hypothesised that this residue plays a pivotal role in enabling ultra-high-affinity binding and protecting PyoS2-producing strains from self-inflicted death. Together with the relatively small binding interface between the two proteins, we sought to introduce mutational changes and install bulkier non-proteinogenic labels at the IPE of PyoS2 to obstruct the binding interface and thereby potentially overcome ImS2-dependent PyoS2 resistance of *P. aeruginosa*.

IV.3.1.2 Selection of Sites for PyoS2 Labelling

Despite the fact that most S-type pyocins exploit the highly conserved Ton machinery for cellular import, no reports have been shared about using this pathway to transport small-molecule drugs conjugated to bacteriocins into the bacterial cell. Even more, the exclusive presence of the Ton machinery in Gram-negative bacteria and the outstandingly high strain-specific nature of TonB box motifs make this uptake system and particularly the central TonB protein, an attractive target for the selective delivery of drugs and novel drug conjugates. S-type pyocins naturally hijack the TonB-dependent machinery to cross the bacterial membrane and deliver their cytotoxic domain into the cytoplasm or, in the case of PyoS5, to the inner membrane, inducing cell death. This makes them an ideal vector for leveraging Ton-mediated import to deliver conjugated molecules into the target cells of *P. aeruginosa*. In this context, a serious effort was invested into elucidating the mode of action and the translocation mechanism of PyoS2, making it the best-studied pyocin within the sphere of S-type pyocins.

Before developing a labelling strategy of PyoS2 to exploit its translocation for the co-transport of putative drugs into *P. aeruginosa*, a comprehensive understanding of the translocation mechanism is of great importance. During translocation across the bacterial membrane of the target cell, only the C-terminal killing domain is transported into the cytoplasm through FtsH-catalysed proteolytic processing, while the NTD and the two middle domains remain in the periplasm (cf. Figure IV.7). Hence, in order to co-transport potential small-molecule drugs into the bacterial cytoplasm, the drugs must be covalently attached to the CTD. The DNase domain within the CTD is approximately 14.5 kDa in size and exhibits the structurally highly conserved HNH nuclease fold, which is found among all HNH DNase bacteriocins from different species. To use this HNH nuclease domain of PyoS2 for the covalent attachment of small molecules, we prospected for surface-exposed amino acid side chains that are located within the flexible loop structures of the protein rather than within conserved α-helices or β-strands to reduce undesired interference with the structural integrity of the relatively small HNH nuclease and its conserved fold and avoid unintended consequences for membrane translocation.

By analysing the crystal structure of the cognate PyoS2/ImS2 complex (PDB 4QKO), it was possible to extract four suitable positions of PyoS2 for covalent labelling with small molecules, namely Q570, K602, Y640, and the C-terminus (cf. Figure IV.10A, purple residues).[701] While Q570 is located within loop 1, the lysine residue K602 is located in a short unstructured region between β-strand 2 and helix III. Similarly behaves the C-terminus of the killing domain, which is a very short unstructured appendix to helix VI and in direct proximity to the DNA binding groove (cf. Figure IV.11). The aforementioned residues Q570, K602, and the C-terminus are neither involved in ImS2 binding nor close to the IPE of PyoS2. Lastly, residue Y640 was purposely selected as a site for protein modification, as the tyrosine residue belongs to the unstructured loop 4 of the DNase domain, which is involved in the stabilisation of interstitial waters and a central part of PyoS2's IPE that interacts with the DNase binding motif of the immunity protein ImS2 (helix II – loop 2 – helix III) (cf. Chapter IV.3.1.1). Therefore, it was hypothesised that mutations at this particular position or additional *in vitro* labelling with bulky small-molecule labels could potentially weaken the PyoS2/ImS2 interaction and render PyoS2/ImS2-producing strains sensitive to PyoS2 Y640 derivatives.

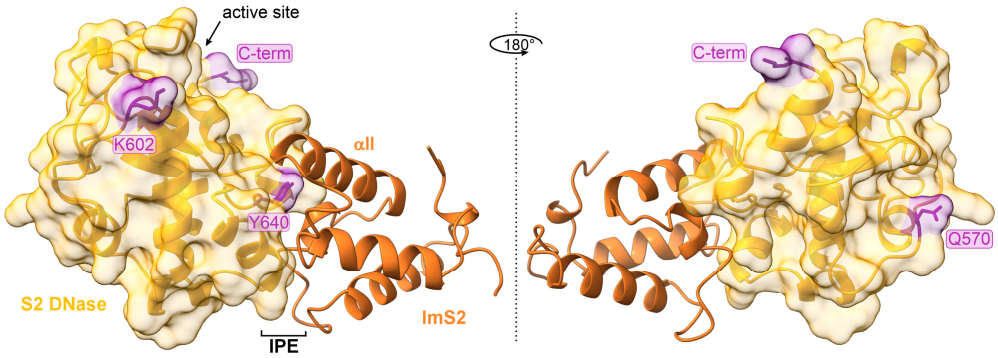
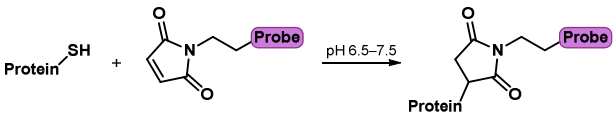


Figure IV.11. Relative position of PyoS2 residues selected for mutagenesis and thiol-maleimide labelling.

The IPE of PyoS2 spans from helix V to the initial residues of loop 6 of the DNase and forms the interface that enables femtomolar binding of PyoS2 and its cognate immunity ImS2. Within the cognate complex, the central residue Y640 is flanked by the PyoS2 residues I651 (loop 5) and V632 (helix V) and the K652 residue (loop 5) covers the aromatic system from above (cf. Figure IV.10D). All residues hold the Y640 residue firmly in place by hydrophobic interactions between the side chains and the Y640 ring system and K652 further stabilises the central residue by acting as hydrogen acceptor for the Y640 hydroxy group. On the other side, the aliphatic ImS2 residues I35 and V38 within the α-helix II mirror the flanking behaviour and stabilise Y640 by hydrophobic interactions (cf. Figure IV.10D). Lastly, the polar ImS2 side chains of H34 and Y55 contribute with strong interactions through the formation of hydrogen bonds in the plane with the Y640 hydroxy group and π-stacking from below between the aromatic ring systems.

To enable the covalent attachment of small-molecule labels to the cytotoxic domain of PyoS2, a reliable and frequently utilised bioorthogonal tool from click chemistry was chosen, namely the thiol-Michael addition between thiols and maleimides (Scheme IV.3).[451] This nucleophilic addition reaction between a thiol-functionalised protein (reduced cysteines or non-natural amino acids) and a maleimide-functionalised drug or probe is highly selective and quantitative at near-neutral pH. As PyoS2 intrinsically lacks cysteine residues, the residues Q570, K602, and Y640 were planned to be substituted by cysteine residues through site-specific mutagenesis. Furthermore, the C-terminal cysteine residue (C-Cys) was designed to protrude from the terminal PyoS2 amino acid K689. After protein purification and reduction of the free cysteine residues with mild reducing agents [e.g. dithiothreitol, β-mercaptoethanol, or tris(2-carboxyethyl)phosphine], the addition of maleimide-functionalised small-molecule labels would then result in stable and covalent post-translational protein modifications.



Scheme IV.3. Michael addition of a thiol-containing protein and a maleimide moiety with an arbitrary probe, yielding a covalent protein-maleimide conjugate.

Taken together, the topology of the cognate complex of PyoS2 and ImS2, along with the few residues mediating ultra-high-affinity binding, served as a foundation for developing the hypothesis that small mutational changes or labelling with bulky fluorophores at the IPE might (partially) prevent complex association. This could potentially lead to PyoS2-associated cytotoxicity, even in the presence of ImS2. To enable maleimide labelling of the HNH

DNase domain, cysteine residues will be introduced in flexible loop positions across the nuclease, of which only residue Y640 lies within the IPE.

IV.3.1.3 Design of DNase-Inactive PyoS2 Mutants

The intrinsic killing activity of PyoS2 through DNA degradation makes growth inhibition of susceptible bacteria a convenient readout for cellular uptake of PyoS2 into the cytoplasm of the target cell. However, to verify that the killing activity of wild-type PyoS2 stems from the nuclease activity of the C-terminal PyoS2 nuclease domain, we set out to inactivate the nuclease domain through mutagenesis. Furthermore, these nuclease-inactive mutants serve as effective readouts for assessing the toxicity of PyoS2-conjugated molecules. In the absence of nuclease activity, any observed bactericidal or bacteriostatic effects can be exclusively attributed to the conjugated small-molecule labels or drugs.

The DNase domain features the HNH nuclease fold that is common within the HNH nuclease superfamily and a conserved structural motif in restriction endonucleases, HNH DNase bacteriocins (cf. Figure IV.10B), transposases, among others.[738, 739] All HNH superfamily members are DNA-interacting enzymes, and most of them use an alkaline metal cofactor (e.g. Mg^{2+}, Zn^{2+}) found in the ββα-metal (His-metal finger) motif within the DNA-binding pocket (Figure IV.12).

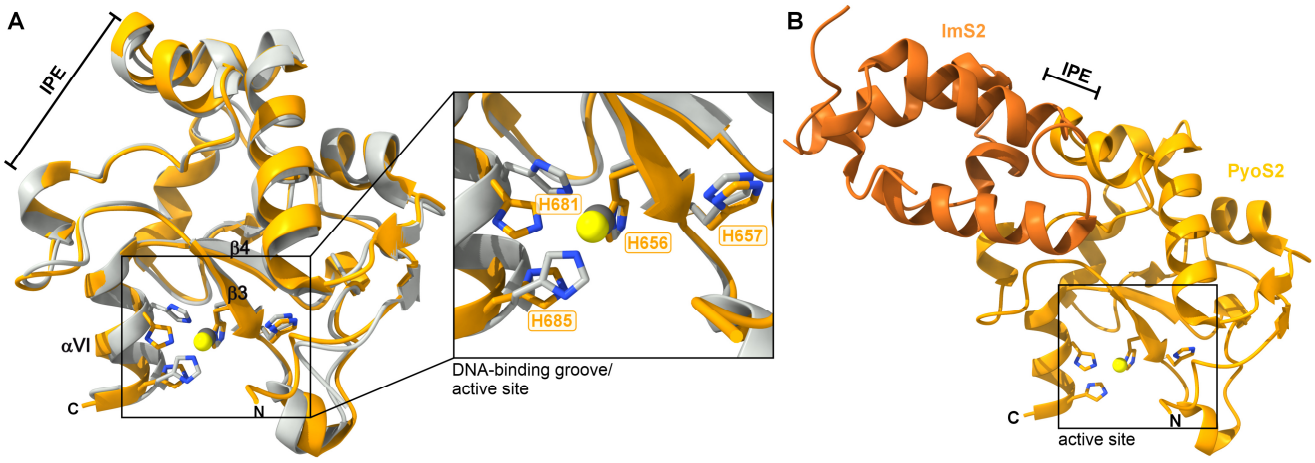


Figure IV.12. Location and geometry of the active site of HNH DNase bacteriocins. **A**. Structural alignment of ColE7 (grey) and PyoS2 (yellow) cartoon models from their corresponding crystal structures (PDB 1M08, ColE7 only; PDB 4QKO, PyoS2/ImS2 complex) with an overall RMSD of 0.97 Å. The Mg^{2+} (yellow sphere) and Zn^{2+} (grey sphere) cofactors of PyoS2 and ColE7 are shown, respectively, complexed by PyoS2 histidine side chains of H656, H681, and H685 or ColE7 residues H544, H569, and H573. The PyoS2 histidine residues buried within the active site are required for coordination of the metal cofactor (αVI: H685 and H681, β3: H656) and for general base catalysis (β3: H657). **B**. Crystal structure of PyoS2 with its immunity protein ImS2, highlighting the relative location of the active site and non-competitive binding of ImS2 at the IPE of PyoS2.

The α-helix VI of the His-metal finger fits into the minor groove of DNA and the β-hairpin formed between β-strands 3 and 4 aligns to the DNA backbone.[739] The interaction with the DNA backbone is enforced by metal-mediated complexation of the negatively charged phosphate from the DNA backbone. This complexation leads to a polarisation of the P–O bond within the DNA backbone and facilitates DNA strand scission through nucleophilic attack of the P–O bond by a nucleophilic species within the HNH DNase active site. The Lewis acidic metal cofactor itself is held in place by the complexation through three Lewis basic residues in direct proximity. In ColE7, PyoAP41, and PyoS2, these basic residues are represented by histidine residues, respectively. Concurrently, a

fourth histidine residue is used as a general base to deprotonate a water molecule that attacks the scissile phosphate group from the DNA backbone in a nucleophilic substitution reaction, leading to site-unspecific hydrolysis of the DNA strand.[739, 740]

Mutational analysis of Doudeva *et al*. on the HNH nuclease bacteriocin ColE7 revealed that the histidine residues H545 (general base) and H573 (metal complexation) are essential for hydrolytic activity. While H573 mutations significantly reduced nuclease activity through reduced metal binding capacity, H545 mutations were able to fully abolish the endonuclease activity.[740] Similar results were observed for ColE9 by Walker *et al*. for the histidine residues H102 (general base) and H131 (metal complexation).[741] Based on these insights, the corresponding histidine residues of PyoS2 were identified from an alignment of crystal structures with ColE7 to enable rational design of a PyoS2 nuclease knock-out (Figure IV.12). In the crystal structure of PyoS2, the identified active site histidine residues H656 and H657 are both located in β-strand 3 and part of the β-hairpin between β-strand 3 and 4. However, as H657 and H656 point in opposite directions of the β-strand, their functional role significantly diverges. While H656 is part of the tripartite metal-chelating histidine ensemble, H657 is utilised as the general base to deprotonate the water molecule for nucleophilic attack of the P–O bond in the DNA backbone. Furthermore, the histidine residues H681 and H685 complete the tripartite metal complexation ensemble and are located in helix VI that is embedded into the minor groove of DNA. Consequently, the residues H657 and H685 were selected for mutational replacement by alanine residues. Since alanine is a small hydrophobic amino acid without basic character, replacement of H657 and H685 is hypothesised to result in abolished nuclease activity of PyoS2.

IV.3.1.4 Rational Design of a PyoS2 Mutant with Deficiency for Interaction with ImS2

The ultra-high-affinity interaction reported for PyoS2 and its immunity protein ImS2 is surprisingly owing to only a few interprotein contacts (cf. Chapter IV.3.1.1). Hence, it was inferred that this interaction can be disrupted by rationally mutating the majority of amino acids located within the IPE, which are critical for the interaction with ImS2 and thus contribute to ultra-high-affinity binding of both binding partners (cf. Table IV.2). A PyoS2 mutant, incapable of interacting with ImS2, would be a superior bacteriocin for clinical applications, as innate (ImS2-dependent) PyoS2-resistance would not protect *P. aeruginosa* strains from the mutant pyocin. Comparing this extensive mutagenesis approach with the interface labelling approach with the PyoS2 Y640C mutant from the previous chapter (cf. Chapter IV.3.1.2), it is assumed that a single amino acid substitution might be countered by *P. aeruginosa* by spontaneous mutations within the immunity protein under appropriate evolutionary selection pressure. However, the *in vitro* attachment of bulky man-made labels to the DNase domain or reshaping of the IPE of PyoS2 by extensive mutagenesis could provide a means to avoid spontaneous ImS2 escape mutants that confer resistance to single point mutants of PyoS2 with impaired ImS2-binding. Furthermore, these two approaches, namely extensive mutagenesis and fluorophore attachment, might help us to deepen our understanding of the molecular mechanism of ultra-high-affinity binding between bacteriocins and their cognate immunity proteins in general.

Although the analysis of the protein-protein binding interface of PyoS2/ImS2 with PDBePISA provided essential insights into interacting residues, the crystal structure of the cognate complex also reveals that the highlighted residues of PyoS2 are also involved in intraprotein stabilisation of the PyoS2 DNase domain itself. Thus, conservative mutations, predominantly resembling the character of the original amino acids but still notably reducing the affinity to ImS2, were desired to avoid a negative impact on HNH nuclease fold and DNase activity while concurrently decreasing the affinity towards the cognate immunity protein. Hence, the DNase mutations N626D (loop 3), D635A (helix V), Y640A (loop 4), E643D and Q646N (3_{10} helix), as well as K652N (loop 5) were

selected for this study (Figure IV.13A). To simplify naming of this PyoS2 mutant carrying six amino acid substitutions, the PyoS2 variant N626D D635A Y640A E643D Q646N K652N was named *"ImS2-interaction deficient"* (ID) in the following sections of this thesis. While PyoS2 is a relatively large protein that consists of 689 amino acids, its DNase domain contributes with 134 amino acids (19.4%) to the protein. With the aim to substitute six surface-accessible amino acids within the 134 amino acid comprising DNase domain (4.48% of DNase), the PyoS2 ID mutant was modelled via AlphaFold and aligned with the PyoS2 crystal structure first to ensure that the conserved HNH nuclease fold is unaffected by the selected substitutions (Figure IV.13B). Both structures merged with an overall RMSD of 0.69 Å, showing a high conformity between both models. Consequently, it was assumed that the introduced mutations of PyoS2 ID do not impair the overall structural integrity of the HNH nuclease fold.

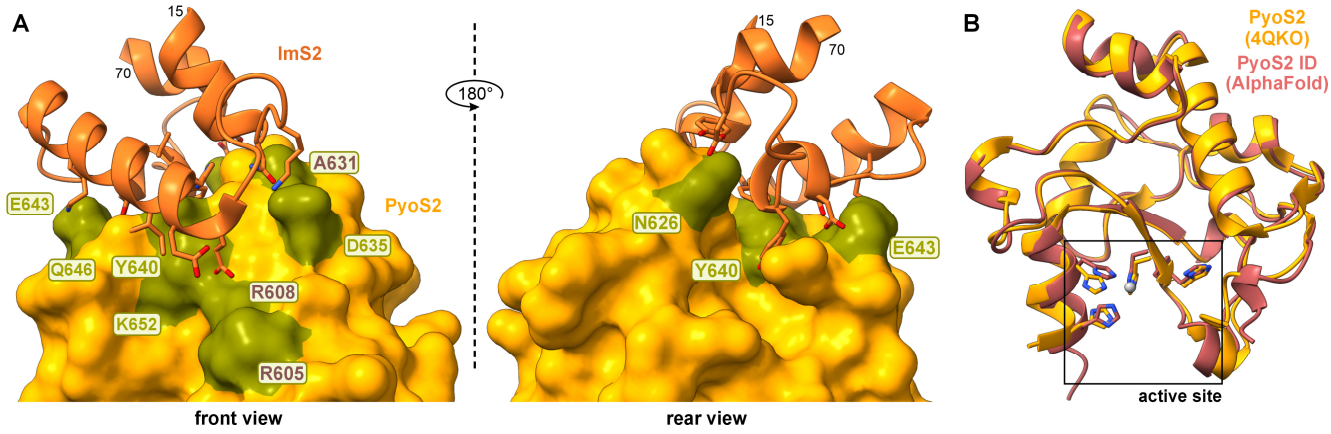


Figure IV.13. Rational design of the PyoS2 ID mutant. **A**. Front and rear view of the immunity protein exosite of PyoS2 (yellow) in complex with ImS2 (orange). The amino acids responsible for interprotein contacts are highlighted in green for PyoS2 and as sticks in the ImS2 model. The residues refer to Table IV.2. Those residues selected for mutagenesis are labelled in green, others in brown. **B**. Structural alignment between DNase domains of PyoS2 from the PDB crystal structure 4QKO and a PyoS2 ID AlphaFold model. The four histidine residues from the active site are highlighted. Models were aligned with an RMSD of 0.69 Å.

IV.3.2 Purification of PyoS2 and DNase Knock-Outs

Pyocins originate from *P. aeruginosa*, an opportunistic human pathogen whose genetic engineering is tightly regulated by legal restrictions. Hence, heterologous protein expression in the genetically tractable bacterium *E. coli* was selected as a more feasible approach to access derivatives of the antimicrobial protein PyoS2. All proteins were expressed from pET21a(+) vectors in the heterologous host *E. coli* BL21(DE3) by utilising the T7 polymerase expression system. To enable the heterologous protein expression without harming the Gram-negative expression host through PyoS2-induced DNA damage, the *pyoS2* sequence from *P. aeruginosa* PAO1 (*pys2*, locus tag PA1150, NCBI NP_249841.1) was expressed in tandem with its ultra-high-affinity immunity partner *imS2* (*imm2*, PA1151, NCBI NP_249842.1). A C-terminally attached hexa-histidine-tag (His-tag) on ImS2 facilitates protein purification of the PyoS2/ImS2 complex through immobilised metal affinity chromatography. The installation of the His-tag on ImS2 instead of PyoS2 is an elegant strategy to avoid interference of the purification tag with the N-terminus of PyoS2 (needed for translocation) or its C-terminus (close to the DNase active site). To validate the DNase activity of wild-type PyoS2 and assess the impact of replacing histidine residues in its active site, the histidine mutants H657A (general base), H685A (metal complexation), and the double mutant H657A H685A were expressed, guided by prior design considerations for a DNase knock-out of PyoS2 (see Chapter IV.3.1.3).

Since the prospect of a future application of PyoS2 in animal models requires highly pure and untagged protein, we aimed for a two-step purification approach that provides PyoS2 in exceptional purity. The downstream processing after heterologous large-scale expression was initiated by the recovery of the bulk cells from the fermentation broth via centrifugation and cell lysis. Since the desired PyoS2 variants are co-purified in a stoichiometric 1:1 complex with the cognate His-tagged immunity protein ImS2 (ImS2-His_6; referred to as ImS2), a solution had to be found to separate the ultra-high-affinity binding partners. The effective approach was inspired by the congeneric colicins and a previously published method for their purification.[742] Jakes *et al*. could show that the ultra-high-affinity interaction between the rRNase colicin ColE3 and its immunity protein ImE3 can be dissociated only under strong denaturing conditions, such as chaotropic salts or denaturing agents like sodium dodecyl sulfate (SDS). Similarly, we attempted to temporally weaken the strong inhibitory complex between PyoS2 and its cognate binding partner ImS2 by partial unfolding through the chaotropic salt guanidinium hydrochloride (Gdn HCl), which would allow the separation of both binding partners by affinity chromatography.

To do so, the stable complex was first immobilised on a Ni-NTA resin, mediated by the complexation of the NTA-chelated Ni^{2+} ions by the His-tag attached to the C-terminus of the immunity protein. Next, bulk protein and weakly bound complex were removed from the matrix by prolonged washing with Tris buffer. This step is essential to remove any unbound PyoS2/ImS2 complex from the matrix that would otherwise result in ImS2 impurities in the PyoS2-containing eluate after complex disruption. PyoS2 was then attempted to elute by the gradual addition of chaotropic salt. At a concentration of 4 M Gdn HCl the complex started to dissociate on the column and at a concentration of 6 M Gdn HCl, thorough elution of PyoS2 was achieved without leaching of ImS2 from the column (Figure IV.14A). In the presence of 250 mM imidazole, ImS2 finally eluted from the column due to competitive binding of free imidazole to the Ni-NTA matrix and displacement of the hexa-histidine affinity tag of ImS2.

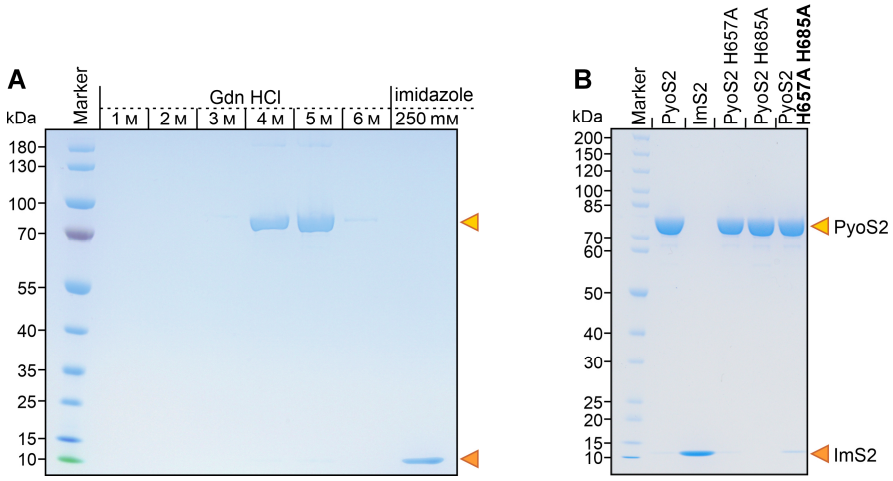


Figure IV.14. Guanidinium hydrochloride-induced separation of PyoS2 and ImS2 via affinity chromatography and SDS gels of purified PyoS2 variants and ImS2. **A**. Stepwise elution of PyoS2 from the Ni-NTA immobilised PyoS2/ImS2-His_6 complex through sequential increase of Gdn HCl concentrations (1–6 M) and complex disruption. **B**. SDS gel of purified PyoS2 (wild-type), ImS2, the histidine mutants H657A, H685A, and the H657A H685A double mutant. 2 µg of protein were loaded per well. Protein sizes: ImS2-His_6 – 11 kDa, PyoS2 – 74 kDa.

Hence, PyoS2 and the histidine mutants H657A, H685A, and the H657A H685A double mutant were first purified by Ni-NTA chromatography to separate the toxin from its immunity protein at a Gdn HCl concentration of 6 M. In the following, the excess of chaotropic salt was removed through dialysis, during which PyoS2 efficiently refolded. Lastly, preparative size exclusion chromatography (SEC) was employed to separate monomeric PyoS2 from

dimeric and aggregated species and to furthermore remove trace impurities of host proteins and ImS2 from the desired monodisperse PyoS2 variants. This methodology provided the desired PyoS2 wild-type protein and the histidine mutants H657A, H685A, and the H657A H685A double mutant in excellent purity (Figure IV.14B). Additionally, this methodology also provided toxin-free ImS2 that is required for further experiments.

IV.3.3 Validation of wild-type PyoS2 and DNase Knock-Outs

All nuclease bacteriocins sharing the HNH nuclease fold introduce nicks or cleave dsDNA in a sequence-unspecific manner, leading to bacterial cell death through genomic and plasmid DNA degradation *in vivo*. However, binding of the cognate immunity protein at the IPE of the PyoS2 DNase domain induces minor conformational changes that effectively abolish catalytic activity by forming an ultra-high-affinity complex. To investigate the kinetics of PyoS2-mediated DNA cleavage in the absence or presence of the immunity protein ImS2 *in vitro*, a time-resolved plasmid nicking assay with pET21a(+) plasmid DNA substrate was performed.[743] This assay exploits the ability of PyoS2 to convert supercoiled plasmid DNA (intact DNA) into nicked (ssDNA break) or linear (dsDNA break) DNA forms. Agarose gel electrophoresis was then used to separate these DNA forms, allowing assessment of DNase activity in different PyoS2 mutants and the effect of ImS2 binding.

HNH nucleases are metal-dependent enzymes whose catalytic mechanism requires the presence of divalent metal cations (Me^{2+}) at the active site for binding and hydrolysis of the nucleic acid substrate. Therefore, a preliminary experiment was conducted to identify the metal with the strongest impact on PyoS2 DNase activation. The addition of Mg^{2+} salts was shown to result in the strongest activation of catalytic DNase activity of wild-type PyoS2, while Mn^{2+} and Zn^{2+} showed minor to no activation, respectively (Figure IX.7, Supporting Information). Hence, Mg^{2+} was added to all subsequent plasmid nicking reactions to enable the highest DNase activity.

Next, the time-resolved plasmid nicking assay was employed to verify whether the selected purification method yielded correctly folded and catalytically active wild-type PyoS2 that would be able to interact with the cognate immunity protein ImS2. Additionally, this assay was used to assess the impact of histidine mutations H657A, H685A, and the H657A H685A double mutant on PyoS2's DNase activity. To ensure thorough complexation of the DNase and thereby full inhibition of PyoS2's catalytic activity, the cognate immunity protein ImS2 with femtomolar binding affinity was optionally added at a slight stoichiometric excess of 5.25 µM, while PyoS2 variants were used at a 5 µM concentration (1.05-fold excess of ImS2). The incubation was performed for 90 min and samples were taken at different time points to analyse the cleavage patterns and DNA forms by agarose gel electrophoresis, revealing time-resolved insights into DNA hydrolysis kinetics. Furthermore, densitometric analysis (analysis of pixel densities) was applied to the corresponding agarose gels for relative quantification of time-dependent changes in the three defined DNA forms (nicked, linear, and supercoiled). Compared to plasmid nicking experiments used in the past, involving tritiated (^3H isotope) plasmid DNA and the monitoring of nuclease activity via scintillation counting of radioactivity,[743] the densitometric analysis of pixel densities from a fluorescence image is a straightforward approach and less harmful for researchers and the environment. Statistical significance of all datasets was then validated using the densitometric data, based on Pearson correlation and permutation analyses. Kinetic parameters of supercoiled DNA degradation were deduced from linear regression and stretched exponential decay fits.

First, DNase activity of wild-type PyoS2 was evaluated to ensure correct folding of the toxin after purification and to establish a reference for comparative analyses with other PyoS2 mutants of interest (Figure IV.15A). In the absence of the immunity protein, PyoS2-catalysed DNA hydrolysis led to the disappearance of the supercoiled DNA species after 10 min. As the supercoiled DNA was predominantly interconverted into linear DNA by

introduced double-strand breaks, this particular DNA form showed a temporary incline in concentration in the early phase of the assay. The concurrent decline of supercoiled DNA and the strong increase in linear DNA in the early phase of the assay are also emphasised by a strong negative Pearson coefficient[7] of –0.90. Further, the PyoS2-catalysed digestion of the supercoiled DNA followed a stretched exponential decay. The exponential fit function derived from the data set was used to calculate the half-life of supercoiled DNA, which was then used to characterise various mutants and conjugates of PyoS2. For wild-type PyoS2, the supercoiled DNA form exhibited a half-life ($t_{1/2}$) of 3.20 min (for fit parameters see Table IX.5, Supporting Information). After 40 min, the nicked DNA was completely converted into linear DNA and after 70 min incubation time, residual linear DNA had been hydrolysed into smaller fragments with inhomogeneous size distribution (DNA smear).

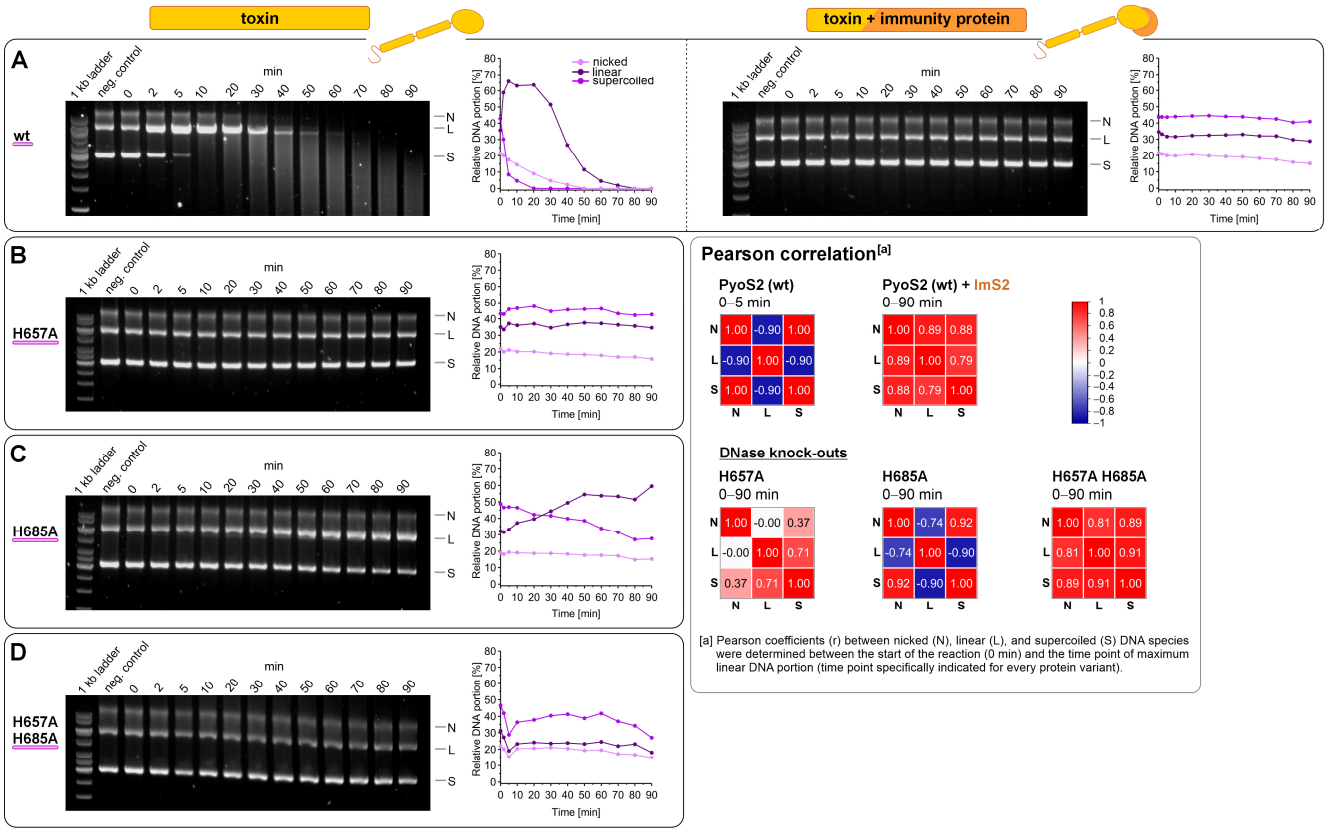


Figure IV.15. DNase kinetics of PyoS2 (wt), its neutralisation by ImS2, and kinetics of DNase active site mutants. DNA digest of pET21a(+) plasmid DNA with 5 µM PyoS2 or a mixture of 5 µM PyoS2 and 5.25 µM ImS2 was monitored over 90 min and analysed by agarose gel electrophoresis (200 ng of DNA per time point). A negative control contained an equivalent amount of DNA, but no enzyme. Graphs were generated by densitometric analyses and display the relative portion of DNA (nicked, linear, supercoiled) in relation to incubation time. Pearson coefficients were determined from 0 min to the time point where the highest linear DNA portion was observed to distinguish assay-related coincident decrease of all DNA species (no DNase activity) from real DNase activity (particularly negative correlation between supercoiled and linear DNA). Fit parameters are summarised in Table IX.5, Table IX.6, and Table IX.7 (Supporting Information).

[7] The Pearson coefficient (r) measures how two variables change together. In DNA degradation, it captures the inverse relationship between supercoiled DNA degradation and interconversion into linear DNA. Active DNA degradation yields a strong negative correlation (r close to –1), meaning that as supercoiled DNA decreases, linear DNA increases. An r near 0 would indicate no coordinated conversion between the DNA forms. A Pearson coefficient of close to +1 would mean supercoiled DNA decreases in synchrony with another variable also decreasing. Active DNA degradation requires negative correlation.

The addition of ImS2 to the reaction fully protected the DNA from PyoS2's DNase activity throughout the 90-min observation period, underlined by a strong positive Pearson correlation between all three DNA forms (nicked, linear, and supercoiled) between 0.79 and 1.00.

The putatively DNase-inactive histidine mutants PyoS2 H657A (general base) and the double mutant PyoS2 H657A H685A showed no residual DNase activity as expected (Figure IV.15B and IV.15D) [strong positive Pearson correlation of 0.71 and 0.91, respectively, between supercoiled and linear DNA]. Hence, residue H657 must play a crucial role in the catalytic cycle of DNA hydrolysis and the substitution of H657 fully abolishes DNase activity of the HNH nuclease. In contrast, the histidine mutant PyoS2 H685A (metal-coordination) still displayed partial cleavage of DNA, represented by a slow decrease of the relative portion of the supercoiled DNA form from initially 48% to 28% after 90 min (Figure IV.15C) and a strongly negative Pearson coefficient of −0.90 between the linear and supercoiled DNA species. According to the very slow decrease of supercoiled DNA over the observation period of 90 min, the half-life of supercoiled DNA for the H685A mutant was analysed with a linear fit model ($t_{1/2,supercoiled}$: 101 min, cf. Table IX.6, Supporting Information). For the DNase-inactive mutant PyoS2 H657A instead, the relative portion of supercoiled DNA remained unchanged at approximately 43% over the 90-min observation period.

Although metal binding in the H685A mutant seems to be compromised, as seen from the overall reduced DNase activity in comparison to wild-type PyoS2, the other two histidine residues H656 and H681 at the metal-coordination site can partially compensate for the substitution of histidine H685 and retain basal DNase activity. Those results are in accordance with earlier studies on the role of the two histidine residues in the homologous DNase colicin ColE7.[740] Although replacement of the general base H657 would be sufficient to knock out the DNase activity of PyoS2 mutants, further experiments will be conducted with the H657A H685A double mutants.

IV.3.4 Conjugation of PyoS2 to Small Molecule Fluorophore Labels

IV.3.4.1 Expression and Purification of PyoS2 Cysteine Mutants for Labelling

The translocation of the DNase domain of PyoS2 into the cytoplasm of a target cell makes this particular domain of the PyoS2 protein a promising vector for the co-transport of cytotoxic small molecules into cells of *P. aeruginosa* (cf. Figure IV.7). Guided by prior design considerations for the DNase labelling of PyoS2 (see Chapter IV.3.1.2), the four labelling sites Q570, K602, Y640, and the C-terminus were selected to introduce reactive cysteine residues in these positions. Those residues are potent nucleophiles that can be used to react with other functionalised electrophiles, such as alkyl iodides or maleimides, to form stable covalent conjugates. Because of the close positioning of the DNase loop 4 residue Y640 next to the stabilising network of interstitial water molecules at the PyoS2/ImS2 interface and its exposed orientation mediating direct polar interactions with ImS2, we decided to substitute the IPE residue Y640 with a nucleophilic cysteine residue, which facilitates further site-selective functionalisation with other functionalised electrophiles, such as alkyl iodides or maleimides, to form stable covalent conjugates. When attached to the IPE, those conjugates could putatively block the PyoS2/ImS2 complex association. Based on earlier studies, this work opted for maleimide chemistry, as the chemical functionalization of cysteines with maleimides (mostly *N*-ethylmaleimide) is a rarely used strategy to mitigate, or even prevent, the association of protein complexes through generating a physical barrier at the protein-protein interface.[744-746]

To generate the reactive PyoS2 mutants with surface-accessible cysteine residues in the first place, the PyoS2 mutants Q570C, K602C, Y640C, and C-Cys and their respective DNase knock-outs carrying the additional H657A H685A substitution, were expressed in the heterologous host *E. coli* BL21(DE3). Although protein production

under the established conditions was confirmed for all of the aforementioned protein variants, the PyoS2 Y640C mutant failed to express homogenously (Figure IV.16A). The Y640C mutation, located within the IPE of PyoS2, may disrupt ImS2 binding, leading to toxicity in the heterologous host. This impairment in ImS2 association could result in insufficient protection of the host DNA from PyoS2-mediated hydrolysis, ultimately causing a cytotoxic phenotype. As the PyoS2 DNase cleaves the host DNA indiscriminately, the host might mitigate the damage by introducing frame-shift or nonsense mutations in the *pyoS2 Y640C* sequence or by losing the corresponding plasmid. During expression of PyoS2 Y640C, the host BL21(DE3) still grew under selection pressure of ampicillin and the expression of immunity protein ImS2 seemed to be unaffected even though no PyoS2 Y640C appeared on the SDS gel (Figure IV.16A). Hence, it was hypothesised that the strain retains the pET21 expression vector under the selected expression conditions, but a mutated variant of it. This mutation might be introduced by homologous recombination, a mechanism which can help organisms to disrupt or replace toxic genes with non-toxic sequences, thereby neutralising their harmful effects while preserving bacterial viability (*vide infra*). Although plasmid sequencing could reveal potential involvement of homologous recombination as a mechanistic cause for the failing expression of PyoS2 Y640C, we subsequently focused on optimising expression conditions instead to retrieve strong expression of the PyoS2 Y640C protein in the heterologous expression host *E. coli*.

Due to failed protein expression for the variant Y640C, individual expression conditions [varying expression temperature (20 °C vs. 37 °C) and time point of expression induction (early exponential after 3 h vs. late exponential after 8 h)] and their impact on PyoS2 Y640C expression were consequently evaluated in three individual clones of BL21(DE3) transformants carrying the PyoS2 Y640C harbouring expression vector (Figure IV.16B). The clones exhibited strongly diverging expression profiles for the desired PyoS2 Y640C protein. Clone 3 was not observed to produce any protein, independent of the incubation temperature or the growth phase at which expression was induced. In contrast, clone 1 and clone 2 displayed varying protein production, with clone 2 demonstrating the strongest protein production. In clone 2, protein yields were highest at a moderate temperature of 20 °C compared to the optimal growth temperature of *E. coli* at 37 °C. Furthermore, induction during the late exponential phase (after 8 h) significantly outperformed protein production in comparison to protein yields after induction during the early exponential phase (after 3 h). Given the inconsistent and unreliable protein expression of the PyoS2 Y640C variant in *E. coli* BL21(DE3), it was concluded that alternative T7 expression strains with a known tolerance to toxic proteins should be explored.

To validate the expression of PyoS2 Y640C in other expression host candidates, the alternative *E. coli* strains C43(DE3), Rosetta 2(DE3) pLysS, and JM109(DE3) were selected for further testing. C43(DE3) is a phenotypically selected mutant of BL21(DE3) and carries uncharacterised mutations that increase its tolerance towards toxic (membrane) proteins.[747] *E. coli* Rosetta 2(DE3) was engineered by Novagen to employ alternative codon usage to assist heterologous expression of eukaryotic proteins with rare codons. Its additional plasmid pLysS harbours the gene encoding T7 lysozyme. This protein binds to the T7 polymerase and is a known transcriptional regulator, tightly repressing basal expression.[748] And lastly, to minimise the risk of undesired inactivation of the potentially toxic *pyoS2 Y640C* gene through homologous recombination, the recombination-deficient strain *E. coli* JM109(DE3) (*recA*$^{-}$) was used as an alternative expression host.[749] While the standard expression host *E. coli* BL21(DE3) encodes a functional recombination machinery (*recA*$^{+}$), potentially leading to the inactivation of toxic genes via homologous recombination, the genetic constitution of strain JM109(DE3) would prohibit this undesired mechanism of DNA degradation.

After transforming the three alternative hosts with the target plasmid, carrying the sequence for the PyoS2 Y640C protein, the previously established expression conditions for PyoS2 proteins [TB media, induction at optical

density (OD_{600}) 0.6–0.8, 500 µM IPTG, 20 °C] were applied to three individual clones per strain. Strain JM109(DE3) did not grow in liquid culture, even in the absence of expression inducer IPTG, which is why this strain was excluded right away as a suitable expression host. The direct comparison of Rosetta 2(DE3) pLysS and C43(DE3) did not reveal significant differences in PyoS2 Y640C protein levels for any of the tested clones and strains (Figure IV.16C) when only examining the protein titre for a defined number of cells. However, strain C43(DE3) exhibited significantly improved growth in contrast to Rosetta 2(DE3) pLysS, reflected by the three-times higher cell density. While strain C43(DE3) reached a final cell density of OD_{600} 15.6 ± 0.3 after overnight protein expression, Rosetta 2(DE3) pLysS reached a final OD_{600} of 6.1 ± 0.2. Consequently, the toxin-resilient strain *E. coli* C43(DE3) was selected as the most suitable and tolerant host for the high-yielding large-scale expression of apparently toxic PyoS2 Y640C.

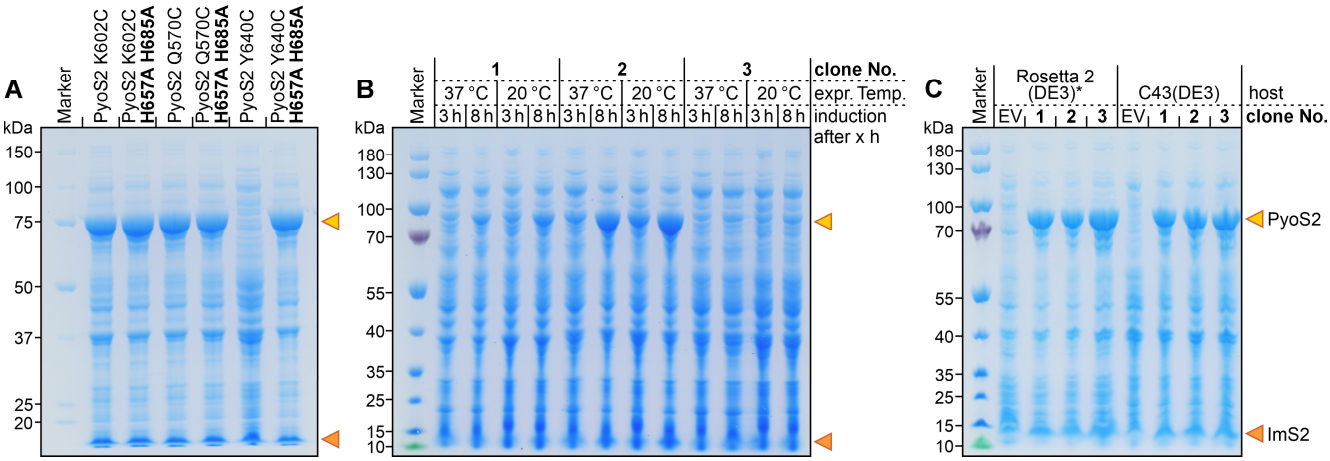


Figure IV.16. SDS-PAGE analysis of PyoS2 variant expression in different *E. coli* strains. Proteins were separated under denaturing conditions on 4-12% Bis-Tris PAGE gels at a loading of OD_{600} 0.1/well (whole cells). **A**. Heterologous expression of various PyoS2 cysteine mutants in *E. coli* BL21(DE3). **B**. Inhomogeneous expression of PyoS2 Y640C from three individual clones of BL21(DE3) with varying time points of induction (3 h vs. 8 h) and expression temperatures (20 °C vs. 37 °C). **C**. Reliable expression of PyoS2 Y640C from *E. coli* Rosetta 2(DE3) pLysS or *E. coli* C43(DE3). Protein sizes: ImS2 – 11 kDa; PyoS2 – 74 kDa. *Rosetta 2(DE3) pLysS.

Due to the generally higher tolerance of *E. coli* C43(DE3) towards toxic proteins and the observed homogenous expression of the toxic protein variant PyoS2 Y640C, which could not be expressed in the standard expression host *E. coli* BL21(DE3), all large-scale expressions of PyoS2 cysteine mutants were carried out in the heterologous host *E. coli* C43(DE3). In the following, the established two-step purification protocol provided pure cysteine mutants of PyoS2 and their respective DNase knock-outs (Figure IV.17), suitable for *in vitro* labelling with thiol-reactive small-molecule electrophiles.

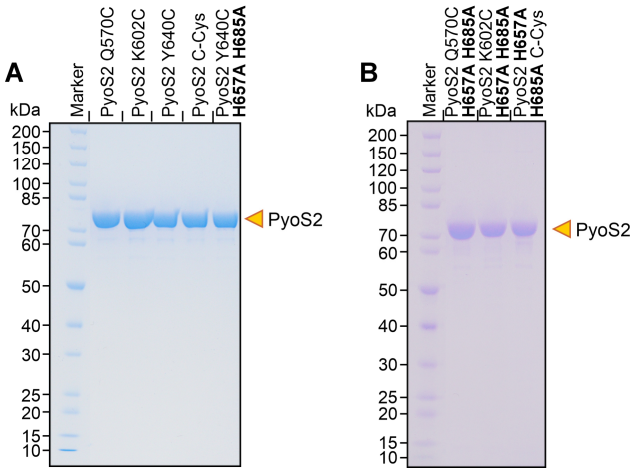


Figure IV.17. SDS gels of purified cysteine mutants of PyoS2. 2 µg of protein were loaded per well. Protein size: PyoS2 – 74 kDa.

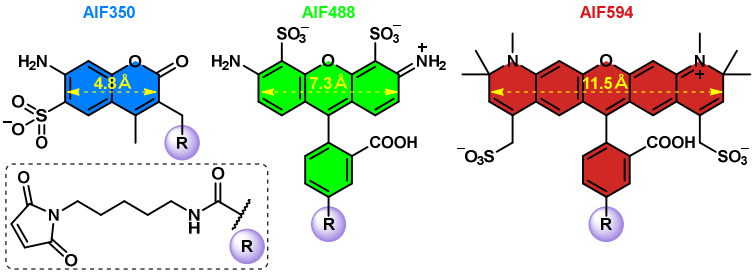
IV.3.4.2 Maleimide Labelling of PyoS2 Cysteine Mutants with Non-Toxic Fluorophores

The selection of an appropriate labelling chemistry is a crucial step for the labelling of the PyoS2 DNase to generate PyoS2 conjugates. First, we were aiming to synthesise conjugates between PyoS2 and fluorophores, which do not possess cytotoxic activity on their own. However, the labelling of PyoS2 with typical small-molecule fluorophores of <1 kDa would result in a negligible mass difference between unlabelled PyoS2 species and their conjugates. Hence, the two protein species cannot be separated by common SEC. Consequently, a thorough and homogeneous labelling of PyoS2 is a prerequisite to studying PyoS2 conjugates *in vitro* and their application *in vivo*. For this reason, the reliable and quantitative labelling of reactive cysteines with maleimide-functionalised small-molecule probes via thiol-Michael click chemistry was chosen in the first place. As the thiol-Michael reaction renders excellent conversions under mild reaction conditions in aqueous systems at near neutral pH, this type of chemistry is ideal for the functionalisation of proteins or other biomolecules.[750, 751] The preparation of PyoS2 conjugates with small-molecule labels is an essential intermediate step to study whether DNase labelling at the sites Q570C, K602C, Y640C, or C-Cys affects PyoS2 DNase activity *in vitro*, its membrane translocation, or the overall cell killing activity against *P. aeruginosa*. Furthermore, PyoS2 labelling could be auxiliary in answering the initial hypothesis of reduced affinity of ImS2 towards its cognate toxin PyoS2 by obstructing the binding of the immunity protein at the binding interface in the labelled mutant Y640C. As a reminder, Y640 is positioned in loop 4 of PyoS2 and located at the heart of PyoS2's IPE, allegedly contributing to ultra-high-affinity binding with ImS2 through polar and unpolar side chain contacts, water binding, and hydrogen bond interactions (cf. Figure IV.10D).

To further investigate the effects of interface labelling on PyoS2's DNase activity and the complex association between PyoS2 and ImS2, three commercial non-toxic AlphaFluor (AlF) fluorophores with a C_5 maleimide linker and varying probe diameter/hydrodynamic radius, namely AlF350, AlF488, and AlF594 (Scheme IV.4), were selected for thiol-Maleimide labelling of the PyoS2 DNase domain.[8] AlF350 is the smallest probe with a conjugated 2*H*-chrome-2-one scaffold. The other two probes, AlF488 and AlF594, are equipped with an additional benzoic acid moiety, connected through a biaryl axis to fused conjugated three-ring or five-ring π-systems, respectively.

[8] AlphaFluor (AlF) fluorophores are structurally identical with AlexaFluor fluorophores. However, the name AlexaFluor is protected under trademark law by Thermo Fisher Scientific, which is why the fluorophores of other manufacturers are marketed under a different name. In accordance with general naming conventions for these kind of fluorophores in biochemical publications, the fluorescent probes will be labelled consistently as AlphaFluor fluorophores in the following text.

With an increasing size of the conjugated system, the energy of the aromatic system decreases, resulting in a spectral red-shift toward longer wavelengths.



Scheme IV.4. Maleimide-functionalised fluorophores for thiol-maleimide labelling of PyoS2. Chemical structure of AlphaFluor 350 (AIF350), AlphaFluor 488 (AIF488), and AlphaFluor 594 (AIF594) C_5 maleimides. The ring colour corresponds to the colour at the absorbance maximum. Diameters were measured with Chem3D and do not include ring substituents.

After selecting the desired PyoS2 cysteine mutants and appropriate maleimide-functionalised AIF fluorophores for protein labelling, the PyoS2-AlphaFluor conjugates were prepared. Therefore, potential interprotein disulfide bridges in the PyoS2 cysteine mutants were initially reduced with the reducing agent dithiothreitol (DTT) and excess reducing agent was subsequently removed through desalting.[719] Thiol-maleimide labelling of PyoS2 mutants was then carried out with a 3-fold excess of maleimide-functionalised AIF probes and desalting was again employed for the separation of free unreacted dye from labelled protein to furnish the desired conjugates. The PyoS2-AIF conjugates were further validated by SDS-PAGE (Figure IV.18A) and coupled LC-MS analysis (cf. Table IX.4, Supporting Information).

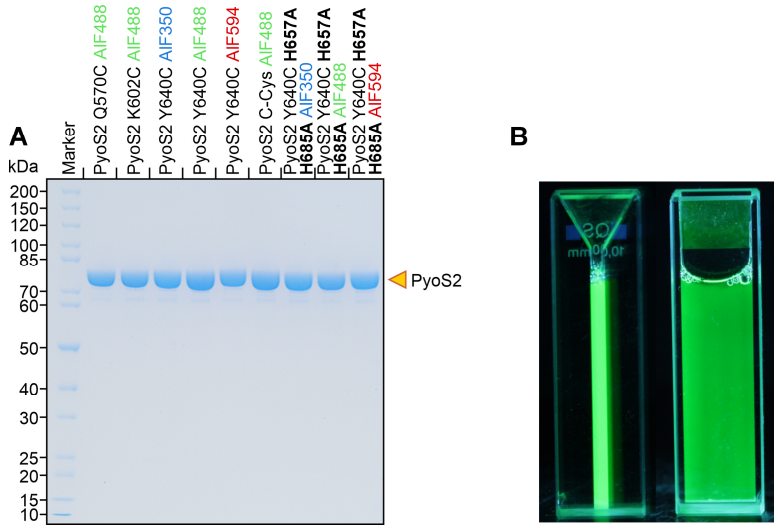


Figure IV.18. SDS gel of AIF-labelled PyoS2 variants and green fluorescence of an AIF488 conjugate. **A**. 2 µg of PyoS2-AIF conjugates were loaded per well. Protein size: PyoS2 – 74 kDa; Label sizes: AIF350 C_5 maleimide – 579 Da, AIF488 C_5 maleimide – 721 Da, AIF594 C_5 maleimide – 909 Da. **B**. Green fluorescence of the PyoS2 Y640C-AIF488 conjugate under excitation with UV-A light (315–400 nm) emitted by an Hg lamp.

Finally, the following PyoS2-AIF conjugates were obtained to address the key research questions outlined below:

- Does the labelling site of PyoS2-AIF conjugates impact the *in vitro* DNase activity and binding of ImS2?
  Variants: **Q570C**-AIF488, **K602C**-AIF488, **Y640C**-AIF488, **C-Cys**-AIF488

- Does a varying size/diameter of attached labels affect *in vitro* DNase activity, ImS2 association, and antibacterial activity *in vivo*?
  Variants: Y640C-**AlF350**, Y640C-**AlF488**, Y640C-**AlF594**
- Are conjugated AlphaFluor fluorophores toxic to *P. aeruginosa* when PyoS2 DNase activity is knocked out?
  Variants: Y640C H657A H685-**AlF350**, Y640C H657A H685-**AlF488**, Y640C H657A H685-**AlF594**

IV.3.5 Labelling at the PyoS2/ImS2 Interface Impairs Association of the Inhibitory Complex *In Vitro*

To determine whether DNase labelling affects nuclease activity of PyoS2, whether the specific labelling site influences DNase activity, and whether fluorophore labelling impacts the binding between PyoS2 and ImS2, AlF488 conjugates of the PyoS2 cysteine mutants (Q570C, K602C, Y640C, and C-Cys) were investigated for *in vitro* DNase activity. In order to do so, the previously introduced plasmid nicking assay (cf. Chapter IV.3.3) was employed to monitor cleavage of plasmid DNA over a period of 90 min for the selected PyoS2 cysteine mutants and their respective AlF-labelled conjugates.

Of all four tested conjugates, Q570C-AlF488 showed the highest DNase activity but was still less active than wild-type PyoS2 (Figure IV.19A; for wild-type cf. Figure IV.15A). Although supercoiled DNA was already fully cleaved similar to wild-type PyoS2 after 10 min ($t_{1/2,\text{supercoiled}}$: 2.65 min vs. 3.20 min), traces of linear DNA were still present after 90 min incubation time. In contrast, with wild-type PyoS2, the linear DNA was completely digested after 70 min of incubation. Nevertheless, strong fragmentation into smaller DNA species (DNA smear) through unspecific hydrolysis was still observed (average size after 90 min is 3000 bp, for wild-type average is 500 bp), indicating an overall minor impact of the fluorophore labelling in position Q570C on the catalytic activity of PyoS2. Of all four labelling sites selected for fluorophore attachment (Q570, K602, Y640, and the C-terminus), Q570 is the most distant labelling site from the DNase active site. Furthermore, residue Q570 is not located near other DNase residues that interact with the DNA substrate, making labelling in this particular position least likely to impact hydrolytic cleavage of the DNA substrate and its binding to the DNase (Figure IV.20).

In the reactions with all three other PyoS2-AlF488 conjugates, namely K602C, Y640C, and C-Cys, the supercoiled DNA was fully cleaved within the observation period of 90 min. While the conjugates K602C-AlF488 and C-Cys-AlF488 (Figure IV.19B and IV19D, respectively) were able to fully cleave the supercoiled DNA after 50 min ($t_{1/2,\text{supercoiled}}$: 13.6 min vs. 15.1 min), the interface mutant Y640C-AlF488 (Figure IV.19C) enabled the digestion of the supercoiled DNA form within only 20 min ($t_{1/2,\text{supercoiled}}$: 4.00 min). However, in contrast to wild-type PyoS2, large relative amounts of linear DNA were still present in the reactions with all three conjugates after 90 min. Despite the low half-life of the supercoiled form of the dsDNA substrate in the plasmid nicking reaction with PyoS2 Y640C-AlF488, 90.4% of linear DNA (relative to supercoiled and nicked DNA) remained after 90 min reaction time. The conjugates K602C-AlF488 and C-Cys-AlF488 showed a lower relative amount of linear DNA being present (65.9% vs. 69.5%), but still all conjugates were considerably less active than the Q570C-AlF488 conjugate (11.2% linear DNA remaining). Also, unspecific DNA cleavage into smaller fragments (DNA smear) was drastically reduced for conjugate K602C-AlF488, while unspecific fragmentation was only present to a negligible extent in the Y640C and C-Cys conjugates.

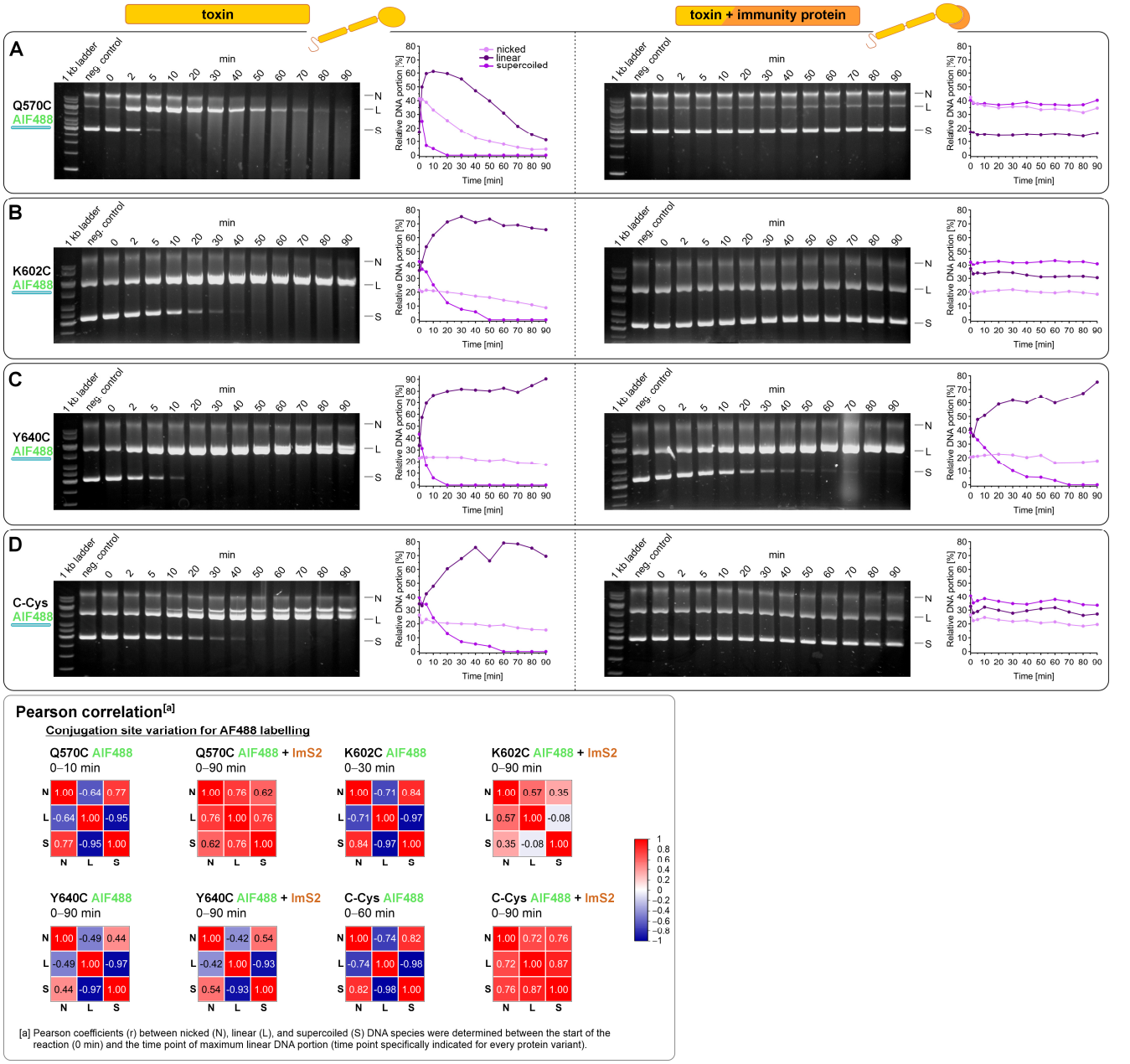


Figure IV.19. DNase kinetics of AlF488-labelled PyoS2 conjugates, and their neutralisation by ImS2. DNA digest of pET21a(+) plasmid DNA with 5 µM PyoS2 variants or a mixture of 5 µM PyoS2 and 5.25 µM ImS2 was monitored over 90 min and analysed by agarose gel electrophoresis (200 ng of DNA per time point). A negative control contained an equivalent amount of DNA, but no enzyme. Graphs were generated by densitometric analyses and display the relative portion of DNA (nicked, linear, supercoiled) in relation to incubation time. Pearson coefficients were determined from 0 min to the time point where the highest linear DNA portion was observed to distinguish assay-related coincident decrease of all DNA species (no DNase activity) from real DNase activity (particularly negative correlation between supercoiled and linear DNA). Fit parameters are summarised in Table IX.5 and Table IX.7 (Supporting Information).

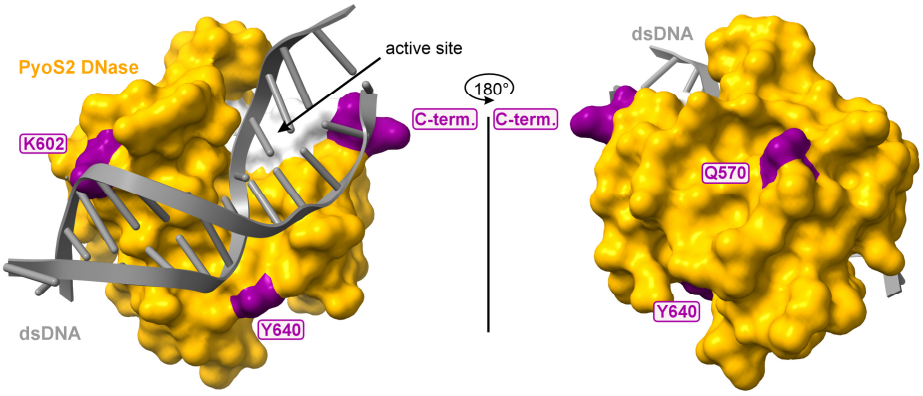


Figure IV.20. Positions of PyoS2 DNase residues selected for maleimide labelling (purple), relative to the dsDNA substrate (grey) and the active site (white). While K602, Y640, and the C-terminus are in very close proximity to the DNA binding pocket of the PyoS2 DNase, the residue Q570 lies on the DNA far side.

When the immunity protein ImS2 was added to all conjugates, no DNA hydrolysis was observed for the AlF488 conjugates of the PyoS2 mutants Q570C, K602C, and C-Cys. However, for the PyoS2 Y640C-AlF488 conjugate, the plasmid nicking assay revealed residual DNase activity of the conjugate, even in the presence of ImS2 in excess (1.05-fold excess). Although the linearisation of DNA by the Y640C-AlF488 conjugate was reduced in the presence of ImS2 in comparison to the ImS2-free reaction (75.4% vs. 90.4% after 90 min), the supercoiled form of plasmid DNA was still fully cleaved within 70 min and thoroughly transformed into linear DNA ($t_{1/2,\text{supercoiled}}$: 18.1 min). This observation clearly evidences that engineering of the PyoS2/ImS2 interface through the attachment of bulky fluorophores increases the structural mismatch between PyoS2 and ImS2, thereby reducing the affinity of the complex and overcoming the natural mechanism of PyoS2 immunity *in vitro*, which partially proves the initial hypothesis of this work.

After finding significant differences in DNase activity between PyoS2-AlF conjugates with AlphaFluor488 fluorophores attached at different labelling sites within the DNase, further investigations on how the label size influences DNase activity and in particular the interaction with ImS2 were of interest. Therefore, the PyoS2 mutant Y640C, which showed hampered interaction with the immunity protein, was selected for further *in vitro* DNase analyses. To modulate the label size (hydrodynamic radius, diameter of the conjugate system), the Y640C site was used in conjugation with the AlF350, AlF488, and AlF594 fluorophore dyes.

In the absence of ImS2, all three Y640C-AlF conjugates, namely Y640C-AlF350, Y640C-AlF488, and Y640C-AlF594, showed the same kinetics in regard to the decline of the supercoiled DNA species (Figure IV.21, B–D). Within 20 min, all three conjugates had converted the supercoiled form of plasmid DNA into the nicked or linear form.

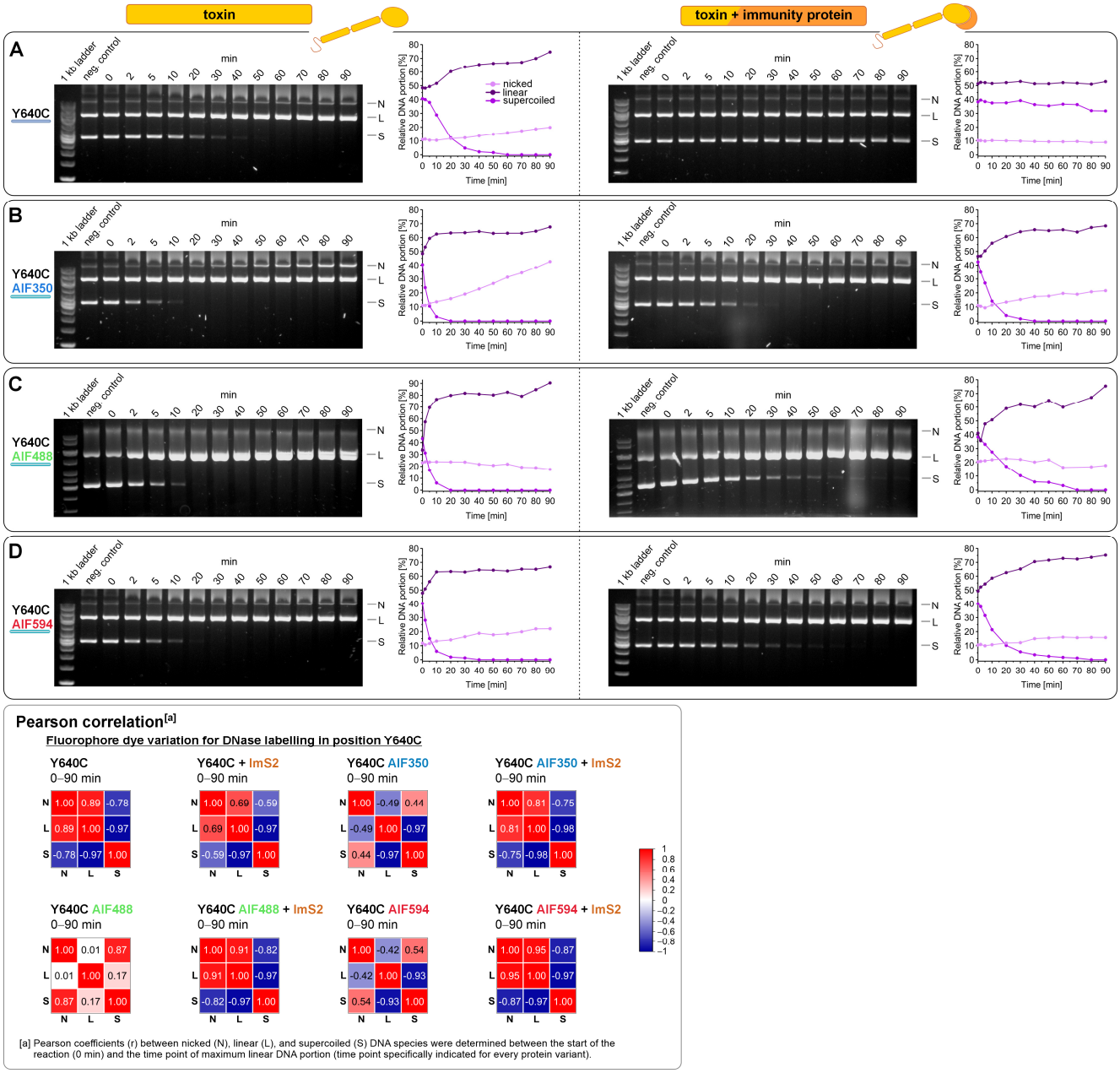


Figure IV.21. DNase kinetics of PyoS2 Y640C, its AIF dye conjugates, and their neutralisation by ImS2. DNA digest of pET21a(+) plasmid DNA with 5 µM PyoS2 variants or a mixture of 5 µM PyoS2 and 5.25 µM ImS2 was monitored over 90 min and analysed by agarose gel electrophoresis (200 ng of DNA per time point). A negative control contained an equivalent amount of DNA, but no enzyme. Graphs were generated by densitometric analyses and display the relative portion of DNA (nicked, linear, supercoiled) in relation to incubation time. The value for 70 min (nicked and linear form) for PyoS2 Y640C-AIF488 in complex with ImS2 was excluded due to faulty densitometric data, based on the bright smear on the corresponding agarose gel. Pearson coefficients were determined from 0 min to the time point where the highest linear DNA portion was observed to distinguish assay-related coincident decrease of all DNA species (no DNase activity) from real DNase activity (particularly negative correlation between supercoiled and linear DNA). Fit parameters are summarised in Table IX.5, Table IV.6, and Table IX.7 (Supporting Information).

With a supercoiled DNA half-life of 2.80 min, the AIF350 conjugate degraded this particular DNA form as fast as wild-type PyoS2 ($t_{1/2,supercoiled}$: 3.20 min). But also, the two conjugates with the bulkier AIF488 and AIF594 fluorophores exhibited only slightly decreased DNase activity ($t_{1/2,supercoiled}$: 4.00 min and 3.86 min). However, while wild-type PyoS2 fully degraded all DNA forms into smaller fragments within the observation period of 90 min (cf.

Figure IV.15A), the AlF-labelled Y640C conjugates maintained a high relative portion of nicked and linear DNA after 90 min. To our surprise, the unlabelled mutant Y640C (Figure IV.21A) exhibited lower catalytic activity than all three AlF-labelled Y640C conjugates, requiring an extended reaction time of 50 min for a complete consumption of supercoiled DNA ($t_{1/2,supercoiled}$: 15.3 min).

When the ultra-high-affinity binding partner ImS2 was added to the plasmid nicking reactions, all Y640C-AlF conjugates exhibited reduced DNase activity in comparison to the ImS2-free reactions. This circumstance was deduced from the increased half-life of the supercoiled DNA species when the immunity protein was present [$t_{1/2,supercoiled}$: 7.19 min (AlF350), 18.1 min (AlF488), and 11.54 min (AlF594)]. Nonetheless, all conjugates still showcased thorough hydrolysis of supercoiled DNA 30–60 min post reaction initialisation (Figure IV.21, B-D). As all Y640C-AlF conjugates remain catalytically active even in the presence of excess immunity protein (1.05-fold excess), hampered ImS2-binding of these conjugates poses a high threat to DNA integrity *in vitro*. However, to date, no clear trend has been observed concerning the size of the attached fluorophore dye and its influence on DNase activity and ImS2 binding. The unlabelled Y640C mutant instead was apparently inhibited by ImS2 (Figure IV.21A). Although no obvious DNA hydrolysis was observable by eye, the densitometric analysis and Pearson correlation suggested a very slow but steady decrease of the supercoiled DNA form over 90 min ($t_{1/2,supercoiled}$: 291 min, r = 0.17). This low but measurable DNase activity of Y640C in the presence of ImS2 might also explain the observed toxic phenotype of PyoS2 Y640C during protein expression in the heterologous host *E. coli* BL21(DE3) despite co-expression of ImS2 (cf. Chapter IV.3.4.1).

An interesting but rather unexpected finding of this experiment is the diminished DNase activity of unlabelled PyoS2 Y640C in comparison to its AlF-labelled counterparts. Intuitively, one would expect the flexibility of proteins to decrease upon labelling with bulky fluorophores; therefore, decreased DNase activity upon labelling would have been hypothesised at first. Nonetheless, fluorophore labelling somehow rescued DNase activity, emphasised by the supercoiled DNA half-life as a measure of DNA stability. The supercoiled DNA half-life was increased from 3.20 min for wild-type PyoS2 to 15.3 min by introducing the single point mutation Y640C into PyoS2. However, after fluorophore labelling, the half-life decreased again to 2.80–4.00 min for the AlF-labelled Y640C conjugates. It may only be speculated why the attachment of the AlF labels leads to enhanced DNase activity in comparison to the unlabelled mutant Y640C. Here, it is supposed that the maleimide portion of the AlF labels might partially resemble the original Y640 residue and thereby stabilise the original protein fold of PyoS2 by restoring important intraprotein contacts for DNase activity, which have been lost upon substituting the Y640 residue against the small amino acid cysteine (Figure IV.22). Although the active site of PyoS2 with its metal-chelating histidine residues is distant from the mutation site Y640 at the immunity protein exosite, the small size of the DNase domain (14.5 kDa) is responsible for the bound dsDNA to pass residue Y640 in a very close distance of only 6.2 Å (Figure IV.22A).

Another close look into Y640-harbouring loop 4 and the surrounding secondary structure elements of the PyoS2 DNase reveals only three intraprotein contacts between Y640 and other amino acids from the DNase domain (Figure IV.22C). The hydrophobic residues V632 within α-helix V and I651 within loop 5 embrace the hydroxybenzyl ring of Y640 and stabilise its orientation through lateral hydrophobic interactions. Furthermore, the lysine residue K652 embeds Y640 from above through hydrophobic interactions between the aliphatic lysine alkyl chain and the aromatic system of Y640, supported by hydrogen bonds between the terminal hydroxy group of tyrosine Y640 and the ε-amino group of lysine K652. In contrast to Y640, lysine K652 is directly involved in the binding of the DNA substrate (vide infra), which is why it is assumed that its orientation is critical for the stabilisation of the PyoS2-dsDNA complex. Furthermore, the DNA rests on the meandering origin of loop 5 that is connected to the short 3_{10}-helix (Figure IV.22B). In the modelled cysteine mutant Y640C, the small amino acid cysteine does

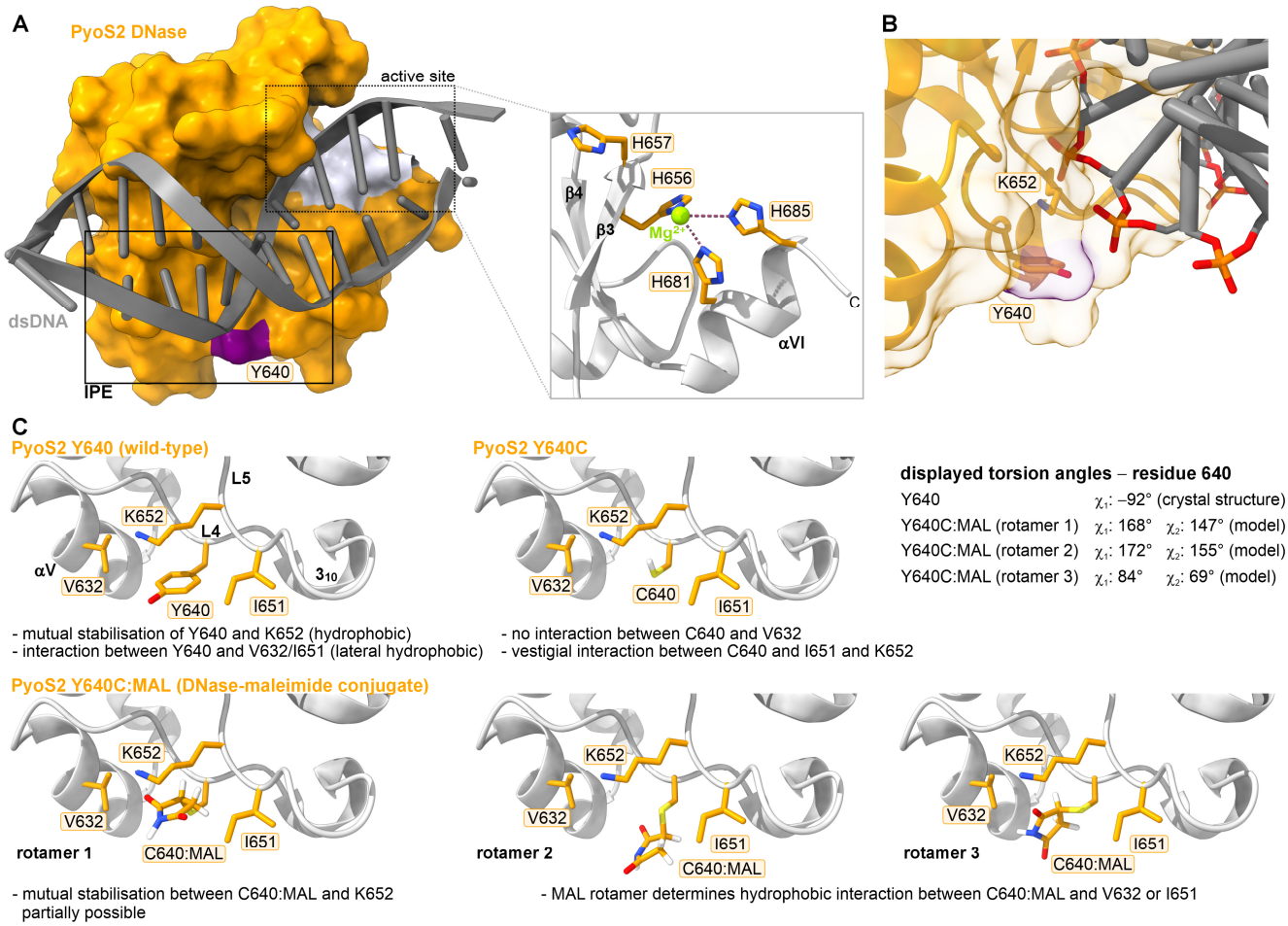


Figure IV.22. Snapshots of the PyoS2 DNase explaining the observed effects of AlF-labelling on DNase activity. **A**. PyoS2 crystal structure (PDB 4QKO) aligned with dsDNA from the co-crystallised ColE2-DNA complex. The active site (grey) contains the metal-chelating histidines (H656, H681, and H685) and the general base (H657) and is the catalytic heart of PyoS2's hydrolytic DNase activity. The Y640 residue is highlighted in purple. **B**. Y640 is not directly interacting with the dsDNA substrate but is in close proximity to it, explaining why maleimide labelling with bulky fluorophores (e.g. AF594) negatively affects DNA binding and thereby reduces DNase activity in comparison to the smaller PyoS2 Y640C AF350 conjugate. **C**. Excerpt of PyoS2's IPE with the original Y640 residue, the unlabelled Y640C substitution, and maleimide-labelled Y640C:MAL (three rotamers shown, no fluorophore attached), highlighting the mutual stabilisation of Y640 and K652 in PyoS2 and the partial restoration of intraDNase contacts upon maleimide labelling. All mutants for image **C** were prepared through *in silico* manipulation of the original PDB structure of PyoS2. Abbreviations: 3_{10} – 3_{10}-helix; MAL – maleimide.

not allow similar intraprotein contacts as the original amino acid Y640 in wild-type PyoS2 (Figure IV.22C). In fact, all contacts with V632 are lost and only a small and negligible overlap between Cβ of C640 and the residues I651 and K652 remains for stabilisation of the loop structures. As the activity of Y640C is significantly reduced in comparison to the bulky AlF conjugates, it is hypothesised that the gained flexibility within loop 4 and loop 5 through the missing mutual stabilisation in the small size cysteine substitution is responsible for the observed effects of diminished DNase activity. Besides reduced affinity towards its DNA substrate, lacking stabilisation of loop 5 might also lead to increased flexibility in the neighbouring 3_{10}-helix and β-strand 3. β-Strand 3 harbours the catalytically important histidine residues H656 (general base mechanism) and H657 (metal-coordination) and unreasonably high flexibility could also lead to decreased catalytic efficiency of the DNase.

A possible explanation for an increased DNase activity of the AlF-labelled Y640C variants despite the significant increase in size could be a partial restoration of intraprotein contacts with V632, I651, and K652 via the introduced

maleimide moiety of the conjugated C_5 maleimide fluorophore probe (Figure IV.22C). Depending on the rotamer of the 2,5-dioxopyrrolidine dipole, contacts between the hydrocarbon backbone of the artificial heterocycle and PyoS2 protein side chain residues can either restore hydrophobic interactions with V632 or I651. Concurrently, the lysine residue K652 can maintain interactions with the polar portion of the 2,5-dioxopyrrolidine label through its terminal amino group or via its hydrophobic alkyl chain with the interior hydrocarbon scaffold of the maleimide label. Although these experimental findings can be well explained by analysing the structural model of PyoS2 and its mutants, the assumptions made are merely speculative and only focus on the reactive maleimide portion of the introduced AlF-labels. Other contributions (size, electrostatic interactions) are not further discussed in this section, as no significant difference between the conjugates with varying probe size was detectable (cf. Figure IV.21, B–D).

In summary, the presented results clearly reveal notable differences in DNase activity, caused by labelling with AlF488 dyes in varying positions of the DNase domain. The least negative impact on DNase activity was observed for the labelling site Q570C, as this particular residue neither lies close to the active site nor close to DNase residues that interact with the DNA substrate. The residues K602C, Y640C, and C-Cys instead are all in close proximity to DNA-interacting residues and the C-terminal cysteine C-Cys is moreover directly protruding from the active site of the DNase (cf. Figure IV.20). While labelling of the DNase in the positions Q570C, K602C, and C-Cys did not affect ImS2 binding and neutralisation of DNase activity through the cognate immunity, the Y640C-AlF488 conjugate was shown to retain DNase activity in the presence of ImS2. Furthermore, the maleimide labelling seems to restore important intraprotein contacts within the DNase domain, leading to its stabilisation and increased catalytic DNase activity in contrast to the unlabelled mutant Y640C. Although the statement of impaired association of the PyoS2/ImS2 complex for the Y640-AlF conjugates is limited to *in vitro* DNase activity for now, it is the first report of overruling the immunity protein-mediated protection from bacteriocins.

Since the toxin-antitoxin relationship found between PyoS2 and ImS2 is representative for all other S-type pyocins and most other bacteriocins from Gram-negative bacteria, the natural dissemination of immunity proteins is a major barrier to a broader application of those antimicrobial proteins. Therefore, the labelling strategy developed in this work presents an auspicious approach to bypass the innate bacterial immunity *in vivo*. Thereby, this strategy has the potential to significantly enhance the applicability of bacteriocins to target pathogenic bacteria which have accumulated antimicrobial resistance to multiple common antibiotics.

IV.3.6 PyoS2 ID Mutants are Highly Deficient in ImS2 Binding but Show Strongly Impaired DNase Activity

One fundamental hypothesis of this work was that the ultra-high-affinity interaction between PyoS2 and ImS2 can be disrupted by strategically mutating PyoS2 residues which are involved in complex association. In the previous chapter it was found that the single Y640C amino acid substitution at the IPE within the DNase domain of PyoS2 weakens the interaction between PyoS2 and ImS2, thereby allowing the DNase toxin to remain partially active even in the presence of ImS2 (cf. Chapter IV.3.5). As this effect is further enhanced through the *in vitro* attachment of bulky fluorophore dyes to the DNase domain, we hypothesised that an equally enhanced effect of weakened PyoS2/ImS2 interaction can be triggered by multiple amino acid substitutions, causing a critical structural change of the IPE. The previously presented mutant PyoS2 ID ("*interaction deficient*") was specifically designed for this purpose, carrying multiple mutations within the IPE of PyoS2 in those positions that are known to mediate intraprotein contacts with ImS2 (cf. Chapter IV.3.1.4, Table IV.2). A PyoS2 mutant fully incapable of interacting with ImS2 would be a superior bacteriocin for clinical applications, as innate (ImS2-dependent) PyoS2-resistance would not protect *P. aeruginosa* strains from the mutant pyocin, leading to a broader antimicrobial spectrum than

that of the corresponding wild-type pyocin. Furthermore, utilisation of an interaction-deficient mutation of PyoS2 would reduce the practical effort needed to produce the previously employed PyoS2-AIF conjugates, as the downstream *in vitro* labelling step for the covalent attachment of the fluorophore is eliminated.

In the common experimental sequence towards antimicrobial susceptibility testing of PyoS2 mutants and conjugates – comprising the essential steps of DNA cloning, heterologous protein production, and protein purification of PyoS2 ID – the first attempt using the previously established workflow for single cysteine mutants of PyoS2 failed already at the step of molecular cloning. Seemingly, the cloning of the *pyoS2 ID* comprising vectors posed a significant challenge to the cloning host *E. coli* DH5α. Although all *pyoS2* genes (including *pyoS2 ID* variants) are under control of the tightly-regulated T7 promoter in the pET21a(+) plasmids, no DH5α transformants carrying copies of the *pyoS2 ID* or *pyoS2 ID Y640C* containing vectors were able to grow in liquid LB growth media, even in the absence of expression inducer IPTG. This is even more surprising, because strain DH5α does not carry a chromosomal copy of the T7 polymerase and gene expression should be strictly suppressed in theory. But in fact, even strains incapable of producing the T7 RNA polymerase are capable of extremely low basal expression of genes under control of the T7 promoter. This background expression of target genes was previously linked to the transcriptional readthrough of *E. coli*'s own RNA polymerase during transcription of genes located upstream of the target gene under control of the inducible T7 promoter.[752] Reports on this phenomenon are scarce and always linked to highly toxic proteins, for which already a few protein copies in the cell can cause cellular death.
Indeed, problems in PyoS2 protein expression had been previously noted for the PyoS2 Y640C mutant with the point mutation located at the IPE (cf. Chapter IV.3.4.1). However, these issues were limited to overexpression of protein in the heterologous host *E. coli* BL21(DE3) and the cloning of the respective plasmid in DH5α had not shown any sign of complications. And yet, the *pyoS2 ID* variants seem to be more challenging, even in the process of cloning.
The common *E. coli* DH5α cloning strain lacks a functional copy of the DNA recombinase *recA* gene, leading to higher plasmid stability and avoiding undesired mutations in the target genes via homologous recombination.[753, 754] Contrariwise, RecA activity can be used by *E. coli* strains to inactivate toxic genes that lead to defective phenotypes or cell death. When recognising DNA damage, RecA promotes self-cleavage of the LexA repressor and thereby activates the cellular SOS response to repair DNA damage.[755] Consequently, the absence of chromosomal *recA* sabotages the SOS response and DNA damage repair. Since PyoS2 carries DNase activity in its CTD, the toxin induces damage to the genomic information of the host cell unless thoroughly protected through co-expression and ultra-tight binding of the cognate immunity protein ImS2. For wild-type PyoS2, this complex between PyoS2 and ImS2 forms through ultra-high-affinity association and protects the expression host from being harmed. Nevertheless, low basal expression through a leaky T7 promoter seemed to be sufficient to kill PyoS2 ID-producing strains despite the co-expression of immunity protein ImS2, leading to the first assumption of strongly inhibited interaction between both proteins. At this point, it should be noted that structure modelling with AlphaFold did not indicate any misfolding of the mutant PyoS2 ID, which contains a total of six amino acid substitutions (cf. Figure IV.13B). As the PyoS2 ID proteins were already toxic to the *E. coli* cloning strain DH5α in the absence of expression inducer and resulted in full inhibition of growth in liquid culture, an alternative cloning host with higher resilience to toxins and toxic proteins was needed. From the previous experience with the *E. coli* expression strain C43(DE3) and its tolerance against high levels of the toxic PyoS2 Y640C variant, this particular strain was selected for cloning and expression of the PyoS2 ID and PyoS2 ID Y640C proteins.

With *E. coli* C43(DE3), the cloning of all pET21a(+) expression vectors with *pyoS2 ID* variants proceeded smoothly without any further complications. Nonetheless, the purification of the PyoS2 ID toxins also turned out

to be more difficult than expected. The attempted Ni-NTA purification of PyoS2 ID variants did not provide a matrix-bound complex of PyoS2/ImS2-His_6 as previously observed for wild-type PyoS2. Instead, only the His-tagged immunity protein ImS2 remained immobilised on the column, leaving the PyoS2 ID mutants unbound in the flow-through together with the bulk protein of the *E. coli* expression host. Consequently, the strongly impaired binding behaviour of PyoS2 ID to its immunity partner ImS2 required an adapted purification procedure to allow isolation of pure PyoS2 ID toxins. Therefore, a modified protocol, including Ni-NTA purification, an additional ion exchange chromatography,[756] and SEC was established. In detail, the crude cell lysates were applied to the Ni-NTA resin to remove ImS2-His_6 from the solution. A buffer exchange of the PyoS2-containing flow through to a low ionic strength potassium phosphate buffer (10 mM, pH 7) via dialysis caused significant precipitation of bulk protein. Subsequently, the cleared supernatant containing the PyoS2 ID proteins with a net-positive charge (the isoelectric point is approximately 9.0) was applied to a custom-packed CM Sepharose FF cation exchange column and more bulk protein was removed by washing with the same buffer. Instead of inducing target protein elution with a pH shift, PyoS2 ID elution was achieved by increasing the ionic strength with NaCl to a concentration of 400 mM. Then, the purification continued on a SEC resin as common for all other purifications to yield highly pure PyoS2 ID derivatives (Figure IV.23). Lastly, the PyoS2 ID Y640C variant was labelled with the AlF488 fluorophore as described earlier (cf. Chapter IV.3.4.2).

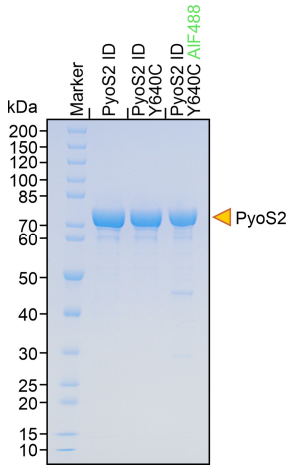


Figure IV.23. SDS gel of PyoS2 ID variants and its AlF488 conjugate. 2 µg of protein were loaded per well. Protein size: PyoS2 – 74 kDa;

Finally, the *"interaction deficient"* PyoS2 ID mutants and its AlF488-labelled conjugate were subjected to the *in vitro* DNase assay to probe residual plasmid nicking activity and interaction of the protein derivatives with the immunity protein ImS2 (Figure IV.24). All three ID protein variants (PyoS2 ID, ID Y640C, and ID Y640C-AlF488) exhibited significantly impaired DNase activity and could not fully convert the supercoiled DNA species within the limited observation window of 90 min. Despite a very low incline of linear DNA during the sampling period of 90 min, Pearson correlation analysis and permutation analysis confirmed a statistically significant incline of the linear DNA form, proving active degradation of supercoiled DNA through the PyoS2 ID variants (Figure IV.24, Figure IX.10, Table IX.7, and Table IX.8, Supporting Information). The detailed analysis of interconversion between the three DNA forms through densitometric analysis of the agarose gels suggested a decline in supercoiled DNA cleavage and DNase activity in the order PyoS2 ID > ID Y640C > ID Y640C-AlF488, emphasised by supercoiled DNA half-life and conversion ($t_{1/2,supercoiled}$: 83.8 min vs. 127 min vs. 239 min; conversion: 56.6% vs. 44.2% vs. 22.1%). Most importantly, all three PyoS2 ID variants sustained their residual DNase activity independent of the presence or absence of the immunity protein with supercoiled DNA half-life between 109 min

and 196 min. Thus, it was concluded that the introduced mutations drastically reduce the affinity between both binding partners but must also cause undesired structural changes within the DNase domain, leading to the drastic reduction of DNase activity.

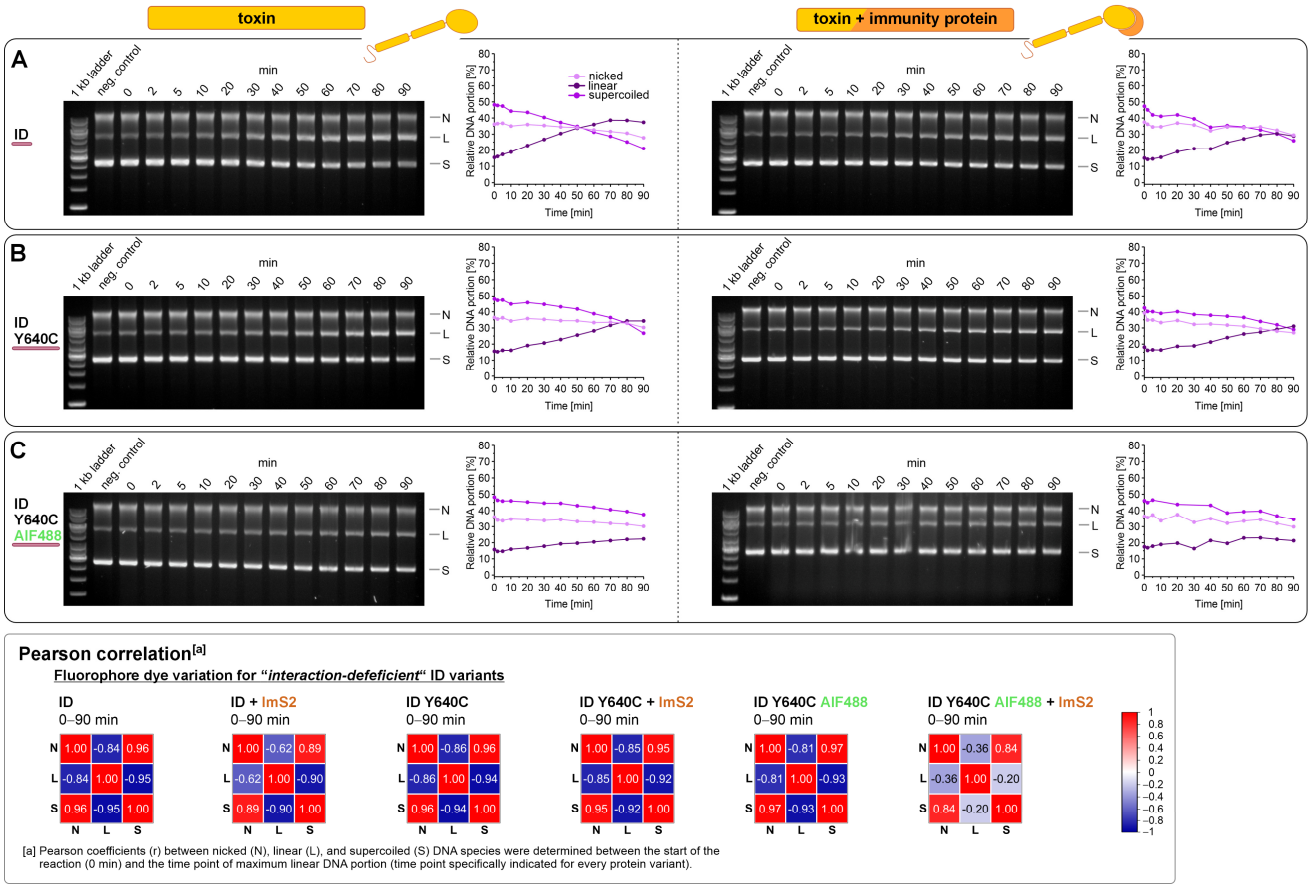


Figure IV.24. DNase kinetics of PyoS2 ID variants, and their neutralisation by ImS2. DNA digest of pET21a(+) plasmid DNA with 5 µM PyoS2 variants or a mixture of 5 µM PyoS2 and 5.25 µM ImS2 was monitored over 90 min and analysed by agarose gel electrophoresis (200 ng of DNA per time point). A negative control contained an equivalent amount of DNA, but no enzyme. Graphs were generated by densitometric analyses and display the relative portion of DNA (nicked, linear, supercoiled) in relation to incubation time. The value for 10 min and 30 min (nicked and linear form) for PyoS2 Y640C-AlF488 in complex with ImS2 was excluded due to faulty densitometric data, based on the bright smear on the corresponding agarose gel. Pearson coefficients were determined from 0 min to the time point where the highest linear DNA portion was observed to distinguish assay-related coincident decrease of all DNA species (no DNase activity) from real DNase activity (particularly negative correlation between supercoiled and linear DNA). Fit parameters are summarised in Table IX.5, Table IV.6, and Table IX.7 (Supporting Information).

Since the introduced mutations of PyoS2 ID seem to be sufficient to effectively impair PyoS2/ImS2 association but also severely reduce DNase activity, the additional attachment of DNase activity affecting fluorophore labels is not favoured. Although further mutational analyses will be needed to decipher the impact of every single amino acid substitution of the PyoS2 ID mutant on its DNase activity to minimise ImS2 binding while retaining the highest possible DNase activity, the current results may already outline the role of certain amino acid residues. A closer look into the structure of the DNase domain previously revealed that all six amino acids (N626, D635, Y640, E643, Q646, and K652) are involved in ImS2 binding to the IPE of PyoS2 (cf. Chapter IV.3.1.4). However, this examination disregarded the potential role of these particular residues in the binding of the DNA substrate. Since drastically decreased DNase activity was observed for all PyoS2 ID mutants in comparison to wild-type PyoS2 or

even the single cysteine mutants, the crucial involvement of certain PyoS2 ID residues in DNA binding is likely. For further computational investigation of this matter, the AlphaFold 3 algorithm was employed to generate structural models of wild-type PyoS2 and PyoS2 ID in complex with the Mg^{2+} cofactor and dsDNA (Figure IV.25).

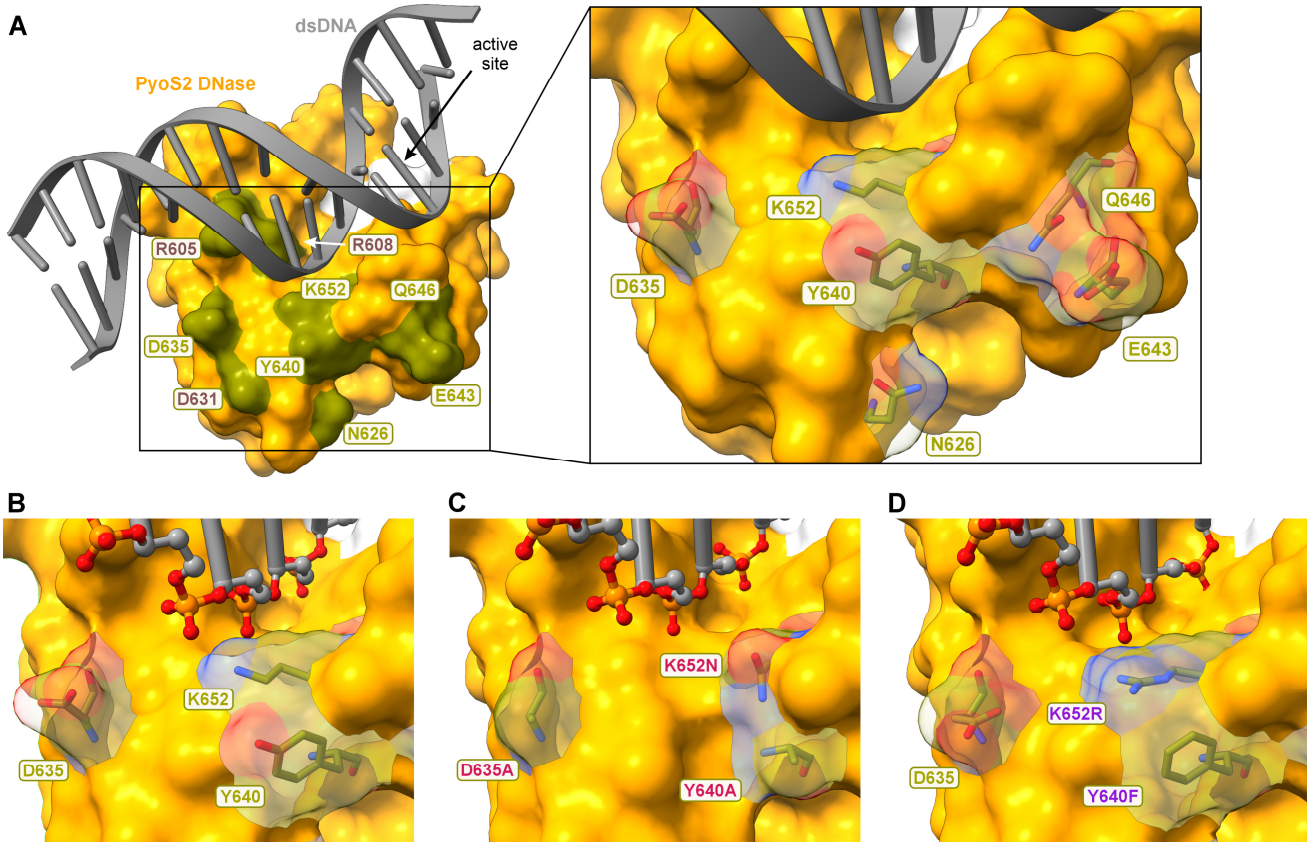


Figure IV.25. Alignment of the PyoS2 DNase domain with its DNA substrate. Protein folds and binding of the DNA substrate were modelled with AlphaFold 3. **A**. IPE residues from the PyoS2 DNase are highlighted (green). Those residues selected for mutagenesis to generate PyoS2 ID are labelled in green, while others are labelled in brown. Active site histidines (H656, H657, H681, H685) are highlighted in white. **B**. Interaction of K652 with the P–O moiety of the DNA backbone and its stabilisation from below through hydrophobic interaction with the aromatic residue of Y640 in wild-type PyoS2. **C**. PyoS2 ID with the mutations N635A, Y640A, and K652N in complex with the DNA substrate. The lower support of the DNA P–O backbone from K652 is lost in this mutant. **D**. Suggested adaptation of PyoS2 ID through conservative substitutions K652R and Y640F to increase DNA binding but maintain overall low ImS2 affinity in comparison to the current PyoS2 ID version.

First, a structural alignment between the crystal structure of PyoS2 (PDB 4QKO) and the AlphaFold model of PyoS2 was generated with an RMSD of 0.69 Å between the two structures (not shown). Thus, the AlphaFold algorithm provides an accurate model of PyoS2, eligible for the analysis of mutational effects on binding of the DNA substrate. Second, the AlphaFold model revealed that the PyoS2 residues N626, D635, E643, and Q646 are not involved in interaction with the double-stranded DNA (Figure IV.25A). Hence, their mutation towards other amino acids, such as in mutant PyoS2 ID, may affect the overall DNase fold, but a direct effect on DNA binding is unlikely. But also, no apparent influence of the N626D, D635A, E643D, and Q646N substitutions on the integrity of the DNase fold was observed in the model of PyoS2 ID. After excluding four of the six amino acid residues in the PyoS2 ID mutant as responsible for the drastic loss of DNase activity, the focus was shifted to the remaining residues, Y640 and K652. Particularly the side chain of K652 is directly involved in the interaction with the backbone of the double-stranded DNA substrate (Figure IV.25B). In the DNA-bound structure, the negatively charged P–O moiety from the backbone of the nucleic acid species rests on the distal part of the positively charged

K652 ε-amino side chain. Furthermore, the aliphatic moiety of the K652 side chain is stabilised from below through hydrophobic interactions with the aromatic π-system of Y640. Hence, a concurrent substitution of K652 and Y640 through smaller amino acids (Y640A and K652N in PyoS2 ID) would probably result in a drastically diminished DNA binding affinity in this region of the DNase domain (Figure IV.25C). Consequently, future optimisation of PyoS2 ID should mainly focus on residues K652 and Y640. Since the single amino acid substitution Y640C on its own is already known to notably decrease DNase activity of PyoS2 (cf. Chapter IV.3.5 and IV.3.7), a vital role of Y640 for the stabilisation of the K652 side chain is assumed. Therefore, advanced protein derivatives of PyoS2 ID should exploit conservative amino acid substitutions in these two positions, Y640 and K652, to retain stabilisation of DNA substrate on one hand, but still reduce the interaction of the DNase with the cognate immunity protein ImS2 on the other hand. In this regard, the two mutations Y640F and K652R are proposed to enhance stabilisation of the DNA backbone in comparison to the currently investigated PyoS2 ID variant carrying the Y640A and K652N mutation (Figure IV.25D).

In conclusion, the PyoS2 ID mutant retained low DNase activity while being highly deficient in its interaction with the immunity protein ImS2. The displayed cytotoxicity resulting from this binding defect was so high that even very low basal expression in the *E. coli* DH5α cloning strain, mediated by transcriptional readthrough of *E. coli*'s own RNA polymerase,[752] caused thorough growth suppression in liquid media. Moreover, this experiment proves that the PyoS2/ImS2 interface can be shaped by mutagenesis to modulate the affinity of ImS2 towards PyoS2, as hypothesised earlier in this chapter.

IV.3.7 Long-Term Exposure of DNA to PyoS2 Variants Discloses Hidden Aspects of Mutagenesis and Labelling *In Vitro*

The previous chapters presented strong evidence that mutations and the attachment of bulky fluorophores at the IPE of PyoS2 partially overrule neutralisation of PyoS2 DNase activity through binding of ImS2. Nevertheless, the kinetic investigation of *in vitro* DNase activity with a limited analysis window of 90 min showed only marginal differences between PyoS2 mutants and conjugates with very low DNase activity. Therefore, a single-time-point analysis after 15 h of DNA hydrolysis was additionally performed to directly compare all mutants and conjugates in one experiment (Figure IV.26A). Moreover, all supercoiled DNA half-lifes determined earlier through densitometric analysis were compiled (Figure IV.26B). Together, these data allow us to draw a conclusion on the systematic impact of conjugation and mutagenesis on PyoS2 *in vitro* DNase activity.

In compliance with the previous kinetic investigation, wild-type PyoS2 was the most active DNase bacteriocin. It degraded all DNA forms (linear, supercoiled, nicked) thoroughly over 15 h into small DNA fragments (smear) with an average size of <100 bp (Figure IV.26A) and a supercoiled DNA half-life of 3.20 min (Figure IV.26B). However, in association with ImS2, no DNase activity was detected ($t_{1/2}$ = >15 h). Thus, the cognate immunity ImS2 fully protects the DNA from degradation by binding to the IPE of the PyoS2 DNase domain. All unlabelled single cysteine mutants of PyoS2 completely degraded the three forms of DNA and left smaller, unspecified fragments behind. The Q570C mutant came closest to wild-type PyoS2 activity (100–500 bp fragments), followed by the C-Cys mutant (100–750 bp fragments). The K602C and Y640C cysteine mutants showed clear impairment of DNase activity as indicated by the broader size distribution of residual DNA fragments (250–3000 bp). While the interaction with ImS2 fully protected the plasmid DNA from hydrolysis through the Q570C, K602C, or C-Cys mutants over 15 h, only the Y640C mutant drew a different picture and unleashed DNase activity despite the presence of ImS2 in a slight excess ($t_{1/2}$ = 292 min). Although the small portion of supercoiled DNA being converted into linear and nicked DNA by PyoS2 Y640C may appear unspectacular, it was

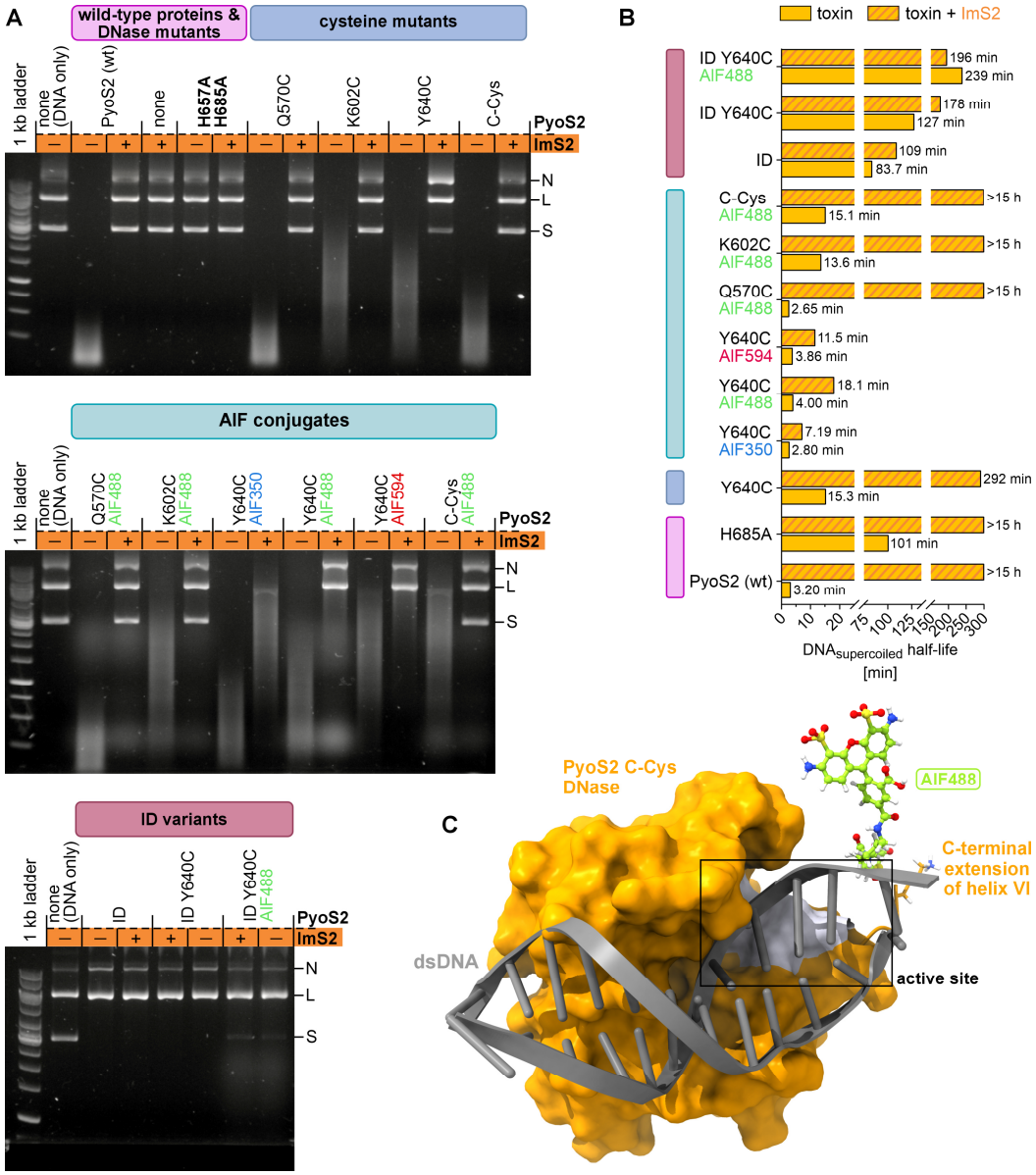


Figure IV.26. Plasmid nicking assay with extended incubation time (15 h) for all PyoS2 mutants and AIF conjugates in the presence (+) or absence (–) of ImS2. **A**. Isolated pET21a(+) plasmid DNA was incubated with 5 μM PyoS2 variants with ImS2 at 5.25 μM as indicated in the figure. Samples were incubated for 15 h and a volume equivalent to 200 ng DNA was collected for analysis via agarose gel electrophoresis. A negative control contained an equivalent amount of DNA, but no enzyme. The nicked, linear, and supercoiled DNA forms are labelled with the respective symbols N, L, and S. DNA digest is visualised by interconversion of DNA forms or by degradation of DNA into smaller fragments (smear). **B**. Half-life of supercoiled DNA for selected DNase-active PyoS2 mutants and conjugates in the presence and absence of ImS2. Half-lifes were calculated from the time-resolved plasmid nicking assay, as shown in Figure IV.15, Figure IV.19, Figure IV.21, and Figure IV.24. **C**. PyoS2 C-Cys-AIF488 DNase domain (wild-type PyoS2 DNase from the PDB structure 4QKO in yellow) with additionally modelled C-terminal residues (Gly Gly Lys Cys), aligned with dsDNA from the co-crystallised ColE2-DNA complex (grey, PDB 1ZNS) to highlight the DNA binding site of PyoS2. The active site (grey) contains the metal-chelating histidines (H656, H681, and H685) and the general base (H657) and is the catalytic heart of PyoS2's hydrolytic DNase activity. The ultimately modelled amino acid in the PDB structure is K686, but the residues ^{687}GGK^{689} are missing. Thus, the C-terminal GGK peptide and the C-terminally attached cysteine residue C690 were modelled in a flexible loop, appending from helix VI at the active site. The peptide in conjugation with the maleimide-functionalised AIF488 fluorophore dye (green) is presented in only one of many potential conformations to visualise the putative interference of the AIF488-label with DNA association and dissociation from the DNase domain.

still sufficient to display a cytotoxic phenotype during protein production in the heterologous expression host *E. coli* BL21(DE3) (cf. Chapter IV.3.4.1, Figure IV.16).

Next, labelling of the DNase domain with AlF488 fluorophores at positions Q570C, K602C, or Y640C did not impact DNase activity compared to the same protein mutants without attached fluorophore labels (Figure IV.26A). But for the C-terminally modified fluorophore conjugate C-Cys-AlF488, a drastic shift of the DNA fragments towards larger sizes was identified in comparison to the unlabelled PyoS2 C-Cys mutant (3000 bp vs. <250 bp average DNA fragment size). Even linear DNA was not fully degraded by the C-Cys-AlF488 conjugate after 15 h, indicating severe impairment of the structural integrity of the PyoS2 DNase domain or a negatively affected binding of the DNA towards the active site. In the case of mutant C-Cys, the latter explanation comes to fruition, as the labelling site lies at the end of helix VI of the DNase. Helix VI harbours the active site residues H681 and H685 and interacts with the minor groove of the DNA substrate. Apparently, the fluorophore protruding into the active site is partially blocking both the dsDNA substrate from entering or the hydrolysed DNA from leaving the active site (Figure IV.26C). Similar to the unlabelled proteins, only the AlF conjugates of mutant Y640C can catalyse DNA hydrolysis in the presence of the cognate immunity protein ImS2. Additionally, it is worth mentioning that the fluorophore-labelled conjugate Y640C-AlF350 possessed even higher DNase activity than the unlabelled protein PyoS2 Y640C. This observation, previously described already in the kinetic investigation of DNase activity (cf. Chapter IV.3.5 and IV.3.7), was attributed to a partial restoration of stabilising intraprotein contacts within the PyoS2 DNase domain. It was hypothesised that the introduction of the maleimide moiety resembles the original amino acid Y640 and recovers some stabilising interactions with the DNase residues K652, V632, and I651. However, the non-labelled mutant Y640C is unable to maintain these stabilising contacts (cf. Figure IV.22), most likely causing the witnessed reduction in DNase activity of this mutant (complete digestion of all three DNA forms for PyoS2 Y640-AlF conjugates after 15 h vs. 43% of initial supercoiled DNA remaining for unlabelled PyoS2 Y640C).

In general, a clear trend regarding the effect of increasing label sizes on PyoS2 DNase activity can be deduced from the corresponding gel (Figure IV.26A). In the absence of ImS2, the DNase activity of Y640C conjugates is decreasing with increasing label size (DNase activity: AlF350 > AlF488 > AlF594), as it can be seen from the increasing average size of unspecific hydrolysis products with increasing label size. However, all three conjugates still thoroughly digest the three full-length forms of DNA (linear, supercoiled, and nicked). When the immunity is added, the highest DNase activity is retained for the small AlF350 label and the majority of DNA is hydrolysed into smaller fragments. Even in the presence of ImS2, the activity of the PyoS2 Y640C-AlF350 conjugate is comparable to that of PyoS2 Y640C-AlF594 in the absence of ImS2. Although the other two Y640C-AlF conjugates with the AlF488 and AlF594 labels are also active, only the supercoiled DNA form has fully disappeared after 15 h. Partial fragmentation into smaller fragments occurs for both conjugates, but to a lesser extent for the conjugate with the larger AlF594 dye.

With PyoS2 ID mutants carrying six mutations at the IPE of PyoS2, only residual DNase activity was detected over 15 h (Figure IV.26A). Nevertheless, all variants displayed comparable DNase activity, characterised by complete (ID and ID Y640C) or at least partial digestion (ID Y640C-AlF488) of supercoiled DNA. Furthermore, no notable difference between the presence or absence of the cognate immunity protein ImS2 was spotted, as represented by the corresponding supercoiled DNA half-lives (Figure IV.26B).

Taking the presented data of the plasmid nicking assay and the analysed DNase activity of PyoS2 variants and conjugates into account, several conclusions for future studies on PyoS2 conjugates may be drawn. Mutations as small as single amino acid substitutions at the IPE of PyoS2 (at position Y640) have been shown to be of great

value to overcome the mechanism of immunity protein-mediated neutralisation of HNH DNase activity, as these mutations are suitable to reduce the affinity between PyoS2 and ImS2. In consequence, the ultra-high-affinity binding of both proteins is weakened, causing an insufficient protection of DNA from the hydrolytic activity of PyoS2. To enhance the structural mismatch between PyoS2 and ImS2, additional mutations at the IPE were introduced (PyoS2 ID) or covalent thiol-maleimide labelling in position Y640C with non-toxic AlF fluorophores was performed. Here, it was proven that the smaller the AlF label is, the higher the retained DNase activity in the presence of ImS2 *in vitro*. It is assumed that large labels interfere with DNA binding distant from the active site, as the DNA rests on the meandering origin of loop 5 that is connected to the short 3_{10}-helix and in close proximity to Y640C-harbouring loop 4, where the labels are attached (cf. Figure IV.22, A and B). However, all AlF-labelled conjugates of mutant Y640C displayed higher DNase activity than the unlabelled mutant Y640C itself, supposedly due to restored intraprotein contacts between the introduced maleimide moiety from the fluorophore and the surrounding amino acids V632, I651, and K652 from helix V and loop 5 of the DNase. These partially restored interactions consequently lead to stabilisation of the DNase HNH nuclease fold and a recovery of DNase activity. While the *"interaction-deficient"* variants of PyoS2 ID experienced no apparent inhibition of DNase activity in the presence of ImS2, their DNase activity seemed to be drastically impaired. Therefore, a step-by-step analysis would be required to unravel the role of every single amino acid (N626 D635 Y640 E643 Q646 K652) from the PyoS2 ID mutant for binding of the DNA substrate and its contribution to DNase activity. Furthermore, in-depth studies could reveal suitable amino acid substitutes for every position to minimise the interaction with ImS2 and concurrently maximise the sustained DNase activity. As the net positive charge of the DNase was hypothesised to be crucial for protein translocation and delivery of the DNase domain into the cytoplasm of host cells, as shown for DNase colicins,[727] the rational protein design should also pay regard to the issue of electrostatics.

In summary, extensive mutagenesis and labelling of PyoS2 at the IPE have proven great potential to expand the catalytic DNase activity of PyoS2 to those conditions where the antitoxin ImS2 is present. Therefore, the novel protein mutants and conjugates could potentially overrule the innate immunity protein-mediated PyoS2-resistance of PyoS2-producing *P. aeruginosa* strains. Moreover, using our current knowledge of predicted or experimentally validated HNH nuclease bacteriocins and the highly conserved binding mode of their respective immunity proteins, the presented strategy might be a general approach to extend the antibacterial spectrum of pyocins, colicins, or bacteriocins in general to provide alternatives to current treatment options against multidrug-resistant Gram-negative human pathogens.

IV.3.8 Impaired Binding of ImS2 to the PyoS2 DNase Overrules PyoS2-Resistance of *Pseudomonas aeruginosa* PAO1

Nuclease bacteriocins, such as PyoS2, and their respective immunity proteins bind each other with ultra-high affinity in the femtomolar range.[733, 734] The binding affinities shared by all HNH nuclease bacteriocins ensure thorough protection for producing strains from DNase activity of their own pyocins and save them from self-inflicted damage. Furthermore, the high binding affinity towards immunity proteins prevents the strains from being killed by pyocin-producing competitors in the fight for ecological niches. The clinical isolate and laboratory strain *P. aeruginosa* PAO1 was used as a donor strain to access the *pyoS2* gene (locus PA1150) and its cognate immunity gene *imS2* (locus PA1151).[757] Although genome analysis of *P. aeruginosa* PAO1 reveals the presence of the correct FpvA type I siderophore receptor (*fpvA*, locus PA2398) that is needed for OMP hijacking and translocation of PyoS2 into the target cell,[713] PAO1 is inherently resistant to PyoS2, due to the induced expression of ImS2 as part of the SOS response upon recognition of DNA damage.[731, 758] While this co-expression of

immunity proteins is a life-saving warrantor in a highly competitive microbiome, this widespread protein-mediated bacteriocin-resistance limits the application potential of bacteriocins as an antimicrobial agent.

Earlier in this thesis, it was hypothesised that the conserved translocation mechanism of PyoS2 can be exploited to use PyoS2 as a carrier molecule for potential small-molecule drugs. This would allow the drugs to bypass the impermeable membrane of *P. aeruginosa* and be selectively delivered into the cells of the opportunistic pathogen. Furthermore, to expand the application range to pathogens expressing the cognate immunity protein ImS2 against PyoS2, it was speculated that the ultra-high-affinity interaction between PyoS2 and ImS2 can be weakened by manipulating the IPE of the PyoS2 DNase domain via mutagenesis (PyoS2 ID derivatives) or by *in vitro* labelling (AlphaFluor conjugates). While the latter hypothesis was already proven for the PyoS2 Y640C-AlF conjugates and the PyoS2 ID derivatives *in vitro* (cf. Chapter IV.3.5 and IV.3.6), leading to DNA hydrolysis by such PyoS2 conjugates in the presence of excess immunity protein, it remains unclear whether the impaired binding behaviour of the PyoS2/ImS2 complex can be observed *in vivo* as well. The implications of such impaired binding could potentially decrease the fitness of *P. aeruginosa* or even exert lethal effects on otherwise PyoS2-resistant strains.

To address this open question, the PyoS2 conjugates, labelled with AlF fluorophores at various sites (Q570C, K602C, Y640C, and C-Cys), were devised to explore their cellular import as a prerequisite for selective drug delivery to specific species and strains. As the cytotoxic activity of PyoS2 is only displayed in the DNA-containing cytoplasm of a target cell, an observed killing activity of the DNase-active PyoS2-AlF conjugates would prove the active import of the DNase domain and the conjugated payload through the bacterial cell wall into the target cell. To test this fundamental hypothesis, the *P. aeruginosa* strains PAO1 and W15Dec1 were selected as an expedient read-out for bacteriocin killing activity. Strain PAO1 is a clinical isolate and the best-characterised strain of *P. aeruginosa*. Since this strain encodes the *pyoS2*, *imS2*, and *fpvAI* genes within its genome, it produces PyoS2, ImS2, and the FpvAI receptor. The expression of ImS2 confers inherent resistance to strain PAO1 against PyoS2 produced by other *P. aeruginosa* strains, making it a suitable negative control for this experiment. In contrast, W15Dec1 is an environmental *P. aeruginosa* isolate from a Belgian river and was previously identified as PyoS2-sensitive.[614] This sensitivity requires the presence of the PyoS2 OM receptor FpvAI and furthermore hints towards the absence of an appropriate immunity protein, making W15Dec1 a suitable positive control in this context. Cellular import and DNase-mediated PyoS2 killing activity were probed in a soft agar overlay assay in which cells of *P. aeruginosa* are immobilised in hardened agar and then challenged with different concentrations of PyoS2 variants. For this initial experiment, a toxin concentration of 5 µM was selected. Although this concentration is significantly higher than the minimal inhibitory concentration of wild-type PyoS2 for sensitive or hypersensitive strains (nanomolar to picomolar range, respectively),[759, 760] this concentration was particularly chosen to assess residual killing activity of potentially less toxic PyoS2 mutants.

First, wild-type PyoS2 and ImS2 were used to verify PyoS2-sensitivity of the literature-known strain *P. aeruginosa* W15Dec1. Here, the purified PyoS2 showed killing activity against W15Dec1 at a protein concentration of 5 µM while its immunity protein ImS2 did not (Figure IV.27). Simultaneously, the PAO1 strain was confirmed to be PyoS2-resistant as expected from the *pyoS2_imS2*$^{+}$ genotype. To verify that the killing activity observed upon PyoS2 treatment stems from the nuclease activity of the C-terminal PyoS2 DNase domain, the active site mutants PyoS2 H657A, PyoS2 H685A, and the double mutant PyoS2 H657A H685A were further evaluated. Treatment of W15Dec1 with the PyoS2 H685A mutant resulted in low residual killing activity, insinuating impaired complexation of the divalent Mg^{2+} cofactor. The remaining activity may stem from partial compensation of metal binding by the residual chelating histidines H656 and H681 within the active site. In fact, this residual killing activity of mutant H685A is consistent with the residual *in vitro* DNase activity of this particular mutant, which was described earlier

in this thesis (cf. Chapter IV.3.2, cf. Figure IV.15C). Also in agreement with the results from the *in vitro* DNase assay was the abolished killing activity of PyoS2, mediated by the histidine substitution H675A and the double mutantion H675A H685A (Figure IV.27).

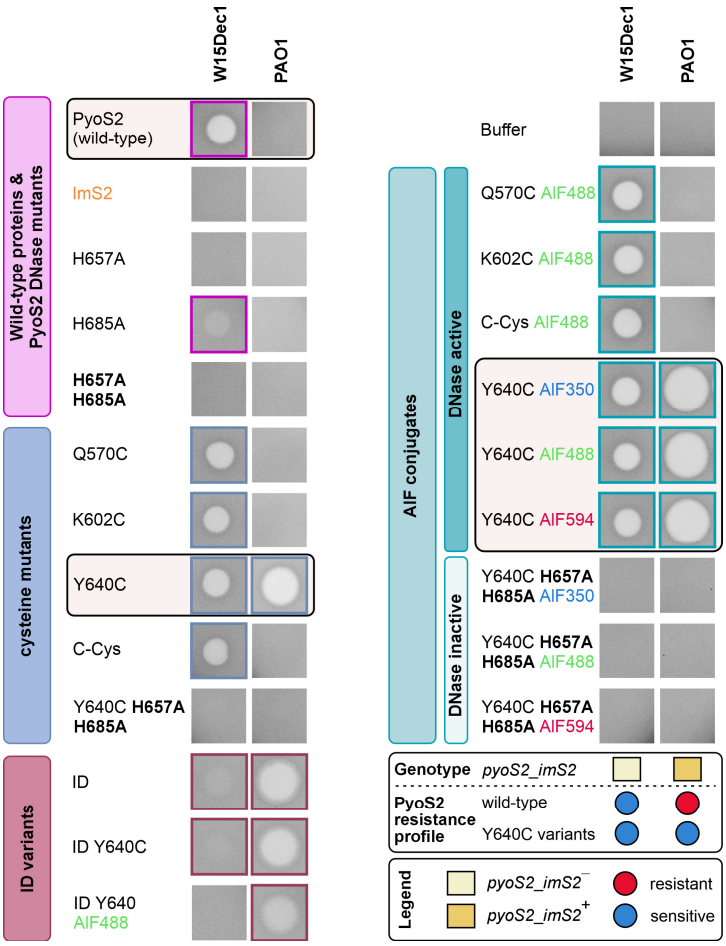


Figure IV.27. Plate killing assay with strains W15Dec1 (PyoS2-sensitive) and PAO1 (PyoS2-resistant) and several PyoS2 mutants and conjugates at 5 µM. 5 µL of 5 µM toxin solutions in dialysis buffer were spotted on hardened agar. Sterile dialysis buffer was used as a negative control. Clear spots indicate antimicrobial activity through bactericidal activity. PyoS2 variants for which antimicrobial activity was observed are highlighted by coloured frames.

This supports previous findings on HNH bacteriocins regarding the essential role of the general base histidine in DNase activity.[740, 741] The abolished DNase and killing activity of the double mutant PyoS2 H657A H685A *in vivo* led to the conclusion that the PyoS2 double knock-out is a suitable means to sense antibacterial activity of PyoS2 conjugates that is unrelated to the DNA-degrading mechanism of PyoS2 and caused by the conjugated payload instead.

Next, protein variants of PyoS2, which carry surface-accessible cysteine residues and are therefore promising for the transport of cargo molecules into target cells of *P. aeruginosa*, were evaluated *in vivo*. Those unlabelled cysteine mutants (Q570C, K602C, Y640C, C-Cys) had been previously tested *in vitro* and were shown to retain high DNase activity, even after fluorophore labelling with AlphaFluor dyes (cf. Chapter IV.3.5). By testing the killing activity of the unlabelled cysteine mutants and their AlF-labelled counterparts *in vivo*, potential interference of the introduced mutations and the fluorophore labels with membrane translocation during the TonB-dependent protein import was examined.

Therefore, the four unlabelled DNase-active cysteine mutants of PyoS2 (Q570C, K602C, Y640C, C-Cys) and their AlphaFluor conjugates were tested for bactericidal activity against W15Dec1 and PAO1. All mutants with an intact metal-binding site at the active site displayed bactericidal activity against W15Dec1 (Figure IV.27). This observation confirms that all cysteine mutants and conjugates are translocated into the target cell, independent of the selected labelling site (Q570C vs. K602C vs. Y640C vs. C-Cys) or the label size (AlF350, AlF488, and AlF594). While the selected labelling site and the size of the conjugated fluorophore dye had been shown to notably impact DNase activity *in vitro* (cf. Chapter IV.3.7), the *in vivo* tests with the PyoS2-sensitive strain W15Dec1 caused the same sensitive phenotype for all variants and conjugates. This is particularly surprising, as the fused ring system of the largest AlphaFluor594 dye has a diameter of 11.5 Å, and is therefore only slightly smaller than the diameter of the FpvAI receptor barrel lumen with 13 Å. Summarising the current data, it was successfully shown that all PyoS2 cysteine mutants and their AlF conjugates are translocated into the target cell of the W15Dec1 positive control strain and maintain DNase activity, leading to thorough killing of the bacteria. Another important presupposition made earlier was the non-toxic behaviour of the conjugated fluorophore dyes *in vivo*. This precondition was investigated by using AlF-labelled DNase knock-outs (H657A H685A double substitution) of mutant Y640C (Figure IV.27), lacking the intrinsic ability to cause cytotoxicity in the target cell through DNA damage. Hence, observed cytotoxicity for these conjugates would consequently stem from the attached fluorophore labels. However, all analysed AlF-conjugates with DNase knock-out did not exhibit bactericidal activity, demonstrating that the three covalently co-transported fluorophore dye payloads (AlF350, AlF488, and AlF594) are not cytotoxic on their own.

So far, membrane translocation and DNase activity of purified wild-type PyoS2, its cysteine mutants, and their respective AlF-conjugates have been demonstrated by monitoring the killing activity against the PyoS2-sensitive *P. aeruginosa* strain W15Dec1. W15Dec1, intrinsically lacking the ability to produce the cognate immunity protein ImS2, was highly susceptible towards the killing activity of those PyoS2 proteins. To further study the role of ImS2 and the importance of IPE integrity in governing PyoS2-resistance, the created PyoS2 cysteine mutants and their AlF-conjugates were assessed for their activity against the ImS2-producing and PyoS2-resistant strain PAO1. Thereby, we aimed to determine whether the obstructed binding of ImS2 to PyoS2's IPE could potentially overrule the innate PyoS2-resistance of ImS2-producing strains. If so, this would drastically expand the antimicrobial spectrum of pyocins and their potential applications.
The unlabelled cysteine mutants of PyoS2 (Q570C, K602C, and C-Cys) and their respective AlF488 conjugates did not overcome the innate PyoS2-resistance of PAO1 (Figure IV.27). But more importantly, the Y640C mutant and its AlF conjugates efficiently killed PAO1 at a toxin concentration of 5 μM. This observation is also in agreement with *in vitro* DNA hydrolysis through mutant Y640C and its AlF conjugates (cf. Figure IV.21 and Figure IV.26A), which were also maintained in the presence of excess ImS2. In addition, it was noted that the zones of growth inhibition were notably larger for the PyoS2-producer PAO1 than for the PyoS2-sensitive isolate W15Dec1 (+40% for Y640C, +63–67% for Y640C AlF-labelled variants). Although this observation cannot be explained at this stage, one may hypothesise that both strains might show differential levels of receptor expression, TonB1 levels, or cell surface accessibility for the toxins, reinforcing the diverging susceptibility to the extended-spectrum PyoS2 Y640C variant and its AlF-conjugates.

Summarising the current data, a single point mutation at the IPE is remarkably sufficient to disrupt the femtomolar ultra-high-affinity interaction between PyoS2 and its immunity protein ImS2, enabling intracellular DNA cleavage and effective inhibition of bacterial growth. This novel form of extended-spectrum antimicrobial activity through corrupt immunity protein binding, mediated by mutating the central Y640 residue within loop 4 of PyoS2's IPE, proves the central hypothesis of this work. Notably, it has never been shown for bacteriocins earlier, nor has it

been found in original *pyoS2* sequences from genome databases. Thus, it is hypothesised that equivalent mutations in PyoS2 or other bacteriocins would not be viable in natural isolates, as the impaired immunity protein binding would lead to killing of the bacteriocin-producing strain without simultaneous adaptation of the immunity protein sequence.

After finding the encouraging mechanism of the corrupt immunity protein binding in the PyoS2 conjugates of cysteine mutant Y640C, the focus was directed to the PyoS2 ID mutants, harbouring not only one but six mutations at the PyoS2/ImS2 interface. The PyoS2 ID variant (N626D D635A Y640A E643D Q646N K652N) was particularly designed with the intention to enhance the effect of impaired ImS2 binding previously observed for mutant Y640C. Furthermore, extensive mutagenesis was hypothesised to reduce the risk of spontaneous ImS2 escape mutants that counter the Y640C substitution while also reducing the practical effort in comparison to conjugate synthesis, owing to the additional *in vitro* labelling with fluorophore dyes. The *in vitro* studies had already shown that the PyoS2 ID variant partially fulfils the intended goal by diminishing ImS2 binding. However, the six amino acid substitutions at the IPE of PyoS2 also significantly reduced DNase activity *in vitro* (cf. Chapter IV.3.6, Figure IV.24). Therefore, we intended to characterise the *in vivo* killing activity of PyoS2 ID variants against the two *P. aeruginosa* model strains W15Dec1 and PAO1 and to draw a direct comparison between the conjugation approach and the extensive mutagenesis strategy.

The PyoS2-resistant strain PAO1 was unaffected by wild-type PyoS2 but exhibited a strongly sensitive phenotype for the killing activity of all the PyoS2 ID variants (ID > ID Y640C > ID Y640C-AlF488) (Figure IV.27). These results clearly evidence that the PyoS2 ID derivatives translocate across the cell membrane and are an adequate means to kill the PyoS2-resistant strain PAO1. Therefore, the inherent PyoS2-resistance of PyoS2-producing strains of *P. aeruginosa*, mediated through expression of the cognate immunity protein ImS2, can be effectively conquered with mutations or labelling at the IPE of the PyoS2 DNase domain. To our surprise, the PyoS2-sensitive environmental isolate W15Dec1 only exhibited negligible growth inhibition after treatment with PyoS2 ID at a concentration of 5 µM (Figure IV.27). Also, microbial treatment with the cysteine mutant PyoS2 ID Y640C led to very basal growth inhibition and its AlF-labelled conjugate PyoS2 ID Y640C-AlF488 was even completely ineffective without any apparent antibacterial activity. However, wild-type PyoS2 efficiently unleashed its bactericidal activity instead. Combining the observation of efficient bacterial killing of strain W15Dec1 by wild-type PyoS2 and the knowledge of efficient bacterial killing of strain PAO1 by the PyoS2 ID variant hints towards translocation- and ImS2-independent causes for the reduced susceptibility of strain W15Dec1 to PyoS2 ID.

Although this *in vivo* study does not provide answers to the question of why PyoS2 ID variants lose considerable biological activity in comparison to wild-type PyoS2 against the PyoS2-sensitive isolate W15Dec1, but concurrently remain highly active against strain PAO1, four hypotheses can be proposed to explain these observations. Firstly, the simplest answer would be reduced DNase activity, caused by positively or negatively modulated flexibility of helix V and the loops 3 and 4 within the HNH DNase and resulting from the introduced mutations (cf. Chapter IV.3.1.4, cf. Figure IV.13). This hypothesis was already proven by the analysis of *in vitro* DNase activity (cf. Figure IV.24) during which PyoS2 ID variants displayed an overall low DNA hydrolysis efficiency in comparison to all other PyoS2 mutants and conjugates. Nonetheless, reduced DNase activity alone would neither explain why AlF labelling results in decreased antibacterial activity in comparison to the unlabelled variants ID and ID Y640C, nor reveal why strain PAO1 is highly susceptible towards PyoS2 ID while strain W15Dec1 is not. Therefore, the second hypothesis considers a differential accessibility of the FpvAI OM receptor in the two investigated strains. The OSA- and CPA-caps of LPS from *P. aeruginosa* are two lipopolysaccharide modifications that append from the bacterial cells and shield the bacterial membrane from exogenous stress

factors. Currently, 20 individual isoforms of the OSA (serotypes) have been identified in *P. aeruginosa* and differential susceptibility of strains from different serotypes was already shown for the treatment with R-type pyocins.[684, 692] However, a direct link between serotype and susceptibility to S-type pyocins is currently missing. Thirdly, labelling could increase the hydrodynamic radius of the DNase and thereby reduce its translocation efficiency across the bacterial two-membrane system. Although this effect has not been noted previously during experimentation with PyoS2 Y640C-AlF conjugates, it might be possible that the ID mutations decrease the nuclease activity to such an extent that labelling clearly reduces bacterial killing at 5 µM toxin concentration. Lastly, it is assumed that the net positive charge of the DNase domain might play a crucial role in cell membrane translocation and its association with the inner membrane. Walker *et al*. could show a clear linear correlation between the net positive charge of colicins and the growth inhibition caused by direct, electrostatically mediated interaction with the phospholipid inner bilayer of *E. coli*. Strongest growth inhibition was observed for ColE7 with a net positive charge of +13, followed by E2 (+11), E8 (+9), and E9 (+7). Other ColE9 mutants with additional negative substitutions (ColE9 K45E with +5; ColE9 K21E K45E with +3) perfectly aligned within this correlation and supported the theory of partial DNase immersion into the inner membrane to facilitate delivery of the bacteriocin to the inner membrane protease FtsH.[727] Wild-type PyoS2 has a net positive charge of +6 and is already more positively charged than ColE9 with the least net positive charge of +7 from the four wild-type colicins. While the PyoS2 ID mutations Y640C Q646N do not affect the net positive charge of the DNase domain, the mutations N626D D635A E643D K652N decrease the net positive charge from +6 to +5. Furthermore, the attachment of the AlF-label is accompanied by the introduction of three acidic residues (2 x $–SO_3H$, 1 x –COOH) and only two basic amine and imine residues ($–NH_2$, =NH), which results in a decrease in the net positive charge to +4 due to DNase labelling. A similar mechanism of charge-dependent potentiation of killing activity was, for example, observed for the pediocin-like bacteriocin sakacin P, a class IIa bacteriocin from Gram-positive bacteria that does not share DNase activity. As a reduction of the net positive charge of –1 resulted in a 2–15-fold reduction of cell killing potency, electrostatically mediated membrane association seems to be a general mechanism of many bacteriocins being crucial for antimicrobial activity against both Gram-positive and Gram-negative bacteria.[761] However, the net positive charge conservation among S-type HNH DNase pyocins is relatively low. Comparing PyoSX1 (+8), S2 (+6), S1 (+6), S8 (+3), AP41 (0), and S9 (–1) with each other, it becomes quite obvious that FtsH processing and membrane translocation cannot be caused by the net positive charge alone. As little research has been conducted on the inner membrane translocation of S-type bacteriocins, many questions regarding the role of charge-dependent translocation remain unanswered to date. In the context of PyoS2 ID and its conjugate ID Y640C-AlF488, we assume that all three factors (reduced DNase activity, impaired translocation through increased hydrodynamic radius, and net charge increase through ID mutations and labelling) contribute to the decreased antimicrobial activity against PAO1 in comparison to PyoS2 Y640C or its AlF conjugates.

In summary, the principle of obstructing ImS2 binding to the PyoS2 DNase domain via mutagenesis or labelling with fluorophore dyes was successfully translated from *in vitro* to *in vivo* applications. By applying the innovative strategy, the inherently PyoS2-resistant strain *P. aeruginosa* PAO1, capable of synthesising PyoS2 and its immunity protein ImS2 on its own, became sensitive to the PyoS2 ID and PyoS2 Y640C mutants and their conjugates. Therefore, we were not only able to address the PyoS2-sensitive strain W15Dec1 with mutants and conjugates of the PyoS2 protein, but also the naturally PyoS2-resistant strain PAO1. This result emphasises that the novel PyoS2 variants introduced in this work have the potential to find a broader application than the wild-type toxin. Furthermore, the presented finding of corrupt immunity binding emphasises that the natural antimicrobial spectrum of bacteriocins with cognate immunity proteins can be re-defined and expanded by rational engineering of the IPE within the cytotoxic domain.

IV.3.9 PAO1 is Killed by Single Dose Treatment with PyoS2 Y640C Conjugate in Liquid Media

In the previous chapters, changes to the IPE of PyoS2 as small as a single amino acid substitution were shown to have an astonishing effect on immunity protein binding and the protection of DNA from PyoS2's nuclease activity. Impaired association of the ultra-high-affinity complex between PyoS2 and ImS2 not only led to insufficient protection of DNA from degradation *in vitro*, but also rendered the PyoS2-resistant strain *P. aeruginosa* PAO1 sensitive to the engineered PyoS2 Y640C and PyoS2 ID derivatives *in vivo*. The Y640C mutation and subsequent AlF labelling obviously impaired PyoS2/ImS2 binding kinetics, reducing the neutralising effect of ImS2 binding to the DNase domain (cf. Figure IV.21 and Figure IV.26). This disruption facilitated effective bacterial killing, regardless of ImS2 expression (cf. Figure IV.27). To evaluate whether this observation is only made on solid media or also translatable to more dynamic liquid cell culture systems, a liquid growth inhibition assay with planktonic bacteria of *P. aeruginosa* W15Dec1 and PAO1 was performed (Figure IV.28), using the bacterial cell density over time as a measure of strain viability in the presence of bactericidal DNase pyocins.

During the exponential growth phase of the bacterial cultures, the *P. aeruginosa* strains were exposed to wild-type PyoS2 and the most potent PyoS2 Y640C conjugate with the AlF350 fluorophore at a final toxin concentration of 750 nM. The two strains exhibited normal growth behaviour when sterile buffer was added as a negative control, reaching a final OD_{600} of approximately 1.8. For both strains, a significant increase in signal noise was detected (after approximately 400 min for W15Dec1 and 600 min for PAO1). This signal noise was owing to biofilm-associated pellicle formation on the surface of the incubation well, which caused random light scattering when in the focus of the light beam of the instrument. When using wild-type PyoS2, the PyoS2-sensitive strain W15Dec1 was efficiently killed through the toxin (Figure IV.28A). Starting from an OD_{600} of approx. 0.2 at PyoS2 addition, the OD_{600} further increased to 0.25 (23 min delay) until the OD_{600} dropped to 0.11. After 800 min, the OD_{600} began to incline again. A comparable effect was observed for the treatment of W15Dec1 with the PyoS2 Y640C-AlF350 conjugate, with the only difference being a slightly prolonged growth phase after the addition of the toxin before the OD_{600} decline began (49 min delay). Here, it was assumed that the slightly reduced DNase activity of the mutated and AlF-labelled toxin in comparison to wild-type PyoS2 DNase activity – both showed complete conversion of supercoiled, nicked, and linear DNA after 15 h, with unspecific hydrolysis products <300 bp for wild-type PyoS2 and <1000 bp for PyoS2 Y640C-AlF350 remaining (cf. Figure IV.26) – is causative for the observed delay in killing activity. Nonetheless, recovery of the bacterial culture was observed again for the treatment with the PyoS2 conjugate after approximately 800 min of total incubation.

As expected for the PyoS2-resistant isolate PAO1, which naturally produces the immunity protein ImS2 to neutralise the toxin by association in a stoichiometric ultra-high-affinity complex, no significant differences in bacterial growth behaviour between the buffer-containing control and the PyoS2-treated sample were observed (Figure IV.28B). Thus, the presence of PyoS2 in the culture broth does not impact the bacterial growth of this strain in liquid culture. However, when treated with the PyoS2 Y640C-AlF350 conjugate at an OD_{600} of 0.35, PAO1 exhibited a sensitive phenotype as indicated by growth inhibition. Upon addition of the PyoS2 conjugate, a delay (46 min) similar to W15Dec1 was observed until the growth plateau was reached at an OD_{600} of 0.47. After a steady decline in cell density, the culture remained at an OD_{600} of 0.13 for roughly 400 min until the cell density began to increase again after approximately 800 min.

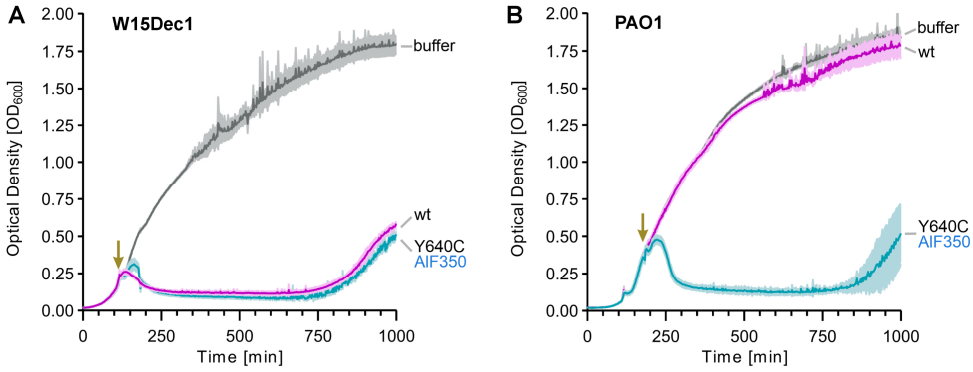


Figure IV.28. Turbidity reduction assay in liquid media with wild-type PyoS2 and PyoS2 Y640C-AlF350 on the PyoS2-sensitive environmental *P. aeruginosa* isolate W15Dec1 (**A**) and the PyoS2-resistant model strain PAO1 (**B**). Growth inhibition of *P. aeruginosa* by single dose treatment with wild-type PyoS2 (red), PyoS2 Y640C-AlF350 (blue) or dialysis buffer (grey) was monitored in lysogeny broth (LB) media at 37 °C at 600 nm over a total time of 1000 min and is displayed as mean value, surrounded by the standard deviation (n=3). Proteins were added (yellow arrow) to a final concentration of 750 nM after 109 min (W15Dec1) or 171 min (PAO1, longer lag phase). LB medium was used as a blank and subtracted from the measured growth curves. Curve jumps at 109 min and 171 min in both datasets are based on the opening of the instrument for the addition of proteins and buffer. The increasing noise during monitoring arises from pellicle formation on the well surface, which induces random light scattering.

The growth data of *P. aeruginosa* PAO1 and W15Dec1 in liquid culture underline that wild-type PyoS2 and the PyoS2 Y640C conjugate with the AlF350 fluorophore dye attached at the IPE of PyoS2 possess the same antibacterial profile for planktonic bacteria as previously observed in the agar-based plate killing assay (cf. Chapter IV.3.8). Most importantly, the corrupt binding of ImS2 in the PyoS2 Y640C-AlF350 conjugate was again able to efficiently conquer the inherent PyoS2-resistance of the PyoS2 producing strain PAO1, while the expression of ImS2 thoroughly neutralised the cytotoxic activity of wild-type PyoS2.

Nevertheless, the highly dynamic turbidity reduction assay leaves one observation unexplained, which had not been made in the static solid agar plate killing assay: the impermanent growth inhibition and subsequent bacterial growth recovery after single-dose treatment with PyoS2 or the PyoS2 Y640C-AlF350 conjugate. Two different phenomena can cause the mentioned effect of bacterial recovery. On the one hand, a smaller subpopulation of dormant bacteria (“persister”) might be formed. Such persisters might exhibit higher resilience towards pyocin treatment. This persistence might be caused by transcriptional downregulation of FpvAI levels in the outer membrane, reducing the overall availability of the PyoS2 primary OM receptor, or by remodelling of the cell-surface polysaccharide CPA as the secondary receptor of PyoS2. For tailocin-like bacteriocins of *Pseudomonas syringae*, high levels of persistence were previously linked to spontaneous mutations in glycosyltransferase genes involved in the biosynthesis of the OSA- or CPA-cap of bacterial LPS.[762] On the other hand, it is hypothesised that the fast recovery of fitness might be attributed to the formed pellicle at the interface between the liquid culture media and air and the utilisation of rich LB growth medium. Hence, minimal media with a different composition could also decelerate the rate of bacterial recovery after single-dose treatment with pyocins and appropriately resemble the nutrient limitation for the bacteria in eukaryotic host environments during infection. Moreover, pellicles are biofilm-like structures containing living bacteria that are mostly protected from the pyocin-containing growth media. Consequently, the bacteria can proliferate unharmed within the pellicle and once enough bacteria from the liquid culture have been sacrificed to stave off all PyoS2 molecules from solution, the culture can grow again without any growth-inhibiting effect being visible. In fact, increased drug tolerance by growth in pellicles is a common strategy in the bacterial kingdom to experience protection from the cytotoxic activity of antibiotics. For

example, the human pathogen *M. tuberculosis* was shown to develop high tolerance against the antibiotic rifampicin when growing in the biofilm-like pellicle. However, mutations leading to defective pellicle formation rendered *M. tuberculosis* sensitive to rifampicin.[763]

The distinct survival instinct of Pseudomonads and their ability to colonise diverse habitats through biofilms apparently reduces the long-term effect of a single-dose pyocin treatment. For a potential application of pyocin conjugates in eukaryotic infection models, treatment in multiple doses, or combinatorial treatment with other drugs or anti-biofilm agents could be auxiliary in breaking the physical barrier of biofilms in the long run. The idea of combinatorial treatment with multiple (typically two) drugs at the same time is not new, but can have superimposing and cumulative effects on both planktonic bacteria and biofilms. For example, combinatorial treatment of *P. aeruginosa*-infected rats with the antibiotics colistin and tobramycin increased the survival rate of infected rats in comparison to treatment with colistin or tobramycin alone.[764] This cited study performed by Herrmann *et al*. also included a clinical trial with eight cystic fibrosis patients that revealed a significant reduction of *P. aeruginosa* in the patients' sputum when being treated with the colistin/tobramycin cocktail. Finally, the authors were able to disclose the differential effect of combinatorial treatment on biofilm clearance by finding that the two drugs tobramycin and colistin address different subpopulations of bacteria within the biofilm.[764] Similarly, the combination of tobramycin and clarithromycin was able to eradicate biofilms of *P. aeruginosa* isolates from cystic fibrosis patients efficiently.[765]

Published works on combinatorial treatments, including bacteriocins and common antibiotics, mostly employ the lantibiotic peptide nisin of Gram-positive *Lactobacillus* species.[766] However, some examples of combinatorial studies have also addressed the Gram-negative pathogens *E. coli*, *M. tuberculosis*, and *P. syringae* by using colicins,[767] cocktails of bacteriocin AS-48 and chemically synthesised bacteriocins,[768, 769], or mixtures of tailocins and L-type pyocins,[770] respectively. Furthermore, concurrent treatment of co-cultivated *Enterococcus faecalis* and *K. pneumoniae* with *E. faecalis*-specific bacteriophages producing the bacteriocin klebicin M was shown to be an effective tool in regulating the bacterial viability within the co-culture.[771] Analogously to our observation of bacterial growth recovery after single-dose treatment of *P. aeruginosa* with PyoS2 and its AIF conjugate (cf. Figure IV.28), the co-treatment with KlebM and bacteriophages led to the recovery of bacterial growth after approximately 10 h. Hence, bacterial recovery through metabolic adaptation is a frequently witnessed side-effect of single-dose treatment with antimicrobials. As bacteriocins are natural antimicrobials used in the fight for resources, bacteria have included combinatorial attacks into their repertoire of microbial warfare. In fact, bacteriocins are an exquisite example to highlight this natural phenomenon. The *P. aeruginosa* model strain PAO1 encodes a whole set of tailocins and S-type pyocins within its genome (R2, F2, S2, S4, S5) to survive in highly competitive ecological niches.[682, 705, 714, 716] Since other strains might be resistant to one bacteriocin by producing the cognate immunity or by simply not presenting the respective bacteriocin receptor in the OM, utilising multiple bacteriocins with different receptor selectivity – as seen for PAO1 – may be beneficial in gaining an advantage over closely related competitors in the fight for resources. Thus, the transfer of this multi-target strategy into application seems to be the logical consequence of this lesson from nature to advance the presented strategy of pyocin conjugates.

In conclusion, using the example of the DNase pyocin PyoS2 and its immunity protein ImS2, it was demonstrated that blocking the interaction surface between PyoS2 and ImS2 through extensive mutagenesis or non-toxic labels provides clear evidence for the disruption of the natural resistance mechanism against PyoS2 both *in vitro* and *in vivo*. The approaches presented in the previous chapters to eliminate immunity protein-mediated resistance to pyocins hold great potential for combating infections caused by the difficult-to-treat opportunistic human pathogen

P. aeruginosa and might be able to challenge the general concept of innate bacterial immunity through the expression of immunity proteins. Consequently, the next goal is the application of pyocins and their conjugates to multidrug-resistant strains of *P. aeruginosa*.

IV.3.10 Characterisation of PyoS2-Related Genetic Determinants in a Strain Collection of MDRs CRPsA

The isolates of *P. aeruginosa* PAO1 and W15Dec1 had proven valuable for the initial verification of our hypothesis of impaired PyoS2/ImS2 binding by mutations and labelling at their binding interface to overcome the innate resistance of ImS2-producing strains. However, to gain a comprehensive overview of the clinical relevance of our discovery of ImS2-insensitive PyoS2 variants, the less virulent model strains W15Dec1 and PAO1 were substituted with highly concerning and clinically relevant isolates of *P. aeruginosa*. Especially for the increased spreading of antimicrobial resistance and the related resistance genes against common antibiotics in hospitals, bacteriocins offer the potential to mitigate the risk of emerging superbugs that lack effective treatment options. Despite the non-controversial potential of pyocins for the development of novel antimicrobials, to date, only one study from the year 2017 tried to address multidrug-resistant strains of *P. aeruginosa* with PyoS8. PyoS8 is a novel S-type pyocin with DNase activity, encoded on the transposon Tn*6035*.[710, 772] Although PyoS8 displayed broad antimicrobial activity against 13 of the selected 16 MDR strains,[772] the currently lacking knowledge about the exploited OM receptor and translocation pathway limits the predictability of PyoS8-sensitivity on the basis of genetic information. In contrast to PyoS8, the uptake mechanism of PyoS2 through the siderophore receptor FpvAI and Ton-mediated membrane translocation is well studied. Therefore, PyoS2 susceptibility is predictable based on genetic determinants (OM receptor and immunity proteins). However, despite its potential as a future treatment option for *P. aeruginosa* infections, a broader study of PyoS2 susceptibility in a large strain collection of MDR isolates has yet to be performed. The limited knowledge on resistance dissemination against PyoS2 in combination with our finding of PyoS2 cysteine mutants and their conjugates being partially “immune” to ImS2 neutralisation was motivation enough to test these rationally designed proteins with an extended antimicrobial spectrum on a larger selection of strains. Therefore, a strain collection of carbapenem-resistant *P. aeruginosa* (CRPsA) clinical isolates from the University Hospital in Düsseldorf was subjected to susceptibility screening with wild-type PyoS2, its introduced mutants, and the AIF conjugates of PyoS2.

In the years from 2002–2020, a total of 113 MDR *P. aeruginosa* isolates were collected from hospitalised patients in Düsseldorf, fulfilling the criteria of nonsusceptibility to ceftazidime, imipenem/meropenem, or combinatorial treatment with piperacillin-tazobactam (β-lactam and β-lactamase inhibitor). While most samples originate from tracheal secretion, urine, or axillary/inguinal swabs, the strain collection comprises clinical isolates originating from 30 different human biofluids, tissues, body regions, or medical instruments (Table IX.9, Supporting Information). Besides antimicrobial susceptibility screening employing broad-spectrum antibiotics with antimicrobial activity against clinically relevant pathogens (amikacin, aztreonam, ceftazidime, ciprofloxacin, cefepime, gentamicin, imipenem, meropenem, piperacillin, piperacillin/tazobactam, tobramycin), CRPsA strains were further analysed by real-time PCR to identify the responsible resistance genes. Carbapenemase genes were identified according to a published procedure of Wendel *et al.* and Schäfer *et al.*, relying on TaqMan multiplex PCR amplification of the genes with two unlabelled forward and reverse primers in conjunction with highly sequence-selective dual-labelled (fluorophore and quencher) DNA probes (Table V.3).[600, 773, 774] Within the strain collection from the University Hospital in Düsseldorf, 71 (63%) *P. aeruginosa* isolates were identified to carry the MBL gene for $bla_{\text{GIM-1}}$, 35 strains (31%) for the MBL $bla_{\text{VIM-2}}$, 3 strains for the carbapenemase-type bla_{GES} (2.7%), and 1 strain each for the MBL genes $bla_{\text{VIM-1}}$ and $bla_{\text{IMP-15}}$, (0.9%). In addition, two strains did not show production

nor genetic determinants of the carbapenemases mentioned above but were still resistant to the carbapenems imipenem and meropenem (MIC >16 µg/mL) by impermeability. The distribution of mobile carbapenemase *bla* genes in this strain collection with an overrepresentation of bla_{GIM-1} underlines the long-term outbreak of GIM-1-producing pathogens in the University Hospital in Düsseldorf.[600] Although the authors refer to a sampling period from 2007–2012, the GIM-1 genotype is still dominant in the year 2020 (Figure IV.29). With bla_{VIM-2} being the second most MBL found within the CRPsA strain collection, the endemic character of VIM-type carbapenemases in European Hospitals is underlined.[612]

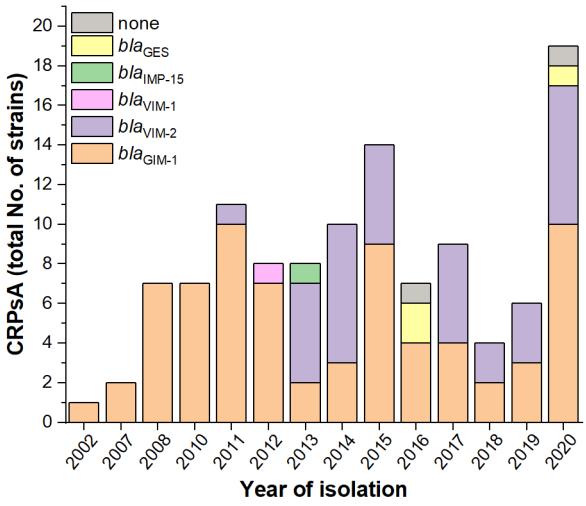


Figure IV.29. Distribution of *bla* resistance genes in the CRPsA strain collection (n=113) of the University Hospital in Düsseldorf over the sampling period (2002–2020). The reported long-term outbreak of GIM-1 refers to the years between 2007 and 2012.[600]

This versatile collection of highly virulent and MDR strains of *P. aeruginosa* was considered for further genetic characterisation and experimental testing to validate the application range of PyoS2 in comparison to the novel engineered variants and conjugates of PyoS2 developed in this work.

IV.3.10.1 Identification of FpvA-Subtypes and PyoS2-Producers by Multiplex PCR

Since pyocins possess cytotoxicity limited to those strains expressing the correct OM receptor for initial entry into the bacterial cell, the genetic setup determines the eligibility of certain strains for pyocin treatment. To experimentally determine the potential susceptibility of *P. aeruginosa* strains towards S-type pyocins with known OM receptors for cell binding and translocation, two unlike approaches are commonly used. The first approach is a straightforward testing method, relying on exposure of the strains of interest to purified pyocins to monitor growth inhibition through bactericidal activity. For treatment with wild-type toxins, this testing approach is sufficient to quickly reveal pyocin susceptibility for certain strains. However, when a strain does not respond to pyocin treatment, this approach is not able to distinguish between several mechanisms, which may lead to ineffectiveness of pyocin treatment. In general, bacterial strains must meet three crucial requirements to become susceptible to S-type pyocins. Firstly, the target cell must display the correct OM receptor on its surface. Secondly, the absence of cognate ultra-high-affinity immunity proteins is required. Lastly, no secondary (immunity protein-independent) resistance mechanisms that inactivate the toxin or impair its cellular uptake may be present. For example, two strains, of which one produces the correct OM receptor for pyocin translocation and the immunity protein and the other does neither produce the correct OM receptor nor the cognate immunity, display the same phenotype of

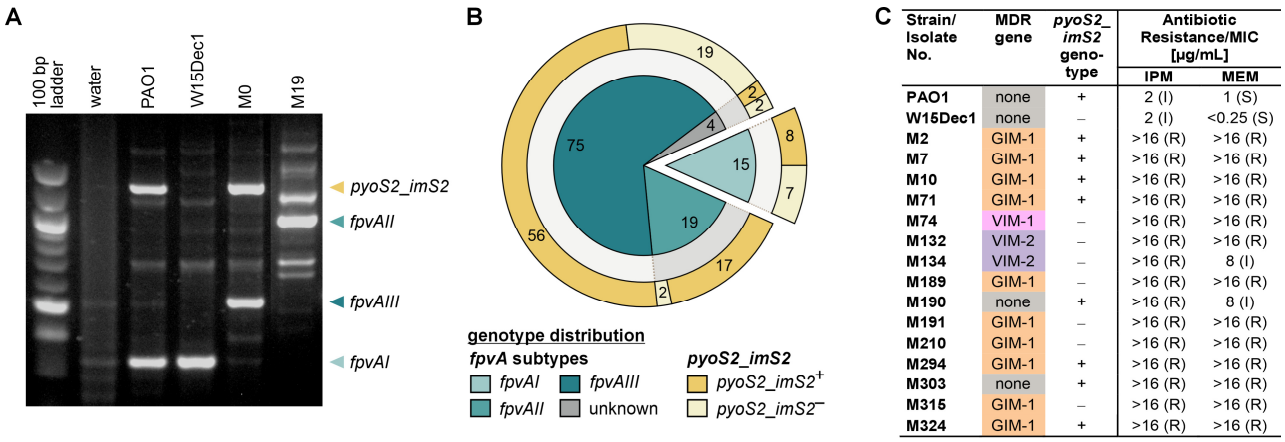
resistance in this phenotypic susceptibility testing. Nevertheless, both strains are genetically diverse and employ different strategies to gain pyocin resistance or insensitivity.

Since engineered toxins were generated in this work, overruling the rules of ImS2-mediated PyoS2-resistance through impaired formation of the stoichiometric ultra-high-affinity complex, the simple method of testing is insufficient to understand the role of genetic determinants in the activity spectrum of these engineered toxins. Therefore, a more elaborate method was applied, combining genetic profiling and antimicrobial testing to understand the capabilities and limitations of PyoS2 variants and conjugates.
Through a PCR-based characterisation of OM receptor subtypes, we first desired to reduce the number of strains for cytotoxicity screenings, as only a small portion of the 113 clinical isolates is assumed to display the correct OM receptor. The receptor binding and translocation domain of PyoS2 binds to the OM pyoverdine siderophore receptor FpvAI. FpvAI is only one subtype of FpvA siderophore receptors (FpvAI–III) found in *P. aeruginosa* for the uptake of respective pyoverdine siderophores (Pvd class I–III).[654, 775] Bodilis *et al*. could show that every strain of *P. aeruginosa* encodes only a single FpvA subtype,[776] thereby naturally limiting the antimicrobial spectrum of those pyocins hijacking FpvA-type receptors. The experimentally validated pyocins PyoS2 (HNH DNase), PyoS4 (tRNase), and PyoS11/SD2 (tRNase), as well as the predicted PyoS7 (rRNase), share high sequence identity in the N-terminal receptor binding domain and translocate through the pore of the Pvd siderophore receptor FpvAI. PyoS3 (non-HNH DNase) binds and translocates through the FpvAII receptor (other OM receptors for experimentally validated pyocins can be found in Table IV.1). However, for the most commonly found FpvAIII subtype, no targeting pyocin has been identified or predicted so far. Since this study solely focuses on PyoS2 and PyoS2-derived conjugates, a multiplex PCR approach with simultaneous detection of the *fpvAI*, *fpvAII*, and *fpvAIII* loci was chosen to reduce the strain collection of 113 strains to those strains encoding a copy of the PyoS2 OM receptor *fpvAI* within the bacterial chromosome. Moreover, naturally PyoS2-resistant strains through their own capability of ImS2-mediated PyoS2 neutralisation were of particular interest for this work. As these strains do not respond to wild-type PyoS2 treatment, the introduced PyoS2 Y640C-AlF conjugates with impaired ImS2 binding might be potential tools to circumnavigate the inherent resistance mechanism. Therefore, the 113 MDR strains from the *P. aeruginosa* strain collection were additionally probed for the genomic tandem of *pyoS2_imS2* to find those strains with innate PyoS2-resistance.

To minimise the practical effort of DNA isolation from the bacterial strains, a colony PCR-inspired approach with heat-induced cell lysis and sedimentation of cell debris was chosen. The remaining supernatant, containing chromosomal and plasmid DNA, was used as a template for subsequent PCR reactions. For simultaneous detection of genome encoded DNA sequences in a multiplex PCR setup with the benefits of sequence selective binding of *fpvAI*, *fpvAII, fpvAIII,* and *pyoS2_imS2*, the short primer pairs (20–22 nucleotides) were designed in such a way that the melting temperature lies between 57 and 62 °C and the GC-content ranges between 50 and 60%. Furthermore, the expected DNA fragments resulting from PCR amplification were designed to differ significantly in size to allow their separation in agarose gel electrophoresis and their unambiguous identification in comparison to a standardised DNA ladder. By utilising the primer pairs FpvAI-F/R, FpvAII-F/R, FpvAIII-F/R, and PyoS2_ImS2-F/R (for sequences cf. Table V.3) and an annealing temperature of 60 °C, the DNA fragments of *fpvAI* (326 bp), *fpvAII* (897 bp), *fpvAIII* (506 bp), and *pyoS2_imS2* (1223 bp) were amplified using the high fidelity Phusion polymerase and subsequently analysed by agarose gel electrophoresis (Figure IX.11A, Supporting Information).
Even though the PCR protocol was optimised for the model strains *P. aeruginosa* PAO1 and W15Dec1 (both *fpvAI*) to reduce the formation of unspecific PCR products, the MDR resistant strains from the *P. aeruginosa* strain collection showed a significantly higher level of undesired PCR side products (Figure IV.30A). The multiplex PCR

analysis of the two model strains finally revealed what was already known from pyocin typing with wild-type PyoS2 and from reference genome analysis of strain PAO1.[757] The PAO1 strain exhibits an *fpvAI* and *pyoS2_imS2*$^{+}$ genotype,[9] which allows for binding of PyoS2 to the cell surface and translocation across the membrane. However, the concurrent expression of ImS2 in the cytoplasm of the target cell confers resistance to the wild-type toxin through association in the ultra-high-affinity complex of PyoS2 and ImS2. The environmental isolate W15Dec1 revealed a *pyoS2_imS2*$^{–}$-deficient genotype and encodes the *fpvAI*-subtype as well. These results render strain W15Dec1 sensitive to wild-type PyoS2 and are in accordance with our data and the reported experimental sensitivity to PyoS2 treatment in the literature.[717]

The analysis of the strain collection from the University Hospital revealed a broad distribution of the *pyoS2_imS2*$^{+}$ genotype (68 strains, 60.2%), pointing at a high level of innate PyoS2-resistance and the ability of PyoS2 production (Figure IV.30B). The remaining strains were characterised by the *pyoS2_imS2*$^{–}$ genotype (45 strains, 39.8%), being putatively susceptible to wild-type PyoS2 treatment. Shifting the focus to *fpvA*-type distribution among the strain collection, a total of 75 strains (66.4%) was genotypically characterised with the *fpvAIII*-subtype, which is not addressable with any of the so-far known S-type pyocins (cf. Table IV.1). Nonetheless, as only *fpvA* subtypes are examined in this particular multiplex setup, the presence of other S-type pyocin receptors within the genome of these strains (*hur*, *fptA*, *crtA*, or any other of the so-far unknown receptors), might still lead to bacterial



C

Strain/ Isolate No.	MDR gene	*pyoS2_ imS2* geno-type	Antibiotic Resistance/MIC [µg/mL]	
			IPM	MEM
PAO1	none	+	2 (I)	1 (S)
W15Dec1	none	–	2 (I)	<0.25 (S)
M2	GIM-1	+	>16 (R)	>16 (R)
M7	GIM-1	+	>16 (R)	>16 (R)
M10	GIM-1	+	>16 (R)	>16 (R)
M71	GIM-1	+	>16 (R)	>16 (R)
M74	VIM-1	–	>16 (R)	>16 (R)
M132	VIM-2	–	>16 (R)	>16 (R)
M134	VIM-2	–	>16 (R)	8 (I)
M189	GIM-1	–	>16 (R)	>16 (R)
M190	none	+	>16 (R)	8 (I)
M191	GIM-1	–	>16 (R)	>16 (R)
M210	GIM-1	–	>16 (R)	>16 (R)
M294	GIM-1	+	>16 (R)	>16 (R)
M303	none	+	>16 (R)	>16 (R)
M315	GIM-1	–	>16 (R)	>16 (R)
M324	GIM-1	+	>16 (R)	>16 (R)

Figure IV.30. Multiplex typing and FpvA siderovar distribution among the CRPsA strain collection. A. Representative agarose gel excerpt for PCR multiplex typing of fpvA subtypes [fpvAI (326 bp), fpvAII (897 bp), fpvAIII (506 bp)] and the pyoS2_imS2 tandem (1223 bp) with water as a negative control and the P. aeruginosa strains PAO1 (fpvAI), W15Dec1 (fpvAI), M0 (fpvAIII), and M19 (fpvAII). B. Pie chart of fpvA and pyoS2_imS2 distribution among 113 clinical isolates of MDR P. aeruginosa. Inner circle: the displayed numbers represent the number of strains classified with the corresponding fpvA siderovar. Outer circle: the displayed numbers represent the number of strains characterised as pyocin-producers (pyoS2_imS2+) or non-producers (pyoS2_imS2–) for each individual siderovar group. C. List of MDR core strains sharing the fpvAI genotype, their pyoS2_imS2 genotype and their MICs against the carbapenems imipenem (IPM) and meropenem (MEM). The full antibiotic susceptibility table can be found in the Supporting Information. Abbreviations: GIM-1 – German imipenemase 1; VIM-1 – Verona integron-encoded metallo-β-lactamase 1; VIM 2 – Verona integron-encoded metallo-β-lactamase 2, R – resistant; I – susceptible with increased exposure; S – susceptible.

[9] In microbiology, gene deletions in genetically engineered strains are conventionally highlighted by the symbol Δ (e.g. *ΔexoU*). However, in many natural bacterial isolates, the absence of these genes of interest is not attributed to gene deletions but is owing to the fact that the corresponding genes have evolutionarily never been acquired. Nevertheless, there is no established naming convention to distinguish between the presence or absence of particular genes. To account for this significant difference, strains in which we could detect the *pyoS2_imS2* tandem were branded with the symbol plus (+, tandem present), while strains without the *pyoS2_imS2* tandem were branded negative (–, tandem not present).

killing when using the respective pyocins hijacking these OM receptors (cf. Table IV.1). Besides four strains with unknown *fpvA* distribution (M68, M195, M206, and M331), 19 strains were identified with the *fpvAII* genotype (16.8%) and further 15 strains (13.3%) with the *fpvAI* genotype. The latter is essential for PyoS2-sensitivity, as only FpvAI is accepted as OM porin for pyocin binding and its translocation into the periplasm of the host cell.

To verify that the latter 15 strains actually carry the genomic copy of *fpvAI* and to sense their *pyoS2_imS2* genotype in order to exclude false positives, the *fpvAI*-positive strains were cross-validated in a less background-producing duplex PCR, only detecting *fpvAI* and *pyoS2_imS2* genotypes (Figure IX.11B, Supporting Information). Eight of these 15 strains were shown to exhibit the *pyoS2_imS2*$^{+}$ genotype (53.3%). At the same time, seven strains were identified to be *pyoS2_imS2*-deficient (Figure IV.30B). The core strain collection of 15 MDR clinical isolates exhibiting the *fpvAI* genotype was used for further antibiotic susceptibility testing (Figure IV.30C, full antibiotic susceptibility testing in Table IX.10 within the Supporting Information). Furthermore, this core strain list was used for experimental validation of sensitivity or resistance to wild-type PyoS2 and its engineered derivatives in the course of this work. All other remaining 98 strains are not of interest for this study dedicated to the DNase bacteriocin PyoS2, as the absence of *fpvAI* confers ImS2-independent insensitivity against PyoS2.

Another multiplex PCR approach, similar to the one used in this work, was previously employed by Bodilis *et al*. in order to characterise the biodiversity of environmental and clinical *P. aeruginosa* isolates, to map the distribution of ferripyoverdine receptors, and to understand the evolution of *fpvA* siderovars.[776] The representative strain collection of 345 isolates (220 clinical and 79 environmental isolates, 46 of miscellaneous origin) was screened for subtypes of the *fpvA* siderovar (*fpvAI*, *fpvAIIa* and *fpvAIIb*, *fpvAIII*) and the related *fpvB* receptor and interestingly, some systematic differences in distribution between environmental and clinical isolates were uncovered. Within the group of clinical isolates, *fpvAI* (29.5%), *fpvAII* (42.3%), and *fpvAIII* (24.5%) were observed to be relatively equally distributed. However, the group of environmental isolates showed a disproportionately high prevalence of the *fpvAI* type siderovar (49.4%), while *fpvAII* (18.2%) and *fpvAIII* (16.5%) were proportionally underrepresented. Comparing these results with the *fpvA* siderovar distribution in our strain collection of 113 MDR clinical isolates, where only 13.3% belong to the *fpvAI* siderovar and 66.4% exhibit the *fpvAIII* genotype, reveals a clearly different distribution pattern. Although the origin of this significant divergence is unknown, one may speculate that certain siderovars might be helpful to conquer or survive in different environments or ecological niches. Especially under the aspect of xenosiderophores (siderophores that are produced by other species but can be taken up by *P. aeruginosa* or *vice versa*) and their role in shaping environmental microbial communities,[777] the high prevalence of *fpvAI* genotypes in environmental isolates might be associated with the beneficial interaction between *P. aeruginosa* and other microbes. Furthermore, certain siderovars might be used by *P. aeruginosa* to associate with other microbes during infections or even to become more tolerant to environmental toxins. Likewise, the siderovar could also be associated with the colonisation of specific tissue types and organs or the development of pathogenicity toward the human host.

Pyoverdine, the natural ligand of FpvA-type siderophore receptors, has been known as an essential virulence factor of *P. aeruginosa* for decades.[778] Nevertheless, a comprehensive analysis of *fpvA* siderovar distributions in clinical isolates – along with their associations with infected tissues, diseases, microbial communities, serotypes, pyocin production, and resistance – remains lacking. This circumstance significantly hinders deciphering the strong divergence of *fpvA* siderovar distribution in *P. aeruginosa* across different published strain collections of clinical isolates and the role of siderovars in developing acute or chronic infections. In light of the strain collection used in this work, it is hypothesised that the overwhelming appearance of the *fpvAIII* siderovar could potentially result from evolutionary selection pressure exerted by pyocins. While the OM siderophore receptors FpvAI and

FpvAII are hijacked by well-known S-type pyocins (FpvAI: S2 and S4, FpvAII: S3), the FpvAIII receptor is not known to be used as a target for antimicrobial peptides from the pyocin family. Thereby, the *fpvAIII* genotype confers a high level of resistance to the prevalent pyocins S2, S3, and S4 to these strains, by which they gain a significant benefit in microbial competition. An additional advantage of strains belonging to the *fpvAIII* siderovar over other bacterial competitors in the proximate environment can be gained by an additional ability to produce their own pyocins. Although our applied multiplex PCR only detects the *pyoS2_imS2* tandem, a disproportionate number of 56 strains (74.6%) from the *fpvAIII* siderovar encode this particular pyocin, while the *pyoS2_imS2* tandem was only detected in 53.3% and 10.5% of the *fpvAI* and *fpvAII* strains, respectively. Hence, the majority of the clinical isolates from the UKD strain collection combine the ability to produce S-type pyocins (represented by PyoS2) while concurrently eluding from the cytotoxic influence and selection pressure of certain S-type pyocins by expressing the non-targetable FpvAIII receptor. A related mechanism to escape from pyocin-derived selection pressure was earlier investigated by Smith and colleagues, who found a higher-than-average sequence divergence in the *fpvAII* locus. As the FpvAII receptor is hijacked by the DNase pyocin PyoS3 for membrane translocation,[715] the authors hypothesised that the observed sequence divergence might occur as a result of selection pressure exerted by iterative exposure to PyoS3.[779]

Multiplex PCR-based approaches like ours, enabling a simultaneous detection of pyocin genes and siderovars that act as pyocin receptors, will be of great importance to predict susceptibility and resistance of *P. aeruginosa* isolates towards S-type pyocins based on genomic DNA. This prediction would drastically reduce the effort of experimental pyocin typing. Therefore, the inclusion of other S-type pyocin targeted OM receptors (*crtA*, *fptA*, *hur*, etc.) and the corresponding pyocin_immunity tandems (*pyoSX1_imSX1*, *pyoS5_imS5*, *pyoG_imG*, etc.) into the presented multiplex setup will be needed to monitor the distribution of pyocins among strain collections and further predict the effectiveness of pyocin treatment *in vitro*.

In summary, 15 CRPsA strains (13.3%) from a strain collection of 113 MDR isolates of *P. aeruginosa* from the University Hospital in Düsseldorf, carrying the *fpvAI* genotype, were identified by the presented multiplex PCR typing. As PyoS2 hijacks the FpvAI OM receptor for protein import and translocation into the target cell, these strains represent an excellent group for the experimental validation of PyoS2 and its engineered derivatives with altered immunity protein binding for the application as alternatives to common antibiotics.

IV.3.11 PyoS2 Y640C and PyoS2 ID Variants are Suitable to Obliterate MDR CRPsA

Earlier in this thesis, it was shown that mutations and small-molecule labelling at the IPE of the DNase bacteriocin PyoS2 impair binding to its cognate ultra-high-affinity immunity protein ImS2. Rational mutagenesis was used to manipulate the interaction between PyoS2 and ImS2, ultimately abolishing ImS2-mediated immunity towards wild-type PyoS2 and leading to the death of the PyoS2-resistant model strain *P. aeruginosa* PAO1. This finding challenges the general concept of innate bacterial immunity through the expression of immunity proteins. Particularly, in the context of MDR CRPsA, engineered bacteriocins could present a novel tool to provide alternative narrow-spectrum antimicrobials to treat these highly virulent and antibiotic-resistant clinical strains from the WHO priority list. Thus, we set out to corroborate our hypothesis by testing wild-type PyoS2, PyoS2 point mutants, AlF-labelled conjugates of PyoS2, and PyoS2 ID derivatives on the core strain collection of CRPsA isolates from the University Hospital in Düsseldorf, harbouring the *fpvAI* genotype. Analogously to previous experiments conducted in this work, the toxicity screening was performed in a soft agar assay by spotting dilutions of PyoS2 variants on immobilised cells of the 15 *fpvAI*-positive *P. aeruginosa* isolates from the core list (Figure IV.31). To briefly recapitulate the expected outcome of this experiment, a *pyoS2_imS2*$^{+}$ genotype is expected to confer resistance to wild-type PyoS2, whereas a *pyoS2_imS2*$^{-}$ genotype would render the corresponding strains

highly sensitive to treatment with the wild-type toxin through the lack of the cognate immunity protein ImS2. Predicted susceptibility and experimental results are additionally summarised in Figure IV.32.

Starting with the eight *P. aeruginosa* isolates, which were genotypically characterised as *pyoS2_imS2*$^{+}$ (M2, M7, M10, M71, M190, M294, M303, and M324), a PyoS2-resistant phenotype was observed upon treatment with wild-type PyoS2. This observation met the expectations of PyoS2-resistance through toxin neutralisation in the ultra-high-affinity complex with ImS2. Turning the focus to the remaining seven genotypically characterised *pyoS2_imS2*$^{-}$ strains (M74, M132, M134, M189, M191, M210, and M315) resulted in a rather unexpected experimental outcome, demonstrating only a limited response to the wild-type toxin. Particularly, only a small fraction of strains, namely M74, M132, and M134, showcased moderate to strong sensitivity to wild-type PyoS2 at a toxin concentration of 5 µM. However, the remaining strains with the *pyoS2_imS2*$^{-}$ genotype (M189, M191, M210, and M315) exhibited an unexpected PyoS2-resistant phenotype. Summarising the susceptibility of the examined *P. aeruginosa* strains to wild-type PyoS2, a total of three strains were killed, representing 20% of the core strain collection (*fpvAI*-positive) of CRPsA isolates.

The utilisation of the single cysteine mutants of PyoS2 (Q570C, K602C, and C-Cys) and their AlF488 conjugates, where the mutation site lies away from the IPE of the DNase domain of PyoS2, provided identical results for all strains from the core strain collection to the testing with wild-type PyoS2.
However, when using the novel PyoS2 variants with the Y640C substitution within the IPE and additional fluorophore dye labels, many of the previously PyoS2-resistant strains became highly sensitive to the engineered extended-spectrum PyoS2 Y640C-AlF conjugates. Eleven of 15 MDR *P. aeruginosa* strains were in total sensitive to PyoS2 Y640C-AlF488, which represents 73% of the strains from the core strain collection being sensitive to the PyoS2 Y640C variants compared to only 20% being sensitive to the wild-type toxin. Including the previously gained knowledge that the Y640C mutation at the IPE of the PyoS2 DNase domain impedes association of the ultra-high-affinity complex between PyoS2 and ImS2 *in vitro* (cf. Chapter IV.3.5) and *in vivo* (cf. Chapter IV.3.8), abolished PyoS2-resistance of ImS2-producing strains can be expected for these engineered proteins. And indeed, eight of the sensitive strains belong to the group of *pyoS2_imS2*$^{+}$ strains (M2, M7, M10, M71, M190, M294, M303, and M324) and three to the group of *pyoS2_imS2*$^{-}$ isolates M74, M132, and M134). Considering that eight of 15 clinical isolates were characterised as inherently PyoS2-resistant by multiplex PCR detection of the *pyoS2_imS2* tandem and subsequent experimental validation with wild-type PyoS2, the introduction of the mutation Y640C in PyoS2 at the IPE and subsequent optional labelling with AlphaFluor fluorophore dyes culminated in thorough extinction of genotypically PyoS2-resistant MDR clinical isolates (100%). Hence, the efficient killing of all eight ImS2-producing and thereby PyoS2-resistant strains through a single amino acid substitution at the IPE in the mutant Y640C in conjunction with small-molecule labelling presents a drastic improvement of the antimicrobial spectrum of wild-type PyoS2.

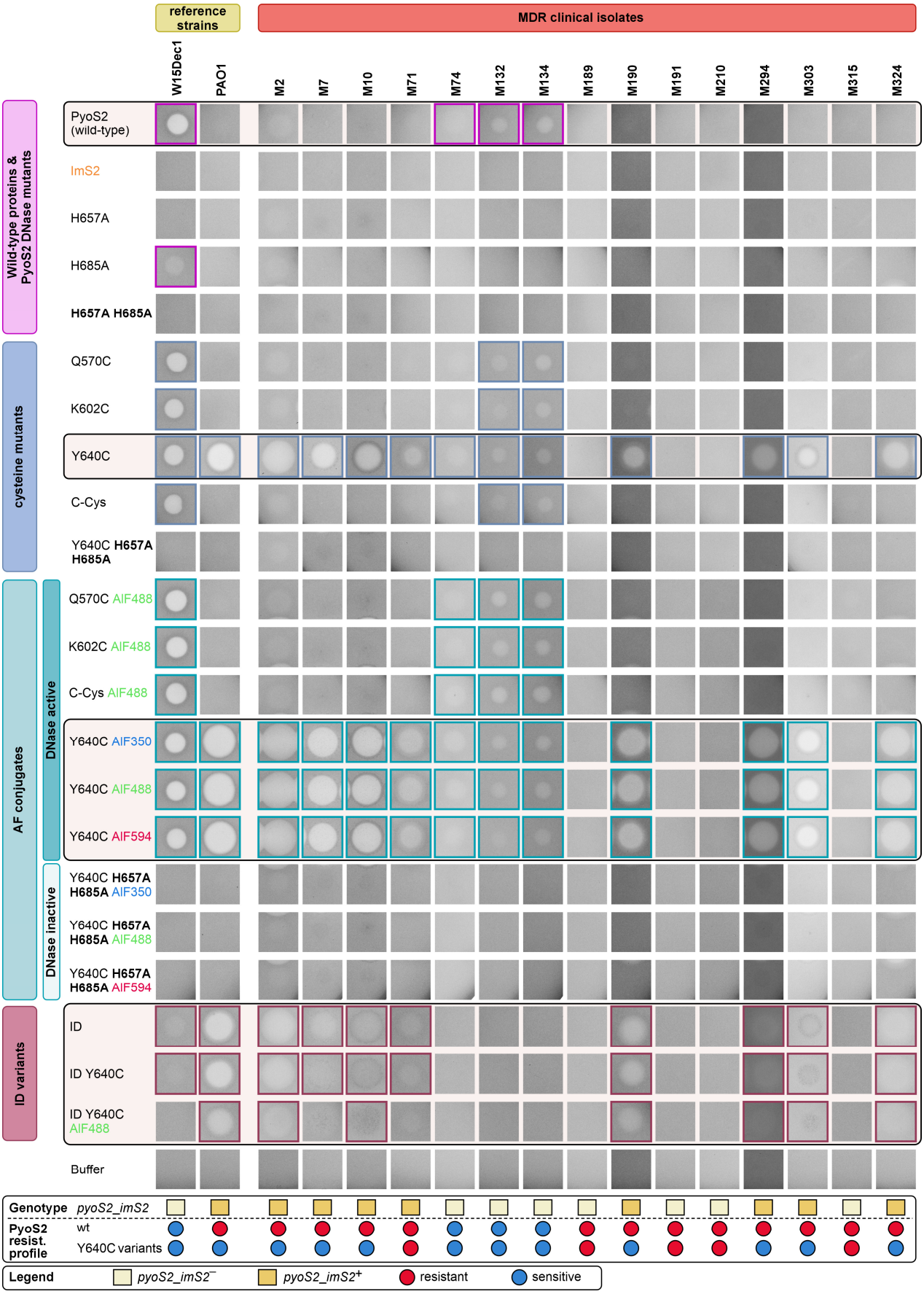


Figure IV.31. Plate killing assay with PyoS2 variants on CRPsA isolates of *P. aeruginosa* from the *fpvAI* siderovar. Bacterial cells were immobilised in LB soft agar and layered over an LB agar plate. Purified proteins and conjugates (5 µL at 5 µM) were spotted onto the plates. Wild-type PyoS2 and the DNase-active extended-spectrum PyoS2 variants are highlighted.

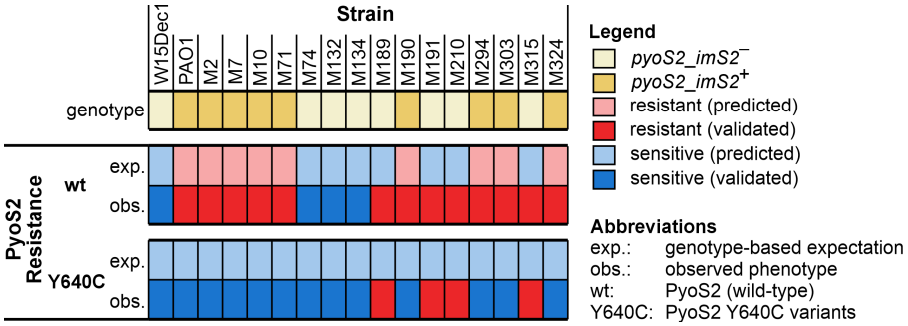


Figure IV.32. Susceptibility of CRPsA strains to wild-type and extended-spectrum PyoS2. Heatmap representation of genome-based susceptibility prediction (based on *fpvAI* and *pyoS2_imS2* loci) and the results of experimental testing with wild-type PyoS2 and the extended-spectrum variants carrying the Y640C mutation at the IPE. This figure summarises the results from Figure IV.31.

The interaction-deficient protein construct PyoS2 ID showed a similar trend in comparison to the killing activity of PyoS2 Y640C or PyoS2 Y640C-AIF conjugates and was also capable of obliterating all eight genotypically PyoS2-resistant isolates. However, the phenotypic characteristics of bacterial killing were weaker than for the Y640C and Y640C-AIF variants, and match the observations made for the model strain PAO1 earlier (cf. Figure IV.27). The apparently lower killing activity of PyoS2 ID in comparison to wild-type PyoS2 was previously accounted to the significantly reduced DNase activity as a result of extensive mutagenesis at the IPE of the DNase domain (cf. Chapter IV.3.6). Furthermore, it was hypothesised that electrostatics of the DNase domain affect membrane translocation of pyocins and an overall reduction of the net positive charge in PyoS2 ID variants impairs the charge-dependent immersion of the DNase into the phospholipid bilayer during membrane translocation into the target cell (cf. Chapter IV.3.8). Lastly, the persistent resistance of genotypically sensitive strains M189, M191, M210, and M315 to PyoS2 ID substantiate the presence of a secondary (ImS2-independent) resistance mechanism against PyoS2 in these particular strains.

Summarising the current results, we could show that wild-type PyoS2 acts only on a small fraction of clinical MDR isolates (3 strains, 20%) from our core strain collection, comprising 15 strains of *P. aeruginosa* harbouring the *fpvAI* genotype that is required for binding and translocation of PyoS2. In total, 80% of the core strain collection exhibited resistance to wild-type PyoS2. This high degree of resistance was partially traced back to a large portion of strains producing the cognate immunity protein ImS2 (8 strains, 53.3%) within this FpvAI$^+$ group. However, from the remaining seven strains, which do not produce the cognate immunity protein ImS2 (46.7%), only three strains were sensitive to the wild-type toxin. Why the other ImS2-deficient strains exhibit a PyoS2-resistant phenotype is currently unknown. By using the engineered protein derivatives and conjugates of PyoS2 with a broadened antimicrobial spectrum that is primarily enabled by the Y640C mutation at the IPE, we were able to increase the sensitivity in our core strain collection from 20% (sensitivity to wild-type PyoS2) to a remarkable 73.3% (sensitivity to PyoS2 Y640C-AIF488). In fact, all eight strains producing the cognate immunity protein ImS2 became sensitive to the PyoS2 Y640C-AIF488 conjugate, facilitated by the corrupted binding of the conjugate to ImS2 and the insufficient neutralisation of the toxin's DNase activity in the presence of ImS2. Further observations of PyoS2-resistant isolates (M189, M191, M210, and M315) remaining persistently resistant to the extended-spectrum pyocins (PyoS2 Y640C and the PyoS2 Y640C-AIF conjugates), despite sharing the *pyoS2_imS2*$^-$ genotype, hint towards a secondary pyocin resistance mechanism of these *fpvAI*-positive *P. aeruginosa* strains, independent of the expression of the cognate immunity protein ImS2.

The presented data in this chapter impressively underline that the uncovered mechanism of corrupt immunity protein binding is not only able to abolish PyoS2-resistance in the *P. aeruginosa* PAO1 model strain, but also in

highly concerning clinical isolates with accumulated multidrug-resistance to last-resort antibiotics. Therefore, the devised strategy of corrupted binding might serve as a blueprint for equivalent modifications in other bacteriocins, aiming for an extended antimicrobial spectrum and to outwit the ultra-high-affinity binding of cognate immunity partners, while maintaining high species and target selectivity. Therefore, the presented strategy of bacteriocin engineering opens new possibilities in treating multidrug-resistant bacterial pathogens and has excellent potential to improve the therapeutic application spectrum of these antimicrobial proteins.

IV.3.12 Whole-Genome Sequencing Reveals Commonalities and Differences in OM Composition

The utilisation of PyoS2 Y640C variants efficiently eliminated PyoS2-resistant MDR clinical isolates of *P. aeruginosa*, whose PyoS2-resistance is caused by a *pyoS2_imS2*$^{+}$ genotype. This resistance is driven by the expression of PyoS2's cognate immunity protein ImS2, which associates with the toxin in an ultra-high-affinity complex and neutralises the toxin by binding at the IPE of the PyoS2 DNase domain. During the *in vivo* testing, four of 15 tested strains (26.7%) from the core list of *fpvAI*-positive CRPsA isolates remained resistant to the engineered PyoS2 Y640-AlF conjugates, which possess the ability to abolish ImS2-mediated PyoS2-resistance by disturbing the association of the cognate toxin/antitoxin complex. However, these strains were expected to be sensitive to wild-type PyoS2 and PyoS2 Y640C-AlF conjugates, as these *pyoS2_imS2*$^{-}$ strains are not capable of producing the cognate immunity protein. Therefore, their resilience must be caused by a secondary resistance mechanism that is independent of ImS2. To investigate the genomics of all *fpvAI*-positive isolates and identify genetic commonalities that may contribute to intractable PyoS2-resistance, Whole-Genome Sequencing (WGS) was performed on all strains from the core strain collection.

IV.3.12.1 Sequencing, Genome Assemblies, and Their Alignment

All genomic DNA samples were processed and sequenced at AZENTA Life Sciences by performing a library preparation in the first place and a short-read Illumina NGS in subsequent steps, providing 150 bp paired-end reads by using the NovaSeq 2x150 setup. Raw data were obtained in the fastq format and the datasets ranged between 1.20 Gb to 5.61 Gb for each individual strain and read (Table V.5, Chapter V.5.10). The Phred quality score is an indicator for the quality of the sequencing data and corresponds to the confidence of every individual base read. A common threshold of >Q20 refers to 99% confidence, while >Q30 refers to a confidence of 99.9%. All datasets of sequencing reads reached a Phred score between Q34.52 and Q35.45, indicating high quality and reliability of the obtained sequencing results. All datasets were trimmed and filtered using fastp and assembled *de novo* with a minimum contig length of 300 bp with Unicyler by using the European Galaxy Server.[780-783] The assembled genomes ranged from 6.67 Mbp to 7.26 Mbp, and all datasets were furthermore subjected to contamination screening. Within the selection of sequenced strains, the GC content was found within a narrow range of 65.7 and 66.2% and each individual genome was constituted from 79 to 149 contigs (>300 bp) with a superb CheckM completeness of >98.5%. All contigs were aligned to the reference genome of *P. aeruginosa* PAO1 (NCBI NC_002516.2) and coding sequences were annotated locally using Bakta.[784] All genomes have been submitted to the NCBI repository and were deposited under GenBank accession numbers (see Chapter V.5.10, Supporting Information) after annotation using NBCI's Prokaryote Genome Annotation Pipeline (PGAP).[785] By using the tBlastn algorithm,[786] common resistance genes, virulence factors, pyocins, and LPS determinants were identified in the sequenced microbial genomes (Figure IX.12, Supporting Information).

IV.3.12.2 The OM Composition Impacts the Cytotoxicity of PyoS2 and Labelled Derivatives Thereof

In the first *in vivo* experiments, using the two *P. aeruginosa* model strains PAO1 and W15Dec1 (cf. Chapter IV.3.8), the PyoS2-sensitive strain W15Dec1 displayed rather small zones of growth inhibition for wild-type PyoS2 treatment at 5 µM, while the PyoS2-resistant strain PAO1 did not show any receptiveness for PyoS2 treatment (MIC >5 µM) (cf. Figure IV.27). However, when PyoS2/ImS2 association was impaired through the introduced mutation Y640C and subsequent AlF-labelling at the IPE of PyoS2, strain PAO1 became highly sensitive to the novel PyoS2-fluorophore conjugate. Although the MIC was not further investigated at first, an apparent discrepancy in the size of the zones of inhibition was noticed between PAO1 and W15Dec1. Particularly, the zones of growth inhibition upon treatment with the PyoS2 Y640C-AlF488 conjugate were significantly larger for strain PAO1 than for the inherently PyoS2-sensitive strain W15Dec1 (cf. Figure IV.27).

Our current understanding of PyoS2 translocation includes binding to the primary receptor FpvAI at the cell surface, translocation via the Ton-pathway into the periplasm, and FtsH processing for import of the DNase domain into the cytoplasm of the target cell. As both investigated strains exhibited a sensitive phenotype upon treatment with the PyoS2 Y640C-AlF488 conjugate, all aforementioned steps of PyoS2 translocation must be functional. Moreover, all three involved protein components are highly conserved on a sequence level, as the Ton-pathway and the IM protease FtsH are essential for cell viability of *P. aeruginosa*. Hence, we concluded that finding the mechanistic cause of differential pyocin sensitivity in these essential membrane components is rather unlikely. Instead, it was hypothesised that other factors in the OM of these *P. aeruginosa* strains might affect the initial affinity of PyoS2 to the targeted cells, thereby modulating the displayed cytotoxicity. Previous works on strain PAO1 and the antibacterial proteins PyoS5, PyoS2, PyoSD2, and PyoSD3 noted strong *in vitro* binding of these S-type pyocins to the D-rhamnose-containing CPA (common polysaccharide antigen) isolated from PAO1,[711, 719] mediated by the CPA-binding domain of the toxins.[719] Moreover, the absence of killing activity in certain isolates was traced back to deficient CPA biosynthesis caused by mutations in the corresponding gene cluster.[707] The CPA is, besides the O-specific antigen, one of the two major cell surface lipopolysaccharides (LPS) of *P. aeruginosa*. This unique structural feature is notable for its conserved biosynthesis cluster, which is exclusively found in *P. aeruginosa*.[787] The biosynthesis of CPA in *P. aeruginosa* PAO1 or the highly virulent isolate PA14 is well-studied and known to be organised in a clustered locus. This gene cluster consists of 13 genes, which encode enzymes involved in D-rhamnose biosynthesis (*gmd*, *rmd*, *wbpW*), as well as an ABC transporter system (*wzt*, *wzm*), and several glycosyl- (*wbpX, wbpY, wbpZ, PA5455, PA5456*), methyl- (*PA5457*, *PA5459*), or acetyltransferases (*PA5458*) (Figure IV.33).[692, 787] Premsuriya *et al*. reported frequent single nucleotide polymorphisms (SNPs) in the *gmd* gene of spontaneous PAO1 mutants resistant to PyoSX1 and PyoSX2, which resulted in premature termination of gmd mRNA translation or the production of nonsense polypeptides.[707] In fact, CPA is the only context in which D-rhamnose can be found in *P. aeruginosa*. Therefore, only a single biosynthesis pathway, including the functional interplay between Gmd, Rmd, and WbpW enzymes, is able to provide the GDP-D-rhamnos precursor essential for CPA assembly. Hence, defects in the corresponding genes lead to CPA-deficient phenotypes and a lack of CPA display on the cell surface. Consequently, the loss of functional CPA biosynthesis and the entailed lack of CPA's D-rhamnose homopolymer being displayed on the cell surface is assumed to significantly decrease the affinity of S-type pyocins to the target cell, being a secondary (ImS2-independent) cause for pyocin resistance.

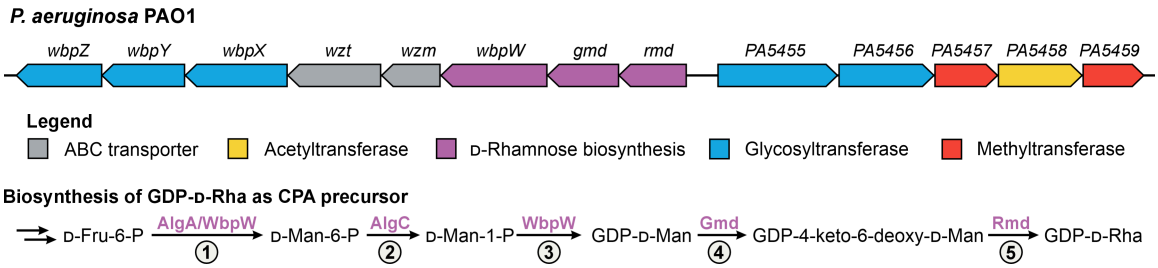


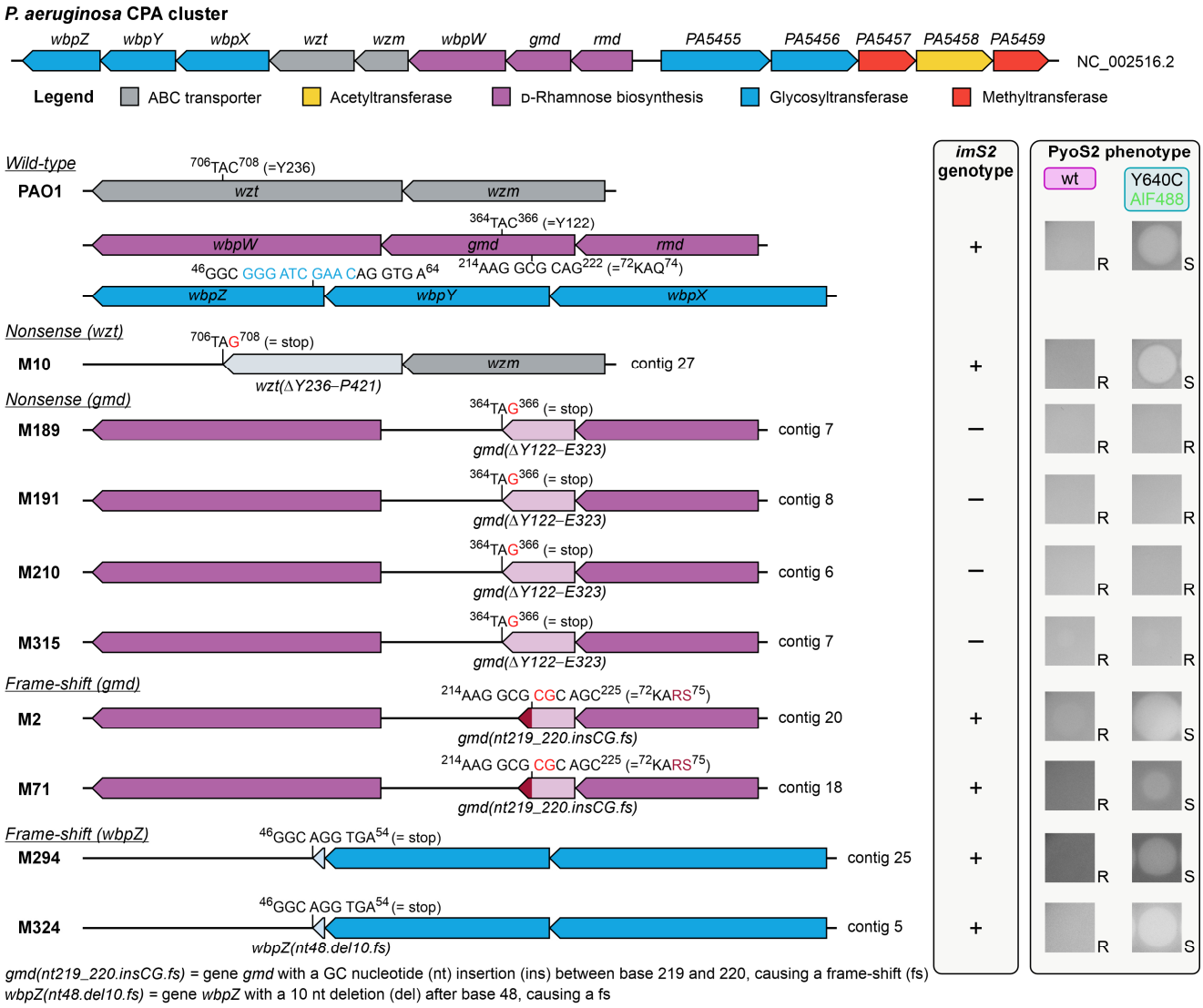
Figure IV.33. CPA biosynthesis cluster of *P. aeruginosa* PAO1 and the biosynthesis pathway of GDP-D-rhamnose as CPA precursor. In the first step of D-rhamnose biosynthesis, D-Fructose-6-phosphate is isomerised to D-mannose-6-phosphate by the phosphomannose isomerase activity of WbpW (or AlgA) (**1**), followed by a second isomerisation reaction towards D-mannose-1-phosphate catalysed by AlgC (**2**). Subsequently, the D-mannose-1-phosphate is equipped with a guanosine nucleotide through the guanylyltransferase activity of WbpW (**3**). Its product GDP-D-mannose is then dehydrated by the GDP-mannose 4,6-dehydratase (Gmd) to GDP-4-keto-6-deoxy-D-mannose (**4**) and in a final step reduced to GDP-D-rhamnose by the GDP-4-keto-6-deoxy-D-mannose reductase (Rmd) (**5**). Abbreviations: GDP – guanosine diphosphate; Fru – fructose; Man – mannose; Rha – rhamnose.

To further investigate a link between the ImS2-independent PyoS2 resistance of isolates M189, M191, M210, and M315 from the strain collection of CRPsA isolates, all CPA clusters of the 15 sequenced MDR clinical isolates and control strain W15Dec1 were analysed in comparison to the reference genome of PAO1. Therefore, the gene clusters from the locally assembled and annotated genomes were subjected to the tBLASTn algorithm.[788] The translated amino acid sequences of PAO1 loci between *wbpZ* and *PA5459* (cf. Figure IV.33), representing the outer boundaries of the CPA biosynthesis cluster, were used as a template and blasted for homologous sequences in the local translated nucleotide databases of every individual strain. Given the established knowledge of impaired CPA biosynthesis in mutants with stop codon mutations leading to shortened proteins, the initial investigation primarily focused on start and stop codon mutations. Thereby, apparent patterns fitting the biological data of unexpected PyoS2-resistance to the wild-type toxin in the absence of ImS2 were prospected.

IV.3.12.2.1 Mutations in the Glycosyltransferase WbpZ and in the ATPase Subunit Wzt Show No Impact on PyoS2 Sensitivity

The BLAST analysis of *P. aeruginosa* genomes for noticeable and recurring aberrations or SNPs in the CPA biosynthesis cluster neither detected anomalies in the glycosyltransferase genes *wbpX*, *wbpY*, *PA5455*, and *PA5456*, nor in the acetyl- and methyltransferase loci *PA5457*, *PA5458*, and *PA5459.* Also, no truncated mutants of the *wzm* membrane subunit of the CPA efflux ABC transporter were found among the 16 sequenced strains. However, three strains were identified in total, carrying nonsense or frame-shift mutations in the *wzt* and *wbpZ* locus, respectively. In strain M10 (*pyoS2_imS2*$^{+}$ genotype), the cytoplasmic ATPase subunit *wzt* of the CPA efflux ABC transporter showed a nonsense SNP. A point mutation (C-to-G) in the tyrosine codon ^{706}TAC^{708} recodes the corresponding codon into a stop codon, leading to premature truncation and the absence of the C-terminal amino acids Y236–P421 in the translated protein (44% shorter than wild-type Wzt) (Figure IV.34). Additionally, strains M294 and M324 (both *pyoS2_imS2*$^{+}$ genotype) were identified to encode a 10 bp deletion the *wbpZ* gene, encoding the cytoplasmic glycosyltransferase WbpZ, which inititates CPA polymerisation the cytoplasm.[789, 790] The deletion after nucleotide 48 of the coding sequence causes a –1 shift of the reading frame and premature truncation after 17 amino acids from the N-terminal formyl-methionine initiator (Figure IV.34). In fact, both proteins Wzt and WbpZ are essential for a functional biosynthesis of the D-rhamnose homopolymer in the cytoplasm and its subsequent transport into the periplasm for further processing and CPA assembly into the OM (cf. Figure IV.38, see page 249, *vide infra*). Hence, all three strains are CPA-deficient and incapable of synthesising the CPA

antigen. Although the CPA antigen was previously shown to act as a secondary receptor for many S-type pyocins and its absence renders strain PAO1 insensitive to S-type pyocin treatment,[707, 711, 719] the described strains M10, M294, and M324 displayed a sensitive phenotype when challenged with the extended-spectrum PyoS2 Y640C-AlF488 conjugate. Therefore, it becomes clear that factors other than just the presence or the absence of the CPA antigen influence the susceptibility of *P. aeruginosa* to pyocins.



gmd(nt219_220.insCG.fs) = gene *gmd* with a GC nucleotide (nt) insertion (ins) between base 219 and 220, causing a frame-shift (fs)
wbpZ(nt48.del10.fs) = gene *wbpZ* with a 10 nt deletion (del) after base 48, causing a fs

Figure IV.34. Schematic representation of identified mutations in the CPA cluster of *P. aeruginosa* isolates. Displayed are the wild-type CPA cluster of *P. aeruginosa* PAO1, encoding 13 genes that are essential for functional CPA biosynthesis, and recurring polymorphisms found in the CPA cluster of MDR isolates via BLAST genome analysis. All other strains not explicitly shown share the wild-type locus of PAO1. The killing activity of PyoS2 variants was tested in the soft agar assay with 5 µM solutions of PyoS2 and PyoS2 Y640C-AlF488. Clear spots indicate bacterial growth inhibition through bactericidal activity. Abbreviations: S – sensitive; R – resistant.

To explain our observations, two possible mechanisms can be hypothesised. Firstly, the unfunctional ATPase Wzt(ΔY236–P421) subunit of the Wzm/Wzt ABC transporter and the unfunctional glycosyltransferase WbpZ(nt48.del10.fs) could be replaced by other unknown ABC-related ATPase subunit X and glycosyltransferases Y from the bacterial proteome. However, Lam and co-workers previously investigated genomic *wzm* and *wzt* mutants of strain PAO1, both of which were unable to display assembled CPA on their cell

surface while maintaining intact OSA.[791] Hence, this hypothesis is implausible. Secondly, it may be hypothesised that the three strains neither display CPA nor the OSA on their cell surface and thereby become hypersusceptible to the treatment with PyoS2 Y640C-AlF488 due to a lack of protective LPS shielding of the cell surface. The absence of the OSA on the cell surface might then also displace the need for CPA to enhance cellular binding of PyoS2, as the primary FpvAI receptor is easily accessible for the toxin. However, the lack of experimental data at this point does not allow for any further conclusions that would support or refute the hypotheses above.

IV.3.12.2.2 Mutations in the *gmd* Locus Impair CPA Biosynthesis and Cause Secondary PyoS2 Resistance

Besides the SNP in the ATPase subunit of Wzt of strain M10 and the 10-bp deletions in the *wbpZ* glycosyltransferase locus of strain M294 and M324, more anomalies in the CPA biosynthesis cluster were found in the portion responsible for GDP-D-rhamnose synthesis, all located in the genomic *gmd* locus of the GDP-mannose 4,6-dehydratase Gmd. In a functional CPA cluster, the Gmd enzyme converts GDP-D-mannose to GDP-4-keto-6-deoxy-D-mannose. The latter product, in turn, is the direct biosynthesis precursor of GDP-D-rhamnose, the GDP-activated monomeric subunit of the cell surface-exposed D-rhamnose homopolymer of the common polysaccharide antigen. Although the BLAST output of all strains seemed inconspicuous at first glance with an indicated identity of 100%, careful examination of the data uncovered two distinct types of anomalies, both affecting the C-terminus of the Gmd protein. Within the 16 sequenced strains, a total of six strains were found carrying mutations in the *gmd* gene.

Four of the six strains with mutations in the *gmd* locus were found to be M189, M191, M210, and M315. As a reminder, all four strains exhibited unexpected and persistent resistance to the engineered PyoS2 Y640C variants with impaired ImS2 binding (cf. Figure IV.32). The BLAST analysis of the *gmd* locus in the assembled genomes of these strains revealed a consistent query coverage of 100% and an identity of 322 of 323 amino acids (99.69%). The discrepancy of just one amino acid is caused by a recurring SNP (C-to-G) in all four strains. This C-to-G nonsense point mutation in position 366 of the nucleotide sequence determines a codon exchange from Y122 (TAC) to a stop codon (TAG) that leads to premature termination of the gmd mRNA translation in M189, M191, M210, and M315 and results in a C-terminally truncated Gmd(ΔY122–E323) protein that is assumed to be non-functional (Figure IV.34). Remarkably, these four strains had been previously identified as *pyoS2_imS2*$^{-}$ in multiplex PCR typing and were thus expected to be sensitive to wild-type PyoS2. However, all of them exhibited an unexpected PyoS2-resistant phenotype (cf. Chapter IV.3.11). As the *P. aeruginosa* genome does not encode other enzymes with homologous function to Gmd, the four strains M189, M191, M210, and M315 are incapable of producing the cell surface lipopolysaccharide CPA through a lack of GDP-D-rhamnose precursor molecules. Consequently, the absence of displayed CPA on the cell surface also explains the PyoS2-resistant phenotype of these strains, since the CPA-binding domain of PyoS2 cannot bind to its secondary receptor anymore and FpvAI binding alone is apparently not strong enough to induce translocation and cell killing. Although this specific SNP has not been described in the literature, the resulting mechanism of *gmd* inactivation is analogous to that observed in the spontaneous PyoSX2-resistant *P. aeruginosa* mutant SX2-R1. Premsuriya *et al*. found this mutant with a C-to-G mutation in position 150 of the *gmd* locus, causing a single amino acid substitution from Y150 to a stop codon.[707] Despite the fact that this Gmd(ΔY150–E323) mutant from the literature is 28 amino acids longer than the truncated Gmd(ΔY122–E323) protein found in our strains M189, M191, M210, and M315, both nonsense mutants of the Gmd dehydratase protein lose their biological function and confer secondary PyoS2-resistance to those strains even in the absence of cognate immunity proteins.

Besides the nonsense mutation in the *gmd* locus of strains M189, M191, M210, and M315, leading to the unfunctional Gmd(ΔY122–E323) protein, two additional strains from the core list of MDR isolates were found to harbour a frame-shift mutation in the same locus (Figure IV.34). The strains M2 and M71 carry a two-nucleotide insertion of CG between the bases ^{219}G and C^{220} of the *gmd* locus, causing a +2 shift in the reading frame of *gmd* and the translation of a non-native sequence from alanine A72 before the translation stops after arginine R95. In consequence, the C-terminally truncated Gmd(nt219_220.insCG.fs) mutant is even shorter than the nonsense mutant Gmd(ΔY122–E323) and does not retain sufficient sequence similarity to the original Gmd enzyme to remain catalytically active and to produce the CPA precursor molecule GDP-4-keto-6-deoxy-D-mannose. Hence, the strains M2 and M71 are certainly unable to produce functional CPA and to display the lipopolysaccharide on their cell surface. Multiplex PCR typing previously identified both isolates to carry the *pyoS2_imS2*$^{+}$ genotype, rendering them resistant to wild-type PyoS2 through neutralisation of the toxin by ultra-high-affinity binding to ImS2. However, in the presence of the novel conjugate PyoS2 Y640-AlF488 with impaired association of ImS2 to the IPE of the DNase domain, both strains were sensitive to the engineered bacterial toxin. This experimental finding is rather non-intuitive, as it contradicts the hypothesis that PyoS2 can only translocate across the membrane in the presence of functional CPA on the cell surface. The observation of bacterial killing by PyoS2 Y640C-AlF488 despite the absence of the secondary receptor CPA on the surface of the target strains M2 and M71 implies that a so-far unknown factor must be present, influencing cell surface binding and membrane translocation of PyoS2 conjugates in these two particular strains. If this hypothesis were verified, these findings could challenge our current understanding of cellular binding of S-type pyocins.

IV.3.12.2.3 The O-Serotype Determines the Sensitivity to PyoS2

So far, a consistent nonsense mutation in the *gmd* locus of the CRPsA strains M189, M191, M210, and M315 was identified as a common cause for CPA-deficiency that renders all four strains resistant to wild-type PyoS2 and the engineered PyoS2 Y640C toxins. However, CPA-deficiency was also detected in strains M2, M10, M71, M294, and M315, but interestingly, these strains retained sensitivity to the extended-spectrum PyoS2 Y640C conjugates. In search of the unknown factor that prevents PyoS2 from translocating into the strains M189, M191, M210, and M315, but concurrently helps PyoS2 to overcome CPA-deficiency in the strains M2, M10, M71, M294, and M324, an interesting but neglected observation from previous experiments was recalled. Earlier it was shown that utilisation of the PyoS2 Y640C variants causes more efficient killing against the PyoS2-resistant strain PAO1 than it does against the PyoS2-sensitive isolate W15Dec1 (cf. Figure IV.27). This conclusion was made based on the zones of growth inhibition, which were notably larger for the PyoS2-producer PAO1 than for the PyoS2-sensitive isolate W15Dec1 (+40% for Y640C, +63–67% for Y640C AlF-labelled variants). Although this finding initially received little attention, it has now been questioned whether this interesting revelation can be substantiated by genetic features.

To explore this question further, we decided to use the available core strain collection of *fpvAI*-positive CRPsA strains from the University Hospital in Düsseldorf, whose genetic constitution is known from WGS. By determining the MIC as a measure of bacterial killing efficiency and the sensitivity of strains to wild-type PyoS2 and PyoS2 Y640C-AlF488 treatment in the first place (Figure IV.35), we aimed at mining for genetic commonalities that might uncover the unknown factor that modulates sensitivity to PyoS2.

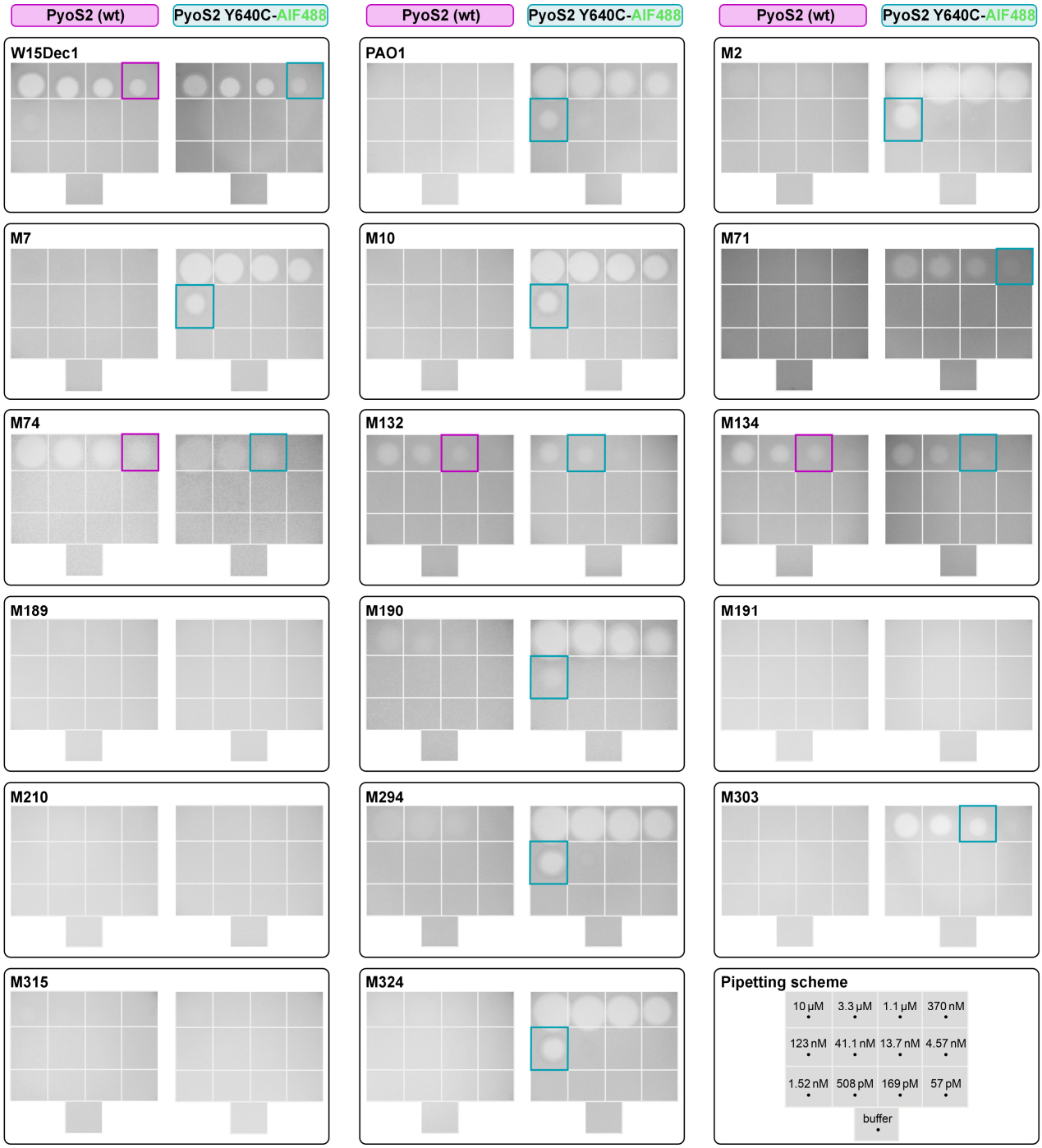


Figure IV.35. Determination of MICs for wild-type PyoS2 and the PyoS2 Y640C-AIF488 conjugate on CRPsA strains from the core strain collection (*fpvAI* siderovar). Bacterial cells were immobilised in LB soft agar and layered over an LB agar plate. 5 µL of purified proteins and conjugates at a concentration of between 10 µM to 57 pM were spotted onto the plates according to the pipetting scheme. Sterile dialysis buffer was used as a negative control. Clear spots indicate zones of bacterial growth inhibition. Minimal inhibitory concentrations (MICs) are highlighted by coloured frames.

In the following section, only the MICs obtained for PyoS2 Y640C-AIF488 in a toxin concentration range between 10 µM and 57 pM will be described, as this engineered toxin kills independently of ImS2 expression and thereby possesses a broader antimicrobial spectrum than the wild-type toxin PyoS2. In general, the observed MICs greatly varied and ranged from >10 µM (resistant) to low nanomolar concentrations (123 nM). As noted earlier, the CRPsA strains M189, M190, M210, and M315 were fully resistant to the PyoS2 Y640C-AIF488 conjugate, caused by the

deficiency in biosynthesis of the secondary PyoS2 receptor CPA (cf. Chapter IV.3.12.2.2). Furthermore, a higher sensitivity of strain PAO1 was observed (123 nM) than for the environmental isolate W15Dec1 (370 nM), an effect which had been previously noted in the first *in vivo* characterisation of PyoS2 variants (cf. Figure IV.27). Additional strains characterised by a MIC of 123 nM, equivalent to the one obtained for PAO1, were M2, M7, M10, M190, M294, and M324. A larger fraction of strains also exhibited a MIC of 1.1 µM, namely M71, M74, M134, and M303. Notably, these strains also exhibited relatively small zones of growth inhibition in comparison to other strains (PAO1, M2, M7, among others). And lastly, with strain M132, only one CRPsA isolate was identified to feature a MIC of 3.3 µM. Although no apparent common feature between strains that group into a certain MIC cluster can be seen at first glance, we hypothesised that the cell surface constitution (other than the CPA lipopolysaccharide) might play an important role in accessibility of the cell surface and the primary FpvAI receptor for binding and translocation of the tested PyoS2 toxins and conjugates.

The most important player in shaping the landscape of the Gram-negative OM is the serotype-dependent polysaccharide moiety of LPS, the O-specific antigen (OSA). While the D-Rha-containing homopolymer CPA can be found in only one form, 20 different O-specific antigens have been identified in *P. aeruginosa* to date. The 20 serotypes cluster into twelve genetically well-defined and distinct serogroups.[692, 792] Per definition, serotypes classify bacterial strains based on the antigenic variation of their O-specific antigen of LPS. The antigenic variation itself is owing to polysaccharides, which vary in sugar constitution, branching, linkage, and length. The serotyping system, based on the utilisation of serotype-specific antisera, was originally established to distinguish unique immune reactivity patterns observed for every individual OSA and serotype. All strains of a certain organism belonging to the same serotype exploit the same unique OSA gene cluster, leading to the presentation of chemically concordant OSA that is displayed on their cell surface. In 2016, the group of Lars Jelsbak developed the *Pseudomonas aeruginosa* serotyper (PAst) algorithm that allows the precise prediction of serogroups based on the corresponding OSA gene cluster in a free-to-use web application.[792, 793] This web application largely supersedes the experimental need for serotyping with serotype-specific antisera. By exploiting this web tool (PAst 1.0), the serogroups of all 15 MDR clinical isolates and the two control strains W15Dec1 and PAO1 were predicted. The fact that PAO1 is the best characterised *P. aeruginosa* strain and its O5 serotype has been known for decades served as an intrinsic control for the OSA prediction.[794] And indeed, the PAst web server predicted the O5 serogroup for strain PAO1. All other strains were indexed into serogroups O1 (W15Dec1), O4 (M132), O6 (M2, M7, M10, M71, M294, M324), O7 (M74), or O11 (M134, M189, M190, M191, M210, M303, M315). Hence, the serogroups O6 (35.3%) and O11 (41.2%) represent the largest fraction of all analysed strains from our core strain collection sharing the *fpvAI* genotype.

A closer look into PyoS2 Y640C-AlF488 sensitive strains with previously identified defects in CPA biosynthesis genes *wzt* (M10), *wbpZ* (M294 and M324), and *gmd* (M2 and M71) revealed a common O6 serotype. In contrast, all strains resistant to PyoS2 Y640C-AlF488 (MIC >10 µM) with defects in the CPA biosynthesis gene *gmd* (M189, M191, M210, and M315) co-group into the O11 serogroup, suggesting a serotype-specific loss of antibacterial activity of PyoS2 conjugates in the absence of the secondary CPA receptor. At this point, two potential explanations can be considered for the differential resistance pattern observed in serotypes O6 and O11 upon CPA biosynthesis deficiency. On the one hand, the O6 antigen might serve as an additional PyoS2 receptor and compensate for the loss of CPA, while O11 does not. On the other hand, the O6 antigen might be less densely packed on the cell surface, providing less effective shielding of the bacterial membrane compared to the O11 antigen, thereby facilitating the accessibility of the primary receptor FpvAI for binding and translocation of PyoS2. To further correlate the observed ImS2-independent antibacterial activity of the engineered PyoS2 Y640C-AlF488 conjugate – reflected in the MIC values – with the O-serogroup, MICs for all 17 strains were plotted against their

predicted O-serogroups (Figure IV.36A). Co-grouping of certain strains would then allow to search for commonalities in OSA composition (Figure IV.36B) or for genomic commonalities within these groups that would explain the observed resistance/sensitivity pattern towards the PyoS2 Y640C-AlF488 conjugate.

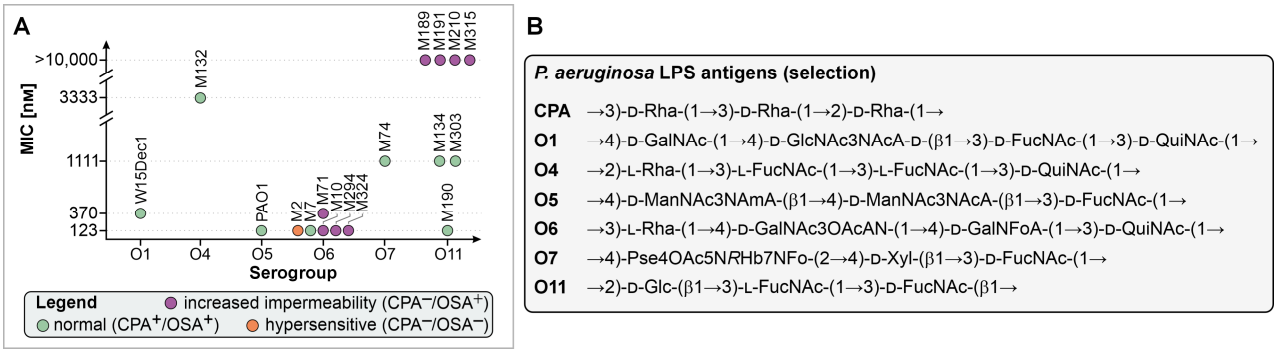


Figure IV.36. Clustering of predicted O-serogroups and correlation with the susceptibility to PyoS2 Y640C-AlF488 conjugates. **A**. The serogroups of all *fpvAI*-positive *P. aeruginosa* 17 isolates, predicted with the PAst web server, are plotted against the MIC for the PyoS2-AlF488 conjugate that overcomes ImS2-dependent PyoS2-resistance. **B**. Diversity of repeating oligosaccharide units of *P. aeruginosa* LPS antigens for the detected serogroups within the core strain collection of CRPsA isolates. Repeating unit constitutions were fetched from Lam *et al*.[692] and showcase overall low congruency in sugar composition and constitution between different LPS antigens of *P. aeruginosa*.

The MIC of PyoS2 Y640C-AlF488 against strains with intact CPA biosynthesis cluster exhibited a broad O-serogroup-dependent range. While strains belonging to the O6 (M7, M294, and M324) and O5 (PAO1) serogroups showed high sensitivity with MICs at 123 nM, the O1 serogroup (W15Dec1) was slightly less susceptible with a MIC of 370 nM. The serogroups O7 and O11 exhibited only moderate sensitivity to the PyoS2 Y640-AlF488 conjugate at 1.1 µM, however, the O11 strain M190 showed highly susceptible behaviour with a MIC of 123 nM. The serogroup O4 (M132) was least sensitive to PyoS2 Y640C-AlF488 with an accompanying MIC of 3.3 µM. Although the sample size of 17 strains is not sufficient to comprise all serogroups in a statistically significant manner, the analysis of CPA-deficient genotypes and their co-clustering provided a revealing insight. While the presence of a functional CPA cluster in strains from the O11 serogroup leads to MICs between 123 nM and 1.1 µM, the absence of CPA on the cell surface – caused by the nonsense mutation introduced into the *gmd* locus and the consequent inability to produce the GDP-D-Rha precursors of CPA – renders the O11 serogroup resistant to PyoS2 Y640C-AlF488 treatment. As all four strains from this resistant O11 cluster (M189, M191, M210, and M315) do not genetically encode the cognate PyoS2 resistance protein ImS2, this resistance (MIC >10 µM) is fully ImS2-independent. By opposing the CPA-deficient strains from the O11 serogroup with resistance to the PyoS2 Y640C-AlF488 conjugate to the other five CPA-deficient strains from the O6 serogroup (M2, M10, M71, M294, and M324), a remarkable difference in the observed pyocin susceptibility was manifested. Although the CPA-deficient strain M71 from the O6 serogroup showed slightly reduced sensitivity to the PyoS2 Y640C-AlF488 conjugate (MIC 1.1 µM) compared to CPA$^+$ strains from the same serogroup (123 nM), the other four CPA-deficient strains, M2, M10, M294, and M324, retained sensitivity at a level comparable to CPA$^+$ O6 strains (all 123 nM).

To further investigate the differences in sensitivity to the PyoS2 Y640C-AlF488 conjugate observed for the O6 strains, the highly conserved O6 IATS (International Antigenic Typing Scheme) gene clusters of M2, M7, M10, M71, M294, and M324 were analysed in a nucleotide multiple sequence alignment in comparison to the *P. aeruginosa* IATS O6 reference strain (GenBank AF035937.1). The O6 gene cluster contains all essential genes needed to synthesise the O6 polysaccharide antigen that is displayed on the cell surface of these strains.

Anomalies in the biosynthesis of the O6 antigen could therefore lead to altered membrane accessibility and enhanced or impaired binding of pyocins to their OM receptors. The opposing analysis of coding sequences from the O6 IATS clusters of all O6 strains revealed the presence of a single nucleotide insertion in the *wbpL* gene of strain M2. This guanine insertion between nucleotides 142 and 143 of the *wbpL* coding sequence causes a shift in the reading frame that converts *wbpL* into a non-functional pseudogene and causes premature translation termination (Figure IV.37).

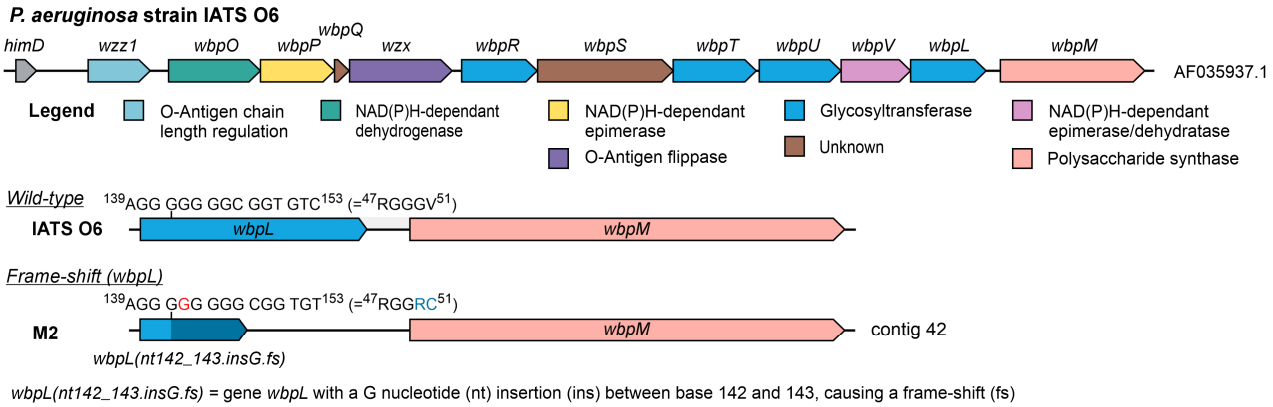


Figure IV.37. Schematic representation of observed anomalies in the IATS O6 cluster of *P. aeruginosa* isolates. Displayed are the wild-type IATS O6 cluster of *P. aeruginosa* IATS O6, encoding 12 genes (*himD* not included) that are essential for functional OSA-capped LPS biosynthesis and the display of the O6 serotype, and polymorphisms found via BLAST genome analysis in the OSA cluster of the O6 predicted *P. aeruginosa* isolate M2. All other strains not explicitly shown share the wild-type O6 locus of strain IATS O6 (M7, M10, M71, M294, and M324) or other serotypes (cf. Figure IV.36).

WbpL is a glycosyltransferase that is essential for both CPA and OSA biosynthesis.[789] During the CPA and OSA assembly in the bacterial cytoplasm, WbpL initiates the CPA and OSA polymerisation through the transfer of *N*-acetylglucosamine (NAG or GlcNAc) or 2-acetamido-2-deoxyfucose (Fuc2NAc) onto the membrane-anchored bactoprenol pyrophosphate, respectively (Figure IV.38).[789] This liposaccharide then serves as a membrane anchor and a prerequisite for subsequent D-Rha homopolymer elongation in CPA biosynthesis or the attachment of OSA-specific polysaccharide units.[692] Once the cytoplasmic antigen assembly has been finalised, two independent routes are taken to deliver the bactoprenol-coupled OSA and CPA antigens to the periplasmic leaflet of the inner membrane: an ABC transporter (Wzm/Wzt) dependent route for the CPA D-Rha homopolymer and a flippase-dependent (Wzx) transport for the OSA polysaccharide units. The antigen ligase WaaL directly transfers the fully assembled CPA antigen onto the reducing terminus of the lipid A outer core, while OSA ligation requires the polymerisation of repeating units via Wzy and Wzz first. Finally, the CPA- and OSA-capped LPS are transported to the cell surface via the Lpt pathway and integrated into the outer leaflet of the OM.

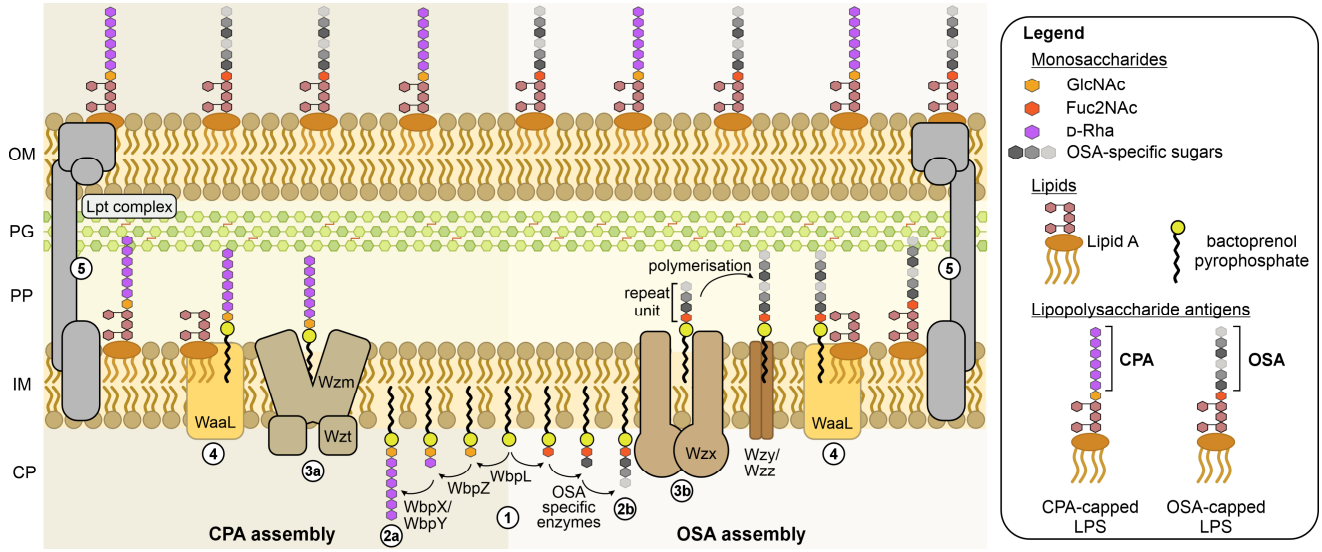


Figure IV.38. Assembly pathways for the CPA and OSA antigens of *P. aeruginosa* PAO1 (O5 serotype). The CPA is assembled in an ABC transporter-dependent pathway, while the OSA ligation involves the flippase/translocase Wzx. The synthesis of both antigens is initiated by the transfer of GlcNAc (CPA) or Fuc2NAc (OSA) onto membrane-anchored bactoprenol pyrophosphate, catalysed by the glycosyltransferase WbpL (**1**). While the CPA antigen is fully assembled in the cytoplasm (**2a**) and brought to the periplasmic leaflet of the IM via the ABC transporter Wzm/Wzt (**3a**), the OSA is synthesised in the cytoplasm in small repeating units (**2b**), which are then polymerised in the periplasm through the action of the polysaccharide polymerases Wzy and Wzz (**3b**). The LPS ligase WaaL transfers the CPA and OSA antigen onto Lipid A (**4**) and the fully assembled and capped LPS molecules are brought to the cell surface through the membrane-spanning Lpt complex (**5**). Abbreviations: IM – inner membrane; OM – outer membrane; PG – peptidoglycan; PP – periplasm. Figure design inspired by Burrows *et al*.[795]

A comprehensive genomic analysis of the CRPsA strains from the core strain collection of *fpvAI*-positive clinical isolates from the University Hospital in Düsseldorf, with respect to the biosynthesis of cell surface lipopolysaccharide antigens CPA and OSA, uncovered numerous deviations from the annotated reference clusters of strain PAO1 (CPA biosynthesis) and IATS O6 (O6 OSA biosynthesis) in our library of *P. aeruginosa* strains. The following paragraphs will summarise the resulting consequences for antigen biosynthesis and assembly, and the implications for PyoS2 binding and translocation:

Identified SNPs in the *wbpL* and *gmd* loci of isolate M2 from the O6 serogroup suggest a compromised biosynthesis of CPA and the O6-specific antigen (CPA^{-}/OSA^{-} phenotype) in this particular strain. Although the secondary PyoS2 receptor CPA is missing on the cell surface, the concurrent disability of this strain to synthesise the cell surface-covering OSA apparently enables strong binding of the PyoS2 Y640C-AlF488 conjugate to the FpvAI receptor. Hence, the absence of the O6 antigen with its shielding function renders strain M2 hypersusceptible to the engineered PyoS2 conjugate, even in the absence of the common polysaccharide antigen.

Other strains belonging to the O6 serogroup, namely M10, M71, M294, and M324, exhibited a nonsense mutation in the *wzt* locus (M10) or frame-shift mutations in the *gmd* (M71) or *wbpZ* (M294 and M324) loci, respectively. All three mutations render the corresponding CPA biosynthesis genes inactive pseudogenes and cause a premature translation stop. Thus, all these strains sharing the O6 serotype suffer from an impaired CPA biosynthesis, while their OSA biosynthesis and assembly pathway is apparently unaffected (CPA^{-}/OSA^{+} phenotype). In comparison to the only O6 serogroup strain M7, which possesses an intact CPA and LPS biosynthesis (CPA^{+}/OSA^{+} phenotype) and displays killing activity of the PyoS2 Y640C-AlF488 conjugate at 123 nM, the loss of CPA in strain

M71 (CPA$^-$/OSA$^+$) increases the MIC towards 1.1 µM. Other CPA$^-$ strains (M10, M294, and M324) remain highly susceptible at a MIC of 123 nM. Although the decreased susceptibility of strain M71 is presumably caused by the absence of CPA and a consequently reduced binding affinity of PyoS2 to the cell surface, while shielding through the cell surface-displayed O6 antigen is maintained, it remains unknown why strain M71 with an identical CPA/OSA phenotype exhibits diverging sensitivity to PyoS2. Besides the mentioned CPA and OSA biosynthesis genes, numerous genes[10] responsible for Lipid A and LPS biosynthesis, LPS assembly, and LPS transport were screened for anomalies. However, no evident explanations for the diverging phenotypes of the CPA-deficient strains were found.

Although experimental analyses of the CPA or OSA pattern for the investigated strains are to be performed to validate the *in silico* detected defects in CPA and OSA biosynthesis, the distribution and clustering of the 17 *fpvAI* strains strongly suggest involvement of another layer of determinants influencing pyocin immunity. The clustering of strains based on MICs and serotypes proposes that the surface-displayed OSA affects binding to target cells in a serotype-dependent manner. By exploiting the engineered PyoS2 Y640C-AlF488 conjugate that abolishes the natural mechanism of toxin neutralisation by sabotaging the formation of the ultra-high-affinity complex between PyoS2 and ImS2, we were able to reveal serotype-dependent cell binding and killing for S-type pyocins of *P. aeruginosa* for the first time.

This mechanism of bacteriocin resistance is an already known phenomenon for R-type pyocins (these tailocins do not associate with immunity proteins) of *P. aeruginosa* and has also been shown to be responsible for colicin-insensitivity of uropathogenic *E. coli*.[684, 796] A comparative study with 50 *P. aeruginosa* isolates and the phage-tail-like R-type pyocins R1, R2, and R5 conducted by Köhler *et al*. could correlate the serotype with R-type pyocin resistance/insensitivity. While the susceptible strains belonged to the serotypes O1, O3, and O6, the resistant strains exhibited the O10, O11, or O12 serotypes. The authors of this study hypothesised that the packing density of the respective OSA might account for the serotype-dependent killing or pyocin resistance of these serotypes.[684] These data coincide with our results of high susceptibility of CPA-producing serotypes O1 and O6 and reduced susceptibility of O11. If the CPA-binding domain of PyoS2 does not find its secondary CPA receptor through defects in the CPA biosynthesis pathway, the O11 serotype becomes fully PyoS2-resistant (cf. Figure IV.36). However, the absence of CPA in the O6 serotype does not fully abolish sensitivity to wild-type PyoS2 (cf. M74) and thus perfectly reflects the cytotoxic activity of R-type pyocins on these serotypes.

Although the serotype-dependent insensitivity of *E. coli* strains to colicins and *P. aeruginosa* strains to R-type pyocins has been known for many years, two key mechanistic differences between the S-type pyocin PyoS2 studied here and bacteriocins from the R-type pyocin and colicin families studied elsewhere have kept the serotype-dependent cell binding of S-type pyocins unnoticed until now.
First of all, unlike *E. coli*-targeting colicins and *P. aeruginosa*-targeting R-type pyocins, PyoS2 and other S-type pyocins possess a CPA-binding domain. The D-Rha-containing CPA homopolymer is a unique surface polysaccharide found only in *P. aeruginosa*. Our experiments showed that defects in CPA biosynthesis – and the resulting absence of CPA on the cell surface – negatively impact S-type pyocin binding and translocation in a serotype-dependent manner (cf. Figure IV.36). Since functional CPA biosynthesis is essential for PyoS2 to maintain killing activity against serotype O11, we hypothesise that the CPA-binding domain in S-type pyocins evolved to enhance killing efficacy against *P. aeruginosa* strains with densely packed OSA. Consequently, binding

[10] Lipid A and LPS biosynthesis (*migA*, *dnpA*, *waaA*, *waaC*, *waaF*, *waaL*, *waaP*, *waaG*, *wapG*, *wapH*, *wapO*, *wapP*, *wapR*, *galU*, *algC*, *gmhA*, *gmhB*, *rfaE/hldE*, *rfaD/hldD*, *rmlA–D*, *ytfN*, *pagL*, *arnT*, *lpxA–D*, *lpxH*, *lpxK*), LPS assembly (*wzz2*, complete IATS O6 cluster: *wbpO*, *wbpP*, *wbpQ*, *wzx*, *wbpR*, *wbpS*, *wbpT*, *wbpU*, *wbpV*, *wbpL*, *wbpM*), and LPS transport (*lptA–G*).

and translocation of S-type pyocins depend on both serotype and CPA. In contrast, colicin binding and translocation rely solely on *E. coli* serotypes, making serotype-dependent colicin insensitivity more readily observable than for S-type pyocins.
Furthermore, phage-derived R-type pyocins lack not only a CPA-binding domain but also cognate immunity proteins, meaning *P. aeruginosa* resistance or sensitivity to R-type pyocins is determined solely by serotype but independent of genome-encoded resistance proteins and the display of CPA on the cell surface. In contrast, resistance to S-type pyocins can arise either from serotype-dependent factors or immunity protein-mediated mechanisms, making genetic analysis necessary to distinguish the exact cause of resistance. Our novel extended-spectrum PyoS2 Y640C conjugates, which exhibit killing activity independent of ImS2-mediated resistance, are able to eliminate the variable of resistance conferred by immunity proteins, which is why the observed phenotypes upon treatment of *P. aeruginosa* with these conjugates are purely serotype-dependent.

The display of the CPA or the OSA on the cell surface is not crucial for the survival of *P. aeruginosa*. Nevertheless, both antigens are common determinants of bacterial virulence. The D-Rha-containing CPA homopolymer was shown to be established in the formation of robust biofilms, and CPA-deficient strains were affected in cell morphology and biofilm matrix production.[797] Deficiency in OSA biosynthesis or its display on the cell surface impairs adhesion to surfaces and swimming and swarming motility of *P. aeruginosa*.[625, 798] Close structural homologies between the CPA of *P. aeruginosa* and the OSA of phytopathogens also raised the question of whether CPA biosynthesis was acquired and evolved to enable *P. aeruginosa* to colonise plants and form biofilm on plants and soil.[625] Thus, loss of both antigens is assumed to come along with drawbacks in virulence against animals and plants and a weakened shielding of the bacterial envelope against the host immune response or environmental stress. Consequently, one might ask about the evolutionary benefit of these strains to lose either CPA, OSA or even both biosynthesis and assembly pathways, since this factor might also cause pyocin resistance if these antimicrobial toxins are broadly applied as antibiotics. In the first place, the loss of CPA or OSA caps might be driven by prolonged exposure to S-type pyocins (CPA binding),[719] R- and F-type pyocins (OSA/LPS core binding),[684, 685] or even bacteriophages (CPA binding by bacteriophage A7).[799] A loss of antigens might thereby increase the bacterial resilience towards these toxins and secure their survival in a competitive environmental niche. A second attempt to identify selection pressures promoting the loss of CPA or OSA is also based on co-colonising bacteria. Immunologically impaired cystic fibrosis patients are known to acquire long-lasting infections with opportunistic pathogens.[800] While *S. aureus* predominates in the childhood of these patients, the microbiome shifts towards *P. aeruginosa* as the dominant species in later years. Studies focusing on genomic adaptations of *P. aeruginosa* through co-evolution in the presence of *S. aureus* evidenced the accumulation of mutations in the LPS biosynthesis genes or the Wsp cell signalling pathways. Here, it was not only shown that the evolutionary genome adaptations caused a fitness gain in co-cultures with *S. aureus* but also increased cell impermeability and β-lactam resistance.[800] Considering that all isolates examined in this work, except W15Dec1, were derived from human patients, it is plausible that these strains have evolved LPS modifications as part of their adaptive strategies during the transition from chronic to acute infections.[801] By this strategy, long-term infections with chronic persistence are enabled, and the bacterium evades immune detection through the mammalian host.

In summary, the utilisation of the PyoS2 Y640C variants allowed us to correlate the persistent and ImS2-independent insensitivity to PyoS2 conjugates of genotypically sensitive strains to a dysfunction in the synthesis of the common polysaccharide antigen and the packing density of the cell surface displayed O-serotype. Thereby, we were able to reveal serotype-dependent cell binding and killing of S-type pyocins of *P. aeruginosa* for the first time. Moreover, the presented data underline the importance of advancing our current understanding of genetic

determinants behind OSA and CPA biosynthesis and their impact on the morphology of the bacterial cell membrane. While engineered PyoS2 Y640C variants with a corrupt immunity protein binding showed drastically improved potential in overcoming the mechanism of innate bacterial immunity through impaired complex association with cognate immunity proteins, further therapeutic solutions will be needed to reshape the outer membrane composition and thereby increase the antimicrobial spectrum of engineered bacteriocins even further.

IV.3.13 Utilisation of PyoS2 Conjugates to Traverse Potential Drugs Across the Bacterial Membrane

All so far presented PyoS2 conjugates from this work resort to non-toxic AlphaFluor fluorophore labels. These particular fluorophores were primarily selected for their broad commercial availability and the experimental focus on investigating labelling effects on PyoS2 DNase activity and ImS2 interaction. As discussed in previous chapters, PyoS2-AlphaFluor conjugates with non-toxic small-molecule labels have provided valuable insights into the uptake of PyoS2 conjugates via the Ton-pathway and the subsequent delivery of conjugated small molecules into the cytoplasm of *P. aeruginosa*. With its intrinsically high impermeability, the two-membrane system of *P. aeruginosa* poses a serious burden for antibiotics and other effector molecules to cross. Therefore, the exploitation of the conserved import mechanism of S-type pyocins to traverse conjugated therapeutics into *P. aeruginosa* is a promising strategy to selectively bypass the protective membrane of *P. aeruginosa* while leaving other microorganisms unaffected. Consequently, the advancement of S-type pyocins as generalised transport vehicles for bioactive drugs is a key milestone towards therapeutic application of these narrow-spectrum antimicrobial toxins. The utilisation of bacteriocins from Gram-negative or Gram-positive bacteria as specialised vehicles for the target-specific transport of potential drugs would present a completely novel strategy to combat the growing concern of antimicrobial resistance.

In this respect, we returned to the cytotoxic prodiginine scaffold, which is generally known to display antitumoral, broad antibacterial, and immunosuppressive bioactivities (cf. Chapter II.5.4). Prior studies have shown that prodigiosin effectively inhibits bacterial growth of *Enterococcus faecalis*, oxacillin-resistant *S. aureus*, and *Streptococcus pyogenes*, whereas so-far uncharacterised mechanisms render oxacillin-resistant *E. coli*, *P. aeruginosa*, and *A. baumannii* resistant to prodigiosin treatment.[802] Although a lack of experimental evidence allows for drawing only limited conclusions about the underlying mechanism of insensitivity to prodigiosin, it is reasonable to assume that multidrug efflux pumps (e.g. Mex RND pumps) extrude the hydrophobic drug from the bacterial membrane and thereby confer elevated resistance. This hypothesis is supported by the fact that the natural production of prodigiosin and carbapenem in *Serratia* sp. underlies a hierarchical network of regulatory proteins, including the transcriptional repressor PigZ. PigZ also controls the expression of a four-component RND drug efflux pump (ZrpADBC) that might increase drug tolerance through the removal of prodigiosin and carbapenem antibiotics from the producing cell.[803] Despite a missing experimental link between prodigiosin resistance and RND efflux, the persistent prodigiosin resistance of *P. aeruginosa* – a difficult-to-treat pathogen that employs numerous drug efflux pumps to drastically reduce the permeability of its membrane – was taken as a motivation to investigate covalent prodigiosin conjugates, which have the potential to elude the influence of drug efflux pumps. In this regard, the conserved import mechanism of PyoS2 via the FpvAI sideropore receptor and the Ton machinery was selected to traverse the prodigiosin-impermeable membrane of *P. aeruginosa* in a Trojan Horse Strategy by using PyoS2-prodigiosin conjugates.

The choice of the protein PyoS2 as a Trojan Horse shall address two major drawbacks currently limiting a broader application of the prodigiosin scaffold as a therapeutic option. Firstly, the covalent conjugation of the hydrophilic protein PyoS2 (74 kDa) to lipophilic prodigiosin (0.32 kDa) leads to increased size, polarity, and solubility of the

prodigiosin payload in comparison to free prodigiosin; factors that are important to conceal the prodigiosin payload from potential cell defence mechanisms and to evade its expulsion from the targeted cell by active efflux. And secondly, prodigiosin is known to deploy passive membrane diffusion for penetration of biological membranes and cells. However, this unselective mechanism also results in limited target specificity of prodiginine alkaloids and undesired off-target effects. By coupling the uptake of prodiginines to the active and conserved Ton-dependent uptake mechanisms of PyoS2 (cf. Figure IV.7), we aim to introduce a novel species- and strain-specific delivery tool for the prodigiosin payload into the Gram-negative bacterium *P. aeruginosa*.

IV.3.13.1 Design and Preparation of PyoS2-Prodigiosin Conjugates

In order to generate covalent conjugates of the antimicrobial protein PyoS2 and prodigiosin derivatives, the established thiol-maleimide chemistry was exploited to attach maleimide-functionalised probes to cysteine residues of PyoS2 mutants. This type of chemistry had already been proven valuable in the preparation of AlF fluorophore dye conjugates of PyoS2 earlier in this work (cf. Chapter IV.3.4.2). Since all introduced labelling sites (Q570C, K602C, Y640C, and C-Cys) within the PyoS2 DNase domain had been shown to retain the ability of PyoS2 to translocate into the bacterial cytoplasm and maintain catalytic DNase activity, the equivalent positions were utilised for attachment of prodiginine labels without risking the DNase to be fully inactivated. DNase-active conjugates with the above-mentioned labelling sites were planned to be used to probe cellular import of the conjugates through bacterial growth inhibition on PyoS2-sensitive strains. However, as DNase-active PyoS2-prodigiosin conjugates might display dual activity, caused by simultaneous PyoS2-related DNase activity and prodigiosin-related action, a second control was implemented. Therefore, DNase-inactive conjugates with the PyoS2 double knock-out mutation H657A H685A (cf. Chapter IV.3.1.3) were used to exclusively monitor potential growth inhibition that stems from the attached prodigiosin label. For the conjugation of prodiginines to the PyoS2 protein carrier via maleimide chemistry, the A-, B-, and C-ring maleimide-functionalised prodiginines **III-169·HCl**, **III-170·HCl**, and **III-171·HCl**, which have been accessed through a multistep total synthesis earlier in this work (cf. Chapter II.5.4), were used (Figure IV.39).

Cysteine labelling of purified PyoS2 mutants was performed as described previously for AlF fluorophores after initial reduction of potential disulfide bridges with the reducing agent dithiothreitol (DTT) and removal of excess reducing agent through desalting. Thiol-maleimide labelling with a 3-fold excess of maleimide-functionalised prodiginine probes **III-169·HCl**, **III-170·HCl**, and **III-171·HCl** and desalting for the separation of free dye from labelled protein furnished the desired conjugates, which were further validated by coupled LC-MS analysis for their mass (cf. Table IX.11, Supporting Information) and by SDS-PAGE (Figure IX.13, Supporting Information). Finally, the maleimide-labelling of PyoS2 mutants provided 12 DNase-active and 12 DNase-inactive PyoS2-prodiginine conjugates that were used for further biological evaluation (Figure IV.39). The labelling of the colourless proteins with the pink-purple prodiginines resulted in noticeably different colouration of the conjugates, even when the same label was used in combination with different proteins. These differences are likely attributed to unlike microenvironments on the protein surface, resulting from altered labelling sites. As prodiginines can occur in different tautomers and the equilibrium between protonated and deprotonated prodiginine species shows strong pH dependence (cf. Scheme III.36), accumulated acidic or basic amino acid residues in close proximity to the labelling site may affect this equilibrium and change the spectral properties of the attached prodiginines. Besides differences in colouring, the PyoS2-prodigiosin conjugates also exhibited a significantly higher viscosity than the previously introduced fluorophore-labelled AlF conjugates of PyoS2. This incline in viscosity may be caused by strong hydrophobic interactions between prodiginine labels in solution or through partial unfolding of the protein resulting from interaction with the hydrophobic prodiginine labels. Whether the increased viscosity

impacts the translocation mechanism of PyoS2 or the cytotoxicity of the PyoS2-prodiginine conjugates remains to be shown.

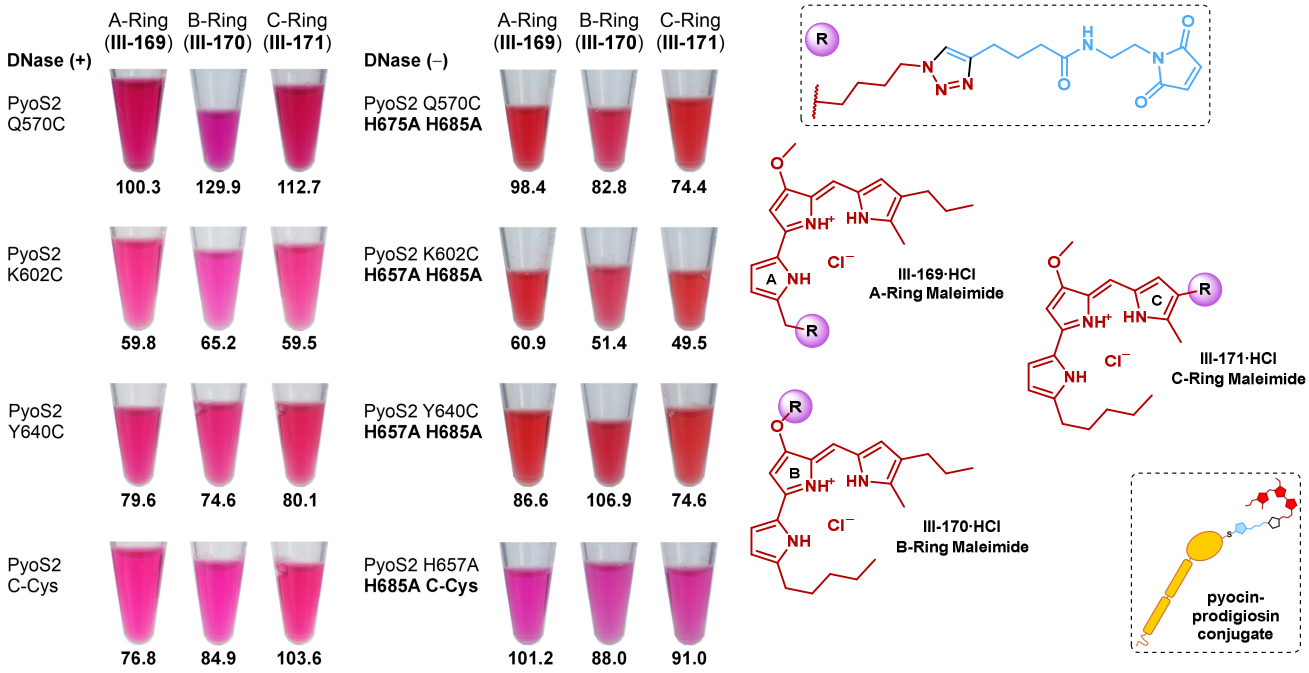


Figure IV.39. Protein conjugates of the bacterial protein toxin PyoS2 of *P. aeruginosa* with A-, B-, and C-ring prodigiosin maleimides **III-169·HCl**, **III-170·HCl**, and **III-171·HCl**, respectively. Pink protein solutions (in 25 mM Tris-HCl, 150 mM NaCl, pH 8) indicate labelling of the colourless wild-type protein with pink-purple prodigiosin maleimides. Numbers below the tubes represent protein concentrations (µM), determined with the Pierce 660 nm assay.

All prodiginine-labelled PyoS2 conjugates exhibited an intense bright-red to purple colour, a typical characteristic of the small-molecule prodiginine labels with absorption of visible light between 530 and 550 nm. Earlier in this work, quantification of unlabelled PyoS2 protein variants was achieved by UV quantification at 280 nm using the calculated molar extinction coefficients. However, spectroscopic characterisation of the maleimide-functionalised prodiginines (**III-169·HCl**, **III-170·HCl**, and **III-171·HCl**) revealed two major issues that would impede quantification of PyoS2-prodiginine conjugates by using this UV-based method.

At first glance, absorption spectra of the prodiginine maleimides **III-169·HCl**, **III-170·HCl**, and **III-171·HCl** in acidified ethanol suggested a relatively low absorbance at 280 nm in comparison to the absorption at the absorbance maximum. This relation would allow quantification of the protein moiety in PyoS2-prodiginine conjugates at 280 nm through correction of the absorption contributed by the attached prodiginine label at this wavelength, while the amount of conjugated prodiginine can be quantified at 530 nm. However, PyoS2, like many other proteins, is only soluble in aqueous buffers with a near-neutral pH and denatures in alcoholic solvents with very low pH. Moreover, the calculated molar extinction coefficient for PyoS2 (retrieved from Expasy) is only reliable for aqueous solvents, but is not applicable to the acidified ethanol used for prodiginine quantification. The hydrophobic prodiginines **III-169·HCl**, **III-170·HCl**, and **III-171·HCl**, in turn, are not soluble in aqueous solutions and their extinction coefficients are experimentally determined from ethanolic solutions at pH 1 to ensure full solvation and protonation of the basic alkaloid scaffold. These solvent and solubility limitations create an incompatibility of UV-based quantification of PyoS2 and prodiginines: while PyoS2 denatures in acidified ethanol, the prodiginines are not soluble in aqueous solutions and undergo a shift of maximum absorption through

protonation equilibria. Consequently, alternative methods are required to ensure accurate quantification of these PyoS2-prodiginine conjugates, facilitating their further antibacterial evaluation *in vivo*.

First, utilisation of an aqueous buffer system with 20% EtOH as a co-solvent was attempted to improve the solubility of prodiginines and maintain the correct folding of PyoS2 variants at the same time. Here, spectroscopic measurements showed that a co-solvent concentration of 20% EtOH was the highest allowable concentration that avoided solvent-induced denaturation of the protein (data not shown). Moreover, we noted a severe decrease in absorption for the three prodiginines **III-169·HCl**, **III-170·HCl**, and **III-171·HCl** at the absorption maximum, when the acidified solvent was replaced by the aqueous neutral pH buffer with 20% EtOH as a co-solvent (for spectra see Figure IX.14, for extinction coefficients see Table IX.12, Supporting Information). The strong solvent-dependence of optical properties is well-known for the colourful prodiginine alkaloids.[391] The hydrophobic nature of the alkaloid scaffold most likely causes aggregation into nanoparticles in water or aqueous solutions with low co-solvent concentrations, such as 20% EtOH, resulting in decreased absorption and a possible shift in the absorption spectrum. This aggregation distorts the molecular interactions responsible for visible light absorption and would explain the observed decline of visible light absorption at the absorption maximum in the aqueous buffer/EtOH solvent system. However, in pure polar-protic alcoholic solvents, such as acidified EtOH, prodiginines dissolve well, maintaining their chromophore in a proper monomeric structure and allowing for the full absorption of light in the visible range.

Concomitant with the decreased absorption at the absorption maximum at approximately 530 nm, the relative absorption at 280 nm was significantly elevated in the mixed solvent of buffer and 20% EtOH as co-solvent. The relative absorption between 280 nm and the absorption maximum ($Abs_{280}/Abs_{\lambda,max}$) is typically used to calculate correction factors. These are needed to correct the light absorption of the conjugate at 280 nm to solely quantify the protein-related absorption and subtract the portion contributed by the label. These correction factors typically range between 0.1–0.3. However, for the prodiginines **III-169·HCl**, **III-170·HCl**, and **III-171·HCl**, the high absorption at 280 nm in relation to strongly reduced absorption at the wavelength of maximum absorption would lead to correction factors of up to 0.48 in buffer with 20% EtOH as co-solvent (only up to 0.07 in acidified EtOH). Hence, those elevated correction factors would introduce high errors into the corrected protein absorption values at 280 nm and might in turn lead to erroneous protein quantification of PyoS2-prodiginine conjugates. In summary, neither of the two presented solvent systems (acidified EtOH or buffer with 20% EtOH co-solvent) is a suitable means to reliably quantify PyoS2-prodiginine conjugates via UV absorption measurements.

Based on the limitations encountered with UV-Vis-based methods for quantifying PyoS2-prodiginine conjugates, we opted for a colorimetric assay for protein quantification instead, relying on complex formation between the protein and the assay reagent. Here, the commercially available Pierce 660 nm assay was selected as the most suitable option, given that the detection wavelength for the protein-dye complex does not overlap with the absorption range of prodiginines. The Pierce 660 nm assay itself relies on a proprietary metal-dye complex that binds to proteins under acidic conditions. The formed metal dye-protein complex exhibits a shifted absorption maximum and enables quantification at 660 nm (prodiginine absorption <630 nm, cf. Figure IX.14, Supporting Information). According to the manufacturer, Pierce and UV quantification may substantially differ in regard to the amino acid constitution of the analysed protein. To assess the accuracy of the Pierce 660 nm assay for quantifying PyoS2, we first established a calibration curve using bovine serum albumin (BSA), with protein amounts determined by weight (Figure IV.40A). Next, we quantified a wild-type PyoS2 sample via UV_{280} absorbance and prepared a dilution series for Pierce 660 nm measurement (Figure IV.40B). The absorbance values from the Pierce assay of PyoS2 were then used to calculate PyoS2 concentrations based on the BSA calibration curve (cf.

Figure IV.40A). A strong correlation (R^2 = 0.992) was observed between the calculated PyoS2 concentrations and the expected values, indicating that the Pierce 660 nm assay provides reliable quantification for PyoS2 (Figure IV.40C). Hence, BSA and PyoS2 calibrations can both be used to reliably quantify the protein portion of PyoS2-prodigiosin conjugates.

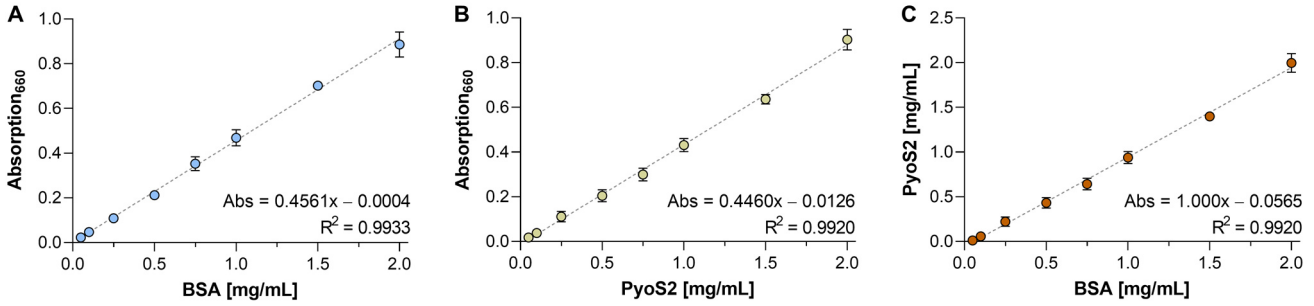


Figure IV.40. Calibration of the Pierce 660 nm assay with bovine serum albumin (BSA) and PyoS2. **A**. Linear fit of the measured absorption at 660 nm for a BSA calibration solution (determined by weight) after 5 min incubation with the assay reagent (n=3). **B**. Linear fit of the measured absorption at 660 nm for a PyoS2 calibration solution (determined based on the UV_{280} signal and the calculated molar extinction coefficient) (n=3). **C**. Correlation plot between the BSA concentration (determined by weight) and the PyoS2 concentration (calculated by application of the linear fit of the BSA calibration curve **A** to the individual experimental data points of PyoS2 absorption from curve **B**). The slope of 1.000±0.0192 represents the congruency of BSA and PyoS2 in Pierce 660 nm quantification and allows for the quantification of PyoS2 conjugates, based on a BSA calibration curve. Slopes and y-intercepts are given in the right corner of each diagram.

IV.3.13.2 PyoS2-Prodigiosin Conjugates Enter the Bacterial Cytoplasm, But Only Display DNase Activity

To assess whether PyoS2 conjugates are suitable to co-transport potential drugs concealed as “Trojan Horses” (other than the AlphaFluor dyes investigated in Chapter IV.3.8), all 24 PyoS2-prodigiosin conjugates (12 DNase-active and 12 DNase-inactive conjugates) were tested on the PyoS2-sensitive environmental *P. aeruginosa* isolate W15Dec1. As a reminder, W15Dec1 genomically encodes the pyoverdine type I siderophore receptor *fpvAI* and neither produces wild-type PyoS2 nor the cognate PyoS2 immunity protein ImS2 itself. The DNase-active conjugates with A-, B-, or C-ring attached prodiginine labels within the DNase domain (positions Q570C, K602C, Y640C, and C-Cys) were employed at first instance to probe for cellular import of the conjugates. As the DNase of PyoS2 is cleaved at the inner membrane by the protease FtsH from the N-terminal portion of the protein and is the only domain being translocated into the cytoplasm, the conjugates are co-transported into the cell. The DNase activity then allows for the cleavage of chromosomal DNA, inhibiting bacterial growth and leading to cell death. Therefore, zones of bacterial growth inhibition in a soft agar setup with immobilised cells of the *P. aeruginosa* strain certainly indicate successful uptake and import of the PyoS2 conjugates and their attached prodiginine labels via the conserved Ton-pathway.

The 12 DNase-active PyoS2-prodiginine conjugates all displayed cytotoxic activity and inhibited bacterial cell growth at a concentration of 10 µM (Figure IV.41). This marks successful translocation of the protein conjugates into the target cells, where they retained their cytotoxic DNase activity, overall demonstrating their ability to hijack the FpvAI receptor to cross the bacterial membrane system and to enter the cytoplasm of the target cell. These findings align with the observations of successful membrane translocation made for AlphaFluor conjugates of PyoS2 earlier in this work. The here described observations of PyoS2-prodiginine conjugate import were consistent regardless of the labelling site (Q570C, K602C, Y640C, or C-Cys) or the selected pyrrole moiety for

linker attachment on the prodiginine scaffold (A-, B-, or C-ring). Thus, this experiment demonstrates that the conjugation of small molecules to PyoS2 can be effectively utilised for their highly specific intracellular delivery into *P. aeruginosa*.

Next, our effort was directed to validating cytotoxicity related to the prodiginine payloads of the PyoS2-prodiginine conjugates. In previous studies, the soluble tripyrrole alkaloid prodigiosin (**III-1ab**) was shown not to possess any biological activity against *P. aeruginosa*.[802] Here, we hypothesised that the high impermeability of the *P. aeruginosa* membrane and active expulsion from the membrane via efflux pumps are the cause for prodigiosin insensitivity of the Gram-negative pathogen. This literature statement was verified by using the soluble prodigiosin **III-1ab** as a negative control, as no growth inhibition was observed for the treatment of strain W15Dec1 with the natural product.

After having confirmed that freely diffusible prodiginines do not show biological activity against *P. aeruginosa*, the DNase-inactive PyoS2-prodiginine conjugates were further evaluated. With the demonstrated evidence that the conjugates translocate across the cell membrane and enter the cytoplasm of the target cell, any observed cytotoxicity of the DNase-inactive PyoS2-prodiginine conjugates can be attributed solely to the delivered prodigiosin payloads. As the insensitivity of strain W15Dec1 to soluble prodigiosin **III-1ab** is assumed to be related to active repulsion from the membrane, thereby preventing the small-molecule alkaloid from membrane penetration, we hypothesised that PyoS2-coupled import of prodiginine cargo molecules could potentially overcome the cellular defence mechanisms of drug efflux and provoke a prodigiosin-sensitive phenotype of *P. aeruginosa*. In this regard, the treatment of strain W15Dec1 with the 12 DNase-inactive PyoS2-prodiginine conjugates did not lead to any cytotoxic activity, represented by unimpaired bacterial growth on the solid media. Even at a conjugate concentration of 10 µM, the DNase-inactive PyoS2-prodiginine conjugates with prodiginine labels did not show any sign of growth inhibition (Figure IV.41). In comparison, the MIC for wild-type PyoS2 treatment on the identical W15Dec1 strain was determined to be 370 nM (cf. Figure IV.36). Compiling the results of DNase-inactive conjugates, we finally conclude that the conjugated prodiginines have lost their cytotoxic activity upon conjugation to the PyoS2 carrier protein.

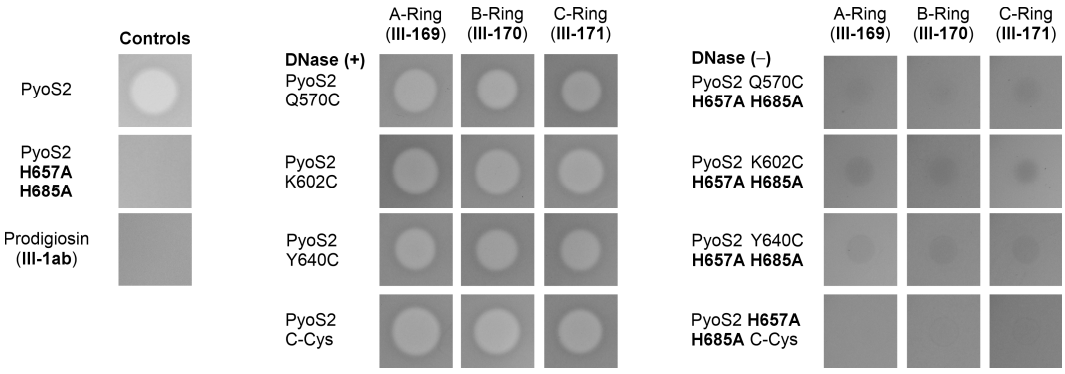


Figure IV.41. Cytotoxicity of PyoS2 conjugates with A-, B-, and C-ring prodiginine maleimides **III-169**, **III-170**, and **III-171** against *P. aeruginosa* W15Dec1. 10 µM protein solutions of DNase-active or DNase-inactive (H657A H685A double mutant) PyoS2-prodiginine conjugates were spotted onto immobilised cells of *P. aeruginosa* W15Dec1 in soft agar. Clear zones indicate bacterial growth inhibition through PyoS2 translocation and cytoplasmic DNA degradation, mediated by the DNase activity of PyoS2. Wild-type PyoS2 (DNase-active), PyoS2 H657A H685A (DNase-inactive), and prodigiosin (**III-1ab**) were used as controls.

To identify potential constraints that might hinder the cytotoxic activity of prodiginine payloads following bacterial cell entry, both components of the PyoS2-prodiginine conjugates should be critically evaluated.

Unlike eukaryotic drug conjugate systems, which often exploit active import mechanisms driven by drug conjugation to essential nutrients such as vitamins or metabolites to achieve high intracellular concentrations,[367, 804-807] pyocins operate via a fundamentally different mechanism. Pyocins hijack the conserved TonB-dependent transport machinery by mimicking siderophore binding to their respective receptors, which is why pyocins are not taken up deliberately to maintain sufficient nutrient supply. As a result, it is conceivable that only a small number of pyocin molecules successfully enter the target cell. Ultimately, even a single PyoS2 molecule may be sufficient to disrupt DNA metabolism and kill the cell. This phenomenon has parallels in *E. coli* colicins, where lethal "single-hit" events have been proposed since the 1960s.[674, 808, 809] While low intracellular concentrations of PyoS2 may still provoke death of the bacterial target cell by causing lethal DNA damage, low concentrations in the case of PyoS2-drug conjugates might be insufficient to unleash the cytotoxic activity of the conjugated drug.
Considering a picomolar to nanomolar intracellular concentration of pyocins or pyocin-small molecule conjugates – deduced from the nanomolar MIC of 370 nM of wild-type PyoS2 against strain W15Dec1 – implies that the conjugated drugs (here: prodigiosin) must be biologically active at an equal concentration range between picomolar and nanomolar scales to act as potent intracellular cytotoxic agents. However, this requirement poses a challenge, as prodiginines typically exhibit micromolar cytotoxicity. Previous studies have shown that soluble prodigiosin lacks bactericidal activity against *P. aeruginosa* and has MICs in the micromolar range for other bacteria, such as *S. aureus* (MIC: 3–6 µM).[802] Similarly, cycloprodigiosin demonstrated limited antibacterial activity against *E. coli* BL21(DE3),[302] suggesting that prodiginines are inherently insufficient for cytotoxicity at the low concentrations required for effective delivery via pyocins.

A key feature of prodiginines is their ability to freely diffuse across membranes. This property is needed to effectively disrupt membrane potentials via H^+ and Cl^- ion symport,[329, 330, 488, 810-812] the most contributing factor to cytotoxicity in living cells. However, this property of unhindered membrane diffusion is lost when prodiginines are covalently attached to PyoS2, a large, hydrophilic protein of 74 kDa that cannot passively diffuse or thread through bacterial membrane porins. Consequently, the covalent conjugation of prodiginines to PyoS2 likely eliminates the primary mechanisms driving prodiginine toxicity. Evidence from other studies investigating covalent prodigiosin conjugates performed by the group of Alison Thompson further supports this hypothesis.[367, 369, 370] Covalent prodiginine conjugates, such as tamoxifen-prodiginine and estradiol-prodiginine conjugates, targeting the ER receptor of ER-overexpressing breast cancer cell lines, showed low growth inhibition on ER-positive eukaryotic cell lines at 10 µM. For example, a 20% growth reduction was observed for the MCF-7 cell line after treatment with 10 µM tamoxifen-prodiginine conjugate, while growth promotion was spotted for ER-negative cell lines BT-549 and HS 578T. However, the ER-negative cell line MDA-MB-231 also displayed a strong response to the drug, which could not be explained by binding to the desired ER receptor, diminishing the overall argument of gained selectivity.[369] Previous works on similar cell lines but with soluble prodigiosin (**III-1ab**) have reported an IC_{50} of 1.10 µM and 1.14 µM against cell lines MCF-7 and MDA-MB-231, respectively.[813] Thereby, conjugation to tamoxifen and estradiol had significantly reduced the cytotoxic potency in comparison to free prodigiosin with a moderate gain in selectivity. These findings highlight the trade-off between conjugation and cytotoxic efficacy for the prodigiosin scaffold.

Other explanations regarding the lacking prodiginine-related cytotoxicity of PyoS2-prodiginine conjugates address accessibility of the conjugated drug for potential intracellular targets. As mentioned earlier, the major biological target of prodiginines is the lipid bilayer and its depolarisation. However, additional intracellular targets of prodiginine alkaloids have already been described for eukaryotic and prokaryotic cell lines.[258, 259, 327, 814] In the prokaryotic context, Danevčič *et al.* observed an inhibition of RNA and protein biosynthesis in *E. coli* upon prodigiosin treatment, which could be linked to limited availability of energy in the form of ATP, caused by loss of

the proton gradient and inhibition of bacterial F-type ATPase activity.[329, 814] Hence, the vast number of readily identified cellular targets of prodigiosin or closely related prodiginine alkaloids suggests that additional, as yet unknown, cellular structures or mechanisms may be targeted by prodigiosin.
In this regard, a proper interaction and unimpaired binding between prodigiosin and the unidentified target are inevitable to unfold the cytotoxic potential. As prodigiosin is a hydrophobic/lipophilic tripyrrole alkaloid, it may be hypothesised that site-specific interactions with potential targets are mainly driven by hydrophobic interactions. However, the conjugation of the hydrophobic prodiginine scaffold to our hydrophilic protein carrier PyoS2 indeed increased the water solubility of the conjugates, but it might also negatively affect binding to cellular target structures through steric or polar repulsion between the target and the carrier protein. As the small prodiginine labels have a rough size estimation of ~700 Da, which equals approximately 1% of the protein mass of PyoS2 with 74 kDa, the global polarity of the large hydrophilic protein will also vastly alter the microenvironment of the small hydrophobic prodiginine label and thereby affect its interaction with other molecules.
In contrast to our introduced PyoS2-prodigiosin conjugates, the small-molecule conjugates presented by Marchal *et al*. between the hydrophobic carrier molecules tamoxifen- or estradiol and prodigiosin (cf. Scheme III.12) supposedly retain the hydrophobic properties of the conjugated prodiginine payload, thereby facilitating hydrophobic interactions with its putative cellular targets. Nonetheless, the opportunity of changing the drug's polarity through conjugation to the hydrophilic PyoS2 protein might be a reasonable feature of future PyoS2-drug conjugates, especially for those payloads which scarcely enter the target cell by passive mechanisms.

Resulting from the hypothesised obstructed binding of PyoS2-conjugated prodiginines to putative targets, we furthermore infer that a cleavable linker for cytoplasmic drug release could enhance the biological activity of the conjugated prodiginines while maintaining enrichment of the drug in cells of *P. aeruginosa*, mediated by the PyoS2 carrier. The triazole linker exploited in this work was purposely designed to be non-cleavable (insensitive towards pH changes or enzymatic hydrolysis), as the generation of freely diffusible prodiginines upon cleavage was hypothesised initially to counteract the aim of gaining target selectivity through conjugation of prodigiosin to PyoS2. This is because once prodiginines are released from the carrier, their unhindered passive diffusion across the membrane boundaries of cells would also affect other bacterial or eukaryotic cells nearby and consequently liquidate the gained target selectivity through PyoS2 conjugation. However, our results clearly show that conjugation of prodiginines to PyoS2 is accompanied by the loss of their biological activity, which means a local drug release mechanism will be needed to unleash the biological activity of the conjugated payload. By using other non-diffusible and more potent drugs for conjugation to PyoS2 in the future, intracellular release of the payload could potentially multiply the cytotoxicity while maintaining high target selectivity through PyoS2-mediated enrichment of the drug in cells of *P. aeruginosa*.
The systematically studied class of ADCs harbours numerous examples of drug payloads, for which cleavable linkers are essentially needed to activate the drug. However, the conjugated drug in general dictates whether it tolerates non-cleavable linkers or whether it loses its cytotoxic potential upon conjugation. A prominent example where linker cleavability is an essential prerequisite for cytotoxicity is the ADC payload MMAE (cf. Scheme II.5), a highly potent antimitotic agent that inhibits cell division in eukaryotic cells through inhibiting tubulin polymerisation. Due to its high cytotoxicity and unselective targeting mechanism, MMAE can not be used as a drug on its own, but ADCs with non-cleavable MMAE payloads lose their cytotoxic potential as a consequence of covalent attachment. Only in conjunction with a protease-cleavable peptide linker, antibody-MMAE conjugates show exceptional and selective killing activity against cancer cell lines upon antibody degradation and drug release by lysosomal acid proteases.[46, 462] By comparing the organisation of eukaryotic cells targeted by ADCs with the organisation of a prokaryotic cell targeted by PyoS2 conjugates, the lack of compartmentalisation of bacterial cells is one of the most striking differences. Hence, the common mechanism of ADC internalisation and

drug release via lysosomal fusion and proteolytic degradation of the antibody is not applicable in bacteria. Although S-type pyocins are, in principle, protease-sensitive and only the C-terminal cytotoxic domain is imported into the cytoplasm after FtsH cleavage at the inner membrane,[727] the DNase remains fully intact after its translocation into the cytoplasm and is not further dismantled by proteolytic degradation. Consequently, in PyoS2-drug conjugates, the drug access might remain essentially obstructed by the remains of PyoS2 in the form of a folded DNase domain and would therefore require active drug release from the protein carrier by means of a cleavable linker to make use of the drug's cytotoxic activity.

A couple of cleavable linker structures have been specifically designed for the application in bacteria. Boyce *et al*. devised a modified phage display, by which the identification of protease-cleavable linkers was possible in high throughput. One important requirement was the identification of periplasmic protease-cleavable linkers, as the researchers aimed for the application of siderophore-drug conjugates and their specific release in the bacterial periplasmic space.[497] The most potent identified peptide linker was finally applied to deliver and release the cyclic lipopeptide antibiotic daptomycin in active form into MDR and pathogenic *Acinetobacter* species, achieving biological activity of daptomycin on Gram-negative bacteria for the first time (MIC: 1–5 μM). The newly acquired cytotoxicity against Gram-negative pathogens was rated a striking success, particularly since unconjugated daptomycin is ineffective against Gram-negative bacteria (MIC >39 μM) and is only active on Gram-positive bacteria.

Another example of protease-cleavable linkers specifically designed for antibacterial applications showcases the beneficial effect of drug release on antibacterial activity against MDR *E. coli*. Wang *et al*. generated a chimeric protein (termed R7) between the human LPS-binding protein LBP14 and the toxic peptide L7.[815] Both domains were finally connected through a furin-cleavable linker – furin is a surface-exposed eukaryotic protease – with the RKRR peptide sequence for on-site release of both domains to enhance the toxic effect of the L7 domain and enable effective LPS neutralisation through the LBP14 domain. Besides stabilising effects on both domains, the conjugation via protease-cleavable linker was also found to increase antibacterial activity in comparison to LBP14 or L7 alone (2–4-fold increase). Lastly, the application of conjugate R7 in a mouse model infected with MDR *E. coli* was shown to significantly increase the survival of the treated group (100% survival for >7 days), while the control group had died after 2 days.

Both presented studies (siderophore-daptomycin conjugates and conjugate R7) using protease-cleavable linkers to release and enhance the effectiveness of antimicrobial agents highlight the value of cleavable linkers for the target-specific delivery of drugs to bacterial pathogens. However, neither strategy is compatible with our introduced PyoS2-drug conjugates, as they rely on proteases that trigger premature drug release on the cell surface or in the bacterial periplasm. Since PyoS2-prodiginine conjugates rely on the delivery of the prodiginine payload into the bacterial cytoplasm, adapted linker structures would be needed, which remain intact in the periplasm or the extracellular environment but are selectively cleaved in the cytoplasm of the target cell. Such linkers were used by Neumann *et al*. to couple the release of fluoroquinolone antibiotics from a siderophore carrier to the redox potential of the cellular compartments.[816] The extracellular environment and the bacterial periplasm are both oxidative, while the bacterial cytoplasm is reductive. By harnessing a self-immolative disulfide linker that is expected to be stable under oxidative conditions but undergoes glutathione-assisted reductive cleavage under reducing conditions, the researchers aimed to selectively trigger drug release upon reaching the cytoplasm of the target cell. Lastly, the conjugates between the fluoroquinolone antibiotic ciprofloxacin and the tricatecholate siderophore enterobactin exhibited only limited antibacterial activity against *E. coli*, which is why the authors of

this study concluded that disulfide linkers – despite distinctive advantages in preventing premature release of the payload –may not be generally applicable to conjugate and release bioactive antibiotics.

Many more strategies have been developed in recent years,[495, 667, 817, 818] unravelling the potential mechanisms of drug release from protein- or siderophore-drug conjugates in pathogenic or MDR bacteria to address the rising concern of widespread antibiotic resistance. In this regard, we could show for the first time that the antimicrobial protein PyoS2 from the opportunistic human pathogen *P. aeruginosa* is an effective vector to selectively deliver small-molecule effectors into the bacterial cell. Exemplified by PyoS2-AlphaFluor dye conjugates and PyoS2-prodiginine conjugates, the protein carrier from the family of S-type pyocins has proven reliable in the highly strain-specific cytoplasmic delivery of the conjugated payloads via the conserved Ton-pathway. This approach holds great potential for transporting additional toxic molecules with enhanced antimicrobial activity into cells in the future, offering alternative treatment strategies to counter the growing global threat of antimicrobial resistance.

IV.4 Summary Chapter IV – Conjugates of Pyocin S2 Target MDR Isolates of *P. aeruginosa*

Chapter IV of this work focused on the investigation of the antimicrobial protein pyocin S2 from the opportunistic human pathogen *Pseudomonas aeruginosa*, aiming to probe for current restraints limiting a broader application as an antimicrobial agent and to mitigate these limitations to develop PyoS2 as an alternative to established antibiotics. The increasing bacterial resistance to conventional antibiotics, including last-resort broad-spectrum antibiotics from the carbapenem class, renders *P. aeruginosa* a difficult-to-treat pathogen and generally makes antibiotic resistance a rapidly growing threat to global health and prosperity. Due to their narrow spectrum of activity and high host specificity, bacteriocins of Gram-negative pathogens, exemplified here by the DNase pyocin PyoS2, are a widely discussed but poorly explored alternative for treating severe infections caused by antibiotic-resistant bacteria. Particularly, the widespread distribution of cognate immunity proteins, naturally protecting pyocin-producing strains from the cytotoxic action of the toxin, poses a challenge to a broader application of these natural antimicrobial proteins. As immunity protein expression and ultra-high-affinity binding to the bacteriocin render the toxins inactive, the natural distribution of immunity proteins drastically limits the number of bacteriocin-sensitive strains. Hence, overcoming this primary pyocin-resistance mechanism of immunity protein binding is one of the major hurdles towards broadly applicable and highly potent pyocin antimicrobials for treating severe nosocomial infections with MDR *P. aeruginosa*. Therefore, this thesis aimed not only to probe the current limitations of wild-type PyoS2 as an antimicrobial agent against clinically relevant *P. aeruginosa* strains, but also to engineer PyoS2 variants that are insensitive to ImS2 binding.

This engineering strategy was advanced by analysing the immunity protein exosite (IPE) of PyoS2 (binding inferface between PyoS2 and ImS2, critical region for ultra-high-affinity binding) and the identification of a central tyrosine residue in position 640 of loop 4 within the DNase domain of PyoS2 (Figure IV.42B). This Y640 residue interacts with ImS2 residues H34, I35, and Y56, located in helix II of ImS2, through hydrogen bonds and hydrophobic side chain interactions and is additionally involved in the complexation of conserved interstitial water molecules at the PyoS2/ImS2 interface (cf. Chapter IV.3.1.1). Hence, it was hypothesised that substitution of this Y640 residue through an unlike smaller amino acid could potentially weaken the ultra-high-affinity binding of PyoS2 to ImS2, thereby rendering the natural mechanism of PyoS2 resistance ineffective. To investigate the effects of interface engineering, cysteine residues were introduced into the DNase domain of PyoS2 from *P. aeruginosa* PAO1 via site-directed mutagenesis. However, of four selected residues, namely Q570, K602, Y640, and the C-terminus, only Y640 is located at the PyoS2/ImS2 interface within PyoS2's IPE. Subsequently, the wild-type S-type pyocin PyoS2, its natural immunity protein ImS2, and the cysteine mutants of PyoS2 were heterologously expressed in *E. coli* and purified for further *in vitro* and *in vivo* studies (cf. Chapter IV.3.2 and Chapter IV.3.4.1). Additional post-translational *in vitro* labelling of the cysteine residues with thiol-reactive non-toxic C_5-maleimide-functionalised AlphaFluor fluorophores (AlF350, AlF488, and AlF594) was performed to not only add small-molecule cargos to the DNase domain but also increase the structural mismatch between the IPE of PyoS2 and the immunity protein ImS2 (cf. Chapter IV.3.4).

Initial *in vivo* experiments with the PyoS2-sensitive environmental isolate *P. aeruginosa* W15Dec1 and the PyoS2-resistant producer strain *P. aeruginosa* PAO1 – both presenting the FpvAI siderophore receptor at their outer membrane, which PyoS2 hijacks for translocation across the membrane – demonstrated that fluorophore labelling distant from the PyoS2/ImS2 interface at positions Q570C, K602C, and C-Cys (C-terminal) did not affect the antimicrobial spectrum of the conjugates or their TonB-dependent import mechanism (cf. Chapter IV.3.8). Consequently, these AlF-conjugates exhibited an identical antimicrobial spectrum as wild-type PyoS2, retaining biological activity against strain W15Dec1 but not against PAO1(Figure IV.42A), which neutralises PyoS2 through non-competitive binding by its cognate immunity protein ImS2. Strikingly, the PyoS2 mutant Y640C and its AlF

conjugates displayed antimicrobial activity against both strains, the PyoS2-sensitive strain W15Dec and the PyoS2-resistant strain PAO1. With residue Y640 lying right in the centre of PyoS2's IPE (Figure IV.42B), it was hypothesised that this particular mutation disrupts the association of the stochiometric protein complex. This impairment likely compromised the protection of cellular DNA from degradation by PyoS2-AIF conjugates. Further *in vitro* analyses of DNase activity confirmed that the presence of ImS2 efficiently neutralised all conjugates (Q570C, K602C, and C-Cys in conjunction with AIF488) except for the Y640C-AIF conjugates, which retained detectable DNase activity despite the presence of ImS2 (Figure IV.42C, cf. Chapter IV.3.7). This property explains the observed susceptibility of the inherently PyoS2-resistant PAO1 strain towards PyoS2 Y640C and its fluorophore-labelled AIF conjugates. Additionally, substituting the aromatic side chain at Y640 was associated with a reduction in the structural stability of the adjacent DNase residue K652 needed for stabilising interaction with the backbone of the DNA substrate, culminating in diminished DNase activity. However, stabilisation was partially recovered and compensated for by introducing the non-aromatic maleimide moiety during AIF conjugation via thiol-maleimide chemistry (cf. Chapter IV.3.5).
Since the widespread ImS2-mediated natural resistance to PyoS2 significantly limits its broad application against *P. aeruginosa* infections, this first demonstration of overcoming the hereditary protective mechanism represents a major milestone in advancing bacteriocins from Gram-negative bacteria as viable therapeutic agents. Remarkably, this profound effect was achieved by the targeted substitution of a single critical amino acid at the structurally conserved toxin-immunity protein interface (cf. Figure IV.42B). Moreover, the *in vivo* data impressively underline for the first time that the active TonB-dependent import mechanism of PyoS2 can be exploited to import small-molecule cargo into cells of *P. aeruginosa* and thereby bypass the protective efflux mechanisms, rendering the membrane of *P. aeruginosa* highly impermeable for drugs. This co-transport and the coupling of drug import to the TonB-pathway hold great potential for target-selective delivery of potential drugs into MDR strains of *P. aeruginosa*.

To further assess the therapeutic value of this engineering strategy of the PyoS2/ImS2 interface to obliterate the immunity protein-dependent resistance mechanisms of bacteriocins, a collection of 113 highly virulent and carbapenem-resistant *P. aeruginosa* isolates from the University Hospital Düsseldorf was investigated (cf. Chapter IV.3.10). First, the collection was analysed via multiplex PCR to determine the prevalence of the *fpvAI* genotype. The TonB-dependent siderophore receptor FpvAI in the OM serves as a receptor and translocator of PyoS2 and is hijacked by the bacteriocin to enter the target cell. Of the three *fpvA* siderovar types found in *P. aeruginosa* (*fpvAI*, *fpvAII,* and *fpvAIII*), only the *fpvAI* subtype serves as a receptor for PyoS2, making strains of this type the primary candidates for phenotypic testing with PyoS2 and protein derivatives thereof. In this specific strain collection, a total of 15 strains (13.3%) were classified as belonging to the *fpvAI* siderovar. Of these, 8 strains encoded the genomic tandem *pyoS2_imS2*, rendering them genotypically resistant to PyoS2 and its DNA-targeting nuclease activity. Phenotypic characterisation with purified protein revealed that only 3 of the 15 *fpvAI* strains – of which 7 are genotypically PyoS2-sensitive – were actually susceptible to wild-type PyoS2 (20%), suggesting the existence of an additional ImS2-independent resistance mechanism in 4 of the genotypically sensitive isolates (cf. Chapter IV.3.11). In contrast, the conjugate PyoS2 Y640C-AIF488 with a broadened antimicrobial spectrum exhibited activity against 11 of 15 strains (73.3%), remarkably including all 8 genotypically PyoS2-resistant strains. Hence, the novel PyoS2 Y640C-AIF conjugate with engineered PyoS2/ImS2 interface effectively abolished ImS2-dependent resistance to PyoS2 even in those strains, where conventional β-lactam antibiotics failed due to the expression of carbapenemase genes.

A comprehensive genome analysis of all 15 *fpvAI* siderovar isolates through Whole-Genome Sequencing supported the hypothesis that the persistent secondary (ImS2-independent) resistance to PyoS2 in the 4

genotypically PyoS2-sensitive isolates is linked to defective synthesis of the D-rhamnose homopolymer common polysaccharide antigens (CPA) (Figure IV.42D, cf. Chapter IV.3.12.2). CPA acts as a secondary receptor for S-type pyocins on the cell surface, with their binding mediated by a dedicated domain within the tandemly repeated kinked three-helix bundle of PyoS2. Identified defects were attributed to mutations in the D-rhamnose

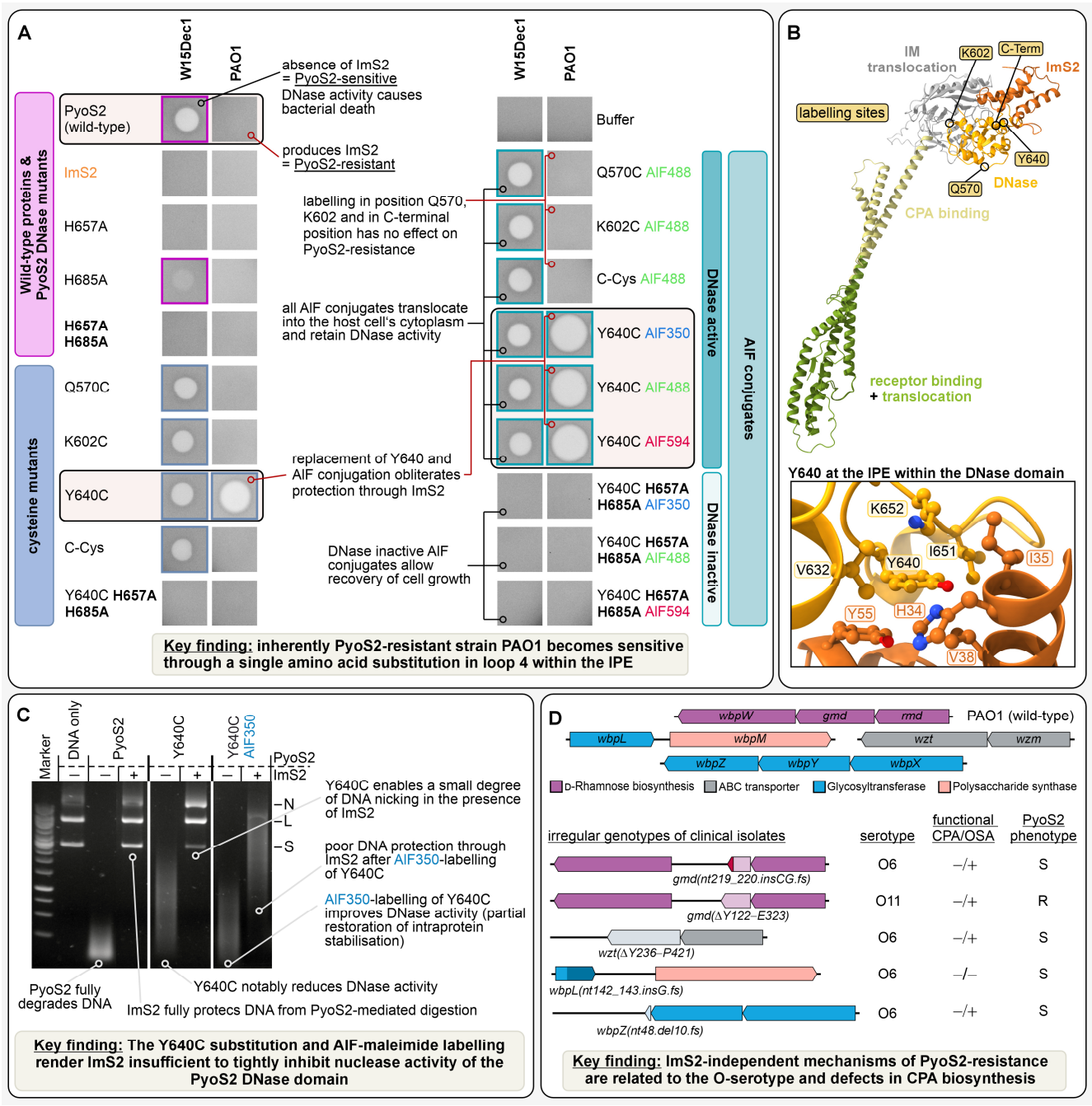


Figure IV.42. Overview of key findings of this pyocin S2-related Chapter IV. **A**. Cell killing assay of PyoS2 and its AIF-labelled conjugates with the PyoS2-sensitive environmental isolate *P. aeruginosa* W15Dec1 and the PyoS2-resistant strain *P. aeruginosa* PAO1. Both strains encode the PyoS2 receptor FpvAI. Clear zones indicate bacterial growth inhibition. **B**. Predicted protein structure of PyoS2 with highlighted domains and selected labelling sites. The zoomed-in excerpt visualises the atomic environment of Y640, located in the centre of the immunity protein exosite of PyoS2. **C**. Plasmid nicking assay (excerpt) after 15 h of incubation with various PyoS2 variants. Plasmid DNA species (N – nicked, L – linear, S – supercoiled) are separated in an agarose gel. **D**. Immunity protein-independent PyoS2-resistance of CRPsA clinical isolates is caused by defects in the CPA biosynthesis and serotype-dependent.

biosynthesis gene *gmd*, in the Wzt ATPase domain of the CPA-ABC transporter (Wzm/Wzt), or in the glycosyltransferase genes *wbpZ* and *wbpL*, all leading to nonsense and frame-shift mutations that cause premature translation termination and render those loci inactive pseudogenes. Moreover, strong evidence was found for a protective role of the O-serotype (cf. Chapter IV.3.12.2.3). In isolates of the O11 serotype, nonsense mutations in the *gmd* locus conferred complete resistance to PyoS2 and its conjugates (MIC >10 µM), even in the absence of ImS2. In contrast, similar mutations in O6 serotype strains only reduced cytotoxicity but did not abolish the killing activity of PyoS2 conjugates. A concurrent defect in the glycosyltransferase *wbpL* locus, involved in the biosynthesis of both O-antigen and CPA, restored PyoS2 activity. This suggests that the O-antigen provides an additional protective effect for the outer membrane, which CPA-binding circumvents during pyocin translocation into target cells.

In summary, this work demonstrated that disrupting the stoichiometric PyoS2/ImS2 complex, which has femtomolar binding affinity, can be achieved through a single mutation within the IPE of PyoS2, enhanced by *in vitro* labelling using bulky non-toxic small molecules. This proof of principle for the corrupt immunity protein binding provided in this thesis can be leveraged to broaden the natural activity spectrum of pyocins, provided that a corresponding immunity protein conferred hereditary resistance to the respective wild-type pyocin. Although this study focused on PyoS2, a pyocin targeting the FpvAI siderophore receptor with a naturally limited distribution among *P. aeruginosa*, the developed concept is highly likely to be transferable to other nuclease pyocins with ubiquitous outer membrane receptors. Furthermore, PyoS2 was successfully established as a vector for transporting small-molecule cargos (fluorophores and prodiginines) into live cells of *P. aeruginosa*, bypassing the impermeable cell membrane as a defensive barrier against antimicrobial agents. By exploiting the conserved mechanism of Ton-mediated pyocin import and the uncovered principle of corrupt binding between pyocins and their cognate immunity proteins, the application potential of these narrow-spectrum antimicrobial peptides as drug vectors and as alternatives to common antibiotics is drastically expanded. While this work exclusively focused on the opportunistic human pathogen *P. aeruginosa*, the principle of corrupt immunity protein binding may be even more effectively applied to other Gram-negative human pathogens (e.g. *E. coli*, *K. pneumoniae*), as the CPA biosynthesis trait and its associated binding domain are unique to *P. aeruginosa* and its pyocins. Collectively, this work launched advanced strategies that might challenge the general concept of innate bacterial immunity to bacteriocins through the expression of cognate immunity proteins, thereby providing highly selective antimicrobial agents with extended spectrum as novel therapeutic solutions against Gram-negative pathogens amidst the global antimicrobial resistance crisis.

IV.5 Outlook Chapter IV

This original work achieved several milestones in streamlining bacteriocins from Gram-negative bacteria – exemplified here by the S-type HNH DNase pyocin S2 from the opportunistic human pathogen *Pseudomonas aeruginosa* PAO1 – as promising antimicrobial agents for therapeutic applications. Through a combination of rational protein engineering and bioorthogonal click chemistry, PyoS2 variants were generated that are no longer inhibited by their cognate immunity protein, ImS2, and exhibit potent killing activity against clinical strains that are inherently resistant to wild-type PyoS2 and to last-resort carbapenem antibiotics (CRPsA). Furthermore, this study demonstrated that the conserved Ton-dependent import mechanism of PyoS2 can be exploited to deliver small-molecule cargo into *P. aeruginosa* cells, circumventing the pathogen's natural mechanisms of drug efflux, rendering the bacterial membrane impermeable to drugs. Collectively, the newly introduced strategy of corrupt immunity protein binding and the use of PyoS2 as a drug delivery vector have the potential to reshape our understanding of bacteriocin immunity and to overcome current limitations that hinder the clinical application of Gram-negative bacteriocins as alternatives to conventional antibiotics in the face of the growing antimicrobial resistance crisis. The following chapter highlights open research questions and future perspectives, and devises strategies to develop bacteriocins and their conjugates as advanced tools in the fight against the global threat of widespread antimicrobial resistance and avert a post-antibiotic era.

IV.5.1 Characterisation of O-Serotypes and Isolation of LPS to Verify Malfunctions in OSA and CPA Biosynthesis and Overcome Secondary Pyocin Resistance

In this work, Whole-Genome Sequencing (WGS) was applied to investigate the genomic background of MDR clinical *P. aeruginosa* isolates and to correlate genomic features with the observed ImS2-independent resistance of certain strains to treatment with wild-type PyoS2 and its Y640C conjugates with extended antimicrobial spectrum. WGS of all 17 *P. aeruginosa* strains from the core strain collection, sharing the *fpvAI* genotype, revealed defects in the OSA and CPA biosynthesis of strain M2 (hypersusceptible to treatment with the PyoS2 Y640C variants) and defects in the CPA biosynthesis of 8 further strains (M10, M71, M189, M191, M210, M294, M315, and M324) on the genomic level. Based on these results, it was hypothesised that the O-serotype might influence the ImS2-independent resistance to treatment with PyoS2, hence the specific type of LPS modification on the cell surface. And indeed, the *in silico* analysis of serotypes and subsequent clustering of all strains from the core strain collection of *fpvAI*-positive strains (serotype vs. minimal inhibitory concentration) suggested a strong correlation between the serotype and susceptibility to treatment with PyoS2 and its conjugates. Although the bioinformatically predicted absence of the secondary PyoS2 receptor CPA was accompanied by an effective shielding of the bacterial membrane in strains of the O11 serotype, the O6 serotype marginally influenced the susceptibility to PyoS2 treatment in the absence of CPA. Nonetheless, the bioinformatic predictions suggesting dysfunctional biosynthesis of OSA and CPA, and a lack of both antigens on the cell surface in strains with persistent ImS2-independent PyoS2 resistance, still require experimental validation.

Future studies could provide experimental evidence for the O-serotype-dependent translocation of pyocins through the isolation of lipopolysaccharide (LPS) fractions from strains with diverging pyocin sensitivity. LPS isolation is a straightforward procedure, including removal of cellular proteins – via heat-assisted denaturation and protease degradation – and extraction of the lipopolysaccharide from the membrane fraction with a hot solution of phenol-chloroform. A consecutive charge- and size-dependent separation of heterogeneous LPS species (CPA and different LPS isoforms with varying OSA chain length) via SDS-PAGE allows for the visualisation of variance in LPS constitution, altered polysaccharide chain lengths, and changes within the LPS core. Combined with untargeted silver staining and monoclonal antibodies with high selectivity for certain LPS

epitopes, defects in LPS and CPA biosynthesis can be mapped.[787, 819, 820] Even though the genetic analysis of currently assigned OSA and CPA biosynthesis genes in all *fpvAI* strains did not reveal any other peculiarities than the mutations in *wzt*, *gmd*, *wbpZ*, and *wbpL*, we still observed diverging phenotypes and MICs within the O6 and O11 serogroups upon treatment with extended-spectrum PyoS2 variants (cf. Figure IV.36). Therefore, we assume that further uncharacterised alterations in the LPS core structure or the OSA could contribute to the observed patterns of pyocin resistance and susceptibility. Moreover, experimental serotyping of these isolates will be needed to confirm the supposed O-serogroups derived from bioinformatic analysis of the OSA clusters with the PAst web tool.

By fully understanding the mechanisms of secondary and immunity protein-independent pyocin resistance through alterations of the bacterial membrane, we might be able to develop strategies to prevent these microbes from evading the bactericidal activity of pyocins. These strategies might, for example, involve engineering of pyocins to increase the affinity towards the primary OM receptor, the rational design of OSA-binding domains instead of the CPA-binding domain within the cytotoxic domain of S-type pyocins, or a combinatorial treatment of pyocins and OSA-specific glycosidases to cut back the membrane shielding polysaccharide for enhanced binding of pyocins to their primary receptors in the outer membrane.
To find suitable proteins that can be engineered to OSA-specific glycosidases or might be eligible as OSA-binding domains for enhanced binding of pyocins to specific serotypes, the eukaryotic immune system and bacteriophages are a rich source of inspiration. For example, LPS-binding proteins (OSA and CPA are both LPS species) are part of the human immune system to defend the organism against bacterial predators and neutralise the virulence factor LPS.[821] Even more diverse structures capable of interacting with bacterial LPS can be found in the domain of bacteriophages. Phages have evolved their tail fibres to bind bacterial LPS as a primary receptor at the onset of the viral replication cycle, but also non-replicative phage-derived tailocins, such as R- and F-type pyocins, share this property.[684, 770] Besides binding to the cell surface-exposed LPS, bacteriophage tail fibres may additionally possess OSA-specific glycosidase or lyase activity that is used to trim down the cell surface polysaccharide and strengthen the viral attachment to the host cell.[822] One such enzyme (LKA1gp49) has been found recently in the tail spike of the *P. aeruginosa*-specific phage LKA1, degrading the O5-specific polysaccharide through lyase activity.[823] This strategy could also be adapted to enhance cellular binding of pyocins and minimise the immunity protein-independent resistance to pyocins in those serotypes with dense LPS packing (e.g. serotype O11).

Taken together, the transfer of nature-derived LPS binding motifs into pyocins and the generation of chimeric pyocins with altered affinity towards the bacterial membrane and its lipopolysaccharide modifications might be one of the vital strategies to further broaden the innate activity spectrum of pyocins within the species of *P. aeruginosa* in the future.

IV.5.2 Transfer of Impaired Toxin/Immunity Association to Other Pyocins and Bacteriocins of Gram-Negative Bacteria

Although nuclease bacteriocins share an outstandingly high structural conservation of nuclease fold and their interaction with their cognate immunity proteins, their sequence conservation, particularly within the IPE, is rather low (Figure IV.43, E and F). After finding out about the pivotal role and the functional importance of tyrosine Y640 for the establishment of the ultra-high-affinity association with the cognate immunity ImS2 (Figure IV.43A), we immediately asked ourselves whether this knowledge is transferrable to other HNH DNase bacteriocins (Figure IV.43, B–D). A simple multiple sequence alignment of eleven representative HNH DNase domains from colicin, klebicins, and pyocins reveals that the tyrosine residue found in PyoS2 is part of a motif with low sequence

conservation (only in PyoS1, PyoS2, and PyoAP41 the residue is tyrosine) and the residues found at this particular position vary among different toxins (Figure IV.43E). Other residues in equivalent positions are phenylalanine (PyoS8, PyoSX1, ColE2, ColE9), threonine (KlebB, Kleb2), valine (PyoS9), and lysine (ColE7). Since these central residues of the immunity protein exosite are not only different in size but also in charge and polarity, intraprotein contacts within the DNase and interprotein contacts between toxin and cognate immunity proteins must be adapted accordingly to maintain nuclease activity and enable ultra-high-affinity binding between toxins and their immunity proteins (cf. Figure IV.43E). While the overall protein sequence conservation of amino acid residues contributing to the immunity protein exosite is relatively poor, the mechanistically essential residues for metal complexation and DNA hydrolysis are conserved without exception.

To gain deeper insights into the stabilising intraprotein contacts between Y640 of PyoS2 and other residues from the PyoS2 DNase domain, as well as its interprotein interactions with the immunity protein ImS2, the crystal structure of the PyoS2/ImS2 complex (PDB 4QKO) was thoroughly analysed to map the network of interacting amino acids. Furthermore, this network was compared with other structural models of DNase/immunity complexes, focusing on the following DNases: colicin E2 (central residue F533, PDB 3U43[824]), colicin E7 (central residue K528, PDB 7CEI[825]), and pyocin AP41 (central residue Y722, PDB 4UHP). The comparative analysis revealed that it is not the protein sequence and the particular type of interactions (hydrophobic, polar, ionic, etc.) that are conserved within the network. Instead, the structural conservation is exceptionally high, meaning the absolute position of residues and their geometrical alignment relative to each other (Figure IV.43E and IV.43G). Based on the uncovered high degree of structural conservation of the immunity protein exosite among the investigated HNH nuclease bacteriocins, it is possible to predict which amino acids are essential for ultra-high-affinity binding of cognate immunity proteins from the primary amino acid sequence of both interaction partners, namely bacteriocins and immunity proteins.

Taking the destructive effect of the single amino acid substitution Y640C of PyoS2 on ImS2-binding into account, we hypothesise that single point mutations and small molecule conjugation in the central position of other HNH nuclease bacteriocins will trigger equivalent effects. These will result in the corrupted binding of cognate immunity proteins in the first place and will enable antimicrobial activity against those strains producing the cognate immunity. This conclusion is of great importance, as this novel kind of bacteriocin conjugates could entirely obliterate primary (immunity protein-associated) resistance to nuclease bacteriocins and redefine the antimicrobial spectrum of these toxins and their therapeutic application potential.

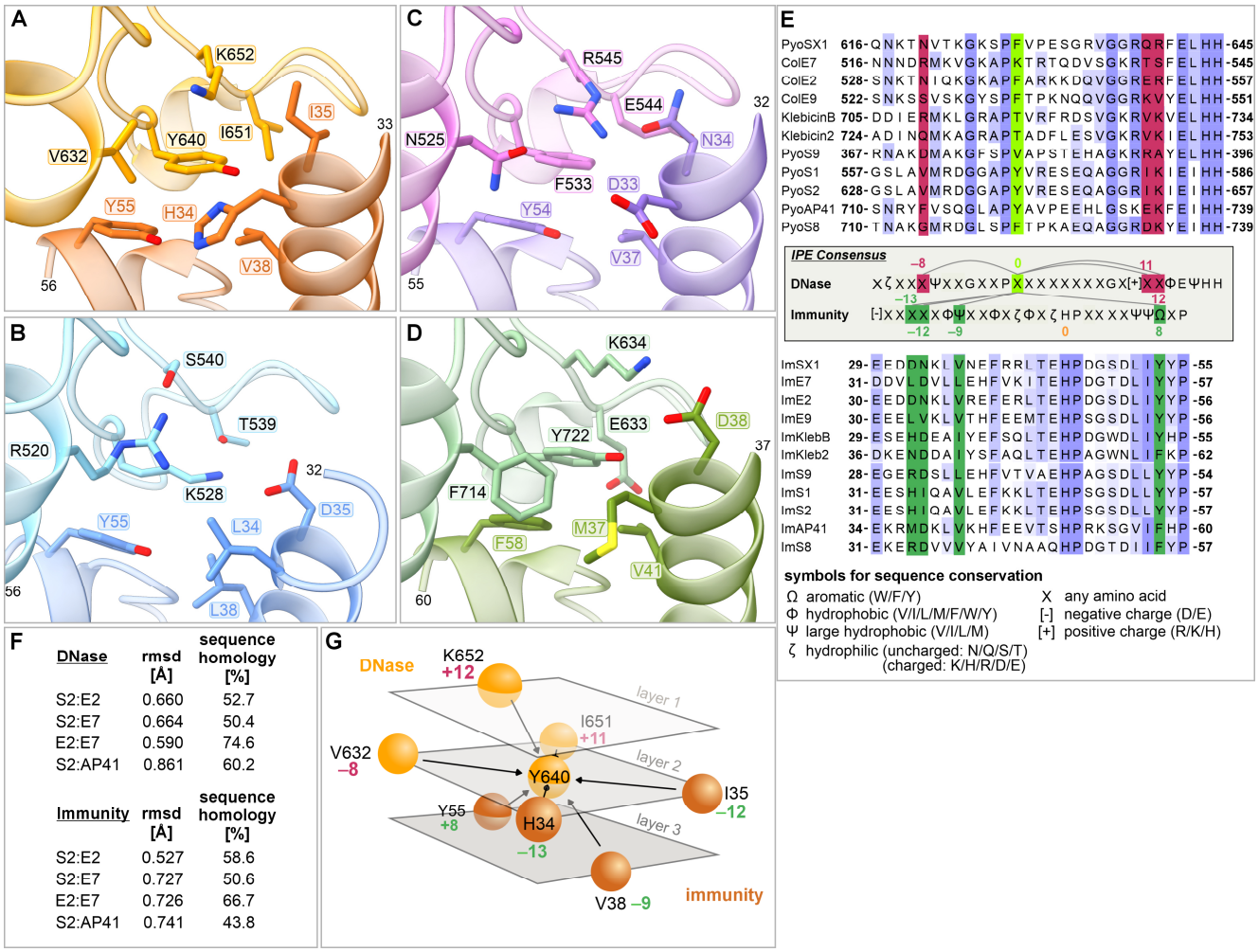


Figure IV.43. Conserved topology of DNase domains and their immunity interaction within HNH nuclease bacteriocins. **A–D**. Structural models of the DNase/immunity interface around the central amino acid. Surrounding secondary structure motifs were removed for better visibility. **A**. PyoS2/ImS2 model (PDB 4QKO) with the central amino acid Y640. **B**. ColE7/ImE7 model (PDB 7CEI) with the central amino acid K528. **C**. ColE2/ImE2 model (PDB 3U43) with the central amino acid F533. **D**. PyoAP41/ImAP41 model (PDB 4UHP) with the central amino acid Y722. **E**. Multiple sequence alignment of HNH DNase bacteriocins from *E. coli*, *P. aeruginosa*, and *K. pneumoniae* and their immunity proteins. Based on the high structural conservation, we devised a "consensus" sequence of both binding partners around the central DNase residue (bright green). Amino acids that interact with the central residue are either accentuated in red (DNase) or dark green (immunity protein). Overall sequence conservation is highlighted in shades of blue. Sequence conservation within the consensus was named per the normalised nomenclature of peptide motifs.[826] **F**. Comparison of conservation among the amino acid sequence and the tertiary structure within HNH DNase domains and their cognate immunity proteins. Structural conservation is represented by the rmsd (measured in Å) of two PDB models, while sequence conservation (measured in %) is represented by the homology. Structural and sequence alignments were performed with ChimeraX and the Expasy SIM alignment tool for protein sequences. **G**. Three-layered model highlighting the geometrical interaction of DNase and immunity residues to stabilise the central residue within the IPE. The representative model was devised based on structures **A–D** and shows the interaction between PyoS2 and ImS2. The model is applicable to all DNase bacteriocins from multiple sequence alignment (**E**) by using the red, light green, and dark green highlighted residues.

Other typical approaches in bacteriocin research to increase the diversity of available toxins are the generation of novel toxins based on domain swapping and creating non-natural chimeric bacteriocins with retained receptor binding and translocation domains but novel cytotoxic domains. Existing examples are a pyoS5:PmnH chimera and lysin-bacteriocin chimeras (lysocins), such as the PyoS2-GN4 or the pesticin-T4 lysozyme chimeras.[827-829]

PmnH itself is a genuine bacteriocin from *Pseudomonas synxantha* strain BG33R and exhibits unusual domain organisation, as the protein is equipped with two cytotoxic domains (colicin M-like and pore-forming). However, only pore-forming activity has been confirmed by previous studies.[830]
The lysins GN4 and T4 lysozyme originate from the *P. aeruginosa* PAJU2 phage and *E. coli* T7 bacteriophage, respectively, and both degrade the periplasmic PG of the host cell. Originally evolved for hypotonic cell lysis and phage progeny liberation, lysins are an alternative class of small antimicrobial hydrolases that cause cell death by bactericidal activity. While the authors highlighted evasion of bacteriocin immunity proteins for the lysocins and an advantage over natural bacteriocins,[828, 829] bacteriocin chimeras with cytotoxic domains originating from other bacteriocins do not have this advantage without restrictions. The problem arising from using these chimeras is the natural origin of the DNase domains. When, for example, an N-terminal receptor binding and translocation domain from the *P. aeruginosa* pyocin S2 is fused with a DNase domain of the *E. coli* colicin E2, none of the known *P. aeruginosa* strains could protect themselves from DNA degradation, as the colicin immunity protein is not found amongst Pseudomonads. However, since certain strains of *E. coli* naturally produce the cognate ImE2 immunity protein and the treatment of *P. aeruginosa* with the chimeric S2:E2 toxin exerts selective pressure on the bacterial target strain, the acquisition of the *E. coli* immunity protein via horizontal gene transfer could be favoured. Hence, the chimeric protein would lose its competence. When comparing the chimeric proteins to our PyoS2 conjugates, no natural immunity proteins are known to confer resistance to the DNase mutants and DNase conjugates of PyoS2 with impaired immunity protein association described in this work for the first time. And even if resistance occurs on the basis of immunity protein mutations, a simple exchange of the attached label might already do the trick and make the adapted immunity protein useless again.

IV.5.3 Investigation on the Restoration of Catalytic DNase Activity of PyoS2 Y640C Through Maleimide-Functionalisation

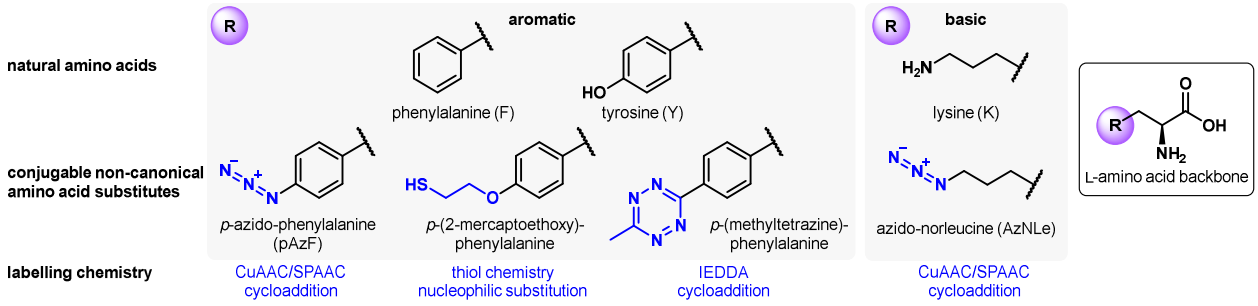
In Chapter IV.3.7, we could show that while the mutation Y640C rendered the neutralisation of DNase activity by ImS2 binding ineffective and was able to overcome ImS2-mediated PyoS2-resistance of *P. aeruginosa* PAO1, the point mutation led at the same time to a perceptible loss of DNase activity for the unlabelled mutant Y640C in comparison to wild-type PyoS2. As highlighted in the former chapter, the structurally conserved residues V632, I651, and K652 stabilise the tyrosine residue Y640, and this stabilisation might not only be essential for ultra-high-affinity binding of the immunity but also efficient hydrolytic activity of the DNase. Particularly, residue K652 directly interacts with the DNA substrate, which is why its orientation and stabilisation through Y640 from below was hypothesised to facilitate DNA binding and cleavage. In addition to the drastic loss of DNase activity in mutant Y640C, it was also noted that the labelling with the AlphaFluor maleimides in position Y640C can partially restore DNase activity and increases the cleavage efficiency of supercoiled DNA in comparison to the unlabelled mutant ($t_{1/2,\text{supercoiled}}$: wild-type = 3.20 min; Y640C = 15.3 min; Y640C-AlF488 = 4.00 min) (cf. Figure IV.26, A and B). The smaller the introduced fluorophore, the higher the *in vitro* DNase activity detected for the AlF-labelled PyoS2 Y640C mutant. Although the recovery of DNase activity via attachment of bulky non-proteinogenic labels to a protein seems contra intuitive at first glance, a closer look into the protein structure suggested that the maleimide residue formed in consequence of covalent protein labelling can partially compensate the loss of stabilising intraprotein contacts, which were lost upon substitution of the Y640 residue with the small amino acid cysteine in the PyoS2 Y640C mutant (cf. Figure IV.22C).

To test this hypothesis, *in vitro* labelling of mutant PyoS2 Y640C with a fluorophore-free maleimide (e.g. *N*-methylmaleimide) can be conducted to investigate its effect on DNase activity in comparison to unlabelled PyoS2

Y640C. Furthermore, the knowledge about the utility of stabilisation in this central position could be auxiliary in modifying and labelling other DNase bacteriocins, which do not harbour a tyrosine residue in this position.

Particularly, while other HNH DNase bacteriocins may have different residues at this central position of the immunity protein exosite for interacting with their cognate immunity proteins (e.g. threonine, lysine, and phenylalanine, cf. Figure IV.43E), the stabilising interactions exerted by neighbouring side chains could serve as a guide for selecting suitable labelling chemistry. This would enable bacteriocin labelling while preserving the original stabilising intraprotein interactions with spatially adjacent residues. Thereby, it might be possible to generate highly functional HNH DNase bacteriocin conjugates that are still able to evade immunity protein neutralisation by the employed mechanism of steric repulsion and a lack of stabilising interprotein interactions between DNase domains and immunity proteins.

Besides *in vitro* labelling with artificial probes via click chemistry, the co-translational incorporation of non-canonical amino acids can also be considered for such derivatisation. Non-canonical amino acids are widely used and are known for having both stabilising and destabilising effects on essential protein properties, such as thermal stability and catalytic activity.[831] The so-called stop codon suppression is the most common strategy for incorporating non-canonical amino acids. Since particularly aromatic non-canonical amino acids are selectively incorporated into proteins by engineered aminoacyl tRNA synthetases, the introduction of other aromatic amino acids with reactive side chain groups opens the door for different kinds of labelling chemistry that might be useful for future labelling of pyocin DNase domains (e.g. CuAAC with azides, thiol-maleimide and thiol-Michael, inverse electron-demand Diels-Alder with tetrazines) with small molecules (Scheme IV.5).
Considering organic azides as highly versatile and reactive moieties for a post-translational *in vitro* protein modification via CuAAC and SPAAC click chemistry, a suitable conjugable non-canonical amino acid substitute for the central tyrosine and phenylalanine residues in DNase bacteriocins might be *para*-azido-L-phenylalanine. At the same time, azido-norleucine could replace lysine (Scheme IV.5).[831-834] Both non-canonical amino acids resemble the size and polarity of the original amino acid, thereby maintaining stabilising contacts within the DNase domain needed for highly efficient cleavage of DNA substrates. However, both azide-functionalised non-canonical amino acids are additionally compatible with bioorthogonal CuAAC and SPAAC click chemistry, allowing for further functionalisation with non-proteinogenic labels such as fluorophore dyes. Thereby, the ultra-high-affinity binding of cognate immunity proteins could be effectively disrupted, leading to killing activity of bacteriocin conjugates against immunity protein-producing strains, while the DNase activity is maximised. An experimental validation of the proposed non-canonical amino acid incorporation into bacteriocins and their subsequent site-specific labelling with additional ligands will require further attention in the future.



Scheme IV.5. Natural amino acids found in the central position of HNH DNase/immunity protein interfaces and their potential non-canonical amino acid substitutes. By mimicking the original polarity and size of the replaced amino acid, DNase activity is assumed to be least affected, while labelling with small molecules is still enabled. Thereby, cytotoxic activity is maximised while immunity protein binding is still impaired, causing DNA degradation in ImS2-producing *P. aeruginosa* strains.

IV.5.4 Stopped-Flow Fluorescence Measurements to Analyse DNase/Immunity Dissociation Constants

In this work, a severe impact of mutations within the immunity protein exosite on the affinity between the DNase bacteriocin and its cognate immunity protein was found. Firstly, the protein expression of PyoS2 Y640C and PyoS2 ID resulted in toxic phenotypes and necessitated the utilisation of toxin-resilient strains for protein production. Secondly, retained DNase activity in the presence of excess ImS2 for the PyoS2 Y640C-AlF conjugates readily proved impaired complex association *in vitro*. And lastly, the straight elution of the PyoS2 ID mutant from the Ni-NTA resin without any need to crack open the PyoS2 ID/ImS2 complex with the chaotropic salt Gdn·HCl emphasised impaired complex association. Nevertheless, none of the mentioned experiments or applied methods is able to provide quantitative information on the exerted effect on PyoS2/ImS2 binding. The DNase domain of HNH DNase bacteriocins and their cognate immunity proteins are known to form a tight complex through ultra-high-affinity binding in the femtomolar range.[701, 733, 835] As a result of this fast diffusion-controlled association and very slow complex dissociation, many standardised methods for dissociation constant characterisation are not eligible for interactions with such high affinity. In the past, stopped-flow fluorescence measurements were the method of choice to monitor the ultra-fast association between the ColE9 DNase and its cognate ImE9 immunity protein. At the same time, radioactive subunit exchange was used to follow complex dissociation.[733] While the latter method requires specialised equipment and safety precautions, stopped-flow measurements are more accessible and relatively easy to perform. Thus, stopped-flow fluorescence measurements could be an ideal method to quantify the effects of single point mutations (e.g. PyoS2 Y640C) or fluorophore labelling at the PyoS2/ImS2 binding interface on the affinity of the cognate complex. Understanding the role of individual amino acid residues in complex formation and their impact on the ultra-high-affinity binding of both proteins will be instrumental in advancing our strategy to block toxin-immunity interactions. This, in turn, would help overcome the natural immunity protein-mediated resistance to bacteriocins and enable the use of engineered bacteriocins as antimicrobials against multidrug-resistant bacteria.

IV.5.5 PyoS2 Conjugates in Eukaryotic Infection Models and Their Application in Antibiotic Formulations

Class I and II bacteriocins of Gram-positive lactic acid bacteria (e.g. nisin and pediocin PA-1) are relatively small (<10 kDa) and readily applied for the preservation of food on an industrial scale.[677, 836] Class III bacteriocins of Gram-negative bacteria with larger size (>30 kDa) are still in the phase of mechanistic exploration instead. Although dozens of representatives of class III bacteriocins, such as colicins, pyocins, or other narrow-spectrum antimicrobial peptides, were shown to possess killing activity against the group of ESKAPE pathogens,[674] none of these bacteriocins from Gram-negative bacteria have made it into a broad application yet.[677] Although our current knowledge about the applicability of Gram-negative bacteriocins is predominantly predicated on works with *P. aeruginosa* and its pyocins, academic studies from the past 10 years have drawn an encouraging image of a future application of these bacteriocins on the basis of *in vivo* mouse model studies.[837-839] In 2016, the University of Glasgow filed a patent on the pulmonary application of pyocins (featuring S5, L1, S2, AP41, and SD2 pyocins), aiming for a reduction of respiratory *P. aeruginosa* infections in mice. Most importantly, the delivery of bacterial proteins to the lung neither activated the eukaryotic immune response nor caused any damage to the lung tissue, while pyocin treatment significantly reduced the bacterial load at the focus of infection.[840, 841] Thus, previous insights into pyocin-based therapeutic approaches, along with our findings on the broadened activity spectrum of certain PyoS2 mutants and conjugates with reduced ImS2 binding, strongly support the applicability and high potential of Gram-negative bacteriocins for treating bacterial infections in the future. As the ultra-high-affinity interaction of S-type pyocins and their cognate immunity proteins is structurally highly conserved and even

adapted by colicins and other nuclease bacteriocins, our conjugation strategy devised for PyoS2-AlphaFluor conjugates offers a broadly applicable mechanism to knock out the innate immunity of nuclease bacteriocin-producing strains in general. To further study the exerted effects of such immunity-insensitive conjugates in *in vivo* models (e.g. in terms of efficacy and tolerability, metabolic stability, and lastly their effect on bacterial load in acute infections), animal studies will be of high importance. The treatment of highly virulent MDR clinical isolates of *P. aeruginosa* with immunity-insensitive pyocin conjugates can be analysed in direct comparison to common antibiotic treatment. Since different types of acute bacterial infections – such as bacterial sepsis, superficial burn wound infections, or respiratory tract infections – may require distinct antibiotic formulations and methods of drug administration, developing and testing a range of pyocin conjugate treatments in appropriate mouse infection models would help assess their effectiveness *in vivo*. While respiratory tract infections could be potentially treated by spray inhalation of pyocin-containing aerosols or by intranasal application,[839-841] bacterial sepsis might require intravenous injection of pyocins. In contrast, applying pyocins on superficial burn wounds would necessitate the development of pyocin-containing salve formulations[842] for topical administration or injectables for subcutaneous application. Since all tissues and biofluids in the human body drastically diverge in their pH, sugar composition, the composition of hydrolytic proteases, as well as the composition in immunologically active proteins and cells, a differentiated study of the stability of pyocins in these therapeutically relevant environments is essential to forecast their applicability for the treatment of Gram-negative pathogens with accumulated antimicrobial resistance in humans or animals.

IV.5.6 Development of S-Type Pyocin Targeting Novel Outer Membrane Receptors

S-Type pyocins hijack outer membrane porins for their membrane translocation and their entry into the target cell. Consequently, binding to these OM porins is the crucial initiating step of pyocin toxicity, also determining the application potential of pyocins or pyocin-derived antimicrobials. All known receptors used for pyocin translocation belong to the group of siderophore receptors and address either FpvA-type receptors (FpvAI, FpvAII), FptA, CrtA, or Hur. In this regard, the group of FpvA-type receptors is of special interest, as every *P. aeruginosa* strain produces exactly one type of FpvA receptor for the uptake of ferripyoverdine siderophores, namely subtype FpvAI, FpvAII, or FpvAIII for the uptake of ferripyoverdine siderophores. Therefore, a selection of bacteriocins targeting all three subtypes could potentially cover all strains of *P. aeruginosa*. However, only FpvAI- and FpvAII-targeting pyocins (S2 and S3, respectively) have been identified to date. Our multiplex PCR study on 113 MDR clinical isolates from the University Hospital in Düsseldorf revealed an overwhelming fraction of 66.4% of strains belonging to the group of FpvAIII-producing strains. Hence, an actual FpvAIII-targeting pyocin could multiply the effectiveness of S-type pyocins and engineered conjugates by addressing a broader selection of *P. aeruginosa* strains.

Despite a lack of a pyocin, explicitly targeting the widespread FpvAIII receptor, strains from the *fpvAIII* siderovar might still be tractable with FptA-, Hur-, or CrtA-targeting pyocins, such as PyoS5, PyoG, or PyoSX1 and PyoSX2, respectively. Even more tempting seems the utilisation of those pyocins targeting essential OM β-barrel proteins. Such an example is BamA, the central component of the β-barrel assembly machinery in Gram-negative bacteria. To access such pyocins with unnatural receptor recognition, the directed evolution of known pyocin receptor binding and translocation domains might be a reasonable strategy. However, several prerequisites must be met by these engineered pyocins to gain novel types of receptor binding but maintain Ton-mediated and FtsH-assisted translocation.

First, the engineered toxin must exhibit sufficiently high affinity for its target receptor to facilitate entry into the porin lumen. However, the interaction must not be excessively strong, as efficient translocation into the periplasm

of the target cell requires the force-dependent TonB1-mediated import. In fact, dissociation constants for bacteriocin/receptor interactions span a wide range, from picomolar (PyoS2/FpvAI; K_D: 240 pM),[662] to low nanomolar (ColE3/BtuB; K_D: 0.9 nM),[843] or even low micromolar (PyoS5/FptA; K_D: 6.5 µM) affinities.[719] Hence, the selected examples emphasise the very broad range of receptor binding affinities of different bacteriocins, which are all highly potent toxins with antibacterial activity against *P. aeruginosa* in the nanomolar range. Consequently, the latitude for engineering unnatural bacteriocin receptor binding affinities is immense.
Second, the introduced mutations, governing unnatural receptor recognition, must still induce conformational changes within the targeted receptors upon binding of the engineered pyocin to uncover the TonB box of the force-labile portion of the periplasmic receptor plug domain for TonB1 recruitment and initiation of membrane translocation.
And lastly, the introduced mutations must still maintain the high degree of structural conservation of the N-terminal receptor binding and translocation domains of S-type pyocins in two tandemly repeated kinked three-helix bundles that enables partial domain unfolding during the process of translocation (cf. Figure IV.7 and Figure IV.8). For the afore mentioned reasons, changing receptor selectivity of a multi-domain protein through an untargeted approach like directed evolution appears to be a viable solution.

Particularly, the large number of variables and amino acid contact points make directed evolution and engineering of highly complex protein interactions a challenging endeavour. Consequently, directed evolution is typically applied for engineering stand-alone enzymes with biotechnological application potential, aiming for a broadened substrate scope or enhanced stability under certain conditions.[844, 845] While these adjustments often require minor changes of the catalyst's structure and only a handful of amino acid substitutions, changing the receptor selectivity of cell-targeting "toxins", such as pyocins, is a more complex task involving multiple protein domains within the pyocin of interest and the interaction of multiple proteins during translocation across the bacterial membrane. And yet, there is a significant public interest in broadening the host range of antimicrobial proteins in the current antimicrobial resistance crisis, by removing those factors limiting a wider application of pyocins via protein engineering. Those factors arise from the natural host and receptor recognition mechanism of pyocins and include the CPA-binding domain for enhanced cellular binding, the TonB box for recruitment of the Ton machinery, and most importantly, the architecture of the N-terminal receptor binding domain – mediating binding between the pyocin and its outer membrane receptor.

Consistent with the high demand for novel therapeutic solutions for treating infections with multidrug-resistant bacteria, directed evolution and structure-guided engineering are readily applied strategies to fulfil the need for expanded host range antimicrobials.[846] Although bacteriocins and their receptors are not among those antimicrobials and targets for which host range expansion was demonstrated so far, some examples from the world of prokaryotic viruses – whose adsorption to the target cell is to some extent similar to bacteriocins – have highlighted alterations to viral host selectivity (narrowing and broadening) by engineering receptor-interacting proteins by means of directed evolution.[847-849] For example, Liang *et al.* were able to evolve tail fibre proteins of the *E. coli*-targeting bacteriophage T7, allowing for newly acquired binding affinity and lytic activity against *Yersinia enterocolitica*.[847] In contrast, Holtzman *et al*. developed a continuous evolution system, leading to a contraction of the host range of bacteriophage T7.[848]
The relatively few studies dealing with the directed evolution of phages as highly complex antimicrobials underline the challenges of untargeted engineering of multi-domain protein-based antimicrobials. Nonetheless, the presented experimental approaches for untargeted protein evolution might be used as positive examples of how directed protein evolution can serve to obtain engineered pyocin variants with altered host recognition mechanisms and broadened activity spectrum in the future. Thereby, we might meet the global demand of highly

active and selective antibiotics with tunable host range selectivity, effectively targeting multidrug-resistant bacteria, such as CRPsA and other concerning microbial pathogens from the WHO priority list.[554, 555]

IV.5.7 Pyocins as Trojan Horse for Targeted Delivery of Antimicrobial Drugs into Multidrug-Resistant *Pseudomonas aeruginosa*

S-Type pyocins exploit a conserved machinery (Ton or Tol) for their highly specific uptake into *P. aeruginosa* and hijack OM receptors by mimicking the binding of their natural ligands. Since these receptors and the import machinery are only present in Gram-negative bacteria, this route is very appealing for the selective intracellular delivery of potential antimicrobials into strains which are otherwise difficult to address with conventional therapeutics. By using non-toxic fluorophores and the potential drugs from the family of prodigiosin alkaloids for covalent attachment to the DNase domain of PyoS2, we showed that the DNase transport into the target cell's cytoplasm remains intact upon labelling and that the labelled DNase domain exerts bactericidal activity by degrading DNA. Hence, PyoS2 conjugates have already passed the first and most important hurdle in drug-targeted delivery by transporting the conjugated small-molecule "drugs" to the desired destination, the bacterial cytoplasm of the difficult-to-treat organism *P. aeruginosa*.
Besides DNase activity contributed by the PyoS2 vector, no additional biological activity has so far been observed for the attached drug payloads from the PyoS2 conjugates, namely the AlphaFluor dyes (inherently non-toxic) and the prodiginine-maleimides. Therefore, some aspects remain to be investigated and optimised to engineer PyoS2-drug conjugates to potent antimicrobial drugs with dual activity, namely DNase activity from the PyoS2 vector and any other cytotoxic antimicrobial activity from the conjugated payload. Earlier in this work, it was hypothesised that two major reasons might prevent the conjugated prodiginine alkaloids from being toxic to the targeted bacterial cells. These define the space for future optimisation of the conjugates.

In the first place, the intracellular concentration of PyoS2 might be too low to allow the co-transported drug payload (here: prodigiosin) to reach its needed cytotoxic threshold. Therefore, the intracellular concentration of the PyoS2 DNase domain following translocation across the membrane should first be determined, as this provides the foundation for selecting appropriate payloads for protein conjugation.
Non-invasive in-cell quantification of proteins is a truly challenging and nontrivial task. In the past years, several methods have been published to address this issue, but the typical application is the quantification of protein expression. Liu *et al*. used a paired microfluidics/immunoblotting strategy to quantify a prostate cancer biomarker in eukaryotic cells.[850] However, bacterial cells are unlike smaller and are only a tenth or a hundredth of an eukaryotic cell and thus far more difficult to capture. Furthermore, the quantification via immunoblotting requires the availability of antibodies for the protein of interest, which is not given for most bacterial proteins. Although specific epitope tags that function as epitopes for antibodies might do the trick, these tags might negatively affect the translocation of our pyocins into the cell. To avoid interference of artificial tags with pyocin translocation, the readily approved and relatively small AlphaFluor fluorophore labels of the PyoS2-AlF conjugates generated in this work can be used for fluorescence quantification via single particle tracking. Although this has never been done for the intracellular quantification of bacteriocins, a similar study investigated a Cy5-labelled ColE1 mutant, which could not fully translocate into the cell.[851] Instead, the protein was quantified on the cell surface. Since constant excitation of the cell surface-located fluorophore dyes with high-energy lasers causes photobleaching over time, there is a short moment in which a single fluorescence-emitting molecule remains before complete bleaching occurs. The brightness of this single molecule was then used for calibration and the brightness of the original fluorescence was used for an estimation of the number of bacteriocin molecules on the cell surface. With this approach, Liu *et al.* could show that approximately 20 bacteriocin molecules are bound to their outer membrane

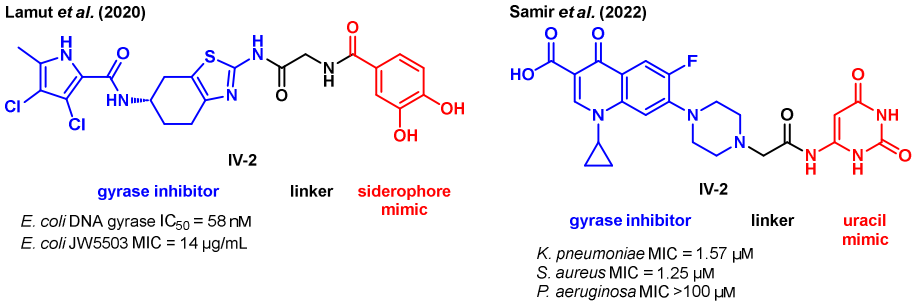
receptor on the cell surface. Based on these data, one could assume that up to 20 bacteriocin molecules can translocate into the target cell by hijacking the Ton or Tol pathway. Consequently, up to 20 conjugated drug payload molecules could be transported into the target cell by using bacteriocin-drug conjugates for selective targeting of bacterial strains.

To adapt this particle tracking approach for quantification of intracellular pyocins, an adapted procedure with tryptic digest of cell surface-localised pyocin-fluorophore conjugates would be needed, degrading all conjugates which have not translocated across the membrane and only quantifying those conjugates which have been internalised (cytoplasmic + periplasmic). Further adjustments could potentially unravel the genuine fluorescence of cytoplasmic conjugates, as only conjugates with cytoplasmic localisation exhibit cytotoxic activity by DNA degradation and are relevant for pyocin-drug conjugates with payloads that are only active in the cytoplasm. Quantification of truly cytoplasmic pyocin conjugates could be tackled by Förster resonance energy transfer (FRET) between co-localised pyocin-fluorophore conjugates (e.g. AlphaFluor dyes) and fluorescently labelled immunity proteins. The heterologous expression of a genetically encoded fluorescent ImS2 chimera in *P. aeruginosa*, for example, through translational fusion with the green fluorescent protein GFP,[852] would enable ultra-high-affinity association of the ImS2-GFP chimera with PyoS2-AlphaFluor conjugates upon membrane translocation of the toxin and lead to spatial adjacency of both fluorophores. If the fluorophores are correctly selected – showing an overlap of the fluorescence emission spectrum of one fluorophore with the fluorescence excitation spectrum of the other fluorophore – their close proximity would result in a detectable FRET signal (non-radiative energy transfer between donor and acceptor fluorophore).[71, 852] Via *in vitro* calibration of the FRET brightness resulting from a single PyoS2-AlF/ImS2-GFP complex, non-invasive in-cell quantification of pyocins would be possible. Besides quantification of intracellular PyoS2 DNase titres, the discussed FRET sensors could also be used to determine dissociation constants between ImS2 and all fluorescently labelled PyoS2 variants, enabling a quantitative assessment of mutation and labelling effects on the ultra-high-affinity complex of PyoS2 and ImS2.[853]

The second potential reason for the lack of payload-associated cytotoxicity of PyoS2-prodiginine conjugates evaluated in this work could lie in the design of the non-cleavable triazole-maleimide linker connecting the PyoS2 vector and the prodiginine payload. Here, a missing release mechanism of the conjugated payload from the large hydrophilic protein vector most likely restrains the prodiginine warhead from showing bioactivity, as limited passive membrane diffusion of the alkaloid is required to uncouple membrane potentials. Hence, independent of the intracellular conjugate titre, the installation of a cleavable linker should be addressed to facilitate an optimal availability of the cytotoxic cargo for interaction with its designated intracellular target. Suitable payloads for future PyoS2-drug conjugate research are those antimicrobials which are, in an unconjugated state, typical substrates of unspecific efflux pumps and get thereby expelled from the periplasmic space, such as gyrase inhibitors from the quinolone, diazanaphthalene, or pyridopyrimidine families.[854] Since conjugation of the payload with the large hydrophilic protein PyoS2 drastically changes the overall polarity and the hydrodynamic radius of the drug, the conjugates would no longer be recognised as efflux pump substrates. In combination with the active uptake of the conjugates via the Ton pathway, the conjugates can traverse the otherwise impermeable bacterial membrane.

Returning to the briefly touched topic of bacterial gyrase inhibitors, for which conjugation to small-molecule carriers had shown promising results with nanomolar to micromolar antimicrobial activities, conjugation to PyoS2 could be a highly strain-specific alternative for intracellular delivery. Previous studies using tetrahydrobenzo[*d*]thiazole- or fluoroquinolone-based conjugates, whose active cellular uptake was linked to siderophore or nucleotide mimic carriers, respectively, were able to circumvent the active drug efflux from the target cell (Scheme IV.6). For example, Lamut *et al*. described the utilisation of a catechol-based siderophore **IV-1** to direct the conjugated 4,5,6,7-tetrahydrobenzo[*d*]thiazole-2,6-diamine antibiotic into the target cell. Thereby, inhibitory concentrations

against the *E. coli* DNA gyrase of up to 58 nM and antibacterial activities against *E. coli*, *P. aeruginosa*, and *A. baumannii* were observed.[855] An alternative study of Samir *et al.* employed an uracil-based nucleotide mimic for the targeted import of a ciprofloxacin fluoroquinolone antibiotic **IV-2** to display bactericidal activity against *E. coli*, *K. pneumoniae*, and methicillin-resistant *S. aureus* at low micromolar concentrations.[856] However, *P. aeruginosa* remained highly resistant to the conjugate (MIC: >100 µM). Both cited studies used a non-cleavable aminoacetamide linker. However, due to the relatively small size of the exploited siderophore and nucleotide carriers, the carriers are assumed to have a minor impact on the drug payload (solubility, polarity, etc.). Concurrently, the antimicrobial data underline that these gyrase inhibitors are highly potent antimicrobial agents, even with additional structure modifications originating from the conjugation.



Scheme IV.6. Bioactive small-molecule conjugates of DNA gyrase inhibitors as putative lead structures for next-generation PyoS2-drug conjugates.[855, 856]

Therefore, gyrase inhibitors that inhibit the bacterial cytoplasmic DNA gyrase in target cells are ideal candidates for a second-generation of PyoS2-drug conjugates, combining novel potent warheads and a cleavable linker design for site-selective drug release from the protein carrier in the bacterial cytoplasm. Although or maybe because these antibiotics have never been conjugated to proteinogenic vectors before, the highly selective import of pyocins via the Ton-pathway might be a suitable model to address the lacking bioactivity of these precious gyrase inhibitors against multidrug-resistant strains of the opportunistic human pathogen *P. aeruginosa*. Thereby, it might be possible to selectively target this Gram-negative bacterium, which becomes a global threat through the frequent acquisition of antibiotic resistance genes, by circumventing the membrane permeability-regulating defence mechanisms (e.g. drug efflux pumps) and thereby evading its protective mechanism that makes this particular bacterium so difficult to treat with common antibiotic therapies.

V Materials and Methods

V.1 Ethical Compliance Statement

The utilisation of clinical isolates of MDR strains of *Pseudomonas aeruginosa* from hospitalised human patients with the study number **2021-1324** (*Microbiological evaluation of pyocin S2 conjugates as substitutes for antibiotics and the treatment of multidrug-resistant Gram-negative bacteria*) was reviewed and approved by the ethics commission of the Faculty of Medicine from the Heinrich Heine University Düsseldorf.

V.2 Software

Table V1. Software used throughout this thesis.

Software	Purpose	Provider
AlphaFold Protein Structure Database	Structure prediction of proteins and complexes	Google DeepMind and EMBL-EBI[857-859]
BLAST2 2.15.0 (Basic Local Alignment Search Tool)	Sequence homology search for proteins and nucleic acids	National Center for Biotechnology Information (NCBI)[786, 788]
Beta-Lactamase Database (BLDB)	β-Lactamase sequences for homology search	Naas *et al*.[611]
ChemDraw Professional 22.2.0.3300	Chemical drawing tool	PerkinElmer Informatics
Clustal Omega	Multiple sequence alignments	Sievers *et al*.[860]
CorelDRAW 24.5.0.731	Drawing software for vector graphics	Corel Corporation
Corel PHOTO-PAINT 24.5.0.731	Processing of photographs	Corel Corporation
DSSP Server	Standardised secondary structure assignment from PDB models	Wolfgang Kabsch and Christian Sander[861, 862]
Endnote X9.3.1	Literature management	Clarivate
ensochemLab 7.0.5	Electronic lab journal	ensoSoftware GmbH
Expasy ProtParam	Calculation of protein parameters	SIB Swiss Institute of Bioinformatics[863]
Expasy SIM	Alignment tool for protein sequences	SIB Swiss Institute of Bioinformatics[864]
The European Galaxy Server	Processing of sequencing raw data, genome assembly and annotation	The Galaxy Community[783]
GraphPad Prism 8	Scientific figures and graphs	GraphPad Prism Software
ImageJ 1.54f	Densitometry	Wayne Rasband and contributors, National Institute of Health (NIH), USA[865]
Jalview 2.11.3.3	Multiple sequence alignment editor	Barton Group, University of Dundee, Scotland, UK[866]
MestReNova 14.1.1-24571	Processing and evaluation of NMR data	MestreLab Research
Microsoft Excel	Writing and editing of spreadsheets	Microsoft Corporation
Microsoft Word	Writing and editing of text documents	Microsoft Corporation
Origin 2021b v9.8.5.201	Scientific figures and graphs	OriginLab Corporation

Table V.1 (continued).

PDBePISA	Interface analysis of crystal complexes	Krissinel and Henrick[737]
Prokaryotic Genome Annotation Pipeline (PGAP)	Annotation of microbial genomes in GenBank-compliant format	National Center for Biotechnology Information (NCBI)[785]
Pseudomonas aeruginosa serotyper 1.0 (PAst), web server tool	Analysis of the OSA gene cluster for *in silico* serotyping of *P. aeruginosa* isolates into 20 serogroups	Sandra Wingaard Thrane, Infection Microbiology Group, Technical University of Denmark[792, 793]
RStudio	Statistical data analysis and visualisation	Posit[867]
SnapGene 6.1.2	Cloning tool	GSL Biotech LLC
SwissADME	Pharmacokinetic evaluation	SwissDrugDesign[868]
UCSF ChimeraX 1.8	Molecular visualisation and analysis of protein structures and complexes	University of California, USA[869]

V.3 Chemical Methods

V.3.1 General Information

V.3.1.1 Naming of Compounds

All chemicals used and compounds synthesised throughout this thesis were named following the naming conventions of the IUPAC (International Union of Pure and Applied Chemistry) nomenclature. Numbering of specific atoms for the analytical purpose of NMR assignments may vary from the IUPAC nomenclature and is only used for explicit correlation. All synthesised compounds and their unique experimental identifiers are summarised in Chapter VII.

V.3.1.2 Fine Chemicals, Solvents, and Reagent Handling

All commercial chemicals were purchased from Sigma Aldrich (Merck), Tokyo Chemical Industry (TCI), ThermoScientific, VWR, BLDpharm, Fluorochem, Biosynth, Fluka, Alfa Aesar, Fisher Chemicals, and Th. Geyer in purities >97% (except benzyl azide, 94%, Alfa Aesar). 2-(4-Methylamino)phenyl)benzo[*d*]thiazol-6-ol (Pittsburgh Compound B, PiB, Product No. BD244053) and acetylene-PEG_4-biotin (Product No. BD00808704) were acquired from BLDpharm in a purity of 95%. Cholesteryl-TEG-azide (Product No. 794384-100MG, purity not indicated) and Obatoclax mesylate (≥98%, HPLC, Product No. SML3118) were purchased from Sigma Aldrich (Merck). Purification of technical-grade organic solvents from VWR, Carl Roth, or Fisher Chemical was achieved by distillation. Anhydrous toluene, THF, Et_2O, and CH_2Cl_2 were obtained from the MBraun MB-SPS 800 solvent purification system. Other solvents (*i*PrOH, MeOH, EtOH, EtOAc, DMSO, DMF, $CHCl_3$, and 1,2-dichloroethane) were dried over activated molecular sieve for >72 h. According to the procedure of Burfield and Smithers, extra dry DMF was prepared by two sequential drying steps over activated 3 Å molecular sieve for ≥72 h.[870] Dry glyme (99.5+%, extra dry over molecular sieve) was purchased from Thermo Scientific Chemicals. Degreased cotton wool (Brand) for filtration purposes was again degreased by washing with distilled *n*-pentane, PE, or CH_2Cl_2. Reactions under inert conditions were performed under N_2 atmosphere with pre-dried glassware under the standard laboratory Schlenk technique. If stated in the synthetic instructions, solvents were degassed using the freeze-pump-thaw procedure (3x). 2,2,6,6-Tetramethylpiperidine (TMP) was refluxed for 4 h over CaH_2, distilled under normal pressure, and stored over 4 Å molecular sieve. All synthesised compounds were stored under an Ar atmosphere at –20 °C.

V.3.1.3 Analytical and Preparative Chromatography

Thin-layer chromatography (TLC) was performed for analytical purposes by using coated Macherey-Nagel POLYGRAM SIL G/UV_{254} plates (40 x 80 x 0.2 mm) or POLYGRAM ALOX N/UV_{254} plates (40 x 80 x 0.2 mm). Visualisation of different compounds on TLC plates was achieved by using various staining methods, including excitation under UV light, $KMnO_4$ stain (7.5 g/L $KMnO_4$, 50 g/L K_2CO_3, 625 mg/L NaOH in water), iron(III) chloride stain (10 g/L $FeCl_3$ in H_2O/MeOH 1:1), *p*-anisaldehyde stain (300 mL glacial acetic acid, 6 mL conc. H_2SO_4, 3 mL *p*-anisaldehyde), CAM stain (25 g/L phosphomolybdic acid, 10 g/L $Ce(SO_4)_2$ x 4 H_2O, 60 mL/L conc. H_2SO_4, fill up with water), and an azide-specific stain[166] (solution A: 100 g/L PPh_3 in CH_2Cl_2; solution B: 10 g/L ninhydrin in EtOH, 10 mL/L glacial AcOH). The plates were dipped into the corresponding reagent solution and developed by gentle heating with a heat gun. Preparative flash chromatography was performed with Macherey-Nagel silica gel 60 (40–63 µm, 230–400 mesh) or ACROS Organics neutral aluminium oxide (Brockmann I, 40–300 µm). Dry column vacuum chromatography (DCVC) was only performed with Merck silica gel 60 (15–40 µm) and custom-made DCVC columns according to Pedersen and Rosenbohm.[397]

V.3.2 Analytical Methods

V.3.2.1 Quantitative and Non-Quantitative Nuclear Magnetic Resonance Spectroscopy (qNMR and NMR)

^{1}H, ^{11}B, ^{13}C, ^{19}F, DEPT135, ^{1}H-^{1}H-COSY, ^{1}H-^{13}C-HSQC, ^{1}H-^{13}C-HMBC, ^{1}H-^{1}H-ROESY, and ^{1}H-^{1}H-TOCSY NMR data were collected on a Bruker Avance/DRX 600 or Avance/DRX 300 spectrometer. $CDCl_3$, DMSO-d_6, CD_2Cl_2, or MeOD were used as solvents and their respective chemical shifts ($CDCl_3$: ^{1}H – 7.26 ppm, ^{13}C – 77.16 ppm; DMSO-d_6: ^{1}H – 2.50 ppm, ^{13}C – 39.52 ppm, CD_2Cl_2: ^{1}H – 5.32 ppm, ^{13}C – 53.84 ppm; MeOD: ^{1}H – 3.31 ppm, ^{13}C – 49.00 ppm) used for referencing.[871] Due to the significant amount of quaternary carbon atoms in MBC- and prodiginine derivatives, the default NMR scan numbers were significantly increased for ^{13}C (6000–8000 scans), COSY (10 scans), HSQC (10 scans), and HMBC (60–100 scans) pulse sequences to allow complete annotation of signals to corresponding ^{1}H and ^{13}C atoms. The atom numbers in NMR assignments refer to the corresponding atom numbering of the structures within experimental procedures and may vary from the IUPAC numbering. Chemical shifts (δ) are indicated in parts per million (ppm) and the corresponding signals characterised by their multiplicities: singlet (s), doublet (d), triplet (t), quartet (q), pentet/quintet (p), hextet (h), heptet/septet (h), centred multiplet (m_c), multiplet (m), broad singlet (brs), or complex higher order multiplicities. Coupling constants (*J*) are given in Hertz.

Quantitative ^{1}H NMR spectroscopy (qNMR) was employed to evaluate the purity of chemically synthesised prodigiosin samples for biological testing on cancer cell lines RT-112 and RT-112^{res}. In contrast to previous works,[391] the commercial qNMR standard 4-methoxyphenol and other standards, such as 1,3,5-trimethoxybenzene and ethyl 4-(dimethylamino)benzoate, were not applicable due to overlapping signals with the complex molecules of interest. Therefore, triphenylmethane was used as an alternative secondary qNMR standard. Briefly, triphenylmethane and prodiginines were weighed into a 1.5 mL reaction tube and dissolved in 500 µL $CDCl_3$. For each prodiginine, four independent sets of ^{1}H qNMR samples were prepared. Spectra were measured at 600 MHz to determine the purity, calculated by equation V.1. For the calculation of purities, the methyl group of triphenylmethane (5.52 ppm) and the methoxy group of prodiginines (3.95 ppm) were integrated in a range of ± 50 Hz from the centre of the signal.

$$P_{Prod} = \frac{I_{Prod}}{I_{Std}} \cdot \frac{N_{Std}}{N_{Prod}} \cdot \frac{M_{Prod}}{M_{Std}} \cdot \frac{m_{Std}}{m_{Prod}} \cdot P_{Std} \quad \text{(V.1)}$$

Prod: Product
Std: Standard
m: Mass
N: Number of absorbing Protons
M: Molecular weight
I: Signal area/integral
P: Purity (in percent)

V.3.2.2 Fourier-Transform Infrared Spectroscopy (FT-IR)

Infrared spectra were recorded on a PerkinElmer SpectrumTwo spectrometer. Samples were measured without solvents (neat) and either applied as liquids or solids to the measuring crystal. IR spectra of thin films of material were then recorded via attenuated total reflection (ATR) and the data were Fourier transformed to display the spectrum with wavenumbers (cm^{-1}) as units.

V.3.2.3 High-Resolution Mass Spectrometry (HRMS)

Samples were dissolved at concentrations lower than 1.00 mg/mL in suitable volatile solvents (EtOAc, EtOH, MeOH, $CHCl_3$, MeCN, or water) and submitted to high-resolution mass spectrometry (HRMS) at CeMSA in Düsseldorf. HRMS data were recorded on a Bruker maXis instrument with a standard collision energy of 8 eV and electrospray ionisation (ESI). However, for Boc-protected 1*H*-pyrroles, a reduction to 2–4 eV was obligatory, as Boc-protecting groups showed strong fragmentation towards the carbamic acid $[M–56.0626]^+$ at 8 eV.

V.3.2.4 Melting points

The Büchi melting point apparatus B-540 was employed for melting point determination with a temperature increment of 2 °C/min.

V.3.2.5 Optical Rotation

The optical rotation of polarised light through interaction with optically active and chiral substances was measured on a Krüss P8000-TF polarimeter at the Sodium-D wavelength (589 nm). Samples were dissolved in the indicated solvent and tempered at 20.0 °C to determine the optical rotation in a cuvette of 1 dm optical path length. The concentration-dependent optical rotation α was transformed into the specific rotation $[\alpha]_D^{20.0}$ by using equation V.2. Measurements were performed in triplicate.

$$[\alpha]_D^{20.0} = \frac{\alpha}{c \cdot d} \quad \text{(V.2)}$$

$[\alpha]_D^{20.0}$: Specific rotation [α] at 20.0 °C and 589 nm (Na-D line)
α: Observed optical rotation
d: Cuvette light path length [dm]
c: Analyte concentration [g/mL]

V.3.2.6 Coupled Gas Chromatography-Mass Spectrometry (GC-MS)

Coupled GC-MS measurements were performed to evaluate the progress of certain reactions and the relative portion of volatile compounds in complex mixtures. For this purpose, a Trace 1310 gas chromatograph (Thermo

Scientific) with a coupled ISQTM QD Single Quadrupole mass spectrometer was used. All samples were dissolved in MTBE or EtOAc, and 1 µL per sample was injected into the split injector (heated to 250 °C). At a carrier gas flow rate of 1 mL/min, samples were separated on an Optima 5MS column (30 m x 0.25 mm, 0.25 µm particle size, Macherey-Nagel) with Helium carrier gas according to the following temperature profile: hold 60 °C for 1 min; heating at 15 °C/min increment up to 185 °C; heating at 120 °C/min increment up to 280 °C; hold 280 °C for 5 min. The transfer line to the MS instrument was heated at 280 °C, and the samples were ionised by electron impact ionisation at 230 °C and 70 eV. Spectra were recorded in an *m/z* range from 50−1000 with a scan time of 0.2 s.

V.3.2.7 Coupled Liquid Chromatography-Mass Spectrometry (LC-MS)

Coupled LC-MS measurements were performed on a Thermo Scientific UltiMate 3000 UHPLC instrument with an Atlantis T3 3 µm, 3 x 100 mm column (Waters) and an ISQ-ES mass spectrometer for prodigiosin quantification from enzymatic *in vitro* ligation reactions. Sample volumes of 5 µL were injected at a temperature of 30 °C and a flow rate of 0.60 mL/min. UV detection was realised at 535 nm with a photo diode array detector. Gradient elution with MeOH + 0.1% formic acid (solvent A) and Millipore water + 0.1% formic acid (solvent B) facilitated the separation of prodiginines from MBC and pyrrole precursors. Elution profile: −5−0 min with 10% solvent A, 0−4 min with 10−60% solvent A, 4−6 min with 60−100% solvent A, 6−13 min with 100% solvent A. The following parameters were used for the ISQ-MS detection – mode: positive, vaporiser temperature: 282 °C, ITT temperature: 300 °C, source voltage positive ions: 3000 V, source voltage negative ions: −2000 V, sheath gas pressure: 49.9 psig, aux gas pressure: 5.7 psig, sweep gas pressure: 0.5 psig, mass area 10−1000, CID 20.

V.3.2.8 Quantification of Prodiginines from LC Chromatograms

Based on the measured and approximated molar extinction coefficients for chemically synthesised prodiginine references, quantification of prodiginines in methanolic extracts from *in vitro* assays was performed. Therefore, equation V.4, devised by Torsi *et al*., was deployed.[872]

$$c\left[\frac{\mu mol}{\mu L}\right] = \frac{n[\mu mol]}{V_{inj}[\mu L]} \tag{V.3}$$

with

$$n[mol] = E[AU \cdot min] \cdot F[\frac{L}{min}] \cdot \frac{1}{\varepsilon[M^{-1}cm^{-1}] \cdot d[cm]} \tag{V.4}$$

c: Prodiginine concentration in the methanolic extract
n: Amount of substance applied to chromatography
V_{inj}: Injected volume applied to chromatography
E: Integrated extinction at 535 nm
F: Chromatographic flow rate
ε: Molar extinction coefficient at 535 nm
d: Flow cell path length

The UV traces at 535 nm and the extracted ion chromatograms (EIC) of the appropriate *m/z* ratio for the proposed products were generated from the total ion chromatograms (TIC). EIC spectra were used to validate the estimated product masses, and UV absorbance at 535 nm was utilised to calculate the corresponding peak areas by integration. For quantification of prodiginines from the methanolic extracts, the mean value of absorbance from triplicate samples was used to determine the amount of substance that had been injected into the chromatographic system (equation V.4), based on the extinction coefficients, which had been determined experimentally or by

approximation. From the results of equation V.4, the concentrations in methanolic extracts were calculated by equation V.3.

V.3.2.9 Experimental Determination of Molar Extinction Coefficients

Molar extinction coefficients of prodiginines were determined by spectroscopic measurements to enable their quantification from methanolic extracts of enzymatic *in vitro* ligation reactions. In detail, chemically synthesised solid prodiginines were weighed in and dissolved in acidic EtOH (+ 4% 1 M HCl) to give a 10 mM solution. Using serial 1:10 dilutions, the stock was diluted to 10 µM in acidic EtOH. Firstly, the absorption spectra of 10 µM solutions were collected on a Shimadzu UV-1800 UV spectrophotometer, using the following instrument settings: 20 °C, 200–800 nm, 1.0 nm increment, Hellma Analytics quartz glass cuvette SUPRASIL QS (d = 10 mm light path length).

Secondly, from the diluted 10 µm stock, three concentrations were prepared in acidic EtOH, namely 1 µM, 3 µM, and 5 µM. The extinction was measured at 20 °C for each concentration at 535 nm, 545 nm and at the wavelength of maximum absorption, if the wavelength varied from the two aforementioned and the solvent background was subtracted on the instrument. The procedure was repeated three times for each compound. Resulting from the Beer-Lambert law (E = ε·c·d), the molar extinction E was plotted against the molar concentration c and the molar extinction coefficient ε was determined from the slope of a linear regression curve using OriginLab.

V.3.2.10 Approximation of Molar Extinction Coefficients

In the prodigiosin ligase-catalysed biocatalytic synthesis approach of A-ring alkylated prodiginines, several new derivatives with propyl and heptyl substitution on the C-ring were synthesised. However, analytical references of these compounds had not been synthesised through preparative chemistry, as only the pentyl derivatives were used for cytotoxicity screening, analytical validation, and compound characterisation. Thus, no experimental molar extinction coefficients are available for quantifying propyl- and heptyl-substituted prodiginines from biocatalytic syntheses, based on the UV trace of LC chromatograms. To circumvent the need for additional chemical synthesis of these compounds, an approximation of molar extinction coefficients was attempted using the linear correlation between experimental extinction coefficients of prodiginine derivatives with a constant methyl substitution on the A-ring and a variable propyl, pentyl, or heptyl substitution on the C-ring. After plotting the mean value of experimental extinction coefficients for prodiginines **III-1ba·HCl**, **III-1bb·HCl**, and **III-1bc·HCl** against the C-ring chain length, the following equation was deduced from the linear regression curve (equation V.5).

$$\varepsilon^*_{535}(n) = 762.5\ M^{-1}cm^{-1} \cdot n + 123007\ M^{-1}cm^{-1} \qquad \text{(V.5)}$$

ε*: Approximated molar extinction coefficient
n: A-ring chain length of prodiginines

Under the assumption that the slope of 762.5 M^{-1} cm^{-1} would behave similarly with increasing chain length on the A-ring, approximated extinction coefficients at 535 nm were calculated for prodiginines with propyl or heptyl substitution on the C-ring for the missing prodiginine derivatives with variable A-ring substitution (Table III.6).

V.3.3 Other Methods

V.3.3.1 General Procedure for the TLC-Based CuAAC Screening for Ligand Comparison

Organic azides and alkynes were acquired from commercial sources and used without further purification or prepared by chemical synthesis. The screening of Cu-ligands was performed in accordance with the protocol from

Michaels and Zhu.[25] Stock solutions of azides (0.80 M) and alkynes (0.82 M) were prepared in *t*BuOH. A 0.4 M stock solution of $Cu(OAc)_2$ was prepared in water and stored for a maximum of two weeks at 4 °C. If needed, Cu-ligands (10 µmol, 5 mol%) were weighed into a reaction vial and dissolved by the addition of 250 µL azide and 250 µL alkyne solution in *t*BuOH. For the ligand comparison between TDETA and TBTA under reducing conditions with sodium ascorbate, 10 µL of 2 M sodium ascorbate (20 µmol, 10 mol%) was additionally added. Once fully dissolved, 25 µL $Cu(OAc)_2$ stock solution (10 µmol, 5 mol%) was added to the reactants, and the reaction vials were stirred in an aerobic atmosphere in a shaker at 1400 RPM for up to 60 min. Reaction progress was monitored using TLC with 7 µL reaction sample per time point. Between 0 and 15 min, samples were collected every 2.5 min and between 15 and 60 min, every 5 min. TLC plates were developed in an appropriate mobile phase and consumption of azide was visualised by UV light for aromatic azides or with azide stain for aliphatic azides.[11] When complete conversion was reported or at the latest after 60 min reaction time, reaction mixtures were applied to a short pipette-sized plug of neutral aluminium oxide and the mini-column was flushed with 2 mL of EtOAc to elute the product and remove copper salts. After solvent removal under reduced pressure, ^{1}H NMR spectra were recorded in $CDCl_3$ to determine conversions, and spectra were compared to reference spectra of chemically synthesised triazolyl products **II-57a**–**g**.

V.3.3.2 Fluorometric Analysis of Tripodal Tetradentate Cu-ligands

Analysis of CuAAC acceleration by tetradentate amine ligands (TDETA, TBTA, THPTA) in aqueous solutions was performed following the literature procedure from Hong *et al.*[118, 119] For the assay, the final concentrations were used as follows: 100 µM propargyl alcohol (**II-55**), 50 µM 3-azido-7-hydroxycoumarin (**II-58**), 50 µM $CuSO_4$ x 5 H_2O, 250 µM ligand, 5 mM sodium ascorbate, 100 mM KP_i (pH 7)/DMSO (95:5) at 21 °C.

In detail, 40 µL 0.5 M KP_i buffer (pH 7), 20 µL 1.0 mM propargyl alcohol (**II-55**) in water, 10 µL 1.0 mM 3-azido-7-hydroxycoumarin (**II-58**) in DMSO, 100 µL water, and 20 µL 50 mM sodium ascorbate were mixed per reaction. For convenience, the ingredients were combined in a master-mix immediately before the experiments were started, and then 190 µL of this mix was distributed into the wells of the 96-well plate (Greiner 96-well black, F-bottom, Chimney well, polypropylene). The reactions were then initiated by adding 10 µL of a pre-mixed Cu-ligand complex containing 1.0 mM $CuSO_4$ and 5.0 mM ligand (1:5 ratio). To obtain a Cu-ligand of 1:3 or 1:1, the pre-mix concentrations of ligands were adjusted to 3.0 mM and 1.0 mM, accordingly. Stock solutions of TDETA and THPTA were prepared in water, stock solutions of TBTA in DMSO/*t*BuOH (1:4). The blank fluorescence signal was recorded using a mixture of 190 µL master-mix and 10 µL of water for THPTA, TDETA, and the ligand-free reactions, or 10 µL of water/DMSO/*t*BuOH (1:1.8:7.2) for TBTA reactions. The fluorescence output was immediately measured on a Tecan Infinite M1000 Pro plate reader with the following instrument settings: Mode: Fluorescence Intensity, Kinetic; Mode: Top; Interval Time: Minimal; Shaking: 5 sec, 2 mm amplitude, 654 RPM frequency; λ_{Ex}: 407 nm; λ_{Em}: 477 nm; Band Width: 10 nm; Manual Gain: 40 (no gain regulation); Flash Frequency: 100 Hz; Number of Flashes: 15; Duration: 1.5 h; Integration Time: 20 µs; Lag Time: 0 µs; Settle Time: 0 ms; Z-Position: Calculated from A1 (21391 µm).

Calibration of the fluorescence signal in relation to conversion was performed using those conditions that are known to give complete conversion of the hydroxycoumarin azide, namely 50 µM $CuSO_4$, 150 µM THPTA, 100 µM propargyl alcohol (**II-55**), 50 µM 3-azido-7-hydroxycoumarin (**II-58**), 5.0 mM sodium ascorbate in 100 mM KP_i buffer

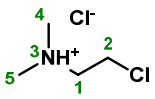
[11] 1-Azidooctane (**II-48**) gave a brown spot when the TLC plate was freshly dipped into the ninhydrin staining solution after reduction of the organic azide towards the primary amine via triphenylphosphine treatment. However, after heating, the spots were sometimes hardly visible but sensitivity could be increased when the plate was briefly dipped into $KMnO_4$ dip. The former azide showed up as purple spots on yellow background on wet TLC plates but disappeared quickly when the plates where heated.

(pH 7)/DMSO (95:5).[118, 119] The fluorescence output for quadruplicate calibration samples was baseline corrected by subtracting the fluorescence output of the Cu-free controls and the mean value generated. After plotting the mean fluorescence signal against the time axis, the maximum fluorescence signal was defined as 100% conversion. Conversions for all other ligands and their varying Cu:ligand ratios were determined relative to the maximum fluorescence output of the calibration sample. All experiments were performed in quadruplicate, and plots were generated with GraphPad Prism.

V.3.4 Synthetic Procedures

(2-Chloroethyl)dimethylamine hydrochloride (II-39·HCl)

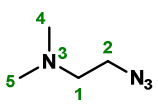
A 250 mL three-necked flask under N_2 atmosphere, equipped with a reflux condenser and a $CaCl_2$-filled drying tube, was sequentially charged with 2-(dimethylamino)-ethanol (15.9 g, 178 mmol, 1.00 eq.) and dry $CHCl_3$ (80 mL), and the solution was stirred at 21 °C. $SOCl_2$ (15.5 mL, 214 mmol, 1.20 eq.) was added dropwise to this solution with a syringe pump over 2 h. A solid precipitated, but when further $SOCl_2$ was added, the solid partially dissolved again. The mixture was heated to reflux at 70 °C for 3 h to give a white solid. Residual solvent was removed *in vacuo*, and the white to pale-yellow residue was suspended in dry EtOH (500 mL) while stirring. The solvent was evaporated to a minimal amount, the resulting solid was dispersed in dry CH_2Cl_2, and the white solid was recovered by filtration (3x). The yellow filtrate was discarded and the precipitate was washed with 100 mL of dry CH_2Cl_2 and dried under vacuum to give 2-chloro-*N*,*N*-dimethylethanamine hydrochloride as a fine white powder (25.1 g, 174 mmol, 98%).



Mp 203.6−206.7 °C (decomposition). **^{1}H NMR** (600 MHz, DMSO-d_6, δ): 11.16 (s, 1H, 3-H), 4.01 (t, *J* = 6.8 Hz, 2H, 2-H), 3.44 (t, *J* = 6.8 Hz, 2H, 1-H), 2.77 (s, 6H, 4-H, 5-H). **^{13}C NMR** (151 MHz, DMSO-d_6, δ): 56.6 (C-1), 42.2 (C-4, C-5), 37.5 (C-2). **FT-IR** (cm^{-1}, neat): 3007, 2975, 2959, 2909, 2625, 2564, 2509, 2471, 1484, 1466, 1429, 1413, 1389, 1319, 1283, 1248, 1178, 1133, 1066, 1058, 1038, 1003, 967, 924, 854, 795, 752, 681, 474. **HRMS** (ESI) *m*/*z*: $[M - Cl]^+$ calcd for $C_4H_{11}ClN$, 108.0575; found, 108.0574. **CAS** 4584-46-7.

2-Azido-*N*,*N*-dimethylethan-1-amine (II-43)

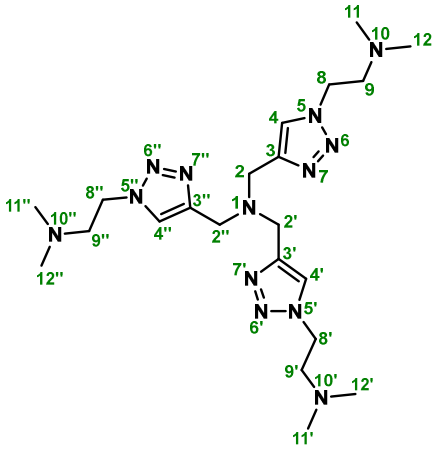
In a 500 mL round-bottom flask under N_2 atmosphere, 2-chloro-*N*,*N*-dimethylethanamine hydrochloride (**II-39·HCl**, 12.8 g, 88.7 mmol, 1.00 eq.) was dissolved in deionised water (180 mL, 0.5 M), and then sodium azide (11.5 g, 178 mmol, 2.00 eq.) was added. The mixture was stirred at 80 °C for 18 h. After cooling, the mixture was adjusted to pH 10 by adding 1 M sodium hydroxide solution and extracted with Et_2O (6 x 100 mL). The combined organic phases were dried over $MgSO_4$ and filtered over degreased cotton wool. The solvent was removed under reduced pressure and the ethereal phase was repeatedly diluted in *n*-pentane to minimise the loss of volatile product. In this step, the use of *n*-pentane during concentration allowed higher pressures for solvent evaporation (>800 mbar) and assisted co-evaporation of Et_2O. Nevertheless, prolonged exposure to low pressures for complete solvent removal was avoided. In addition, concentration was performed in an over-dimensioned flask to allow condensation of the low-boiling product on the glass surface of the product flask. The desired azide (**II-43**, 10.0 g, 87.9 mmol, 99%) was obtained after solvent evaporation under reduced pressure as a colourless and very volatile liquid and used without further purification. Storage at –20 °C under argon.



^{1}H NMR (600 MHz, $CDCl_3$, δ): 3.33 (t, *J* = 6.3 Hz, 2H, 1-H), 2.48 (t, *J* = 6.3 Hz, 2H, 2-H), 2.25 (s, 6H, 4-H, 5-H). **^{13}C NMR** (151 MHz, $CDCl_3$, δ): 58.2 (C-2), 49.1 (C-1), 45.5 (C-4, C-5). **FT-IR** (cm^{-1}, neat): 2975, 2946, 2862, 2822, 2772, 2095, 1456, 1375, 1346, 1276, 1179, 1153, 1098, 1042, 972, 943, 845, 778, 667, 644, 556, 528. **HRMS** (ESI) *m*/*z*: $[M + H]^+$ calcd for $C_4H_{11}N_4$, 115.0978; found, 115.0979. **CAS** 86147-04-8.

2-(4-((Bis((1-(2-(dimethylamino)ethyl)-1*H*-1,2,3-triazol-4-yl)methyl)amino)methyl)-1*H*-1,2,3-triazol-1-yl)-*N*,*N*-dimethylethan-1-amine (II-44, TDETA)

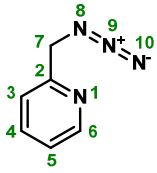
Under N_2 atmosphere, 2-azido-*N*,*N*-dimethylethan-1-amine (**II-43**, 8.77 g, 67.8 mmol, 6.00 eq.) and tripropargylamine (1.68 g, 12.8 mmol, 1.00 eq.) were dissolved in 25.6 mL *t*BuOH/H_2O (3:1) (2 mL/mmol tripropargylamine). Aqueous $Cu(OAc)_2$ (233 mg, 1.28 mmol, 0.10 eq., 0.4 M) was added, causing a colour shift to turquoise. Immediately followed by aqueous sodium ascorbate (507 mg, 2.56 mmol, 0.20 eq., 0.8 M), the reaction turned clear yellow, and a large burst of heat was observed within 1 min. After a few minutes, the clear yellow solution had turned turbid yellow. The reaction was further stirred at 20 °C for 14 h. The solvent was removed *in vacuo* to leave a thick yellow oil, which was dissolved in MeOH and applied to a plug of neutral aluminium oxide (50−200 µm, Brockman I, 8 cm) to remove copper by filtration.[12] Methanolic fractions of the eluted product were concentrated and dissolved in CH_2Cl_2. Celite was added, and the solvent was removed *in vacuo* to immobilise the product. The solid was then applied to silica chromatography with CH_2Cl_2 + 6% 7 N NH_3 in MeOH as eluent. Removal of solvent, redissolving in CH_2Cl_2 and repeated precipitation with PE, followed by drying under high vacuum, yielded the desired ligand TDETA (**II-44**, 5.72 g, 12.1 mmol, 94%) as a fluffy odourless white solid. Storage at 4 °C under argon.



R_f (CH_2Cl_2 + 7% 7 N NH_3 in MeOH): 0.32 ($KMnO_4$ stain). **Mp** 96.7−99.0 °C. **^{1}H NMR** (600 MHz, $CDCl_3$, δ): 7.81 (s, 3H, 4-H, 4'-H, 4"-H), 4.41 (t, *J* = 6.5 Hz, 6H, 8-H, 8'-H, 8"-H), 3.71 (s, 6H, 2-H, 2'-H, 2"-H), 2.74 (t, *J* = 6.5 Hz, 6H, 9-H, 9'-H, 9"-H), 2.24 (s, 18H, 11-H, 11'-H, 11"-H, 12-H, 12'-H, 12"-H). **^{13}C NMR** (151 MHz, $CDCl_3$, δ): 143.9 (C-3, C-3', C-3"), 124.3 (C-4, C-4', C-4"), 58.9 (C-9, C-9', C-9"), 48.3 (C-8, C-8', C-8"), 47.2 (C-2, C-2', C-2"), 45.5 (C-11, C-11', C-11", C-12, C-12', C-12"). **FT-IR** (cm^{-1}, neat): 3146, 3118, 3079, 2978, 2945, 2861, 2822, 2767, 1553, 1458, 1384, 1354, 1330, 1322, 1267, 1224, 1212, 1154, 1115, 1105, 1083, 1045, 968, 953, 929, 866, 844, 806, 780, 745, 712, 702, 678, 666, 655, 548, 516, 466. **HRMS** (ESI) *m*/*z*: $[M + H]^+$ calcd for $C_{21}H_{40}N_{13}$, 474.3524; found, 474.3516. **CAS** 2922309-56-4.

2-(Azidomethyl)pyridine (II-46)

2-(Azidomethyl)pyridine was synthesised according to a modified protocol from Ogden *et al.*[161] To 2-(chloromethyl)pyridine hydrochloride (2.00 g, 12.2 mmol, 1.00 eq.) and sodium azide (2.38 g, 36.6 mmol, 3.00 eq.) in a 250 mL round-bottom flask were added 48.8 mL of water (4 mL/mmol hydrochloride). The reaction was heated to 50 °C and allowed to stir for 21 h. The orange-brown solution was cooled to room temperature and adjusted to pH 10–11 with 1 M NaOH. The aqueous phase that had turned red-brown was then extracted with CH_2Cl_2 (3 × 50 mL, aqueous phase remains bright orange). The yellow organic phase was dried with $MgSO_4$, filtered over degreased cotton wool and the product **II-46** obtained as a deep yellow oil (1.44 g, 10.8 mmol, 88%) after solvent removal. The azide was used without further purification and stored at –20 °C under argon.



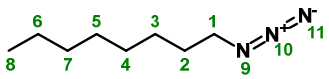
R_f (PE/EtOAc 65:35): 0.38 (UV). **^{1}H NMR** (600 MHz, $CDCl_3$, δ): 8.61 – 8.56 (m_c, 1H, 6-H), 7.70 (qt, *J* = 7.7 Hz, 1H, 4-H), 7.33 (d, *J* = 7.9 Hz, 1H, 3-H), 7.25 – 7.21 (m_c, 1H, 5-H), 4.47 (s, 2H, 7-H). **^{13}C NMR** (151 MHz, $CDCl_3$, δ): 155.8 (C-2), 149.8 (C-6), 137.1 (C-4), 123.0 (C-5), 122.1 (C-3), 55.8 (C-7). **FT-IR** (cm^{-1}, neat): 3053, 3013, 2930, 2868, 2095, 1591, 1571, 1474, 1436, 1342, 1271, 1218, 1149, 1098, 1048, 996, 960, 918, 887, 835, 756, 729, 666, 627, 586, 556. **HRMS** (ESI) *m*/*z*: $[M + H]^+$ calcd for $C_6H_7N_4$, 135.0665; found, 135.0666. **CAS** 609770-35-6.

1-Azidooctane (II-48)

1-Azidooctane was synthesised according to a modified protocol from Gannarapu *et al.*[162] 1-Iodooctane (4.50 g, 18.7 mmol, 1.00 eq.) and sodium azide (3.66 g, 56.2 mmol, 3.00 eq.) were added to a round-bottom flask and dissolved in acetone/water (3:1) (75 mL, 4 mL/mmol 1-iodooctane). The homogenous, clear solution was heated to 50 °C for 18 h.

[12] Aqueous extraction of TDETA from organic solvents is not possible, as the ligand remains in the aqueous phase!

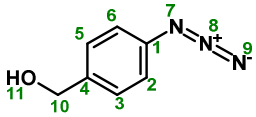
After completion, the reaction was cooled to room temperature and 50 mL of water was added for dilution. The aqueous phase was then extracted with *n*-pentane (5 x 50 mL). The combined extracts were washed with brine (2 x 50 mL), the organic phases were dried over anhydrous Na_2SO_4, and filtered over degreased cotton wool. Careful solvent removal under reduced pressure provided the product **II-48** as a volatile colourless liquid in quantitative yield (2.88 g, 18.6 mmol, 99%). The azide was used without further purification and stored at –20 °C under argon.



R_f (PE/Et_2O 95:5): 0.84 (azide stain). **^{1}H NMR** (600 MHz, $CDCl_3$, δ): 3.25 (t, *J* = 7.0 Hz, 2H, 1-H), 1.60 (p, *J* = 7.1 Hz, 2H, 2-H), 1.36 (p, *J* = 7.0 Hz, 6.6 Hz, 2H, 3-H), 1.33 – 1.23 (m, 8H, 4-H, 5-H, 6-H, 7-H), 0.88 (t, *J* = 6.9 Hz, 3H, 8-H). **^{13}C NMR** (151 MHz, $CDCl_3$, δ): 51.6 (C-1), 31.9 (C-6), 29.3 (C-4), 29.3 (C-5), 29.0 (C-2), 26.9 (C-3), 22.8 (C-7), 14.2 (C-8). **FT-IR** (cm^{-1}, neat): 2956, 2926, 2856, 2092, 1466, 1457, 1377, 1349, 1259, 1124, 933, 901, 723, 675, 640, 558. **CAS** 7438-05-3.

(4-Azidophenyl)methanol (II-50)

(4-Azidophenyl)methanol was synthesised according to a modified protocol from Park *et al*.[164] A 250 mL three-necked flask under N_2 atmosphere, equipped with a quick-fit thermometer and connection to the Schlenk line, was charged with a mixture of commercially available 4-aminobenzyl alcohol (3.00 g, 24.4 mmol, 1.00 eq.) and sodium nitrite (2.52 g, 36.5 mmol, 1.50 eq.) in distilled water (50 mL). Aqueous 6 M HCl (16.2 mL, 87.4 mmol, 4.00 eq.) was added dropwise at 0 °C (syringe pump at 1.0 mL/min). The resulting olive-green suspension was stirred at 0 °C for 30 min over which time the solid had dissolved to give a brown solution. Sodium azide (6.34 g, 97.4 mmol, 4.00 eq.) in 15 mL water was added dropwise to the reaction mixture at 0 °C (syringe pump at 1.0 mL/min) and after completion of the addition, the orange suspension was stirred at room temperature for 2 h. The product mixture was extracted with Et_2O (3 x 50 mL), the combined organic layers were washed with brine (50 mL), dried with anhydrous Na_2SO_4, and filtered over degreased cotton wool. The product was obtained in quantitative yield as an orange viscous oil (3.61 g, 24.2 mmol, 99%) and crystallised at –20 °C. The azide was used without further purification and stored at –20 °C under argon.



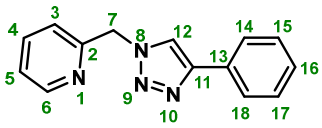
R_f (Et_2O): 0.66 (UV). **Mp** 32.0−34.8 °C. **^{1}H NMR** (600 MHz, $CDCl_3$, δ): 7.34 (d, *J* = 8.1 Hz, 2H, 3-H, 5-H), 7.01 (d, *J* = 8.2 Hz, 2H, 2-H, 6-H), 4.65 (s, 2H, 10-H), 1.92 (brs, 1H, 11-H). **^{13}C NMR** (151 MHz, $CDCl_3$, δ): 139.5 (C-1), 137.7 (C-4), 128.6 (C-3, C-5), 119.2 (C-2, C-6), 64.8 (C-10). **FT-IR** (cm^{-1}, neat): 3307, 2927, 2875, 2408, 2256, 2103, 1608, 1582, 1506, 1458, 1419, 1368, 1285, 1208, 1179, 1129, 1112, 1025, 1011, 827, 814, 773, 718, 711, 704, 696, 688, 667, 644, 535, 493, 486, 467. **CAS** 31499-54-4.

General Preparative Procedure for Preparative CuAAC Reactions to Access Products II-57a−g

Organic azide (1.0 eq.) and alkyne (1.05 eq.) are weighed into a 12 mL vial. The ligand TDETA **II-44** (5.0 mol%) is added and the reactants are dissolved in *t*BuOH (0.38 M final azide concentration). Aqueous solutions of $Cu(OAc)_2$ (0.4 M, 5.0 mol%) and sodium ascorbate (0.1 eq.) are added sequentially to initiate the click reaction. The vials are incubated at 20 °C in a shaker and stirred for 60 min at 700 RPM. Reaction solutions are diluted with MeOH and immobilised on Celite. Purification using flash chromatography on silica provides the products as white to off-white solids.

2-((4-Phenyl-1*H*-1,2,3-triazol-1-yl)methyl)pyridine (II-57a)

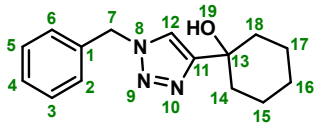
Following the general procedure for preparative CuAAC reactions, 2-(azidomethyl)pyridine (**II-46**, 96.8 mg, 722 µmol, 1.00 eq.) and phenylacetylene (**II-53**, 77.4 mg, 77.4 µmol, 1.05 eq.) in *t*BuOH (1.90 mL) are converted in the presence of TDETA (**II-44**, 17.1 mg, 36.1 µmol, 5.0 mol%), 90.2 µL $Cu(OAc)_2$ (6.56 mg, 36.1 µmol, 5.0 mol%, 0.4 M in water), and 144.4 µL sodium ascorbate (14.3 mg, 72.2 µmol, 0.1 eq., 0.5 M in water) to triazole **II-57a**. Chromatography on silica with PE/EtOAc (80:20) provided the product (**II-57a**, 162 mg, 685 µmol, 95%) as a white solid.



R_f (EtOAc): 0.38 (UV). **Mp** 80.0−83.1 °C. **^{1}H NMR** (600 MHz, $CDCl_3$, δ): 8.61 (d, *J* = 4.6 Hz, 1H, 6-H), 7.93 (s, 1H, 12-H), 7.84 – 7.80 (m_c, 2H, 14-H, 18-H), 7.68 (dt, *J* = 7.7 Hz, 1.8 Hz, 1H, 5-H), 7.40 (t, *J* = 7.7 Hz, 2H, 15-H, 17-H), 7.31 (tt, *J* = 7.2 Hz, 1.3 Hz, 1H, 16-H), 7.28 – 7.24 (m, 1H, 4-H), 7.23 (d, *J* = 7.8 Hz, 1H, 3-H), 5.69 (s, 2H, 7-H). **^{13}C NMR** (151 MHz, $CDCl_3$, δ): 154.7 (C-2), 149.9 (C-6), 148.4 (C-11), 137.5 (C-5), 130.7 (C-13), 128.9 (C-15, C-17), 128.3 (C-16), 125.8 (C-14, C-18), 123.6 (C-4), 122.6 (C-3), 120.3 (C-12), 55.9 (C-7). **FT-IR** (cm^{-1}, neat): 3129, 3096, 3085, 3062, 3048, 3009, 2979, 2938, 1607, 1586, 1571, 1483, 1472, 1465, 1437, 1422, 1364, 1321, 1287, 1227, 1201, 1149, 1078, 1050, 1031, 994, 975, 945, 915, 893, 834, 814, 792, 768, 754, 727, 707, 694, 624, 599, 508, 478, 455. **HRMS** (ESI) *m/z*: $[M + H]^+$ calcd for $C_{14}H_{13}N_4$, 237.1135; found, 237.1138. **CAS** 1192206-01-1.

1-(1-Benzyl-1*H*-1,2,3-triazol-4-yl)cyclohexan-1-ol (II-57b)

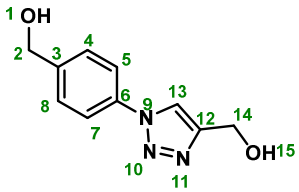
Following the general procedure for preparative CuAAC reactions, benzyl azide (**II-2**, 107 mg, 752 µmol, 1.00 eq., 94%) and 1-ethynyl-1-cyclohexanol (**II-54**, 98.1 mg, 790 µmol, 1.05 eq.) in *t*BuOH (1.98 mL) are converted in the presence of TDETA (**II-44**, 17.8 mg, 37.6 µmol, 5.0 mol%), 94.0 µL $Cu(OAc)_2$ (6.83 mg, 37.6 µmol, 5.0 mol%, 0.4 M in water), and 150.4 µL sodium ascorbate (14.9 mg, 75.2 µmol, 0.1 eq., 0.5 M in water) to triazole **II-57b**. Chromatography on silica with CH_2Cl_2/MeOH (95:5) provided the product (**II-57b**, 180 mg, 701 µmol, 93%) as a white solid.



R_f (CH_2Cl_2/MeOH 92:8): 0.44 ($FeCl_3$, then $KMnO_4$ stain)[13]. **Mp** 123.3−126.0 °C. **^{1}H NMR** (600 MHz, $CDCl_3$, δ): 7.39 – 7.33 (m, 4H, 3-H, 4-H, 5-H, 12-H), 7.28 – 7.25 (m, 2H, 2-H, 6-H), 5.50 (s, 2H, 7-H), 2.36 (s, 1H, 19-H), 1.98 – 1.90 (m_c, 2H, 14''-H, 18''-H), 1.88 – 1.81 (m, 2H, 14'-H, 18'-H), 1.77 – 1.68 (m_c, 2H, 15''-H, 17''-H), 1.65 – 1.58 (m_c, 1H, 16''-H), 1.57 – 1.49 (m, 2H, 15'-H, 17'-H), 1.38 – 1.29 (m_c, 1H, 16'-H). **^{13}C NMR** (151 MHz, $CDCl_3$, δ): 156.2 (C-11), 134.8 (C-1), 129.2 (C-3, C-5), 128.8 (C-4), 128.2 (C-2, C-6), 119.6 (C-12), 69.7 (C-13), 54.3 (C-7), 38.2 (C-14, C-18), 25.5 (C-16), 22.1 (C-15, C-17). **FT-IR** (cm^{-1}, neat): 3294, 2932, 2922, 2855, 1737, 1604, 1585, 1498, 1456, 1453, 1426, 1398, 1365, 1352, 1334, 1316, 1266, 1250, 1218, 1180, 1159, 1141, 1131, 1077, 1063, 1054, 1037, 1029, 999, 980, 931, 910, 893, 853, 832, 796, 779, 729, 717, 696, 662, 619, 582, 516, 506, 497, 459. **HRMS** (ESI) *m/z*: $[M + H]^+$ calcd for $C_{15}H_{20}N_3O$, 258.1601; found, 258.1600. **CAS** 83027-66-1.

(4-(4-(Hydroxymethyl)-1*H*-1,2,3-triazol-1-yl)phenyl)methanol (II-57c)

Following the general procedure for preparative CuAAC reactions, (4-azidophenyl)methanol (**II-50**, 117 mg, 782 µmol, 1.00 eq.) and propargyl alcohol (**II-55**, 46.0 mg, 821 µmol, 1.05 eq.) in *t*BuOH (2.06 mL) are converted in the presence of TDETA (**II-44**, 18.5 mg, 39.1 µmol, 5.0 mol%), 97.7 µL $Cu(OAc)_2$ (7.10 mg, 39.1 µmol, 5.0 mol%, 0.4 M in water), and 156.3 µL sodium ascorbate (15.5 mg, 78.2 µmol, 0.1 eq., 0.5 M in water) to triazole **II-57c**. Chromatography on silica with CH_2Cl_2/MeOH (90:10) provided the product (**II-57c**, 149 mg, 728 µmol, 93%) as a white solid.



R_f (CH_2Cl_2/MeOH 90:10): 0.28 (UV). **Mp** 129.8−132.9 °C. **^{1}H NMR** (600 MHz, DMSO-d_6, δ): 8.64 (s, 1H, 13-H), 7.85 (d, *J* = 8.4 Hz, 2H, 5-H, 7-H), 7.51 (d, *J* = 8.2 Hz, 2H, 4-H, 8-H), 5.33 (t, *J* = 5.7 Hz, 1H, 1-H), 5.31 (t, *J* = 5.6 Hz, 1H, 15-H), 4.61 (d, *J* = 5.5 Hz, 2H, 14-H), 4.57 (d, *J* = 5.7 Hz, 2H, 2-H). **^{13}C NMR** (151 MHz, DMSO-d_6, δ): 149.0 (C-12), 143.0 (C-3), 135.4 (C-6), 127.6 (C-4, C-8), 120.9 (C-13), 119.7 (C-5, C-7), 62.2 (C-2), 55.0 (C-14). **FT-IR** (cm^{-1}, neat): 3339, 3176, 3135, 3101, 2859, 2748, 2635, 1610, 1595, 1562, 1518, 1456, 1444, 1407, 1357, 1326, 1286, 1245, 1228, 1214, 1194, 1174, 1108, 1065, 1037, 1020, 994, 951, 849, 821, 803, 760,

[13] Triazoles **II-57b** and **II-57d** showed weak UV-active spots on TLC plates only at very high concentrations, and were moreover difficult to stain with $KMnO_4$ stain and insensitive to low sample loading. Other staining methods, such as *p*-anisaldehyde, iodine, phosphomolybdic acid (PMA), ninhydrin, Dragendorff's reagent, and cerium ammonium molybdate (CAM) failed. However, the result of the $KMnO_4$ stain could be significantly increased when TLC plates were first dipped into 1% $FeCl_3$ solution and gently heated, before dipping the plates into $KMnO_4$ stain and heating again.

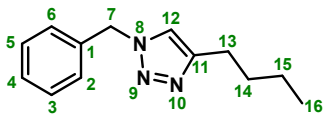
735, 696, 671, 639, 625, 529, 520, 493, 463. **HRMS** (ESI) *m/z*: $[M + H]^+$ calcd for $C_{10}H_{12}N_3O_2$, 206.0924; found, 206.0928. **CAS** 1026133-60-7.

Recycling of the Cu-ligand TDETA II-44

Although TDETA **II-44** was used in catalytic amounts of 5 mol% throughout the experiments on analytical and preparative scale, we sought recycling of the precious ligand TDETA. Recycling and re-usability of the ligand might be of increased interest for industrial applications or reactions on a large scale. The click reaction between (4-azidophenyl)methanol (**II-50**) and propargyl alcohol (**II-55**) to form triazole **II-57c** on a scale of 4 mmol was chosen as a representative example for the recycling of the Cu-ligand TDETA **II-44**. Briefly, (4-Azidophenyl)methanol (**II-50**, 600 mg, 4.02 mmol, 1.00 eq.), propargyl alcohol (**II-55**, 237 mg, 4.22 mmol, 1.05 eq.), and TDETA (**II-44**, 95.3 mg, 201 µmol, 5.00 mol%) were dissolved in *t*BuOH (11.1 mL). Addition of aqueous solutions of 0.4 M $Cu(OAc)_2$ (503 µL, 36.5 mg, 201 µmol, 5.00 mol%) and 0.5 M sodium ascorbate (805 µL, 79.7 mg, 402 µmol, 10.00 mol%) started the reaction, which was allowed to stir for 60 min. The solvent was evaporated, leaving a thick yellow oil, which was subsequently taken up in MeOH and immobilised on Celite. Chromatography on silica using CH_2Cl_2/MeOH (90:10) provided the triazole product **II-57c** as a white solid in a yield of 99% (814 mg, 3.96 mmol). However, the ligand did not elute under these conditions. Thus, the column was washed with a small amount of CH_2Cl_2 and then further processed with CH_2Cl_2 + 8% 7 N NH_3 in MeOH to provide the recovered copper-free ligand TDETA **II-44** in a yield of 80% (76.2 mg, 161 mmol), proving that recycling of TDETA is feasible and adequate.

1-Benzyl-4-butyl-1*H*-1,2,3-triazole (II-57d)

Following the general procedure for preparative CuAAC reactions, benzyl azide (**II-2**, 103 mg, 730 µmol, 1.00 eq., 94%) and 1-hexyne (**II-56**, 63.0 mg, 767 µmol, 1.05 eq.) in *t*BuOH (2.04 mL) are converted in the presence of TDETA (**II-44**, 17.3 mg, 36.5 µmol, 5.0 mol%), 91.3 µL $Cu(OAc)_2$ (6.63 mg, 36.5 µmol, 5.0 mol%, 0.4 M in water), and 146.0 µL sodium ascorbate (14.5 mg, 73.0 µmol, 0.1 eq., 0.5 M in water) to triazole **II-57d**. Chromatography on silica with CH_2Cl_2/MeOH (95:5) provided the product (**II-57d**, 146 mg, 680 µmol, 93%) as a white solid.

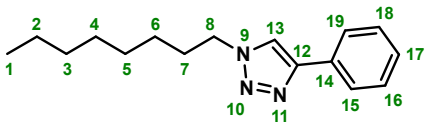


R_f (CH_2Cl_2/MeOH 92:8): 0.74 ($FeCl_3$, then $KMnO_4$ stain)[14]. **Mp** 59.6−61.4 °C. **^{1}H NMR** (600 MHz, $CDCl_3$, δ): 7.39 – 7.32 (m, 3H, 3-H, 4-H, 5-H), 7.27 – 7.23 (m, 2H, 2-H, 6-H), 7.17 (s, 1H, 12-H), 5.49 (s, 2H, 7-H), 2.69 (t, *J* = 7.8 Hz, 2H, 13-H), 1.62 (p, *J* = 7.7 Hz, 2H, 14-H), 1.36 (h, *J* = 7.4 Hz, 2H, 15-H), 0.91 (t, *J* = 7.4 Hz, 3H, 16-H). **^{13}C NMR** (151 MHz, $CDCl_3$, δ): 149.1 (C-11), 135.2 (C-1), 129.2 (C-3, C-5), 128.7 (C-4), 128.1 (C-2, C-6), 120.6 (C-12), 54.1 (C-7), 31.6 (C-14), 25.5 (C-13), 22.5 (C-15), 13.9 (C-16). **FT-IR** (cm^{-1}, neat): 3114, 3064, 3035, 2967, 2960, 2923, 2875, 2857, 1706, 1557, 1495, 1459, 1448, 1434, 1365, 1352, 1332, 1310, 1295, 1287, 1228, 1215, 1206, 1176, 1131, 1102, 1073, 1052, 1033, 1002, 930, 901, 856, 825, 797, 748, 731, 704, 692, 673, 642, 574, 478, 469. **HRMS** (ESI) *m/z*: $[M + H]^+$ calcd for $C_{13}H_{18}N_3$, 216.1495; found, 216.1498. **CAS** 871689-95-1.

1-Octyl-4-phenyl-1*H*-1,2,3-triazole (II-57e)

Following the general procedure for preparative CuAAC reactions, 1-azidooctane (**II-48**, 110 mg, 706 µmol, 1.00 eq.) and phenylacetylene (**II-53**, 75.7 mg, 741 µmol, 1.05 eq.) in *t*BuOH (1.86 mL) are converted in the presence of TDETA (**II-44**, 16.7 mg, 35.3 µmol, 5.0 mol%), 88.2 µL $Cu(OAc)_2$ (6.41 mg, 35.3 µmol, 5.0 mol%, 0.4 M in water), and 141.2 µL sodium ascorbate (14.0 mg, 70.6 µmol, 0.1 eq., 0.5 M in water) to triazole **II-57e**. Chromatography on silica with PE/EtOAc (80:20) provided the product (**II-57e**, 176 mg, 682 µmol, 97%) as a white solid.

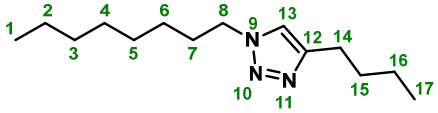
[14] Triazoles **II-57b** and **II-57d** showed weak UV-active spots on TLC plates only at very high concentrations, and were moreover difficult to stain with $KMnO_4$ stain and insensitive to low sample loading. Other staining methods, such as *p*-anisaldehyde, iodine, phosphomolybdic acid (PMA), ninhydrin, Dragendorff's reagent, and cerium ammonium molybdate (CAM) failed. However, the result of the $KMnO_4$ stain could be significantly increased when TLC plates were first dipped into 1% $FeCl_3$ solution and gently heated, before dipping the plates into $KMnO_4$ stain and heating again.



R_f (PE/EtOAc 60:40): 0.64 (UV). **Mp** 77.8−79.6 °C. **^{1}H NMR** (600 MHz, $CDCl_3$, δ): 7.83 (d, *J* = 7.6 Hz, 2H, 15-H, 19-H), 7.74 (s, 1H, 13-H), 7.42 (t, *J* = 7.6 Hz, 2H, 16-H, 18-H), 7.33 (t, *J* = 7.4 Hz, 1H, 17-H), 4.39 (t, *J* = 7.3 Hz, 2H, 8-H), 1.95 (p, *J* = 7.2 Hz, 2H, 7-H), 1.39 – 1.31 (m, 4H, 5-H, 6-H), 1.31 – 1.20 (m, 6H, 2-H, 3-H, 4-H), 0.87 (t, *J* = 6.9 Hz, 3H, 1-H). **^{13}C NMR** (76 MHz, $CDCl_3$, δ): 147.9 (C-12), 130.9 (C-14), 129.0 (C-16, C-18), 128.2 (C-17), 125.8 (C-15, C-19), 119.5 (C-13), 50.6 (C-8), 31.8 (C-3), 30.5 (C-7), 29.2 (C-4), 29.1 (C-5), 26.6 (C-6), 22.7 (C-2), 14.2 (C-1). **FT-IR** (cm^{-1}, neat): 3121, 3093, 3064, 3045, 2954, 2917, 2871, 2848, 1609, 1578, 1485, 1464, 1439, 1374, 1357, 1335, 1303, 1215, 1166, 1079, 1052, 1025, 1003, 976, 913, 839, 761, 708, 694, 527, 517, 491, 465. **HRMS** (ESI) *m/z*: $[M + H]^+$ calcd for $C_{16}H_{24}N_3$, 258.1965; found, 258.1969. **CAS** 853052-50-3.

4-Butyl-1-octyl-1*H*-1,2,3-triazole (II-57f)

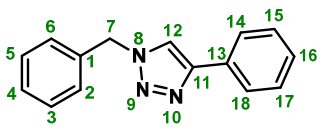
Following the general procedure for CuAAC, 1-azidooctane (**II-48**, 116 mg, 749 µmol, 1.00 eq.) and 1-hexyne (**II-56**, 64.6 mg, 786 µmol, 1.05 eq.) in *t*BuOH (1.97 mL) are converted in the presence of TDETA (**II-44**, 17.7 mg, 37.4 µmol, 5.0 mol%), 93.6 µL $Cu(OAc)_2$ (6.80 mg, 37.4 µmol, 5.0 mol%, 0.4 M in water), and 149.8 µL sodium ascorbate (14.8 mg, 74.9 µmol, 0.1 eq., 0.5 M in water) to triazole **II-57f**. Chromatography on silica with PE/EtOAc (80:20) to yield the triazole (**II-57f**, 173 mg, 728 µmol, 97%) as a colourless oil that crystallised at room temperature.



R_f (PE/EtOAc 60:40): 0.55 ($KMnO_4$ stain). **^{1}H NMR** (600 MHz, $CDCl_3$, δ): 7.23 (s, 1H, 13-H), 4.29 (t, *J* = 7.3 Hz, 2H, 8-H), 2.71 (t, *J* = 7.7 Hz, 2H, 14-H), 1.87 (p, *J* = 7.1 Hz, 2H, 7-H), 1.65 (p, *J* = 7.7 Hz, 2H, 15-H), 1.38 (h, *J* = 7.4 Hz, 2H, 16-H), 1.33 – 1.29 (m, 4H, 5-H, 6-H), 1.29 – 1.20 (m, 6H, 2-H, 3-H, 4-H), 0.93 (t, *J* = 7.4 Hz, 3H, 17-H), 0.87 (t, *J* = 6.9 Hz, 3H, 1-H). **^{13}C NMR** (151 MHz, $CDCl_3$, δ): 148.5 (C-12), 120.4 (C-13), 50.3 (C-8), 31.8 (C-3), 31.8 (C-15), 30.5 (C-7), 29.2 (C-5), 29.1 (C-4), 26.7 (C-6), 25.5 (C-14), 22.7 (C-2), 22.5 (C-16), 14.2 (C-1), 14.0 (C-17). **FT-IR** (cm^{-1}, neat): 3130, 3076, 2955, 2926, 2856, 1551, 1464, 1459, 1437, 1378, 1315, 1215, 1142, 1106, 1046, 927, 784, 724, 664. **HRMS** (HRMS-ESI) *m/z*: $[M + H]^+$ calcd for $C_{14}H_{28}N_3$, 238.2278; found, 238.2282. **CAS** 1144506-45-5.

1-Benzyl-4-phenyl-1*H*-1,2,3-triazole (II-57g)

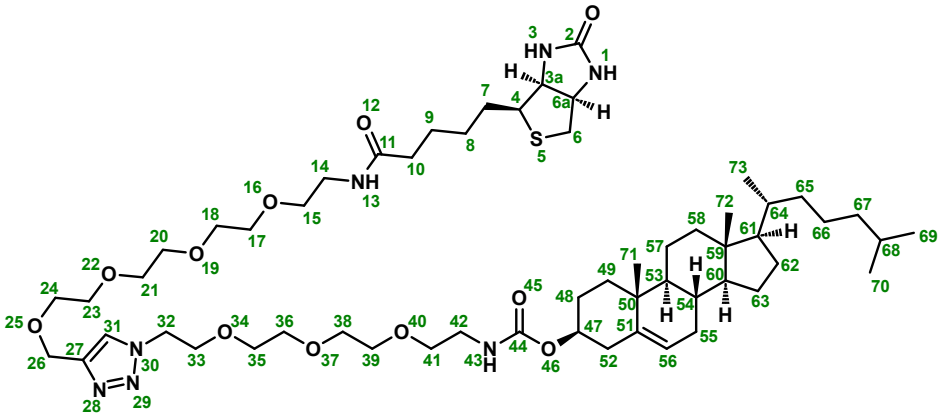
Following the general procedure for preparative CuAAC reactions, benzyl azide (**II-2**, 101 mg, 716 µmol, 1.00 eq., 94%) and phenylacetylene (**II-53**, 76.8 mg, 752 µmol, 1.05 eq.) in *t*BuOH (1.88 mL) are converted in the presence of TDETA (**II-44**, 17.0 mg, 35.8 µmol, 5.0 mol%), 89.5 µL $Cu(OAc)_2$ (6.50 mg, 35.8 µmol, 5.0 mol%, 0.4 M in water), and 143.2 µL sodium ascorbate (14.2 mg, 71.6 µmol, 0.1 eq., 0.5 M in water) to triazole **II-57g**. Chromatography on silica with CH_2Cl_2/MeOH gradient (100:0 to 95:5) provided the product (**II-57g**, 156 mg, 663 µmol, 93%) as a white solid.



R_f (PE/EtOAc 60:40): 0.54 (UV). **R_f** (PE/CH_2Cl_2 20:80): 0.22 (UV). **Mp** 127.5−131.3 °C. **^{1}H NMR** (600 MHz, $CDCl_3$, δ): 7.80 – 7.78 (m_c, 2H, 14-H, 18-H), 7.66 (s, 1H, 12-H), 7.40 – 7.34 (m, 5H, 3-H, 4-H, 5-H, 15-H, 17-H), 7.32 – 7.28 (m, 3H, 2-H, 6-H, 16-H), 5.55 (s, 2H, 7-H). **^{13}C NMR** (151 MHz, $CDCl_3$, δ): 148.2 (C-11), 134.7 (C-1), 130.6 (C-13), 129.2 (C-3, C-5), 128.9 (C-15, C-17), 128.8 (C-4), 128.2 (C-16), 128.1 (C-2, C-6), 125.7 (C-14, C-18), 119.6 (C-12), 54.2 (C-7). **FT-IR** (cm^{-1}, neat): 3143, 3081, 3029, 2976, 1987, 1966, 1607, 1579, 1552, 1494, 1482, 1469, 1450, 1428, 1362, 1334, 1323, 1294, 1282, 1256, 1224, 1210, 1194, 1174, 1158, 1141, 1076, 1046, 1026, 1002, 993, 972, 952, 924, 909, 857, 825, 808, 786, 768, 728, 707, 695, 651, 617, 588, 507, 480. **HRMS** (HRMS-ESI) *m/z*: $[M + H]^+$ calcd for $C_{15}H_{14}N_3$, 236.1182; found, 236.1186. **CAS** 108717-96-0.

(3*S*,8*S*,9*S*,10*R*,13*R*,14*S*,17*R*)-10,13-Dimethyl-17-((*R*)-6-methylheptan-2-yl)-2,3,4,7,8,9,10,11,12,13,14,15,16,17-tetradecahydro-1*H*-cyclopenta[*a*]phenanthren-3-yl (2-(2-(2-(2-(4-(15-oxo-19-((3a*S*,4*S*,6a*R*)-2-oxohexahydro-1*H*-thieno[3,4-*d*]imidazol-4-yl)-2,5,8,11-tetraoxa-14-azanonadecyl)-1*H*-1,2,3-triazol-1-yl)ethoxy)ethoxy)ethoxy)ethyl)carbamate (II-67)

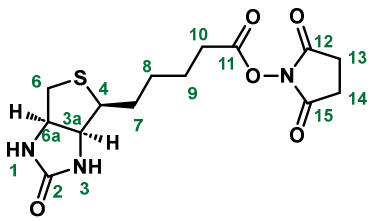
A 50 mL round-bottom flask was charged with acetylen-PEG$_4$-biotin (**II-65**, 63.0 mg, 130 µmol, 1.00 eq.), cholesteryl-TEG-azide (**II-66**, 99.0 mg, 157 µmol, 1.20 eq.), and TDETA (**II-44**, 6.20 mg, 13.08 µmol, 0.10 eq.). $CHCl_3$ (6.5 mL, 50 µL/µmol biotin) was added to dissolve the solids. A solution of $Cu(OAc)_2$ (1.31 mL, 2.38 mg, 13.1 µmol, 0.10 eq., 10 mM in EtOH) was added, and additional EtOH (5.2 mL) was supplemented to give a 1:1 mixture of $CHCl_3$/EtOH. Aqueous sodium ascorbate (131 µL, 5.18 mg, 26.2 µmol, 0.20 eq., 200 mM in water) was added, and the reaction was stirred at 21 °C for 19 h. The solvent was removed *in vacuo*, the crude product dissolved in CH_2Cl_2/MeOH (92:8), and chromatographed on silica in the same solvent mixture. The desired click product (**II-67**, 126 mg, 116 µmol, 88%) was obtained as a colourless to white foam.



R_f (CH_2Cl_2/MeOH 90:10): 0.40 ($KMnO_4$ stain). **^{1}H NMR** (900 MHz, $CDCl_3$, δ): 7.76 (s, 1H), 6.89 (s, 1H), 6.46 (s, 1H), 5.56 (d, *J* = 57.9 Hz, 1H), 5.35 (dt, *J* = 5.1, 2.2 Hz, 1H), 5.25 (t, *J* = 5.8 Hz, 1H), 4.66 (s, 2H), 4.54 (t, *J* = 4.9 Hz), 4.47 (dp, *J* = 16.1, 4.8 Hz, 2H), 4.30 (s, 1H), 3.87 (t, *J* = 4.9 Hz), 3.69 (t, *J* = 4.5 Hz), 3.65 – 3.58 (m, 19H), 3.54 (dt, *J* = 10.9, 5.0 Hz, 4H), 3.46 – 3.36 (m, 2H), 3.34 (q, *J* = 5.4 Hz, 2H'), 3.12 (s, 1H), 2.88 (dd, *J* = 13.4, 4.7 Hz, 1H), 2.72 (d, *J* = 12.6 Hz, 1H), 2.38 – 2.27 (m, 2H), 2.24 (dd, *J* = 20.6, 9.8 Hz, 2H), 2.22 – 2.17 (m, 2H), 1.99 (dt, *J* = 12.8, 3.6 Hz, 1H), 1.94 (dtd, *J* = 17.6, 5.2, 2.7 Hz, 1H), 1.89 – 1.77 (m, 4H), 1.76 – 1.70 (m, 1H), 1.65 (tq, *J* = 14.0, 7.2 Hz, 3H), 1.58 – 1.45 (m, 4H), 1.43 (tdt, *J* = 14.9, 10.4, 4.6 Hz, 4H), 1.35 (dddd, *J* = 11.4, 9.1, 6.7, 3.9 Hz, 1H), 1.33 – 1.27 (m, *J* = 3.8, 2H), 1.23 (tdd, *J* = 13.4, 11.5, 3.1 Hz, 1H), 1.18 – 1.01 (m, 7H), 0.98 (s, 4H), 1.01 – 0.95 (m, 1H), 0.93 (td, *J* = 11.8, 4.7 Hz, 1H), 0.90 (d, *J* = 6.5 Hz, 3H), 0.85 (dd, *J* = 6.6, 4.3 Hz, 6H), 0.66 (s, 3H). **^{13}C NMR** (226 MHz, $CDCl_3$, δ): 173.5, 164.0, 156.3, 144.8, 139.9, 124.1, 122.6, 74.4, 70.61, 70.57, 70.55, 70.50, 70.31, 70.24, 70.18, 70.10, 69.68, 69.57, 64.6, 61.9, 60.3, 56.8, 56.2, 55.7, 50.3, 50.1, 42.4, 40.74, 40.69, 39.8, 39.6, 39.2, 38.7, 37.1, 36.6, 36.3, 36.0, 35.9, 31.99, 31.94, 28.33, 28.30, 28.27, 28.18, 28.12, 25.7, 24.4, 23.9, 22.9, 22.7, 21.1, 19.5, 18.8, 12.0. **FT-IR** (cm^{-1}, neat): 3289, 3225, 3130, 3090, 2932, 2901, 2866, 1704, 1644, 1544, 1535, 1461, 1442, 1377, 1365, 1353, 1323, 1305, 1282, 1264, 1246, 1136, 1099, 1048, 1032, 1019, 959, 947, 926, 888, 856, 837, 814, 800, 776, 761, 725, 699, 650, 596, 572, 546, 489, 486, 460, 454. **HRMS** (ESI) *m/z*: $[M + H]^+$ calcd for $C_{57}H_{98}N_7O_{11}S$, 1088.7040; found, 1088.7045. **Specific rotation** $[\alpha]_D^{20.0}$ = 5.52 ± 0.30 ($CHCl_3$, c = 1.002 g/100 mL).

2,5-Dioxopyrrolidin-1-yl 5-((3a*S*,4*S*,6a*R*)-2-oxohexahydro-1*H*-thieno[3,4-*d*]imidazol-4-yl)pentanoate (II-63)

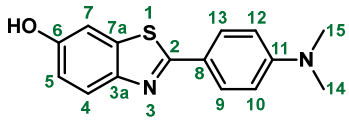
The NHS-activated biotin was synthesised according to Siewert *et al.*[192] In a 100 mL Schlenk flask under N_2 atmosphere, D-(+)-biotin (**II-60**,1.00 g, 4.09 mmol, 1.00 eq.) and fresh disuccinimidyl carbonate (1.36 g, 5.32 mmol, 1.30 eq.) were suspended in extra dry DMF (18.4 mL, 4.5 mL/mmol biotin). Triethylamine (2.28 mL, 16.4 mmol, 4.00 eq.) was added, and the resulting suspension was stirred at 19 °C, giving a clear solution after a few minutes. After approximately 60 min, a white solid started to precipitate and stirring was continued for a total reaction time of 25 h. The solvent was removed under reduced pressure and the resulting solid was triturated in diethyl ether. Filtration over a fritted glass funnel (pore size 4) and subsequent washing with EtOAc and Et_2O removed off-white impurities and left a fine white powder (repeated twice). Drying under high vacuum provided the biotin-NHS ester (**II-63**, 1.33 g, 3.90 mmol, 95%) as a white solid.



R_f (CH_2Cl_2/MeOH 90:10): 0.44 ($KMnO_4$ stain). **Mp** 206.4–212.9 °C. **^{1}H NMR** (600 MHz, DMSO-d_6, δ): 6.42 (s, 1H, 1-H), 6.36 (s, 1H, 3-H), 4.31 (dd, *J* = 7.7, 5.1 Hz, 1H, 6a-H), 4.15 (ddd, *J* = 7.4, 4.5, 1.8 Hz, 1H, 3a-H), 3.11 (ddd, *J* = 8.3, 6.4, 4.4 Hz, 1H, 4-H), 2.86 – 2.81 (dd, 1H, 6''-H, overlap with 13-H and 14-H), 2.81 (s, 4H, 13-H, 14-H, overlap with 6''-H), 2.69 – 2.64 (m, 2H, 10-H), 2.58 (d, *J* = 12.4 Hz, 1H, 6'-H), 1.69 – 1.60 (m, 3H, 7''-H, 9-H), 1.50 (tt, *J* = 13.9, 7.1 Hz, 1H, 7'-H), 1.42 (pt, *J* = 8.1, 3.7 Hz, 2H, 8-H). **^{13}C NMR** (151 MHz, DMSO-d_6, δ): 170.3 (C-12, C-15), 168.9 (C-11), 162.7 (C-2), 61.0 (C-3a), 59.2 (C-6a), 55.2 (C-4), 39.9 (C-6), 30.0 (C-10), 27.8 (C-7), 27.6 (C-8), 25.4 (C-13, C-14), 24.3 (C-9). **FT-IR** (cm^{-1}, neat): 3346, 3230, 3117, 3066, 2942, 2918, 2875, 1818, 1788, 1745, 1728, 1697, 1465, 1436, 1432, 1369, 1325, 1314, 1306, 1296, 1278, 1261, 1248, 1209, 1167, 1150, 1123, 1110, 1070, 1061, 1048, 1012, 993, 954, 917, 884, 860, 834, 813, 800, 739, 701, 655, 606, 582, 570, 549, 492, 486. **HRMS** (ESI) *m/z*: $[M + H]^+$ calcd for $C_{14}H_{20}N_3O_5S$, 342.1118; found, 342.1119. **CAS** 35013-72-0.

2-(4-(Dimethylamino)phenyl)benzo[*d*]thiazol-6-ol (II-71)

Procedure A from commercially available Pittsburgh Compound B (**II-68**): In a 100 mL Schlenk flask under N_2 atmosphere, Pittsburgh Compound B (**II-68**) (250 mg, 975 µmol, 1.00 eq.) and paraformaldehyde (158 mg, 5.27 mmol, 5.40 eq.) were three times vacuum/nitrogen backfilled. The compounds were suspended in dry THF (24.9 mL, 25.5 mL/mmol PiB) and stirred for 15 min at 19 °C to give a milky beige suspension. The solution was cooled to 0 °C and sodium cyanoborohydride (331 mg, 5.27 mmol, 5.40 eq.) was added in one portion. At 0 °C, glacial acetic acid (301 µL, 5.27 mmol, 5.40 eq.) was added dropwise to the THF solution. Stirring was continued for 25 min at 0 °C, then 25 min at 19 °C and finally for 13 h at 50 °C. The reaction was quenched with ice water (20 mL) and subsequently extracted with CH_2Cl_2 (3 x 50 mL). THF (stabiliser-free) was added during the extractive workup to assist phase separation and the transfer of the bright yellow fluorescent solution into the organic phase. Organic phases were combined and washed with saturated $NaHCO_3$ (2 x 50 mL) to give a colourless extract, followed by brine (1 x 50 mL). Drying over $MgSO_4$ and filtration over degreased cotton wool provided an ivory extract. The solvent was removed under reduced pressure and a fine, bright yellow solid was obtained. The solid was suspended in *i*Pr_2O/EtOAc (1:1) and filtered with a fritted funnel (pore size 4). The yellow powder was washed with *i*Pr_2O/EtOAc (1:1) and *i*PrOH. The recovered Me-PiB **II-71** was obtained and the procedure was repeated once to yield the title compound (255 mg, 942 µmol, 97%) as a bright yellow powder.

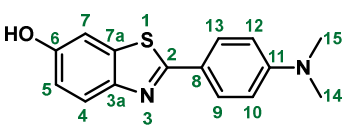


R_f (CH_2Cl_2/THF 90:10): 0.59 (UV and CAM stain). **Mp** 287.3–294.9 °C (decomposition). **^{1}H NMR** (600 MHz, DMSO-d_6, δ): 9.71 (s, 1H, OH), 7.80 (d, *J* = 8.4 Hz, 2H, 9, 13-H), 7.72 (d, *J* = 8.7 Hz, 1H, 4-H), 7.33 (d, *J* = 2.5 Hz, 1H, 7-H), 6.92 (dd, *J* = 8.7, 2.4 Hz, 1H, 5-H), 6.80 (d, *J* = 8.4 Hz, 2H, 10-H, 12-H), 3.00 (s, 6H, 14-H, 15-H). **^{13}C NMR** (151 MHz, DMSO-d_6, δ): 164.2 (C-2), 155.0 (C-6), 151.8 (C-11), 147.4 (C-3a), 135.2 (C-7a), 127.9 (C-9, C-13), 122.4 (C-4), 120.6 (C-8), 115.5 (C-5), 111.8 (C-10, C-12), 106.7 (C-7), 39.7 (C-14, C-15). **FT-IR** (cm^{-1}, neat): 3065, 3040, 3012, 2939, 2892, 2804, 2762, 2675, 2594, 2547, 2503, 2458, 1605, 1558, 1538, 1489, 1474, 1450, 1427, 1410, 1369, 1346, 1321, 1278, 1240, 1225, 1207, 1194, 1168, 1126, 1063, 1052, 1004, 972, 946, 938, 906, 838, 807, 732, 710, 697, 625, 589, 546, 509, 503, 480. **HRMS** (ESI) *m/z*: $[M + H]^+$ calcd for $C_{15}H_{15}N_2OS$, 271.0900; found, 271.0903. **CAS** 566169-94-6.

2-(4-(Dimethylamino)phenyl)benzo[*d*]thiazol-6-ol (II-71)

Procedure B[241, 250] from compound **II-90**: In a 500 mL Schlenk flask under N_2 atmosphere, methoxy-protected Me-PiB (**II-90**, 5.00 g, 17.6 mmol, 1.00 eq.) was dissolved in dry CH_2Cl_2 (175 mL, 10 mL/mmol PiB derivative) and the brown-purple solution was cooled to 0 °C. BBr_3 (5.01 mL, 52.8 mmol, 3.00 eq.) was slowly added at 0 °C. After the addition was completed, a greenish solid precipitated and stirring was continued for 30 min at 0 °C. The suspension was allowed to warm to 27 °C and stirring was continued for 17 h during which time a dark film had solidified on the surface of the flask. The reaction was cooled to 0 °C and carefully quenched by the addition of water (150 mL) to give an orange suspension. The solid was scraped from the surface and the pH adjusted with 3 M NaOH to approximately 12–14. The resulting green slurry was filtered, and the green solid was washed with water and Et_2O (wash fraction was orange due

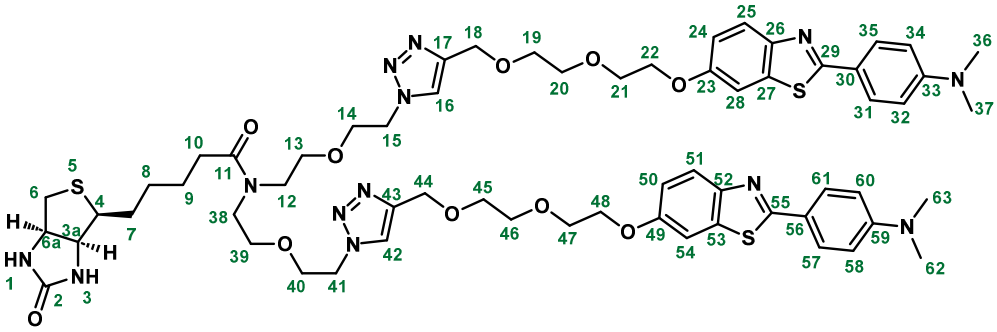
to HBr) to give the demethylated Me-PiB (**II-71**, 3.86 g, 14.3 mmol, 81%) as a green amorphous solid after solvent removal and drying under high vacuum.



R_f (CH_2Cl_2/THF 90:10): 0.52 (UV and CAM stain). **Mp** 286.9–291.9 °C. **^{1}H NMR** (600 MHz, DMSO-d_6, δ): 9.73 (s, 1H, OH), 7.79 (d, *J* = 8.9 Hz, 2H, 9-H, 13-H), 7.73 (d, *J* = 8.7 Hz, 1H, 4-H), 7.33 (d, *J* = 2.5 Hz, 1H, 7-H), 6.92 (dd, *J* = 8.7, 2.5 Hz, 1H, 5-H), 6.79 (d, *J* = 8.8 Hz, 2H, 10-H, 12-H), 2.99 (s, 5H, 14-H, 15-H). **^{13}C NMR** (151 MHz, DMSO-d_6, δ): 164.2 (C-2), 155.0 (C-6), 151.7 (C-11), 147.3 (C-3a), 135.2 (C-7a), 127.9 (C-9, C-13), 122.4 (C-4), 120.6 (C-8), 115.5 (C-5), 111.9 (C-10, C-12), 106.7 (C-7), 39.7 (C-14, C-15). **FT-IR** (cm^{-1}, neat): 3067, 3014, 2893, 2808, 2767, 2678, 2595, 2552, 2460, 1606, 1558, 1538, 1489, 1476, 1452, 1446, 1411, 1370, 1347, 1320, 1279, 1240, 1225, 1207, 1195, 1170, 1126, 1062, 1053, 1005, 972, 946, 938, 907, 836, 808, 755, 732, 710, 698, 647, 626, 589, 547, 510, 503, 481. **HRMS** (ESI) *m/z*: $[M + H]^+$ calcd for $C_{15}H_{15}N_2OS$, 271.0900; found, 271.0902. **CAS** 566169-94-6.

N,*N*-Bis(2-(2-(4-((2-(2-((2-(4-(dimethylamino)phenyl)benzo[*d*]thiazol-6-yl)oxy)ethoxy)ethoxy)methyl)-1*H*-1,2,3-triazol-1-yl)ethoxy)ethyl)-5-((3a*S*,4*S*,6a*R*)-2-oxohexahydro-1*H*-thieno[3,4-*d*]imidazol-4-yl)pentanamide (II-73, cCAP-1)

To a 100 mL round-bottom flask under N_2 atmosphere, biotin bis-azide (**II-79**, 34.1 mg, 72.6 µmol, 1.00 eq.), alkynylated Me-PiB (**II-93**, 59.0 mg, 149 µmol, 2.05 eq.), and TDETA (**II-44**, 10.3 mg, 21.8 µmol, 0.30 eq.) were added. The compounds were dissolved in $CHCl_3$ (25.4 mL, 0.35 mL/µmol biotin). $Cu(OAc)_2$ (2.18 mL, 3.96 mg, 21.8 µmol, 0.30 eq., 10 mM in EtOH) and additional EtOH (23.2 mL) were added to give a 1:1 mixture of $CHCl_3$/EtOH. An aqueous solution of sodium ascorbate (182 µL, 7.19 mg, 36.3 µmol, 0.50 eq., 200 mM in water) was then added and the pale-yellow reaction was stirred at 19 °C for 23 h. The reaction was concentrated *in vacuo* and the slimy yellow residue was taken up in CH_2Cl_2/MeOH (95:5) before being applied to a silica column. The column was washed with CH_2Cl_2/MeOH (95:5) and the product then eluted with CH_2Cl_2/MeOH (90:10). A yellow oil was obtained after solvent removal that slowly transformed into a pale-yellow foam, as which the desired bis-click product cCAP-1 (**II-73**, 80.7 mg, 63.9 µmol, 88%) was finally obtained after extensive drying.

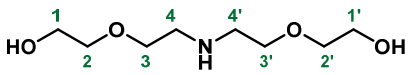


R_f (CH_2Cl_2/MeOH 80:20): 0.76 (UV and yellow spot with CAM stain). **Mp** 79.5–90.3 °C (the yellow flakes start rapid shrinking at 65 °C and show a broad melting point). **^{1}H NMR** (600 MHz, $CDCl_3$, δ): 7.88 (d, *J* = 8.8 Hz, 4H, 31-H, 35-H, 57-H, 61-H), 7.83 (d, *J* = 8.9 Hz, 2H, 25-H, 51-H), 7.60 (s, 1H, 42-H), 7.57 (s, 1H, 16-H), 7.35 – 7.29 (m, 2H, 28-H, 54-H), 7.03 (dt, *J* = 8.9, 2.3 Hz, 2H, 24-H, 50-H), 6.72 (d, *J* = 8.8 Hz, 4H, 32-H, 34-H, 58-H, 60-H), 5.78 (s, 1H, 3-H), 4.88 (s, 1H, 1-H), 4.68 (d, *J* = 7.2 Hz, 4H, 18-H, 44-H), 4.46 – 4.39 (m, 5H, 6a-H, 15-H, 41-H), 4.26 (t, *J* = 6.1 Hz, 1H, 3a-H), 4.19 – 4.14 (m, 4H, 22-H, 48-H), 3.86 (q, *J* = 4.1 Hz, 4H, 21-H, 47-H), 3.78 – 3.68 (m, 12H, 14-H, 19-H, 20-H, 40-H, 45-H, 46-H), 3.49 (t, *J* = 5.4 Hz, 2H, 13-H), 3.38 (t, *J* = 5.2 Hz, 4H, 12-H, 39-H), 3.29 (t, *J* = 5.6 Hz, 2H, 38-H), 3.09 (td, *J* = 7.4, 4.6 Hz, 1H, 4-H), 3.03 (s, 12H, 36-H, 37-H, 62-H, 63-H), 2.84 (dd, *J* = 12.8, 5.0 Hz, 1H, 6''-H), 2.66 (d, *J* = 12.8 Hz, 1H, 6'-H), 2.24 (td, *J* = 7.4, 3.1 Hz, 2H, 10-H), 1.68 (ddd, *J* = 16.8, 13.0, 6.7 Hz, 1H, 7'-H), 1.63 – 1.50 (m, 3H, 7''-H, 9-H), 1.38 (tq, *J* = 15.6, 7.5, 7.0 Hz, 2H, 8-H). **^{13}C NMR** (151 MHz, $CDCl_3$, δ): 173.5 (C-11), 166.78 (C-29 or C-55), 166.75 (C-29 or C-55), 163.2 (C-2), 156.38 (C-23 or C-49), 156.36 (C-23 or C-49), 152.1 (C-33, C-59), 149.23 (C-26 or C-52), 149.21 (C-26 or C-52), 145.3 (C-43), 145.1 (C-17), 135.9 (C-27, C-53), 128.6 (C-31, C-35, C-57, C-61), 123.6 (C-42), 123.5 (C-16), 122.84 (C-25 or C-51), 122.83 (C-25 or C-51), 121.65 (C-30 or C-56), 121.63 (C-30 or C-56), 115.6 (C-50), 115.6 (C-24), 111.9 (C-32, C-34, C-58, C-60), 105.6 (C-28, C-54), 70.9 (C-20, C-46), 70.0 (C-21, C-47), 69.9 (C-19, C-45), 69.5 (C-13), 69.5 (C-40), 69.3 (C-39), 69.1 (C-14), 68.3 (C-22, C-48) 64.8 (C-44), 64.8 (C-18), 61.9 (C-3a), 60.1 (C-6a),

55.5 (C-4), 50.2 (C-15, C-41), 48.6 (C-38), 46.0 (C-12), 40.7 (C-6), 40.3 (C-36, C-37, C-62, C-63), 32.4 (C-10), 28.3 (C-7, C-8), 24.9 (C-9). **FT-IR** (cm^{-1}, neat): 3241, 3214, 3135, 3090, 3079, 2906, 2865, 2817, 1701, 1633, 1604, 1560, 1532, 1491, 1445, 1430, 1362, 1313, 1285, 1263, 1223, 1188, 1169, 1122, 1064, 1049, 1007, 966, 941, 884, 817, 772, 751, 725, 712, 702, 687, 628, 607, 589, 556, 517, 484, 461. **HRMS** (ESI) *m/z*: $[M + H]^+$ calcd for $C_{62}H_{80}N_{13}O_{10}S_3$, 1262.5308; found, 1262.5293.

2,2'-((Azanediylbis(ethane-2,1-diyl))bis(oxy))bis(ethan-1-ol) (II-74)

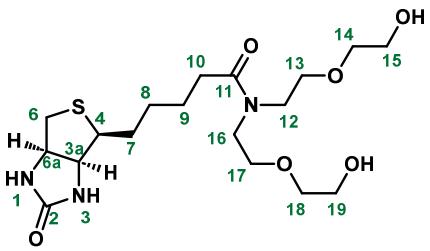
The amino alcohol linker was synthesised according to Bordunov *et al.*[231] In a 1 L three-necked flask under N_2 atmosphere, a solution of 2-(2-chloroethoxy)ethanol (**II-75**, 25.2 g, 202 mmol, 1.00 eq.) in dry toluene (50 mL, 0.25 mL/mmol chloride) was added dropwise to a refluxing mixture of 2-(2-aminoethoxy)ethanol (**II-76**, 53.1 g, 505 mmol, 2.50 eq.) and sodium carbonate (23.6 g, 222 mmol, 1.10 eq.) in dry toluene (500 mL, 2.50 mL/mmol chloride). The mixture was stirred under reflux at 160 °C for 63 h using a glass column filled with 50 mL activated 4 Å molecular sieve and a condenser on top. The molecular sieve was washed with toluene and the wash fraction was added to the reaction vessel. The solid was removed by filtration and the filtrate was dried with 60 g $MgSO_4$ to clear the solution. The solution was then filtered again and the solvent was removed under reduced pressure. The solids from the first and second filtration (NaCl and $MgSO_4$) were merged and thoroughly washed with MTBE. After solvent evaporation, the crude product was obtained as a thick pale-yellow oil. The residue was distilled under vacuum at 2.6 x 10^{-1} mbar (no Vigreux column and short bridge to prevent product from decomposition at high temperature, distillation bridge and flask wrapped in tin foil and paper towels for insulation) to provide the title compound (**II-74**, 25.8 g, 134 mmol, 66%) as viscous pale-yellow oil.



R_f (CH_2Cl_2/MeOH 60:40): 0.14 (concentration dependent, $KMnO_4$ stain). **Bp** 170–173 °C (0.26 mbar). **^{1}H NMR** (600 MHz, $CDCl_3$, δ): 3.70 – 3.66 (m, 4H, 1-H, 1'-H), 3.61 – 3.57 (m, 4H, 3-H, 3'-H), 3.58 – 3.54 (m, 4H, 2-H, 2'-H), 2.84 – 2.79 (m, 4H, 4-H, 4'-H). **^{13}C NMR** (151 MHz, $CDCl_3$, δ): 72.8 (C-2, C-2'), 69.9 (C-3, C-3'), 61.7 (C-1, C-1'), 49.1 (C-4, C-4'). **FT-IR** (cm^{-1}, neat): 3291, 2858, 1653, 1454, 1352, 1281, 1248, 1115, 1066, 945, 887, 836, 659, 527, 459. **HRMS** (ESI) *m/z*: $[M + H]^+$ calcd for $C_8H_{20}NO_4$, 194.1387; found, 194.1387. **CAS** 54384-47-3.

N,*N*-Bis(2-(2-hydroxyethoxy)ethyl)-5-((3a*S*,4*S*,6a*R*)-2-oxohexahydro-1*H*-thieno[3,4-*d*]imidazol-4-yl)pentanamide (II-77)

Under N_2 atmosphere, a 100 mL round-bottom flask was charged with biotin-NHS ester (**II-63**, 600 mg, 1.76 mmol, 1.00 eq.) and amino alcohol (**II-74**, 408 mg, 2.11 mmol, 1.20 eq.). The flask was subjected to three cycles of vacuum/nitrogen backfill before extra dry DMF (35.4 mL, 20.1 mL/mmol NHS ester) was added. Stirring for 15 min rendered a colourless solution, to which triethylamine (735 µL, 5.27 mmol, 3.00 eq.) was added, and after 2 h of stirring, the solution was heated to 60 °C for an additional 2 h. The reaction was concentrated *in vacuo* (60 °C), leaving a thick colourless oil. A short filter column of neutral aluminium oxide (8 cm) with CH_2Cl_2/MeOH (70:30, 400 mL) was used to efficiently remove released NHS (remains on the baseline of Alox TLC plates). Combined fractions were then applied to a column of silica and the product was eluted with CH_2Cl_2/MeOH (80:20) to yield the desired biotin-bis-PEG_2-alcohol **II-77** as colourless sticky oil (570 mg, 1.36 mmol, 77%) after solvent evaporation, which is only soluble in MeOH, DMSO, and DMF.

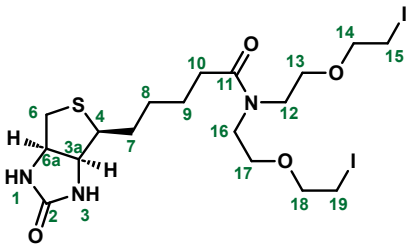


R_f (silica, CH_2Cl_2/MeOH 70:30): 0.57 ($KMnO_4$ stain). **R_f** (neutral aluminium oxide, CH_2Cl_2/MeOH 90:10): 0.23 ($KMnO_4$ stain). **^{1}H NMR** (600 MHz, MeOD, δ): 4.49 (ddd, *J* = 7.9, 5.0, 0.9 Hz, 1H, 6a-H), 4.31 (dd, *J* = 7.9, 4.4 Hz, 1H, 3a-H), 3.68 – 3.63 (m, 8H, 15-H, 16-H, 17-H, 19-H), 3.63 – 3.58 (m, *J* = 4.1, 3.7 Hz, 4H, 12-H, 13-H), 3.55 (dd, *J* = 5.5, 4.3 Hz, 2H, 18-H), 3.52 (dd, *J* = 5.5, 4.2 Hz, 2H, 14-H), 3.22 (ddd, *J* = 8.8, 6.0, 4.4 Hz, 1H, 4-H), 2.93 (dd, *J* = 12.7, 5.0 Hz, 1H, 6''-H), 2.71 (d, *J* = 12.7 Hz, 1H, 6'-H), 2.53 – 2.45 (m, 2H, 10-H), 1.75 (ddt, *J* = 13.0, 9.2, 6.3 Hz, 1H, 7''-H), 1.70 – 1.57 (m, 3H, 7'-H, 9-H), 1.50 – 1.42 (m, 2H, 8-H). **^{13}C NMR** (151 MHz, MeOD, δ): 176.2 (C-11), 166.1 (C-2), 73.8 (C-18), 73.6 (C-14), 70.3 (C-17), 70.1 (C-13), 63.3 (C-3a), 62.2

(C-19), 62.2 (C-15), 61.6 (C-6a), 57.1 (C-4), 50.0 (C-16), 47.3 (C-12), 41.1 (C-6), 33.7 (C-10), 29.9 (C-8), 29.6 (C-7), 26.4 (C-9). **FT-IR** (cm^{-1}, neat): 3280, 2923, 2863, 1689, 1617, 1456, 1426, 1354, 1330, 1265, 1219, 1118, 1058, 886, 761, 725, 684, 595, 539. **HRMS** (ESI) *m/z*: $[M + H]^+$ calcd for $C_{18}H_{34}N_3O_6S$, 420.2163; found, 420.2166. **CAS** 2100306-75-8.

N,*N*-Bis(2-(2-iodoethoxy)ethyl)-5-((3a*S*,4*S*,6a*R*)-2-oxohexahydro-1*H*-thieno[3,4-*d*]imidazol-4-yl)pentanamide (II-78)

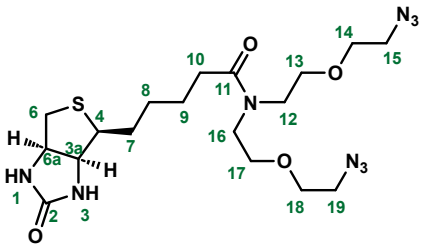
In a 50 mL Schlenk flask under N_2 atmosphere, bis-hydroxy-functionalised biotin (**II-77**, 505 mg, 1.20 mmol, 1.00 eq.) was dissolved in extra dry DMF (10.8 mL). In a separate Schlenk flask, a solution of methyltriphenoxyphosphonium iodide (2.18 g, 4.82 mmol, 4.00 eq.) in extra dry DMF (19.3 mL, 250 mM) was added to the biotin mixture and the solution was stirred at 21 °C for 14 h to give a clear colourless solution. Then, isopropyl alcohol (921 µL, 12.0 mmol, 10.0 eq.) was added to quench the excess of halogenating reagent. The solution was stirred at 21 °C for 1 h, the reaction mixture was transferred with MeOH to a round-bottom flask, and then the solvent was removed by rotary evaporation (60 °C) to give a colourless oil. The residue was purified on silica with CH_2Cl_2/MeOH (98:2, then 93:7) to yield the biotin-bis-PEG-iodide **II-78** as a colourless viscous oil (544 mg, 850 µmol, 71%).



R_f (CH_2Cl_2/MeOH 90:10): 0.49 ($KMnO_4$ stain and weak UV activity). **^{1}H NMR** (600 MHz, $CDCl_3$, δ): 5.72 (s, 1H, 3-H), 5.29 (s, 1H, 1-H), 4.51 (dd, *J* = 7.8, 4.9 Hz, 1H, 6a-H), 4.32 (ddd, *J* = 7.8, 4.6, 1.5 Hz, 1H, 3a-H), 3.70 (dq, *J* = 12.3, 6.3, 5.8 Hz, 4H, 14-H, 18-H), 3.66 – 3.60 (m, 6H, 16-H, 13-H, 17-H), 3.57 (q, *J* = 5.0 Hz, 2H, 12-H), 3.24 (t, *J* = 6.4 Hz, 4H, 15-H, 19-H), 3.18 (td, *J* = 7.4, 4.5 Hz, 1H, 4-H), 2.91 (dd, *J* = 12.8, 5.0 Hz, 1H, 6''-H), 2.74 (d, *J* = 12.8 Hz, 1H, 6'-H), 2.50 – 2.38 (m, 2H, 10-H), 1.75 (ddd, *J* = 13.5, 6.8, 2.0 Hz, 1H, 7''-H), 1.68 (hept, *J* = 7.2 Hz, 3H, 7'-H, 9-H), 1.51 – 1.43 (m, 2H, 8-H). **^{13}C NMR** (151 MHz, $CDCl_3$, δ): 173.7 (C-11), 163.5 (C-2), 71.8 (C-18), 71.5 (C-14), 69.5 (C-17), 69.1 (C-13), 62.0 (C-3a), 60.3 (C-6a), 55.5 (C-4), 49.2 (C-16), 46.5 (C-12), 40.8 (C-6), 32.7 (C-10), 28.5 (C-8), 28.5 (C-7), 25.2 (C-9), 3.7 (C-19), 3.1 (C-15). **FT-IR** (cm^{-1}, neat): 3384, 3283, 2921, 2861, 2405, 1684, 1629, 1446, 1422, 1355, 1337, 1314, 1299, 1263, 1229, 1171, 1120, 993, 933, 864, 760, 721, 681, 663, 612, 592, 565, 535, 521, 513, 509, 482, 473, 456. **HRMS** (ESI) *m/z*: $[M + H]^+$ calcd for $C_{18}H_{32}I_2N_3O_4S$, 640.0197; found, 640.0207.

N,*N*-Bis(2-(2-azidoethoxy)ethyl)-5-((3a*S*,4*S*,6a*R*)-2-oxohexahydro-1*H*-thieno[3,4-*d*]imidazol-4-yl)pentanamide (II-79)

In a 25 mL round-bottom flask under N_2 atmosphere, bis-iodinated biotin (**II-78**, 349 mg, 546 µmol, 1.00 eq.) was dissolved in extra dry DMF (3.27 mL, 6.0 mL/mmol bis-iodide). Sodium azide (142 mg, 2.18 mmol, 4.00 eq.) was added in a single batch and the pale-yellow suspension was stirred for 2 h at 19 °C. The solution had become colourless and a white solid had precipitated. Heating at 50 °C was then continued for 14 h. The reaction was diluted with ice water (50 mL) and extracted with EtOAc (5 x 30 mL). Merged organic phases were washed with cold water (2 x 50 mL) and brine (1 x 50 mL), dried over $MgSO_4$, and filtered over degreased cotton wool. After solvent evaporation, the colourless oil was purified on silica with CH_2Cl_2/MeOH (95:5) to yield the biotin-bis-PEG-azide (**II-79**, 222 mg, 472 µmol, 87%) as a hard colourless glass.

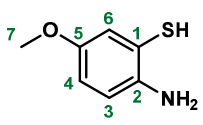


R_f (CH_2Cl_2/MeOH 90:10): 0.44 (CAM stain). **^{1}H NMR** (600 MHz, $CDCl_3$, δ): 5.52 (s, 1H, 3-H), 5.04 (s, 1H, 1-H), 4.44 (ddt, *J* = 7.7, 5.0, 1.2 Hz, 1H, 6a-H), 4.25 (ddd, *J* = 7.8, 4.6, 1.5 Hz, 1H, 3a-H), 3.60 – 3.54 (m, 10H, 13-H, 14-H, 16-H, 17-H, 18-H), 3.52 (dd, *J* = 5.5, 4.0 Hz, 2H, 12-H), 3.34 – 3.25 (m, 4H, 15-H, 19-H), 3.11 (td, *J* = 7.4, 4.6 Hz, 1H, 4-H), 2.85 (dd, *J* = 12.8, 5.0 Hz, 1H, 6''-H), 2.67 (d, *J* = 12.8 Hz, 1H, 6'-H), 2.36 (td, *J* = 7.3, 2.0 Hz, 2H, 10-H), 1.71 – 1.63 (m, 1H, 7''-H), 1.65 – 1.57 (m, 3H, 7'-H, 9-H), 1.41 (dtt, *J* = 13.7, 8.9, 4.9 Hz, 2H, 8-H). **^{13}C NMR** (151 MHz, $CDCl_3$, δ): 173.6 (C-11), 163.4 (C-2), 70.3, 70.0, 69.9, 69.6, 61.9 (C-3a), 60.2 (C-6a), 55.4 (C-4), 50.9 (C-15, C-19), 49.1 (C-16), 46.5 (C-12), 40.7 (C-6), 32.6 (C-10), 28.4 (C-8), 28.4 (C-7), 25.1 (C-9). **FT-IR**

(cm^{-1}, neat): 3317, 3240, 3093, 2930, 2907, 2869, 2809, 2103, 2088, 1704, 1667, 1621, 1459, 1424, 1415, 1367, 1344, 1330, 1287, 1272, 1249, 1235, 1201, 1164, 1116, 1097, 1063, 1009, 989, 953, 937, 914, 898, 885, 859, 846, 813, 810, 801, 727, 679, 643, 620, 598, 567, 556, 541, 502, 491, 456. **HRMS** (ESI) *m/z*: $[M + H]^+$ calcd for $C_{18}H_{32}N_9O_4S$, 470.2293; found, 470.2301.

2-Amino-5-methoxybenzenethiol (II-88)

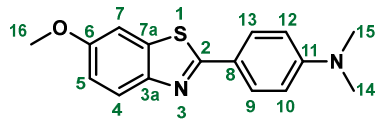
In a 1 L round-bottom flask, 2-amino-6-methoxy-benzothiazole (**II-87**, 35.0 g, 194 mmol, 1.00 eq.) was suspended in 40% NaOH in water (485 mL, 194 g, 4.85 mol, 25.0 eq.), ethylene glycol (43.4 mL, 0.78 mmol, 4.00 eq.) was added and the mixture was subsequently degassed by freeze-pump-thaw (2 cycles). The suspension was refluxed at 140 °C for 39 h (it remains a white-grey suspension). While cooling to 0 °C in an ice bath, the reaction mixture turned purple and was diluted with ice water (1 L) in a 5 L Erlenmeyer flask to give a red-brown solution. Acidification with concentrated HCl to pH 2–3 shifted the colour from red-brown to green and then yellow, before a bright-yellow solid precipitated (total HCl amount is 440 mL). Neutralisation with 20% K_2CO_3 (pH 5–6) was followed by repeated extraction with MTBE (8 x 200 mL) during which the aqueous phase remained turbid and a green solid precipitated. Merged organic phases were washed with brine (500 mL) and dried over $MgSO_4$. After solvent evaporation, the product **II-88** was obtained as orange oil and crystallised at room temperature to give a yellow solid (23.0 g, 148 mmol, 76%).



R_f (PE/EtOAc 20:80): 0.66 (UV and $KMnO_4$ stain). **Mp** 70.3–73.8 °C. **^{1}H NMR** (600 MHz, $CDCl_3$, δ): 6.80 (dd, *J* = 8.8, 2.9 Hz, 1H, 6-H), 6.71 – 6.66 (m, 2H, 3-H, 4-H), 4.06 (s, 2H, 8-H), 3.60 (s, 3H, 10-H). **^{13}C NMR** (151 MHz, $CDCl_3$, δ): 152.0 (C-5), 142.8 (C-2), 120.2 (C-3), 119.5 (C-6), 119.4 (C-1), 116.8 (C-4), 55.9 (C-10). **FT-IR** (cm^{-1}, neat): 3277, 2909, 2884, 2866, 2850, 2803, 1605, 1563, 1557, 1528, 1490, 1449, 1427, 1409, 1360, 1348, 1320, 1287, 1259, 1220, 1187, 1169, 1136, 1120, 1097, 1065, 1040, 1004, 966, 942, 882, 844, 835, 816, 752, 724, 702, 687, 678, 653, 626, 609, 590, 563, 554, 540, 514, 485, 475. **HRMS** (ESI) *m/z*: $[M + H]^+$ calcd for $C_7H_{10}NOS$, 156.0478; found, 156.0477. **CAS** 6274-29-9.

4-(6-Methoxybenzo[*d*]thiazol-2-yl)-*N*,*N*-dimethylaniline (II-90)

In a 100 mL round-bottom flask under N_2 atmosphere, 4-(dimethylamino)benzaldehyde (**II-89**, 3.30 g, 2.12 mmol, 1.00 eq.) and 2-aminothiophenol (**II-88**, 4.46 g, 28.8 mmol, 1.30 eq.) in DMSO (44.2 mL, 2.0 mL/mmol aldehyde) were stirred at room temperature until fully dissolved. The deep orange solution was stirred at 125 °C for 2 h to form a black-yellow coloured solution. The septum was removed and stirring under air continued for 30 min while heating. The dark brown solution was diluted with water (150 mL) to precipitate a greenish solid. Further dilution with water and suction filtration provided a solid, which was further washed with water and distilled EtOH and finally dried under vacuum to give the product (**II-90**, 5.19 g, 18.2 mmol, 82%) as an amorphous green solid. The product was used without further purification.

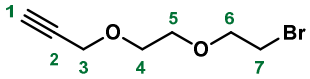


R_f (CH_2Cl_2/THF 90:10): 0.73 (UV). **Mp** 176.5–178.0 °C. **^{1}H NMR** (600 MHz, $CDCl_3$, δ): 7.92 (d, *J* = 8.5 Hz, 2H, 9-H, 13-H), 7.88 (d, *J* = 8.9 Hz, 1H, 7-H), 7.31 (d, *J* = 2.5 Hz, 1H, 4-H), 7.04 (dd, *J* = 8.9, 2.5 Hz, 1H, 5-H), 6.74 (d, *J* = 8.6 Hz, 2H, 10-H, 12-H), 3.88 (s, 3H, 16-H), 3.05 (s, 6H, 14-H, 15-H). **^{13}C NMR** (151 MHz, $CDCl_3$, δ): 166.7 (C-2), 157.3 (C-6), 152.1 (C-11), 148.7 (C-3a), 135.7 (C-7a), 128.7 (C-9, C-13), 122.8 (C-7), 121.6 (C-8), 115.1 (C-5), 111.9 (C-10, C-12), 104.5 (C-4), 55.9 (C-16), 40.4 (C-14, C-15). **FT-IR** (cm^{-1}, neat): 3011, 2966, 2935, 2906, 2865, 2834, 2805, 1604, 1557, 1530, 1487, 1461, 1444, 1429, 1411, 1366, 1318, 1284, 1260, 1241, 1222, 1187, 1167, 1116, 1057, 1022, 1005, 967, 958, 945, 891, 832, 814, 806, 751, 732, 722, 694, 686, 626, 591, 547, 510, 484. **HRMS** (ESI) *m/z*: $[M + H]^+$ calcd for $C_{16}H_{17}N_2OS$, 285.1056; found, 285.1058. **CAS** 10205-71-7.

3-(2-(2-Bromoethoxy)ethoxy)prop-1-yne (II-92)

In a 100 mL Schlenk flask under N_2 atmosphere, a solution of alcohol (**II-91**, 1.07 g, 7.42 mmol, 1.00 eq.) and carbon tetrabromide (2.95 g, 8.91 mmol, 1.20 eq.) in dry CH_2Cl_2 (61.8 mL, 120 mM) was prepared. A solution of PPh_3 (2.34 g, 8.91 mmol, 1.20 eq.) in dry CH_2Cl_2 (10 mL) was added to the pale yellow CBr_4 solution at ambient temperature and the

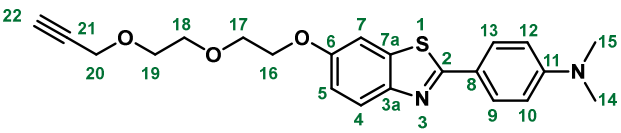
reaction mixture, which had quickly turned yellow, was stirred for 72 h at 19 °C. The solvent was removed under reduced pressure to yield the crude product as a brown oil. The oil was dissolved in CH_2Cl_2 and immobilised on Celite (PPh_3 and $O{=}PPh_3$ stick to Celite) by solvent removal. Purification was then performed by chromatography on silica with PE/EtOAc (80:20) to give the brominated alkyne (**II-92**, 1.52 g, 7.34 mmol, 99%) as a colourless liquid with characteristic odour in near-quantitative yield.



R_f (PE/EE 80:20): 0.39 ($KMnO_4$ stain). **^{1}H NMR** (600 MHz, $CDCl_3$, δ): 4.22 (d, *J* = 2.4 Hz, 2H, 3-H), 3.82 (t, *J* = 6.4 Hz, 2H, 6-H), 3.74 – 3.67 (m, 4H, 4-H, 5-H), 3.48 (t, *J* = 6.4 Hz, 2H, 7-H), 2.44 (t, *J* = 2.3 Hz, 1H, 1-H). **^{13}C NMR** (151 MHz, $CDCl_3$, δ): 79.7 (C-2), 74.8 (C-1), 71.4 (C-6), 70.5 (C-5), 69.2 (C-4), 58.6 (C-3), 30.3 (C-7). **FT-IR** (cm^{-1}, neat): 3291, 3019, 2866, 2115, 1459, 1442, 1423, 1352, 1277, 1246, 1227, 1186, 1100, 1041, 1008, 952, 920, 881, 841, 668, 573, 512. **HRMS** (ESI) *m/z*: $[M + Na]^+$ calcd for $C_7H_{11}BrNaO_2$, 228.9835; found, 228.9829. **CAS** 1287660-82-5.

N,*N*-Dimethyl-4-(6-(2-(2-(prop-2-yn-1-yloxy)ethoxy)ethoxy)benzo[*d*]thiazol-2-yl)aniline (II-93)

To a 100 mL flask under N_2 atmosphere, Me-PiB (**II-71**, 86.5 mg, 320 µmol, 1.00 eq.), alkyne bromide (**II-92**, 99.4 mg, 480 µmol, 1.50 eq.), and ground potassium hydroxide (53.9 mg, 960 µmol, 3.00 eq.) were added and suspended in dry glyme (43.2 mL, 0.5 mL/mg PiB). The reaction was vigorously stirred at 80 °C for 20 h, giving a brown dispersion. After cooling to room temperature, the solvent was removed and the green-brown residue diluted with water (150 mL) and CH_2Cl_2 (400 mL). As the organic phase was very turbid, EtOH was added to clear the organic phase and allow phase separation. Phases were separated and the aqueous phase was extracted with CH_2Cl_2 (3 x 150 mL, EtOH added if needed). Merged organic phases were washed with saturated $NaHCO_3$ (250 mL) and dried over $MgSO_4$. After filtration and subsequent evaporation of solvent, the crude product was yielded as an olive green solid. Purification on silica with PE/CH_2Cl_2/MeOH (40:59:1) provided a beige-brown solid that contained aliphatic impurities of unknown origin. The solid was suspended in *i*PrOH and applied to a glass pipette column (filled with silica). The column was thoroughly washed with *i*PrOH, giving a yellow eluate that contained minor product and all undesired aliphatic impurities. The product remained as a beige solid on top of the silica and was eluted stepwise with CH_2Cl_2/MeOH (1:1), CH_2Cl_2, and then MeOH. The process was repeated with the *i*PrOH fraction to increase the yield. Although near-full conversion was reported from TLC, the title compound was obtained as an amorphous beige-yellow solid (**II-93**, 66.5 mg, 168 µmol, 52%) in a moderate yield.



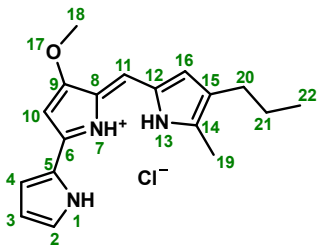
R_f (CH_2Cl_2/THF 90:10): 0.68 (UV and CAM stain). **Mp** 116.5–120.6 °C. **^{1}H NMR** (600 MHz, $CDCl_3$, δ): 7.90 (d, J = 9.0 Hz, 2H, 9-H, 13-H), 7.85 (d, *J* = 8.9 Hz, 1H, 4-H), 7.34 (d, *J* = 2.5 Hz, 1H, 7-H), 7.06 (dd, *J* = 8.9, 2.5 Hz, 1H, 5-H), 6.74 (d, *J* = 9.0 Hz, 2H, 10-H, 12-H), 4.22 (d, *J* = 2.4 Hz, 2H, 20-H), 4.22 – 4.18 (m, 2H, 16-H), 3.90 (dd, *J* = 5.6, 4.0 Hz, 2H, 17-H), 3.80 – 3.76 (m, 2H, 18-H), 3.76 – 3.72 (m, 2H, 19-H), 3.05 (s, 6H, 14-H, 15-H), 2.43 (t, *J* = 2.4 Hz, 1H, 22-H). **^{13}C NMR** (151 MHz, $CDCl_3$, δ): 166.7 (C-2), 156.4 (C-6), 152.1 (C-11), 149.3 (C-3a), 135.9 (C-7a), 128.7 (C-9, C-13), 122.9 (C-4), 121.8 (C-8), 115.6 (C-5), 111.9 (C-10, C-12), 105.6 (C-7), 79.8 (C-21), 74.7 (C-22), 70.8 (C-18), 70.0 (C-17), 69.3 (C-19), 68.3 (C-16), 58.6 (C-20), 40.3 (C-14, C-15). **FT-IR** (cm^{-1}, neat): 3277, 2909, 2884, 2866, 2850, 2803, 1605, 1563, 1557, 1528, 1490, 1449, 1427, 1409, 1360, 1348, 1320, 1287, 1259, 1220, 1187, 1169, 1136, 1120, 1097, 1065, 1040, 1004, 966, 942, 882, 835, 816, 752, 724, 702, 687, 678, 653, 626, 609, 590, 554, 540, 514, 485, 475. **HRMS** (ESI) *m/z*: $[M + H]^+$ calcd for $C_{22}H_{25}N_2O_3S$, 397.1580; found, 397.1584.

(*Z*)-4'-Methoxy-5'-((5-methyl-4-propyl-1*H*-pyrrol-2-yl)methylene)-1*H*,5'*H*-[2,2'-bipyrrol]-1'-ium chloride (III-1aa·HCl)

Propylprodigiosin **III-1aa** was synthesised in a Palladium-catalysed Suzuki-Miyaura cross-coupling reaction between unsubstituted Boc-pyrrole boronic acid **III-76** and triflate **III-96** to evaluate different Palladium ligands and precatalysts [$Pd(PPh_3)_4$ **III-120**, dppf **III-121**, SPhos **III-122**, XPhos **III-123**, and RuPhos **III-124**].

A 25 mL Schlenk flask was charged with triflate **III-96** (50.0 mg, 132 µmol, 1.00 eq.), *N*-Boc-pyrrole-2-boronic acid (**III-76**, 55.8 mg, 264 µmol, 2.00 eq.), ligand (see Table III.5, 7.93 µmol, 0.06 eq.), and $Pd(OAc)_2$ (1.48 mg, 6.61 µmol,

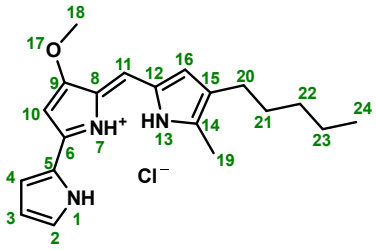
0.05 eq.), and the reaction vessel was three times vacuum/nitrogen backfilled. For the $Pd(PPh_3)_4$ precatalyst instead, no additional ligand or $Pd(OAc)_2$ was added and the precatalyst was used at a final concentration of 5 mol% (7.64 mg, 6.61 µmol, 0.05 eq.). The solids were dissolved in degassed *n*BuOH (728 µL) and supplemented by the addition of a solution of K_3PO_4 (56.1 mg, 264 µmol, 2.00 eq.) in degassed water (182 µL). The reactions were stirred under N_2 atmosphere at 40 °C or 60 °C for 18 h (cf. Table III.5). Finally, the reaction solution was diluted with CH_2Cl_2 (5 mL) and a saturated aqueous solution of $NaHCO_3$ (5 mL) was added. The aqueous phase was repeatedly extracted with CH_2Cl_2 (3 x 5 mL). After drying the merged organic phases over $MgSO_4$, an orange extract was obtained. Purification by column chromatography on silica with CH_2Cl_2 + 7 N NH_3 in MeOH (gradient, 0–1%), followed by a second column on silica using CH_2Cl_2 with 7 N NH_3 in MeOH (isocratic, 1%), and acidification with 1 M HCl In Et_2O provided the product as a red solid in yields between 18–84% (for isolated yields see Table III.5).



^{1}H NMR (300 MHz, $CDCl_3$, δ): 12.66 (brs, 2H, 7-H, 13-H), 12.53 (brs, 1H, 1-H), 7.20 (td, *J* = 2.6 Hz, 1.2, 1H, 2-H), 6.92 (s, 1H, 11-H), 6.89 (td, *J* = 1.8 Hz, 1H, 4-H), 6.66 (d, *J* = 2.0 Hz, 1H, 16-H), 6.33 (dt, *J* = 4.3, 1.8 Hz, 1H, 3-H), 6.06 (d, *J* = 1.6 Hz, 1H, 10-H), 3.98 (s, 3H, 18-H), 2.53 (s, 3H, 19-H), 2.36 (t, *J* = 7.5 Hz, 2H, 20-H), 1.55 (h, *J* = 7.4 Hz, 2H, 21-H), 0.93 (t, *J* = 7.3 Hz, 3H, 22-H). **^{13}C NMR** (76 MHz, $CDCl_3$, δ): 165.9 (C-9), 147.8 (C-6), 147.0 (C-14), 128.5 (C-15), 128.3 (C-16), 127.0 (C-2), 125.2 (C-12), 122.3 (C-5), 120.8 (C-8), 117.2 (C-4), 116.1 (C-11), 111.8 (C-3), 93.0 (C-10), 58.9 (C-18), 27.5 (C-20), 23.4 (C-21), 13.9 (C-22), 12.5 (C-19). **FT-IR** (cm^{-1}, neat): 3153, 3097, 3069, 3010, 2958, 2926, 2870, 1629, 1601, 1574, 1542, 1510, 1450, 1352, 1250, 1130, 1066, 1042, 987, 957, 880, 836, 808, 780, 744, 720, 698, 649, 621, 594. **HRMS** (ESI) *m/z*: $[M - Cl]^+$ calcd for $C_{18}H_{22}N_3O$, 296.1757; found, 296.1757.

(*Z*)-4'-Methoxy-5'-((5-methyl-4-pentyl-1*H*-pyrrol-2-yl)methylene)-1*H*,5'*H*-[2,2'-bipyrrol]-1'-ium chloride (III-1ab·HCl, prodigiosin·HCl)

Under N_2 atmosphere, 2-methyl-3-pentyl-1*H*-pyrrole (**III-15b**, 651 mg, 4.31 mmol, 2.50 eq.) and Boc-MBC (**III-174**, 500 mg, 1.72 mmol, 1.00 eq.) were dissolved in MeOH (40 mL) and cooled to 0 °C. HCl in MeOH (1.25 M, 3.58 mL, 2.24 mmol, 1.30 eq.) was added dropwise, and the solution was stirred for 60 min at 21 °C. A second portion of HCl in MeOH (1.25 M, 3.58 mL, 2.24 mmol, 1.30 eq.) was added and the solution was further stirred at 21 °C for 18 h. The reaction was quenched by the addition of 25% NH_3 (*aq*.) and the solvent was evaporated under reduced pressure. The residue was diluted with CH_2Cl_2 (100 mL) and washed with brine (2 x 100 mL). The organic phase was dried over $MgSO_4$, filtered over degreased cotton wool, and the solvent was removed in *vacuo*. Chromatography on silica using CH_2Cl_2 + 0.7% 7 N NH_3 in MeOH, followed by chromatography on silica using *n*-pentane/CH_2Cl_2 (60:40) + 4% 7 N NH_3 in MeOH, and acidification with 1 M HCl in Et_2O afforded the desired the HCl salt of prodigiosin (**III-1ab·HCl**, 423 mg, 1.17 mmol, 68%) as a deep purple amorphous solid.



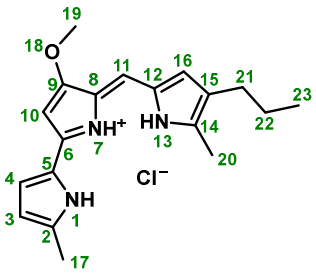
Mp 135.5–139.9 °C. **^{1}H NMR** (300 MHz, $CDCl_3$, δ): 12.69 (brs, 2H, 7-H, 13-H), 12.55 (brs, 1H, 1-H), 7.22 (td, 1H, 2-H), 6.94 (s, 1H, 11-H), 6.91 (ddd, 1H, 4-H), 6.67 (d, 1H, 16-H), 6.34 (dt, 1H, 3-H), 6.07 (d, 1H, 10-H), 3.99 (s, 3H, 18-H), 2.54 (s, 3H, 19-H), 2.38 (t, 2H, 20-H), 1.52 (p, 2H, 21-H), 1.39 – 1.22 (m, 4H, 22-H, 23-H), 0.88 (t, 3H, 24-H). **^{13}C NMR** (76 MHz, $CDCl_3$, δ): 165.9 (C-9), 147.8 (C-6), 147.1 (C-14), 128.6 (C-15), 128.5 (C-16), 127.0 (C-2), 125.3 (C-12), 122.4 (C-5), 120.8 (C-8), 117.2 (C-4), 116.1 (C-11), 111.9 (C-3), 93.0 (C-10), 58.8 (C-18), 31.6 (C-22), 29.9 (C-21), 25.4 (C-20), 22.6 (C-23), 14.2 (C-24), 12.6 (C-19). **FT-IR** (cm^{-1}, neat): 3215, 3154, 3098, 3070, 3011, 2954, 2924, 2853, 1633, 1604, 1575, 1544, 1509, 1469, 1148, 1412, 1385, 1351, 1278, 1264, 1250, 1198, 1135, 1065, 1042, 998, 988, 956, 888, 879, 836, 808, 785, 744, 716, 697, 650, 622, 594, 544, 502, 461. **HRMS** (ESI) *m/z*: $[M - Cl]^+$ calcd for $C_{20}H_{26}N_3O$, 324.2070; found, 324.2077. t_R (LC-MS method): 7.67 min. **CAS** 56144-17-3.

General Procedure for the Synthesis of 5-Alkylated Prodiginines III-1ba–gb

MBC and pyrrole derivatives were transformed to prodiginines under acid catalysis as performed by Boger and Patel.[873] An MBC derivative **III-14a**–**g** (1.00 eq.) is dissolved in MeOH (10 mM solution). After the addition of 1*H*-pyrrole **III-15a**-**c** (2.00 eq.), the solution is cooled to 0 °C. After 15 min of stirring, 1.25 M HCl in MeOH (1.80 eq.) is added dropwise. With completed HCl addition, the reaction is thawed and then stirred at 21 °C overnight. Water is added and the mixture is then quenched with 25% NH_3 (*aq*.). The product is extracted with CH_2Cl_2 (3 x 50 mL). Merged organic phases are dried over $MgSO_4$ and filtered over degreased cotton wool. After removal of the solvent, the residue is chromatographed on silica with CH_2Cl_2 and 0.7% 7 N NH_3 in MeOH. Product-containing fractions are merged and chromatographed on silica with *n*-pentane/CH_2Cl_2 (60:40) and 4% 7 N NH_3 in MeOH to remove unconverted MBC precursor. Evaporation of the solvent and acidification with 1 M HCl in Et_2O yields a purple film that is precipitated by repeated addition of PE and solvent evaporation. Finally, the desired prodiginines **III-1ba–gb** are obtained as deep purple amorphous solids.

(*Z*)-4'-Methoxy-5-methyl-5'-((5-methyl-4-propyl-1*H*-pyrrol-2-yl)methylene)-1*H*,5'*H*-[2,2'-bipyrrol]-1'-ium chloride (III-1ba·HCl)

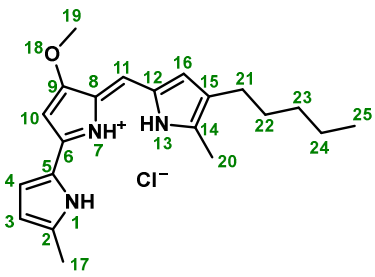
Following the general procedure for the synthesis of 5-alkylated prodiginines, carbaldehyde (**III-14b**, 54.0 mg, 0.26 mmol, 1.00 eq.), pyrrole (**III-15a**, 65.2 mg, 0.53 mmol, 2.00 eq.) and HCl in MeOH (381 µL, 0.48 mmol, 1.80 eq.) were converted to the HCl salt of prodigiosin analogue (**III-14ba**, 60.1 mg, 0.17 mmol, 66%, 95.7% ± 0.85% purity by qNMR) and the product was obtained as a deep purple amorphous solid.



Mp 158.6–160.5 °C. **^{1}H NMR** (300 MHz, $CDCl_3$, δ): 12.63 – 12.44 (brs, 2H, 1-NH, 13-H), 12.38 (brs, 1H, 7-H), 6.85 – 6.77 (m, 2H, 4-H, 11-H), 6.59 (d, *J* = 1.8 Hz, 1H, 16-H), 6.03 (t, *J* = 3.1 Hz, 1H, 3-H), 5.97 (d, *J* = 1.7 Hz, 1H, 10-H), 3.94 (s, 3H, 19-H), 2.50 (s, 3H, 20-H), 2.43 (s, 3H, 17-H), 2.34 (t, *J* = 7.5 Hz, 2H, 21-H), 1.54 (h, *J* = 7.4, 2H, 22-H), 0.92 (t, *J* = 7.3 Hz, 3H, 23-H). **^{13}C NMR** (76 MHz, $CDCl_3$, δ): 165.7 (C-9), 147.7 (C-6), 145.1 (C-14), 139.6 (C-2), 127.5 (C-15), 127.2 (C-16), 124.9 (C-12), 121.3 (C-8), 121.0 (C-5), 118.9 (C-4), 114.6 (C-11), 111.4 (C-3), 92.6 (C-10), 58.7 (C-19), 27.5 (C-21), 23.5 (C-22), 13.9 (C-23), 13.6 (C-17), 12.3 (C-20). **FT-IR** (cm^{-1}, neat): 3221, 3164, 3143, 3115, 3115, 3105, 3066, 3010, 2958, 2914, 2873, 2859, 2854, 2818, 1635, 1608, 1552, 1537, 1517, 1493, 1441, 1415, 1403, 1370, 1338, 1252, 1208, 1184, 1159, 1128, 1083, 1045, 995, 980, 967, 909, 891, 884, 867, 844, 823, 792, 769, 752, 743, 732, 668, 647, 638, 621, 548, 478. **HRMS** (ESI) *m/z*: $[M - Cl]^+$ calcd for $C_{19}H_{24}N_3O$, 310.1914; found, 310.1911. t_R (LC-MS method): 7.56 min.

(*Z*)-4'-Methoxy-5-methyl-5'-((5-methyl-4-pentyl-1*H*-pyrrol-2-yl)methylene)-1*H*,5'*H*-[2,2'-bipyrrol]-1'-ium chloride (III-1bb·HCl)

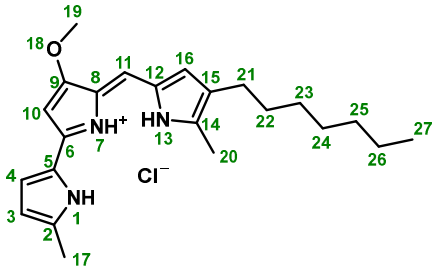
Following the general procedure for the synthesis of 5-alkylated prodiginines, carbaldehyde (**III-14b**, 100 mg, 0.49 mmol, 1.00 eq.), pyrrole (**III-15b**, 148 mg, 0.98 mmol, 2.00 eq.) and HCl in MeOH (705 µL, 0.88 mmol, 1.80 eq.) were converted to the HCl salt of prodigiosin analogue (**III-1bb·HCl**, 150 mg, 0.40 mmol, 82%, 89.5% ± 0.94% purity by qNMR) and the product was obtained as a deep purple amorphous solid.



Mp 77.6–80.1 °C. **^{1}H NMR** (300 MHz, $CDCl_3$, δ): 12.54 (brs, 2H, 1-H, 13-H), 12.44 (brs, 1H, 7-H), 6.87 – 6.81 (m, 2H, 4-H, 11-H), 6.61 (d, 1H, 16-H), 6.11 – 6.03 (m, 1H, 3-H), 6.00 (d, *J* = 1.9 Hz, 1H, 10-H), 3.97 (s, 3H, 19-H), 2.52 (s, 3H, 20-H), 2.45 (s, 3H, 17-H), 2.38 (t, *J* = 7.6 Hz, 2H, 21-H), 1.53 (p, *J* = 7.4 Hz, 2H, 22-H), 1.30 (qq, 4H, 23-H, 24-H), 0.94 – 0.80 (m, 3H, 25-H). **^{13}C NMR** (76 MHz, $CDCl_3$, δ): 165.8 (C-9), 147.7 (C-16), 145.3 (C-14), 139.7 (C-2), 127.8 (C-15), 127.3 (C-16), 125.0 (C-12), 121.3 (C-8), 121.1 (C-5), 118.9 (C-4), 114.7 (C-11), 111.4 (C-3), 92.6 (C-10), 58.8 (C-19), 31.6 (C-23), 30.1 (C-22), 25.5 (C-21), 22.6 (C-24), 14.2 (C-15), 13.7 (C-17), 12.4 (C-20). **FT-IR** (cm^{-1}, neat): 3171, 3141, 3101, 3067, 2954, 2922, 2855, 1630, 1605, 1579, 1538, 1493, 1447, 1414, 1402, 1348, 1286, 1253, 1207, 1151, 1130, 1099, 1078, 1037, 994, 965, 899, 882, 841, 805, 785, 768, 732, 698, 666, 643, 623, 550, 502. **HRMS** (ESI) *m/z*: $[M - Cl]^+$ calcd for $C_{21}H_{28}N_3O$, 338.2227; found, 338.2228. t_R (LC-MS method): 7.83 min.

(*Z*)-4'-Methoxy-5-methyl-5'-((5-methyl-4-heptyl-1*H*-pyrrol-2-yl)methylene)-1*H*,5'*H*-[2,2'-bipyrrol]-1'-ium chloride (III-1bc·HCl)

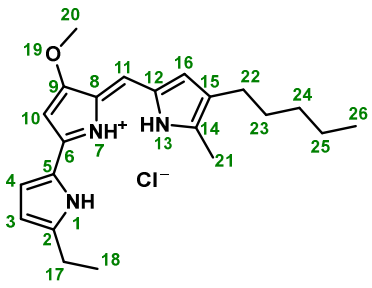
Following the general procedure for the synthesis of 5-alkylated prodiginines, carbaldehyde (**III-14b,** 50.0 mg, 0.24 mmol, 1.00 eq.), pyrrole (**III-15c**, 87.8 mg, 0.49 mmol, 2.00 eq.) and HCl in MeOH (353 µL, 0.44 mmol, 1.80 eq.) were converted to the HCl salt of prodigiosin analogue (**III-1bc·HCl**, 79.0 mg, 0.20 mmol, 80%, 97.3% ± 0.87% purity by qNMR) and the product was obtained as a deep purple amorphous solid.



Mp 120.5–122.6 °C. **^{1}H NMR** (300 MHz, $CDCl_3$, δ): 12.50 (brs, 2H, 1-H, 13-H), 12.38 (brs, 1H, 7-H), 6.84 – 6.78 (m, 2H, 4-H, 11-H), 6.59 (d, *J* = 2.4 Hz, 1H, 16-H), 6.03 (dd, *J* = 1.9 Hz, 1H, 3-H), 5.97 (d, *J* = 1.9 Hz, 1H, 10-H), 3.94 (s, 3H, 19-H), 2.50 (s, 3H, 20-H), 2.43 (s, 3H, 17-H), 2.36 (t, *J* = 7.5 Hz, 2H, 21-H), 1.51 (p, *J* = 7.3 Hz, 2H, 22-H), 1.36 – 1.17 (m, 8H, 23-H, 24-H, 26-H, 27-H), 0.92 – 0.79 (m, 3H, 28-H). **^{13}C NMR** (76 MHz, $CDCl_3$, δ): 165.7 (C-9), 147.6 (C-6), 145.1 (C-14), 139.6 (C-2), 127.7 (C-15), 127.2 (C-16), 125.0 (C-12), 121.2 (C-8), 121.0 (C-5), 118.9 (C-4), 114.6 (C-11), 111.4 (C-3), 92.6 (C-10), 58.7 (C-19), 31.9 (C-26), 30.3 (C-22), 29.3 (C-24), 29.2 (C-23), 25.5 (C-21), 22.8 (C-27), 14.2 (C-28), 13.6 (C-17), 12.3 (C-20). **FT-IR** (cm^{-1}, neat): 3223, 3171, 3144, 3116, 3073, 3062, 2953, 2921, 2851, 1629, 1605, 1581, 1540, 1516, 1494, 1447, 1403, 1369, 1347, 1289, 1257, 1205, 1174, 1089, 1042, 976, 887, 841, 829, 818, 810, 792, 779, 765, 741, 726, 705, 683, 661, 642, 605, 543, 517, 505, 476. **HRMS** (ESI) *m/z*: $[M - Cl]^+$ calcd for $C_{23}H_{32}N_3O$, 366.2540; found, 366.2546. t_R (LC-MS method): 7.95 min.

(*Z*)-5-Ethyl-4'-methoxy-5'-((5-methyl-4-pentyl-1*H*-pyrrol-2-yl)methylene)-1*H*,5'*H*-[2,2'-bipyrrol]-1'-ium chloride (III-1cb·HCl)

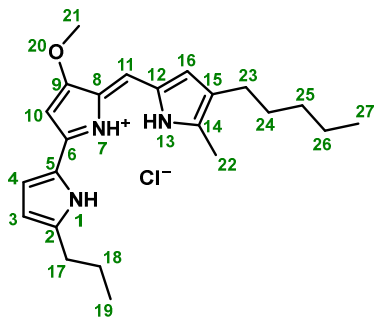
Following the general procedure for the synthesis of 5-alkylated prodiginines, carbaldehyde (**III-14c**, 50.0 mg, 0.24 mmol, 1.00 eq.), pyrrole (**III-15b**, 87.8 mg, 0.49 mmol, 2.00 eq.) and HCl in MeOH (353 µL, 0.44 mmol, 1.80 eq.) were converted to the HCl salt of prodigiosin analogue (**III-1cb·HCl**, 79.0 mg, 0.20 mmol, 80%, 94.6% ± 0.59% purity by qNMR) and the product was obtained as a deep purple amorphous solid.



Mp 111.9–117.3 °C. **^{1}H NMR** (300 MHz, $CDCl_3$, δ): 12.58 (brs, 1H, 13-H), 12.49 (brs, 2H, 1-H, 7-H), 6.89 – 6.79 (m, 2H, 4-H, 11-H), 6.61 (d, *J* = 2.5 Hz, 1H, 16-H), 6.09 (dd, *J* = 3.7, 2.4 Hz,1H, 3-H), 6.00 (d, *J* = 2.0 Hz, 1H, 10-H), 3.96 (s, 3H, 20-H), 2.80 (q, *J* = 7.6 Hz, 2H, 17-H), 2.51 (s, 3H, 21-H), 2.37 (t, *J* = 7.7 Hz, 2H, 22-H), 1.59 – 1.46 (m, 2H, 23-H), 1.38 (t, *J* = 7.6 Hz, 3H, 18-H), 1.36 – 1.21 (m, 4H, 24-H, 25-H), 0.92 – 0.83 (m_c, 3H, 26-H). **^{13}C NMR** (76 MHz, $CDCl_3$, δ): 165.7 (C-9), 147.8 (C-6), 146.0 (C-2), 145.2 (C-14), 127.8 (C-15), 127.3 (C-16), 125.0 (C-12), 121.3 (C-8), 121.1 (C-5), 118.7 (C-4), 114.6 (C-11), 110.0 (C-3), 92.6 (C-10), 58.7 (C-20), 31.6 (C-24), 30.0 (C-23), 25.5 (C-22), 22.6 (C-25), 21.6 (C-17), 14.2 (C-26), 13.4 (C-18), 12.3 (C-21). **FT-IR** (cm^{-1}, neat): 3221, 3171, 3145, 3118, 3063, 2950, 2923, 2853, 1632, 1606, 1580, 1547, 1540, 1493, 1447, 1402, 1375, 1360, 1308, 1290, 1257, 1202, 1174, 1146, 1077, 1058, 1043, 1004, 985, 969, 887, 841, 820, 807, 785, 764, 737, 648, 626, 610. **HRMS** (ESI) *m/z*: $[M - Cl]^+$ calcd for $C_{22}H_{30}N_3O$, 352.2383; found, 352.2387. t_R (LC-MS method): 7.92 min.

(*Z*)-4'-Methoxy-5-propyl-5'-((5-methyl-4-pentyl-1*H*-pyrrol-2-yl)methylene)-1*H*,5'*H*-[2,2'-bipyrrol]-1'-ium chloride (III-1db·HCl)

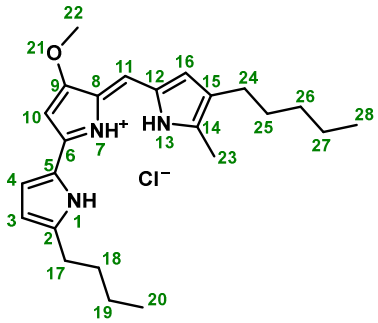
Following the general procedure for the synthesis of 5-alkylated prodiginines, carbaldehyde (**III-14d**, 116 mg, 0.50 mmol, 1.00 eq.), pyrrole (**III-15b**, 151 mg, 1.00 mmol, 2.00 eq.) and HCl in MeOH (719 µL, 0.90 mmol, 1.80 eq.) were converted to the HCl salt of prodigiosin analogue (**III-1db·HCl**, 116 mg, 0.29 mmol, 58%, 99.5% ± 0.94% purity by qNMR) and the product was obtained as a deep purple amorphous solid.



Mp 105.7–107.5 °C. **^{1}H NMR** (300 MHz, $CDCl_3$, δ): 12.59 (brs, 1H, 13-H), 12.51 (brs, 2H, 1-H, 7-H), 6.88 – 6.83 (m, 2H, 4-H, 11-H), 6.62 (d, *J* = 2.5 Hz, 1H, 16-H), 6.10 (dd, *J* = 3.8, 2.2 Hz, 1H, 3-H), 6.01 (d, *J* = 1.9 Hz, 1H, 10-H), 3.98 (s, 3H, 21-H), 2.75 (t, *J* = 7.6 Hz, 2H, 17-H), 2.52 (s, 3H, 22-H), 2.38 (t, *J* = 7.6 Hz, 2H, 23-H), 1.82 (h, *J* = 7.4 Hz, 2H, 18-H), 1.52 (p, *J* = 7.4 Hz, 2H, 24-H), 1.38 – 1.22 (m, 4H, 25-H, 26-H), 0.99 (t, *J* = 7.3 Hz, 3H, 19-H), 0.93 – 0.84 (m_c, 3H, 27-H). **^{13}C NMR** (76 MHz, $CDCl_3$, δ): 165.7 (C-9), 147.8 (C-6), 145.3 (C-14), 144.7 (C-2), 127.8 (C-15), 127.3 (C-16), 125.0 (C-12), 121.3 (C-8), 121.1 (C-5), 118.7 (C-4), 114.7 (C-11), 110.7 (C-3), 92.6 (C-10), 58.8 (C-21), 31.6 (C-25), 30.4 (C-17), 30.1 (C-24), 25.5 (C-23), 22.7 (C-26), 22.6 (C-18), 14.2 (C-27), 14.0 (C-19), 12.4 (C-22). **FT-IR** (cm^{-1}, neat): 3170, 3144, 3111, 3010, 2961, 2927, 2869, 2857, 1632, 1605, 1577, 1537, 1519, 1495, 1463, 1447, 1407, 1384, 1346, 1284, 1251, 1207, 1187, 1151, 1131, 1065, 1044, 998, 972, 955, 891, 883, 836, 816, 806, 786, 728, 695, 677, 655, 623, 545, 505, 477. **HRMS** (ESI) *m/z*: $[M - Cl]^+$ calcd for $C_{23}H_{32}N_3O$, 366.2540; found, 366.2542. t_R (LC-MS method): 8.02 min.

(*Z*)-5-Butyl-4'-methoxy-5'-((5-methyl-4-pentyl-1*H*-pyrrol-2-yl)methylene)-1*H*,5'*H*-[2,2'-bipyrrol]-1'-ium chloride (III-1eb·HCl)

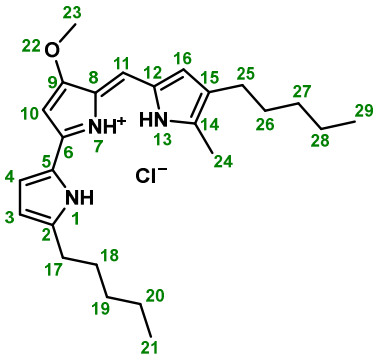
Following the general procedure for the synthesis of 5-alkylated prodiginines, carbaldehyde (**III-14e**, 120 mg, 0.49 mmol, 1.00 eq.), pyrrole (**III-15b**, 147 mg, 0.97 mmol, 2.00 eq.) and HCl in MeOH (702 µL, 0.88 mmol, 1.80 eq.) were converted to the HCl salt of prodigiosin analogue (**III-1eb·HCl**, 148 mg, 0.36 mmol, 73%, 99.9% ± 0.40% purity by qNMR) and the product was obtained as a deep purple amorphous solid.



Mp 96.7–100.7 °C. **^{1}H NMR** (300 MHz, $CDCl_3$, δ): 12.59 (brs, 1H, 13-H), 12.51 (brs, 2H, 1-H, 7-H), 6.88 – 6.83 (m, 2H, 4-H, 11-H), 6.62 (d, *J* = 2.6 Hz, 1H, 16-H), 6.10 (dd, *J* = 3.8, 2.2 Hz, 1H, 3-H), 6.01 (d, *J* = 1.9 Hz, 1H, 10-H), 3.98 (s, 3H, 22-H), 2.77 (t, *J* = 7.7 Hz, 2H, 17-H), 2.52 (s, 3H, 23-H), 2.38 (t, *J* = 7.5 Hz, 2H, 24-H), 1.83 – 1.69 (m, 2H, 18-H), 1.60 – 1.46 (m, 3H, 25-H), 1.40 (h, *J* = 7.5 Hz, 2H, 19-H), 1.35 – 1.23 (m, 4H, 26-H, 27-H), 0.95 (t, *J* = 7.3 Hz, 3H, 20-H), 0.92 – 0.84 (m_c, 3H, 28 H). **^{13}C NMR** (76 MHz, $CDCl_3$, δ): 165.7 (C-9), 147.8 (C-6), 145.3 (C-14), 145.0 (C-2), 127.8 (C-15), 127.3 (C-16), 125.0 (C-12), 121.3 (C-8), 121.0 (C-5), 118.7 (C-4), 114.6 (C-11), 110.6 (C-3), 92.6 (C-10), 58.8 (C-22), 31.6 (C-26), 31.3 (C-18), 30.1 (C-25), 28.0 (C-17), 25.5 (C-24), 22.7 (C-27), 22.5 (C-19), 14.2 (C-28), 13.9 (C-20), 12.4 (C-23). **FT-IR** (cm^{-1}, neat): 3170, 3142, 3109, 3008, 2960, 2926, 2856, 1632, 1605, 1577, 1536, 1495, 1464, 1452, 1406, 1350, 1299, 1257, 1240, 1208, 1186, 1151, 1131, 1066, 1043, 1000, 972, 956, 891, 882, 837, 816, 806, 785, 732, 695,.675, 655, 545, 505, 475. **HRMS** (ESI) *m/z*: $[M - Cl]^+$ calcd for $C_{24}H_{34}N_3O$, 380.2696; found, 380.2704. t_R (LC-MS method): 8.11 min.

(*Z*)-4'-Methoxy-5-pentyl-5'-((5-methyl-4-pentyl-1*H*-pyrrol-2-yl)methylene)-1*H*,5'*H*-[2,2'-bipyrrol]-1'-ium chloride (III-1fb·HCl)

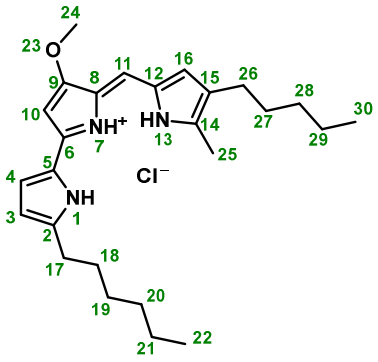
Following the general procedure for the synthesis of 5-alkylated prodiginines, carbaldehyde (**III-14f**, 130 mg, 0.50 mmol, 1.00 eq.), pyrrole (**III-15b**, 151 mg, 1.00 mmol, 2.00 eq.) and HCl in MeOH (719 µL, 0.90 mmol, 1.80 eq.) were converted to the HCl salt of prodigiosin analogue (**III-1fb·HCl**, 100 mg, 0.23 mmol, 47%, 99.9% ± 0.78% purity by qNMR) and the product was obtained as a deep purple amorphous solid.



Mp 98.0–99.7 °C. **^{1}H NMR** (300 MHz, $CDCl_3$, δ): 12.60 (brs, 1H, 13-H), 12.51 (brs, 2H, 1-H, 7-H), 6.88 – 6.83 (m, 2H, 4-H, 11-H), 6.62 (d, *J* = 2.5 Hz, 1H, 16-H), 6.10 (dd, *J* = 3.7, 2.2 Hz, 1H, 3-H), 6.01 (d, *J* = 1.9 Hz, 1H, 10-H), 3.98 (s, 3H, 23-H), 2.77 (t, *J* = 7.7 Hz, 2H, 17-H), 2.52 (s, 3H, 24-H), 2.38 (t, *J* = 7.6 Hz, 2H, 25-H), 1.79 (tp, *J* = 7.6, 2.4 Hz, 2H, 18-H), 1.53 (p, *J* = 7.5 Hz, 2H, 26-H), 1.43 – 1.21 (m, 8H, 19-H, 20-H, 27-H, 28-H), 0.95 – 0.82 (m, 6H, 21-H, 29-H). **^{13}C NMR** (76 MHz, $CDCl_3$, δ): 165.7 (C-9), 147.8 (C-6), 145.3 (C-14), 145.0 (C-2), 127.8 (C-15), 127.3 (C-16), 125.0 (C-12), 121.3 (C-8), 121.0 (C-5), 118.7 (C-4), 114.6 (C-11), 110.6 (C-3), 92.6 (C-10), 58.8 (C-23), 31.6 (C-19, C-27), 30.1 (C-26), 28.9 (C-18), 28.3 (C-17), 25.5 (C-25), 22.7 (C-28), 22.5 (C-20), 14.2 (C-21, C-21), 12.4 (C-24). **FT-IR** (cm^{-1}, neat): 3171, 3144, 3111, 3058, 3015, 2952, 2925, 2870, 2854, 1632, 1606, 1578, 1537, 1495, 1464, 1451, 1406, 1383, 1349, 1322, 1285, 1254, 1208, 1186, 1045, 971, 955, 891, 882, 836, 816, 805, 789, 731, 708, 696, 685, 675, 656, 622, 546, 505, 471. **HRMS** (ESI) *m/z*: $[M - Cl]^+$ calcd for $C_{25}H_{36}N_3O$, 394.2853; found, 394.2855. t_R (LC-MS method): 8.09 min.

(*Z*)-5-Hexyl-4'-methoxy-5'-((5-methyl-4-pentyl-1*H*-pyrrol-2-yl)methylene)-1*H*,5'*H*-[2,2'-bipyrrol]-1'-ium chloride (III-1gb·HCl)

Following the general procedure for the synthesis of 5-alkylated prodiginines, carbaldehyde (**III-14g**, 140 mg, 0.51 mmol, 1.00 eq.), pyrrole (**III-15b**, 154 mg, 1.02 mmol, 2.00 eq.) and HCl in MeOH (735 µL, 0.92 mmol, 1.80 eq.) were converted to the HCl salt of prodigiosin analogue (**III-1gb·HCl**, 109 mg, 0.25 mmol, 48%, 99.3% ± 3.73% purity by qNMR) and the product was obtained as a deep purple amorphous solid.

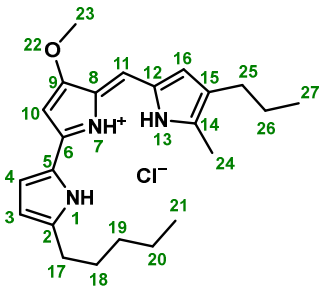


Mp 96.6–98.7 °C. **^{1}H NMR** (300 MHz, $CDCl_3$, δ): 12.57 (brs, 1H, 13-H), 12.47 (brs, 2H, 1-H, 7-H), 6.86 – 6.81 (m, 2H, 4-H, 11-H), 6.60 (d, *J* = 2.5 Hz, 1H, 16-H), 6.08 (dd, *J* = 3.7, 2.3 Hz, 1H, 3-H), 5.99 (d, *J* = 1.9 Hz, 1H, 10-H), 3.96 (s, 3H, 24-H), 2.75 (t, *J* = 7.7 Hz, 2H, 17-H), 2.51 (s, 3H, 25-H), 2.37 (t, *J* = 7.6 Hz, 2H, 26-H), 1.77 (p, *J* = 7.5 Hz, 2H, 18-H), 1.52 (p, *J* = 7.4 Hz, 2H, 27-H), 1.42 – 1.20 (m, 10H, 19-H, 20-H, 21-H, 28-H, 29-H), 0.93 – 0.81 (m, 6H, 22-H, 30-H). **^{13}C NMR** (76 MHz, $CDCl_3$, δ): 165.7 (C-9), 147.7 (C-6), 145.1 (C-14), 144.9 (C-2), 127.7 (C-15), 127.2 (C-16), 125.0 (C-12), 121.3 (C-8), 121.0 (C-5), 118.7 (C-4), 114.5 (C-11), 110.6 (C-3), 92.6 (C-10), 58.7 (C-24), 31.64 and 31.57 (C-20, C-28), 30.0 (C-27), 29.17 and 29.12 (C-7, C-8), 28.3 (C-17), 25.4 (C-26), 22.73 and 22.63 (C-21, C-29), 14.20 and 14.17 (C-22, C-30), 12.3 (C-25). **FT-IR** (cm^{-1}, neat): 3171, 3144, 3115, 3072, 3015, 2953, 2919, 2868, 2855, 1636, 1613, 1580, 1549, 1539, 1497, 1466, 1450, 1421, 1407, 1386, 1362, 1333, 1293, 1263, 1253, 1215, 1204, 1185, 1157, 1129, 1101, 1092, 1044, 991, 978, 969, 891, 843, 817, 808, 782, 767, 735, 709, 694, 653, 625, 614, 553, 497, 456. **HRMS** (ESI) *m/z*: $[M - Cl]^+$ calcd for $C_{26}H_{38}N_3O$, 408.3009; found, 408.3017. t_R (LC-MS method): 8.30 min.

(*Z*)-4'-Methoxy-5'-((5-methyl-4-propyl-1*H*-pyrrol-2-yl)methylene)-5-pentyl-1*H*,5'*H*-[2,2'-bipyrrol]-1'-ium chloride (III-1fa·HCl)

A 50 mL Schlenk flask with magnetic stirring bar was sequentially charged with $Pd(OAc)_2$ (14.8 mg, 66.1 µmol, 0.05 eq.), SPhos (**III-122**, 32.6 mg, 79.3 µmol, 0.06 eq.), alkyl triflate (**III-96**, 500 mg, 1.32 mmol, 1.00 eq.), alkyl boronic acid (**III-140f**, 743 mg, 2.64 mmol, 2.00 eq.), and was evacuated/N_2-refilled three times. Degassed *n*BuOH (7.28 mL) was added and the mixture was stirred at 20 °C until homogeneous. A solution of K_3PO_4 (561 mg, 2.64 mmol, 2.00 eq., 1.45 M) in degassed H_2O (1.82 mL) was added in one portion to initiate the Suzuki reaction. The reaction vessel was lowered into a pre-heated heating mantle at 60 °C and the orange solution was stirred under argon for 13 h. The red-orange solution was diluted with CH_2Cl_2, and brine (50 mL) was added. The phases were separated and the aqueous phase was repeatedly extracted with CH_2Cl_2 (25 mL portions) until the organic phase remained nearly colourless. Merged organic phases were dried over $MgSO_4$, filtered over degreased cotton wool (**!**), and the solvent was removed *in vacuo*. The deep red film was chromatographed on silica using a gradient of CH_2Cl_2 + 0.7–3% NH_3 (7 N in MeOH).

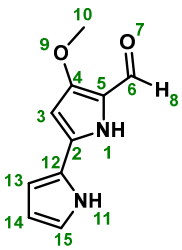
Acidification of product fractions with 1 M HCl in Et_2O, immobilisation on Celite, and chromatography on neutral aluminium oxide (Brockmann I) with *n*-pentane/EtOAc (0–80% EtOAc) provided the product as a purple film. The film was dissolved in a minimal amount of CH_2Cl_2 and acidified again. Repeated treatment with *n*-pentane assisted precipitation of the HCl salt **III-1fa·HCl** as an amorphous purple powder (383 mg, 954 µmol, 72%) upon solvent evaporation.



Mp 99.5–101.1 °C. **^{1}H NMR** (300 MHz, $CDCl_3$, δ): 2.59 (brs, 1H, 13-H), 12.50 (brs, 2H, 1-H, 7-H), 6.85 (m, 2H, 4-H, 11-H), 6.61 (d, *J* = 2.4 Hz, 1H, 16-H), 6.09 (dd, *J* = 3.9, 2.2 Hz, 1H, 3-H), 6.01 (d, *J* = 1.9 Hz, 1H, 10-H), 3.98 (s, 3H, 23-H), 2.76 (t, *J* = 7.7 Hz, 2H, 17-H), 2.52 (s, 3H, 24-H), 2.36 (t, *J* = 7.5 Hz, 2H, 25-H), 1.78 (dp, *J* = 7.5 Hz, 2H, 18-H), 1.55 (h, *J* = 7.4 Hz, 2H, 26-H), 1.44 – 1.27 (m, *J* = 3.9 Hz, 4H, 19-H, 20-H), 0.93 (t, *J* = 7.3 Hz, 4H, 27-H), 0.93 – 0.84 (m_c, *J* = 6.9, 3.9 Hz, 3H, 21-H). **^{13}C NMR** (76 MHz, $CDCl_3$, δ): 165.7 (C-9), 147.8 (C-6), 145.2 (C-14), 145.0 (C-2), 127.5 (C-15), 127.3 (C-16), 125.0 (C-12), 121.3 (C-8), 121.0 (C-5), 118.8 (C-4), 114.6 (C-11), 110.6 (C-3), 92.6 (C-10), 58.8 (C-23), 31.6 (C-19), 28.9 (C-18), 28.3 (C-17), 27.6 (C-25), 23.6 (C-26), 22.5 (C-20), 14.2 (C-21), 13.9 (C-27), 12.4 (C-24). **FT-IR** (cm^{-1}, neat): 3168, 3145, 3112, 3091, 3063, 2953, 2926, 2867, 2857, 1606, 1579, 1547, 1539, 1493, 1448, 1403, 1378, 1354, 1254, 1204, 1149, 1046, 976, 670, 886, 882, 838, 822, 808, 766, 740, 647, 627, 610. **HRMS** (ESI) *m/z*: $[M - Cl]^+$ calcd for $C_{23}H_{32}N_3O$, 366.2540; found, 366.2546.

4-Methoxy-1*H*,1'*H*-[2,2'-bipyrrole]-5-carbaldehyde (III-14a, MBC)

In a 10 mL microwave vial, Boc-MBC (**III-174**, 500 mg, 1.72 mmol, 1.00 eq.) was suspended in 2,2,2-trifluoroethanol (4.96 mL, 68.9 mmol, 40.0 eq.) and heated at constant power of 50 W up to 120 °C in a CEM Discover laboratory microwave. During subsequent cooling, the product crystallised from a dark purple to black solution. The product was recovered by filtration and repeatedly washed with EtOAc to remove residual purple impurities. The deprotected bipyrrole MBC (**III-14a**, 267 mg, 1.40 mmol, 81%) was finally obtained as a metallic silver powder.



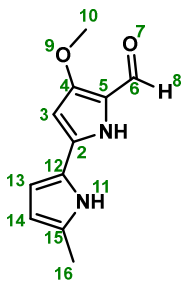
Mp 250–265 °C (decomposition). **^{1}H NMR** (600 MHz, DMSO-d_6, δ): 11.43 (s, 1H, 1-H), 11.24 (s, 1H, 11-H), 9.30 (s, 1H, 8-H), 6.91 (m, 1H, 15-H), 6.75 (s, 1H, 13-H), 6.27 (m, 1H, 3-H), 6.12 (m, 1H, 14-H), 3.83 (s, 3H, 10-H). **^{13}C NMR** (151 MHz, DMSO-d_6, δ): 171.6 (C-6), 158.6 (C-4), 133.1 (C-2), 123.3 (C-12), 120.3 (C-15), 117.4 (C-5), 109.3 (C-14), 108.3 (C-13), 90.9 (C-3), 57.7 (C-10). **FT-IR** (cm^{-1}, neat): 3245, 3192, 3125, 3039, 2952, 2840, 1593, 1546, 1517, 1504, 1422, 1358, 1346, 1302, 1276, 1234, 1187, 1160, 1116, 1044, 1013, 974, 829, 810, 770, 740, 694, 667, 625, 612, 604, 587, 463. **HRMS** (ESI) *m/z*: $[M + H]^+$ calcd for $C_{10}H_{11}N_2O_2$, 191.0815; found, 191.0818. t_R (LC-MS method): 7.01 min. **CAS** 10476-41-2.

General Procedure for the Synthesis of 5'-*n*-Alkylated MBC Derivatives III-14b–g

A Schlenk flask with magnetic stirring bar is sequentially charged with $Pd(OAc)_2$ (5.0 mol-%), SPhos (**III-122**, 6.0 mol-%), bromide **III-75** (1.00 eq.), crude Boc-protected pyrrole boronic acid **III-140b**–**g** (3.00 eq.) and evacuated/N_2-refilled three times. Degassed *n*BuOH is added and the mixture is stirred at 20 °C until homogeneous. A 1.45 M solution of K_3PO_4 (2.00 eq.) in degassed water is added to give an *n*BuOH/water ratio of 4:1. The reaction vessel is lowered into a pre-heated 60 °C bath and the orange solution is stirred under argon overnight. The solvent is evaporated, water (50 mL) is added to the slurry and the mixture is then extracted with EtOAc (3 x 50 mL). Combined organic phases are washed with brine (2 x 25 mL), dried over $MgSO_4$, filtered over degreased cotton wool, and the solvent is removed under reduced pressure. The resulting solid is recovered by filtration and washed with cold distilled *n*-pentane. The green solid, which contains a mixture of partially deprotected and Boc-protected carbaldehyde, is refluxed for 6 h at 90 °C in 45 eq. 2,2,2-trifluoroethanol. Evaporation of the solvent and trituration of the remaining solid in *n*-pentane provides the alkylated MBC derivatives **III-14b**–**g** as green solids, which are recovered by filtration and washed with distilled *n*-pentane and Et_2O and then dried under high vacuum.

4-Methoxy-5'-methyl-1*H*,1'*H*-[2,2'-bipyrrole]-5-carbaldehyde (III-14b)

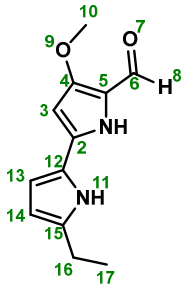
Following the general procedure for the synthesis of 5'-*n*-alkylated MBC derivatives, bromide (**III-75**, 800 mg, 3.09 mmol, 1.00 eq.), boronic acid (**III-140b**, 2.60 g, 9.26 mmol, 3.00 eq.), SPhos (**III-122**, 76.0 mg, 0.19 mmol, 6 mol-%), $Pd(OAc)_2$ (34.7 mg, 0.15 mmol, 5 mol-%), and K_3PO_4 (1.31 g, 6.17 mmol, 2.00 eq.) were converted to 4-methoxy-5'-methyl-1*H*,1'*H*-[2,2'-bipyrrole]-5-carbaldehyde (**III-14b**, 379 mg, 1.86 mmol, 60%) after 15 h reaction time. The product was obtained as a green powder.



Mp 250–275 °C (decomposition). **^{1}H NMR** (600 MHz, DMSO-d_6, δ): 11.27 (s, 1H, 1-H), 11.00 (s, 1H, 11-H), 9.26 (s, 1H, 8-H), 6.66 – 6.58 (m, 1H, 13-H), 6.23 – 6.16 (m, 1H, 3-H), 5.84 – 5.77 (m, 1H, 14-H), 3.82 (s, 3H, 10-H), 2.22 (s, 3H, 16-H). **^{13}C NMR** (151 MHz, DMSO-d_6, δ): 171.1 (C-6). 158.8 (C-4), 133.5 (C-2), 130.1 (C-15), 122.0 (C-12), 117.2 (C-5), 108.8 (C-13), 107.6 (C-14), 90.3 (C-3), 57.7 (C-10), 12.7 (C-16). **FT-IR** (cm^{-1}, neat): 3254, 3205, 3127, 3071, 2954, 2837, 1585, 1546, 1514, 1426, 1357, 1333, 1296, 1280, 1254, 1203, 1177, 1164, 1033, 1018, 1000, 991, 972, 833, 790, 770, 697, 653, 624, 589, 482. **HRMS** (ESI) *m/z*: $[M + H]^+$ calcd for $C_{11}H_{13}N_2O_2$, 205.0973; found, 205.0973. t_R (LC-MS method): 7.54 min.

5'-Ethyl-4-methoxy-1*H*,1'*H*-[2,2'-bipyrrole]-5-carbaldehyde (III-14c)

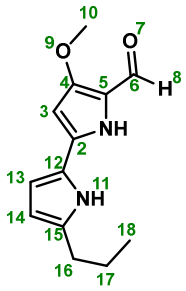
Following the general procedure for the synthesis of 5'-*n*-alkylated MBC derivatives, bromide (**III-75**, 850 mg, 3.28 mmol, 1.00 eq.), boronic acid (**III-140c**, 2.35 g, 9.84 mmol, 3.00 eq.), SPhos (**III-122**, 80.8 mg, 0.20 mmol, 6 mol-%), $Pd(OAc)_2$ (36.8 mg, 0.16 mmol, 5 mol-%), and K_3PO_4 (1.39 g, 6.56 mmol, 2.00 eq.) were converted to 5'-ethyl-4-methoxy-1*H*,1'*H*-[2,2'-bipyrrole]-5-carbaldehyde (**III-14c**, 375 mg, 1.72 mmol, 52%) after 14 h reaction time. The product was obtained as a green powder.



Mp 243.7–245.5 °C. **^{1}H NMR** (300 MHz, DMSO-d_6, δ): 11.27 (s, 1H, 1-H), 10.95 (s, 1H, 11-H), 9.26 (d, 1H, 8-H), 6.70 – 6.53 (m, 1H, 13-H), 6.30 – 6.13 (m, 1H, 3-H), 5.92 – 5.75 (m, 1H, 14-H), 3.92 – 3.69 (m, 3H, 10-H), 2.65 – 2.53 (m, 2H, 16-H), 1.19 (q, 3H, 17-H). **^{13}C NMR** (76 MHz, DMSO-d_6, δ): 171.1 (C-6), 158.8 (C-4), 136.6 (C-15), 133.6 (C-2), 122.0 (C-12), 117.2 (C-5), 108.7 (C-13), 106.2 (C-14), 90.4 (C-3), 57.7 (C-10), 20.4 (C-16), 13.7 (C-17). **FT-IR** (cm^{-1}, neat): 3250, 3197, 2972, 2833, 1593, 1553, 1513, 1445, 1422, 1357, 1302, 1284, 1248, 1199, 1175, 1161, 1147, 1039, 1014, 990, 832, 766, 740, 698, 588, 484. **HRMS** (ESI) *m/z*: $[M + H]^+$ calcd for $C_{12}H_{15}N_2O_2$, 219.1128; found, 219.1132. t_R (LC-MS method): 7.93 min. **CAS** 325460-98-8.

4-Methoxy-5'-propyl-1*H*,1'*H*-[2,2'-bipyrrole]-5-carbaldehyde (III-14d)

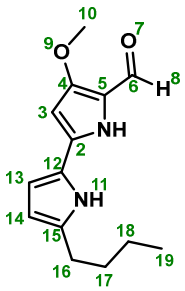
Following the general procedure for the synthesis of 5'-*n*-alkylated MBC derivatives, bromide (**III-75**, 800 mg, 3.09 mmol, 1.00 eq.), boronic acid (**III-140d**, 2.34 g, 9.26 mmol, 3.00 eq.), SPhos (**III-122**, 76.0 mg, 0.19 mmol, 6 mol-%), $Pd(OAc)_2$ (34.7 mg, 0.15 mmol, 5 mol-%), and K_3PO_4 (1.31 g, 6.17 mmol, 2.00 eq.) were converted to 4-methoxy-5'-propyl-1*H*,1'*H*-[2,2'-bipyrrole]-5-carbaldehyde (**III-14d**, 497 mg, 2.14 mmol, 69%) after 17 h reaction time. The product was obtained as a green powder.



Mp 224.7–226.8 °C. **^{1}H NMR** (600 MHz, DMSO-d_6, δ): 11.27 (s, 1H, 1-H), 10.94 (s, 1H, 11-H), 9.26 (s, 1H, 8-H), 6.65 – 6.57 (m, 1H, 13-H), 6.22 (s, 1H, 3-H), 5.86 – 5.81 (m, 1H, 14-H), 3.83 (s, 3H, 10-H), 2.53 (t, J = 7.5 Hz, 2H, 16-H), 1.60 (h, J = 7.4 Hz, 2H, 17-H), 0.91 (t, J = 7.3 Hz, 3H, 18-H). **^{13}C NMR** (151 MHz, DMSO-d_6, δ): 171.1 (C-6), 158.7 (C-4), 135.0 (C-15), 133.5 (C-2), 121.9 (C-12), 117.1 (C-5), 108.6 (C-13), 106.8 (C-14), 90.4 (C-3), 57.7 (C-10), 29.2 (C-16), 22.4 (C-17), 13.6 (C-18). **FT-IR** (cm^{-1}, neat): 3253, 3201, 3135, 3071, 3008, 2956, 2929, 2870, 2381, 1593, 1553, 1516, 1462, 1447, 1421, 1356, 1343, 1302, 1248, 1224, 1199, 1176, 1161, 1041, 1016, 986, 831, 769, 692, 664, 624, 587, 484, 453. **HRMS** (ESI) *m/z*: $[M + H]^+$ calcd for $C_{13}H_{17}N_2O_2$, 233.1285; found, 233.1286. t_R (LC-MS method): 8.23 min.

5'-Butyl-4-methoxy-1*H*,1'*H*-[2,2'-bipyrrole]-5-carbaldehyde (III-14e)

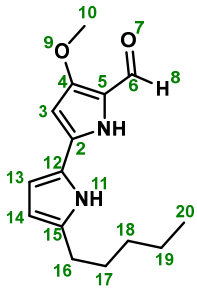
Following the general procedure for the synthesis of 5'-*n*-alkylated MBC derivatives, bromide (**III-75**, 700 mg, 2.70 mmol, 1.00 eq.), boronic acid (**III-140e**, 2.17 g, 8.10 mmol, 3.00 eq.), SPhos (**III-122**, 66.5 mg, 0.16 mmol, 6 mol-%), $Pd(OAc)_2$ (30.3 mg, 0.14 mmol, 5 mol-%), and K_3PO_4 (1.15 g, 5.40 mmol, 2.00 eq.) were converted to 5'-butyl-4-methoxy-1*H*,1'*H*-[2,2'-bipyrrole]-5-carbaldehyde (**III-14e**, 499 mg, 2.03 mmol, 75%) after 17 h reaction time. The product was obtained as a green powder.



Mp 203.5–205.6 °C. **^{1}H NMR** (300 MHz, DMSO-d_6, δ): 11.26 (s, 1H, 1-H), 10.93 (s, 1H, 11-H), 9.26 (s, 1H, 8-H), 6.65 – 6.57 (m, 1H, 13-H), 6.22 (t, 1H, 3-H), 5.86 – 5.80 (m, 1H, 14-H), 3.83 (s, 3H, 10-H), 2.55 (t, *J* = 8.1 Hz, 2H, 16-H), 1.57 (p, *J* = 7.6 Hz, 2H, 17-H), 1.40 – 1.25 (m, 2H, 18-H), 0.90 (t, *J* = 7.3 Hz, 3H, 19-H). **^{13}C NMR** (76 MHz, DMSO-d_6, δ): 171.1 (C-6), 158.8 (C-4), 135.2 (C-15), 133.5 (C-2), 121.9 (C-12), 117.1 (C-5), 108.7 (C-13), 106.8 (C-14), 90.4 (C-3), 57.7 (C-10), 31.3 (C-17), 26.9 (C-16), 21.8 (C-18), 13.7 (C-19). **FT-IR** (cm^{-1}, neat): 3257, 3208, 3002, 2952, 2928, 2856, 2835, 1596, 1553, 1516, 1427, 1361, 1342, 1303, 1243, 1198, 1163, 1038, 1024, 985, 834, 782, 741, 724, 691, 667, 587, 488. **HRMS** (ESI) *m/z*: $[M + H]^+$ calcd for $C_{14}H_{19}N_2O_2$, 247.1441; found, 247.1446. t_R (LC-MS method): 8.56 min.

4-Methoxy-5'-pentyl-1*H*,1'*H*-[2,2'-bipyrrole]-5-carbaldehyde (III-14f)

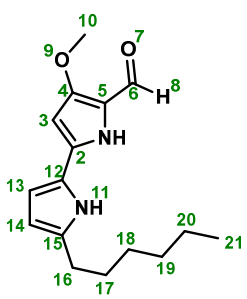
Following the general procedure for the synthesis of 5'-*n*-alkylated MBC derivatives, bromide (**III-75**, 800 mg, 3.09 mmol, 1.00 eq.), boronic acid (**III-140f**, 2.60 g, 9.26 mmol, 3.00 eq.), SPhos (**III-122**, 76.0 mg, 0.19 mmol, 6 mol-%), $Pd(OAc)_2$ (34.7 mg, 0.15 mmol, 5 mol-%), and K_3PO_4 (1.31 g, 6.17 mmol, 2.00 eq.) were converted to 4-methoxy-5'-pentyl-1*H*,1'*H*-[2,2'-bipyrrole]-5-carbaldehyde (**III-14f**, 605 mg, 2.33 mmol, 75%) after 15 h reaction time. The product was obtained as a green powder.



Mp 196.2–199.5 °C. **^{1}H NMR** (600 MHz, DMSO-d_6, δ): 11.26 (s, 1H, 1-H), 10.93 (s, 1H, 11-H), 9.25 (s, 1H, 8-H), 6.68 – 6.56 (m, 1H, 13-H), 6.27 – 6.14 (m, 1H, 3-H), 5.88 – 5.78 (m, 1H, 14-H), 3.82 (s, 3H, 10-H), 2.54 (t, *J* = 7.7 Hz, 2H, 16-H), 1.58 (p, *J* = 7.5 Hz, 2H, 17-H), 1.30 (tt, *J* = 7.3 Hz, 4H, 18-H, 19-H), 0.87 (t, *J* = 6.9 Hz, 3H, 20-H). **^{13}C NMR** (151 MHz, DMSO-d_6, δ): 171.6 (C-6), 159.3 (C-4), 135.7 (C-15), 134.0 (C-2), 122.4 (C-12), 117.7 (C-5), 109.2 (C-13), 107.3 (C-14), 90.9 (C-3), 58.2 (C-10), 31.4 (C-18), 29.3 (C-17), 27.6 (C-16), 22.4 (C-19), 14.4 (C-20). **FT-IR** (cm^{-1}, neat): 3255, 3204, 3105, 3071, 2953, 2929, 2839, 1599, 1554, 1518, 1428, 1361, 1340, 1304, 1287, 1255, 1231, 1202, 1163, 1034, 1023, 987, 833, 781, 742, 724, 692, 667, 588, 490, 454. **HRMS** (ESI) *m/z*: $[M + H]^+$ calcd for $C_{15}H_{21}N_2O_2$, 261.1598; found, 261.1601. t_R (LC-MS method): 7.78 min.

5'-Hexyl-4-methoxy-1*H*,1'*H*-[2,2'-bipyrrole]-5-carbaldehyde (III-14g)

Following the general procedure for the synthesis of 5'-*n*-alkylated MBC derivatives, bromide (**III-75**, 800 mg, 3.09 mmol, 1.00 eq.), boronic acid (**III-140g**, 2.73 g, 9.26 mmol, 3.00 eq.), SPhos (**III-122**, 76.0 mg, 0.19 mmol, 6 mol-%), $Pd(OAc)_2$ (34.7 mg, 0.15 mmol, 5 mol-%), and K_3PO_4 (1.31 g, 6.17 mmol, 2.00 eq.) were converted to 5'-hexyl-4-methoxy-1*H*,1'*H*-[2,2'-bipyrrole]-5-carbaldehyde (**III-14g**, 678 mg, 2.47 mmol, 80%) after 14 h reaction time. The product was obtained as a green powder.



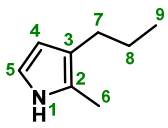
Mp 171.8–174.6 °C. **^{1}H NMR** (600 MHz, DMSO-d_6, δ): 11.26 (s, 1H, 1-H), 10.93 (s, 1H, 11-H), 9.26 (s, 1H, 8-H), 6.65 – 6.57 (m, 1H, 13-H), 6.23 – 6.19 (m, 1H, 3-H), 5.87 – 5.78 (m, 1H, 14-H), 3.83 (s, 3H, 10-H), 2.54 (t, *J* = 7.7 Hz, 2H, 16-H), 1.58 (p, *J* = 7.4 Hz, 2H, 17-H), 1.34 – 1.23 (m, 6H, 18-H, 19-H, 20-H), 0.85 (t, 3H, 21-H). **^{13}C NMR** (151 MHz, DMSO-d_6, δ): 171.1 (C-6), 158.7 (C-4), 135.2 (C-15), 133.5 (C-2), 121.9 (C-12), 117.1 (C-5), 108.7 (C-13), 106.8 (C-14), 90.4 (C-3), 57.7 (C-10), 31.0 (C-19), 29.1 (C-17), 28.3 (C-18), 27.2 (C-16), 22.0 (C-20), 13.9 (C-21). **FT-IR** (cm^{-1}, neat): 3223, 3117, 2954, 2924, 2855, 1664, 1464, 1458, 1377, 1368, 1258, 1217, 1168, 1113, 994, 956, 943, 830, 823, 724, 651, 614. **HRMS** (ESI) *m/z*: $[M + H]^+$ calcd for $C_{16}H_{23}N_2O_2$, 275.1754; found, 275.1758. t_R (LC-MS method): 9.01 min.

General Procedure for the Synthesis of 3-Alkyl-2-Methyl-1*H*-Pyrroles III-15a–c

For the synthesis of 2,3-alkylpyrroles according to Trofimov, a mixture of (*E*/*Z*)-oximes (1.00 eq.), pestled KOH (5.00 eq)., and water (13.7 µL/mmol oxime) was added to a three-necked flask under N_2 atmosphere. Degassed and dried DMSO (1.92 mL/mmol oxime) was added under N_2 atmosphere. The reaction was refluxed at 100 °C and a solution of 1,2-dichloroethane (3.50 eq.) in degassed DMSO (0.21 mL/mmol oxime) was added with a syringe pump over 2 h. A second batch of KOH (5.00 eq.) was added under ice cooling after the first hour of 1,2-dichloroethane addition (dichloroethane-feeding is paused during KOH addition) before the dichloroethane addition was continued for a further 60 min. Once the dichloroethane addition was completed, the reaction was refluxed for 2 h. The reaction was cooled to 0 °C and ice water was added for quenching. Extraction was performed with Et_2O (3 x 100 mL). Combined organic phases were dried over $MgSO_4$, filtered over degreased cotton wool, and the solvent was removed *in vacuo*. Chromatographic purification on silica provided the products **III-15a–c** as yellow oils.

2-Methyl-3-propyl-1*H*-pyrrole (III-15a)

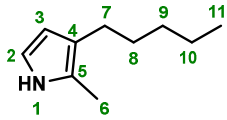
Following the general procedure for the synthesis of 3-alkyl-2-methyl-1*H*-pyrroles, a mixture of (*E*/*Z*)-hexan-2-one oxime (**III-93a**, 12.0 g, 104 mmol, 1.00 eq.), 1,2-dichloroethane (28.80 mL, 365 mmol, 3.50 eq.), and KOH (58.4 g, 1.04 mol, 10.0 eq.) is converted to 6.99 g (56.7 mmol, 54%) 2-methyl-3-propyl-1*H*-pyrrole (**III-15a**). After purification with PE/CH_2Cl_2 (85:15) + 1% triethylamine, the product is obtained as a yellow oil.



R_f (PE/EtOAc 80:20): 0.57 (UV and $KMnO_4$ stain). **^{1}H NMR** (600 MHz, $CDCl_3$, δ): 7.70 (s, 1H, 1-H), 6.60 (t, *J* = 2.7 Hz, 1H, 5-H), 6.02 (t, *J* = 2.7 Hz, 1H, 4-H), 2.37 (t, *J* = 7.5 Hz, 2H, 7-H), 2.19 (s, 3H, 6-H), 1.56 (h, *J* = 7.5 Hz, 2H, 8-H), 0.95 (t, *J* = 7.3 Hz, 3H, 9-H). **^{13}C NMR** (151 MHz, $CDCl_3$, δ): 123.4 (C-2), 119.7 (C-3), 114.9 (C-5), 109.0 (C-4), 28.2 (C-7), 24.6 (C-8), 14.2 (C-9), 11.2 (C-6). **FT-IR** (cm^{-1}, neat): 3378, 2956, 2925, 2869, 1464, 1455, 1376, 1249, 1106, 1066, 955, 904, 889, 832, 801, 712, 663, 549. **HRMS** (ESI) *m/z*: $[M + H]^+$ calcd for $C_8H_{14}N$, 124.1121; found, 124.1120. **t_R** (LC-MS method): 7.90 min. **CAS** 75145-97-0.

2-Methyl-3-pentyl-1*H*-pyrrole (III-15b)

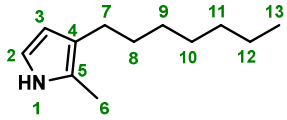
Following the general procedure for the synthesis of 3-alkyl-2-methyl-1*H*-pyrroles, a mixture of (*E*/*Z*)-octan-2-one oxime (**III-93b**, 12.0 g, 83.8 mmol, 1.00 eq.), 1,2-dichloroethane (23.2 mL, 293 mmol, 3.50 eq.), and KOH (47.0 g, 838 mmol, 10.0 eq.) is converted to 6.89 g (45.6 mmol, 54%) 2-methyl-3-pentyl-1*H*-pyrrole (**III-15b**). After purification with PE/CH_2Cl_2 (90:10) + 1% triethylamine, the product is obtained as a yellow volatile oil.



^{1}H NMR (600 MHz, $CDCl_3$, δ): 7.70 (brs, 1H, 1-H), 6.60 (t, *J* = 2.7 Hz, 1H, 5-H), 6.02 (t, *J* = 2.8 Hz, 1H, 4-H), 2.39 (t, *J* = 7.7 Hz, 2H, 7-H), 2.19 (s, 3H, 6-H), 1.54 (p, *J* = 7.4 Hz, 2H, 8-H), 1.38 – 1.28 (m, 4H, 9-H, 10-H), 0.90 (3 H, t, *J* = 6.7 Hz, 11-H). **^{13}C NMR** (151 MHz, $CDCl_3$, δ): 123.3 (C-2), 119.9 (C-3), 114.9 (C-5), 109.0 (C-4), 31.9 (C-9), 31.2 (C-8), 26.0 (C-7), 22.8 (C-10), 14.3 (C-11), 11.2 (C-6). **FT-IR** (cm^{-1}, neat): 3376, 2956, 2923, 2854, 1464, 1444, 1378, 1246, 1107, 1064, 954, 901, 831, 771, 670, 551. **HRMS** (ESI) *m/z*: $[M + H]^+$ calcd for $C_{10}H_{18}N$, 152.1434; found, 152.1434. **t_R** (LC-MS method): 8.52 min. **CAS** 18320-91-7.

3-Heptyl-2-methyl-1*H*-pyrrole (III-15c)

Following the general procedure for the synthesis of 3-alkyl-2-methyl-1*H*-pyrroles, decan-2-one oxime (**III-93c**, 7.50 g, 43.8 mmol, 1.00 eq.), 1,2-dichloroethane (12.1 mL, 153 mmol, 3.50 eq.), and KOH (24.6 g, 438 mmol, 10.0 eq.) are converted to 4.11 g (22.9 mmol, 52%) 3-heptyl-2-methyl-1*H*-pyrrole (**III-15c**). After purification with PE/CH_2Cl_2 (85:15) + 1% triethylamine, the product is obtained as a yellow volatile oil.

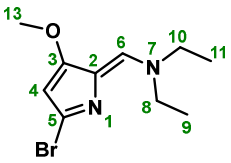


^{1}H NMR (600 MHz, $CDCl_3$, δ): 7.71 (brs, 1H, 1-H), 6.60 (t, *J* = 2.7 Hz, 1H, 5-H), 6.02 (t, *J* = 2.8 Hz, 1H, 4-H), 2.39 (t, 2H, 7-H), 2.19 (s, 3H, 6-H), 1.58 – 1.48 (m, 2H, 8-H), 1.38 – 1.23 (m, 8H, 9-H, 10-H, 11-H, 12-H), 0.89 (t, 3H, 13-H). **^{13}C NMR** (151 MHz, $CDCl_3$, δ): 123.3 (C-2), 119.9 (C-3), 114.9 (C-5), 109.0 (C-4), 32.1 (C-11), 31.5 (C-8), 29.7 (C-10), 29.4 (C-9), 26.1 (C-7), 22.8 (C-12), 14.3 (C-13), 11.2 (C-6). **FT-IR** (cm^{-1}, neat): 3485, 3377, 2955, 2923, 2871, 1583, 1463, 1445,

1377, 1272, 1247, 1144, 1108, 1064, 953, 901, 831, 711, 668, 646, 634, 548, 485, 468. **HRMS** (ESI) *m/z*: $[M + H]^+$ calcd for $C_{12}H_{22}N$, 180.1747; found, 180.1749. t_R (LC-MS method): 9.01 min. **CAS** 2649513-86-8.

(*Z*)-*N*-[(5-Bromo-3-methoxy-2H-pyrrol-2-ylidene)methyl]-*N*-ethylethanamine (III-75)

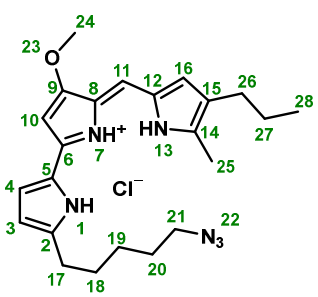
Bromide **III-75** was synthesised according to a published procedure from Chawrai *et al*.[286] In a 500 mL Schlenk flask under N_2 atmosphere, *N*,*N*-diethylformamide (10.7 g, 106 mmol, 3.00 eq.) was dissolved in dry CH_2Cl_2 (40 mL) and cooled to 0 °C. Phosphoryl bromide (25.4 g, 88.5 mmol, 2.50 eq.) was dissolved in dry CH_2Cl_2 and slowly added to the diethylformamide solution at 0 °C via transfer cannula. The solution was stirred for 1 h at 0 °C, during which time the solution had turned yellow and a white solid had precipitated. A solution of 4-methoxy-3-pyrrolin-2-one (**III-74**, 4.00 g, 35.4 mmol, 1.00 eq.) in dry CH_2Cl_2 (60 mL) was slowly added to the Vilsmeier reagent at 0 °C. After complete addition, the reaction was allowed to warm to 21 °C, stirred for 30 min at 21 °C and then heated for 3 h at 40°C. Finally, the reaction was refluxed for 2 h at 50 °C. The reaction was quenched with ice water (400 mL), phases were separated and the aqueous phase was adjusted to pH 7–8 with aqueous 1 M NaOH. The aqueous phase was then extracted with CH_2Cl_2 (5 x 100 mL) and the merged organic phases were washed with brine (2 x 150 mL). Drying over $MgSO_4$ and filtration provided the crude product as a brown oil. Chromatography on silica with PE/EtOAc (80:20) + 1% TEA yielded the desired product (**III-75**, 5.55 g, 21.4 mmol, 61%) as an orange oil, which crystallised at –20 °C.



Mp 43.3–45.0 °C. **^{1}H NMR** (600 MHz, $CDCl_3$, δ): 6.99 (s, 1H, 6-H), 5.59 (s, 1H, 4-H), 4.12 (q, *J* = 7.1 Hz, 2H, 8-H), 3.76 (s, 3H, 13-H), 3.39 (q, *J* = 7.2 Hz, 2H, 10-H), 1.29 (q, *J* = 7.1 Hz, 6H, 9-H, 11-H). **^{13}C NMR** (151 MHz, $CDCl_3$, δ): 165.5 (C-3), 138.7 (C-6), 133.8 (C-5), 120.9 (C-2), 96.6 (C-4), 58.1 (C-13), 51.2 (C-10), 44.7 (C-8), 14.7 (C-11), 12.6 (C-9). **FT-IR** (cm^{-1}, neat): 2974, 2938, 2876, 2866, 1630, 1525, 1486, 1459, 1448, 1406, 1382, 1325, 1275, 1185, 1106, 1076, 1058, 992, 944, 908, 858, 813, 801, 775, 719, 683, 676, 642, 565, 525, 478. **HRMS** (ESI) *m/z*: $[M + H]^+$ calcd for $C_{10}H_{16}BrN_2O$, 259.0441; found, 259.0443. **CAS** 960509-42-6.

(*Z*)-5-(5-Azidopentyl)-4'-methoxy-5'-((5-methyl-4-propyl-1*H*-pyrrol-2-yl)methylene)-1*H*,5'*H*-[2,2'-bipyrrol]-1'-ium chloride (III-89·HCl)

A 50 mL Schlenk flask with magnetic stirring bar was sequentially charged with $Pd(OAc)_2$ (32.6 mg, 145 µmol, 0.05 eq.), SPhos (**III-122**, 71.6 mg, 174 µmol, 0.06 eq.), triflate (**III-96**, 1.10 g, 2.91 mmol, 1.00 eq.), azide boronic acid (**III-114**, 2.81 g, 8.72 mmol, 3.00 eq.) and evacuated/N_2-refilled three times. Degassed *n*BuOH (16.0 mL) was added and the mixture was stirred at 20 °C until homogeneous. A solution of K_3PO_4 (1.23 g, 5.81 mmol, 2.00 eq., 1.45 M) in degassed H_2O (4.00 mL) was added in one portion to initiate the Suzuki reaction. The reaction vessel was lowered into a pre-heated heating mantle at 60 °C and the orange solution was stirred under argon for 15 h. The red-orange solution was diluted with CH_2Cl_2, and brine (50 mL) was added. The phases were separated and the aqueous phase was repeatedly extracted with CH_2Cl_2 (25 mL portions) until the organic phase remained nearly colourless. Merged organic phases were dried over $MgSO_4$, filtered over degreased cotton wool (**!**), and the solvent was removed *in vacuo*. The deep red film was chromatographed on silica using CH_2Cl_2 + 0.7–3% NH_3 (7 N in MeOH) as eluent. Acidification of product fractions with 1 M HCl in Et_2O, immobilisation on Celite, and chromatography on neutral aluminium oxide (Brockmann I) with *n*-pentane/EtOAc (0–100% EtOAc) provided the product as a purple film. The film was dissolved in a minimal amount of CH_2Cl_2 and acidified again. Drugin solvent removal, repeated treatment with *n*-pentane assisted precipitation of the HCl salt **III-89·HCl** as an amorphous purple powder (827 mg, 1.87 mmol, 64%).

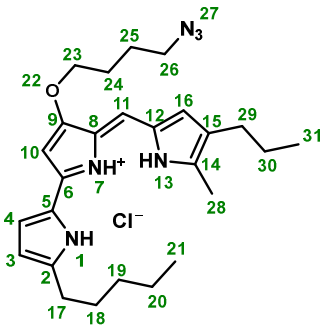


Mp 75.4–79.2 °C. **^{1}H NMR** (300 MHz, $CDCl_3$, δ): 12.52 (brs, 1H, 13-H), 12.47 (brs, 1H, 1-H), 12.39 (brs, 1H, 7-H), 6.84 – 6.77 (m, 2H, 4-H, 11-H), 6.58 (d, *J* = 2.2 Hz, 1H, 16-H), 6.05 (dd, *J* = 3.9, 2.2 Hz, 1H, 3-H), 5.98 (d, *J* = 1.9 Hz, 1H, 10-H), 3.92 (s, 3H, 24-H), 3.25 (t, *J* = 6.9 Hz, 2H, 21-H), 2.75 (t, *J* = 7.6 Hz, 2H, 17-H), 2.49 (s, 3H, 25-H), 2.33 (t, *J* = 7.5 Hz, 2H, 26-H), 1.81 (p, *J* = 7.6 Hz, 2H, 18-H), 1.69 – 1.55 (m, *J* = 7.3 Hz, 1H, 20-H) 1.53 (h, *J* = 7.5 Hz, 2H, 27-H), 1.49 – 1.36 (m, 3H, 19-H), 0.91 (t, *J* = 7.3 Hz, 3H, 28-H). **^{13}C NMR** (76 MHz, $CDCl_3$, δ): 165.7 (C-9), 147.6 (C-6), 145.2 (C-14), 143.8 (C-2), 127.5 (C-15), 127.3 (C-16), 124.9 (C-12), 121.15 (C-8), 121.09 (C-5), 118.6 (C-4), 114.6

(C-11), 110.6 (C-3), 92.6 (C-10), 58.7 (C-24), 51.4 (C-21), 28.6 (C-18, C-20), 28.1 (C-17), 27.5 (C-26), 26.4 (C-19), 23.4 (C-27), 13.8 (C-28), 12.3 (C-25). **FT-IR** (cm^{-1}, neat): 3162, 3139, 3113, 3070, 2930, 2868, 2178, 2102, 1738, 1705, 1629, 1601, 1537, 1495, 1464, 1448, 1437, 1414, 1403, 1358, 1337, 1292, 1247, 1216, 1201, 1183, 1161, 1128, 1081, 1063, 1044, 998, 990, 976, 965, 902, 884, 838, 790, 778, 762, 731, 659, 634, 622, 556, 552, 509, 475. **HRMS** (ESI) *m/z*: $[M - Cl]^+$ calcd for $C_{23}H_{31}N_6O$, 407.2554; found, 407.2556.

(*Z*)-4'-(4-Azidobutoxy)-5'-((5-methyl-4-propyl-1*H*-pyrrol-2-yl)methylene)-5-pentyl-1*H*,5'*H*-[2,2'-bipyrrol]-1'-ium chloride (III-90·HCl)

A 100 mL Schlenk flask with magnetic stirring bar was sequentially charged with $Pd(OAc)_2$ (28.0 mg, 125 µmol, 0.05 eq.), SPhos (**III-122**, 61.4 mg, 150 µmol, 0.06 eq.), triflate (**III-137**, 1.15 g, 2.49 mmol, 1.00 eq.), alkyl boronic acid (**III-140f**, 1.40 g, 4.98 mmol, 2.00 eq.) and evacuated/N_2-refilled three times. Degassed *n*BuOH (13.7 mL) was added and the mixture was stirred at 20 °C until homogeneous. A solution of K_3PO_4 (1.06 g, 4.98 mmol, 2.00 eq., 1.45 M) in degassed H_2O (3.43 mL) was added in one portion to initiate the Suzuki reaction. The reaction vessel was lowered into a pre-heated heating mantle at 60 °C and the orange solution was stirred under argon for 13 h. The red-orange solution was diluted with CH_2Cl_2, and brine (50 mL) was added. The phases were separated and the aqueous phase was repeatedly extracted with CH_2Cl_2 (25 mL portions) until the organic phase remained nearly colourless. Merged organic phases were dried over $MgSO_4$, filtered over degreased cotton wool (**!**), and the solvent was removed *in vacuo*. The deep red film was chromatographed on silica using CH_2Cl_2 + 0.7% NH_3 (7 N in MeOH) as eluent. Acidification of product fractions with 1 M HCl in Et_2O, immobilisation on Celite, and chromatography on neutral aluminium oxide (Brockmann I) with *n*-pentane/EtOAc (0–100% EtOAc) provided the product as a purple film. The film was dissolved in a minimal amount of CH_2Cl_2 and acidified again. During solvent removal, repeated treatment with *n*-pentane assisted precipitation of the HCl salt **III-90·HCl** as an amorphous purple powder (651 mg, 1.34 mmol, 54%).

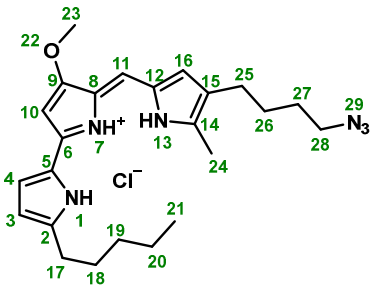


Mp 72.4–75.8 °C. **^{1}H NMR** (300 MHz, $CDCl_3$, δ): 12.60 (brs, 1H, 13-H), 12.50 (brs, 2H, 1-H, 7-H), 6.85 (s, 1H, 11-H), 6.84 (dd, *J* = 3.8, 2.5 Hz, 1H, 4-H), 6.65 (d, *J* = 2.6 Hz, 1H, 16-H), 6.09 (dd, *J* = 3.9, 2.2 Hz, 1H, 3-H), 5.99 (d, *J* = 1.8 Hz, 1H, 10-H), 4.16 (t, *J* = 6.1 Hz, 2H, 23-H), 3.40 (t, *J* = 6.5 Hz, 2H, 26-H), 2.76 (t, *J* = 7.7 Hz, 2H, 17-H), 2.52 (s, 3H, 28-H), 2.37 (t, *J* = 7.5 Hz, 2H, 29-H), 2.01 – 1.88 (m, 2H, 25-H), 1.87 – 1.72 (m, 4H, 18-H, 24-H), 1.56 (h, *J* = 7.4 Hz, 2H, 30-H), 1.41 – 1.29 (m, 4H, 19-H, 20-H), 0.93 (t, *J* = 7.3 Hz, 3H, 31-H), 0.88 (d, *J* = 6.9 Hz, 3H, 21-H). **^{13}C NMR** (76 MHz, $CDCl_3$, δ): 164.6 (C-9), 147.8 (C-6), 145.4 (C-14), 145.0 (C-2), 127.6 (C-15), 127.4 (C-16), 125.0 (C-12), 121.4 (C-8), 121.0 (C-5), 118.7 (C-4), 114.5 (C-11), 110.6 (C-3), 93.0 (C-10), 71.2 (C-23), 51.1 (C-26), 31.6 (C-19), 28.9 (C-18), 28.3 (C-17), 27.6 (C-29), 26.3 (C-25), 25.6 (C-24), 23.5 (C-30), 22.5 (C-20), 14.2 (C-21), 13.9 (C-31), 12.4 (C-28). **FT-IR** (cm^{-1}, neat): 3161, 3137, 3107, 3060, 2956, 2927, 2869, 2861, 2096, 1628, 1603, 1576, 1545, 1533, 1493, 1441, 1336, 1245, 1199, 1152, 1128, 1078, 1042, 999, 966, 893, 846, 820, 784, 770, 734, 684, 664, 624, 566, 479. **HRMS** (ESI) *m/z*: $[M - Cl]^+$ calcd for $C_{26}H_{37}N_6O$, 449.3023; found, 449.3031.

(*Z*)-5'-((4-(4-Azidobutyl)-5-methyl-1*H*-pyrrol-2-yl)methylene)-4'-methoxy-5-pentyl-1*H*,5'*H*-[2,2'-bipyrrol]-1'-ium chloride (III-91·HCl)

A 50 mL Schlenk flask with magnetic stirring bar was sequentially charged with $Pd(OAc)_2$ (19.5 mg, 87.0 µmol, 0.05 eq.), SPhos (**III-122**, 42.9 mg, 104 µmol, 0.06 eq.), triflate (**III-158**, 754 mg, 1.74 mmol, 1.00 eq.), alkyl boronic acid (**III-140f**, 987 mg, 3.48 mmol, 2.00 eq.) and evacuated/N_2-refilled three times. Degassed *n*BuOH (9.59 mL) was added and the mixture was stirred at 20 °C until homogeneous. A solution of K_3PO_4 (739 mg, 3.48 mmol, 2.00 eq., 1.45 M) in degassed H_2O (2.40 mL) was added in one portion to initiate the Suzuki reaction. The reaction vessel was lowered into a pre-heated heating mantle at 60 °C and the orange solution stirred under argon for 13 h. The red-orange solution was diluted with CH_2Cl_2 and brine (50 mL), the phases were separated, and the aqueous phase was repeatedly extracted with CH_2Cl_2 (25 mL portions) until the organic phase remained nearly colourless. Merged organic phases were dried over $MgSO_4$, filtered over degreased cotton wool (**!**), and the solvent was removed *in vacuo*. The deep red film was

chromatographed on silica using CH_2Cl_2 + 0.7–3% NH_3 (7 N in MeOH) as eluent. Acidification of product fractions with 1 M HCl in Et_2O, immobilisation on Celite, and chromatography on neutral aluminium oxide (Brockmann I) with *n*-pentane/EtOAc (0–100% EtOAc) provided the product as purple film. The film was dissolved in a minimal amount of CH_2Cl_2 and acidified again. During solvent removal, repeated treatment with *n*-pentane assisted precipitation of the HCl salt **III-91·HCl** as an amorphous purple powder (367 mg, 803 µmol, 46%).



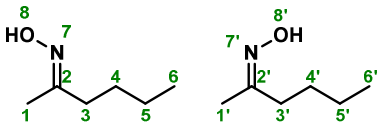
Mp 112.4–113.2 °C. **^{1}H NMR** (300 MHz, $CDCl_3$, δ): 12.60 (brs, 1H, 13-H), 12.51 (brs, 2H, 1-H, 7-H), 6.87 (dd, *J* = 3.9, 2.5 Hz, 1H, 4-H), 6.85 (s, 1H, 11-H), 6.60 (d, *J* = 2.6 Hz, 1H, 16-H), 6.10 (dd, *J* = 3.9, 2.2 Hz, 1H, 3-H), 6.01 (d, *J* = 1.8 Hz, 1H, 10-H), 3.98 (s, 3H, 23-H), 3.37 – 3.21 (m_c, 2H, 28-H), 2.76 (t, *J* = 7.7 Hz, 2H, 17-H), 2.52 (s, 3H, 24-H), 2.48 – 2.35 (m_c, 2H, 25-H), 1.86 – 1.71 (m_c, *J* = 6.4 Hz, 2H, 18-H), 1.70 – 1.56 (m, 4H, 26-H, 27-H), 1.43 – 1.27 (m, 4H, 19-H, 20-H) 0.89 (m_c, *J* = 6.9 Hz, 3H, 21-H). **^{13}C NMR** (76 MHz, $CDCl_3$, δ): 165.9 (C-9), 148.1 (C-6), 145.3 (C-2), 144.5 (C-14), 126.8 (C-16), 126.5 (C-15), 125.0 (C-12), 121.6 (C-8), 121.0 (C-5), 119.1 (C-4), 114.4 (C-11), 110.8 (C-3), 92.7 (C-10), 58.8 (C-23), 51.4 (C-28), 31.6 (C-19), 28.9 (C-18), 28.6 (C-27), 28.3 (C-17), 27.4 (C-26), 25.0 (C-25), 22.5 (C-20), 14.2 (C-21), 12.3 (C-24). **FT-IR** (cm^{-1}, neat): 3172, 3146, 3108, 3075, 3013, 2924, 2856, 2095, 1634, 1607, 1579, 1538, 1519, 1495, 1447, 1406, 1348, 1257, 1209, 1168, 1155, 1128, 1046, 997, 972, 893, 882, 841, 813, 794, 732, 696, 651, 618, 601, 546, 504. **HRMS** (ESI) *m/z:* $[M - Cl]^+$ calcd for $C_{24}H_{33}N_6O$, 421.2710; found, 421.2717.

General Procedure for the Synthesis of (*E*/*Z*)-Oximes III-93a–c

A round-bottom flask with a stirring bar was charged with sodium acetate (2.00 eq.) and hydroxylamine hydrochloride (1.50 eq.). The solids were suspended in a solution of EtOH/water (4:1, 3.33 mL/mmol ketone) and the ketone (1.00 eq.) was added. The reaction mixture was then heated to reflux for 4 h and afterwards allowed to cool to room temperature. Excess EtOH was removed under reduced pressure and the residue was diluted with water (100 mL). The aqueous solution was extracted with EtOAc (3 x 200 mL). The combined organic layers were then washed with saturated $NaHCO_3$ (2 x 100 mL) and water (2 x 100 mL), dried over $MgSO_4$, filtered, and concentrated *in vacuo*. The oxime products were obtained as colourless or weak yellow oils in quantitative to near-quantitative yields.

(*E*/*Z*)-Hexan-2-one oxime (III-93a)

Following the general procedure for the synthesis of (*E*/*Z*)-oximes, hexan-2-one (**III-92a**, 15.0 g, 150 mmol, 1.00 eq.), sodium acetate (24.6 g, 300 mmol, 2.00 eq.), and hydroxylamine hydrochloride (15.7 g, 226 mmol, 1.50 eq.) were converted to (*E*/*Z*)-hexan-2-one oxime **III-93a** (16.9 g, 147 mmol, 98%). After solvent evaporation, the product was obtained as a weak yellow oil and used without further purification.

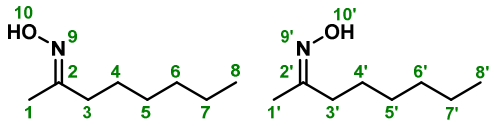


(*E*/*Z*)-Ratio: 73:27 (NMR). <u>*E*-Isomer:</u> **^{1}H NMR** (600 MHz, $CDCl_3$, δ): 9.09 (s, 1H, 8-OH), 2.23 – 2.15 (m, 2H, 3-H), 1.87 (s, 3H, 1-H), 1.52 – 1.44 (m, 2H, 4-H), 1.32 (h, *J* = 7.3 Hz, 2H, 5-H), 0.90 (t, *J* = 7.4 Hz, 3H, 6-H). **^{13}C NMR** (151 MHz, $CDCl_3$, δ): 158.8 (C-2), 35.6 (C-3), 28.5 (C-4), 22.4 (C-5), 13.9 (C-6), 13.5 (C-1). <u>*Z*-Isomer:</u> **^{1}H NMR** (600 MHz, $CDCl_3$, δ): 9.09 (s, 1H, 8'-OH), 2.40 – 2.34 (m, 2H, 3'-H), 1.85 (s, 3H, 1'-H), 1.52 – 1.44 (m, 2H, 4'-H), 1.36 (h, *J* = 7.4 Hz, 2H, 5'-H), 0.92 (t, *J* = 7.4 Hz, 3H, 6'-H). **^{13}C NMR** (151 MHz, $CDCl_3$, δ): 159.2 (C-2'), 28.5 (C-3'), 27.8 (C-4'), 23.0 (C-5'), 20.0 (C-1'), 14.0 (C-6'). **FT-IR** (cm^{-1}, neat): 3222, 3118, 2957, 2928, 2873, 2862, 1664, 1467, 1433, 1368, 1331, 1262, 1207, 1105, 1010, 951, 919, 878, 823, 742, 648, 613. **HRMS** (ESI) *m/z*: $[M + H]^+$ calcd for $C_6H_{14}NO$, 116.1070; found, 116.1071. **CAS** 5577-48-0.

(*E*/*Z*)-Octan-2-one oxime (III-93b)

Following the general procedure for the synthesis of (*E*/*Z*)-oximes, octan-2-one (**III-92b**, 12.0 g, 93.6 mmol, 1.00 eq.), sodium acetate (15.4 g, 187 mmol, 2.00 eq.), and hydroxylamine hydrochloride (9.76 g, 140 mmol, 1.50 eq.) were

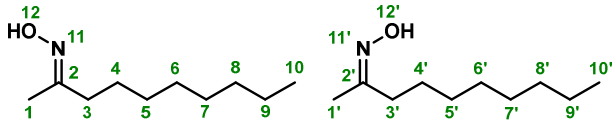
converted to (*E*/*Z*)-octan-2-one oxime **III-93b** (13.4 g, 93.2 mmol, >99%). After solvent evaporation, the product was obtained as a colourless oil and used without further purification.



(*E*/*Z*)-Ratio: 76:24 (NMR). *E*-Isomer: **^{1}H NMR** (600 MHz, $CDCl_3$, δ): 8.58 (brs, 1H, 10-OH), 2.24 – 2.12 (m, 2H, 3-H), 1.87 (s, 3H, 1-H), 1.53 – 1.45 (m, 2H, 4-H), 1.36 – 1.22 (m, 6H, 5-H, 6-H, 7-H), 0.872 (t, 3H, 8-H). **^{13}C NMR** (151 MHz, $CDCl_3$, δ): 158.9 (C-2), 35.9 (C-3), 31.70 (C-6), 29.0 (C-5), 26.4 (C-4), 22.7 (C-7), 14.2 (C-8), 13.5 (C-1). *Z*-Isomer: **^{1}H NMR** (600 MHz, $CDCl_3$, δ): 8.58 (brs, 1H, 10'-OH), 2.41 – 2.32 (m, 2H, 3'-H), 1.86 (s, 3H, 1'-H), 1.53 – 1.45 (m, 2H, 4'-H), 1.36 – 1.22 (m, 6H, 5'-H, 6'-H, 7'-H), 0.879 (t, 3H, 8'-H). **^{13}C NMR** (151 MHz, $CDCl_3$, δ): 159.3 (C-2'), 31.73 (C-6‘), 29.5 (C-5'), 28.8 (C-3'), 25.6 (C-4'), 22.7 (C-7), 19.9 (C-1'), 14.2 (C-8'). **FT-IR** (cm^{-1}, neat): 3224, 3120, 2955, 2926, 2858, 1664, 1466, 1458, 1376, 1369, 1261, 1247, 1179, 1111, 1031, 954, 943, 828, 796, 742, 726, 651, 613. **HRMS** (ESI) *m/z*: $[M + H]^+$ calcd for $C_8H_{18}NO$, 144.1383; found, 144.1383. **CAS** 7207-49-0.

(*E*/*Z*)-Decan-2-one oxime (III-93c)

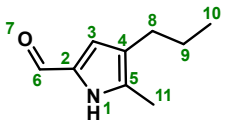
Following the general procedure for the synthesis of (*E*/*Z*)-oximes, decan-2-one (**III-92c**, 7.50 g, 48.0 mmol, 1.00 eq.), sodium acetate (7.88 g, 96.1 mmol, 2.00 eq.), and hydroxylamine hydrochloride (5.00 g, 72.0 mmol, 1.50 eq.) were converted to (*E*/*Z*)-decan-2-one oxime **III-93c** (8.22 g, 48.0 mmol, >99%). After solvent evaporation, the product was obtained as a colourless oil and used without further purification.



(*E*/*Z*)-Ratio: 76:24 (NMR). *E*-Isomer: **^{1}H NMR** (600 MHz, $CDCl_3$, δ): 8.14 (brs, 1H, 12-OH), 2.20 – 2.14 (m, 2H, 3-H), 1.88 (s, 3H, 1-H), 1.49 (p, 2H, 4-H), 1.19 – 1.35 (m, 10H, 5-H, 6-H, 7-H, 8-H, 9-H), 0.871 (t, 3H, 10-H). **^{13}C NMR** (151 MHz, $CDCl_3$, δ): 159.0 (C-2), 35.9 (C-3), 32.0 (C-8), 29.5 (C-6), 29.33 (C-5), 29.32 (C-7), 26.4 (C-4), 22.8 (C-9), 14.2 (C-10), 13.5 (C-1). **^{1}H NMR** (600 MHz, $CDCl_3$, δ): 8.14 (brs, 1H, 12'-OH), 2.38 – 2.33 (m, 2H, 3'-H), 1.86 (s, 3H, 1'-H), 1.49 (p, 2H, 4' H), 1.35 – 1.19 (m, 10H, 5'-H, 6'-H, 7' H, 8'-H, 9'-H), 0.874 (t, 3H, 10'-H). **^{13}C NMR** (151 MHz, $CDCl_3$, δ): 159.4 (C-2'), 32.0 (C-8'), 29.9 (C-6'), 29.5 (C-5'), 29.32 (C-7'), 28.7 (C-3'), 25.6 (C-4'), 22.8 (C-9'), 19.9 (C-1'), 14.2 (C-10'). **FT-IR** (cm^{-1}, neat): 3223, 3117, 2954, 2924, 2855, 1664, 1464, 1458, 1377, 1368, 1258, 1217, 1168, 1113, 994, 956, 943, 830, 823, 724, 651, 614. **HRMS** (ESI) *m/z*: $[M + H]^+$ calcd for $C_{10}H_{22}NO$, 172.1696; found, 172.1699. **CAS** 13326-89-1.

5-Methyl-4-propyl-1*H*-pyrrole-2-carbaldehyde (III-94)

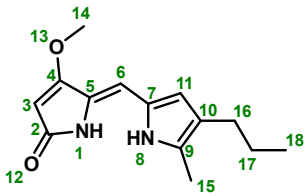
To a 250 mL Schlenk flask with stirring bar under N_2 atmosphere was added dry DMF (2.10 mL, 27.3 mmol, 1.20 eq.) and cooled to 0 °C. Phosphoryl chloride (2.54 mL, 27.3 mmol, 1.20 eq.) was added dropwise at 0 °C and the Vilsmeier reagent solidified as a white clump. The reagent was suspended in dry 1,2-dichloroethane (6.8 mL, 0.3 mL/mmol pyrrole) and stirred for 30 min at 0 °C. A solution of 2-methyl-3-propyl-1*H*-pyrrole (**III-15a**, 2.80 g, 22.7 mmol, 1.00 eq.) in 1,2-dichloroethane (13.6 mL, 0.6 mL/mmol pyrrole) was added dropwise and the reaction mixture was refluxed for 2 h after completion of the dichloroethane addition. A solution of sodium acetate (11.2 g, 136 mmol, 6.00 eq.) in water (34.1 mL, 4 mol/L) was slowly added and refluxing was continued for 30 min. The reaction was cooled to ambient temperature and extracted with CH_2Cl_2 (4 x 100 mL). Merged organic phases were dried over Na_2SO_4, filtered, and the solvent was removed *in vacuo* to yield a brown residue. Chromatographic purification on silica with PE/CH_2Cl_2 (92:8) + 1% TEA provided the product (**III-94**, 3.29 g, 21.8 mmol, 96%) as a light-yellow crystalline solid.



R_f (PE/EtOAc 80:20): 0.28 (UV and $KMnO_4$ stain). **Mp** 74.8–76.4 °C. **^{1}H NMR** (600 MHz, $CDCl_3$, δ): 9.78 (s, 1H, H-1), 9.30 (s, 1H, H-6), 6.75 (d, *J* = 2.6 Hz, 1H, 3-H), 2.37 (t, *J* = 7.6 Hz, 2H, 8-H), 2.28 (s, 3H, 11-H), 1.56 (h, *J* = 7.4 Hz, 2H, 9-H), 0.94 (t, *J* = 7.3 Hz, 3H, 10-H). **^{13}C NMR** (151 MHz, $CDCl_3$, δ): 177.7 (C-6), 135.9 (C-5), 130.6 (C-2), 124.5 (C-4), 122.6 (C-3), 27.8 (C-8), 23.9 (C-9), 14.0 (C-10), 11.7 (C-11). **FT-IR** (cm^{-1}, neat): 3166, 3091, 3062, 2961, 2932, 2869, 2844, 1622, 1615, 1514, 1464, 1414, 1378, 1342, 1276, 1157, 1143, 1050, 839, 812, 741, 730, 673, 635, 625, 518. **HRMS** (ESI) *m/z*: $[M + H]^+$ calcd for $C_9H_{14}NO$, 152.1070; found, 152.1073.

(*Z*)-4-Methoxy-5-((5-methyl-4-propyl-1*H*-pyrrol-2-yl)methylene)-1,5-dihydro-2*H*-pyrrol-2-one (III-95)

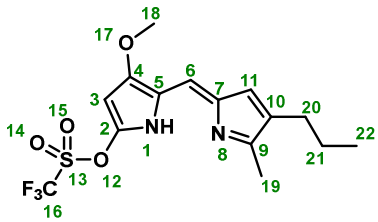
To a 500 mL Schlenk flask under N_2 atmosphere were added 5-methyl-4-propyl-1*H*-pyrrole-2-carbaldehyde (**III-94**, 4.00 g, 26.5 mmol, 1.00 eq.) and 4-methoxy-3-pyrrolin-2-one (**III-74**, 5.98 g, 52.9 mmol, 2.00 eq.) and the solids were dissolved in degassed DMSO (92.6 mL, 3.5 mL/mmol carbaldehyde). Degassed 2 M NaOH (*aq*.) (74.1 mL, 2.8 mL/mmol carbaldehyde) was added and the reaction was stirred for 24 h at 60 °C. A yellow solid precipitated during the reaction. The product was partitioned between EtOAc (150 mL) and water (150 mL), the phases were separated, and the aqueous phase was subsequently extracted with EtOAc (5 x 100 mL). Merged organic phases were washed with water (100 mL) and brine (150 mL), dried over Na_2SO_4, filtered, and the solvent was removed *in vacuo*. The canary yellow crude product was then suspended in *n*-heptane and filtered. The filter cake was washed repeatedly with *n*-heptane, dropwise with *i*Pr_2O/acetone (1:1), and again with *n*-heptane to remove a brown impurity. After drying under high vacuum, the desired product (**III-95**, 5.96 g, 24.2 mmol, 91%) was obtained as a gold-yellow powder.



Mp 195.1 °C (decomposition). **^{1}H NMR** (600 MHz, $CDCl_3$, δ): 10.87 (brs, 1H, 1-H), 10.30 (brs, 1H, 8-H), 6.28 (s, 1H, 6-H), 6.24 (d, *J* = 2.5 Hz, 1H, 11-H), 5.09 (d, *J* = 1.1 Hz, 1H, 3-H), 3.88 (s, 3H, 14-H), 2.35 (t, *J* = 7.6 Hz, 2H, 16-H), 2.34 (s, 3H, 15-H), 1.55 (h, *J* = 7.4 Hz, 2H, 17-H), 0.94 (t, *J* = 7.3 Hz, 3H, 18-H). **^{13}C NMR** (151 MHz, $CDCl_3$, δ): 173.2 (C-2), 168.0 (C-4), 132.5 (C-9), 124.3 (C-7), 122.6 (C-5), 122.5 (C-10), 118.0 (C-11), 102.9 (C-6), 90.0 (C-3), 58.3 (C-14), 27.8 (C-16), 24.2 (C-17), 14.1 (C-18), 11.5 (C-15). **FT-IR** (cm^{-1}, neat): 3345, 3144, 2952, 2918, 1680, 1643, 1574, 1484, 1438, 1384, 1347, 1219, 1131, 1007, 976, 870, 802, 768, 704, 680, 642, 630, 546, 474, 467. **HRMS** (ESI) *m/z*: $[M + H]^+$ calcd for $C_{14}H_{19}N_2O_2$, 247.1441; found, 247.1447.

(*Z*)-4-Methoxy-5-((5-methyl-4-propyl-2*H*-pyrrol-2-ylidene)methyl)-1*H*-pyrrol-2-yl trifluoromethanesulfonate (III-96)

In a 250 mL Schlenk flask under N_2 atmosphere, trifluoromethanesulfonic anhydride (984 µL, 5.85 mmol, 1.20 eq., **freshly opened!**) was added dropwise to a solution of dipyrrinone (**III-95**, 1.20 g, 4.87 mmol, 1.00 eq.) in CH_2Cl_2 (95 mL, 19.5 mL/mmol) at 0 °C. After stirring at this temperature for 1 h, the dark brown reaction mixture was poured into aqueous 2% $NaHCO_3$ (250 mL), the phases were separated and the aqueous phase was repeatedly extracted with MTBE (3 x 20 mL). The combined organic layers were washed with brine (200 mL), dried over Na_2SO_4, filtered, and the solvent was evaporated *in vacuo*. Before the complete removal of the solvent, *n*-pentane was repeatedly added to assist in the precipitation of the product. Thorough solvent removal provided the pure triflate (**III-96**, 1.75 g, 4.62 mmol, 95%) without the need for purification as a deep brown-yellow amorphous solid.

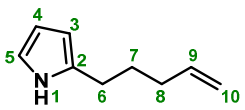


Mp 67.4–68.7 °C. **^{1}H NMR** (300 MHz, $CDCl_3$, δ): 10.70 (brs, 1H, 1-H), 6.97 (s, 1H, 6-H), 6.52 (s, 1H, 11-H), 5.41 (s, 1H, 3-H), 3.86 (s, 3H, 18-H), 2.35 (t, *J* = 7.5 Hz, 2H, 20-H), 2.30 (s, 3H, 19-H), 1.55 (h, *J* = 7.4 Hz, 2H, 21-H), 0.93 (td, *J* = 7.3, 2.9 Hz, 3H, 22-H). **^{13}C NMR** (76 MHz, $CDCl_3$, δ): 167.6 (C-4), 160.4 (C-2), 138.6 (C-9), 131.5 (C-5), 127.5 (C-7), 125.7 (C-10), 123.3 (C-11), 122.0 (C-6), 118.8 (q, *J* = 321.0 Hz, C-16), 86.9 (C-3), 58.8 (C-18), 27.8 (C-20), 23.9 (C-21), 13.9 (C-22), 12.3 (C-19). **^{19}F NMR** (282 MHz, $CDCl_3$, δ): –72.71 (s, –CF_3). **FT-IR** (cm^{-1}, neat): 3347, 2958, 2935, 2873, 1619, 1544, 1505, 1474, 1451, 1416, 1371, 1332, 1260, 1234, 1210, 1147, 1126, 1085, 1053, 1007, 970, 926, 887, 821, 797, 766, 747, 734, 713, 690, 650, 637, 621, 600, 571, 543, 519, 483. **HRMS** (ESI) *m/z*: $[M + H]^+$ calcd for $C_{15}H_{18}F_3N_2O_4S$, 379.0934; found, 379.0938.

2-(Pent-4-en-1-yl)-1*H*-pyrrole (III-97)

Under N_2 atmosphere, $NaBH_4$ (4.97 g, 131 mmol, 2.80 eq.) was suspended in dry *i*PrOH (150 mL). The acylated pyrrole (**III-100**, 7.00 g, 46.9 mmol, 1.00 eq.) was dissolved in dry *i*PrOH (200 mL) and slowly added to the $NaBH_4$ suspension at 0 °C. Afterwards, the solution was refluxed for 22 h at 98 °C. The reaction mixture was cooled to 0 °C, quenched with saturated NH_4Cl, and extracted with EtOAc (3 x 150 mL). The merged organic phases were washed with water (2 x 150 mL) and dried over Na_2SO_4. After solvent evaporation, the crude product was purified over silica using PE/Et_2O

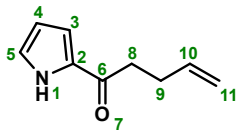
(98:2) + 0.5% TEA and the alkene pyrrole **III-97** was obtained as an instable volatile colourless syrup (4.97 g, 36.7 mmol, 78%) that darkened over time at –20 °C under argon.



R_f (PE/EtOAc 80:20): 0.64 (UV and $KMnO_4$ stain). **^{1}H NMR** (600 MHz, $CDCl_3$, δ): 7.91 (brs, 1H, 1-H), 6.69 (q, *J* = 2.5, 1.6 Hz, 1H, 5-H), 6.18 (q, *J* = 3.2, 2.6 Hz, 1H, 4-H), 5.97 (t, *J* = 3.2 Hz, 1H, 3-H), 5.87 (ddt, *J* = 16.9, 10.0, 6.7 Hz, 1H, 9-H), 5.08 (dq, *J* = 17.1, 1.7 Hz, 1H, 10a-H), 5.03 (dt, *J* = 10.3, 1.6 Hz, 1H, 10b-H), 2.65 (t, *J* = 7.8 Hz, 2H, 6-H), 2.16 (q, *J* = 7.5, 6.6 Hz, 2H, 8-H), 1.76 (p, *J* = 7.5 Hz, 2H, 7-H). **^{13}C NMR** (151 MHz, $CDCl_3$, δ): 138.5 (C-9), 132.5 (C-2), 116.2 (C-5), 115.0 (C-10), 108.4 (C-4), 105.1 (C-3), 33.4 (C-8), 28.9 (C-7), 27.1 (C-6). **FT-IR** (neat, cm^{-1}): 3380, 3096, 3076, 2995, 2976, 2931, 2856, 1640, 1567, 1472, 1456, 1439, 1428, 1403, 1347, 1335, 1304, 1292, 1117, 1094, 1025, 992, 958, 911, 884, 787, 713, 644, 639, 575, 564, 557, 547, 537, 526, 514, 509, 502. **HRMS** (ESI) *m/z:* $[M + H]^+$ calcd for $C_9H_{14}N$, 136.1121; found, 136.1127. **CAS** 249575-98-2.

1-(1*H*-Pyrrol-2-yl)pent-4-en-1-one (III-100)

Under N_2 atmosphere, a solution of 4-pentenoic acid (**III-98**, 7.07 g, 70.6 mmol, 1.00 eq.), 2,2'-dipyridyl disulfide (20.2 g, 91.8 mmol, 1.30 eq.), and PPh_3 (24.1 g, 91.8 mmol, 1.30 eq.) in dry toluene (90 mL) was stirred at 25 °C for 4 h for activation of the carboxylic acid. The reaction mixture was then cooled to –78 °C and a solution of pyrrolylmagnesium chloride [formed by deprotonation of 1*H*-pyrrole (19.6 mL, 283 mmol, 4.00 eq.) with methylmagnesium chloride (3 M in THF, 70.6 mL, 212 mmol, 3.00 eq.) in dry toluene (400 mL) at –40 °C, stirred for at least 20 min] was introduced with a transfer cannula. After stirring for 1 h at –78 °C, the reaction was quenched with saturated NH_4Cl at –78 °C, and the aqueous layer was repeatedly extracted with MTBE (3 x 200 mL). The organic phase was successively washed with 5% K_2CO_3 (250 mL), water (400 mL), and brine (400 mL). After drying over Na_2SO_4 and concentration under reduced pressure, chromatography over silica (*n*-pentane/EtOAc 98:2) afforded the product (**III-100**, 8.49 g, 56.9 mmol, 81%) as a colourless syrup that crystallised at –20 °C.



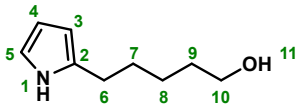
R_f (PE/EtOAc 80:20): 0.37 (UV and $KMnO_4$ stain). **Mp** 33.3–36.4 °C. **^{1}H NMR** (600 MHz, $CDCl_3$, δ): 9.41 (brs, 1H, 1-H), 7.03 (td, *J* = 2.8, 1.4 Hz, 1H, 5-H), 6.92 (ddd, *J* = 4.0, 2.6, 1.4 Hz, 1H, 3-H), 6.28 (dt, *J* = 3.8, 2.5 Hz, 1H, 4-H), 5.88 (ddt, *J* = 16.8, 10.2, 6.5 Hz, 1H, 10-H), 5.08 (dq, *J* = 17.1, 1.6 Hz, 1H, 11a-H), 5.00 (dq, *J* = 10.2, 1.3 Hz, 1H, 11b-H), 2.87 (dd, *J* = 7.4, 6.8 Hz, 2H, 8-H), 2.48 (qt, *J* = 7.3, 1.3 Hz, 2H, 9-H). **^{13}C NMR** (151 MHz, $CDCl_3$, δ): 190.0 (C-6), 137.5 (C-10), 132.1 (C-2), 124.5 (C-5), 116.1 (C-3), 115.4 (C-11), 110.8 (C-4), 37.2 (C-8), 29.0 (C-9). **FT-IR** (cm^{-1}, neat): 3280, 3079, 2978, 2911, 1737, 1632, 1545, 1426, 1402, 1318, 1297, 1244, 1136, 1113, 1099, 1043, 999, 836, 748, 606, 514, 505, 462. **HRMS** (ESI) *m/z*: $[M + H]^+$ calcd for $C_9H_{12}NO$, 150.0913; found, 150.0916. **CAS** 150513-99-8.

5-(1*H*-Pyrrol-2-yl)pentan-1-ol (III-101)

Reaction screening: To a 25 mL Schlenk flask under N_2 atmosphere is added pyrrole ethyl ester (**III-109**, 55.5–123.8 mg, 1.00 eq.) and the pyrrole is dissolved in dry solvent (THF, *i*PrOH, glyme, or 1,4-dioxane) to a final concentration of 0.25 M. The solution is cooled at 0 °C for 15 min while stirring. Reducing agents ($LiAlH_4$, DIBAL-H, $NaBH_4$, or $LiBH_4$, for equivalents see Table III.4) are added and the solutions are heated at the specified temperature for varying duration (cf. Table III.4). For reaction quenching and subsequent analysis, 100 µL of the reaction solution is quenched by the careful addition of water (100 µL). Then, 15% NaOH (100 µL) and water (100 µL) are sequentially added and the aqueous phase is extracted with 1 mL MTBE. The organic phase is dried over $MgSO_4$ and analysed via GC-MS according to Chapter V.3.2.1. For product distribution, see Table III.4.

Highly optimised preparative procedure: To a 1 L three-necked flask with a reflux condenser under N_2 atmosphere was added the pyrrole ethyl ester (**III-109**, 20.3 g, 97.0 mmol, 1.00 eq.) and was dissolved in dry 1,2-dimethoxy ethane (388 mL, 4 mL/mmol pyrrole). The orange solution was degassed by consecutive freeze-pump-thaw cycles (3x) and finally cooled to 0 °C for 20 min. Under a slow stream of N_2, $LiAlH_4$ (18.4 g, 485 mmol, 5.00 eq.) was added carefully in a single batch (vigorous gas and local heat development) and the solution stirred for 5 min at 0 °C (gas development had stopped). Afterwards, the slurry was refluxed at 90 °C for 90 min (preheated heating block). For the workup procedure according to Fieser,[396] the reaction mixture was cooled to 0 °C for 10 min before 18.4 mL of ice water (1 mL/g

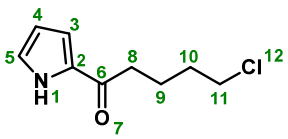
$LiAlH_4$) was added dropwise to the well-ventilated solution (condenser still in place! If the stirring bar starts to get clogged, the solution is diluted with Et_2O). After vigorous stirring for 15 min, 18.4 mL of cold 15% (w/v) NaOH (1 mL/g $LiAlH_4$) were slowly added, followed by 55.2 mL of ice water (3 mL/g $LiAlH_4$). The solution was stirred for 15 min at 0 °C and then for a further 30 min at 20 °C to give a pale-yellow slurry with fine white precipitate. The precipitated aluminium salts were filtered off over a fritted filter (P3) and thoroughly suspended in MTBE, followed by several washing steps with MTBE. Brine (500 mL) was added to the merged clear yellow filtrate and wash fractions, the phases were separated and the aqueous phase was then extracted with MTBE (2 x 150 mL). Merged organic phases were dried over $MgSO_4$, filtered, and the solvent removed *in vacuo*. The viscous yellow oil was dissolved in MTBE and immobilised on Celite by careful evaporation of the solvent. The solid was applied to DCVC (7 cm bed height, 8 cm column diameter, column equilibrated in PE + 1.5% TEA) on Merck silica 60 (15–40 µm) with a PE/MTBE gradient (0 to 70% MTBE with 4.5% increment per fraction, then constant elution at PE/MTBE 30:70 over 15 fractions and 8 fractions with PE/EtOAc 20:80, 100 mL fraction size volume) to afford the product (**III-101**, 13.7 g, 89.4 mmol, 92%) as viscous yellow.



R_f (PE/MTBE 10:90): 0.53 ($KMnO_4$ stain). **R_f** (PE/MTBE 40:60): 0.24 ($KMnO_4$ stain). **^{1}H NMR** (300 MHz, $CDCl_3$, δ): 8.08 (brs, 1H, 1-H), 6.67 (td, *J* = 2.6, 1.5 Hz, 1H, 5-H), 6.14 (q, *J* = 2.9 Hz, 1H, 4-H), 5.95 – 5.90 (m, 1H, 3-H), 3.65 (td, *J* = 6.8, 2.1 Hz, 2H, 10-H), 2.62 (t, *J* = 7.6 Hz, 2H, 6-H), 1.73 – 1.54 (m, 5H, 7-H, 9-H, 11-OH), 1.50 – 1.36 (m, 2H, 8-H). **^{13}C NMR** (76 MHz, $CDCl_3$, δ): 132.6 (C-2), 116.2 (C-5), 108.3 (C-4), 105.0 (C-3), 62.9 (C-10), 32.5 (C-9), 29.5 (C-7), 27.7 (C-6), 25.5 (C-8). **FT-IR** (cm^{-1}, neat): 3370, 3145, 3098, 2931, 2857, 1568, 1472, 1462, 1429, 1403, 1349, 1311, 1302, 1276, 1259, 1228, 1118, 1096, 1065, 1048, 1025, 958, 884, 787, 718, 607, 582, 570. **HRMS** (ESI) *m/z*: $[M + H]^+$ calcd for $C_9H_{16}NO$, 154.1226; found, 154.1229. **CAS** 1797443-11-8.

5-Chloro-1-(1*H*-pyrrol-2-yl)pentan-1-one (III-103)

Under N_2 atmosphere, 1*H*-pyrrole (8.95 mL, 129 mmol, 2.00 eq.) was dissolved in dry toluene (260 mL). Methylmagnesium chloride (22.8 mL, 67.7 mmol, 1.05 eq., 2.97 M in THF) was introduced at 21 °C and the mixture was stirred for 60 min at this temperature before the pyrrolylmagnesium chloride was cooled to –40 °C for 30 min. 5-Chloropentanoyl chloride (**III-102**, 8.29 mL, 64.5 mmol, 1.00 eq.) in dry toluene (65 mL) was cooled to –78 °C and the pyrrolylmagnesium chloride was added to the acid chloride with a transfer cannula. After stirring for 3 h at –78 °C, the green-brown solution was allowed to warm to 21 °C and stirred for a further 24 h. The reaction was quenched at 0 °C with saturated NH_4Cl, causing a colour shift to dark green. After phase separation, the aqueous layer was repeatedly extracted with MTBE (3 x 150 mL). The brown organic phase was successively washed with 5% K_2CO_3, water, and brine (each 250 mL), and dried over $MgSO_4$. Concentration under reduced pressure provided a viscous brown liquid that slowly crystallised at –20 °C. Purification was achieved on silica with *n*-pentane/CH_2Cl_2/MTBE (85:8:7) and a long column of 50 cm to give the product (**III-103**, 6.19 g, 33.3 mmol, 52%) as a weak brown solid. Separation of two product isomers (probably 2- and 3-acylated pyrrole) is **only** possible in the presence of 5–10% CH_2Cl_2, since all two-component solvent mixtures failed in separation.



R_f (*n*-pentane/CH_2Cl_2/MTBE 60:30:10): 0.32 (UV and anisaldehyde stain). **Mp** 58.9–60.4 °C. **^{1}H NMR** (600 MHz, $CDCl_3$, δ): 9.36 (brs, 1H, 1-H), 7.03 (td, *J* = 2.7, 1.3 Hz, 1H, 5-H), 6.91 (ddd, *J* = 3.8, 2.5, 1.3 Hz, 1H, 3-H), 6.28 (dt, *J* = 3.8, 2.6 Hz, 1H, 4-H), 3.57 (t, *J* = 6.1 Hz, 2H, 11-H), 2.81 (t, *J* = 6.8 Hz, 2H, 8-H), 1.93 – 1.82 (m, 4H, 9-H, 10-H). **^{13}C NMR** (151 MHz, $CDCl_3$, δ): 190.2 (C-6), 132.0 (C-2), 124.6 (C-5), 116.1 (C-3), 110.9 (C-4), 44.8 (C-11), 37.0 (C-8), 32.3 (C-9), 22.4 (C-10). **FT-IR** (cm^{-1}, neat): 3285, 3127, 2988, 2952, 2897, 1638, 1545, 1430, 1405, 1372, 1313, 1271, 1139, 1112, 1053, 1037, 1002, 925, 834, 756, 735, 718, 606, 525. **HRMS** (ESI) *m/z*: $[M + H]^+$ calcd for $C_9H_{13}ClNO$, 186.0680; found, 186.0679. **CAS** 160295-19-2.

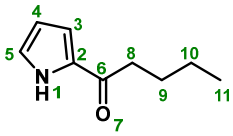
2-(5-Chloropentyl)-1*H*-pyrrole (III-104)

Reaction screening: To a 25 mL Schlenk flask under N_2 atmosphere is added $NaBH_4$ (varying amounts), as well as the additives $CeCl_3$ and NaOH (optional). The solids are suspended in 3 mL of dry *i*PrOH or *i*PrOH/THF (1:2) and the suspensions are cooled to 0 °C (for additives and equivalents see Table III.3). Finally, the chlorinated pyrrole (**III-103**,

50.0 mg, 1.00 eq.) is added and the reactions are heated at 95 °C. For reaction quenching and subsequent analysis, 50 µL of the reaction solution is quenched by carefully adding water (500 µL) and the aqueous phase is extracted with 1 mL MTBE. The organic phase is dried over $MgSO_4$ and analysed via GC-MS according to Chapter V.3.2.1. For product distribution, see Table III.3.

(1*H*-Pyrrol-2-yl)pentan-1-one (III-105f)

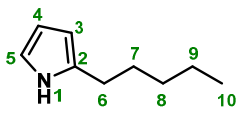
In a 1 L Schlenk flask under N_2 atmosphere, aluminium(III) chloride (15.9 g, 119 mmol, 1.20 eq.) was suspended in dry CH_2Cl_2 (450 mL) and pentanoyl chloride (**III-138f**, 11.8 mL, 99.5 mmol, 1.00 eq.) was added slowly to the aluminium salt. After stirring for 30 min at 21 °C to dissolve the inorganic salt, the red solution was cooled to 0 °C and a solution of 1*H*-pyrrole (7.60 mL, 110 mmol, 1.10 eq.) in dry CH_2Cl_2 (50 mL) was slowly transferred to the acid chloride solution, causing a colour shift from brown to deep orange. The reaction was stirred for a further 1 h at 0 °C, then slowly thawed to 24 °C and stirred at this temperature for 13 h, yielding a deep orange coloured solution. At 0 °C, saturated NH_4Cl (*aq.*) was used for reaction quenching. The phases were separated and the aqueous phase was subsequently extracted with CH_2Cl_2 (3 x 150 mL). The organic phases were merged, washed with saturated $NaHCO_3$ (2 x 150 mL) and brine (1 x 150 mL), dried over $MgSO_4$, filtered, and concentrated *in vacuo*. The oily residue was purified by column chromatography on silica with *n*-pentane/MTBE (90:10) to afford the product (**III-105f**, 9.14 g, 60.5 mmol, 61%) as an orange oil.



R_f (PE/EtOAc 80:20): 0.38 (UV and $KMnO_4$ stain). **^{1}H NMR** (600 MHz, $CDCl_3$, δ): 10.22 (brs, 1H, 1-H), 7.05 (td, *J* = 2.7, 1.3 Hz, 1H, 5-H), 6.93 (ddd, *J* = 3.8, 2.4, 1.3 Hz, 1H, 3-H), 6.27 (dt, *J* = 3.8, 2.5 Hz, 1H, 4-H), 2.78 (t, *J* = 7.6 Hz, 2H, 8-H), 1.72 (p, *J* = 7.6 Hz, 2H, 9-H), 1.40 (h, *J* = 7.4 Hz, 2H, 10-H), 0.94 (t, *J* = 7.4 Hz, 3H, 11-H). **^{13}C NMR** (151 MHz, $CDCl_3$, δ): 191.6 (C-6), 132.1 (C-2), 125.0 (C-5), 116.4 (C-3), 110.5 (C-4), 37.9 (C-8), 27.6 (C-9), 22.7 (C-10), 14.0 (C-11). **FT-IR** (cm^{-1}, neat): 3276, 2958, 2931, 2872, 1710, 1631, 1545, 1427, 1402, 1307, 1294, 1126, 1093, 1046, 923, 883, 844, 748, 606. **HRMS** (ESI) *m/z*: $[M + H]^+$ calcd for $C_9H_{14}NO$, 152.1070; found, 152.1068. **CAS** 89789-53-7.

2-Pentyl-1*H*-pyrrole (III-106f)

In a 500 mL Schlenk flask under N_2 atmosphere, $NaBH_4$ (6.17 g, 163 mmol, 2.80 eq.) was suspended in dry *i*PrOH (100 mL) and cooled to 0 °C. A solution of the acyl pyrrole (**III-105f**, 8.81 g, 58.3 mmol, 1.00 eq.) in dry *i*PrOH (200 mL) was added to the sodium borohydride suspension at 0 °C. Afterwards, the solution was refluxed for 17 h at 99 °C. The reaction was quenched with water at 0 °C, and after the addition of more water (300 mL), the product was extracted with MTBE (3 x 250 mL). Merged organic phases were washed with brine (250 mL), dried over $MgSO_4$, filtered, and the solvent was removed *in vacuo*. The residual oil was purified by column chromatography on silica with *n*-pentane/MTBE (98:2) + 0.5% TEA and the alkyl pyrrole **III-106f** was obtained as a colourless oil (7.16 g, 52.2 mmol, 90%).

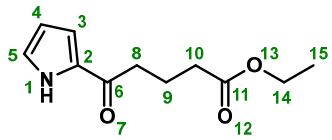


R_f (PE/EtOAc 80:20): 0.58 ($KMnO_4$ stain). **^{1}H NMR** (600 MHz, $CDCl_3$, δ): 7.90 (brs, 1H, 1-H), 6.70 – 6.66 (m, 1H, 5-H), 6.16 (p, *J* = 2.6 Hz, 1H, 4-H), 5.94 (t, *J* = 2.7 Hz, 2H, 3-H), 2.65 – 2.59 (m, 2H, 6-H), 1.69 – 1.61 (m, 2H, 7-H), 1.40 – 1.32 (m, 4H, 8-H, 9-H), 0.96 – 0.89 (m, 3H, 10-H). **^{13}C NMR** (151 MHz, $CDCl_3$, δ): 133.0 (C-2), 116.1 (C-5), 108.3 (C-4), 105.0 (C-3), 31.7 (C-8), 29.5 (C-7), 27.8 (C-6), 22.6 (C-9), 14.2 (C-10). **FT-IR** (cm^{-1}, neat): 3383, 3096, 2956, 2926, 2857, 1567, 1467, 1459, 1426, 1378, 1119, 1096, 1024, 957, 883, 783, 710, 562. **HRMS** (ESI) *m/z*: $[M + H]^+$ calcd for $C_9H_{16}N$, 138.1277; found, 138.1275. **CAS** 1551-12-8.

Ethyl 5-oxo-5-(1*H*-pyrrol-2-yl)pentanoate (III-109)

In a 2 L two-necked flask under N_2 atmosphere, aluminium(III) chloride (22.4 g, 168 mmol, 1.20 eq.) was added to dry CH_2Cl_2 (1 L) and cooled to 0 °C. Ethyl glutaryl chloride (**III-108**, 21.9 mL, 140 mmol, 1.00 eq.) was added slowly to the transparent suspension and the mixture was stirred for 30 min at 0 °C until the salt had completely dissolved. A solution of 1*H*-pyrrole (10.7 mL, 154 mmol, 1.10 eq.) in dry CH_2Cl_2 (70 mL) was transferred to the acid chloride solution, causing a colour shift from yellow to orange. The reaction was stirred for a further 3 h at 0 °C, then thawed to 20 °C overnight,

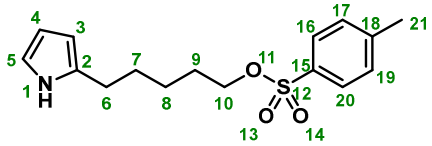
and stirred at this temperature for 15 h, yielding a deep orange/brown-coloured solution. At 0 °C, saturated NH_4Cl (*aq*.) was slowly introduced for reaction quenching. The phases were separated and the aqueous phase was subsequently extracted with CH_2Cl_2 (3 x 100 mL). The organic phases were merged, washed with saturated $NaHCO_3$ (2 x 250 mL) and brine (1 x 250 mL), dried over $MgSO_4$, filtered, and the solvent was removed *in vacuo*. The brown oily residue was dissolved in EtOAc, immobilised on Celite by evaporation and applied to dry column vacuum chromatography (8 cm bed height, 9 cm column diameter, DCVC) on Merck silica 60 (15–40 µm) with a PE/MTBE gradient (0 to 80% MTBE with 3% increment per fraction and 100 mL fraction volume) to afford the product (**III-109**, 20.9 g, 100 mmol, 72%) as an orange oil.



R_f (PE/MTBE 60:40): 0.32 ($KMnO_4$ stain). **^{1}H NMR** (300 MHz, $CDCl_3$, δ): 9.88 (brs, 1H, 1-H), 7.04 (td, *J* = 2.7, 1.3 Hz, 1H, 5-H), 6.93 (ddd, *J* = 3.8, 2.4, 1.3 Hz, 1H, 3-H), 6.26 (dt, *J* = 3.8, 2.5 Hz, 1H, 4-H), 4.13 (q, *J* = 7.1 Hz, 2H, 14-H), 2.84 (t, *J* = 7.3 Hz, 2H, 8-H), 2.40 (t, *J* = 7.3 Hz, 2H, 10-H), 2.05 (p, *J* = 7.3 Hz, 2H, 9-H), 1.24 (t, *J* = 7.1 Hz, 3H, 15-H). **^{13}C NMR** (76 MHz, $CDCl_3$, δ): 190.1 (C-6), 173.4 (C-11), 132.0 (C-2), 124.9 (C-5), 116.5 (C-3), 110.7 (C-4), 60.5 (C-14), 36.9 (C-8), 33.7 (C-10), 20.3 (C-9), 14.3 (C-15). **FT-IR** (cm^{-1}, neat): 3284, 2978, 2939, 2906, 2875, 1729, 1635, 1546, 1403, 1375, 1302, 1245, 1212, 1185, 1159, 1138, 1111, 1043, 934, 914, 882, 873, 853, 843, 753, 606, 515, 505. **HRMS** (ESI) *m/z*: $[M + H]^+$ calcd for $C_{11}H_{16}NO_3$, 210.1125; found, 210.1127.

5-(1*H*-Pyrrol-2-yl)pentyl 4-methylbenzenesulfonate (III-111)

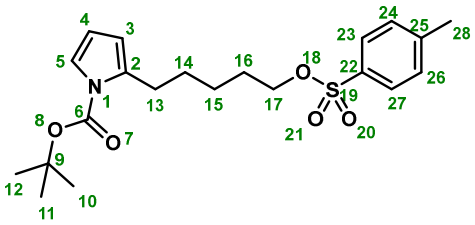
In a 500 mL Schlenk flask under N_2 atmosphere, pyrrole (**III-101**, 7.59 g, 49.5 mmol, 1.00 eq.) and DMAP (605 mg, 4.95 mmol, 0.10 eq.) were dissolved in dry CH_2Cl_2 (165 mL, 3.34 mL/mmol pyrrole) and DIPEA (25.4 mL, 149 mmol, 3.00 eq.) was added under cooling to 0 °C. At 0 °C, a solution of recrystallised *p*TsCl (14.2 g, 74.3 mmol, 1.50 eq.) in dry CH_2Cl_2 (83 mL) was slowly added to the pyrrolic solution and the solution was allowed to warm to ambient temperature. The reaction was stirred for 16.5 h at 26 °C. Ice water (250 mL) was added for quenching, the phases were separated, and the aqueous phase was extracted with CH_2Cl_2 (3 x 50 mL). Merged organic phases were dried over $MgSO_4$, filtered, and the solvent was removed *in vacuo*. Column chromatography on silica using a PE/CH_2Cl_2 gradient (70:30, then 60:40, then 30:70) as eluent provided the product (**III-111**, 10.1 g, 32.9 mmol, 66%) as a light-yellow oil. Considering re-isolation of unconverted pyrrole (1.04 g, 6.81 mmol), a total yield of 77% was achieved.



R_f (PE/MTBE 40:60): 0.48 ($KMnO_4$ stain). **^{1}H NMR** (600 MHz, $CDCl_3$, δ): 7.97 (brs, 1H, 1-H), 7.78 (d, *J* = 8.4 Hz, 2H, 16-H, 20-H), 7.35 (d, *J* = 8.1 Hz, 2H, 17-H, 19-H), 6.66 (td, *J* = 2.6, 1.5 Hz, 1H, 5-H), 6.12 (q, *J* = 2.9 Hz, 1H, 4-H), 5.87 (d, *J* = 3.0 Hz, 1H, 3-H), 4.02 (t, *J* = 6.4 Hz, 2H, 10-H), 2.56 (t, *J* = 7.6 Hz, 2H, 6-H), 2.45 (s, 3H, 21-H), 1.71 – 1.63 (m, 2H, 9-H), 1.58 (p, *J* = 7.7 Hz, 2H, 7-H), 1.38 (dp, *J* = 7.5, 6.3 Hz, 2H, 8-H). **^{13}C NMR** (151 MHz, $CDCl_3$, δ): 144.8 (C-18), 133.6 (C-15), 132.2 (C-2), 130.0 (C-17, C-19), 128.0 (C-16, C-20), 116.3 (C-5), 108.4 (C-4), 105.2 (C-3), 70.6 (C-10), 29.1 (C-7), 28.8 (C-9), 27.6 (C-6), 25.2 (C-8), 21.7 (C-21). **FT-IR** (cm^{-1}, neat): 3409, 2933, 2859, 1597, 1570, 1495, 1463, 1350, 1306, 1292, 1211, 1188, 1173, 1120, 1097, 1021, 943, 904, 884, 814, 782, 713, 691, 662, 574, 553, 496. **HRMS** (ESI) *m/z*: $[M + H]^+$ calcd for $C_{16}H_{22}NO_3S$, 308.1315; found, 308.1318.

tert-Butyl 2-(5-(tosyloxy)pentyl)-1*H*-pyrrole-1-carboxylate (III-112)

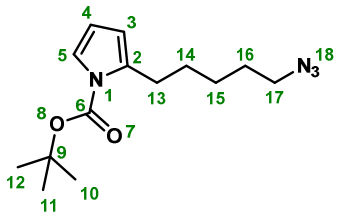
To a 250 mL Schlenk flask under N_2 atmosphere were added 5-(1*H*-pyrrol-2-yl)pentyl 4-methylbenzenesulfonate (**III-111**, 9.24 g, 30.1 mmol, 1.00 eq.) and DMAP (367 mg, 3.01 mmol, 0.10 eq.) and the solids were dissolved in dry CH_2Cl_2 (25 mL). A solution of Boc_2O (7.87 g, 36.1 mmol, 1.20 eq.) in CH_2Cl_2 (100 mL) was added to the prior solution at 31 °C and the reaction was stirred for 22 h at 31 °C. The solvent was removed under reduced pressure and the orange oily residue purified by column chromatography on silica using a gradient of PE/CH_2Cl_2 (60:40 up to 20:80). The product **III-112** was afforded as a colourless viscous oil (9.93 g, 24.4 mmol, 81%).



R_f (PE/MTBE 70:30): 0.52 (UV and $KMnO_4$ stain). **^{1}H NMR** (300 MHz, $CDCl_3$, δ): 7.81 – 7.75 (m_c, 2H, 23-H, 27-H), 7.37 – 7.30 (m_c, 2H, 24-H, 26-H), 7.17 (dd, *J* = 3.4, 1.8 Hz, 1H, 5-H), 6.05 (t, *J* = 3.3 Hz, 1H, 4-H), 5.89 (ddt, *J* = 3.4, 1.9 Hz, 1H, 3-H), 4.02 (t, *J* = 6.5 Hz, 2H, 17-H), 2.78 (t, 2H, 13-H), 2.44 (s, 3H, 28-H), 1.74 – 1.62 (m, 2H, 16-H), 1.61 – 1.48 (m, 11H, 10-H, 11-H, 12-H, 14-H), 1.45 – 1.31 (m, 2H, 15-H). **^{13}C NMR** (76 MHz, $CDCl_3$, δ): 149.5 (C-6), 144.8 (C-25), 135.9 (C-2), 133.3 (C-22), 129.9 (C-24, C-26), 128.0 (C-23, C-27), 120.9 (C-5), 111.0 (C-3), 109.9 (C-4), 83.4 (C-9), 70.6 (C-17), 28.8 (C-16), 28.6 (C-13), 28.2 (C-14), 28.1 (C-10, C-11, C-12), 25.2 (C-15), 21.7 (C-28). **FT-IR** (cm^{-1}, neat): 2977, 2935, 2864, 1737, 1598, 1495, 1477, 1458, 1407, 1396, 1367, 1359, 1329, 1255, 1235, 1210, 1188, 1176, 1127, 1098, 1060, 1019, 1012, 950, 906, 882, 842, 829, 815, 773, 759, 727, 689, 664, 600, 577, 555, 493. **HRMS** (ESI) *m/z*: $[M + H]^+$ calcd for $C_{21}H_{30}NO_5S$, 408.1839; found, 408.1845.

tert-Butyl 2-(5-azidopentyl)-1*H*-pyrrole-1-carboxylate (III-113)

In a 100 mL Schlenk flask under N_2 atmosphere, the tosyl-protected 4-(2-methyl-1*H*-pyrrol-3-yl)butyl 4-methylbezenesulfonate (**III-112**, 8.75 g, 21.5 mmol, 1.00 eq.) was dissolved in dry DMF (85.8 mL, 4 mL/mmol pyrrole). Sodium azide (4.19 g, 64.4 mmol, 3.00 eq.) was added and the reaction was furnished by the addition of five catalytic drops of DIPEA. The mixture was stirred for 17 h at 21 °C after which time a white solid had precipitated. The reaction was quenched by the addition of ice water (50 mL) and the product was afterwards extracted with Et_2O (5 x 50 mL). Merged organic phases were washed with water (2 x 100 mL), dried over $MgSO_4$, filtered, and the solvent was removed *in vacuo* to give a yellow residue. Purification of the crude product by column chromatography on silica with *n*-pentane/CH_2Cl_2 (80:20) yielded the desired product **III-113** as a colourless oil (5.94 g, 21.3 mmol, 99%).

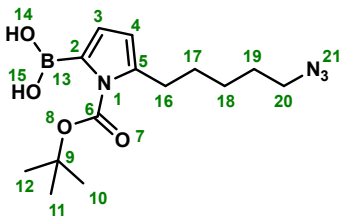


R_f (*n*-pentane/CH_2Cl_2 60:40): 0.36 (UV and $KMnO_4$ stain). **^{1}H NMR** (600 MHz, $CDCl_3$, δ): 7.18 (dd, *J* = 3.4, 1.8 Hz, 1H, 5-H), 6.07 (t, *J* = 3.3 Hz, 1H, 4-H), 5.95 (ddt, *J* = 3.4, 1.8 Hz, 1H, 3-H), 3.27 (t, *J* = 7.1 Hz, 2H, 17-H), 2.86 (t, *J* = 7.6 Hz, 2H, 13-H), 1.65 (pd, *J* = 7.4 Hz, 4H, 14-H, 16-H), 1.59 (s, 9H, 10-H, 11-H, 12-H), 1.49 – 1.42 (m, 2H, 15-H). **^{13}C NMR** (151 MHz, $CDCl_3$, δ): 149.6 (C-6), 136.1 (C-2), 121.0 (C-5), 111.0 (C-3), 110.0 (C-4), 83.4 (C-9), 51.6 (C-17), 28.9 (C-13), 28.8 (C-16), 28.6 (C-14), 28.2 (C-10, C-11, C-12), 26.6 (C-15). **FT-IR** (cm^{-1}, neat): 3159, 3109, 2979, 2935, 2862, 2093, 1738, 1495, 1478, 1457, 1408, 1395, 1370, 1329, 1319, 1255, 1236, 1169, 1156, 1125, 1059, 1011, 883, 851, 804, 772, 721, 674, 599, 558, 495, 463. **HRMS** (ESI) *m/z*: $[M + H]^+$ calcd for $C_{14}H_{23}N_4O_2$, 279.1816; found, 279.1814.

(5-(5-Azidopentyl)-1-(*tert*-butoxycarbonyl)-1*H*-pyrrol-2-yl)boronic acid (III-114)

In a 100 mL Schlenk flask under N_2 atmosphere, TMP (7.02 mL, 41.6 mmol, 2.00 eq.) was dissolved in dry THF (49.1 mL, 2.36 mL/mmol pyrrole) and cooled to –78 °C. *n*-Butyl lithium (17.8 mL, 43.7 mmol, 2.10 eq., 2.46 M in *n*-hexane) was added dropwise to the TMP solution in THF at 0.5 mL/min (syringe pump). After completion of the addition and further stirring for 30 min at –78 °C, the mixture was allowed to warm to 0 °C over 30 min and was then cooled again to –78 °C. In a 500 mL three-necked flask under N_2 atmosphere, equipped with a cold thermometer and connection to the line, was *tert*-butyl 2-(5-azidopentyl)-1*H*-pyrrole-1-carboxylate (**III-113**, 5.79 g, 20.8 mmol, 1.00 eq.) dissolved in dry THF (83.2 mL, 4.00 mL/mmol pyrrole) and cooled to –78 °C. The LiTMP was then added dropwise with a transfer cannula to the glass surface of the flask with the pyrrolic THF solution at the slowest possible speed by adding positive pressure of argon to the Schlenk flask. The internal temperature was constantly kept below –70 °C and the rate was adjusted if needed. The reaction mixture was stirred for 2 h at –78 °C, before a solution of $B(OMe)_3$ (6.96 mL, 62.4 mmol, 3.00 eq.) in dry THF (22.3 mL, 1.07 mL/mmol pyrrole) was added dropwise at 1.00 mL/min (syringe pump). The solution was stirred for 1 h at –78 °C, before excess of dry ice was removed from the cooling bath. The reaction was allowed to warm to 21 °C over 15 h. The reaction was quenched at 0 °C by the dropwise addition of 0.20 M HCl (260 mL, 52.0 mmol, 2.50 eq.). Phases were separated and the aqueous phase was extracted with Et_2O (3 x 150 mL). Merged organic phases were washed with water (2 x 100 mL) and brine (2 x 100 mL), dried over a minimal amount $MgSO_4$, filtered, and the solvent was removed *in vacuo*. As the product typically did not precipitate upon removal of the

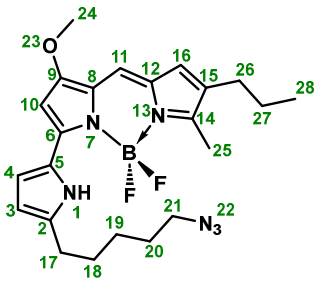
ethereal solvent, the residue was taken up in Et_2O and washed again with 0.2 M HCl (2 x 50 mL). After drying over $MgSO_4$, filtration, and slow concentration under reduced pressure, stabiliser-free *i*Pr_2O was added when the Et_2O had been reduced to a minimal amount to ease product precipitation (the product is less soluble in *i*Pr_2O than Et_2O, but undergoes decomposition in even less polar hydrocarbon solvents, such as *n*-pentane or *n*-heptane). The solution was cooled to 0 °C and the solid recovered by filtration, followed by washing with a minimal amount of cold *i*Pr_2O. The product **III-114** was obtained as a delicate yellow powder (2.75 g, 8.55 mmol, 41%) after quick (**!**) drying under vacuum (prolonged drying under vacuum provokes black spots to appear in the solid product, which propagate quickly until the product has completely decomposed). Longer storage at –20 °C under Ar atmosphere is not feasible and the product decomposes within <3 days.



Mp 65.4–66.6 °C. **^{1}H NMR** (300 MHz, $CDCl_3$, δ): 7.06 (brs, 2H, 14-OH, 15-OH), 7.01 (d, *J* = 3.4 Hz, 1H, 3-H), 6.04 (d, *J* = 3.3 Hz, 1H, 4-H), 3.28 (t, *J* = 6.8 Hz, 2H, 20-H), 2.82 (t, *J* = 7.6 Hz, 2H, 16-H), 1.63 (s, 9H, 10-H, 11-H, 12-H), 1.71 – 1.57 (m, 4H, 17-H, 19-H), 1.52 – 1.38 (m, 2H, 18-H). **^{13}C NMR** (76 MHz, $CDCl_3$, δ): 153.3 (C-6), 141.9 (C-5), 127.4 (C-3), 112.8 (C-4), 86.0 (C-9), 51.4 (C-20), 30.7 (C-16), 29.0 (C-17), 28.9 (C-19), 28.1 (C-10, C-11, C-12), 26.6 (C-18). **^{11}B NMR** (96 MHz, $CDCl_3$, δ): 25.3 [s, –*B*$(OH)_2$]. **FT-IR** (cm^{-1}, neat): 3358, 3152, 3010, 2986, 2975, 2942, 2882, 2864, 2127, 2082, 1705, 1699, 1571, 1494, 1471, 1460, 1429, 1400, 1375, 1369, 1356, 1344, 1289, 1265, 1256, 1235, 1213, 1202, 1166, 1131, 1120, 1084, 1056, 1022, 1002, 948, 891, 863, 835, 806, 780, 763, 731, 696, 681, 656, 615, 582, 559, 510, 465. **HRMS** (ESI) *m/z*: $[M + H]^+$ calcd for $C_{14}H_{23}BN_4NaO_4$, 345.1705; found, 345.1705.

3-(5-(5-Azidopentyl)-1*H*-pyrrol-2-yl)-5,5-difluoro-1-methoxy-7-methyl-8-propyl-5*H*-5λ^4,6λ^4-dipyrrolo[1,2-*c*:2',1'-*f*][1,3,2]diazaborinine (III-125)

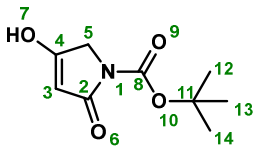
To a tin foil-covered 25 mL Schlenk flask under N_2 atmosphere was added the prodigiosin A-ring azide HCl salt (**III-89·HCl**, 101 mg, 227 µmol, 1.00 eq.). The solid was dissolved in dry CH_2Cl_2 (10 mL) (pink solution) before dry DIPEA (194 µL, 1.14 mmol, 5.00 eq.) (red-orange) was added at 20 °C. After stirring for 15 min, the reaction was cooled to 0 °C. Boron trifluoride etherate (112 µL, 909 µmol, 4.00 eq.) was added dropwise at 0 °C to the solution. Once the addition was completed, stirring at 0 °C was continued for 5 h before the reaction was slowly warmed to 20 °C overnight. After a total reaction time of 21 h, the reaction was quenched at 0 °C with 5 mL of ice water. Additional ice water (25 mL) was added and the phases were separated. The aqueous phase was extracted with $CHCl_3$ (3 x 5 mL). After drying of the combined organic phases over $MgSO_4$ and filtration over degreased cotton wool, the flask was covered with tin foil and the solvent was evaporated under reduced pressure. The crude purple product was chromatographed on silica using PE/CH_2Cl_2 (80:20) to provide the BODIPY A-ring azide **III-125** as a pink fluorescent liquid that solidified to a purple solid (81.3 mg, 179 µmol, 79%) after evaporation of solvent and precipitation with *n*-pentane.



R_f (PE/CH_2Cl_2 80:20): 0.47 (visible light). **Mp** 99.9–100.8 °C. **^{1}H NMR** (600 MHz, $CDCl_3$, δ): 10.26 (t, *J* = 9.9 Hz, 1H, 1-H), 6.92 (s, 1H, 11-H), 6.83 (dd, *J* = 3.8, 2.5 Hz, 1H, 4-H), 6.54 (s, 1H, 16-H), 6.07 (dd, *J* = 2.6 Hz, 1H, 3-H), 6.04 (s, 1H, 10-H), 3.93 (s, 3H, 24-H), 3.29 (t, *J* = 7.0 Hz, 2H, 21-H), 2.76 (t, *J* = 7.5 Hz, 2H, 17-H), 2.49 (s, 3H, 25-H), 2.38 (t, *J* = 7.6 Hz, 2H, 26-H), 1.75 (p, *J* = 7.6 Hz, 2H, 18-H), 1.66 (p, *J* = 7.2 Hz, 2H, 20-H), 1.57 (h, *J* = 7.4 Hz, 2H, 27-H), 1.53 – 1.44 (m, 2H, 19-H), 0.97 (t, *J* = 7.3 Hz, 3H, 28-H). **^{13}C NMR** (151 MHz, $CDCl_3$, δ): 163.5 (C-9), 149.3 (C-6), 147.2 (C-14), 141.0 (C-2), 130.5 (C-12), 130.1 (C-15), 128.0 (C-8), 122.6 (C-5), 122.3 (C-16), 118.2 (C-4), 115.9 (C-11), 109.5 (C-3), 96.2 (C-10), 58.5 (C-24), 51.5 (C-21), 28.8 (C-20), 28.7 (C-18), 28.1 (C-26), 28.1 (C-17), 26.4 (C-19), 23.6 (C-27), 14.1 (C-28), 12.4 (C-25). **^{11}B NMR** (96 MHz, $CDCl_3$, δ): 1.35 (t, *J* = 36.9 Hz). **^{19}F NMR** (282 MHz, $CDCl_3$, δ): –139.7 (dd, *J* = 72.5, 34.7 Hz). **FT-IR** (cm^{-1}, neat): 3430, 2957, 2926, 2872, 2864, 2135, 2084, 1606, 1585, 1546, 1510, 1466, 1457, 1448, 1420, 1397, 1370, 1355, 1302, 1278, 1238, 1312, 1278, 1220, 1205, 1185, 1155, 1141, 1086, 1075, 1050, 1024, 1014, 983, 960, 907, 891, 880, 856, 829, 809, 795, 779, 738, 692, 676, 660, 636, 615, 556, 520, 482, 455. **HRMS** (ESI) *m/z*: $[M + Na]^+$ calcd for $C_{23}H_{29}BF_2N_6NaO$, 477.2356; found, 477.2353.

tert-Butyl 4-hydroxy-2-oxo-2,5-dihydro-1*H*-pyrrole-1-carboxylate (III-126)

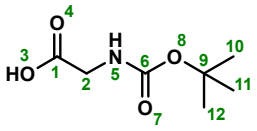
To a 1 L Schlenk flask under N_2 atmosphere was added Boc-Gly-OH (**III-128**, 15.0 g, 85.6 mmol, 1.00 eq.), dissolved in dry CH_2Cl_2 (428 mL, 0.2 M solution of Boc-Gly-OH), and cooled to –5 °C [NH_4Cl/ice bath with (25:75 w/w) ratio]. Recrystallised Meldrum's acid (13.6 g, 94.2 mmol, 1.10 eq.) and DMAP (23.0 g, 188 mmol, 2.20 eq.) were added and stirring was continued until dissolved. Isopropyl chloroformate (47.1 mL, 94.2 mmol, 1.10 eq., 2 M in toluene) was added at –5 °C over 60 min with a syringe pump. The weak yellow solution was stirred for 3 h at –5 °C. Afterwards, the mixture was quenched and washed with cold 10% citric acid (2 x 500 mL), cold water (2 x 500 mL), and cold brine (2 x 500 mL). The organic layer was dried over $MgSO_4$, filtered, and the solvent evaporated to give a slurry solid. Drying under high vacuum provided the crude acylated Meldrum's acid as a dry yellow amorphous solid. This crude material was then refluxed in N_2-bubbled dry EtOAc (500 mL) for 2 h to give an intense yellow solution with some precipitate before the solvent was removed under reduced pressure. The product was filtered, washed with Et_2O, and dried under high vacuum overnight. The Boc-protected tetramic acid (**III-126**, 11.1 g, 55.5 mmol, 65%) was obtained as an amorphous beige powder.



Mp >320 °C (decomposition). **^{1}H NMR** (600 MHz, DMSO-d_6) 12.13 (s, 1H, 7-OH), 4.88 (s, 1H, 3-H), 4.14 (s, 2H, 5-H), 1.44 (s, 9H, 12-H, 13-H, 14-H). **^{13}C NMR** (151 MHz, DMSO-d_6, δ): 174.4 (C-4), 169.2 (C-2), 148.9 (C-8), 94.3 (C-3), 80.8 (C-11), 49.4 (C-5), 27.8 (C-12, C-13, C-14). **FT-IR** (cm^{-1}, neat): 2980, 2937, 1756, 1599, 1432, 1413, 1364, 1302, 1240, 1209, 1151, 1077, 1033, 847, 800, 774, 752, 741, 730, 626, 604, 592, 482, 460. **HRMS** (ESI) *m/z*: [M + Na]$^+$ calcd for $C_9H_{13}NNaO_4$, 222.0737; found, 222.0737. **CAS** 182352-48-3.

N-Boc-Glycine (III-128)

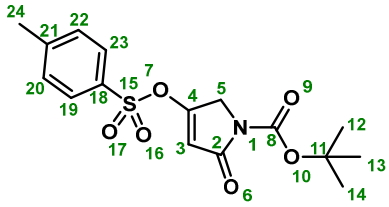
N-Boc-Glycine was synthesised according to a procedure of Mroczkiewicz *et al*.[874] To a solution of NaOH (4.69 g, 117 mmol, 1.10 eq.) in water (117 mL), glycine (**III-127**, 8.00 g, 107 mmol, 1.00 eq.) and *t*BuOH (82 mL) were added. Then, Boc_2O (23.3 g, 107 mmol, 1.00 eq.) was added at 23 °C. After stirring at 23 °C for 15 h, the reaction mixture was washed with *n*-pentane (3 × 150 mL). The combined organic layers were extracted with saturated $NaHCO_3$ solution (2 × 150 mL). The aqueous layers (from pentane and $NaHCO_3$ wash) were combined and acidified with solid $KHSO_4$ up to pH 2 and extracted with Et_2O (5 × 150 mL). The organic layers were combined, dried over MgSO4, and evaporated to dryness to leave a thick yellow oil. The oil was dissolved in EtOAc and the solvent was removed *in vacuo*. After vacuum drying, the residue crystallised as an amorphous solid. Grinding provided the Boc-protected amino acid (**III-128**, 17.6 g, 101 mmol, 94%) as a fine white powder.



Mp 87.3–89.0 °C. **^{1}H NMR** (600 MHz, DMSO-d_6, δ): 12.43 (brs, 1H, 3-OH), 7.05 (t, J = 6.2 Hz, 1H, 5-H), 3.57 (d, J = 6.2 Hz, 2H, 2-H), 1.38 (s, 9H, 10-H, 11-H, 12-H). **^{13}C NMR** (151 MHz, DMSO-d_6, δ): 171.8 (C-1), 155.9 (C-6), 78.1 (C-9), 41.8 (C-2), 28.2 (C-10, C-11, C-12). **FT-IR** (cm^{-1}, neat): 3407, 3343, 3107, 2979, 2938, 1739, 1667, 1530, 1453, 1408, 1368, 1298, 1280, 1256, 1196, 1157, 1055, 958, 882, 857, 780, 768, 674, 659, 582, 567, 457. **CAS** 4530-20-5.

tert-Butyl 2-oxo-4-(tosyloxy)-2,5-dihydro-1*H*-pyrrole-1-carboxylate (III-130)

Under N_2 atmosphere, *N*-Boc-protected tetramic acid (**III-126**, 2.50 g, 12.6 mmol, 1.00 eq.) was dissolved in dry CH_2Cl_2 (125 mL) and *p*TsCl (2.51 g, 13.2 mmol, 1.05 eq.) was added at 0 °C to give a yellow slurry. DIPEA (4.29 mL, 25.1 mmol, 2.00 eq.) was added dropwise at 0 °C to this solution over 30 min (143 µL/min with a syringe pump) to yield a clear yellow solution turning dark brown to black over time. The resulting mixture was stirred for 6 h at 21 °C. Then, the reaction mixture was washed with 5% HCl (15 mL), 5% $NaHCO_3$ (25 mL), and brine (25 mL), dried over $MgSO_4$, and filtered. The solvent was removed *in vacuo*, and the residue was chromatographed on silica using PE/EtOAc (80:20) to give the *O*-tosylated Boc-protected tetramic acid (**III-126**, 3.75 g, 10.6 mmol, 84%) as a white solid.



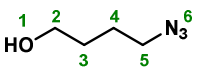
R_f (PE/EtOAc 80:20): 0.12 (UV and $KMnO_4$ stain). **R_f** (PE/EtOAc 60:40): 0.41 (UV and $KMnO_4$ stain). **Mp** 104.8–106.5 °C. **^{1}H NMR** (600 MHz, $CDCl_3$, δ): 7.84 (d, *J* = 8.0 Hz, 2H, 19-H, 23-H), 7.41 (d, *J* = 7.9 Hz, 2H, 20-H, 22-H), 5.74 (s, 1H, 3-H), 4.21 (s, 2H, 5-H), 2.48 (s, 3H, 24-H), 1.51 (s, 9H, 12-H, 13-H, 14-H). **^{13}C NMR** (151 MHz, $CDCl_3$, δ): 167.0 (C-2), 162.9 (C-4), 148.9 (C-8), 147.3 (C-21), 131.1 (C-18), 130.5 (C-20, C-22), 128.7 (C-19, C-23), 107.8 (C-3), 83.6 (C-11), 49.6 (C-5), 28.2 (C-12, C-13, C-14), 22.0 (C-24). **FT-IR** (cm^{-1}, neat): 3136, 3007, 2995, 2967, 2956, 2932, 2883, 1737, 1709, 1625, 1595, 1491, 1480, 1461, 1448, 1396, 1372, 1361, 1346, 1304, 1259, 1206, 1190, 1179, 1159, 1121, 1082, 1038, 1015, 1008, 993, 935, 858, 842, 810, 800, 783, 745, 725, 701, 676, 661, 599, 561, 549, 502, 493, 480, 468. **HRMS** (ESI) *m/z*: $[M + H]^+$ calcd for $C_{16}H_{20}NO_6S$, 354.1006; found, 189.0679. **CAS** 443680-33-9.

tert-Butyl 4-(hex-5-en-1-yloxy)-2-oxo-2,5-dihydro-1*H*-pyrrole-1-carboxylate (III-131)

To a 10 mL vial under N_2 atmosphere were added tosyl pyrrolidinone (**III-130**, 200 mg, 0.57 mmol, 1.00 eq.) and DABCO (69.8 mg, 0.62 mmol, 1.10 eq.). The solids were dissolved in dry CH_2Cl_2 (3.8 mL, 0.15 M) before 5-hexen-1-ol (134 µL, 1.13 mmol, 2.00 eq.) was added. The reaction was then stirred at 21 °C for 18 h. A few minutes after initiating the reaction, protonated DABCO precipitated as a white solid. However, the desired *O*-functionalised reaction product **III-131** was not identified in a crude NMR.

4-Azidobutan-1-ol (III-132)

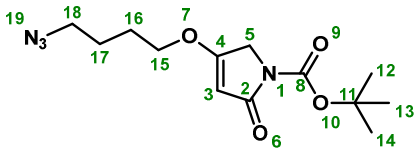
In a 250 mL Schlenk flask under N_2 atmosphere, 4-chloro-1-butanol (**III-133**, 5.00 g, 46.1 mmol, 1.00 eq., >85% with variable traces of THF) was dissolved in dry DMF (92.1 mL, 0.5 M). Sodium azide (4.49 g, 69.1 mmol, 1.50 eq.) was added in a single batch, followed by five catalytic drops of DIPEA. The reaction was stirred for 22 h at 70 °C. After cooling to ambient temperature, the reaction was quenched by the slow introduction of ice water (100 mL) and the aqueous phase was repeatedly extracted with Et_2O (6 x 100 mL). Merged organic phases were dried over $MgSO_4$, filtered, and the solvent was removed *in vacuo*. Chromatographic purification of the crude product on silica with *n*-pentane/Et_2O (50:50) provided the product (**III-132**, 4.63 g, 40.2 mmol, 87%) as a light-yellow oil.



R_f (PE/EtOAc 60:40): 0.29 ($KMnO_4$ stain). **^{1}H NMR** (600 MHz, $CDCl_3$, δ): 3.66 (q, *J* = 5.1 Hz, 2H, 2-H), 3.31 (t, *J* = 6.7 Hz, 2H, 5-H), 1.74 (d, *J* = 5.3 Hz, 1H, 1-H), 1.68 (h, *J* = 6.7 Hz, 1H, 4-H), 1.64 (h, *J* = 6.7 Hz, 2H, 3-H). **^{13}C NMR** (151 MHz, $CDCl_3$, δ): 62.4 (C-2), 51.5 (C-5), 30.0 (C-3), 25.6 (C-4). **FT-IR** (cm^{-1}, neat): 3333, 2941, 2870, 2505, 2090, 1666, 1451, 1351, 1250, 1173, 1058, 1033, 992, 949, 924, 824, 745, 659, 636, 558, 504. **HRMS** (ESI) *m/z*: $[M + Na]^+$ calcd for $C_4H_9N_3NaO$, 138.0638; found, 138.0636. **CAS** 54953-78-5.

tert-Butyl 4-(4-azidobutoxy)-2-oxo-2,5-dihydro-1*H*-pyrrole-1-carboxylate (III-134)

In a 500 mL Schlenk flask under N_2 atmosphere, Boc-protected tetramic acid (**III-126**, 5.00 g, 25.1 mmol, 1.00 eq.), PPh_3 (7.24 g, 27.6 mmol, 1.10 eq.), and 4-azido-1-butanol (**III-132**, 4.34 g, 37.7 mmol, 1.50 eq.) were dissolved in dry THF (83.7 mL) at 21 °C (yellow slurry). Diethyl azodicarboxylate (DEAD, 4.3 mL, 27.6 mmol, 1.10 eq.) was added under vigorous stirring to give a brown homogenous solution and stirring was continued for 22 h. The solvent was then evaporated under reduced pressure and the remaining oil was purified by column chromatography on silica with a gradient of *n*-pentane/Et_2O (50:50 to 0:100) to give the desired product as a yellow oil with high viscosity and water content. The product **III-134** was lyophilised overnight to yield a light yellow amorphous solid (4.14 g, 14.0 mmol, 56%).

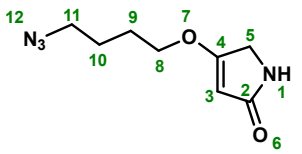


R_f (PE/EtOAc 40:60): 0.35 (UV and $KMnO_4$ stain). **R_f** (EtOAc): 0.66 (UV and $KMnO_4$ stain). **Mp** 31.8–33.8 °C. **^{1}H NMR** (600 MHz, $CDCl_3$, δ): 5.07 (s, 1H, 3-H), 4.18 (s, 2H, 5-H), 4.00 (t, *J* = 6.2 Hz, 2H, 15-H), 3.35 (t, *J* = 6.7 Hz, 2H, 18-H), 1.91 – 1.82 (m, 2H, 16-H), 1.77 – 1.68 (m, 2H, 17-H), 1.53 (s, 9H, 12-H, 13-H, 14-H). **^{13}C NMR** (151 MHz, $CDCl_3$, δ): 173.6 (C-4), 169.3 (C-2), 149.5 (C-8), 95.5 (C-3), 82.8 (C-11), 71.2 (C-15), 51.0 (C-18), 49.5 (C-5), 28.3 (C-12, C-13, C-14), 26.0 (C-16), 25.6 (C-17).

FT-IR (cm^{-1}, neat): 2977, 2935, 2874, 2094, 1774, 1734, 1706, 1622, 1451, 1394, 1368, 1322, 1296, 1256, 1240, 1159, 1091, 1071, 1036, 978, 914, 843, 806, 773, 733, 670. **HRMS** (ESI) *m/z*: $[M + H]^+$ calcd for $C_{13}H_{21}N_4O_4$, 297.1557; found, 297.1556.

4-(4-Azidobutoxy)-1,5-dihydro-2*H*-pyrrol-2-one (III-135)

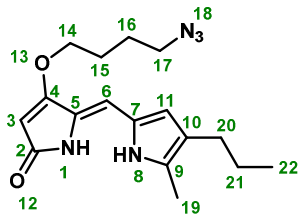
In a 250 mL Schlenk flask under N_2 atmosphere, the Boc-protected pyrrolidinone azide (**III-134**, 3.80 g, 12.8 mmol, 1.00 eq.) was dissolved in dry CH_2Cl_2 (64.1 mL, 5.0 mL/mmol pyrrolidinone) and cooled to 0 °C for 30 min. Trifluoroacetic acid (64.1 mL, equal volume as CH_2Cl_2) was added slowly and the reaction was warmed to 21 °C. After 90 min stirring at room temperature, the reaction was quenched by slowly adding saturated aqueous $NaHCO_3$ until pH 7 and then extracted with CH_2Cl_2 (3 x 100 mL). The combined organic layers were washed with water (50 mL) and brine (50 mL), dried over $MgSO_4$, and filtered. After evaporation of the solvent under reduced pressure, the nearly pure pyrrolinone was obtained as a weak yellow solid. Column chromatography on silica with CH_2Cl_2/MeOH (97:3) furnished the desired product as a yellow solid (**III-135**, 2.21 g, 11.3 mmol, 88%).



R_f (EtOAc): 0.11 (UV and $KMnO_4$ stain). **Mp** 80.0–82.7 °C. **^{1}H NMR** (600 MHz, $CDCl_3$, δ): 5.66 (brs, 1H, 1-H), 5.06 (s, 1H, 3-H), 3.99 (t, *J* = 6.2 Hz, 2H, 8-H), 3.93 (s, 2H, 5-H), 3.35 (t, *J* = 6.7 Hz, 2H, 11-H), 1.90 – 1.83 (m, 2H, 9-H), 1.77 – 1.71 (m, 2H, 10-H). **^{13}C NMR** (151 MHz, $CDCl_3$, δ): 175.5 (C-2), 175.0 (C-4), 94.6 (C-3), 70.9 (C-8), 51.1 (C-11), 46.9 (C-5), 26.0 (C-9), 25.6 (C-10). **FT-IR** (cm^{-1}, neat): 3185, 3070, 2954, 2883, 2857, 2092, 1657, 1614, 1454, 1402, 1345, 1300, 1286, 1228, 1204, 1191, 1090, 1038, 985, 943, 933, 918, 799, 717, 651, 633, 542, 507. **HRMS** (ESI) *m/z*: $[M + H]^+$ calcd for $C_8H_{13}N_4O_2$, 197.1033; found, 197.1035.

(*Z*)-4-(4-Azidobutoxy)-5-((5-methyl-4-propyl-1*H*-pyrrol-2-yl)methylene)-1,5-dihydro-2*H*-pyrrol-2-one (III-136)

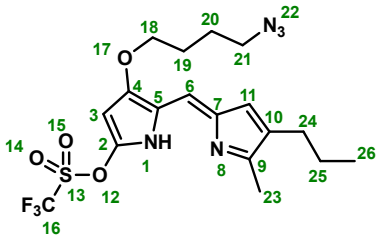
To a 100 mL Schlenk flask under N_2 atmosphere were added 5-methyl-4-propyl-1*H*-pyrrole-2-carbaldehyde (**III-94**, 900 mg, 5.95 mmol, 1.00 eq.) and 4-(4-azidobutoxy)-1,5-dihydro-2*H*-pyrrol-2-one (**III-135**, 2.10 g, 10.7 mmol, 1.80 eq.) and the solids were dissolved in degassed DMSO (20.8 mL, 3.5 mL/mmol carbaldehyde). Degassed 2 M NaOH (*aq*.) (16.7 mL, 2.8 mL/mmol carbaldehyde) was added and the reaction was stirred for 24 h at 60 °C. A yellow solid precipitated during the reaction. The product was then partitioned between EtOAc (75 mL) and water (50 mL), the phases were separated, and the aqueous phase was extracted with EtOAc (5 x 75 mL). Merged organic phases were washed with water (100 mL) and brine (150 mL), dried over Na_2SO_4, filtered, and the solvent was removed *in vacuo*. The canary yellow crude product was suspended in *n*-heptane and filtered. The filter cake was washed repeatedly with *n*-heptane, dropwise with *i*Pr_2O/acetone (1:1), and again with *n*-heptane to remove a brown impurity. After drying under high vacuum, the desired product (**III-136**, 1.22 g, 3.71 mmol, 62%) was obtained as a gold-yellow powder.



Mp 150.6–153.3 °C. **^{1}H NMR** (600 MHz, $CDCl_3$, δ): 10.63 (brs, 1H, 1-H), 10.15 (brs, 1H, 8-H), 6.27 (s, 1H, 6-H), 6.26 (d, *J* = 3.0 Hz, 1H, 11-H), 5.07 (d, *J* = 1.6 Hz, 1H, 3-H), 4.06 (t, *J* = 6.1 Hz, 2H, 14-H), 3.39 (t, *J* = 6.7 Hz, 2H, 17-H), 2.35 (t, *J* = 7.5 Hz, 2H, 20-H), 2.33 (s, 3H, 19-H), 1.96 – 1.89 (m, 2H, 15-H), 1.83 – 1.76 (m, 2H, 16-H), 1.55 (h, *J* = 7.4 Hz, 2H, 21-H), 0.93 (t, *J* = 7.3 Hz, 3H, 22-H). **^{13}C NMR** (151 MHz, $CDCl_3$, δ): 173.2 (C-2), 166.9 (C-4), 132.3 (C-9), 124.3 (C-7), 122.8 (C-5), 122.7 (C-10), 117.8 (C-11), 102.7 (C-6), 90.5 (C-3), 70.6 (C-14), 51.2 (C-17), 27.9 (C-20), 26.2 (C-15), 25.7 (C-16), 24.2 (C-21), 14.1 (C-22), 11.5 (C-19). **FT-IR** (cm^{-1}, neat): 3345, 3158, 3030, 2953, 2927, 2868, 2153, 2126, 2080, 1660, 1635, 1566, 1481, 1471, 1415, 1355, 1263, 1233, 1212, 1131, 1114, 1075, 1039, 1007, 1001, 974, 880, 814, 785, 718, 678, 653, 627, 579, 485. **HRMS** (ESI) *m/z*: $[M + H]^+$ calcd for $C_{17}H_{24}N_5O_2$, 330.1925; found, 330.1923.

(*Z*)-4-(4-Azidobutoxy)-5-((5-methyl-4-propyl-2*H*-pyrrol-2-ylidene)methyl)-1*H*-pyrrol-2-yl trifluoromethanesulfonate (III-137)

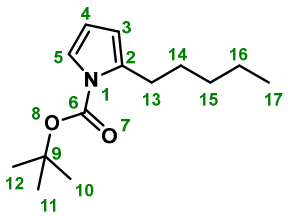
A 100 mL Schlenk flask under N_2 atmosphere was charged with dipyrrinone (**III-136**, 1.00 g, 3.04 mmol, 1.00 eq.) and the solid was dissolved in dry CH_2Cl_2 (60 mL, 19.5 mL/mmol). At 0 °C, trifluoromethanesulfonic anhydride (613 µL, 3.64 mmol, 1.20 eq., **freshly opened!**) was added dropwise to the solution of dipyrrinone **III-136** over 30 min. After additional stirring at this temperature for 1 h, the dark brown reaction mixture was poured into 2% $NaHCO_3$ (200 mL) and the aqueous phase was repeatedly extracted with MTBE (3 x 50 mL). The combined organic layers were washed with brine (200 mL), dried over Na_2SO_4, filtered, and the solvent was removed *in vacuo* to a minimal volume. Excess *n*-pentane was added repeatedly during evaporation to support precipitation. After complete evaporation of the solvent, the pure triflate **III-137** was obtained as a brown-yellow amorphous solid (1.37 g, 2.96 mmol, 98%) after extensive drying.



Mp 47.9–49.3 °C. **^{1}H NMR** (300 MHz, $CDCl_3$, δ): 10.70 (brs, 1H, 1-H), 6.98 (s, 1H, 6-H), 6.53 (s, 1H, 11-H), 5.38 (s, 1H, 3-H), 4.02 (t, *J* = 5.9 Hz, 2H, 18-H), 3.38 (t, *J* = 6.5 Hz, 2H, 21-H), 2.35 (t, *J* = 7.5 Hz, 2H, 24-H), 2.30 (s, 3H, 23-H), 1.96 – 1.84 (m, 2H, 19-H), 1.84 – 1.71 (m, 2H, 20-H), 1.55 (h, *J* = 7.4 Hz, 2H, 25-H), 0.93 (t, *J* = 7.3 Hz, 3H, 26-H). **^{13}C NMR** (76 MHz, $CDCl_3$, δ): 166.4 (C-4), 160.5 (C-2), 138.6 (C-9), 131.7 (C-5), 127.4 (C-7), 125.7 (C-10), 123.3 (C-11), 121.9 (C-6), 118.8 (q, *J* = 321.0 Hz, C-16), 87.2 (C-3), 71.1 (C-18), 51.2 (C-21), 27.8 (C-24), 26.3 (C-19), 25.7 (C-20), 23.8 (C-25), 13.9 (C-26), 12.3 (C-23). **^{19}F NMR** (282 MHz, $CDCl_3$, δ): –72.7 (s, –C*F*$_3$). **FT-IR** (cm^{-1}, neat): 3351, 3137, 2959, 2938, 2875, 2846, 2189, 2097, 1622, 1568, 1547, 1503, 1468, 1421, 1397, 1366, 1336, 1257, 1242, 1231,1207, 1150, 1139, 1125, 1078, 1010, 996, 974, 931, 916, 896, 823, 810, 765, 757, 738, 684, 654, 637, 623, 592, 576, 555, 520, 494. **HRMS** (ESI) *m/z*: $[M + H]^+$ calcd for $C_{18}H_{23}F_3N_5O_4S$, 462.1417; found, 462.1422.

1-*tert*-Butyloxycarbonyl 2-pentyl-1*H*-pyrrole (III-139f)

In a 250 mL Schlenk flask under N_2 atmosphere, 2-pentyl-1*H*-pyrrole (**III-106f**, 6.77 g, 49.4 mmol, 1.00 eq.) and DMAP (603 mg, 4.94 mmol, 0.10 eq.) were dissolved in dry CH_2Cl_2 (40 mL). A solution of Boc_2O (12.9 g, 59.2 mmol, 1.20 eq.) in dry CH_2Cl_2 (100 mL) was added to the prior solution at 25 °C, turning instantly yellow, and the reaction was stirred for 18 h at 25 °C. The solvent was removed under reduced pressure and the orange residue purified by column chromatography on silica using *n*-pentane/MTBE (99:1) as eluent. The Boc-protected pyrrole **III-139f** was afforded as a pale-yellow liquid (11.4 g, 48.1 mmol, 97%).



R$_f$ (PE/EtOAc 80:20): 0.88 ($KMnO_4$ stain). **^{1}H NMR** (600 MHz, $CDCl_3$, δ): 7.19 (dd, *J* = 3.4, 1.8 Hz, 1H, 5-H), 6.07 (t, *J* = 3.3 Hz, 1H, 4-H), 5.95 (ddt, *J* = 3.3, 1.9 Hz, 1H, 3-H), 2.85 – 2.80 (m, 2H, 13-H), 1.66 – 1.55 (m, 11H, 10-H, 11-H, 12-H, 14-H), 1.40 – 1.31 (m, 4H, 15-H, 16-H), 0.93 – 0.87 (m, 3H, 17-H). **^{13}C NMR** (151 MHz, $CDCl_3$, δ): 149.7 (C-6), 136.7 (C-2), 120.9 (C-5), 110.8 (C-3), 110.0 (C-4), 83.3 (C-9), 31.8 (C-15), 29.0 (C-13), 28.8 (C-14), 28.2 (C-10, C-11, C-12), 22.7 (C-16), 14.2 (C-17). **FT-IR** (cm^{-1}, neat): 2957, 2931, 2871, 2861, 1738, 1495, 1478, 1458, 1408, 1394, 1369, 1326, 1317, 1254, 1235, 1166, 1125, 1059, 1010, 963, 883, 851, 844, 800, 772, 715, 599, 560, 497, 461. **HRMS** (ESI) *m/z*: $[M + H]^+$ calcd for $C_{14}H_{24}NO_2$, 238.1802; found, 238.1801.

General Procedure for the Synthesis of Boc-Protected Pyrroles III-139b–e and III-139g

Acylation of 1*H*-pyrrole: The 2-acylation of 1*H*-pyrrole was performed according to the protocol of Ono *et al*.[393] In a Schlenk flask under N_2 atmosphere, the acid chlorides **III-138c–e** and **III-138g** (1.00 eq.) were dissolved in dry CH_2Cl_2 (3.74 mL/mmol acid chloride) and cooled to 0 °C. Anhydrous aluminium chloride (1.20 eq.) was added slowly to give a yellow suspension and the mixture was allowed to warm to 24 °C over 30 min. The solution was cooled to 0 °C again and a solution of 1*H*-pyrrole (1.10 eq.) in dry CH_2Cl_2 (0.42 mL/mmol acid chloride) was slowly transferred to the acid chloride solution. The reaction was stirred for a further 1 h at 0 °C, then slowly thawed to 21 °C, and stirred overnight. A saturated solution of NH_4Cl was used at 0 °C for reaction quenching. The phases were separated, the aqueous phase

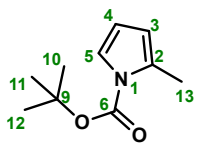
was subsequently extracted with CH_2Cl_2 (3 x 150 mL) and the combined organic phases were washed with saturated $NaHCO_3$ (2 x 150 mL) and brine (1 x 150 mL). Drying over $MgSO_4$, filtration over degreased cotton wool, and solvent removal *in vacuo* provided the crude acylation products **III-105c–e** and **III-150g** as brown oils, which were used without further purification and contained mostly 2-acylated 1*H*-pyrroles and minor impurities of 3-acylated 1*H*-pyrroles.

Reduction of acylated 1*H*-pyrrole: The reduction of 2-acylated 1*H*-pyrroles to 2-alkyl-1*H*-pyrroles was performed according to the protocol of Fürstner *et al*.[263] Under N_2 atmosphere, $NaBH_4$ (2.80 eq.) was suspended in dry *i*PrOH (0.90 mL/mmol acylated pyrrole) and cooled to 0 °C. The crude acylated pyrroles **III-105c–e** and **III-105g** (1.00 eq.) were dissolved in dry *i*PrOH (3.15 mL/mmol acylated pyrrole), precooled to 0 °C, and added to the $NaBH_4$ suspension at 0 °C. Afterwards, the solution was refluxed overnight at 99 °C. The reaction was quenched with water at 0 °C, additional water (300 mL) was added, and the product was extracted with MTBE (3 x 200 mL). Merged organic phases were washed with brine (2 x 200 mL), dried over $MgSO_4$, and filtered over degreased cotton wool. After solvent removal, the oily brown crude products, which contained mostly 2-alkylated 1*H*-pyrroles **III-106c–e** and **III-106g** and minor impurities of 3-alkylated 1*H*-pyrroles, were used without further purification.

Boc-protection of alkylated 1*H*-pyrrole: Boc-protection of 2-alkyl-1*H*-pyrroles was realised according to the protocol of Fürstner *et al*.[263] In a Schlenk flask under N_2 atmosphere, crude alkylated 1*H*-pyrroles **III-106c–e** and **III-106g** or commercially available 2-methyl-1*H*-pyrrole (**III-106b**) (1.00 eq.) and DMAP (0.10 eq.) were dissolved in dry CH_2Cl_2 (1.42 mL/mmol alkylated pyrrole). A solution of Boc_2O (1.20 eq.) in dry CH_2Cl_2 (2.37 mL/mmol alkylated pyrrole) was added to the prior solution at ambient temperature and the reaction was stirred overnight. The solvent was removed under reduced pressure and the residues were purified by chromatography on silica using *n*-pentane/MTBE (99:1). The analytically pure Boc-protected 2-alkylated 1*H*-pyrroles **III-139b–e** and **III-139g** were afforded as colourless to yellow liquids.

1-*tert*-Butyloxycarbonyl 2-methyl-1*H*-pyrrole (III-139b)

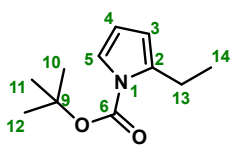
In a Schlenk flask under N_2 atmosphere, 2-methyl-1*H*-pyrrole (**III-106b**, 3.03 g, 37.4 mmol, 1.40 eq.) and DMAP (326 mg, 2.67 mmol, 0.10 eq.) were dissolved in dry CH_2Cl_2 (20 mL). A solution of Boc_2O (5.83 g, 26.7 mmol, 1.00 eq.) in CH_2Cl_2 (100 mL) was added to the pyrrole at 20 °C, turning instantly yellow, and the reaction was stirred for 18 h at 21 °C. The solvent was removed under reduced pressure and the orange residue purified by chromatography on silica using *n*-pentane/MTBE (98:2), yielding the Boc-protected 2-methylpyrrole (**III-139b**, 3.88 g, 21.39 mmol, 80%) of a colourless liquid.



^{1}H NMR (600 MHz, $CDCl_3$, δ): 7.18 (dd, *J* = 3.4 Hz, *J* = 1.8 Hz, 1H, 5-H), 6.06 (t, *J* = 3.3 Hz, 1H, 4-H), 5.92 (tt, *J* = 1.9 Hz, *J* = 1.0 Hz, 1H, 3-H), 2.43 (d, *J* = 1.1 Hz, 3H, 13-H), 1.59 (s, 9H, 10-H, 11-H, 12-H). **^{13}C NMR** (151 MHz, $CDCl_3$, δ): 149.9 (C-6), 131.7 (C-2), 120.7 (C-5), 111.9 (C-3), 110.0 (C-4), 83.4 (C-9), 28.2 (C-10, C-11, C-12), 15.6 (C-13). **FT-IR** (cm^{-1}, neat): 2979, 2928, 1737, 1497, 1396, 1370, 1329, 1308, 1254, 1237, 1170, 1127, 1065, 983, 883, 851, 798, 772, 715, 676, 597, 552. **HRMS** (ESI) *m/z*: $[M + H]^+$ calcd for $C_{10}H_{16}NO_2$, 182.1176; found, 182.1176. **CAS** 72590-65-9.

1-*tert*-Butyloxycarbonyl 2-ethyl-1*H*-pyrrole (III-139c)

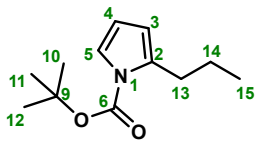
Following the general procedure for the synthesis of Boc-protected pyrroles, 1-*tert*-butyloxycarbonyl 2-ethyl-1*H*-pyrrole (**III-139c**) was synthesised from acetyl chloride (**III-138c**, 9.95 g, 127 mmol, 1.00 eq.) and obtained as a pale-yellow liquid (11.8 g, 60.3 mmol, 48% over three steps).



^{1}H NMR (600 MHz, $CDCl_3$, δ): 7.19 (dd, *J* = 3.4 Hz, 1H, 5-H), 6.08 (t, *J* = 3.3 Hz, 1H, 4-H), 5.96 (tt, *J* = 3.0 Hz, 1H, 3-H), 2.87 (qd, *J* = 7.4 Hz, 2H, 13-H), 1.59 (s, 9H, 10-H, 11-H, 12-H), 1.23 (t, *J* = 7.4 Hz, 3H, 14-H). **^{13}C NMR** (151 MHz, $CDCl_3$, δ): 149.7 (C-6), 138.2 (C-2), 120.9 (C-5), 110.04 (C-4), 110.01 (C-3), 83.4 (C-9), 28.2 (C-10, C-11, C-12), 22.4 (C-13), 13.4 (C-14). **FT-IR** (cm^{-1}, neat): 2973, 2934, 2877, 1739, 1497, 1479, 1458, 1409, 1395, 1369, 1326, 1293, 1256, 1233, 1167, 1132, 1124, 1066, 1058, 1047, 1015, 977, 953, 882, 853, 840, 814, 772, 719. **HRMS** (ESI) *m/z*: $[M + H]^+$ calcd for $C_{11}H_{18}NO_2$, 196.1332; found, 196.1331. **CAS** 437717-00-5.

1-*tert*-Butyloxycarbonyl 2-propyl-1*H*-pyrrole (III-139d)

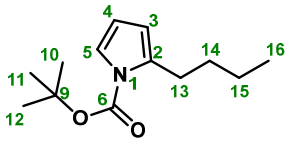
Following the general procedure for the synthesis of Boc-protected pyrroles, 1-*tert*-butyloxycarbonyl 2-propyl-1*H*-pyrrole (**III-139d**) was synthesised from propanoic acid chloride (**III-138d**, 10.7 g, 115 mmol, 1.00 eq.) and obtained as a colourless liquid (12.5 g, 59.8 mmol, 52% over three steps).



^{1}H NMR (600 MHz, $CDCl_3$, δ): 7.19 (dd, *J* = 3.4 Hz, *J* = 1.8 Hz, 1H, 5-H), 6.08 (t, *J* = 3.3 Hz, 1H, 4-H), 5.95 (ddt, *J* = 3.0 Hz, *J* = 2.0 Hz, 1H, 3-H), 2.87 – 2.75 (m, 2H, 13-H), 1.64 (h, *J* = 7.4 Hz, 2H, 14-H), 1.59 (s, 9H, 10-H, 11-H, 12-H), 0.98 (t, *J* = 7.4 Hz, 3H, 15-H). **^{13}C NMR** (151 MHz, $CDCl_3$, δ): 149.7 (C-6), 136.5 (C-2), 120.9 (C-5), 111.0 (C-3), 110.0 (C-4), 83.3 (C-9), 31.1 (C-13), 28.2 (C-10, C-11, C-12), 22.3 (C-14), 14.1 (C-15). **FT-IR** (cm^{-1}, neat): 3006, 2961, 2933, 2873, 1739, 1495, 1479, 1457, 1436, 1407, 1394, 1369, 1327, 1318, 1254, 1169, 1127, 1060, 1010, 972, 907, 895, 884, 849, 801, 772, 716, 599, 495. **HRMS** (ESI) *m/z*: $[M + H]^+$ calcd for $C_{12}H_{20}NO_2$, 210.1489; found, 210.1488.

1-*tert*-Butyloxycarbonyl 2-butyl-1*H*-pyrrole (III-139e)

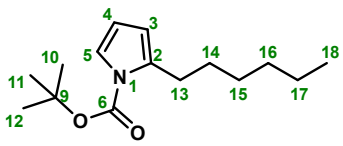
Following the general procedure for the synthesis of Boc-protected pyrroles, 1-*tert*-butyloxycarbonyl 2-butyl-1*H*-pyrrole (**III-139e**) was synthesised from butanoic acid chloride (**III-138e**, 10.3 g, 96.5 mmol, 1.00 eq.) and obtained as a pale-yellow oil (9.55 g, 42.8 mmol, 44% over three steps).



^{1}H NMR (600 MHz, $CDCl_3$, δ): 7.19 (dd, *J* = 3.4 Hz, *J* = 1.8 Hz, 1H, 5-H), 6.07 (t, *J* = 3.3 Hz, 1H, 4-H), 5.95 (td, *J* = 1.9 Hz, 1H, 3-H), 2.88 – 2.80 (m, 2H, 13-H), 1.63 – 1.56 (m, 2H, 14-H), 1.59 (s, 9H, 10-H, 11-H, 12-H), 1.40 (h, *J* = 7.4 Hz, 2H, 15-H), 0.94 (t, *J* = 7.4 Hz, 3H, 16-H). **^{13}C NMR** (151 MHz, $CDCl_3$, δ): 149.7 (C-6), 136.7 (C-2), 120.9 (C-5), 110.8 (C-3), 110.0 (C-4), 83.3 (C-9), 31.2 (C-14), 28.8 (C-13), 28.2 (C-10, C-11, C-12), 22.7 (C-15), 14.2 (C-16). **FT-IR** (cm^{-1}, neat): 2958, 2932, 2872, 2863, 1737, 1495, 1478, 1458, 1407, 1394, 1369, 1325, 1315, 1254, 1235, 1221, 1166, 1123, 1059, 1013, 999, 883, 852, 804, 772, 714, 599. **HRMS** (ESI) *m/z*: $[M + H]^+$ calcd for $C_{13}H_{22}NO_2$, 224.1645; found, 224.1641. **CAS** 1431620-53-9.

1-*tert*-Butyloxycarbonyl 2-hexyl-1*H*-pyrrole (III-139g)

Following the general procedure for the synthesis of Boc-protected pyrroles, 1-*tert*-butyloxycarbonyl 2-hexyl-1*H*-pyrrole (**III-139g**) was synthesised from hexanoic acid chloride (**III-138g**, 15.0 g, 111 mmol, 1.00 eq.) and obtained as a colourless oil (12.1 g, 48.2 mmol, 43% over three steps).

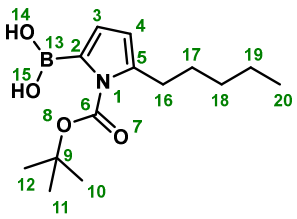


^{1}H NMR (600 MHz, $CDCl_3$, δ): 7.19 (dd, *J* = 3.4 Hz, *J* = 1.8 Hz, 1H, 5-H), 6.07 (t, *J* = 3.3 Hz, 1H, 4-H), 5.95 (td, *J* = 1.9 Hz, 1H, 3-H), 2.86 – 2.77 (m, 2H, 13-H), 1.59 (s, 9H, 10-H, 11-H, 12-H), 1.64 – 1.57 (m, 2H, 14-H), 1.42 – 1.34 (m, 2H, 15-H), 1.35 – 1.24 (m, 4H, 16-H, 17-H), 0.94 – 0.83 (m, 3H, 18-H). **^{13}C NMR** (151 MHz, $CDCl_3$, δ): 149.7 (C-6), 136.7 (C-2), 120.9 (C-5), 110.8 (C-3), 110.0 (C-4), 83.3 (C-9), 31.9 (C-16), 29.3 (C-14), 29.1 (C-15), 28.2 (C-10, C-11, C-12), 22.8 (C-17), 14.2 (C-18). **FT-IR** (cm^{-1}, neat): 2956, 2927, 2858, 1740, 1495, 1478, 1458, 1407, 1394, 1369, 1327, 1319, 1253, 1234, 1165, 1127, 1061, 1008, 887, 851, 803, 772, 715. **HRMS** (ESI) *m/z*: $[M + H]^+$ calcd for $C_{15}H_{26}NO_2$, 252.1958; found, 252.1959.

(1-(*tert*-Butoxycarbonyl)-5-pentyl-1*H*-pyrrol-2-yl)boronic acid (III-140f)

In a 250 mL Schlenk flask under N_2 atmosphere, TMP (10.7 mL, 63.2 mmol, 2.00 eq.) was dissolved in dry THF (74.6 mL, 2.36 mL/mmol pyrrole) and cooled to –78 °C. *n*-Butyl lithium (27.1 mL, 66.4 mmol, 2.10 eq., 2.45 M in *n*-hexane) was added dropwise to the TMP solution in THF at 0.9 mL/min (syringe pump). After completion of the addition and further stirring for 15 min at –78 °C, the mixture was allowed to warm to 0 °C over 30 min and was then cooled again to –78 °C. In a 500 mL three-necked flask under N_2 atmosphere, equipped with a cold thermometer and connection to the Schlenk line, was *tert*-butyl 2-pentyl-1*H*-pyrrole-1-carboxylate (**III-139f**, 7.50 g, 31.6 mmol, 1.00 eq.) dissolved in dry THF (126.4 mL, 4.00 mL/mmol pyrrole) and cooled to –78 °C. The LiTMP was then added dropwise

with a transfer cannula to the glass surface of the flask with the pyrrolic THF solution at the slowest possible speed by adding positive pressure of argon to the Schlenk flask. The internal temperature was constantly kept below –70 °C and the rate was adjusted if needed. The reaction mixture was stirred for 2 h at –78 °C, before a solution of $B(OMe)_3$ (10.6 mL, 94.8 mmol, 3.00 eq.) in dry THF (33.8 mL, 1.07 mL/mmol pyrrole) was added dropwise at 0.75 mL/min (syringe pump). The solution was stirred for 15 min at –78 °C, then 30 min at 0 °C, and finally stirred for 12 h at 23 °C. The reaction was quenched at 0 °C by the dropwise addition of 0.20 M HCl (332 mL, 66.4 mmol, 2.10 eq.). Phases were separated and the aqueous phase was extracted with Et_2O (3 x 150 mL). Merged organic phases were washed with water (2 x 250 mL) and brine (2 x 250 mL), dried over a minimal amount $MgSO_4$, filtered, and the solvent was removed *in vacuo*. As the product typically did not precipitate upon removal of the ethereal solvent, the residue was taken up in stabiliser-free *i*Pr_2O (the product is less soluble in *i*Pr_2O than Et_2O, but undergoes decomposition in even less polar hydrocarbon solvents, such as *n*-pentane or *n*-heptane) and washed again with 0.2 M HCl (2 x 150 mL). After drying over $MgSO_4$, filtration, and slow solvent removal, the boronic acid started to precipitate as a light-yellow solid. The suspension was cooled to –20 °C, the boronic acid recovered by filtration and washed with cold *i*Pr_2O. When the *i*Pr_2O wash fraction was treated with water and left to evaporate the ether, more boronic acid crystals formed at the surface as a brown solid. Trituration with cold toluene provided another fraction of pure product as a white solid. The isolated boronic acid **III-140f** was obtained as an amorphous white solid (5.84 g, 20.8 mmol, 66%) after drying. Storage for a longer period at –20 °C under an Ar atmosphere is feasible.



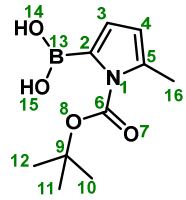
Mp 75.2–75.8 °C. **^{1}H NMR** (300 MHz, $CDCl_3$, δ): 7.35 (brs, 2H, 14-OH, 15-OH), 7.02 (d, *J* = 3.4 Hz, 1H, 3-H), 6.04 (d, *J* = 3.4 Hz, 1H, 4-H), 2.79 (t, *J* = 7.7 Hz, 2H, 16-H), 1.70 – 1.51 (m, 11H, 10-H, 11-H, 12-H, 17-H), 1.34 (dt, *J* = 7.3 Hz, 3.7, 4H, 18-H, 19-H), 0.96 – 0.85 (m_c, *J* = 6.7 Hz, 3H, 20-H). **^{13}C NMR** (76 MHz, $CDCl_3$, δ): 153.4 (C-6), 142.6 (C-5), 127.5 (C-3), 112.7 (C-4), 85.9 (C-9), 31.8 (C-18), 30.9 (C-16), 29.2 (C-17), 28.1 (C-10, C-11, C-12), 22.7 (C-19), 14.2 (C-20). **^{11}B NMR** (96 MHz, $CDCl_3$, δ): 25.5 [s, –*B*$(OH)_2$]. **FT-IR** (cm^{-1}, neat): 3364, 3190, 2960, 2936, 2928, 2873, 2861, 1697, 1572, 1494, 1467, 1428, 1399, 1378, 1362, 1347, 1337, 1266, 1256, 1239, 1198, 1198, 1166, 1111, 1060, 1048, 1018, 1002, 949, 863, 832, 795, 779, 761, 732, 710, 682, 657, 615, 583, 510, 466. **HRMS** (ESI) *m/z*: $[M + H]^+$ calcd for $C_{14}H_{25}BNO_4$, 282.1871; found, 282.1874.

General Procedure for the Synthesis of Pyrrole-2-boronic Acids III-140b–e and III-140g

Boc-protected pyrrole-2-boronic acids were accessed following the procedure of Cai and Snider.[399] In a Schlenk flask under N_2 atmosphere, *n*-butyl lithium (2.10 eq., 2.5 M in hexane) is added dropwise to a solution of distilled 2,2,6,6-tetramethylpiperidine (2.00 eq.) in dry THF (2.36 mL/mmol pyrrole) at –78 °C. After stirring for 15 min, the mixture is allowed to warm to 0 °C over 30 min and then cooled again to –78 °C. In a three-necked flask, Boc-2-alkyl-1*H*-pyrrole **III-139b–e** and **III-139g** (1.00 eq.) is dissolved in dry THF (4.00 mL/mmol pyrrole) and cooled to –78 °C. The LiTMP is then transferred dropwise to the pyrrolic solution in THF with a transfer cannula. The internal temperature is constantly kept below –70 °C and the rate is adjusted if needed. The reaction mixture is stirred for 2 h at –78 °C, before $B(OMe)_3$ (3.00 eq.) in THF (1.07 mL/mmol pyrrole) is added slowly. The solution is stirred for 15 min at –78 °C, then 30 min at 0 °C, and finally at 21 °C overnight. The reaction is quenched at 0 °C by dropwise addition of 0.20 M HCl (*aq*.) (2.10 eq.). The aqueous phase is extracted with Et_2O (3 x 50 mL). Merged organic phases are washed with water (100 mL), brine (100 mL), and dried over $MgSO_4$. The solvent is almost completely removed by evaporation at room temperature (water bath at 20 °C). The residue in Et_2O/THF is transferred to a Schlenk flask and residual solvent is removed *in vacuo* while stirring to prevent bumping and the crude product is recovered as a viscous orange solid or oil. The delicate crude product is used without further purification for the next synthetic step on the same day.

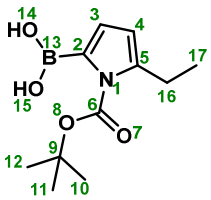
NMR data of crude boronic acids III-140b–e and III-140g:

(1-(*tert*-Butoxycarbonyl)-5-methyl-1*H*-pyrrol-2-yl)boronic acid (III-140b)



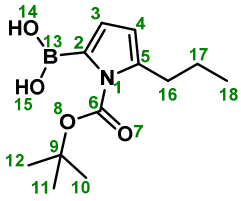
^{1}H NMR (300 MHz, $CDCl_3$, δ): 7.09 (brs, 2H, 14-OH, 15-OH), 7.00 (d, *J* = 3.3 Hz, 1H, 3-H), 6.01 (dd, *J* = 3.2 Hz, 1H, 4-H), 2.42 (s, 3H, 16-H), 1.62 (s, 9H, 10-H, 11-H, 12-H). **^{13}C NMR** (76 MHz, $CDCl_3$, δ): 153.4 (C-6), 137.8 (C-5), 127.6 (C-3), 113.8 (C-4), 85.9 (C-9), 28.2 (C-10, C-11, C-12), 17.8 (C-16). **^{11}B NMR** (96 MHz, $CDCl_3$, δ): 26.5 [s, –*B*$(OH)_2$]. **CAS** 282528-59-0.

(1-(*tert*-Butoxycarbonyl)-5-ethyl-1*H*-pyrrol-2-yl)boronic acid (III-140c)



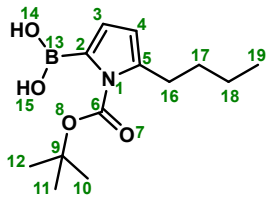
^{1}H NMR (300 MHz, $CDCl_3$, δ): 7.01 (d, *J* = 3.4 Hz, 1H, 3-H), 6.66 (brs, 2H, 14-OH, 15-OH), 6.06 (dt, *J* = 3.4 Hz, 1H, 4-H), 2.83 (q, *J* = 7.5 Hz, 2H, 16-H), 1.63 (s, 9H, 10-H, 11-H, 12-H), 1.27 – 1.19 (m, 3H, 17-H). **^{13}C NMR** (76 MHz, $CDCl_3$, δ): 153.4 (C-6), 144.1 (C-5), 127.5 (C-3), 111.8 (C-4), 85.9 (C-9), 28.1 (C-10, C-11, C-12), 24.1 (C-16), 13.9 (C-17). **^{11}B NMR** (96 MHz, $CDCl_3$, δ): 25.8 [s, –*B*$(OH)_2$]. **CAS** 1808944-76-4.

(1-(*tert*-Butoxycarbonyl)-5-propyl-1*H*-pyrrol-2-yl)boronic acid (III-140d)



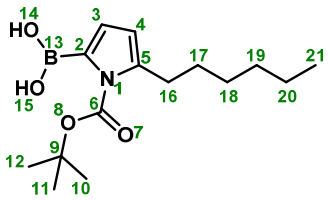
^{1}H NMR (300 MHz, $CDCl_3$, δ): 7.00 (d, *J* = 3.3 Hz, 1H, 3-H), 6.04 (d, *J* = 3.3 Hz, 1H, 4-H), 2.77 (t, *J* = 7.8 Hz, 2H, 16-H), 1.67 – 1.58 (m, 11H, H-10, H-11, H-12, H-17), 0.97 (t, *J* = 7.5 Hz, 3H, 18-H). **^{13}C NMR** (76 MHz, $CDCl_3$, δ): 153.3 (C-6), 142.2 (C-5), 127.2 (C-3), 112.8 (C-4), 85.8 (C-9), 32.8 (C-16), 28.0 (C-10, C-11, C-12), 22.7 (C-17), 13.9 (C-18). **^{11}B NMR** (96 MHz, $CDCl_3$, δ): 25.0 [s, –*B*$(OH)_2$].

(1-(*tert*-Butoxycarbonyl)-5-butyl-1*H*-pyrrol-2-yl)boronic acid (III-140e)



^{1}H NMR (300 MHz, $CDCl_3$, δ): 7.00 (d, *J* = 3.3 Hz, 1H, 3-H), 6.71 (brs, 2H, 14-OH, 15-OH), 6.04 (d, *J* = 3.3 Hz, 1H, 4-H), 2.80 (t, *J* = 7.6 Hz, 1H, 16-H), 1.63 (s, 9H, 10-H, 11-H, 12-H), 1.62 – 1.52 (m, 2H, 17-H), 1.47 – 1.33 (m, 2H, 18-H), 0.94 (t, *J* = 7.3 Hz, 3H, 19-H). **^{13}C NMR** (76 MHz, $CDCl_3$, δ): 153.4 (C-6), 142.6 (C-5), 127.4 (C-3), 112.6 (C-4), 85.9 (C-9), 31.6 (C-17), 30.6 (C-16), 28.1 (C-10, C-11, C-12), 22.7 (C-18), 14.1 (C-19). **^{11}B NMR** (96 MHz, $CDCl_3$, δ): 25.5 [s, –*B*$(OH)_2$].

(1-(*tert*-Butoxycarbonyl)-5-hexyl-1*H*-pyrrol-2-yl)boronic acid (III-140g)

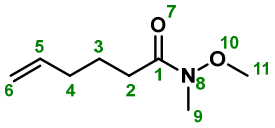


^{1}H NMR (300 MHz, $CDCl_3$, δ): 7.00 (d, *J* = 3.3 Hz, 1H, 3-H), 6.04 (d, *J* = 3.4 Hz, 1H, 4-H), 2.79 (t, *J* = 7.6 Hz, 2H, 16-H), 1.63 (s, 9H, 10-H, 11-H, 12-H), 1.62 – 1.53 (m, 2H, 17-H), 1.43 – 1.22 (m, 6H, 18-H, 19-H, 20-H), 0.94 – 0.83 (m_c, 3H, 21-H). **^{13}C NMR** (76 MHz, $CDCl_3$, δ): 153.4 (C-6), 142.6 (C-5), 127.4 (C-3), 112.6 (C-4), 85.8 (C-9), 31.9 (C-19), 30.9 (C-16), 29.5 (C-17), 29.3 (C-18), 28.1 (C-10, C-11, C-12), 22.7 (C-20), 14.2 (C-21). **^{11}B NMR** (96 MHz, $CDCl_3$, δ): 25.5 [s, –*B*$(OH)_2$].

***N*-Methoxy-*N*-methylhex-5-enamide (III-142)**

A 1 L Schlenk flask under N_2 atmosphere was charged with 5-hexenoic acid (**III-141**, 9.96 g, 87.3 mmol, 1.00 eq.) and the acid was dissolved in dry CH_2Cl_2 (300 mL). *N*,*O*-Dimethylhydroxylamine hydrochloride (10.2 g, 105 mmol, 1.20 eq.), *N*-(3-dimethylaminopropyl)-*N*-ethylcarbodiimide hydrochloride (20.1 g, 105 mmol, 1.20 eq.), and DMAP (16.0 g, 131 mmol, 1.50 eq.) were added sequentially. The reaction was stirred at 21 °C for 23 h, quenched with saturated NH_4Cl, and the phases were separated. The aqueous phase was extracted with CH_2Cl_2 (3 x 150 mL) and the merged organic phases were dried over $MgSO_4$. The solution was filtered and the desired product (**III-142**, 13.6 g, 86.3 mmol,

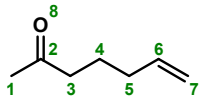
99%) was obtained as a volatile colourless liquid after solvent evaporation. The product was used without further purification.



R_f (PE/EtOAc 40:60): 0.54 ($KMnO_4$ stain). **^{1}H NMR** (600 MHz, $CDCl_3$, δ): 5.78 (dtd, *J* = 16.7, 9.6 Hz, 1H, 5-H), 5.02 (dt, *J* = 17.1, 1.8 Hz, 1H, 6a-H), 4.96 (d, *J* = 10.0 Hz, 1H, 6b-H), 3.66 (s, 3H, 11-H), 3.16 (s, 3H, 9-H), 2.42 (t, *J* = 7.7 Hz, 2H, 2-H), 2.10 (q, *J* = 7.3 Hz, 2H, 4-H), 1.73 (p, *J* = 7.8, 7.3 Hz, 2H, 3-H). **^{13}C NMR** (151 MHz, $CDCl_3$, δ): 174.6 (C-1), 138.3 (C-5), 115.2 (C-6), 61.3 (C-11), 33.4 (C-4), 32.3 (C-9), 31.2 (C-2), 23.8 (C-3). **FT-IR** (cm^{-1}, neat): 3077, 2995, 2973, 2938, 2911, 2870, 2821, 1663, 1460, 1441, 1415, 1384, 1349, 1318, 1177, 1151, 1117, 1092, 996, 912, 859, 799, 782, 762, 745, 733, 722, 635, 610, 564, 496. **HRMS** (ESI) *m/z*: $[M + H]^+$ calcd for $C_8H_{16}NO_2$, 158.1176; found, 158.1176. **CAS** 122334-35-4.

Hept-6-en-2-one (III-143)

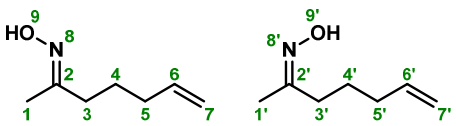
Under N_2 atmosphere, the Weinreb amide (**III-142**, 23.1 g, 147 mmol, 1.00 eq.) was dissolved in dry THF (500 mL) and cooled to 0 °C. Methylmagnesium chloride (98.1 mL, 294 mmol, 2.00 eq., 3.0 M in THF) was added dropwise over 30 min and the reaction was stirred for a further 3 h at 0 °C. At 0 °C, saturated NH_4Cl was carefully added for quenching and the reaction was further stirred for 15 min. The phases were separated and the aqueous phase was diluted with water until the solid had nearly dissolved. Then the aqueous phase was extracted with *n*-pentane (3 x 150 mL). Merged organic phases were dried over $MgSO_4$, filtered, and the solvent was carefully removed *in vacuo* to yield the product (**III-143**, 15.2 g, 136 mmol, 92%) as a volatile light-yellow liquid. The product was used without further purification.



R_f (PE/EtOAc 80:20): 0.57 ($KMnO_4$ stain). **^{1}H NMR** (600 MHz, $CDCl_3$, δ): 5.76 (ddt, *J* = 17.0, 10.2, 6.7 Hz, 1H, 6-H), 5.01 (dq, *J* = 17.0, 1.7 Hz, 1H, 7a-H), 4.97 (ddt, *J* = 10.2, 2.5, 1.2 Hz, 1H, 7b-H), 2.43 (t, *J* = 7.4 Hz, 2H, 3-H), 2.13 (s, 3H), 2.05 (qd, *J* = 7.0, 1.4 Hz, 2H, 5-H), 1.67 (p, *J* = 7.4 Hz, 2H, 4-H). **^{13}C NMR** (151 MHz, $CDCl_3$, δ): 208.9 (C-2), 138.1 (C-6), 115.4 (C-7), 43.0 (C-3), 33.2 (C-5), 30.1 (C-1), 23.0 (C-4). **FT-IR** (cm^{-1}, neat): 3078, 2998, 2976, 2935, 2867, 1715, 1641, 1439, 1414, 1361, 1305, 1224, 1164, 1112, 1067, 1048, 1037, 995, 913, 734, 640, 585, 556, 532. **HRMS** (ESI) *m/z*: $[M + H]^+$ calcd for $C_7H_{13}O$, 113.0961; found, 113.0959. **CAS** 21889-88-3.

(*E*/*Z*)-Hept-6-en-2-one oxime (III-144)

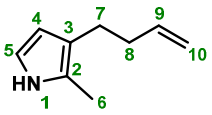
A 500 mL round-bottom flask was charged with sodium acetate (17.6 g, 214 mmol, 2.00 eq.) and hydroxylamine hydrochloride (11.2 g, 161 mmol, 1.50 eq.) and the reactants were dissolved in 357 mL EtOH/water (4:1, 3.33 mL/mmol ketone). 6-Hepten-2-one (**III-143**, 12.0 g, 107 mmol, 1.00 eq.) was added to the suspension and the reaction mixture was heated to reflux for 4 h. The reaction was cooled to ambient temperature and excess EtOH was removed under reduced pressure. Water (100 mL) was added to the crude mixture and the aqueous phase was subsequently extracted with EtOAc (3 x 100 mL). Combined organic phases were then washed with saturated $NaHCO_3$ (2 x 100 mL) and water (2 x 100 mL), dried over $MgSO_4$, filtered, and concentrated *in vacuo*. The oxime product (**III-144**, 12.8 g, 100 mmol, 94%) was obtained as a yellow liquid with a fruity smell and used without further purification.



(*E*/*Z*)-Ratio: 72:28 (NMR). <u>*E*-Isomer</u>: **^{1}H NMR** (600 MHz, $CDCl_3$, δ): 8.62 (brs, 1H, 9-OH), 5.81 (tdt, *J* = 17.2, 10.4, 6.7 Hz, 1H, 6-H), 5.02 (dq, *J* = 17.1, 1.7 Hz, 1H, 7a-H), 4.97 (ddd, *J* = 10.2, 1.2 Hz, 1H, 7b-H), 2.20 (t, *J* = 7.6 Hz, 2H, 3-H), 2.07 (q, *J* = 7.2 Hz, 2H, 5-H), 1.88 (s, 3H, 1-H), 1.610 (p, *J* = 7.6 Hz, 2H, 4-H). **^{13}C NMR** (151 MHz, $CDCl_3$, δ): 158.6 (C-2), 138.2 (C-6), 115.2 (C-7), 35.4 (C-3), 33.3 (C-5), 25.6 (C-4), 13.5 (C-1). <u>*Z*-Isomer</u>: **^{1}H NMR** (600 MHz, $CDCl_3$, δ): 8.51 (brs, 1H, 9'-OH), 5.81 (tdt, *J* = 17.2, 10.4, 6.7 Hz, 1H, 6'-H), 5.04 (dq, *J* = 17.1, 1.8 Hz, 1H, 7'a-H), 5.00 – 4.95 (m, *J* = 10.2, 1.2 Hz, 1H, 7'b-H), 2.40 – 2.35 (m, *J* = 8.1 Hz, 2H, 3'-H), 2.10 (q, *J* = 7.7 Hz, 2H, 5'-H), 1.87 (s, 3H, 1'-H), 1.608 (q, *J* = 7.7 Hz, 2H, 4'-H). **^{13}C NMR** (151 MHz, $CDCl_3$, δ): 159.0 (C-2'), 138.3 (C-6'), 115.1 (C-7'), 33.8 (C-5'), 28.2 (C-3'), 24.9 (C-4'), 20.0 (C-1'). **FT-IR** (cm^{-1}, neat): 3226, 3119, 3078, 2977, 2927, 2862, 1664, 1641, 1456, 1440, 1417, 1368, 1303, 1278, 1256, 1233, 1207, 1188, 1166, 1113, 1024, 996, 954, 912, 815, 760, 741, 632, 577, 557, 535, 523. **HRMS** (ESI) *m/z*: $[M + H]^+$ calcd for $C_7H_{14}NO$, 128.1070; found, 128.1071. **CAS** 57606-77-6.

3-(But-3-en-1-yl)-2-methyl-1*H*-pyrrole (III-145)

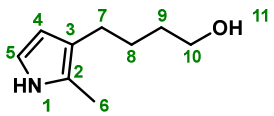
(*E*/*Z*)-Hept-6-en-2-one oxime (**III-144**, 14.3 g, 112 mmol, 1.00 eq.), pestled KOH (31.5 g, 562 mmol, 5.00 eq.), and water (1.54 mL, 13.7 µL/mmol oxime) were sequentially added to a 500 mL three-necked flask under N_2 atmosphere. Degassed and dried DMSO (216 mL, 1.92 mL/mmol oxime) was added. The reaction was heated at 100 °C and a solution of 1,2-dichloroethane (31.1 mL, 394 mmol, 3.50 eq.) in degassed DMSO (23.6 mL, 0.21 mL/mmol oxime) was added with a syringe pump over 2 h. A second batch of KOH (31.5 g, 562 mmol, 5.00 eq.) was added under ice cooling after the first hour of 1,2-dichloroethane addition (dichloroethane-feeding is paused during KOH addition) before the dichloroethane addition was continued for a further 1 h. Once the addition of dichloroethane was completed, the reaction was heated at 100 °C for 2 h. The reaction was cooled to 0 °C and ice water (400 mL) was added for quenching until potassium salts were completely dissolved. Extraction was performed with Et_2O (3 x 200 mL). Combined organic phases were dried over $MgSO_4$, filtered over degreased cotton wool, and the solvent was removed *in vacuo*. Kugelrohr distillation at 120–140 °C at 3 x 10^{-2} mbar provided the impure product as an orange liquid. Further chromatographic purification on silica with *n*-pentane/Et_2O (95:5) + 1% TEA provided the monopyrrole (**III-145**, 9.00 g, 66.6 mmol, 59%) as a yellow-orange liquid.



R_f (*n*-pentane/Et_2O 95:5): 0.24 ($KMnO_4$ stain). **R_f** (PE/EtOAc 80:20): 0.58 ($KMnO_4$ stain). **^{1}H NMR** (600 MHz, $CDCl_3$, δ): 7.73 (brs, 1H, 1-H), 6.61 (t, *J* = 2.7 Hz, 1H, 5-H), 6.05 (t, *J* = 2.7 Hz, 1H, 4-H), 5.92 (ddt, *J* = 17.1, 10.1, 6.5 Hz, 1H, 9-H), 5.07 (dq, *J* = 17.2, 1.7 Hz, 1H, 10a-H), 5.02 – 4.92 (dq, *J* = 10.1, 1.3 Hz, 1H, 10b-H), 2.51 (dt, *J* = 8.6, 7.4 Hz, 2H, 7-H), 2.31 (m, *J* = 7.2 Hz, 2H, 8-H), 2.20 (s, 3H, 6-H). **^{13}C NMR** (151 MHz, $CDCl_3$, δ): 139.2 (C-9), 123.5 (C-2), 119.0 (C-3), 115.1 (C-5), 114.4 (C-10), 108.9 (C-4), 35.5 (C-8), 25.7 (C-7), 11.2 (C-6). **FT-IR** (cm^{-1}, neat): 3378, 3075, 2975, 2917, 2851, 1639, 1585, 1464, 1439, 1415, 1378, 1338, 1274, 1247, 1201, 1192, 1107, 1090, 1064, 995, 955, 909, 834, 786, 714, 669, 651, 601, 554, 547, 538, 531, 522, 510. **HRMS** (ESI) *m/z*: $[M + H]^+$ calcd for $C_9H_{14}N$, 136.1121; found, 136.1122.

4-(2-Methyl-1*H*-pyrrol-3-yl)butan-1-ol (III-146)

From the hydroboration-oxidation route: To a 500 mL three-necked flask under N_2 atmosphere was added alkene pyrrole (**III-145**, 2.93 g, 21.7 mmol, 1.00 eq.). The pyrrole was dissolved in dry and degassed THF (179 mL, 8.24 mL/mmol pyrrole, 0.25 M pyrrole) and stirred for 15 min at 0 °C. A solution of 9-BBN (69.3 mL, 34.7 mmol, 1.60 eq., 0.5 M in THF) was added over 15 min with a syringe pump while keeping the reaction at 0 °C (pale yellow). Stirring was continued at 0 °C for 1 h, followed by reflux at 75 °C for 3 h (pale orange). At 0 °C, 36.2 mL 3 M NaOH (*aq*.) (turning yellow) and then 34.4 mL 30% H_2O_2 (first pinkish, then yellow, then turbid colourless) were added dropwise. After 1 h at 0 °C (boric acid precipitated as a white solid), the reaction was allowed to warm to 20 °C and stirred for a further 17 h. The reaction was diluted with ice water and repeatedly extracted with CH_2Cl_2 (3 x 75 mL). Merged organic phases (pale-yellow) were dried over $MgSO_4$, filtered, and the solvent was removed *in vacuo*. The orange crude product was chromatographed on silica with PE/EtOAc (70:30) + 1% TEA to yield the desired product (**III-146**, 2.89 g, 18.9 mmol, 87%) as a pale-yellow viscous oil.

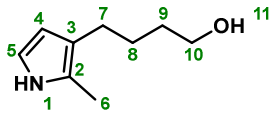


R_f (PE/EtOAc 20:80): 0.62 ($KMnO_4$ stain). **^{1}H NMR** (600 MHz, $CDCl_3$, δ): 7.83 (brs, 1H, 1-H), 6.59 (t, *J* = 2.7 Hz, 1H, 5-H), 6.02 (t, *J* = 2.8 Hz, 1H, 4-H), 3.66 (t, *J* = 6.1 Hz, 2H, 10-H), 2.43 (t, *J* = 6.9 Hz, 2H, 7-H), 2.19 (s, 3H, 6-H), 1.67 – 1.56 (m, *J* = 6.9 Hz, 4H, 8-H, 9-H). **^{13}C NMR** (151 MHz, $CDCl_3$, δ): 123.4 (C-2), 119.2 (C-3), 115.1 (C-5), 108.8 (C-4), 63.1 (C-10), 32.7 (C-9), 27.4 (C-8), 25.7 (C-7), 11.1 (C-6). **FT-IR** (cm^{-1}, neat): 3367, 3094, 2929, 2857, 2736, 1668, 1585, 1544, 1445, 1378, 1276, 1261, 1246, 1206, 1176, 1136, 1102, 1058, 1028, 979, 957, 932, 900, 835, 715, 667, 596, 562. **HRMS** (ESI) *m/z*: $[M + H]^+$ calcd for $C_9H_{16}NO$, 154.1226; found, 154.1228.

4-(2-Methyl-1*H*-pyrrol-3-yl)butan-1-ol (III-146)

From the acylation route: Highly optimised procedure: To a 250 mL three-necked flask under N_2 atmosphere, equipped with reflux condenser and thermometer, were added NaOH (2.73 g, 68.2 mmol, 3.20 eq.) and acylated pyrrole carboxylate (**III-152**, 4.80 g, 21.3 mmol, 1.00 eq.). The solids were then suspended in anhydrous ethylene glycol (53.3 mL, 2.5 mL/mmol pyrrole) and the mixture was degassed by two consecutive freeze-pump-thaw cycles. The

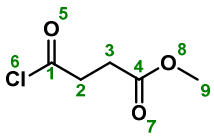
reaction mixture was stirred at 60 °C until all solids had completely dissolved. The flask was then lowered into a pre-heated heating vessel at 130 °C and stirred for 15 min from the point where the internal temperature had reached 120 °C to convert the starting material to the corresponding acid under mild conditions (solution gets orange, no decarboxylation or polymerisation). Then, the reaction was lowered immediately into a pre-heated vessel at 210 °C for decarboxylation and maintained at 180 °C for exactly 12 min (**!**) from the point where the internal temperature had reached 180 °C (heating to 180 °C required approx. 2 min, turning brown). The solution was immediately cooled with an ice bath and diluted with water (400 mL). The aqueous phase was extracted with EtOAc (3 x 150 mL), the merged organic phases were washed with brine (2 x 300 mL), dried over $MgSO_4$, filtered, and the solvent was removed *in vacuo* to provide a viscous brown oil. Column chromatography on silica with CH_2Cl_2/EtOAc (80:20) yielded the desired pyrrole **III-146** as a viscous yellow-orange oil (2.52 g, 16.4 mmol, 77%).



R_f (CH_2Cl_2/EtOAc 60:40): 0.48 (UV and $KMnO_4$ stain). **^{1}H NMR** (600 MHz, $CDCl_3$, δ): 7.80 (brs, 1H, 1-H), 6.60 (t, *J* = 2.7 Hz, 1H, 5-H), 6.02 (t, *J* = 2.8 Hz, 1H, 4-H), 3.66 (t, *J* = 6.1 Hz, 2H, 10-H), 2.44 (t, *J* = 7.0 Hz, 2H, 7-H), 2.19 (s, 3H, 6-H), 1.62 (dq, *J* = 7.1, 3.3 Hz, 4H, 8-H, 9-H). **^{13}C NMR** (151 MHz, $CDCl_3$, δ): 123.4 (C-2), 119.3 (C-3), 115.1 (C-5), 108.8 (C-4), 63.1 (C-10), 32.7 (C-9), 27.4 (C-8), 25.7 (C-7), 11.1 (C-6). **FT-IR** (cm^{-1}, neat): 3365, 3094, 2929, 2857, 1722, 1586, 1444, 1379, 1338, 1275, 1256, 1246, 1208, 1173, 1137, 1102, 1058, 1032, 980, 959, 932, 901, 834, 715, 672, 665, 600, 563, 510, 504. **HRMS** (ESI) *m/z*: $[M + Na]^+$ calcd for $C_9H_{15}NNaO$, 176.1046; found, 176.1044.

Methyl 4-chloro-4-oxobutanoate (III-148)

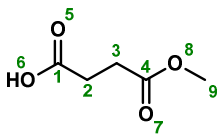
To a 100 mL round-bottom flask under N_2 atmosphere were added fine powdered 4-methoxy-4-oxobutanoic acid (**III-150**, 12.0 g, 90.8 mmol, 1.00 eq.) and thionyl chloride (45.4 mL, 627 mmol, 6.90 eq., 0.50 mL/mmol acid) before the clear solution was heated to 40 °C for 4 h and then to 75 °C for 30 min. Afterwards, excess thionyl chloride was removed under reduced pressure and traces forced out by stepwise co-evaporation with CH_2Cl_2 (4 x 5 mL) to yield the title compound **III-148** as a volatile light-yellow liquid (13.0 g, 86.6 mmol, 95%), which was used without further purification.



R_f (CH_2Cl_2/MeOH 95:5): 0.70 ($KMnO_4$ stain). **^{1}H NMR** (600 MHz, $CDCl_3$, δ): 3.71 (s, 3H, 9-H), 3.22 (t, *J* = 6.5 Hz, 2H, 2-H), 2.68 (t, *J* = 6.6 Hz, 2H, 3-H). **^{13}C NMR** (151 MHz, $CDCl_3$, δ): 173.2 (C-1), 171.5 (C-4), 52.3 (C-9), 41.9 (C-2), 29.2 (C-3). **FT-IR** (cm^{-1}, neat): 3004, 2956, 2851, 1789, 1735, 1439, 1410, 1397, 1369, 1346, 1305, 1264, 1236, 1207, 1175, 1062, 1050, 1025, 986, 962, 917, 886, 839, 789, 761, 712, 658, 583, 488. **CAS** 1490-25-1.

4-Methoxy-4-oxobutanoic acid (III-150)

To a 250 mL three-necked flask under N_2 atmosphere, succinic anhydride (**III-149**, 20.0 g, 200 mmol, 1.00 eq.) and dry MeOH (70 mL) were added. The suspension was subsequently heated and refluxed for 2 h at 70 °C. After cooling to ambient temperature, the solvent was removed under reduced pressure to yield a colourless liquid with a sweet odour. The title compound **III-150** solidified as a white crystalline (26.3 g, 199 mmol, >99%) solid at room temperature in quantitative yield and was used without further purification after drying under high vacuum.

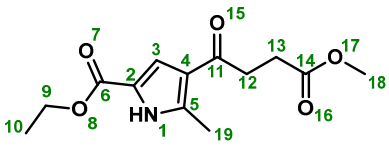


R_f (CH_2Cl_2/MeOH 96:4): 0.35 (concentration dependent, $KMnO_4$ stain). **Mp** 54.8–58.1 °C. **^{1}H NMR** (600 MHz, $CDCl_3$, δ): 11.49 (brs, 1H, 6-OH), 3.70 (s, 3H, 9-H), 2.69 (t, *J* = 6.8 Hz, 2H, 2-H), 2.63 (t, *J* = 6.8 Hz, 2H, 3-H). **^{13}C NMR** (151 MHz, $CDCl_3$, δ): 178.3 (C-1), 172.7 (C-4), 52.1 (C-9), 29.1 (C-2), 28.8 (C-3). **FT-IR** (cm^{-1}, neat): 3010, 2980, 2956, 2933, 2756, 2668, 2620, 2591, 2570, 1728, 1688, 1437, 1416, 1365, 1344, 1299, 1253, 1232, 1198, 1171, 1068, 1003, 971, 943, 852, 843, 688, 669, 641, 580, 554, 533. **HRMS** (ESI) *m/z*: $[M + H]^+$ calcd for $C_5H_9O_4$, 133.0495; found, 133.0496. **CAS** 3878-55-5.

Ethyl 4-(4-methoxy-4-oxobutanoyl)-5-methyl-1*H*-pyrrole-2-carboxylate (III-151)

A 500 mL Schlenk flask under N_2 atmosphere was charged with anhydrous $AlCl_3$ (17.4 g, 131 mmol, 2.00 eq.). The salt was suspended in dry CH_2Cl_2 (120 mL, 1.86 mL/mmol pyrrole) and subsequently cooled to 0 °C. Methyl 4-chloro-4-

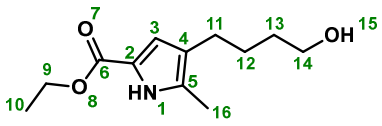
oxobutanoate (**III-148**, 12.5 g, 82.9 mmol, 1.27 eq.) was added at 0 °C and the suspension was stirred for 30 min at 21 °C, after which time the salt had mostly dissolved (the solution had turned brown-yellow). Then, a solution of ethyl 5-methyl-1*H*-pyrrole-2-carboxylate (**III-147**, 10.0 g, 65.3 mmol, 1.00 eq.) in dry CH_2Cl_2 (60 mL, 0.93 mL/mmol pyrrole) was added and the reaction mixture was stirred at 21 °C for 15 h. The reaction was quenched at 0 °C with ice water (150 mL), the phases were separated, and the aqueous phase was extracted with CH_2Cl_2 (3 × 75 mL). The combined organic layers were washed with brine (2 x 150 mL), dried over $MgSO_4$, filtered, and the solvent was removed in *vacuo* to provide the crude product as a pink-purple solid. Chromatography on silica with CH_2Cl_2/EtOAc gradient (100:0 to 80:20) gave the product (**III-151**, 14.6 g, 54.5 mmol, 84%) as a light-yellow solid.



R_f (PE/EtOAc 70:30): 0.39 (UV). **Mp** 127.2–130.7 °C. **^{1}H NMR** (600 MHz, CD_2Cl_2, δ): 9.90 (brs, 1H, 1-H), 7.26 (d, *J* = 2.5 Hz, 1H, 3-H), 4.32 (q, *J* = 7.1 Hz, 2H, 9-H), 3.66 (s, 3H, 18-H), 3.10 (t, *J* = 6.7 Hz, 2H, 12-H), 2.65 (t, *J* = 6.7 Hz, 2H, 13-H), 2.55 (s, 3H, 19-H), 1.36 (t, *J* = 7.1 Hz, 3H, 10-H). **^{13}C NMR** (151 MHz, CD_2Cl_2, δ): 194.7 (C-11), 173.9 (C-14), 161.4 (C-6), 139.8 (C-5), 122.0 (C-4), 121.0 (C-2), 116.6 (C-3), 61.2 (C-9), 51.9 (C-18), 35.1 (C-12), 28.2 (C-13), 14.5 (C-10), 14.1 (C-19). **FT-IR** (cm^{-1}, neat): 3301, 2994, 2961, 2940, 2912, 1710, 1661, 1569, 1500, 1445, 1411, 1375, 1362, 1341, 1306, 1267, 1225, 1190, 1178, 1125, 1090, 1035, 999, 987, 956, 908, 876, 847, 798, 766, 703, 671, 655, 615, 577, 502. **HRMS** (ESI) *m/z*: $[M + H]^+$ calcd for $C_{13}H_{18}NO_5$, 268.1179; found, 268.1180.

Ethyl 4-(4-hydroxybutyl)-5-methyl-1*H*-pyrrole-2-carboxylate (III-152)

In a 250 mL Schlenk flask under N_2 atmosphere, acylated pyrrole carboxylate (**III-151**, 8.00 g, 29.9 mmol, 1.00 eq.) was dissolved in dry THF (49.4 mL, 1.65 mL/mmol carboxylate) to give a clear pale-yellow solution. $NaBH_4$ (2.50 g, 62.9 mmol, 2.10 eq.) was added at room temperature under gas development and a pale-yellow suspension remained in the reaction flask. Subsequently, boron trifluoride etherate (10.3 mL, 83.81 mmol, 2.80 eq.) was added with a syringe pump over 20 min at 0.517 mL/min, followed by 3 h stirring at 21 °C (a white solid precipitates). The reaction was carefully quenched at 0 °C by the addition of glacial acetic acid (4.5 mL) and water (55 mL) until the solution became clear yellow. The wet THF phase was extracted with CH_2Cl_2 (5 x 100 mL). Merged organic phases were washed with saturated $NaHCO_3$ (2 x 100 mL) and brine (2 x 200 mL) [the aqueous phase remains turbid while the organic phase is turbid yellow], dried over $MgSO_4$, filtered, and the solvent was removed *in vacuo*. The sticky yellow residue was almost pure product and crystallised upon thorough removal of THF at high vacuum to give an amorphous salmon pink solid (**III-152**, 5.40 g, 24.0 mmol, 80%). If the product did not crystallise or the melting point did not match, boric acid impurities were likely to be present.

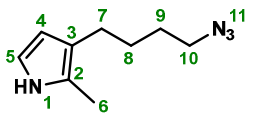


R_f (PE/EtOAc 50:50): 0.34 (UV). **Mp** 79.3–81.9 °C. **^{1}H NMR** (600 MHz, $CDCl_3$, δ): 9.39 (brs, 1H, 1-H), 6.69 (d, *J* = 2.7 Hz, 1H, 3-H), 4.27 (q, *J* = 7.2 Hz, 2H, 9-H), 3.65 (t, *J* = 5.4 Hz, 2H, 14-H), 2.39 (t, *J* = 6.7 Hz, 2H, 11-H), 2.20 (s, 3H, 16-H), 1.64 – 1.54 (m, 4H, 12-H, 13-H), 1.33 (t, *J* = 7.1 Hz, 3H, 10-H). **^{13}C NMR** (151 MHz, $CDCl_3$, δ): 161.6 (C-6), 130.8 (C-5), 122.3 (C-4), 119.8 (C-2), 115.8 (C-3), 62.9 (C-14), 60.1 (C-9), 32.4 (C-13), 27.0 (C-12), 25.5 (C-11), 14.6 (C-10), 11.4 (C-16). **FT-IR** (cm^{-1}, neat): 3302, 3270, 2988, 2937, 2932, 2864, 1656, 1581, 1504, 1499, 1485, 1460, 1417, 1375, 1340, 1323, 1264, 1221, 1203, 1127, 1059, 1023, 982, 940, 924, 910, 883, 838, 821, 776, 769, 685, 670, 645, 618, 608, 562, 551, 508, 480, 457. **HRMS** (ESI) *m/z*: $[M + H]^+$ calcd for $C_{12}H_{20}NO_3$, 226.1438; found, 226.1436.

3-(4-Azidobutyl)-2-methyl-1*H*-pyrrole (III-155)

Tosylation: In a 100 mL round-bottom flask under N_2 atmosphere, the hydroxy pyrrole (**III-146**, 1.38 g, 8.99 mmol, 1.00 eq.) and DMAP (1.65 g, 13.5 mmol, 1.50 eq.) were dissolved in dry CH_2Cl_2 (25.7 mL, 350 mM pyrrole) and stirred for 10 min at 20 °C. At 0 °C, a solution of *p*TsCl (25.2 mL, 2.40 g, 12.6 mmol, 1.40 eq., 500 mM in dry CH_2Cl_2) was added dropwise over 25 min and stirring was continued at 0 °C for 4 h before the reaction was slowly warmed to 20 °C overnight. After stirring for 18 h, the yellow reaction solution was quenched at 0 °C by slowly adding ice water (30 mL) and stirring for 15 min. More ice water (170 mL) was added, phases were separated, and the turbid aqueous phase

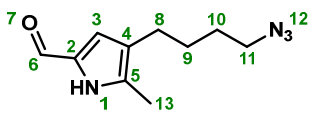
was subsequently extracted with CH_2Cl_2 (3 x 25 mL). Azide substitution: After drying over Na_2SO_4, filtration, and partial solvent evaporation (**not evaporated to dryness! Otherwise, the product will degrade and polymerise**), the yellow residue of tosylate **III-154** was transferred to a 50 mL round-bottom flask and was dissolved in dry DMF (12 mL). The excess CH_2Cl_2 was further removed under reduced pressure (>30 mbar) and sodium azide (2.05 g, 31.5 mmol, 3.50 eq.) was added under argon atmosphere to the clear orange solution of tosylate **III-154**. After adding five catalytic drops of dry DIPEA, the reaction was stirred overnight for 21 h at 20 °C (green-brown with precipitate) and quenched at 0 °C by adding ice water (25 mL). After further dilution with ice water (100 mL), the residue was extracted with Et_2O (3 x 50 mL). Merged organic phases were washed with ice water (2 x 100 mL, getting yellow) and dried over $MgSO_4$. After filtration, the crude product was obtained as an orange oil after solvent evaporation and chromatographed on silica with PE/CH_2Cl_2 (95:5) + 0.5% TEA to yield the azide **III-155** as a yellow-orange oil (1.14 g, 6.37 mmol, 71% over two steps).



R_f (PE/CH_2Cl_2 20:80): 0.67 (UV and anisaldehyde stain). **R_f** (PE/EtOAc 60:40): 0.82 (UV and anisaldehyde stain). **^{1}H NMR** (600 MHz, $CDCl_3$, δ): 7.75 (brs, 1H, 1-H), 6.61 (t, *J* = 2.7 Hz, 1H, 5-H), 6.02 (t, *J* = 2.8 Hz, 1H, 4-H), 3.29 (t, *J* = 6.6 Hz, 2H, 10-H), 2.45 (t, *J* = 7.1 Hz, 2H, 7-H), 2.20 (s, 3H, 6-H), 1.73–1.54 (m, 4H, 8-H, 9-H). **^{13}C NMR** (151 MHz, $CDCl_3$, δ): 123.5 (C-2), 118.8 (C-3), 115.2 (C-5), 108.8 (C-4), 51.6 (C-10), 28.7 (C-8), 28.4 (C-9), 25.5 (C-7), 11.1 (C-6). **FT-IR** (cm^{-1}, neat): 3452, 3376, 2930, 2857, 2091, 1731, 1667, 1585, 1542, 1462, 1453, 1445, 1408, 1370, 1352, 1298, 1266, 1249, 1178, 1138, 1101, 1065, 1008, 955, 917, 901, 857, 835, 714, 674, 664, 641, 557, 491, 484, 477. **HRMS** (ESI) *m/z*: $[M + H]^+$ calcd for $C_9H_{15}N_4$, 179.1291; found, 179.1290.

4-(4-Azidobutyl)-5-methyl-1*H*-pyrrole-2-carbaldehyde (III-156)

To a 25 mL two-necked flask under N_2 atmosphere was added dry DMF (523 µL, 6.79 mmol, 1.20 eq.) and the solvent was cooled to 0 °C. Phosphoryl chloride (633 µL, 6.79 mmol, 1.20 eq.) was added dropwise at 0 °C to precipitate the Vilsmeier reagent as a white solid. At 0 °C, the Vilsmeier reagent was diluted with degassed dry 1,2-dichloroethane (1.70 mL, 0.3 mL/mmol pyrrole) and stirred at 0 °C for 30 min. The azide pyrrole (**III-155**, 1.00 g, 5.66 mmol, 1.00 eq.) in 1,2-dichloroethane (3.40 mL, 0.6 mL/mmol pyrrole) was added dropwise at 0 °C over 10 min, followed by stirring for 2 h at 0 °C and 2 h at 100 °C under reflux. A solution of NaOAc (2.79 g, 34.0 mmol, 6.00 eq.) in water (8.50 mL, 4 mol/L) was added and refluxing was continued for 30 min. After cooling to ambient temperature, the deep brown mixture was diluted with water (50 mL) and extracted with CH_2Cl_2 (3 x 30 mL). Merged organic phases were washed with brine (100 mL), dried over $MgSO_4$, filtered, and the solvent was removed *in vacuo*. Purification of the crude product on silica with CH_2Cl_2/EtOAc (85:15) provided the product **III-156** as orange oil that crystallised at ambient temperature to give a yellow to orange solid (1.09 g, 5.28 mmol, 93%).

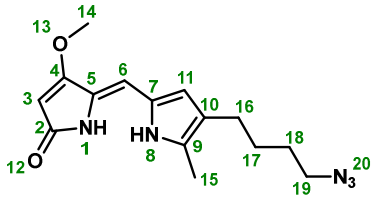


R_f (CH_2Cl_2/EtOAc 75:25): 0.50 (UV and $KMnO_4$ stain). **Mp** 62.1–64.5 °C. **^{1}H NMR** (600 MHz, $CDCl_3$, δ): 10.55 (s, 1H, 1-H), 9.28 (s, 1H, 6-H), 6.77 (d, *J* = 2.8 Hz, 1H, 3-H), 3.29 (t, *J* = 5.8 Hz, 2H, 11-H), 2.43 (t, *J* = 6.5 Hz, 2H, 8-H), 2.30 (s, 3H, 13-H), 1.67 – 1.59 (m, 4H, 9-H, 10-H). **^{13}C NMR** (151 MHz, $CDCl_3$, δ): 177.7 (C-6), 136.6 (C-5), 130.6 (C-2), 123.7 (C-4), 122.7 (C-3), 51.4 (C-11), 28.6 (C-9), 27.7 (C-10), 25.2 (C-8), 11.6 (C-13). **FT-IR** (cm^{-1}, neat): 3167, 3127, 3100, 3066, 3018, 2987, 2944, 2925, 2856, 2174, 2087, 1614, 1567, 1516, 1467, 1441, 1419, 1379, 1345, 1308, 1279, 1254, 1231, 1172, 1144, 1132, 1081, 1053, 1003, 984, 919, 901, 847, 816, 795, 781, 735, 678, 652, 636, 627, 559, 523, 456. **HRMS** (ESI) *m/z*: $[M + Na]^+$ calcd for $C_{10}H_{14}N_4NaO$, 229.1060; found, 229.1058.

(*Z*)-5-((4-(4-Azidobutyl)-5-methyl-1*H*-pyrrol-2-yl)methylene)-4-methoxy-1,5-dihydro-2*H*-pyrrol-2-one (III-157)

To a 100 mL Schlenk flask under N_2 atmosphere were added 4-(azidobutyl)-5-methyl-1*H*-pyrrole-2-carbaldehyde (**III-156**, 1.20 g, 5.83 mmol, 1.00 eq.) and 4-methoxy-3-pyrrolin-2-one (**III-74**, 1.32 g, 11.7 mmol, 2.00 eq.) and the solids were dissolved in degassed DMSO (20.4 mL, 3.5 mL/mmol carbaldehyde). Degassed 2 M NaOH (*aq.*) (16.3 mL, 2.8 mL/mmol carbaldehyde) was added and the reaction was stirred at 60 °C for 24 h. A yellow solid precipitated during the reaction. The product was partitioned between EtOAc (100 mL) and water (50 mL), the phases were separated, and

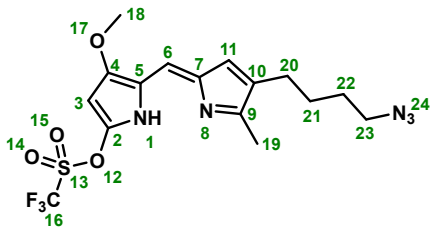
the aqueous phase was extracted with EtOAc (5 x 75 mL). Merged organic phases were washed with water (100 mL) and brine (150 mL), dried over Na_2SO_4, filtered, and the solvent was removed *in vacuo*. The canary yellow crude product was suspended in *n*-heptane and filtered. The filter cake was then washed repeatedly with *n*-heptane, dropwise with *i*Pr_2O/acetone (1:1), and again with *n*-heptane to remove a brown impurity. After drying under high vacuum, the desired product (**III-157**, 1.55 g, 5.15 mmol, 88%) was obtained as a gold-yellow powder.



Mp 126.8–130.6 °C. **^{1}H NMR** (300 MHz, $CDCl_3$, δ): 10.77 (brs, 1H, 1-H), 10.26 (brs, 1H, 8-H), 6.27 (s, 1H, 6-H), 6.23 (d, *J* = 2.6 Hz, 1H, 11-H), 5.10 (d, *J* = 1.5 Hz, 1H, 3-H), 3.89 (s, 3H, 14-H), 3.28 (t, *J* = 6.3 Hz, 2H, 19-H), 2.42 (t, *J* = 6.7 Hz, 2H, 16-H), 2.34 (s, 3H, 15-H), 1.72 – 1.52 (m, *J* = 6.6, 3.3 Hz, 4H, 17-H, 18-H). **^{13}C NMR** (76 MHz, $CDCl_3$, δ): 173.2 (C-2), 168.1 (C-4), 132.2 (C-9), 124.5 (C-7), 122.8 (C-5), 121.7 (C-10), 117.6 (C-11), 102.7 (C-6), 90.2 (C-3), 58.3 (C-14), 51.6 (C-19), 28.6 (C-18), 28.1 (C-17), 25.2 (C-16), 11.5 (C-15). **FT-IR** (cm^{-1}, neat): 3338, 3167, 3145, 3027, 2937, 2910, 2855, 2083, 1667, 1634, 1569, 1481, 1466, 1437, 1386, 1346, 1311, 1276, 1261, 1221, 1174, 1148, 1119, 1063, 1042, 1006, 973, 870, 824, 808, 790, 780, 737, 716, 673, 641, 631, 556, 546, 510, 493, 473, 457. **HRMS** (ESI) *m/z*: $[M + H]^+$ calcd for $C_{15}H_{20}N_5O_2$, 302.1612; found, 302.1614.

(*Z*)-5-((4-(4-Azidobutyl)-5-methyl-2*H*-pyrrol-2-ylidene)methyl)-4-methoxy-1*H*-pyrrol-2-yl trifluoromethanesulfonate (III-158)

In a 250 mL Schlenk flask under N_2 atmosphere, trifluoromethanesulfonic anhydride (402 µL, 2.39 mmol, 1.20 eq., **freshly opened!**) was added dropwise to a solution of dipyrrinone (**III-157**, 600 mg, 1.99 mmol, 1.00 eq.) in CH_2Cl_2 (39 mL, 19.5 mL/mmol dipyrrinone) at 0 °C. After stirring at this temperature for 1 h, the dark brown reaction mixture was poured into 2% $NaHCO_3$ (*aq*., 200 mL), the phases were separated and the aqueous phase was repeatedly extracted with MTBE (3 x 50 mL, solids from the reaction flask were solubilised with a minimal amount of EtOAc). The combined organic layers were washed with brine (200 mL), dried over Na_2SO_4, filtered, and the solvent evaporated *in vacuo*. Before complete removal of the solvent, *n*-pentane was repeatedly added to assist in the evaporation of MTBE and EtOAc. Thorough solvent removal provided the pure triflate (**III-158**, 805 mg, 1.86 mmol, 93%) without the need for purification as a deep brown-yellow oil.

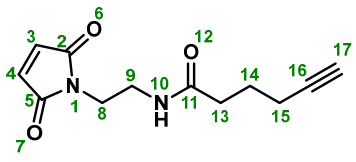


^{1}H NMR (300 MHz, $CDCl_3$, δ): 10.69 (brs, 1H, 1-H), 6.96 (s, 1H, 6-H), 6.50 (s, 1H, 11-H), 5.40 (s, 1H, 3-H), 3.85 (s, 3H, 17-H), 3.33 – 3.24 (m_c, *J* = 6.2 Hz, 2H, 22-H), 2.46 – 2.36 (m_c, *J* = 6.8 Hz, 2H, 19-H), 2.29 (s, 3H, 18-H), 1.74 – 1.48 (m, 4H, 20-H, 21-H). **^{13}C NMR** (76 MHz, $CDCl_3$, δ): 167.8 (C-4), 160.8 (C-2), 137.9 (C-9), 132.0 (C-5), 127.5 (C-7), 124.6 (C-10), 122.7 (C-11), 121.8 (C-6), 118.8 (q, *J* = 321.2 Hz, C-15), 87.0 (C-3), 58.8 (C-17), 51.4 (C-22), 28.5 (C-20), 27.7 (C-21), 25.2 (C-19), 12.2 (C-18). **^{19}F NMR** (282 MHz, $CDCl_3$, δ): –72.7 (s, –C*F*$_3$). **FT-IR** (cm^{-1}, neat): 3335, 2937, 2861, 2094, 1623, 1552, 1478, 1418, 1371, 1333, 1265, 1234, 1210, 1174, 1130, 1086, 1011, 973, 886, 830, 793, 767, 747, 709, 653, 625, 604, 573, 520, 487. **HRMS** (ESI) *m/z*: $[M + H]^+$ calcd for $C_{16}H_{19}F_3N_5O_4S$, 434.1104; found, 434.1102.

Bifunctional Alkyne-Maleimide Linker

N-(2-(2,5-Dioxo-2,5-dihydro-1*H*-pyrrol-1-yl)ethyl)hex-5-ynamide (III-159)

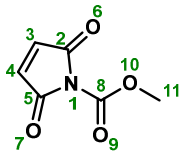
To a 500 mL Schlenk flask under N_2 atmosphere were added PyBOP (7.47 g, 14.4 mmol, 1.40 eq., **freshly opened!),** anhydrous DIPEA (3.85 mL, 22.6 mmol, 2.20 eq.), and the maleimide trifluoroacetate (**III-165**, 3.00 g, 11.79 mmol, 1.15 eq.). The reactants were stirred in dry CH_2Cl_2 (103 mL, 10 mL/mol acid) until nearly dissolved. 5-Hexynoic acid (1.15 g, 10.3 mmol, 1.00 eq.) was added and the bright yellow mixture was stirred for 18 h at 20 °C, after which the solution had become ivory coloured. All volatile materials were evaporated under reduced pressure and the residue was dissolved in EtOAc (150 mL). The organic solution was washed with saturated $NaHCO_3$ (3 x 50 mL), dried over $MgSO_4$, filtered, and the solvent was removed *in vacuo*. The orange oil was applied to chromatography on silica with CH_2Cl_2/MeOH (97:3) to yield the alkyne-maleimide-linker (**III-159**, 2.10 g, 8.97 mmol, 87%) as a white solid.



R_f (PE/EtOAc 20:80): 0.38 ($KMnO_4$ stain). **R_f** (CH_2Cl_2/MeOH 90:10): 0.59 ($KMnO_4$ stain). **Mp** 83.2–86.8 °C. **^{1}H NMR** (300 MHz, $CDCl_3$, δ): 6.66 (s, 2H, 3-H, 4-H), 5.78 (s, 1H, 10-H), 3.69 – 3.55 (m, 2H, 8-H), 3.46 – 3.32 (m, 2H, 9-H), 2.26 – 2.17 (t, *J* = 7.3 Hz, 2H, 13-H), 2.22 – 2.08 (dt, *J* = 6.7, 2.7 Hz, 2H, 15-H), 1.90 (t, *J* = 2.6 Hz, 1H, 17-H), 1.75 (p, *J* = 7.1 Hz, 2H, 14-H). **^{13}C NMR** (76 MHz, $CDCl_3$, δ): 172.7 (C-11), 171.0 (C-2, C-5), 134.4 (C-3, C-4), 83.6 (C-16), 69.3 (C-17), 39.0 (C-9), 37.7 (C-8), 35.0 (C-13), 24.1 (C-14), 17.9 (C-15). **FT-IR** (cm^{-1}, neat): 3461, 3308, 3263, 3175, 3100, 2968, 2948, 2927, 2913, 2887, 1767, 1743, 1696, 1650, 1600, 1588, 1549, 1459, 1447, 1417, 1387, 1329, 1315, 1269, 1219, 1171, 1108, 1044, 1026, 980, 952, 908, 829, 785, 765, 722, 696, 678, 641, 625, 579, 571, 475. **HRMS** (ESI) *m/z*: $[M + H]^+$ calcd for $C_{12}H_{15}N_2O_3$, 235.1077; found, 235.1081. **CAS** 2785323-77-3.

Methyl 2,5-dioxo-2,5-dihydro-1*H*-pyrrole-1-carboxylate (III-161)

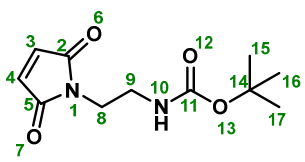
A 500 mL Schlenk flask with stirring bar under N_2 atmosphere was charged with maleimide (**III-160**, 3.00 g, 30.9 mmol, 1.00 eq.) and the solid was dissolved in dry EtOAc (150 mL). Anhydrous *N*-methyl morpholine (3.45 mL, 30.9 mmol, 1.00 eq.) was added. The resulting clear solution was cooled to 0 °C and stirred for 20 min. Methyl chloroformate (3.58 mL, 46.4 mmol, 1.50 eq.) was added dropwise at 0 °C and the faint pink reaction was stirred for 30 min at 0 °C, followed by 2 h at 20 °C. Solids were collected by filtration over a Büchner funnel and washed with EtOAc (100 mL). The filtrate was washed with water (100 mL) and brine (100 mL), dried over $MgSO_4$, filtered, and the solvent was removed under reduced pressure. The resulting faint pink crude product was chromatographed on silica using PE/EtOAc (70:30) to provide the product **III-161** as a white solid (3.57 g, 23.0 mmol, 74%) after solvent evaporation.



R_f (PE/EtOAc 50:50): 0.38 ($KMnO_4$ stain). **Mp** 64.5–66.9 °C. **^{1}H NMR** (600 MHz, $CDCl_3$, δ): 6.85 (d, *J* = 0.8 Hz, 2H, 3-H, 4-H), 3.98 (s, 3H, 11-H). **^{13}C NMR** (151 MHz, $CDCl_3$, δ): 165.7 (C-2, C-5), 148.2 (C-8), 135.4 (C-3, C-4), 54.4 (C-11). **FT-IR** (cm^{-1}, neat): 3190, 3111, 3102, 3091, 2971, 2905, 1801, 1756, 1709, 1596, 1453, 1439, 1391, 1332, 1280, 1256, 1187, 1137, 1103, 1059, 1034, 921, 840, 815, 769, 760, 693, 640, 592, 488. **HRMS** (ESI) *m/z*: $[M + H]^+$ calcd for $C_6H_6NO_4$, 156.0291; found, 156.0293. **CAS** 55750-48-6.

tert-Butyl (2-(2,5-dioxo-2,5-dihydro-1*H*-pyrrol-1-yl)ethyl)carbamate (III-164)

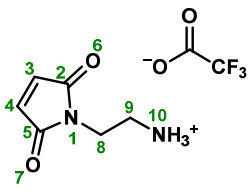
A 500 mL round-bottom flask was charged with *tert*-butyl 2-aminoethylcarbamate (**III-161**, 3.41 g, 21.3 mmol, 1.10 eq.) and the oil was dissolved in saturated $NaHCO_3$ (*aq.*) (96.7 mL, 5 mL/mmol maleimide) by stirring for 15 min at 23 °C, followed by stirring at 0 °C for 15 min. Finely ground methyl carbamate (**III-161**, 3.00 g, 19.3 mmol, 1.00 eq.) was then added to the clear solution at 0 °C. Stirring at 0 °C was continued for 3 h (white solid precipitates), followed by 30 min at 20 °C. Water (150 mL) was added and the aqueous phase was extracted with EtOAc (3 x 150 mL). Merged organic phases were dried over $MgSO_4$, filtered, and the solvent was removed *in vacuo* to yield a weak pink solid. For chromatography, the solid was dissolved in a minimal amount of EtOAc and then diluted with an equal volume of PE. Chromatography on silica with PE/EtOAc (75:25) provided the product (**III-164**, 3.52 g, 14.7 mmol, 76%) as a hygroscopic, fluffy white solid after removal of residual moisture by vacuum desiccation over anhydrous $CaCl_2$ for 10 days.



R_f (PE/EtOAc 50:50): 0.42 (UV and $KMnO_4$ stain). **Mp** 127.2–128.9 °C. **^{1}H NMR** (600 MHz, $CDCl_3$, δ): 6.71 (s, 2H, 3-H, 4-H), 4.73 (s, 1H, 10-H), 3.66 (t, *J* = 5.6 Hz, 2H, 8-H), 3.33 (q, *J* = 5.8 Hz, 2H, 9-H), 1.40 (s, 9H, 15-H, 16-H, 17-H). **^{13}C NMR** (151 MHz, $CDCl_3$, δ): 170.9 (C-2, C-5), 156.1 (C-11), 134.3 (C-3, C-4), 79.7 (C-14), 39.6 (C-9), 38.2 (C-8), 28.5 (C-15, C-16, C-17). **FT-IR** (cm^{-1}, neat): 3348, 3087, 2979, 2938, 1701, 1678, 1515, 1434, 1404, 1367, 1361, 1323, 1288, 1252, 1167, 1144, 1103, 1060, 1039, 1014, 943, 877, 844, 784, 761, 739, 691, 642, 612, 574, 536, 492, 464. **HRMS** (ESI) *m/z*: $[M + H]^+$ calcd for $C_{11}H_{17}N_2O_4$, 241.1183; found, 241.1185. **CAS** 134272-63-2.

2-(2,5-Dioxo-2,5-dihydro-1*H*-pyrrol-1-yl)ethan-1-aminium 2,2,2-trifluoroacetate (III-165)

The Boc-protected maleimide (**III-164**, 3.00 g, 12.5 mmol, 1.00 eq.) was dissolved under N_2 atmosphere in CH_2Cl_2 (31.2 mL, 0.4 M) and cooled to 0 °C. TFA (6.73 mL, 87.4 mmol, 7.00 eq.) was added slowly to the maleimide and the solution was stirred overnight for 20 h at 20 °C. The solvent was removed and the pale-yellow oil taken up in approximately 7 mL CH_2Cl_2 and diluted with Et_2O to precipitate a solid. If clumped, brief sonication was used to give a fine suspension of solids. The suspension was cooled at –20 °C for 3 h before the solid was filtered off, washed with Et_2O, *n*-pentane, and dried under high vacuum to provide the ammonium salt (**III-165**, 3.11 g, 12.2 mmol, 98%) as a white hygroscopic solid.

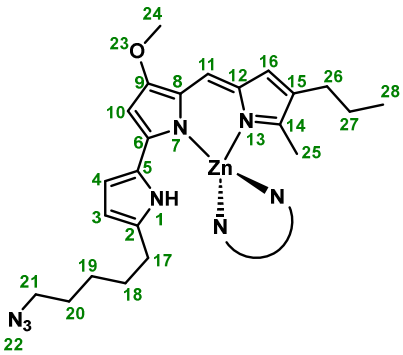


Mp 125.9–127.7 °C. **^{1}H NMR** (600 MHz, D_2O, δ): 6.88 (s, 2H, 3-H, 4-H), 3.82 (t, *J* = 5.8 Hz, 2H, 8-H), 3.21 (t, *J* = 5.8 Hz, 2H, 9-H). **^{13}C NMR** (151 MHz, D_2O, δ): 172.8 (C-2, C-5), 134.8 (C-3, C-4), 38.5 (C-9), 35.1 (C-8). **FT-IR** (cm^{-1}, neat): 3036, 2926, 2843, 2744, 2653, 2551, 2477, 2436, 1711, 1671, 1626, 1584, 1536, 1465, 1440, 1426, 1413, 1395, 1370, 1331, 1202, 1176, 1156, 1120, 1061, 1041, 1022, 948, 901, 850, 829, 799, 719, 698, 640, 609, 599, 520, 500. **HRMS** (ESI) *m/z*: $[M - CF_3CO_2]^+$ calcd for $C_6H_9N_2O_2$, 141.0659; found, 141.0660. **CAS** 146474-00-2.

Homo-Dimeric Zinc Complexes of Prodigiosin Azides

Prodigiosin A-Ring Azide Zinc Complex (III-166)

Under N_2 atmosphere, prodigiosin A-ring azide (**III-89·HCl**, 333 mg, 751 µmol, 1.00 eq.) and zinc(II) acetate dihydrate (990 mg, 4.51 mmol, 6.00 eq.) were dissolved in MeOH (75 mL). $CHCl_3$ (75 mL) and DIPEA (1.83 mL, 10.5 mmol, 14.0 eq.) were added sequentially and the reaction was stirred at 21 °C for 18 h. The solvent was evaporated and the crude product was dissolved in CH_2Cl_2. Purification over basic aluminium oxide with CH_2Cl_2 eluted the desired product. Starting material remained on the column and was eluted with EtOH. Evaporation of the solvent provided a red solid, which was repeatedly precipitated with *n*-pentane. The EtOH fraction was concentrated *in vacuo* and treated again with DIPEA and $Zn(OAc)_2$ dihydrate in $CHCl_3$/MeOH to allow further product isolation. The process was repeated four times in total. The desired prodigiosin A-ring azide zinc complex (**III-166**, 241 mg, 275 µmol, 73%) was obtained as an amorphous red solid after repetitive precipitation with *n*-pentane, which is soluble in CH_2Cl_2 and partially soluble in PE.

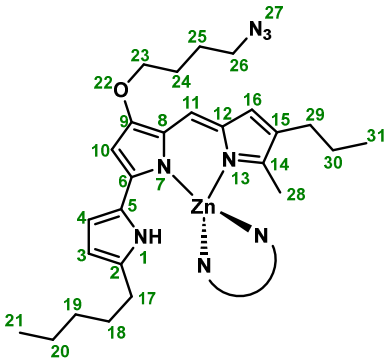


R_f (PE/EtOAc 80:20): 0.49 (visible light). **Mp** 108.4–110.0 °C. **^{1}H NMR** (300 MHz, $CDCl_3$, δ): 9.24 (t, *J* = 2.5 Hz, 1H, 1-H), 7.09 (s, 1H, 11-H), 6.70 (s, 1H, 16-H), 6.48 (d, *J* = 3.5 Hz, 2.4, 1H, 4-H), 6.07 (s, 1H, 10-H), 5.81 (dd, *J* = 3.6, 2.3 Hz, 1H, 3-H), 3.95 (s, 3H, 24-H), 3.24 (t, *J* = 7.0 Hz, 2H, 21-H), 2.30 (t, *J* = 7.6 Hz, 2H, 26-H), 2.20 (t, *J* = 7.1 Hz, 2H, 17-H), 1.88 (s, 3H, 25-H), 1.63 – 1.46 (m, 2H, 20-H), 1.45 (p, *J* = 7.4 Hz, 2H, 27-H), 1.39 – 1.22 (m, 3H, 18-H, 19-H), 0.91 (t, *J* = 7.3 Hz, 3H, 28-H). **^{13}C NMR** (76 MHz, $CDCl_3$, δ): 165.3 (C-9), 154.2 (C-14), 151.8 (C-6), 137.5 (C-2), 135.0 (C-12), 130.4 (C-15), 129.1 (C-8), 126.6 (C-16), 125.9 (C-5), 119.7 (C-11), 112.8 (C-4), 107.6 (C-3), 94.9 (C-10), 58.2 (C-24), 51.5 (C-21), 29.6 (C-19), 28.7 (C-20), 28.4 (C-26), 27.9 (C-17), 26.5 (C-18), 23.5 (C-27), 14.2 (C-25), 14.1 (C-28). **FT-IR** (cm^{-1}, neat): 3316, 3100, 3007, 2954, 2927, 2869, 2856, 2092, 1587, 1544, 1533, 1510, 1451, 1393, 1366, 1306, 1263, 1228, 1200, 1180, 1143, 1125, 1094, 1078, 1044, 1016, 992, 979, 909, 846, 825, 803, 784, 767, 737, 714, 672, 655, 632, 594, 558, 524, 513, 498. **HRMS** (ESI) *m/z*: $[M + H]^+$ calcd for $C_{46}H_{59}N_{12}O_2Zn$, 875.4170; found, 875.4139.

Prodigiosin B-Ring Azide Zinc Complex (III-167)

Under N_2 atmosphere, prodigiosin B-ring azide (**III-90·HCl**, 434 mg, 895 µmol, 1.00 eq.) and zinc(II) acetate dihydrate (1.18 g, 5.37 mmol, 6.00 eq.) were dissolved in MeOH (90 mL). $CHCl_3$ (90 mL) and DIPEA (2.18 mL, 12.5 mmol, 14.0 eq.) were added sequentially and the reaction was stirred at 21 °C for 18 h. Celite was added and the solvent was evaporated. The immobilised product was applied to chromatography on silica with PE/CH_2Cl_2 (60:40). After product

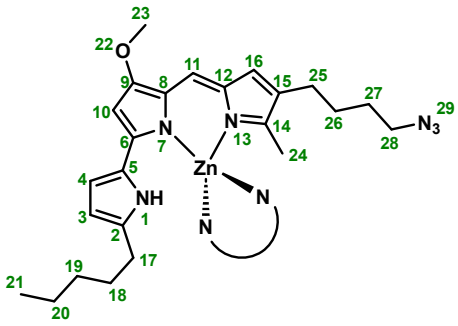
elution, the column was flushed with EtOAc to elute uncomplexed starting material. Evaporation of the solvent provided a red solid, which was repeatedly precipitated with PE to obtain the desired prodigiosin B-ring azide zinc complex as an amorphous, fluffy red solid. The EtOAc fraction was treated again with DIPEA and $Zn(OAc)_2$ dihydrate in $CHCl_3$/MeOH after solvent evaporation due to partial decomplexation of Zn complex during workup. The process was repeated three times in total. The desired prodigiosin B-ring azide zinc complex was obtained as a fluffy red solid (**III-167**, 309 mg, 322 µmol, 72%), which is soluble in CH_2Cl_2 and PE but rather insoluble in MeOH.



R_f (PE/EtOAc 80:20): 0.54 (visible light). **Mp** 167.1–168.9 °C. **^{1}H NMR** (300 MHz, $CDCl_3$, δ): 9.18 (t, *J* = 2.5 Hz, 1H, 1-H), 7.06 (s, 1H, 11-H), 6.69 (s, 1H, 16-H), 6.44 (dd, *J* = 3.6, 2.4 Hz, 1H, 4-H), 6.00 (s, 1H, 10-H), 5.78 (dd, *J* = 3.5, 2.3 Hz, 1H, 3-H), 4.10 (td, *J* = 6.0, 3.4 Hz, 2H, 23-H), 3.42 (t, *J* = 6.5 Hz, 2H, 26-H), 2.28 (t, *J* = 7.5 Hz, 2H, 29-H), 2.20 – 2.12 (m, 2H, 17-H), 2.02 – 1.91 (m, 2H, 24-H), 1.90 – 1.79 (m, 2H, 25-H), 1.86 (s, 3H, 28-H), 1.59 – 1.43 (m, *J* = 7.5 Hz, 2H, 30-H), 1.37 – 1.12 (m, *J* = 6.8 Hz, 6H, 18-H, 19-H, 20-H), 0.89 (t, *J* = 7.5 Hz, 6H, 21-H, 31-H). **^{13}C NMR** (76 MHz, $CDCl_3$, δ): 164.2 (C-9), 154.0 (C-14), 152.0 (C-6), 138.2 (C-2), 135.0 (C-12), 130.3 (C-15), 129.3 (C-8), 126.6 (C-16), 125.8 (C-5), 119.6 (C-11), 112.8 (C-4), 107.4 (C-3), 95.3 (C-10), 70.3 (C-23), 51.3 (C-26), 31.8 (C-19), 29.8 (C-18), 28.5 (C-29), 28.1 (C-17), 26.6 (C-24), 25.9 (C-25), 23.5 (C-30), 22.6 (C-20), 14.3 (C-28), 14.3 (C-21), 14.1 (C-31). **FT-IR** (cm^{-1}, neat): 3312, 3168, 3105, 2954, 2927, 2869, 2857, 2091, 1587, 1540, 1528, 1509, 1452, 1435, 1389, 1358, 1305, 1257, 1227, 1192, 1144, 1126, 1076, 1040, 1018, 990, 978, 901, 855, 848, 827, 804, 767, 738, 692, 664, 632, 564, 511, 486, 474. **HRMS** (ESI) *m/z*: $[M + H]^+$ calcd for $C_{52}H_{70}N_{12}O_2Zn$, 958.5031; found, 958.5013.

Prodigiosin C-Ring Azide Zinc Complex (III-168)

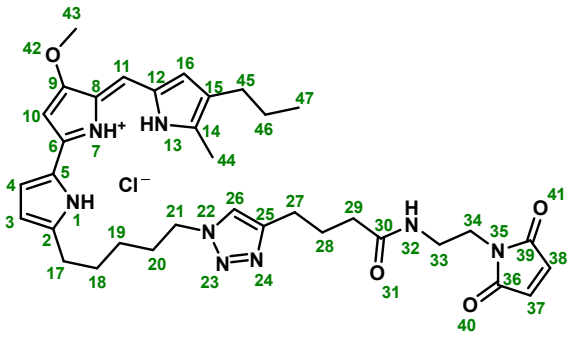
Under N_2 atmosphere, prodigiosin C-ring azide (**III-91·HCl**, 227 mg, 497 µmol, 1.00 eq.) and zinc(II) acetate dihydrate (654 mg, 2.98 mmol, 6.00 eq.) were dissolved in MeOH (50 mL). $CHCl_3$ (50 mL) and DIPEA (1.21 mL, 6.95 mmol, 14.0 eq.) were added sequentially and the reaction was stirred at 21 °C for 18 h. Celite was added and the solvent was evaporated. The immobilised product was applied to chromatography on silica with PE/CH_2Cl_2 (60:40). After product elution, the column was flushed with EtOAc to elute uncomplexed starting material. Evaporation of the solvent provided a red solid, which was repeatedly precipitated with PE. The EtOAc fraction was treated again with DIPEA and $Zn(OAc)_2$ dihydrate in $CHCl_3$/MeOH after solvent evaporation due to partial decomplexation of Zn complex during workup. The process was repeated three times in total. The desired prodigiosin C-ring azide zinc complex was obtained as a fine powdered red solid (**III-168**, 163 mg, 180 µmol, 72%), which is soluble in CH_2Cl_2, less soluble in MeOH, and rather insoluble in PE.



R_f (PE/EtOAc 80:20): 0.54 (visible light). **Mp** 127.8–129.5 °C. **^{1}H NMR** (300 MHz, $CDCl_3$, δ): 9.19 (t, *J* = 2.3 Hz, 1H, 1-H), 7.05 (s, 1H, 11-H), 6.65 (s, 1H, 16-H), 6.47 (dd, *J* = 3.6, 2.6 Hz, 1H, 4-H), 6.04 (s, 1H, 10-H), 5.78 (dd, *J* = 3.5, 2.4 Hz, 1H, 3-H), 3.93 (s, 3H, 23-H), 3.28 – 3.17 (m, 2H, 28-H), 2.38 – 2.28 (m, 2H, 25-H), 2.20 – 2.11 (m, 2H, 17-H), 1.84 (s, 3H, 24-H), 1.64 – 1.50 (m_c, 4H, 26-H, 27-H), 1.34 – 1.12 (m, 6H, 18-H, 19-H, 20-H), 0.88 (t, *J* = 6.9 Hz, 3H, 21-H). **^{13}C NMR** (76 MHz, $CDCl_3$, δ): 165.6 (C-9), 153.2 (C-14), 152.4 (C-6), 138.5 (C-2), 134.9 (C-12), 129.5 (C-8), 129.1 (C-15), 126.2 (C-16), 125.7 (C-5), 119.7 (C-11), 113.2 (C-4), 107.5 (C-3), 95.0 (C-10), 58.2 (C-23), 51.5 (C-28), 31.8 (C-19), 29.8 (C-18), 28.7 (C-27), 28.1 (C-17), 27.4 (C-26), 25.9 (C-25), 22.6 (C-20), 14.2 (C-21), 14.2 (C-24). **FT-IR** (cm^{-1}, neat): 3320, 2957, 2929, 2870, 2855, 2089, 1590, 1549, 1510, 1454, 1423, 1393, 1366, 1303, 1267, 1232, 1200, 1180, 1147, 1129, 1117, 1086, 1075, 1063, 1044, 1024, 992, 976, 909, 848, 831, 815, 798, 786, 769, 735, 715, 671, 633, 595, 567, 558, 517, 495, 468, 459. **HRMS** (ESI) *m/z*: $[M + H]^+$ calcd for $C_{48}H_{62}N_{12}O_2Zn$, 902.4405; found, 902.4388.

(*Z*)-5-(5-(4-(4-((2-(2,5-Dioxo-2,5-dihydro-1*H*-pyrrol-1-yl)ethyl)amino)-4-oxobutyl)-1*H*-1,2,3-triazol-1-yl)pentyl)-4'-methoxy-5'-((5-methyl-4-propyl-1*H*-pyrrol-2-yl)methylene)-1*H*,5'*H*-[2,2'-bipyrrol]-1'-ium chloride (III-169·HCl)

To a 100 mL round-bottom flask under N_2 atmosphere, prodigiosin A-ring azide zinc complex (**III-166**, 205 mg, 234 µmol, 1.00 eq., final 5 mM) and alkyne-maleimide linker (**III-159**, 274 mg, 1.17 mmol, 5.00 eq.) were added and the solids were dissolved in CH_2Cl_2 (15.6 mL). EtOH (15.2 mL) was added to dissolve the linker. Solutions of TDETA (**II-44**, 4.29 mL, 122 mg, 258 µmol, 1.10 eq., 60 mM in EtOH) and sodium ascorbate (703 µL, 69.6 mg, 351 µmol, 1.50 eq., 500 mM in water) were added. The reaction was started by the addition of a freshly prepared solution of $Cu(OAc)_2$ (11.7 mL, 42.5 mg, 234 µmol, 1.00 eq., 20 mM in EtOH) and it was stirred for 60 min at 21 °C (final ratio of CH_2Cl_2/EtOH 1:2). The reaction was diluted with CH_2Cl_2 (100 mL) and washed with 1 M aqueous HCl (100 mL) to disrupt the zinc complex. Phases were separated and the aqueous phase was extracted with CH_2Cl_2 (15 mL portions) until the organic phase remained weakly pink. Merged organic phases were washed with brine (2 x 100 mL), dried over anhydrous Na_2SO_4, and filtered over degreased cotton wool (**!**). After solvent evaporation, the purple residue was purified by column chromatography on silica with a gradient of CH_2Cl_2/MeOH (0–3% MeOH with 1% iterations, then 6% and 10%). The red product fractions eluted at 3–6% MeOH. The solvent was removed *in vacuo* and the residue was purified on silica with isocratic elution in CH_2Cl_2/MeOH (97:3). After solvent evaporation, the residue was dissolved in CH_2Cl_2 and repeatedly precipitated with *n*-pentane. Drying under high vacuum provided the desired product **III-169·HCl** as a deep purple solid (254 mg, 93.6 µmol, 80%).

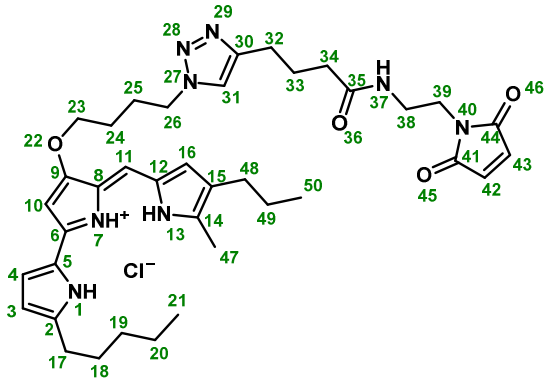


R_f (CH_2Cl_2/MeOH 90:10): 0.44 (visible light). **Mp** 58.5–62.3 °C. **^{1}H NMR** (300 MHz, $CDCl_3$, δ): 12.50 (brs, 1H, 13-H), 12.46 (brs, 1H, 1-H), 12.40 (brs, 1H, 7-H), 7.47 (s, 1H, 26-H), 6.88 (s, 1H, 11-H), 6.85 (dd, *J* = 3.9, 2.1 Hz, 1H, 4-H), 6.64 (s, 2H, 37-H, 38-H), 6.63 (d, *J* = 2.8 Hz, 1H, 16-H), 6.55 (t, *J* = 5.9 Hz, 1H, 32-H), 6.07 (dd, *J* = 4.0, 1.9 Hz, 1H, 3-H), 6.04 (d, *J* = 1.3 Hz, 1H, 10-H), 4.33 (t, *J* = 7.0 Hz, 2H, 21-H), 3.99 (s, 3H, 43-H), 3.70 – 3.61 (m, 2H, 34-H), 3.48 – 3.38 (m, 2H, 33-H), 2.75 (t, *J* = 7.5 Hz, 2H, 17-H), 2.67 (t, *J* = 7.0 Hz, 2H, 27-H), 2.50 (s, 3H, 44-H), 2.36 (t, *J* = 7.5 Hz, 2H, 45-H), 2.15 (t, *J* = 7.2 Hz, 2H, 29-H), 2.02 – 1.76 (m, *J* = 7.5, 7.4 Hz, 6H, 18-H, 19-H, 28-H), 1.55 (h, *J* = 7.4 Hz, 2H, 46-H), 1.45 – 1.26 (m, 2H, 20-H), 0.92 (t, *J* = 7.3 Hz, 3H, 47-H). **^{13}C NMR** (76 MHz, $CDCl_3$, δ): 173.4 (C-30), 171.0 (C-36, C-39), 165.9 (C-9), 147.7 (C-6), 147.1 (C-25), 145.5 (C-14), 143.7 (C-2), 134.3 (C-37, C-38), 127.8 (C-15), 127.7 (C-16), 125.0 (C-12), 121.6 (C-26), 121.2 (C-5, C-8), 118.7 (C-4), 114.9 (C-11), 110.9 (C-3), 92.7 (C-10), 58.8 (C-43), 49.9 (C-21), 38.5 (C-33), 37.8 (C-34), 35.3 (C-29), 29.9 (C-19), 28.4 (C-18), 27.9 (C-17), 27.6 (C-45), 25.8 (C-20), 25.4 (C-28), 24.4 (C-27), 23.5 (C-46), 13.9 (C-47), 12.4 (C-44). **FT-IR** (cm^{-1}, neat): 3173, 3112, 3072, 2931, 2864, 1705, 1631, 1602, 1577, 1537, 1495, 1436, 1404, 1355, 1253, 1208, 1152, 1131, 1097, 1080, 1043, 994, 969, 895, 884, 823, 805, 782, 734, 695, 648, 623. **HRMS** (ESI) *m/z*: $[M - Cl]^+$ calcd for $C_{35}H_{45}N_8O_4$, 641.3558; found, 641.3570.

(*Z*)-4'-(4-(4-(4-((2-(2,5-Dioxo-2,5-dihydro-1*H*-pyrrol-1-yl)ethyl)amino)-4-oxobutyl)-1*H*-1,2,3-triazol-1-yl)butoxy)-5'-((5-methyl-4-propyl-1*H*-pyrrol-2-yl)methylene)-5-pentyl-1*H*,5'*H*-[2,2'-bipyrrol]-1'-ium chloride (III-170·HCl)

To a 100 mL round-bottom flask under N_2 atmosphere, prodigiosin B-ring azide zinc complex (**III-167**, 130 mg, 135 µmol, 1.00 eq., final 5 mM) and alkyne-maleimide linker (**III-159**, 159 mg, 677 µmol, 5.00 eq.) were added, and the solids were dissolved in CH_2Cl_2 (9.02 mL). EtOH (8.79 mL) was added to dissolve the linker. Solutions of TDETA (**II-44**, 2.48 mL, 70.5 mg, 149 µmol, 1.10 eq., 60 mM in EtOH) and sodium ascorbate (406 µL, 40.2 mg, 203 µmol, 1.50 eq., 500 mM in water) were added. The reaction was started by the addition of a freshly prepared solution of $Cu(OAc)_2$ (6.77 mL, 24.9 mg, 135 µmol, 1.00 eq., 20 mM in EtOH) and it was stirred for 60 min at 21 °C (final ratio of CH_2Cl_2/EtOH 1:2). The reaction was diluted with CH_2Cl_2 (100 mL) and washed with 1 M aqueous HCl (100 mL) to disrupt the zinc complex. Phases were separated and the aqueous phase was extracted with CH_2Cl_2 (15 mL portions) until the organic phase was weakly pink. Merged organic phases were washed with brine (2 x 100 mL), dried over anhydrous Na_2SO_4,

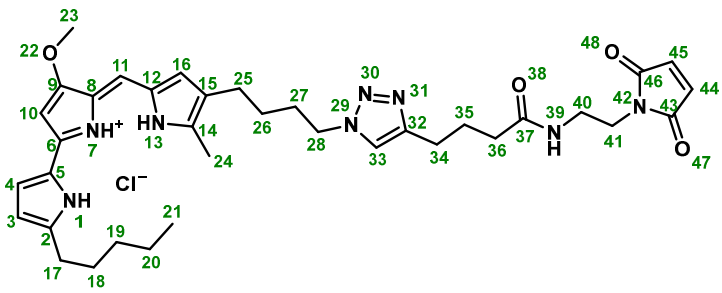
and filtered over degreased cotton wool (**!**). After solvent evaporation, the purple residue was purified by column chromatography on silica with a gradient of CH_2Cl_2/MeOH (0–4% MeOH, 1% iterations). The red product fractions eluted at 3% MeOH. The solvent was removed *in vacuo* and the residue was purified on silica with isocratic elution in CH_2Cl_2/MeOH (96:4). After solvent evaporation, the residue was dissolved in CH_2Cl_2 and repeatedly precipitated with *n*-pentane. Drying under high vacuum provided the desired product **III-170·HCl** as a deep purple solid (145 mg, 50.3 µmol, 74%).



R_f (CH_2Cl_2/MeOH 90:10): 0.54 (visible light). **Mp** 49.3–52.3 °C. **^{1}H NMR** (300 MHz, $CDCl_3$, δ): 12.59 (brs, 1H, 13-H), 12.49 (brs, 2H, 1-H, 7-H), 7.36 (s, 1H, 31-H), 6.87 – 6.82 (m, 2H, 4-H, 11-H), 6.69 (s, 2H, 42-H, 43-H), 6.66 (s, 1H, 16-H), 6.21 (t, *J* = 5.2 Hz, 1H, 37-H), 6.10 (d, *J* = 3.8 Hz, 1H, 3-H), 5.97 (s, 1H, 10-H), 4.42 (t, *J* = 6.9 Hz, 2H, 26-H), 4.14 (t, *J* = 6.1 Hz, 2H, 23-H), 3.70 – 3.63 (m, 2H, 39-H), 3.48 – 3.40 (m, 2H, 38-H), 2.76 (t, *J* = 7.7 Hz, 2H, 17-H), 2.72 (t, *J* = 7.4 Hz, 2H, 32-H), 2.52 (s, 3H, 47-H), 2.37 (t, *J* = 7.5 Hz, 2H, 48-H), 2.18 (t, *J* = 7.2 Hz, 2H, 34-H), 2.18 – 2.05 (m, 2H, 25-H), 1.93 (p, *J* = 7.2 Hz, 2H, 33-H), 1.92 – 1.82 (m, 2H, 24-H), 1.77 (p, *J* = 7.4 Hz, 2H, 18-H), 1.56 (h, *J* = 7.4 Hz, 2H, 49-H), 1.42 – 1.27 (m, 4H, 19-H, 20-H), 0.93 (t, *J* = 7.3 Hz, 3H, 50-H), 0.92 – 0.84 (m_c, *J* = 6.8 Hz, 3H, 21-H). **^{13}C NMR** (76 MHz, $CDCl_3$, δ): 173.1 (C-35), 171.0 (C-41, C-44), 164.4 (C-9), 147.74 (C-30), 147.70 (C-6), 145.5 (C-14), 145.1 (C-2), 134.3 (C-42, C-43), 127.7 (C-15), 127.5 (C-16), 125.0 (C-12), 121.3 (C-8), 121.1 (C-31), 120.9 (C-5), 118.9 (C-4), 114.5 (C-11), 110.7 (C-3), 93.1 (C-10), 70.8 (C-23), 49.7 (C-26), 38.8 (C-38), 37.8 (C-39), 35.5 (C-34), 31.6 (C-19), 28.9 (C-18), 28.3 (C-17), 27.6 (C-48), 26.9 (C-25), 26.0 (C-24), 25.4 (C-33), 24.7 (C-32), 23.5 (C-49), 22.5 (C-20), 14.2 (C-21), 13.9 (C-50), 12.4 (C-47). **FT-IR** (cm^{-1}, neat): 3167, 3111, 3064, 2953, 2927, 2869, 2859, 1706, 1631, 1602, 1576, 1538, 1495, 1435, 1405, 1389, 1353, 1338, 1250, 1202, 1151, 1131, 1099, 1079, 1043, 1000, 968, 888, 849, 822, 806, 784, 734, 695, 661, 623, 600, 568, 550, 502, 474, 467, 457. **HRMS** (ESI) *m/z*: $[M - Cl]^+$ calcd for $C_{38}H_{51}N_8O_4$, 683.4028; found, 683.4028.

(*Z*)-5'-((4-(4-(4-(4-((2-(2,5-Dioxo-2,5-dihydro-1*H*-pyrrol-1-yl)ethyl)amino)-4-oxobutyl)-1*H*-1,2,3-triazol-1-yl)butyl)-5-methyl-1*H*-pyrrol-2-yl)methylene)-4'-methoxy-5-pentyl-1*H*,5'*H*-[2,2'-bipyrrol]-1'-ium chloride (III-171·HCl)

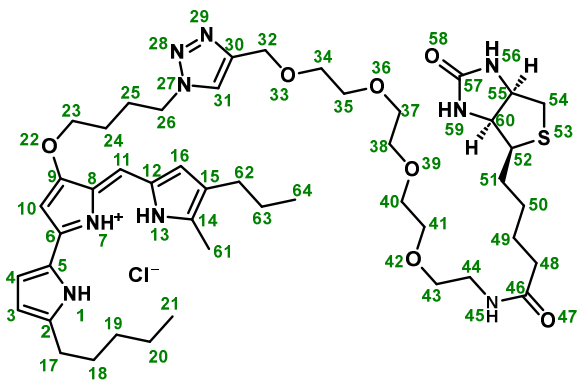
To a 100 mL round-bottom flask under N_2 atmosphere, prodigiosin C-ring azide zinc complex (**III-168**, 100 mg, 111 µmol, 1.00 eq., final 5 mM) and alkyne-maleimide linker (**III-159**, 129 mg, 553 µmol, 5.00 eq.) were added and the solids were dissolved in CH_2Cl_2 (5.50 mL). EtOH (9.00 mL) was added to dissolve the linker. Solutions of TDETA (**II-44**, 2.03 mL, 57.6 mg, 122 µmol, 1.10 eq., 60 mM in EtOH) and sodium ascorbate (332 µL, 32.9 mg, 166 µmol, 1.50 eq., 500 mM in water) were added. The reaction was started by the addition of a freshly prepared solution of $Cu(OAc)_2$ (5.53 mL, 20.1 mg, 111 µmol, 1.00 eq., 20 mM in EtOH) and it was stirred for 60 min at 21 °C (final ratio of CH_2Cl_2/EtOH 1:3). The reaction was diluted with CH_2Cl_2 (100 mL) and washed with 1 M aqueous HCl (100 mL) to disrupt the zinc complex. Phases were separated and the aqueous phase was extracted with CH_2Cl_2 (15 mL portions) until the organic phase was weakly pink. Merged organic phases were washed with brine (2 x 100 mL), dried over anhydrous Na_2SO_4, and filtered over degreased cotton wool (**!**). After solvent evaporation, the purple residue was purified by column chromatography on silica with a gradient of CH_2Cl_2/MeOH (0–3% MeOH with 1% iterations). The red product fractions eluted at 3% MeOH. The solvent was removed *in vacuo* and the residue was purified on silica with isocratic elution in CH_2Cl_2/MeOH (97:3). After solvent evaporation, the residue was dissolved in CH_2Cl_2 and repeatedly precipitated with *n*-pentane. Drying under high vacuum provided the desired product **III-171·HCl** as a deep purple solid (123 mg, 44.3 µmol, 80%).



R_f (CH_2Cl_2/MeOH 90:10): 0.52 (visible light). **Mp** 55.3–64.5 °C (broad transition). **^{1}H NMR** (300 MHz, $CDCl_3$, δ): 12.57 (brs, 1H, 13-H), 12.50 (brs, 2H, 1-H, 7-H), 7.29 (s, 1H, 33-H), 6.88 (dd, *J* = 3.9, 2.3 Hz, 1H, 4-H), 6.84 (s, 1H, 11-H), 6.68 (s, 2H, 44-H, 45-H), 6.56 (d, *J* = 2.5 Hz, 1H, 16-H), 6.30 (t, *J* = 6.0 Hz, 1H, 39-H), 6.11 (dd, *J* = 3.9, 2.1 Hz, 1H, 3-H), 6.02 (d, *J* = 1.7 Hz, 1H, 10-H), 4.32 (t, *J* = 7.1 Hz, 2H, 28-H), 3.99 (s, 3H, 23-H), 3.71 – 3.63 (m, 2H, 41-H), 3.50 – 3.40 (m, 2H, 40-H), 2.76 (t, *J* = 7.7 Hz, 2H, 17-H), 2.72 (t, *J* = 7.1 Hz, 2H, 34-H), 2.49 (s, 3H, 24-H), 2.44 (t, *J* = 7.4 Hz, 2H, 25-H), 2.18 (t, *J* = 7.2 Hz, 2H, 36-H), 1.94 (p, *J* = 7.2 Hz, 2H, 35-H), 1.96 – 1.83 (m, 2H, 27-H), 1.78 (pd, *J* = 7.3 Hz, 2H, 18-H), 1.55 (p, *J* = 7.5 Hz, 2H, 26-H), 1.41 – 1.27 (m, 4H, 19-H, 20-H), 0.99 – 0.77 (m_c, *J* = 6.8 Hz, 3H, 21-H). **^{13}C NMR** (76 MHz, $CDCl_3$, δ): 173.3 (C-37), 171.0 (C-43, C-46), 165.9 (C-9), 148.3 (C-6), 147.4 (C-32), 145.5 (C-2), 144.3 (C-14), 134.3 (C-44, C-45), 126.7 (C-16), 126.0 (C-15), 124.9 (C-12), 121.8 (C-8), 121.0 (C-5), 120.9 (C-33), 119.3 (C-4), 114.4 (C-11), 110.9 (C-3), 92.8 (C-10), 58.8 (C-23), 50.1 (C-28), 38.7 (C-40), 37.8 (C-41), 35.4 (C-36), 31.6 (C-19), 29.9 (C-27), 28.9 (C-18), 28.3 (C-17), 27.2 (C-26), 25.5 (C-35), 24.8 (C-25), 24.6 (C-34), 22.5 (C-20), 14.2 (C-21), 12.3 (C-24). **FT-IR** (cm^{-1}, neat): 3169, 3112, 3067, 2929, 2859, 1706, 1631, 1603, 1578, 1538, 1495, 1436, 1404, 1357, 1253, 1206, 1162, 1132, 1118, 1044, 994, 969, 895, 884, 839, 822, 797, 787, 734, 695, 650, 624, 503. **HRMS** (ESI) *m/z*: $[M - Cl]^+$ calcd for $C_{36}H_{47}N_8O_4$, 655.3715; found, 655.3723.

(*Z*)-5'-((5-Methyl-4-propyl-1*H*-pyrrol-2-yl)methylene)-4'-(4-(4-(15-oxo-19-((3a*S*,4*S*,6a*R*)-2-oxohexahydro-1*H*-thieno[3,4-*d*]imidazol-4-yl)-2,5,8,11-tetraoxa-14-azanonadecyl)-1*H*-1,2,3-triazol-1-yl)butoxy)-5-pentyl-1*H*,5'*H*-[2,2'-bipyrrol]-1'-ium chloride (III-172·HCl)

To a 25 mL round-bottom flask, prodigiosin B-ring azide zinc complex (**III-167**, 48.5 mg, 50.5 µmol, 1.00 eq.), biotin-PEG_4-acetylene (**II-65**, 53.5 mg, 111 µmol, 2.20 eq., 95%), and TDETA (**II-44**, 25.1 mg, 53.0 µmol, 1.05 eq.) were added, and the solids were dissolved in $CHCl_3$ (2.00 mL). Subsequently, EtOH (1.48 mL) and solutions of $Cu(OAc)_2$ (2.52 mL, 9.17 mg, 50.5 µmol, 1.00 eq., 20 mM in EtOH) and sodium ascorbate (151 µL, 15.0 mg, 75.7 µmol, 1.50 eq., 500 mM in water) were added. The reaction was stirred at 20 °C for 110 min in a final ratio of $CHCl_3$/EtOH (1:2). The purple reaction solution was diluted with $CHCl_3$ (30 mL) and washed with 1 M HCl (30 mL) to disrupt the zinc complex. The aqueous phase was extracted with $CHCl_3$ (3 x 3 mL), and the merged organic phases were dried over $MgSO_4$ and filtered. After solvent evaporation, the purple crude product was chromatographed on silica with a gradient of CH_2Cl_2/MeOH (0–30% MeOH, with 5%, 10%, 15%, 20% and 30% steps), followed by a second chromatographic separation on silica with CH_2Cl_2/MeOH (0% MeOH, then 20% MeOH). After solvent removal, the biotinylated B-ring prodiginine **III-172·HCl** was obtained as a purple film (82.9 mg, 22.0 µmol, 87%).

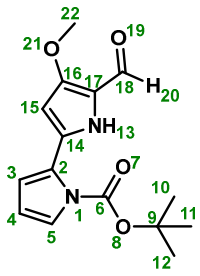


R_f (CH_2Cl_2/MeOH 70:30): 0.86 (visible light and $KMnO_4$ stain). **^{1}H NMR** (600 MHz, $CDCl_3$, δ): 12.56 (brs, 1H, 13-H), 12.45 (brs, 2H, 1-H, 7-H), 7.64 (s, 1H, 31-H), 6.88 (t, *J* = 5.4 Hz, 1H, 45-H), 6.84 (dd, *J* = 4.0, 2.1 Hz, 1H, 4-H), 6.82 (s, 1H, 11-H), 6.70 (brs, 1H, 56-H), 6.66 – 6.63 (m, 1H, 16-H), 6.07 (dd, *J* = 3.9, 2.2 Hz, 1H, 3-H), 5.99 (d, *J* = 1.9 Hz, 1H, 10-H), 5.78 (brs, 1H, 59-H), 4.66 (s, 2H, 32-H), 4.46 (dd, *J* = 7.5 Hz, 4.9, 1H, 55-H), 4.44 (t, *J* = 7.0 Hz, 2H, 26-H), 4.26 (dd, *J* = 7.8, 4.6 Hz, 1H, 60-H), 4.13 (t, *J* = 6.2 Hz, 2H, 23-H), 3.70 – 3.65 (m, 2H), 3.65 – 3.62 (m, 2H), 3.61 (s, 4H), 3.60 – 3.56 (m, 4H), 3.52 (t, *J* = 5.1 Hz, 2H, 43-H), 3.43 – 3.31 (m, 2H, 44-H), 3.08 (td, *J* = 7.4, 4.5 Hz, 1H, 52-H), 2.85 (dd, *J* = 12.8, 4.9 Hz, 1H, 54a-H), 2.73 (t, *J* = 7.8 Hz, 2H, 17-H), 2.70 (d, *J* = 12.7 Hz, 1H, 54b-H), 2.49 (s, 3H, 61-H), 2.34 (t, *J* = 7.5 Hz, 2H, 62-H), 2.18 (t, *J* = 7.5 Hz, 2H, 48-H), 2.10 (p, *J* = 7.2 Hz, 2H, 25-H), 1.89 – 1.82 (m, 2H, 24-H), 1.79 – 1.72 (m_c, 2H, 18-H), 1.73 – 1.65 (m, 1H, 51a-H), 1.66 – 1.57 (m, *J* = 7.4 Hz, 3H, 49-H, 51b-H), 1.53 (h, *J* = 7.3 Hz, 2H, 63-H), 1.43 – 1.34 (m, 2H, 50-H), 1.36 – 1.29 (m, 4H, 19-H, 20-H), 0.91 (t, *J* = 7.3 Hz, 3H, 64-H), 0.89

– 0.84 (m_c, *J* = 6.7 Hz, 3H, 21-H). **^{13}C NMR** (151 MHz, $CDCl_3$, δ): 173.5 (C-46), 164.4 (C-9), 164.1 (C-57), 147.7 (C-6), 145.27 (C-30), 145.25 (C-14), 144.9 (C-2), 127.6 (C-15), 127.4 (C-16), 124.9 (C-12), 122.8 (C-31), 121.2 (C-8), 120.9 (C-5), 118.9 (C-4), 114.4 (C-11), 110.6 (C-3), 93.1 (C-10), 70.8 (C-23), 70.58, 70.57, 70.48, 70.42, 70.13, 69.93, 69.86, 64.7 (C-32), 61.8 (C-60), 60.3 (C-55), 55.7 (C-52), 49.8 (C-26), 40.6 (C-54), 39.2 (C-44), 35.9 (C-48), 31.5 (C-19), 28.8 (C-18), 28.23 (C-17), 28.22 (C-50), 28.1 (C-51), 27.5 (C-62), 26.9 (C-25), 25.9 (C-24), 25.7 (C-49), 23.45 (C-63), 22.43 (C-20), 14.1 (C-21), 13.9 (C-64), 12.3 (C-61). **FT-IR** (cm^{-1}, neat): 3221, 3172, 3134, 3112, 3072, 2925, 2862, 1699, 1664, 1631, 1603, 1577, 1539, 1404, 1354, 1338, 1309, 1253, 1203, 1130, 1083, 1044, 1001, 970, 887, 845, 806, 783, 735, 683, 661, 624, 598, 566, 550, 545, 503, 486, 478, 469, 463. **HRMS** (ESI) *m/z*: $[M - Cl]^+$ calcd for $C_{47}H_{72}N_9O_7S$, 906.5270; found, 906.5265.

tert-Butyl 5'-formyl-4'-methoxy-1*H*,1'*H*-[2,2'-bipyrrole]-1-carboxylate (III-174, Boc-MBC)

Boc-protected MBC was synthesised according to an original procedure from Aldrich *et al*. and modified by Klein *et al*.[469, 875] In a 500 mL Schlenk flask under N_2 atmosphere, tetrakis(triphenylphosphine)palladium(0) (1.18 g, 1.02 mmol, 0.05 eq.) was suspended in degassed toluene (11 mL). A solution of bromide (**III-75**, 5.30 g, 20.5 mmol, 1.00 eq.) and *N*-Boc-pyrrole-2-boronic acid MIDA ester (**III-173**, 9.88 g, 30.7 mmol, 1.50 eq.) in degassed 1,4-dioxane/water (9:1, 180 mL) were added to the Pd precatalyst. After adding Na_2CO_3 (6.51 g, 61.4 mmol, 3.00 eq.), the reaction was heated to 90 °C for 1 h. Anhydrous K_3PO_4 (8.68 g, 40.9 mmol, 2.00 eq.) was supplemented to the reaction and after an additional 90 min of reflux, a second batch of Pd catalyst (1.18 g, 1.02 mmol, 0.05 eq.) was added. After 5 h of reflux, the solution was cooled to ambient temperature and ice water (400 mL) was added. The pH was adjusted with 30 mL 2 M HCl to pH 7–8, followed by extraction with CH_2Cl_2 (3 x 150 mL). Merged organic phases were dried over $MgSO_4$, filtered, and the solvent was removed *in vacuo*. Purification on silica with PE/EtOAc (80:20) provided the product (**III-174**, 2.57 g, 8.86 mmol, 43%) as a beige solid.



Mp 145–150 °C (decomposition). **^{1}H NMR** (600 MHz, $CDCl_3$, δ): 10.70 (brs, 1H, 13-H), 9.54 (brs, 1H, 20-H), 7.33 (dd, *J* = 3.4 Hz, *J* = 1.8 Hz, 1H, 5-H), 6.67 (dd, J = 3.6 Hz, J = 1.8 Hz, 1H, 3-H), 6.25 (t, *J* = 3.5 Hz, 1H, 4-H), 6.08 (d, *J* = 2.7 Hz, 1H, 15-H), 3.89 (s, 3H, 22-H), 1.62 (s, 9H, 10-H, 11-H, 12-H). **^{13}C NMR** (151 MHz, $CDCl_3$, δ): 174.5 (C-18), 157.8 (C-16), 149.9 (C-6), 130.3 (C-14), 126.2 (C-2), 124.7 (C-5), 118.4 (C-17), 117.0 (C-3), 111.6 (C-4), 94.9 (C-15), 85.9 (C-9), 58.1 (C-22), 28.1 (C-10, C-11, C-12). **FT-IR** (cm^{-1}, neat): 3207, 3156, 3111, 3013, 2993, 2977, 2936, 2857, 2831, 1744, 1597, 1546, 1504, 1455, 1445, 1389, 1366, 1304, 1284, 1255, 1230, 1189, 1170, 1160, 1138, 1082, 1067, 1041, 1015, 918, 878, 843, 821, 768, 732, 692, 639, 585, 571, 497. **HRMS** (ESI) *m/z*: $[M + H]^+$ calcd for $C_{16}H_{21}N_2O_4$, 291.1339; found, 291.1344. **CAS** 1213263-03-6.

V.4 Microbiological Methods

V.4.1 Sterilisation

Bacterial cultivation media, water, and media supplements (antibiotics, IPTG) were sterilised to prevent contamination of laboratory microbes and media with environmental microorganisms or to inactivate genetically modified organisms (GMOs). Therefore, cultivation media, consumables, and glassware were sterilised by autoclaving in a steam autoclave at 121 °C for 20 min. Heat-sensitive media supplements were filter-sterilised by forcing the liquids through a sterile 0.22 µm polyvinyl difluoride (PVDF) syringe filter.

V.4.2 Bacterial Cultivation Media

All cultivation media were prepared with deionised water. Liquid cultures of bacteria were either grown in sterile lysogeny broth (10 g/L tryptone, 5 g/L yeast extract, and 10 g/L NaCl, adjusted to pH 7.2 with NaOH) or terrific broth (50.8 g/L pre-mix, supplemented with 4 mL/L glycerol, Carl Roth). Solid LB-agar was prepared by adding 1.4% (w/v) agar-agar to the medium before autoclaving. LB soft-agar, containing 0.7% agar-agar, was prepared by mixing sterile hot LB medium and molten LB-agar in a 1:1 ratio. Commercial Columbia agar + 5% sheep blood (COS agar, Biomérieux) was used for the plating of clinical *P. aeruginosa* isolates.

V.4.3 Antibiotics and Media Supplements

Ampicillin and kanamycin were used as antibiotics for microbial selection. 1000x antibiotic stock solutions were prepared in water before 0.22 µm filter-sterilisation and storage at –20 °C. While ampicillin was used at a final concentration of 100 µg/mL for pET21a vectors (harbouring the β-lactamase *bla* gene), kanamycin was used at 50 µg/mL for pET28a vectors, which confers kanamycin resistance by expressing the aminoglycoside phosphotransferase Kan^R. IPTG was used as an inducer for the heterologous expression of genes under control of the *lac* operon and the T7 polymerase. Stock solutions of 500 mM were prepared in water and IPTG was added to a final concentration of 500 µM during cultivation. Antibiotics and IPTG were stored at –20 °C and were freshly supplemented to liquid media or molten agar before hardening. All solutions were filter-sterilised.

V.4.4 Bacterial Strains

Table V.2. Bacterial strains used in this work.

Strain	Genotype or relevant characteristic	Reference
	Pseudomonas aeruginosa	
PAO1	Clinical isolate, burn wound, PyoS2-resistant, ATCC 15692	[757]
W15Dec1	Environmental isolate from a Belgian river, PyoS2-sensitive	[614]
M strains	MDR clinical isolates from hospitalised patients (for details see Table IX.9, SI)	this work
	Escherichia coli	
DH5α	F^- *endA1 glnV44 thi-1 recA1 relA1 gyrA96 deoR nupG purB20* φ80*dlacZ*ΔM15 *Δ(lacZYA-argF)*U169, hsdR17($r_K^- m_K^+$), λ^-	[754]
BL21(DE3)	*E. coli* strain B, F^- *ompT gal dcm lon* hsdSB($r_B^- m_B^-$) *λ*(DE3) [*lacI lacUV5-T7p07 ind1 sam7 nin5*]) [$malB^+$]$_{K\text{-}12}$(λ^S)	[876]
C43(DE3)	*E. coli* strain BL21, F^- *ompT gal dcm* hsdSB($r_B^- m_B^-$) *λ*(DE3), uncharacterised mutations confer resistance to toxic proteins	[747]
JM109(DE3)	*endA1 recA1 gyrA96 thi hsdR17(rk⁻ mk⁺), relA1, supE44, λ⁻, Δ(lac-proAB),* [*F', traD36, proAB, lacI^{q}ZΔM15*], *λ*(DE3)	[749]
Rosetta 2(DE3) pLysS	F^- *ompT hsdSB*($r_B^- m_B^-$) *gal dcm* pRARE2 (Cam^R) pLysS (Cam^R)	Novagen

V.4.5 Bacterial Precultures

Precultures of single bacterial colonies (selected from agar) were used to ensure genetic homogeneity and fitness within an experiment, and furthermore, render all bacteria in the same growth phase. Precultures were typically prepared in 5 mL LB medium, supplemented with antibiotics if needed, and the medium was inoculated with a single colony from plated colonies on LB-agar. The cultures were grown at 37 °C in a rotary shaker and used for all kinds of microbial work. Specific strains and cultivation media for individual experiments are mentioned in the corresponding experimental section.

V.4.6 Preparation of Chemically Competent Cells

Chemically competent cells of *E. coli* strains were used for the facilitated uptake of DNA for cloning or protein synthesis purposes. To prepare competent cells, a sterile 500 mL Erlenmeyer flask with LB Medium (50 mL, no antibiotics added) is inoculated to an OD_{600} of 0.05 with a preculture of the desired bacterial strain of *E. coli*. Cells are incubated at 37 °C (130 RPM) to an OD_{600} of 0.3–0.4 and harvested by centrifugation (10,000 x g, 10 min, 4 °C). The supernatant is discarded and the cells are permanently kept on ice for all following steps. The pellet is carefully resuspended in filter-sterilised and ice-cold 100 mM $CaCl_2$ and the cell suspension is kept on ice for at least 2 h. Longer incubation periods result in greater competence. The incubation period is followed by sedimentation of the cells by centrifugation (10,000 x g, 10 min, 4 °C) and careful resuspension of the pellet in filter-sterilised and ice-cold 100 mM $CaCl_2$, 15% glycerol. Aliquots of 20–50 µL are transferred into cooled sterile 1.5 mL reaction tubes and shock-frozen in liquid nitrogen. The aliquots of chemically competent cells are stored at –80 °C until needed.

V.4.7 Heat-Shock Transformation of Chemically Competent Cells

Transformation of competent bacterial cells was achieved using the heat-shock procedure. Chemically competent cells are thawed on ice and then supplemented with 1 µL of purified plasmid DNA or up to 1/10 of the volume with non-purified ligation mixtures. Incubation on ice is continued for 30 min, followed by a brief heat-shock at 42 °C for 45 s. Cells are further chilled on ice for 10 min, before 700 µL of LB medium (no antibiotics added) are added. Incubation at 37 °C on a rotary shaker for 1.5 h allows phenotypic expression of plasmid-harboured enzymes that confer antibiotic resistance needed for selection. Cells are then briefly sedimented via centrifugation (7,000 x g, 2 min, 20 °C) and 600 µL of the supernatant is discarded. The pellet is resuspended in the residual medium and suitable volumes are plated on LB agar (supplemented with antibiotics) for colony selection. Plates are incubated at 37 °C overnight, and colonies are used for colony-PCR, plasmid preparation for sequencing or amplification, or protein synthesis.

V.4.8 Cryo-Preservation of Bacterial Strains

Cryo-preservation of bacteria was used for long-term storage of microbes. First, 500 µL of glycerol is aliquoted into 1.5 mL screw-cap tubes and autoclaved. Second, the sterile cryo-preservative is thoroughly mixed with 500 µL of exponential phase cultures of *E. coli* or *P. aeruginosa* by pipetting. Cryo-cultures are then frozen in liquid nitrogen and stored at –80 °C until needed.

V.4.9 Heterologous Protein Synthesis

Proteins were heterologously produced through the pET-based T7 expression system in *E. coli* BL21(DE3) or *E. coli* C43(DE3) (only for PyoS2 Y640C and PyoS2 ID derivatives). The coding sequences under the control of

the T7 promoter were either expressed from pET21a(+) vectors, harbouring the *pyoS2_imS2-His$_6$* tandem, or from pET28a(+) vector, harbouring the coding genes *pigC*, *tamQ*, and *treaP* for the prodigiosin ligating enzymes.

V.4.9.1 Protein Synthesis of PyoS2 Mutants and ImS2

Precultures of *E. coli* BL21(DE3) or C41(DE3), transformed with the pET21a(+) expression vectors, were prepared by inoculating LB media (100 µg/mL amp) with a single colony of the respective strain. Cultures were incubated overnight at 37 °C (130 RPM).

For the heterologous protein synthesis of PyoS2 mutants, 2 L of TB medium (100 µg/mL amp) in a 5 L Erlenmeyer flask was inoculated to an OD_{600} of 0.05 with the preculture and grown at 37 °C (130 RPM) until an OD_{600} of 0.6–0.8 was reached. Cultures were allowed to chill at RT for 30 min prior to induction with 500 µM IPTG. Protein production was then carried out overnight at 25 °C (130 RPM). Expression cultures were harvested by centrifugation (4,500 RPM, 15 min, 4 °C), the supernatant was discarded, the cell pellets were resuspended in an appropriate amount of binding buffer (20 mM Tris-HCl, 500 mM NaCl, 5 mM imidazole, pH 7.5), and cell suspensions stored at –20 °C until needed.

V.4.9.2 Protein Synthesis of Prodiginine Ligases

Precultures of *E. coli* BL21(DE3), harbouring the pET28a(+) expression vectors (see Table V.4), were prepared by inoculating LB media (50 µg/mL kan) with a single colony of the respective strain. Cultures were incubated overnight at 37 °C (130 RPM).

For the heterologous protein synthesis of the prodiginine ligases PigC, TamQ, TreaP, and the pET28a(+) empty vector control, 2 x 1 L of TB medium (50 µg/mL kanamycin) in a 3 L baffled flask was inoculated to an OD_{600} of 0.05 with the preculture and grown at 37 °C (130 RPM) until an OD_{600} of 0.6–0.9 was reached. Cultures were allowed to chill at RT for 15 min prior to induction with 100 µM IPTG. Protein production was then carried out overnight at 25 °C (130 RPM). Expression cultures were harvested by centrifugation (4,500 RPM, 15 min, 4 °C), the supernatant was discarded, and the dry cell pellets were stored at –20 °C until further use.

V.4.10 Plate Killing Assay

The plate killing assay was used to assess the cytotoxic potential of pyocin S2 and its conjugates against selected strains of *P. aeruginosa*. To display cytotoxic activity, PyoS2 must display cellular binding, membrane translocation, and intracellular DNase activity. First, LB medium is inoculated with a single colony of the desired *P. aeruginosa* strain and incubated overnight at 37 °C on a rotary shaker. 20 mL of LB medium is then inoculated with 200 µL of overnight culture and incubated at 37 °C for 2.5–3 h to obtain a visible turbidity (OD_{600} not measured). 5 mL of this exponential day culture is mixed with 45 mL liquid 0.7% LB soft-agar (kept at 50 °C until needed) and 7 mL of this culture is immediately added to a 1.4% LB agar plate to cover the 1.4% LB agar base with a layer of immobilised cells. After hardening at room temperature, the plates are briefly dried under the safety cabinet and 5 µL of protein dilutions (10 µM–57 pM) in sterile-filtered dialysis buffer is spotted onto the surface. After evaporating excess liquid under the safety cabinet, the plates are incubated overnight at 37 °C and the killing activity is subsequently documented by photography. Clear spots of inhibited bacterial growth indicate cytotoxic activity related to PyoS2 treatment.

V.4.11 Liquid Growth Inhibition Assay

The liquid growth inhibition assay was used to validate PyoS2 killing and killing activity of its conjugates against *P. aeruginosa* PAO1 and W15Dec1 in liquid media. To do so, LB medium is inoculated with a single colony of the

desired *P. aeruginosa* strain and incubated overnight at 37 °C on a rotary shaker. 20 mL of LB medium is then inoculated with overnight cultures of *P. aeruginosa* PAO1 or W15Dec1 to an OD_{600} of 0.05 and distributed to a 24-well plate (ThermoScientific, Nunclon Delta Surface, Catalogue No. 142475, sterile, flat well bottom, transparent with lid) with 2 mL per well. The plate is incubated in a MolecularDevices SpectraMax ID3 plate reader at 37 °C with medium shaking, and the optical density is monitored at 600 nm in intervals of 2 min (for instrument settings see below). For strain W15Dec1, 30 µL of filter-sterilised dialysis buffer, 30 µL of 50 µM PyoS2 (750 nM final concentration), or 30 µL of 50 µM PyoS2 Y640C-AlF350 (750 nM final concentration) is added after 1:49 h. For strain PAO1, the same proteins and volumes are added after 2:51 h. Monitoring of triplicate samples is continued until a total incubation time of 1000 min is reached. Dialysis buffer is used as a negative control and LB medium as a blank sample for background subtraction.

The following data record parameters were used:
Device: Molecular Devices SpectraMax iD3; Temperature: 37 °C; Mode: Kinetic [Time: 15:00 h, Interval: 02:00 min, Reads: 451, Min. Interval: 01:57 min, Absorbance: 600 nm]; Plate type: 24 well standard clear bottom (landscape, lidded, 23 mm height); Additional settings: shake before first read (5 s, medium speed, orbital), shake between reads (100 s, medium speed, orbital), speed read (On), read order (Row), show optimizer (On).
Before the first read, plate optimisation was performed (ca. 9 min) with the filled plate already in the instrument at 37 °C.

V.4.12 Isolation and Identification of *P. aeruginosa* Strains from Human Patients

Multidrug-resistant *P. aeruginosa* strains were isolated from anonymised clinical specimens obtained from human patients at the University Hospital Düsseldorf between 2002 and 2020. Isolation and identification were performed using standard diagnostic microbiology procedures, including culturing on selective and non-selective agar media (e.g., cetrimide agar, blood agar). Species were confirmed by using matrix-assisted laser desorption/ionisation-time of flight (MALDI-TOF) mass spectrometry (Vitek MS, bioMérieux, Germany) and antimicrobial susceptibility testing with the semi-automatic VITEK-2 system (bioMérieux, Nürtingen, Germany) and agar-diffusion using EUCAST guidelines (v 12.0, 2020) and breakpoints. For long-term storage, bacterial strains were preserved at −80 °C in Microbank vials (Pro-Lab Diagnostics Inc., Toronto, Canada). For a detailed list of clinical isolates used in this work, see Table IX.9 (Supporting Information). For the results of antimicrobial susceptibility testing (only available for the core strain collection of *fpvAI*-positive isolates), see Table IX.10 (Supporting Information).

V.4.13 Characterisation of ESBL and Carbapenemase Genes

All *P. aeruginosa* isolates showing resistance to the carbapenems imipenem/meropenem during antimicrobial susceptibility testing were subjected to multiplex real-time PCR analysis to identify the encoded ESBL or carbapenemase resistance genes. Strains were plated on MacConkey agar and a single colony was suspended in 20 mM Tris-HCl, 1 mM EDTA, pH 8 (200 µL). Cells were lysed by heating at 95 °C for 10 min, followed by centrifugation (10,000 x g, 10 min, 4 °C). The DNA-containing supernatant (150 µL) was transferred into a new tube and stored at −20 °C for further analyses via multiplex PCR.

The isolated DNA of all *P. aeruginosa* isolates was then analysed in an in-house TaqMan-based multiplex real-time PCR protocol, established for the detection of the most common carbapenemase genes (*bla*$_{IMP}$, *bla*$_{VIM-1}$, *bla*$_{VIM-2}$, *bla*$_{GIM-1}$, *bla*$_{GES}$, *bla*$_{OXA-48}$, *bla*$_{NDM-1}$ and *bla*$_{KPC}$).[600, 773] DNA oligonucleotides and fluorescently-labelled TaqMan probes used for the detection of β-lactamase resistance genes are summarised in Table V.3.

V.5 Molecular Biology Methods

V.5.1 DNA Oligonucleotides

DNA oligonucleotides were used as primers for DNA sequencing according to Sanger, for PCR amplification of genes in the process of molecular cloning, for PCR-based multiplex detection of siderophore subtypes in *P. aeruginosa*, or as molecular probes for MBL genes in MDR clinical isolates of *P. aeruginosa*. These oligonucleotides were ordered at Sigma Aldrich (Merck) in quantities of 0.025 µmol (desalted), dissolved in deionised water to 100 µM upon arrival, and stored at –20 °C. All DNA oligonucleotides used throughout this work are summarised in Table V.3.

Table V.3. DNA oligonucleotides for cloning of PyoS2 mutants, Sanger sequencing, and multiplex PCR characterisation in MDR isolates of *P. aeruginosa* regarding their *fpvA* subtypes (this work) and MBL genes (at UKD Düsseldorf).

Primer	Sequence (5'-3')	Purpose
	Cloning Primers	
TWE01	TATGGCTAGCATGGCTGTCAATGATTACG	*pyoS2_imS2_His$_6$* cloning into pET21a(+)
TWE02	TAATACTCGAGACCGGCCTTAAAGCCAGGAAGC	
TWE09	GGAAATCTTGGACTTCATATCAACACTTCCCTCCCTTGTGGATTTC	Introduction of a *C*-terminal cysteine residue in PyoS2
TWE10	GAAATCCACAAGGGAGGGAAGTGTTGATATGAAGTCCAAGATTTCC	
TWE17	CGTAATCATTGACAGCCATATGTATATCTCCTTCTTAAAG	Deletion of 3 N-terminal AA from the *Nhe*I cloning
TWE18	CTTTAAGAAGGAGATATACATATGGCTGTCAATGATTACG	
TWE13	GAATAAAGATCGAAATCCACGCAAAGGTTCGAATAGCAGATG	AA substitution H657A into the cytotoxic domain of PyoS2
TWE14	CATCTGCTATTCGAACCTTTGCGTGGATTTCGATCTTTATTC	
TWE15	CAAAACGTCATATAGAAATCGCAAAGGGAGGGAAGTGATATG	AA substitution H685A into the cytotoxic domain of PyoS2
TWE16	CATATCACTTCCCTCCCTTTGCGATTTCTATATGACGTTTTG	
TWE19	GAAATCTTGGACTTCATATCAACACTTCCCTCCCTTTGCGATTTC	Addition of *C*-term. cysteine to PyoS2 H657A H685A
TWE20	GAAATCGCAAAGGGAGGGAAGTGTTGATATGAAGTCCAAGATTTC	
TWE23	CCGAAAGTCCCGCCAGTTACAGAATGTCTTACCACGTAG	Introduction of the AA substitution K602C in PyoS2
TWE24	CTACGTGGTAAGACATTCTGTAACTGGCGGGACTTTCGG	
TWE25	GAGCCAATTACCGCTGACGGGACATCCCTTGCCAGTCGCAGCACCAG	Introduction of the AA substitution Q570C in PyoS2
TWE26	CTGGTGCTGCGACTGGCAAGGGATGTCCCGTCAGCGGTAATTGGCTC	
TWE29	CCTGTTCTGACTCTCTGACACAAGGAGCCCCTCCATCTCTCATTACAGC	Introduction of the AA substitution Y640C in PyoS2
TWE30	GCTGTAATGAGAGATGGAGGGGCTCCTTGTGTCAGAGAGTCAGAACAGG	
TWE49	[Phos]CATTACAGCTAAACTACCAGGATCAAACTGTTTACTTAACTCAG	AA substitutions N626D D635A in PyoS2
TWE50	[Phos]AGAGCTGGAGGGGCTCCTTATGTCAGAGAGTCAGAAC	
TWE51	[Phos]ATTTTCTGAATCTCTGACAGCAGGAGCCCCTCCAGCTCTCATTAC	[a]
TWE52	[Phos]GCTGGCGGGAGAATAAATATCGAAATCCACCACAAGGTTCGAATAG	[b]
TWE53	[Phos]ATTTTCTGAATCTCTGACACAAGGAGCCCCTCCAGCTCTCATTAC	[c]
	Sequencing Primers	
T7	TAATACGACTCACTATAGGG	For T7-based pET vectors
T7term	CTAGTTATTGCTCAGCGGT	For T7-based pET vectors
Seq_TWE01	TAGAGGGAACCGTAACCTCGTAC	For *pyoS2_imS2* inserts
Seq_TWE03	CCGGTAGTGTAATCACCCCAGGATAG	For *pyoS2_imS2* inserts
Seq_TWE04	CGATCTATGTGATGTTCAGGGATC	For *pyoS2_imS2* inserts

Table V.3 (continued).

***fpvA* and *pyoS2_imS2* Multiplex Primers for Detection in *P. aeruginosa* Genomes**		
FpvAI-F	CGAAGGCCAGAACTACGAGA	*fpvAI* detection
FpvAI-R	TGTAGCTGGTGTAGAGGCTCAA	(326 bp fragment)
FpvAII-F	TACCTCGACGGCCTGCACAT	*fpvAII* detection
FpvAII-R	GAAGGTGAATGGCTTGCCGTA	(897 bp fragment)
FpvAIII-F	ACTGGGACAAGATCCAAGAGAC	*fpvAIII* detection
FpvAIII-R	CTGGTAGGACGAAATGCGAG	(506 bp fragment)
PyoS2_ImS2-F	CAAGCGATCTCCGATGCGATTG	*pyoS2_imS2* detection
PyoS2_ImS2-R	CTCCAGCTGGGCTATCTTCTC	(1223 bp fragment)
Carbapenemase Multiplex Primers and Dual-Labelled TaqMan Probes		
NDM1-S	6-FAM-GCGACTTGGCCTTGCTGTCCTTG-BHQ-1	NDM-1 probe
NDM1-F	CGGCATCACCGAGATTGC	NDM-1 forward primer
NDM1-R	CACCGACATCGCTTTTGGT	NDM-1 reverse primer
VIM-1-S	6-FAM-CTTCTATCCTGGTGCTGCGCATTCG-BHQ-1	VIM-1 probe
VIM-1-F	TGCGCTTCGGTCCAGTAGA	VIM-1 forward primer
VIM-1-R	TGACGGGACGTATACAACCAGAT	VIM-1 reverse primer
VIM-2-S	6-FAM-CTTCTATCCTGGTGCTGCGCATTCG-BHQ-1	VIM-2 probe
VIM-2-F	GCGCTTCGGTCCAGTAGAAC	VIM-2 forward primer
VIM-2-R	CTCGCAGACGGGACGTACA	VIM-2 reverse primer
KPC-S	6-FAM-CAGTCGGAGACAAAACCGGAACCTGC-BHQ-1	KPC probe
KPC-F	GCAGCGGCAGCAGTTTGTTGATT	KPC forward primer
KPC-R	GTAGACGGCCAACACAATAGGTGC	KPC reverse primer
OXA-48-S	Hex-CTGGCTGCGCTCCGATACGTGTAACTTATTG-BHQ-1	OXA-48 probe
OXA-48-F	TTCGGCCACGGAGCAAATCAG	OXA-48 forward primer
OXA-48-R	GATGTGGGCATATCCATATTCATCGCA	OXA-48 reverse primer
GES-S	TexasRed-CGACCTCAGAGATACAACTACGCCTATTGC-BHQ-2	GES probe
GES-F	CGGTTTCTAGCATCGGGACACAT	GES forward primer
GES-R	CCGCCATAGAGGACTTTAGCMACA	GES reverse primer
GIM-S	Hex-ACACGAAGTTGTTATTATCCTGGGCGACTGAC-BHQ-1	GIM-1 probe
GIM-F	CGACACACCTTGGTCTGAAGAA	GIM-1 forward primer
GIM-R	GATGCTAGCCATAACCTGGTATCC	GIM-1 reverse primer
IMP-S	Hex-CGATCTATCCCCACGTATGCATCTGAATTAACA-BHQ-1	IMP probe
IMP-F	GGGCGGAATAGAGTGGCTTA	IMP forward primer
IMP-R	GGCTTGAACCTTACCGTCTTTTT	IMP reverse primer

[a] Introduction of the AA substitutions N626D D635A Y640A E643D Q646N K652N in PyoS2 (referred to as PyoS2 ID). [b] Introduction of the AA substitutions N626D D635A E643D Q646N K652N and Y640A or Y640C in PyoS2 (referred to as PyoS2 ID or PyoS2 ID Y640C, respectively). [c] Introduction of the AA substitutions N626D D635A Y640C E643D Q646N K652N in PyoS2 (referred to as PyoS2 ID Y640C). Abbreviations: AA – amino acid; BHQ-1 – black Hole Quencher 1; 6-FAM – 6-carboxyfluorescein; Hex – hexachlorofluorescein.

V.5.2 Plasmids

Plasmid DNA was used to transform susceptible bacteria of *E. coli* with exogenous DNA for cloning and heterologous protein synthesis. All plasmids used or generated in this work are based on the pBR322 plasmid and the T7 polymerase system under the control of the LacI repressor protein and the *lac* operator. The plasmids and their genetic features are summarised in Table V.4. All plasmids were stored in deionised water at –20 °C for daily use and at –80 °C for long-term storage.

Table V.4. Plasmids used and generated in this work. The genotype displayed by each plasmid is specified, primer pairs and the corresponding template DNAs for the generation of the listed plasmids and the PCR-based methods are given.

Plasmid	Genotype	Encoded Proteins	Method	Template	Primers[a]	Reference
Empty Vectors						
pET21a(+)	*amp*^{R}, pBR322 Ori, T7 promoter, T7 terminator, *lacI*, *lacO*	None	–	–	–	Novagen
pET28a(+)	*kan*^{R}, pBR322 Ori, T7 promoter, T7 terminator, *lacI*, *lacO*	None	–	–	–	Novagen
Pyocin S2 Vectors						
pTWE01	pET21a(+), *MAS-pyoS2*, *imS2-His$_6$*	MAS-PyoS2, ImS2-His$_6$	RL	PAO1 gDNA	01 / 02	this work
pTWE04	pET21a(+), *pyoS2-H657A-H685A*, *imS2-His$_6$*	PyoS2 H657A H685A, ImS2-His$_6$	QC	pTWE08	15 / 16	this work
pTWE05	pET21a(+), *pyoS2-H657A-H685A-C-Cys*, *imS2-His$_6$*	PyoS2 H657A H685A C-Cys, ImS2-His$_6$	QC	pTWE04	19 / 20	this work
pTWE08	pET21a(+), *pyoS2-H657A*, *imS2-His$_6$*	PyoS2 H657A, ImS2-His$_6$	QC	pTWE10	13 / 14	this work
pTWE09	pET21a(+), *pyoS2-H685A*, *imS2-His$_6$*	PyoS2 H685A, ImS2-His$_6$	QC	pTWE10	15 / 16	this work
pTWE10	pET21a(+), *pyoS2*, *imS2-His$_6$*	PyoS2, ImS2-His$_6$	QC	pTWE01	17 / 18	this work
pTWE13	pET21a(+), *pyoS2-C-Cys*, *imS2-His$_6$*	PyoS2 C-Cys, ImS2-His$_6$	QC	pTWE10	09 / 10	this work
pTWE14	pET21a(+), *pyoS2-K602C*, *imS2-His$_6$*	PyoS2 K602C, ImS2-His$_6$	QC	pTWE10	23 / 24	this work
pTWE15	pET21a(+), *pyoS2-K602C-H657A-H685A*, *imS2-His$_6$*	PyoS2 K602C H657A H685A, ImS2-His$_6$	QC	pTWE04	23 / 24	this work
pTWE16	pET21a(+), *pyoS2-Q570C*, *imS2-His$_6$*	PyoS2 Q570C, ImS2-His$_6$	QC	pTWE10	25 / 26	this work
pTWE17	pET21a(+), *pyoS2-Q570C-H657A-H685A*, *imS2-His$_6$*	PyoS2 Q570C H657A H685A, ImS2-His$_6$	QC	pTWE04	25 / 26	this work
pTWE18	pET21a(+), *pyoS2-Y640C*, *imS2-His$_6$*	PyoS2 Y640C, ImS2-His$_6$	QC	pTWE10	29 / 30	this work
pTWE19	pET21a(+), *pyoS2-Y640C-H657A-H685A*, *imS2-His$_6$*	PyoS2 Y640C H657A H685A, ImS2-His$_6$	QC	pTWE04	29 / 30	this work
pTWE21	pET21a(+), *pyoS2 ID*, *imS2-His$_6$*	PyoS2 ID, ImS2-His$_6$	RTH	pTWE30	51 / 52	this work
pTWE24	pET21a(+), *pyoS2 ID-Y640C*, *imS2-His$_6$*	PyoS2 ID Y640C, ImS2-His$_6$	RTH	pTWE30	52 / 53	this work
pTWE30	pET21a(+), *pyoS2-N626D-D635A*, *imS2-His$_6$*	PyoS2 N626D D635A, ImS2-His$_6$	RTH	pTWE10	49 / 50	this work
Prodigiosin Ligase Vectors						
pPIGC_3	pET28a(+), *pigC*	PigC	–	–	–	[391]
pET28a(+)::*tamQ*	pET28a(+), *tamQ*	TamQ	–	–	–	[877]
pET28a(+)::*treaP*	pET28a(+), *treaP*	TreaP	–	–	–	[877]

[a] TWE Primer No.'s from Table V.3. Abbreviations: PyoS2 ID – PyoS2 interaction-deficient (PyoS2 N626D D635A Y640A E643D Q646N K652N); QC – QuickChange; RL – Restriction-Ligation; RTH – Round-the-Horn.

V.5.3 Molecular Cloning Methods

Molecular cloning was used to integrate specific genes of interest into high-copy number cloning vectors and to introduce site-specific mutations, which facilitate purification of heterologously produced proteins (His-tag), change the properties of certain proteins (e.g. inactivation), or enable their *in vitro* labelling (cysteine substitutions). All methods applied in this thesis are predicated on the polymerase chain reaction (PCR), which resembles the natural phenomenon of DNA replication in a cell-free environment and allows site-specific manipulation of DNA fragments by utilising customised DNA oligonucleotides, called primers. The thermostable Phusion High-Fidelity DNA polymerase (2 U/µL, Thermo Fisher Scientific) was used for all cloning and DNA amplification applications, described in the following section. Furthermore, FastDigest restriction endonucleases (DpnI, XhoI, and NheI, Thermo Fisher Scientific), the T4 DNA ligase (5 U/µL, Thermo Fisher Scientific), 10 mM dNTP mix (Thermo Fisher Scientific), and FastAP alkaline phosphatase (1 U/µL, Thermo Fisher Scientific) were used for the following cloning procedures.

V.5.3.1 Restriction-Ligation (RL) Cloning

RL Cloning is the traditional cloning method and makes use of unique sequence recognition patterns of DNA endonucleases (restriction enzymes) in combination with DNA ligases. These endonucleases cut dsDNA and produce 5'-phosphorylated fragments with palindromic 5'-overhangs (sticky ends) or without overhangs (blunt ends). When two fragments with identical overhangs align, hybridisation between pairing DNA bases takes place and both fragments can be merged by DNA ligating enzymes (Figure V.1). As the 5'-end is already phosphorylated, RL ligation cloning supersedes the use of phosphorylated oligonucleotides. However, to reduce self-ligation of the vector backbone, which would result in false-positive clones during microbial selection on antibiotic-supplemented agar, the vector backbone can be dephosphorylated using alkaline phosphatase. While restriction enzymes in principle can be applied to any DNA molecule (genomic DNA, plasmid DNA, oligonucleotides, environmental DNA, etc.), restriction sites are typically not located in the sequence where needed for sophisticated DNA manipulation. Thus, DNA fragments of interest are commonly amplified by PCR first, to increase the DNA concentration on the one hand, and allow the attachment of custom DNA fragments on the other hand. These custom DNA fragments can be used to introduce or remove restriction sites, start and stop codons, barcodes, or tags for protein purification.

In this work, the tandem sequence of *pyocin S2* and its *immunity protein imS2* was first PCR-amplified from isolated genomic DNA of *P. aeruginosa* PAO1. Through the design of oligonucleotides TWE01 and TWE02, the 5'-end of the sequence was equipped with an NheI restriction site and the 3'-end with an XhoI site for cloning into the multiple cloning site of the pET21a(+) expression vector. As the multiple cloning site of the expression vector is equipped with an NheI restriction site downstream of the T7 promoter and an additional XhoI site upstream of the T7 terminator, the *pyoS2_imS2* tandem can be heterologously expressed in suitable T7 DNA polymerase expression strains. Moreover, the XhoI site of the plasmid is in frame with a C-terminal hexa-His-tag, which was purposely added to the C-terminus of the *imS2* gene by utilisation of the XhoI restriction site.

For PCR-amplification of the *pyoS2_imS2* tandem from genomic DNA of *P. aeruginosa*, the following ingredients were mixed in a PCR tube: 5x HF buffer (10 µL), DMSO (3 µL), 10 mM dNTP mix (1 µL), 10 µM forward primer (1 µL, TWE01), 10 µM reverse primer (1 µL, TWE02), DNA template (1 µL of 30 ng/µL *P. aeruginosa* PAO1 genomic DNA), nuclease-free water (32.5 µL), Phusion polymerase (0.5 µL).
In the following step, the target DNA sequence was amplified according to the following PCR protocol:

Initial denaturation: 2 min – 98 °C; [30x cycles: denaturation: 30 s – 98 °C; annealing: 30 s – 72 °C; elongation: 75 s – 72 °C]; final elongation: 10 min – 72 °C; storage: infinite – 10 °C. Then, the PCR product was purified via agarose gel electrophoresis (Chapter V.5.5) and eluted from the gel (Chapter V.5.6).

In the next step, the 3 ng of pET21a(+) vector and 6 ng of the PCR product of *pyoS2_imS2* were separately digested with NheI and XhoI FastDigest restriction endonucleases for 1 h at 37 °C to generate sticky DNA overhangs. Therefore, DNA was mixed with 10x FastDigest buffer (2 µL) and both restriction enzymes (each 1 µL), before being finally filled with water to a total reaction volume of 20 µL. After completion of the restriction reaction, the linearised vector backbone was subjected to dephosphorylation with alkaline phosphatase (1 µL) at 37 °C for 10 min to minimise self-ligation of the vector backbone during the ligation reaction.

Next, the vector backbone and insert were ligated using T4 DNA ligase. Therefore, vector and insert were mixed in a 1:3 molar ratio (1.5 ng of vector backbone and 2 ng of insert used) and supplemented with 10x T4 DNA ligase buffer (2 µL), T4 DNA ligase (1 µL), and nuclease-free water to a total reaction volume of 20 µL. After ligation at ambient temperature for 2 h, *E. coli* DH5α was transformed according to the heat-shock protocol (Chapter V.4.7) with 5 µL of the purified RL PCR product and plated on LB agar with supplemented antibiotics. Plasmid DNA was subsequently isolated from single transformants (Chapter V.5.7) and the gene of interest verified by Sanger sequencing (Chapter V.5.8).

V.5.3.2 Quick-Change (QC) Cloning

Quick-Change site-directed mutagenesis allows for restriction-independent cloning and was used to introduce point mutations into the sequence of *pyoS2* (cf. Table V.4). The two primers are complementary and harbour the desired mutation in the middle of the sequence (Figure V.1). Caused by the complementary primer design, the melting temperatures are very high, which makes GC-rich sequences difficult to address. Moreover, the melting temperature limits the length of the mutable sequence. Therefore, sequential primer addition to the PCR reaction is a reasonable approach to reduce undesired interactions between the DNA oligonucleotides. As both primers bind to the identical section of the DNA template, a PCR product cannot serve as a template for a second round of mutagenesis, which is why the QC method only provides a linear increase of PCR product. To separate the unmutated template vector from mutated PCR products, the DNA endonuclease DpnI is used. This bacterial endonuclease cleaves methylated and hemimethylated DNA, but leaves non-methylated DNA untouched. As the *E. coli* DNA adenine methylase (DAM) methylates chromosomal and plasmid DNA for increased protection and stability *in vivo*, the template plasmids isolated from this organism are DpnI degradable. In contrast, the *in vitro*-generated PCR products are non-methylated, which is why PCR products remain unharmed in solution. A remarkable benefit of QC cloning is the fact that both synthesised DNA strands share complementary ends, which originate from the designed DNA oligonucleotides. Thus, the strands readily hybridise and form a stable nicked plasmid. The high stability supersedes the use of DNA ligating enzymes *in vitro*. Instead, the DNA can be immediately used for transformation, and the DNA nicks are repaired by the *E. coli* DNA ligase *in vivo* after uptake.

For QC mutagenesis, the following representative protocol with sequential primer addition (developed for the cloning of pTWE10) was used:
5x HF or GC buffer (10 µL), DMSO (3 µL), 10 mM dNTP mix (1 µL), 10 µM forward primer (1 µL, TWE17), nuclease-free water (33.5 µL), template DNA (1 µL, pTWE01 at 30 ng/µL), Phusion polymerase (0.5 µL). The reverse primer was added after 20 PCR reaction cycles, allowing for reduced annealing temperatures during the PCR-amplification.
In the following step, the target DNA sequence was amplified according to the following two-step PCR protocol:

Step 1: Initial denaturation: 2 min – 98 °C; [20x cycles: denaturation: 30 s – 98 °C; annealing: 30 s – 55 °C; elongation: 120 s – 72 °C].
Then, the reverse primer (1 µL, TWE18) was added to the PCR product and a second amplification sequence was performed.
Step 2: Initial denaturation: 2 min – 98 °C; [20x cycles: denaturation: 30 s – 98 °C; annealing: 30 s – 55 °C; elongation: 120 s – 72 °C]; final elongation: 10 min – 72 °C; storage: infinite – 10 °C.

Subsequently, FastDigest DpnI (1 µL) was added to the PCR reaction to degrade the hemi-methylated template DNA. After incubation at 37 °C for 1 h, the PCR product was purified via agarose gel electrophoresis (Chapter V.5.5) and eluted from the gel (Chapter V.5.6). *E. coli* DH5α was transformed according to the heat-shock protocol (Chapter V.4.7) with 5 µL of the purified QC PCR product and plated on LB agar with supplemented antibiotics. Plasmid DNA was subsequently isolated from single transformants (Chapter V.5.7) and the gene of interest verified by Sanger sequencing (Chapter V.5.8).

V.5.3.3 Round-the-Horn (RTH) Cloning

Round-the-Horn site-directed mutagenesis was employed to introduce multiple site-specific mutations into the sequence of *pyoS2* in one mutagenesis step (Table V.4). While QC cloning suffers from very high melting temperatures of the complementary primer sets and linear amplification of DNA fragments, RTH cloning offers a straightforward alternative to circumvent these issues. RTH primers are 5'-phosphorylated and, in contrast to regular primer-assisted amplification of genes or DNA fragments, these primers bind "back-to-back" (Figure V.1). In consequence, these primers possess lower melting temperatures and cover a larger section of the sequence, allowing for the introduction of multiple far-distant mutations at the same time. Furthermore, the whole plasmid is exponentially amplified rather than a single gene. After DpnI digestion of the methylated DNA template, only the non-methylated PCR product remains unharmed and through the utilisation of phosphorylated primers, the linearised plasmid can be ligated with T4 DNA ligase *in vitro* before bacterial strains are transformed with the newly synthesised circular DNA.

For RTH mutagenesis, the following representative protocol (developed for the cloning of pTWE21) was used:
5x HF buffer (10 µL), DMSO (3 µL), 10 mM dNTP mix (1 µL), 10 µM forward primer (1 µL, TWE51), 10 µM reverse primer (1 µL, TWE52), DNA template (1 µL, pTWE30 at 30 ng/µL), nuclease-free water (32.5 µL), Phusion polymerase (0.5 µL).
In the following step, the target DNA sequence was amplified according to the following PCR protocol:
Initial denaturation: 2 min – 98 °C; [30x cycles: denaturation: 30 s – 98 °C; annealing: 30 s – 60 °C; elongation: 120 s – 72 °C]; final elongation: 10 min – 72 °C; storage: infinite – 10 °C.

Subsequently, FastDigest DpnI (1 µL) was added to the PCR reaction to degrade the methylated template DNA. After incubation at 37 °C for 1 h, the PCR product was purified via agarose gel electrophoresis (Chapter V.5.5) and eluted from the gel (Chapter V.5.6).
In the next step, the linearised vector was circularised in a ligation reaction. Therefore, 50 ng of the purified PCR product were mixed with 10x T4 ligase buffer (5 µL), T4 DNase ligase (1 µL) and supplemented with nuclease-free water to a total reaction volume of 50 µL. After ligation at ambient temperature for 2 h, *E. coli* DH5α was transformed according to the heat-shock protocol (Chapter V.4.7) with 5 µL of the purified RTH PCR product and plated on LB agar with supplemented antibiotics. Plasmid DNA was subsequently isolated from single transformants (Chapter V.5.7) and the gene of interest verified by Sanger sequencing (Chapter V.5.8).

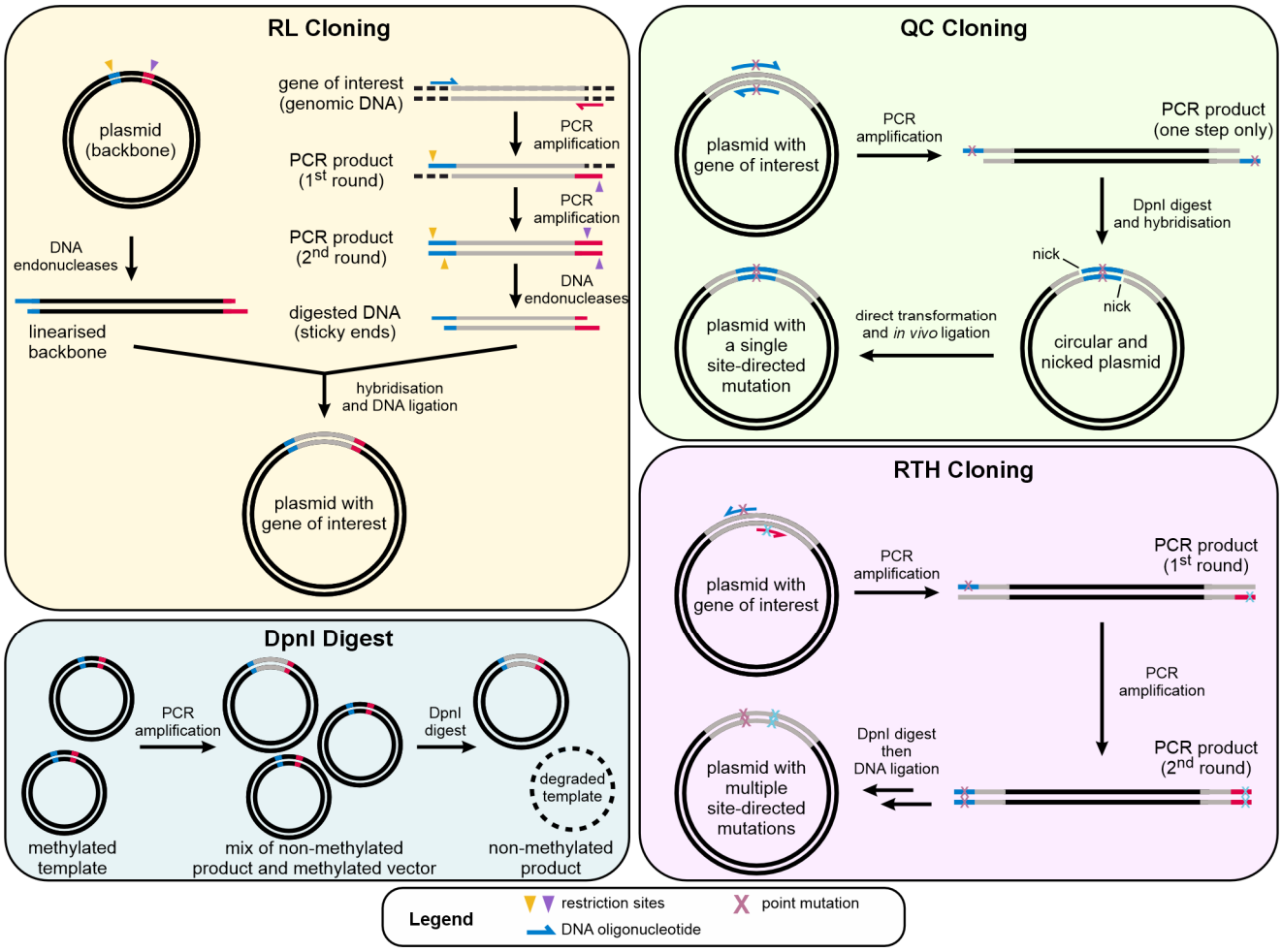


Figure V.1. Applied methods for molecular cloning and site-directed mutagenesis of *pyoS2* and *imS2* from *P. aeruginosa* PAO1. While Restriction-Ligation (RL) Cloning makes use of DNA endonucleases and their unique recognition patterns to join DNA fragments with complementary overhangs, Quick-Change (QC) and Round-the-Horn (RTH) Cloning use modified oligonucleotides to introduce site-specific mutations. Furthermore, both of the latter methods profit from the nucleolytic activity of DpnI. The bacterial endonuclease DpnI cleaves methylated and hemimethylated DNA, but leaves non-methylated DNA untouched. As the *E. coli* DNA adenine methylase (DAM) methylates chromosomal and plasmid DNA for increased protection and stability *in vivo*, the template plasmids isolated from this organism are DpnI degradable. In contrast, the *in vitro*-generated PCR products are non-methylated, which is why PCR products remain unharmed in solution.

V.5.4 DNA Quantification

DNA was quantified using a NanoDrop OneC Nanovolume UV-Vis Spectrophotometer (Thermo Fisher Scientific) by exploitation of the intrinsic absorption of aromatic DNA bases at 260 nm. Sample volumes of 1 µL were applied to the crystal and the absorption A_{260} was measured. Deionised water was used as a blank sample. Furthermore, the purity of isolated DNA was assessed using the quotient A_{260}/A_{280} which is approximately 1.8 for pure DNA. Values smaller 1.8 indicate contaminations with proteins, whereas values greater 1.8 indicate the presence of RNA impurities.

V.5.5 Agarose Gel Electrophoresis

Agarose gel electrophoresis was employed to separate and visualise DNA fragments in the processes of cloning (for purification of PCR products and endonuclease-treated DNA), genomic DNA isolation (for purity assessment of *P. aeruginosa* genomic DNA), and plasmid nicking assays (to evaluate time-resolved DNA fragmentation).

Firstly, a 0.8% agarose solution in 1x TAE buffer was prepared and heated in a microwave until the agarose was fully dissolved. After cooling to 60 °C, but before polymerisation at room temperature, the non-toxic and DNA intercalating stain GelRed was added to a final concentration of 1x (10,000x stock in water) and thoroughly dissolved in the agarose solution. The agarose was poured into a suitable mould and left at ambient temperature for polymerisation. The gel was then loaded with adequate amounts of DNA samples, which were premixed with 6x DNA loading dye to a 1x dye concentration and finalised by the addition of 2.5 µL of 1 kb DNA ladder. The gels were run in 1x TAE buffer [40 mM Tris, 20 mM acetate, 1 mM EDTA, pH 8.6 (not adjusted)] at 180 V for 45 min and subsequently analysed and documented on an INTAS Science Imaging gel documentation system, which visualises DNA by excitation of the DNA intercalated GelRed dye with UV light.

V.5.6 DNA Isolation from Agarose Gels

PCR products or enzymatically digested DNA fragments were isolated from preparative agarose gels by the commercial Innuscreen innuPREP DOUBLEpure Kit for further utilisation. In detail, DNA encapsulated within an agarose gel was visualised on a UV transillumination table and the desired band was cut from the gel using a scalpel. The gel fragment was placed in a 2 mL reaction tube and 650 µL of Gel Solubiliser was added. The tube was incubated at 50 °C for 10 min and sporadically inverted to dissolve the gel. 50 µL of Binding Optimiser was added and after thorough mixing, the solution was added to the spin filters. Samples were centrifuged (11,000 x g, 1 min, 20 °C), the flow-through discarded, and the process repeated until all solubilised DNA was consumed. Spin filters were subsequently washed with 700 µL Washing Solution LS by centrifugation (11,000 x g, 1 min, 20 °C) and after removal of the flow through, the process was repeated once. Finally, the spin filters were dried from residual EtOH by centrifugation (21,300 x g, 2 min, 20 °C) and placed in a sterile 1.5 mL reaction tube. 30–50 µL of preheated (50 °C) water was added and after incubation for 1 min at ambient temperature, the DNA was recovered by centrifugation (11,000 x g, 1 min, 20 °C).

V.5.7 Isolation of Plasmid DNA

Plasmid DNA was either isolated for replication and reproduction of existing DNA constructs or to clone new DNA fragments into expression vectors and sequencing of these constructs. Using the commercial IST Innuscreen innuPREP Plasmid Mini Kit 2.0, the DNA was either isolated from *E. coli* DH5α or *E. coli* C43(DE3). DH5α is a laboratory strain, specifically designed for the high-yielding production of recombinant DNA. The strain is deficient in DNA recombinases and homologous recombination through a point mutation in *recA1* and does not express active DNA endonucleases, caused by the *endA1* mutation.[754, 878] In contrast, C43(DE3) is an expression strain, harbouring the lambda DE3 phage within its genome that allows heterologous expression of genes under the control of the T7 promoter. Other than *E. coli* BL21(DE3), C43(DE3) is equipped with additional uncharacterised point mutations, which confer high tolerance towards the heterologous expression of toxic proteins.[747] While DH5α was unable to grow in liquid cultures when transformed with plasmids carrying genetic variants of *pyoS2 ID*, the attribute of high tolerance against toxic metabolites of C43(DE3) rendered this strain ideal for cloning of pET21 vectors with mutants of *pyoS2 ID*.

Bacterial strains transformed with plasmid DNA via the heat-shock procedure were used to inoculate 5 mL of LB medium (supplemented with suitable antibiotics) and the cultures were grown overnight at 37 °C on a rotary shaker. Cells were sedimented by centrifugation (20,000 x g, 2 min, 20 °C) and the supernatant was discarded. The pellet was resuspended in 250 µL resuspension buffer, and alkaline lysis was initiated by adding 250 µL lysis buffer. After a maximum of 5 min incubation, 350 µL of neutralisation buffer was added to precipitate proteins and cell debris by forming an insoluble potassium-SDS-protein complex. After centrifugation (21,300 x g, 10 min, 4 °C),

the supernatant was carefully transferred into the spin filter and passed through the membrane via centrifugation (11,000 x g, 1 min, 20 °C). The procedure was repeated until all supernatant from the neutralisation step was consumed. The flow-through was discarded and the spin filters were successively washed with 500 µL of washing solution A and 700 µL of washing solution B, accompanied by a centrifugation step (11,000 x g, 20 °C, 1 min) for each washing solution. The spin filter was dried from residual washing solution by centrifugation (21,300 x g, 2 min, 20 °C) and transferred into a sterile 1.5 mL reaction tube. The precipitated plasmid DNA on the membrane was allowed to refold in 20–50 µL of sterile water (preheated to 50 °C) for 2 min and then recovered by centrifugation (11,000 x g, 20 °C, 1.5 min). Plasmid DNA was stored at –20 °C.

V.5.8 Sequencing of Plasmid DNA

Isolated plasmid DNA was sequenced using fluorescently labelled deoxynucleotides in the chain-termination approach with dideoxynucleotides, referred to as Sanger sequencing.[879] All DNA inserts of newly generated plasmids were thoroughly validated by Sanger sequencing by the commercial supplier Eurofins Genomics, using the sequencing primers found in Table V.3.

V.5.9 Isolation of Genomic DNA of *P. aeruginosa*

The genomic DNA of *P. aeruginosa* W15Dec1 and 15 MDR clinical isolates for subsequent Whole-Genome Sequencing was isolated using the Qiagen Blood & Cell Culture DNA Mini Kit and the protocol for preparation of Gram-negative bacterial samples. Briefly, the strains were grown overnight in LB medium at 37 °C and an OD_{600} of 2.0 was harvested by centrifugation (6,000 x g, 10 min, 21 °C). The supernatant was discarded and the pellet was thoroughly resuspended in 1 mL buffer B1 (supplemented with 2 µL 100 mg/mL RNase A) by vortexing. 20 µL of lysozyme stock solution (100 mg/mL in water) and 45 µL of Qiagen protease (reconstituted in 1.4 mL water) were added, and the bacterial suspension was incubated for 45 min at 37 °C for lysis. 350 µL of buffer B2 was added and the tube was vortexed for 5 s, followed by an incubation at 50 °C for 30 min. The sample was vortexed again for 10 s and applied to the Qiagen Genomic-Tip 20/G (equilibrated with 1 mL buffer QBT). After complete immersion of the sample into the resin, the 20/G column was washed with buffer QC (4 x 1 mL). Subsequently, the genomic DNA was eluted with prewarmed buffer QF at 50 °C (2 x 1 mL) and collected in a 15 mL tube. DNA was then precipitated by adding 1.4 mL *i*PrOH (0.7 volumes) at 20 °C and carefully inverting the tube 20 times. Immediate pelleting of the DNA by centrifugation (15,000 x g, 20 min, 4 °C) and careful removal of the supernatant yielded a white pellet, which was then washed with ice-cold 70% EtOH (1 mL, kept at –20 °C) by brief vortexing for 2 s and centrifugation (15,000 x g, 30 min, 4 °C). The supernatant was carefully discarded, and the pellet was air-dried for 10 min. Finally, the genomic DNA was resuspended by the addition of 2 mL TE buffer (10 mM Tris-HCl, 1 mM EDTA, pH 8.0) and incubation overnight at 55 °C with shaking at 400 RPM. A final centrifugation step (15,000 x g, 10 min, 4 °C) was applied to separate undissolved particles from reconstituted genomic DNA. The nucleic acid isolates were concentrated in a vacuum centrifuge at 60 °C to the desired concentration, then frozen in liquid nitrogen and finally stored at –20 °C until needed.

V.5.10 Whole-Genome Sequencing and Genome Assembly

Sequencing library preparation and whole genome sequencing of *P. aeruginosa* genomic DNA was performed by AZENTA/Genewiz (Leipzig, Germany) on an Illumina platform with the NovaSeq 2x150 bp paired-end configuration. A total amount of 2000 ng of genomic DNA of *P. aeruginosa* W15Dec1 and the 15 MDR clinical isolates from the core strain collection (see Figure IV.30C) was diluted in TE buffer (10 mM Tris-HCl, 1 mM EDTA, pH 8.0) to a final concentration of 200 ng/µL and a volume of 100 µL was submitted to AZENTA for NGS

sequencing. The obtained paired-end raw sequencing data in fastq format were uploaded to the European Galaxy Project webserver (usegalaxy.eu) for the subsequent processing and assembly steps.[783]

Raw paired-end 2×150 bp Illumina reads were first assessed with FastQC to evaluate base quality, adapter content, and sequence composition, and the reports were summarised with MultiQC. Adapter removal, quality trimming, and read filtering were then performed with fastp,[781] with parameters adjusted as follows: adapter sequence auto-detection enabled; qualified quality Phred score: 20; unqualified percent limit: 40; minimum read length: 50 bp; polyG tail trimming enabled (Illumina NovaSeq mode); and 3′ end trimming based on quality (window size: 4 bp; mean quality threshold: 20). The processed reads were re-analysed with FastQC, and the results were aggregated using MultiQC to confirm improvements in read quality.

De novo assembly was performed with Unicycler,[782] which internally employs SPAdes for short-read assembly, Bowtie2 for read alignment, BLAST+ for repeat resolution, and two iterations of polishing with Pilon to remove substitution and indel errors. Normal bridging mode was used and contigs shorter than 300 bp were excluded to reduce assembly artefacts. Assembly quality and completeness were evaluated using QUAST (for contiguity metrics), BUSCO (for single-copy orthologue recovery), and NCBI FCS-GX (for contamination screening). Read alignments were processed with SAMtools, and coverage across the assembled genome was visualised in JBrowse2. Annotation was conducted with Bakta[784] using a minimum contig size threshold of 300 bp, the Bakta database v5.1, and the AMRFinderPlus database v3.12, with the genus specified as *Pseudomonas* to optimise functional annotation. Genome assemblies and annotations were visualised and customised using Artemis[880] (Wellcome Sanger Institute).

Final genome assemblies (FASTA format) were deposited in the NCBI genome repository under the BioProject PRJNA1336694 and annotated using NCBI's PGAP pipeline.[785] The following DDBJ/ENA/GenBank accession numbers were assigned: W15Dec1 (JBRLAX000000000), M2 (JBRLBM000000000), M7 (JBRLBL000000000), M10 (JBRLBK010000000), M71 (JBRLBJ010000000), M74 (JBRLBI010000000), M132 (JBRLBH010000000), M134 (JBRLBG000000000), M189 (JBRLBF000000000), M190 (JBRLBE000000000), M191 (JBRLBD000000000), M210 (JBRLBC000000000), M294 (JBRLBB000000000), M303 (JBRLBA000000000), M315 (JBRLAZ000000000), and M324 (JBRLAY000000000). The sequencing raw data parameters and parameters of the final genome assemblies are summarised in Table V.5.

Table V.5. Data report for sequenced *P. aeruginosa* genomes of MDR isolates. Raw data were received in the fastq format.

Strain	Barcode Sequence	No. of Reads	Yield (Mbp)	Mean Q Score	% Bases (Q Score >30)	No. of Contigs	Genome (bp)	Min. Contig Size (bp)	Max. Contig Size (bp)	L50 Size (bp)	N50 Size (bp)	GC (%)	Complete-ness
W15Dec1	ATCGTCTC/ CAGGCGAA	9,285,458	2,786	34.83	87.76	79	6,698,123	300	901,982	6	372,878	66.20	99.4
M2	CCTTGTGA/ GGAGCTAG	3,853,188	1,156	35.24	90.07	122	7,258,366	307	519035	14	143,135	65.72	98.5
M7	CTCACCAT/ CCGGCATA	5,463,608	1,639	35.40	90.87	124	7,091,967	307	765,435	8	311,725	65.94	99.3
M10	CAAATTCT/ CCAACATT	3,398,215	1,019	35.45	91.13	85	7,033,220	326	584,220	9	241,750	65.82	99.3
M71	CTCCTCAC/ TATCCGAT	3,967,006	1,190	35.33	90.49	149	7,238,610	300	376,687	17	137,045	65.75	98.5
M74	ATGTGCAA/ GTCACTAT	3,794,165	1,138	35.19	89.77	99	6,534,215	302	551,780	11	209,766	66.24	99.0
M132	GCAAATGT/ CAGGGAGC	4,947,554	1,484	35.44	91.08	106	6,846,215	301	661,865	7	305,805	65.79	98.6
M134	ACGCATGG/ AATTGACT	3,555,544	1,067	35.41	90.93	97	6,931,305	301	565,035	10	256,649	65.95	99.1
M189	ACACCACC/ AGCGTATT	4,388,589	1,317	35.32	90.51	142	6,835,758	300	399,387	13	182,508	66.01	98.8
M190	CACGCTGA/ ACGAAGTT	5,314,039	1,594	35.31	90.45	81	6,759,937	311	906,563	5	501,743	66.21	99.1
M191	TCCCAGCC/ GGCAGTTC	3,909,803	1,173	35.36	90.68	127	6,845,055	301	473,968	12	191,227	66.00	98.8
M210	CTATTCGT/ ACAATGCT	4,795,581	1,439	35.43	91.03	125	6,842,250	301	432,145	12	210,216	66.01	98.8
M294	GAGCCATT/ TCCTGGTC	4,422,716	1,327	35.27	90.15	80	7,253,112	338	967,364	7	344,495	65.83	99.5
M303	ATTAATCG/ AATGCTGT	5,509,038	1,653	34.97	88.58	89	6,666,631	320	517,511	9	289,533	66.15	99.1
M315	GAAGGAGC/ TGCAGAAC	3,486,526	1,046	35.40	90.85	108	6,773,815	301	504,715	12	187,024	66.10	98.3
M324	GATTACAA/ CCGGACAG	16,344,276	4,903	34.52	86.19	96	7,198,687	303	902,517	7	325,602	65.84	99.5

V.5.10.1 Genome Mining for Serotypes, and Defects in LPS Biogenesis, Resistance Genes, and Virulence Factors

Assembled genomes of *P. aeruginosa* isolates from the core strain collection of *fpvAI*-positive strains from the University Hospital in Düsseldorf (cf. Figure IV.30C) were screened for certain genes of interest and single nucleotide polymorphisms by using the local NCBI blast+ algorithms (v2.17.0) tBLASTn[786] and BLASTp.[788] Therefore, the assembled genomes were searched against reference sequences of all proteins of interest (LPS biosynthesis genes, pyocins, and antibiotic resistance genes, for a detailed list of genes see Figure IX.12), retrieved from reference genomes of *P. aeruginosa* strains, and the loci were subsequently mapped against the PGAP annotation files using Python (v3.13.7) to identify overlaps between blast search results and annotated features.

- **Strain PAO1** (NC_002516.2, IATS serogroup O5; source for all reference sequences except those specified in the following paragraph),[757]
- **Strain IATS:O6** (GenBank AF035937.1, reference for IATS serogroup O6),[881]
- **Strain PA103** (GenBank AF147795.1, reference for IATS serogroup O11),[882]
- **Strain UCBPP-PA14** (NC_008463.1, source for exoU, accession number WP_003134060.1)
- **Strain DSM 50071** (GenBank CP012001.1, source for pyocin S1, accession number AKO87955.1)
- **Strain P12** (GenBank X77996.1, source for pyocin S3, accession number CAA54958.1)
- **Strain 105738** (LOHK01000018.1, source for pyocin S6, accession number KYO98147.1)
- **Strain BWHPSA018** (GenBank AXQK01000000.1, source for pyocin S7, accession number ERW54179.1)
- **Strain BL04** (GenBank AXPW00000000.1, source for pyocin S9, accession number ERV82772.1)
- **Strain PABL056** (Genome Assembly GCF_000290555.2, source for pyocin S10, accession number WP_025991911.1)
- **Strain BWHPSA019** (AXQJ01000003.1, source for pyocin SD1, accession number WP_023116694.1)
- **Strain MSH-10** (NZ_KE138672.1, source for pyocin SD2, gene not annotated; accession number of the cognate immunity protein WP_003101816.1)
- **Strain PA7** (NC_009656.1, source for pyocin SD3, accession number ABR82489.1)
- **Strain WH-SGI-V-07287** (LLUM01000014.1, source for pyocin SX1, accession number KSR45004.2)
- **Strain 2_1_26** (GenBank ACWU01000201.1, source for pyocin SX2, accession number EHF11209.1)
- **Strain BWHPSA046** (GenBank AZZH01000005.1, source for pyocin G, accession number ETV05907.1)
- **Strain PAF41-2** (GenBank D12705.1, source for pyocin AP41, accession number BAA02196.1)
- **Strain 7NSK2** (source for FpvAIIa, accession number AF537095.2)
- **Strain ATCC 27853** (NZ_CP015117.1, source for FpvAIIb, accession number WP_016852868.1 (wrong annotation))
- **Strain 59.20** (NZ_NSUN00000000.1, source for FpvAIII, accession number AAN62912.1)

Besides the CPA and OSA biosynthesis genes listed in Figure IX.12 (Supporting Information), the following LPS biosynthesis genes were screened for anomalies that would explain ImS2-independent resistance to PyoS2 Y640C proteins:
Lipid A and LPS biosynthesis: *migA*, *dnpA*, *waaA*, *waaC*, *waaF*, *waaL*, *waaP*, *waaG*, *wapG*, *wapH*, *wapO*, *wapP*, *wapR*, *galU*, *algC*, *gmhA*, *gmhB*, *rfaE/hldE*, *rfaD/hldD*, *rmlA–D*, *ytfN*, *pagL*, *arnT*, *lpxA-D*, *lpxH*, *lpxK*.
LPS assembly: *wzz2.*
Complete IATS O6 cluster: *wbpO*, *wbpP*, *wbpQ*, *wzx*, *wbpR*, *wbpS*, *wbpT*, *wbpU*, *wbpV*, *wbpL*, *wbpM*.
Complete IATS O11 cluster: *wzz*, *wzx*, *wzy*, *wbjA*, *wbjB*, *wbjC*, *wbjD*, *wbjE*, *wbjF*, *wbpL*, *wbpM*.
LPS transport: *lpt–G*.
However, no common anomalies were detected in the loci mentioned above.

Multiple sequence alignments of nucleotide and protein sequences were generated with Clustal Omega[860] and were visualised and edited with Jalview.[866] Prediction of O-serogroups based on bacterial genomes was performed with the web version of the *Pseudomonas aeruginosa* serotyper 1.0 (PAst 1.0).[792, 793] Reference sequences of β-lactamase resistance genes were retrieved from the Beta-Lactamase Database (BLDB).[611]

V.6 Biochemical Methods

V.6.1 Protein Purification of PyoS2 Variants and ImS2

V.6.1.1 Cell Lysis

For purification, the resuspended and frozen host cells after expression of the desired protein construct (Chapter V.4.9.1) were first thawed, then supplemented with protease inhibitor (1 mM PMSF, 100 mM in *i*PrOH), and finally disrupted by sonication (3 x 10 min, 40% amplitude, 5 min rest on ice). Cell debris was removed by centrifugation (15,000 x g, 2 x 30 min, 4 °C) and the supernatant was separated from the pellet. The pellet was discarded and the cleared lysate was used for subsequent affinity purification.

V.6.1.2 Immobilised Nickel Affinity Chromatography

The cleared lysate of all PyoS2 variant expressions was transferred onto a 20 mL (4 x 5 mL) Qiagen Ni-NTA Superflow column[15], equilibrated in binding buffer, and afterwards thoroughly washed with binding buffer (min. 35–40 CV) to remove unbound PyoS2/ImS2-His_6 complex and bulk host proteins from the resin. All PyoS2 mutants (except PyoS2 ID variants, see Chapter V.6.1.3) were purified as previously described for colicins by disrupting the column bound PyoS2/ImS2-His_6 complex by washing with 3 CV of the chaotropic salt-containing complex disruption buffer (20 mM Tris-HCl, 500 mM NaCl, 6 M guanidine hydrochloride, pH 7.5), leaving only the His-tagged ImS2 bound to the NTA resin.[883] After washing the column with 2 CV of binding buffer, the immunity protein was separately eluted with elution buffer (20 mM Tris-HCl, 500 mM NaCl, 250 mM imidazole, pH 7.5). PyoS2-containing and ImS2-containing fractions were merged separately, and EDTA was added to a final concentration of 1 mM. PyoS2 fractions were then dialysed overnight at 4 °C against 5 L of dialysis buffer (25 mM Tris-HCl, 150 mM NaCl, pH 8), using 12–14 kDa dialysis tubing (Spectra/Por 4 Dialysis Membrane, Standard RC Tubing, 12–14 kDa MWCO), to remove the chaotropic salt and allow gentle refolding of the protein. For ImS2-His_6, imidazole from the elution buffer was removed by successive rounds of centrifugal concentration (Sartorius Vivaspin 20, 3 kDa MWCO) and washing with dialysis buffer. All PyoS2 proteins (except PyoS2 ID variants) and ImS2-His_6 were finally purified by size exclusion chromatography.

V.6.1.3 Ion Exchange Chromatography (IEX)

Ion exchange chromatography was **only** performed for PyoS2 ID derivatives, as these proteins with strongly defective ImS2-binding eluted immediately from the Ni-NTA resin with the bulk protein of the expression host, while only His-tagged ImS2 remained bound to the column. Consequently, an adapted purification procedure was established.

First, PyoS2 ID derivatives that had eluted from the Ni-NTA column were dialysed overnight at 4 °C into IEX start buffer (10 mM KP_i buffer, pH 7.0).[756] The bulk precipitate was removed by centrifugation (15,000 x g, 45 min, 4 °C), yielding a pale-yellow liquid. After filtration through a 0.22 µm syringe filter, the protein solution was then applied to a 160 mL CM Sepharose FF cation exchange (CIEX) column (custom packed, XK 26/40 body). The column was washed with start buffer until the UV signal remained stable below 15 mAU (ca. 3 CV) and PyoS2 ID derivatives were finally eluted with IEX elution buffer (10 mM KP_i buffer, 400 mM NaCl, pH 7). Subsequent dialysis at 4 °C overnight into 5 L dialysis buffer (25 mM Tris-HCl, 150 mM NaCl, pH 8.0), using 12–14 kDa dialysis tubing

[15] Ni-NTA columns were stripped with ETDA (20 mM Na_3PO_4, 500 mM NaCl, 50 mM Na_2-EDTA, pH 7.4) and cleaned with 1 M NaOH before each run, to avoid cross contamination of DNase-active and -inactive PyoS2 variants.

(Spectra/Por 4 Dialysis Membrane, Standard RC Tubing, 12–14 kDa MWCO), prepared the protein for size exclusion chromatography.

V.6.1.4 Size Exclusion Chromatography (SEC)

The last step in the purification of all proteins (PyoS2 mutants, PyoS2 ID mutants, and ImS2-His_6) was size exclusion chromatography. Therefore, dialysed proteins were concentrated using centrifugal concentrators (Sartorius Vivaspin 20, 10 kDa MWCO for PyoS2 and 3 kDa MWCO for ImS2) and loaded onto a Cytiva HiLoad 26/600 Superdex 200 prep grade column, equilibrated in dialysis buffer. The same buffer was used as eluent (1.25 CV) and only monomeric protein species were merged and concentrated to the desired concentration by centrifugal concentration for further usage (aggregates and dimers were discarded). Furnished proteins were frozen in liquid N_2 and stored at −20 °C until needed.

V.6.2 Maleimide Labelling of PyoS2 Cysteine Mutants

Purified cysteine mutants of PyoS2 were thawed on ice and DTT was added to a final concentration of 10 mM to reduce putative disulfide bridges. Incubation was carried out for 60 min on ice. Excess of reducing agent was removed by desalting into labelling buffer (25 mM Tris-HCl, 150 mM NaCl, pH 7.5) on a Cytiva HiLoad desalting column (5 mL). PyoS2-containing fractions were merged and the protein concentration was determined by UV-Vis measurements at 280 nm. The desired fluorophore maleimide (Alpha Fluor 350 C5 maleimide, Alpha Fluor 488 C5 maleimide, or Alpha Fluor 594 C5 maleimide, AAT Bioquest, 10 mM in DMSO) was added to a 3-fold excess and incubated at RT under gentle agitation in the dark for 1.5 h. DTT was added to a final concentration of 5 mM for quenching and the labelled proteins were subsequently separated from unreacted fluorophore by desalting into dialysis buffer (25 mM Tris-HCl, 150 mM NaCl, pH 8.0). After reduction of the volume to the desired protein concentration by centrifugal concentration at 4 °C, labelled proteins were stored at −20 °C until needed.

V.6.3 Determination of Maleimide Labelling Efficiency

After maleimide labelling, PyoS2-AlF conjugates were subjected to absorption measurements in dialysis buffer to determine protein concentrations and the labelling efficiency according to the manufacturer (AAT Bioquest). Therefore, the protein absorption was measured at 280 nm and the absorption of the attached AlphaFluor fluorophore dyes was measured at 343 nm (AlF350, ε_{343}: 19,000 M^{-1} cm^{-1}), 499 nm (AlF488, ε_{499}: 71,000 M^{-1} cm^{-1}), or 590 nm (AlF594, ε_{590}: 90,000 M^{-1} cm^{-1}) using a Shimadzu UV-1800 UV spectrophotometer and Hellma Analytics quartz glass cuvette SUPRASIL QS (d = 10 mm light path length). Labelling efficiency was determined as described in the manufacturer's protocol with the following correction factors for the correction of fluorophore absorption at 280 nm: 0.19 (AlF350), 0.11 (AlF488), and 0.56 (AlF594). All fluorescently labelled proteins used for *in vitro* DNase assays and *in vivo* cytotoxicity screening with live cells of *P. aeruginosa* were labelled with greater than 98% efficiency.

V.6.4 Protein Quantification

V.6.4.1 UV-Based Protein Quantification

Purified proteins were quantified by measuring the absorption of aromatic amino acids under UV light at 280 nm according to the Beer-Lambert Law. For this purpose, molar extinction coefficients and molecular weights were predicted and calculated based on the primary amino acid sequence with the Expasy ProtParam tool.[863] The following parameters were calculated for the purified PyoS2 proteins generated and used in this work (Table V.6).

Table V.6. Molecular weights and predicted molar extinction coefficients of PyoS2 mutants.

Protein	No. of amino acids[a]	Mass [Da][a]	ε_{280nm} [M^{-1} cm^{-1}]
PyoS2 (wild-type)	688	73722.65	65780
ImS2	94	10973.28	11460
H657A	688	73656.58	65780
H685A	688	73656.58	65780
H657A H685A	688	73590.52	65780
Q570C	688	73697.65	65780
K602C	688	73697.61	65780
Y640C	688	73662.61	64290
C-Cys	689	73825.78	65780
Q570C H657A H685A	688	73565.53	65780
K602C H657A H685A	688	73565.49	65780
Y640C H657A H685A	688	73530.48	64290
H657A H685A C-Cys	689	73693.66	65780

[a] Calculated without the methionine initiator.

V.6.4.2 Pierce 660 nm Protein Quantification

Since prodiginines possess significant absorption at 280 nm, the prodiginine labels of Pyos2-prodiginine conjugates interfere with UV-based quantification. Hence, the alternative and commercially available Pierce 660 nm assay (ThermoScientific) was used for their quantification, as the detection wavelength of 660 nm does not overlap with the absorption of prodiginines (λ_{max} = 530–550 nm).

Prodigiosin-labeled proteins were quantified using the Pierce 660 nm assay, calibrated and validated with bovine serum albumin (determined by weight) and pyocin S2 (determined by UV quantification) (cf. Figure IV.40). Briefly, proteins of unknown concentration were diluted 1:10 in dialysis buffer (25 mM Tris-HCl, 150 mM NaCl, pH 8.0) and 10 µL of this dilution placed in a 96-well plate (four replicates per protein). For BSA, 10 µL of distinct concentrations in a range from 50–2000 µg mL^{-1} (diluted in dialysis buffer) were placed in a 96-well plate. 150 µL of the Pierce 660 nm assay reagent[884] [Thermo Scientific, Product No. 22660, composition: 50 mM succinic acid, 1.0 mM sodium oxalate, 3.5 mM sodium benzoate, 0.26 mM pyrocatechol violet, 0.16 mM sodium molybdate, 4% (w/v) methanol, 0.2% (w/v) polyvinyl alcohol, and 0.1% (w/v) polyvinyl pyrrolidone] were added with a multi-channel pipette and briefly mixed by pipetting. Plates were incubated for 5 min at ambient temperature, followed by quick shaking and measurement of the absorption at 660 nm. Data sets were fitted by linear regression and protein concentrations were determined based on this fit. For fitting parameters, see Figure IV.40B.

V.6.5 Sodium Dodecyl Sulfate Polyacrylamide Gel Electrophoresis (SDS-PAGE)

SDS-PAGE was performed to validate the expression of certain proteins under varying growth conditions or to assess the purity of isolated proteins. In detail, purified proteins were diluted in dialysis buffer (25 mM Tris-HCl, 150 mM NaCl, pH 8.0) to a concentration of 0.33 µg/µL and mixed with 4x SDS sample buffer (200 mM Tris-HCl, pH 6.8, 8% w/v SDS, 0.4% w/v bromophenol blue, 40% w/v glycerol, 400 mM β-mercaptoethanol) to give a final concentration of 0.25 µg/µL. Samples were heated at 98 °C for 10 min and used without centrifugation. 5 µL marker (ThermoScientific PageRuler Unstained Protein Ladder, Ref 26614) and 8 µL protein sample (equals 2 µg of protein per well) were applied to a commercial Invitrogen NuPAGE 4–12% Bis-Tris gel (1.0 mm x 15 well, Ref NP0323BOX). Gels were run at 180 V for 46 min in 1x NuPAGE MOPS SDS running buffer (50 mM MOPS, 50 mM Tris Base, 0.1% SDS, 1 mM EDTA, pH 7.7, Ref NP0001). After three times washing with water and incubation

with colloidal Coomassie o/n, stained gels were incubated in water with a cellulose tissue to destain the background. Gels were then documented by photography.

V.7 Special Methods

V.7.1 Multiplex PCR for Detection of *fpvAI–III* and *pyoS2_imS2*

Clinical isolates of *P. aeruginosa* were tested for their eligibility to produce PyoS2 and its immunity protein ImS2 and their ability to translocate PyoS2 via the FpvAI siderophore transporter. Therefore, an analytical multiplex PCR was developed to simultaneously detect the fpvAI, fpvAII, and fpvAIII subtypes and pyoS2_imS2 from the bacterial genome. First, all tested strains were grown overnight on COS agar and a single colony per strain was suspended in 50 µL sterile water and heated for 10 min at 98 °C for disruption. After centrifugation (20,000 x g, 10 min, 4 °C) to remove cell debris and denatured proteins, the DNA-containing supernatant was transferred into sterile PCR tubes and used as a template for the following polymerase reaction.

Per 20 µL PCR reaction 5x HF buffer (4 µL), DMSO (1.2 µL), 10 mM dNTP mix (0.4 µL), template DNA (0.4 µL, DNA-containing supernatant), primer (0.4 µL for each primer from a 7.5 µM stock in water), water (10.6 µL), and Phusion DNA polymerase (0.2 µL) are mixed. The primer pairs FpvAI-F/FpvAI-R, FpvAII-F/FpvAII-R, FpvAIII-F/FpvAIII-R and PyoS2/ImS2-F and PyoS2/ImS2-R (cf. Table V.3) are used for simultaneous detection of *fpvAI-III* and *pyoS2_imS2*. For amplification, the samples are processed in a PCR cycler: denaturation for 2 min at 98 °C, 25 cycles of amplification (30 sec at 98 °C, 30 sec at 59.7 °C, 30 sec at 72 °C), and final elongation for 10 min at 72 °C. 4 µL of 6x DNA loading dye is added to each reaction and 9 µL of this solution is applied to agarose gels. Samples are separated on a 2% agarose gel (in 1x TAE buffer) at 100 V for 100 min. 2 µL 100 bp QuickLoad marker (New England Biolabs) is used as a reference. Apparent *fpvAI*-positive strains were verified by an additional duplex PCR using the primer pairs FpvAI-F/FpvAI-R and PyoS2/ImS2-F and PyoS2/ImS2-R.

V.7.2 Plasmid Nicking Assay

The plasmid nicking assay was used to validate DNase activity of PyoS2 mutants and PyoS2 conjugates, relative to wild-type PyoS2 and their inhibition through the inhibitory protein ImS2. For characterisation of PyoS2 DNase activity without ImS2 inhibition, PyoS2 variants were thawed on ice and diluted to 40 µM in plasmid nicking buffer (25 mM Tris-HCl, 150 mM NaCl, 10 mM $MgCl_2$, pH 8.0). For DNase activity in the presence of the innate PyoS2 inhibitor ImS2, both proteins were diluted in the same tube to 40 µM and 42 µM, respectively, and incubated at RT for 20 min to allow complex formation and incorporation of the Mg^{2+} cofactor. pET21a(+) plasmid DNA (177.3 ng/µL, stock solution in water) was used as a DNA substrate for the nuclease bacteriocin PyoS2.

In a 1.5 mL reaction tube, pET21a(+) plasmid DNA (assay concentration 26.7 ng/µL), plasmid nicking buffer and PyoS2 (assay concentration 5 µM) or alternatively PyoS2/ImS2 (assay concentration 5 µM/5.25 µM) are mixed to give a final volume of 90 µL. The plasmid nicking is carried out at 30 °C (400 RPM). For the kinetic experiment, 7.5 µL of the reaction mixture is taken after 2, 5, 10, 20, 30, 40, 50, 60, 70, 80, and 90 min and immediately quenched by adding to a solution of 0.25 µL 1 M EDTA and 1.25 µL 6x DNA loading dye. A 0 min sample is prepared separately by mixing DNA, plasmid nicking buffer, and quenching buffer in advance and finally adding the enzyme to a final concentration of 5 µM PyoS2 (optional: 5.25 µM ImS2). pET21a(+) DNA without any enzyme serves as a negative control. Alternatively, the same setup is used for long-term monitoring of DNA degradation. For this long-term monitoring, only a single sample is taken after 15 h.

For the analysis of DNase-catalysed pET21a(+) DNA digest, 2 µL of 1 kb DNA ladder and 9 µL quenched reaction mixture (200 ng/DNA per well) for each time point are loaded onto a 0.8% agarose gel (with 1x GelRed stain) in 1x TAE buffer and the gel is developed for 40 min at 180 V. Gels were subsequently analysed and documented on an INTAS Science Imaging gel documentation system, which visualises DNA by excitation of the DNA intercalated dye with UV light.

V.7.3 Densitometric Analysis of DNase Activity

Photographs of DNase agarose gels were analysed with Fiji ImageJ2 to quantify the relative amount of nicked, linear, and supercoiled DNA from the measured pixel density. The average pixel density of unloaded wells was subtracted as background, and the corrected gels were further analysed using the gel analyser tool. A uniform "rectangle" was drawn around each form of DNA individually and the lanes were plotted against pixels. Using the "straight" line tool, a baseline was introduced manually for each peak and the integral was calculated as pixel density with the "wand (tracing) tool". The obtained pixel densities Y for each DNA form and time point were then normalised to the sum of nicked (N), linear (L), and supercoiled (S) DNA at the t=0 time point (t=0 equals 100%, equation V.6) and their relative percentage for each time point t_x plotted against the time.

$$Y_{x,norm}\ [\%] = 100 \cdot \frac{Y_x}{Y_{N,0} + Y_{L,0} + Y_{S,0}} \qquad \text{(V.6)}$$

Y_x = Pixel density at time point x
$Y_{N,0}$ = Pixel density of nicked DNA at t=0
$Y_{L,0}$ = Pixel density of linear DNA at t=0
$Y_{S,0}$ = Pixel density of supercoiled DNA at t=0
$Y_{x,norm}$ = Relative percentage of nicked, linear, or supercoiled DNA at t_x (relative to t=0)

To quantitatively describe the degradation of supercoiled DNA over time, each dataset was independently fitted to a stretched exponential decay model (for highly active DNase mutants, equation V.7) or to a linear model (for DNase mutants with residual activity, equation V.9). Therefore, the relative portions of supercoiled DNA were extracted for every time point via densitometric analysis from the corresponding agarose gel of the time coursed experiment (see Chapter V.7.2). Subsequently, the plotted data (relative $DNA_{supercoiled}$ portion vs. time) were analysed according to equation V.7 or V.9). Furthermore, Pearson correlation analyses (equation V.11) and permutation analyses (equation V.12) were performed.

V.7.3.1 Stretched Exponential Decay (Kohlrausch–Williams–Watts Function)

Each dataset was independently fitted to a stretched exponential decay model of the form

$$y(t) = y_0 \cdot e^{-(k \cdot t)^b} \qquad \text{(V.7)}$$

with

$$t_{\frac{1}{2}} = \frac{[\ln(2)]^{1/b}}{k} \qquad \text{(V.8)}$$

b = stretching exponent
y = measured variable [supercoiled DNA portion at time x]
y_0 = initial amplitude at t=0 [% of supercoiled DNA at t=0]
k = decay rate
$t_{1/2}$ = half-life of supercoiled DNA

using nonlinear least-squares regression implemented in R (nlsLM, minpack.lm package). The initial value y_0, decay rate parameter k, and stretching exponent b were estimated for each dataset, and 95% confidence intervals were derived when the fit permitted. Goodness-of-fit was assessed via the coefficient of determination (R^2), residual standard error (RSE), and visual inspection of residuals. The half-life $t_{1/2}$, the time at which the fitted signal decayed to 50% of y_0, was estimated numerically by linear interpolation. For each fit, three diagnostic plots were generated: (i) the raw data with fitted curve, (ii) residuals versus time, and (iii) a log-linear transformation of the observed signal to assess conformity to exponential behaviour.

The exponential decay analysis was performed for the following datasets of PyoS2 mutants and conjugates with an apparent exponential decrease of supercoiled DNA species (high DNase activity):

PyoS2 (toxin only): PyoS2 (wild-type); PyoS2 Q570C-AlF488; PyoS2 K602C-AlF488; PyoS2 Y640C; PyoS2 Y640C-AlF350; PyoS2 Y640C-AlF488; PyoS2 Y640C-AlF594; PyoS2 C-Cys-AlF488.

PyoS2 (+ImS2): PyoS2 Y640C-AlF350 + ImS2; PyoS2 Y640C-AlF488 + ImS2; PyoS2 Y640C-AlF594 + ImS2.

Values of supercoiled DNA half-life and fit parameters are summarised in Table IX.5, and graphical analyses are shown in Figure IX.8 (Supporting Information).

V.7.3.2 Linear Regression

Each dataset was independently analysed using linear regression according to the following model

$$y(t) = b \cdot t + y_0 \tag{V.9}$$

with

$$t_{\frac{1}{2}} = \frac{\frac{y_0}{2} - y(0)}{b} \tag{V.10}$$

b	=	slope; rate of change
y	=	measured variable (supercoiled DNA portion at time x)
y_0	=	y-Intercept (fitted parameter)
$t_{1/2}$	=	half-life of supercoiled DNA
$y(0)$	=	Supercoiled DNA portion at t=0 min (experimental)

with time as the independent variable and the relative portion of supercoiled DNA as the dependent variable. The analysis was performed in R using the *lm()* function, and summary statistics were extracted using the *broom* package. The initial signal intensity y_0 was defined as the value of the first time point in each dataset. The half-life $t_{1/2}$, defined as the time at which the fitted linear model predicted a signal of $y_0/2$, was calculated algebraically from the model intercept and slope according to equation V.10. Goodness-of-fit was assessed using the coefficient of determination (R^2), adjusted R^2, standard error, p-value for the slope, and the F-statistic. Diagnostic plots were generated for each dataset, including (i) the fitted regression line overlaid on the experimental data, and (ii) the residuals plotted against the fitted values.

The linear regression analysis was performed for the following datasets of PyoS2 mutants and conjugates with an apparent linear decrease of supercoiled DNA species:

PyoS2 (toxin only): PyoS2 H685A; PyoS2 ID; PyoS2 ID Y640C; PyoS2 ID Y640C-AlF488.

PyoS2 (+ImS2): PyoS2 Y640C + ImS2; PyoS2 ID + ImS2; PyoS2 ID Y640C + ImS2; PyoS2 ID Y640C-AlF488 + ImS2.

Values of supercoiled DNA half-life and fit parameters are summarised in Table IX.6, graphical analyses are shown in Figure IX.9 (Supporting Information).

V.7.3.3 Pearson Correlation Analysis

To assess whether the observed concurrent decline of supercoiled, linear, and nicked plasmid DNA species over time was attributable to assay-related degradation (systematic error) rather than DNase-mediated cleavage, a Pearson correlation analysis was conducted using OriginLab.

In theory, enzymatic digestion of supercoiled plasmid DNA by an active PyoS2 DNase is expected to initially yield an increase in linear DNA – the intermediate between supercoiled and fully degraded products – before its eventual degradation into smaller fragments. In contrast, DNase-inactive protein variants showing a synchronous decline across all DNA forms (without a transient increase in linear DNA) may reflect assay-related artefacts such as sample degradation or binding of DNA to the plastic of the reaction tubes.

Pearson's correlation coefficient (r) was used to measure the strength and direction of the linear relationship between the abundance profiles of the different DNA species over time. The Pearson correlation coefficient is defined as:

$$r = \frac{\sum_{i=1}^{n}(x_i - \bar{x})(y_i - \bar{y})}{\sqrt{\sum_{i=1}^{n}(x_i - \bar{x})^2}\sqrt{\sum_{i=1}^{n}(y_i - \bar{y})^2}} \qquad \text{(V.11)}$$

x_i and y_i = Values of two variables (e.g. intensity of supercoiled and nicked DNA) at time point *i*
$\bar{x}$ and $\bar{y}$ = Mean values of respective datasets
n = Number of time points measured

In this context, a strong positive correlation (r close to +1) between all three DNA species suggests a shared mode of signal loss, such as systematic assay degradation rather than enzymatic action. Conversely, weak or negative correlations may indicate true enzymatic cleavage behaviour, where one species (e.g. supercoiled) declines while another (e.g. linear) transiently increases.

This analysis helped differentiate between protein variants with genuine DNase activity and those whose apparent effects on DNA integrity arose from assay-related phenomena. Pearson coefficients and correlation graphs are summarised in Figure IV.15, Figure IV.19, Figure IV.21, and Figure IV.24.

V.7.3.4 Permutation Analysis

To assess whether the slow increase in linear plasmid DNA over time – observed in time-resolved plasmid nicking assays with low-activity DNase mutants – was statistically significant, a permutation analysis was performed using R with 10,000 random permutations and a 95% confidence interval. Permutation testing is a non-parametric method that evaluates significance by comparing the observed test statistic (here, the coefficient of determination R^2 from a linear regression of linear DNA vs. time) against a distribution of R^2 values generated from randomly shuffled data under the null hypothesis. This approach avoids assumptions about data normality and is well-suited for small or irregular biological datasets.

The test statistic used was the coefficient of determination (R^2), calculated as:

$$R^2 = 1 - \frac{\sum_{i=1}^{n}(y_i - \hat{y})^2}{\sum_{i=1}^{n}(y_i - \bar{y})^2} \qquad \text{(V.12)}$$

y_i = Observed linear DNA at time point *i*
$\hat{y}_i$ = Predicted value from regression
$\bar{y}$ = Mean values of all observed values
n = Number of time points measured

The empirical p-value was determined as the proportion of permuted R^2 values greater than or equal to the observed R^2. Three plots were used to interpret the regression output: i) Histogram of permuted R^2 values [distribution of R^2 under the null hypothesis], ii) residuals vs. time [assessment of model fit; randomly scattered residuals suggest homoscedasticity and linearity], and iii) observed vs. predicted values [agreement between actual and fitted values]. Together, the R^2 value and permutation-derived p-value provided statistical validation for a genuine, time-dependent increase in linear DNA, distinguishing low-level DNase activity from random variation or assay noise. All graphs and fit parameters generated during the permutation analysis can be found in Figure IX.10 and Table IX.7 (Supporting Information).

V.7.4 Electrospray Ionisation Mass Spectrometry (ESI-MS) of Proteins

Purified and labelled PyoS2 and ImS2 proteins were analysed and verified by LC-coupled ESI-MS measurements at the Central Institute of Engineering, Electronics and Analytics (ZEA-3) at the Jülich Research Center. Concentrated samples were diluted 1:10 with water and separated on an Accucore 150-C4 HPLC column (100 mm x 4.6 mm, 2.6 µm particle size), using a 5–95% gradient of acetonitrile. The eluents water and acetonitrile were supplemented with 0.025% heptafluorobutyric acid (HFBA) for ion-pairing and 1% formic acid (FA). Eluent A (water + 0.025% HFBA + 1% FA), eluent B (MeCN + 0.025% HFBA + 1% FA).

V.7.5 Analytical *In Vitro* Biocatalysis with Prodiginine Ligating Enzymes

Cells from heterologous expression batches of prodiginine ligating enzymes (cf. Chapter V.4.9.2) were resuspended in 50 mM KP_i buffer (pH 7.0) to a final mass concentration of 0.2 g/mL and cooled on ice. To disrupt the cells, sonication on ice was performed (40% amplitude, 3 x 5 min with 5 min rest on ice between each cycle, 0.5 s pulse and 0.5 s rest per pulse cycle). The 1*H*-pyrroles **III-15a–c** and the MBC derivatives **III-14a–g** were freshly dissolved in DMSO to a final concentration of 20 mM. For ATP, a 62.5 mM stock solution in water was prepared from the disodium salt Na_2-ATP x 3 H_2O.

In a 1.5 mL reaction tube, 10 µL of 62.5 mM ATP, 25 µL of 20 mM MBC, and 25 µL of 20 mM pyrrole were mixed. Subsequently, the reaction was initiated by supplementation with 440 µL of homogenous sonicated cells in KP_i buffer with a concentration of 0.20 g/mL (cell debris was not removed, as the enzymes are attached to the inner membrane). After carefully inverting the tubes, the reactions were incubated at 30 °C and 300 RPM for a total reaction time of 4 h. Afterwards, the analytical reactions were centrifuged (20,300 x g, 20 min, 4 °C) and the supernatant was discarded. Depending on the further utilisation of samples, two workup procedures were used as follows.

Workup for LC-MS measurements: The cell debris was resuspended in 400 µL of MeOH, assisted by an ultrasound bath. Centrifugation (20,300 x g, 20 min, 4 °C) was used to remove cell debris and the prodiginine-containing supernatant was transferred into a new reaction tube. MeOH was evaporated in a vacuum centrifuge at 45 °C and the residue was taken up in 200 µL of water. Extraction with CH_2Cl_2 (2 x 200 µL) and successive

evaporation of the solvent provided a red-purple residue, which was dissolved in 200 µL MeOH, filtered through a 0.45 µm syringe filter, and subjected to LC-MS analysis (see Chapter V.3.2.7) for prodiginine quantification from the UV trace (see Chapter V.3.2.8).

Workup for photographic documentation: The cell debris was resuspended in 300 µL acidic EtOH (+ 4% 1 M HCl) and the resuspension process was assisted by an ultrasound bath. Centrifugation (20,300 x g, 20 min, 4 °C) was used to remove cell debris and the supernatant was then transferred into a new 1.5 mL reaction tube for documentation. Photographs were recorded on a Canon EOS 6D digital reflex camera with the following instrument settings: ISO 250, shutter speed 1/13 s^{-1}, aperture F/13, focal distance 100 mm, and manual white balance. For the purpose of image processing in Corel PHOTO-PAINT 2019, photographs were saved as .CR2 (Canon Raw 2) raw image files. By using Corel, all images (including the colour and grey control card) were edited to alter the light exposure from 0.0 to 1.0, and the brightness was increased from 0 to 25. Each reaction tube was saved individually as a TIFF file with a transparent background and 600 dpi resolution.

V.7.6 Labelling and Purification of Trastuzumab-Prodigiosin ADCs

The monoclonal antibody variant trastuzumab-NEJ4, carrying four cysteine mutations, was labelled with the maleimide-functionalised prodiginines **III-169**, **III-170**, and **III-171** in accordance with the labelling procedure of PyoS2 (see Chapter V.6.2). However, the maleimide was used in a 10-fold excess. Afterwards, hydrophobic interaction chromatography was performed for the separation of trastuzumab-prodigiosin conjugates from an excess of the maleimide-functionalised prodiginines. An Agilent 1260 Infinity series device (Agilent, Santa Clara, CA, USA) with a variable wavelength detector was used with a TSKgel Butyl-NRP (4.6 × 35 mm, 2.5 µm) column (Tosoh Bioscience, Griesheim, Germany). Absorbance was measured at 220 nm. Eluents consisted of eluent A [1.5 M $(NH_4)_2SO_4$, 25 mM Tris-HCl, pH 7.5] and eluent B (25 mM Tris-HCl, pH 7.5). 2.5 min of isocratic flow (0% eluent B) was followed by a 25 min gradient flow to reach 100% B. After that, the column was washed with 100% eluent B for 2.5 min and isocratic flow with 0% B for 5 min. Protein-containing fractions were merged and concentrated to the desired volume. The antibody-drug ratio (labelling efficiency) was not determined.

V.7.7 Cellular Binding Assays of Trastuzumab-Prodigiosin ADCs

The eukaryotic cell line utilised to evaluate binding of the HER2-targeting antibody trastuzumab ADCs was the human SK-BR-3, which is known to overexpress the HER2 receptor. A431 cells served as a negative control (ADC constructs were only tested at 10 nM here). 5 x 10^4 cells per well were incubated with dilution series of trastuzumab and trastuzumab-prodigiosin ADCs, respectively, in binding buffer (1× PBS with 0.1% m/v bovine serum albumin) in a U-bottom 96-well plate for 30 min at 4 °C. After washing with binding buffer, 7 µL of a 1:80 dilution of Goat anti-Human IgG Fc secondary antibody conjugates with the R-phycoerythrin fluorophore (PE), eBioscience (AB_465926, ThermoFisher Scientific, Darmstadt, Germany) was added to each well for staining and cells were incubated for additional 20 min at 4 °C. Subsequently, cells were washed with binding buffer and analysed in the cytometer (CytoFLEX, Beckman Coulter GmbH, Krefeld, Germany). The mean fluorescence was calculated and plotted against the ADC concentration for data analysis.

V.7.8 Cellular Viability Assays with Trastuzumab-Prodigiosin ADCs

6 x 10^3 cells/well were seeded in a U-bottom 96-well plate in 90 µL of medium and incubated overnight at 37 °C and 5% CO_2. The next day, 10 µL of a dilution series of each trastuzumab-prodigiosin ADC was added and cells were incubated for 3 days at 37°C and 5% CO_2. To evaluate the cell viability in the presence of trastuzumab-

prodigiosin ADCs, the CellTiter 96® Non-Radioactive Cell Proliferation Assay (MTT) (Promega GmbH, Walldorf, Germany) was performed, following the instructions of the supplier. Absorbance measurements were conducted with a CLARIOstar Plus (BMG Labtech, Ortenberg, Germany) plate reader.

VI References

[1] A. Fleming, *Br. J. Exp. Pathol.* **1929**, *10*(3), 226-236; 'On the Antibacterial Action of Cultures of a Penicillium, with Special Reference to Their Use in the Isolation of *B. influenzae*', PubMed ID 11545337.

[2] R. Hare, *Med. Hist.* **1982**, *26*(1), 1-24; 'New Light on the History of Penicillin'; DOI 10.1017/S0025727300040758.

[3] K. Sambyal, R. V. Singh, *J. Genet. Eng. Biotechnol.* **2021**, *19*(1):156, 1-11; 'Exploitation of *E. coli* for the production of penicillin G amidase: a tool for the synthesis of semisynthetic β-lactam antibiotics'; DOI 10.1186/s43141-021-00263-7.

[4] P. N. Bryan, *Biochim. Biophys. Acta* **2000**, *1543*(2), 203-222; 'Protein engineering of subtilisin'; DOI 10.1016/S0167-4838(00)00235-1.

[5] World Health Organization (WHO): 10 Global Health Issues to Track in 2021, **2020**, https://www.who.int/news-room/spotlight/10-global-health-issues-to-track-in-2021, accessed 24/11/2024.

[6] WHO Global Strategy on Health, Environment and Climate Change: The transformation needed to improve lives and wellbeing sustainably through healthy environments, **2020**, https://iris.who.int/bitstream/handle/10665/331959/9789240000377-eng.pdf?sequence=1, accessed 24/11/2024.

[7] vfa. Die forschenden Pharma-Unternehmen: Milestones in pharmaceutical development, **2018**, https://www.vfa.de/de/englische-inhalte/milestones-in-pharmaceutical-development.html, accessed 25/11/2024.

[8] M. Lahlou, *Pharmacol. Pharm.* **2013**, *4*, 17-31; 'The Success of Natural Products in Drug Discovery'; DOI 10.4236/pp.2013.43A003.

[9] M. I. Choudhary, W. J. Thomsen, **2001**, *Bioassay Techniques for Drug Development (1st Edition)*, CRC Press, Boca Raton, FL, USA; ISBN 978-0429219818, DOI 10.3109/9780203304532.

[10] P. Suresh, P. K. Basu, *J. Pharm. Innov.* **2008**, *3*, 175-187; 'Improving Pharmaceutical Product Development and Manufacturing: Impact on Cost of Drug Development and Cost of Goods Sold of Pharmaceuticals'; DOI 10.1007/s12247-008-9043-1.

[11] M. Butters, D. Catterick, A. Craig, A. Curzons, D. Dale, A. Gillmore, S. P. Green, I. Marziano, J.-P. Sherlock, W. White, *Chem. Rev.* **2006**, *106*(7), 3002-3027; 'Critical Assessment of Pharmaceutical Processes - A Rationale for Changing the Synthetic Route'; DOI 10.1021/cr050982w.

[12] H. C. Kolb, M. G. Finn, K. B. Sharpless, *Angew. Chem. Int. Ed.* **2001**, *40*(11), 2004-2021; 'Click Chemistry: Diverse Chemical Function from a Few Good Reactions'; DOI 10.1002/1521-3773(20010601)40:11<2004::AID-ANIE2004>3.0.CO;2-5.

[13] H. C. Kolb, M. G. Finn, K. B. Sharpless, *Angew. Chem.* **2001**, *113*(11), 2056-2075; 'Click-Chemie: Diverse Chemische Funktionalität mit einer Handvoll guter Reaktionen'; DOI 10.1002/1521-3757(20010601)113:11<2056::AID-ANGE2056>3.0.CO;2-W.

[14] C. R. Bertozzi, **2011**, *44*(9), 651-653; 'A Decade of Bioorthogonal Chemistry'; DOI 10.1021/ar200193f.

[15] H. C. Kolb, K. B. Sharpless, *Drug Discov. Today* **2003**, *8*(24), 1128-1137; 'The growing impact of click chemistry on drug discovery'; DOI 10.1016/s1359-6446(03)02933-7.

[16] S. Neumann, M. Biewend, S. Rana, W. H. Binder, *Macromol. Rapid Comm.* **2020**, *41*(1):1900359, 1-32; 'The CuAAC: Principles, Homogeneous and Heterogeneous Catalysts, and Novel Developments and Applications'; DOI 10.1002/marc.201900359.

[17] R. Huisgen, *Angew. Chem. Int. Ed.* **1963**, *2*(10), 565-598; '1,3-Dipolar Cycloadditions. Past and Future'; DOI 10.1002/anie.196305651.

[18] R. Huisgen, *Proc. Chem. Soc.* **1961**, 357-396; '1,3-Dipolar Cycloadditions'; DOI 10.1039/PS9610000357.

[19] M. Breugst, H. U. Reissig, *Angew. Chem. Int. Ed.* **2020**, *59*(30), 12293-12307; 'The Huisgen Reaction: Milestones of the 1,3-Dipolar Cycloaddition'; DOI 10.1002/anie.202003115.

[20] M. Breugst, H. U. Reissig, *Angew. Chem.* **2020**, *132*(30), 12389-12404; 'Die Huisgen-Reaktion: Meilensteine der 1,3-dipolaren Cycloaddition'; DOI 10.1002/ange.202003115.

[21] N. J. Agard, J. A. Prescher, C. R. Bertozzi, *J. Am. Chem. Soc.* **2004**, *126*(46), 15046-15047; 'A strain-Promoted [3 + 2] Azide−Alkyne Cycloaddition for Covalent Modification of Biomolecules in Living Systems'; DOI 10.1021/ja044996f.

[22] C. W. Tornøe, C. Christensen, M. Meldal, *J. Org. Chem.* **2002**, *67*(9), 3057-3064; 'Peptidotriazoles on Solid Phase: [1,2,3]-Triazoles by Regiospecific Copper (I)-Catalyzed 1,3-Dipolar Cycloadditions of Terminal Alkynes to Azides'; DOI 10.1021/jo011148j.

[23] V. V. Rostovtsev, L. G. Green, V. V. Fokin, K. B. Sharpless, *Angew. Chem. Int. Ed.* **2002**, *41*(14), 2596-2599; 'A Stepwise Huisgen Cycloaddition Process: Copper(I)-Catalyzed Regioselective “Ligation” of Azides and Terminal Alkynes'; DOI 10.1002/1521-3773(20020715)41:14<2596::AID-ANIE2596>3.0.CO;2-4.

[24] V. V. Rostovtsev, L. G. Green, V. V. Fokin, K. B. Sharpless, *Angew. Chem.* **2002**, *114*(14), 2708-2711; 'A Stepwise Huisgen Cycloaddition Process: Copper(I)-Catalyzed Regioselective “Ligation” of Azides and Terminal Alkynes'; DOI 10.1002/1521-3757%2820020715%29114%3A14<2708%3A%3AAID-ANGE2708>3.0.CO%3B2-0.

[25] H. A. Michaels, L. Zhu, *Chem. Asian J.* **2011**, *6*(10), 2825-2834; 'Ligand-Assisted, Copper(II) Acetate-Accelerated Azide–Alkyne Cycloaddition'; DOI 10.1002/asia.201100426.

[26] G. Wittig, A. Krebs, *Chem. Ber.* **1961**, *94*(12), 3260-3275; 'Zur Existenz niedergliedriger cycloalkine, I'; DOI 10.1002/cber.19610941213.

[27] H. Meier, H. Petersen, H. Kolshorn, *Chem. Ber.* **1980**, *113*(7), 2398-2409; 'Die Ringspannung von Cycloalkinen und ihre spektroskopischen Auswirkungen'; DOI 10.1002/cber.19801130708.

[28] R. B. Turner, A. D. Jarrett, P. Goebel, B. J. Mallon, *J. Am. Chem. Soc.* **1973**, *95*(3), 790-792; 'Heats of Hydrogenation. IX. Cyclic Acetylenes and Some Miscellaneous Olefins'; DOI 10.1021/ja00784a025.

[29] S. J. Luchansky, S. Argade, B. K. Hayes, C. R. Bertozzi, *Biochemistry* **2004**, *43*(38), 12358-12366; 'Metabolic Functionalization of Recombinant Glycoproteins'; DOI 10.1021/bi049274f.

[30] P. C. Weber, D. H. Ohlendorf, J. J. Wendoloski, F. R. Salemme, *Science* **1989**, *243*(4887), 85-88; 'Structural Origins of High-Affinity Biotin Binding to Streptavidin'; DOI 10.1126/science.2911722.

[31] A. Rondon, F. Degoul, *Bioconjugate Chem.* **2019**, *31*(2), 159-173; 'Antibody Pretargeting Based on Bioorthogonal Click Chemistry for Cancer Imaging and Targeted Radionuclide Therapy'; DOI 10.1021/acs.bioconjchem.9b00761.
[32] V. O. Rodionov, S. I. Presolski, D. Díaz Díaz, V. V. Fokin, M. G. Finn, *J. Am. Chem. Soc.* **2007**, *129*(42), 12705-12712; 'Ligand-Accelerated Cu-Catalyzed Azide−Alkyne Cycloaddition: A Mechanistic Report'; DOI 10.1021/ja072679d.
[33] V. O. Rodionov, S. I. Presolski, S. Gardinier, Y.-H. Lim, M. G. Finn, *J. Am. Chem. Soc.* **2007**, *129*(42), 12696-12704; 'Benzimidazole and Related Ligands for Cu-Catalyzed Azide−Alkyne Cycloaddition'; DOI 10.1021/ja072678l.
[34] S. I. Presolski, V. Hong, S.-H. Cho, M. G. Finn, *J. Am. Chem. Soc.* **2010**, *132*(41), 14570-14576; 'Tailored Ligand Acceleration of the Cu-Catalyzed Azide−Alkyne Cycloaddition Reaction: Practical and Mechanistic Implications'; DOI 10.1021/ja105743g.
[35] F. Manzenrieder, R. Luxenhofer, M. Retzlaff, R. Jordan, M. G. Finn, *Angew. Chem. Int. Ed.* **2011**, *50*(11), 2649-2653; 'Stabilization of Virus-like Particles with Poly(2-oxazoline)s'; DOI 10.1002/anie.201006134.
[36] F. Manzenrieder, R. Luxenhofer, M. Retzlaff, R. Jordan, M. G. Finn, *Angew. Chem.* **2011**, *123*(11), 2649-2653; 'Stabilization of Virus-like Particles with Poly(2-oxazoline)s'; DOI 10.1002/ange.201006134.
[37] J. E. Hein, V. V. Fokin, *Chem. Soc. Rev.* **2010**, *39*(4), 1302-1315; 'Copper-catalyzed azide–alkyne cycloaddition (CuAAC) and beyond: new reactivity of copper(I) acetylides'; DOI 10.1039/b904091a.
[38] M. Yang, J. Li, P. R. Chen, *Chem. Soc. Rev.* **2014**, *43*(18), 6511-6526; 'Transition metal-mediated bioorthogonal protein chemistry in living cells'; DOI 10.1039/c4cs00117f.
[39] S. Li, H. Cai, J. He, H. Chen, S. Lam, T. Cai, Z. Zhu, S. J. Bark, C. Cai, *Bioconjugate Chem.* **2016**, *27*(10), 2315-2322; 'Extent of the Oxidative Side Reactions to Peptides and Proteins During the CuAAC Reaction'; DOI 10.1021/acs.bioconjchem.6b00267.
[40] J. C. Jewett, E. M. Sletten, C. R. Bertozzi, *J. Am. Chem. Soc.* **2010**, *132*(11), 3688-3690; 'Rapid Cu-Free Click Chemistry with Readily Synthesized Biarylazacyclooctynones'; DOI 10.1021/ja100014q.
[41] J. M. Baskin, J. A. Prescher, S. T. Laughlin, N. J. Agard, P. V. Chang, I. A. Miller, A. Lo, J. A. Codelli, C. R. Bertozzi, *Proc. Natl. Acad. Sci. U.S.A.* **2007**, *104*(43), 16793–16797; 'Copper-free click chemistry for dynamic *in vivo* imaging'; DOI 10.1073/pnas.0707090104.
[42] Y. He, L. Liu, L. Cheng, *Molecules* **2023**, *28*(9):3715, 1-10; 'A Short Review of Research Progress on the Synthesis Approaches of Aza-Dibenzocyclooctyne Derivatives'; DOI 10.3390/molecules28093715.
[43] M. Abdollahpour-Alitappeh, M. Lotfinia, T. Gharibi, J. Mardaneh, B. Farhadihosseinabadi, P. Larki, B. Faghfourian, K. S. Sepehr, K. Abbaszadeh-Goudarzi, G. Abbaszadeh-Goudarzi, B. Johari, M. R. Zali, N. Bagheri, *J. Cell. Physiol.* **2019**, *234*(5), 5628-5642; 'Antibody–drug conjugates (ADCs) for cancer therapy: Strategies, challenges, and successes'; DOI 10.1002/jcp.27419.
[44] J. M. Lambert, C. Q. Morris, *Adv. Ther.* **2017**, *34*, 1015-1035; 'Antibody–drug conjugates (ADCs) for personalized treatment of solid tumors: a review'; DOI 10.1007/s12325-017-0519-6.
[45] N. Jain, S. W. Smith, S. Ghone, B. Tomczuk, *Pharm. Res.* **2015**, *32*(11), 3526-3540; 'Current ADC Linker Chemistry'; DOI 10.1007/s11095-015-1657-7.
[46] F. Riccardi, M. Dal Bo, P. Macor, G. Toffoli, *Front. Pharmacol.* **2023**, *14*:1274088, 1-21; 'A comprehensive overview on antibody-drug conjugates: from the conceptualization to cancer therapy'; DOI 10.3389/fphar.2023.1274088.
[47] S. J. Walsh, J. D. Bargh, F. M. Dannheim, A. R. Hanby, H. Seki, A. J. Counsell, X. Ou, E. Fowler, N. Ashman, Y. Takada, A. Isidro-Llobet, J. S. Carroll, J. S. Parker, D. R. Spring, *Chem. Soc. Rev.* **2021**, *50*(2), 1305-1353; 'Site-selective modification strategies in antibody–drug conjugates'; DOI 10.1039/d0cs00310g.
[48] M. Damelin, W. Zhong, J. Myers, P. Sapra, *Pharm. Res.* **2015**, *32*, 3494-3507; 'Evolving Strategies for Target Selection for Antibody-Drug Conjugates'; DOI 10.1007/s11095-015-1624-3.
[49] V. Boni, M. R. Sharma, A. Patnaik, *Am. Soc. Clin. Oncol. Educ. Book* **2020**, *40*, e58-e74; 'The Resurgence of Antibody Drug Conjugates in Cancer Therapeutics: Novel Targets and Payloads'; DOI 10.1200/EDBK_ 281107.
[50] S.-F. Yu, B. Zheng, M. Go, J. Lau, S. Spencer, H. Raab, R. Soriano, S. Jhunjhunwala, R. Cohen, M. Caruso, P. Polakis, J. Flygare, A. G. Polson, *Clin. Cancer Res.* **2015**, *21*(14), 3298-3306; 'A Novel Anti-CD22 Anthracycline-Based Antibody–Drug Conjugate (ADC) that Overcomes Resistance to Auristatin-Based ADCs'; DOI 10.1158/1078-0432.CCR-14-2035.
[51] E. C. Vatansever, J. Kang, A. Tuley, E. S. Ward, W. R. Liu, *Bioorg. Med. Chem.* **2020**, *28*(24), 1-6; 'An optimal “Click” formulation strategy for antibody-drug conjugate synthesis'; DOI 10.1016/j.bmc.2020.115808.
[52] R. Dudchak, M. Podolak, S. Holota, O. Szewczyk-Roszczenko, P. Roszczenko, A. Bielawska, R. Lesyk, K. Bielawski, *Bioorg. Chem.* **2023**, *143*:106982, 1-16; 'Click chemistry in the synthesis of antibody-drug conjugates'; DOI 10.1016/j.bioorg.2023.106982.
[53] G. Castro-Falcón, G. S. Seiler, Ö. Demir, M. K. Rathinaswamy, D. Hamelin, R. M. Hoffmann, S. L. Makowski, A.-C. Letzel, S. J. Field, J. E. Burke, R. E. Amaro, C. C. Hughes, *J. Med. Chem.* **2018**, *61*(23), 10463-10472; 'Neolymphostin A is a Covalent Phosphoinositide 3-Kinase (PI3K)/Mammalian Target of Rapamycin (mTOR) Dual Inhibitor that Employs an Unusual Electrophilic Vinylogous Ester'; DOI 10.1021/acs.jmedchem.8b00975.
[54] H. Nagata, H. Yano, K. Sasaki, S. Sato, S. Nakanishi, I. Takahashi, T. Tamaoki, *Biosci. Biotechnol. Biochem.* **2002**, *66*(3), 501-507; 'Inhibition of Lymphocyte Kinase Lck and Phosphatidylinositol 3-kinase by a Novel Immunosuppressant, Lymphostin'; DOI 10.1271/bbb.66.501.
[55] D. Zhou, J. Casavant, E. I. Graziani, H. He, J. Janso, F. Loganzo, S. Musto, N. Tumey, C. J. O'Donnell, R. Dushin, *Bioorg. Med. Chem. Lett.* **2019**, *29*(7), 943-947; 'Novel PIKK inhibitor antibody-drug conjugates: Synthesis and anti-tumor activity'; DOI 10.1016/j.bmcl.2019.01.009.
[56] F. Alemi, A. Raei Sadigh, F. Malakoti, Y. Elhaei, S. H. Ghaffari, M. Maleki, Z. Asemi, B. Yousefi, N. Targhazeh, M. Majidinia, *J. Cell. Physiol.* **2022**, *237*(1), 313-328; 'Molecular mechanisms involved in DNA repair in human cancers: An overview of PI3k/Akt signaling and PIKKs crosstalk'; DOI 10.1002/jcp.30573.
[57] G. Valabrega, F. Montemurro, M. Aglietta, *Ann. Oncol.* **2007**, *18*(6), 977-984; 'Trastuzumab: mechanism of action, resistance and future perspectives in HER2-overexpressing breast cancer'; DOI 10.1093/annonc/mdl475.

[58] D. J. Slamon, G. M. Clark, S. G. Wong, W. J. Levin, A. Ullrich, W. L. McGuire, *Science* **1987**, *235*(4785), 177-182; 'Human Breast Cancer: Correlation of Relapse and Survival with Amplification of the HER-2/*neu* Oncogene'; DOI 10.1126/science.3798106.
[59] P. K. Qasba, *Bioconjugate Chem.* **2015**, *26*(11), 2170-2175; 'Glycans of Antibodies as a Specific Site for Drug Conjugation using Glycosyltransferases'; DOI 10.1021/acs.bioconjchem.5b00173.
[60] R. Jefferis, *Nat. Rev. Drug Discov.* **2009**, *8*(3), 226-234; 'Glycosylation as a strategy to improve antibody-based therapeutics'; DOI 10.1038/nrd2804.
[61] P. Thompson, E. Ezeadi, I. Hutchinson, R. Fleming, B. Bezabeh, J. Lin, S. Mao, C. Chen, L. Masterson, H. Zhong, D. Toader, P. Howard, H. Wu, C. Gao, N. Dimasi, *ACS Med. Chem. Lett.* **2016**, *7*(11), 1005-1008; 'Straightforward Glycoengineering Approach to Site-Specific Antibody–Pyrrolobenzodiazepine Conjugates'; DOI 10.1021/acsmedchemlett.6b00278.
[62] J. A. Hartley, *Expert Opin. Investig. Drugs* **2011**, *20*(6), 733-744; 'The development of pyrrolobenzodiazepines as antitumour agents'; DOI 10.1517/13543784.2011.573477.
[63] A. C. Tiberghien, J.-N. Levy, L. A. Masterson, N. V. Patel, L. R. Adams, S. Corbett, D. G. Williams, J. A. Hartley, P. W. Howard, *ACS Med. Chem. Lett.* **2016**, *7*(11), 983-987; 'Design and Synthesis of Tesirine, a Clinical Antibody–Drug Conjugate Pyrrolobenzodiazepine Dimer Payload'; DOI 10.1021/acsmedchemlett.6b00062.
[64] A. Kumar, K. Kinneer, L. Masterson, E. Ezeadi, P. Howard, H. Wu, C. Gao, N. Dimasi, *Bioorg. Med. Chem. Lett.* **2018**, *28*(23-24), 3617-3621; 'Synthesis of a heterotrifunctional linker for the site-specific preparation of antibody-drug conjugates with two distinct warheads'; DOI 10.1016/j.bmcl.2018.10.043.
[65] D. Dornan, F. Bennett, Y. Chen, M. Dennis, D. Eaton, K. Elkins, D. French, M. A. T. Go, A. Jack, J. R. Junutula, H. Koeppen, J. Lau, J. McBride, A. Rawstron, X. Shi, N. Yu, S.-F. Yu, P. Yue, B. Zheng, A. Ebsen, A. G. Polson, *Blood* **2009**, *114*(13), 2721-2729; 'Therapeutic potential of an anti-CD79b antibody–drug conjugate, anti–CD79b-vc-MMAE, for the treatment of non-Hodgkin lymphoma'; DOI 10.1182/blood-2009-02-205500.
[66] M. R. Lewis, C. A. Boswell, R. Laforest, T. L. Buettner, D. Ye, J. M. Connett, C. J. Anderson, *Cancer Biother. Radiopharm.* **2001**, *16*(6), 483-494; 'Conjugation of Monoclonal Antibodies with TETA Using Activated Esters: Biological Comparison of ^{64}Cu-TETA-1A3 with ^{64}Cu-BAT-2IT-1A3'; DOI 10.1089/10849780152752083.
[67] N. Wu, C. S. Kang, I. Sin, S. Ren, D. Liu, V. C. Ruthengael, M. R. Lewis, H.-S. Chong, *J. Biol. Inorg. Chem.* **2016**, *21*, 177-184; 'Promising bifunctional chelators for copper 64-PET imaging: practical ^{64}Cu radiolabeling and high in vitro and in vivo complex stability'; DOI 10.1007/s00775-015-1318-7.
[68] M. Shokeen, C. J. Anderson, *Acc. Chem. Res.* **2009**, *42*(7), 832-841; 'Molecular Imaging of Cancer with Copper-64 Radiopharmaceuticals and Positron Emission Tomography (PET)'; DOI 10.1021/ar800255q.
[69] W. Lee, S. Sarkar, R. Pal, J. Y. Kim, H. Park, P. T. Huynh, A. Bhise, K. N. Bobba, K. I. Kim, Y. S. Ha, N. Soni, W. Kim, K. Lee, J.-M. Jung, S. Rajkumar, K. C. Lee, J. Yoo, *ACS Appl. Bio Mater.* **2021**, *4*(3), 2544-2557; 'Successful Application of CuAAC Click Reaction in Constructing ^{64}Cu-Labeled Antibody Conjugates for Immuno-PET Imaging'; DOI 10.1021/acsabm.0c01555.
[70] A. V. F. Massicano, B. V. Marquez-Nostra, S. E. Lapi, *Mol. Imaging* **2018**, *17*, 1-11; 'Targeting HER2 in Nuclear Medicine for Imaging and Therapy'; DOI 10.1177/1536012117745386.
[71] T. Förster, *Ann. Phys.* **1948**, *437*(1-2), 55-75; 'Zwischenmolekulare Energiewanderung und Fluoreszenz'; DOI 10.1002/andp.19484370105.
[72] J. Schoch, M. Staudt, A. Samanta, M. Wiessler, A. Jäschke, *Bioconjugate Chem.* **2012**, *23*(7), 1382-1386; 'Site-Specific One-Pot Dual Labeling of DNA by Orthogonal Cycloaddition Chemistry'; DOI 10.1021/bc300181n.
[73] E. A. Motea, A. J. Berdis, *Biochim. Biophys. Acta, Proteins Proteomics* **2010**, *1804*(5), 1151-1166; 'Terminal deoxynucleotidyl transferase: the story of a misguided DNA polymerase'; DOI 10.1016/j.bbapap.2009.06.030.
[74] F. Miura, T. Fujino, K. Kogashi, Y. Shibata, M. Miura, H. Isobe, T. Ito, *Nucleic Acids Res.* **2018**, *46*(16):e95, 1-11; 'Triazole linking for preparation of a next-generation sequencing library from single-stranded DNA'; DOI 10.1093/nar/gky452.
[75] A. Routh, S. R. Head, P. Ordoukhanian, J. E. Johnson, *J. Mol. Biol.* **2015**, *427*(16), 2610-2616; 'ClickSeq: Fragmentation-Free Next-Generation Sequencing via Click Ligation of Adaptors to Stochastically Terminated 3′-Azido cDNAs'; DOI 10.1016/j.jmb.2015.06.011.
[76] M. Helm, Y. Motorin, *Nat. Rev. Genet.* **2017**, *18*(5), 275-291; 'Detecting RNA modifications in the epitranscriptome: predict and validate'; DOI 10.1038/nrg.2016.169.
[77] W. V. Gilbert, T. A. Bell, C. Schaening, *Science* **2016**, *352*(6292), 1408-1412; 'Messenger RNA modifications: Form, distribution, and function'; DOI 10.1126/science.aad8711.
[78] N. Pozhydaieva, M. Wolfram-Schauerte, H. Keuthen, K. Höfer, *Curr. Opin. Microbiol.* **2024**, *77*:102417, 1-12; 'The enigmatic epitranscriptome of bacteriophages: putative RNA modifications in viral infections'; DOI 10.1016/j.mib.2023.102417.
[79] Y. G. Chen, W. E. Kowtoniuk, I. Agarwal, Y. Shen, D. R. Liu, *Nat. Chem. Biol.* **2009**, *5*(12), 879-881; 'LC/MS analysis of cellular RNA reveals NAD-linked RNA'; DOI 10.1038/nchembio.235.
[80] N. Lentz, S. Reuge, M. Albrecht, *ACS Catal.* **2023**, *13*(14), 9839-9844; 'NADH-Type Hydride Storage and Release on a Functional Ligand for Efficient and Selective Hydrogenation Catalysis'; DOI 10.1021/acscatal.3c02343.
[81] G. D. Birkmayer, **2009**, *NADH, the Biological Hydrogen: The Secret of Our Life Energy*, Basic Health Publications, Inc., Laguna Beach, California, USA; ISBN 978-1-59120-262-2.
[82] N. S. Chandel, *Cold Spring Harb. Perspect. Biol.* **2021**, *13*(5):a040535, 1-12; 'Glycolysis'; DOI 10.1101/cshperspect.a040535.
[83] H. Cahová, M.-L. Winz, K. Höfer, G. Nübel, A. Jäschke, *Nature* **2015**, *519*(7543), 374-377; 'NAD captureSeq indicates NAD as a bacterial cap for a subset of regulatory RNAs'; DOI 10.1038/nature14020.
[84] T. F. Walseth, H. C. Lee, *Biochim. Biophys. Acta, Mol. Cell Res.* **1993**, *1178*(3), 235-242; 'Synthesis and characterization of antagonists of cyclic-ADP-ribose-induced Ca^{2+} release'; DOI 10.1016/0167-4889(93)90199-y.

[85] S. Lee, S. Inzerillo, G. Y. Lee, E. M. Bosire, S. K. Mahato, J. Song, *Trends Microbiol.* **2022**, *30*(3), 254-267; 'Glycan-mediated molecular interactions in bacterial pathogenesis'; DOI 10.1016/j.tim.2021.06.011.
[86] P. Stanley, K. W. Moremen, N. E. Lewis, N. Taniguchi, M. Aebi, **2022**, '*N-Glycans*' in *Essentials of Glycobiology, Fourth Edition*, Cold Spring Harbor Laboratory Press, New York, USA; ISBN 978-1-621824-22-0, DOI 10.1101/9781621824213.
[87] Y. Y. Zhao, M. Takahashi, J. G. Gu, E. Miyoshi, A. Matsumoto, S. Kitazume, N. Taniguchi, *Cancer Sci.* **2008**, *99*(7), 1304-1310; 'Functional roles of *N*-glycans in cell signaling and cell adhesion in cancer'; DOI 10.1111/j.1349-7006.2008.00839.x.
[88] A. Paul, D. Segal, E. Zacco, *Neural Regen. Res.* **2021**, *16*(11), 2215-2216; 'Glycans to improve efficacy and solubility of protein aggregation inhibitors'; DOI 10.4103/1673-5374.310688.
[89] B. Winchester, *Glycobiol.* **2005**, *15*(6), 1R-15R; 'Lysosomal metabolism of glycoproteins'; DOI 10.1093/glycob/cwi041.
[90] R. Marchetti, R. E. Forgione, F. N. Fabregat, C. Di Carluccio, A. Molinaro, A. Silipo, *Curr. Opin. Struct. Biol.* **2021**, *68*, 74-83; 'Solving the structural puzzle of bacterial glycome'; DOI 10.1016/j.sbi.2020.12.003.
[91] G. B. Pier, *Int. J. Med. Microbiol.* **2007**, *297*(5), 277-295; '*Pseudomonas aeruginosa* lipopolysaccharide: A major virulence factor, initiator of inflammation and target for effective immunity'; DOI 10.1016/j.ijmm.2007.03.012.
[92] H. L. Rocchetta, L. L. Burrows, J. S. Lam, *Microbiol. Mol. Biol. Rev.* **1999**, *63*(3), 523-553; 'Genetics of *O*-Antigen Biosynthesis in *Pseudomonas aeruginosa*'; DOI 10.1128/MMBR.63.3.523-553.1999.
[93] H. Nikaido, M. Vaara, *Microbiol. Rev.* **1985**, *49*(1), 1-32; 'Molecular Basis of Bacterial Outer Membrane Permeability'; DOI 10.1128/mr.49.1.1-32.1985.
[94] J. Hirabayashi, A. Kuno, H. Tateno, *Electrophoresis* **2011**, *32*(10), 1118-1128; 'Lectin-based structural glycomics: A practical approach to complex glycans'; DOI 10.1002/elps.201000650.
[95] L. Cipolla, L. Gabrielli, D. Bini, L. Russo, N. Shaikh, *Nat. Prod. Rep.* **2010**, *27*(11), 1618-1629; 'Kdo: a critical monosaccharide for bacteria viability'; DOI 10.1039/c004750n.
[96] A. Dumont, A. Malleron, M. Awwad, S. Dukan, B. Vauzeilles, *Angew. Chem. Int. Ed.* **2012**, *51*(13), 3143-3146; 'Click-Mediated Labeling of Bacterial Membranes Through Metabolic Modification of the Lipopolysaccharide Inner Core'; DOI 10.1002/anie.201108127.
[97] A. Dumont, A. Malleron, M. Awwad, S. Dukan, B. Vauzeilles, *Angew. Chem.* **2012**, *124*(13), 3197-3200; 'Click-Mediated Labeling of Bacterial Membranes Through Metabolic Modification of the Lipopolysaccharide Inner Core'; DOI 10.1002/ange.201108127.
[98] J. E. Stencel-Baerenwald, K. Reiss, D. M. Reiter, T. Stehle, T. S. Dermody, *Nat. Rev. Microbiol.* **2014**, *12*(11), 739-749; 'The sweet spot: defining virus–sialic acid interactions'; DOI 10.1038/nrmicro3346.
[99] M. Ohuchi, N. Asaoka, T. Sakai, R. Ohuchi, *Microbes Infect.* **2006**, *8*(5), 1287-1293; 'Roles of neuraminidase in the initial stage of influenza virus infection'; DOI 10.1016/j.micinf.2005.12.008.
[100] L. Byrd-Leotis, R. D. Cummings, D. A. Steinhauer, *Int. J. Mol. Sci.* **2017**, *18*(7):1541, 1-22; 'The Interplay between the Host Receptor and Influenza Virus Hemagglutinin and Neuraminidase'; DOI 10.3390/ijms18071541.
[101] M. Weïwer, C. C. Chen, M. M. Kemp, R. J. Linhardt, *Eur. J. Org. Chem.* **2009**, *2009*(16), 2611–2620; 'Synthesis and Biological Evaluation of Non-Hydrolyzable 1,2,3-Triazole-Linked Sialic Acid Derivatives as Neuraminidase Inhibitors'; DOI 10.1002/ejoc.200900117.
[102] L. V. Gubareva, M. J. Robinson, R. C. Bethell, R. G. Webster, *J. Virol.* **1997**, *71*(5), 3385-3390; 'Catalytic and Framework Mutations in the Neuraminidase Active Site of Influenza Viruses That Are Resistant to 4-Guanidino-Neu5Ac2en'; DOI 10.1128/jvi.71.5.3385-3390.1997.
[103] B. T. Worrell, J. A. Malik, V. V. Fokin, *Science* **2013**, *340*(6131), 457-460; 'Direct Evidence of a Dinuclear Copper Intermediate in Cu(I)-Catalyzed Azide-Alkyne Cycloadditions'; DOI 10.1126/science.1229506.
[104] A. Moen, D. G. Nicholson, *J. Chem. Soc., Faraday Trans.* **1995**, *91*(19), 3529-3535; 'Reduction of Copper(II) with Subsequent Disproportionation of Copper(I) during the Hydrothermal Syntheses of Microporous Silicoaluminium Phosphates SAPO-5 and-11'; DOI 10.1039/FT9959103529.
[105] J. Fielden, J. Sprott, D.-L. Long, P. Kögerler, L. Cronin, *Inorg. Chem.* **2006**, *45*(7), 2886-2895; 'Controlling Aggregation of Copper(II)-Based Coordination Compounds: From Mononuclear to Dinuclear, Tetranuclear, and Polymeric Copper Complexes'; DOI 10.1021/ic051647t.
[106] C. Nolte, P. Mayer, B. F. Straub, *Angew. Chem. Int. Ed.* **2007**, *46*(12), 2101-2103; 'Isolation of a Copper(I) Triazolide: A “Click” Intermediate'; DOI 10.1002/anie.200604444.
[107] L. M. Gaetke, C. K. Chow, *Toxicology* **2003**, *189*(1-2), 147-163; 'Copper toxicity, oxidative stress, and antioxidant nutrients'; DOI 10.1016/S0300-483X(03)00159-8.
[108] M. Meldal, F. Diness, *Trends Chem.* **2020**, *2*(6), 569-584; 'Recent Fascinating Aspects of the CuAAC Click Reaction'; DOI 10.1016/j.trechm.2020.03.007.
[109] G. R. Abel Jr, Z. A. Calabrese, J. Ayco, J. E. Hein, T. Ye, *Bioconjugate Chem.* **2016**, *27*(3), 698-704; 'Measuring and Suppressing the Oxidative Damage to DNA During Cu(I)-Catalyzed Azide–Alkyne Cycloaddition'; DOI 10.1021/acs.bioconjchem.5b00665.
[110] F. Vatansever, W. C. M. A. de Melo, P. Avci, D. Vecchio, M. Sadasivam, A. Gupta, R. Chandran, M. Karimi, N. A. Parizotto, R. Yin, G. P. Tegos, M. R. Hamblin, *FEMS Microbiol. Rev.* **2013**, *37*(6), 955-989; 'Antimicrobial strategies centered around reactive oxygen species–bactericidal antibiotics, photodynamic therapy, and beyond'; DOI 10.1111/1574-6976.12026.
[111] J. Shen, P. T. Griffiths, S. J. Campbell, B. Utinger, M. Kalberer, S. E. Paulson, *Sci. Rep.* **2021**, *11*(1):7417, 1-14; 'Ascorbate oxidation by iron, copper and reactive oxygen species: Review, model development, and derivation of key rate constants'; DOI 10.1038/s41598-021-86477-8.
[112] I. Bremner, *Am. J. Clin. Nutr.* **1998**, *67*(5), 1069S-1073S; 'Manifestations of copper excess'; DOI 10.1093/ajcn/67.5.1069S.

[113] C. Uttamapinant, A. Tangpeerachaikul, S. Grecian, S. Clarke, U. Singh, P. Slade, K. R. Gee, A. Y. Ting, *Angew. Chem. Int. Ed.* **2012**, *51*(24), 5852-5856; 'Fast, Cell-Compatible Click Chemistry with Copper-Chelating Azides for Biomolecular Labeling'; DOI 10.1002/anie.201108181.
[114] C. Uttamapinant, A. Tangpeerachaikul, S. Grecian, S. Clarke, U. Singh, P. Slade, K. R. Gee, A. Y. Ting, *Angew. Chem.* **2012**, *124*(24), 5954-5958; 'Fast, Cell-Compatible Click Chemistry with Copper-Chelating Azides for Biomolecular Labeling'; DOI 10.1002/ange.201108181.
[115] C. Zhang, P. Dai, A. A. Vinogradov, Z. P. Gates, B. L. Pentelute, *Angew. Chem.* **2018**, *130*(22), 6569-6573; 'Site-Selective Cysteine–Cyclooctyne Conjugation'; DOI 10.1002/ange.201800860.
[116] C. Zhang, P. Dai, A. A. Vinogradov, Z. P. Gates, B. L. Pentelute, *Angew. Chem. Int. Ed.* **2018**, *57*(22), 6459-6463; 'Site-Selective Cysteine–Cyclooctyne Conjugation'; DOI 10.1002/anie.201800860.
[117] B. M. El-Zaatari, A. U. Shete, B. J. Adzima, C. J. Kloxin, *Phys. Chem. Chem. Phys.* **2016**, *18*(36), 25504-25511; 'Towards understanding the kinetic behaviour and limitations in photo-induced copper(I) catalyzed azide–alkyne cycloaddition (CuAAC) reactions'; DOI 10.1039/c6cp04950h.
[118] V. Hong, S. I. Presolski, C. Ma, M. G. Finn, *Angew. Chem. Int. Ed.* **2009**, *48*(52), 9879-9883; 'Analysis and Optimization of Copper-Catalyzed Azide–Alkyne Cycloaddition for Bioconjugation'; DOI 10.1002/anie.200905087.
[119] V. Hong, S. I. Presolski, C. Ma, M. G. Finn, *Angew. Chem.* **2009**, *121*(52), 10063-10067; 'Analysis and Optimization of Copper-Catalyzed Azide–Alkyne Cycloaddition for Bioconjugation'; DOI 10.1002/ange.200905087.
[120] R. Berg, B. F. Straub, *Beilstein J. Org. Chem.* **2013**, *9*(1), 2715-2750; 'Advancements in the mechanistic understanding of the copper-catalyzed azide–alkyne cycloaddition'; DOI 10.3762/bjoc.9.308.
[121] Q. Wang, T. R. Chan, R. Hilgraf, V. V. Fokin, K. B. Sharpless, M. G. Finn, *J. Am. Chem. Soc.* **2003**, *125*(11), 3192-3193; 'Bioconjugation by Copper(I)-Catalyzed Azide-Alkyne [3 + 2] Cycloaddition'; DOI 10.1021/ja021381e.
[122] T. R. Chan, R. Hilgraf, K. B. Sharpless, V. V. Fokin, *Org. Lett.* **2004**, *6*(17), 2853-2855; 'Polytriazoles as Copper(I)-Stabilizing Ligands in Catalysis'; DOI 10.1021/ol0493094.
[123] Y.-M. Wu, J. Deng, X. Fang, Q.-Y. Chen, *J. Fluor. Chem.* **2004**, *125*(10), 1415-1423; 'Regioselective synthesis of fluoroalkylated [1,2,3]-triazoles by Huisgen cycloaddition'; DOI 10.1016/j.jfluchem.2004.02.016.
[124] T. Hasegawa, M. Umeda, M. Numata, T. Fujisawa, S. Haraguchi, K. Sakurai, S. Shinkai, *Chem. Lett.* **2006**, *35*(1), 82-83; 'Click Chemistry on Curdlan: A Regioselective and Quantitative Approach to Develop Artificial β-1,3-Glucans with Various Functional Appendages'; DOI 10.1246/cl.2006.82.
[125] M. Roice, I. Johannsen, M. Meldal, *QSAR Comb. Sci.* **2004**, *23*(8), 662-673; 'High Capacity Poly(ethylene glycol) Based Amino Polymers for Peptide and Organic Synthesis'; DOI 10.1002/qsar.200420021.
[126] P. L. Golas, N. V. Tsarevsky, B. S. Sumerlin, K. Matyjaszewski, *Macromolecules* **2006**, *39*(19), 6451-6457; 'Catalyst Performance in “Click” Coupling Reactions of Polymers Prepared by ATRP: Ligand and Metal Effects'; DOI 10.1021/ma061592u.
[127] P. Zardi, J. Piękoś, C. Bravin, K. Wurst, F. Droghetti, M. Natali, G. Licini, A. Zambon, C. Zonta, *Dalton Trans.* **2024**, *53*(33), 13831-13836; 'Novel ligands from direct benzylic functionalisation of tris(2-pyridylmethyl)amine'; DOI 10.1039/D4DT02022G.
[128] V. D. Bock, H. Hiemstra, J. H. van Maarseveen, *Eur. J. Org. Chem.* **2006**, *2006*(1), 51-68; 'Cu^{I}-Catalyzed Alkyne–Azide “Click” Cycloadditions from a Mechanistic and Synthetic Perspective'; DOI 10.1002/ejoc.200500483.
[129] C. Besanceney-Webler, H. Jiang, T. Zheng, L. Feng, D. S. del Amo, W. Wang, L. M. Klivansky, F. L. Marlow, Y. Liu, P. Wu, *Angew. Chem.* **2011**, *123*(35), 8201-8206; 'Increasing the Efficacy of Bioorthogonal Click Reactions for Bioconjugation: A Comparative Study'; DOI 10.1002/ange.201101817.
[130] C. Besanceney-Webler, H. Jiang, T. Zheng, L. Feng, D. S. del Amo, W. Wang, L. M. Klivansky, F. L. Marlow, Y. Liu, P. Wu, *Angew. Chem. Int. Ed.* **2011**, *50*(35), 8051-8056; 'Increasing the Efficacy of Bioorthogonal Click Reactions for Bioconjugation: A Comparative Study'; DOI 10.1002/anie.201101817.
[131] D. S. del Amo, W. Wang, H. Jiang, C. Besanceney, A. C. Yan, M. Levy, Y. Liu, F. L. Marlow, P. Wu, *J. Am. Chem. Soc.* **2010**, *132*(47), 16893-16899; 'Biocompatible Copper(I) Catalysts for *in Vivo* Imaging of Glycans'; DOI 10.1021/ja106553e.
[132] W. Wang, S. Hong, A. Tran, H. Jiang, R. Triano, Y. Liu, X. Chen, P. Wu, *Chem. Asian J.* **2011**, *6*(10), 2796-2802; 'Sulfated Ligands for the Copper (I)-Catalyzed Azide–Alkyne Cycloaddition'; DOI 10.1002/asia.201100385.
[133] Z. Zhou, C. J. Fahrni, *J. Am. Chem. Soc.* **2004**, *126*(29), 8862-8863; 'A Fluorogenic Probe for the Copper(I)-Catalyzed Azide−Alkyne Ligation Reaction: Modulation of the Fluorescence Emission via ^{3}(n, π*)−^{1}(π,π*) Inversion'; DOI 10.1021/ja049684r.
[134] S. Garg, J. n. M. Shreeve, *J. Mater. Chem.* **2011**, *21*(13), 4787-4795; 'Trifluoromethyl- or pentafluorosulfanyl-substituted poly-1,2,3-triazole compounds as dense stable energetic materials'; DOI 10.1039/c0jm04229c.
[135] H. S. G. Beckmann, H. M. Möller, V. Wittmann, *Beilstein J. Org. Chem.* **2012**, *8*(1), 819-826; 'High-affinity multivalent wheat germ agglutinin ligands by one-pot click reaction'; DOI 10.3762/bjoc.8.91.
[136] S. Chakraborty, D.-F. Tai, *Tetrahedron Lett.* **2014**, *55*(14), 2274-2276; 'Synthesis of triazole cages containing C_3-symmetric α-cyclic tripeptide scaffold'; DOI 10.1016/j.tetlet.2014.02.089.
[137] T. M. Weber, J. Pietruszka, *Synthesis* **2023**, *55*(14), 2128-2133; 'Synthesis of a Water-Soluble Tridentate (Dimethylamino)ethyl Cu(I)/Cu(II)-Ligand'; DOI 10.1055/a-2034-9427.
[138] N. B. Munro, S. S. Talmage, G. D. Griffin, L. C. Waters, A. P. Watson, J. F. King, V. Hauschild, *Environ. Health Perspect.* **1999**, *107*(12), 933-974; 'The Sources, Fate, and Toxicity of Chemical Warfare Agent Degradation Products'; DOI 10.1289/ehp.99107933.
[139] Organisation for the Prohibition of Chemical Weapons (OPCW), https://www.opcw.org, accessed 27/10/2022.
[140] S. L. Smith, *Can. Med. Assoc. J.* **2017**, *189*(8), E321-E322; 'War! What is it good for? Mustard gas medicine'; DOI 10.1503/cmaj.161032.

[141] P. P. Schnurr, J. D. Ford, M. J. Friedman, B. L. Green, B. J. Dain, A. Sengupta, *J. Consult. Clin. Psychol.* **2000**, *68*(2), 258-268; 'Predictors and Outcomes of Posttraumatic Stress Disorder in World War II Veterans Exposed to Mustard Gas'; DOI 10.1037/0022-006X.68.2.258.
[142] H. P. Benschop, G. P. van der Schans, D. Noort, A. Fidder, R. H. Mars-Groenendijk, L. P. A. de Jong, *J. Anal. Toxicol.* **1997**, *21*(4), 249-251; 'Verification of Exposure to Sulfur Mustard in Two Casualties of the Iran-Iraq Conflict'; DOI 10.1093/jat/21.4.249.
[143] Chemical Weapons Convention 2020 (OPCW), **2020**, https://www.opcw.org/sites/default/files/documents/CWC/CWC_en.pdf, accessed 27/10/2022.
[144] D. G. Goswami, D. Kumar, N. Tewari-Singh, D. J. Orlicky, A. K. Jain, R. Kant, R. C. Rancourt, D. Dhar, S. Inturi, C. Agarwal, *Exp. Toxicol. Pathol.* **2015**, *67*(2), 161-170; 'Topical nitrogen mustard exposure causes systemic toxic effects in mice'; DOI 10.1016/j.etp.2014.11.006.
[145] V. R. Sunil, K. N. Vayas, J. Radbel, E. Abramova, A. Gow, J. D. Laskin, D. L. Laskin, *Toxicol. Appl. Pharmacol.* **2022**, *456*:116257, 1-9; 'Impaired energy metabolism and altered functional activity of alveolar type II epithelial cells following exposure of rats to nitrogen mustard'; DOI 10.1016/j.taap.2022.116257.
[146] P. Solopov, M. Marinova, C. Dimitropoulou, R. M. L. Colunga Biancatelli, J. D. Catravas, *Inhal. Toxicol.* **2020**, *32*(4), 141-154; 'Development of chronic lung injury and pulmonary fibrosis in mice following acute exposure to nitrogen mustard'; DOI 10.1080/08958378.2020.1757791.
[147] W. B. Mattes, J. A. Hartley, K. W. Kohn, *Nucleic Acids Res.* **1986**, *14*(7), 2971-2987; 'DNA sequence selectivity of guanine–N7 alkylation by nitrogen mustards'; DOI 10.1093/nar/14.7.2971.
[148] D. Lorke, *Arch. Toxicol.* **1983**, *54*(4), 275-287; 'A New Approach to Practical Acute Toxicity Testing'; DOI 10.1007/BF01234480.
[149] R. Vijayaraghavan, A. Kulkarni, S. C. Pant, P. Kumar, P. V. L. Rao, N. Gupta, A. Gautam, K. Ganesan, *Toxicol. Appl. Pharmacol.* **2005**, *202*(2), 180-188; 'Differential toxicity of sulfur mustard administered through percutaneous, subcutaneous, and oral routes'; DOI 10.1016/j.taap.2004.06.020.
[150] Q.-Q. Wang, R. A. Begum, V. W. Day, K. Bowman-James, *Org. Biomol. Chem.* **2012**, *10*(44), 8786-8793; 'Sulfur, oxygen, and nitrogen mustards: stability and reactivity'; DOI 10.1039/c2ob26482j.
[151] F. A. Patty, **1981**, *Patty's Industrial Hygiene and Toxicology, Vol. 2A (Toxicology)*, John Wiley & Sons, Inc., Hoboken, New Jersey, USA; ISBN 978-0471160427.
[152] B. Renshaw, **1946**, *Summary Technical Report of Division 9, NDRC, Chemical Warfare Agents, and Related Chemical Problems (Parts III–VI), Vol. 1*, Office of Scientific Research and Development, National Defense Research Commitee (Washington, D. C., USA).
[153] National Technical Reports Library: Basic Toxicity of 2-Chloro-*N*,*N*-dimethylethylamine Hydrochloride with Cover Letter, **1992**, https://ntrl.ntis.gov/NTRL/dashboard/searchResults/titleDetail/OTS0557828.xhtml, Accession Number OTS0546424, accessed 11/10/2022.
[154] Most Traded Scheduled Chemicals 2022 (OPCW), **2022**, https://www.opcw.org/sites/default/files/documents/2021/12/Most%20Traded%20Scheduled%20Chemicals%202022%20%28MTSC%29.pdf, accessed 27/10/2022.
[155] C. Xiao, Y. Cheng, Y. Zhang, J. Ding, C. He, X. Zhuang, X. Chen, *J. Polym. Sci., Part A: Polym. Chem.* **2014**, *52*(5), 671-679; 'Side Chain Impacts on pH- and Thermo-Responsiveness of Tertiary Amine Functionalized Polypeptides'; DOI 10.1002/pola.27048.
[156] Y. Bernhard, E. Gigot, V. Goncalves, M. Moreau, N. Sok, P. Richard, R. A. Decréau, *Org. Biomol. Chem.* **2016**, *14*(19), 4511-4518; 'Direct subphthalocyanine conjugation to bombesin *vs.* indirect conjugation to its lipidic nanocarrier'; DOI 10.1039/c6ob00530f.
[157] A. C. Engler, D. K. Bonner, H. G. Buss, E. Y. Cheung, P. T. Hammond, *Soft Matter* **2011**, *7*(12), 5627-5637; 'The synthetic tuning of clickable pH responsive cationic polypeptides and block copolypeptides'; DOI 10.1039/c1sm05064h.
[158] A. Kirby, M. Suchý, A. Brouwer, A. Shuhendler, *Chem. Commun.* **2019**, *55*(37), 5371-5374; 'Mapping aldehydic load *in vivo* by positron emission tomography with [^{18}F]NA_3BF_3'; DOI 10.1039/c9cc01831j.
[159] A. Polavarapu, J. A. Stillabower, S. G. W. Stubblefield, W. M. Taylor, M.-H. Baik, *J. Org. Chem.* **2012**, *77*(14), 5914-5921; 'The Mechanism of Guanine Alkylation by Nitrogen Mustards: A Computational Study'; DOI 10.1021/jo300351g.
[160] G. Reddy, J. Song, M. S. Mecchi, M. S. Johnson, *Mutat. Res.* **2010**, *700*(1-2), 26-31; 'Genotoxicity assessment of two hypergolic energetic propellant compounds'; DOI 10.1016/j.mrgentox.2010.04.019.
[161] M. D. Ogden, C. L. Hoch, S. I. Sinkov, G. P. Meier, G. J. Lumetta, K. L. Nash, *J. Solut. Chem.* **2011**, *40*(11), 1874-1888; 'Complexation Studies of Bidentate Heterocyclic *N*-Donor Ligands with Nd(III) and Am(III)'; DOI 10.1007/s10953-011-9762-7.
[162] M. R. Gannarapu, S. B. Vasamsetti, N. Punna, S. Kotamraju, N. Banda, *Med. Chem. Commun.* **2015**, *6*(8), 1494-1500; 'Synthesis of novel 1-substituted triazole linked 1,2-benzothiazine 1,1-dioxido propenone derivatives as potent anti-inflammatory agents and inhibitors of monocyte-to-macrophage differentiation'; DOI 10.1039/c5md00171d.
[163] S. M. Joshi, A. de Cózar, V. Gómez-Vallejo, J. Koziorowski, J. Llop, F. P. Cossío, *Chem. Commun.* **2015**, *51*(43), 8954-8957; 'Synthesis of radiolabelled aryl azides from diazonium salts: experimental and computational results permit the identification of the preferred mechanism'; DOI 10.1039/c5cc01913c.
[164] S. J. Park, S. K. Yeon, Y. Kim, H. J. Kim, S. Kim, J. Kim, J. W. Choi, B. Kim, E. H. Lee, R. Kim, *J. Med. Chem.* **2022**, *65*(4), 3539-3562; 'Discovery of Novel Sphingosine-1-Phosphate-1 Receptor Agonists for the Treatment of Multiple Sclerosis'; DOI 10.1021/acs.jmedchem.1c01979.
[165] V. Bevilacqua, M. King, M. Chaumontet, M. Nothisen, S. Gabillet, D. Buisson, C. Puente, A. Wagner, F. Taran, *Angew. Chem. Int. Ed.* **2014**, *53*(23), 5872-5876; 'Copper-Chelating Azides for Efficient Click Conjugation Reactions in Complex Media'; DOI 10.1002/anie.201310671.
[166] B. Cegielska, K. M. Kacprzak, *Chem. Anal. (Warsaw, Pol.)* **2009**, *54*(4), 807-812; 'Simple and Convenient Protocol for Staining of Organic Azides on TLC Plates by Ninhydrin. A New Application of an Old Reagent'.

[167] W. R. Streit, P. Entcheva, *Appl. Microbiol. Biotechnol.* **2003**, *61*, 21-31; 'Biotin in microbes, the genes involved in its biosynthesis, its biochemical role and perspectives for biotechnological production'; DOI 10.1007/s00253-002-1186-2.
[168] J. Zempleni, S. S. K. Wijeratne, Y. I. Hassan, *Biofactors* **2009**, *35*(1), 36-46; 'Biotin'; DOI 10.1002/biof.8.
[169] Y. M. Xu, J. Y. Du, A. T. Y. Lau, *Proteomics* **2014**, *14*(17-18), 2047-2060; 'Posttranslational modifications of human histone H3: An update'; DOI 10.1002/pmic.201300435.
[170] A. Chapman-Smith, T. W. Morris, J. C. Wallace, J. E. Cronan, *J. Biol. Chem.* **1999**, *274*(3), 1449-1457; 'Molecular Recognition in a Post-Translational Modification of Exceptional Specificity: Mutants of the Biotinylated Domain of Acetyl-CoA Carboxylase Defective in Recognition by Biotin Protein Ligase'; DOI 10.1074/jbc.274.3.1449.
[171] L. Chaiet, F. J. Wolf, *Arch. Biochem. Biophys.* **1964**, *106*, 1-5; 'The properties of Streptavidin, a Biotin-Binding Protein Produced by *Streptomycetes*'; DOI 10.1016/0003-9861(64)90150-x.
[172] N. M. Green, **1975**, '*Avidin*' in *Advances in Protein Chemistry, Vol. 29*, 85-133, Academic Press Inc., Cambridge, Massachusetts, USA; ISBN 978-0-12-034229-7, DOI 10.1016/S0065-3233(08)60411-8.
[173] O. H. Laitinen, T. P. Kuusela, S. Kukkurainen, A. Nurminen, A. Sinkkonen, V. P. Hytönen, *BMC Ecol. Evol.* **2021**, *21*(53), 1-14; 'Bacterial avidins are a widely distributed protein family in Actinobacteria, Proteobacteria and Bacteroidetes'; DOI 10.1186/s12862-021-01784-y.
[174] F. Tausig, F. J. Wolf, *Biochem. Biophys. Res. Commun.* **1964**, *14*, 205-209; 'Streptavidin - A Substance with Avidin-Like Properties Produced by Microorganisms'; DOI 10.1016/0006-291X(64)90436-X.
[175] J. Li, G. Brader, E. Helenius, T. Kariola, E. T. Palva, *Plant J.* **2012**, *70*(2), 315-326; 'Biotin deficiency causes spontaneous cell death and activation of defense signaling'; DOI 10.1111/j.1365-313X.2011.04871.x.
[176] M. González, C. E. Argaraña, G. D. Fidelio, *Biomol. Eng.* **1999**, *16*(1-4), 67-72; 'Extremely high thermal stability of streptavidin and avidin upon biotin binding'; DOI 10.1016/s1050-3862(99)00041-8.
[177] S. E. Ross, S. D. Carson, L. M. Fink, *BioTechniques* **1986**, *4*(4), 350-354; 'Effects of Detergents on Avidin-Biotin Interaction'.
[178] C. M. Dundas, D. Demonte, S. Park, *Appl. Microbiol. Biotechnol.* **2013**, *97*, 9343-9353; 'Streptavidin–biotin technology: improvements and innovations in chemical and biological applications'; DOI 10.1007/s00253-013-5232-z.
[179] I.-H. Cho, E.-H. Paek, H. Lee, J. Y. Kang, T. S. Kim, S.-H. Paek, *Anal. Biochem.* **2007**, *365*(1), 14-23; 'Site-directed biotinylation of antibodies for controlled immobilization on solid surfaces'; DOI 10.1016/j.ab.2007.02.028.
[180] M. Ganji, I. A. Shaltiel, S. Bisht, E. Kim, A. Kalichava, C. H. Haering, C. Dekker, *Science* **2018**, *360*(6384), 102-105; 'Real-time imaging of DNA loop extrusion by condensin'; DOI 10.1126/science.aar7831.
[181] A. Koide, J. Wojcik, R. N. Gilbreth, A. Reichel, J. Piehler, S. Koide, *Protein Eng. Des. Sel.* **2009**, *22*(11), 685-690; 'Accelerating phage-display library selection by reversible and site-specific biotinylation'; DOI 10.1093/protein/gzp053.
[182] W. X. Ren, J. Han, S. Uhm, Y. J. Jang, C. Kang, J.-H. Kim, J. S. Kim, *Chem. Commun.* **2015**, *51*(52), 10403-10418; 'Recent development of biotin conjugation in biological imaging, sensing, and target delivery'; DOI 10.1039/C5CC03075G.
[183] R. Gambari, G. Feriotto, C. Rutigliano, N. Bianchi, C. Mischiati, *J. Pharmacol. Exp. Ther.* **2000**, *294*(1), 370-377; 'Biospecific Interaction Analysis (BIA) of Low-Molecular Weight DNA-Binding Drugs', PubMed ID 10871335.
[184] J. M. Eeftens, J. van der Torre, D. R. Burnham, C. Dekker, *BMC Biophys.* **2015**, *8*, 1-7; 'Copper-free click chemistry for attachment of biomolecules in magnetic tweezers'; DOI 10.1186/s13628-015-0023-9.
[185] K. J. Roux, D. I. Kim, B. Burke, D. G. May, *Curr. Protoc. Protein Sci.* **2018**, *91*(1), 19.23.11-19.23.15; 'BioID: a screen for protein-protein interactions'; DOI 10.1002/cpps.51.
[186] T. C. Branon, J. A. Bosch, A. D. Sanchez, N. D. Udeshi, T. Svinkina, S. A. Carr, J. L. Feldman, N. Perrimon, A. Y. Ting, *Nat. Biotechnol.* **2018**, *36*(9), 880-887; 'Efficient proximity labeling in living cells and organisms with TurboID'; DOI 10.1038/nbt.4201.
[187] M. Rodrigues, P. Bhattacharjee, A. Brinkmalm, D. T. Do, C. M. Pearson, S. De, A. Ponjavic, J. A. Varela, K. Kulenkampff, I. Baudrexel, D. Emin, F. S. Ruggeri, J. E. Lee, A. R. Carr, T. P. J. Knowles, H. Zetterberg, T. N. Snaddon, S. Gandhi, S. F. Lee, D. Klenerman, *Nat. Chem.* **2022**, *14*(9), 1045-1053; 'Structure-specific amyloid precipitation in biofluids'; DOI 10.1038/s41557-022-00976-3.
[188] E. de Boer, P. Rodriguez, E. Bonte, J. Krijgsveld, E. Katsantoni, A. Heck, F. Grosveld, J. Strouboulis, *Proc. Natl. Acad. Sci. U.S.A.* **2003**, *100*(13), 7480-7485; 'Efficient biotinylation and single-step purification of tagged transcription factors in mammalian cells and transgenic mice'; DOI 10.1073/pnas.1332608100.
[189] A. A. Welcher, A. R. Torres, D. C. Ward, *Nucleic Acids Res.* **1986**, *14*(24), 10027-10044; 'Selective enrichment of specific DNA, cDNA and RNA sequences using biotinylated probes, avidin and copper-chelate agarose'; DOI 10.1093/nar/14.24.10027.
[190] G. Elia, *Proteomics* **2008**, *8*(19), 4012-4024; 'Biotinylation reagents for the study of cell surface proteins'; DOI 10.1002/pmic.200800097.
[191] C. E. Murar, F. Thuaud, J. W. Bode, *J. Am. Chem. Soc.* **2014**, *136*(52), 18140-18148; 'KAHA Ligations That Form Aspartyl Aldehyde Residues as Synthetic Handles for Protein Modification and Purification'; DOI 10.1021/ja511231f.
[192] B. Siewert, M. Langerman, A. Pannwitz, S. Bonnet, *Eur. J. Inorg. Chem.* **2018**, *2018*(37), 4117-4124; 'Synthesis and Avidin Binding of Ruthenium Complexes Functionalized with a Light-Cleavable Free Biotin Moiety'; DOI 10.1002/ejic.201800644.
[193] M. Tantama, W.-C. Lin, S. Licht, *J. Am. Chem. Soc.* **2008**, *130*(47), 15766-15767; 'An activity-based protein profiling probe for the nicotinic acetylcholine receptor'; DOI 10.1021/ja805868x.
[194] B. Liu, *Trends Chem.* **2019**, *1*(8), 763-778; 'Bio-orthogonal Click Chemistry for *In Vivo* Bioimaging'; DOI 10.1016/j.trechm.2019.08.003.
[195] J. M. Baskin, C. R. Bertozzi, *QSAR Comb. Sci.* **2007**, *26*(11-12), 1211-1219; 'Bioorthogonal Click Chemistry: Covalent Labeling in Living Systems'; DOI 10.1002/qsar.200740086.

[196] S. R. Park, J. Hauver, Y. Zhang, A. Revyakin, R. A. Coleman, R. Tjian, S. Chu, A. Pertsinidis, *Structure* **2020**, *28*(12), 1337-1343.e1334; 'A Single-Molecule Surface-Based Platform to Detect the Assembly and Function of the Human RNA Polymerase II Transcription Machinery'; DOI 10.1016/j.str.2020.07.009.
[197] R. C. Oslund, T. Reyes-Robles, C. H. White, J. H. Tomlinson, K. A. Crotty, E. P. Bowman, D. Chang, V. M. Peterson, L. Li, S. Frutos, M. Vila-Perelló, D. Vlerick, K. Cromie, D. H. Perlman, S. Ingale, S. D. O' Hara, L. R. Roberts, G. Piizzi, E. C. Hett, D. J. Hazuda, O. O. Fadeyi, *Nat. Chem. Biol.* **2022**, *18*(8), 850-858; 'Detection of cell–cell interactions via photocatalytic cell tagging'; DOI 10.1038/s41589-022-01044-0.
[198] D. S. Schade, L. Shey, R. P. Eaton, *Endocr. Pract.* **2020**, *26*(12), 1514-1523; 'Cholesterol Review: A Metabolically Important Molecule'; DOI 10.4158/EP-2020-0347.
[199] A. H. Payne, D. B. Hales, *Endocr. Rev.* **2004**, *25*(6), 947-970; 'Overview of Steroidogenic Enzymes in the Pathway from Cholesterol to Active Steroid Hormones'; DOI 10.1210/er.2003-0030.
[200] G. Saher, B. Brügger, C. Lappe-Siefke, W. Möbius, R.-i. Tozawa, M. C. Wehr, F. Wieland, S. Ishibashi, K.-A. Nave, *Nat. Neurosci.* **2005**, *8*(4), 468-475; 'High cholesterol level is essential for myelin membrane growth'; DOI 10.1038/nn1426.
[201] R. A. Cooper, *J. Supramol. Struct.* **1978**, *8*(4), 413-430; 'Influence of Increased Membrane Cholesterol on Membrane Fluidity and Cell Function in Human Red Blood Cells'; DOI 10.1002/jss.400080404.
[202] H. Ma, K.-J. Shieh, *Am. J. Sci.* **2006**, *2*(1), 46-50; 'Cholesterol and Human Health'.
[203] T. Vuorela, A. Catte, P. S. Niemelä, A. Hall, M. T. Hyvönen, S.-J. Marrink, M. Karttunen, I. Vattulainen, *PLoS Comput. Biol.* **2010**, *6*(10):e1000964, 1-14; 'Role of Lipids in Spheroidal High Density Lipoproteins'; DOI 10.1371/journal.pcbi.1000964.
[204] J. A. Glomset, *J. Lipid Res.* **1968**, *9*(2), 155-167; 'The plasma lecithin: cholesterol acyltransferase reaction'; DOI 10.1016/S0022-2275(20)43114-1.
[205] E. A. Fisher, J. E. Feig, B. Hewing, S. L. Hazen, J. D. Smith, *Arterioscler. Thromb. Vasc. Biol.* **2012**, *32*(12), 2813-2820; 'High-Density Lipoprotein Function, Dysfunction, and Reverse Cholesterol Transport'; DOI 10.1161/ATVBAHA.112.300133.
[206] A. Colpo, *J. Am. Phys. Surg.* **2005**, *10*(3), 83-89; 'LDL Cholesterol: "Bad" Cholesterol or Bad Science?'.
[207] J. Simons, *Fortune* **2003**, *147*(1), 58-68; 'The $10 Billion Pill', 12602122.
[208] C. Stancu, A. Sima, *J. Cell. Mol. Med.* **2001**, *5*(4), 378-387; 'Statins: mechanism of action and effects'; DOI 10.1111/j.1582-4934.2001.tb00172.x.
[209] S. G. Mlodinow, M. K. Onysko, J. W. Vandiver, M. L. Hunter, T. D. Mahvan, *J. Fam. Pract.* **2014**, *63*(9), 497-506; 'Statin Adverse Effects: Sorting out the Evidence', PubMed ID 25353029.
[210] A. Henninot, J. C. Collins, J. M. Nuss, *J. Med. Chem.* **2018**, *61*(4), 1382-1414; 'The Current State of Peptide Drug Discovery: Back to the Future?'; DOI 10.1021/acs.jmedchem.7b00318.
[211] B. D. Welch, A. P. VanDemark, A. Heroux, C. P. Hill, M. S. Kay, *Proc. Natl. Acad. Sci. U.S.A.* **2007**, *104*(43), 16828-16833; 'Potent D-Peptide Inhibitors of HIV-1 Entry'; DOI 10.1073/pnas.0708109104.
[212] M. Muttenthaler, G. F. King, D. J. Adams, P. F. Alewood, *Nat. Rev. Drug Discov.* **2021**, *20*(4), 309-325; 'Trends in peptide drug discovery'; DOI 10.1038/s41573-020-00135-8.
[213] W. Jaroszewicz, J. Morcinek-Orłowska, K. Pierzynowska, L. Gaffke, G. Węgrzyn, *FEMS Microbiol. Rev.* **2022**, *46*(2):fuab052, 1-25; 'Phage display and other peptide display technologies'; DOI 10.1093/femsre/fuab052.
[214] A. A. D'Souza, R. Shegokar, *Expert Opin. Drug Deliv.* **2016**, *13*(9), 1257-1275; 'Polyethylene glycol (PEG): a versatile polymer for pharmaceutical applications'; DOI 10.1080/17425247.2016.1182485.
[215] Alzheimer's Association, *Alzheimer's Dementia* **2019**, *15*(3), 321-387; '2019 Alzheimer's disease facts and figures'; DOI 10.1016/j.jalz.2019.01.010.
[216] A. Serrano-Pozo, M. P. Frosch, E. Masliah, B. T. Hyman, *Cold Spring Harb. Perspect. Med.* **2011**, *1*(1):a006189, 1-24; 'Neuropathological Alterations in Alzheimer Disease'; DOI 10.1101/cshperspect.a006189.
[217] S. H. W. Scheres, B. Ryskeldi-Falcon, M. Goedert, *Nature* **2023**, *621*(7980), 701-710; 'Molecular pathology of neurodegenerative diseases by cryo-EM of amyloids'; DOI 10.1038/s41586-023-06437-2.
[218] D. Willbold, B. Strodel, G. F. Schröder, W. Hoyer, H. Heise, *Chem. Rev.* **2021**, *121*(13), 8285-8307; 'Amyloid-type Protein Aggregation and Prion-like Properties of Amyloids'; DOI 10.1021/acs.chemrev.1c00196.
[219] D. Twohig, H. M. Nielsen, *Mol. Neurodegener.* **2019**, *14*(1), 1-19; 'α-synuclein in the pathophysiology of Alzheimer's disease'; DOI 10.1186/s13024-019-0320-x.
[220] P. C. Donaghy, I. G. McKeith, *Alzheimer's Res. Ther.* **2014**, *6*(4), 1-12; 'The clinical characteristics of dementia with Lewy bodies and a consideration of prodromal diagnosis'; DOI 10.1186/alzrt274.
[221] A. L. Boxer, R. Sperling, *Cell* **2023**, *186*(22), 4757-4772; 'Accelerating Alzheimer's therapeutic development: The past and future of clinical trials'; DOI 10.1016/j.cell.2023.09.023.
[222] J. Stockmann, I. M. W. Verberk, N. Timmesfeld, R. Denz, B. Budde, J. Lange-Leifhelm, P. Scheltens, W. M. van der Flier, A. Nabers, C. E. Teunissen, K. Gerwert, *Alzheimer's Res. Ther.* **2020**, *12*, 1-13; 'Amyloid-β misfolding as a plasma biomarker indicates risk for future clinical Alzheimer's disease in individuals with subjective cognitive decline'; DOI 10.1186/s13195-020-00738-8.
[223] H. LeVine III, **1999**, '*[18] Quantification of β-Sheet Amyloid Fibril Structures with Thioflavin T*' in *Amyloid, Prions, and Other Protein Aggregates. Methods in Enzymology, Vol. 309*, 274-284, Academic Press Inc., Cambridge, Massachusetts, USA; ISBN 978-0-12-182210-1, DOI 10.1016/s0076-6879(99)09020-5.
[224] W. E. Klunk, H. Engler, A. Nordberg, Y. Wang, G. Blomqvist, D. P. Holt, M. Bergström, I. Savitcheva, G. F. Huang, S. Estrada, B. Ausén, M. L. Debnath, J. Barletta, J. C. Price, J. Sandell, B. J. Lopresti, A. Wall, P. Koivisto, G. Antoni, C. A. Mathis, B. Långström, *Ann. Neurol.* **2004**, *55*(3), 306-319; 'Imaging Brain Amyloid in Alzheimer's Disease with Pittsburgh Compound-B'; DOI 10.1002/ana.20009.
[225] M. T. Fodero-Tavoletti, D. P. Smith, C. A. McLean, P. A. Adlard, K. J. Barnham, L. E. Foster, L. Leone, K. Perez, M. Cortés, J. G. Culvenor, Q.-X. Li, K. M. Laughton, C. C. Rowe, C. L. Masters, R. Cappai, V. L. Villemagne, *J. Neurosci.*

2007, *27*(39), 10365-10371; '*In Vitro* Characterization of Pittsburgh Compound-B Binding to Lewy Bodies'; DOI 10.1523/JNEUROSCI.0630-07.2007.
[226] R. M. Meade, D. P. Fairlie, J. M. Mason, *Mol. Neurodegener.* **2019**, *14*(29), 1-14; 'Alpha-synuclein structure and Parkinson's disease – lessons and emerging principles'; DOI 10.1186/s13024-019-0329-1.
[227] A. Siderowf, L. Concha-Marambio, D.-E. Lafontant, C. M. Farris, Y. Ma, P. A. Urenia, H. Nguyen, R. N. Alcalay, L. M. Chahine, T. Foroud, D. Galasko, K. Kieburtz, K. Merchant, B. Mollenhauer, K. L. Poston, J. Seibyl, T. Simuni, C. M. Tanner, D. Weintraub, A. Videnovic, S. H. Choi, R. Kurth, C. Caspell-Garcia, C. S. Coffey, M. Frasier, L. M. A. Oliveira, S. J. Hutten, T. Sherer, K. Marek, C. Soto, *Lancet Neurol.* **2023**, *22*(5), 407-417; 'Assessment of heterogeneity among participants in the Parkinson's Progression Markers Initiative cohort using α-synuclein seed amplification: a cross-sectional study'; DOI 10.1016/S1474-4422(23)00109-6.
[228] A. Schaffrath, S. Schleyken, A. Seger, H. Jergas, P. Özdüzenciler, M. Pils, L. Blömeke, A. Cousin, J. Willbold, T. Bujnicki, O. Bannach, G. R. Fink, D. Willbold, M. Sommerauer, M. T. Barbe, G. Tamgüney, *NPJ Parkinsons Dis.* **2023**, *9*(1):14, 1-11; 'Patients with isolated REM-sleep behavior disorder have elevated levels of alpha-synuclein aggregates in stool'; DOI 10.1038/s41531-023-00458-4.
[229] A. Okuzumi, T. Hatano, G. Matsumoto, S. Nojiri, S.-i. Ueno, Y. Imamichi-Tatano, H. Kimura, S. Kakuta, A. Kondo, T. Fukuhara, Y. Li, M. Funayama, S. Saiki, D. Taniguchi, T. Tsunemi, D. McIntyre, J.-J. Gérardy, M. Mittelbronn, R. Kruger, Y. Uchiyama, N. Nukina, N. Hattori, *Nat. Med.* **2023**, *29*(6), 1448-1455; 'Propagative α-synuclein seeds as serum biomarkers for synucleinopathies'; DOI 10.1038/s41591-023-02358-9.
[230] L. Concha-Marambio, S. Pritzkow, M. Shahnawaz, C. M. Farris, C. Soto, *Nat. Protoc.* **2023**, *18*(4), 1179-1196; 'Seed amplification assay for the detection of pathologic alpha-synuclein aggregates in cerebrospinal fluid'; DOI 10.1038/s41596-022-00787-3.
[231] A. V. Bordunov, P. C. Hellier, J. S. Bradshaw, N. K. Dalley, X. Kou, X. X. Zhang, R. M. Izatt, *J. Org. Chem.* **1995**, *60*(19), 6097-6102; 'Synthesis of New Pyridinoazacrown Ethers Containing Aromatic and Heteroaromatic Proton Ionizable Substituents'; DOI 10.1021/jo00124a022.
[232] J. P. H. Verheyden, J. G. Moffatt, *J. Org. Chem.* **1970**, *35*(7), 2319-2326; 'Halo Sugar Nucleosides. I. Iodination of the Primary Hydroxyl Groups of Nucleosides with Methyltriphenoxyphosphonium Iodide'; DOI 10.1021/jo00832a047.
[233] J. P. H. Verheyden, J. G. Moffatt, *J. Org. Chem.* **1970**, *35*(9), 2868-2877; 'Halo Sugar Nucleosides. II. Iodination of Secondary Hydroxyl Groups of Nucleosides with Methyltriphenoxyphosphonium Iodide'; DOI 10.1021/jo00834a002.
[234] P. Li, J. Li, L. Wang, L. J. Di, *Proteomics* **2017**, *17*(20):1700002, 1-10; 'Proximity Labeling of Interacting Proteins: Application of BioID as a Discovery Tool'; DOI 10.1002/pmic.201700002.
[235] M. B. Parrott, M. A. Barry, *Mol. Ther.* **2000**, *1*(1), 96-104; 'Metabolic Biotinylation of Recombinant Proteins in Mammalian Cells and in Mice'; DOI 10.1006/mthe.1999.0011.
[236] S. Kang, L. Mou, J. Lanman, S. Velu, W. J. Brouillette, P. E. Prevelige Jr., *Rapid Commun. Mass Spectrom.* **2009**, *23*(11), 1719-1726; 'Synthesis of biotin-tagged chemical cross-linkers and their applications for mass spectrometry'; DOI 10.1002/rcm.4066.
[237] J. D. Esko, Y. Tor, 'Assisted Enzyme Replacement Therapy', World Patent WO 2011/034951 A2, 1-107, **2011**, https://patentimages.storage.googleapis.com/86/6b/a1/32d1e8c4de1038/WO2011034951A2.pdf.
[238] J. D. Esko, Y. Tor, 'Assisted Enzyme Replacement Therapy', U.S. Patent US 2018/0311321 A1, 1-78, **2018**, https://patentimages.storage.googleapis.com/76/77/05/466759597b8749/US20180311321A1.pdf.
[239] I. Kaur, P. Kaur, K. Singh, *Dyes Pigm.* **2020**, *176*:108198, 1-8; '2-(2′-Hydroxyphenyl)benzothiazole derivatives: Emission and color tuning'; DOI 10.1016/j.dyepig.2020.108198.
[240] H. Reed, T. R. Paul, W. J. Chain, *J. Org. Chem.* **2018**, *83*(18), 11359-11368; 'Synthesis of Halogenated Anilines by Treatment of *N*,*N*-Dialkylaniline *N*-Oxides with Thionyl Halides'; DOI 10.1021/acs.joc.8b01590.
[241] Y. Huang, H.-J. Cho, N. Bandara, L. Sun, D. Tran, B. E. Rogers, L. M. Mirica, *Chem. Sci.* **2020**, *11*(30), 7789-7799; 'Metal-chelating benzothiazole multifunctional compounds for the modulation and ^{64}Cu PET imaging of Aβ aggregation'; DOI 10.1039/d0sc02641g.
[242] I. Diner, J. Dooyema, M. Gearing, L. C. Walker, N. T. Seyfried, *Bioconjugate Chem.* **2017**, *28*(10), 2627-2637; 'Generation of clickable Pittsburgh Compound B for the detection and capture of β-Amyloid in Alzheimer's Disease Brain'; DOI 10.1021/acs.bioconjchem.7b00500.
[243] C. Xue, T. Y. Lin, D. Chang, Z. Guo, *R. Soc. Open Sci.* **2017**, *4*(1):116257, 1-12; 'Thioflavin T as an amyloid dye: fibril quantification, optimal concentration and effect on aggregation'; DOI 10.1098/rsos.160696.
[244] B. J. Lopresti, W. E. Klunk, C. A. Mathis, J. A. Hoge, S. K. Ziolko, X. Lu, C. C. Meltzer, K. Schimmel, N. D. Tsopelas, S. T. DeKosky, J. C. Price, *J. Nucl. Med.* **2005**, *46*(12), 1959-1972; 'Simplified Quantification of Pittsburgh Compound B Amyloid Imaging PET Studies: A Comparative Analysis', PubMed ID 16330558.
[245] J. N. Rybak, S. B. Scheurer, D. Neri, G. Elia, *Proteomics* **2004**, *4*(8), 2296-2299; 'Purification of biotinylated proteins on streptavidin resin: a protocol for quantitative elution'; DOI 10.1002/pmic.200300780.
[246] A. Jain, R. Liu, B. Ramani, E. Arauz, Y. Ishitsuka, K. Ragunathan, J. Park, J. Chen, Y. K. Xiang, T. Ha, *Nature* **2011**, *473*(7348), 484-488; 'Probing cellular protein complexes using single-molecule pull-down'; DOI 10.1038/nature10016.
[247] T. R. Chan, V. V. Fokin, *QSAR Comb. Sci.* **2007**, *26*(11-12), 1274-1279; 'Polymer-Supported Copper(I) Catalysts for the Experimentally Simplified Azide–Alkyne Cycloaddition'; DOI 10.1002/qsar.200740131.
[248] M. M. A. Mitry, F. Greco, H. M. I. Osborn, *Chem. Eur. J.* **2023**, *29*(20):e202203942, 1-24; '*In Vivo* Applications of Bioorthogonal Reactions: Chemistry and Targeting Mechanisms'; DOI 10.1002/chem.202203942.
[249] S. Li, L. Wang, F. Yu, Z. Zhu, D. Shobaki, H. Chen, M. Wang, J. Wang, G. Qin, U. J. Erasquin, L. Ren, Y. Wang, C. Cai, *Chem. Sci.* **2017**, *8*(3), 2107-2114; 'Copper-catalyzed click reaction on/in live cells'; DOI 10.1039/c6sc02297a.
[250] C. A. Mathis, Y. Wang, D. P. Holt, G.-F. Huang, M. L. Debnath, W. E. Klunk, *J. Med. Chem.* **2003**, *46*(13), 2740-2754; 'Synthesis and Evaluation of ^{11}C-Labeled 6-Substituted 2-Arylbenzothiazoles as Amyloid Imaging Agents'; DOI 10.1021/jm030026b.

[251] R. Croteau, T. M. Kutchan, N. G. Lewis, **2015**, '*Natural Products (Secondary Metabolites)*' in *Biochemistry and Molecular Biology of Plants, 2nd Edition*, 1250-1319, John Wiley & Sons, Inc., Hoboken, New Jersey, USA; ISBN 978-0-470-71421-8.
[252] J. Bérdy, *J. Antibiot.* **2005**, *58*(1), 1-26; 'Bioactive Microbial Metabolites'; DOI 10.1038/ja.2005.1.
[253] A. L. Demain, S. Sánchez, **2019**, '*Microbial Synthesis of Primary Metabolites: Current Trends and Future Prospects*' in *Fermentation Microbiology and Biotechnology, Fourth Edition*, 57-74, CRC Press, Boca Raton, Florida, USA; ISBN 978-1138581029, DOI 10.1201/9780429506987.
[254] S. Mathur, C. Hoskins, *Biomed. Rep.* **2017**, *6*(6), 612-614; 'Drug development: Lessons from nature'; DOI 10.3892/br.2017.909.
[255] D. W. P. Tay, N. Z. X. Yeo, K. Adaikkappan, Y. H. Lim, S. J. Ang, *Sci. Data* **2023**, *10*(1):296, 1-8; '67 million natural product-like compound database generated via molecular language processing'; DOI 10.1038/s41597-023-02207-x.
[256] J. W.-H. Li, J. C. Vederas, *Science* **2009**, *325*(5937), 161-165; 'Drug Discovery and Natural Products: End of an Era or an Endless Frontier?'; DOI 10.1126/science.1168243.
[257] R. Breslow, *J. Chem. Educ.* **1998**, *75*(6), 705-718; 'Bioorganic Chemistry: A Natural and Unnatural Science'; DOI 10.1021/ed075p705.
[258] A. Fürstner, *Angew. Chem.* **2003**, *115*(31), 3706-3728; 'Chemie und Biologie des Roseophilins und der Prodigiosin-Alkaloide: 2500 Jahre im Überblick'; DOI 10.1002/ange.200300582.
[259] A. Fürstner, *Angew. Chem. Int. Ed.* **2003**, *42*(31), 3582-3603; 'Chemistry and Biology of Roseophilin and the Prodigiosin Alkaloids: A Survey of the Last 2500 Years'; DOI 10.1002/anie.200300582.
[260] S. A. Parikh, H. Kantarjian, A. Schimmer, W. Walsh, E. Asatiani, K. El-Shami, E. Winton, S. Verstovsek, *Clin. Lymphoma Myeloma Leuk.* **2010**, *10*(4), 285-289; 'Phase II Study of Obatoclax Mesylate (GX15-070), a Small-Molecule BCL-2 Family Antagonist, for Patients with Myelofibrosis'; DOI 10.3816/CLML.2010.n.059.
[261] A. D. Schimmer, S. O'Brien, H. Kantarjian, J. Brandwein, B. D. Cheson, M. D. Minden, K. Yee, F. Ravandi, F. Giles, A. Schuh, *Clin. Cancer Res.* **2008**, *14*(24), 8295-8301; 'A Phase I Study of the Pan Bcl-2 Family Inhibitor Obatoclax Mesylate in Patients with Advanced Hematologic Malignancies'; DOI 10.1158/1078-0432.CCR-08-0999.
[262] A. D. Schimmer, A. Raza, T. H. Carter, D. Claxton, H. Erba, D. J. DeAngelo, M. S. Tallman, C. Goard, G. Borthakur, *PLoS One* **2014**, *9*(10):e108694, 1-10; 'A multicenter phase I/II study of obatoclax mesylate administered as a 3-or 24-hour infusion in older patients with previously untreated acute myeloid leukemia'; DOI 10.1371/journal.pone.0108694.
[263] A. Fürstner, J. Grabowski, C. W. Lehmann, *J. Org. Chem.* **1999**, *64*(22), 8275-8280; 'Total Synthesis and Structural Refinement of the Cyclic Tripyrrole Pigment Nonylprodigiosin'; DOI 10.1021/jo991021i.
[264] H. Rapoport, C. D. Willson, *J. Am. Chem. Soc.* **1962**, *84*(4), 630-635; 'The Preparation and Properties of Some Methoxypyrroles'; DOI 10.1021/ja00863a025.
[265] D. L. Boger, M. Patel, *J. Org. Chem.* **1988**, *53*(7), 1405-1415; 'Total Synthesis of Prodigiosin, Prodigiosene, and Desmethoxyprodigiosin: Diels-Alder Reactions of Heterocyclic Azadienes and Development of an Effective Palladium(II)-Promoted 2,2'-Bipyrrole Coupling Procedure'; DOI 10.1021/jo00242a013.
[266] H. H. Wasserman, L. J. Lombardo, *Tetrahedron Lett.* **1989**, *30*(13), 1725-1728; 'The Chemistry of Vicinal Tricarbonyls a Total Synthesis of Prodigiosin'; DOI 10.1016/S0040-4039(00)99566-2.
[267] H. H. Wasserman, G. C. Rodgers, D. D. Keith, *J. Am. Chem. Soc.* **1969**, *91*(5), 1263-1264; 'Metacycloprodigiosin, a Tripyrrole Pigment from *Streptomyces longisporus ruber*'; DOI 10.1021/ja01033a065.
[268] R. E. Johnson, T. de Rond, V. N. G. Lindsay, J. D. Keasling, R. Sarpong, *Org. Lett.* **2015**, *17*(14), 3474-3477; 'Synthesis of Cycloprodigiosin Identifies the Natural Isolate as a Scalemic Mixture'; DOI 10.1021/acs.orglett.5b01527.
[269] M. D. Clift, R. J. Thomson, *J. Am. Chem. Soc.* **2009**, *131*(40), 14579-14583; 'Development of a Merged Conjugate Addition/Oxidative Coupling Sequence. Application to the Enantioselective Total Synthesis of Metacycloprodigiosin and Prodigiosin R1'; DOI 10.1021/ja906122g.
[270] J. H. Frederich, P. G. Harran, *J. Am. Chem. Soc.* **2013**, *135*(10), 3788-3791; 'Modular Access to Complex Prodiginines: Total Synthesis of (+)-Roseophilin via its 2-Azafulvene Prototropisomer'; DOI 10.1021/ja400473v.
[271] A. Fürstner, K. Radkowski, H. Peters, *Angew. Chem. Int. Ed.* **2005**, *44*(18), 2777-2781; 'Chasing a Phantom by Total Synthesis: The Butylcycloheptylprodigiosin Case'; DOI 10.1002/anie.200462215.
[272] A. Fürstner, K. Radkowski, H. Peters, *Angew. Chem.* **2005**, *117*(18), 2669-2873; 'Chasing a Phantom by Total Synthesis: The Butylcycloheptylprodigiosin Case'; DOI 10.1002/ange.200462215.
[273] A. Fürstner, H. Weintritt, *J. Am. Chem. Soc.* **1998**, *120*(12), 2817-2825; 'Total Synthesis of Roseophilin'; DOI 10.1021/ja973846k.
[274] D. X. Hu, D. M. Withall, G. L. Challis, R. J. Thomson, *Chem. Rev.* **2016**, *116*(14), 7818-7853; 'Structure, Chemical Synthesis, and Biosynthesis of Prodiginine Natural Products'; DOI 10.1021/acs.chemrev.6b00024.
[275] N. R. Williamson, P. C. Fineran, F. J. Leeper, G. P. C. Salmond, *Nat. Rev. Microbiol.* **2006**, *4*(12), 887-899; 'The biosynthesis and regulation of bacterial prodiginines'; DOI 10.1038/nrmicro1531.
[276] A. K. P. Harris, N. R. Williamson, H. Slater, A. Cox, S. Abbasi, I. Foulds, H. T. Simonsen, F. J. Leeper, G. P. C. Salmond, *Microbiology* **2004**, *150*(11), 3547-3560; 'The *Serratia* gene cluster encoding biosynthesis of the red antibiotic, prodigiosin, shows species- and strain-dependent genome context variation'; DOI 10.1099/mic.0.27222-0.
[277] A. M. Cerdeño, M. J. Bibb, G. L. Challis, *Chem. Biol.* **2001**, *8*(8), 817-829; 'Analysis of the prodiginine biosynthesis gene cluster of Streptomyces coelicolor A3 (2): new mechanisms for chain initiation and termination in modular multienzymes'; DOI 10.1016/S1074-5521(01)00054-0.
[278] K. J. Picott, J. A. Deichert, E. M. deKemp, G. Schatte, F. Sauriol, A. C. Ross, *MedChemComm* **2019**, *10*(3), 478-483; 'Isolation and characterization of tambjamine MYP1, a macrocyclic tambjamine analogue from marine bacterium *Pseudoalteromonas citrea*'; DOI 10.1039/c9md00061e.
[279] S. M. Salem, P. Kancharla, G. Florova, S. Gupta, W. Lu, K. A. Reynolds, *J. Am. Chem. Soc.* **2014**, *136*(12), 4565-4574; 'Elucidation of Final Steps of the Marineosins Biosynthetic Pathway through Identification and Characterization of the Corresponding Gene Cluster'; DOI 10.1021/ja411544w.

[280] E. A. Coco, K. E. Narva, J. S. Feitelson, *Mol. Genet. Genom.* **1991**, *227*, 28-32; 'New classes of *Streptomyces coelicolor* A3(2) mutants blocked in undecylprodigiosin (Red) biosynthesis'; DOI 10.1007/BF00260702.
[281] X. Wang, T. Isbrandt, E. Ø. Christensen, J. Melchiorsen, T. O. Larsen, S.-D. Zhang, L. Gram, *Microbiol. Spectr.* **2021**, *9*(2):e01171-21, 1-11; 'Identification and Verification of the Prodigiosin Biosynthetic Gene Cluster (BGC) in *Pseudoalteromonas rubra* S4059'; DOI 10.1128/spectrum.01171-21.
[282] N. L. Grenade, D. S. Chiriac, A. R. O. Pasternak, J. L. Babulic, B. E. Rowland, G. W. Howe, A. C. Ross, *ACS Chem. Biol.* **2023**, *18*(2), 223-229; 'Discovery of a Tambjamine Gene Cluster in Streptomyces Suggests Convergent Evolution in Bipyrrole Natural Product Biosynthesis'; DOI 10.1021/acschembio.2c00685.
[283] N. R. Williamson, H. T. Simonsen, R. A. A. Ahmed, G. Goldet, H. Slater, L. Woodley, F. J. Leeper, G. P. C. Salmond, *Mol. Microbiol.* **2005**, *56*(4), 971-989; 'Biosynthesis of the red antibiotic, prodigiosin, in *Serratia*: identification of a novel 2-methyl-3-*n*-amyl-pyrrole (MAP) assembly pathway, definition of the terminal condensing enzyme, and implications for undecylprodigiosin biosynthesis in *Streptomyces*'; DOI 10.1111/j.1365-2958.2005.04602.x.
[284] H. H. Wasserman, C. K. Shaw, R. J. Sykes, R. J. Cushley, *Tetrahedron Lett.* **1974**, *15*(33), 2787-2790; 'The Biosynthesis of Metacycloprodigiosin and Undecylprodigiosin'; DOI 10.1016/S0040-4039(01)91743-5.
[285] H. H. Wasserman, R. J. Sykes, P. Peverada, C. K. Shaw, R. J. Cushley, S. R. Lipsky, *J. Am. Chem. Soc.* **1973**, *95*(20), 6874-6875; 'Biosynthesis of Prodigiosin. Incorporation Patterns of ^{13}C-Labeled Alanine, Proline, Glycine, and Serine Elucidated by Fourier Transform Nuclear Magnetic Resonance'; DOI 10.1021/ja00801a080.
[286] S. R. Chawrai, N. R. Williamson, G. P. C. Salmond, F. J. Leeper, *Chem. Commun.* **2008**, *16*, 1862-1864; 'Chemoenzymatic synthesis of prodigiosin analogues – exploring the substrate specificity of PigC'; DOI 10.1039/b719353j.
[287] M. J. Jaremko, T. D. Davis, J. C. Corpuz, M. D. Burkart, *Nat. Prod. Rep.* **2020**, *37*(3), 355-379; 'Type II Non-ribosomal Peptide Synthetase Proteins: Structure, Mechanism, and Protein–Protein Interactions'; DOI 10.1039/c9np00047j.
[288] C. Dresen, M. Richter, M. Pohl, S. Lüdeke, M. Müller, *Angew. Chem. Int. Ed.* **2010**, *37*(49), 6600-6603; 'The Enzymatic Asymmetric Conjugate Umpolung Reaction'; DOI 10.1002/anie.201000632.
[289] C. Dresen, M. Richter, M. Pohl, S. Lüdeke, M. Müller, *Angew. Chem.* **2010**, *122*(37), 6750-6753; 'The Enzymatic Asymmetric Conjugate Umpolung Reaction'; DOI 10.1002/ange.201000632.
[290] N. R. Williamson, S. Chawrai, F. J. Leeper, G. P. C. Salmond, **2010**, '*Prodiginines and their Potential Utility as Proapoptotic Anticancer Agents*' in *Emerging Cancer Therapy: Microbial Approaches and Biotechnological Tools*, 333-366, John Wiley & Sons, Inc., Hoboken, New Jersey, USA; ISBN 978-0470444672, DOI 10.1002/9780470626528.ch15.
[291] Z. You, X. Liu, S. Zhang, Y. Wang, *Biochem. Eng. J.* **2018**, *134*, 1-11; 'Characterization of a prodigiosin synthetase PigC from *Serratia marcescens* jx-1 and its application in prodigiosin analogue synthesis'; DOI 10.1016/j.bej.2018.01.034.
[292] S. Brands, H. U. C. Brass, A. S. Klein, J. G. Sikkens, M. D. Davari, J. Pietruszka, A. J. Ruff, U. Schwaneberg, *Catal. Sci. Technol.* **2021**, *11*(8), 2805-2815; 'KnowVolution of prodigiosin ligase PigC towards condensation of short-chain prodiginines'; DOI 10.1039/d0cy02297g.
[293] K. J. Picott, J. A. Deichert, E. M. deKemp, V. Snieckus, A. C. Ross, *ChemBioChem* **2020**, *21*(7), 1036-1042; 'Purification and Kinetic Characterization of the Essential Condensation Enzymes Involved in Prodiginine and Tambjamine Biosynthesis'; DOI 10.1002/cbic.201900503.
[294] S. W. Haynes, P. K. Sydor, A. E. Stanley, L. Song, G. L. Challis, *Chem. Commun.* **2008**, *16*, 1865-1867; 'Role and substrate specificity of the *Streptomyces coelicolor* RedH enzyme in undecylprodiginine biosynthesis'; DOI 10.1039/b801677a.
[295] H. U. C. Brass, A. S. Klein, S. Nyholt, T. Classen, J. Pietruszka, *Adv. Synth. Catal.* **2019**, *361*(11), 2659-2667; 'Condensing Enzymes from *Pseudoalteromonadaceae* for Prodiginine Synthesis'; DOI 10.1002/adsc.201900183.
[296] R. M. Salih, Doctoral Thesis, 'Investigations of Carbocyclisation Reactions in Prodiginine Alkaloid Biosynthesis', University of Warwick (Warwick, England), **2017**; https://wrap.warwick.ac.uk/id/eprint/107843/1/WRAP_Theses_Salih_2017.pdf.
[297] T. Kawasaki, F. Sakurai, S.-y. Nagatsuka, Y. Hayakawa, *J. Antibiot.* **2009**, *62*(5), 271-276; 'Prodigiosin biosynthesis gene cluster in the roseophilin producer *Streptomyces griseoviridis*'; DOI 10.1038/ja.2009.27.
[298] D.-K. Kim, Y.-K. Park, J.-S. Lee, J.-H. F Kim, H.-Y. Jeong, B.-S. Kim, C.-H. Lee, *J. Microbiol. Biotechnol.* **2006**, *16*(12), 1912-1918; 'Analysis of a Prodigiosin Biosynthetic Gene Cluster from the Marine Bacterium *Hahella chejuensis* KCTC 2396'.
[299] C. Burke, T. Thomas, S. Egan, S. Kjelleberg, *Environ. Microbiol.* **2007**, *9*(3), 814-818; 'The use of functional genomics for the identification of a gene cluster encoding for the biosynthesis of an antifungal tambjamine in the marine bacterium *Pseudoalteromonas tunicata*'; DOI 10.1111/j.1462-2920.2006.01177.x.
[300] W. R. Hearn, M. K. Elson, R. H. Williams, J. Medina-Castro, *J. Org. Chem.* **1970**, *35*(1), 142-146; 'Prodigiosene [5-(2-Pyrryl)-2,2'-dipyrrylmethene] and Some Substituted Prodigiosenes'; DOI 10.1021/jo00826a032.
[301] A. S. Klein, A. Domröse, P. Bongen, H. U. C. Brass, T. Classen, A. Loeschcke, T. Drepper, L. Laraia, S. Sievers, K.-E. Jaeger, J. Pietruszka, *ACS Synth. Biol.* **2017**, *6*(9), 1757-1765; 'New Prodigiosin Derivatives Obtained by Mutasynthesis in *Pseudomonas putida*'; DOI 10.1021/acssynbio.7b00099.
[302] A. S. Klein, H. U. C. Brass, D. P. Klebl, T. Classen, A. Loeschcke, T. Drepper, S. Sievers, K. E. Jaeger, J. Pietruszka, *ChemBioChem* **2018**, *19*(14), 1545-1552; 'Preparation of cyclic prodiginines by mutasynthesis in *Pseudomonas putida* KT2440'; DOI 10.1002/cbic.201800154.
[303] S. M. O'Brien, D. F. Claxton, M. Crump, S. Faderl, T. Kipps, M. J. Keating, J. Viallet, B. D. Cheson, *Blood* **2009**, *113*(2), 299-305; 'Phase I study of obatoclax mesylate (GX15-070), a small molecule pan–Bcl-2 family antagonist, in patients with advanced chronic lymphocytic leukemia'; DOI 10.1182/blood-2008-02-137943.
[304] D. Fehér, R. S. Barlow, P. S. Lorenzo, T. K. Hemscheidt, *J. Nat. Prod.* **2008**, *71*(11), 1970-1972; 'A 2-Substituted Prodiginine, 2-(*p*-Hydroxybenzyl)prodigiosin, from *Pseudoalteromonas rubra*'; DOI 10.1021/np800493p.

[305] D. M. Withall, S. W. Haynes, G. L. Challis, *J. Am. Chem. Soc.* **2015**, *137*(24), 7889-7897; 'Stereochemistry and Mechanism of Undecylprodigiosin Oxidative Carbocyclization to Streptorubin B by the Rieske Oxygenase RedG'; DOI 10.1021/jacs.5b03994.
[306] C. Perry, E. L. C. De los Santos, L. M. Alkhalaf, G. L. Challis, *Nat. Prod. Rep.* **2018**, *35*(7), 622-632; 'Rieske non-heme iron-dependent oxygenases catalyse diverse reactions in natural product biosynthesis'; DOI 10.1039/c8np00004b.
[307] A. E. T. Silva, L. A. Guimarães, E. G. Ferreira, M. d. C. M. Torres, A. B. da Silva, P. C. Branco, F. A. S. Oliveira, G. G. Z. Silva, D. V. Wilke, E. R. Silveira, O. D. L. Pessoa, P. C. Jimenez, L. V. Costa-Lotufo, *J. Braz. Chem. Soc.* **2017**, *28*, 465-474; 'Bioprospecting Anticancer Compounds from the Marine-Derived Actinobacteria *Actinomadura* sp. Collected at the Saint Peter and Saint Paul Archipelago (Brazil)'; DOI 10.21577/0103-5053.20160297.
[308] F. E. Sakai-Kawada, C. G. Ip, K. A. Hagiwara, J. D. Awaya, *Front. Microbiol.* **2019**, *10*:1715, 1-9; 'Biosynthesis and Bioactivity of Prodiginine Analogs in Marine Bacteria, *Pseudoalteromonas*: A Mini Review'; DOI 10.3389/fmicb.2019.01715.
[309] P. C. Dorrestein, E. Yeh, S. Garneau-Tsodikova, N. L. Kelleher, C. T. Walsh, *Proc. Natl. Acad. Sci. U.S.A.* **2005**, *102*(39), 13843-13848; 'Dichlorination of a pyrrolyl-*S*-carrier protein by $FADH_2$-dependent halogenase PltA during pyoluteorin biosynthesis'; DOI 10.1073/pnas.0506964102.
[310] R. D'Alessio, A. Bargiotti, O. Carlini, F. Colotta, M. Ferrari, P. Gnocchi, A. Isetta, N. Mongelli, P. Motta, A. Rossi, M. Rossi, M. Tibolla, E. Vanotti, *J. Med. Chem.* **2000**, *43*(13), 2557-2565; 'Synthesis and Immunosuppressive Activity of Novel Prodigiosin Derivatives'; DOI 10.1021/jm001003p.
[311] M. S. Melvin, M. W. Calcutt, R. E. Noftle, R. A. Manderville, *Chem. Res. Toxicol.* **2002**, *15*(5), 742-748; 'Influence of the A-ring on the Redox and Nuclease Properties of the Prodigiosins: Importance of the Bipyrrole Moiety in Oxidative DNA Cleavage'; DOI 10.1021/tx025508p.
[312] K. Kumar, V. Kumar, *RSC Adv.* **2015**, *5*(15), 10899-10920; 'Prodigiosin alkaloids: recent advancements in total synthesis and their biological potential'; DOI 10.1039/c4ra10296g.
[313] R. I. S. Díaz, J. Regourd, P. V. Santacroce, J. T. Davis, D. L. Jakeman, A. Thompson, *Chem. Commun.* **2007**(26), 2701-2703; 'Chloride anion transport and copper-mediated DNA cleavage by C-ring functionalized prodigiosenes'; DOI 10.1039/b701919j.
[314] E. Marchal, S. Rastogi, A. Thompson, J. T. Davis, *Org. Biomol. Chem.* **2014**, *12*(38), 7515-7522; 'Influence of B-ring modifications on proton affinity, transmembrane anion transport and anti-cancer properties of synthetic prodigiosenes'; DOI 10.1039/c4ob01399a.
[315] J. L. Sessler, L. R. Eller, W. S. Cho, S. Nicolaou, A. Aguilar, J. T. Lee, V. M. Lynch, D. J. Magda, *Angew. Chem. Int. Ed.* **2005**, *44*(37), 5989-5992; 'Synthesis, Anion-Binding Properties, and *In Vitro* Anticancer Activity of Prodigiosin Analogues'; DOI 10.1002/anie.200501740.
[316] J. L. Sessler, L. R. Eller, W. S. Cho, S. Nicolaou, A. Aguilar, J. T. Lee, V. M. Lynch, D. J. Magda, *Angew. Chem.* **2005**, *117*(37), 6143-6146; 'Synthesis, Anion-Binding Properties, and *In Vitro* Anticancer Activity of Prodigiosin Analogues'; DOI 10.1002/ange.200501740.
[317] R. B. Gennis, *Biophys. J.* **2016**, *110*(9), 1909-1911; 'Proton Dynamics at the Membrane Surface'; DOI 10.1016/j.bpj.2016.04.001.
[318] J. T. Davis, P. A. Gale, O. A. Okunola, P. Prados, J. C. Iglesias-Sánchez, T. Torroba, R. Quesada, *Nat. Chem.* **2009**, *1*(2), 138-144; 'Using small molecules to facilitate exchange of bicarbonate and chloride anions across liposomal membranes'; DOI 10.1038/NCHEM.178.
[319] G. Deckers-Hebestreit, K. Altendorf, *Annu. Rev. Microbiol.* **1996**, *50*(1), 791-824; 'The F_0F_1-type ATP Synthases of Bacteria: Structure and Function of the F_0 Complex'; DOI 10.1146/annurev.micro.50.1.791.
[320] M. S. Melvin, J. T. Tomlinson, G. R. Saluta, G. L. Kucera, N. Lindquist, R. A. Manderville, *J. Am. Chem. Soc.* **2000**, *122*(26), 6333-6334; 'Double-Strand DNA Cleavage by Copper·Prodigiosin'; DOI 10.1021/ja0000798.
[321] A. Fürstner, E. J. Grabowski, *ChemBioChem* **2001**, *2*(9), 706-709; 'Studies on DNA Cleavage by Cytotoxic Pyrrole Alkaloids Reveal the Distinctly Different Behavior of Roseophilin and Prodigiosin Derivatives'; DOI 10.1002/1439-7633(20010903)2:9<706::AID-CBIC706>3.0.CO;2-J.
[322] G. Park, J. T. Tomlinson, M. S. Melvin, M. W. Wright, C. S. Day, R. A. Manderville, *Org. Lett.* **2003**, *5*(2), 113-116; 'Zinc and Copper Complexes of Prodigiosin: Implications for Copper-Mediated Double-Strand DNA Cleavage'; DOI 10.1021/ol027165s.
[323] B. Montaner, W. Castillo-Avila, M. Martinell, R. Öllinger, J. Aymami, E. Giralt, R. Pérez-Tomás, *Toxicol. Sci.* **2005**, *85*(2), 870-879; 'DNA Interaction and Dual Topoisomerase I and II Inhibition Properties of the Anti-Tumor Drug Prodigiosin'; DOI 10.1093/toxsci/kfi149.
[324] D. M. Petibone, W. Majeed, D. A. Casciano, *J. Appl. Toxicol.* **2017**, *37*(1), 23-37; 'Autophagy function and its relationship to pathology, clinical applications, drug metabolism and toxicity'; DOI 10.1002/jat.3393.
[325] D. Glick, S. Barth, K. F. Macleod, *J. Pathol.* **2010**, *221*(1), 3-12; 'Autophagy: cellular and molecular mechanisms'; DOI 10.1002/path.2697.
[326] I. Tanida, T. Ueno, E. Kominami, **2008**, '*LC3 and Autophagy*' in *Autophagosome and Phagosome. Methods in Molecular Biology, Vol. 445*, 77-88, Humana Press Inc., Totowa, New Jersey, USA; ISBN 978-1-58829-853-9, DOI 10.1007/978-1-59745-157-4_4.
[327] V. A. Stamelos, N. Fisher, H. Bamrah, C. Voisey, J. C. Price, W. E. Farrell, C. W. Redman, A. Richardson, *PLoS One* **2016**, *11*(3):e0150696, 1-20; 'The BH3 Mimetic Obatoclax Accumulates in Lysosomes and Causes Their Alkalinization'; DOI 10.1371/journal.pone.0150696.
[328] W. Castillo-Ávila, M. Abal, S. Robine, R. Pérez-Tomás, *Life Sci.* **2005**, *78*(2), 121-127; 'Non-apoptotic concentrations of prodigiosin (H^+/Cl^- symporter) inhibit the acidification of lysosomes and induce cell cycle blockage in colon cancer cells'; DOI 10.1016/j.lfs.2005.04.059.

[329] H. Konno, H. Matsuya, M. Okamoto, T. Sato, Y. Tanaka, K. Yokoyama, T. Kataoka, K. Nagai, H. H. Wasserman, S. Ohkuma, *J. Biochem.* **1998**, *124*(3), 547-556; 'Prodigiosins Uncouple Mitochondrial and Bacterial F-ATPases: Evidence for their H^+/Cl^- Symport Activity'; DOI 10.1093/oxfordjournals.jbchem.a022147.
[330] T. Sato, H. Konno, Y. Tanaka, T. Kataoka, K. Nagai, H. H. Wasserman, S. Ohkuma, *J. Biol. Chem.* **1998**, *273*(34), 21455-21462; 'Prodigiosins as a New Group of H^+/Cl^- Symporters that Uncouple Proton Translocators'; DOI 10.1074/jbc.273.34.21455.
[331] K. Daïri, Y. Yao, M. Faley, S. Tripathy, E. Rioux, X. Billot, D. Rabouin, G. Gonzalez, J.-F. Lavallée, G. Attardo, *Org. Process Res. Dev.* **2007**, *11*(6), 1051-1054; 'A Scalable Process for the Synthesis of the Bcl Inhibitor Obatoclax'; DOI 10.1021/op7001613.
[332] Teva Branded Pharmaceutical Products R&D, Inc. (Cephalon): "Efficacy and Safety of Obatoclax Mesylate in Combination With Carboplatin and Etoposide Compared With Carboplatin and Etoposide Alone in Chemotherapy-Naive Patients With Extensive-Stage Small Cell Lung Cancer", **2012**, https://www.clinicaltrials.gov/study/NCT01563601, Clinical Trials.gov ID NCT01563601, accessed 06/08/2024.
[333] M. Konopleva, J. Watt, R. Contractor, T. Tsao, D. Harris, Z. Estrov, W. Bornmann, H. Kantarjian, J. Viallet, I. Samudio, M. Andreeff, *Cancer Res.* **2008**, *68*(9), 3413-3420; 'Mechanisms of Antileukemic Activity of the Novel Bcl-2 Homology Domain-3 Mimetic GX15-070 (Obatoclax)'; DOI 10.1158/0008-5472.CAN-07-1919.
[334] S. Songia, A. Mortellaro, S. Taverna, C. Fornasiero, E. A. Scheiber, E. Erba, F. Colotta, A. Mantovani, A.-M. Isetta, J. Golay, *J. Immunol.* **1997**, *158*(8), 3987-3995; 'Characterization of the New Immunosuppressive Drug Undecylprodigiosin in Human Lymphocytes: Retinoblastoma Protein, Cyclin-Dependent Kinase-2, and Cyclin-Dependent Kinase-4 as Molecular Targets'; DOI 10.4049/jimmunol.158.8.3987.
[335] S. L. Schreiber, G. R. Crabtree, *Immunol. Today* **1992**, *13*(4), 136-142; 'The mechanism of action of cyclosporin A and FK506'; DOI 10.1016/0167-5699(92)90111-J.
[336] T. Azuma, N. Watanabe, H. Yagisawa, H. Hirata, M. Iwamura, Y. Kobayashi, *Immunopharmacology* **2000**, *46*(1), 29-37; 'Induction of apoptosis of activated murine splenic T cells by cycloprodigiosin hydrochloride, a novel immunosuppressant'; DOI 10.1016/S0162-3109(99)00153-8.
[337] S. B. Han, H. M. Kim, Y. H. Kim, C. W. Lee, E.-S. Jang, K. H. Son, S. U. Kim, Y. K. Kim, *Int. J. Immunopharmacol.* **1998**, *20*(1-3), 1-13; 'T-cell specific immunosuppression by prodigiosin isolated from *Serratia marcescens*'; DOI 10.1016/s0192-0561(97)00062-3.
[338] S. M. Stepkowski, R. A. Erwin-Cohen, F. Behbod, M.-E. Wang, X. Qu, N. Tejpal, Z. S. Nagy, B. D. Kahan, R. A. Kirken, *Blood* **2002**, *99*(2), 680-689; 'Selective inhibitor of Janus tyrosine kinase 3, PNU156804, prolongs allograft survival and acts synergistically with cyclosporine but additively with rapamycin'; DOI 10.1182/blood.V99.2.680.
[339] S. M. Stepkowski, Z. S. Nagy, M. E. Wang, F. Behbod, R. Erwin-Cohen, B. D. Kahan, R. A. Kirken, *Transplant. Proc.* **2001**, *33*(7-8), 3272-3273; 'PNU156804 Inhibits Jak3 Tyrosine Kinase and Rat Heart Allograft Rejection'; DOI 10.1016/s0041-1345(01)02390-9.
[340] T. Kataoka, J. Magae, K. Kasamo, H. Yamanishi, A. Endo, M. Yamasaki, K. Nagai, *J. Antibiot.* **1992**, *45*(10), 1618-1625; 'Effects of Prodigiosin 25-C on Cultured Cell Lines: Its Similarity to Monovalent Polyether Ionophores and Vacuolar Type H^+-ATPase Inhibitors'; DOI 10.7164/antibiotics.45.1618.
[341] O. Boyman, J. Sprent, *Nat. Rev. Immunol.* **2012**, *12*(3), 180-190; 'The role of interleukin-2 during homeostasis and activation of the immune system'; DOI 10.1038/nri3156.
[342] V. Rizzo, A. Morelli, V. Pinciroli, D. Sciangula, R. D'Alessio, *J. Pharm. Sci.* **1999**, *88*(1), 73-78; 'Equilibrium and Kinetics of Rotamer Interconversion in Immunosuppressant Prodigiosin Derivatives in Solution'; DOI 10.1021/js980225w.
[343] A. Mortellaro, S. Songia, P. Gnocchi, M. Ferrari, C. Fornasiero, R. D'Alessio, A. Isetta, F. Colotta, J. e. Golay, *J. Immunol.* **1999**, *162*(12), 7102-7109; 'New Immunosuppressive Drug PNU156804 Blocks IL-2-Dependent Proliferation and NF-κB and AP-1 Activation'; DOI 10.4049/jimmunol.162.12.7102.
[344] B. M. Greenwood, D. A. Fidock, D. E. Kyle, S. H. I. Kappe, P. L. Alonso, F. H. Collins, P. E. Duffy, *J. Clin. Invest.* **2008**, *118*(4), 1266-1276; 'Malaria: progress, perils, and prospects for eradication'; DOI 10.1172/JCI33996.
[345] N. N. Gerber, *J. Antibiot.* **1975**, *28*(3), 194-199; 'A New Prodiginine (Prodigiosin-Like) Pigment from *Streptomyces*. Antimalarial Activity of Several Prodiginines'; DOI 10.7164/antibiotics.28.194.
[346] P. Kancharla, M. Smilkstein, J. X. Kelly, Shweta, S. M. Salem, M. Alhamadsheh, S. W. Haynes, G. L. Challis, K. A. Reynolds, *J. Med. Chem.* **2011**, *54*(15), 5296-5306; 'Antimalarial Activity of Natural and Synthetic Prodiginines'; DOI 10.1021/jm200543y.
[347] P. Kancharla, W. Lu, S. M. Salem, J. X. Kelly, K. A. Reynolds, *J. Org. Chem.* **2014**, *79*(23), 11674-11689; 'Stereospecific Synthesis of 23-Hydroxyundecylprodiginines and Analogues and Conversion to Antimalarial Premarineosins via a Rieske Oxygenase Catalyzed Bicyclization'; DOI 10.1021/jo5023553.
[348] E. Marchal, D. A. Smithen, M. I. Uddin, A. W. Robertson, D. L. Jakeman, V. Mollard, C. D. Goodman, K. S. MacDougall, S. A. McFarland, G. I. McFadden, A. Thompson, *Org. Biomol. Chem.* **2014**, *12*(24), 4132-4142; 'Synthesis and antimalarial activity of prodigiosenes'; DOI 10.1039/c3ob42548g.
[349] M. Isaka, A. Jaturapat, J. Kramyu, M. Tanticharoen, Y. Thebtaranonth, *Antimicrob. Agents Chemother.* **2002**, *46*(4), 1112-1113; 'Potent In Vitro Antimalarial Activity of Metacycloprodigiosin Isolated from *Streptomyces spectabilis* BCC 4785'; DOI 10.1128/AAC.46.4.1112–1113.2002.
[350] F. Wrede, O. Hettche, *Ber. Dtsch. Chem. Ges.* **1929**, *62*, 2678-2687; 'Über das Prodigiosin, den roten Farbstoff des *Bacillus prodigiosus* (I. Mitteil.)'; DOI 10.1002/cber.19290620934.
[351] H. H. Wasserman, A. K. Petersen, M. Xia, J. Wang, *Tetrahedron Lett.* **1999**, *40*(43), 7587-7589; 'Pyrrole-singlet oxygen reactions leading to α,α′-bipyrroles. Synthesis of prodigiosin and analogs'; DOI 10.1016/S0040-4039(99)01538-5.
[352] R. D'Alessio, A. Rossi, *Synlett* **1996**, *1996*(6), 513-514; 'Short synthesis of undecylprodigiosine. A new route to 2,2'-bipyrrolyl-pyrromethene systems'; DOI 10.1055/s-1996-5485.
[353] K. Dairi, S. Tripathy, G. Attardo, J.-F. Lavallée, *Tetrahedron Lett.* **2006**, *47*(15), 2605-2606; 'Two-step synthesis of the bipyrrole precursor of prodigiosins'; DOI 10.1016/j.tetlet.2006.02.035.

[354] S. O. Dozie-Nwachukwu, Y. Danyuo, J. D. Obayemi, O. S. Odusanya, K. Malatesta, W. O. Soboyejo, *Mater. Sci. Eng. C* **2017**, *71*, 268-278; 'Extraction and encapsulation of prodigiosin in chitosan microspheres for targeted drug delivery'; DOI 10.1016/j.msec.2016.09.078.
[355] T. H. Nguyen, S.-L. Wang, T. Q. Phan, T. H. Nguyen, A. D. Nguyen, V. B. Nguyen, *Res. Chem. Intermed.* **2024**, *50*, 2873-2896; 'Enhancing nematicidal effect of prodigiosin via micro-encapsulation using chitosan as a novel carrier substance'; DOI 10.1007/s11164-024-05275-9.
[356] K. Zhao, D. Li, G. Cheng, B. Zhang, J. Han, J. Chen, B. Wang, M. Li, T. Xiao, D. Zhang, J. Zhou, Z. Jin, X. Fan, *Int. J. Mol. Sci.* **2019**, *20*(21):5458, 1-18; 'Targeted Delivery Prodigiosin to Choriocarcinoma by Peptide-Guided Dendrigraft Poly-L-Lysines Nanoparticles'; DOI 10.3390/ijms20215458.
[357] T. M. Clausen, S. Christoffersen, M. Dahlbäck, A. E. Langkilde, K. E. Jensen, M. Resende, M. Ø. Agerbæk, D. Andersen, B. Berisha, S. B. Ditlev, V. V. Pinto, M. A. Nielsen, T. G. Theander, S. Larsen, A. Salanti, *J. Biol. Chem.* **2012**, *287*(28), 23332-23345; 'Structural and Functional Insight into How the *Plasmodium falciparum* VAR2CSA Protein Mediates Binding to Chondroitin Sulfate A in Placental Malaria'; DOI 10.1074/jbc.M112.348839.
[358] J. Nikodinovic-Runic, M. Mojic, Y. Kang, D. Maksimovic-Ivanic, S. Mijatovic, B. Vasiljevic, V. R. Stamenkovic, L. Senerovic, *J. Mater. Chem. B* **2014**, *2*(21), 3271-3281; 'Undecylprodigiosin conjugated monodisperse gold nanoparticles efficiently cause apoptosis in colon cancer cells *in vitro*'; DOI 10.1039/C4TB00300D.
[359] R. Bhole, C. Bonde, P. Kadam, R. Wavwale, *Turk. J. Oncol.* **2021**, *36*(1), 125-132; 'A Comprehensive Review on Photodynamic Therapy (PDT) and Photothermal Therapy (PTT) for Cancer Treatment'; DOI 10.5505/tjo.2020.2400.
[360] S. O. Dozie-Nwachukwu, J. D. Obayemi, Y. Danyuo, N. Anuku, O. S. Odusanya, K. Malatesta, W. O. Soboyejo, *J. Mater. Sci.: Mater. Med.* **2017**, *28*(9):143, 1-13; 'A comparative study of the adhesion of biosynthesized gold and conjugated gold/prodigiosin nanoparticles to triple negative breast cancer cells'; DOI 10.1007/s10856-017-5943-2.
[361] S. O. Dozie-Nwachukwu, J. D. Obayemi, Y. T. Danyuo, G. Etuk-Udo, Y. Chi, J. Hu, N. Anuku, O. S. Odusanya, K. Malatesta, W. O. Soboyejo, *Waste Biomass Valor.* **2017**, *8*, 2045-2059; 'Biosynthesis of Gold Nanoparticles and Gold/Prodigiosin Nanoparticles with Serratia marcescens Bacteria'; DOI 10.1007/s12649-016-9734-7.
[362] R. B. Kassab, M. Elbaz, A. A. A. Oyouni, A. H. Mufti, A. Theyab, A. Al-Brakati, H. A. Mohamed, A. M. S. Hebishy, M. I. Y. Elmallah, M. S. Abdelfattah, A. E. Abdel Moneim, *Environ. Sci. Pollut. Res.* **2022**, *29*(37), 55790-55802; 'Anticolitic activity of prodigiosin loaded with selenium nanoparticles on acetic acid–induced colitis in rats'; DOI 10.1007/s11356-022-19747-1.
[363] Y. Zhou, X. Liang, Z. Dai, *Nanoscale* **2016**, *8*(25), 12394-12405; 'Porphyrin-loaded nanoparticles for cancer theranostics'; DOI 10.1039/c5nr07849k.
[364] R. Kumar, M. N. Zakharov, S. H. Khan, R. Miki, H. Jang, G. Toraldo, R. Singh, S. Bhasin, R. Jasuja, *J. Amino Acids* **2011**, *2011*(1):812540, 1-7; 'The Dynamic Structure of the Estrogen Receptor'; DOI 10.4061/2011/812540.
[365] D. Sharma, N. K. Saxena, N. E. Davidson, P. M. Vertino, *Cancer Res.* **2006**, *66*(12), 6370-6378; 'Restoration of Tamoxifen Sensitivity in Estrogen Receptor–Negative Breast Cancer Cells: Tamoxifen-Bound Reactivated ER Recruits Distinctive Corepressor Complexes'; DOI 10.1158/0008-5472.CAN-06-0402.
[366] Q. Zhong, G. Shi, Q. Zhang, L. Lu, D. Levy, S. Zhong, *Oncotarget* **2014**, *5*(23), 12410-12417; 'Tamoxifen represses alcohol-induced transcription of RNA polymerase III-dependent genes in breast cancer cells'; DOI 10.18632/oncotarget.2678.
[367] C. L. A. Hawco, E. Marchal, M. I. Uddin, A. E. G. Baker, D. P. Corkery, G. Dellaire, A. Thompson, *Bioorg. Med. Chem.* **2013**, *21*(19), 5995-6002; 'Synthesis and biological evaluation of prodigiosene conjugates of porphyrin, estrone and 4-hydroxytamoxifen'; DOI 10.1016/j.bmc.2013.07.042.
[368] C. Figliola, E. Marchal, B. R. Groves, A. Thompson, *RSC Adv.* **2019**, *9*(25), 14078-14092; 'A step-wise synthetic approach is necessary to access γ-conjugates of folate: folate-conjugated prodigiosenes'; DOI 10.1039/c9ra01435g.
[369] E. Marchal, C. Figliola, A. Thompson, *Org. Biomol. Chem.* **2017**, *15*(25), 5410-5427; 'Prodigiosenes conjugated to tamoxifen and estradiol'; DOI 10.1039/c7ob00943g.
[370] E. Marchal, M. I. Uddin, C. L. A. Hawco, A. Thompson, *Can. J. Chem.* **2015**, *93*(5), 526-535; 'Synthesis of Prodigiosene–Estrogen Conjugates: optimization of protecting group strategies and anticancer properties'; DOI 10.1139/cjc-2014-0516.
[371] G. Bianchini, J. M. Balko, I. A. Mayer, M. E. Sanders, L. Gianni, *Nat. Rev. Clin. Oncol.* **2016**, *13*(11), 674-690; 'Triple-negative breast cancer: challenges and opportunities of a heterogeneous disease'; DOI 10.1038/nrclinonc.2016.66.
[372] H. L. Perez, P. M. Cardarelli, S. Deshpande, S. Gangwar, G. M. Schroeder, G. D. Vite, R. M. Borzilleri, *Drug Discov. Today* **2014**, *19*(7), 869-881; 'Antibody–drug conjugates: current status and future directions'; DOI 10.1016/j.drudis.2013.11.004.
[373] Y. Wang, A. G. Cheetham, G. Angacian, H. Su, L. Xie, H. Cui, *Adv. Drug Deliv. Rev.* **2017**, *110*, 112-126; 'Peptide–drug conjugates as effective prodrug strategies for targeted delivery'; DOI 10.1016/j.addr.2016.06.015.
[374] C. H. Chau, P. S. Steeg, W. D. Figg, *Lancet* **2019**, *394*(10200), 793-804; 'Antibody–drug conjugates for cancer'; DOI 10.1016/S0140-6736(19)31774-X.
[375] S. C. Alley, N. M. Okeley, P. D. Senter, *Curr. Opin. Chem. Biol.* **2010**, *14*(4), 529-537; 'Antibody–drug conjugates: targeted drug delivery for cancer'; DOI 10.1016/j.cbpa.2010.06.170.
[376] L. Fiume, M. Manerba, G. Di Stefano, *Expert Opin. Drug Deliv.* **2014**, *11*(8), 1203-1217; 'Albumin–drug conjugates in the treatment of hepatic disorders'; DOI 10.1517/17425247.2014.913567.
[377] C. Lorenz, P. Hadwiger, M. John, H.-P. Vornlocher, C. Unverzagt, *Bioorg. Med. Chem. Lett.* **2004**, *14*(19), 4975-4977; 'Steroid and lipid conjugates of siRNAs to enhance cellular uptake and gene silencing in liver cells'; DOI 10.1016/j.bmcl.2004.07.018.
[378] D. Irby, C. Du, F. Li, *Mol. Pharmaceutics* **2017**, *14*(5), 1325-1338; 'Lipid–drug conjugate for enhancing drug delivery'; DOI 10.1021/acs.molpharmaceut.6b01027.
[379] J. Zheng, G. Zhu, Y. Li, C. Li, M. You, T. Chen, E. Song, R. Yang, W. Tan, *ACS Nano* **2013**, *7*(8), 6545-6554; 'A Spherical Nucleic Acid Platform Based on Self-Assembled DNA Biopolymer for High-Performance Cancer Therapy'; DOI 10.1021/nn402344v.

[380] S. Moktan, C. Ryppa, F. Kratz, D. Raucher, *Invest. New Drugs* **2012**, *30*, 236-248; 'A thermally responsive biopolymer conjugated to an acid-sensitive derivative of paclitaxel stabilizes microtubules, arrests cell cycle, and induces apoptosis'; DOI 10.1007/s10637-010-9560-x.
[381] M. A. Ghaz-Jahanian, F. Abbaspour-Aghdam, N. Anarjan, A. Berenjian, H. Jafarizadeh-Malmiri, *Mol. Biotechnol.* **2015**, *57*(3), 201-218; 'Application of Chitosan-Based Nanocarriers in Tumor-Targeted Drug Delivery'; DOI 10.1007/s12033-014-9816-3.
[382] G. E. Winter, D. L. Buckley, J. Paulk, J. M. Roberts, A. Souza, S. Dhe-Paganon, J. E. Bradner, *Science* **2015**, *348*(6241), 1376-1381; 'Phthalimide conjugation as a strategy for in vivo target protein degradation'; DOI 10.1126/science.aab1433.
[383] M. Kotecha, J. Kluza, G. Wells, C. C. O'Hare, C. Forni, R. Mantovani, P. W. Howard, P. Morris, D. E. Thurston, J. A. Hartley, D. Hochhauser, *Mol. Cancer Ther.* **2008**, *7*(5), 1319-1328; 'Inhibition of DNA binding of the NF-Y transcription factor by the pyrrolobenzodiazepine-polyamide conjugate GWL-78'; DOI 10.1158/1535-7163.MCT-07-0475.
[384] E. Kim, H. Koo, *Chem. Sci.* **2019**, *10*(34), 7835-7851; 'Biomedical applications of copper-free click chemistry: *in vitro*, *in vivo*, and *ex vivo*'; DOI 10.1039/c9sc03368h.
[385] D. Schulz, A. Rentmeister, *ChemBioChem* **2014**, *15*(16), 2342-2347; 'Current Approaches for RNA Labeling *in Vitro* and in Cells Based on Click Reactions'; DOI 10.1002/cbic.201402240.
[386] N. N. Gerber, *Tetrahedron Lett.* **1970**, *11*(11), 809-812; 'A Novel, Cyclic, Tripyrrole Pigment from *Actinomadura* (*Nocardia*) *madurae*'; DOI 10.1016/s0040-4039(01)97837-2.
[387] P. Kancharla, Y. Li, M. Yeluguri, R. A. Dodean, K. A. Reynolds, J. X. Kelly, *J. Med. Chem.* **2021**, *64*(12), 8739-8754; 'Total Synthesis and Antimalarial Activity of 2-(*p*-Hydroxybenzyl)-prodigiosins, Isoheptylprodigiosin, and Geometric Isomers of Tambjamine MYP1 Isolated from Marine Bacteria'; DOI 10.1021/acs.jmedchem.1c00748.
[388] T. M. Weber, A. Leyens, L. Berning, B. Stork, J. Pietruszka, *Catal. Sci. Technol.* **2023**, *13*(21), 6165-6184; 'New prodigiosin derivatives – chemoenzymatic synthesis and physiological evaluation against cisplatin-resistant cancer cells'; DOI 10.1039/d3cy00913k.
[389] B. A. Trofimov, A. I. Mikhaleva, A. N. Vasil'ev, S. E. Korostova, S. G. Shevchenko, *Chem. Heterocycl. Compd.* **1985**, *21*, 46-49; 'Pyrroles from Ketoximes and Acetylene. 29. Synthesis of Alkylpyrroles from Dialkylketoximes and Dichloroethane by Reaction with KOH-DMSO'; DOI 10.1007/BF00505898.
[390] X. Mo, T. D. R. Morgan, H. T. Ang, D. G. Hall, *J. Am. Chem. Soc.* **2018**, *140*(15), 5264-5271; 'Scope and Mechanism of a True Organocatalytic Beckmann Rearrangement with a Boronic Acid/Perfluoropinacol System under Ambient Conditions'; DOI 10.1021/jacs.8b01618.
[391] A. S. Klein, Doctoral Thesis, 'Methoden zur Herstellung von Prodigininen als Wirkstoffe – Eine farbenfrohe Brücke zwischen Chemie und Biologie', Heinrich Heine University Düsseldorf (Düsseldof, Germany), **2018**; ISBN 978-3-95806-343-3; https://docserv.uni-duesseldorf.de/servlets/DerivateServlet/Derivate-49863/Dissertation%20Andreas%20Sebastian%20Klein.pdf.
[392] R. Greenhouse, C. Ramirez, J. M. Muchowski, *J. Org. Chem.* **1985**, *50*(16), 2961-2965; 'Synthesis of Alkylpyrroles by the Sodium Borohydride Reduction of Acylpyrroles'; DOI 10.1021/jo00216a030.
[393] T. Ono, D. Koga, Y. Hisaeda, *Chem. Lett.* **2017**, *46*(2), 260-262; 'Facile Synthesis of 9,10,19,20-Tetraalkylporphycenes'; DOI 10.1246/cl.161019.
[394] E. F. Knights, H. C. Brown, *J. Am. Chem. Soc.* **1968**, *90*(19), 5281-5283; '9-Borabicyclo[3.3. 1]nonane as a Convenient Selective Hydroborating Agent'; DOI 10.1021/ja01021a047.
[395] L. Aldrich, Doctoral Thesis, 'Progress Toward the Total Synthesis of Marineosins A & B; Total Synthesis of Tambjamine K and Unnatural Analogs with Improved Anticancer Activity, and Discovery of Selective M_1 Antagonists', Vanderbilt University Tennessee (Nashville, Tennessee, USA), **2012**; https://ir.vanderbilt.edu/bitstream/handle/1803/12642/Aldrich.pdf?sequence=1&isAllowed=y.
[396] L. F. Fieser, M. Fieser, T.-L. Ho, **2006**, '*Lithium aluminium hydride*' in *Fieser and Fieser's Reagents for Organic Synthesis*, John Wiley & Sons, Inc., Hoboken, New Jersey, USA; ISBN 978-0471264194, DOI 10.1002/9780471264194.fos06257.pub3.
[397] D. S. Pedersen, C. Rosenbohm, *Synthesis* **2001**, *2001*(16), 2431-2434; 'Dry Column Vacuum Chromatography'; DOI 10.1055/s-2001-18722.
[398] S. Martina, V. Enkelmann, G. Wegner, A.-D. Schlüter, *Synthesis* **1991**, *1991*(08), 613-615; '*N*-Protected Pyrrole Derivatives Substituted for Metal-Catalyzed Cross-Coupling Reactions'; DOI 10.1055/s-1991-26526.
[399] X.-C. Cai, B. B. Snider, *J. Org. Chem.* **2013**, *78*(23), 12161-12175; 'Synthesis of the Spiroiminal Moiety and Approaches to the Synthesis of Marineosins A and B'; DOI 10.1021/jo402178r.
[400] M. S. Melvin, J. T. Tomlinson, G. Park, C. S. Day, G. R. Saluta, G. L. Kucera, R. A. Manderville, *Chem. Res. Toxicol.* **2002**, *15*(5), 734-741; 'Influence of the A-Ring on the Proton Affinity and Anticancer Properties of the Prodigiosins'; DOI 10.1021/tx025507x.
[401] L.-C. Campeau, S. Rousseaux, K. Fagnou, *J. Am. Chem. Soc.* **2005**, *127*(51), 18020-18021; 'A Solution to the 2-Pyridyl Organometallic Cross-Coupling Problem: Regioselective Catalytic Direct Arylation of Pyridine *N*-Oxides'; DOI 10.1021/ja056800x.
[402] X. A. F. Cook, A. de Gombert, J. McKnight, L. R. E. Pantaine, M. C. Willis, *Angew. Chem. Int. Ed.* **2021**, *60*(20), 11168-11191; 'The 2-Pyridyl Problem: Challenging Nucleophiles in Cross-Coupling Arylations'; DOI 10.1002/anie.202010631.
[403] X. A. F. Cook, A. de Gombert, J. McKnight, L. R. E. Pantaine, M. C. Willis, *Angew. Chem.* **2021**, *133*(20), 11168-11191; 'The 2-Pyridyl Problem: Challenging Nucleophiles in Cross-Coupling Arylations'; DOI 10.1002/ange.202010631.
[404] E. Tyrrell, P. Brookes, *Synthesis* **2003**, *2003*(4), 469-483; 'The Synthesis and Applications of Heterocyclic Boronic Acids'; DOI 10.1055/s-2003-37721.
[405] A. Y. Fedorov, A. A. Shchepalov, A. V. Bol'shakov, A. S. Shavyrin, Y. A. Kurskii, J.-P. Finet, S. V. Zelentsov, *Russ. Chem. Bull.* **2004**, *53*, 370-375; 'Synthesis of (azidomethyl)phenylboronic acids'; DOI 10.1023/B:RUCB.0000030813.05424.1f.

[406] K. Hanaya, M. K. Miller, Z. T. Ball, *Org. Lett.* **2019**, *21*(7), 2445-2448; 'Nickel(II)-Promoted Amide N–H Arylation of Pyroglutamate–Histidine with Arylboronic Acid Reagents'; DOI 10.1021/acs.orglett.9b00759.
[407] J. Zhou, P. Stapleton, F. H. Xavier-Junior, A. Schatzlein, S. Haider, J. Healy, G. Wells, *Eur. J. Med. Chem.* **2022**, *240*:114571, 1-13; 'Triazole-substituted phenylboronic acids as tunable lead inhibitors of KPC-2 antibiotic resistance'; DOI 10.1016/j.ejmech.2022.114571.
[408] N. Lin, J. Yan, Z. Huang, C. Altier, M. Li, N. Carrasco, M. Suyemoto, L. Johnston, S. Wang, Q. Wang, H. Fang, J. Caton-Williams, B. Wang, *Nucleic Acids Res.* **2007**, *35*(4), 1222-1229; 'Design and synthesis of boronic-acid-labeled thymidine triphosphate for incorporation into DNA'; DOI 10.1093/nar/gkl1091.
[409] L. Florentino, L. López, R. Barroso, M. P. Cabal, C. Valdés, *Angew. Chem.* **2021**, *133*(3), 1293-1300; 'Synthesis of Pyrrolidines by a Csp^3-Csp^3/Csp^3-*N* Transition-Metal-Free Domino Reaction of Boronic Acids with γ-Azido-*N*-Tosylhydrazones'; DOI 10.1002/ange.202010528.
[410] L. Florentino, L. López, R. Barroso, M. P. Cabal, C. Valdés, *Angew. Chem. Int. Ed.* **2021**, *60*(3), 1273-1280; 'Synthesis of Pyrrolidines by a Csp^3-Csp^3/Csp^3-*N* Transition-Metal-Free Domino Reaction of Boronic Acids with γ-Azido-*N*-Tosylhydrazones'; DOI 10.1002/anie.202010528.
[411] P. Kancharla, J. X. Kelly, K. A. Reynolds, *J. Med. Chem.* **2015**, *58*(18), 7286-7309; 'Synthesis and Structure–Activity Relationships of Tambjamines and B-Ring Functionalized Prodiginines as Potent Antimalarials'; DOI 10.1021/acs.jmedchem.5b00560.
[412] N. Miyaura, A. Suzuki, *J. Chem. Soc., Chem. Commun.* **1979**, *19*, 866-867; 'Stereoselective Synthesis of Arylated (*E*)-Alkenes by the Rreaction of Alk-1-enylboranes with Aryl Halides in the Presence of Palladium Catalyst'; DOI 10.1039/C39790000866.
[413] N. Miyaura, K. Yamada, A. Suzuki, *Tetrahedron Lett.* **1979**, *20*(36), 3437-3440; 'A New Stereospecific Cross-Coupling by the Palladium-Catalyzed Reaction of 1-Alkenylboranes with 1-Alkenyl or 1-Alkynyl halides'; DOI 10.1016/S0040-4039(01)95429-2.
[414] N. Miyaura, T. Yanagi, A. Suzuki, *Synth. Commun.* **1981**, *11*(7), 513-519; 'The Palladium-Catalyzed Cross-Coupling Reaction of Phenylboronic Acid with Haloarenes in the Presence of Bases'; DOI 10.1080/00397918108063618.
[415] S. Mo, P. K. Sydor, C. Corre, M. M. Alhamadsheh, A. E. Stanley, S. W. Haynes, L. Song, K. A. Reynolds, G. L. Challis, *Chem. Biol.* **2008**, *15*(2), 137-148; 'Elucidation of the *Streptomyces coelicolor* Pathway to 2-Undecylpyrrole, a Key Intermediate in Undecylprodiginine and Streptorubin B Biosynthesis'; DOI 10.1016/j.chembiol.2007.11.015.
[416] C. N. Johnson, G. Stemp, N. Anand, S. C. Stephen, T. Gallagher, *Synlett* **1998**, *1998*(9), 1025-1027; 'Palladium (0)-Catalysed Arylations using Pyrrole and Indole 2-Boronic Acids'; DOI 10.1055/s-1998-1834.
[417] N. Miyaura, A. Suzuki, *Chem. Rev.* **1995**, *95*(7), 2457-2483; 'Palladium-Catalyzed Cross-Coupling Reactions of Organoboron Compounds'; DOI 10.1021/cr00039a007.
[418] P. Fitton, E. A. Rick, *J. Organomet. Chem.* **1971**, *28*(2), 287-291; 'The Addition of Aryl Halides to Tetrakis(triphenylphosphine)palladium(0)'; DOI 10.1016/S0022-328X(00)84578-7.
[419] C. Amatore, M. Azzabi, A. Jutand, *J. Am. Chem. Soc.* **1991**, *113*(22), 8375-8384; 'Role and Effects of Halide Ions on the Rates and Mechanisms of Oxidative Addition of Iodobenzene to Low-Ligated Zerovalent Palladium Complexes $Pd^0(PPh_3)_2$'; DOI 10.1021/ja00022a026.
[420] D. M. Knapp, E. P. Gillis, M. D. Burke, *J. Am. Chem. Soc.* **2009**, *131*(20), 6961-6963; 'A General Solution for Unstable Boronic Acids: Slow-Release Cross-Coupling from Air-Stable MIDA Boronates'; DOI 10.1021/ja901416p.
[421] S. Bräse, C. Gil, K. Knepper, V. Zimmermann, *Angew. Chem. Int. Ed.* **2005**, *44*(33), 5188-5240; 'Organic Azides: An Exploding Diversity of a Unique Class of Compounds'; DOI 10.1002/anie.200400657.
[422] S. Bräse, C. Gil, K. Knepper, V. Zimmermann, *Angew. Chem.* **2005**, *117*(33), 5320-5374; 'Organische Azide–explodierende Vielfalt bei einer einzigartigen Substanzklasse'; DOI 10.1002/ange.200400657.
[423] S. Ge, J. F. Hartwig, *Angew. Chem. Int. Ed.* **2012**, *51*(51), 12837-12841; 'Highly Reactive, Single-Component Nickel Catalyst Precursor for Suzuki–Miyuara Cross-Coupling of Heteroaryl Boronic Acids with Heteroaryl Halides'; DOI 10.1002/anie.201207428.
[424] P. A. Cox, A. G. Leach, A. D. Campbell, G. C. Lloyd-Jones, *J. Am. Chem. Soc.* **2016**, *138*(29), 9145-9157; 'Protodeboronation of Heteroaromatic, Vinyl, and Cyclopropyl Boronic Acids: pH–Rate Profiles, Autocatalysis, and Disproportionation'; DOI 10.1021/jacs.6b03283.
[425] G. Zhang, Y. Li, J. Liu, *RSC Adv.* **2017**, *7*(56), 34959-34962; 'Acid-promoted metal-free protodeboronation of arylboronic acids'; DOI 10.1039/c7ra05979e.
[426] P.-J. Chen, A. M. Kelly, D. J. Blair, M. D. Burke, *Org. Synth.* **2022**, *99*, 92-112; 'Preparation of MIDA Anhydride and Reaction with Boronic Acids'; DOI 10.15227/orgsyn.099.0092.
[427] M. A. Düfert, K. L. Billingsley, S. L. Buchwald, *J. Am. Chem. Soc.* **2013**, *135*(34), 12877-12885; 'Suzuki-Miyaura Cross-Coupling of Unprotected, Nitrogen-Rich Heterocycles: Substrate Scope and Mechanistic Investigation'; DOI 10.1021/ja4064469.
[428] K. L. Billingsley, K. W. Anderson, S. L. Buchwald, *Angew. Chem. Int. Ed.* **2006**, *45*(21), 3484-3488; 'A Highly Active Catalyst for Suzuki-Miyaura Cross-Coupling Reactions of Heteroaryl Compounds'; DOI 10.1002/anie.200600493.
[429] K. L. Billingsley, K. W. Anderson, S. L. Buchwald, *Angew. Chem.* **2006**, *118*(21), 3564-3568; 'A Highly Active Catalyst for Suzuki-Miyaura Cross-Coupling Reactions of Heteroaryl Compounds'; DOI 10.1002/ange.200600493.
[430] A. M. Hansen, A. L. Sewell, R. H. Pedersen, D.-L. Long, N. Gadegaard, R. Marquez, *Tetrahedron* **2013**, *69*(39), 8527-8533; 'Tunable BODIPY derivatives amenable to 'click' and peptide chemistry'; DOI 10.1016/j.tet.2013.05.037.
[431] J.-J. Shie, Y.-C. Liu, Y.-M. Lee, C. Lim, J.-M. Fang, C.-H. Wong, *J. Am. Chem. Soc.* **2014**, *136*(28), 9953-9961; 'An Azido-BODIPY Probe for Glycosylation: Initiation of Strong Fluorescence upon Triazole Formation'; DOI 10.1021/ja5010174.
[432] A. Paulus, P. Desai, B. Carney, G. Carlucci, T. Reiner, C. Brand, W. A. Weber, *EJNMMI Res.* **2015**, *5*:43, 1-9; 'Development of a clickable bimodal fluorescent/PET probe for *in vivo* imaging'; DOI 10.1186/s13550-015-0120-4.

[433] M. Zhang, E. Hao, J. Zhou, C. Yu, G. Bai, F. Wang, L. Jiao, *Org. Biomol. Chem.* **2012**, *10*(10), 2139-2145; 'Synthesis of pyrrolyldipyrrinato BF_2 complexes by oxidative nucleophilic substitution of boron dipyrromethene with pyrrole'; DOI 10.1039/c2ob06689k.
[434] A. Loudet, K. Burgess, *Chemical reviews* **2007**, *107*(11), 4891-4932; 'BODIPY Dyes and Their Derivatives: Syntheses and Spectroscopic Properties'; DOI 10.1021/cr078381n.
[435] O. S. Vodyanova, B. A. Kochergin, S. D. Usoltsev, Y. S. Marfin, E. V. Rumyantsev, E. L. Aleksakhina, I. K. Tomilova, *J. Photochem. Photobiol. A Chem.* **2018**, *350*, 44-51; 'BODIPY dyes in bio environment: Spectral characteristics and possibilities for practical application'; DOI 10.1016/j.jphotochem.2017.09.049.
[436] W. Zhang, A. Ahmed, H. Cong, S. Wang, Y. Shen, B. Yu, *Dyes Pigm.* **2021**, *185*:108937, 1-14; 'Application of multifunctional BODIPY in photodynamic therapy'; DOI 10.1016/j.dyepig.2020.108937.
[437] P. Agostinis, K. Berg, K. A. Cengel, T. H. Foster, A. W. Girotti, S. O. Gollnick, S. M. Hahn, M. R. Hamblin, A. Juzeniene, D. Kessel, M. Korbelik, J. Moan, P. Mroz, D. Nowis, J. Piette, B. C. Wilson, J. Golab, *CA Cancer J. Clin.* **2011**, *61*(4), 250-281; 'Photodynamic Therapy of Cancer: An Update'; DOI 10.3322/caac.20114.
[438] P. Kancharla, K. A. Reynolds, *Tetrahedron* **2013**, *69*(39), 8375-8385; 'Synthesis of 2,2′-bipyrrole-5-carboxaldehydes and their application in the synthesis of B-ring functionalized prodiginines and tambjamines'; DOI 10.1016/j.tet.2013.07.067.
[439] B. S. Deol, J. R. Alden, J. L. Still, A. V. Robertson, J. Winkler, *Aust. J. Chem.* **1974**, *27*(12), 2657-2662; 'Isolation and structure confirmation of norprodigiosin from a *Serratia marcescens* mutant'; DOI 10.1071/CH9742657.
[440] W. R. Hearn, R. E. Worthington, R. C. Burgus, R. P. Williams, *Biochem. Biophys. Res. Commun.* **1964**, *17*(5), 517-520; 'Norprodigiosin: Occurrence in a mutant of *Serratia marcescens*'; DOI 10.1016/0006-291X(64)90057-9.
[441] D. A. Fort, T. J. Woltering, M. Nettekoven, H. Knust, T. Bach, *Angew. Chem. Int. Ed.* **2012**, *51*(40), 10169-10172; 'Synthesis of Fluorinated Tricyclic Scaffolds by Intramolecular [2+2] Photocycloaddition Reactions'; DOI 10.1002/anie.201204080.
[442] D. A. Fort, T. J. Woltering, M. Nettekoven, H. Knust, T. Bach, *Angew. Chem.* **2012**, *124*(40), 10316-10319; 'Synthesis of Fluorinated Tricyclic Scaffolds by Intramolecular [2+2] Photocycloaddition Reactions'; DOI 10.1002/ange.201204080.
[443] P. Jouin, B. Castro, D. Nisato, *J. Chem. Soc., Perkin Trans. I* **1987**, 1177-1182; 'Stereospecific Synthesis of *N*-Protected Statine and its Analogues via Chiral Tetramic Acid'; DOI 10.1039/P19870001177.
[444] J. Courcambeck, F. Bihel, C. De Michelis, G. Quéléver, J. L. Kraus, *J. Chem. Soc., Perkin Trans.* **2001**, *12*, 1421-1430; 'Design of potential new HIV protease inhibitors: enantioconvergent synthesis of new pyrrolidin-3-ol, and pyrrolidin-3-one peptide conjugates'; DOI 10.1039/b101584m.
[445] S. M. Greening, Doctoral Thesis, 'Synthesis of 2-Aryl Pyrroles, Prodigiosene *F*-BODIPYs and B-Ring Modified Prodigiosenes', Dalhousie University (Halifax, Nova Scotia, Canada) **2019**; https://dalspace.library.dal.ca/bitstream/handle/10222/76816/Greening-Sarah-PhD-CHEM-December-2019.pdf?sequence=1&isAllowed=y.
[446] C. P. Glindemann, A. Backenköhler, M. Strieker, U. Wittstock, P. Klahn, *ChemBioChem* **2019**, *20*(18), 2341-2345; 'Synthesis and Biochemical Evaluation of an Artificial, Fluorescent Glucosinolate (GSL)'; DOI 10.1002/cbic.201900148.
[447] O. Mitsunobu, M. Yamada, *Bull. Chem. Soc. Jpn.* **1967**, *40*(10), 2380-2382; 'Preparation of Esters of Carboxylic and Phosphoric Acid via Quaternary Phosphonium Salts'; DOI 10.1246/bcsj.40.2380.
[448] J. Agramunt, R. Ginesi, E. Pedroso, A. Grandas, *J. Org. Chem.* **2020**, *85*(10), 6593-6604; 'Inverse Electron-Demand Diels–Alder Bioconjugation Reactions Using 7-Oxanorbornenes as Dienophiles'; DOI 10.1021/acs.joc.0c00583.
[449] B. Morgan, D. Dolphin, *J. Org. Chem.* **1987**, *52*(24), 5364-5374; 'Synthesis of Hydrocarbon-Strapped Porphyrins Containing Quinone and Phenolic Groups'; DOI 10.1021/jo00233a011.
[450] D. P. Nair, M. Podgorski, S. Chatani, T. Gong, W. Xi, C. R. Fenoli, C. N. Bowman, *Chem. Mater.* **2014**, *26*(1), 724-744; 'The Thiol-Michael Addition Click Reaction: a Powerful and Widely Used Tool in Materials Chemistry'; DOI 10.1021/cm402180t.
[451] J. M. J. M. Ravasco, H. Faustino, A. Trindade, P. M. P. Gois, *Chem. Eur. J.* **2019**, *25*(1), 43-59; 'Bioconjugation with Maleimides: A Useful Tool for Chemical Biology'; DOI 10.1002/chem.201803174.
[452] T. L. Foley, A. Yasgar, C. J. Garcia, A. Jadhav, A. Simeonov, M. D. Burkart, *Org. Biomol. Chem.* **2010**, *8*(20), 4601-4606; 'Preparation of FRET Reporters to Support Chemical Probe Development'; DOI 10.1039/c0ob00322k.
[453] T. Uehara, T. Rokugawa, M. Kinoshita, S. Nemoto, G. G. Fransisco Lazaro, H. Hanaoka, Y. Arano, *Bioconjugate Chem.* **2014**, *25*(11), 2038-2045; '$^{67/68}$Ga-Labeling Agent That Liberates $^{67/68}$Ga-NOTA-Methionine by Lysosomal Proteolysis of Parental Low Molecular Weight Polypeptides to Reduce Renal Radioactivity Levels'; DOI 10.1021/bc5004058.
[454] L. Buschbeck, J. Christoffers, *J. Org. Chem.* **2018**, *83*(7), 4002-4014; 'Orthogonally Protected Diaminoterephthalate Scaffolds: Installation of Two Functional Units at the Chromophore'; DOI 10.1021/acs.joc.8b00347.
[455] J. Notni, H. J. Wester, *Chem. Eur. J.* **2016**, *22*(33), 11500-11508; 'A Practical Guide on the Synthesis of Metal Chelates for Molecular Imaging and Therapy by Means of Click Chemistry'; DOI 10.1002/chem.201600928.
[456] H. LeVine III, *Anal. Biochem.* **2006**, *356*(2), 265-272; 'Biotin–avidin interaction-based screening assay for Alzheimer's β-peptide oligomer inhibitors'; DOI 10.1016/j.ab.2006.04.036.
[457] R. Pérez-Tomás, B. Montaner, E. Llagostera, V. Soto-Cerrato, *Biochem. Pharmacol.* **2003**, *66*(8), 1447-1452; 'The prodigiosins, proapoptotic drugs with anticancer properties'; DOI 10.1016/S0006-2952(03)00496-9.
[458] G. D. Lewis, I. Figari, B. Fendly, W. Lee Wong, P. Carter, C. Gorman, H. M. Shepard, *Cancer Immunol. Immunother.* **1993**, *37*, 255-263; 'Differential responses of human tumor cell lines to anti-p185^{HER2} monoclonal antibodies'; DOI 10.1007/BF01518520.
[459] J. Regourd, A. Al-Sheikh Ali, A. Thompson, *J. Med. Chem.* **2007**, *50*(7), 1528-1536; 'Synthesis and Anti-Cancer Activity of C-Ring-Functionalized Prodigiosin Analogues'; DOI 10.1021/jm061088f.
[460] J. D. Bargh, A. Isidro-Llobet, J. S. Parker, D. R. Spring, *Chem. Soc. Rev.* **2019**, *48*(16), 4361-4374; 'Cleavable linkers in antibody–drug conjugates'; DOI 10.1039/c8cs00676h.

[461] J.-Z. Du, H.-J. Li, J. Wang, *Acc. Chem. Res.* **2018**, *51*(11), 2848-2856; 'Tumor-Acidity-Cleavable Maleic Acid Amide (TACMAA): A Powerful Tool for Designing Smart Nanoparticles to Overcome Delivery Barriers in Cancer Nanomedicine'; DOI 10.1021/acs.accounts.8b00195.
[462] A. Dal Corso, S. Cazzamalli, R. Gébleux, M. Mattarella, D. Neri, *Bioconjugate Chem.* **2017**, *28*(7), 1826-1833; 'Protease-Cleavable Linkers Modulate the Anticancer Activity of Noninternalizing Antibody–Drug Conjugates'; DOI 10.1021/acs.bioconjchem.7b00304.
[463] L. Berning, D. Schlütermann, A. Friedrich, N. Berleth, Y. Sun, W. Wu, M. J. Mendiburo, J. Deitersen, H. U. C. Brass, M. A. Skowron, M. J. Hoffmann, G. Niegisch, J. Pietruszka, B. Stork, *Molecules* **2021**, *26*(5):1294, 1-17; 'Prodigiosin Sensitizes Sensitive and Resistant Urothelial Carcinoma Cells to Cisplatin Treatment'; DOI 10.3390/molecules26051294.
[464] B. Montaner, R. Pérez-Tomás, *Life Sci.* **2001**, *68*(17), 2025-2036; 'Prodigiosin-induced apoptosis in human colon cancer cells'; DOI 10.1016/s0024-3205(01)01002-5.
[465] U. V. Santer, H. J. Vogel, *Biochim. Biophys. Acta* **1956**, *19*(3), 578-579; 'Prodigiosin synthesis in *Serratia marcescens*: isolation of a pyrrole-containing precursor'; DOI 10.1016/0006-3002(56)90500-5.
[466] H. H. Wasserman, J. E. McKeon, U. V. Santer, *Biochem. Biophys. Res. Commun.* **1960**, *3*(2), 146-149; 'Studies Related to the Biosynthesis of Prodigiosin in *Serratia marcescens*'; DOI 10.1016/0006-291X(60)90211-4.
[467] A. J. J. Lennox, G. C. Lloyd-Jones, *Chem. Soc. Rev.* **2014**, *43*(1), 412-443; 'Selection of boron reagents for Suzuki–Miyaura coupling'; DOI 10.1039/c3cs60197h.
[468] R. Hubbard, C. Rimington, *Biochem. J.* **1950**, *46*(2), 220-225; 'The Biosynthesis of Prodigiosin, the Tripyrrylmethene Pigment from *Bacillus prodigiosus* (*Serratia marcescens*)'; DOI 10.1042/bj0460220.
[469] A. Domröse, A. S. Klein, J. Hage-Hülsmann, S. Thies, V. Svensson, T. Classen, J. Pietruszka, K.-E. Jaeger, T. Drepper, A. Loeschcke, *Front. Microbiol.* **2015**, *6*:972, 1-10; 'Efficient recombinant production of prodigiosin in *Pseudomonas putida*'; DOI 10.3389/fmicb.2015.00972.
[470] W.-C. Chen, M.-J. Tsai, P.-C. Soo, L.-F. Wang, S.-L. Tsai, Y.-K. Chang, Y.-H. Wei, *J. Biosci. Bioeng.* **2018**, *126*(6), 783-789; 'Construction and co-cultivation of two mutant strains harboring key precursor genes to produce prodigiosin'; DOI 10.1016/j.jbiosc.2018.06.010.
[471] F. Yoshimura, H. Nikaido, *J. Bacteriol.* **1982**, *152*(2), 636-642; 'Permeability of *Pseudomonas aeruginosa* Outer Membrane to Hydrophilic Solutes'; DOI 10.1128/jb.152.2.636-642.1982.
[472] C.-H. Yip, S. Mahalingam, K.-L. Wan, S. Nathan, *PLoS One* **2021**, *16*(6):e0253445, 1-24; 'Prodigiosin inhibits bacterial growth and virulence factors as a potential physiological response to interspecies competition'; DOI 10.1371/journal.pone.0253445.
[473] D. Schlütermann, M. A. Skowron, N. Berleth, P. Boehler, J. Deitersen, F. Stuhldreier, N. Wallot-Hieke, W. Wu, C. Peter, M. J. Hoffmann, G. Niegisch, B. Stork, *Urol. Oncol.: Semin. Orig. Invest.* **2018**, *36*(4), 160.e161-160.e113; 'Targeting urothelial carcinoma cells by combining cisplatin with a specific inhibitor of the autophagy-inducing class III PtdIns3K complex'; DOI 10.1016/j.urolonc.2017.11.021.
[474] M. A. Skowron, G. Niegisch, G. Fritz, T. Arent, J. G. H. van Roermund, A. Romano, P. Albers, W. A. Schulz, M. J. Hoffmann, *J. Exp. Clin. Cancer Res.* **2015**, *34*(1), 1-15; 'Phenotype plasticity rather than repopulation from CD90/CK14+ cancer stem cells leads to cisplatin resistance of urothelial carcinoma cell lines'; DOI 10.1186/s13046-015-0259-x.
[475] M. A. Skowron, P. Petzsch, K. Hardt, N. Wagner, M. Beier, S. Stepanow, M. Drechsler, H. Rieder, K. Köhrer, G. Niegisch, M. J. Hoffmann, W. A. Schulz, *Sci. Rep.* **2019**, *9*(1):14476, 1-14; 'Distinctive mutational spectrum and karyotype disruption in long-term cisplatin-treated urothelial carcinoma cell lines'; DOI 10.1038/s41598-019-50891-w.
[476] K. Ma, S. Li, X. Huo, M. Guo, X. Du, C. Li, X. Liu, J. Lv, Z. Chen, *Biochem. Biophys. Res. Commun.* **2020**, *533*(3), 474-480; 'Exploring the mechanism of cisplatin resistance by transcriptome sequencing and reversing the chemoresistance by autophagy inhibition in small cell lung cancer'; DOI 10.1016/j.bbrc.2020.09.023.
[477] M. A. Skowron, M. Melnikova, J. G. H. van Roermund, A. Romano, P. Albers, J. Thomale, W. A. Schulz, G. Niegisch, M. J. Hoffmann, *Int. J. Mol. Sci.* **2018**, *19*(2):590, 1-17; 'Multifaceted mechanisms of cisplatin resistance in long-term treated urothelial carcinoma cell lines'; DOI 10.3390/ijms19020590.
[478] R. M. Drayton, J. W. F. Catto, *Expert Rev. Anticancer Ther.* **2012**, *12*(2), 271-281; 'Molecular mechanisms of cisplatin resistance in bladder cancer'; DOI 10.1586/ERA.11.201.
[479] S.-H. Chen, J.-Y. Chang, *Int. J. Mol. Sci.* **2019**, *20*(17), 4136-4156; 'New Insights into Mechanisms of Cisplatin Resistance: From Tumor Cell to Microenvironment'; DOI 10.3390/ijms20174136.
[480] M. M. Anwar, C. Albanese, N. M. Hamdy, A. S. Sultan, *Cancer Cell Int.* **2022**, *22*(1):419, 1-20; 'Rise of the natural red pigment 'prodigiosin' as an immunomodulator in cancer'; DOI 10.1186/s12935-022-02815-4.
[481] S. L. T. Nguyen, T. C. Nguyen, T. T. Do, T. L. Vu, T. T. Nguyen, T. T. Do, T. H. T. Nguyen, T. H. Le, D. K. Trinh, T. A. T. Nguyen, *Biomed. Res. Int.* **2022**, *2022*(1):4053074, 1-11; 'Study on the Anticancer Activity of Prodigiosin from Variants of *Serratia marcescens* QBN VTCC 910026'; DOI 10.1155/2022/4053074.
[482] T. Mosmann, *J. Immunol. Methods* **1983**, *65*(1-2), 55-63; 'Rapid Colorimetric Assay for Cellular Growth and Survival: Application to Proliferation and Cytotoxicity Assays'; DOI 10.1016/0022-1759(83)90303-4.
[483] T. L. Riss, R. A. Moravec, A. L. Niles, S. Duellman, H. A. Benink, T. J. Worzella, L. Minor, **2016**, '*Cell Viability Assays*' in *Assay Guidance Manual*, Eli Lilly & Company and the National Center for Advancing Translational Sciences Bethesda (MD); PubMed ID NBK53196.
[484] F. McCoy, J. Hurwitz, N. McTavish, I. Paul, C. Barnes, B. O'Hagan, K. Odrzywol, J. Murray, D. Longley, G. McKerr, D. A. Fennell, *Cell Death Dis.* **2010**, *1*(12):e108, 1-13; 'Obatoclax induces Atg7-dependent autophagy independent of beclin-1 and BAX/BAK'; DOI 10.1038/cddis.2010.86.
[485] B. C. Koehler, A. Jassowicz, A.-L. Scherr, S. Lorenz, P. Radhakrishnan, N. Kautz, C. Elssner, J. Weiss, D. Jaeger, M. Schneider, H. Schulze-Bergkamen, *BMC Cancer* **2015**, *15*, 1-11; 'Pan-Bcl-2 inhibitor Obatoclax is a potent late stage autophagy inhibitor in colorectal cancer cells independent of canonical autophagy signaling'; DOI 10.1186/s12885-015-1929-y.

[486] B. Montaner, S. Navarro, M. Piqué, M. Vilaseca, M. Martinell, E. Giralt, J. Gil, R. Pérez-Tomás, *Br. J. Pharmacol.* **2000**, *131*(3), 585-593; 'Prodigiosin from the supernatant of *Serratia marcescens* induces apoptosis in haematopoietic cancer cell lines'; DOI 10.1038/sj.bjp.0703614.
[487] S. Ji, R. Sun, K. Xu, Z. Man, J. Ji, Y. Pu, L. Yin, J. Zhang, Y. Pu, *Toxicol. In Vitro* **2019**, *60*, 107-115; 'Prodigiosin induces apoptosis and inhibits autophagy via the extracellular signal-regulated kinase pathway in K562 cells'; DOI 10.1016/j.tiv.2019.05.003.
[488] S. Ohkuma, T. Sato, M. Okamoto, H. Matsuya, K. Arai, T. Kataoka, K. Nagai, H. H. Wasserman, *Biochem. J.* **1998**, *334*(3), 731-741; 'Prodigiosins uncouple lysosomal vacuolar-type ATPase through promotion of H^+/Cl^- symport'; DOI 10.1042/bj3340731.
[489] F. A. P. C. Gobas, J. M. Lahittete, G. Garofalo, W. Y. Shiu, D. Mackay, *J. Pharm. Sci.* **1988**, *77*(3), 265-272; 'A Novel Method for Measuring Membrane-Water Partition Coefficients of Hydrophobic Organic Chemicals: Comparison with 1-Octanol–Water Partitioning'; DOI 10.1002/jps.2600770317.
[490] D. Kim, J. You, D. H. Lee, H. Hong, D. Kim, Y. Park, *Science* **2024**, *386*(6717), 99-105; 'Photocatalytic furan-to-pyrrole conversion'; DOI 10.1126/science.adq6245.
[491] J. K. Jurjew, *Ber. Dtsch. Chem. Ges. A/B* **1936**, *69*(2), 440-443; 'Katalytische Umwandlungen von heterocyclischen Verbindungen, I. Mitteil.: Umwandlungen von Furan in Pyrrol und Thiophen'; DOI 10.1002/cber.19360690242.
[492] A. Couture, A. Lablache-Combier, *J. Chem. Soc. D.* **1971**, *16*, 891-892; 'Analogy between Furan and Thiophen Photochemistry'; DOI 10.1039/C29710000891.
[493] L. Berning, T. Lenz, A. K. Bergmann, G. Poschmann, H. U. Brass, D. Schlütermann, A. Friedrich, M. J. Mendiburo, C. David, S. Akgün, J. Pietruszka, K. Stühler, B. Stork, *Cell Commun. Signal.* **2023**, *21*(1):275, 1-24; 'The Golgi stacking protein GRASP55 is targeted by the natural compound prodigiosin'; DOI 10.1186/s12964-023-01275-1.
[494] B. Rayner, A. D. Verderosa, V. Ferro, M. A. T. Blaskovich, *RSC Med. Chem.* **2023**, *14*(5), 800-822; 'Siderophore conjugates to combat antibiotic-resistant bacteria'; DOI 10.1039/D2MD00465H.
[495] C. Peukert, A. C. Vetter, H. L. S. Fuchs, K. Harmrolfs, B. Karge, M. Stadler, M. Brönstrup, *Chem. Sci.* **2023**, *14*(20), 5490-5502; 'Siderophore conjugation with cleavable linkers boosts the potency of RNA polymerase inhibitors against multidrug-resistant *E. coli*'; DOI 10.1039/D2SC06850H.
[496] A. Brezden, M. F. Mohamed, M. Nepal, J. S. Harwood, J. Kuriakose, M. N. Seleem, J. Chmielewski, *J. Am. Chem. Soc.* **2016**, *138*(34), 10945-10949; 'Dual Targeting of Intracellular Pathogenic Bacteria With a Cleavable Conjugate of Kanamycin and an Antibacterial Cell-Penetrating Peptide'; DOI 10.1021/jacs.6b04831.
[497] J. H. Boyce, B. Dang, B. Ary, Q. Edmondson, C. S. Craik, W. F. DeGrado, I. B. Seiple, *J. Am. Chem. Soc.* **2020**, *142*(51), 21310-21321; 'Platform to Discover Protease-Activated Antibiotics and Application to Siderophore–Antibiotic Conjugates'; DOI 10.1021/jacs.0c06987.
[498] J. Carlet, P. Collignon, D. Goldmann, H. Goossens, I. C. Gyssens, S. Harbarth, V. Jarlier, S. B. Levy, B. N'Doye, D. Pittet, R. Richtmann, W. H. Seto, J. W. M. Van der Meer, A. Voss, *Lancet* **2011**, *378*(9788), 369-371; 'Society's failure to protect a precious resource: antibiotics'; DOI 10.1016/S01406736(11)60401-7.
[499] J. Carlet, V. Jarlier, S. Harbarth, A. Voss, H. Goossens, D. Pittet, for the Participants of the 3rd World Healthcare-Associated Infections Forum, *Antimicrob. Resist. Infect. Control* **2012**, *1*(11), 1-13; 'Ready for a world without antibiotics? The Pensières Antibiotic Resistance Call to Action'; DOI 10.1186/2047-2994-1-11.
[500] E. Martens, A. L. Demain, *J. Antibiot.* **2017**, *70*(5), 520-526; 'The antibiotic resistance crisis, with a focus on the United States'; DOI 10.1038/ja.2017.30.
[501] R. W. Meek, H. Vyas, L. J. V. Piddock, *PLOS Biol.* **2015**, *13*(10):e1002266, 1-11; 'Nonmedical Uses of Antibiotics: Time to Restrict Their Use?'; DOI 10.1371/journal.pbio.1002266.
[502] Antimicrobial Resistance Collaborators, *Lancet* **2022**, *399*(10325), 629-655; 'Global burden of bacterial antimicrobial resistance in 2019: a systematic analysis'; DOI 10.1016/S0140-6736(21)02724-0.
[503] C. Kim, M. Holm, I. Frost, M. Hasso-Agopsowicz, K. Abbas, *BMJ Glob. Health* **2023**, *8*(7):e011341, 1-13; 'Global and regional burden of attributable and associated bacterial antimicrobial resistance avertable by vaccination: modelling study'; DOI 10.1136/bmjgh-2022-011341.
[504] J. Bengtsson-Palme, M. Milakovic, H. Švecová, M. Ganjto, V. Jonsson, R. Grabic, N. Udikovic-Kolic, *Water Res.* **2019**, *162*, 437-445; 'Industrial wastewater treatment plant enriches antibiotic resistance genes and alters the structure of microbial communities'; DOI 10.1016/j.watres.2019.06.073.
[505] E. Kristiansson, J. Fick, A. Janzon, R. Grabic, C. Rutgersson, B. Weijdegård, H. Söderström, D. G. J. Larsson, *PLoS One* **2011**, *6*(2):e17038, 1-7; 'Pyrosequencing of Antibiotic-Contaminated River Sediments Reveals High Levels of Resistance and Gene Transfer Elements'; DOI 10.1371/journal.pone.0017038.
[506] D. G. J. Larsson, C. de Pedro, N. Paxeus, *J. Hazard. Mater.* **2007**, *148*(3), 751-755; 'Effluent from drug manufactures contains extremely high levels of pharmaceuticals'; DOI 10.1016/j.jhazmat.2007.07.008.
[507] P. Ramachandran, N. K. Rachuri, S. Martha, R. Shakthivel, A. Gundala, T. S. Battu, *J. Pharm. Bioall. Sci.* **2019**, *11*(Suppl 2), S434-S437; 'Implications of Overprescription of Antibiotics: A Cross-Sectional Study'; DOI 10.4103/jpbs.JPBS_62_19.
[508] G.-G. Ying, L.-Y. He, A. J. Ying, Q.-Q. Zhang, Y.-S. Liu, J.-L. Zhao, *Environ. Sci. Technol.* **2017**, *51*(3), 1072-1073; 'China Must Reduce Its Antibiotic Use'; DOI 10.1021/acs.est.6b06424.
[509] K. Poole, *J. Mol. Microbiol. Biotechnol.* **2001**, *3*(2), 255-264; 'Multidrug Efflux Pumps and Antimicrobial Resistance in *Pseudomonas aeruginosa* and Related Organisms', PubMed ID 11321581.
[510] L. M. Sommer, H. K. Johansen, S. Molin, *Microb. Genom.* **2020**, *6*(5):e000370, 1-6; 'Antibiotic resistance in *Pseudomonas aeruginosa* and adaptation to complex dynamic environments'; DOI 10.1099/mgen.0.000370.
[511] D. M. Livermore, *Clin. Infect. Dis.* **2002**, *34*(5), 634-640; 'Multiple Mechanisms of Antimicrobial Resistance in *Pseudomonas aeruginosa*: Our Worst Nightmare?'; DOI 10.1086/338782.
[512] M. Meschiari, S. Volpi, M. Faltoni, G. Dolci, G. Orlando, E. Franceschini, M. Menozzi, M. Sarti, G. Del Fabro, B. Fumarola, F. Guarneri, P. Lanza, S. Lorenzotti, B. Saccani, L. Signorini, E. Van Hauwermeiren, M. Gatti, F. Pea, F.

Castelli, C. Mussini, *JAC Antimicrob. Resist.* **2021**, *3*(4):dlab188, 1-5; 'Real-life experience with compassionate use of cefiderocol for difficult-to-treat resistant *Pseudomonas aeruginosa* (DTR-P) infections'; DOI 10.1093/jacamr/dlab188.
[513] P. D. Tamma, S. L. Aitken, R. A. Bonomo, A. J. Mathers, D. Van Duin, C. J. Clancy, *Clin. Infect. Dis.* **2021**, *72*(7):e169–83, e169-e183; 'Infectious Diseases Society of America Guidance on the Treatment of Extended-Spectrum β-lactamase Producing Enterobacterales (ESBL-E), Carbapenem-Resistant Enterobacterales (CRE), and *Pseudomonas aeruginosa* with Difficult-to-Treat Resistance (DTR-*P. aeruginosa*)'; DOI 10.1093/cid/ciaa1478.
[514] S. Qin, W. Xiao, C. Zhou, Q. Pu, X. Deng, L. Lan, H. Liang, X. Song, M. Wu, *Signal Transduct. Target. Ther.* **2022**, *7*(1), 1-27; '*Pseudomonas aeruginosa*: pathogenesis, virulence factors, antibiotic resistance, interaction with host, technology advances and emerging therapeutics'; DOI 10.1038/s41392-022-01056-1.
[515] D. L. MacLeod, L. E. Nelson, R. M. Shawar, B. B. Lin, L. G. Lockwood, J. E. Dirks, G. H. Miller, J. L. Burns, R. L. Garber, *J. Infect. Dis.* **2000**, *181*(3), 1180-1184; 'Aminoglycoside-Resistance Mechanisms for Cystic Fibrosis *Pseudomonas aeruginosa* Isolates are Unchanged by Long-Term, Intermittent, Inhaled Tobramycin Treatment'; DOI 10.1086/315312.
[516] T. Strateva, D. Yordanov, *J. Med. Microbiol.* **2009**, *58*(9), 1133-1148; '*Pseudomonas aeruginosa* – a phenomenon of bacterial resistance'; DOI 10.1099/jmm.0.009142-0.
[517] L. Nguyen, J. Garcia, K. Gruenberg, C. MacDougall, *Curr. Infect. Dis. Rep.* **2018**, *20*(8), 1-10; 'Multidrug-Resistant *Pseudomonas* Infections: Hard to Treat, But Hope on the Horizon?'; DOI 10.1007/s11908-018-0629-6.
[518] M. McKenna, *Nature* **2013**, *499*(7459), 394-397; 'The last resort: health officials are watching in horror as bacteria become resistant to powerful carbapenem antibiotics – one of the last drugs on the shelf'; DOI 10.1038/499394a.
[519] K. M. Papp-Wallace, A. Endimiani, M. A. Taracila, R. A. Bonomo, *Antimicrob. Agents Chemother.* **2011**, *55*(11), 4943-4960; 'Carbapenems: Past, Present, and Future'; DOI 10.1128/AAC.00296-11.
[520] S. Reardon, *Nature* **2014**, *15*, 135-138; 'WHO warns against 'post-antibiotic' era'; DOI 10.1038/nature.2014.15135.
[521] R. Seifert, B. Schirmer, *Trends Microbiol.* **2021**, *29*(11), 963-966; 'A case to stop the use of the term 'antibiotics''; DOI 10.1016/j.tim.2021.03.017.
[522] M. I. Hutchings, A. W. Truman, B. Wilkinson, *Curr. Opin. Microbiol.* **2019**, *51*, 72-80; 'Antibiotics: past, present and future'; DOI 10.1016/j.mib.2019.10.008.
[523] L. L. Silver, *Clin. Microbiol. Rev.* **2011**, *24*(1), 71-109; 'Challenges of Antibacterial Discovery'; DOI 10.1128/cmr.00030-10.
[524] W. R. Miller, C. A. Arias, *Nat. Rev. Microbiol.* **2024**, *22*(10), 598-616; 'ESKAPE pathogens: antimicrobial resistance, epidemiology, clinical impact and therapeutics'; DOI 10.1038/s41579-024-01054-w.
[525] P.-E. Sum, V. J. Lee, R. T. Testa, J. J. Hlavka, G. A. Ellestad, J. D. Bloom, Y. Gluzman, F. P. Tally, *J. Med. Chem.* **1994**, *37*(1), 184-188; 'Glycylcyclines. 1. A New Generation of Potent Antibacterial Agents Through Modification of 9-Aminotetracyclines'; DOI 10.1021/jm00027a023.
[526] M. T. Guskey, B. T. Tsuji, *Pharmacotherapy* **2010**, *30*(1), 80-94; 'A Comparative Review of the Lipoglycopeptides: Oritavancin, Dalbavancin, and Telavancin'; DOI 10.1592/phco.30.1.80.
[527] K. Andries, P. Verhasselt, J. Guillemont, H. W. H. Göhlmann, J.-M. Neefs, H. Winkler, J. Van Gestel, P. Timmerman, M. Zhu, E. Lee, P. Williams, D. de Chaffoy, E. Huitric, S. Hoffner, E. Cambau, C. Truffot-Pernot, N. Lounis, V. Jalier, *Science* **2005**, *307*(5707), 223-227; 'A Diarylquinoline Drug Active on the ATP Synthase of *Mycobacterium tuberculosis*'; DOI 10.1126/science.1106753.
[528] Y. A. Adebisi, *Global. Health* **2023**, *19*(1):27, 1-7; 'Balancing the risks and benefits of antibiotic use in a globalized world: the ethics of antimicrobial resistance'; DOI 10.1186/s12992-023-00930-z.
[529] World Health Organization (WHO): AWaRe Classification of Antibiotics for Evaluation and Monitoring of Use, 2023, **2023**, https://www.who.int/publications/i/item/WHO-MHP-HPS-EML-2023.04, accessed 05/11/2024.
[530] K. Hiramatsu, H. Hanaki, T. Ino, K. Yabuta, T. Oguri, F. C. Tenover, *J. Antimicrob. Chemother.* **1997**, *40*(1), 135-136; 'Methicillin-resistant *Staphylococcus aureus* clinical strain with reduced vancomycin susceptibility'; DOI 10.1093/jac/40.1.135.
[531] Centers for Disease Control and Prevention (CDC), *MMWR Morb. Mortal. Wkly Rep.* **2006**, *55*(11), 301-305; 'Emergence of *Mycobacterium tuberculosis* with Extensive Resistance to Second-Line Drugs -- Worldwide, 2000-2004', PubMed ID 16557213.
[532] S. Tsiodras, H. S. Gold, G. Sakoulas, G. M. Eliopoulos, C. Wennersten, L. Venkataraman, R. C. Moellering, M. J. Ferraro, *Lancet* **2001**, *358*(9277), 207-208; 'Linezolid resistance in a clinical isolate of *Staphylococcus aureus*'; DOI 10.1016/S0140-6736(01)05410-1.
[533] C. Y. Wang, J. S. Jerng, K. Y. Cheng, L. N. Lee, C. J. Yu, P. R. Hsueh, P. C. Yang, *Clin. Microbiol. Infect.* **2006**, *12*(1), 63-68; 'Pandrug-resistant *Pseudomonas aeruginosa* among hospitalised patients: clinical features, risk-factors and outcomes'; DOI 10.1111/j.1469-0691.2005.01305.x.
[534] A. Mangili, I. Bica, D. R. Snydman, D. H. Hamer, *Clin. Infect. Dis.* **2005**, *40*(7), 1058-1060; 'Daptomycin-Resistant, Methicillin-Resistant *Staphylococcus aureus* Bacteremia'; DOI 10.1086/428616.
[535] M. K. Hayden, K. Rezai, R. A. Hayes, K. Lolans, J. P. Quinn, R. A. Weinstein, *J. Clin. Microbiol.* **2005**, *43*(10), 5285-5287; 'Development of Daptomycin Resistance In Vivo in Methicillin-Resistant *Staphylococcus aureus*'; DOI 10.1128/jcm.43.10.5285-5287.2005.
[536] L. A. Arroyo, A. Garcia-Curiel, M. E. Pachon-Ibanez, A. C. Llanos, M. Ruiz, J. Pachon, J. Aznar, *J. Clin. Microbiol.* **2005**, *43*(2), 903-905; 'Reliability of the E-Test Method for Detection of Colistin Resistance in Clinical Isolates of *Acinetobacter baumannii*'; DOI 10.1128/jcm.43.2.903-905.2005.
[537] Y.-Y. Liu, Y. Wang, T. R. Walsh, L.-X. Yi, R. Zhang, J. Spencer, Y. Doi, G. Tian, B. Dong, X. Huang, L.-F. Yu, D. Gu, H. Ren, X. Chen, L. Lv, D. He, H. Zhou, Z. Liang, J.-H. Liu, J. Shen, *Lancet Infect. Dis.* **2016**, *16*(2), 161-168; 'Emergence of plasmid-mediated colistin resistance mechanism MCR-1 in animals and human beings in China: a microbiological and molecular biological study'; DOI 10.1016/S1473-3099(15)00424-7.

[538] A. Gladki, S. Kaczanowski, P. Szczesny, P. Zielenkiewicz, *BMC bioinformatics* **2013**, *14*:36, 1-10; 'The evolutionary rate of antibacterial drug targets'; DOI 10.1186/1471-2105-14-36.
[539] M. H. Richmond, *J. Antimicrob. Chemother.* **1978**, *4*(Suppl. B), 1-14; 'Factors influencing the antibacterial action of β-lactam antibiotics'; DOI 10.1093/jac/4.suppl_b.1.
[540] M. D. Nailor, J. D. Sobel, *Infect. Dis. Clin. North Am.* **2009**, *23*(4), 965-982; 'Antibiotics for Gram-Positive Bacterial Infections: Vancomycin, Teicoplanin, Quinupristin/Dalfopristin, Oxazolidinones, Daptomycin, Dalbavancin, and Telavancin'; DOI 10.1016/j.idc.2009.06.010.
[541] J. D. Palmer, K. R. Foster, *Proc. Natl. Acad. Sci. U.S.A.* **2022**, *119*(38):e2205407119, 1-11; 'The evolution of spectrum in antibiotics and bacteriocins'; DOI 10.1073/pnas.2205407119.
[542] K. Bush, P. A. Bradford, *Cold Spring Harb. Perspect. Med.* **2016**, *6*(8):a025247, 1-23; 'β-Lactams and β-Lactamase Inhibitors: An Overview'; DOI 10.1101/cshperspect.a025247.
[543] World Health Organization (WHO): Antimicrobial Stewardship Programmes in Health-Care Facilites in Low- and Middle-Income Countries, **2019**, https://iris.who.int/bitstream/handle/10665/329404/9789241515481-eng.pdf, accessed 05/11/2024.
[544] A. Aliashkevich, F. Cava, *FEBS J.* **2022**, *289*(16), 4718-4730; 'LD-transpeptidases: the great unknown among the peptidoglycan cross-linkers'; DOI 10.1111/febs.16066.
[545] J. van Heijenoort, *Microbiol. Mol. Biol. Rev.* **2011**, *75*(4), 636-663; 'Peptidoglycan Hydrolases of *Escherichia coli*'; DOI 10.1128/mmbr.00022-11.
[546] D. J. Tipper, J. L. Strominger, *Proc. Natl. Acad. Sci. U.S.A.* **1965**, *54*(4), 1133-1141; 'Mechanism of Action of Penicillins: A Proposal Based on Their Structural Similarity to Acyl-D-Alanyl-D-Alanine'; DOI 10.1073/pnas.54.4.1133.
[547] C. Walsh, *Nature* **2000**, *406*(6797), 775-781; 'Molecular mechanisms that confer antibacterial drug resistance'; DOI 10.1038/35021219.
[548] S. Magnet, L. Dubost, A. Marie, M. Arthur, L. Gutmann, *J. Bacteriol.* **2008**, *190*(13), 4782-4785; 'Identification of the L,D-transpeptidases for peptidoglycan cross-linking in Escherichia coli'; DOI 10.1128/jb.00025-08.
[549] J.-E. Hugonnet, D. Mengin-Lecreulx, A. Monton, T. den Blaauwen, E. Carbonnelle, C. Veckerle, Y. Brun, V, M. van Nieuwenhze, C. Bouchier, K. Tu, L. B. Rice, M. Arthur, *Elife* **2016**, *5*:e19469, 1-22; 'Factors essential for L,D-transpeptidase-mediated peptidoglycan cross-linking and β-lactam resistance in *Escherichia coli*'; DOI 10.7554/eLife.19469.
[550] J.-L. Mainardi, R. Legrand, M. Arthur, B. Schoot, J. Van Heijenoort, L. Gutmann, *J. Biol. Chem.* **2000**, *275*(22), 16490-16496; 'Novel Mechanism of β-Lactam Resistance Due to Bypass of DD-Transpeptidation in *Enterococcus faecium*'; DOI 10.1074/jbc.M909877199.
[551] E. M. Darby, E. Trampari, P. Siasat, M. S. Gaya, I. Alav, M. A. Webber, J. M. A. Blair, *Nat. Rev. Microbiol.* **2023**, *21*(5), 280-295; 'Molecular mechanisms of antibiotic resistance revisited'; DOI 10.1038/s41579-022-00820-y.
[552] M. Duval, D. Dar, F. Carvalho, E. P. Rocha, R. Sorek, P. Cossart, *Proc. Natl. Acad. Sci. U.S.A.* **2018**, *115*(52), 13359-13364; 'HflXr, a homolog of a ribosome-splitting factor, mediates antibiotic resistance'; DOI 10.1073/pnas.1810555115.
[553] C. J. H. von Wintersdorff, J. Penders, J. M. Van Niekerk, N. D. Mills, S. Majumder, L. B. van Alphen, P. H. M. Savelkoul, P. F. G. Wolffs, *Front. Microbiol.* **2016**, *7*:173, 1-10; 'Dissemination of Antimicrobial Resistance in Microbial Ecosystems through Horizontal Gene Transfer'; DOI 10.3389/fmicb.2016.00173.
[554] World Health Organization (WHO): "WHO Publishes List of Bacteria for Which New Antibiotics are Urgently Needed", **2017**, https://www.who.int/news/item/27-02-2017-who-publishes-list-of-bacteria-for-which-new-antibiotics-are-urgently-needed, accessed 24/04/2024.
[555] World Health Organization (WHO): "New Report Calls for Urgent Action to Avert Antimicrobial Resistance Crisis", **2019**, https://www.who.int/news/item/29-04-2019-new-report-calls-for-urgent-action-to-avert-antimicrobial-resistance-crisis, accessed 24/04/2024.
[556] World Health Organization (WHO): WHO Bacterial Priority Pathogens List, 2024, **2024**, https://iris.who.int/bitstream/handle/10665/376776/9789240093461-eng.pdf?sequence=1, accessed 05/11/2024.
[557] S. K. Gohil, E. Septimus, K. Kleinman, N. Varma, T. R. Avery, L. Heim, R. Rahm, W. S. Cooper, M. Cooper, L. E. McLean, N. G. Nickolay, R. A. Weinstein, H. Burgess, M. H. Coady, E. Rosen, S. Sljivo, K. E. Sands, J. Moody, J. Vigeant, S. Rashid, R. F. Gilbert, K. N. Smith, B. Carver, R. E. Poland, J. Hickok, S. G. Sturdevant, M. S. Calderwood, A. Weiland, D. W. Kubiak, S. Reddy, M. M. Neuhauser, A. Srinivasan, J. A. Jernigan, M. K. Hayden, A. Gowda, K. Eibensteiner, R. Wolf, J. B. Perlin, R. Platt, S. S. Huang, *J. Am. Med. Assoc.* **2024**, *331*(23), 2007-2017; 'Stewardship Prompts to Improve Antibiotic Selection for Pneumonia: The INSPIRE Randomized Clinical Trial'; DOI 10.1001/jama.2024.6248.
[558] S. K. Gohil, E. Septimus, K. Kleinman, N. Varma, T. R. Avery, L. Heim, R. Rahm, W. S. Cooper, M. Cooper, L. E. McLean, N. G. Nickolay, R. A. Weinstein, H. Burgess, M. H. Coady, E. Rosen, S. Sljivo, K. E. Sands, J. Moody, J. Vigeant, S. Rashid, R. F. Gilbert, K. N. Smith, B. Carver, R. E. Poland, J. Hickok, S. G. Sturdevant, M. S. Calderwood, A. Weiland, D. W. Kubiak, S. Reddy, M. M. Neuhauser, A. Srinivasan, J. A. Jernigan, M. K. Hayden, A. Gowda, K. Eibensteiner, R. Wolf, J. B. Perlin, R. Platt, S. S. Huang, *J. Am. Med. Assoc.* **2024**, *331*(23), 2018-2028; 'Stewardship Prompts to Improve Antibiotic Selection for Urinary Tract Infection: The INSPIRE Randomized Clinical Trial'; DOI 10.1001/jama.2024.6259.
[559] S. Leekha, C. L. Terrell, R. S. Edson, *Mayo Clin. Proc.* **2011**, *86*(2), 156-167; 'General Principles of Antimicrobial Therapy'; DOI 10.4065/mcp.2010.0639.
[560] M. Bassetti, A. Vena, A. Croxatto, E. Righi, B. Guery, *Drugs Context* **2018**, *7*:212527, 1-18; 'How to manage *Pseudomonas aeruginosa* infections'; DOI 10.7573/dic.212527.
[561] S. R. Modi, J. J. Collins, D. A. Relman, *J. Clin. Invest.* **2014**, *124*(10), 4212-4218; 'Antibiotics and the gut microbiota'; DOI 10.1172/JCI72333.
[562] M. F. Chellat, L. Raguž, R. Riedl, *Angew. Chem. Int. Ed.* **2016**, *55*(23), 6600-6626; 'Targeting Antibiotic Resistance'; DOI 10.1002/anie.201506818.

[563] M. F. Chellat, L. Raguž, R. Riedl, *Angew. Chem.* **2016**, *128*(23), 6710-6738; 'Targeting Antibiotic Resistance'; DOI 10.1002/ange.201506818.
[564] J. Spížek, J. Novotná, T. Řezanka, A. L. Demain, *J. Ind. Microbiol. Biotechnol.* **2010**, *37*(12), 1241-1248; 'Do we need new antibiotics? The search for new targets and new compounds'; DOI 10.1007/s10295-010-0849-8.
[565] S. Tao, H. Chen, N. Li, T. Wang, W. Liang, *Can. J. Infect. Dis. Med. Microbiol.* **2022**, *2022*(1):3348695, 1-11; 'The Spread of Antibiotic Resistance Genes In Vivo Model'; DOI 10.1155/2022/3348695.
[566] J. M. Munita, C. A. Arias, *Microbiol. Spectr.* **2016**, *4*(2):VMBF-0016-2015, 1-24; 'Mechanisms of Antibiotic Resistance'; DOI 10.1128/microbiolspec.vmbf-0016-2015.
[567] L. Yang, Y. Hu, Y. Liu, J. Zhang, J. Ulstrup, S. Molin, *Environ. Microbiol.* **2011**, *13*(7), 1705-1717; 'Distinct roles of extracellular polymeric substances in *Pseudomonas aeruginosa* biofilm development'; DOI 10.1111/j.1462-2920.2011.02503.x.
[568] M. T. T. Thi, D. Wibowo, B. H. A. Rehm, *Int. J. Mol. Sci.* **2020**, *21*(22):8671, 1-25; '*Pseudomonas aeruginosa* Biofilms'; DOI 10.3390/ijms21228671.
[569] A. H. Delcour, *Biochim. Biophys. Acta* **2009**, *1794*(5), 808-816; 'Outer membrane permeability and antibiotic resistance'; DOI 10.1016/j.bbapap.2008.11.005.
[570] N. Weston, P. Sharma, V. Ricci, L. J. V. Piddock, *Res. Microbiol.* **2018**, *169*(7-8), 425-431; 'Regulation of the AcrAB-TolC efflux pump in Enterobacteriaceae'; DOI 10.1016/j.resmic.2017.10.005.
[571] C. Llanes, D. Hocquet, C. Vogne, D. Benali-Baitich, C. Neuwirth, P. Plésiat, *Antimicrob. Agents Chemother.* **2004**, *48*(5), 1797-1802; 'Clinical Strains of *Pseudomonas aeruginosa* Overproducing MexAB-OprM and MexXY Efflux Pumps Simultaneously'; DOI 10.1128/AAC.48.5.1797-1802.2004.
[572] N. Masuda, E. Sakagawa, S. Ohya, N. Gotoh, H. Tsujimoto, T. Nishino, *Antimicrob. Agents Chemother.* **2000**, *44*(12), 3322-3327; 'Substrate Specificities of MexAB-OprM, MexCD-OprJ, and MexXY-oprM Efflux Pumps in *Pseudomonas aeruginosa*'; DOI 10.1128/aac.44.12.3322-3327.2000.
[573] M. F. Moradali, S. Ghods, B. H. A. Rehm, *Front. Cell. Infect. Microbiol.* **2017**, *7*:39, 1-29; '*Pseudomonas aeruginosa* Lifestyle: A Paradigm for Adaptation, Survival, and Persistence'; DOI 10.3389/fcimb.2017.00039.
[574] L. Huang, C. Wu, H. Gao, C. Xu, M. Dai, L. Huang, H. Hao, X. Wang, G. Cheng, *Antibiotics* **2022**, *11*(4):520, 1-18; 'Bacterial Multidrug Efflux Pumps at the Frontline of Antimicrobial Resistance: An Overview'; DOI 10.3390/antibiotics11040520.
[575] G. A. J. Ayliffe, *Clin. Infect. Dis.* **1997**, *24*(Supplement_1), S74-S79; 'The Progressive Intercontinental Spread of Methicillin-Resistant *Staphylococcus aureus*'; DOI 10.1093/clinids/24.Supplement_1.S74.
[576] Y. Katayama, T. Ito, K. Hiramatsu, *Antimicrob. Agents Chemother.* **2000**, *44*(6), 1549-1555; 'A New Class of Genetic Element, Staphylococcus Cassette Chromosome *mec*, Encodes Methicillin Resistance in *Staphylococcus aureus*'; DOI 10.1128/aac.44.6.1549-1555.2000.
[577] B. Guignard, J. M. Entenza, P. Moreillon, *Curr. Opin. Pharmacol.* **2005**, *5*(5), 479-489; 'β-lactams against methicillin-resistant *Staphylococcus aureus*'; DOI 10.1016/j.coph.2005.06.002.
[578] K. Bush, *Antimicrob. Agents Chemother.* **2018**, *62*(10):e01076-18, 1-20; 'Past and Present Perspectives on β-Lactamases'; DOI 10.1128/aac.01076-18.
[579] O. B. Jonas, A. Irwin, F. C. J. Berthe, F. G. Le Gall, P. V. Marquez, *HNP/Agriculture Global Antimicrobial Resistance Initiative Washington, D.C.: World Bank Group.* **2023**; 'Drug-Resistant Infections: A Threat to Our Economic Future (Vol 2): Final Report. HNP/Agriculture Global Antimicrobial Resistance Initiative Washington, DC: World Bank Group'.
[580] Y. He, J. Lei, X. Pan, X. Huang, Y. Zhao, *Sci. Rep.* **2020**, *10*(1):10205, 1-13; 'The hydrolytic water molecule of Class A β-lactamase relies on the acyl-enzyme intermediate ES* for proper coordination and catalysis'; DOI 10.1038/s41598-020-66431-w.
[581] B. G. Hall, M. Barlow, *Drug Resist. Updat.* **2004**, *7*(2), 111-123; 'Evolution of the serine β-lactamases: past, present and future'; DOI 10.1016/j.drup.2004.02.003.
[582] E. P. Abraham, E. Chain, *Nature* **1940**, *146*(3713), 837-837; 'An Enzyme from Bacteria able to Destroy Penicillin'; DOI 10.1038/146837a0.
[583] A. Mathers, *Microbiol. Spectr.* **2016**, *4*(3):EI10-0010-2015, 1-10; 'Mobilization of Carbapenemase-Mediated Resistance in *Enterobacteriaceae*'; DOI 10.1128/microbiolspec.ei10-0010-2015.
[584] B. Farber, R. C. Moellering Jr., *Bull. N. Y. Acad. Med.* **1982**, *58*(8), 696; 'The Third Generation Cephalosporins', PubMed ID 6762896.
[585] A. Philippon, R. Labia, G. Jacoby, *Antimicrob. Agents Chemother.* **1989**, *33*(8), 1131-1136; 'Extended-Spectrum β-Lactamases'; DOI 10.1128/aac.33.8.1131.
[586] K. Bush, *J. Infect. Chemother.* **2013**, *19*(4), 549-559; 'The ABCD's of β-lactamase nomenclature'; DOI 10.1007/s10156-013-0640-7.
[587] J. S. Kahan, F. M. Kahan, R. Goegelman, S. A. Currie, M. Jackson, E. O. Stapley, T. W. Miller, A. K. Miller, D. Hendlin, S. Mochales, S. Hernandez, H. B. Woodruff, J. Birnbaum, *J. Antibiot.* **1979**, *32*(1), 1-12; 'Thienamycin, a New β-Lactam Antibiotic I. Discovery, Taxonomy, Isolation and Physical Properties'; DOI 10.7164/antibiotics.32.1.
[588] R. B. Sykes, D. P. Bonner, *Am. J. Med.* **1985**, *78*(2A), 2-10; 'Aztreonam: The First Monobactam'; DOI 10.1016/0002-9343(85)90196-2.
[589] J. J. Rahal, C. Urban, D. Horn, K. Freeman, S. Segal-Maurer, J. Maurer, N. Mariano, S. Marks, J. M. Burns, D. Dominick, M. Lim, *J. Am. Med. Assoc.* **1998**, *280*(14), 1233-1237; 'Class Restriction of Cephalosporin Use to Control Total Cephalosporin Resistance in Nosocomial *Klebsiella*'; DOI 10.1001/jama.280.14.1233.
[590] P. M. Lepper, E. Grusa, H. Reichl, J. Högel, M. Trautmann, *Antimicrob. Agents Chemother.* **2002**, *46*(9), 2920-2925; 'Consumption of Imipenem Correlates with β-Lactam Resistance in *Pseudomonas aeruginosa*'; DOI 10.1128/aac.46.9.2920-2925.2002.
[591] K. Bush, *J. Glob. Antimicrob. Resist.* **2013**, *1*(1), 7-16; 'Carbapenemases: Partners in crime'; DOI 10.1016/j.jgar.2013.01.005.

[592] C. Urban, E. Go, N. Mariano, J. J. Rahal, *FEMS Microbiol. Lett.* **1995**, *125*(2-3), 193-197; 'Interaction of sulbactam, clavulanic acid and tazobactam with penicillin-binding proteins of imipenem-resistant and -susceptible *Acinetobacter baumannii*'; DOI 10.1016/0378-1097(94)00497-F.
[593] P. A. Bradford, C. Urban, N. Mariano, S. J. Projan, J. J. Rahal, K. Bush, *Antimicrob. Agents Chemother.* **1997**, *41*(3), 563-569; 'Imipenem Resistance in *Klebsiella pneumoniae* Is Associated with the Combination of ACT-1, a Plasmid-Mediated AmpC β-Lactamase, and the Loss of an Outer Membrane Protein'; DOI 10.1128/aac.41.3.563.
[594] M. Watanabe, S. Iyobe, M. Inoue, S. Mitsuhashi, *Antimicrob. Agents Chemother.* **1991**, *35*(1), 147-151; 'Transferable Imipenem Resistance in *Pseudomonas aeruginosa*'; DOI 10.1128/aac.35.1.147.
[595] H. C. Maltezou, *Int. J. Antimicrob. Agents* **2009**, *33*(5):405.e1-7, 405.e401-405. e407; 'Metallo-β-lactamases in Gram-negative bacteria: introducing the era of pan-resistance?'; DOI 10.1016/j.ijantimicag.2008.09.003.
[596] E. V. Scoulica, I. K. Neonakis, A. I. Gikas, Y. J. Tselentis, *Diagn. Microbiol. Infect. Dis.* **2004**, *48*(3), 167-172; 'Spread of *bla*$_{VIM-1}$-producing *E. coli* in a university hospital in Greece. Genetic analysis of the integron carrying the *bla*$_{VIM-1}$ metallo-β-lactamase gene'; DOI 10.1016/j.diagmicrobio.2003.09.012.
[597] N. D. Hanson, A. Hossain, L. Buck, E. S. Moland, K. S. Thomson, *Antimicrob. Agents Chemother.* **2006**, *50*(6), 2272-2273; 'First Occurrence of a *Pseudomonas aeruginosa* Isolate in the United States Producing an IMP Metallo-β-Lactamase, IMP-18'; DOI 10.1128/AAC.01440-05.
[598] F. Pasteran, D. Faccone, A. Petroni, M. Rapoport, M. Galas, M. Vázquez, A. Procopio, *Antimicrob. Agents Chemother.* **2005**, *49*(1), 474-475; 'Novel Variant (*bla*$_{VIM-11}$) of the Metallo-β-lactamase *bla*$_{VIM}$ Family in a GES-1 Extended-Spectrum-β-Lactamase-Producing *Pseudomonas aeruginosa* Clinical Isolate in Argentina'; DOI 10.1128/AAC.49.1.474–475.2005.
[599] J. Yatsuyanagi, S. Saito, Y. Ito, K. Ohta, J. Kato, S. Harata, N. Suzuki, K.-i. Amano, *Jpn. J. Infect. Dis* **2004**, *57*(3), 130-132; 'Identification of *Pseudomonas aeruginosa* Clinical Strains Harboring the *bla*(VIM-2) Metallo-β-Lactamase Gene in Akita Prefecture, Japan', PubMed ID 15218228.
[600] A. F. Wendel, A. H. B. Brodner, S. Wydra, S. Ressina, B. Henrich, K. Pfeffer, M. A. Toleman, C. R. MacKenzie, *Antimicrob. Agents Chemother.* **2013**, *57*(10), 5162-5165; 'Genetic Characterization and Emergence of the Metallo-β-Lactamase GIM-1 in *Pseudomonas* spp. and *Enterobacteriaceae* during a Long-Term Outbreak'; DOI 10.1128/aac.00118-13.
[601] M. Castanheira, M. A. Toleman, R. N. Jones, F. J. Schmidt, T. R. Walsh, *Antimicrob. Agents Chemother.* **2004**, *48*(12), 4654-4661; 'Molecular Characterization of a β-Lactamase Gene, *bla*$_{GIM-1}$, Encoding a New Subclass of Metallo-β-Lactamase'; DOI 10.1128/aac.48.12.4654-4661.2004.
[602] L. Lauretti, M. L. Riccio, A. Mazzariol, G. Cornaglia, G. Amicosante, R. Fontana, G. M. Rossolini, *Antimicrob. Agents Chemother.* **1999**, *43*(7), 1584-1590; 'Cloning and Characterization of *bla*$_{VIM}$, a New Integron-Borne Metallo-β-Lactamase Gene from a *Pseudomonas aeruginosa* Clinical Isolate'; DOI 10.1128/aac.43.7.1584.
[603] D. Yong, M. A. Toleman, C. G. Giske, H. S. Cho, K. Sundman, K. Lee, T. R. Walsh, *Antimicrob. Agents Chemother.* **2009**, *53*(12), 5046-5054; 'Characterization of a New Metallo-β-Lactamase Gene, *bla*$_{NDM-1}$, and a Novel Erythromycin Esterase Gene Carried on a Unique Genetic Structure in *Klebsiella pneumoniae* Sequence Type 14 from India'; DOI 10.1128/aac.00774-09.
[604] L. Poirel, J.-M. Rodríguez-Martínez, N. Al Naiemi, Y. J. Debets-Ossenkopp, P. Nordmann, *Antimicrob. Agents Chemother.* **2010**, *54*(6), 2420-2424; 'Characterization of DIM-1, an Integron-Encoded Metallo-β-Lactamase from a *Pseudomonas stutzeri* Clinical Isolate in the Netherlands'; DOI 10.1128/aac.01456-09.
[605] D. Yong, M. A. Toleman, J. Bell, B. Ritchie, R. Pratt, H. Ryley, T. R. Walsh, *Antimicrob. Agents Chemother.* **2012**, *56*(12), 6154-6159; 'Genetic and Biochemical Characterization of an Acquired Subgroup B3 Metallo-β-Lactamase Gene, *bla*$_{AIM-1}$, and its Unique Genetic Context in *Pseudomonas aeruginosa* from Australia'; DOI 10.1128/aac.05654-11.
[606] A. El Salabi, P. S. Borra, M. A. Toleman, Ø. Samuelsen, T. R. Walsh, *Antimicrob. Agents Chemother.* **2012**, *56*(5), 2241-2245; 'Genetic and Biochemical Characterization of a Novel Metallo-β-Lactamase, TMB-1, from an *Achromobacter xylosoxidans* Strain Isolated in Tripoli, Libya'; DOI 10.1128/aac.05640-11.
[607] F. Lange, N. Pfennigwerth, R. Hartl, H. Kerschner, D. Achleitner, S. G. Gatermann, M. Kaase, *J. Antimicrob. Chemother.* **2018**, *73*(9), 2331-2335; 'LMB-1, a novel family of class B3 MBLs from an isolate of *Enterobacter cloacae*'; DOI 10.1093/jac/dky215.
[608] M. Kanamori, T. Kirikae, M. O. Watanabe, T. Miyoshi-Akiyama, M. Kanamori, T. Kirikae, *Antimicrob. Agents Chemother.* **2008**, *52*(11), 4194–4197; 'KHM-1, a Novel Plasmid-Mediated Metallo-β-Lactamase from a *Citrobacter freundii* Clinical Isolate'; DOI 10.1128/AAC.01337-07.
[609] M. A. Toleman, A. M. Simm, T. A. Murphy, A. C. Gales, D. J. Biedenbach, R. N. Jones, T. R. Walsh, *J. Antimicrob. Chemother.* **2002**, *50*(5), 673-679; 'Molecular characterization of SPM-1, a novel metallo-β-lactamase isolated in Latin America: report from the SENTRY antimicrobial surveillance programme'; DOI 10.1093/jac/dkf210.
[610] K. Lee, J. H. Yum, D. Yong, H. M. Lee, H. D. Kim, J.-D. Docquier, G. M. Rossolini, Y. Chong, *Antimicrob. Agents Chemother.* **2005**, *49*(11), 4485-4491; 'Novel Acquired Metallo-β-Lactamase Gene, *bla*$_{SIM-1}$, in a Class 1 Integron from *Acinetobacter baumannii* Clinical Isolates from Korea'; DOI 10.1128/aac.49.11.4485-4491.2005.
[611] T. Naas, S. Oueslati, R. A. Bonnin, M. L. Dabos, A. Zavala, L. Dortet, P. Retailleau, B. I. Iorga, *J. Enzyme Inhib. Med. Chem.* **2017**, *32*(1), 917-919; 'Beta-lactamase database (BLDB) – structure and function'; DOI 10.1080/14756366.2017.1344235.
[612] C. Lagatolla, E. A. Tonin, C. Monti-Bragadin, L. Dolzani, F. Gombac, C. Bearzi, E. Edalucci, F. Gionechetti, G. M. Rossolini, *Emerg. Infect. Dis.* **2004**, *10*(3), 535-538; 'Endemic Carbapenem-resistant *Pseudomonas aeruginosa* with Acquired Metallo-β-lactamase Determinants in European Hospital'; DOI 10.3201/eid1003.020799.
[613] J. D. D. Pitout, D. B. Gregson, L. Poirel, J.-A. McClure, P. Le, D. L. Church, *J. Clin. Microbiol.* **2005**, *43*(7), 3129-3135; 'Detection of *Pseudomonas aeruginosa* Producing Metallo-β-Lactamases in a Large Centralized Laboratory'; DOI 10.1128/jcm.43.7.3129-3135.2005.

[614] J. P. Pirnay, S. Matthijs, H. Colak, P. Chablain, F. Bilocq, J. Van Eldere, D. De Vos, M. Zizi, L. Triest, P. Cornelis, *Environ. Microbiol.* **2005**, *7*(7), 969-980; 'Global *Pseudomonas aeruginosa* biodiversity as reflected in a Belgian river'; DOI 10.1111/j.1462-2920.2005.00776.x.
[615] C. Liao, X. Huang, Q. Wang, D. Yao, W. Lu, *Front. Cell. Infect. Microbiol.* **2022**, *12*:926758, 1-17; 'Virulence Factors of *Pseudomonas aeruginosa* and Antivirulence Strategies to Combat Its Drug Resistance'; DOI 10.3389/fcimb.2022.926758.
[616] I. Jurado-Martín, M. Sainz-Mejías, S. McClean, *Int. J. Mol. Sci.* **2021**, *22*(6):3128, 1-35; '*Pseudomonas aeruginosa*: An Audacious Pathogen with an Adaptable Arsenal of Virulence Factors'; DOI 10.3390/ijms22063128.
[617] E. Stachler, A. Kull, T. R. Julian, *Appl. Environ. Microbiol.* **2021**, *87*(20):e00980-21, 1-12; 'Bacteriophage Treatment before Chemical Disinfection Can Enhance Removal of Plastic-Surface-Associated *Pseudomonas aeruginosa*'; DOI 10.1128/aem.00980-21.
[618] D. Reynolds, M. Kollef, *Drugs* **2021**, *81*(18), 2117-2131; 'The Epidemiology and Pathogenesis and Treatment of *Pseudomonas aeruginosa* Infections: An Update'; DOI 10.1007/s40265-021-01635-6.
[619] F. J. Veyrier, A. Dufort, M. A. Behr, *Trends Microbiol.* **2011**, *19*(4), 156-161; 'The rise and fall of the *Mycobacterium tuberculosis* genome'; DOI 10.1016/j.tim.2010.12.008.
[620] A. Ghafoor, I. D. Hay, B. H. A. Rehm, *Appl. Environ. Microbiol.* **2011**, *77*(15), 5238-5246; 'Role of Exopolysaccharides in *Pseudomonas aeruginosa* Biofilm Formation and Architecture'; DOI 10.1128/aem.00637-11.
[621] M. J. Franklin, D. E. Nivens, J. T. Weadge, P. L. Howell, *Front. Microbiol.* **2011**, *2*:167, 1-16; 'Biosynthesis of the *Pseudomonas aeruginosa* extracellular polysaccharides, alginate, Pel, and Psl'; DOI 10.3389/fmicb.2011.00167.
[622] M. Wilton, L. Charron-Mazenod, R. Moore, S. Lewenza, *Antimicrob. Agents Chemother.* **2016**, *60*(1), 544-553; 'Extracellular DNA acidifies biofilms and induces aminoglycoside resistance in Pseudomonas aeruginosa'; DOI 10.1128/AAC.01650-15.
[623] M. Wilton, M. J. Q. Wong, L. Tang, X. Liang, R. Moore, M. D. Parkins, S. Lewenza, T. G. Dong, *Infect. Immun.* **2016**, *84*(8), 2355-2361; 'Chelation of Membrane-Bound Cations by Extracellular DNA Activates the Type VI Secretion System in *Pseudomonas aeruginosa*'; DOI 10.1128/iai.00233-16.
[624] S. L. Drees, S. Fetzner, *Chem. Biol.* **2015**, *22*(5), 611-618; 'PqsE of *Pseudomonas aeruginosa* Acts as Pathway-Specific Thioesterase in the Biosynthesis of Alkylquinolone Signaling Molecules'; DOI 10.1016/j.chembiol.2015.04.012.
[625] S. M. Huszczynski, J. S. Lam, C. M. Khursigara, *Pathogens* **2019**, *9*(1):6, 1-22; 'The Role of *Pseudomonas aeruginosa* Lipopolysaccharide in Bacterial Pathogenesis and Physiology'; DOI 10.3390/pathogens9010006.
[626] W. Engels, J. Endert, M. A. Kamps, C. P. van Boven, *Infect. Immun.* **1985**, *49*(1), 182-189; 'Role of Lipopolysaccharide in Opsonization and Phagocytosis of *Pseudomonas aeruginosa*'; DOI 10.1128/iai.49.1.182-189.1985.
[627] D. Drake, T. C. Montie, *J. Gen. Microbiol.* **1988**, *134*(1), 43-52; 'Flagella, Motility and Invasive Virulence of *Pseudomonas aeruginosa*'; DOI 10.1099/00221287-134-1-43.
[628] C. M. Toutain, N. C. Caizza, M. E. Zegans, G. A. O'Toole, *Res. Microbiol.* **2007**, *158*(5), 471-477; 'Roles for flagellar stators in biofilm formation by *Pseudomonas aeruginosa*'; DOI 10.1016/j.resmic.2007.04.001.
[629] S. R. Coleman, D. Pletzer, R. E. W. Hancock, *J. Infect. Dis.* **2021**, *224*(4), 726-733; 'Contribution of Swarming Motility to Dissemination in a *Pseudomonas aeruginosa* Murine Skin Abscess Infection Model'; DOI 10.1093/infdis/jiaa778.
[630] M. Q. Carter, J. Chen, S. Lory, *J. Bacteriol.* **2010**, *192*(13), 3249-3258; 'The *Pseudomonas aeruginosa* Pathogenicity Island PAPI-1 Is Transferred via a Novel Type IV Pilus'; DOI 10.1128/JB.00041-10.
[631] B. W. Bardoel, K. P. M. van Kessel, J. A. G. van Strijp, F. J. Milder, *J. Mol. Biol.* **2012**, *415*(3), 573-583; 'Inhibition of *Pseudomonas aeruginosa* Virulence: Characterization of the AprA–AprI Interface and Species Selectivity'; DOI 10.1016/j.jmb.2011.11.039.
[632] E. T. Yukl, G. Jepkorir, A. Y. Alontaga, L. Pautsch, J. C. Rodriguez, M. Rivera, P. Moënne-Loccoz, *Biochemistry* **2010**, *49*(31), 6646-6654; 'Kinetic and Spectroscopic Studies of Hemin Acquisition in the Hemophore HasAp from *Pseudomonas aeruginosa*'; DOI 10.1021/bi100692f.
[633] L. L. Anzaldi, E. P. Skaar, *Infect. Immun.* **2010**, *78*(12), 4977-4989; 'Overcoming the Heme Paradox: Heme Toxicity and Tolerance in Bacterial Pathogens'; DOI 10.1128/IAI.00613-10.
[634] R. Jørgensen, A. R. Merrill, S. P. Yates, V. E. Marquez, A. L. Schwan, T. Boesen, G. R. Andersen, *Nature* **2005**, *436*(7053), 979-984; 'Exotoxin A-eEF2 complex structure indicates ADP ribosylation by ribosome mimicry'; DOI 10.1038/nature03871.
[635] L. S. Engel, J. M. Hill, A. R. Caballero, L. C. Green, R. J. O'Callaghan, *J. Biol. Chem.* **1998**, *273*(27), 16792-16797; 'Protease IV, a Unique Extracellular Protease and Virulence Factor from *Pseudomonas aeruginosa*'; DOI 10.1074/jbc.273.27.16792.
[636] M. J. Wargo, M. J. Gross, S. Rajamani, J. L. Allard, L. K. A. Lundblad, G. B. Allen, M. L. Vasil, L. W. Leclair, D. A. Hogan, *Am. J. Respir. Crit. Care Med.* **2011**, *184*(3), 345-354; 'Hemolytic Phospholipase C Inhibition Protects Lung Function During *Pseudomonas aeruginosa* Infection'; DOI 10.1164/rccm.201103-0374OC.
[637] D. M. Foulkes, K. McLean, A. S. Haneef, D. G. Fernig, C. Winstanley, N. Berry, S. B. Kaye, *Microorganisms* **2019**, *7*(12):707, 1-17; '*Pseudomonas aeruginosa* Toxin ExoU as a Therapeutic Target in the Treatment of Bacterial Infections'; DOI 10.3390/microorganisms7120707.
[638] S. Wilhelm, A. Gdynia, P. Tielen, F. Rosenau, K.-E. Jaeger, *J. Bacteriol.* **2007**, *189*(18), 6695-6703; 'The Autotransporter Esterase EstA of *Pseudomonas aeruginosa* Is Required for Rhamnolipid Production, Cell Motility, and Biofilm Formation'; DOI 10.1128/JB.00023-07.
[639] F. Jacob-Dubuisson, C. Locht, R. Antoine, *Mol. Microbiol.* **2001**, *40*(2), 306-313; 'Two-partner secretion in Gram-negative bacteria: a thrifty, specific pathway for large virulence proteins'; DOI 10.1046/j.1365-2958.2001.02278.x.
[640] F. Jiang, N. R. Waterfield, J. Yang, G. Yang, Q. Jin, *Cell Host Microbe* **2014**, *15*(5), 600-610; 'A *Pseudomonas aeruginosa* Type VI Secretion Phospholipase D Effector Targets Both Prokaryotic and Eukaryotic Cells'; DOI 10.1016/j.chom.2014.04.010.
[641] B. R. Otto, A. M. J. J. Verweij-van Vught, D. M. MacLaren, *Crit. Rev. Microbiol.* **1992**, *18*(3), 217-233; 'Transferrins and Heme-Compounds as Iron Sources for Pathogenic Bacteria'; DOI 10.3109/10408419209114559.

[642] K. D. Krewulak, H. J. Vogel, *Biochem. Cell Biol.* **2011**, *89*(2), 87-97; 'TonB or not TonB: is that the question?'; DOI 10.1139/O10-141.
[643] J. E. Cassat, E. P. Skaar, *Cell Host Microbe* **2013**, *13*(5), 509-519; 'Iron in Infection and Immunity'; DOI 10.1016/j.chom.2013.04.010.
[644] C. Ayala-Castro, A. Saini, F. W. Outten, *Microbiol. Mol. Biol. Rev.* **2008**, *72*(1), 110-125; 'Fe-S Cluster Assembly Pathways in Bacteria'; DOI 10.1128/MMBR.00034-07.
[645] Y. V. Verkhovtseva, Y. Y. Filina, D. E. Pukhov, *J. Evol. Biochem. Physiol.* **2001**, *37*, 444-450; 'Evolutionary Role of Iron in Metabolism of Prokaryotes and in Biogeochemical Processes'; DOI 10.1023/A:1012987214946.
[646] P. Cornelis, *Appl. Microbiol. Biotechnol.* **2010**, *86*(6), 1637-1645; 'Iron uptake and metabolism in pseudomonads'; DOI 10.1007/s00253-010-2550-2.
[647] G. Ghssein, Z. Ezzeddine, *Biology* **2022**, *11*(12):1711, 1-18; 'A Review of *Pseudomonas aeruginosa* Metallophores: Pyoverdine, Pyochelin and Pseudopaline'; DOI 10.3390/biology11121711.
[648] C. D. Cox, K. L. Rinehart Jr, M. L. Moore, J. C. Cook Jr, *Proc. Natl. Acad. Sci. U.S.A.* **1981**, *78*(7), 4256-4260; 'Pyochelin: Novel Structure of an Iron-Chelating Growth Promoter for *Pseudomonas aeruginosa*'; DOI 10.1073/pnas.78.7.4256.
[649] J. S. McFarlane, A. L. Lamb, *Biochemistry* **2017**, *56*(45), 5967-5971; 'Biosynthesis of an Opine Metallophore by *Pseudomonas aeruginosa*'; DOI 10.1021/acs.biochem.7b00804.
[650] J. Zhang, T. Zhao, R. Yang, I. Siridechakorn, S. Wang, Q. Guo, Y. Bai, H. C. Shen, X. Lei, *Chem. Sci.* **2019**, *10*(27), 6635-6641; '*De novo* synthesis, structural assignment and biological evaluation of pseudopaline, a metallophore produced by *Pseudomonas aeruginosa*'; DOI 10.1039/c9sc01405e.
[651] I. L. Lamont, P. A. Beare, U. Ochsner, A. I. Vasil, M. L. Vasil, *Proc. Natl. Acad. Sci. U.S.A.* **2002**, *99*(10), 7072-7077; 'Siderophore-mediated signaling regulates virulence factor production in *Pseudomonas aeruginosa*'; DOI 10.1073/pnas.09201699.
[652] M. Shirley, I. L. Lamont, *J. Bacteriol.* **2009**, *191*(18), 5634-5640; 'Role of TonB1 in Pyoverdine-Mediated Signaling in *Pseudomonas aeruginosa*'; DOI 10.1128/JB.00742-09.
[653] H. Budzikiewicz, M. Schäfer, D. U. Fernández, S. Matthijs, P. Cornelis, *Biometals* **2007**, *20*(2), 135-144; 'Characterization of the chromophores of pyoverdins and related siderophores by electrospray tandem mass spectrometry'; DOI 10.1007/s10534-006-9021-3.
[654] M. De Chial, B. Ghysels, S. A. Beatson, V. Geoffroy, J. M. Meyer, T. Pattery, C. Baysse, P. Chablain, Y. N. Parsons, C. Winstanley, S. J. Cordwell, P. Cornelis, *Microbiology* **2003**, *149*(4), 821-831; 'Identification of type II and type III pyoverdine receptors from *Pseudomonas aeruginosa*'; DOI 10.1099/mic.0.26136-0.
[655] K. Brillet, L. Journet, H. Celia, L. Paulus, A. Stahl, F. Pattus, D. Cobessi, *Structure* **2007**, *15*(11), 1383-1391; 'A β Strand Lock Exchange for Signal Transduction in TonB-Dependent Transducers on the Basis of a Common Structural Motif'; DOI 10.1016/j.str.2007.08.013.
[656] A. Silale, B. van den Berg, *Annu. Rev. Microbiol.* **2023**, *77*(1), 67-88; 'TonB-Dependent Transport Across the Bacterial Outer Membrane'; DOI 10.1146/annurev-micro-032421-111116.
[657] A. R. T. Figueiredo, Ö. Özkaya, R. Kümmerli, J. Kramer, *Ecol. Lett.* **2022**, *25*(1), 138-150; 'Siderophores drive invasion dynamics in bacterial communities through their dual role as public good versus public bad'; DOI 10.1111/ele.13912.
[658] G. L. A. Mislin, I. J. Schalk, *Metallomics* **2014**, *6*(3), 408-420; 'Siderophore-dependent iron uptake systems as gates for antibiotic Trojan horse strategies against *Pseudomonas aeruginosa*'; DOI 10.1039/c3mt00359k.
[659] K. Poole, L. Young, S. Neshat, *J. Bacteriol.* **1990**, *172*(12), 6991-6996; 'Enterobactin-Mediated Iron Transport in *Pseudomonas aeruginosa*'; DOI 10.1128/jb.172.12.6991-6996.1990.
[660] M. A. Llamas, M. Sparrius, R. Kloet, C. R. Jiménez, C. Vandenbroucke-Grauls, W. Bitter, *J. Bacteriol.* **2006**, *188*(5), 1882-1891; 'The Heterologous Siderophores Ferrioxamine B and Ferrichrome Activate Signaling Pathways in *Pseudomonas aeruginosa*'; DOI 10.1128/JB.188.5.1882–1891.2006.
[661] Y. Michel-Briand, C. Baysse, *Biochim.* **2002**, *84*(5-6), 499-510; 'The pyocins of *Pseudomonas aeruginosa*'; DOI 10.1016/S0300-9084(02)01422-0.
[662] P. White, A. Joshi, P. Rassam, N. G. Housden, R. Kaminska, J. D. Goult, C. Redfield, L. C. McCaughey, D. Walker, S. Mohammed, C. Kleanthous, *Proc. Natl. Acad. Sci. U.S.A.* **2017**, *114*(45), 12051-12056; 'Exploitation of an iron transporter for bacterial protein antibiotic import'; DOI 10.1073/pnas.1713741114.
[663] Y. Zeng, A. Kulkarni, Z. Yang, P. B. Patil, W. Zhou, X. Chi, S. Van Lanen, S. Chen, *ACS Chem. Biol.* **2012**, *7*(9), 1565-1575; 'Biosynthesis of Albomycin δ_2 Provides a Template for Assembling Siderophore and Aminoacyl-tRNA Synthetase Inhibitor Conjugates'; DOI 10.1021/cb300173x.
[664] O. Kinzel, R. Tappe, I. Gerus, H. Budzikiewicz, *J. Antibiot.* **1998**, *51*(5), 499-507; 'The Synthesis and Antibacterial Activity of two Pyoverdin-ampicillin Conjugates, Entering *Pseudomonas aeruginosa* via the Pyoverdin-mediated Iron Uptake Pathway'; DOI 10.7164/antibiotics.51.499.
[665] H. Budzikiewicz, *Curr. Top. Med. Chem.* **2001**, *1*(1), 73-82; 'Siderophore-Antibiotic Conjugates Used as Trojan Horses Against *Pseudomonas aeruginosa*'; DOI 10.2174/1568026013395524.
[666] S. Noël, V. Gasser, B. Pesset, F. Hoegy, D. Rognan, I. J. Schalk, G. L. Mislin, *Org. Biomol. Chem.* **2011**, *9*(24), 8288-8300; 'Synthesis and biological properties of conjugates between fluoroquinolones and a N3″-functionalized pyochelin'; DOI 10.1039/c1ob06250f.
[667] C. Peukert, V. Gasser, T. Orth, S. Fritsch, V. Normant, O. Cunrath, I. J. Schalk, M. Brönstrup, *J. Med. Chem.* **2022**, *66*(1), 553-576; 'Trojan Horse Siderophore Conjugates Induce *Pseudomonas aeruginosa* Suicide and Qualify the TonB Protein as a Novel Antibiotic Target'; DOI 10.1021/acs.jmedchem.2c01489.
[668] P. D. Cotter, R. P. Ross, C. Hill, *Nat. Rev. Microbiol.* **2013**, *11*(2), 95-105; 'Bacteriocins – a viable alternative to antibiotics?'; DOI 10.1038/nrmicro2937.
[669] M. G. K. Ghequire, R. De Mot, *FEMS Microbiol. Rev.* **2014**, *38*(4), 523-568; 'Ribosomally encoded antibacterial proteins and peptides from *Pseudomonas*'; DOI 10.1111/1574-6976.12079.

[670] M. Zimina, O. Babich, A. Prosekov, S. Sukhikh, S. Ivanova, M. Shevchenko, S. Noskova, *Antibiotics* **2020**, *9*(9):553, 1-21; 'Overview of Global Trends in Classification, Methods of Preparation and Application of Bacteriocins'; DOI 10.3390/antibiotics9090553.
[671] A. Gardner, S. A. West, A. Buckling, *Proc. R. Soc. Lond. B Biol. Sci.* **2004**, *271*(1547), 1529-1535; 'Bacteriocins, spite and virulence'; DOI 10.1098/rspb.2004.2756.
[672] M. Kageyama, M. Kobayashi, Y. Sano, H. Masaki, *J. Bacteriol.* **1996**, *178*(1), 103-110; 'Construction and Characterization of Pyocin-Colicin Chimeric Proteins'; DOI 10.1128/jb.178.1.103-110.1996.
[673] R. A. Alm, S. D. Lahiri, *Antibiotics* **2020**, *9*(7):418, 1-8; 'Narrow-Spectrum Antibacterial Agents – Benefits and Challenges'; DOI 10.3390/antibiotics9070418.
[674] E. Cascales, S. K. Buchanan, D. Duché, C. Kleanthous, R. Lloubès, K. Postle, M. Riley, S. Slatin, D. Cavard, *Microbiol. Mol. Biol. Rev.* **2007**, *71*(1), 158-229; 'Colicin Biology'; DOI 10.1128/MMBR.00036-06.
[675] D. K. Verma, M. Thakur, S. Singh, S. Tripathy, A. K. Gupta, D. Baranwal, A. R. Patel, N. Shah, G. L. Utama, A. K. Niamah, M. L. Chávez-González, C. Flores Gallegos, C. N. Aguilar, P. P. Srivastav, *Food Biosci.* **2022**, *46*:101594, 1-23; 'Bacteriocins as antimicrobial and preservative agents in food: Biosynthesis, separation and application'; DOI 10.1016/j.fbio.2022.101594.
[676] H. Khan, S. Flint, P.-L. Yu, *Int. J. Food Microbiol.* **2010**, *141*(1-2), 1-10; 'Enterocins in food preservation'; DOI 10.1016/j.ijfoodmicro.2010.03.005.
[677] M. L. Chikindas, R. Weeks, D. Drider, V. A. Chistyakov, L. M. T. Dicks, *Curr. Opin. Biotechnol.* **2018**, *49*, 23-28; 'Functions and emerging applications of bacteriocins'; DOI 10.1016/j.copbio.2017.07.011.
[678] F. Jacob, *Ann. Inst. Pasteur* **1954**, *86*(2), 149-160; 'Biosynthèse induite et mode d'action d'une pyocine, antibiotique de *Pseudomonas pyocyanea*', PubMed ID 13158940.
[679] H. Barreteau, A. Bouhss, M. Fourgeaud, J.-L. Mainardi, T. Touzé, F. Gérard, D. Blanot, M. Arthur, D. Mengin-Lecreulx, *J. Bacteriol.* **2009**, *191*(11), 3657-3664; 'Human- and Plant-Pathogenic *Pseudomonas* Species Produce Bacteriocins Exhibiting Colicin M-Like Hydrolase Activity Towards Peptidoglycan Precursors'; DOI 10.1128/JB.01824-08.
[680] M. G. K. Ghequire, J. Dingemans, J. P. Pirnay, D. De Vos, P. Cornelis, R. De Mot, *Microbiologyopen* **2014**, *3*(6), 875-884; 'O serotype-independent susceptibility of *Pseudomonas aeruginosa* to lectin-like pyocins'; DOI 10.1002/mbo3.210.
[681] M. G. K. Ghequire, B. Öztürk, *Appl. Environ. Microbiol.* **2018**, *84*(18):e00716-18, 1-11; 'A Colicin M-Type Bacteriocin from *Pseudomonas aeruginosa* Targeting the HxuC Heme Receptor Requires a Novel Immunity Partner'; DOI 10.1128/AEM.00716-18.
[682] K. Nakayama, K. Takashima, H. Ishihara, T. Shinomiya, M. Kageyama, S. Kanaya, M. Ohnishi, T. Murata, H. Mori, T. Hayashi, *Mol. Microbiol.* **2000**, *38*(2), 213-231; 'The R-type pyocin of *Pseudomonas aeruginosa* is related to P2 phage, and the F-type is related to lambda phage'; DOI 10.1046/j.1365-2958.2000.02135.x.
[683] K. Ikeda, F. Egami, *J. Gen. Appl. Microbiol.* **1973**, *19*(2), 115-128; 'Lipopolysaccharide of *Pseudomonas aeruginosa* with Special Reference to Pyocin R Receptor Activity'; DOI 10.2323/jgam.19.115.
[684] T. Köhler, V. Donner, C. van Delden, *J. Bacteriol.* **2010**, *192*(7), 1921-1928; 'Lipopolysaccharide as Shield and Receptor for R-Pyocin-Mediated Killing in *Pseudomonas aeruginosa*'; DOI 10.1128/JB.01459-09.
[685] S. Saha, C. D. Ojobor, A. S. C. Li, E. Mackinnon, O. I. North, J. Bondy-Denomy, J. S. Lam, A. W. Ensminger, K. L. Maxwell, A. R. Davidson, *J. Bacteriol.* **2023**, *205*(6):e00029-23, 1-17; 'F-Type Pyocins are Diverse Noncontractile Phage Tail-Like Weapons for Killing *Pseudomonas aeruginosa*'; DOI 10.1128/jb.00029-23.
[686] Y. Uratani, T. Hoshino, *J. Bacteriol.* **1984**, *157*(2), 632-636; 'Pyocin R1 Inhibits Active Transport in *Pseudomonas aeruginosa* and Depolarizes Membrane Potential'; DOI 10.1128/jb.157.2.632-636.1984.
[687] M. Ohsumi, T. Shinomiya, M. Kageyama, *J. Biochem.* **1980**, *87*(4), 1119-1126; 'Comparative Study on R-type Pyocins of *Pseudomonas aeruginosa*', PubMed ID 6771248.
[688] Y. Kaziro, M. Tanaka, *J. Biochem.* **1965**, *57*(5), 689-695; 'Studies on the Mode of Action of Pyocin I. Inhibition of Macromolecular Synthesis in Sensitive Cells', PubMed ID 4953867.
[689] G. Lee, U. Chakraborty, D. Gebhart, G. R. Govoni, Z. H. Zhou, D. Scholl, *J. Bacteriol.* **2016**, *198*(20), 2784-2793; 'F-Type Bacteriocins of *Listeria monocytogenes*: a New Class of Phage Tail-Like Structures Reveals Broad Parallel Coevolution between Tailed Bacteriophages and High-Molecular-Weight Bacteriocins'; DOI 10.1128/jb.00489-16.
[690] M. G. K. Ghequire, B. Öztürk, R. De Mot, *Front. Microbiol.* **2018**, *9*:2706, 1-11; 'Lectin-Like Bacteriocins'; DOI 10.3389/fmicb.2018.02706.
[691] M. G. K. Ghequire, R. De Mot, *Microb. Biotechnol.* **2019**, *12*(3), 567-573; 'LlpB represents a second subclass of lectin-like bacteriocins'; DOI 10.1111/1751-7915.13373.
[692] J. S. Lam, V. L. Taylor, S. T. Islam, Y. Hao, D. Kocíncová, *Front. Microbiol.* **2011**, *2*:118, 1-25; 'Genetic and functional diversity of *Pseudomonas aeruginosa* lipopolysaccharide'; DOI 10.3389/fmicb.2011.00118.
[693] L. C. McCaughey, R. Grinter, I. Josts, A. W. Roszak, K. I. Waløen, R. J. Cogdell, J. Milner, T. Evans, S. Kelly, N. P. Tucker, O. Byron, B. Smith, D. Walker, *PLOS Pathog.* **2014**, *10*(2):e1003898, 1-15; 'Lectin-Like Bacteriocins from *Pseudomonas* spp. Utilise D-Rhamnose Containing Lipopolysaccharide as a Cellular Receptor'; DOI 10.1371/journal.ppat.1003898.
[694] M. G. K. Ghequire, A. Garcia-Pino, E. K. M. Lebbe, S. Spaepen, R. Loris, R. De Mot, *PLOS Pathog.* **2013**, *9*(2):e1003199, 1-14; 'Structural Determinants for Activity and Specificity of the Bacterial Toxin LlpA'; DOI 10.1371/journal.ppat.1003199.
[695] M. G. K. Ghequire, T. Swings, J. Michiels, S. K. Buchanan, R. De Mot, *MBio* **2018**, *9*(2):e02138-17, 1-15; 'Hitting with a BAM: selective Killing by Lectin-Like Bacteriocins'; DOI 10.1128/mbio.02138-17.
[696] L. M. Matano, M. J. Coyne, L. García-Bayona, L. E. Comstock, *MBio* **2021**, *12*(5):e02285-21, 1-13; 'Bacteroidetocins Target the Essential Outer Membrane Protein BamA of *Bacteroidales* Symbionts and Pathogens'; DOI 10.1128/mbio.02285-21.
[697] R. E. Harkness, T. Ölschläger, *FEMS Microbiol. Rev.* **1991**, *8*(1), 27-42; 'The biology of colicin M'; DOI 10.1111/j.1574-6968.1991.tb04955.x.

[698] M. El Ghachi, A. Bouhss, H. Barreteau, T. Touzé, G. Auger, D. Blanot, D. Mengin-Lecreulx, *J. Biol. Chem.* **2006**, *281*(32), 22761-22772; 'Colicin M Exerts Its Bacteriolytic Effect via Enzymatic Degradation of Undecaprenyl Phosphate-linked Peptidoglycan Precursors'; DOI 10.1074/jbc.M602834200.
[699] L. Latino, D. Patin, D. Chérier, T. Touzé, C. Pourcel, H. Barreteau, D. Mengin-Lecreulx, *J. Bacteriol.* **2019**, *201*(13):e00164-19, 1-21; 'Impact of FiuA Outer Membrane Receptor Polymorphism on the Resistance of *Pseudomonas aeruginosa* Toward Peptidoglycan Lipid II-Targeting PaeM Pyocins'; DOI 10.1128/jb.00164-19.
[700] A. Shushan, M. Kosloff, *Sci. Rep.* **2021**, *11*(1):3789, 1-15; 'Structural design principles for specific ultra-high affinity interactions between colicins/pyocins and immunity proteins'; DOI 10.1038/s41598-021-83265-2.
[701] A. Joshi, R. Grinter, I. Josts, S. Chen, J. A. Wojdyla, E. D. Lowe, R. Kaminska, C. Sharp, L. McCaughey, A. W. Roszak, R. J. Cogdell, O. Byron, D. Walker, C. Kleanthous, *J. Mol. Biol.* **2015**, *427*(17), 2852-2866; 'Structures of the Ultra-High-Affinity Protein–Protein Complexes of Pyocins S2 and AP41 and Their Cognate Immunity Proteins from *Pseudomonas aeruginosa*'; DOI 10.1016/j.jmb.2015.07.014.
[702] S. Ito, M. Kageyama, F. Egami, *J. Gen. Appl. Microbiol.* **1970**, *16*(3), 205-214; 'Isolation and Characterization of Pyocins from Several Strains of *Pseudomonas aeruginosa*'; DOI 10.2323/jgam.16.3_205.
[703] B. W. Holloway, H. Rossiter, D. Burgess, J. Dodge, *Genet. Res.* **1973**, *22*(3), 239-253; 'Aeruginocin tolerant mutants of *Pseudomonas aeruginosa*'; DOI 10.1017/s0016672300013069.
[704] I. Ohkawa, M. Kageyama, F. Egami, *J. Biochem.* **1973**, *73*(2), 281-289; 'Purification and Properties of Pyocin S2'; DOI 10.1093/oxfordjournals.jbchem.a130085.
[705] A. H. A. Parret, R. De Mot, *Mol. Microbiol.* **2000**, *35*(2), 472-475; 'Novel bacteriocins with predicted tRNase and pore-forming activities in *Pseudomonas aeruginosa* PAO1'; DOI 10.1046/j.1365-2958.2000.01716.x.
[706] I. Atanaskovic, K. Mosbahi, C. Sharp, N. G. Housden, R. Kaminska, D. Walker, C. Kleanthous, *J. Mol. Biol.* **2020**, *432*(13), 3869-3880; 'Targeted Killing of *Pseudomonas aeruginosa* by Pyocin G Occurs *via* the Hemin Transporter Hur'; DOI 10.1016/j.jmb.2020.04.020.
[707] J. Premsuriya, K. Mosbahi, I. Atanaskovic, C. Kleanthous, D. Walker, *Biochem. J.* **2023**, *480*(14), 1035-1049; 'Outer membrane translocation of pyocins via the copper regulated TonB-dependent transporter CrtA'; DOI 10.1042/BCJ20220552.
[708] C. Duport, C. Baysse, Y. Michel-Briand, *J. Biol. Chem.* **1995**, *270*(15), 8920-8927; 'Molecular Characterization of Pyocin S3, a Novel S-Type Pyocin from *Pseudomonas aeruginosa*'; DOI 10.1074/jbc.270.15.8920.
[709] J. Dingemans, M. G. K. Ghequire, M. Craggs, R. De Mot, P. Cornelis, *Microbiologyopen* **2016**, *5*(3), 413-423; 'Identification and functional analysis of a bacteriocin, pyocin S6, with ribonuclease activity from a *Pseudomonas aeruginosa* cystic fibrosis clinical isolate'; DOI 10.1002/mbo3.339.
[710] H. Turano, F. Gomes, R. M. Domingos, M. F. S. Degenhardt, C. L. P. Oliveira, R. C. Garratt, N. Lincopan, L. E. S. Netto, *J. Bacteriol.* **2020**, *202*(21):e00346-20, 1-17; 'Molecular Structure and Functional Analysis of Pyocin S8 from *Pseudomonas aeruginosa* Reveals the Essential Requirement of a Glutamate Residue in the HNH Motif for DNase Activity'; DOI 10.1128/jb.00346-20.
[711] L. C. McCaughey, I. Josts, R. Grinter, P. White, O. Byron, N. P. Tucker, J. M. Matthews, C. Kleanthous, C. B. Whitchurch, D. Walker, *Biochem. J.* **2016**, *473*(15), 2345-2358; 'Discovery, characterization and in vivo activity of pyocin SD2, a protein antibiotic from *Pseudomonas aeruginosa*'; DOI 10.1042/BCJ20160470.
[712] Y. Sano, H. Matsui, M. Kobayashi, M. Kageyama, *J. Bacteriol.* **1993**, *175*(10), 2907-2916; 'Molecular Structures and Functions of Pyocins S1 and S2 in *Pseudomonas aeruginosa*'; DOI 10.1128/jb.175.10.2907-2916.1993.
[713] S. Denayer, S. Matthijs, P. Cornelis, *J. Bacteriol.* **2007**, *189*(21), 7663-7668; 'Pyocin S2 (Sa) Kills *Pseudomonas aeruginosa* Strains via the FpvA Type I Ferripyoverdine Receptor'; DOI 10.1128/JB.00992-07.
[714] Y. Seo, D. R. Galloway, *Biochem. Biophys. Res. Commun.* **1990**, *172*(2), 455-461; 'Purification of the pyocin S2 complex from *Pseudomonas aeruginosa* PAO1: analysis of DNase activity'; DOI 10.1016/0006-291X(90)90694-I.
[715] C. Baysse, J.-M. Meyer, P. Plesiat, V. Geoffroy, Y. Michel-Briand, P. Cornelis, *J. Bacteriol.* **1999**, *181*(12), 3849-3851; 'Uptake of Pyocin S3 Occurs through the Outer Membrane Ferripyoverdine Type II Receptor of *Pseudomonas aeruginosa*'; DOI 10.1128/jb.181.12.3849-3851.1999.
[716] A. Elfarash, Q. Wei, P. Cornelis, *Microbiologyopen* **2012**, *1*(3), 268-275; 'The soluble pyocins S2 and S4 from *Pseudomonas aeruginosa* bind to the same FpvAI receptor'; DOI 10.1002/mbo3.27.
[717] A. Elfarash, J. Dingemans, L. Ye, A. A. Hassan, M. Craggs, C. Reimmann, M. S. Thomas, P. Cornelis, *Microbiology* **2014**, *160*(2), 261-269; 'Pore-forming pyocin S5 utilizes the FptA ferripyochelin receptor to kill *Pseudomonas aeruginosa*'; DOI 10.1099/mic.0.070672-0.
[718] H. Ling, N. Saeidi, B. H. Rasouliha, M. W. Chang, *FEBS Lett.* **2010**, *584*(15), 3354-3358; 'A predicted S-type pyocin shows a bactericidal activity against clinical *Pseudomonas aeruginosa* isolates through membrane damage'; DOI 10.1016/j.febslet.2010.06.021.
[719] H. M. Behrens, E. D. Lowe, J. Gault, N. G. Housden, R. Kaminska, T. M. Weber, C. M. A. Thompson, G. L. A. Mislin, I. J. Schalk, D. Walker, C. V. Robinson, C. Kleanthous, *MBio* **2020**, *11*(2):e03230-19, 1-16; 'Pyocin S5 Import into *Pseudomonas aeruginosa* Reveals a Generic Mode of Bacteriocin Transport'; DOI 10.1128/mbio.03230-19.
[720] Y. Sano, *J. Bacteriol.* **1993**, *175*(3), 912-915; 'The Inherent DNase of Pyocin AP41 Causes Breakdown of Chromosomal DNA'; DOI 10.1128/jb.175.3.912-915.1993.
[721] A. H. A. Parret, R. De Mot, *Trends Microbiol.* **2002**, *10*(3), 107-112; 'Bacteria killing their own kind: novel bacteriocins of *Pseudomonas* and other γ-proteobacteria'; DOI 10.1016/s0966-842x(02)02307-7.
[722] C. Kleanthous, *Nat. Rev. Microbiol.* **2010**, *8*(12), 843-848; 'Swimming against the tide: progress and challenges in our understanding of colicin translocation'; DOI 10.1038/nrmicro2454.
[723] I. Atanaskovic, C. Kleanthous, *Front. Microbiol.* **2019**, *10*:646, 1-12; 'Tools and Approaches for Dissecting Protein Bacteriocin Import in Gram-Negative Bacteria'; DOI 10.3389/fmicb.2019.00646.

[724] H. Celia, I. Botos, X. Ni, T. Fox, N. De Val, R. Lloubes, J. Jiang, S. K. Buchanan, *Commun. Biol.* **2019**, *2*:358, 1-6; 'Cryo-EM structure of the bacterial Ton motor subcomplex ExbB-ExbD provides information on structure and stoichiometry'; DOI 10.1038/s42003-019-0604-2.
[725] N. G. Housden, J. T. S. Hopper, N. Lukoyanova, D. Rodriguez-Larrea, J. A. Wojdyla, A. Klein, R. Kaminska, H. Bayley, H. R. Saibil, C. V. Robinson, C. Kleanthous, *Science* **2013**, *340*(6140), 1570-1574; 'Intrinsically Disordered Protein Threads Through the Bacterial Outer-Membrane Porin OmpF'; DOI 10.1126/science.12378.
[726] C. Sharp, J. Bray, N. G. Housden, M. C. J. Maiden, C. Kleanthous, *PLoS Comput. Biol.* **2017**, *13*(7):e1005652, 1-24; 'Diversity and distribution of nuclease bacteriocins in bacterial genomes revealed using Hidden Markov Models'; DOI 10.1371/journal.pcbi.1005652.
[727] D. Walker, K. Mosbahi, M. Vankemmelbeke, R. James, C. Kleanthous, *J. Biol. Chem.* **2007**, *282*(43), 31389-31397; 'The Role of Electrostatics in Colicin Nuclease Domain Translocation into Bacterial Cells'; DOI 10.1074/jbc.M705883200.
[728] S. Langklotz, U. Baumann, F. Narberhaus, *Biochim. Biophys. Acta, Mol. Cell Res.* **2012**, *1823*(1), 40-48; 'Structure and function of the bacterial AAA protease FtsH'; DOI 10.1016/j.bbamcr.2011.08.015.
[729] G. D. Mawla, S. M. Kamal, L.-Y. Cao, P. Purhonen, H. Hebert, R. T. Sauer, T. A. Baker, U. Römling, *J. Biol. Chem.* **2024**, *300*(2):105622, 1-18; 'The membrane-cytoplasmic linker defines activity of FtsH proteases in *Pseudomonas aeruginosa* clone C'; DOI 10.1016/j.jbc.2023.105622.
[730] M. Vankemmelbeke, B. Healy, G. R. Moore, C. Kleanthous, C. N. Penfold, R. James, *J. Bacteriol.* **2005**, *187*(14), 4900-4907; 'Rapid Detection of Colicin E9-Induced DNA Damage Using *Escherichia coli* Cells Carrying SOS Promoter-*lux* Fusions'; DOI 10.1128/jb.187.14.4900-4907.2005.
[731] D. Walker, M. Rolfe, A. Thompson, G. R. Moore, R. James, J. C. D. Hinton, C. Kleanthous, *J. Bacteriol.* **2004**, *186*(3), 866-869; 'Transcriptional Profiling of Colicin-Induced Cell Death of *Escherichia coli* MG1655 Identifies Potential Mechanisms by Which Bacteriocins Promote Bacterial Diversity'; DOI 10.1128/jb.186.3.866-869.2004.
[732] I. Atanaskovic, C. Sharp, C. Press, R. Kaminska, C. Kleanthous, *MBio* **2022**, *13*(2):e03396-21, 1-15; 'Bacterial Competition Systems Share a Domain Required for Inner Membrane Transport of the Bacteriocin Pyocin G from *Pseudomonas aeruginosa*'; DOI 10.1128/mbio.03396-21.
[733] R. Wallis, G. R. Moore, R. James, C. Kleanthous, *Biochemistry* **1995**, *34*(42), 13743-13750; 'Protein-Protein Interactions in Colicin E9 DNase-Immunity Protein Complexes. 1. Diffusion-Controlled Association and Femtomolar Binding for the Cognate Complex'; DOI 10.1021/bi00042a004.
[734] R. Wallis, K.-Y. Leung, A. J. Pommer, H. Videler, G. R. Moore, R. James, C. Kleanthous, *Biochemistry* **1995**, *34*(42), 13751-13759; 'Protein-Protein Interactions in Colicin E9 DNase-Immunity Protein Complexes. 2. Cognate and Noncognate Interactions That Span the Millilmolar to Femptomolar Affinity Range'; DOI 10.1021/bi00042a005.
[735] K.-C. Hsia, K.-F. Chak, P.-H. Liang, Y.-S. Cheng, W.-Y. Ku, H. S. Yuan, *Structure* **2004**, *12*(2), 205-214; 'DNA Binding and Degradation by the HNH Protein ColE7'; DOI 10.1016/j.str.2004.01.004.
[736] M. J. Maté, C. Kleanthous, *J. Biol. Chem.* **2004**, *279*(33), 34763-34769; 'Structure-based analysis of the metal-dependent mechanism of H-N-H endonucleases'; DOI 10.1074/jbc.M403719200.
[737] E. Krissinel, K. Henrick, *J. Mol. Biol.* **2007**, *372*(3), 774-797; 'Inference of Macromolecular Assemblies from Crystalline State'; DOI 10.1016/j.jmb.2007.05.022.
[738] D. A. Shub, H. Goodrich-Blair, S. R. Eddy, *Trends Biochem. Sci.* **1994**, *19*(10), 402-404; 'Amino acid sequence motif of group I intron endonucleases is conserved in open reading frames of group II introns'; DOI 10.1016/0968-0004(94)90086-8.
[739] J. Jablonska, D. Matelska, K. Steczkiewicz, K. Ginalski, *Nucleic Acids Res.* **2017**, *45*(20), 11479-11494; 'Systematic classification of the His-Me finger superfamily'; DOI 10.1093/nar/gkx924.
[740] L. G. Doudeva, H. Huang, K. C. Hsia, Z. Shi, C. L. Li, Y. Shen, Y. S. Cheng, H. S. Yuan, *Protein Sci.* **2006**, *15*(2), 269-280; 'Crystal structural analysis and metal-dependent stability and activity studies of the ColE7 endonuclease domain in complex with DNA/Zn^{2+} or inhibitor/Ni^{2+}'; DOI 10.1110/ps.051903406.
[741] D. C. Walker, T. Georgiou, A. J. Pommer, D. Walker, G. R. Moore, C. Kleanthous, R. James, *Nucleic Acids Res.* **2002**, *30*(14), 3225-3234; 'Mutagenic scan of the H-N-H motif of colicin E9: implications for the mechanistic enzymology of colicins, homing enzymes and apoptotic endonucleases'; DOI 10.1093/nar/gkf420.
[742] K. S. Jakes, N. D. Zinder, *Proc. Natl. Acad. Sci. U.S.A.* **1974**, *71*(9), 3380-3384; 'Highly Purified Colicin E3 Contains Immunity Protein'; DOI 10.1073/pnas.71.9.3380.
[743] A. J. Pommer, R. Wallis, G. R. Moore, R. James, C. Kleanthous, *Biochem. J.* **1998**, *334*(2), 387-392; 'Enzymological characterization of the nuclease domain from the bacterial toxin colicin E9 from *Escherichia coli*'; DOI 10.1042/bj3340387.
[744] B. Malm, *FEBS Lett.* **1984**, *173*(2), 399-402; 'Chemical modification of Cys-374 of actin interferes with the formation of the profilactin complex'; DOI 10.1016/0014-5793(84)80813-3.
[745] R. Zhang, C. Chen, Z. Sun, F. Tan, J. Zhuang, D. Tian, G. Tong, S. Yuan, *J. Virol.* **2012**, *86*(8), 4670-4681; 'Disulfide Linkages Mediating Nucleocapsid Protein Dimerization Are Not Required for Porcine Arterivirus Infectivity'; DOI 10.1128/jvi.06709-11.
[746] K. K. Phelps, R. A. Walker, *Biochemistry* **2000**, *39*(14), 3877-3885; 'NEM Tubulin Inhibits Microtubule Minus End Assembly by a Reversible Capping Mechanism'; DOI 10.1021/bi992200x.
[747] B. Miroux, J. E. Walker, *J. Mol. Biol.* **1996**, *260*(3), 289-298; 'Over-production of Proteins in *Escherichia coli*: Mutant Hosts that Allow Synthesis of some Membrane Proteins and Globular Proteins at High Levels'; DOI 10.1006/jmbi.1996.0399.
[748] X. Zhang, F. W. Studier, *J. Mol. Biol.* **1997**, *269*(1), 10-27; 'Mechanism of Inhibition of Bacteriophage T7 RNA Polymerase by T7 Lysozyme'; DOI 10.1006/jmbi.1997.1016.
[749] C. Yanisch-Perron, J. Vieira, J. Messing, *Gene* **1985**, *33*(1), 103-119; 'Improved M13 phage cloning vectors and host strains: nucleotide sequences of the M13mpl8 and pUC19 vectors'; DOI 10.1016/0378-1119(85)90120-9.

[750] Y. Zhang, K.-Y. Park, K. F. Suazo, M. D. Distefano, *Chem. Soc. Rev.* **2018**, *47*(24), 9106-9136; 'Recent progress in enzymatic protein labelling techniques and their applications'; DOI 10.1039/c8cs00537k.
[751] K. Renault, J. W. Fredy, P.-Y. Renard, C. Sabot, *Bioconjugate Chem.* **2018**, *29*(8), 2497-2513; 'Covalent Modification of Biomolecules through Maleimide-Based Labeling Strategies'; DOI 10.1021/acs.bioconjchem.8b00252.
[752] J. W. Dubendorf, F. W. Studier, *J. Mol. Biol.* **1991**, *219*(1), 45-59; 'Controlling Basal Expression in an Inducible T7 Expression System by Blocking the Target T7 Promoter with *lac* Repressor'; DOI 10.1016/0022-2836(91)90856-2.
[753] A. Kuzminov, F. W. Stahl, *J. Bacteriol.* **1997**, *179*(3), 880-888; 'Stability of Linear DNA in *recA* Mutant *Escherichia coli* Cells Reflects Ongoing Chromosomal DNA Degradation'; DOI 10.1128/jb.179.3.880-888.1997.
[754] S. G. Grant, J. Jessee, F. R. Bloom, D. Hanahan, *Proc. Natl. Acad. Sci. U.S.A.* **1990**, *87*(12), 4645-4649; 'Differential plasmid rescue from transgenic mouse DNAs into *Escherichia coli* methylation-restriction mutants'; DOI 10.1073/pnas.87.12.4645.
[755] T. Horii, T. Ogawa, T. Nakatani, T. Hase, H. Matsubara, H. Ogawa, *Cell* **1981**, *27*(3), 515-522; 'Regulation of SOS Functions: Purification of *E. coli* LexA Protein and Determination of Its Specific Site Cleaved by the RecA Protein'; DOI 10.1016/0092-8674(81)90393-7.
[756] A. Abdi-Ali, E. A. Worobec, A. Deezagi, F. Malekzadeh, *Can. J. Microbiol.* **2004**, *50*(5), 375-381; 'Cytotoxic effects of pyocin S2 produced by *Pseudomonas aeruginosa* on the growth of three human cell lines'; DOI 10.1139/w04-019.
[757] C. K. Stover, X. Q. Pham, A. L. Erwin, S. D. Mizoguchi, P. Warrener, M. J. Hickey, F. S. L. Brinkman, W. O. Hufnagle, D. J. Kowalik, M. Lagrou, R. L. Garber, L. Goltry, E. Tolentino, S. Westbrock-Wadman, Y. Yuan, L. L. Brody, S. N. Coulter, K. R. Folger, A. Kas, K. Larbig, R. Lim, K. Smith, D. Spencer, G. K.-S. Wong, Z. Wu, I. T. Paulsenk, J. Reizer, M. H. Saier, R. E. W. Hancock, S. Lory, M. V. Olson, *Nature* **2000**, *406*(6799), 959-964; 'Complete genome sequence of *Pseudomonas aeruginosa* PAO1, an opportunistic pathogen'; DOI 10.1038/35023079.
[758] J. Penterman, P. K. Singh, G. C. Walker, *J. Bacteriol.* **2014**, *196*(18), 3351-3359; 'Biological Cost of Pyocin Production During the SOS Response in *Pseudomonas aeruginosa*'; DOI 10.1128/jb.01889-14.
[759] H. M. Behrens, Doctoral Thesis, 'How the protein antibiotic pyocin S5 kills *Pseudomonas aeruginosa*', University of Oxford (Oxford, England), **2019**; https://ora.ox.ac.uk/objects/uuid:8c00e14e-1703-4a36-b4ae-d685bf04dda1/files/m7104332c82ebd2ebeb7508f3d64ee260.
[760] P. White, Doctoral Thesis, 'Bacterial protein import mediated by an iron transporter', University of Oxford (Oxford, England), **2017**; https://ora.ox.ac.uk/objects/uuid:20298bb4-0998-4dad-9dfa-dd9e52854dec/files/m2f8b416c2a2fc0aceb64e773fe86c596.
[761] M. Kazazic, J. Nissen-Meyer, G. Fimland, *Microbiology* **2002**, *148*(7), 2019-2027; 'Mutational analysis of the role of charged residues in target-cell binding, potency and specificity of the pediocin-like bacteriocin sakacin P'; DOI 10.1099/00221287-148-7-2019.
[762] P. P. Kandel, D. A. Baltrus, K. L. Hockett, *J. Bacteriol.* **2020**, *202*(13):e00142-20, 1-6; '*Pseudomonas* Can Survive Tailocin Killing via Persistence-Like and Heterogenous Resistance Mechanisms'; DOI 10.1128/jb.00142-20.
[763] D. Sambandan, D. N. Dao, B. C. Weinrick, C. Vilchèze, S. S. Gurcha, A. Ojha, L. Kremer, G. S. Besra, G. F. Hatfull, W. R. Jacobs Jr, *MBio* **2013**, *4*(3):e00222-13, 1-10; 'Keto-Mycolic Acid-Dependent Pellicle Formation Confers Tolerance to Drug-Sensitive *Mycobacterium tuberculosis*'; DOI 10.1128/mbio.00222-13.
[764] G. Herrmann, L. Yang, H. Wu, Z. Song, H. Wang, N. Høiby, M. Ulrich, S. Molin, J. Riethmüller, G. Döring, *J. Infect. Dis.* **2010**, *202*(10), 1585-1592; 'Colistin-Tobramycin Combinations Are Superior to Monotherapy Concerning the Killing of Biofilm *Pseudomonas aeruginosa*'; DOI 10.1086/656788.
[765] M. Tré-Hardy, C. Nagant, N. El Manssouri, F. Vanderbist, H. Traore, M. Vaneechoutte, J.-P. Dehaye, *Antimicrob. Agents Chemother.* **2010**, *54*(10), 4409-4415; 'Efficacy of the Combination of Tobramycin and a Macrolide in an *In Vitro Pseudomonas aeruginosa* Mature Biofilm Model'; DOI 10.1128/aac.00372-10.
[766] P. Sharma, M. Yadav, *J. Appl. Biol. Biotechnol.* **2023**, *11*(1), 232-243; 'Enhancing antibacterial properties of bacteriocins using combination therapy'; DOI 10.7324/JABB.2023.110206.
[767] S. Upatissa, W. Mun, R. J. Mitchell, *Microbiol. Spectr.* **2023**, *11*(3):e00173-23, 1-6; 'Pairing Colicins B and E5 with *Bdellovibrio bacteriovorus* To Eradicate Carbapenem- and Colistin-Resistant Strains of *Escherichia coli*'; DOI 10.1128/spectrum.00173-23.
[768] A. Martin, M. J. Bland, H. Rodriguez-Villalobos, J.-L. Gala, P. Gabant, *Microb. Drug Resist.* **2023**, *29*(5), 165-174; 'Promising antimicrobial activity and synergy of bacteriocins against *Mycobacterium tuberculosis*'; DOI 10.1089/mdr.2021.0429.
[769] C. Aguilar-Pérez, B. Gracia, L. Rodrigues, A. Vitoria, R. Cebrián, N. Deboosère, O.-r. Song, P. Brodin, M. Maqueda, J. A. Aínsa, *Antimicrob. Agents Chemother.* **2018**, *62*(9):e00359-18, 1-13; 'Synergy between Circular Bacteriocin AS-48 and Ethambutol against *Mycobacterium tuberculosis*'; DOI 10.1128/aac. 00359-18.
[770] S. L. Weaver, E. Casamassima, A. E. Nguyen, D. A. Baltrus, *bioRxiv* **2023**, 1-35; 'Broad intraspecies killing activity in *Pseudomonas syringae* due to the combinatorial action of LPS-interacting bacteriocins'; DOI 10.1101/2023.09.27.559845.
[771] J. Du, S. Meile, J. Baggenstos, T. Jäggi, P. Piffaretti, L. Hunold, C. I. Matter, L. Leitner, T. M. Kessler, M. J. Loessner, S. Kilcher, M. Dunne, *Nat. Commun.* **2023**, *14*(1):4337, 1-10; 'Enhancing bacteriophage therapeutics through in situ production and release of heterologous antimicrobial effectors'; DOI 10.1038/s41467-023-39612-0.
[772] H. Turano, F. Gomes, G. A. Barros-Carvalho, R. Lopes, L. Cerdeira, L. E. S. Netto, A. C. Gales, N. Lincopan, *Antimicrob. Agents Chemother.* **2017**, *61*(5):e00100-17, 1-4; 'Tn*6350*, a Novel Transposon Carrying Pyocin S8 Genes Encoding a Bacteriocin with Activity Against Carbapenemase-Producing *Pseudomonas aeruginosa*'; DOI 10.1128/aac.00100-17.
[773] E. Schäfer, M. Malecki, C. J. Tellez-Castillo, N. Pfennigwerth, L. Marlinghaus, P. G. Higgins, F. Mattner, A. F. Wendel, *Antimicrob. Resist. Infect. Control* **2019**, *8*:208, 1-7; 'Molecular surveillance of carbapenemase-producing *Pseudomonas aeruginosa* at three medical centres in Cologne, Germany'; DOI 10.1186/s13756-019-0665-5.

[774] C. Hardegen, S. Messler, B. Henrich, K. Pfeffer, J. Würthner, C. R. MacKenzie, *Ann. Clin. Microbiol. Antimicrob.* **2010**, *9*:5, 1-7; 'A set of novel multiplex Taqman real-time PCRs for the detection of diarrhoeagenic *Escherichia coli* and its use in determining the prevalence of EPEC and EAEC in a university hospital'; DOI 10.1186/1476-0711-9-5.
[775] I. J. Schalk, C. Hennard, C. Dugave, K. Poole, M. A. Abdallah, F. Pattus, *Mol. Microbiol.* **2001**, *39*(2), 351-361; 'Iron-free pyoverdin binds to its outer membrane receptor FpvA in *Pseudomonas aeruginosa*: a new mechanism for membrane iron transport'; DOI 10.1046/j.1365-2958.2001.02207.x.
[776] J. Bodilis, B. Ghysels, J. Osayande, S. Matthijs, J. P. Pirnay, S. Denayer, D. De Vos, P. Cornelis, *Environ. Microbiol.* **2009**, *11*(8), 2123-2135; 'Distribution and evolution of ferripyoverdine receptors in *Pseudomonas aeruginosa*'; DOI 10.1111/j.1462-2920.2009.01932.x.
[777] R. Niehus, A. Picot, N. M. Oliveira, S. Mitri, K. R. Foster, *Evolution* **2017**, *71*(6), 1443-1455; 'The evolution of siderophore production as a competitive trait'; DOI 10.1111/evo.13230.
[778] J.-M. Meyer, A. Neely, A. Stintzi, C. Georges, I. A. Holder, *Infect. Immun.* **1996**, *64*(2), 518-523; 'Pyoverdin Is Essential for Virulence of *Pseudomonas aeruginosa*'; DOI 10.1128/iai.64.2.518-523.1996.
[779] E. E. Smith, E. H. Sims, D. H. Spencer, R. Kaul, M. V. Olson, *J. Bacteriol.* **2005**, *187*(6), 2138-2147; 'Evidence for Diversifying Selection at the Pyoverdine Locus of *Pseudomonas aeruginosa*'; DOI 10.1128/jb.187.6.2138-2147.2005.
[780] R. D. Olson, R. Assaf, T. Brettin, N. Conrad, C. Cucinell, J. J. Davis, D. M. Dempsey, A. Dickerman, E. M. Dietrich, R. W. Kenyon, M. Kuscuoglu, E. J. Lefkowitz, J. Lu, D. Machi, C. Macken, C. Mao, A. Niewiadomska, M. Nguyen, G. J. Olsen, J. C. Overbeek, B. Parrello, V. Parrello, J. S. Porter, G. D. Pusch, M. Shukla, I. Singh, L. Stewart, G. Tan, C. Thomas, M. VanOeffelen, V. Vonstein, Z. S. Wallace, A. S. Warren, A. R. Wattam, F. Xia, H. Yoo, Y. Zhang, C. M. Zmasek, R. H. Scheuermann, R. L. Stevens, *Nucleic Acids Res.* **2023**, *51*(D1), D678-D689; 'Introducing the Bacterial and Viral Bioinformatics Resource Center (BV-BRC): a resource combining PATRIC, IRD and ViPR'; DOI 10.1093/nar/gkac1003.
[781] S. Chen, Y. Zhou, Y. Chen, J. Gu, *Bioinformatics* **2018**, *34*(17), i884-i890; 'fastp: an ultra-fast all-in-one FASTQ preprocessor'; DOI 10.1093/bioinformatics/bty560.
[782] R. R. Wick, L. M. Judd, C. L. Gorrie, K. E. Holt, *PLoS Comput. Biol.* **2017**, *13*(6):e1005595, 1-22; 'Unicycler: Resolving bacterial genome assemblies from short and long sequencing reads'; DOI 10.1371/journal.pcbi.1005595.
[783] The Galaxy Community, *Nucleic Acids Res.* **2022**, *50*(W1), W345-W351; 'The Galaxy platform for accessible, reproducible and collaborative biomedical analyses: 2022 update'; DOI 10.1093/nar/gkac247.
[784] O. Schwengers, L. Jelonek, M. A. Dieckmann, S. Beyvers, J. Blom, A. Goesmann, *Microb. Genom.* **2021**, *7*(11):000685, 1-13; 'Bakta: rapid and standardized annotation of bacterial genomes via alignment-free sequence identification'; DOI 10.1099/mgen.0.000685.
[785] T. Tatusova, M. DiCuccio, A. Badretdin, V. Chetvernin, E. P. Nawrocki, L. Zaslavsky, A. Lomsadze, K. D. Pruitt, M. Borodovsky, J. Ostell, *Nucleic Acids Res.* **2016**, *44*(14), 6614-6624; 'NCBI prokaryotic genome annotation pipeline'; DOI 10.1093/nar/gkw569.
[786] E. M. Gertz, Y.-K. Yu, R. Agarwala, A. A. Schäffer, S. F. Altschul, *BMC Biol.* **2006**, *4*:41, 1-14; 'Composition-based statistics and translated nucleotide searches: improving the TBLASTN module of BLAST'; DOI 10.1186/1741-7007-4-41.
[787] Y. Hao, J. D. King, S. Huszczynski, D. Kocíncová, J. S. Lam, *MBio* **2013**, *4*(1):e00631-12, 1-9; 'Five New Genes Are Important for Common Polysaccharide Antigen Biosynthesis in *Pseudomonas aeruginosa*'; DOI 10.1128/mbio.00631-12.
[788] S. F. Altschul, W. Gish, W. Miller, E. W. Myers, D. J. Lipman, *J. Mol. Biol.* **1990**, *215*(3), 403-410; 'Basic Local Alignment Search Tool'; DOI 10.1016/S0022-2836(05)80360-2.
[789] H. L. Rocchetta, L. L. Burrows, J. C. Pacan, J. S. Lam, *Mol. Microbiol.* **1998**, *28*(6), 1103-1119; 'Three rhamnosyltransferases responsible for assembly of the A-band D-rhamnan polysaccharide in *Pseudomonas aeruginosa*: a fourth transferase, WbpL, is required for the initiation of both A-band and B-band lipopolysaccharide synthesis'; DOI 10.1046/j.1365-2958.1998.00871.x.
[790] S. Wang, Y. Hao, J. S. Lam, J. Z. Vlahakis, W. A. Szarek, A. Vinnikova, V. V. Veselovsky, I. Brockhausen, *J. Bacteriol.* **2015**, *197*(12), 2012-2019; 'Biosynthesis of the Common Polysaccharide Antigen of *Pseudomonas aeruginosa* PAO1: Characterization and Role of GDP-D-Rhamnose: GlcNAc/GalNAc-Diphosphate-Lipid α1,3-D-Rhamnosyltransferase WbpZ'; DOI 10.1128/JB.02590-14.
[791] H. L. Rocchetta, J. S. Lam, *J. Bacteriol.* **1997**, *179*(15), 4713-4724; 'Identification and Functional Characterization of an ABC Transport System Involved in Polysaccharide Export of A-Band Lipopolysaccharide in *Pseudomonas aeruginosa*'; DOI 10.1128/jb.179.15.4713-4724.1997.
[792] S. W. Thrane, V. L. Taylor, O. Lund, J. S. Lam, L. Jelsbak, *J. Clin. Microbiol.* **2016**, *54*(7), 1782-1788; 'Application of Whole-Genome Sequencing Data for O-Specific Antigen Analysis and *In Silico* Serotyping of *Pseudomonas aeruginosa* Isolates'; DOI 10.1128/jcm.00349-16.
[793] Sandra Wingaard Thrane, Center for Genomic Epidemiology: *Pseudomonas aeruginosa* serotyper 1.0 (PAst), **2017**, https://cge.food.dtu.dk/services/PAst/, accessed 02/02/2024.
[794] J. D. King, D. Kocíncová, E. L. Westman, J. S. Lam, *Innate Immun.* **2009**, *15*(5), 261-312; 'Lipopolysaccharide biosynthesis in *Pseudomonas aeruginosa*'; DOI 10.1177/1753425909106436.
[795] L. L. Burrows, H. L. Rocchetta, J. S. Lam, **2000**, '*Assembly Pathways for Biosynthesis of A-Band and B-Band Lipopolysaccharide in Pseudomonas aeruginosa*' in *Glycomicrobiology*, 127-143, Springer, Boston, Massachusetts, USA, DOI 10.1007/0-306-46821-2_5.
[796] C. Sharp, C. Boinett, A. Cain, N. G. Housden, S. Kumar, K. Turner, J. Parkhill, C. Kleanthous, *J. Bacteriol.* **2019**, *201*(4):e00545-18, 1-12; 'O-Antigen-Dependent Colicin Insensitivity of Uropathogenic *Escherichia coli*'; DOI 10.1128/jb.00545-18.

[797] K. Murphy, A. J. Park, Y. Hao, D. Brewer, J. S. Lam, C. M. Khursigara, *J. Bacteriol.* **2014**, *196*(7), 1306-1317; 'Influence of O Polysaccharides on Biofilm Development and Outer Membrane Vesicle Biogenesis in *Pseudomonas aeruginosa* PAO1'; DOI 10.1128/jb.01463-13.
[798] S. A. Makin, T. J. Beveridge, *Microbiology* **1996**, *142*(2), 299-307; 'The influence of A-band and B-band lipopolysaccharide on the surface characteristics and adhesion of *Pseudomonas aeruginosa* to surfaces'; DOI 10.1099/13500872-142-2-299.
[799] M. Rivera, T. R. Chivers, J. S. Lam, E. J. McGroarty, *J. Bacteriol.* **1992**, *174*(7), 2407-2411; 'Common Antigen Lipopolysaccharide from *Pseudomonas aeruginosa* AK1401 as a Receptor for Bacteriophage A7'; DOI 10.1128/jb.174.7.2407-2411.1992.
[800] M. Tognon, T. Köhler, B. G. Gdaniec, Y. Hao, J. S. Lam, M. Beaume, A. Luscher, A. Buckling, C. Van Delden, *ISME J.* **2017**, *11*(10), 2233-2243; 'Co-evolution with *Staphylococcus aureus* leads to lipopolysaccharide alterations in *Pseudomonas aeruginosa*'; DOI 10.1038/ismej.2017.83.
[801] C. Cigana, L. Curcurù, M. R. Leone, T. Ieranò, N. I. Lorè, I. Bianconi, A. Silipo, F. Cozzolino, R. Lanzetta, A. Molinaro, M. L. Bernardini, A. Bragonzi, *PLoS One* **2009**, *4*(12):e8439, 1-13; '*Pseudomonas aeruginosa* Exploits Lipid A and Muropeptides Modification as a Strategy to Lower Innate Immunity During Cystic Fibrosis Lung Infection'; DOI 10.1371/journal.pone.0008439.
[802] J. C. Lapenda, P. A. Silva, M. C. Vicalvi, K. X. F. R. Sena, S. C. Nascimento, *World J. Microbiol. Biotechnol.* **2015**, *31*, 399-406; 'Antimicrobial activity of prodigiosin isolated from *Serratia marcescens* UFPEDA 398'; DOI 10.1007/s11274-014-1793-y.
[803] T. Gristwood, P. C. Fineran, L. Everson, G. P. C. Salmond, *Mol. Microbiol.* **2008**, *69*(2), 418-435; 'PigZ, a TetR/AcrR family repressor, modulates secondary metabolism via the expression of a putative four-component resistance-nodulation-cell-division efflux pump, ZrpADBC, in *Serratia* sp. ATCC 39006'; DOI 10.1111/j.1365-2958.2008.06291.x.
[804] S. Chen, X. Zhao, J. Chen, J. Chen, L. Kuznetsova, S. S. Wong, I. Ojima, *Bioconjugate Chem.* **2010**, *21*(5), 979-987; 'Mechanism-Based Tumor-Targeting Drug Delivery System. Validation of Efficient Vitamin Receptor-Mediated Endocytosis and Drug Release'; DOI 10.1021/bc9005656.
[805] M. Patra, T. C. Johnstone, K. Suntharalingam, S. J. Lippard, *Angew. Chem.* **2016**, *128*(7), 2596-2600; 'A Potent Glucose–Platinum Conjugate Exploits Glucose Transporters and Preferentially Accumulates in Cancer Cells'; DOI 10.1002/ange.201510551.
[806] M. Patra, T. C. Johnstone, K. Suntharalingam, S. J. Lippard, *Angew. Chem. Int. Ed.* **2016**, *55*(7), 2550-2554; 'A Potent Glucose–Platinum Conjugate Exploits Glucose Transporters and Preferentially Accumulates in Cancer Cells'; DOI 10.1002/anie.201510551.
[807] E. C. Calvaresi, P. J. Hergenrother, *Chem. Sci.* **2013**, *4*(6), 2319-2333; 'Glucose conjugation for the specific targeting and treatment of cancer'; DOI 10.1039/c3sc22205e.
[808] L. Wendt, *J. Bacteriol.* **1970**, *104*(3), 1236-1241; 'Mechanism of Colicin Action: Early Events'; DOI 10.1128/jb.104.3.1236-1241.1970.
[809] A. J. Hedges, *J. Theoret. Biol.* **1966**, *11*(3), 383-410; 'An Examination of Single-Hit and Multi-Hit Hypotheses in Relation to the Possible Kinetics of Colicin Adsorption'; DOI 10.1016/0022-5193(66)90100-7.
[810] K. Tanigaki, T. Sato, Y. Tanaka, T. Ochi, A. Nishikawa, K. Nagai, H. Kawashima, S. Ohkuma, *FEBS Lett.* **2002**, *524*(1-3), 37-42; 'BE-18591 as a new H^+/Cl^- symport ionophore that inhibits immunoproliferation and gastritis'; DOI 10.1016/S0014-5793(02)02996-4.
[811] C. Yamamoto, H. Takemoto, K. Kuno, D. Yamamoto, A. Tsubura, K. Kamata, H. Hirata, A. Yamamoto, H. Kano, T. Seki, K. Inoue, *Hepatology* **1999**, *30*(4), 894-902; 'Cycloprodigiosin Hydrochloride, a New H^+/Cl^- Symporter, Induces Apoptosis in Human and Rat Hepatocellular Cancer Cell Lines *In Vitro* and Inhibits the Growth of Hepatocellular Carcinoma Xenografts in Nude Mice'; DOI 10.1002/hep.510300417.
[812] D. Yamamoto, Y. Kiyozuka, Y. Uemura, C. Yamamoto, H. Takemoto, H. Hirata, K. Tanaka, K. Hioki, A. Tsubura, *J. Cancer Res. Clin. Oncol.* **2000**, *126*, 191-197; 'Cycloprodigiosin hydrochloride, a H^+/Cl^- symporter, induces apoptosis in human breast cancer cell lines'; DOI 10.1007/s004320050032.
[813] V. Soto-Cerrato, E. Llagostera, B. Montaner, G. L. Scheffer, R. Perez-Tomas, *Biochem. Pharmacol.* **2004**, *68*(7), 1345-1352; 'Mitochondria-mediated apoptosis operating irrespective of multidrug resistance in breast cancer cells by the anticancer agent prodigiosin'; DOI 10.1016/j.bcp.2004.05.056.
[814] T. Danevčič, M. Borić Vezjak, M. Zorec, D. Stopar, *PLoS One* **2016**, *11*(9):e0162412, 1-13; 'Prodigiosin – A multifaceted *Escherichia coli* antimicrobial agent'; DOI 10.1371/journal.pone.0162412.
[815] Z. Wang, D. Teng, R. Mao, Y. Hao, N. Yang, X. Wang, J. Wang, *Commun. Biol.* **2023**, *6*(1):1170, 1-15; 'A cleavable chimeric peptide with targeting and killing domains enhances LPS neutralization and antibacterial properties against multi-drug resistant *E. coli*'; DOI 10.1038/s42003-023-05528-0.
[816] W. Neumann, E. M. Nolan, *J. Biol. Inorg. Chem.* **2018**, *23*(7), 1025-1036; 'Evaluation of a reducible disulfide linker for siderophore-mediated delivery of antibiotics'; DOI 10.1007/s00775-018-1588-y.
[817] Y. Xue, H. Bai, B. Peng, B. Fang, J. Baell, L. Li, W. Huang, N. H. Voelcker, *Chemical Society Reviews* **2021**, *50*(8), 4872-4931; 'Stimulus-cleavable chemistry in the field of controlled drug delivery'; DOI 10.1039/d0cs01061h.
[818] C. Zhu, E. K. Schneider, J. Wang, K. Kempe, P. Wilson, T. Velkov, J. Li, T. P. Davis, M. R. Whittaker, D. M. Haddleton, *J. Control. Release* **2017**, *259*, 83-91; 'A traceless reversible polymeric colistin prodrug to combat multidrug-resistant (MDR) gram-negative bacteria'; DOI 10.1016/j.jconrel.2017.02.005.
[819] J. S. Lam, E. M. Anderson, Y. Hao, **2014**, '*LPS Quantitation Procedures*' in *Pseudomonas Methods and Protocols. Methods in Molecular Biology*, 375-402, Humana New York, New York, USA.; ISBN 978-1493904723, DOI 10.1007/978-1-4939-0473-0_31.
[820] T. R. de Kievit, J. S. Lam, *J. Bacteriol.* **1994**, *176*(23), 7129-7139; 'Monoclonal Antibodies That Distinguish Inner Core, Outer Core, and Lipid A Regions of *Pseudomonas aeruginosa* Lipopolysaccharide'; DOI 10.1128/jb.176.23.7129-7139.1994.

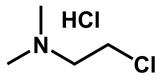
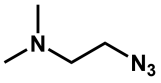
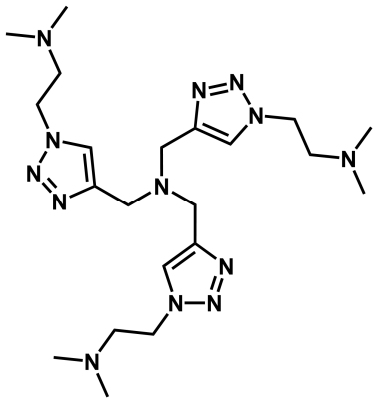
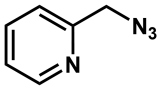
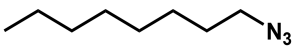
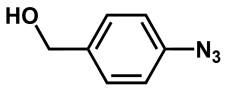
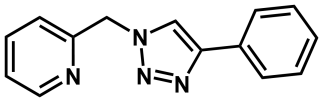
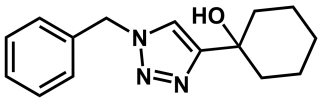
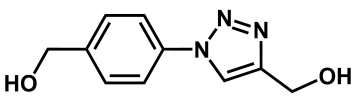
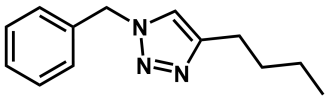
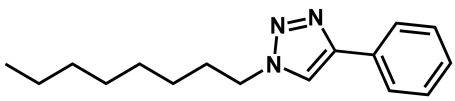
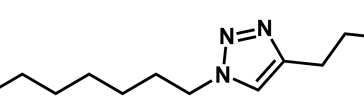
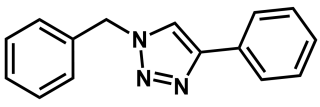
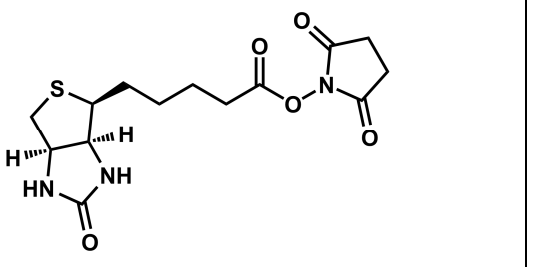
[821] L. Meng, Z. Song, A. Liu, U. Dahmen, X. Yang, H. Fang, *Front. Immunol.* **2021**, *12*:681810, 1-12; 'Effects of Lipopolysaccharide-Binding Protein (LBP) Single Nucleotide Polymorphism (SNP) in Infections, Inflammatory Diseases, Metabolic Disorders and Cancers'; DOI 10.3389/fimmu.2021.681810.
[822] J. Greenfield, X. Shang, H. Luo, Y. Zhou, R. D. Heselpoth, D. C. Nelson, O. Herzberg, *Sci. Rep.* **2019**, *9*(1):7349, 1-11; 'Structure and tailspike glycosidase machinery of ORF212 from *E. coli* O157: H7 phage CBA120 (TSP3)'; DOI 10.1038/s41598-019-43748-9.
[823] T. Olszak, M. M. Shneider, A. Latka, B. Maciejewska, C. Browning, L. V. Sycheva, A. Cornelissen, K. Danis-Wlodarczyk, S. N. Senchenkova, A. S. Shashkov, G. Gula, M. Arabski, S. Wasik, K. A. Miroshnikov, R. Lavigne, P. G. Leiman, Y. A. Knirel, Z. Drulis-Kawa, *Sci. Rep.* **2017**, *7*(1):16302, 1-14; 'The O-specific polysaccharide lyase from the phage LKA1 tailspike reduces *Pseudomonas* virulence'; DOI 10.1038/s41598-017-16411-4.
[824] J. A. Wojdyla, S. J. Fleishman, D. Baker, C. Kleanthous, *J. Mol. Biol.* **2012**, *417*(1-2), 79-94; 'Structure of the Ultra-High-Affinity Colicin E2 DNase–Im2 Complex'; DOI 10.1016/j.jmb.2012.01.019.
[825] T.-P. Ko, C.-C. Liao, W.-Y. Ku, K.-F. Chak, H. S. Yuan, *Structure* **1999**, *7*(1), 91-102; 'The crystal structure of the DNase domain of colicin E7 in complex with its inhibitor Im7 protein'; DOI 10.1016/s0969-2126(99)80012-4.
[826] R. Aasland, C. Abrams, C. Ampe, L. J. Ball, M. T. Bedford, G. Cesareni, M. Gimona, J. H. Hurley, T. Jarchau, V.-P. Lehto, M. A. Lemmon, R. Linding, B. J. Mayer, M. Nagai, M. Sudol, U. Walter, S. J. Winder, *FEBS Lett.* **2002**, *513*(1), 141-144; 'Normalization of nomenclature for peptide motifs as ligands of modular protein domains'; DOI 10.1016/S0014-5793(01)03295-1.
[827] Š. Paškevičius, V. Dapkutė, A. Misiūnas, M. Balzaris, P. Thommes, A. Sattar, Y. Gleba, A. Ražanskienė, *Sci. Rep.* **2022**, *12*(1):5865, 1-14; 'Chimeric bacteriocin S5-PmnH engineered by domain swapping efficiently controls *Pseudomonas aeruginosa* infection in murine keratitis and lung models'; DOI 10.1038/s41598-022-09865-8.
[828] R. D. Heselpoth, C. W. Euler, R. Schuch, V. A. Fischetti, *Antimicrob. Agents Chemother.* **2019**, *63*(6):e00342-19, 1-14; 'Lysocins: Bioengineered Antimicrobials That Deliver Lysins across the Outer Membrane of Gram-Negative Bacteria'; DOI 10.1128/aac.00342-19.
[829] P. Lukacik, T. J. Barnard, P. W. Keller, K. S. Chaturvedi, N. Seddiki, J. W. Fairman, N. Noinaj, T. L. Kirby, J. P. Henderson, A. C. Steven, B. J. Hinnebusch, S. K. Buchanan, *Proc. Natl. Acad. Sci. U.S.A.* **2012**, *109*(25), 9857-9862; 'Structural engineering of a phage lysin that targets Gram-negative pathogens'; DOI 10.1073/pnas.1203472109.
[830] M. G. K. Ghequire, L. Kemland, E. Anoz-Carbonell, S. K. Buchanan, R. De Mot, *MBio* **2017**, *8*(1):e01961-16, 1-12; 'A Natural Chimeric *Pseudomonas* Bacteriocin with Novel Pore-Forming Activity Parasitizes the Ferrichrome Transporter'; DOI 10.1128/mbio.01961-16.
[831] T. Lugtenburg, A. Gran-Scheuch, I. Drienovská, *Protein Eng. Des. Sel.* **2023**, *36*:gzad003, 1-10; 'Non-canonical amino acids as a tool for the thermal stabilization of enzymes'; DOI 10.1093/protein/gzad003.
[832] T. S. Young, I. Ahmad, J. A. Yin, P. G. Schultz, *J. Mol. Biol.* **2010**, *395*(2), 361-374; 'An Enhanced System for Unnatural Amino Acid Mutagenesis in *E. coli*'; DOI 10.1016/j.jmb.2009.10.030.
[833] H. Xiao, A. Chatterjee, S. C. Sei-hyun, K. M. Bajjuri, S. C. Sinha, P. G. Schultz, *Angew. Chem. Int. Ed.* **2013**, *52*(52), 14080-14083; 'Genetic Incorporation of Multiple Unnatural Amino Acids into Proteins in Mammalian Cells'; DOI 10.1002/anie.201308137.
[834] H. Xiao, A. Chatterjee, S. C. Sei-hyun, K. M. Bajjuri, S. C. Sinha, P. G. Schultz, *Angew. Chem.* **2013**, *125*(52), 14330-14333; 'Genetic Incorporation of Multiple Unnatural Amino Acids into Proteins in Mammalian Cells'; DOI 10.1002/ange.201308137.
[835] A. Klein, J. A. Wojdyla, A. Joshi, I. Josts, L. C. McCaughey, N. G. Housden, R. Kaminska, O. Byron, D. Walker, C. Kleanthous, *Biochem. J.* **2016**, *473*(18), 2799-2812; 'Structural and biophysical analysis of nuclease protein antibiotics'; DOI 10.1042/BCJ20160544.
[836] A. W. Negash, B. A. Tsehai, *Int. J. Microbiol.* **2020**, *2020*(1):4374891, 1-7; 'Current Applications of Bacteriocin'; DOI 10.1155/2020/4374891.
[837] M. Redero, J. Aznar, A. I. Prieto, *J. Antimicrob. Chemother.* **2020**, *75*(8), 2188-2196; 'Antibacterial efficacy of R-type pyocins against *Pseudomonas aeruginosa* on biofilms and in a murine model of acute lung infection'; DOI 10.1093/jac/dkaa121.
[838] A. Six, K. Mosbahi, M. Barge, C. Kleanthous, T. Evans, D. Walker, *J. Antimicrob. Chemother.* **2021**, *76*(9), 2317-2324; 'Pyocin efficacy in a murine model of *Pseudomonas aeruginosa* sepsis'; DOI 10.1093/jac/dkab199.
[839] L. C. McCaughey, N. D. Ritchie, G. R. Douce, T. J. Evans, D. Walker, *Sci. Rep.* **2016**, *6*(1):30201, 1-8; 'Efficacy of species-specific protein antibiotics in a murine model of acute *Pseudomonas aeruginosa* lung infection'; DOI 10.1038/srep30201
[840] D. Walker, L. McCaughey, 'Pulmonary Administration of Pyocins for Treating Bacterial Respiratory Infections', World Patent WO 2016/046218 A1, 1-58, **2016**, https://patentimages.storage.googleapis.com/4b/53/34/375eafc09e3673/WO2016046218A1.pdf.
[841] D. Walker, L. McCaughey, 'Pulmonary Administration of Pyocins for Treating Bacterial Respiratory Infections', United States Patent US 2017/0240602 A1, 1-46, **2017**, https://patentimages.storage.googleapis.com/75/54/51/be575e8884e2bc/US20170240602A1.pdf.
[842] A. Alqahtani, L. Mena, D. Scholl, C. Kruczek, J. A. Colmer-Hamood, R. M. Jeter, A. N. Hamood, *Can. J. Microbiol.* **2021**, *67*(12), 919-932; 'Recombinant R2-pyocin cream is effective in treating *Pseudomonas aeruginosa*-infected wounds'; DOI 10.1139/cjm-2021-0207.
[843] G. Kurisu, S. D. Zakharov, M. V. Zhalnina, S. Bano, V. Y. Eroukova, T. I. Rokitskaya, Y. N. Antonenko, M. C. Wiener, W. A. Cramer, *Nat. Struct. Biol.* **2003**, *10*(11), 948-954; 'The structure of BtuB with bound colicin E3 R-domain implies a translocon'; DOI 10.1038/nsb997.
[844] V. G. H. Eijsink, S. Gåseidnes, T. V. Borchert, B. Van Den Burg, *Biomol. Eng.* **2005**, *22*(1-3), 21-30; 'Directed evolution of enzyme stability'; DOI 10.1016/j.bioeng.2004.12.003.
[845] C. Schmidt-Dannert, F. H. Arnold, *Trends Biotechnol.* **1999**, *17*(4), 135-136; 'Directed evolution of industrial enzymes'; DOI 10.1016/s0167-7799(98)01283-9.

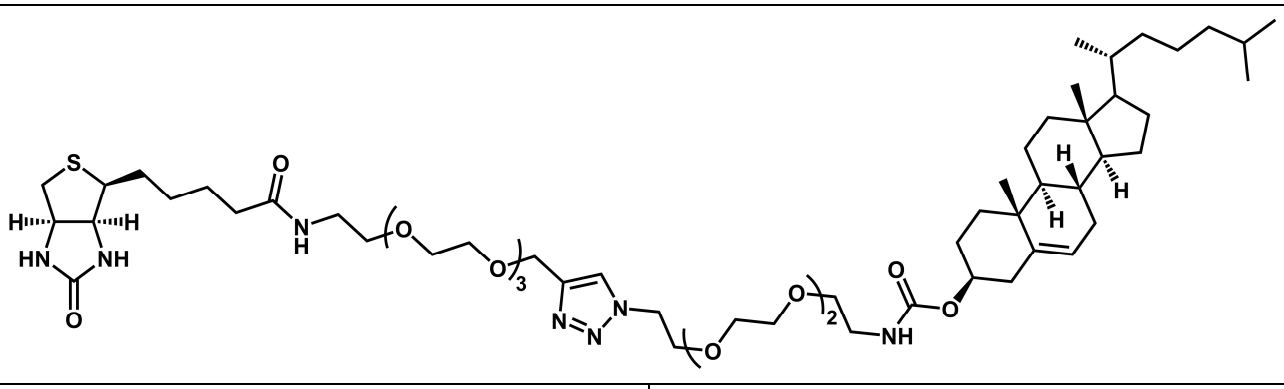
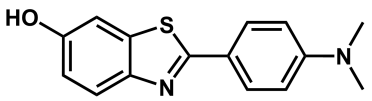
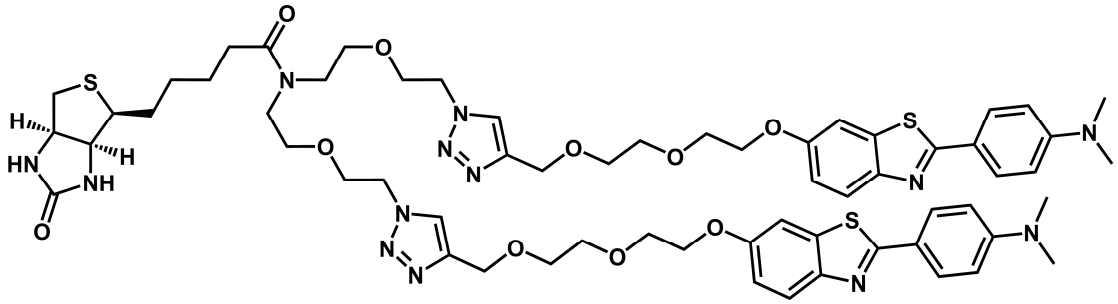
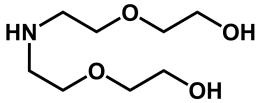
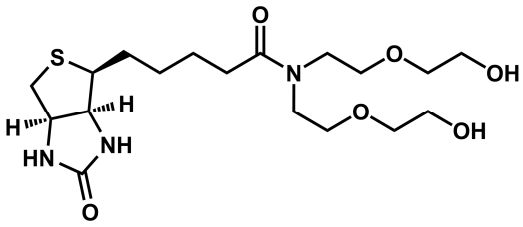
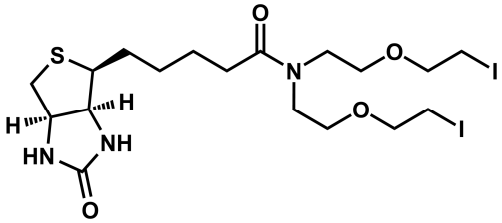
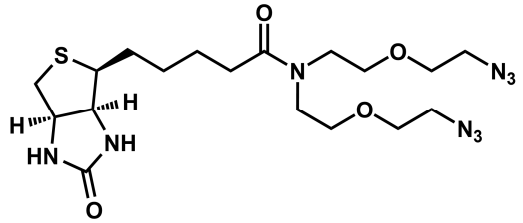
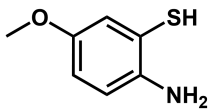
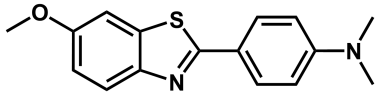
[846] M. Dunne, N. S. Prokhorov, M. J. Loessner, P. G. Leiman, *Curr. Opin. Biotechnol.* **2021**, *68*, 272-281; 'Reprogramming bacteriophage host range: design principles and strategies for engineering receptor binding proteins'; DOI 10.1016/j.copbio.2021.02.006.
[847] J. Liang, H. Zhang, Y. L. Tan, H. Zhao, E. L. Ang, *ACS Synth. Biol.* **2022**, *11*(2), 634-643; 'Directed Evolution of Replication-Competent Double-Stranded DNA Bacteriophage toward New Host Specificity'; DOI 10.1021/acssynbio.1c00319.
[848] T. Holtzman, R. Globus, S. Molshanski-Mor, A. Ben-Shem, I. Yosef, U. Qimron, *Sci. Rep.* **2020**, *10*(1):307, 1-8; 'A continuous evolution system for contracting the host range of bacteriophage T7'; DOI 10.1038/s41598-019-57221-0.
[849] M. Cebriá-Mendoza, R. Sanjuán, P. Domingo-Calap, *Antibiotics* **2019**, *8*(2):46, 1-9; 'Directed Evolution of a Mycobacteriophage'; DOI 10.3390/antibiotics8020046.
[850] W. Liu, R. Zhang, S. Huang, X. Li, W. Liu, J. Zhou, L. Zhu, Y. Song, C. Yang, *Langmuir* **2022**, *38*(26), 7929-7937; 'Quantification of Intracellular Proteins in Single Cells Based on Engineered Picoliter Droplets'; DOI 10.1021/acs.langmuir.2c00341.
[851] A. L. Calkins, Doctoral Thesis, 'Achieving Single-Molecule Tracking in Bacteria During Real-Time Environmental Perturbations', University of Michigan (Ann Arbor, Michigan, USA), **2023**; DOI 10.7302/7473; https://deepblue.lib.umich.edu/bitstream/handle/2027.42/176624/annalc_1.pdf?sequence=1&isAllowed=y.
[852] H. Kim, J. Ju, H. N. Lee, H. Chun, J. Seong, *Sensors* **2021**, *21*(3):795, 1-18; 'Genetically Encoded Biosensors Based on Fluorescent Proteins'; DOI 10.3390/s21030795.
[853] L. Jiang, Z. Xiong, Y. Song, Y. Lu, Y. Chen, J. S. Schultz, J. Li, J. Liao, *Sci. Rep.* **2019**, *9*(1):2050, 1-8; 'Protein–Protein Affinity Determination by Quantitative FRET Quenching'; DOI 10.1038/s41598-018-35535-9.
[854] T. Köhler, M. Michea-Hamzehpour, P. Plesiat, A.-L. Kahr, J.-C. Pechere, *Antimicrob. Agents Chemother.* **1997**, *41*(11), 2540-2543; 'Differential Selection of Multidrug Efflux Systems by Quinolones in *Pseudomonas aeruginosa*'; DOI 10.1128/aac.41.11.2540.
[855] A. Lamut, C. D. Cruz, Ž. Skok, M. Barančoková, N. Zidar, A. Zega, L. P. Mašič, J. Ilaš, P. Tammela, D. Kikelj, *Bioorg. Chem.* **2020**, *95*:103550, 1-13; 'Design, synthesis and biological evaluation of novel DNA gyrase inhibitors and their siderophore mimic conjugates'; DOI 10.1016/j.bioorg.2019.103550.
[856] M. Samir, M. Ramadan, M. H. Abdelrahman, M. A. Elbastawesy, H. M. Halby, M. Abdel-Aziz, G. E.-D. A. Abuo-Rahma, *Bioorg. Med. Chem.* **2022**, *73*:117004, 1-13; 'New potent ciprofloxacin-uracil conjugates as DNA gyrase and topoisomerase IV inhibitors against methicillin-resistant *Staphylococcus aureus*'; DOI 10.1016/j.bmc.2022.117004.
[857] J. Jumper, R. Evans, A. Pritzel, T. Green, M. Figurnov, O. Ronneberger, K. Tunyasuvunakool, R. Bates, A. Žídek, A. Potapenko, A. Bridgland, C. Meyer, S. A. A. Kohl, A. J. Ballard, A. Cowie, B. Romera-Paredes, S. Nikolov, R. Jain, J. Adler, T. Back, S. Petersen, D. Reiman, E. Clancy, M. Zielinski, M. Steinegger, M. Pacholska, T. Berghammer, S. Bodenstein, D. Silver, O. Vinyals, A. W. Senior, K. Kavukcuoglu, P. Kohli, D. Hassabis, *Nature* **2021**, *596*(7873), 583-589; 'Highly accurate protein structure prediction with AlphaFold'; DOI 10.1038/s41586-021-03819-2.
[858] M. Varadi, S. Anyango, M. Deshpande, S. Nair, C. Natassia, G. Yordanova, D. Yuan, O. Stroe, G. Wood, A. Laydon, A. Žídek, T. Green, K. Tunyasuvunakool, S. Petersen, J. Jumper, E. Clancy, R. Green, A. Vora, M. Lutfi, M. Figurnov, A. Cowie, N. Hobbs, P. Kohli, G. Kleywegt, E. Birney, D. Hassabis, S. Velankar, *Nucleic Acids Res.* **2022**, *50*(D1), D439-D444; 'AlphaFold Protein Structure Database: massively expanding the structural coverage of protein-sequence space with high-accuracy models'; DOI 10.1093/nar/gkab1061.
[859] M. Varadi, D. Bertoni, P. Magana, U. Paramval, I. Pidruchna, M. Radhakrishnan, M. Tsenkov, S. Nair, M. Mirdita, J. Yeo, O. Kovalevskiy, K. Tunyasuvunakool, A. Laydon, A. Žídek, H. Tomlinson, D. Hariharan, J. Abrahamson, T. Green, J. Jumper, E. Birney, M. Steinegger, D. Hassabis, S. Velankar, *Nucleic Acids Res.* **2024**, *52*(D1), D368-D375; 'AlphaFold Protein Structure Database in 2024: providing structure coverage for over 214 million protein sequences'; DOI 10.1093/nar/gkad1011.
[860] F. Sievers, A. Wilm, D. Dineen, T. J. Gibson, K. Karplus, W. Li, R. Lopez, H. McWilliam, M. Remmert, J. Söding, J. D. Thompson, D. G. Higgins, *Mol. Syst. Biol.* **2011**, *7*(1):539, 1-6; 'Fast, scalable generation of high-quality protein multiple sequence alignments using Clustal Omega'; DOI 10.1038/msb.2011.75.
[861] W. Kabsch, C. Sander, *Biopolymers* **1983**, *22*(12), 2577-2637; 'Dictionary of Protein Secondary Structure: Pattern Recognition of Hydrogen-Bonded and Geometrical Features'; DOI 10.1002/bip.360221211.
[862] W. G. Touw, C. Baakman, J. Black, T. A. H. te Beek, E. Krieger, R. P. Joosten, G. Vriend, *Nucleic Acids Res.* **2015**, *43*(D1), D364-D368; 'A series of PDB-related databanks for everyday needs'; DOI 10.1093/nar/gku1028.
[863] E. Gasteiger, C. Hoogland, A. Gattiker, S. Duvaud, M. R. Wilkins, R. D. Appel, A. Bairoch, **2005**, '*Protein Identification and Analysis Tools on the Expasy Server*' in *The Proteomics Protocols Handbook. Springer Protocols Handbooks*, 571-607, Humana Press Inc., Tatowa, New Jersey, USA; ISBN 978-1-58829-343-5, DOI 10.1385/1-59259-890-0:571.
[864] X. Huang, W. Miller, *Adv. Appl. Math.* **1991**, *12*(3), 337-357; 'A Time-Efficient, Linear-Space Local Similarity Algorithm'; DOI 10.1016/0196-8858(91)90017-D.
[865] J. Schindelin, I. Arganda-Carreras, E. Frise, V. Kaynig, M. Longair, T. Pietzsch, S. Preibisch, C. Rueden, S. Saalfeld, B. Schmid, J.-Y. Tinevez, D. J. White, V. Hartenstein, K. Eliceiri, P. Tomancak, A. Cardona, *Nat. Methods* **2012**, *9*(7), 676-682; 'Fiji: an open-source platform for biological-image analysis'; DOI 10.1038/nmeth.2019.
[866] A. M. Waterhouse, J. B. Procter, D. M. Martin, M. Clamp, G. J. Barton, *Bioinformatics* **2009**, *25*(9), 1189-1191; 'Jalview Version 2 - a multiple sequence alignment editor and analysis workbench'; DOI 10.1093/bioinformatics/btp033.
[867] Posit Team, **2025**, '*RStudio: Integrated Development Environment for R*', Posit Software, PBC, Boston, MA, USA, URL http://www.posit.co/.
[868] A. Daina, O. Michielin, V. Zoete, *Sci. Rep.* **2017**, *7*:42717, 1-13; 'SwissADME: a free web tool to evaluate pharmacokinetics, drug-likeness and medicinal chemistry friendliness of small molecules'; DOI 10.1038/srep42717.
[869] E. F. Pettersen, T. D. Goddard, C. C. Huang, G. S. Couch, D. M. Greenblatt, E. C. Meng, T. E. Ferrin, *J. Comput. Chem.* **2004**, *25*(13), 1605-1612; 'UCSF Chimera - A Visualization System for Exploratory Research and Analysis'; DOI 10.1002/jcc.20084.

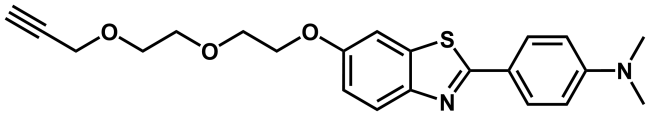
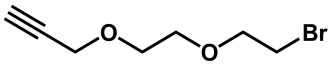
[870] D. R. Burfield, R. H. Smithers, *J. Org. Chem.* **1978**, *43*(20), 3966-3968; 'Desiccant Efficiency in Solvent Drying. 3. Dipolar Aprotic Solvents'; DOI 10.1021/jo00414a038.
[871] G. R. Fulmer, A. J. M. Miller, N. H. Sherden, H. E. Gottlieb, A. Nudelman, B. M. Stoltz, J. E. Bercaw, K. I. Goldberg, *Organometallics* **2010**, *29*(9), 2176-2179; 'NMR Chemical Shifts of Trace Impurities: Common Laboratory Solvents, Organics, and Gases in Deuterated Solvents Relevant to the Organometallic Chemist'; DOI 10.1021/om100106e.
[872] G. Torsi, G. Chiavari, C. Laghi, A. M. Asmundsdottir, F. Fagioli, R. Vecchietti, *J. Chromatogr. A* **1989**, *482*(1), 207-214; 'Determination of the absolute number of moles of an analyte in a flow-through system from peak-area measurements'; DOI 10.1016/S0021-9673(01)93221-2.
[873] D. L. Boger, M. Patel, *Tetrahedron Lett.* **1987**, *28*(22), 2499-2502; 'Total Synthesis of Prodigiosin'; DOI 10.1016/S0040-4039(00)95451-0.
[874] M. Mroczkiewicz, R. Ostaszewski, *Tetrahedron* **2009**, *65*(20), 4025-4034; 'A new and general method for the synthesis of tripeptide aldehydes based on the multi-component Ugi reaction'; DOI 10.1016/j.tet.2009.03.018.
[875] L. N. Aldrich, E. S. Dawson, C. W. Lindsley, *Org. Lett.* **2010**, *12*(5), 1048-1051; 'Evaluation of the Biosynthetic Proposal for the Synthesis of Marineosins A and B'; DOI 10.1021/ol100034p.
[876] F. W. Studier, B. A. Moffatt, *J. Mol. Biol.* **1986**, *189*(1), 113-130; 'Use of Bacteriophage T7 RNA Polymerase to Direct Selective High-Level Expression of Cloned Genes'; DOI 10.1016/0022-2836(86)90385-2.
[877] H. U. C. Braß, Doctoral Thesis, 'Die farbenfrohe Welt der Prodiginine – Neue Enzyme für die Synthese bioaktiver Naturstoffderivate', Heinrich Heine University Düsseldorf (Düsseldorf, Germany), **2020**; ISBN 978-3-95806-523-9; https://docserv.uni-duesseldorf.de/servlets/DerivateServlet/Derivate-59656/Brass_Hannah_Dissertation_print_final_PDFA1b.pdf.
[878] D. Hanahan, J. Jessee, F. R. Bloom, **1991**, '*[4] Plasmid Transformation of Escherichia coli and Other Bacteria*' in *Bacterial Genetic Systems. Methods in Enzymology, Vol. 204*, 63-113, Academic Press Inc., Cambridge, Massachusetts, USA; ISBN 978-0-12-182105-0, DOI 10.1016/0076-6879(91)04006-A.
[879] F. Sanger, S. Nicklen, A. R. Coulson, *Proc. Natl. Acad. Sci. U.S.A.* **1977**, *74*(12), 5463-5467; 'DNA sequencing with chain-terminating inhibitors'; DOI 10.1073/pnas.74.12.5463.
[880] T. Carver, S. R. Harris, M. Berriman, J. Parkhill, J. A. McQuillan, *Bioinformatics* **2012**, *28*(4), 464-469; 'Artemis: an integrated platform for visualization and analysis of high-throughput sequence-based experimental data'; DOI 10.1093/bioinformatics/btr703.
[881] M. Bélanger, L. L. Burrows, J. S. Lam, *Microbiology* **1999**, *145*(12), 3505-3521; 'Functional analysis of genes responsible for the synthesis of the B-band O antigen of *Pseudomonas aeruginosa* serotype O6 lipopolysaccharide'; DOI 10.1099/00221287-145-12-3505.
[882] P. V. Liu, *J. Infect. Dis.* **1973**, *128*(4), 506-513; 'Exotoxins of *Pseudomonas aeruginosa*. I. Factors that Influence the Production of Exotoxin A'; DOI 10.1093/infdis/128.4.506.
[883] R. Wallis, A. Reilly, A. Rowe, G. R. Moore, R. James, C. Kleanthous, *Eur. J. Biochem.* **1992**, *207*(2), 687-695; '*In vivo* and *in vitro* characterization of overproduced colicin E9 immunity protein'; DOI 10.1111/j.1432-1033.1992.tb17096.x.
[884] A. K. Mallia, B. S. Antharavally, 'Pyrocatechol Violet-Metal Protein Assay', U.S. Patent US 7,745,153 B2, 1-12, **2010**, https://patentimages.storage.googleapis.com/29/20/17/a9f3dd0930a311/US7745153.pdf.

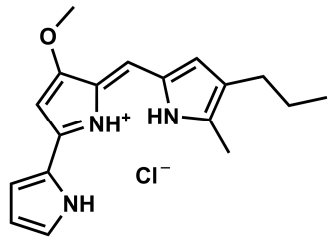
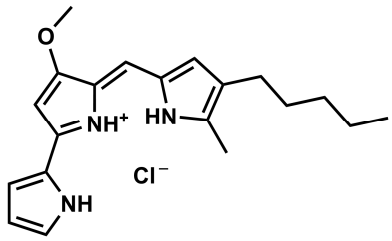
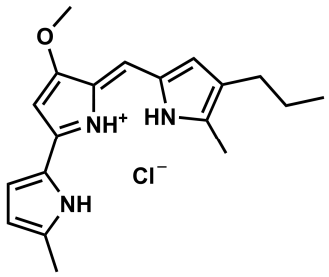
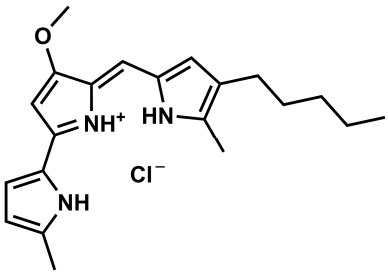
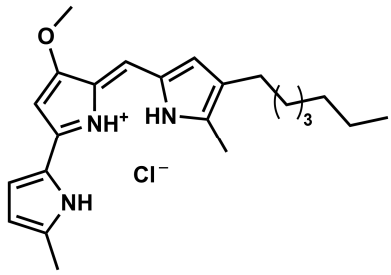
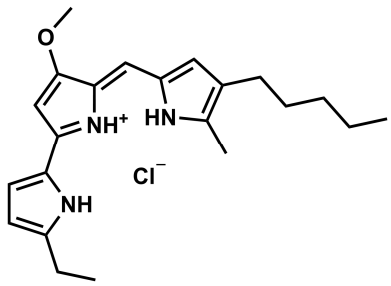
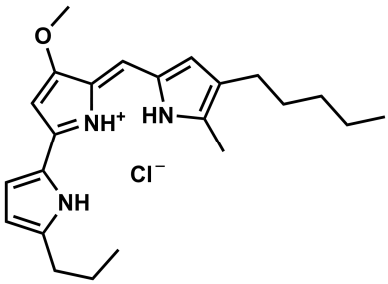
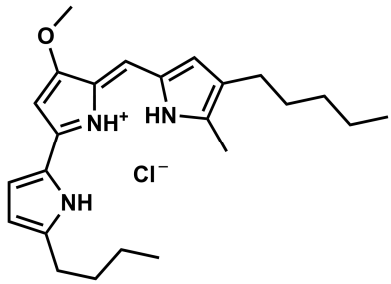
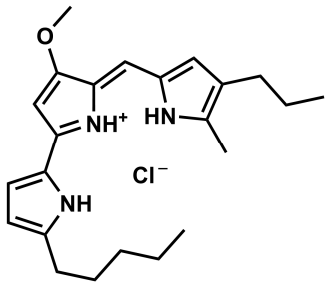
VII Table of Compounds

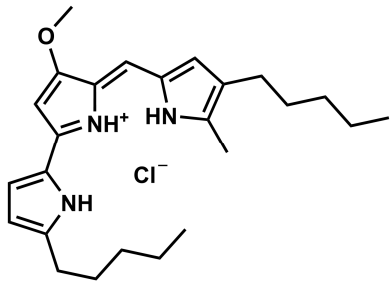
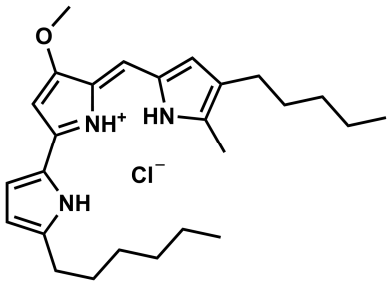
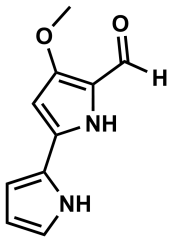
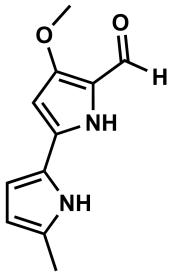
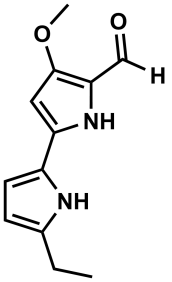
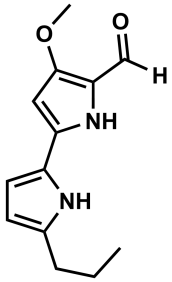
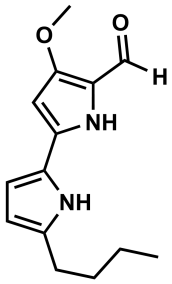
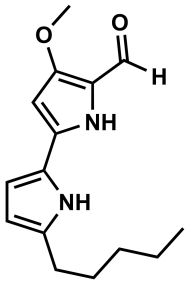
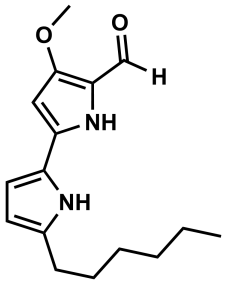
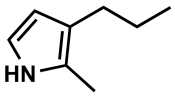
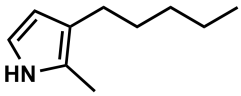
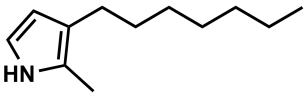
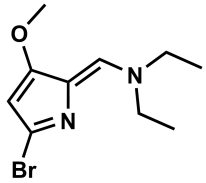
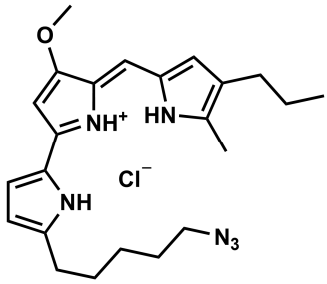
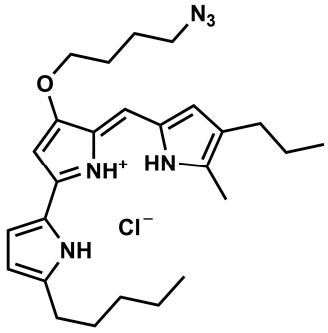
The following compounds described in this work have been synthesised under the corresponding experimental identifiers (TWE_XXX_X).

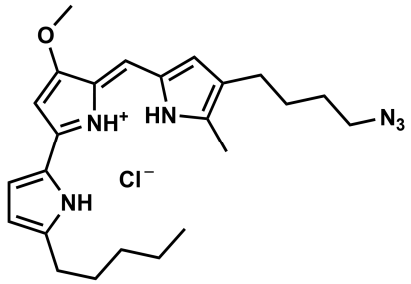
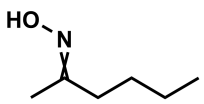
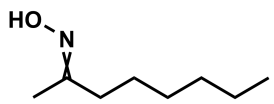
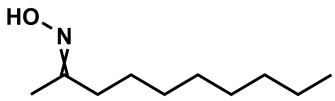
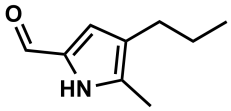
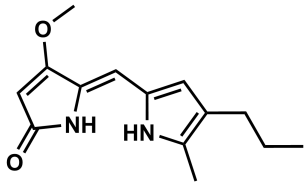
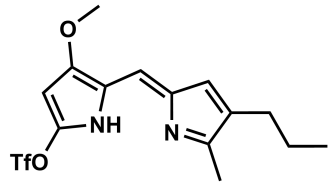
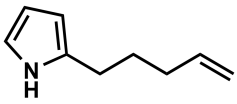
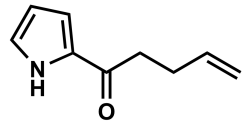
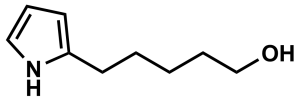
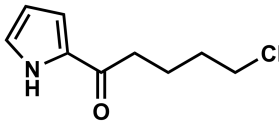
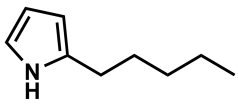
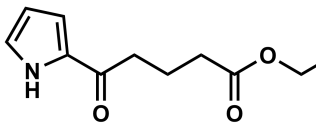
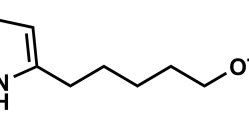
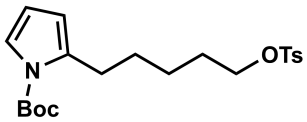
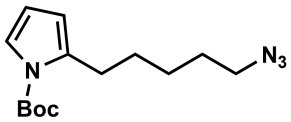
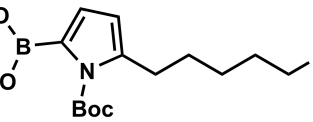
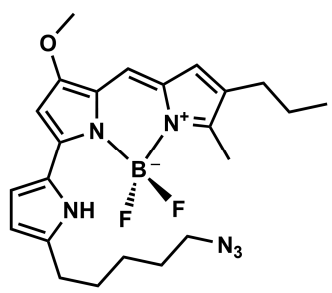
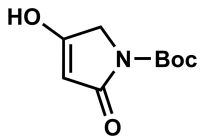
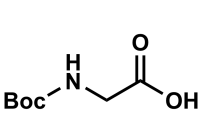
Chapter II					
					
II-39·HCl	TWE_259_1	**II-43**	TWE_265_2	**II-44**	TWE_266_2
					
II-46	TWE_279_1	**II-48**	TWE_278_2	**II-50**	TWE_277_3
					
II-57a	TWE_310_1	**II-57b**	TWE_322_1	**II-57c**	TWE_325_1
					
II-57d	TWE_321_1	**II-57e**	TWE_309_1	**II-57f**	TWE_324_1
					
II-57g	TWE_320_1	**II-63**	TWE_352_1		

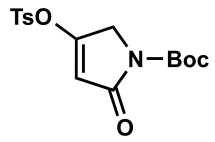
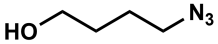
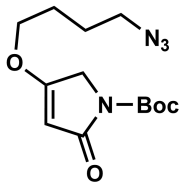
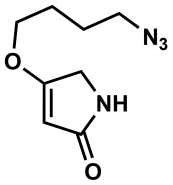
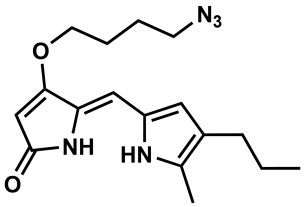
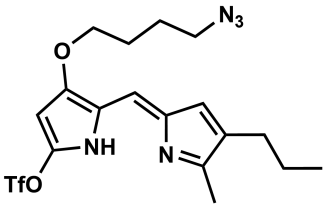
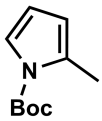
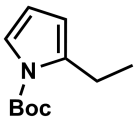
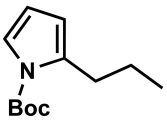
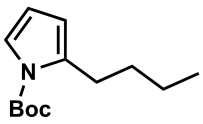
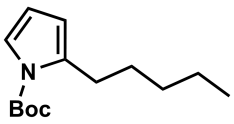
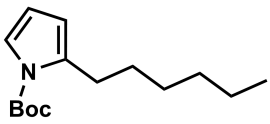
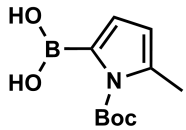
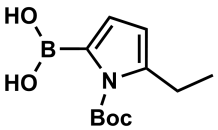
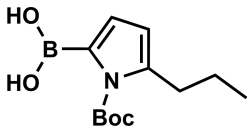
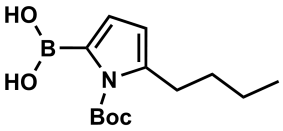
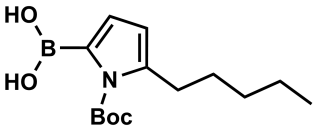
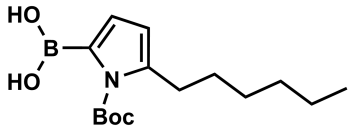
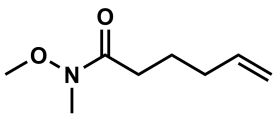
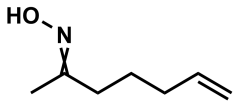
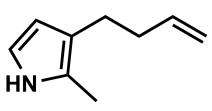
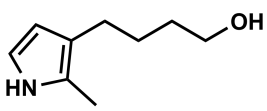
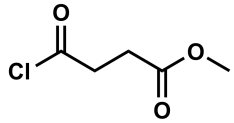
	
II-67	TWE_399_3
	
II-71	TWE_367_4 and TWE_393_2
	
II-73	TWE_384_2
	
II-74	TWE_323_2
II-77	TWE_355_3
	
II-78	TWE_359_2
II-79	TWE_372_1
	
II-88	TWE_388_1
II-90	TWE_392_7

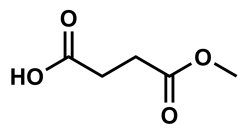
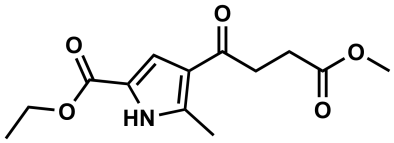
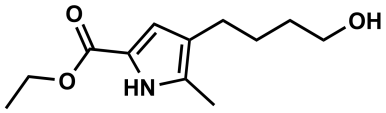
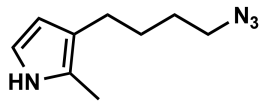
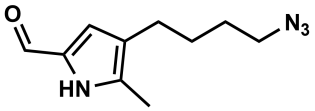
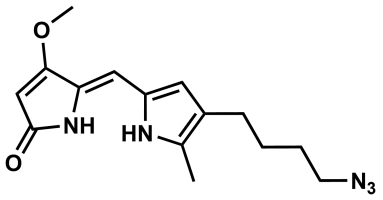
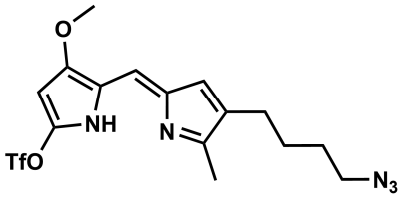
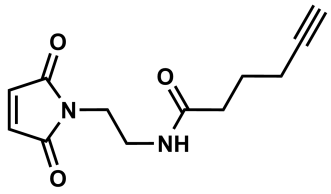
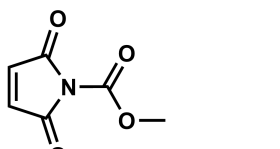
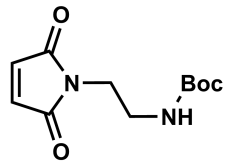
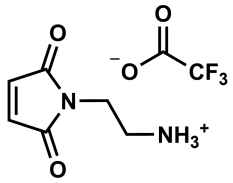
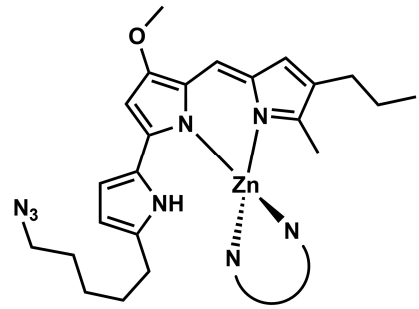
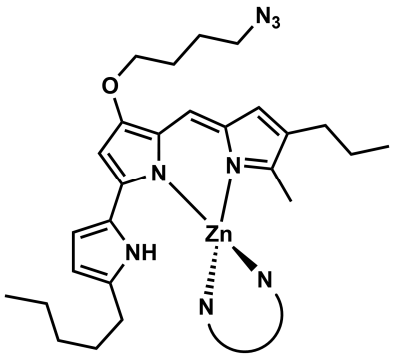
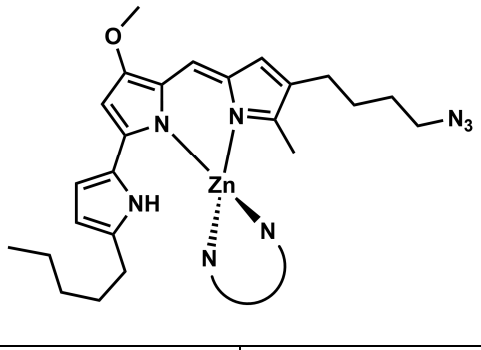
	
II-92	TWE_371_1
	
II-93	TWE_383_1

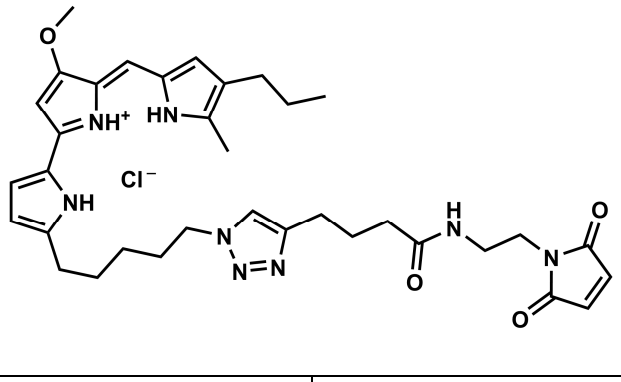
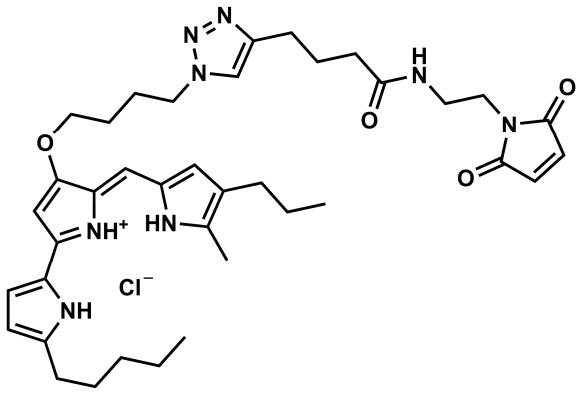
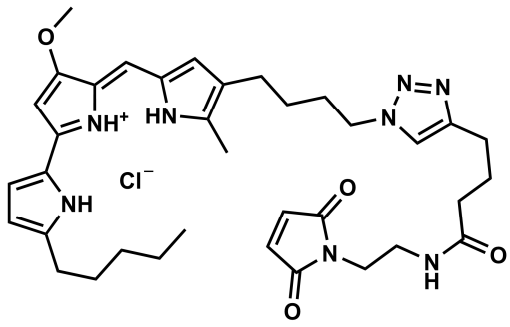
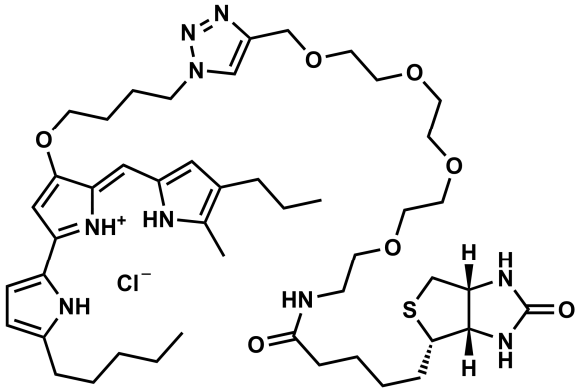
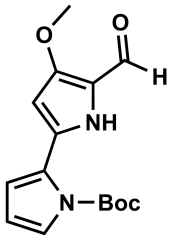
Chapter II.5.4					
					
III-1aa·HCl	TWE_207_1–8 and TWE_229_1	**III-1ab·HCl**	TWE_210_1	**III-1ba·HCl**	TWE_272_1
					
III-1bb·HCl	TWE_244_1	**III-1bc·HCl**	TWE_273_1	**III-1cb·HCl**	TWE_245_1
					
III-1db·HCl	TWE_247_1	**III-1eb·HCl**	TWE_248_1	**III-1fa·HCl**	TWE_243_1

					
III-1fb·HCl	TWE_251_1	**III-1gb·HCl**	TWE_252_1	**III-14a**	TWE_061_001
					
III-14b	TWE_216_2	**III-14c**	TWE_234_1	**III-14d**	TWE_238_2
					
III-14e	TWE_240_1	**III-14f**	TWE_215_2	**III-14g**	TWE_235_2
					
III-15a	TWE_070_3	**III-15b**	TWE_155_1	**III-15c**	TWE_242_1
					
III-75	TWE_058_001 and TWE_214_1	**III-89·HCl**	TWE_226_2	**III-90·HCl**	TWE_220_2

					
III-91·HCl	TWE_219_2	**III-93a**	TWE_069_3	**III-93b**	TWE_152_1
					
III-93c	TWE_241_1	**III-94**	TWE_074_3	**III-95**	TWE_075_2
					
III-96	TWE_192_5	**III-97**	TWE_094_1	**III-100**	TWE_089_1
					
III-101	TWE_174_3	**III-103**	TWE_161_1	**III-105f**	TWE_162_2
					
III-106f	TWE_165_2	**III-109**	TWE_171_4	**III-111**	TWE_176_5
					
III-112	TWE_177_2	**III-113**	TWE_178_2	**III-114**	TWE_225_4
					
III-125	TWE_249_3	**III-126**	TWE_140_3	**III-128**	TWE_129_2

					
III-130	TWE_143_1	**III-132**	TWE_150_2	**III-134**	TWE_149_2
					
III-135	TWE_153_2	**III-136**	TWE_154_2	**III-137**	TWE_218_2
					
III-139b	TWE_212_1	**III-139c**	TWE_Boc_C2	**III-139d**	TWE_Boc_C3
					
III-139e	TWE_Boc_C4	**III-139f**	TWE_167_2	**III-139g**	TWE_Boc_C6
					
III-140b	TWE_213_2	**III-140c**	TWE_232_1	**III-140d**	TWE_237_2
					
III-140e	TWE_239_1	**III-140f**	TWE_208_10	**III-140g**	TWE_233_2
					
III-142	TWE_124_1	**III-143**	TWE_125_3	**III-144**	TWE_126_2
					
III-145	TWE_127_3	**III-146**	TWE_128_3 and TWE_408_5	**III-148**	TWE_403_1

					
III-150	TWE_402_2	**III-151**	TWE_404_1	**III-152**	TWE_407_3
					
III-155	TWE_417_3	**III-156**	TWE_419_1	**III-157**	TWE_141_1
					
III-158	TWE_217_2	**III-159**	TWE_115_4	**III-161**	TWE_110_2
					
III-164	TWE_112_6	**III-165**	TWE_113_7	**III-166**	TWE_227_2
					
III-167	TWE_222_2	**III-168**	TWE_221_2		

			
III-169·HCl	TWE_275_1	**III-170·HCl**	TWE_269_1
			
III-171·HCl	TWE_271_1	**III-172·HCl**	TWE_415_3
			
III-174	TWE_059_001		

VIII Declaration of Originality

Ich versichere an Eides statt, dass die Dissertation von mir selbstständig und ohne unzulässige fremde Hilfe unter Beachtung der „Grundsätze zur Sicherung guter wissenschaftlicher Praxis an der Heinrich-Heine-Universität Düsseldorf“ erstellt worden ist. Die vorliegende Dissertation wurde ausschließlich an der Mathematisch-Naturwissenschaftlichen Fakultät der Heinrich-Heine-Universität Düsseldorf vorgelegt. Es wurde zuvor kein Promotionsversuch unternommen.

Wülfrath, 28.05.2026	M. Weber
Ort und Datum	Tim Moritz Weber

IX Supporting Information

IX.1 Identification and Prevention Strategies of Grease Contaminations

In the last cross-coupling steps of the prodiginine synthesis, recurrent and severe *H*-grease impurities of unknown origin were encountered, which could not be removed by chromatography or washing with distilled *n*-pentane. Non-distilled solvents and in particular cotton wool for filtration of crude reaction products were found to contain significant amounts of non-volatile *H*-grease, which can then be transferred into reaction products as prodiginines or the alkyne maleimide linker without further chance of removal. For this reason, purchased solvents were distilled on lab-scale rotary evaporators to determine the amount of residual *H*-grease and other insoluble impurities present (without prior distillation). In addition, 5 g of commercial cotton wool (Jean Carol Cosmetic-Pleats Naturelle, exp. date 20.03.2029, Lot 0642) were washed with distilled *n*-pentane (2 x 350 mL) and distilled CH_2Cl_2 (2 x 250 mL), and the solvent was evaporated for quantification of insoluble residues. The insoluble residues were dissolved in 500 µL $CDCl_3$ and analysed by ^{1}H NMR spectroscopy (600 MHz, 16 scans, Figure IX.1). From 2 L of solvent were obtained the following quantities of grease (and other non-volatile polymers) (single determination, Table IX.1). Furthermore, 20.82 mg of non-volatile impurities were obtained from 5 g of domestic cotton wool.

Table IX.1. Quantification of non-volatile impurities from commercial organic solvents.

Solvent	Grade	Supplier	Lot	Non-volatiles [mg L^{-1}]
MTBE	99.5%, for synthesis, 25 L tin barrel	Carl Roth	240296596	19.51
n-Pentane	>95%, extra pure, 25 L tin barrel	Carl Roth	391311713	17.75
PE	40–65 °C, anhydrous, 25 L tin barrel	VWR	21J114009	14.78
EtOAc	>99%, technical, 25 L plastic container	VWR	21K024016	17.93
CH_2Cl_2	99%, lab. reagent grade, stab. with amylene, 25 L tin barrel	Fisher Chemical	2100396	94.31

Additionally, other standard laboratory utensils were analysed as sources of grease contaminants, such as foldable rubber and silicone septa (Saint Gobain), nitrile gloves and hand cream (Th. Geyer), commercially available degreased cotton wool (Brand), or Baysilone silicone paste (Bayer) for airtight connection of glass joints (Figure IX.2). As expected, silicone paste and silicone septa contained mostly silicone grease. All other samples showed detectable amounts of *H*-grease. While the nitrile gloves and commercial degreased cotton wool still contained minor amounts of *H*-grease, rubber septa and the laboratory hand cream exhibited significant amounts of the uninvited guest.

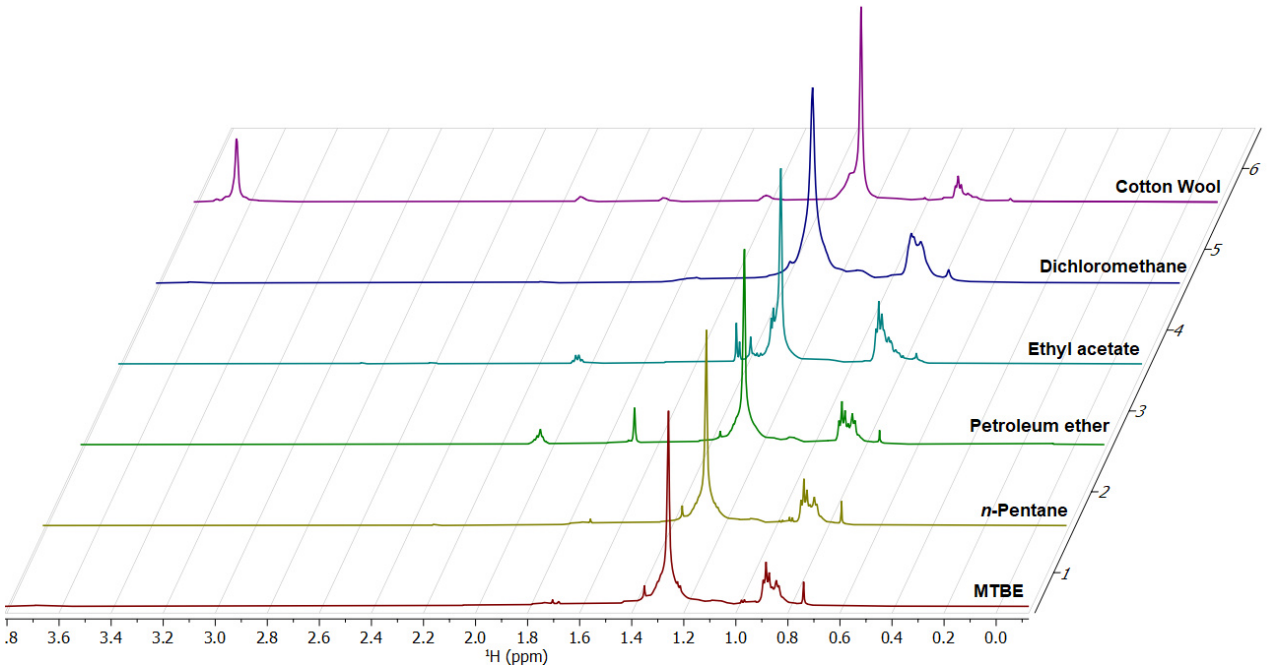


Figure IX.1. Stacked excerpts of ^{1}H NMR spectra of non-volatile residues from solvent evaporation of 2 L of organic solvents or 5 g of domestic cotton wool in $CDCl_3$. *H*-Grease gives a triplet at 0.88 ppm and a broad singlet at 1.26 ppm.[871]

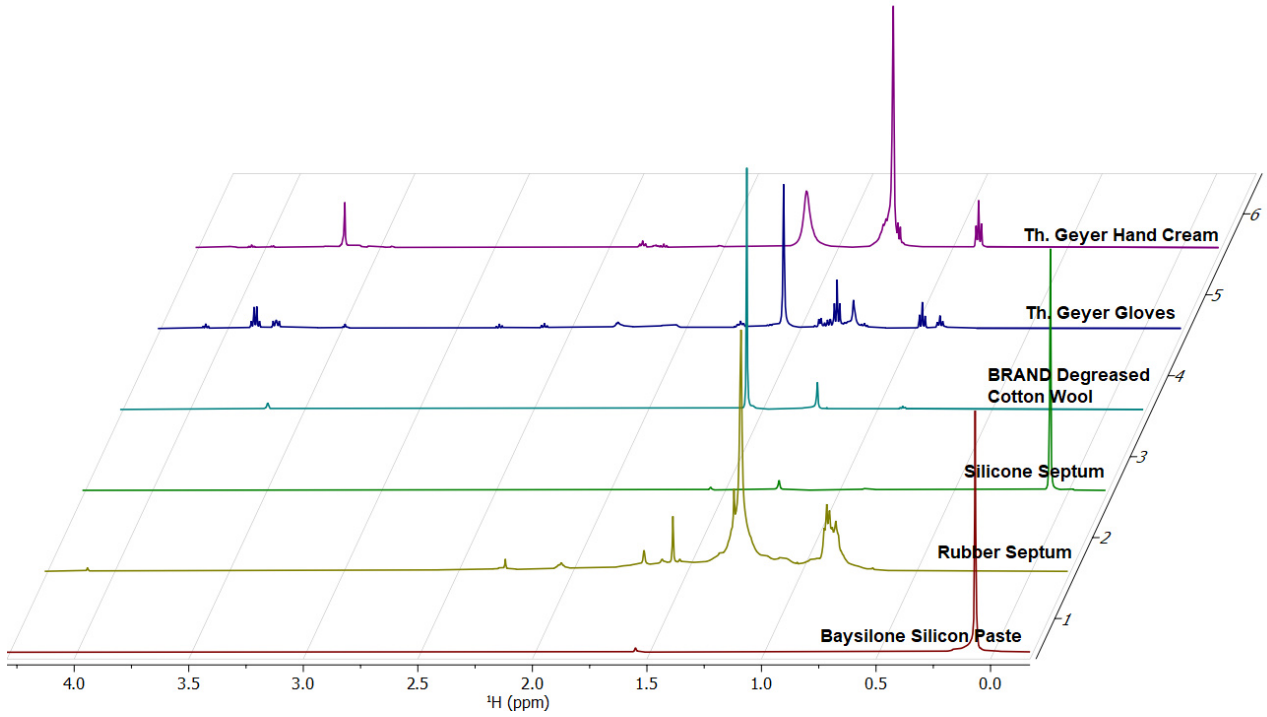


Figure IX.2. Stacked excerpts of ^{1}H NMR spectra of non-volatile residues from standard laboratory utensils $CDCl_3$. H-Grease gives a triplet at 0.88 ppm and a broad singlet at 1.26 ppm, while silicone grease is characterised by a single singlet at 0.07 ppm.[871]

These observations led to the development of the following laboratory practice strategies to avoid the introduction of non-removable grease impurities into prodiginine samples:

(a) All organic solvents were distilled prior to usage and were stored in clean glass containers.

(b) Filtration of crude reaction products was performed over commercially available degreased cotton wool (Brand, Product No. BR28205, cotton roving, degreases cotton wool, approximately 1.3 g m^{-1}), which had been degreased again by washing with distilled *n*-pentane, PE, or CH_2Cl_2.

(c) Plastic articles (pipettes, measuring cylinders, spray bottles) were avoided wherever possible and replaced by adequate substitutes made of borosilicate glass.

(d) Prodigiosin-containing reactions were not sealed with foldable rubber or silicone septa (especially in combination with chlorinated solvents) but with a custom-made adapter that allows utilisation of disposable PTFE-coated septa and avoids long-term exposure of septa to vapour of organic solvents through a PTFE stopcock (Figure IX.3).

(e) Greasing of solvent-exposed glass joints was avoided if not essential.

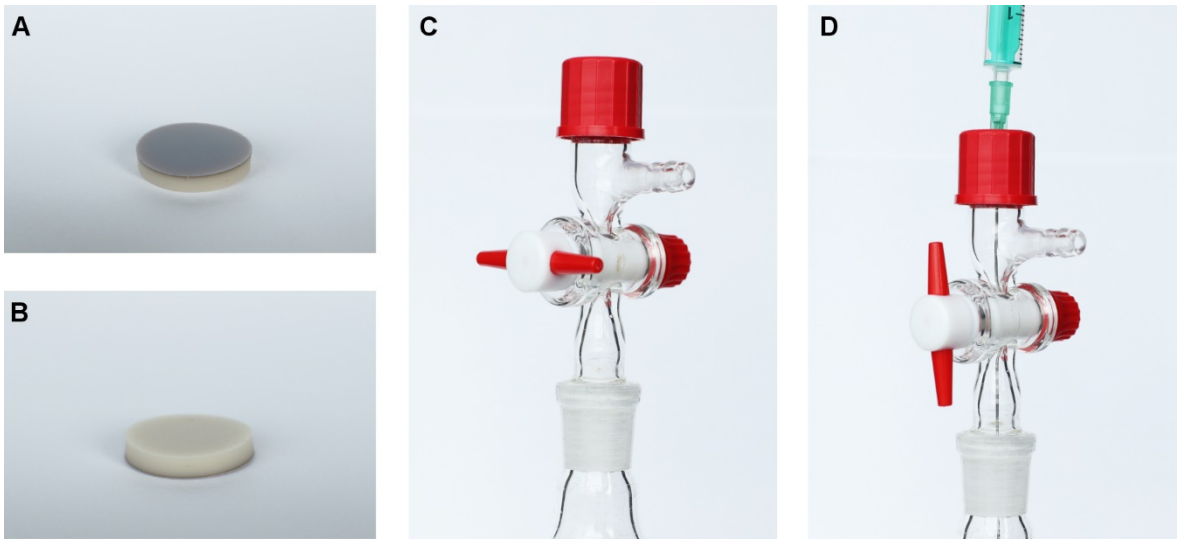


Figure IX.3. Custom-made glass adapter. If connected to a Schlenk flask, solids can be added under an inert atmosphere upon removal of the adapter. If connected to a round-bottom flask instead, every flask can be converted into a Schlenk-type flask for air-sensitive reactions. **A**. BOLA cap seal (PTFE + silicone, Bohlender, Product No. H973-18, 16.8 mm diameter, 3.3 mm thickness), bottom view. **B**. BOLA cap seal, top view. **C**. Custom-made glass adapter with standard ground joint cone (14/23), a one-way PTFE stopcock, an olive with 8 mm outer diameter for connection to the Schlenk line, and a screw thread (GL18) for mounting a screw cap (GL18) with disposable septa (cf. **A** and **B**). **D**. Addition of liquids through the borehole of the PTFE stopcock with a syringe.

IX.2 Substrate Promiscuity of Prodiginine Ligase – Unprocessed Raw Data

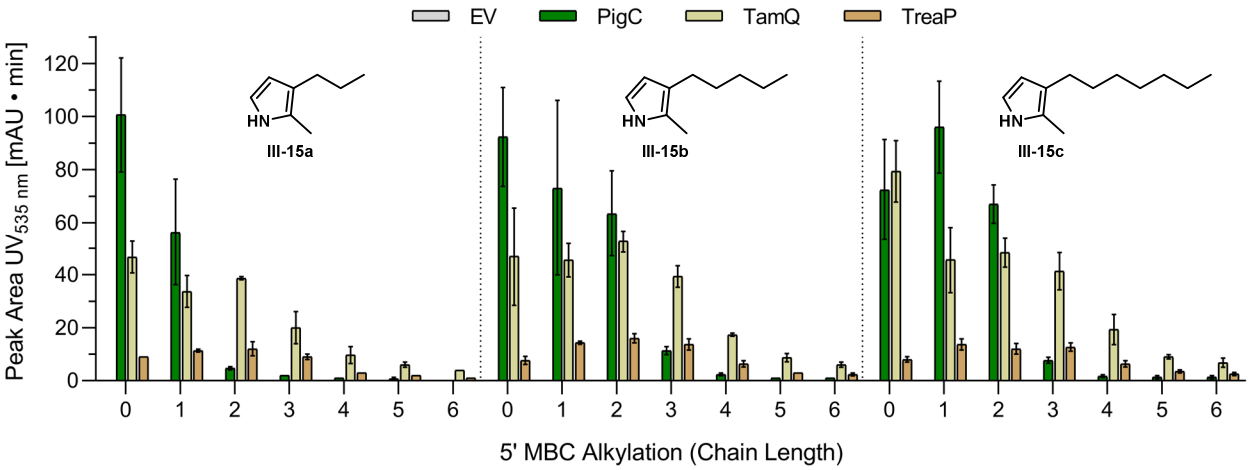


Figure IX.4. Unprocessed raw data of prodiginine quantification from *in vitro* reactions with the prodiginine ligases PigC, TamQ, and TreaP with varying chain lengths on the A- and C-ring. Methanolic extracts of biocatalytic reactions between monopyrroles **III-15a**–**c** and 5'-*n*-alkyl MBC derivatives **III-14a**–**g** were subjected to coupled LC-MS measurements and the UV absorption at 535 nm is plotted against the chain length of the corresponding alkylated MBC derivatives (n=3). Hence, varying extinction coefficients are not taken into account. The used monopyrrole is shown in the diagram.

IX.3 Absorption Properties of A-Ring Alkylated Prodiginines

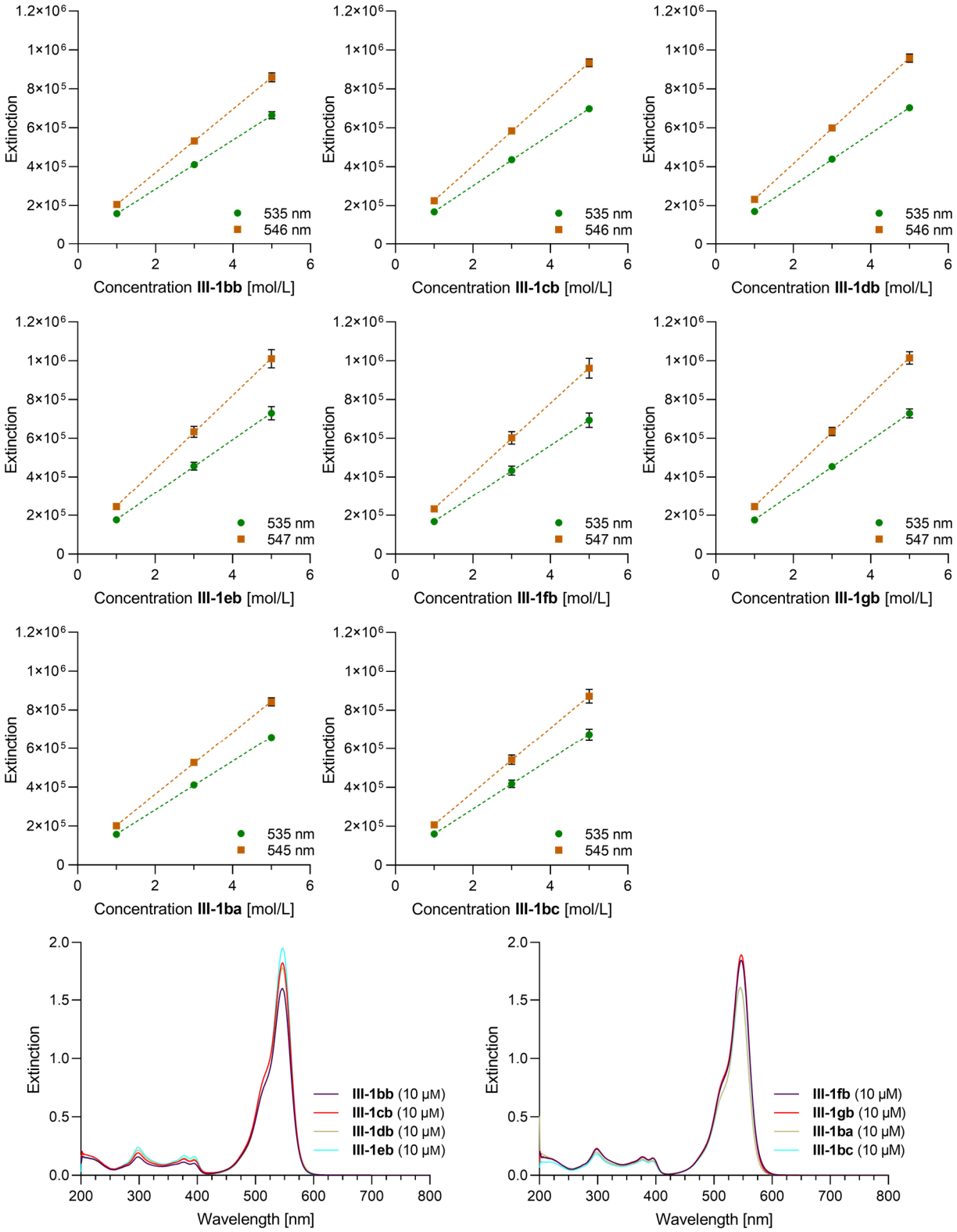


Figure IX.5. Extinction values for different molar concentrations of prodiginines **III-1ba–bc** in acidic ethanol. Measured extinctions at 535 nm and at the absorption maximum of prodiginine solutions at 1 µM, 3 µM, and 5 µM were plotted against the concentrations and the molar extinction coefficients were determined from the slope of linear regression in agreement with the Beer-Lambert law. Absorption spectra of 10 µM prodiginine solutions in acidic ethanol were recorded from 200–800 nm.

Table IX.2. Fit parameters for determination of molar extinction coefficients of prodiginines **III-1ba–bc** from linear regression (n=3).

Prodiginine	λ_{max}	535 nm			λ_{max}		
	[nm]	Slope	Y-Intersect	R^2	Slope	Y-Intersect	R^2
III-1bb·HCl	546	126508	31353	0.9975	163533	42056	0.9976
III-1cb·HCl	546	132425	36969	0.9981	177092	50169	0.9980
III-1db·HCl	546	133375	37697	0.9984	181692	51814	0.9983
III-1eb·HCl	547	138350	39206	0.9929	191400	55522	0.9929
III-1fb·HCl	547	131608	36631	0.9902	182125	52236	0.9903
III-1gb·HCl	547	138200	38244	0.9966	192358	54403	0.9965
III-1ba·HCl	545	125450	32839	0.9979	160358	42714	0.9980
III-1bc·HCl	545	128500	32011	0.9939	166267	42189	0.9941

IX.4 IC_{50} Values of Synthetic Prodiginines Against Urothelial Cancer Cell Lines

Table IX.3. Inhibitory concentrations of prodigiosin (**III-1ab·HCl**), obatoclax mesylate (**III-55·Mes**), prodigiosin azides (**III-89·HCl**, **III-90·HCl**, and **III-91·HCl**) and A-ring alkylated prodiginines **III-1ba–gb·HCl** against urothelial carcinoma cell lines RT-112 (cisplatin sensitive) and RT-112res (cisplatin resistant) after 24 h and 72 h of incubation. The presented IC_{50} (nM) values are visualised as a bar diagram in Figure III.7 in the results and discussion section of Chapter III.3.2.6 and summarise the data from the dose-response curves of the MTT cell viability assay. The displayed errors represent the 95% confidence interval. Lena Berning (Institute of Molecular Medicine I, HHU) experimented and provided the data.

	24 h		72 h		Hydrophobicity[a]
Prodiginine	RT-112	RT-112res	RT-112	RT-112res	[Consensus LogP]
Reference Compounds					
Prodigiosin (III-1ab·HCl)	675 ± 92	157 ± 31.4	73.8 ± 4.90	41.1 ± 3.80	2.54
Obatoclax (III-55·Mes)	3327 ± 548	184 ± 36.3	172 ± 13.8	36.0 ± 2.99	2.91
Prodiginine Azides					
III-89·HCl (A-Ring azide)	736 ± 175	308 ± 74.0	156 ± 19.1	70.5 ± 6.71	2.96
III-90·HCl (B-Ring azide)	7518 ± 4292	1675 ± 541	303 ± 45.8	143 ± 22.5	3.89
III-91·HCl (C-Ring azide)	703 ± 193	353 ± 99.3	142 ± 19.0	64.2 ± 8.57	3.27
Alkylated A-Ring Prodiginines					
III-1ba·HCl	285 ± 60	66.3 ± 10.2	155 ± 20.1	16.1 ± 1.02	2.22
III-1bb·HCl	535 ± 178	1586 ± 44.8	26.3 ± 3.12	18.8 ± 1.25	2.83
III-1bc·HCl	274 ± 48	57.4 ± 9.65	67.7 ± 5.96	15.7 ± 0.77	3.45
III-1cb·HCl	260 ± 51	185 ± 43.6	52.1 ± 3.29	26.3 ± 1.83	3.09
III-1db·HCl	414 ± 64	155 ± 24.0	81.3 ± 7.24	34.0 ± 2.92	3.36
III-1eb·HCl	789 ± 132	201 ± 34.8	90.8 ± 10.2	28.4 ± 2.57	3.67
III-1fa·HCl	752 ± 165	200 ± 55.0	104 ± 12.8	44.4 ± 4.40	3.27
III-1fb·HCl	1650 ± 758	367 ± 80.0	182 ± 19.0	64.9 ± 6.20	3.98
III-1gb·HCl	7752 ± 4588	1648 ± 489	375 ± 41.5	146 ± 1.66	4.29

[a] Hydophobicity/lipophilicity data were predicted with the SwissADME web tool.[868] The consensus LogP value for an equilibrium between octanol and water is calculated as the average of five different prediction models (iLOGP, XLOGP3, WLOGP, MLOGP, and SILICOS-IT).

IX.5 Dose-Response Plots for Cell Viability Screening of Urothelial Carcinoma Cell Lines RT-112 and RT-112res with Prodiginine Azides III-89, III-90, III-91, and the Alkylated Derivative III-1fa

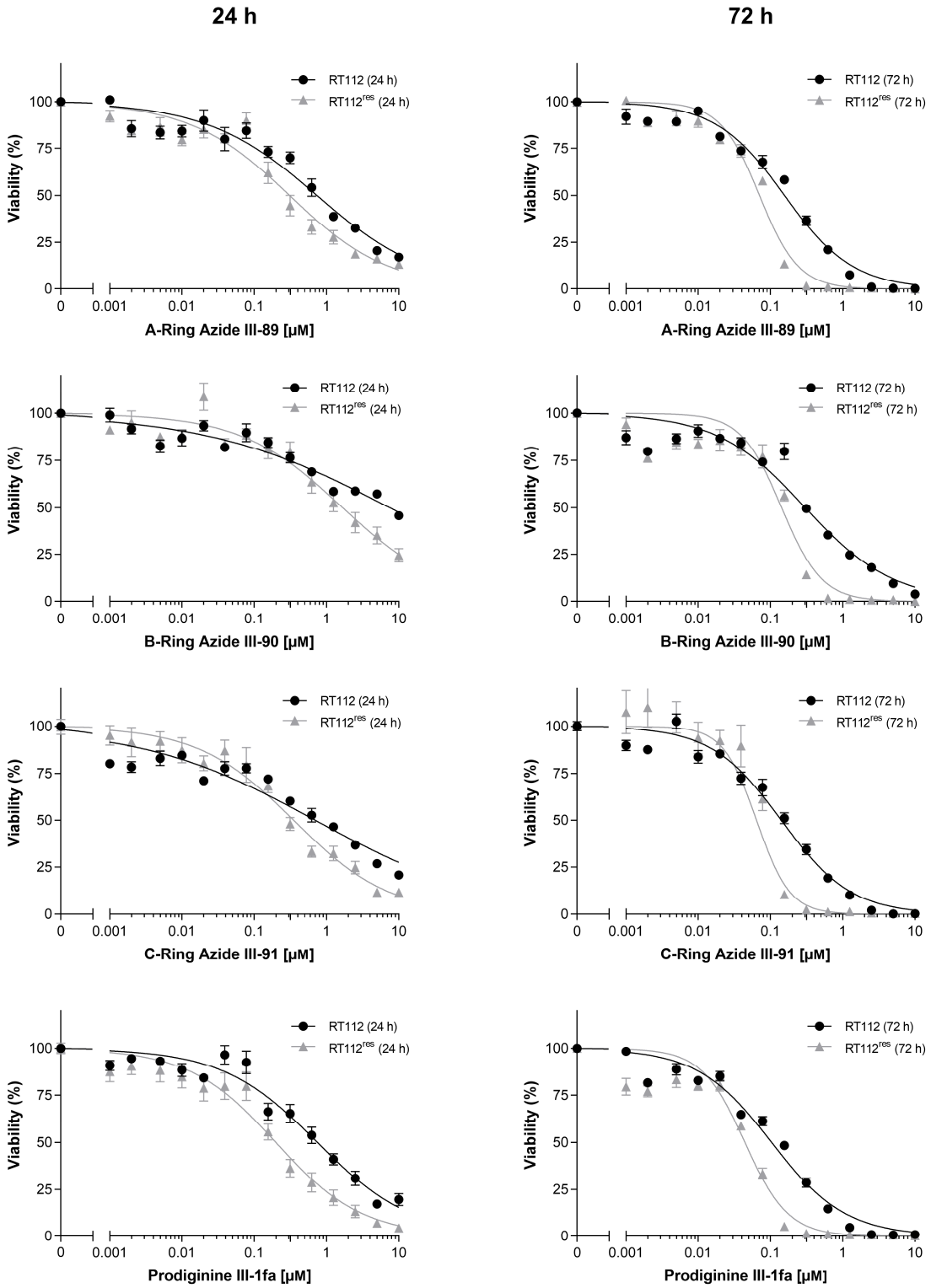


Figure IX.6. Dose-response curves of urothelial cancer cell lines RT-112 (black circles) and the cisplatin-resistant progeny RT-112res (grey triangles) for chemically synthesised prodiginine azides **III-89·HCl**, **III-90·HCl**, and **III-91·HCl** and the alkyl derivative **III-1fa**. Cell viability (n=3) was determined via MTT assay and plotted against the prodiginine concentration (µM). The left column contains the viability read out after 24 h of incubation, and the right column contains the viability read out after 72 h of incubation. Dose-response curves of all other prodiginines from this thesis can be found in the following publication: Weber *et al.*, *Catal. Sci. Technol.* **2023**, 13(*21*), 6165–6184. DOI 10.1039/D3CY00913K.

IX.6 Activation of PyoS2 DNase Activity in the Presence of Divalent Metal Ions

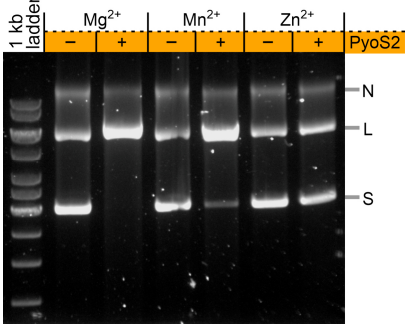


Figure IX.7. Effect of divalent metal cations on activation of PyoS2 DNase activity. pET21a(+) plasmid DNA (200 ng) in dialysis buffer was incubated for 60 min with 10 mM metal salts ($MgCl_2$, $MnSO_4$ x H_2O, or $ZnSO_4$ x 7 H_2O) and optional PyoS2 at a concentration of 500 nM. Samples were analysed via agarose gel electrophoresis. The strongest activation of DNase activity is observed with Mg^{2+} (full cleavage of supercoiled DNA), while Mn^{2+} and Zn^{2+} show minor to no activation, respectively. Abbreviations: L – linear; N – nicked; S – supercoiled.

IX.7 Mass Spectrometry Data of Purified PyoS2 Variants and AIF-Conjugates

Table IX.4. Protein mass spectrometry data for ImS2, PyoS2, and PyoS2 variants.

Protein	Average Mass*† [calc.]	Mass [detect.]	SD
ImS2-His_6	11104.47	11104.60	–
PyoS2	73722.52	73722.90	0.88
PyoS2 H657A	73656.46	73658.58	2.33
PyoS2 H685A	73656.46	73655.83	4.42
PyoS2 **H657A H685A**	73590.40	73590.98	0.76
PyoS2 Q570C	73697.55	73697.56	2.06
PyoS2 Q570C AIF488	74394.53	74391.22	2.17
PyoS2 K602C	73697.61	73694.19	6.19
PyoS2 K602C AIF488	74394.61	74394.15	3.13
PyoS2 Y640C	73662.61	73662.87	2.15
PyoS2 Y640C AIF350	74138.09	74136.08	0.11
PyoS2 Y640C AIF488	74359.60	74359.12	2.63
PyoS2 Y640C AIF594	74548.58	74551.04	1.57
PyoS2 Y640C **H657A H685A**	73530.48	73530.92	1.67
PyoS2 Y640C **H657A H685A** AIF350	74006.96	74005.86	1.34
PyoS2 Y640C **H657A H685A** AIF488	74228.14	74227.03	1.38
PyoS2 Y640C **H657A H685A** AIF594	74416.45	74415.45	6.04
PyoS2 C-Cys	73825.78	73825.75	1.51
PyoS2 C-Cys AIF488	74519.79	74519.85	2.49
PyoS2 ID	73545.40	73546.54	0.49
PyoS2 ID Y640C	73577.46	73577.37	2.00
PyoS2 ID Y640C AIF488	74274.46	74274.59	1.18

Abbreviations: ID – interaction-deficient; SD – standard deviation.

* All proteins and masses were calculated and detected with the initial methionine missing.

† For PyoS2-AlphaFluor conjugates, the average mass was calculated from the PyoS2 molecular weight without initial methionine and masses of the commercial AlphaFluor350 (578.68 g/mol triethylammonium counter ion), AlphaFluor488 (720.66 g/mol, sodium counter ion), and AlphaFluor594 (908.97 g/mol, sodium counter ion) C_5 maleimides. A mass of 23 was subtracted from the indicated molecular weight for sodium as counter ion, and a mass of 102.20 for the triethylammonium counter ion.

IX.8 Statistical Analysis of DNase Activity of PyoS2 and its Mutants and Conjugates

IX.8.1 Exponential Fitting and Half-Life Determination

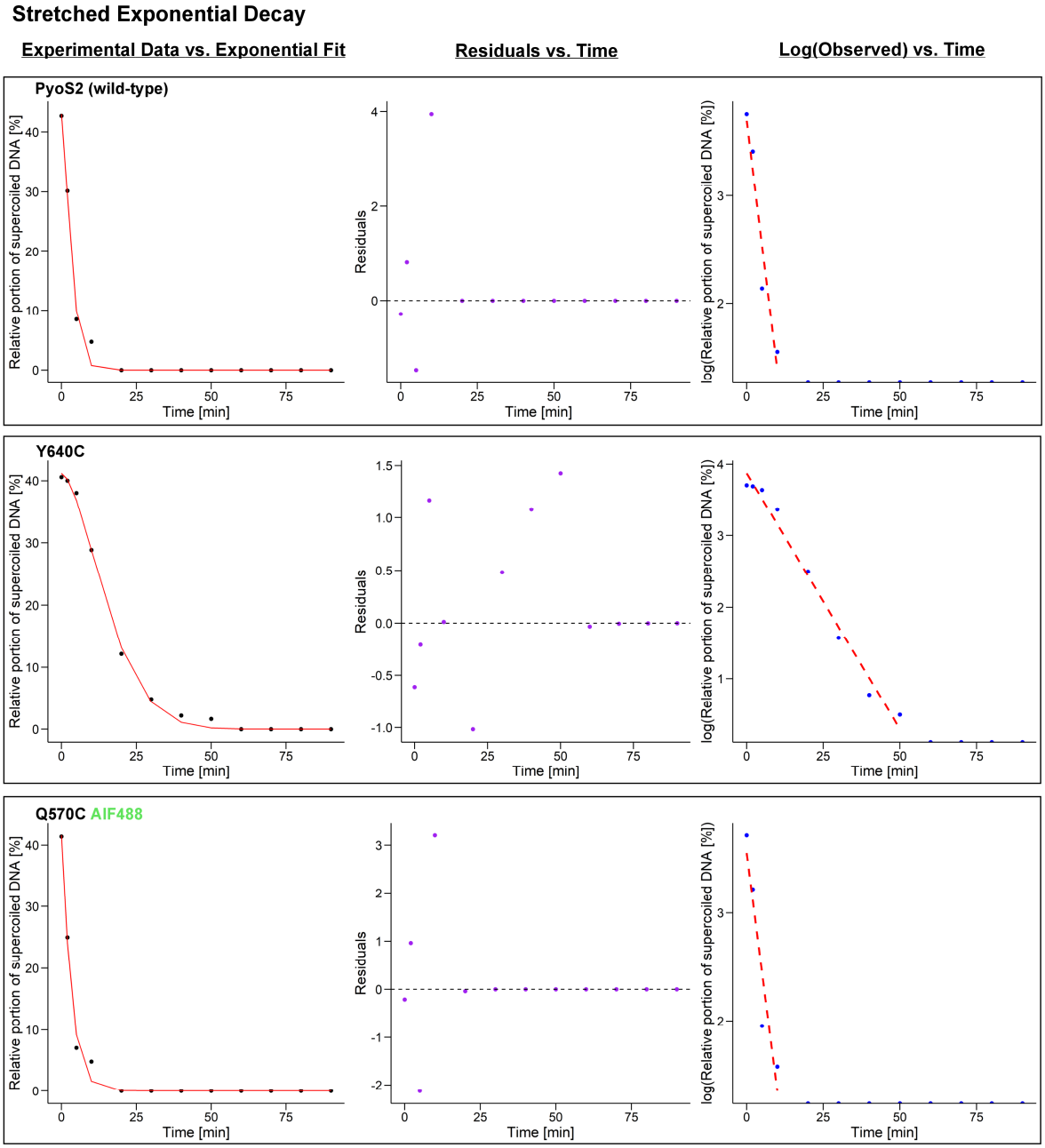


Figure IX.8. Analysis of supercoiled DNA cleavage for highly active PyoS2 proteins with a stretched exponential fit in R. **Left**: Experimental data points (relative portion of supercoiled DNA, from densitometric analysis) and fitted data. **Middle**: Residuals vs. Time. **Right**: logarithmic plot. Parameters of fitted curves and supercoiled DNA half-lives are summarised in Table IX.5 (Supporting Information).

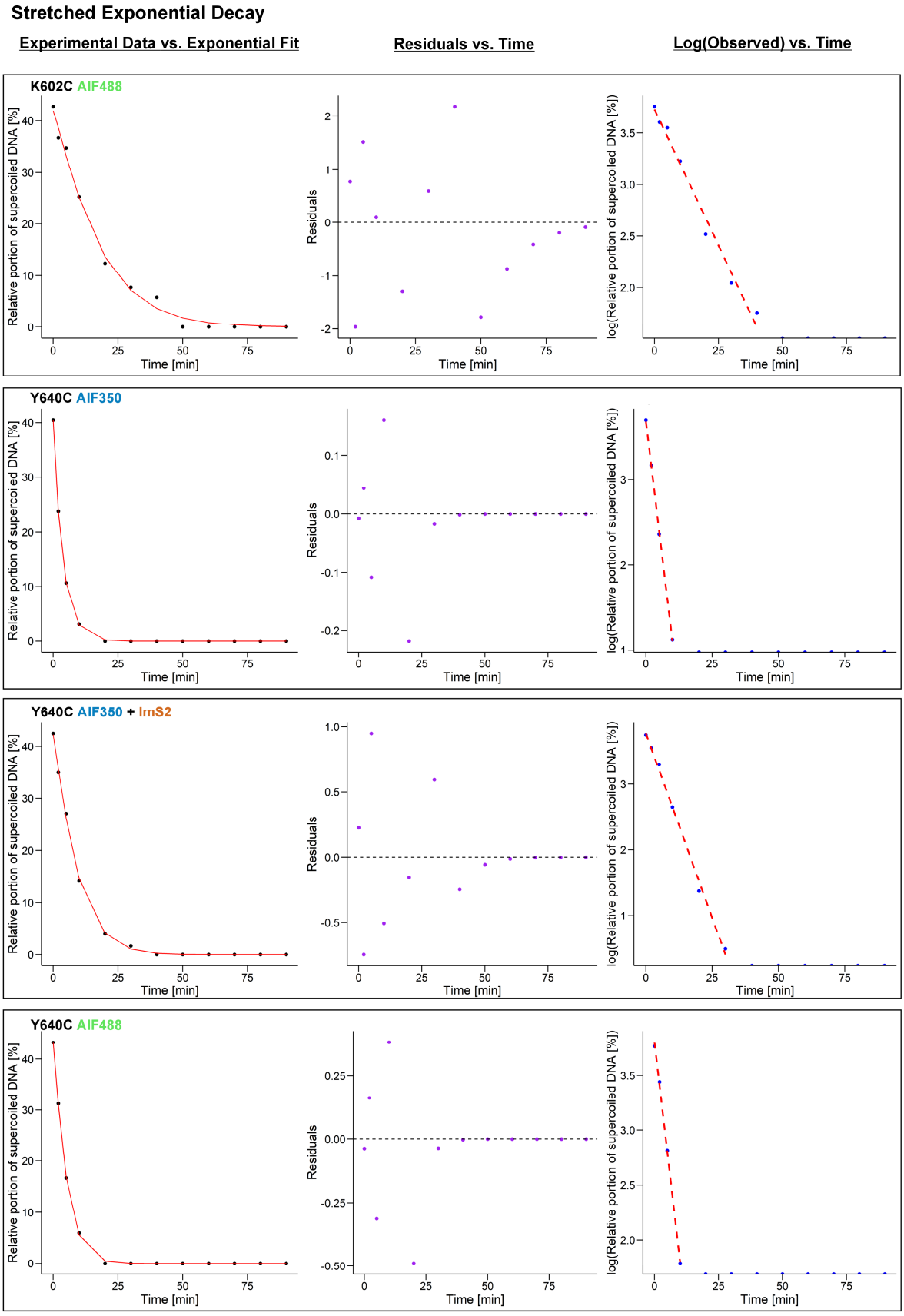


Figure IX.8 (continued).

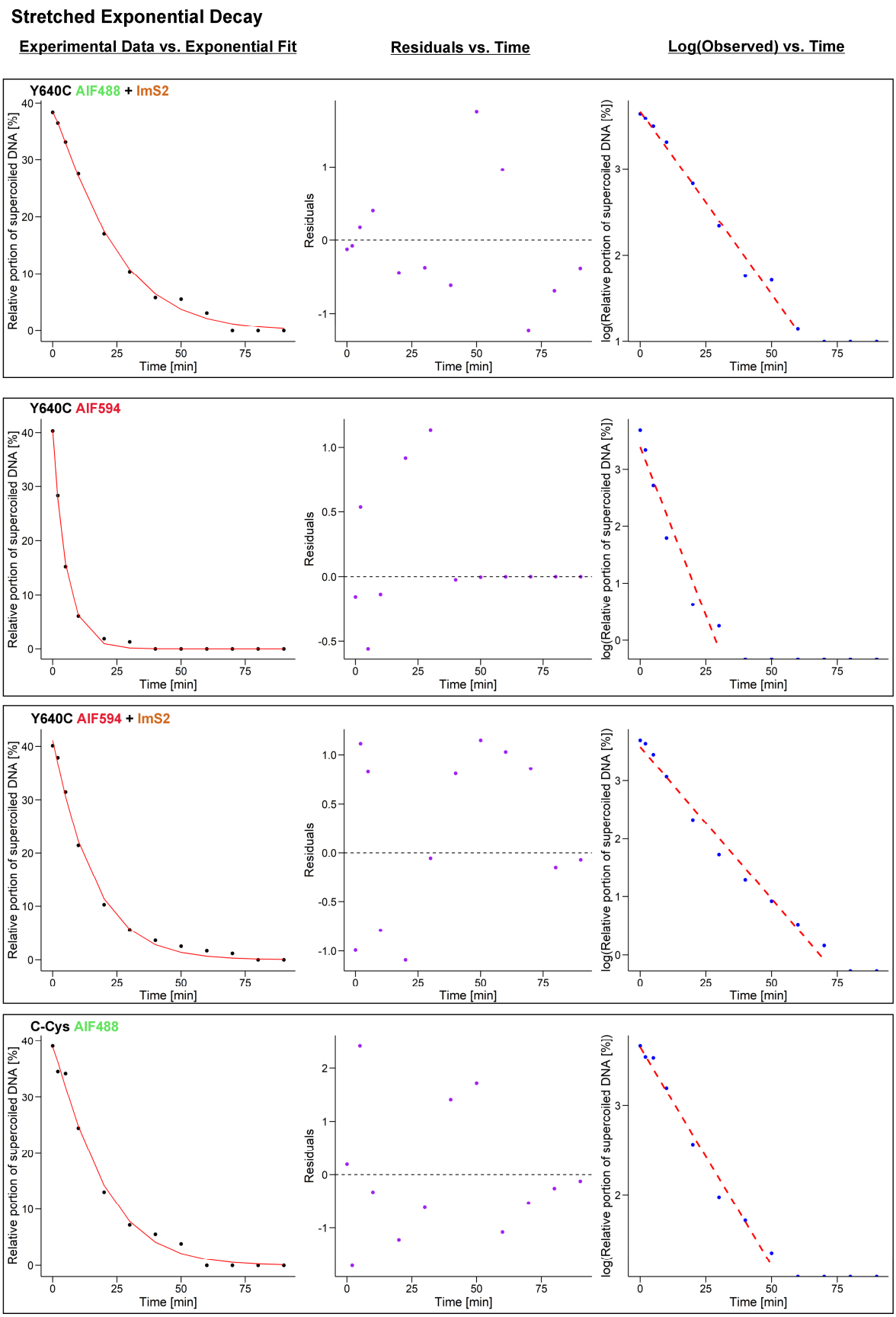


Figure IX.8 (continued).

IX.8.2 Linear Fitting and Half-Life Determination

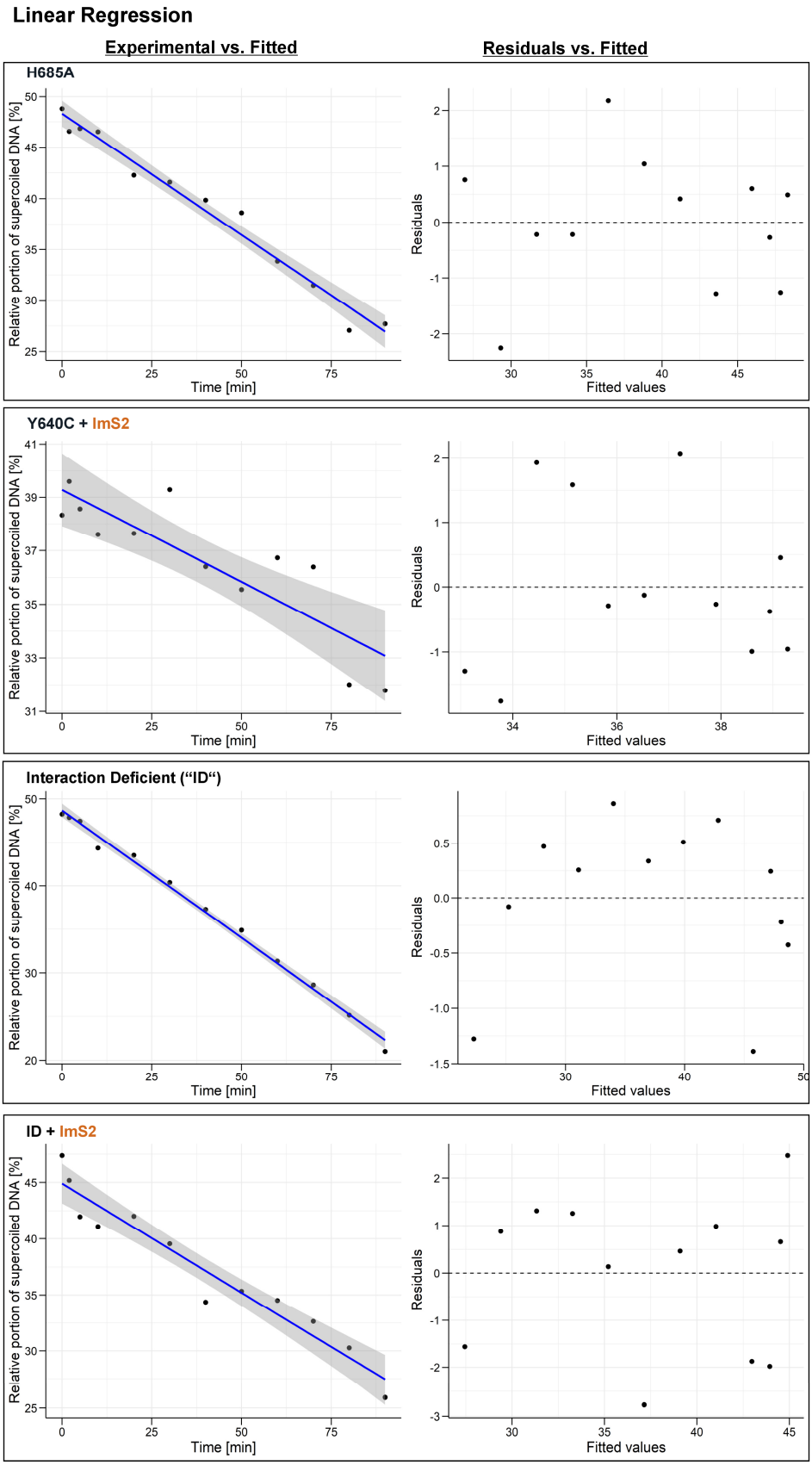


Figure IX.9. Linear regression analysis of supercoiled DNA in R for PyoS2 proteins with low DNase activity. **Left**: Experimental data points (relative portion of supercoiled DNA, from densitometric analysis) and linear regression curve with 95% confidence interval. **Right**: Residuals vs. fitted values. Parameters of fitted curves and supercoiled DNA half-lives are summarised in Table IX.6 (Supporting Information).

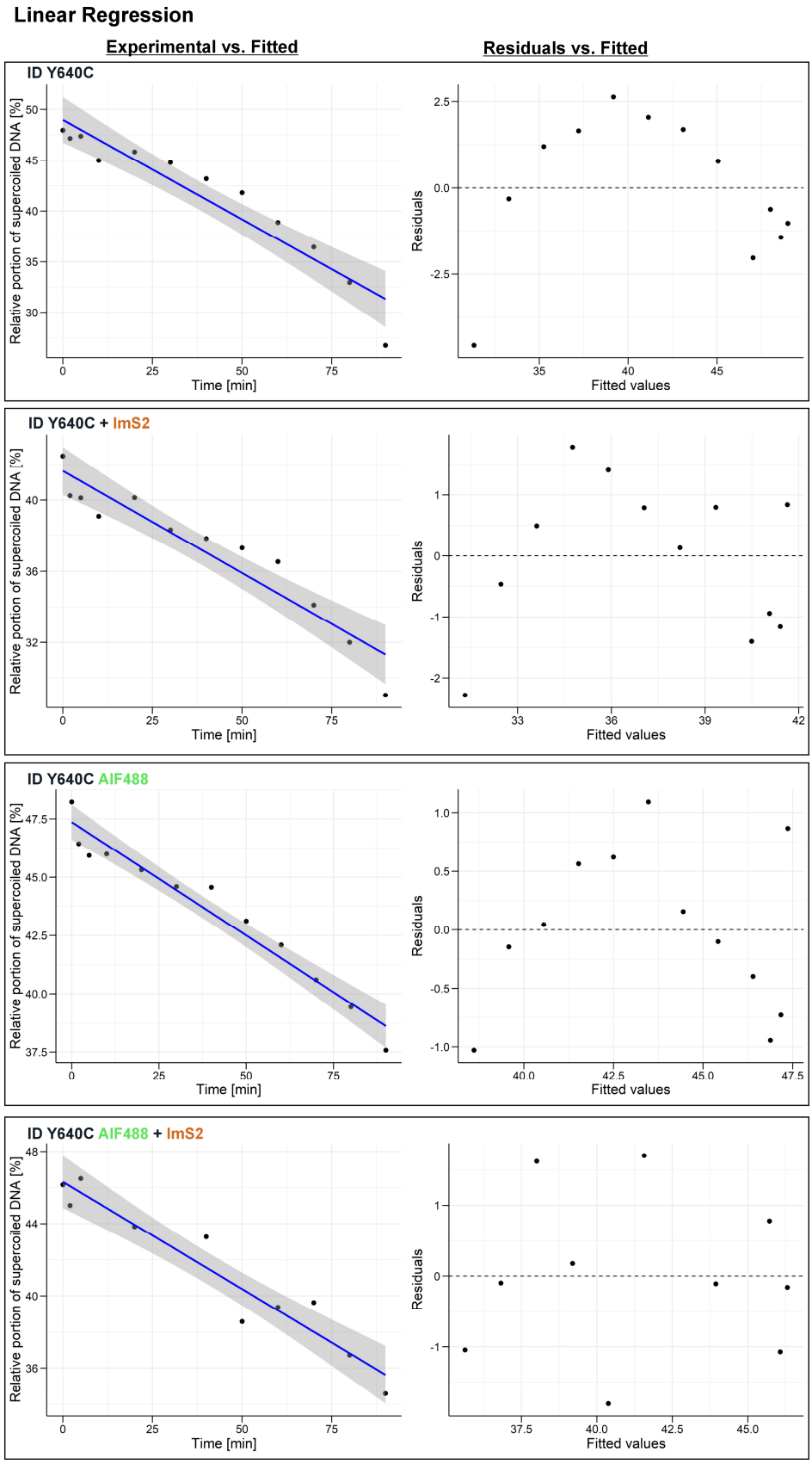


Figure IX.9 (continued).

IX.8.3 Permutation Analysis

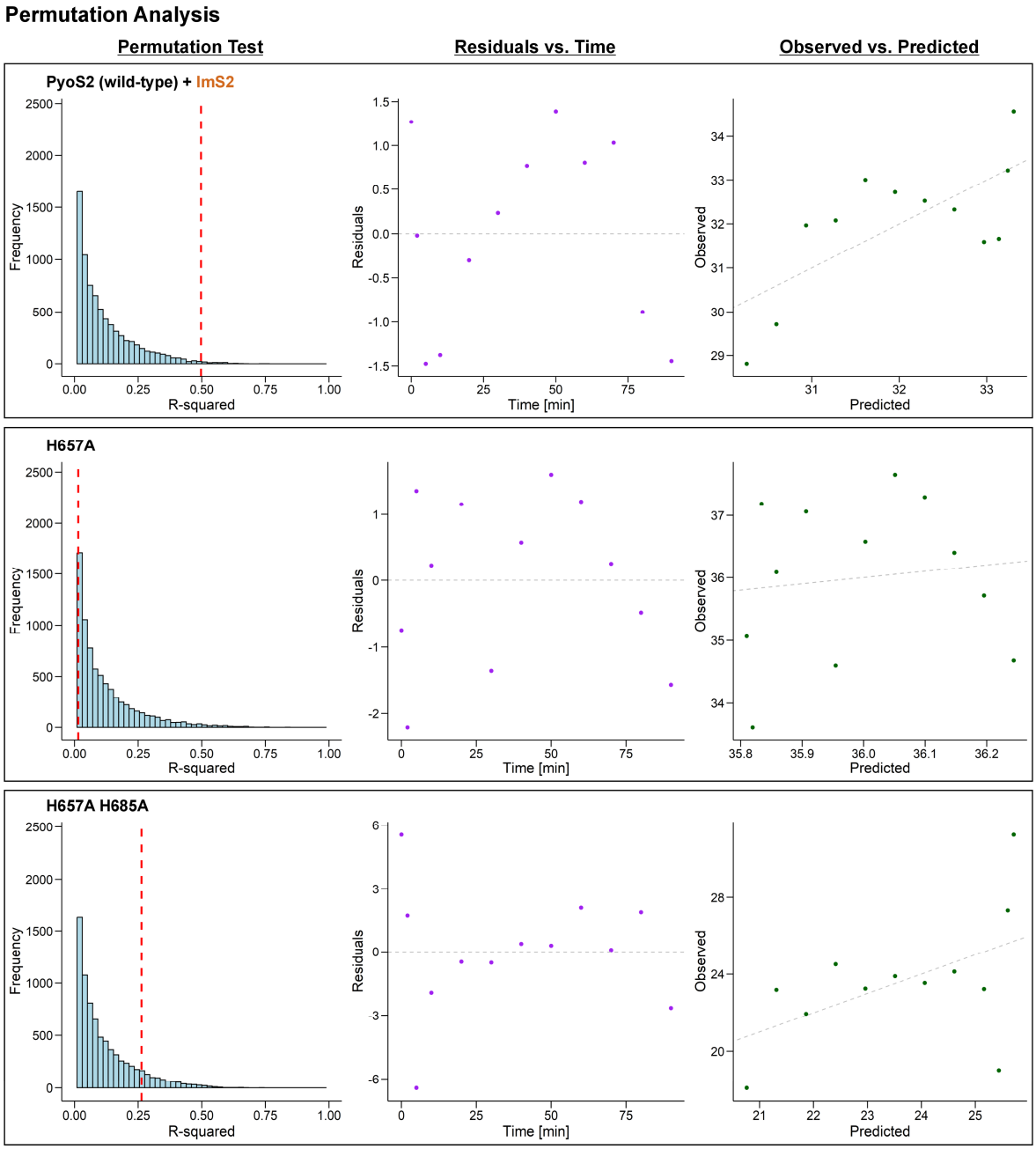


Figure IX.10. Permutation analysis of linear DNA increase for PyoS2 proteins with low DNase activity (is the increase significantly different from random noise?). **Left**: Histogram with plotted R^2 of 10,000 random permutations. The red dotted line highlights the R^2 of the experimental dataset. **Middle**: Plotted residuals of linear regression vs. time. **Right**: Observed vs. predicted DNA concentrations. Parameters of fitted curves are summarised in Table IX.7 (Supporting Information).

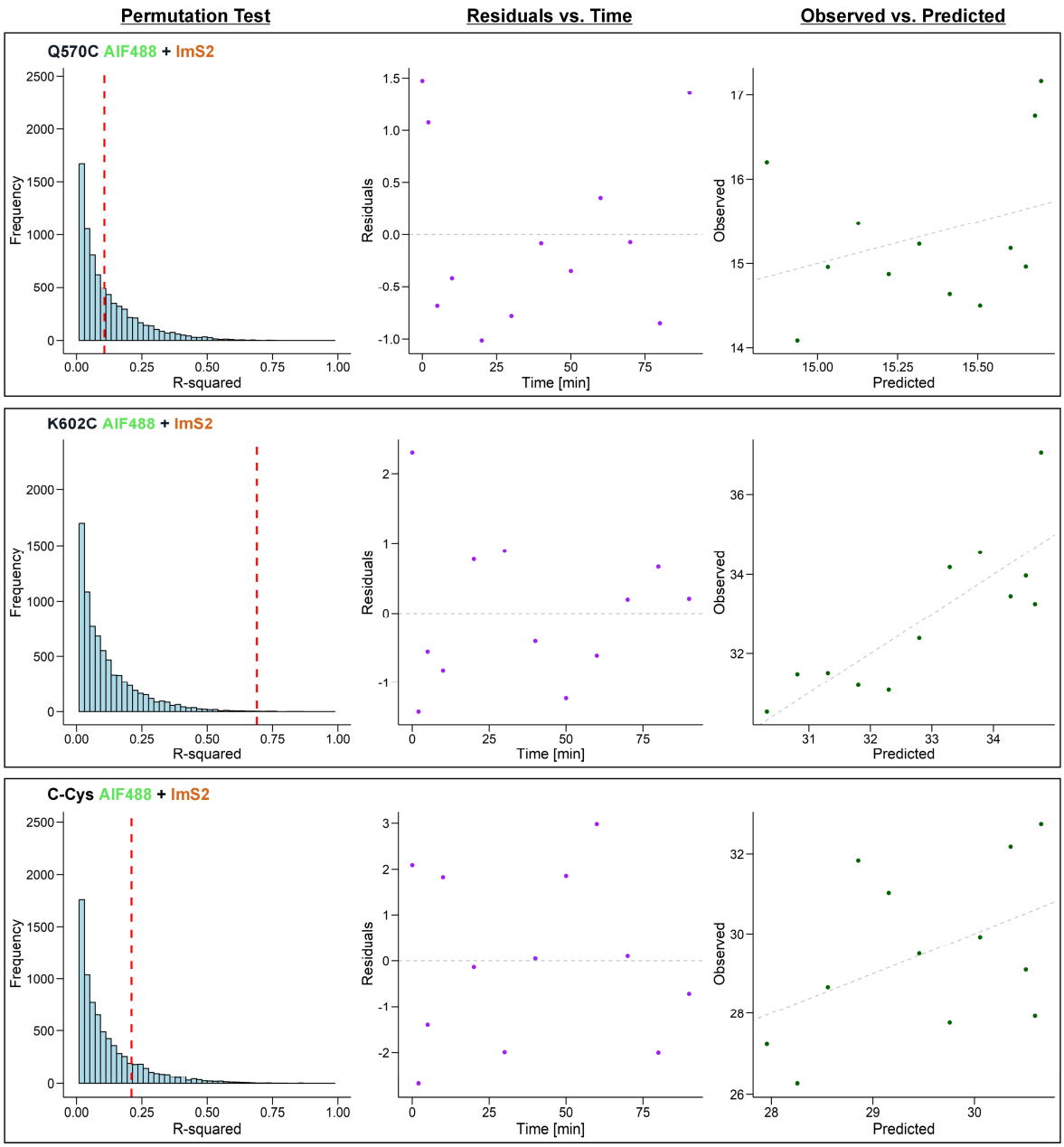


Figure IX.10 (continued).

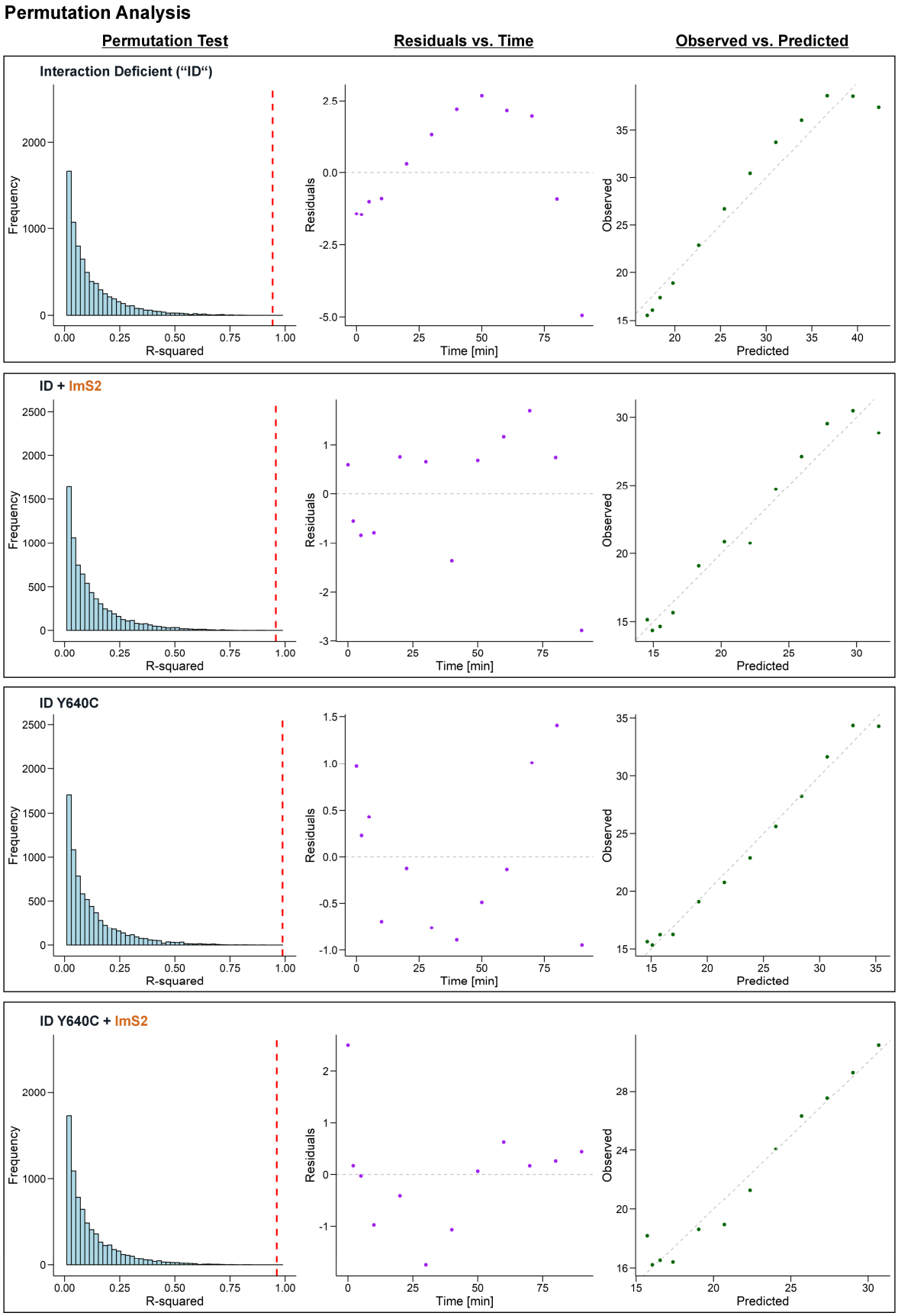


Figure IX.10 (continued).

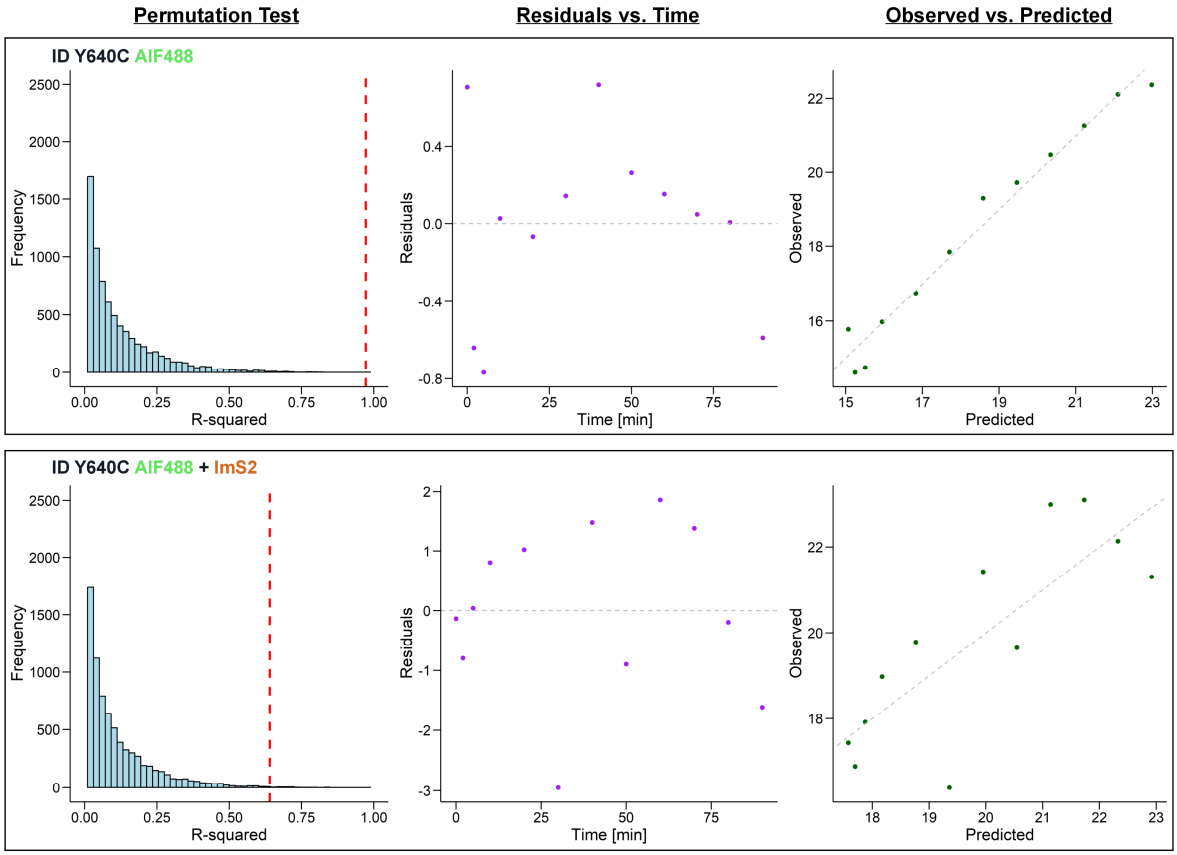


Figure IX.10 (continued).

IX.8.4 Fit Parameters

Table IX.5. Fit data of **supercoiled** DNA degradation by different variants and conjugates of PyoS2 with apparent exponential decline (very high DNase activity). Curves of relative supercoiled DNA portions from densitometric analysis were fitted to a stretched exponential decay function (equation V.7) for the following PyoS2 variants. Fits were generated with R.

		Exponential Decay – Fit Parameters												
Protein (PyoS2 variant)	**Immunity protein**	**y_0 [%]**	**y_0 (lower) [%]**	**y_0 (upper) [%]**	**k $[min]^{-1}$**	**k (lower) $[min]^{-1}$**	**k (upper) $[min]^{-1}$**	**b**	**b (lower)**	**b (upper)**	**R^2**	**RSE**	**Con-verged**	**$t_{1/2}$ [min]**
wild-type	–	43.14	39.90	46.36	0.26	0.22	0.30	1.46	1.04	NA	0.99	1.43	TRUE	3.20
Q570C AlF488	–	41.61	38.65	44.59	0.29	0.25	0.34	1.11	0.81	1.59	0.99	1.32	TRUE	2.65
K602C AlF488	–	42.04	39.35	44.87	0.06	0.05	0.06	1.13	0.95	1.38	0.99	1.40	TRUE	13.62
Y640C	–	41.21	39.83	42.63	0.05	0.05	0.06	1.68	1.47	1.93	1.00	0.83	TRUE	15.26
Y640C AlF350	–	40.46	40.24	40.68	0.27	0.26	0.27	0.99	0.97	1.01	1.00	0.10	TRUE	2.80
Y640C AlF350	+ImS2	42.25	41.18	43.32	0.11	0.10	0.11	1.14	1.05	1.24	1.00	0.50	TRUE	7.19
Y640C AlF488	–	43.36	42.83	43.89	0.19	0.18	0.19	1.13	1.09	1.18	1.00	0.24	TRUE	4.00
Y640C AlF488	+ImS2	38.53	36.96	40.17	0.04	0.04	0.04	1.17	1.04	1.32	1.00	0.89	TRUE	18.06
Y640C AlF594	–	40.46	39.22	41.71	0.19	0.18	0.20	0.99	0.89	1.11	1.00	0.56	TRUE	3.86
Y640C AlF594	+ImS2	41.12	39.22	43.07	0.06	0.06	0.07	1.06	0.94	1.22	1.00	0.97	TRUE	11.54
C-Cys AlF488	–	38.87	36.35	41.54	0.05	0.04	0.06	1.16	0.96	1.43	0.99	1.38	TRUE	15.11

Abbreviations: DNA_L – linear DNA form; DNA_S – supercoiled DNA form; NA – not available; RSE – residual standard error.

Table IX.6. Fit data of **supercoiled** DNA degradation by different variants and conjugates of PyoS2 with apparent linear decline (very low DNase activity). Curves of relative supercoiled DNA portions from densitometric analysis were fitted to a linear fit function (equation V.9) for the following PyoS2 variants. Fits were generated with R. A p-value <0.05 refers to the 95% confidence interval.

		Linear Regression – Fit Parameters								
Protein (PyoS2 variant)	**Immunity protein**	**Intercept y_0 [%]**	**Slope b [%/min]**	**R^2**	**Adjusted R^2**	**Std_error**	**t value**	**p value**	**F statistic**	**$t_{1/2}$ [min]**
H685A	–	48.32	–0.24	0.98	0.97	0.01	–20.04	2.11×10^{-9}	401.48	100.66
Y640C	+ImS2	39.28	–0.07	0.75	0.72	0.01	–5.46	2.79×10^{-4}	29.76	291.94
ID	–	48.69	–0.29	0.99	0.99	0.01	–40.76	1.89×10^{-12}	1661.65	83.73
ID	+ImS2	44.91	–0.19	0.93	0.93	0.02	–11.93	3.09×10^{-7}	142.29	109.37
ID Y640C	–	48.98	–0.20	0.90	0.89	0.02	–9.50	2.53×10^{-6}	90.31	127.47
ID Y640C	+ImS2	41.64	–0.11	0.90	0.89	0.01	–9.27	3.16×10^{-6}	86.00	177.89
ID Y640C AlF488	–	47.36	–0.10	0.95	0.95	0.01	–14.03	6.62×10^{-8}	196.95	239.00
ID Y640C AlF488	+ImS2	46.31	–0.12	0.92	0.91	0.01	–9.87	9.34×10^{-6}	97.46	195.87

Table IX.7. Permutation analysis of slow **linear** DNA accumulation in PyoS2 variants with putative (very low) DNase activity (is the slow increase in linear DNA statistically significantly different from random noise?). Permutations were performed in R (10,000 permutations) and R^2 calculated according to equation V.12. A p-value <0.05 refers to the 95% confidence interval.

		Permutation Analysis – Fit Parameters		
Protein (PyoS2 variant)	**Immunity protein**	**R^2**	**p value**	**Interpretation**
PyoS2 (wild-type)	+ImS2	0.50	7.70×10^{-3}	Moderate congruency between data and linear fit; statistically significant (**no** DNase activity)
H657A	–	0.015	0.70	Very low congruency between data and linear fit (**no** DNase activity)
H657A H685A	–	0.26	8.55×10^{-2}	Low congruency between data and linear fit; statistically significant (**no** DNase activity)
Q570C AlF488	+ImS2	0.11	0.30	Low congruency between data and linear fit; statistically not significant (**no** DNase activity)
K602C AlF488	+ImS2	0.69	1.40×10^{-3}	Moderate congruency between data and linear fit; statistically significant (**no** DNase activity)
C-Cys AlF488	+ImS2	0.21	0.13	Low congruency between data and linear fit; statistically not significant (**no** DNase activity)
ID	–	0.94	0	Very high congruency between data and linear fit; statistically significant (**low** DNase activity)
ID	+ImS2	0.96	0	Very high congruency between data and linear fit; statistically significant (**low** DNase activity)
ID Y640C	–	0.99	0	Very high congruency between data and linear fit; statistically significant (**low** DNase activity)
ID Y640C	+ImS2	0.96	0	Very high congruency between data and linear fit; statistically significant (**low** DNase activity)
ID Y640C AlF488	–	0.97	0	Very high congruency between data and linear fit; statistically significant (**low** DNase activity)
ID Y640C AlF488	+ImS2	0.64	2.70×10^{-3}	Moderate congruency between data and linear fit; statistically significant (**unclear status***)

* From the 15 h DNase activity measurement, it is already known that PyoS2 ID Y640C-AlF488 remains catalytically active in the presence of ImS2.

Table IX.8. Relative increase and decrease of supercoiled and linear DNA in plasmid nicking assay after 90 min reaction time. Relative changes were calculated from relative DNA (DNA form of interest relative to the sum of all DNA forms) portions at 0 min and past 90 min incubation. A relative change of –100% refers to complete conversion for both species. Since supercoiled DNA is converted to linear DNA, the linear DNA form initially increases. Only for PyoS2 variants with high DNase activity does the linear DNA drop to levels lower than at t = 0 min. Numbers in parentheses in the format (t_0/t_{90}) indicate relative percentages of DNA forms at t = 0 min and t = 90 min.[a]

		Relative Change				Relative Change	
Protein (PyoS2 variant)	**Immunity protein**	**$DNA_{supercoiled}$ [%]**	**DNA_{linear} [%]**	**Protein (PyoS2 variant)**	**Immunity protein**	**$DNA_{supercoiled}$ [%]**	**DNA_{linear} [%]**
PyoS2 (wild-type)	–	–100 (42.5/0)	–100 (36.0/0)	Y640C	–	–100 (40.6/0)	+54.0 (48.5/74.6)
PyoS2 (wild-type)	+ImS2	no conversion		Y640C	+ImS2	–17.1 (38.3/31.8)	+3.13 (51.4/53.0)
H657A	–	no conversion		Y640C AlF350	–	–100 (40.5/0)	+39.6 (48.5/67.7)
H685A	–	–43.2 (48.8/27.7)	+85.1 (32.2/59.6)	Y640C AlF350	+ImS2	–100 (42.5/0)	+47.2 (46.5/68.5)
H657A H685A	–	no conversion		Y640C AlF594	–	–100 (40.3/0)	+39.6 (47.9/66.8)
Q570C AlF488	–	–100 (41.4/0)	–35.0 (17.2/11.2)	Y640C AlF594	+ImS2	–100 (40.1/0)	+52.7 (49.3/75.3)
Q570C AlF488	+ImS2	no conversion		ID	–	–56.5 (48.3/21.0)	+140 (15.6/37.4)
K602C AlF488	–	–100 (42.8/0)	+84.5 (35.7/65.9)	ID	+ImS2	–45.4 (47.4/25.9)	+90.4 (15.2/28.8)
K602C AlF488	+ImS2	no conversion		ID Y640C	–	–44.2 (48.0/26.8)	+120 (15.6/34.3)
Y640C AlF488	–	–100 (43.3/0)	+169 (33.6/90.4)	ID Y640C	+ImS2	–31.6 (42.5/29.0)	+108 (18.2/31.1)
Y640C AlF488	+ImS2	–100 (38.4/0)	+83.6 (41.1/75.4)	ID Y640C AlF488	–	–22.1 (48.2/37.6)	+41.9 (15.8/22.4)
C-Cys AlF488	–	–100 (39.1/0)	+101 (34.6/69.5)	ID Y640C AlF488	+ImS2	–25.1 (46.2/34.6)	+22.1 (17.4/21.3)
C-Cys AlF488	+ImS2	no conversion					

[a] The absolute value of the relative change of supercoiled DNA equals the conversion of this particular DNA form (e.g. –100% relative change equals 100% conversion). However, this is not applicable to linear DNA, as this species increases due to the cleavage of supercoiled DNA and decreases due to the unspecific cleavage of linear DNA into smaller fragments at the same time. Therefore, quantitative conclusions from relative changes in linear DNA should only be made in connection with the respective datasets (Figure IV.15, Figure IV.19, Figure IV.21, and Figure IV.24).

IX.9 *P. aeruginosa* Strain Collection

Table IX.9. List of 113 MDR clinical isolates of *P. aeruginosa* tested by multiplex-PCR for *fpvA* subtypes and *pyoS2* genotype. Positive results for *fpvAI*, *fpvAII*, *fpvAIII*, unknown subtypes, and *pyoS2_imS2*$^{+}$ genotypes are indicated in the isolate No. column.

Isolate No.	Resistance Gene	Date of Isolation	Origin of Specimen	Isolate No.	Resistance Gene	Date of Isolation	Origin of Specimen
M0	GIM-1	2002-03-01	tracheal secretion	M127	VIM-2	2014-09-03	scr. anal
M1	GIM-1	2007-12-09	tracheal secretion	M128	VIM-2	2014-09-16	stool
M2	GIM-1	2008-01-18	stool	M132	VIM-2	2014-10-23	tracheal secretion
M3	GIM-1	2008-04-15	tracheal secretion	M134	VIM-2	2015-11-13	drainage aspiration
M4	GIM-1	2008-04-13	urine	M138	VIM-2	2014-12-22	scr. anal
M5	GIM-1	2008-06-04	tracheal secretion	M139	VIM-2	2015-02-25	tracheal secretion
M7	GIM-1	2008-09-14	tracheal secretion	M142	GIM-1	2015-04-21	nasopharyngeal scr.
M8	GIM-1	2008-09-22	tracheal secretion	M143	GIM-1	2015-04-22	sputum
M10	GIM-1	2008-10-10	stool	M144	VIM-2	2015-05-19	nasopharyngeal scr.
M16	GIM-1	2010-02-07	tracheal secretion	M145	GIM-1	2015-06-03	stool
M19	GIM-1	2007-10-10	wound swab	M146	GIM-1	2015-07-06	stool
M25	GIM-1	2010-02-23	urine	M147	VIM-2	2015-07-08	tracheal secretion
M28	GIM-1	2010-05-10	urine	M149	GIM-1	2015-08-11	urine
M29	GIM-1	2010-05-11	tracheal secretion	M150	GIM-1	2015-08-18	tracheal secretion
M45	GIM-1	2010-11-07	tracheal secretion	M151	GIM-1	2015-08-17	nasopharyngeal scr.
M46	GIM-1	2010-12-07	tracheal secretion	M152	GIM-1	2015-09-01	nasopharyngeal scr.
M47	GIM-1	2010-12-09	urine	M159	GIM-1	2015-10-28	urine
M48	GIM-1	2011-03-30	wound swab	M165	VIM-2	2015-12-29	tracheal secretion
M49	GIM-1	2011-05-31	tracheal secretion	M166	GIM-1	2016-01-04	stool
M50	GIM-1	2011-06-16	urine	M171	GES	2016-01-28	catheter stent
M51	GIM-1	2011-06-19	tracheal secretion	M174	GES	2016-03-23	wound swab
M52	GIM-1	2011-06-21	tracheal secretion	M182	GIM-1	2016-07-07	drainage secretion
M53	GIM-1	2011-06-21	tracheal secretion	M189	GIM-1	2016-10-07	abdominal swab
M55	GIM-1	2011-07-03	bronchoalveolar lavage	M190	none	2016-10-25	tracheal secretion
M57	GIM-1	2011-04-05	tracheal secretion	M191	GIM-1	2016-10-25	nasopharyngeal scr.
M58	GIM-1	2011-09-26	wound swab	M195	VIM-2	2017-01-10	brain tissue
M59	VIM-2	2011-10-10	tracheal secretion	M199	GIM-1	2017-02-22	urine
M63	GIM-1	2011-12-25	tracheal secretion	M206	VIM-2	2017-04-09	scr. pharynx
M64	GIM-1	2012-01-23	wound swab	M207	VIM-2	2017-04-09	tracheal secretion
M67	GIM-1	2012-03-16	wound swab	M208	VIM-2	2017-08-18	tracheal secretion
M68	GIM-1	2012-03-19	urine	M209	GIM-1	2017-08-18	tissue
M69	GIM-1	2012-04-02	wound swab	M210	GIM-1	2017-09-25	tracheal secretion
M70	GIM-1	2012-05-07	tracheal secretion	M214	GIM-1	2017-10-24	catheter urine
M71	GIM-1	2012-05-21	pleural aspirate	M219	VIM-2	2017-12-04	swab
M72	GIM-1	2012-06-04	central venous catheter	M224	GIM-1	2018-05-08	sputum
M74	VIM-1	2012-08-22	swab	M228	VIM-2	2018-09-12	scr. axilla/inguinal region
M78	VIM-2	2013-02-01	urine	M230	VIM-2	2018-09-19	swab
M81	GIM-1	2013-03-18	urine	M238	GIM-1	2018-10-31	bronchial secretion
M88	GIM-1	2013-05-19	tracheal secretion	M249	GIM-1	2019-01-23	blood culture
M91	VIM-2	2013-07-12	urine	M259	VIM-2	2019-03-13	central venous catheter
M98	VIM-2	2013-09-30	tracheal swab	M263	VIM-2	2019-06-11	blood culture
M100	VIM-2	2013-10-25	urine	M273	GIM-1	2019-09-12	peritoneal swab
M103	VIM-2	2013-11-15	central venous catheter	M283	GIM-1	2019-10-29	rectal swab
M105	IMP-15	2013-12-06	bronchial secretion	M287	VIM-2	2019-11-28	tracheal secretion
M106	VIM-2	2014-01-10	urethra	M292	VIM-2	2020-01-09	urinary catheter
M108	VIM-2	2014-02-27	stool	M294	GIM-1	2020-01-16	swab anal
M119	GIM-1	2014-07-08	scr. anal	M303	none	2020-03-05	axilla/inguinal swab
M120	GIM-1	2014-07-09	tracheal secretion	M304	GIM-1	2020-03-05	axilla/inguinal swab
M123	GIM-1	2014-07-31	sputum	M305	GES	2020-03-26	urine
M126	VIM-2	2014-08-13	urine	M307	GIM-1	2020-04-09	axilla/inguinal swab

Table IX.9 (continued).

Isolate No.	Resistance Gene	Date of Isolation	Origin of Specimen	Isolate No.	Resistance Gene	Date of Isolation	Origin of Specimen
M313	VIM-2	2020-06-24	axilla/inguinal swab	M325	VIM-2	2020-09-09	urine
M314	GIM-1	2020-06-24	tracheal secretion	M326	GIM-1	2020-09-09	rectal swab
M315	GIM-1	2020-07-13	tracheal secretion	M328	GIM-1	2020-09-30	stool
M320	VIM-2	2020-08-06	axilla/inguinal swab	M331	GIM-1	2020-11-05	unknown
M322	VIM-2	2020-08-12	blood culture	M334	VIM-2	2020-11-25	nasopharyngeal swab
M323	GIM-1	2020-08-26	rectal swab	M335	VIM-2	2020-12-02	axilla/inguinal swab
M324	GIM-1	2020-09-09	intra-operative swab				

Abbreviations: scr – screening; GIM-1 – German imipenemase 1; VIM-1 – Verona integron-encoded metallo-β-lactamase 1; VIM-2 – Verona integron-encoded metallo-β-lactamase 2; GES – Guiana extended-spectrum β-lactamase; IMP-15 – Imipenemase 15.

IX.10 FpvA Siderovars and *pyoS2* Genotypes of MDR *P. aeruginosa* Isolates

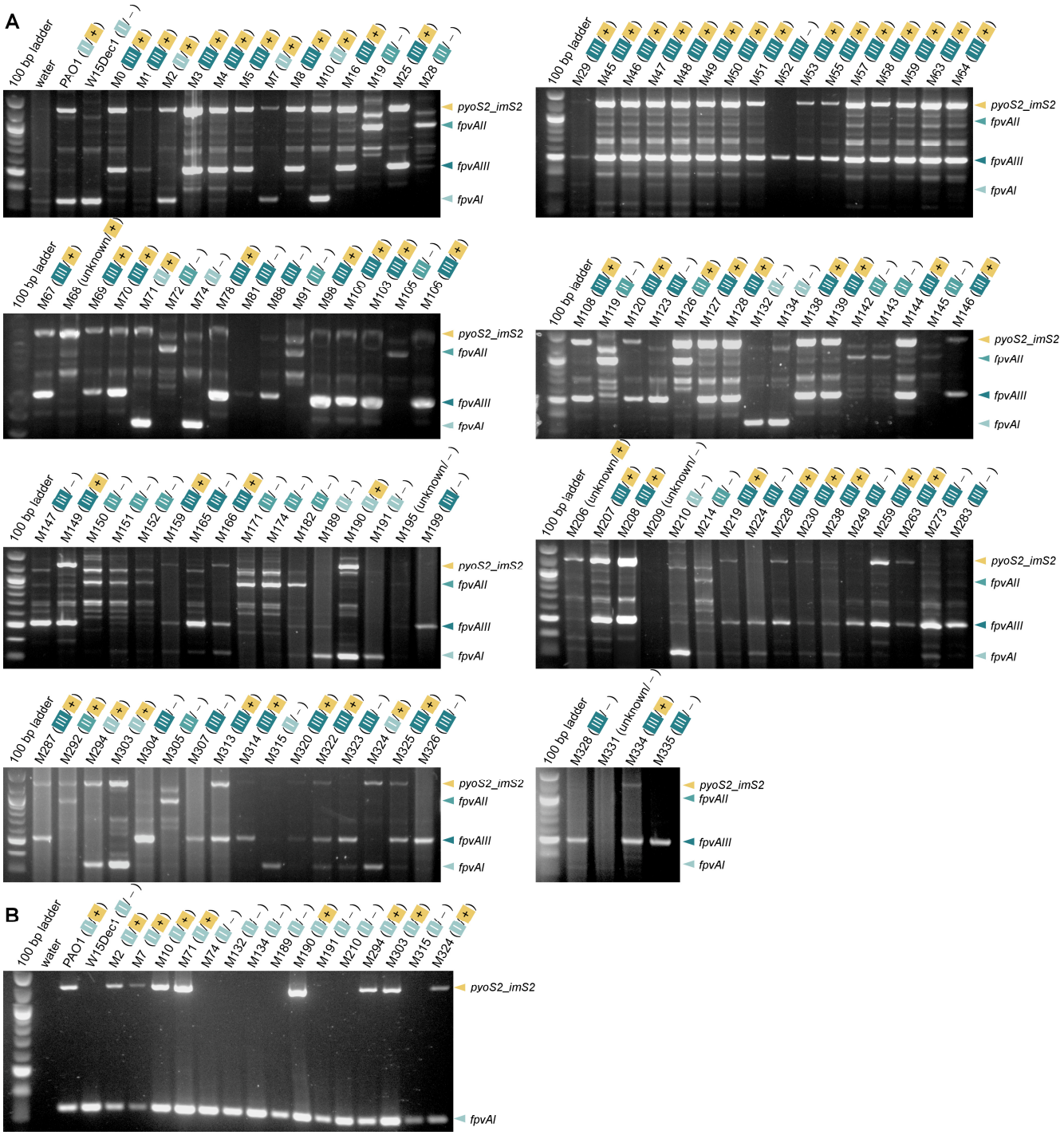


Figure IX.11. Multiplex PCR typing of CRPsA isolates for determining the *fpvA* siderovar and identifying PyoS2 producers. **A**. Agarose gels from multiplex PCR of CRPsA strains from the University Hospital Düsseldorf for detecting amplicons for *fpvAI* (326 bp), *fpvAII* (897 bp), *fpvAIII* (506 bp), and *pyoS2_imS2* (1223 bp) simultaneously. **B**. Agarose gels from duplex PCR of apparently *fpvAI*-positive strains with the primer pairs FpvAI-F/R and PyoS2_ImS2-F/R (CRPsA core strain collection). The Quick-Load 100 bp DNA ladder (New England Biolabs) is used as a size reference. The identified *fpvA* siderovar for every individual strain is indicated by the corresponding number (I, II, or III), followed by the *pyoS2_imS2* genotype [producer (+) or non-producer (–)].

IX.11 Antibiotic Susceptibility of CRPsA Isolates with *fpvAI* Genotype

Table IX.10. Control strains (PAO1 and W15Dec1) and core list of MDR clinical isolates of *P. aeruginosa* with *fpvAI* genotype tested against common antibiotics. The minimal inhibitory concentrations (MIC) are given in µg/mL. Strains were either classified according to EUCAST as sensitive (S), resistant (R), resistant with technical uncertainty (*R), insufficient evidence (IE), or sensitive with increased exposure (I).

Strain/ Isolate No.	MBL Resistance Gene	Antibiotic Resistance – MIC [µg/mL]										
		PIP	PPT	CAZ	CPM	AZT	IPM	MEM	AMI	GEN	TOB	CIP
PAO1	none	<4 (I)	8 (I)	2 (I)	2 (I)	4 (I)	2 (I)	1 (S)	4 (S)	<1 (IE)	<1 (S)	0.5 (I)
W15Dec1	none	8 (*R)	16 (*R)	32 (R)	16 (R)	4 (R*)	2 (I)	<0.25 (S)	4 (S)	2 (IE)	>1 (S)	0.25 (I)
M2	GIM-1	>128 (R)	>128 (R)	>64 (R)	>32 (R)	8 (I)	>16 (R)	>16 (R)	4 (S)	>16 (IE)	>16 (R)	>4 (R)
M7	GIM-1	>128 (R)	>128 (R)	>64 (R)	>32 (R)	16 (*R)	>16 (R)	>16 (R)	8 (S)	>16 (IE)	>16 (R)	>4 (R)
M10	GIM-1	>128 (R)	>128 (R)	>64 (R)	>32 (R)	32 (R)	>16 (R)	>16 (R)	8 (S)	>16 (IE)	>16 (R)	>4 (R)
M71	GIM-1	>128 (R)	>128 (R)	>64 (R)	>32 (R)	8 (I)	>16 (R)	>16 (R)	4 (S)	>16 (IE)	>16 (R)	>4 (R)
M74	VIM-1	>128 (R)	>128 (R)	>64 (R)	>32 (R)	4 (I)	>16 (R)	>16 (R)	8 (S)	>16 (IE)	>16 (R)	0.25 (I)
M132	VIM-2	>128 (R)	>128 (R)	>64 (R)	>32 (R)	8 (I)	>16 (R)	>16 (R)	4 (S)	>16 (IE)	>16 (R)	>4 (R)
M134	VIM-2	>128 (R)	>128 (R)	>64 (R)	>32 (R)	16 (*R)	>16 (R)	8 (I)	2 (S)	>16 (IE)	>16 (R)	0.5 (I)
M189	GIM-1	>128 (R)	>128 (R)	>64 (R)	16 (R)	4 (*R)	>16 (R)	>16 (R)	2 (S)	8 (IE)	>16 (R)	>4 (R)
M190	none	>128 (R)	>128 (R)	32 (R)	16 (R)	16 (*R)	>16 (R)	8 (I)	8 (S)	4 (IE)	<1 (S)	>4 (R)
M191	GIM-1	>128 (R)	>128 (R)	>64 (R)	16 (R)	16 (*R)	>16 (R)	>16 (R)	2 (S)	>16 (IE)	>16 (R)	>4 (R)
M210	GIM-1	>128 (R)	>128 (R)	>64 (R)	>32 (R)	32 (R)	>16 (R)	>16 (R)	4 (S)	>16 (IE)	>16 (R)	>4 (R)
M294	GIM-1	>128 (R)	>128 (R)	>64 (R)	>32 (R)	>64 (R)	>16 (R)	>16 (R)	4 (S)	>16 (IE)	>16 (R)	>4 (R)
M303	none	>128 (R)	>128 (R)	>64 (R)	16 (R)	16 (*R)	>16 (R)	>16 (R)	2 (S)	<1 (IE)	<1 (S)	0.25 (I)
M315	GIM-1	>128 (R)	>128 (R)	>64 (R)	16 (R)	16 (*R)	>16 (R)	>16 (R)	4 (S)	>16 (IE)	>16 (R)	>4 (R)
M324	GIM-1	>128 (R)	>128 (R)	>64 (R)	>32 (R)	>64 (R)	>16 (R)	>16 (R)	4 (S)	>16 (IE)	>16 (R)	>4 (R)

Abbreviations for antibiotics: AMI – Amikacin; AZT – Aztreonam; CAZ – Ceftazidime; CIP – Ciprofloxacin; CPM – Cefepime; GEN – Gentamicin; IPM – Imipenem; MEM – Meropenem; PIP – Piperacillin; PPT – Piperacillin/tazobactam; TOB – Tobramycin. Abbreviations for resistance genes: GIM-1 – German imipenemase 1; VIM-1 – Verona integron-encoded metallo-β-lactamase 1; VIM-2 – Verona integron-encoded metallo-β- lactamase 2.

IX.12 Genetic Determinants of CRPsA Isolates with *fpvAI* Genotype

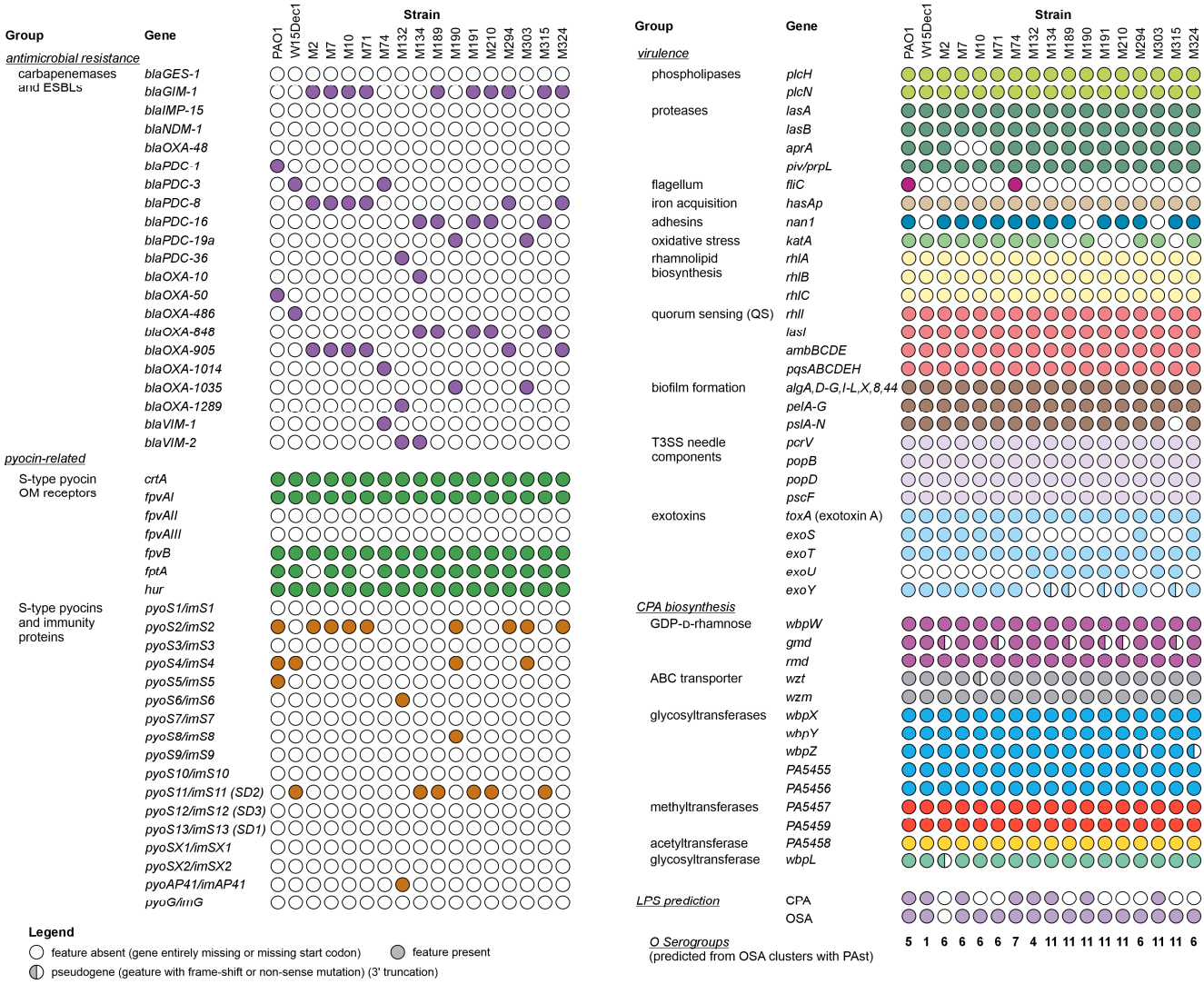


Figure IX.12. Visualisation of genetic determinants for virulence, antibiotic resistance, and pyocin biosynthesis in CRPsA isolates from the core strain collection. The annotated genomes of CRPsA isolates were blasted (tBLASTn) against reference sequences from *P. aeruginosa* strains deposited in the NCBI database.

IX.13 Mass Spectrometry Data of PyoS2-Prodigiosin Conjugates

The lack of reliable extinction coefficients for mixed species of protonated and deprotonated prodiginines and the exerted influence of the protein microenvironment on the protonation state of the prodigiosin scaffold in PyoS2-prodigiosin conjugates required other methods to verify the labelling. For this reason, mass spectrometry was used to detect the masses of PyoS2-prodigiosin conjugates after removal of excess labelling reagent (Table IX.11). Again, as seen before from the varying colouration of the conjugates, several prodigiosin species and their corresponding masses (free base, protonated but without Cl^- anion, HCl salt) were detected. Although this LC-MS-based method does not estimate the labelling efficiency and the proportion of labelled and unlabelled protein, it does verify the successful conjugation of prodigiosin maleimides **III-169**, **III-170**, and **III-171** to the PyoS2 cysteine mutants via thiol-Michael reaction.

Table IX.11. Mass spectrometric analysis of PyoS2-prodigiosin conjugates.

Protein Conjugates	Label	Average Mass[a],[b] [calc.]	Mass [detect.]	SD
PyoS2 Q570C conjugate	A-Ring maleimide (**III-169**)	74338.44[e]	74337.71	0.98
PyoS2 Q570C conjugate	B-Ring maleimide (**III-170**)	74416.98[c]	74420.01	6.61
PyoS2 Q570C conjugate	C-Ring maleimide (**III-171**)	74353.47[d]	74355.05	3.43
PyoS2 Q570C **H657A H685A** conjugate	A-Ring maleimide (**III-169**)	74207.33[d]	74207.60	3.25
PyoS2 Q570C **H657A H685A** conjugate	B-Ring maleimide (**III-170**)	74249.41[d]	74249.65	4.20
PyoS2 Q570C **H657A H685A** conjugate	C-Ring maleimide (**III-171**)	74220.35[e]	74219.42	2.09
PyoS2 K602C conjugate	A-Ring maleimide (**III-169**)	74339.41[d]	74341.38	3.66
PyoS2 K602C conjugate	B-Ring maleimide (**III-170**)	74381.50[d]	74382.10	3.56
PyoS2 K602C conjugate	C-Ring maleimide (**III-171**)	74353.43[d]	74355.50	4.27
PyoS2 K602C **H657A H685A** conjugate	A-Ring maleimide (**III-169**)	74207.29[d]	74207.40	2.56
PyoS2 K602C **H657A H685A** conjugate	B-Ring maleimide (**III-170**)	74248.36[e]	74248.36	2.94
PyoS2 K602C **H657A H685A** conjugate	C-Ring maleimide (**III-171**)	74221.31[d]	74222.80	2.45
PyoS2 Y640C conjugate	A-Ring maleimide (**III-169**)	74303.40[e]	74301.59	1.89
PyoS2 Y640C conjugate	B-Ring maleimide (**III-170**)	74346.49[d]	74348.28	3.97
PyoS2 Y640C conjugate	C-Ring maleimide (**III-171**)	74353.88[c]	74355.20	5.27
PyoS2 Y640C **H657A H685A** conjugate	A-Ring maleimide (**III-169**)	74171.27[e]	74170.92	4.45
PyoS2 Y640C **H657A H685A** conjugate	B-Ring maleimide (**III-170**)	74214.36[d]	74215.47	1.92
PyoS2 Y640C **H657A H685A** conjugate	C-Ring maleimide (**III-171**)	74186.30[d]	74187.35	2.55
PyoS2 C-Cys conjugate	A-Ring maleimide (**III-169**)	744667.58[d]	74467.60	2.12
PyoS2 C-Cys conjugate	B-Ring maleimide (**III-170**)	74508.65[e]	74508.06	1.54
PyoS2 C-Cys conjugate	C-Ring maleimide (**III-171**)	74480.60[e]	74480.02	2.01
PyoS2 **H657A H685A** C-Cys conjugate	A-Ring maleimide (**III-169**)	74335.46[d]	74335.19	3.24
PyoS2 **H657A H685A** C-Cys conjugate	B-Ring maleimide (**III-170**)	74412.99[c]	74412.32	5.83
PyoS2 **H657A H685A** C-Cys conjugate	C-Ring maleimide (**III-171**)	74349.48[d]	74349.37	4.67

[a] All proteins and masses were calculated and detected with the initial methionine missing; [b] For PyoS2 conjugates, the average mass was calculated from the sum of the PyoS2 molecular weight (without initial methionine) and masses of the prodigiosin maleimides **III-169**, **III-170**, and **III-171**; [c] Protein + prodigiosin HCl salt; [d] Protein + protonated prodigiosin (no counter ion); [e] Protein + prodigiosin (free base). Abbreviation: SD – standard deviation.

IX.14 SDS Gels of PyoS2-Prodigiosin Conjugates

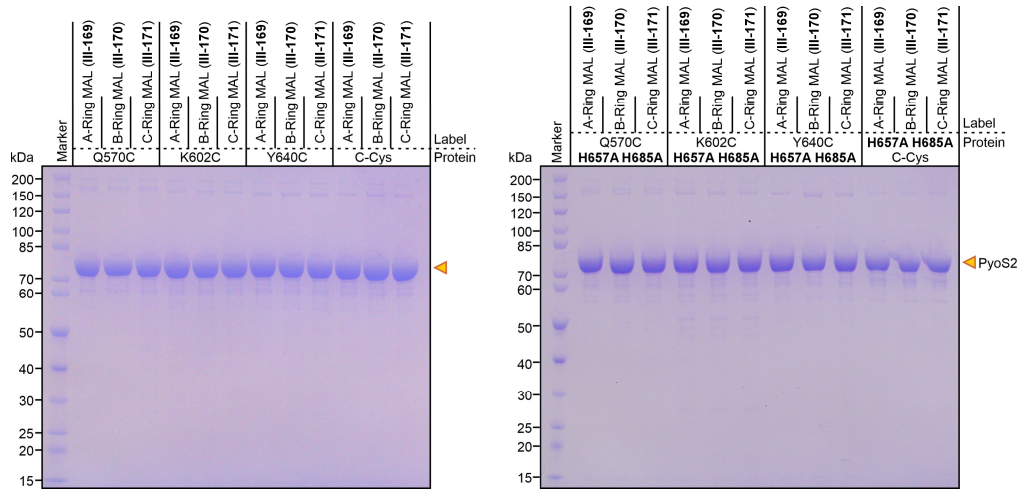


Figure IX.13. SDS gel of PyoS2-prodigiosin conjugates. Proteins are labelled with the maleimide-functionalised prodiginines **III-169**, **III-170**, and **III-171**. 2 µg of PyoS2 conjugates were loaded per well. Protein size: PyoS2 – 74 kDa (wild-type). Abbreviation: MAL – maleimide.

IX.15 Absorption Spectra of Prodiginine Maleimides

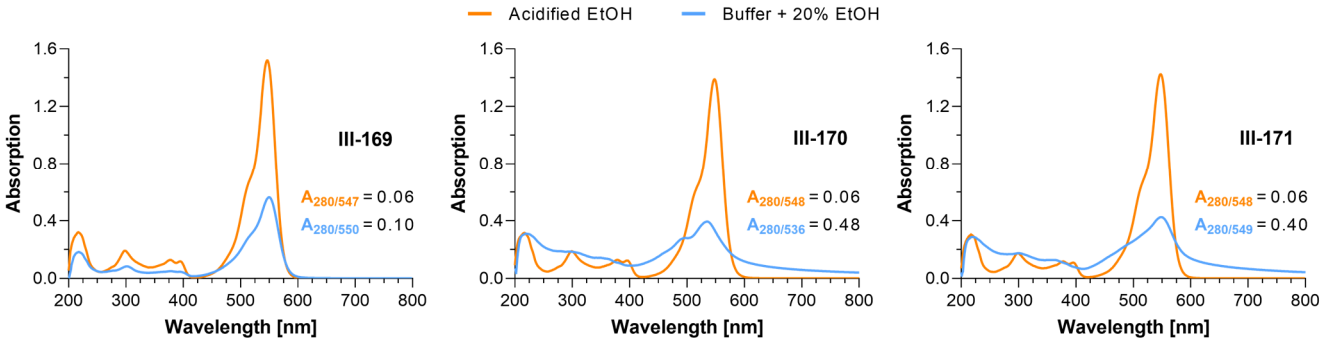


Figure IX.14. Absorption spectra of prodigiosin maleimides in acidified EtOH or buffer with 20% EtOH as co-solvent. Spectra were recorded from 10 µM solutions of prodigiosin maleimides (**III-169·HCl**, **III-170·HCl,** and **III-171·HCl**) in EtOH (+4% 1 M HCl) or in dialysis buffer (25 mM Tris-HCl, 150 mM NaCl, pH 8) + 20% EtOH. Correction factors, calculated from the absorbance ratio between 280 nm and the wavelength of maximum absorption, are indicated in each figure.

IX.16 Extinction Coefficients of Prodigiosin Maleimides

Table IX.12. Molar extinction coefficients of prodigiosin maleimides **III-169**, **III-170**, and **III-171**.

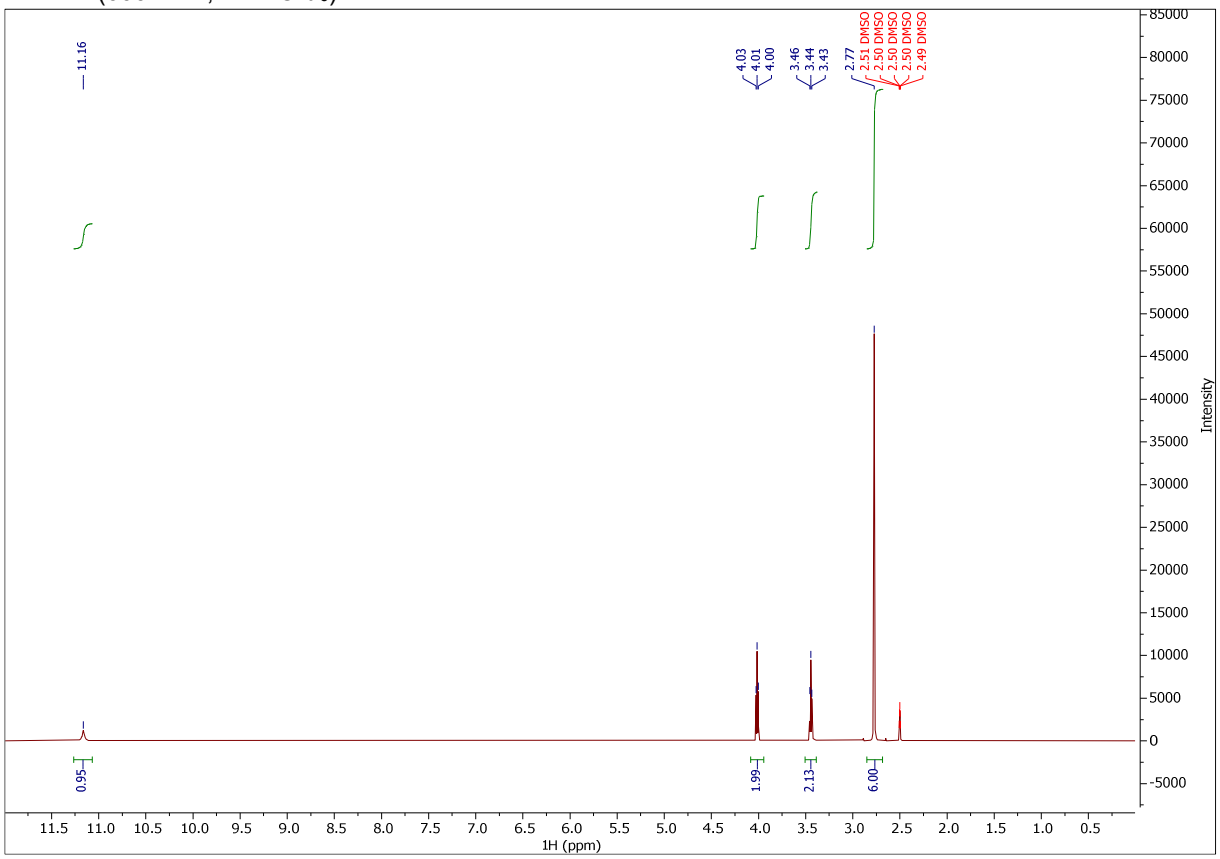
Acidified Ethanol (+4% 1 M HCl)					
Compound	λ_{max} **[nm]**	ε_{535} **[M^{-1} cm^{-1}]**	ε_{546} **[M^{-1} cm^{-1}]**	ε_{547} **[M^{-1} cm^{-1}]**	ε_{548} **[M^{-1} cm^{-1}]**
III-169	546	107833 ± 4496	147725 ± 6117	n.d.	n.d.
III-170	548	96400 ± 866	n.d.	n.d.	147567 ± 7254
III-171	548	107283 ± 1656	n.d.	n.d.	148425 ± 2272
Buffer[a] + 20% Ethanol					
Compound	λ_{max} **[nm]**	ε_{280} **[M^{-1} cm^{-1}]**	ε_{536} **[M^{-1} cm^{-1}]**	ε_{548} **[M^{-1} cm^{-1}]**	ε_{550} **[M^{-1} cm^{-1}]**
III-169	550	2592 ± 365	n.d.	n.d.	38633 ± 2735
III-170	536	18408 ± 793	40900 ± 3089	n.d.	n.d.
III-171	548	15967 ± 344	n.d.	32267 ± 949	n.d.

[a] Dialysis buffer (25 mM Tris-HCl, 150 mM NaCl, pH 8.0); n.d.: not determined. Molar extinction coefficients ε were determined from the slope of a linear regression fit (not shown). All samples were measured in triplicate. Mean values and standard deviations are given.

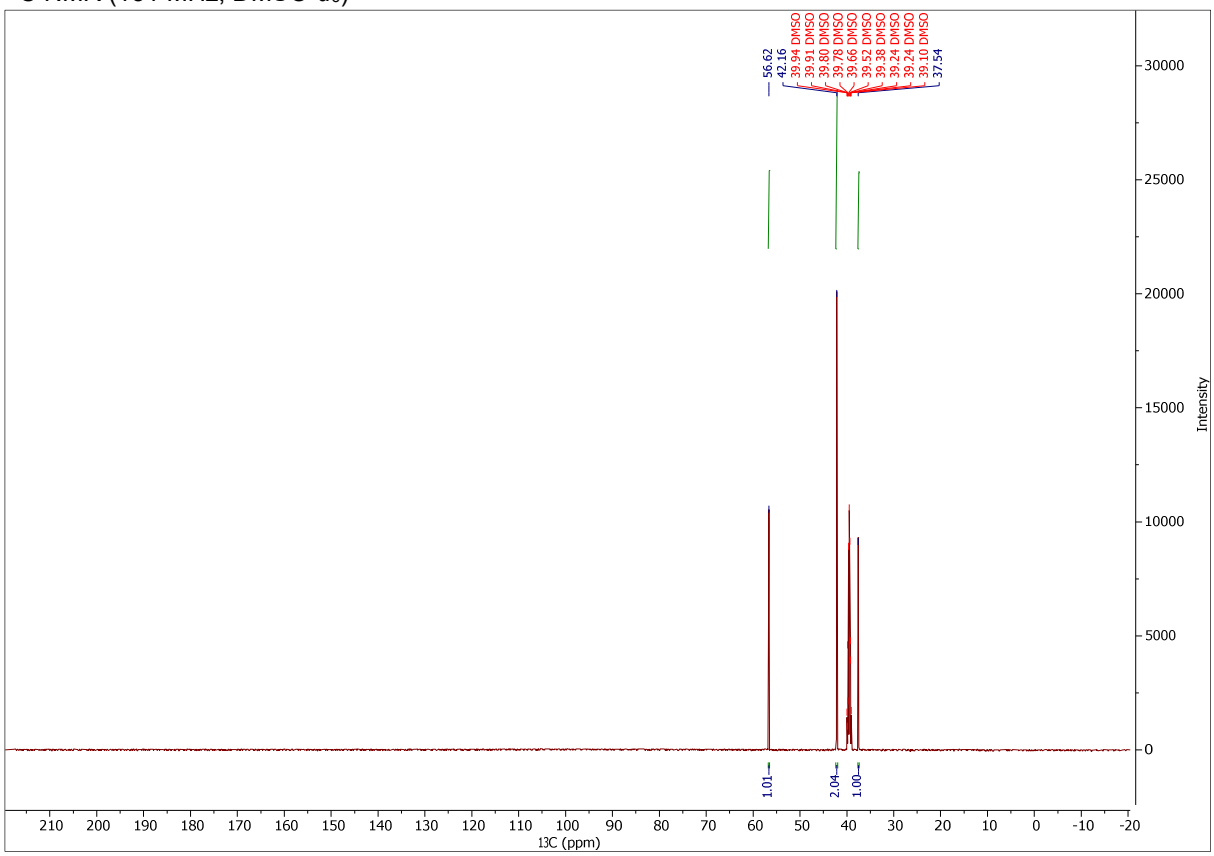
IX.17 NMR Spectra

(2-Chloroethyl)dimethylamine hydrochloride (**II-39·HCl**)

^{1}H NMR (600 MHz, DMSO-d_6)

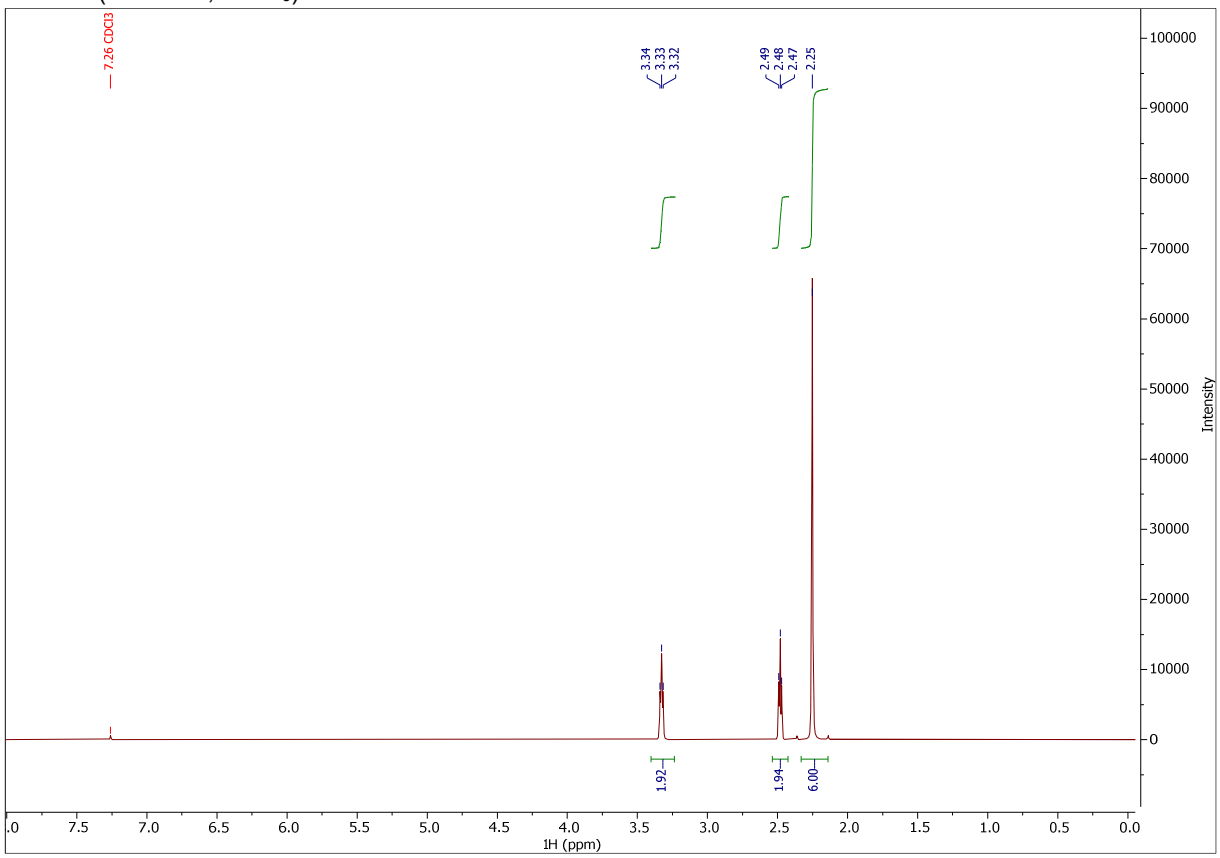


^{13}C NMR (151 MHz, DMSO-d_6)

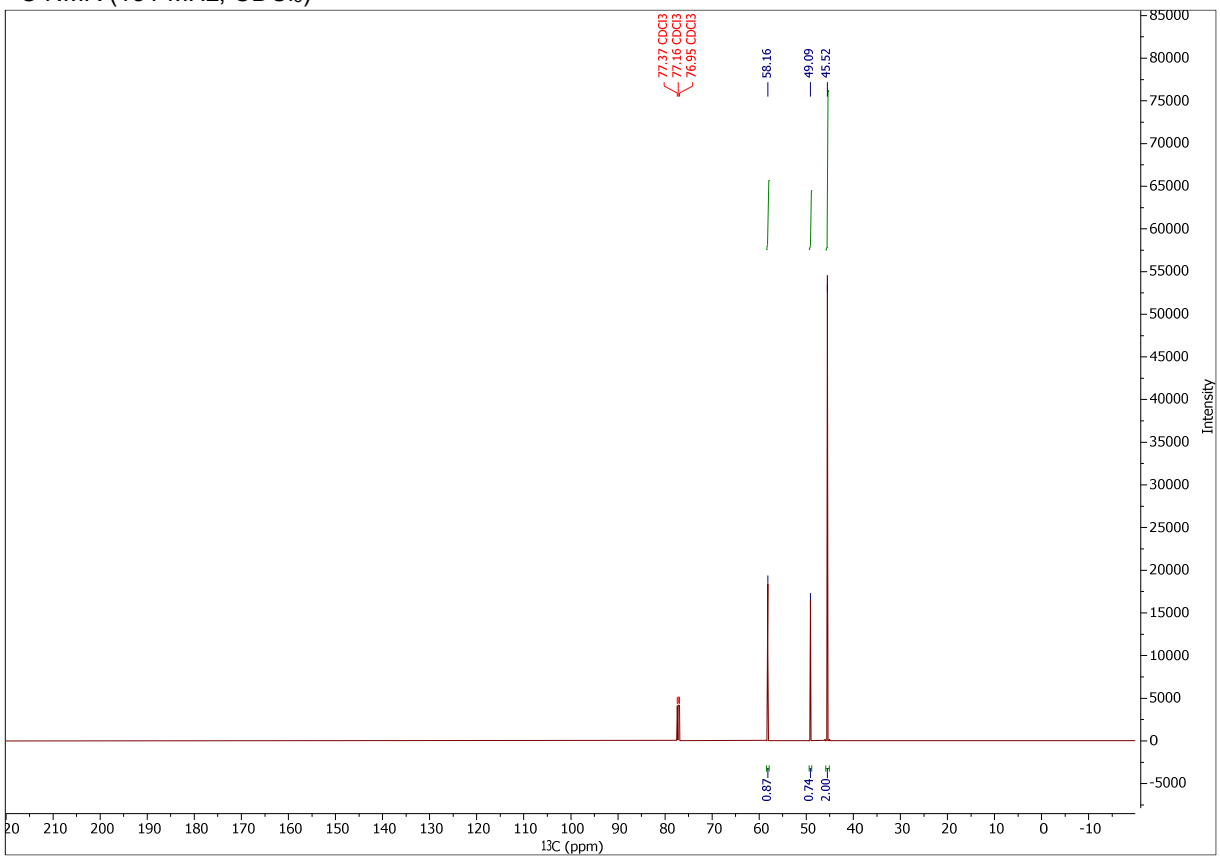


2-Azido-*N*,*N*-dimethylethan-1-amine (**II-43**)

^{1}H NMR (600 MHz, $CDCl_3$)

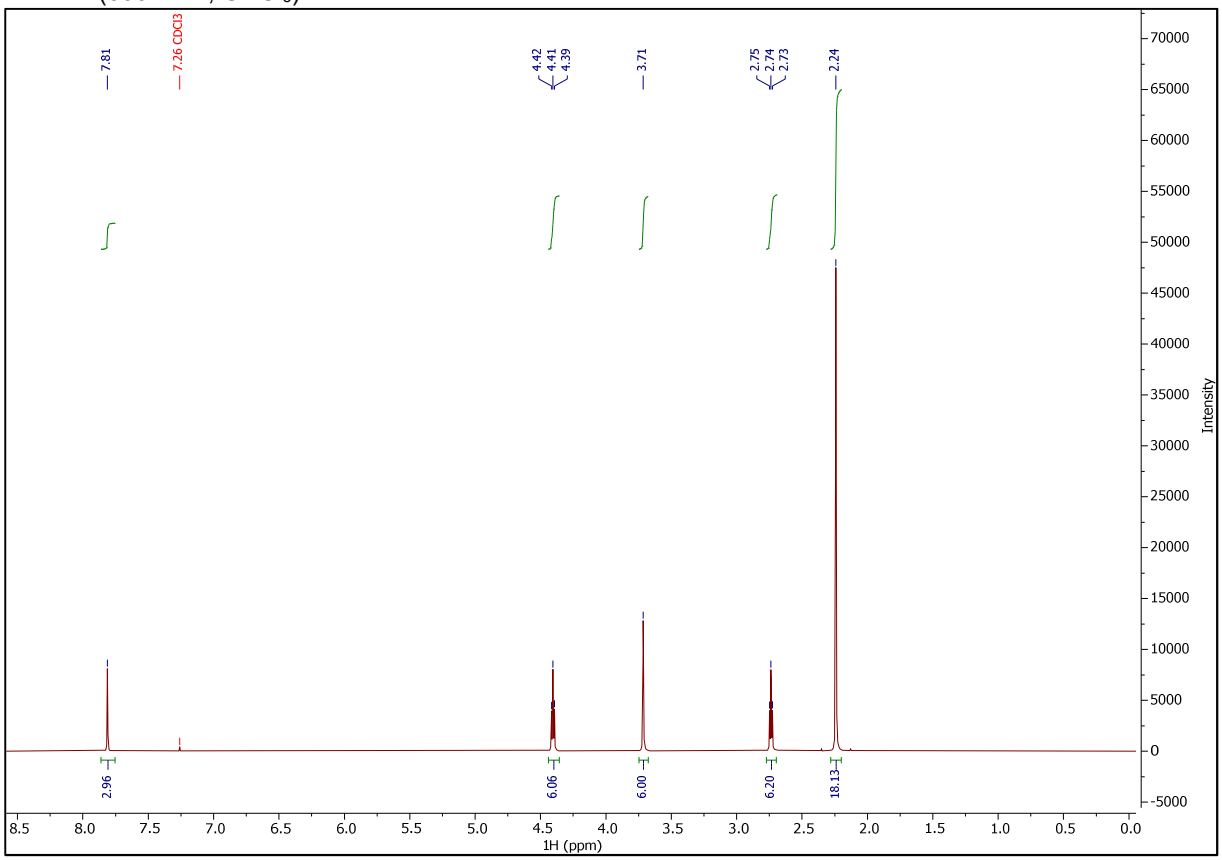


^{13}C NMR (151 MHz, $CDCl_3$)

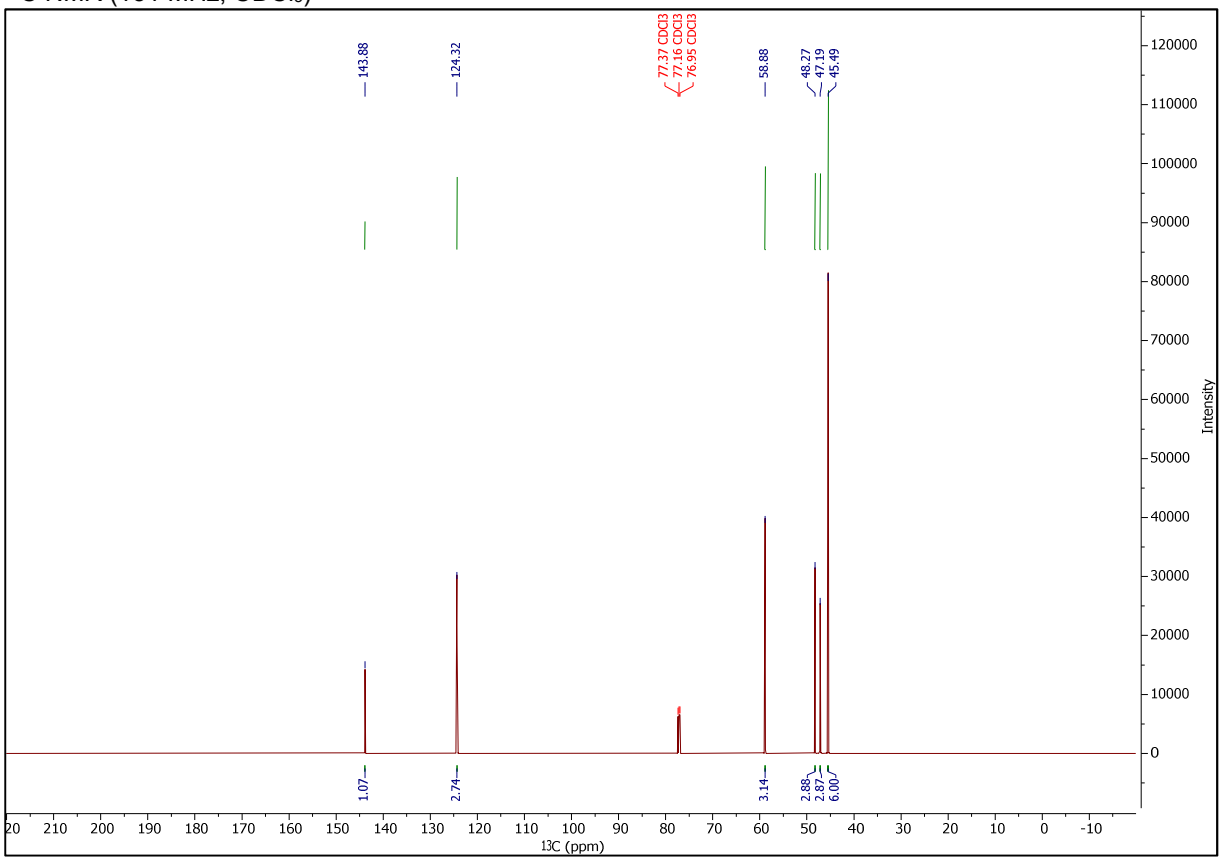


2-(4-((Bis((1-(2-(dimethylamino)ethyl)-1*H*-1,2,3-triazol-4-yl)methyl)amino)methyl)-1*H*-1,2,3-triazol-1-yl)-*N*,*N*-dimethylethan-1-amine (**II-44**, TDETA)

^{1}H NMR (600 MHz, $CDCl_3$)

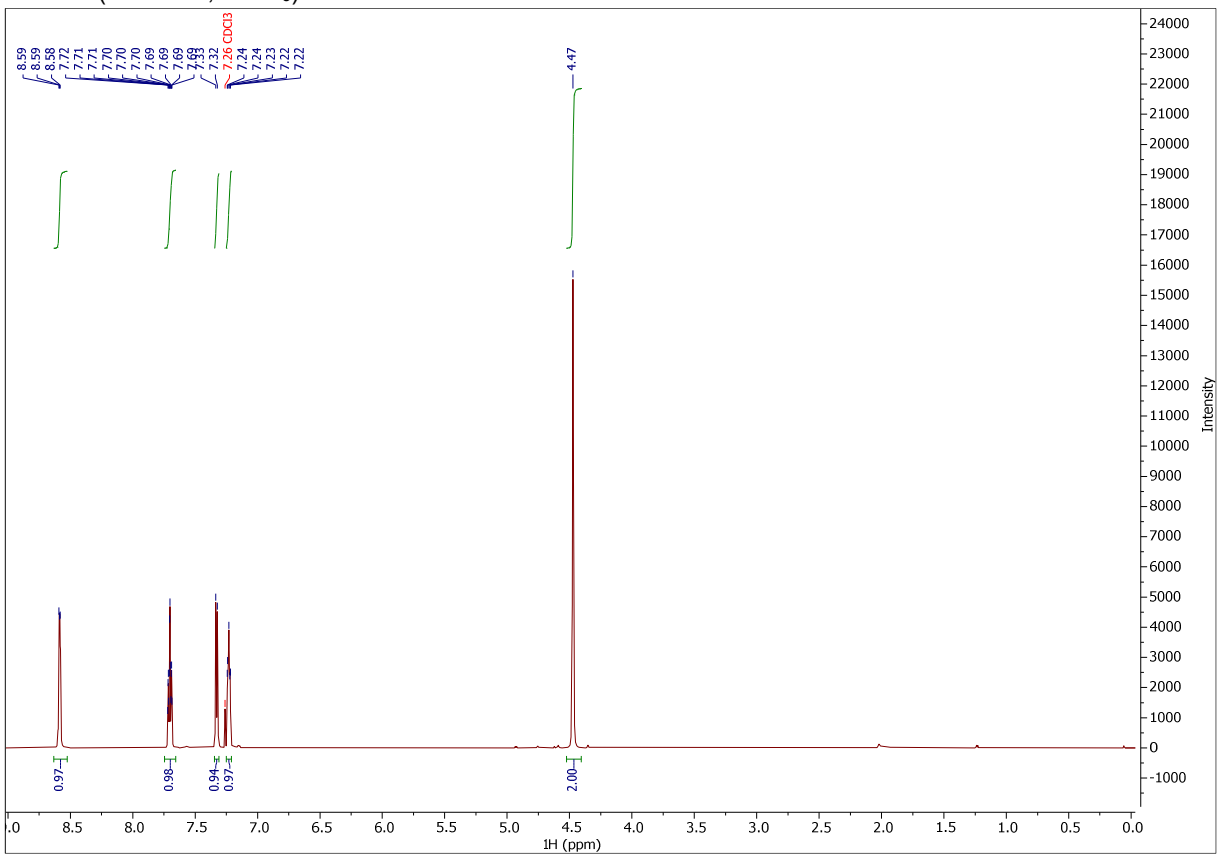


^{13}C NMR (151 MHz, $CDCl_3$)

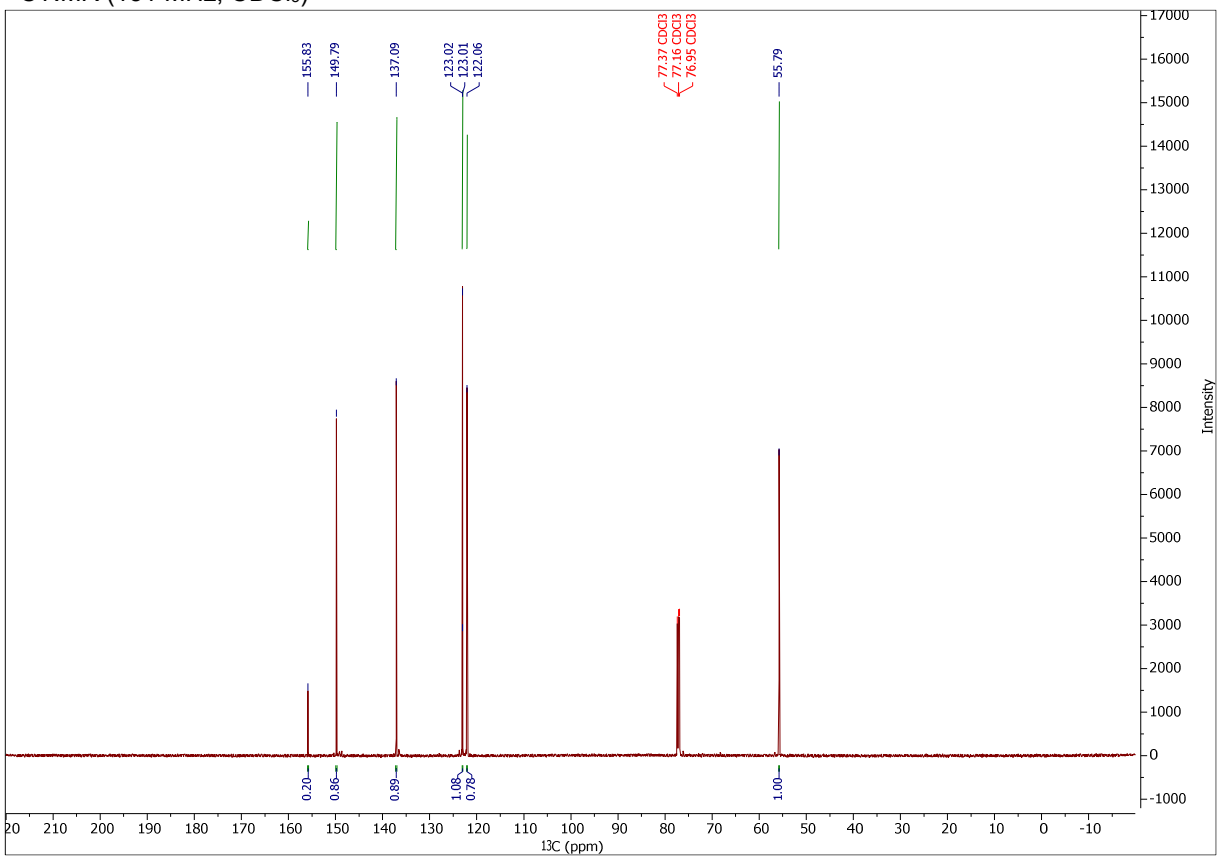


2-(Azidomethyl)pyridine (**II-46**)

^{1}H NMR (600 MHz, $CDCl_3$)

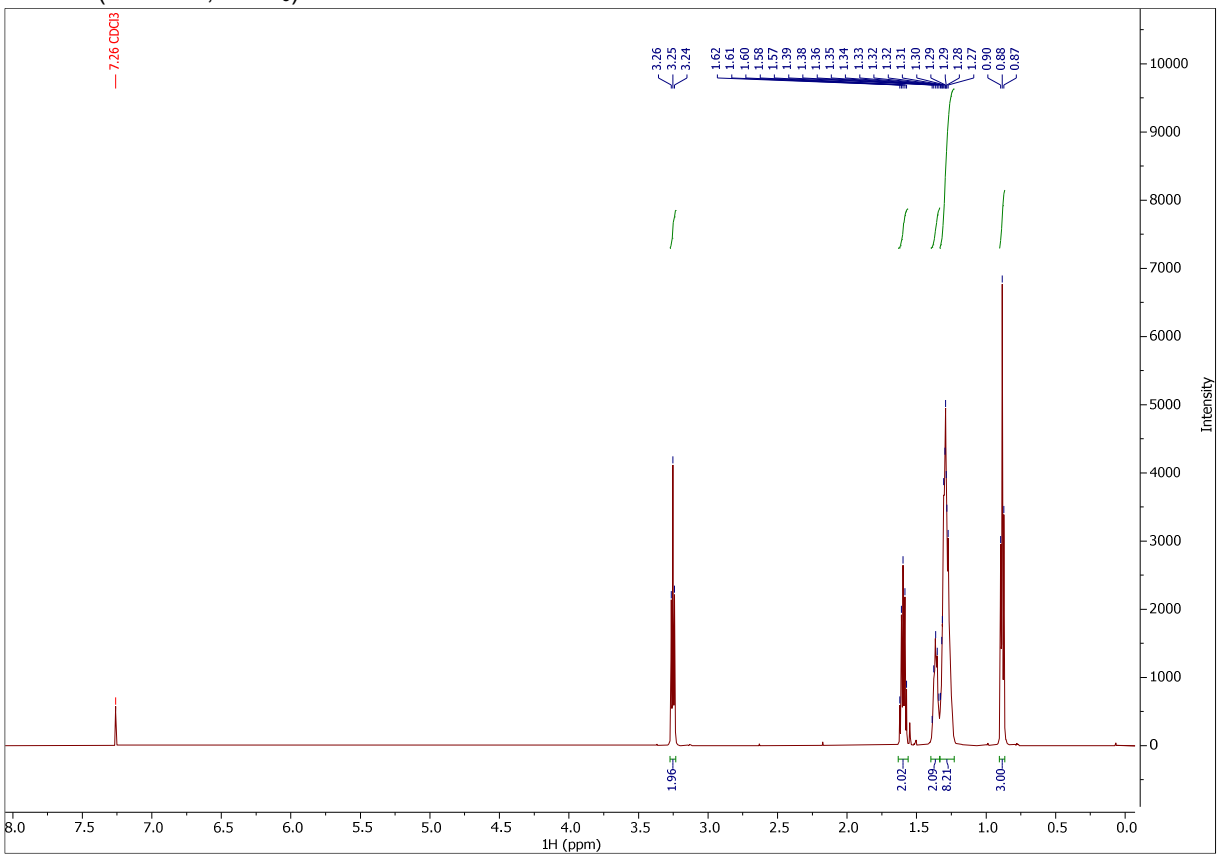


^{13}C NMR (151 MHz, $CDCl_3$)

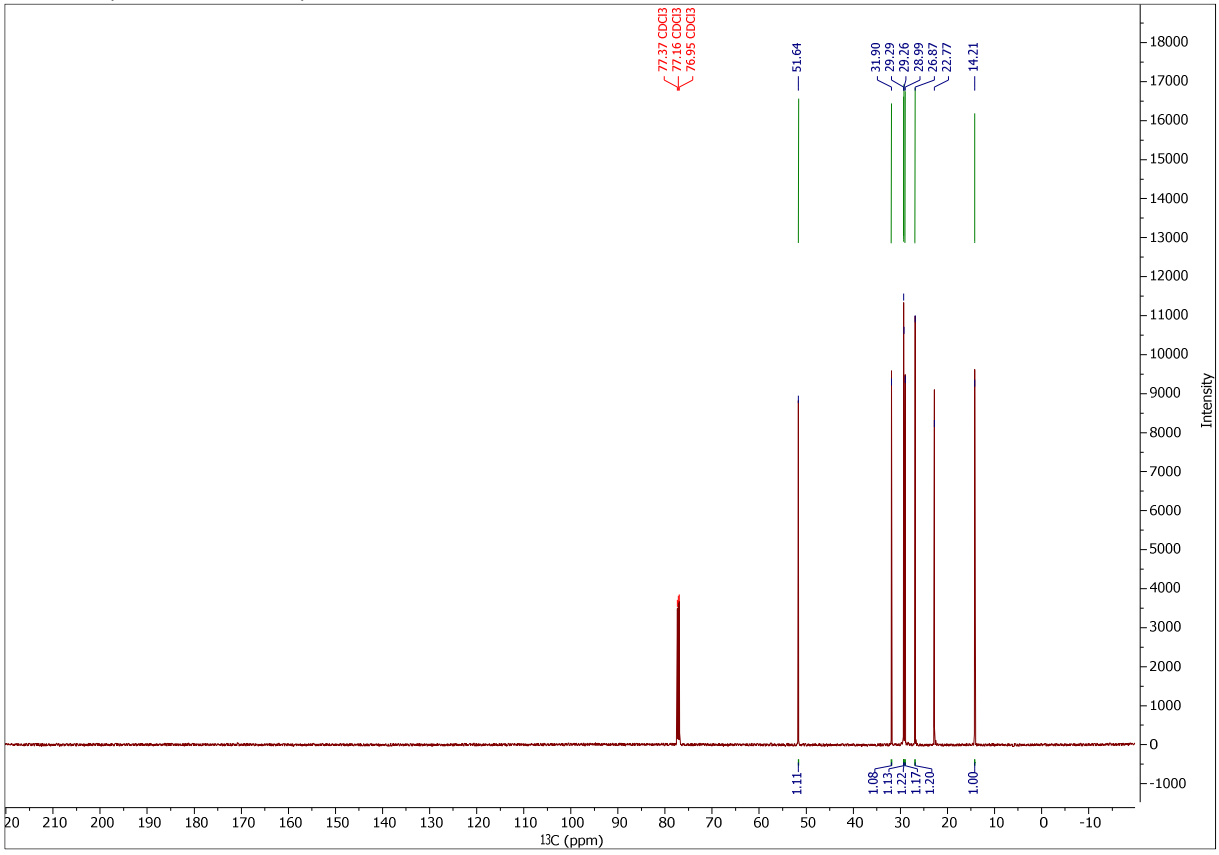


1-Azidooctane (**II-48**)

^{1}H NMR (600 MHz, $CDCl_3$)

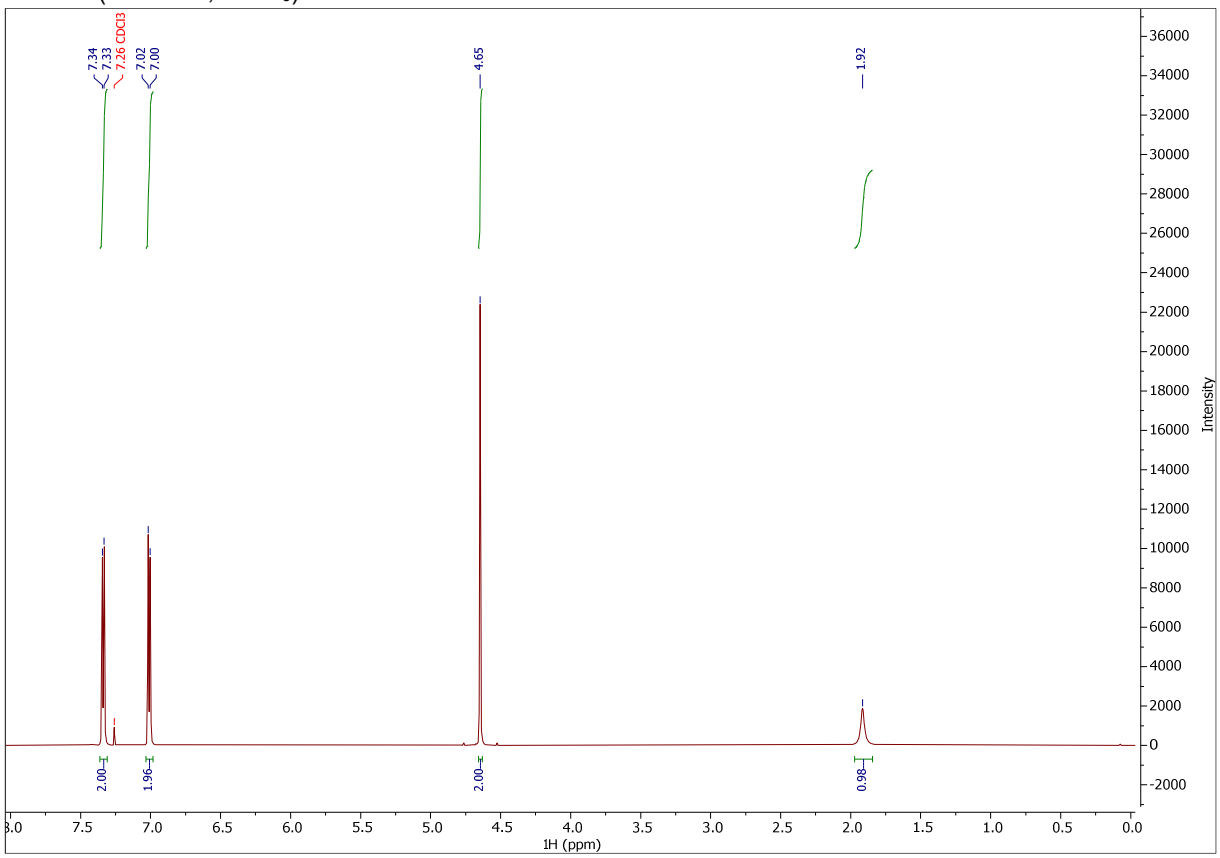


^{13}C NMR (151 MHz, $CDCl_3$)

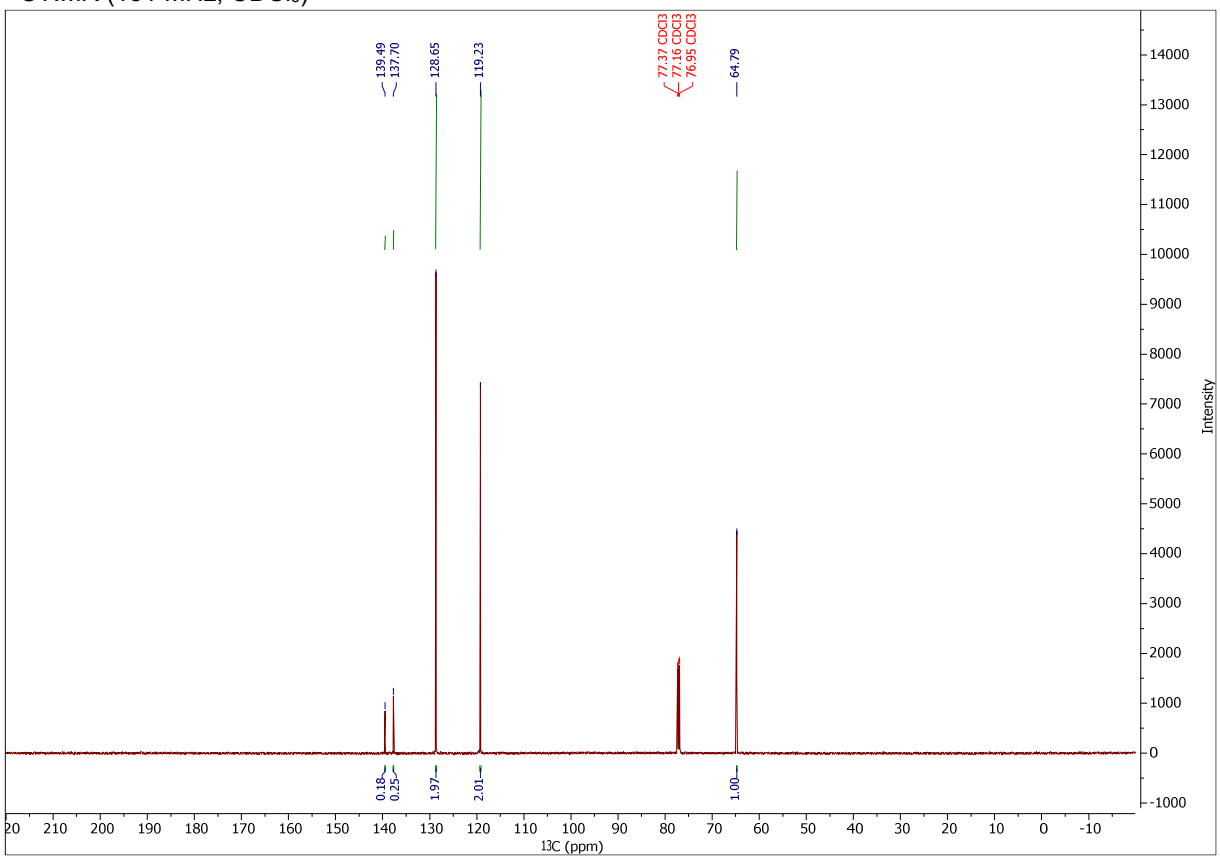


1-Azido-4-(hydroxymethyl)benzene (**II-50**)

^{1}H NMR (600 MHz, $CDCl_3$)

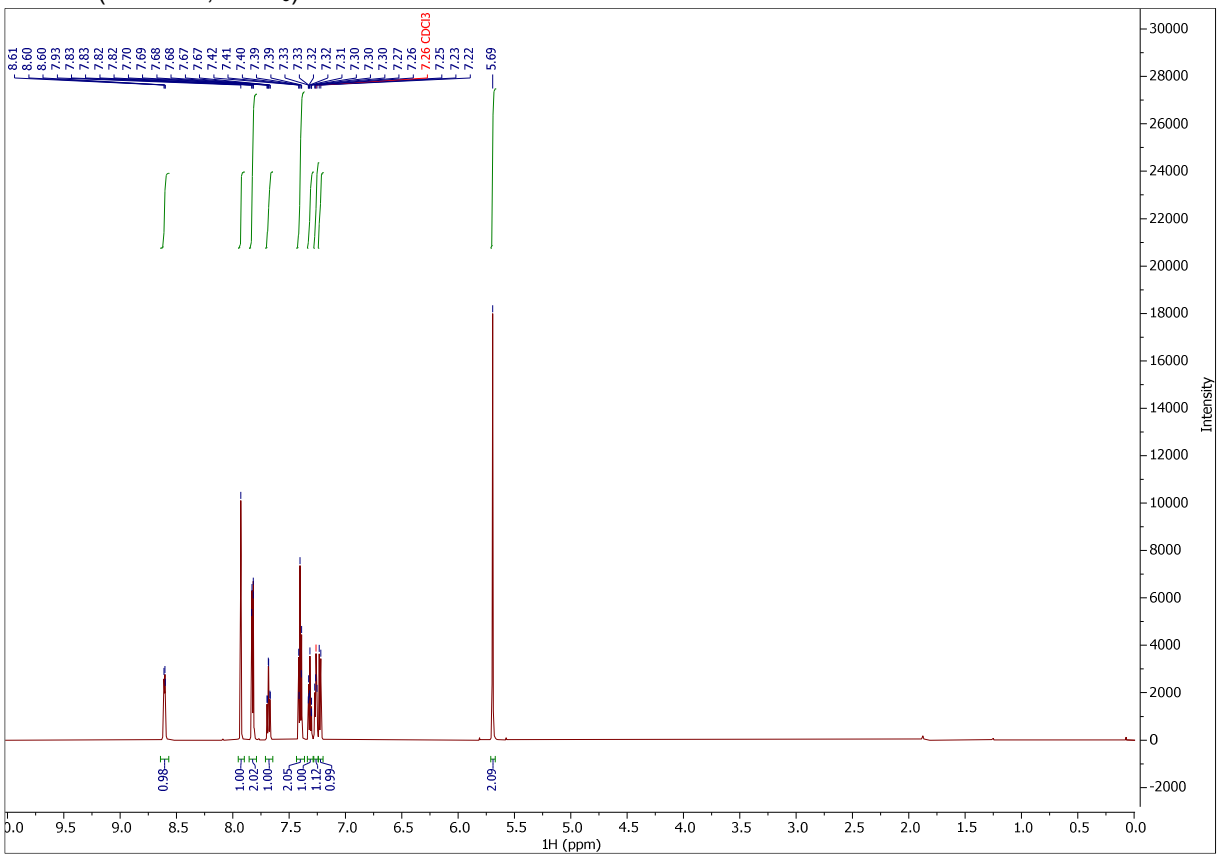


^{13}C NMR (151 MHz, $CDCl_3$)

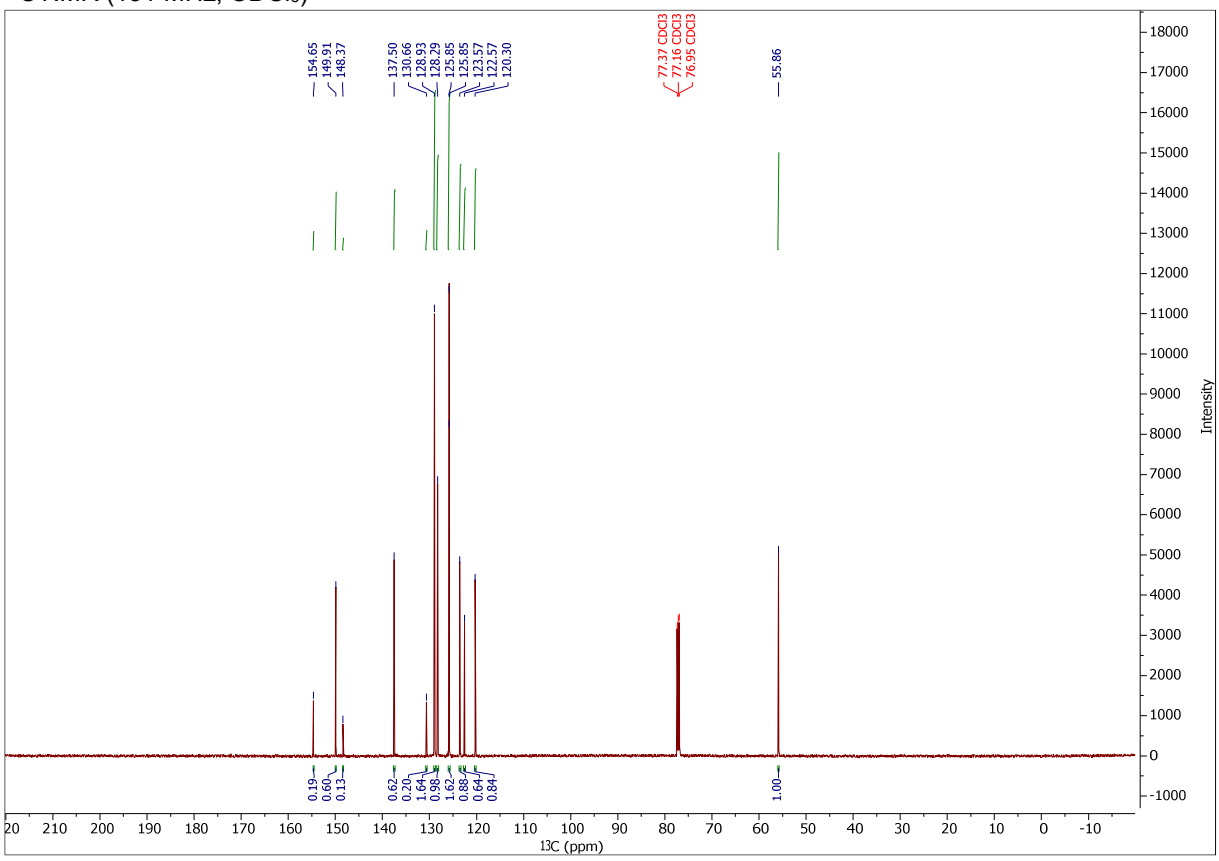


2-((4-Phenyl-1*H*-1,2,3-triazol-1-yl)methyl)pyridine (**II-57a**)

^{1}H NMR (600 MHz, $CDCl_3$)

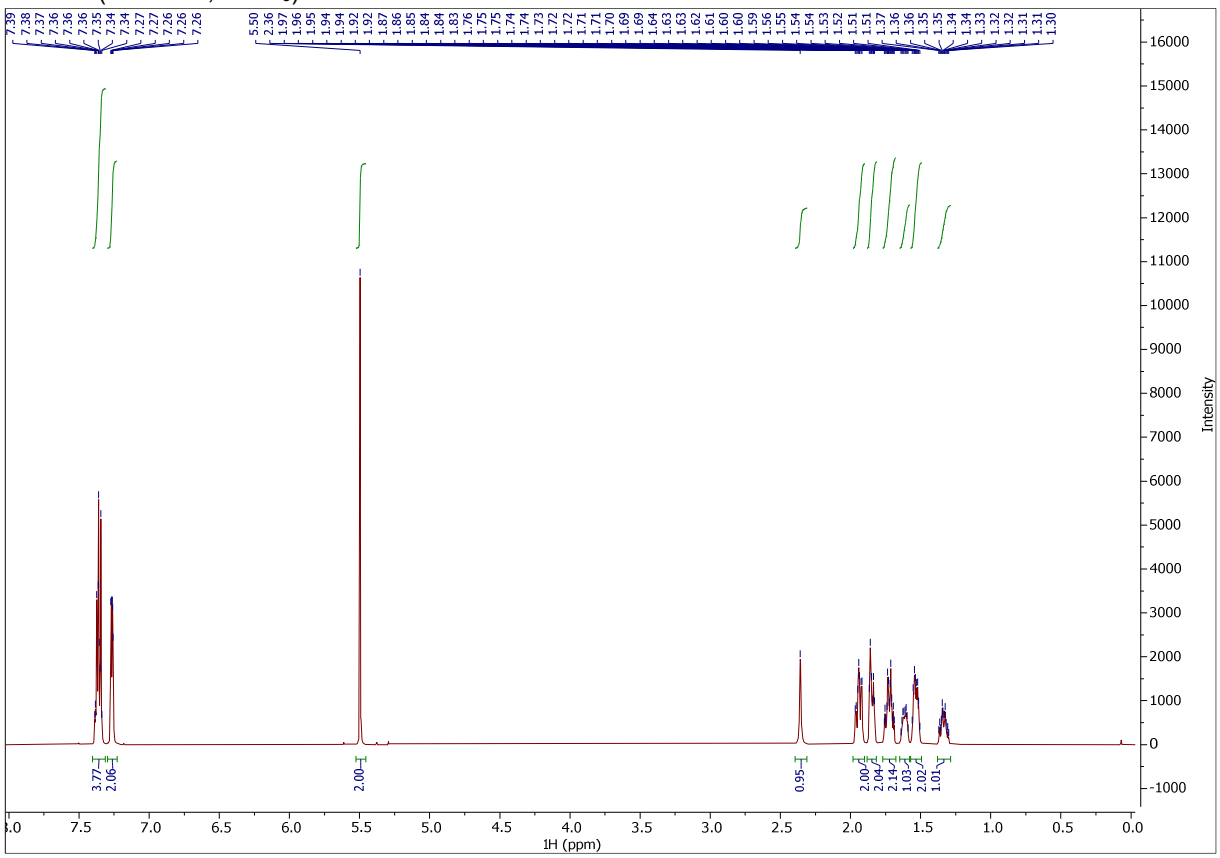


^{13}C NMR (151 MHz, $CDCl_3$)

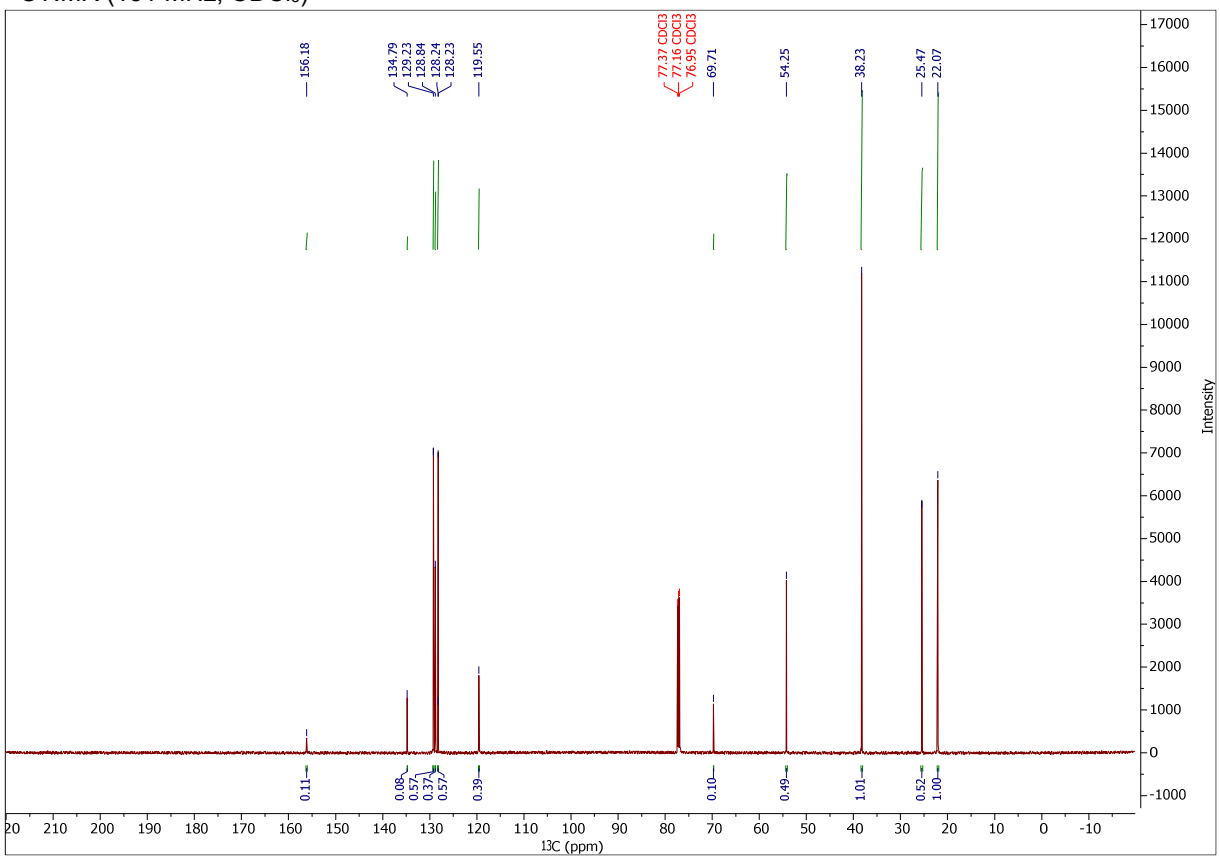


1-(1-Benzyl-1*H*-1,2,3-triazol-4-yl)cyclohexan-1-ol (**II-57b**)

^{1}H NMR (600 MHz, $CDCl_3$)

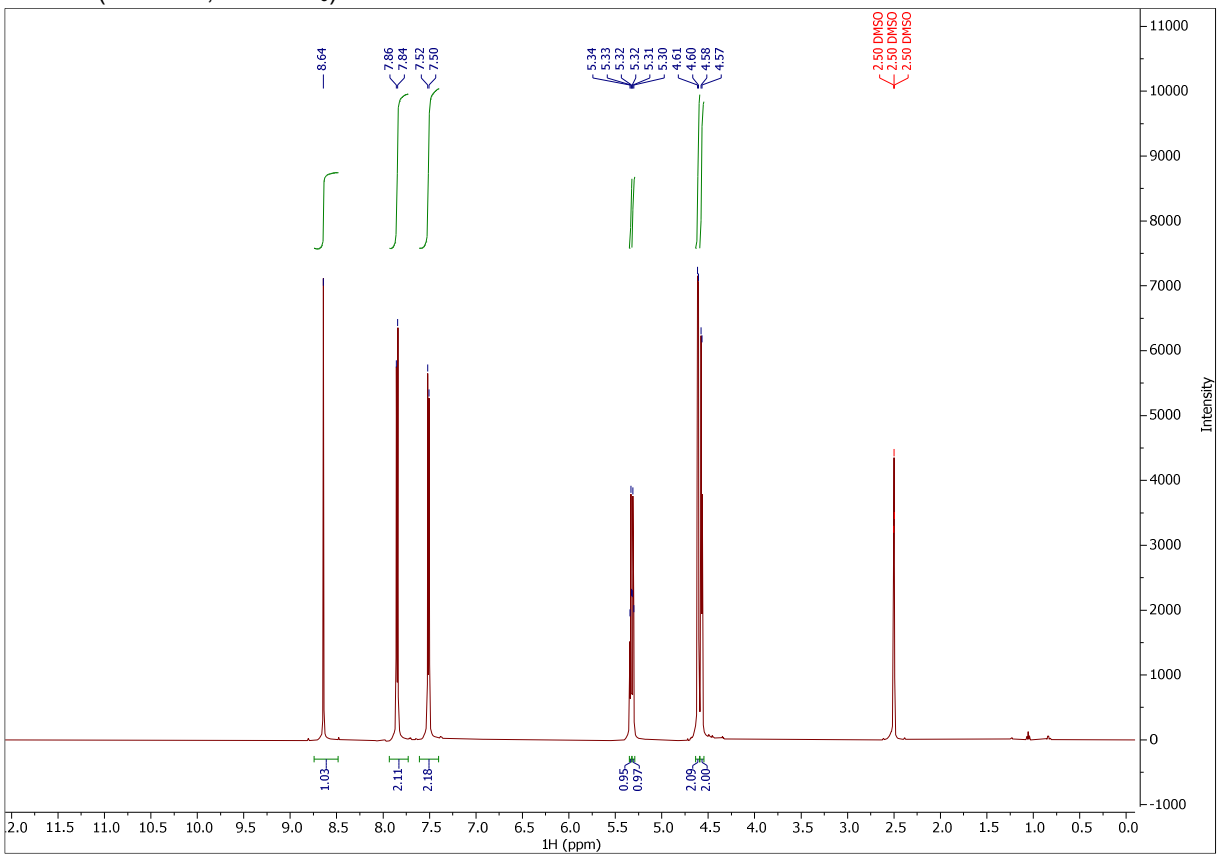


^{13}C NMR (151 MHz, $CDCl_3$)

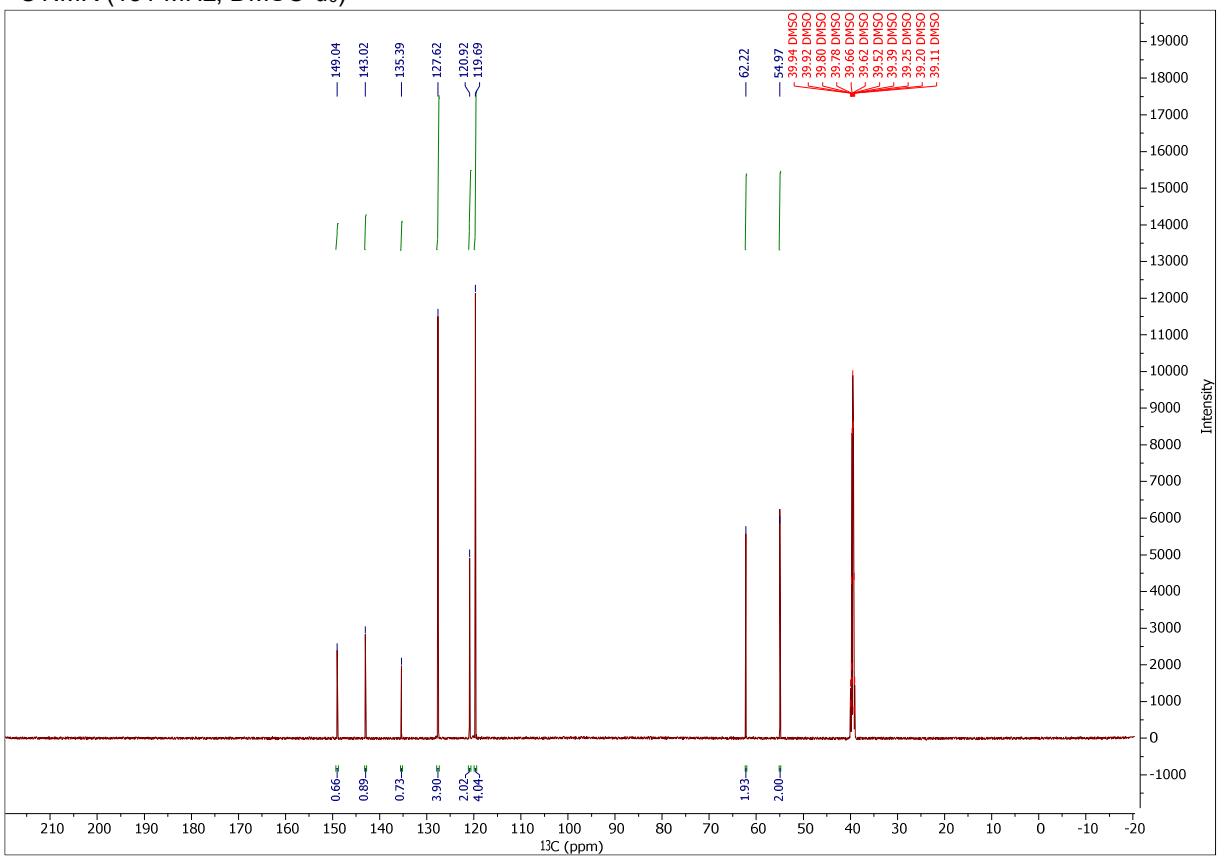


(4-(4-(Hydroxymethyl)-1*H*-1,2,3-triazol-1-yl)phenyl)methanol (**II-57c**)

^{1}H NMR (600 MHz, DMSO-d_6)

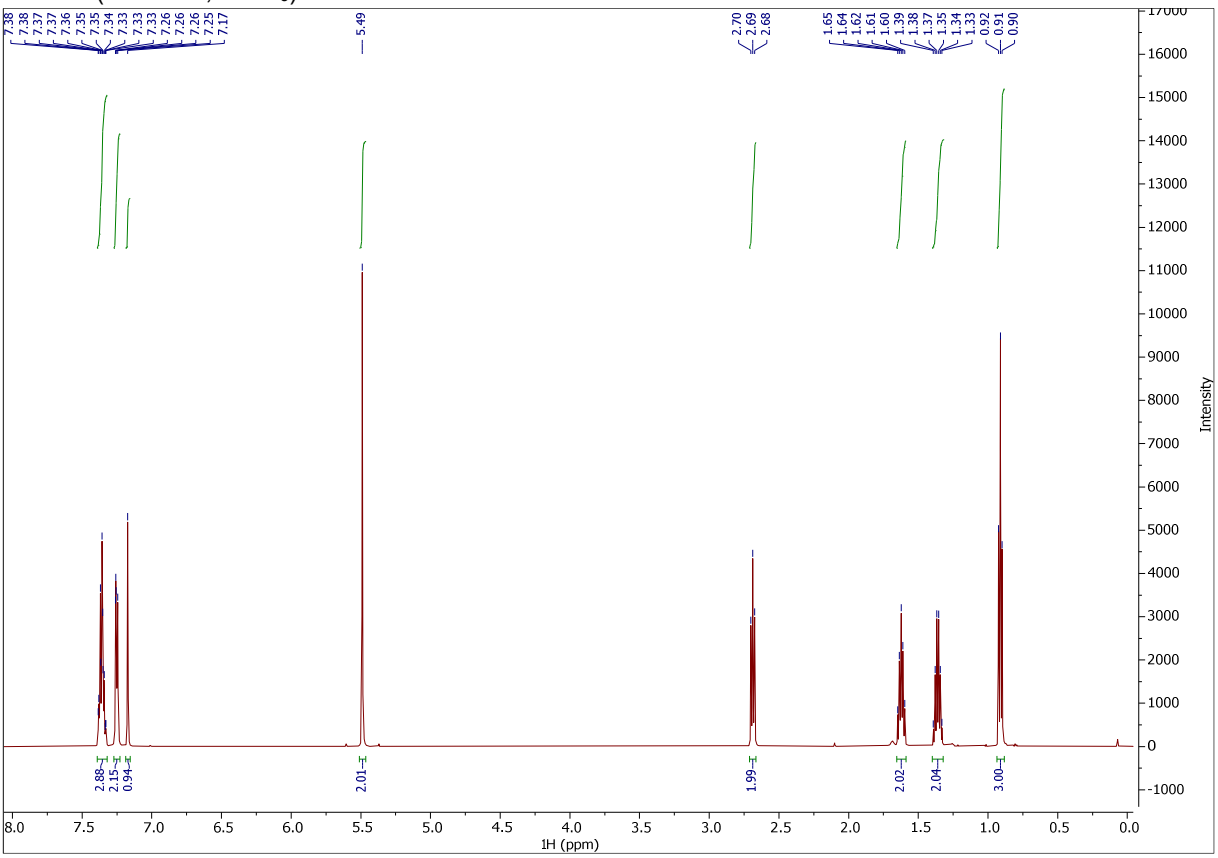


^{13}C NMR (151 MHz, DMSO-d_6)

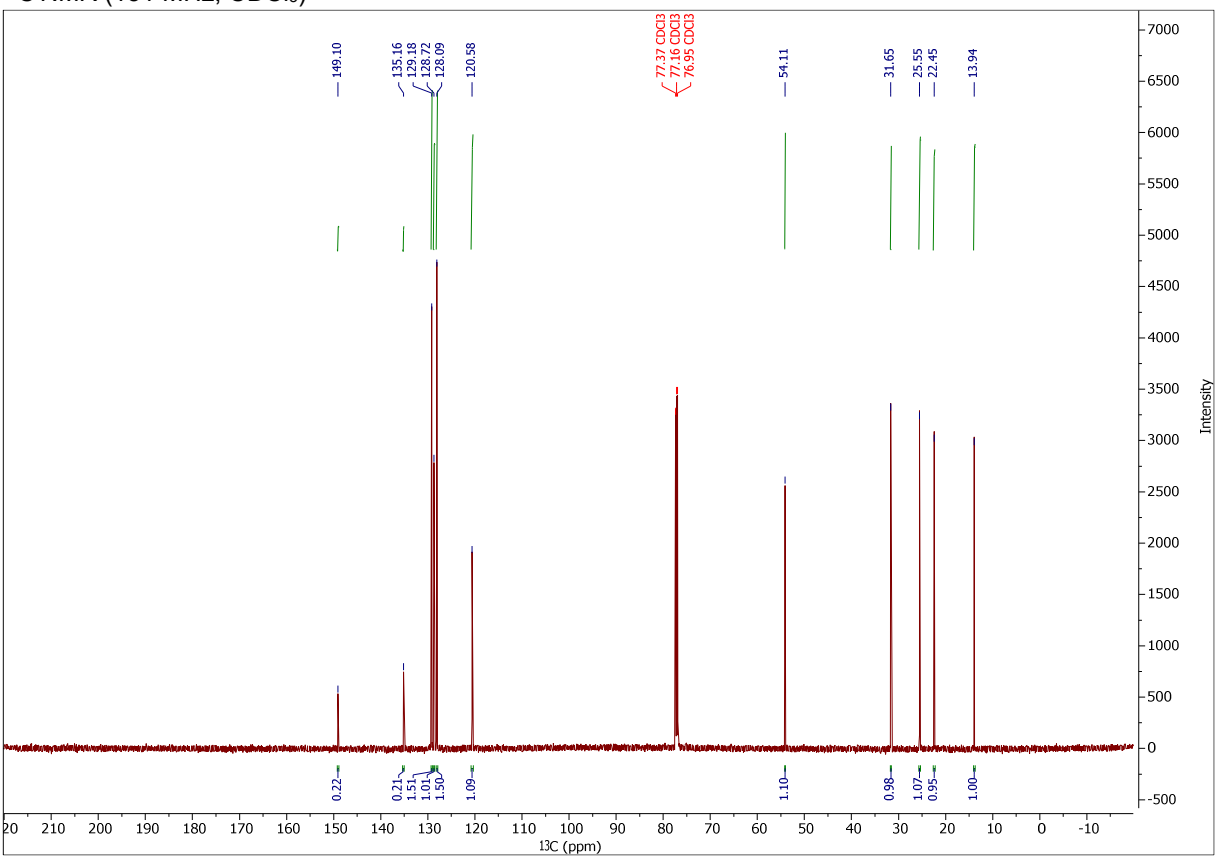


1-Benzyl-4-butyl-1*H*-1,2,3-triazole (**II-57d**)

^{1}H NMR (600 MHz, $CDCl_3$)

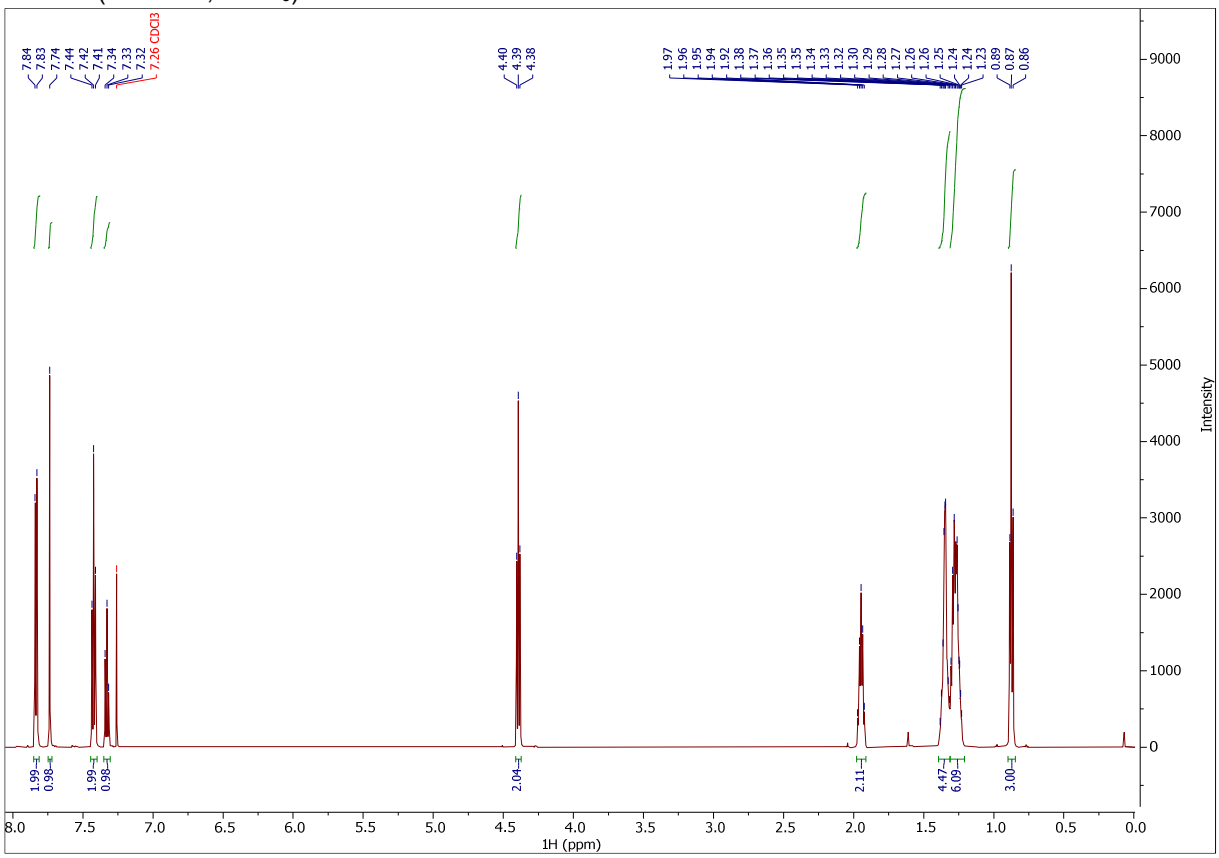


^{13}C NMR (151 MHz, $CDCl_3$)

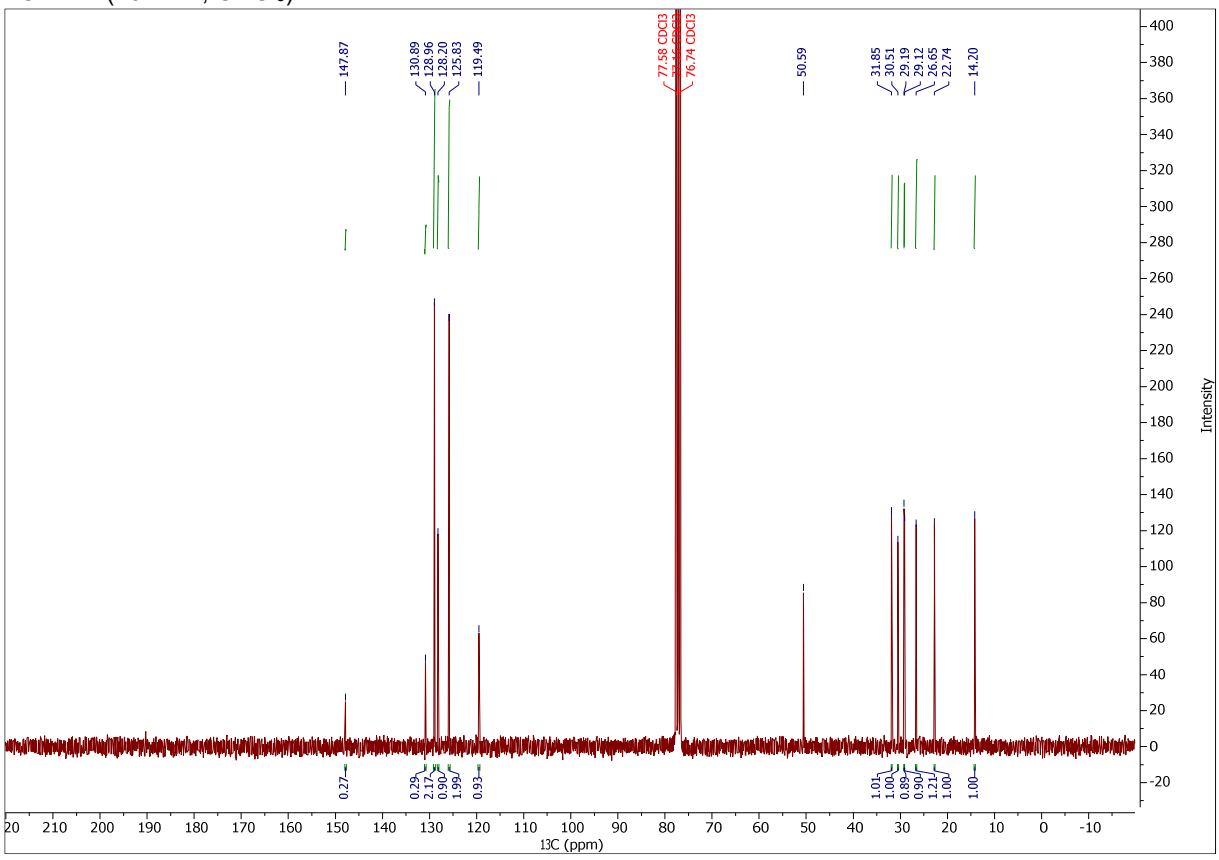


1-Octyl-4-phenyl-1*H*-1,2,3-triazole (**II-57e**)

^{1}H NMR (600 MHz, $CDCl_3$)

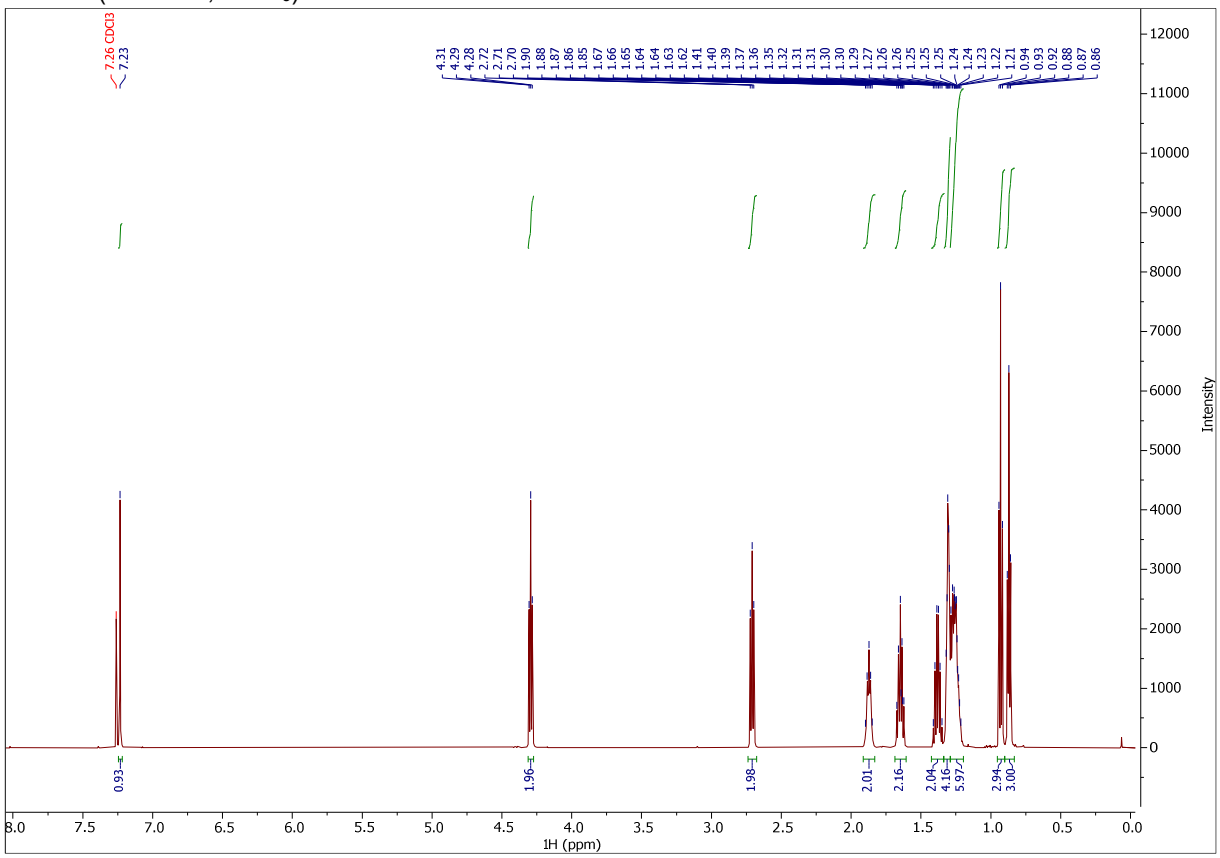


^{13}C NMR (76 MHz, $CDCl_3$)

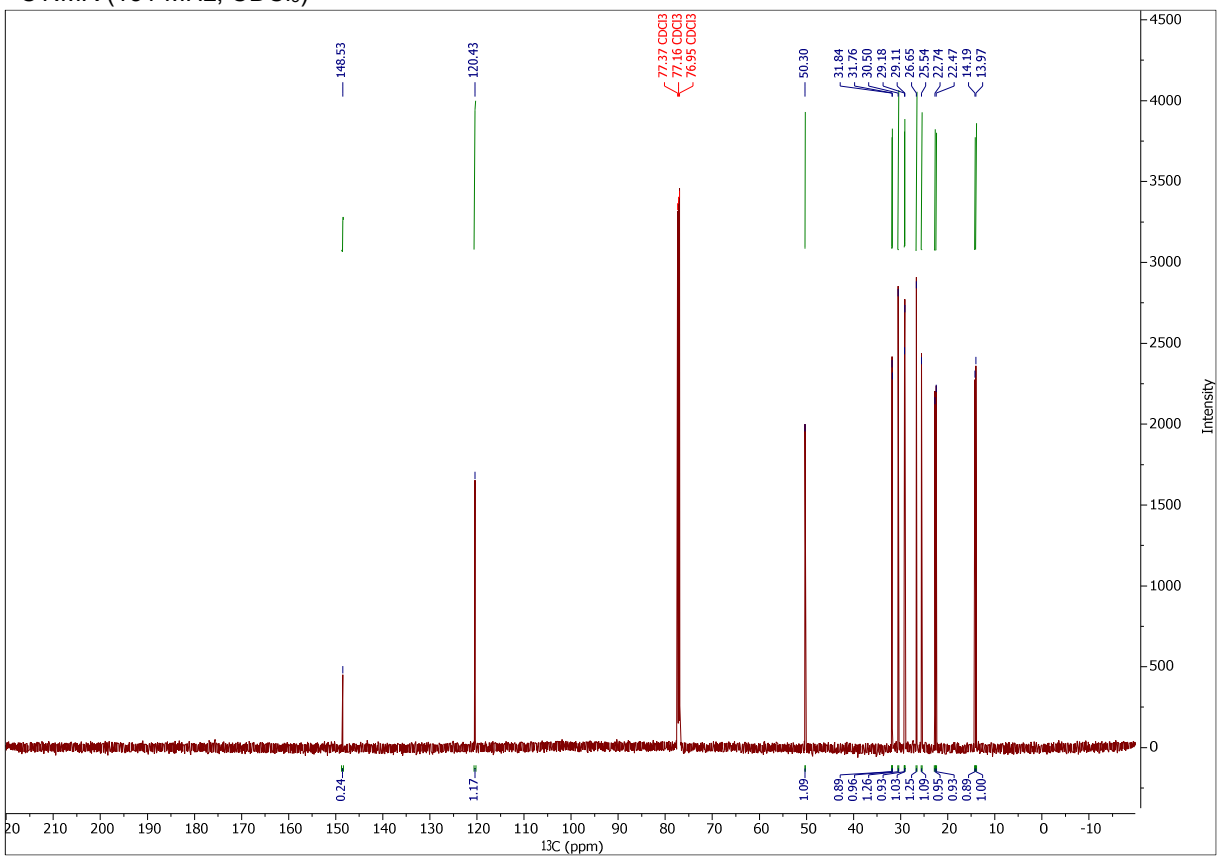


4-Butyl-1-octyl-1*H*-1,2,3-triazole (**II-57f**)

^{1}H NMR (600 MHz, $CDCl_3$)

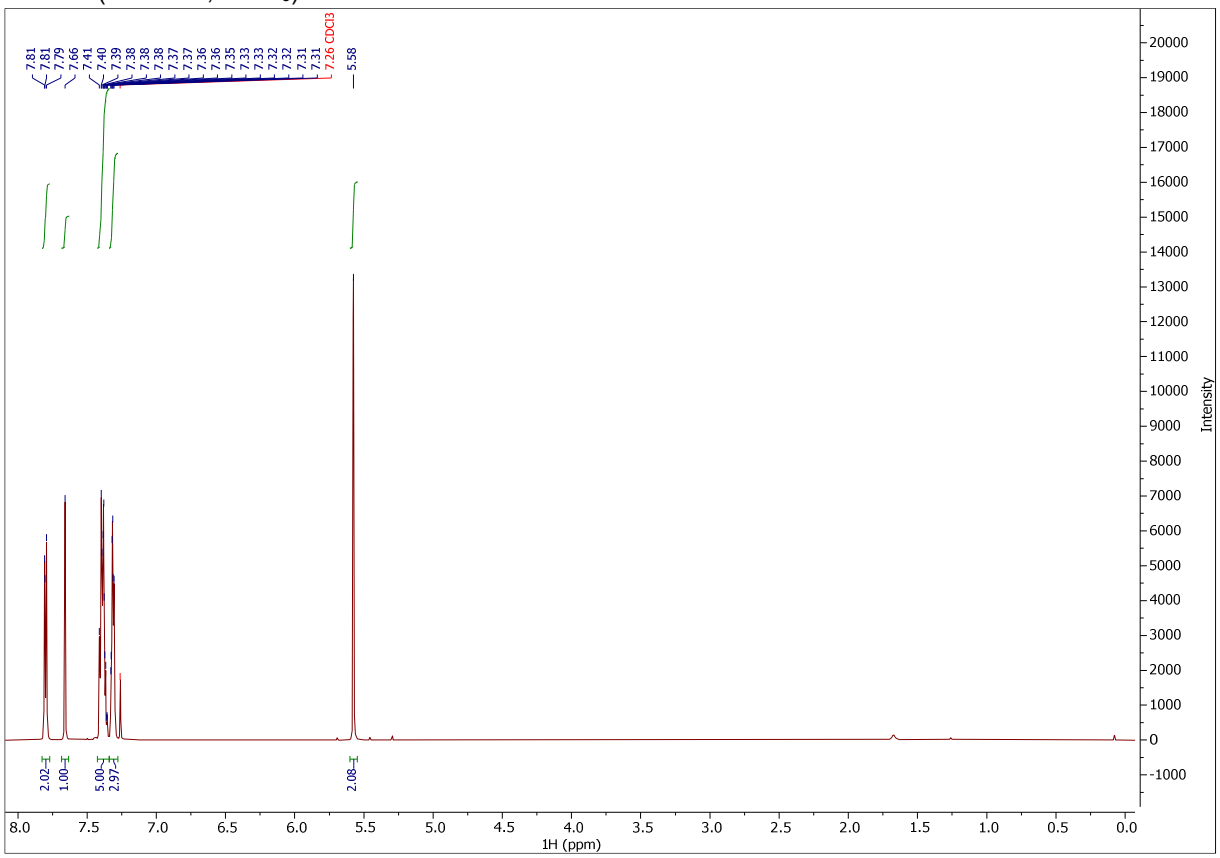


^{13}C NMR (151 MHz, $CDCl_3$)

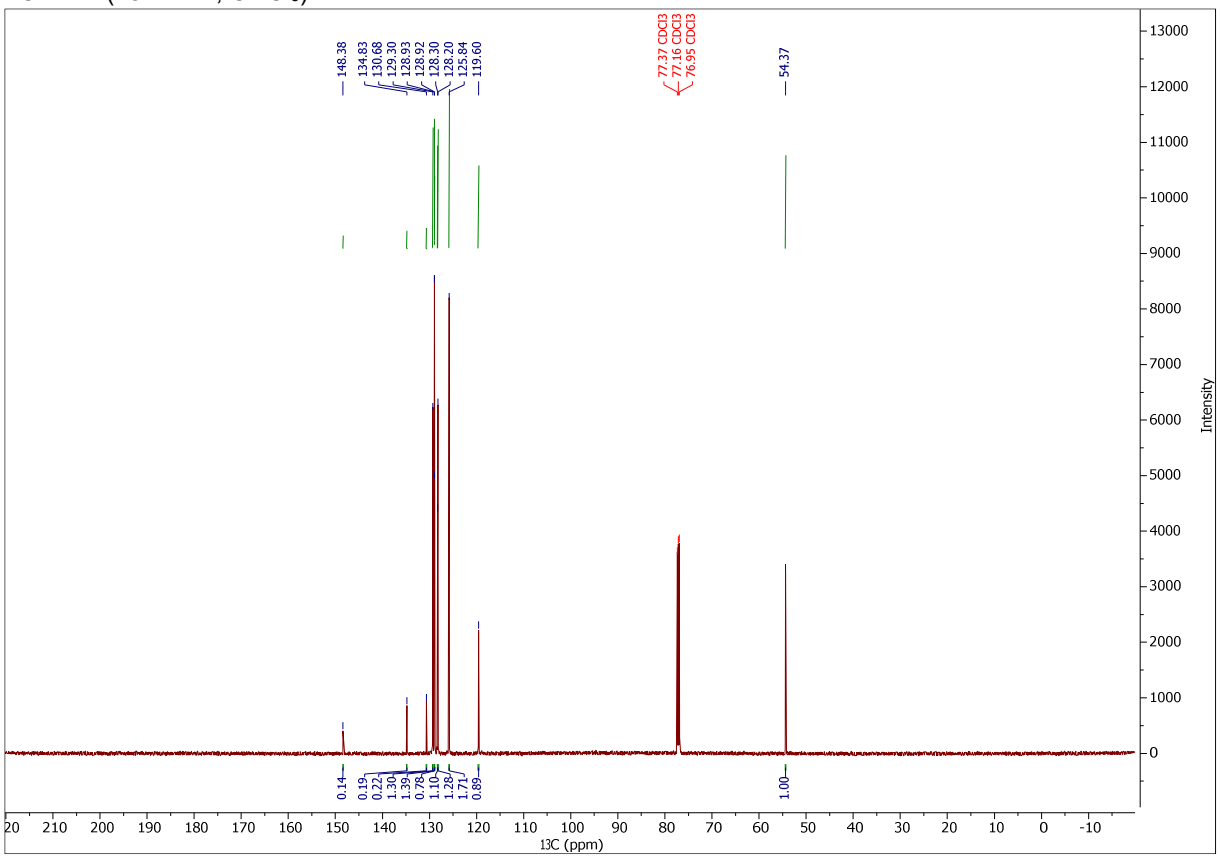


1-Benzyl-4-phenyl-1*H*-1,2,3-triazole (**II-57g**)

^{1}H NMR (600 MHz, $CDCl_3$)

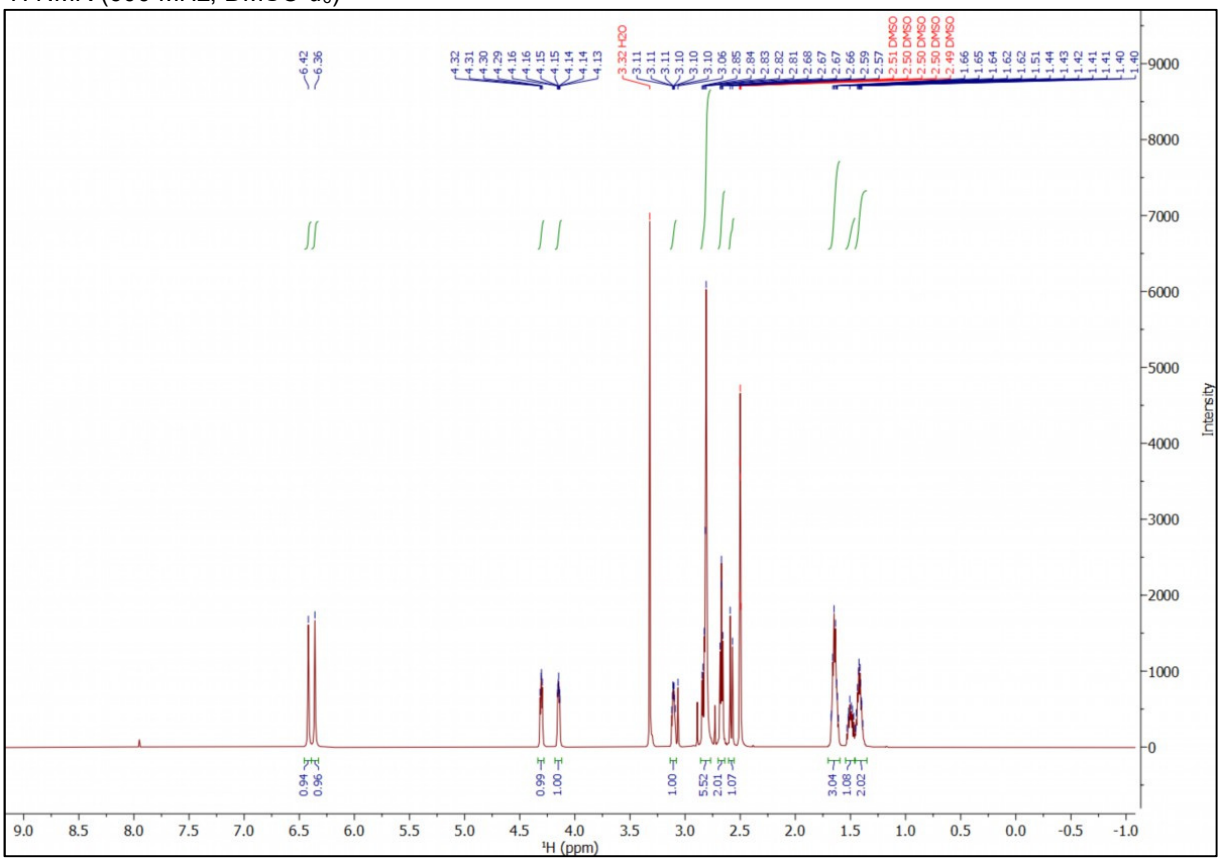


^{13}C NMR (151 MHz, $CDCl_3$)

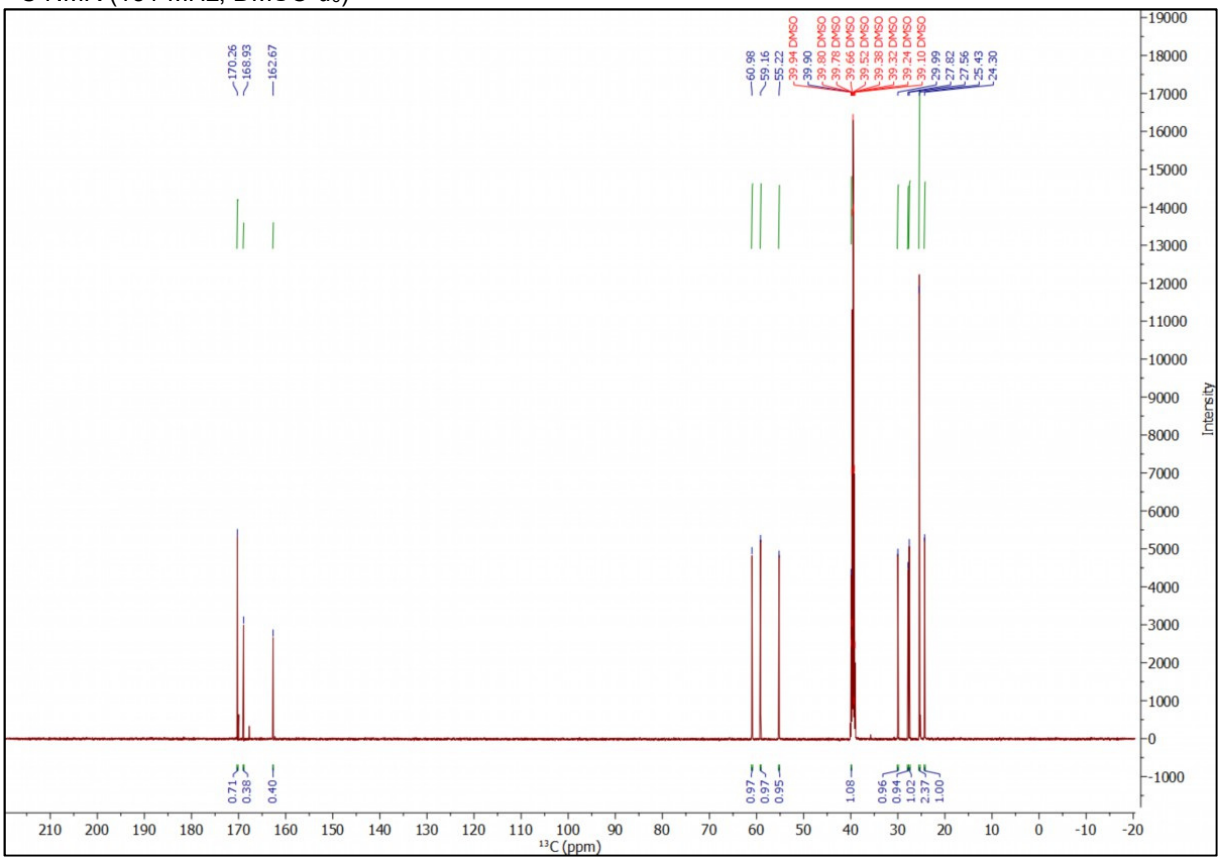


2,5-Dioxopyrrolidin-1-yl 5-((3a*S*,4*S*,6a*R*)-2-oxohexahydro-1*H*-thieno[3,4-*d*]imidazol-4-yl)pentanoate (**II-63**)

^{1}H NMR (600 MHz, DMSO-d_6)

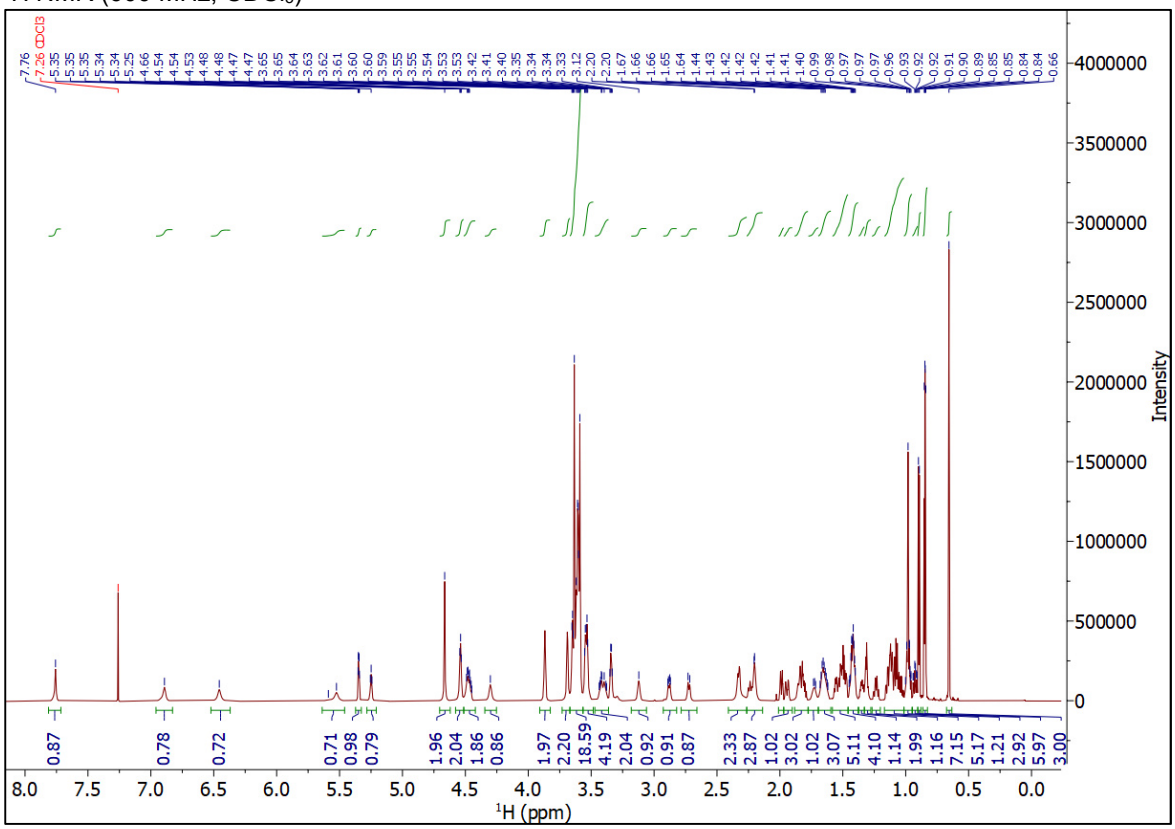


^{13}C NMR (151 MHz, DMSO-d_6)

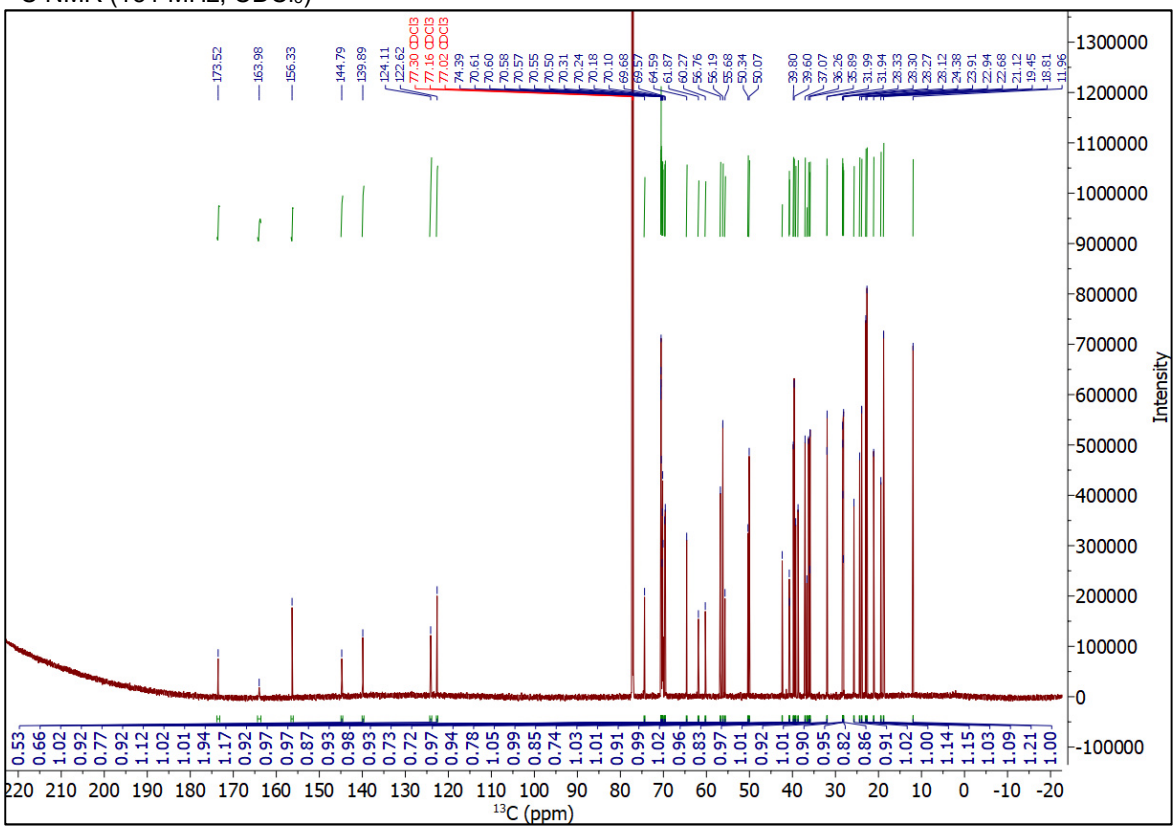


(3*S*,8*S*,9*S*,10*R*,13*R*,14*S*,17*R*)-10,13-Dimethyl-17-((*R*)-6-methylheptan-2-yl)-2,3,4,7,8,9,10,11,12,13,14,15,16,17-tetradecahydro-1*H*-cyclopenta[*a*]phenanthren-3-yl (2-(2-(2-(2-(4-(15-oxo-19-((3a*S*,4*S*,6a*R*)-2-oxohexahydro-1*H*-thieno[3,4-*d*]imidazol-4-yl)-2,5,8,11-tetraoxa-14-azanonadecyl)-1*H*-1,2,3-triazol-1-yl)ethoxy)ethoxy)ethoxy)ethyl)-carbamate (**II-67**)

^{1}H NMR (600 MHz, $CDCl_3$)

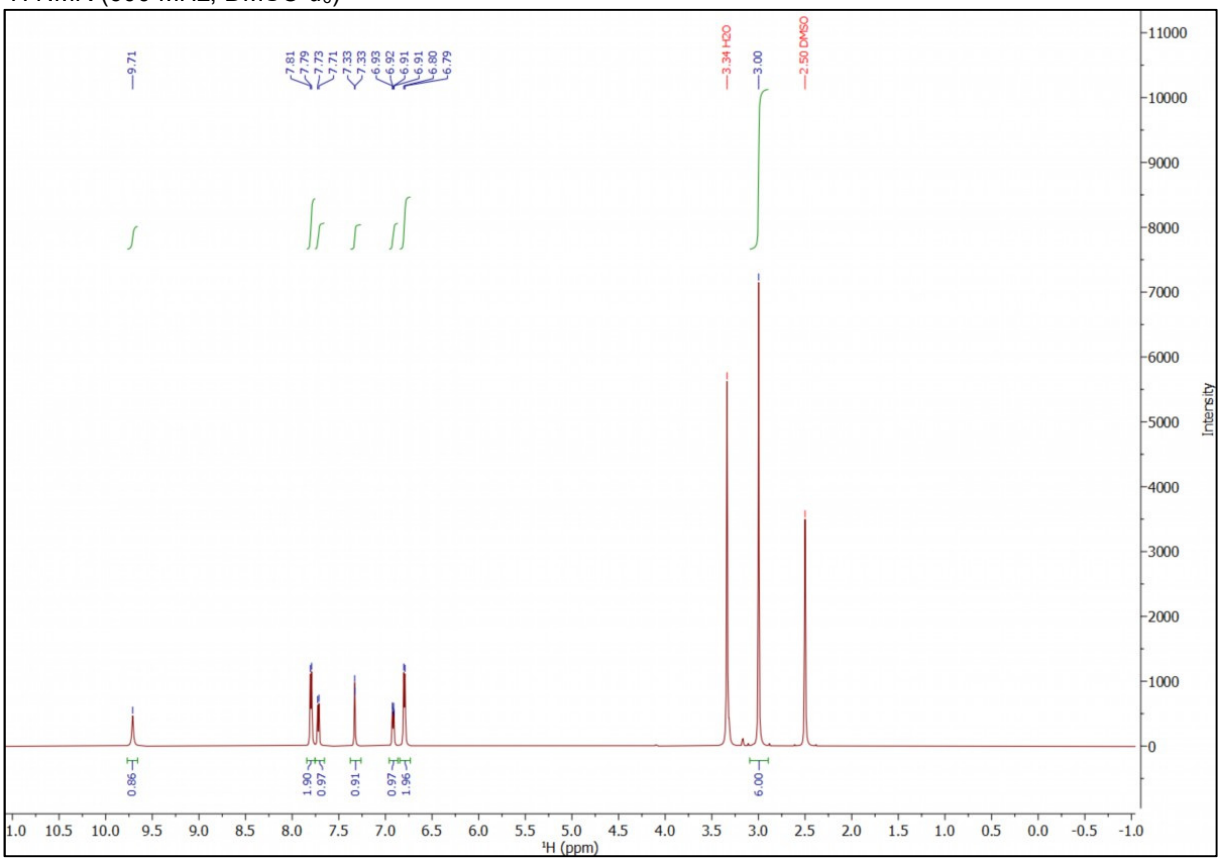


^{13}C NMR (151 MHz, $CDCl_3$)

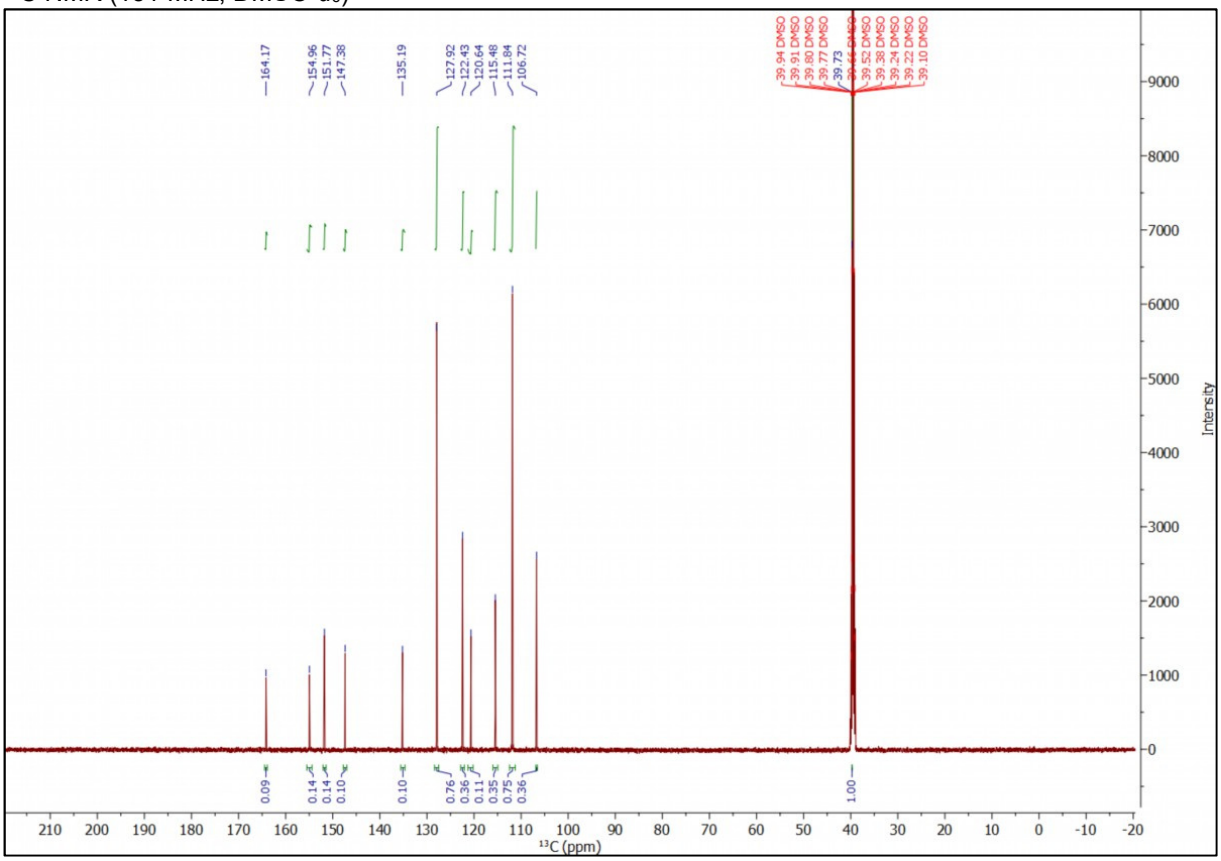


2-(4-(Dimethylamino)phenyl)benzo[*d*]thiazol-6-ol (**II-71**) [from **procedure A**]

^{1}H NMR (600 MHz, DMSO-d_6)

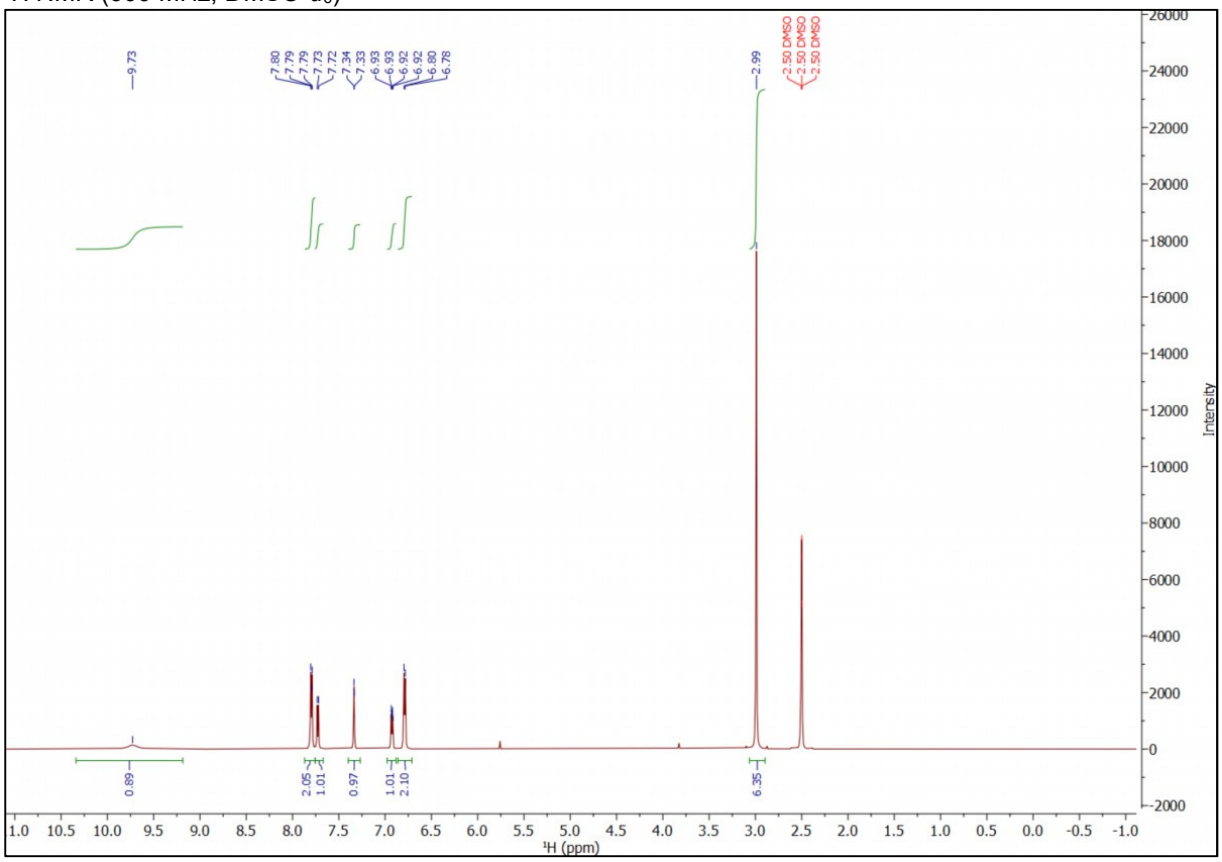


^{13}C NMR (151 MHz, DMSO-d_6)

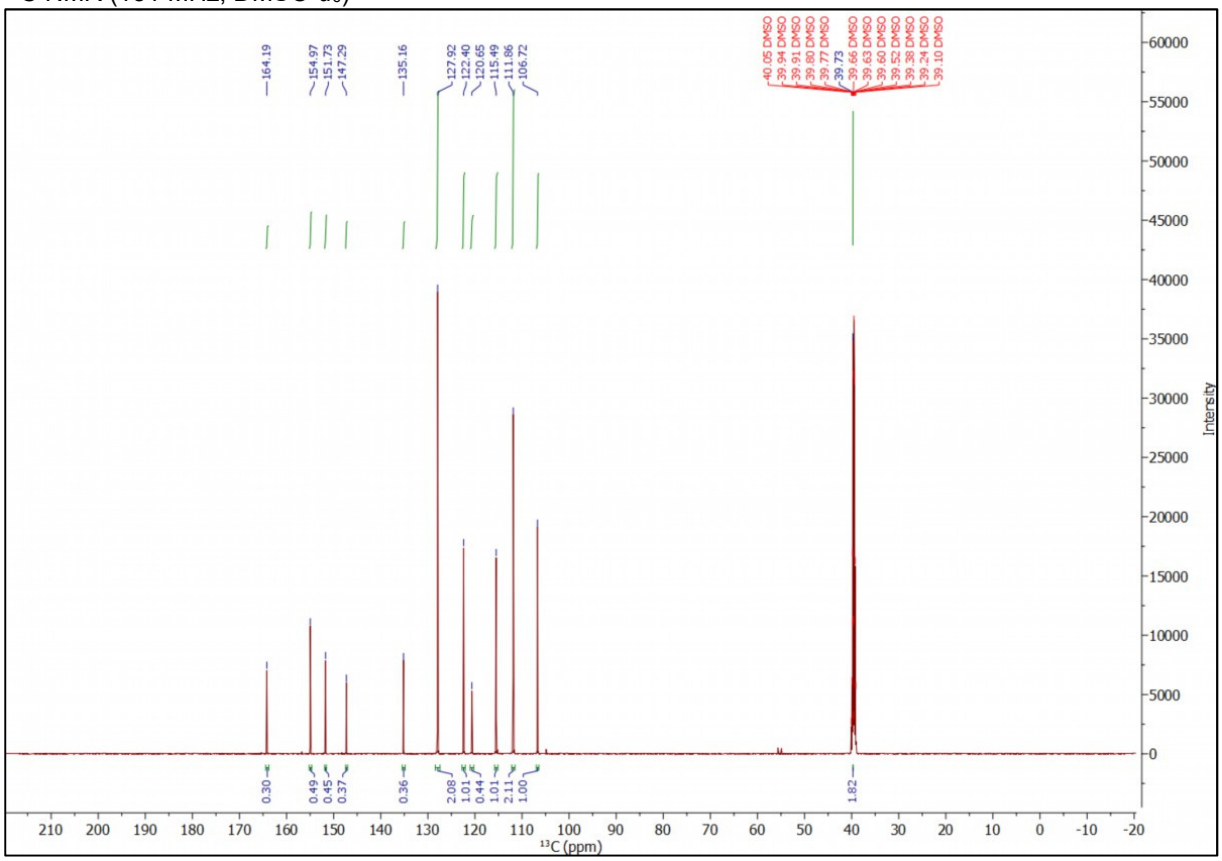


2-(4-(Dimethylamino)phenyl)benzo[*d*]thiazol-6-ol (**II-71**) [from **procedure B**]

^{1}H NMR (600 MHz, DMSO-d_6)

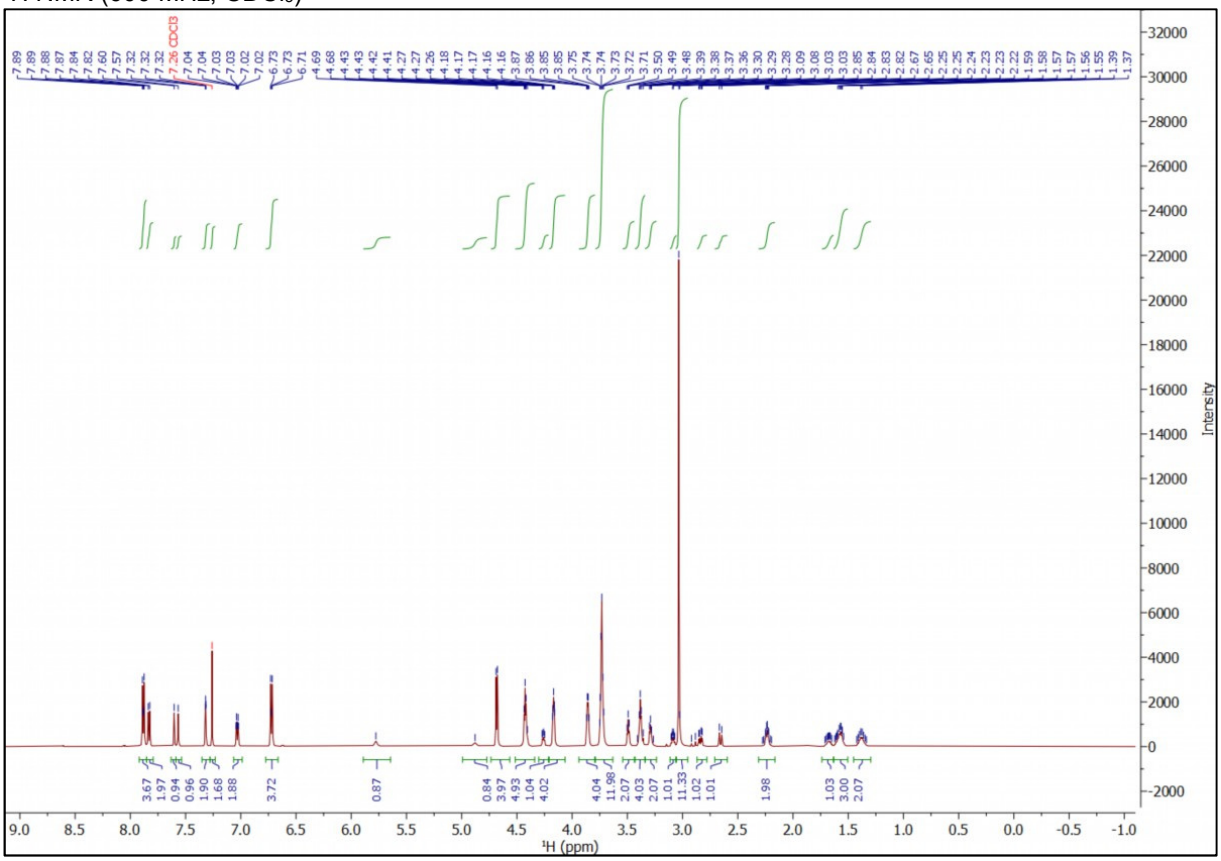


^{13}C NMR (151 MHz, DMSO-d_6)

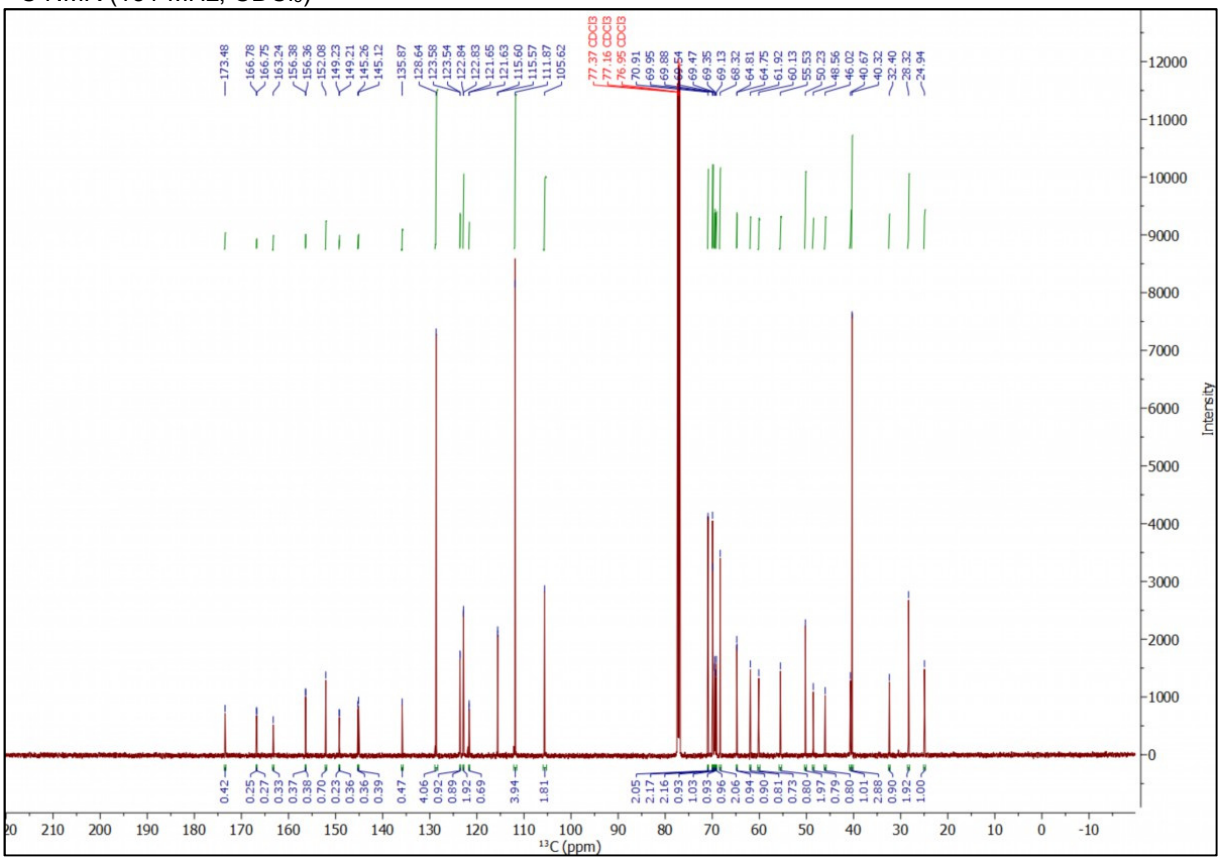


N,*N*-Bis(2-(2-(4-((2-(2-((2-(4-(dimethylamino)phenyl)benzo[*d*]thiazol-6-yl)oxy)ethoxy)ethoxy)methyl)-1*H*-1,2,3-triazol-1-yl)ethoxy)ethyl)-5-((3a*S*,4*S*,6a*R*)-2-oxohexahydro-1*H*-thieno[3,4-*d*]imidazol-4-yl)pentanamide (**II-73**, cCAP-1)

^{1}H NMR (600 MHz, $CDCl_3$)

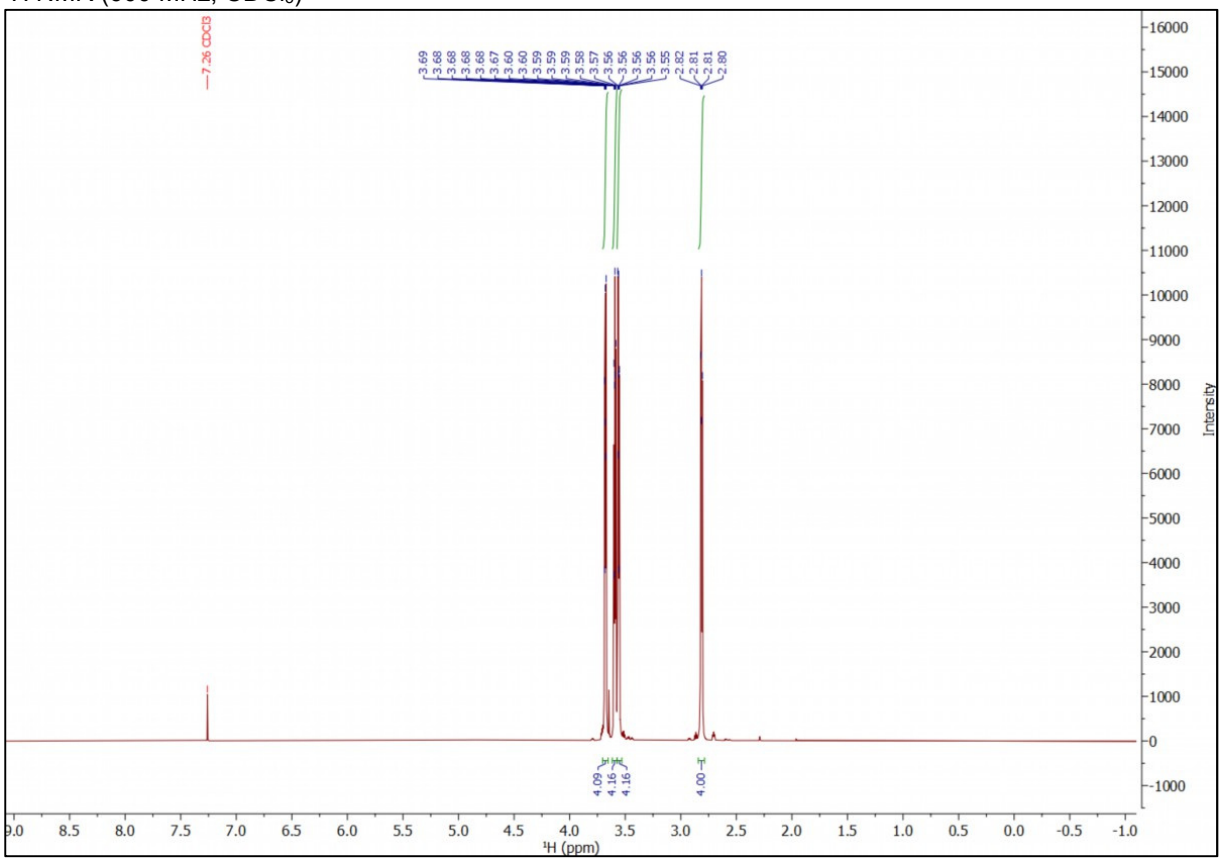


^{13}C NMR (151 MHz, $CDCl_3$)

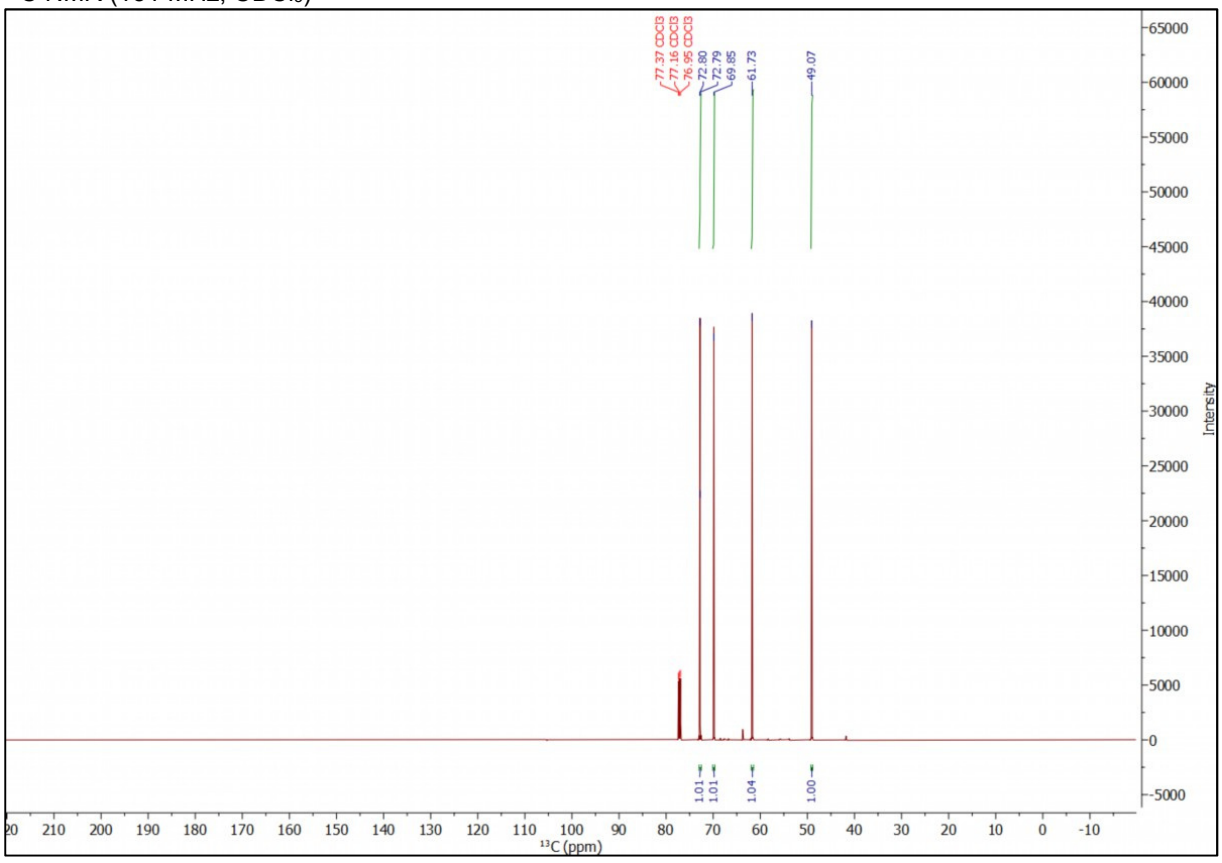


2,2'-((Azanediylbis(ethane-2,1-diyl))bis(oxy))bis(ethan-1-ol) (**II-74**)

^{1}H NMR (600 MHz, $CDCl_3$)

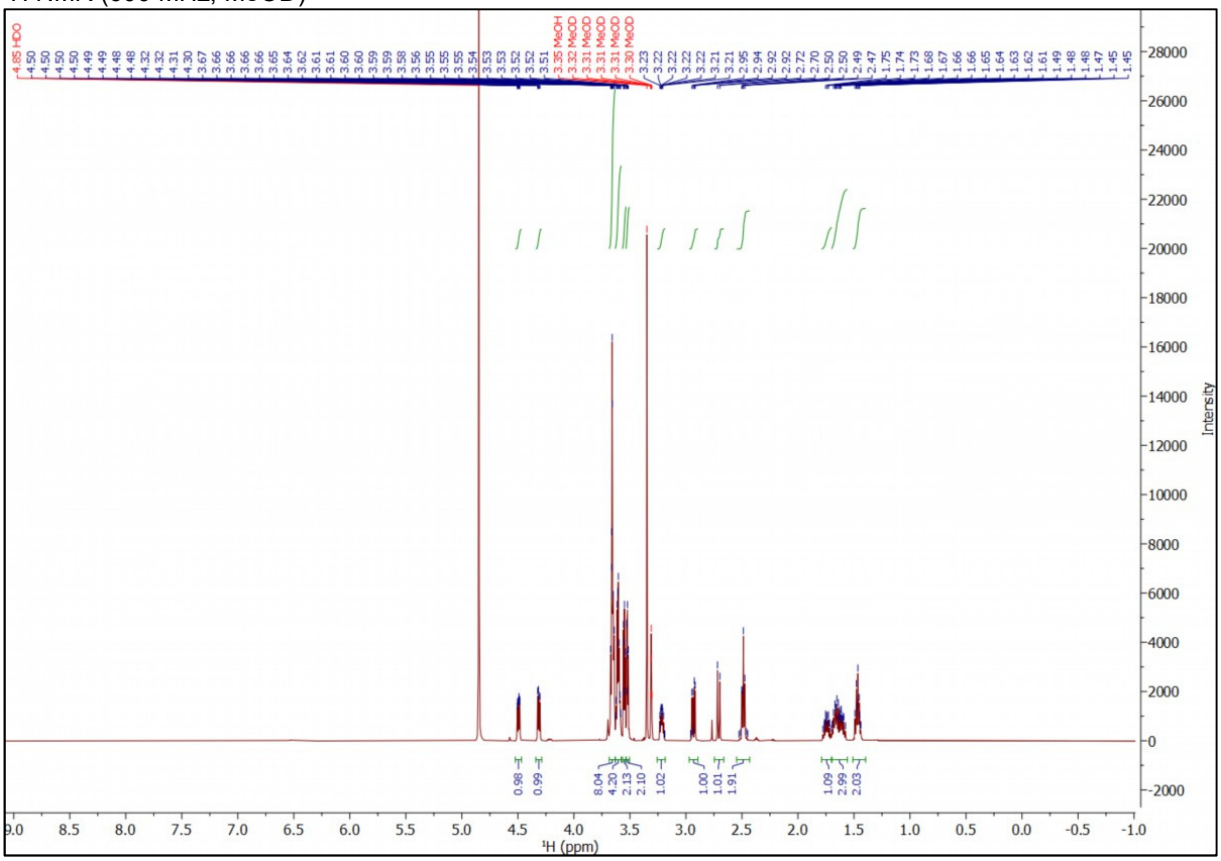


^{13}C NMR (151 MHz, $CDCl_3$)

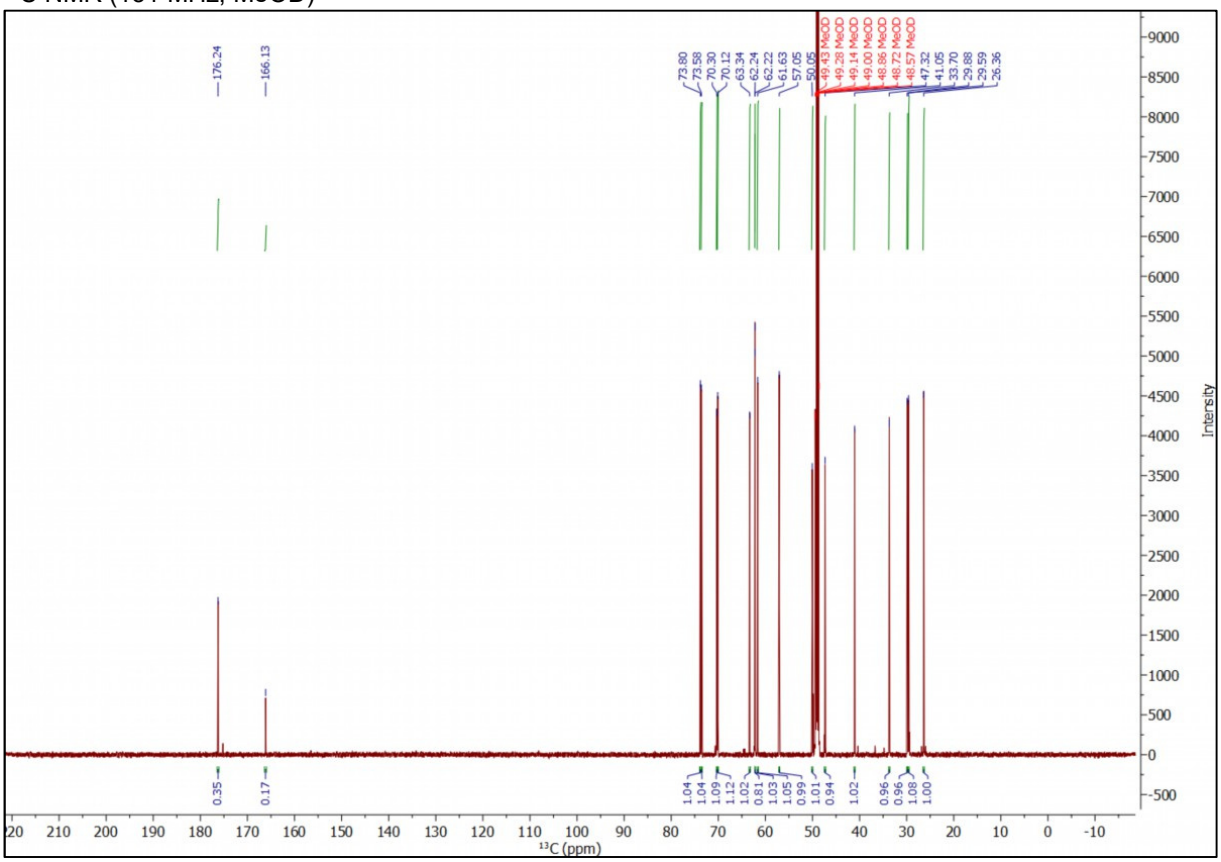


N,*N*-Bis(2-(2-hydroxyethoxy)ethyl)-5-((3a*S*,4*S*,6a*R*)-2-oxohexahydro-1*H*-thieno[3,4-*d*]imidazol-4-yl)pentanamide (**II-77**)

^{1}H NMR (600 MHz, MeOD)

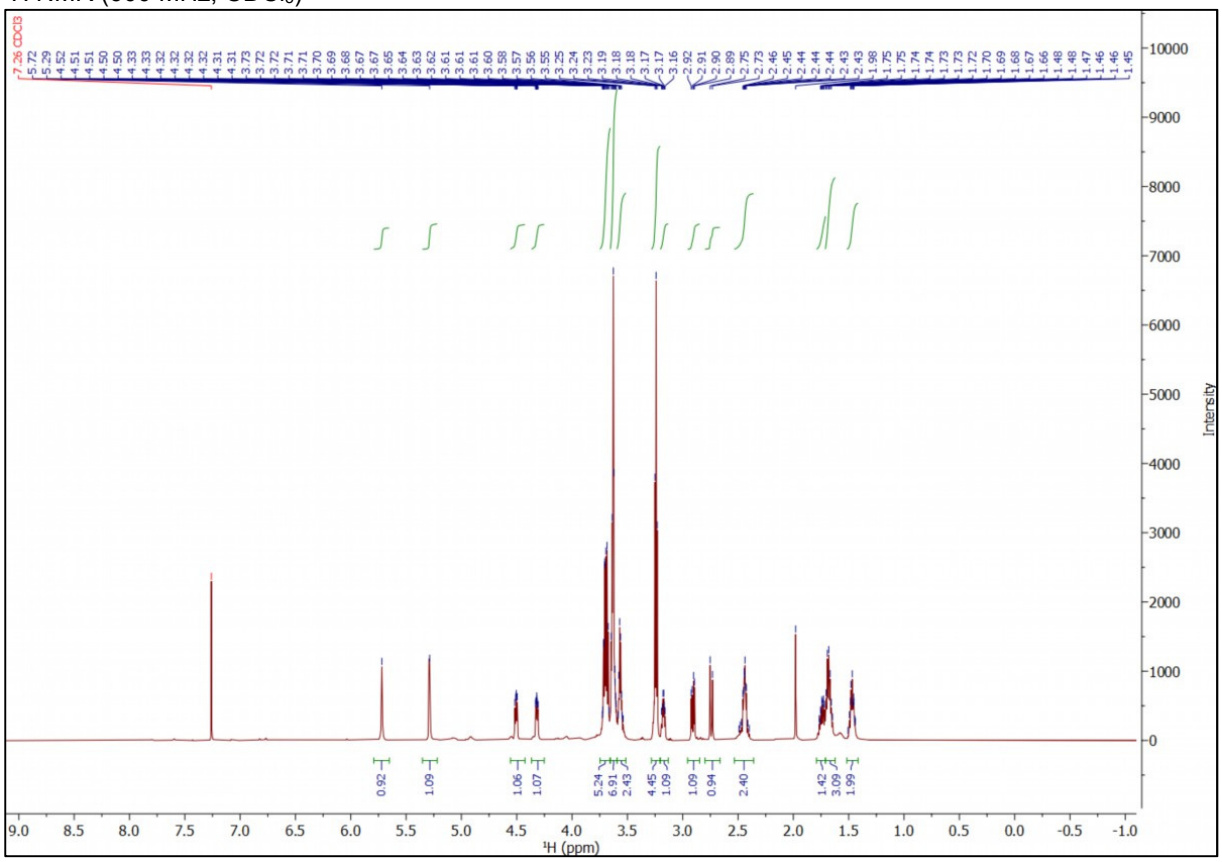


^{13}C NMR (151 MHz, MeOD)

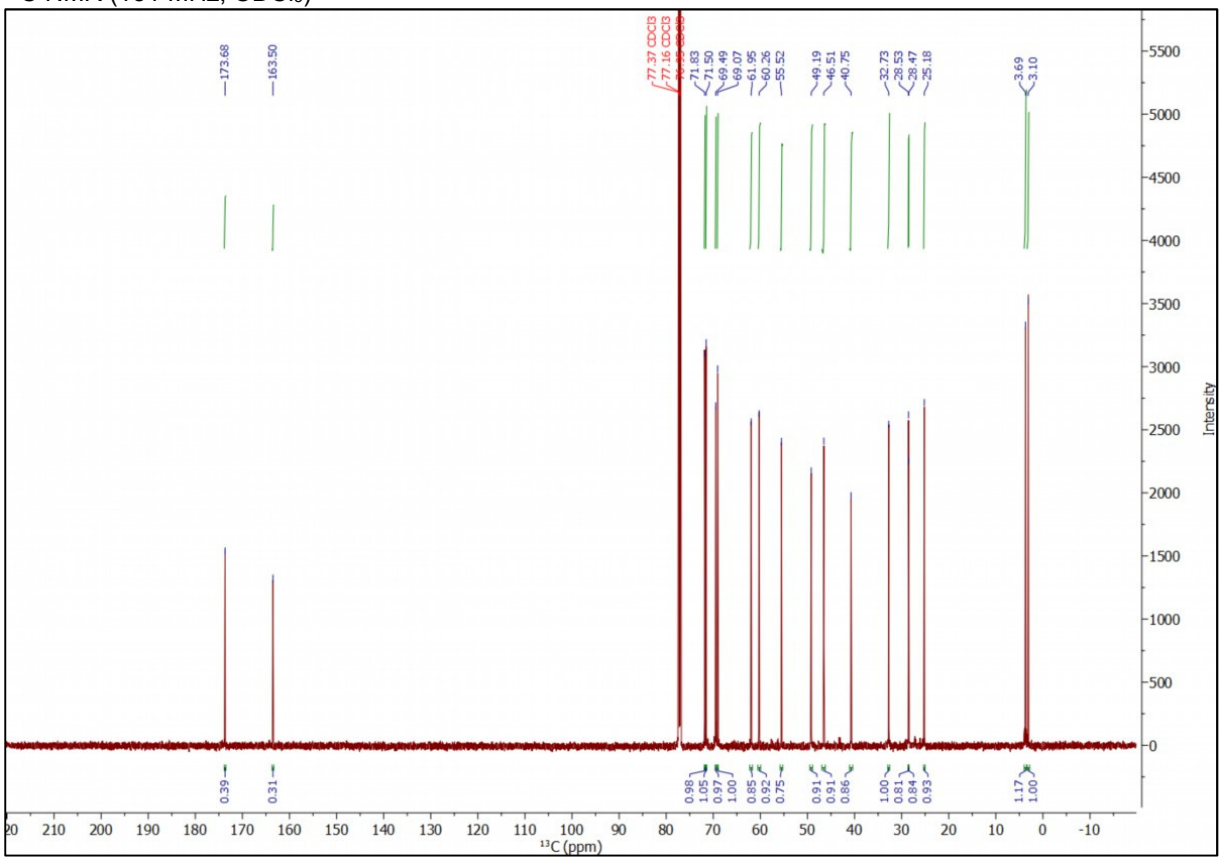


N,*N*-Bis(2-(2-iodoethoxy)ethyl)-5-((3a*S*,4*S*,6a*R*)-2-oxohexahydro-1*H*-thieno[3,4-*d*]imidazol-4-yl)pentanamide (**II-78**)

^{1}H NMR (600 MHz, $CDCl_3$)

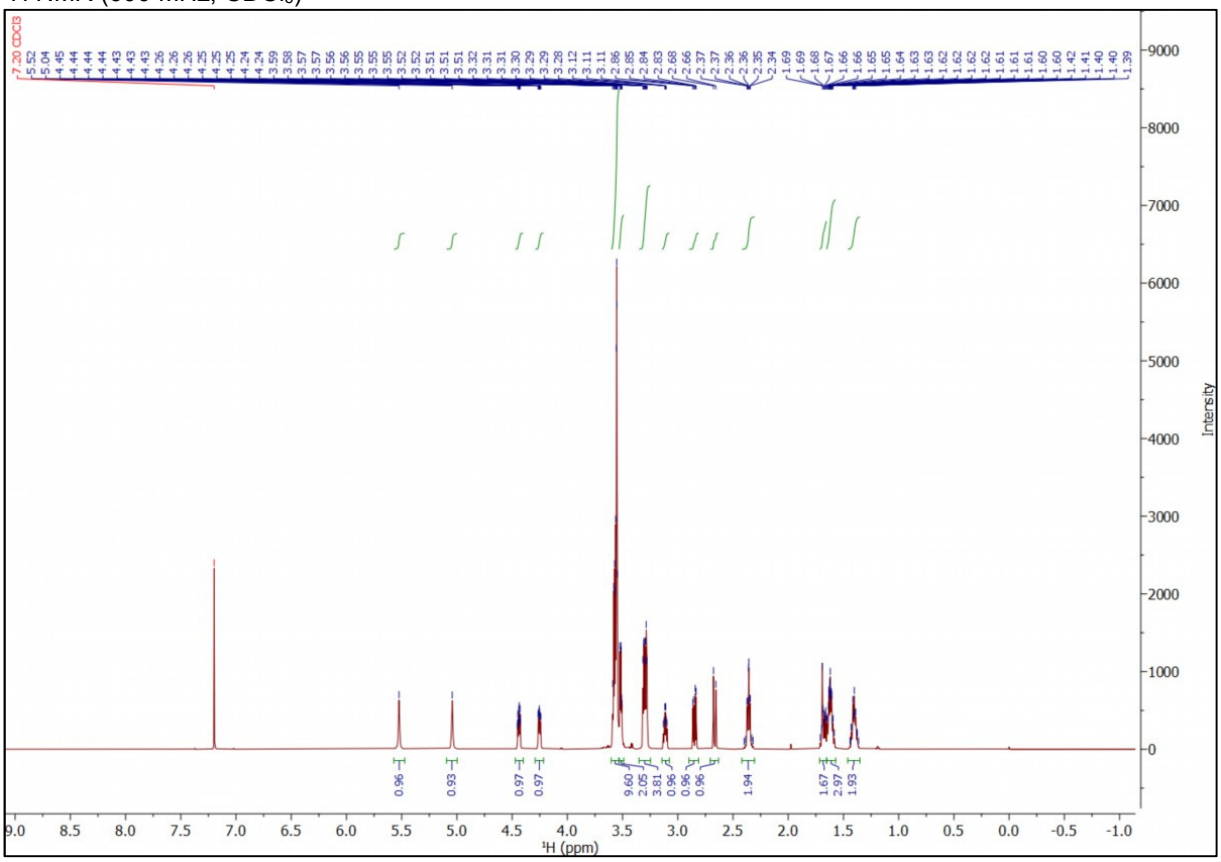


^{13}C NMR (151 MHz, $CDCl_3$)

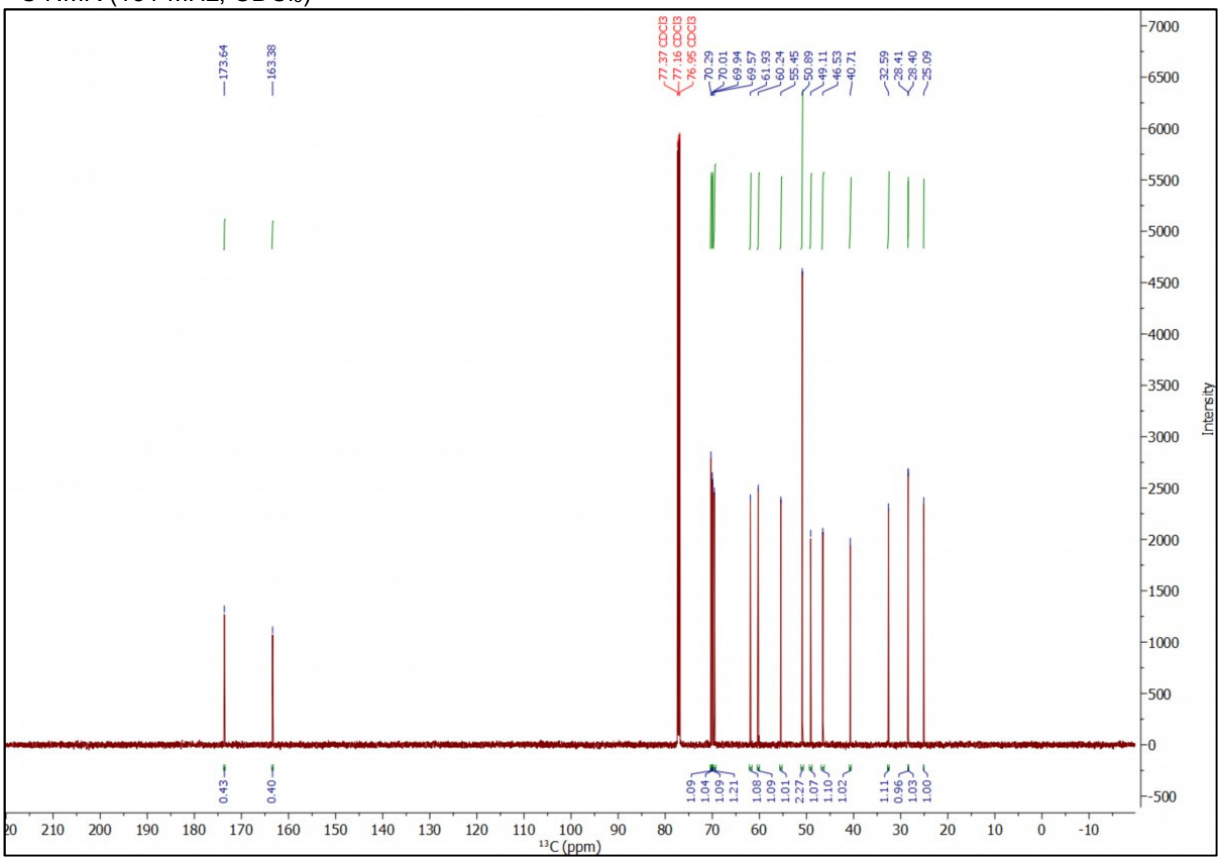


N,*N*-Bis(2-(2-azidoethoxy)ethyl)-5-((3a*S*,4*S*,6a*R*)-2-oxohexahydro-1*H*-thieno[3,4-*d*]imidazol-4-yl)pentanamide (**II-79**)

^{1}H NMR (600 MHz, $CDCl_3$)

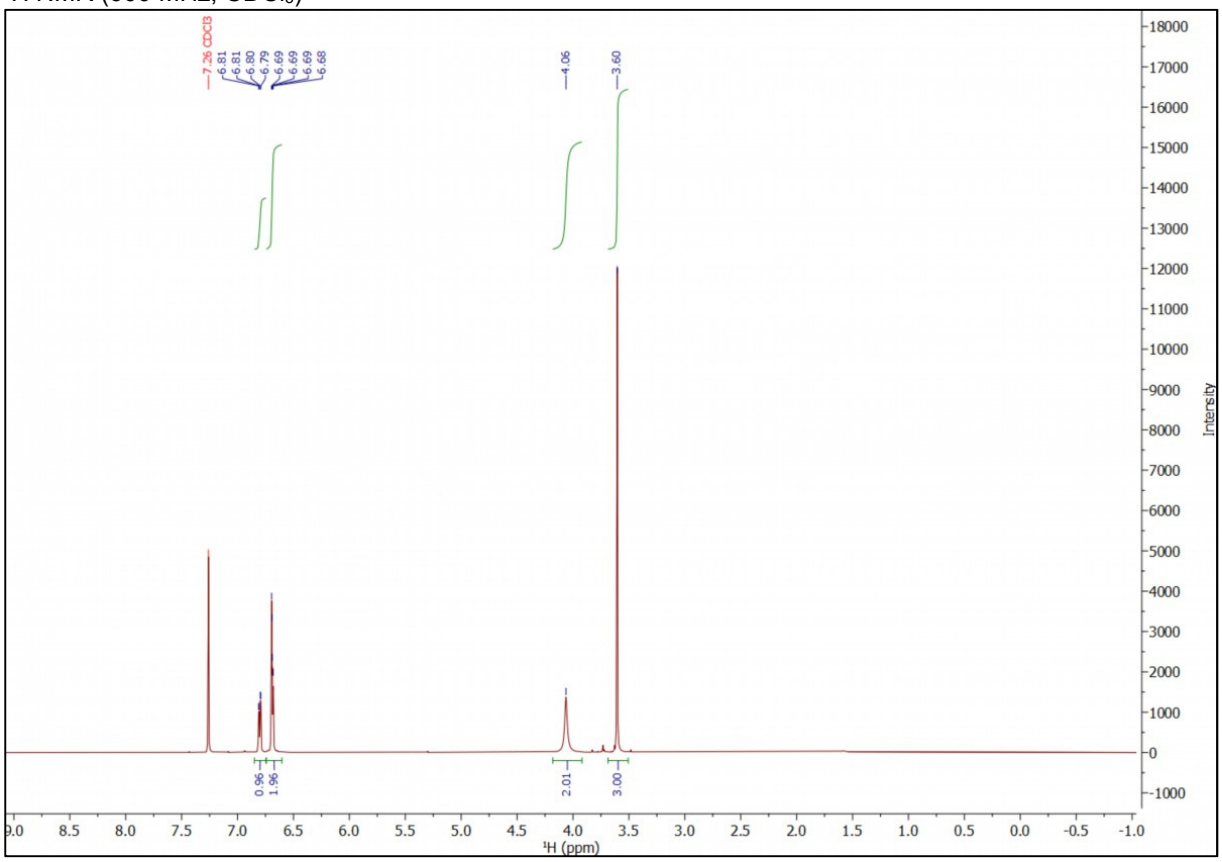


^{13}C NMR (151 MHz, $CDCl_3$)

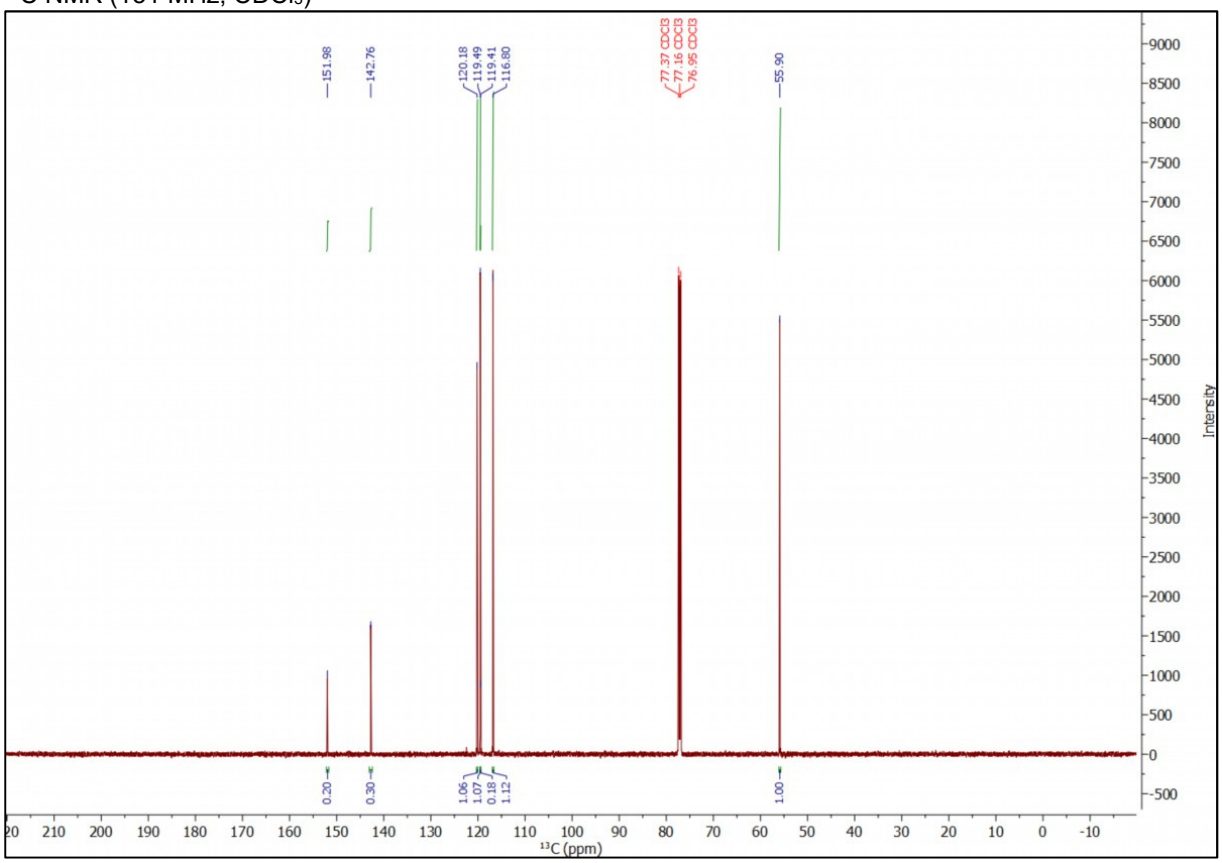


2-Amino-5-methoxybenzenethiol (**II-88**)

^{1}H NMR (600 MHz, $CDCl_3$)

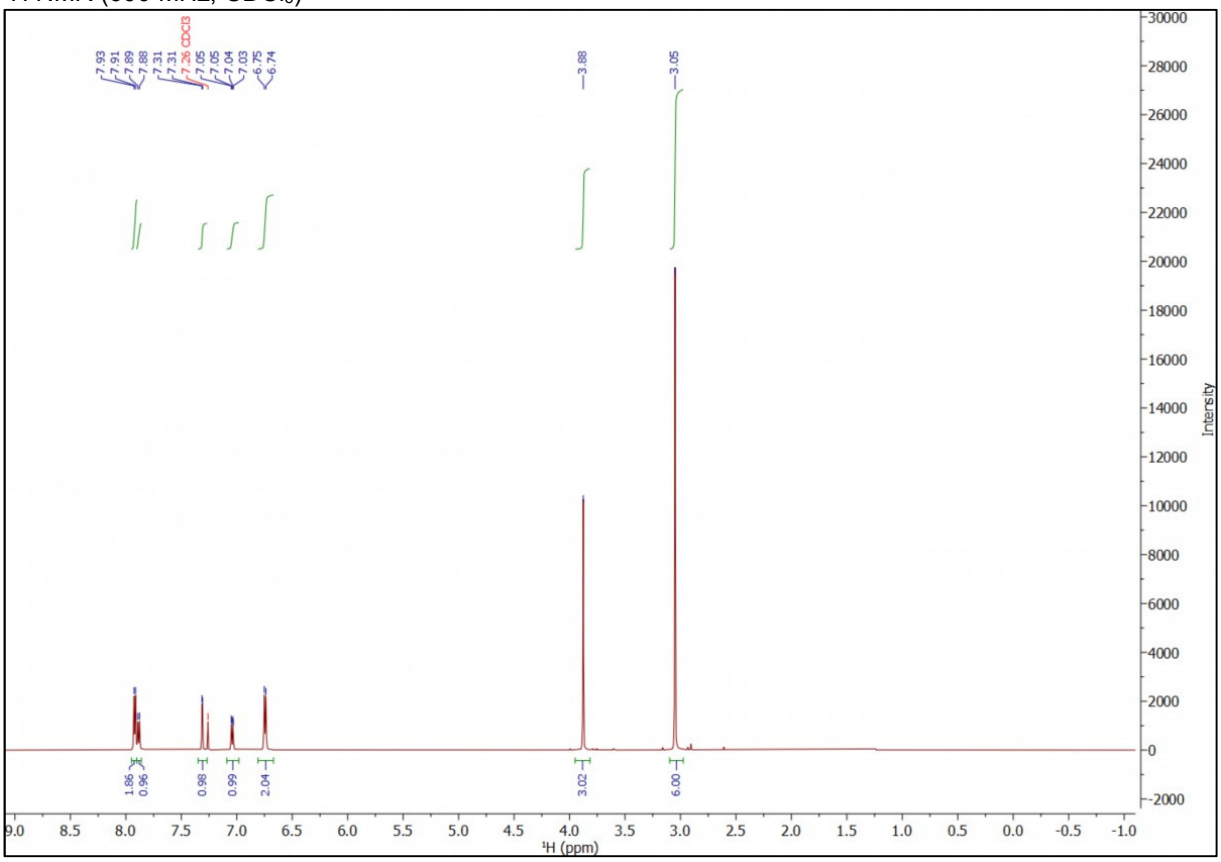


^{13}C NMR (151 MHz, $CDCl_3$)

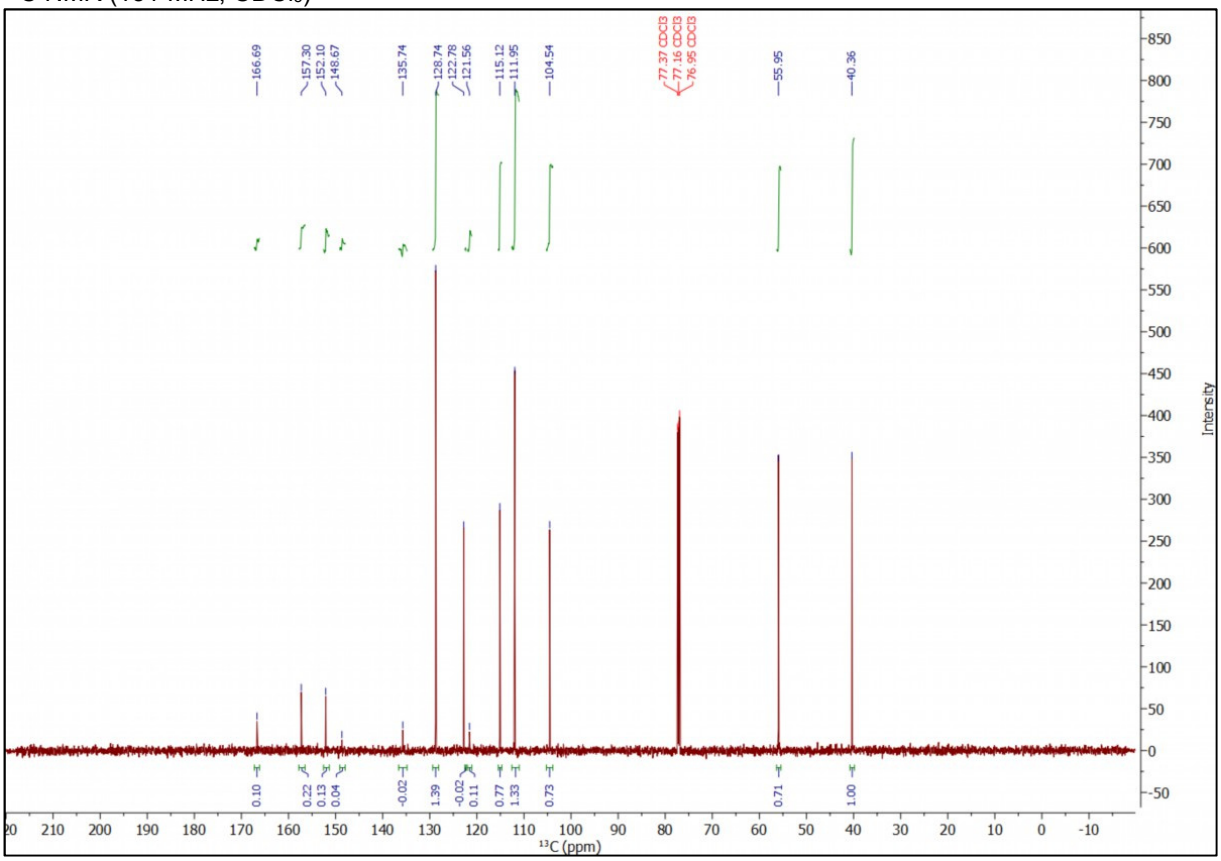


4-(6-Methoxybenzo[*d*]thiazol-2-yl)-*N*,*N*-dimethylaniline (**II-90**)

^{1}H NMR (600 MHz, $CDCl_3$)

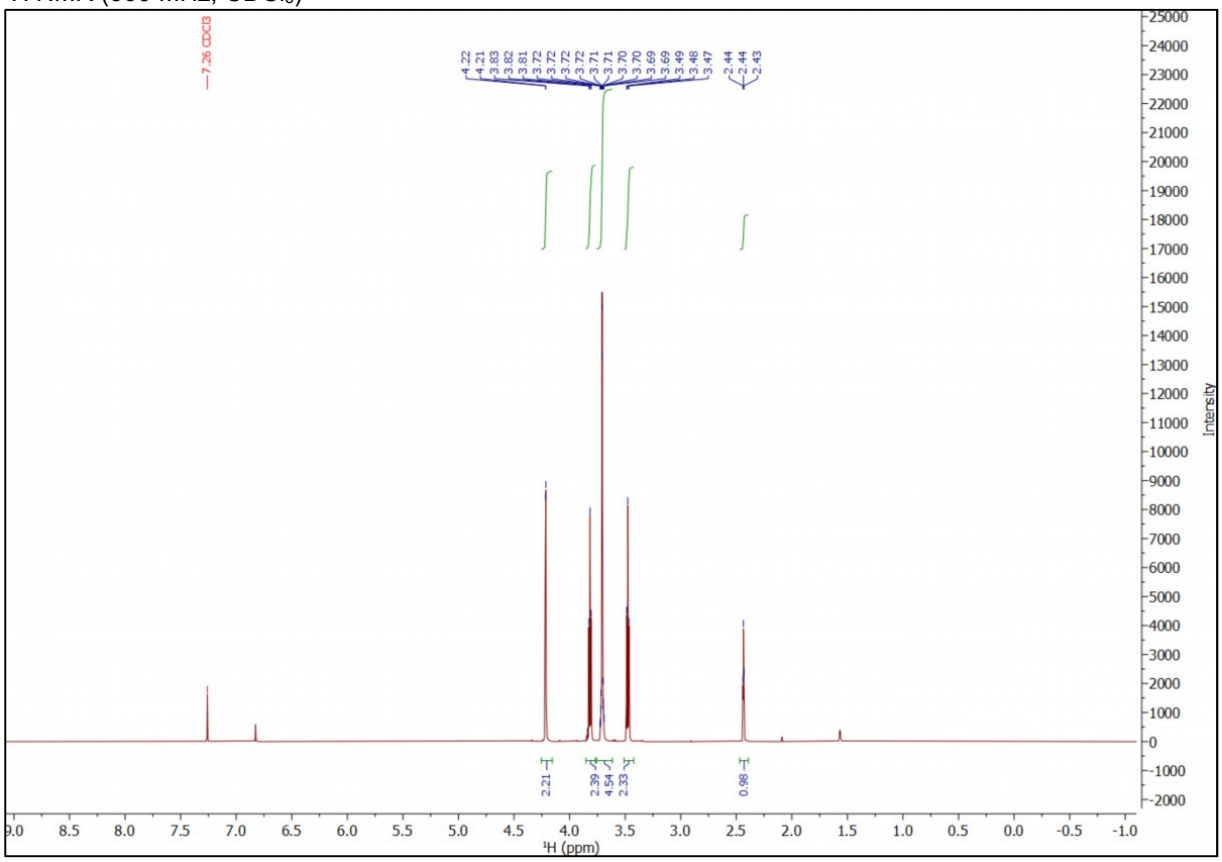


^{13}C NMR (151 MHz, $CDCl_3$)

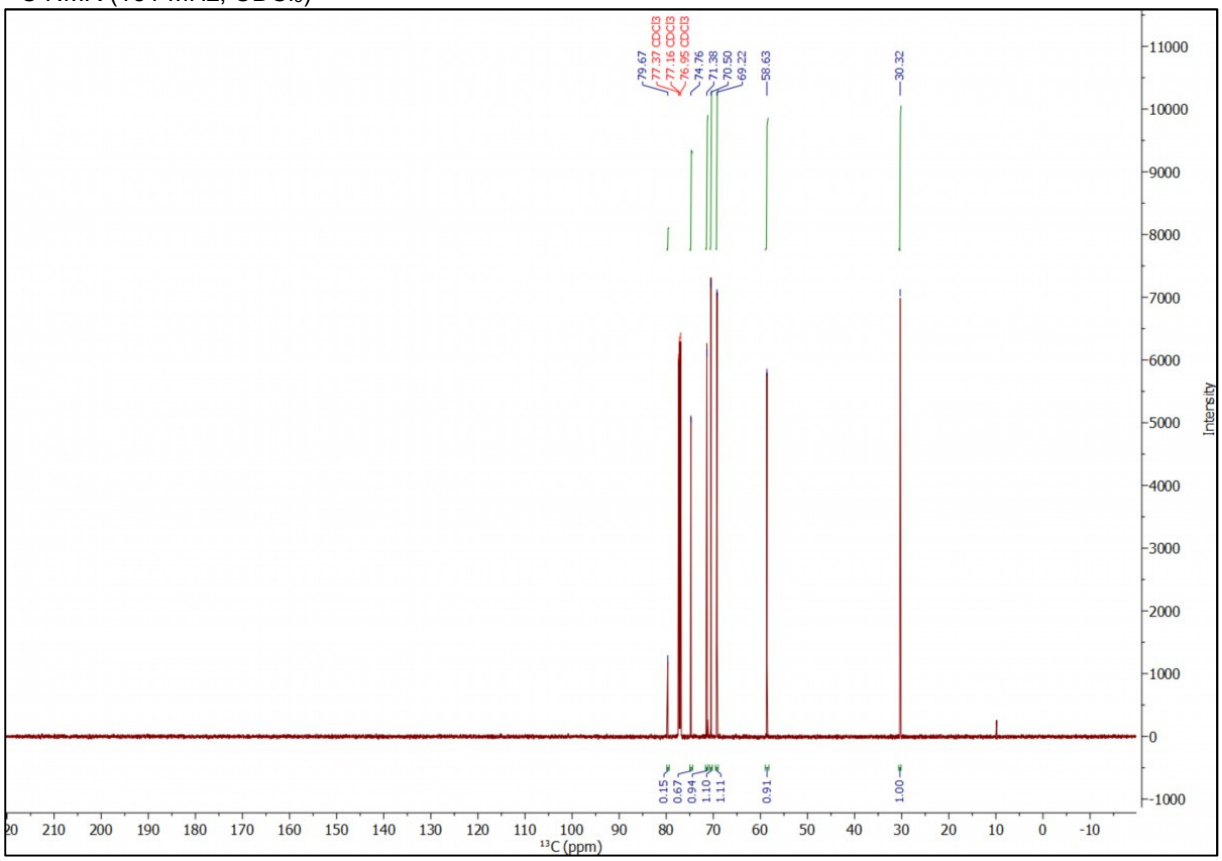


3-(2-(2-Bromoethoxy)ethoxy)prop-1-yne (**II-92**)

^{1}H NMR (600 MHz, $CDCl_3$)

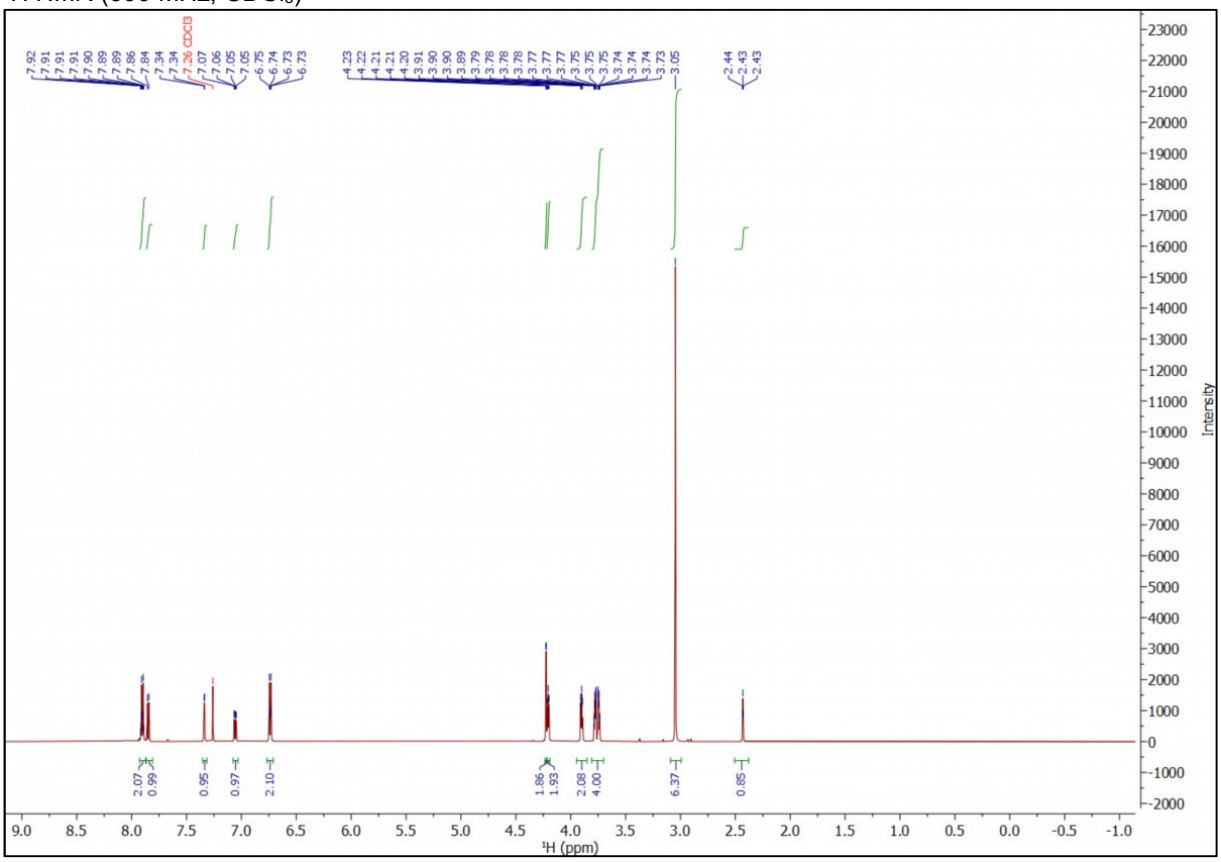


^{13}C NMR (151 MHz, $CDCl_3$)

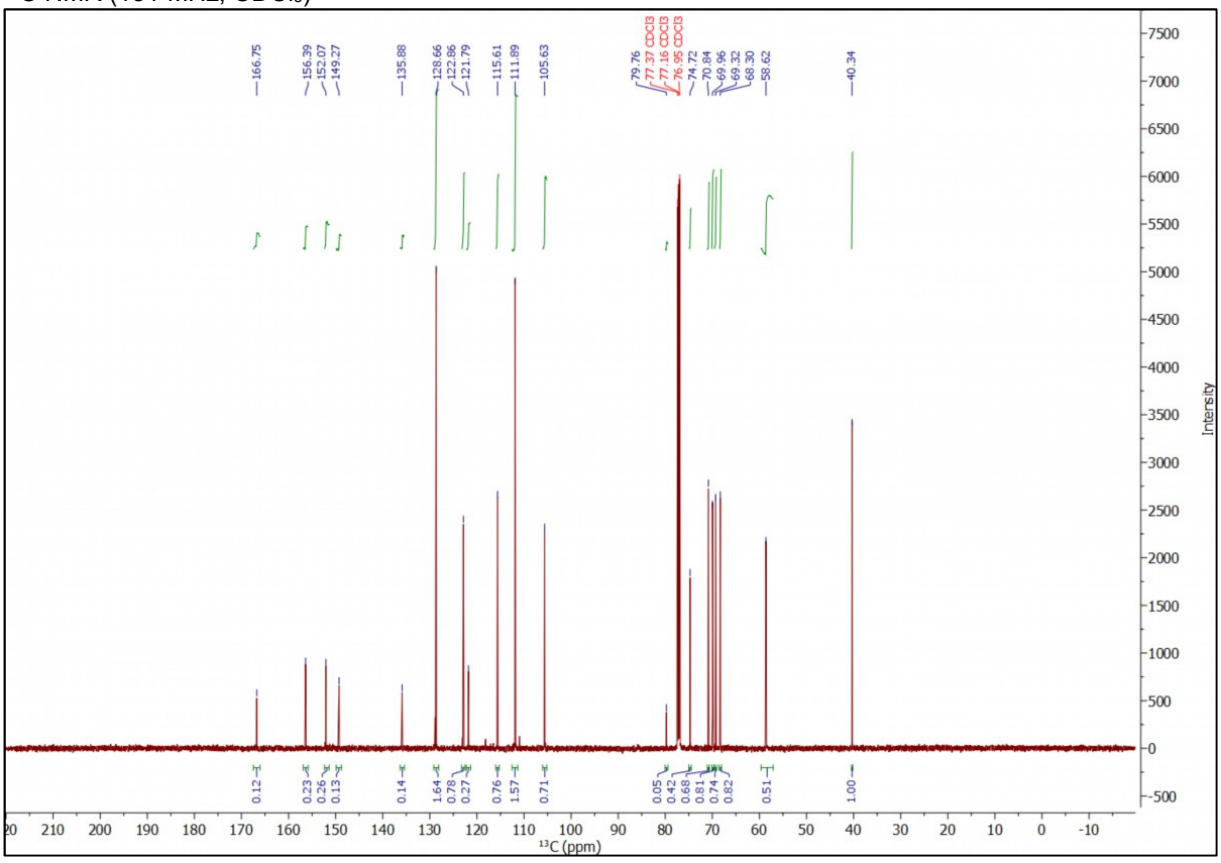


N,*N*-Dimethyl-4-(6-(2-(2-(prop-2-yn-1-yloxy)ethoxy)ethoxy)benzo[*d*]thiazol-2-yl)aniline (**II-93**)

^{1}H NMR (600 MHz, $CDCl_3$)

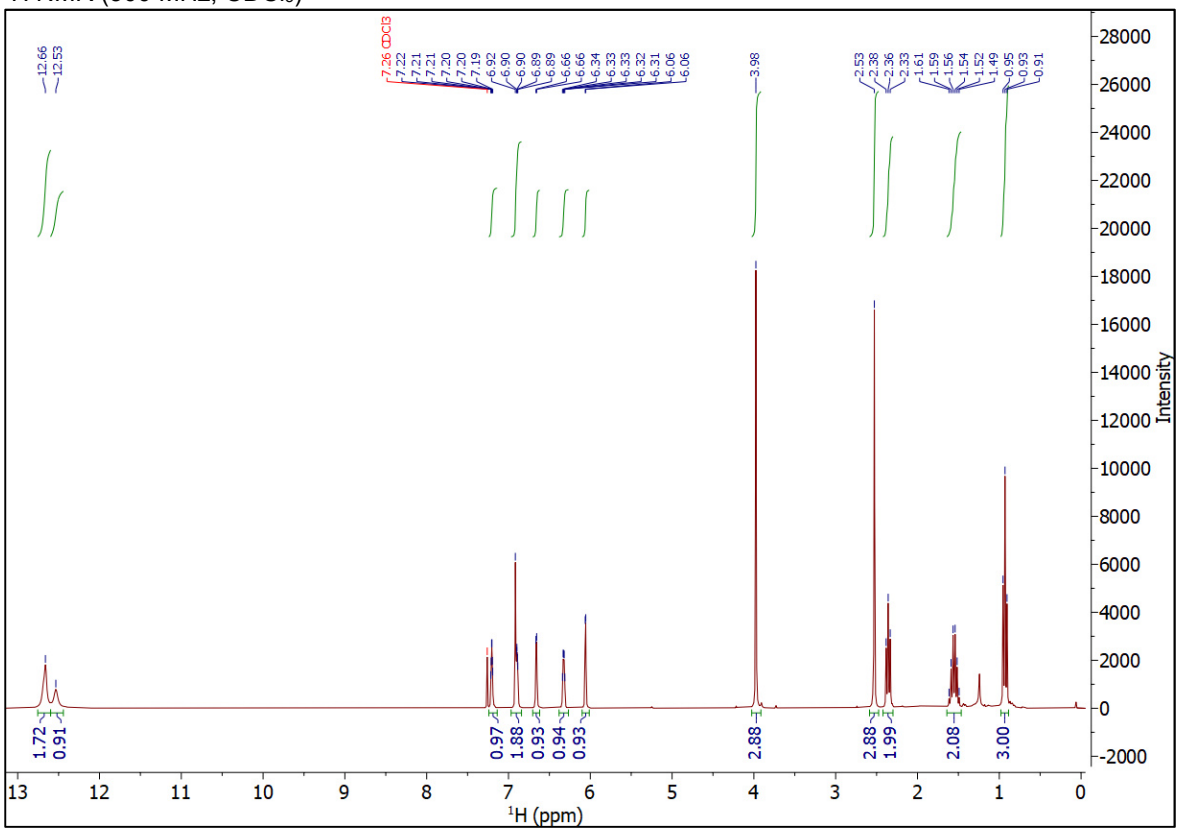


^{13}C NMR (151 MHz, $CDCl_3$)

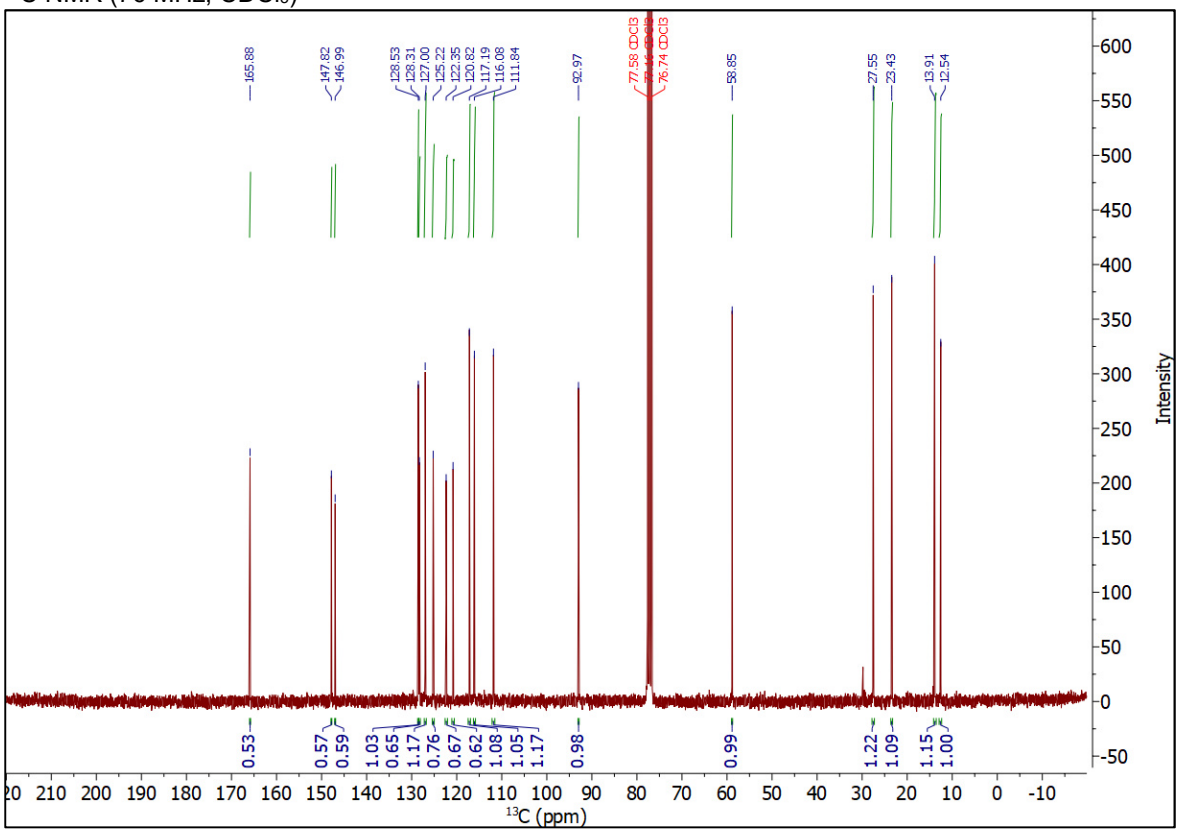


(*Z*)-4'-methoxy-5'-((5-methyl-4-propyl-1*H*-pyrrol-2-yl)methylene)-1*H*,5'*H*-[2,2'-bipyrrol]-1'-ium chloride (**III-1aa·HCl**)

^{1}H NMR (300 MHz, $CDCl_3$)

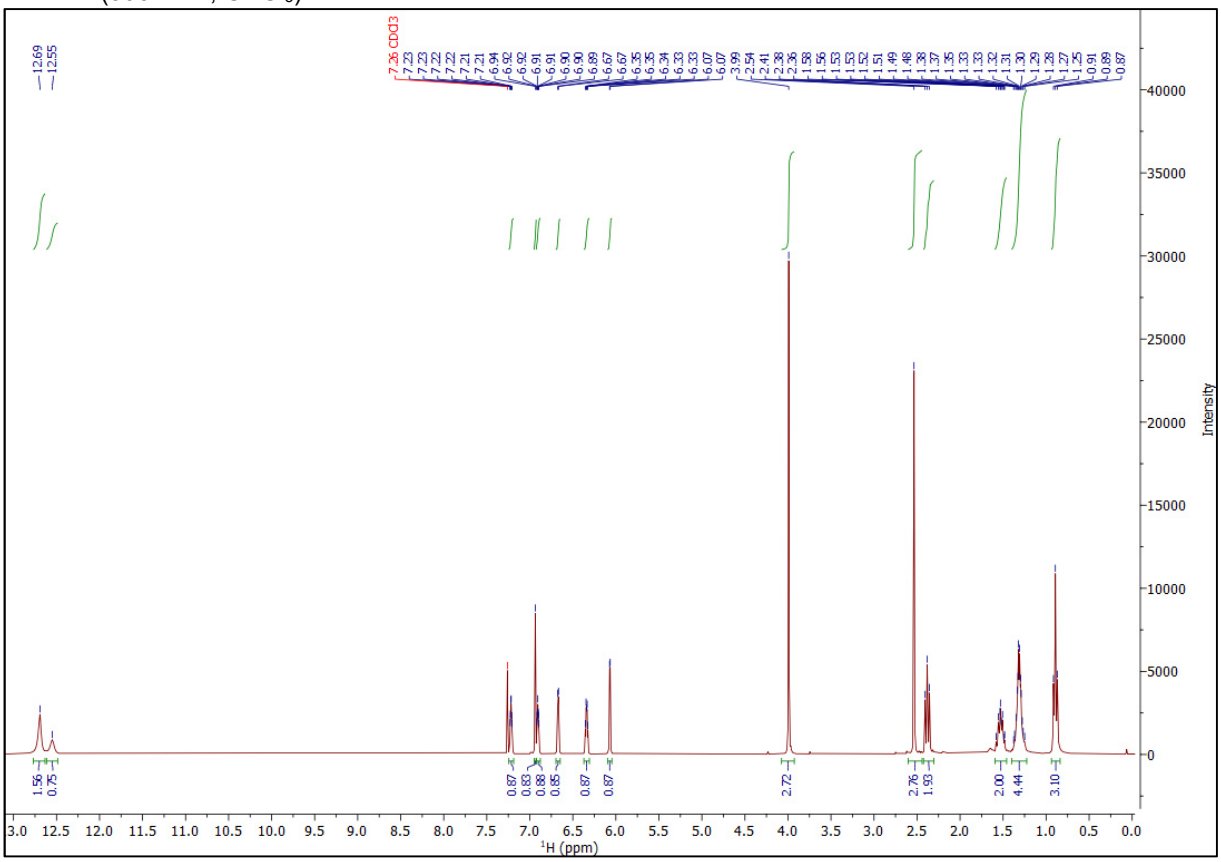


^{13}C NMR (76 MHz, $CDCl_3$)

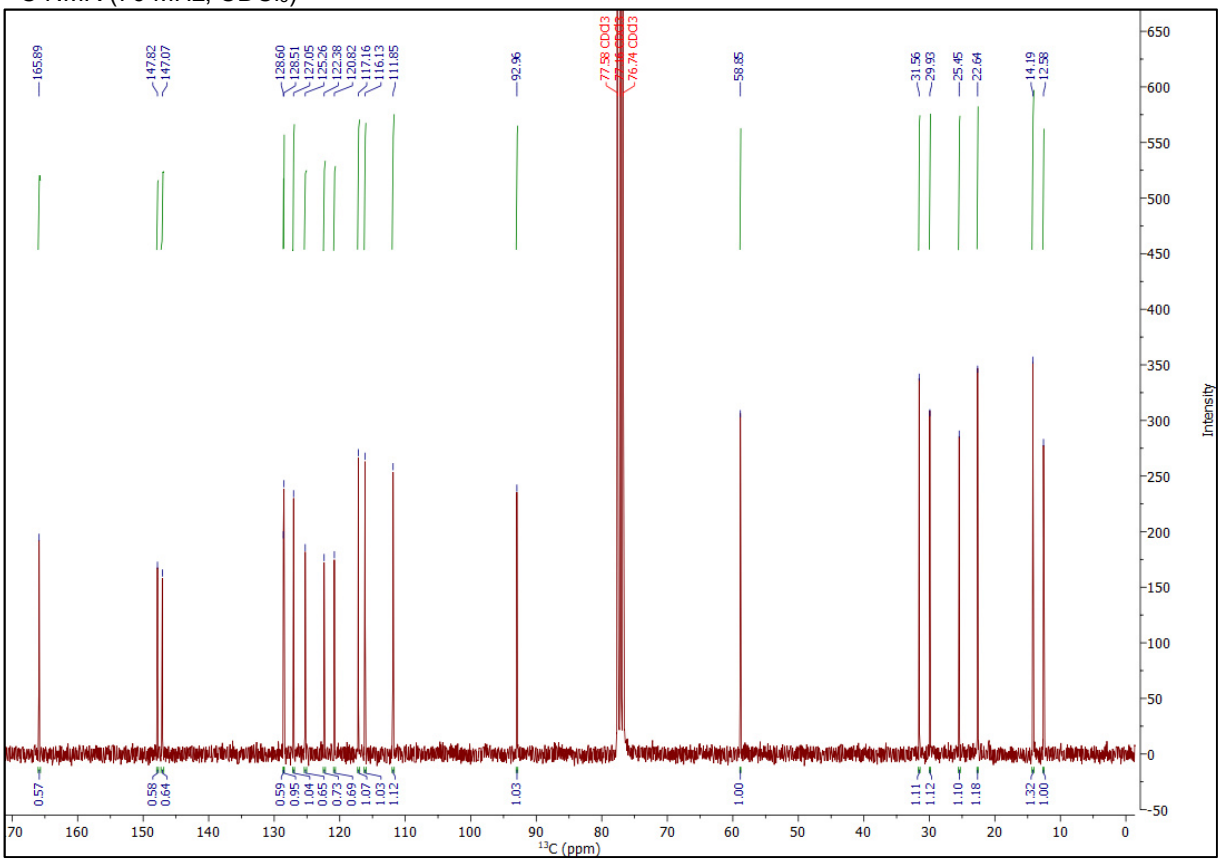


(*Z*)-4'-Methoxy-5'-((5-methyl-4-pentyl-1*H*-pyrrol-2-yl)methylene)-1*H*,5'*H*-[2,2'-bipyrrol]-1'-ium chloride (**III-1ab·HCl**, prodigiosin)

^{1}H NMR (300 MHz, $CDCl_3$)

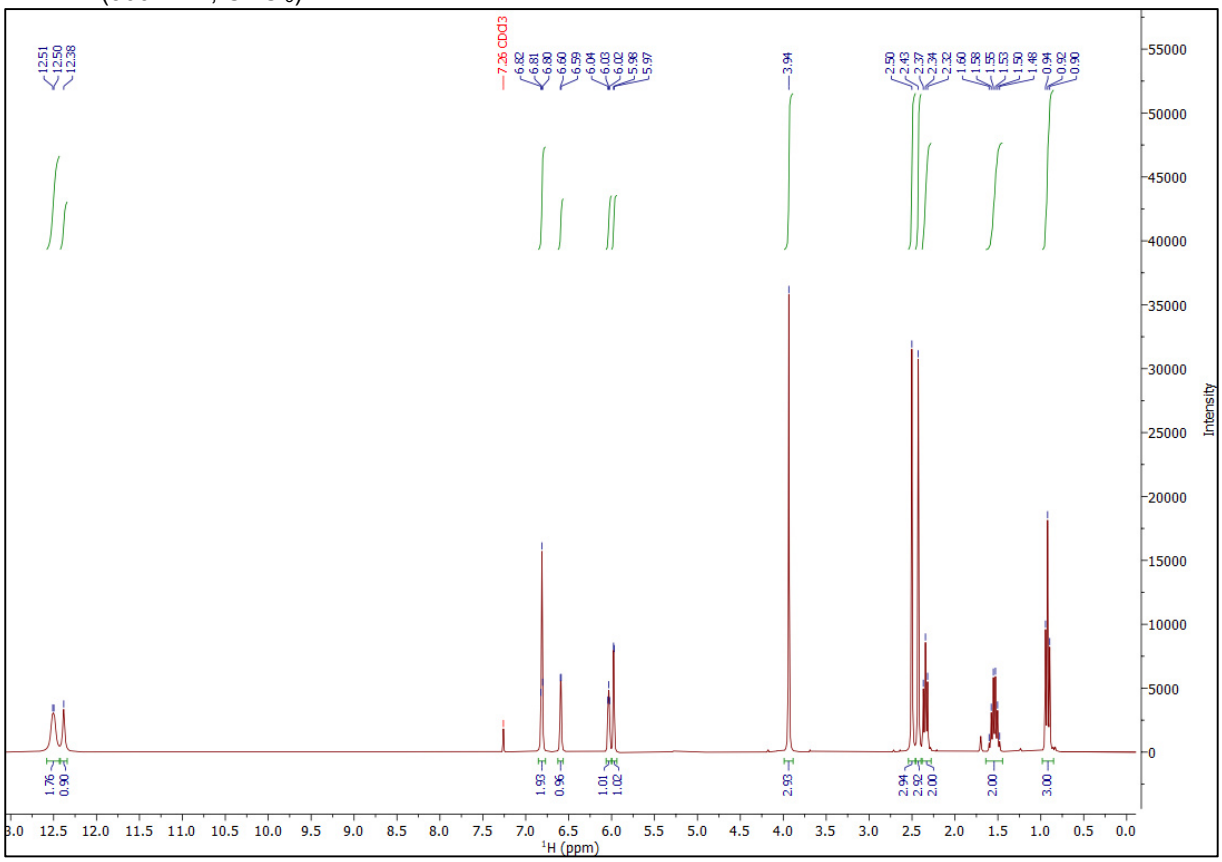


^{13}C NMR (76 MHz, $CDCl_3$)

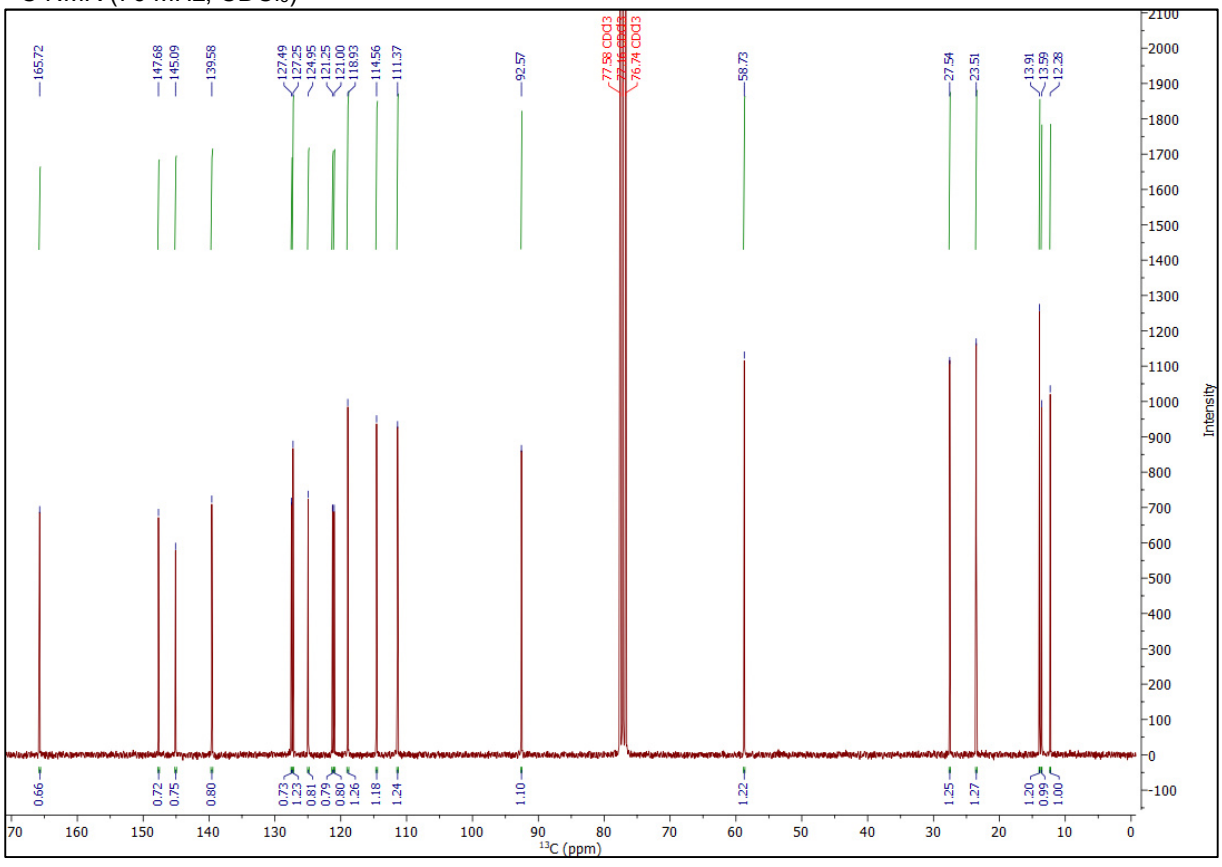


(*Z*)-4'-Methoxy-5-methyl-5'-((5-methyl-4-propyl-1*H*-pyrrol-2-yl)methylene)-1*H*,5'*H*-[2,2'-bipyrrol]-1'-ium chloride (**III-1ba·HCl**)

^{1}H NMR (300 MHz, $CDCl_3$)

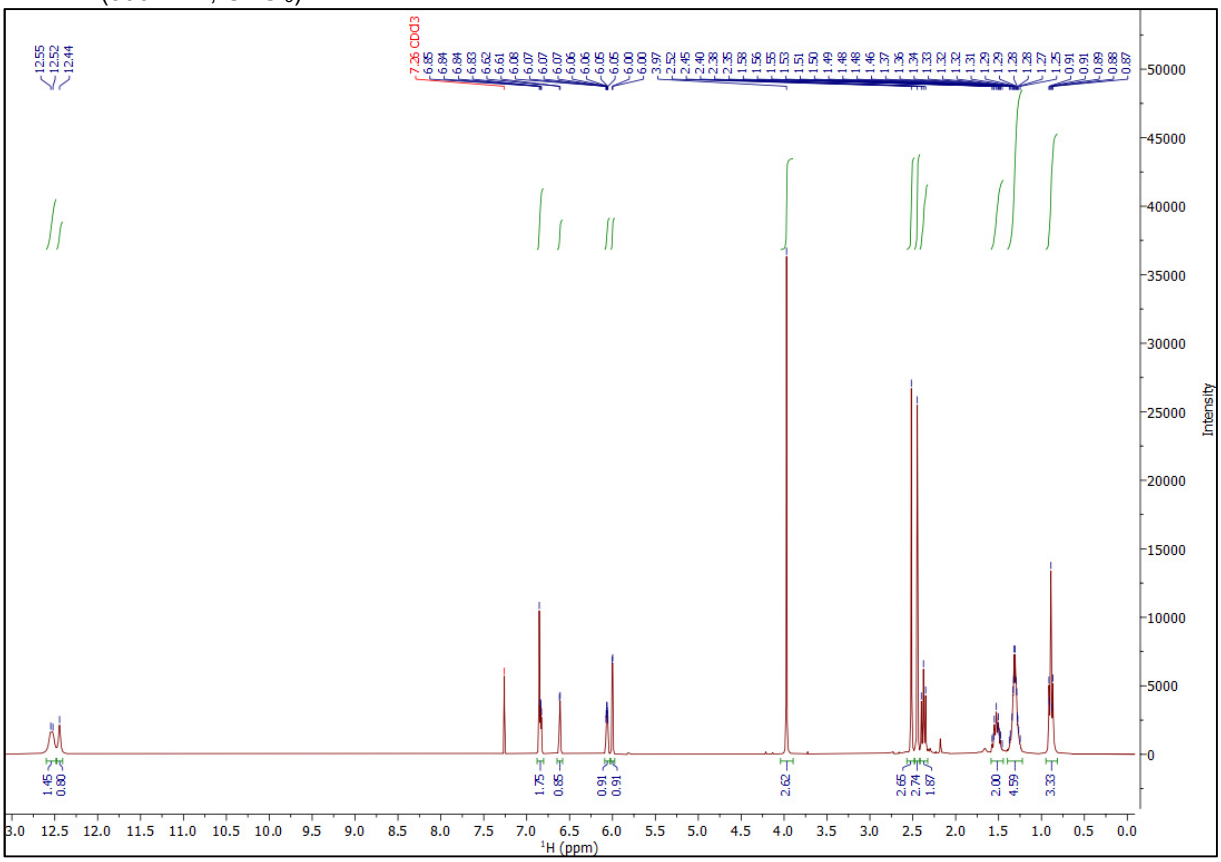


^{13}C NMR (76 MHz, $CDCl_3$)

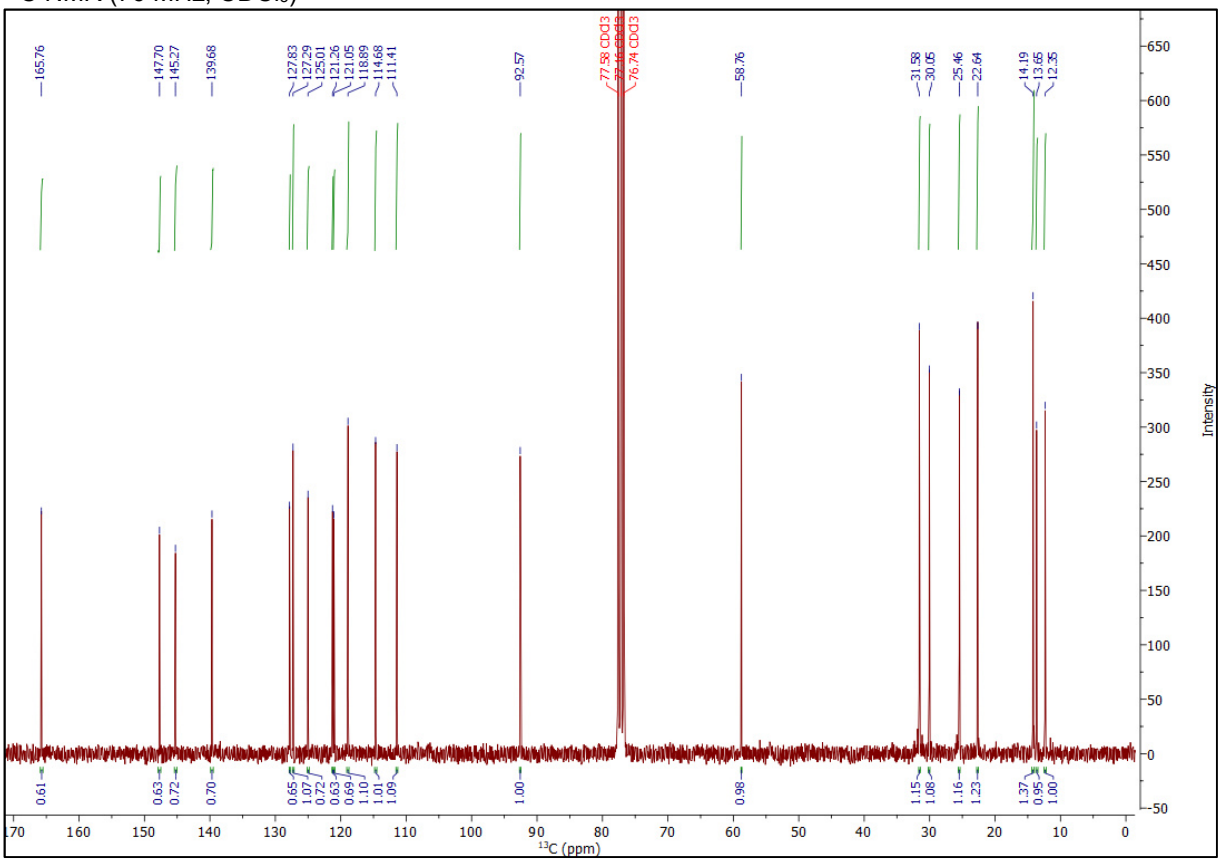


(*Z*)-4'-Methoxy-5-methyl-5'-((5-methyl-4-pentyl-1*H*-pyrrol-2-yl)methylene)-1*H*,5'*H*-[2,2'-bipyrrol]-1'-ium chloride (**III-1bb·HCl**)

^{1}H NMR (300 MHz, $CDCl_3$)

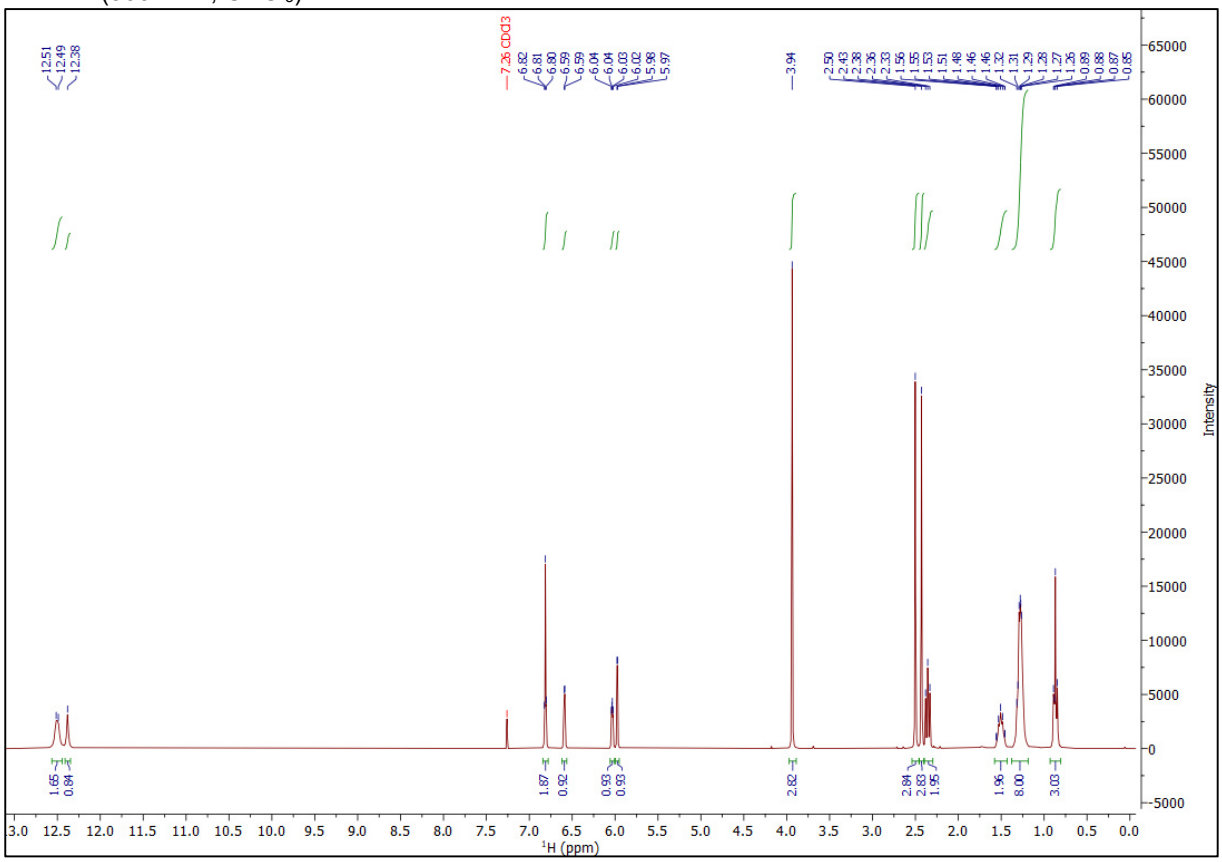


^{13}C NMR (76 MHz, $CDCl_3$)

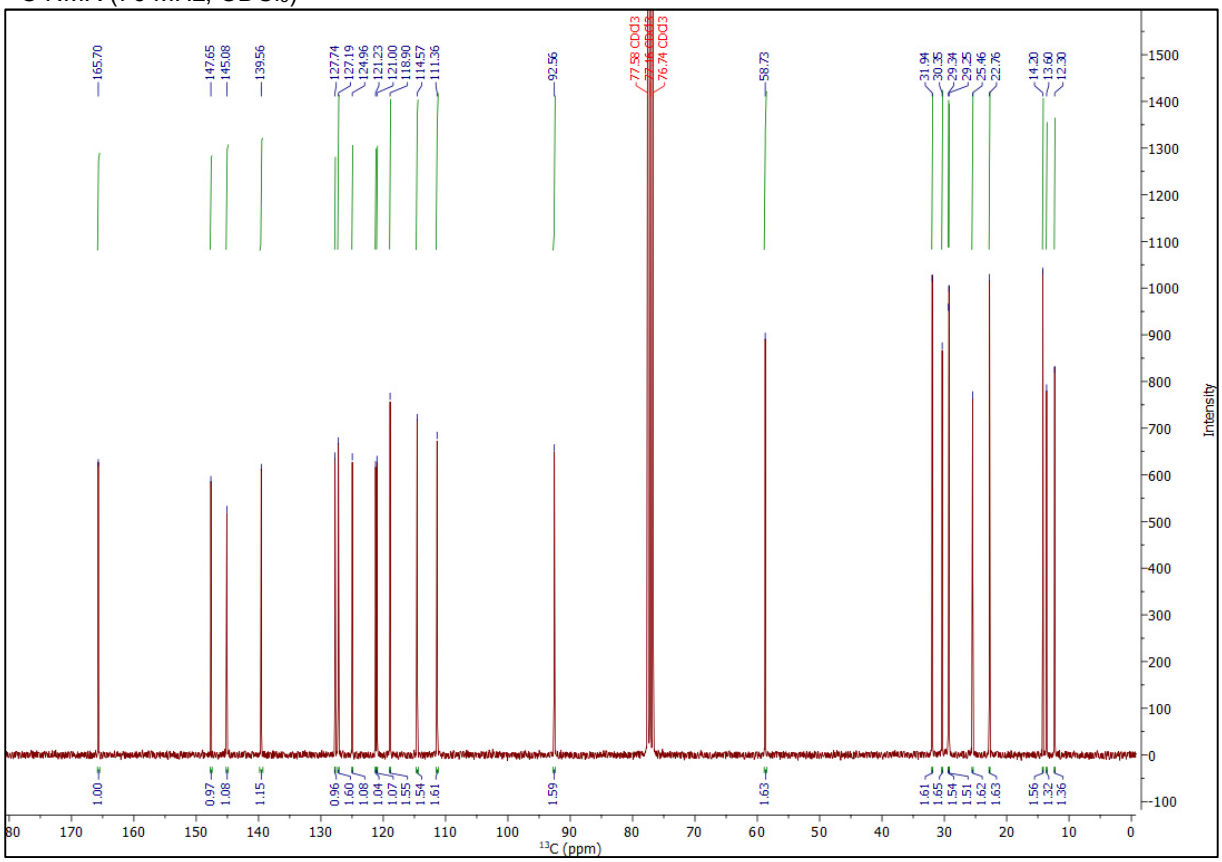


(*Z*)-4'-Methoxy-5-methyl-5'-((5-methyl-4-heptyl-1*H*-pyrrol-2-yl)methylene)-1*H*,5'*H*-[2,2'-bipyrrol]-1'-ium chloride (**III-1bc·HCl**)

^{1}H NMR (300 MHz, $CDCl_3$)

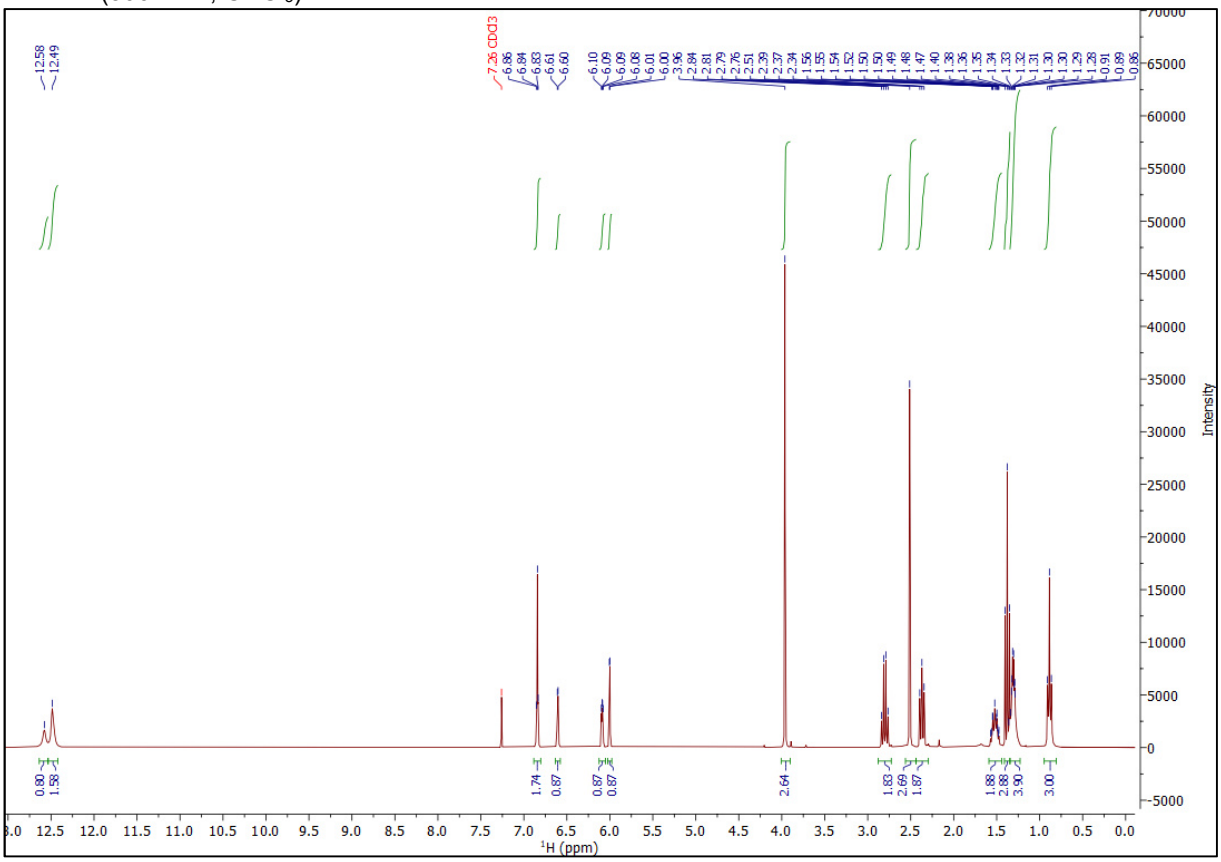


^{13}C NMR (76 MHz, $CDCl_3$)

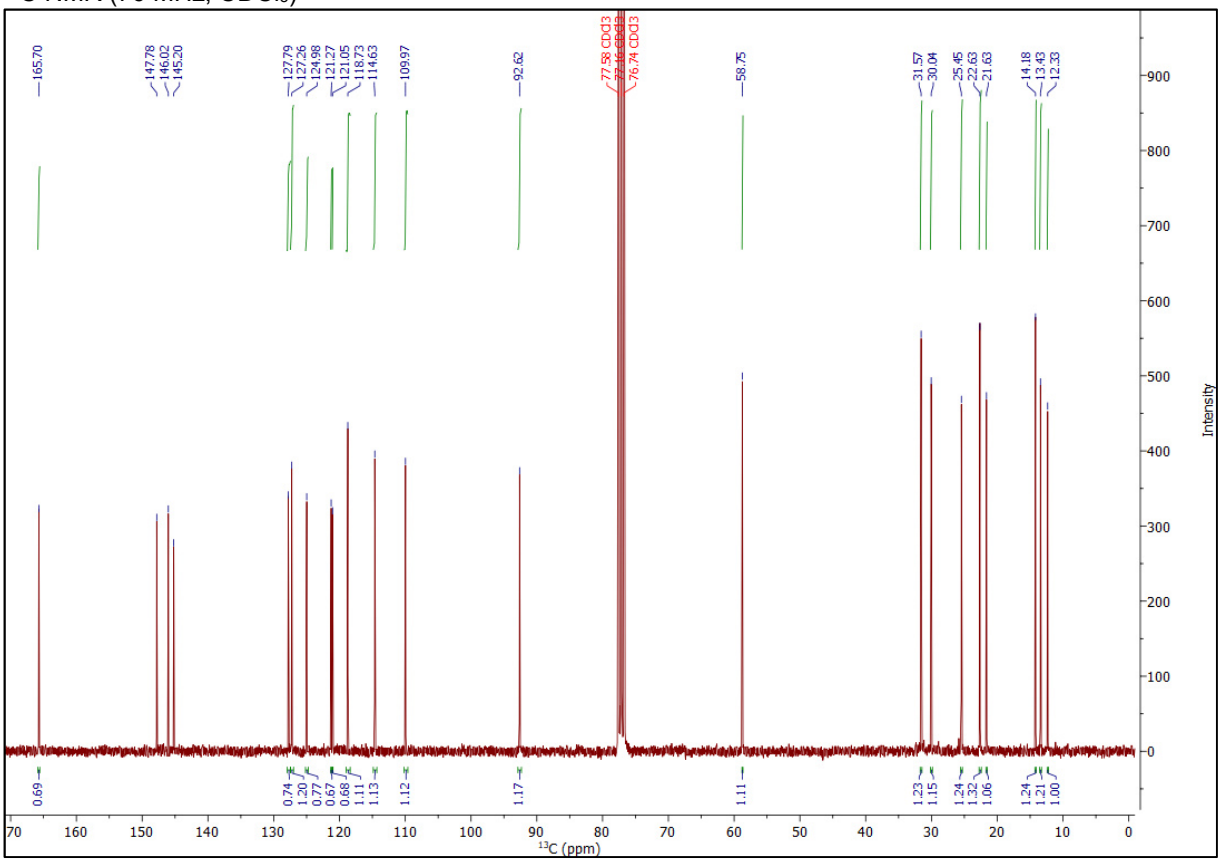


(*Z*)-5-Ethyl-4'-methoxy-5'-((5-methyl-4-pentyl-1*H*-pyrrol-2-yl)methylene)-1*H*,5'*H*-[2,2'-bipyrrol]-1'-ium chloride (**III-1cb·HCl**)

^{1}H NMR (300 MHz, $CDCl_3$)

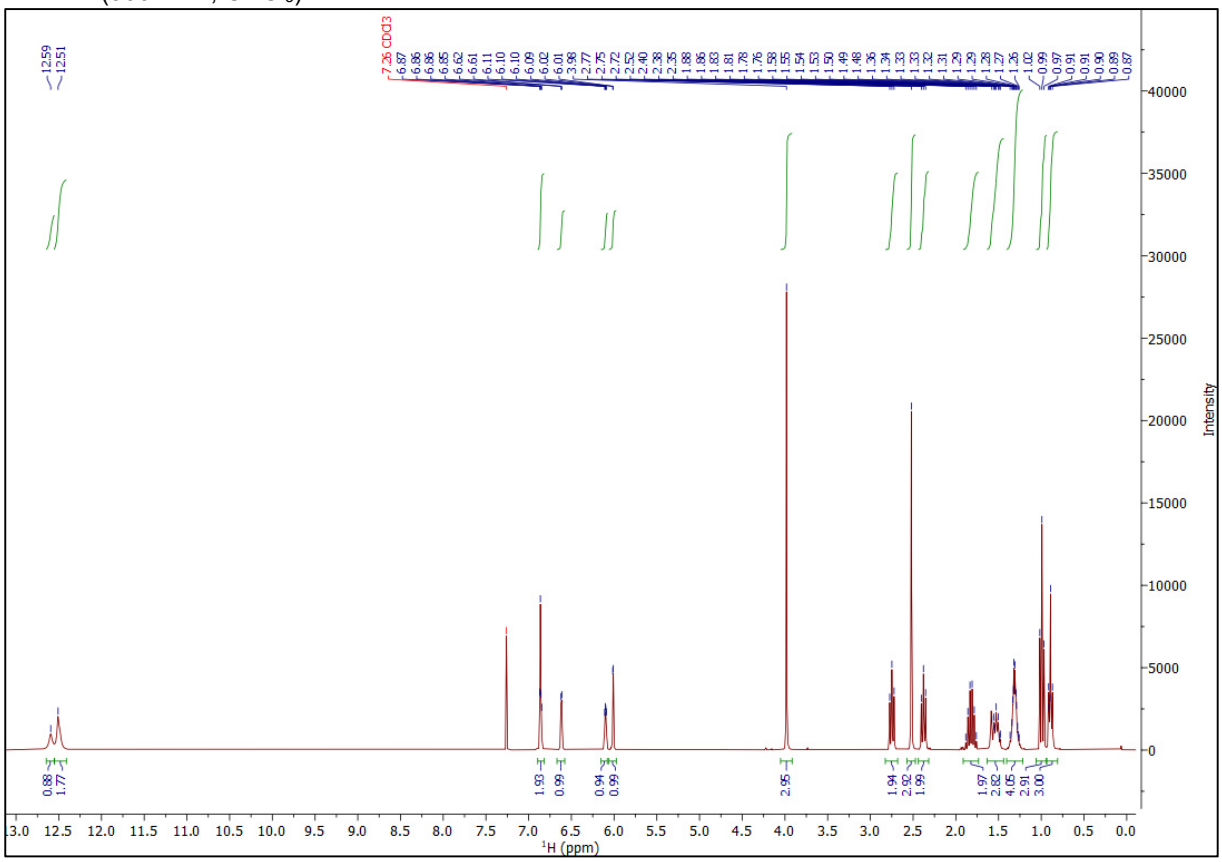


^{13}C NMR (76 MHz, $CDCl_3$)

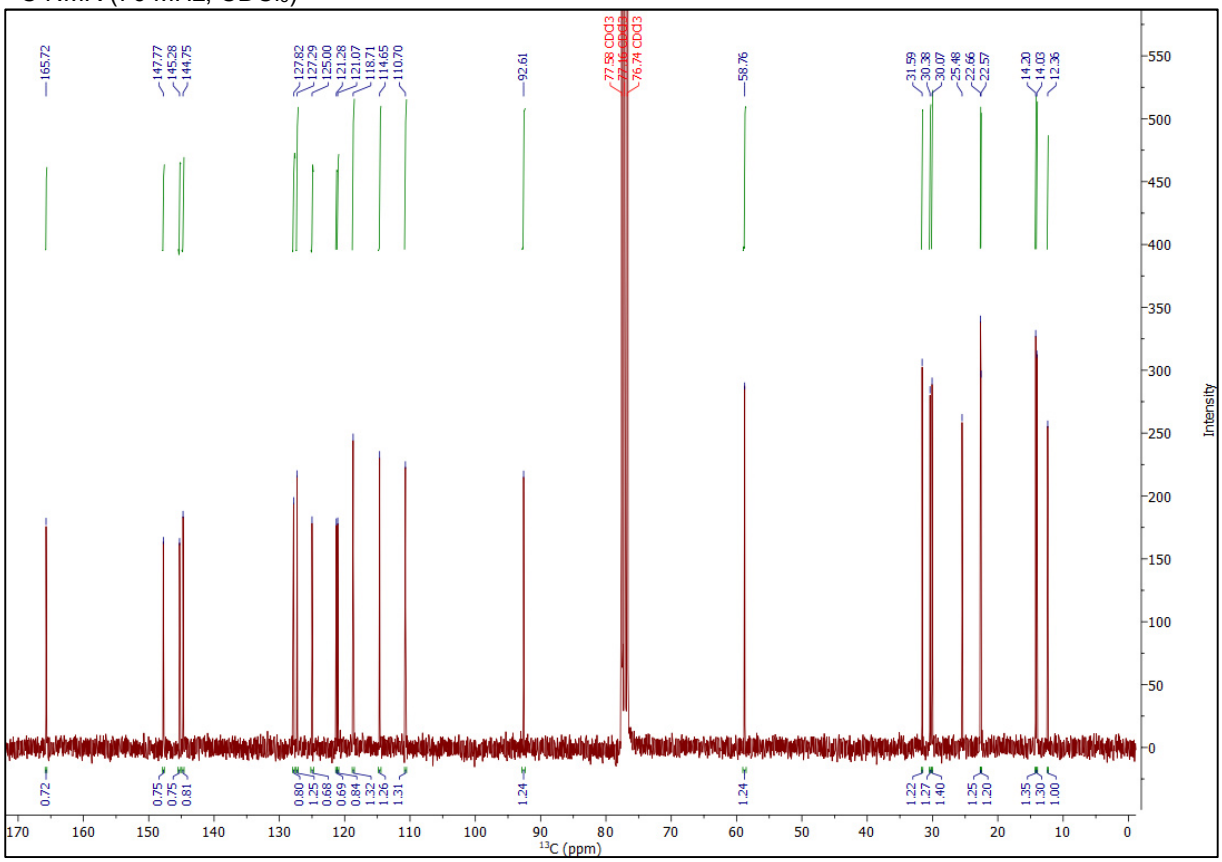


(*Z*)-4'-Methoxy-5-propyl-5'-((5-methyl-4-pentyl-1*H*-pyrrol-2-yl)methylene)-1*H*,5'*H*-[2,2'-bipyrrol]-1'-ium chloride (**III-1db·HCl**)

^{1}H NMR (300 MHz, $CDCl_3$)

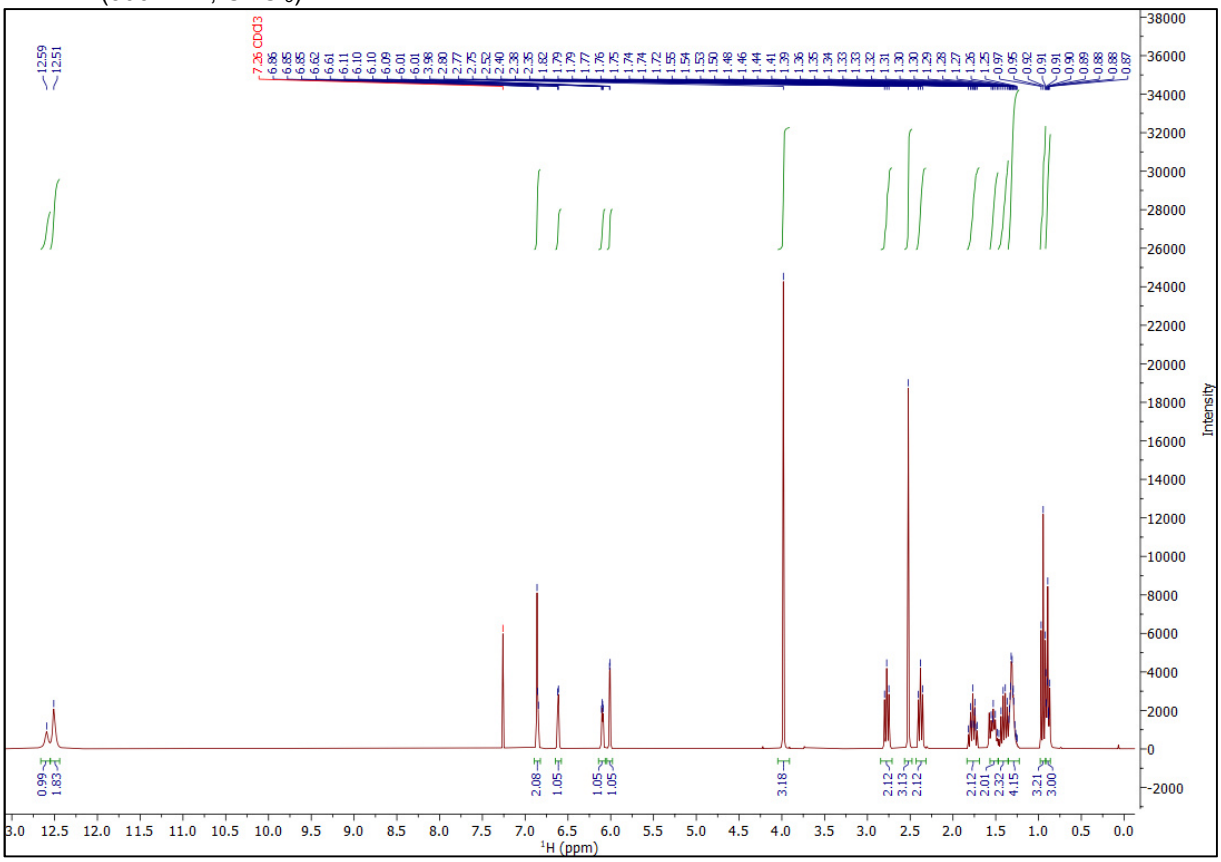


^{13}C NMR (76 MHz, $CDCl_3$)

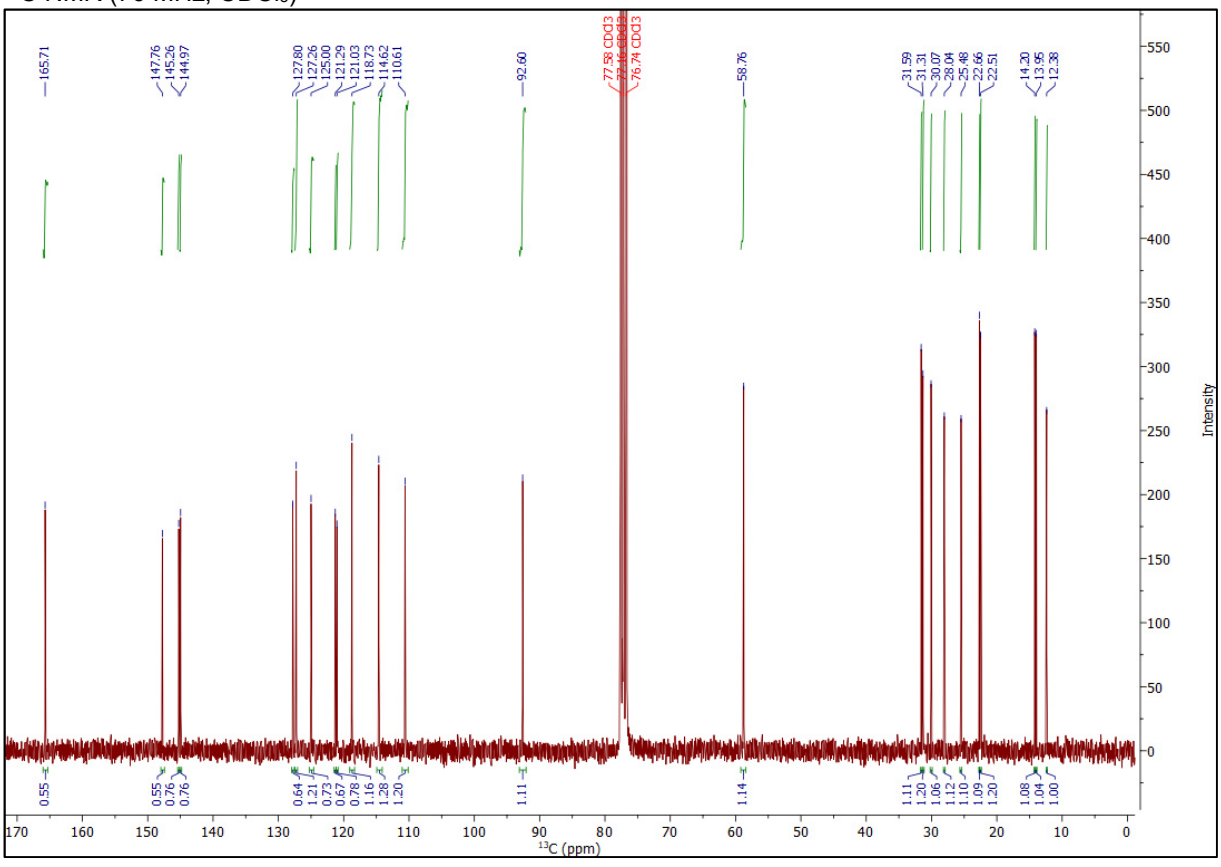


(*Z*)-5-Butyl-4'-methoxy-5'-((5-methyl-4-pentyl-1*H*-pyrrol-2-yl)methylene)-1*H*,5'*H*-[2,2'-bipyrrol]-1'-ium chloride (**III-1eb·HCl**)

^{1}H NMR (300 MHz, $CDCl_3$)

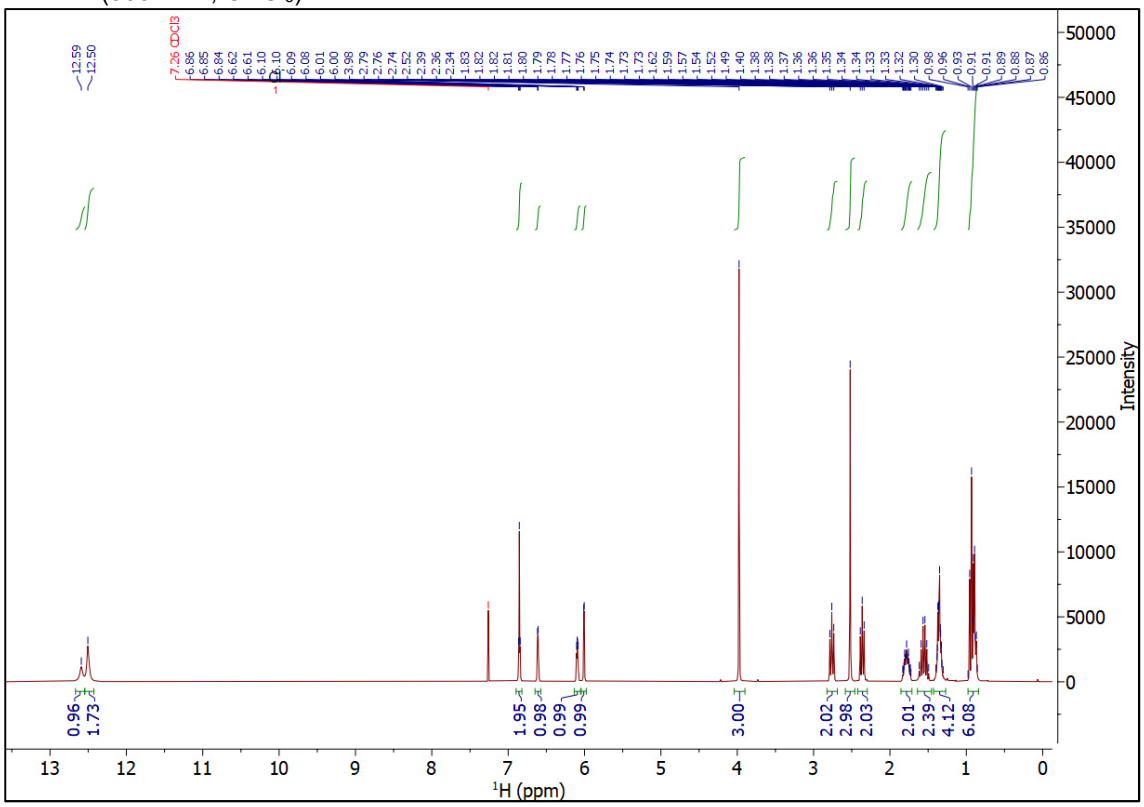


^{13}C NMR (76 MHz, $CDCl_3$)

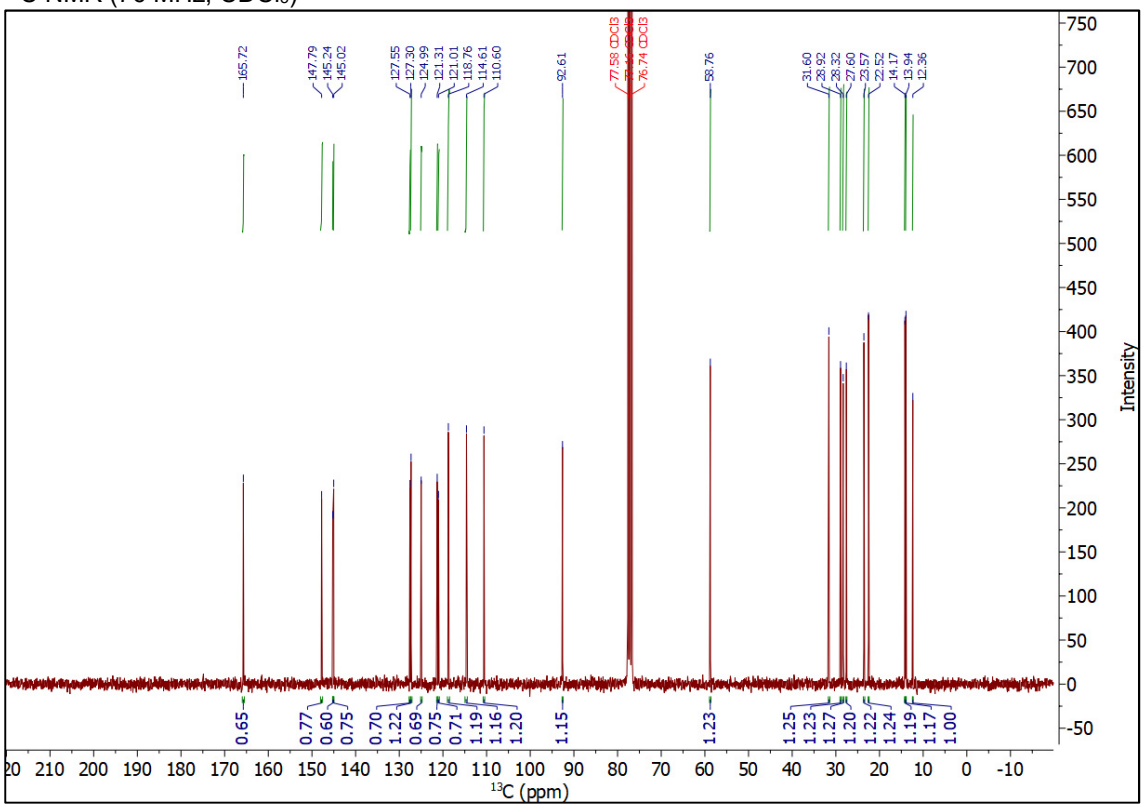


(*Z*)-4'-Methoxy-5'-((5-methyl-4-propyl-1*H*-pyrrol-2-yl)methylene)-5-pentyl-1*H*,5'*H*-[2,2'-bipyrrol]-1'-ium chloride (**III-1fa·HCl**)

^{1}H NMR (300 MHz, $CDCl_3$)

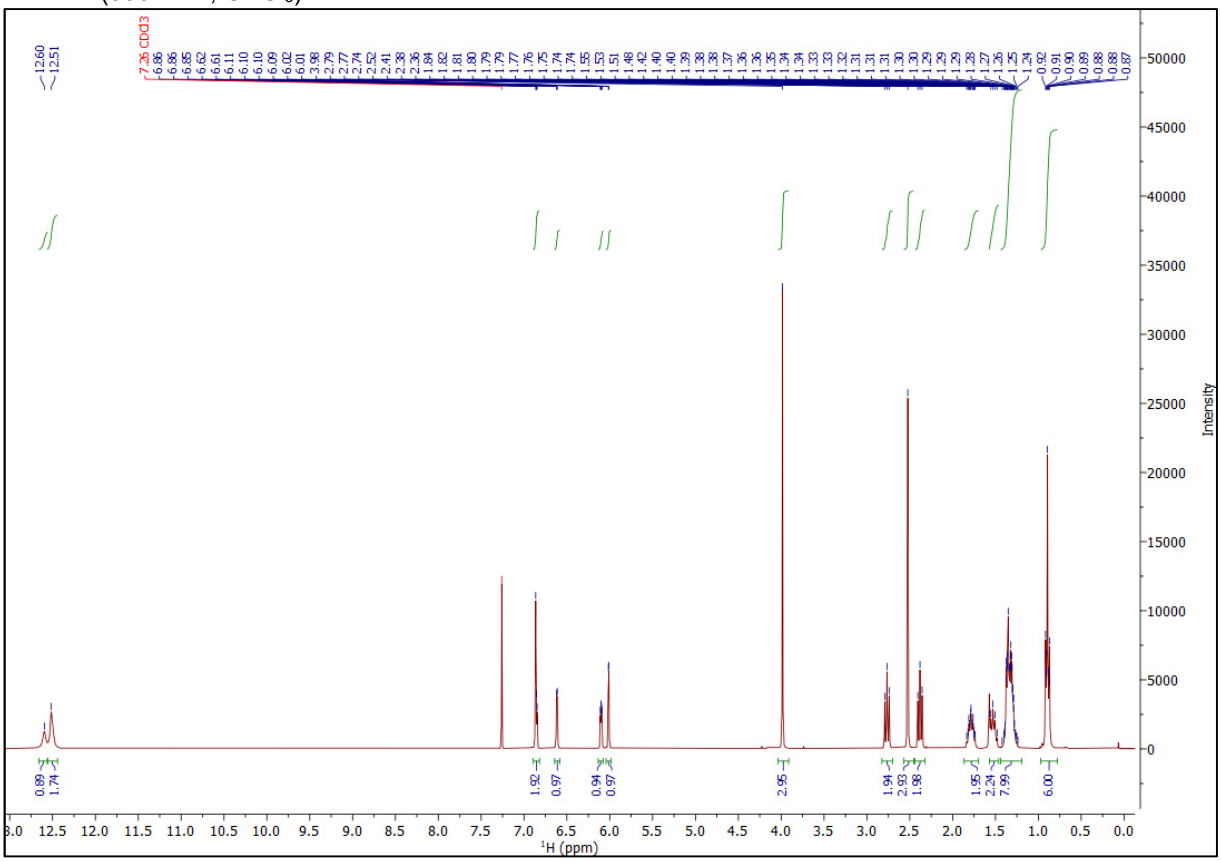


^{13}C NMR (76 MHz, $CDCl_3$)

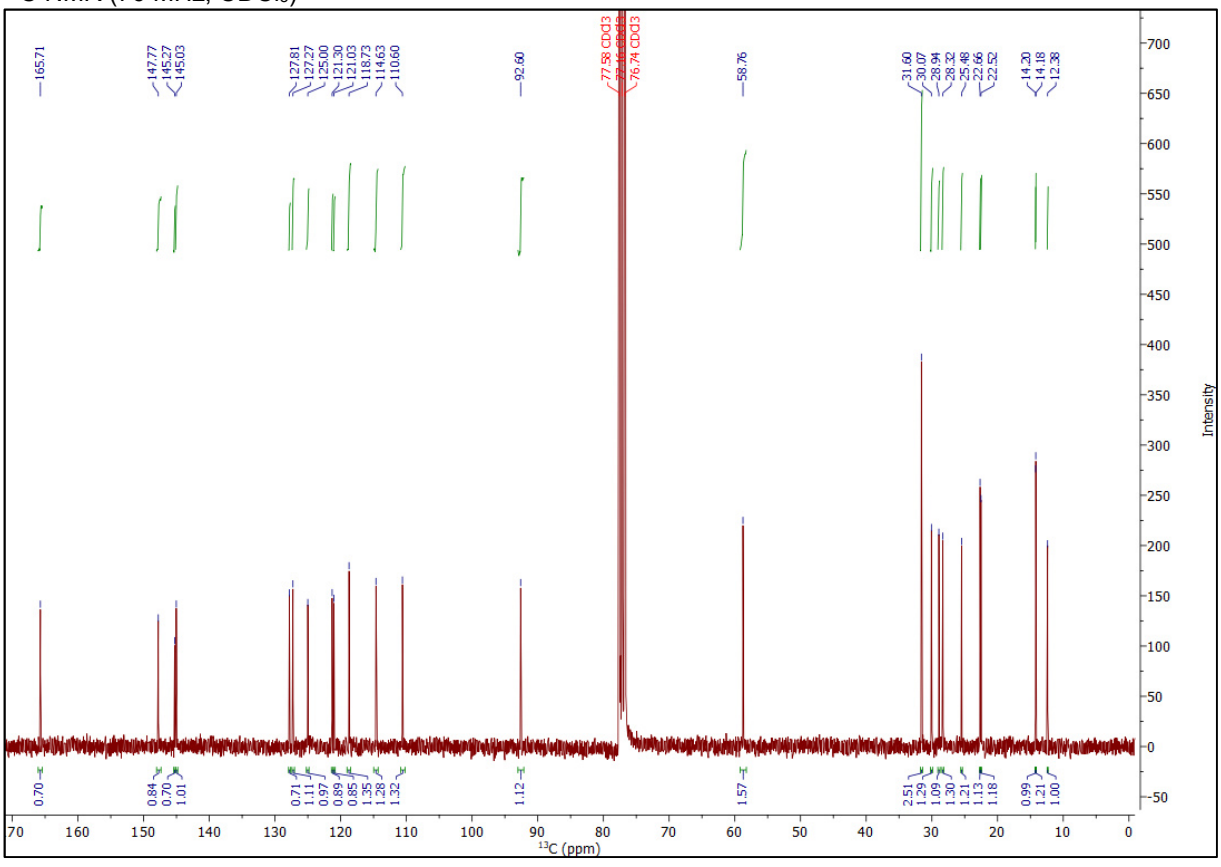


(*Z*)-4'-Methoxy-5-pentyl-5'-((5-methyl-4-pentyl-1*H*-pyrrol-2-yl)methylene)-1*H*,5'*H*-[2,2'-bipyrrol]-1'-ium chloride (**III-1fb·HCl**)

^{1}H NMR (300 MHz, $CDCl_3$)

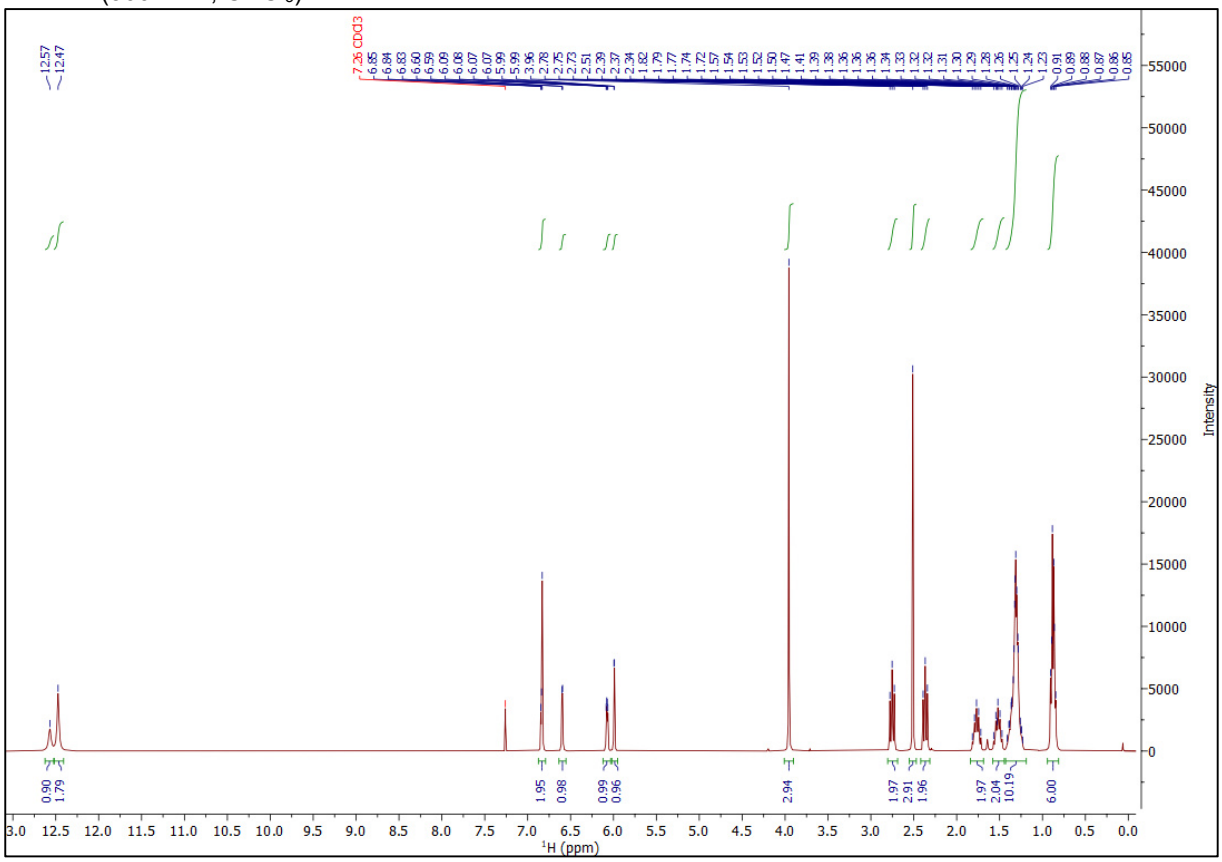


^{13}C NMR (76 MHz, $CDCl_3$)

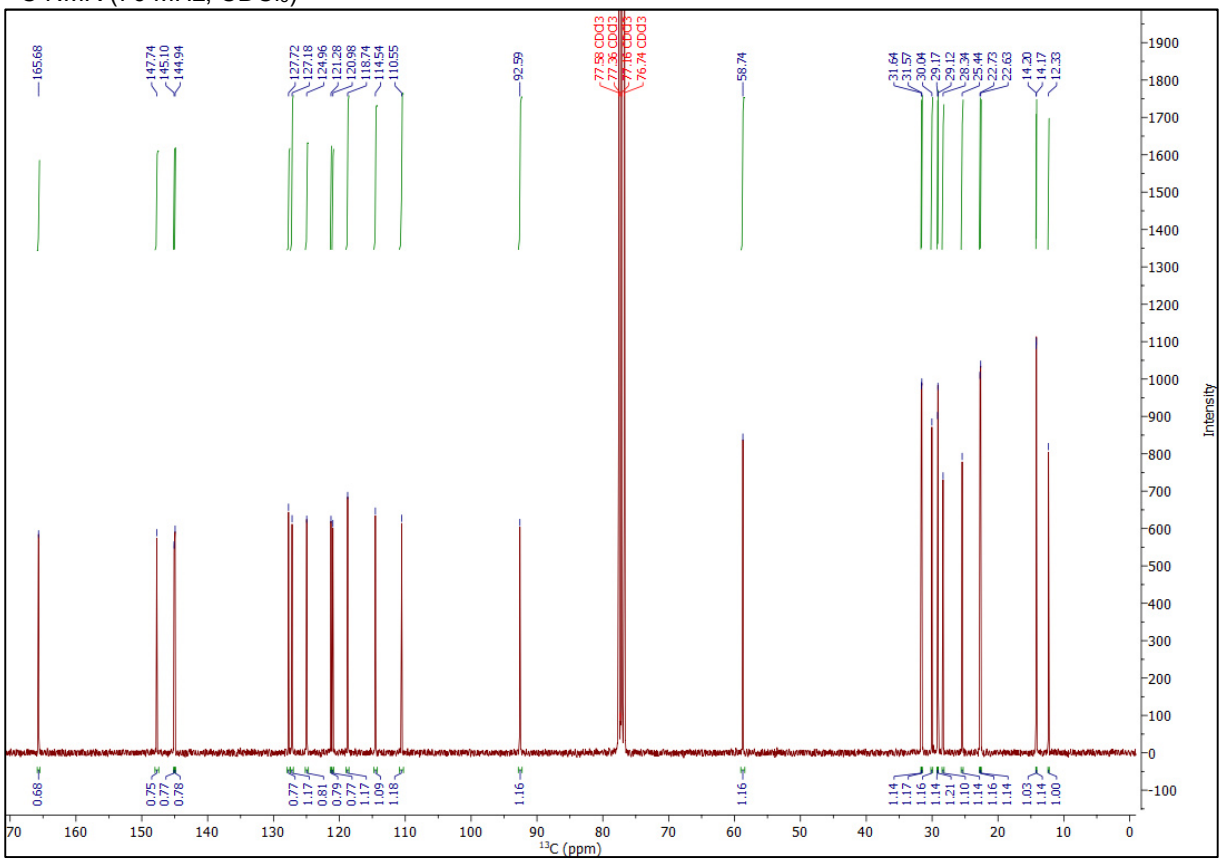


(*Z*)-5-Hexyl-4'-methoxy-5'-((5-methyl-4-pentyl-1*H*-pyrrol-2-yl)methylene)-1*H*,5'*H*-[2,2'-bipyrrol]-1'-ium chloride (**III-1gb·HCl**)

^{1}H NMR (300 MHz, $CDCl_3$)

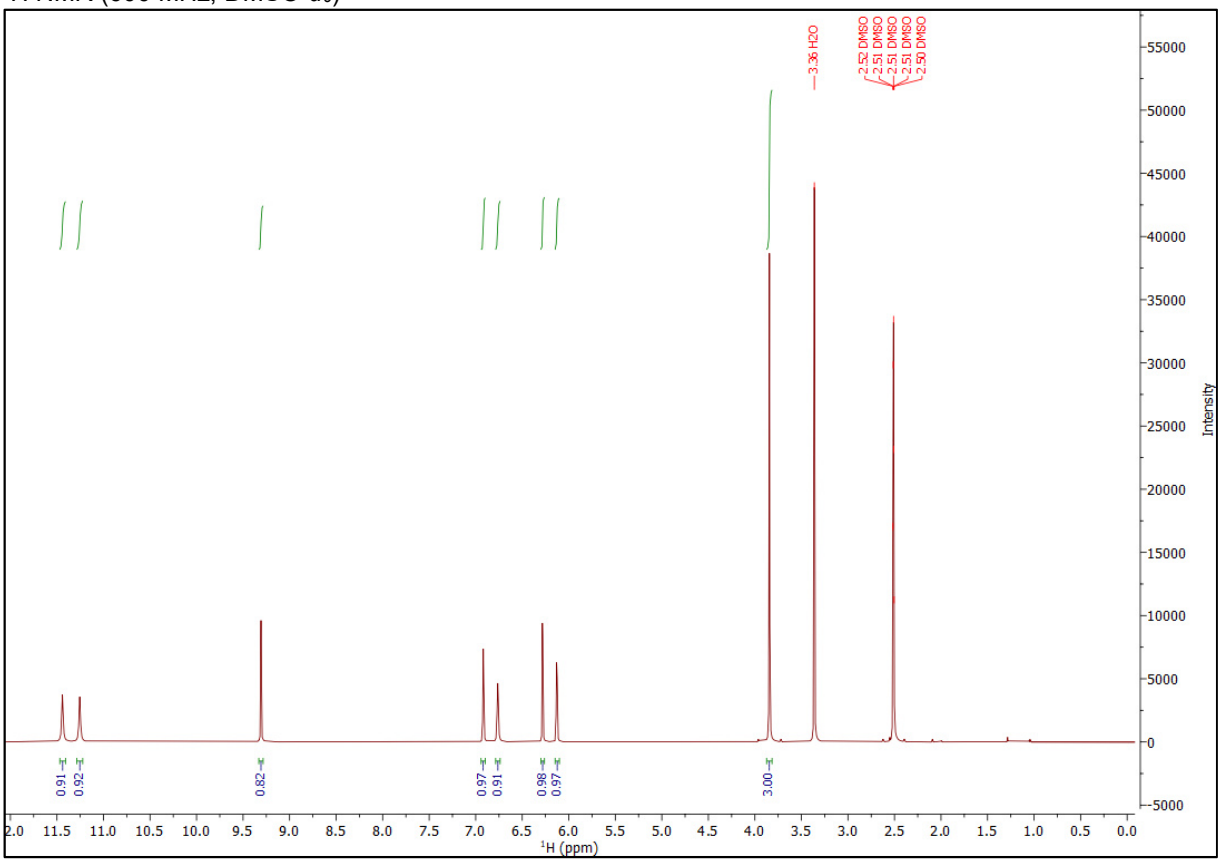


^{13}C NMR (76 MHz, $CDCl_3$)

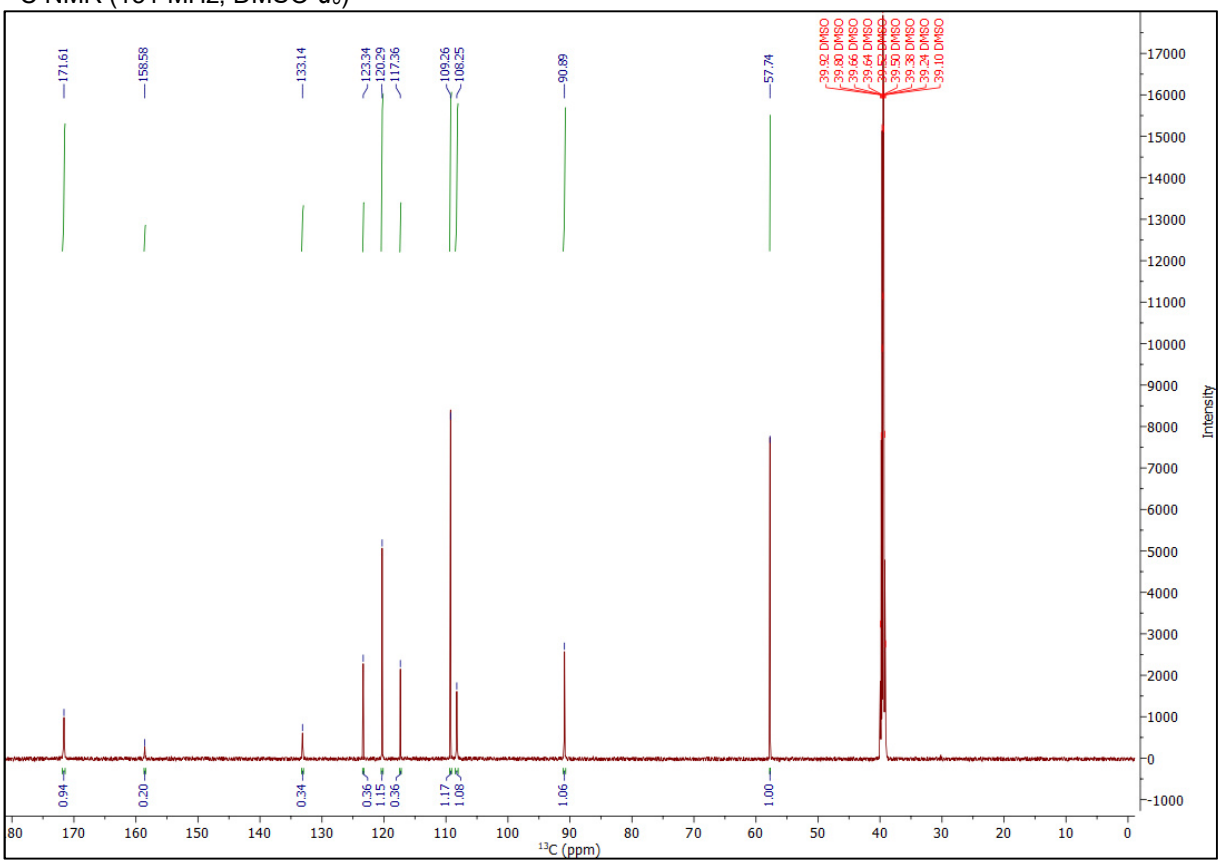


4-Methoxy-1*H*,1'*H*-[2,2'-bipyrrole]-5-carbaldehyde (**III-14a**)

^{1}H NMR (600 MHz, DMSO-d_6)

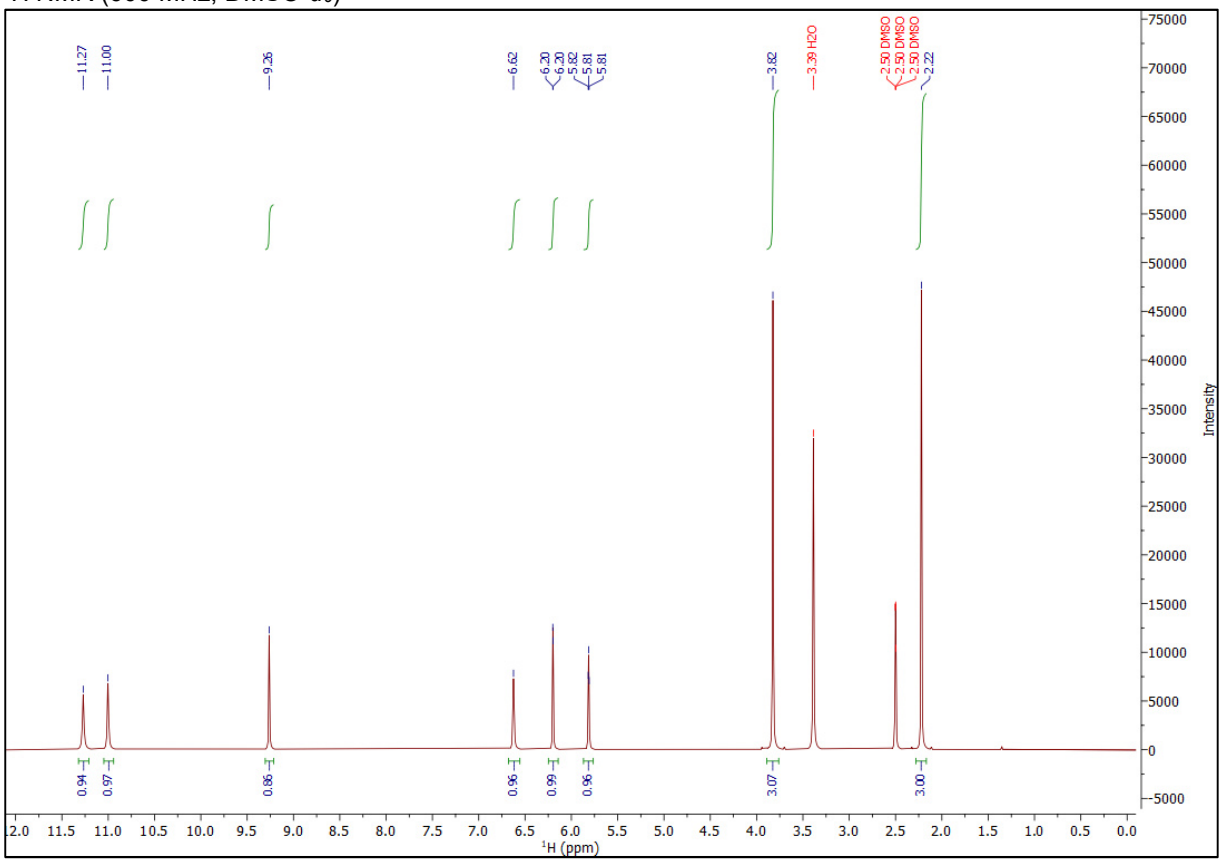


^{13}C NMR (151 MHz, DMSO-d_6)

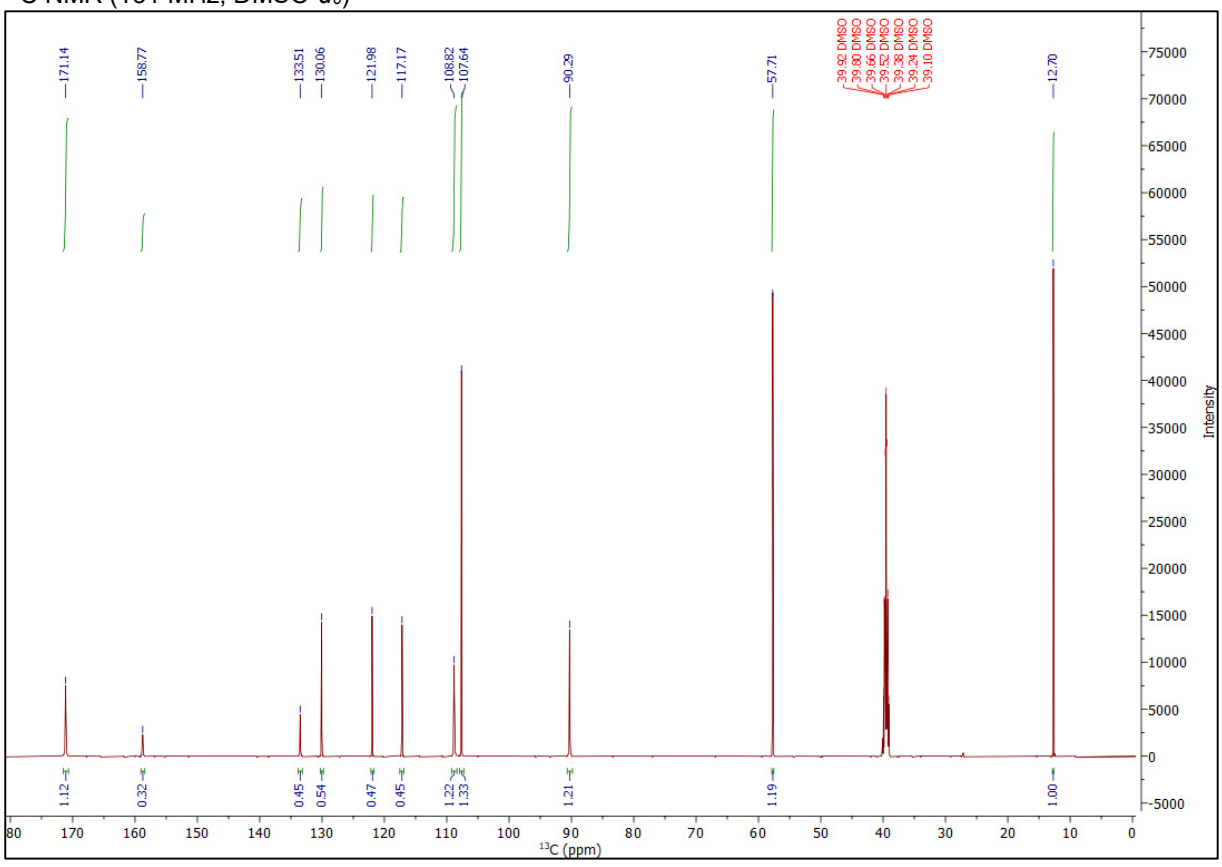


4-Methoxy-5'-methyl-1*H*,1'*H*-[2,2'-bipyrrole]-5-carbaldehyde (**III-14b**)

^{1}H NMR (600 MHz, DMSO-d_6)

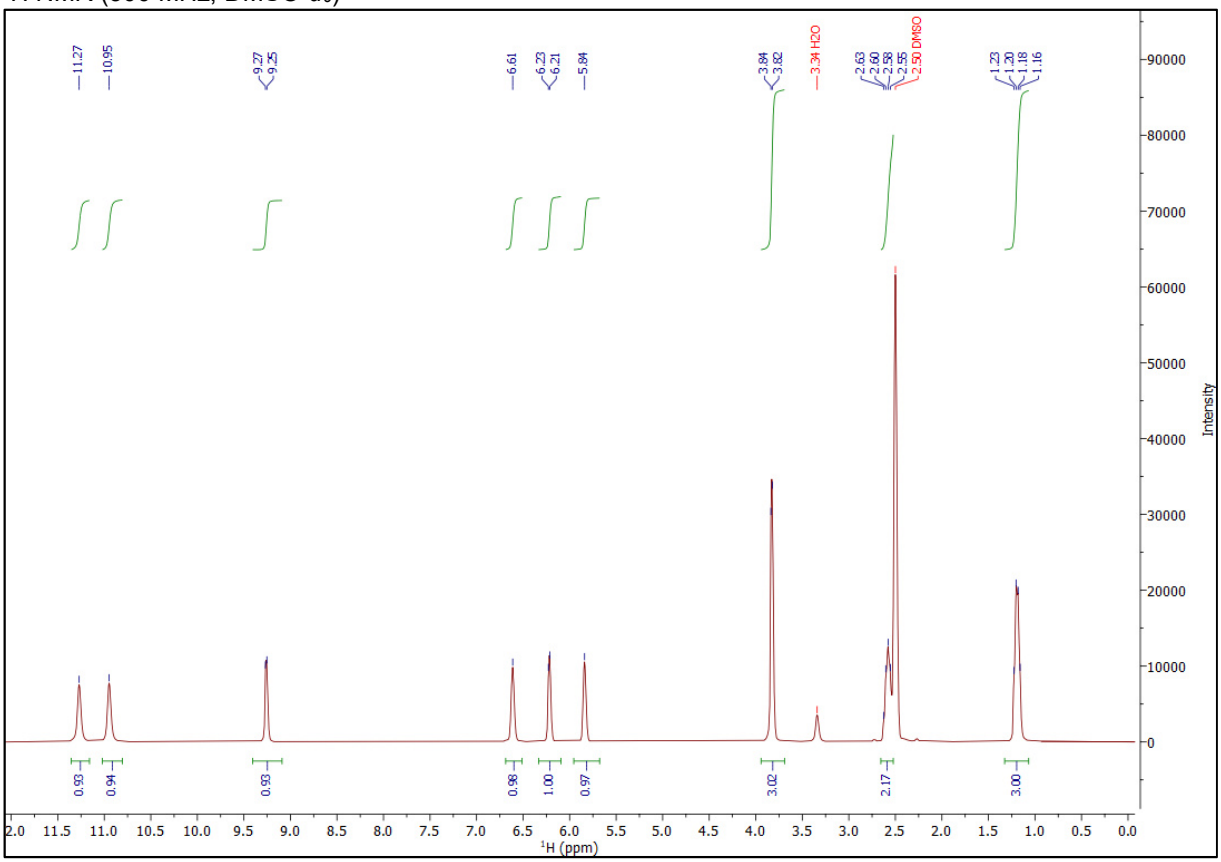


^{13}C NMR (151 MHz, DMSO-d_6)

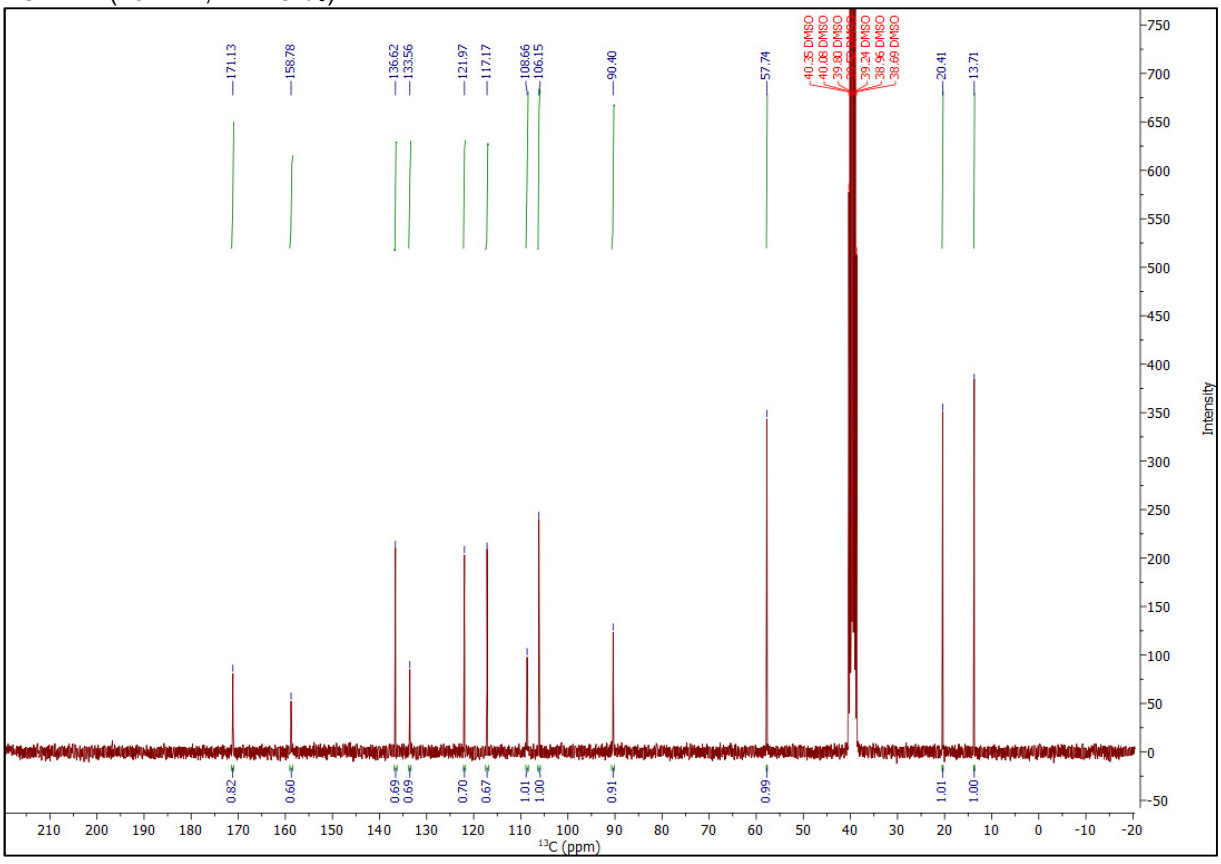


5'-Ethyl-4-methoxy-1*H*,1'*H*-[2,2'-bipyrrole]-5-carbaldehyde (**III-14c**)

^{1}H NMR (300 MHz, DMSO-d_6)

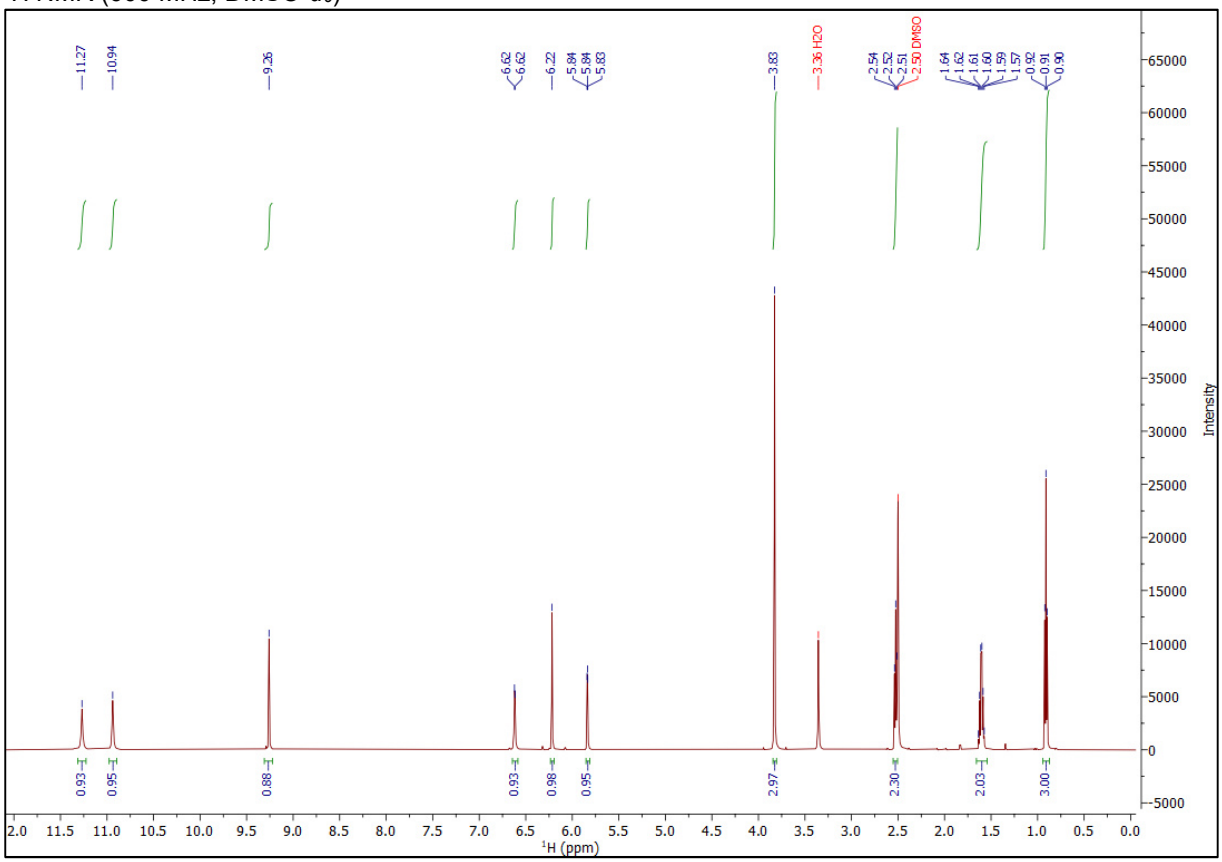


^{13}C NMR (76 MHz, DMSO-d_6)

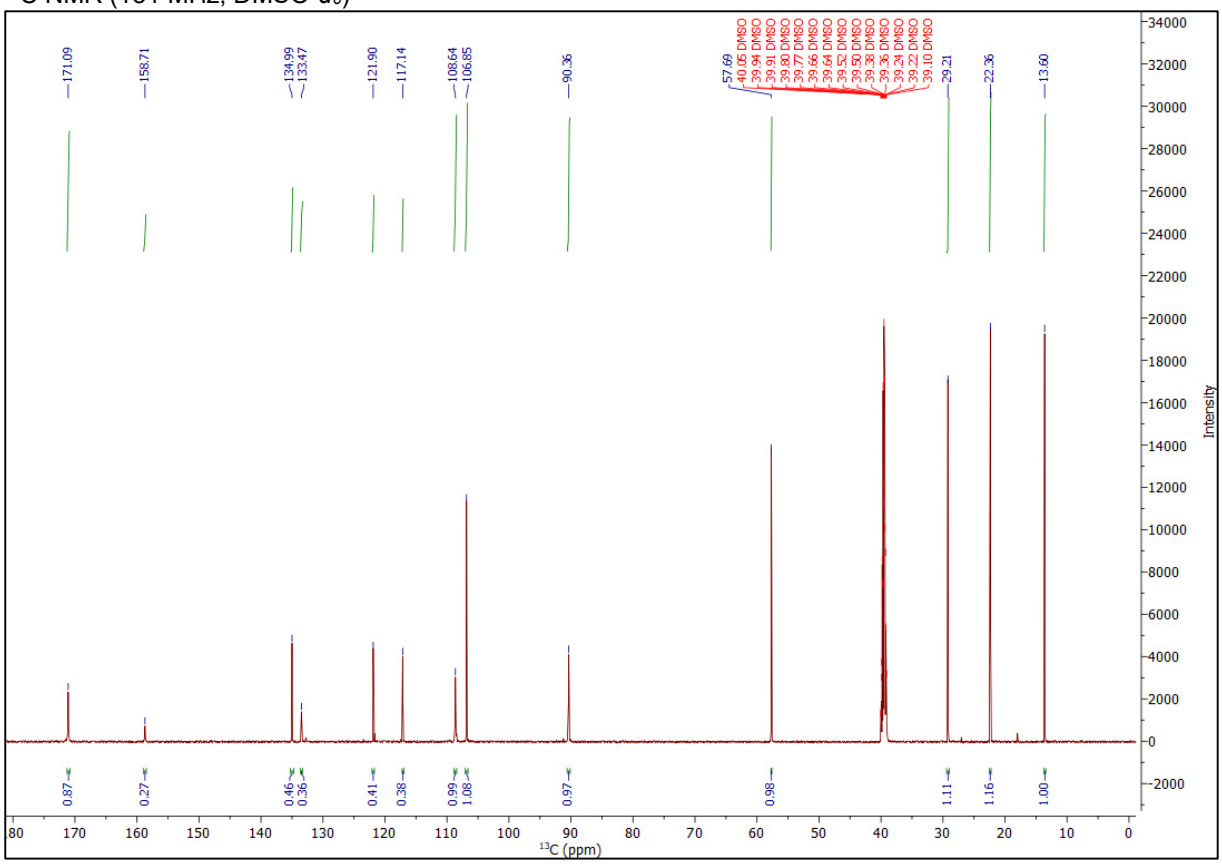


4-Methoxy-5'-propyl-1*H*,1'*H*-[2,2'-bipyrrole]-5-carbaldehyde (**III-14d**)

^{1}H NMR (600 MHz, DMSO-d_6)

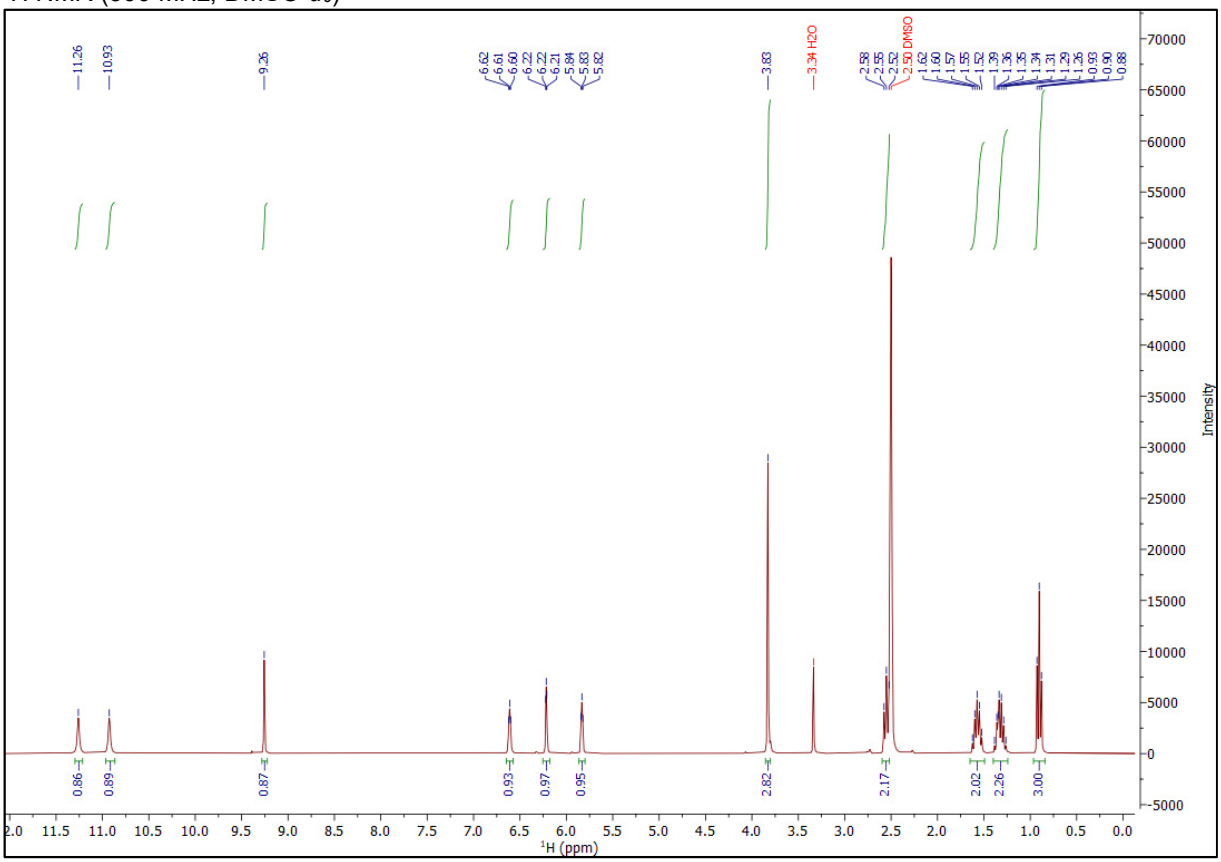


^{13}C NMR (151 MHz, DMSO-d_6)

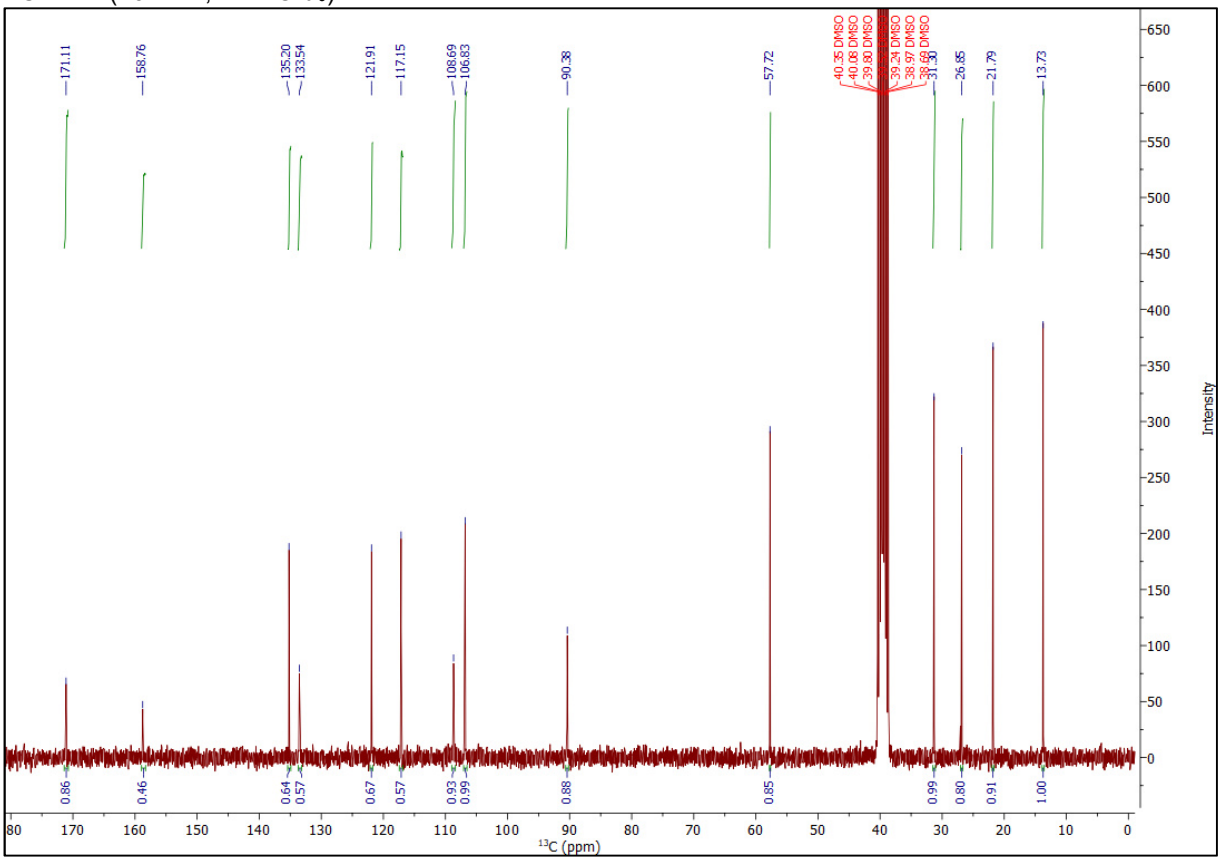


5'-Butyl-4-methoxy-1*H*,1'*H*-[2,2'-bipyrrole]-5-carbaldehyde (**III-14e**)

^{1}H NMR (300 MHz, DMSO-d_6)

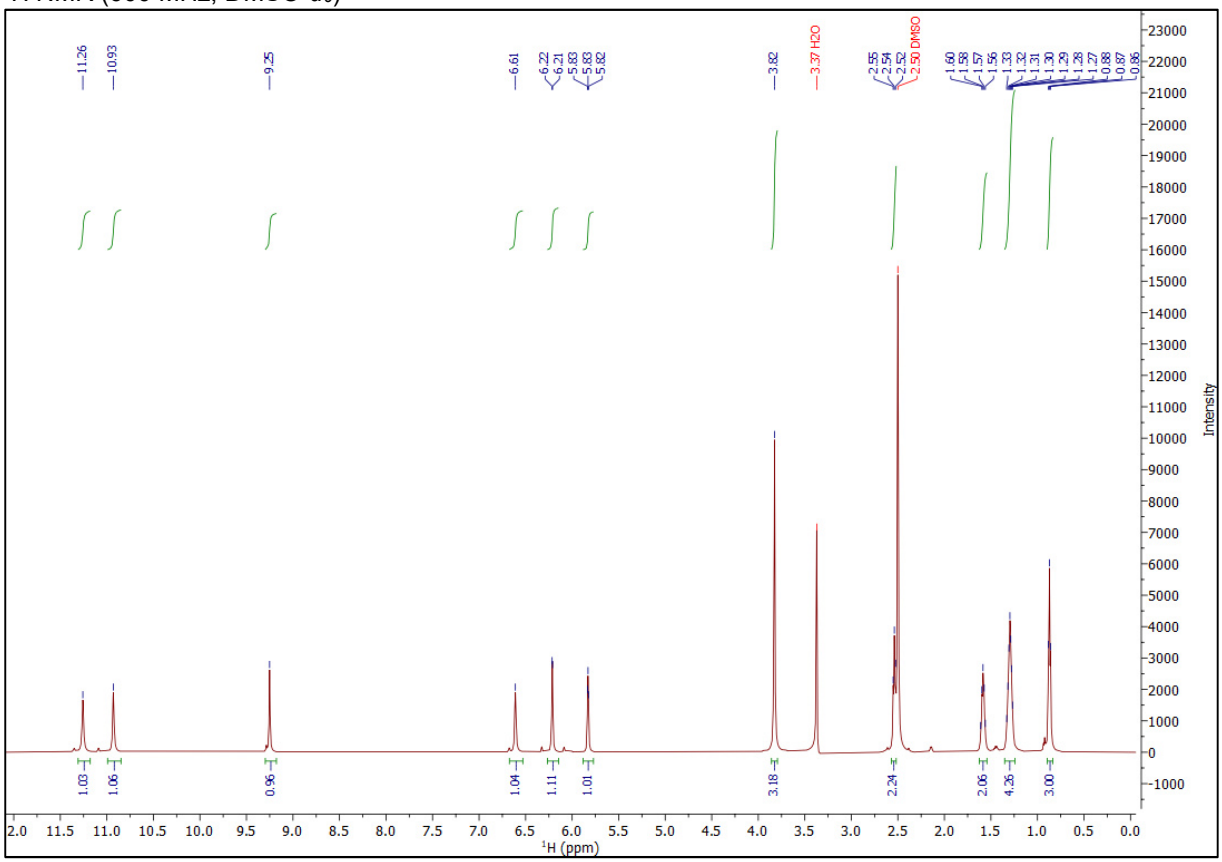


^{13}C NMR (76 MHz, DMSO-d_6)

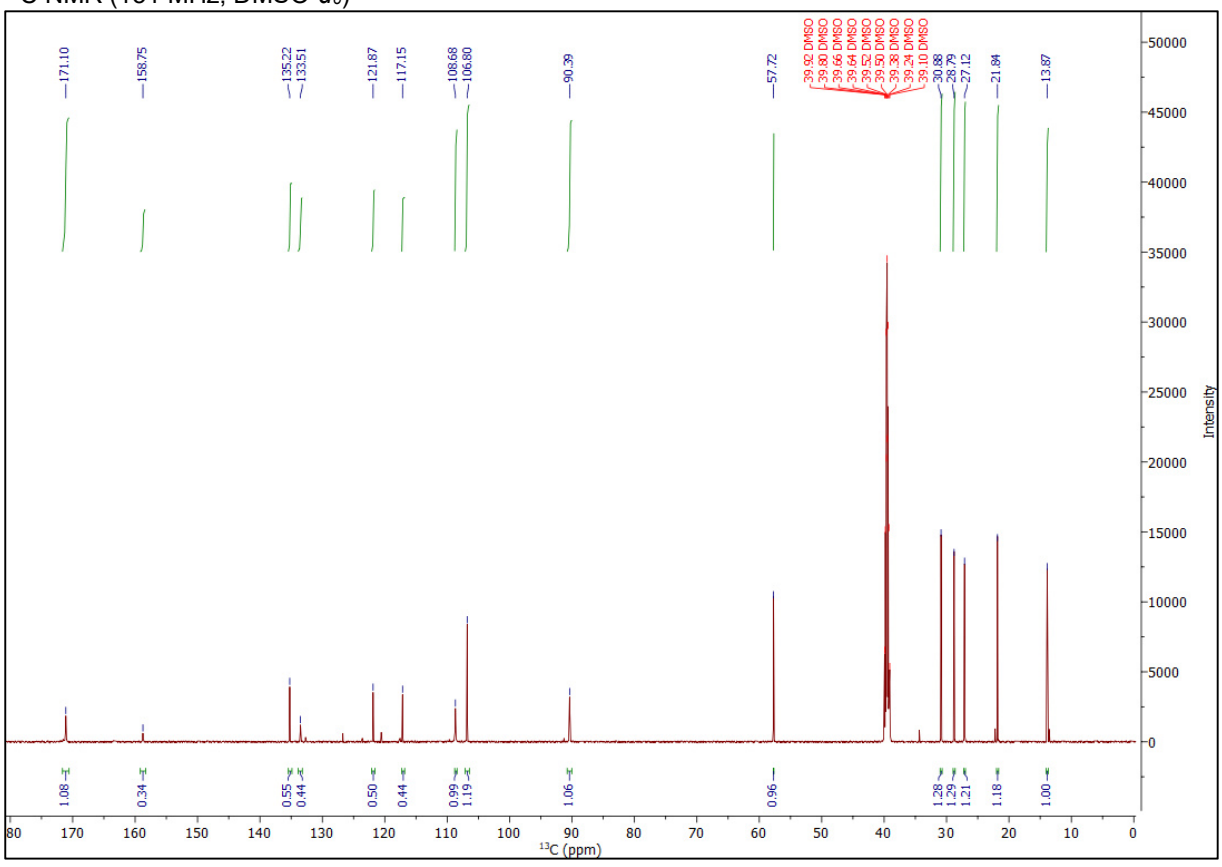


4-Methoxy-5'-pentyl-1*H*,1'*H*-[2,2'-bipyrrole]-5-carbaldehyde (**III-14f**)

^{1}H NMR (600 MHz, DMSO-d_6)

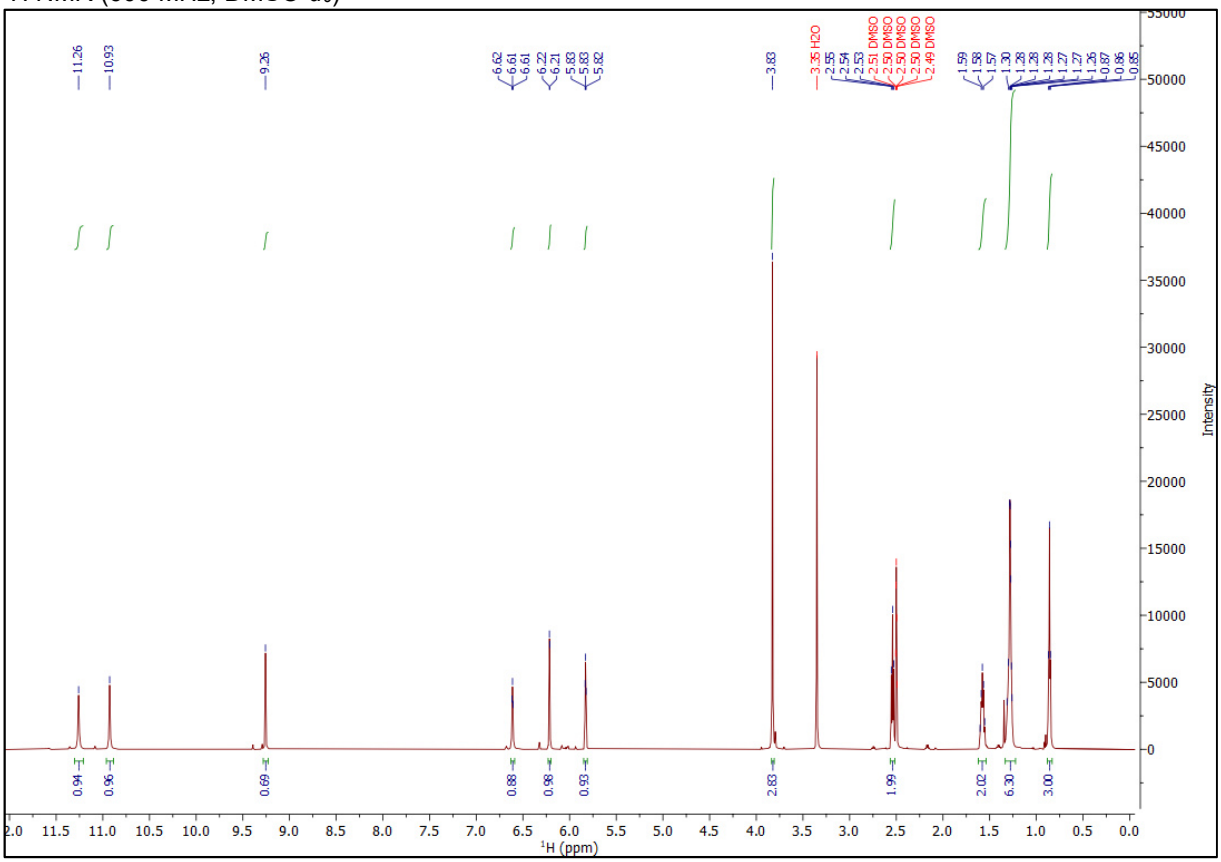


^{13}C NMR (151 MHz, DMSO-d_6)

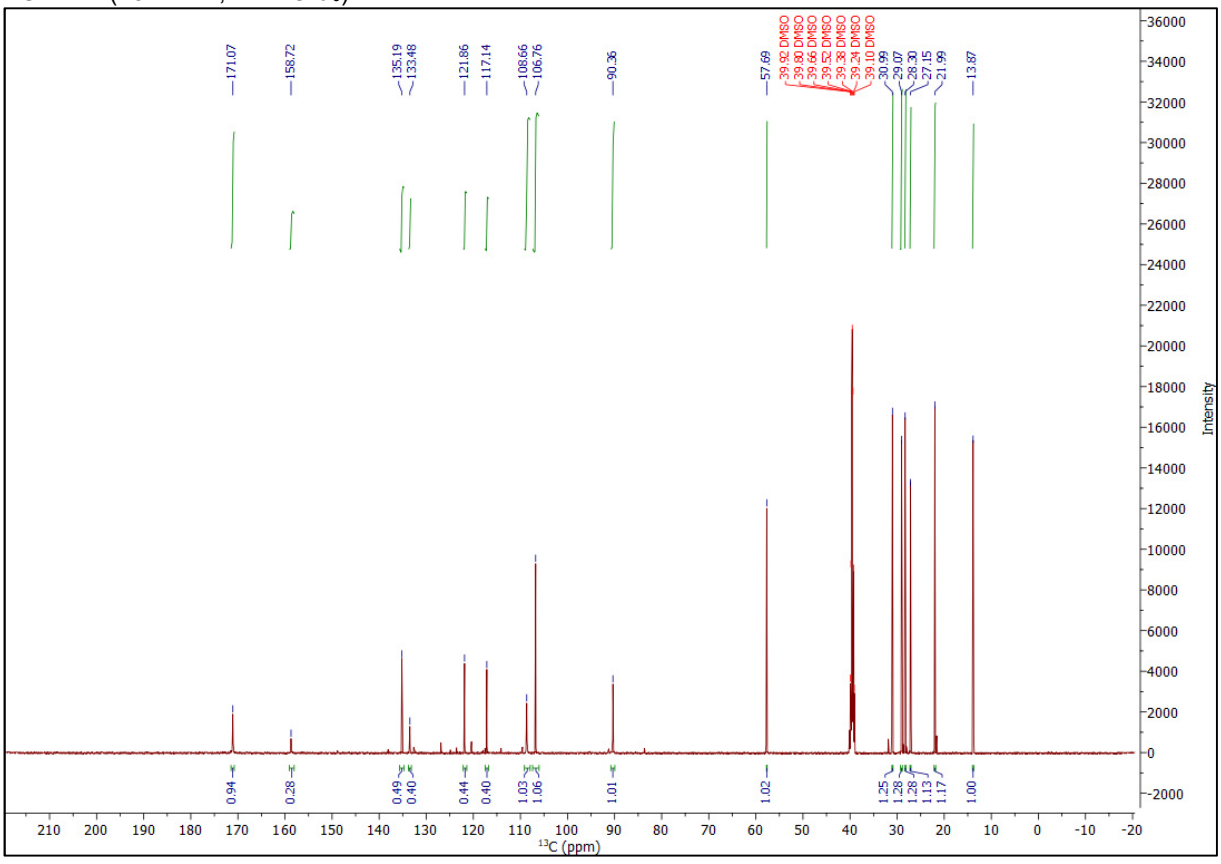


5'-Hexyl-4-methoxy-1*H*,1'*H*-[2,2'-bipyrrole]-5-carbaldehyde (**III-14g**)

^{1}H NMR (600 MHz, DMSO-d_6)

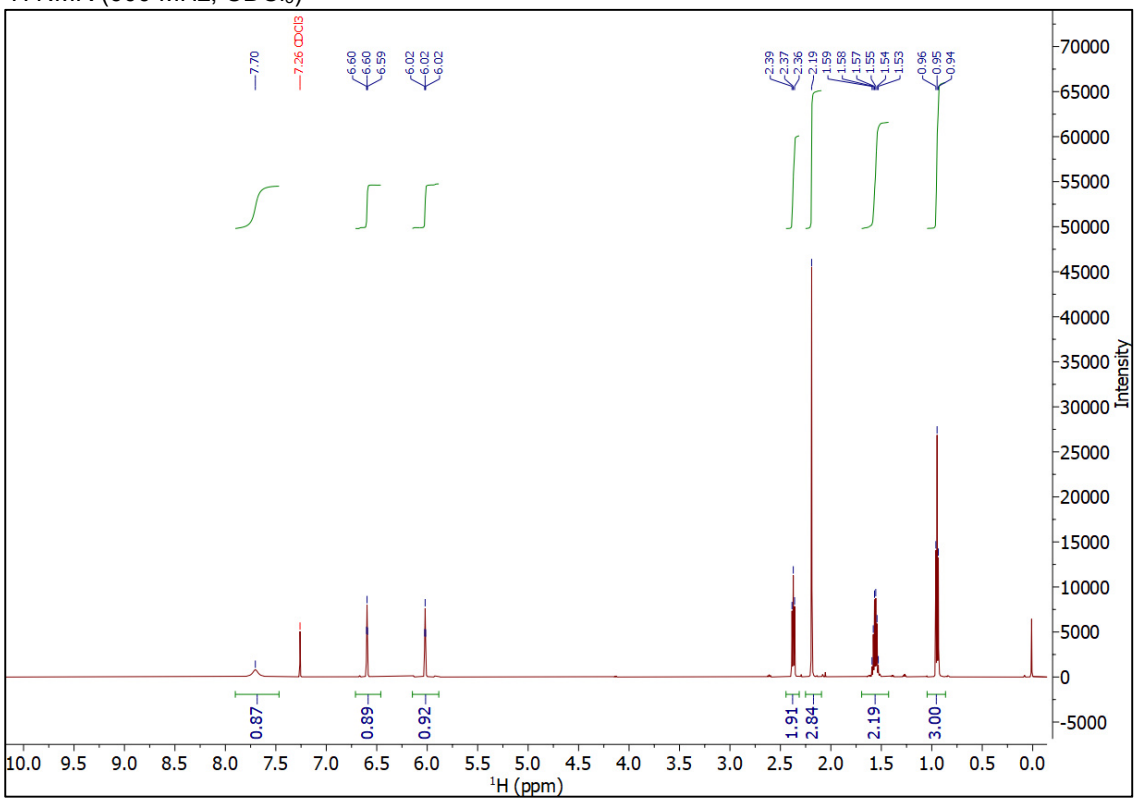


^{13}C NMR (151 MHz, DMSO-d_6)

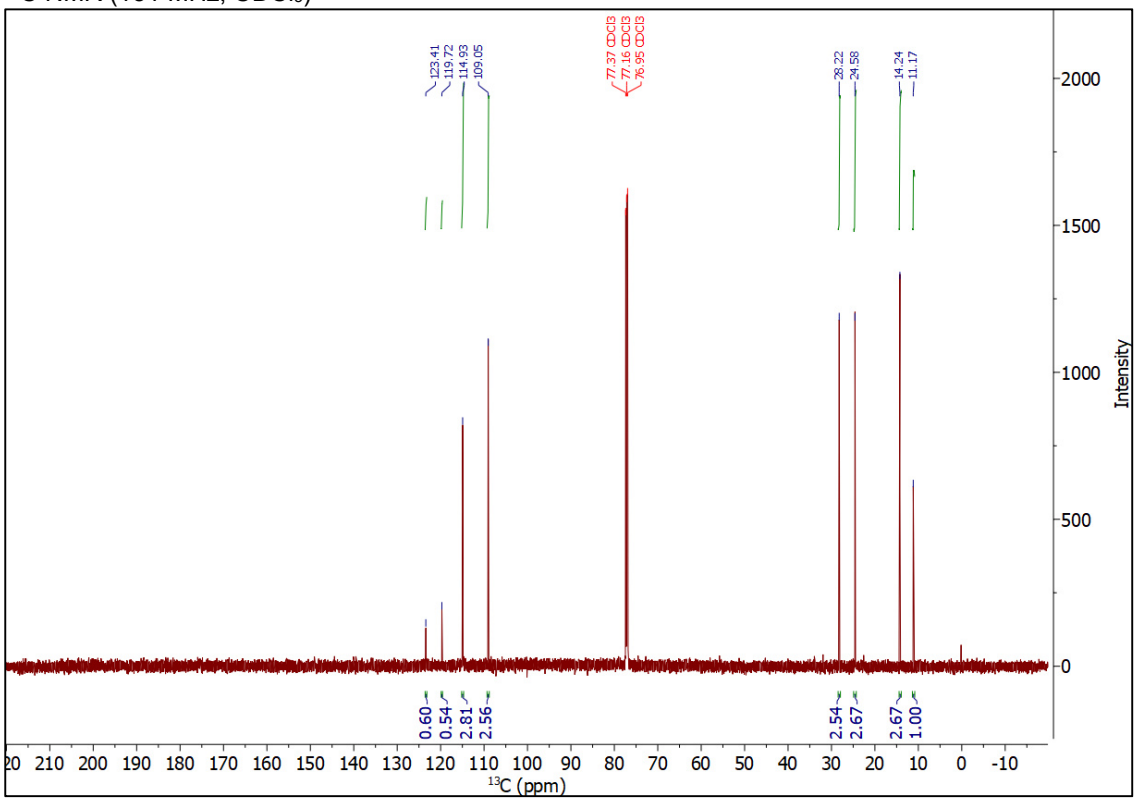


2-Methyl-3-propyl-1H-pyrrole (**III-15a**)

^{1}H NMR (600 MHz, $CDCl_3$)

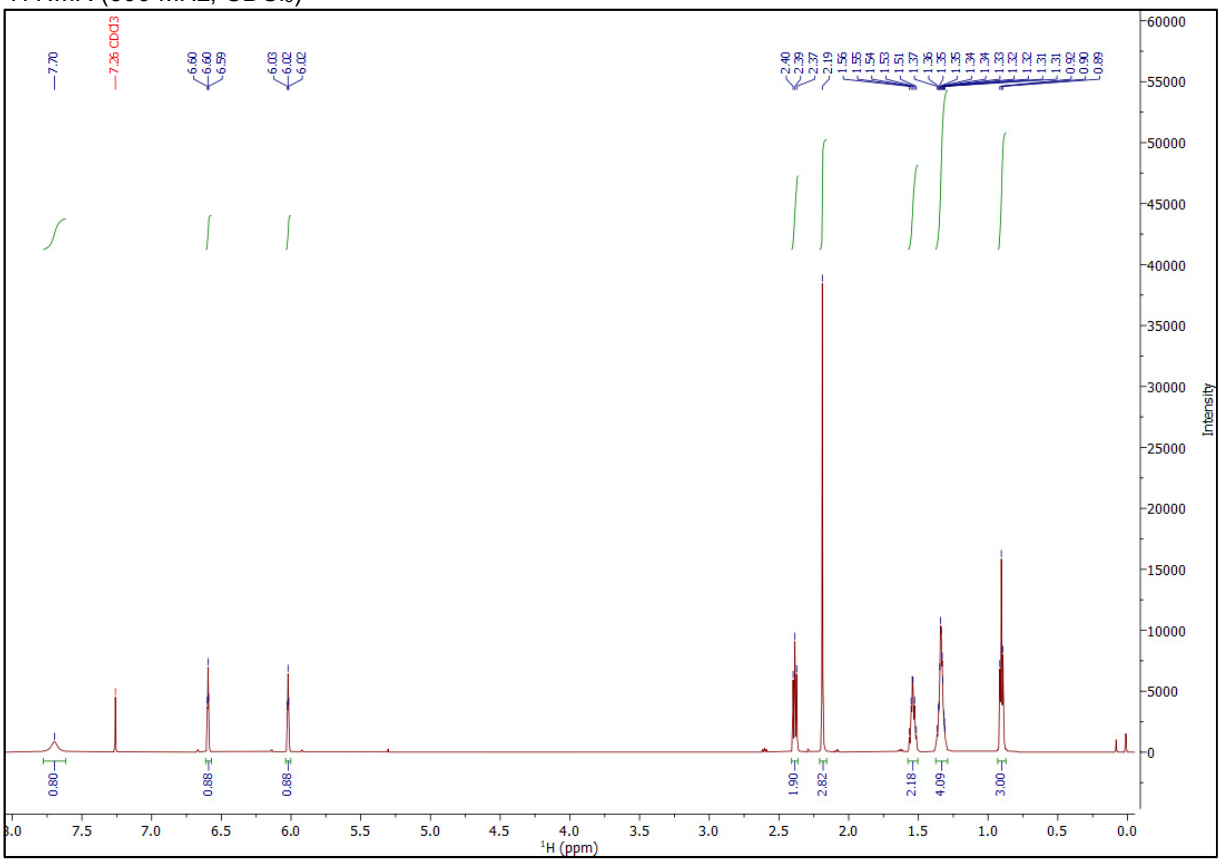


^{13}C NMR (151 MHz, $CDCl_3$)

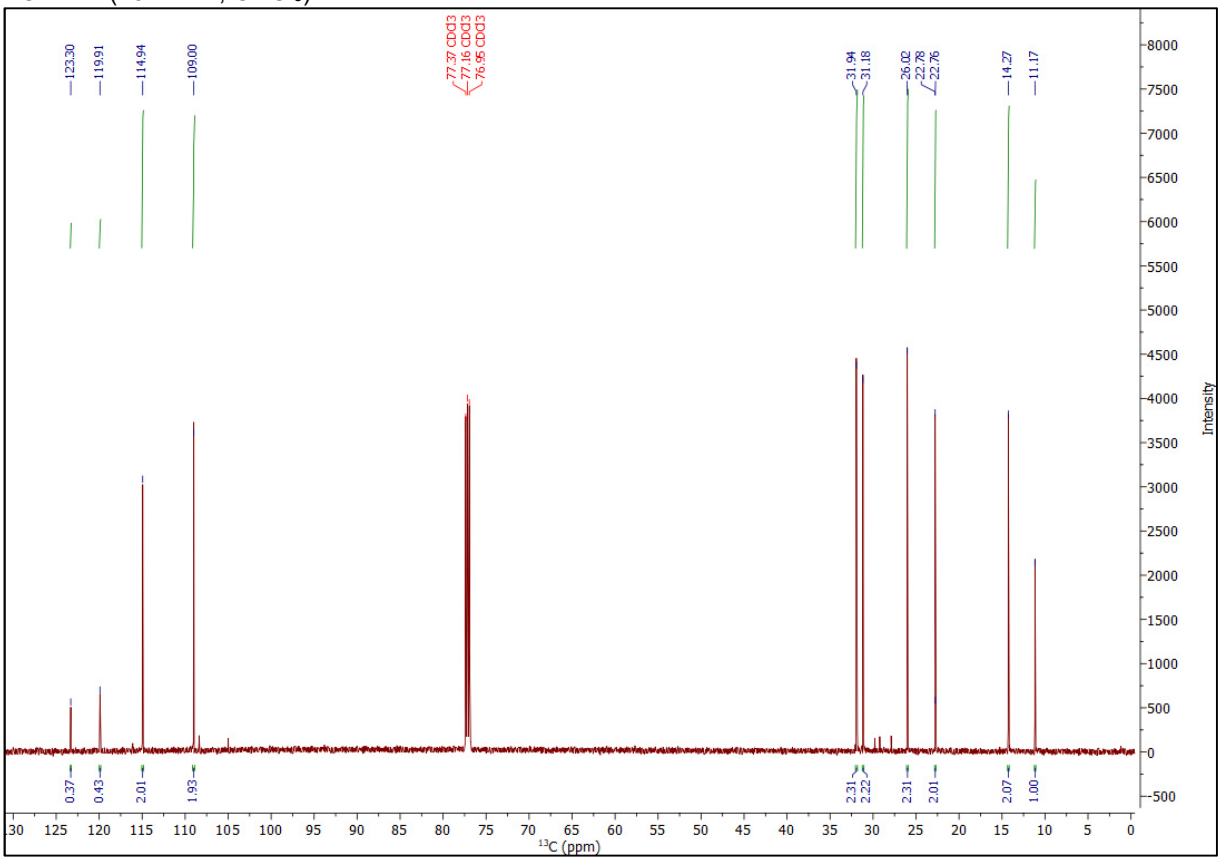


2-Methyl-3-pentyl-1*H*-pyrrole (**III-15b**)

^{1}H NMR (600 MHz, $CDCl_3$)

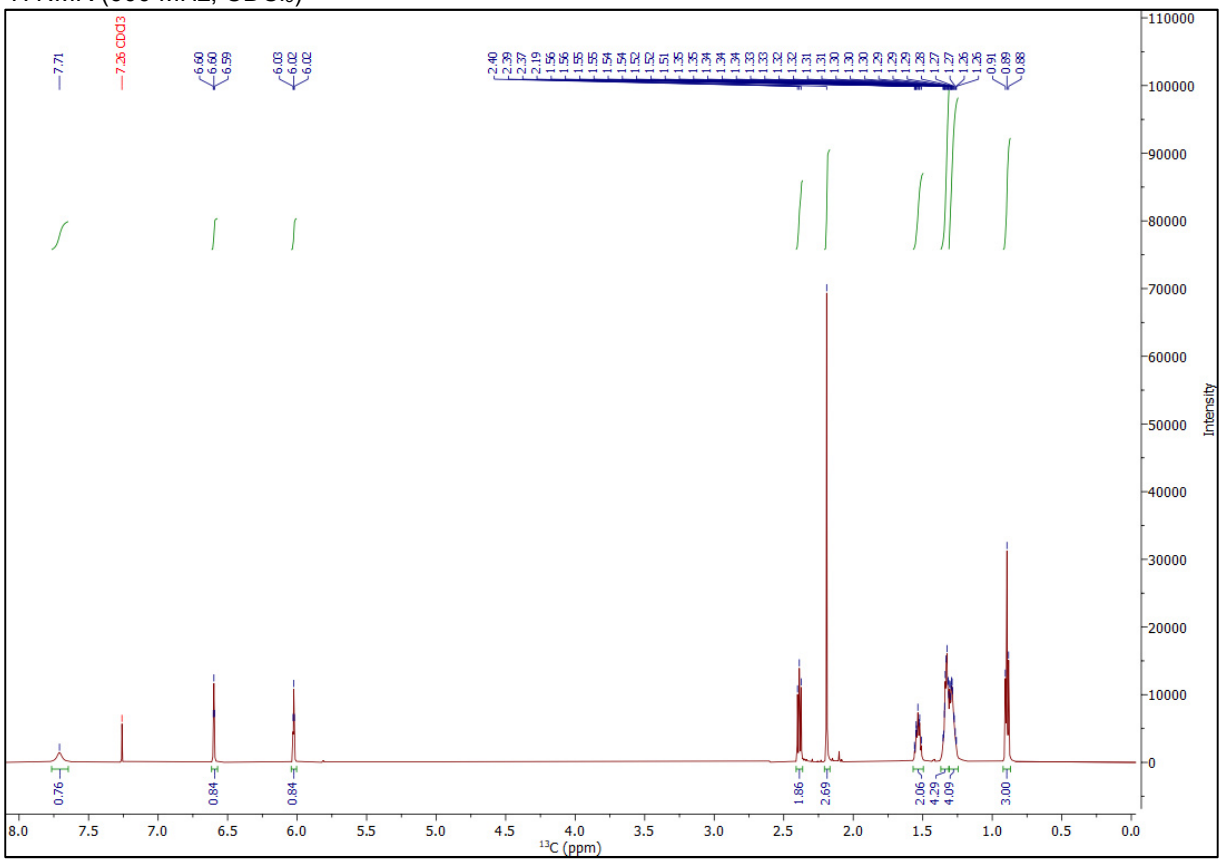


^{13}C NMR (151 MHz, $CDCl_3$)

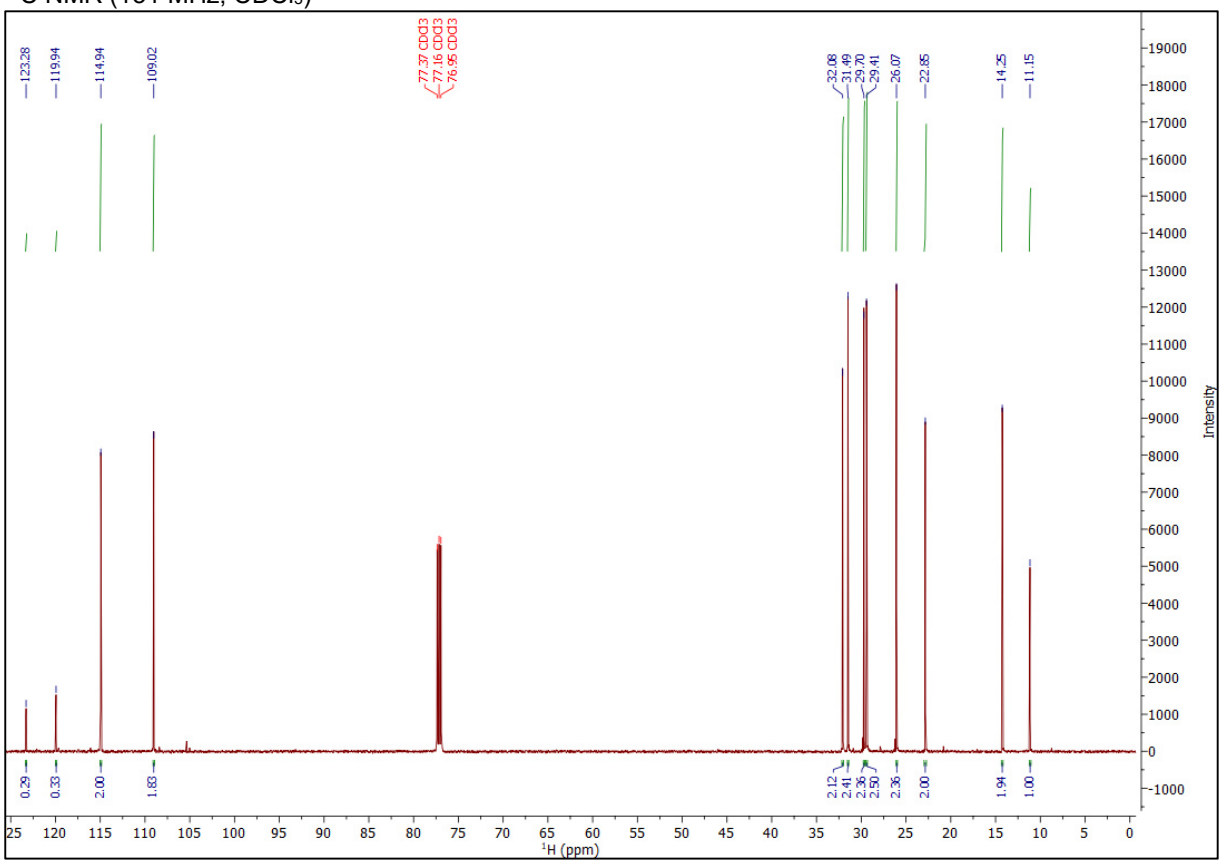


3-Heptyl-2-methyl-1*H*-pyrrole (**III-15c**)

^{1}H NMR (600 MHz, $CDCl_3$)

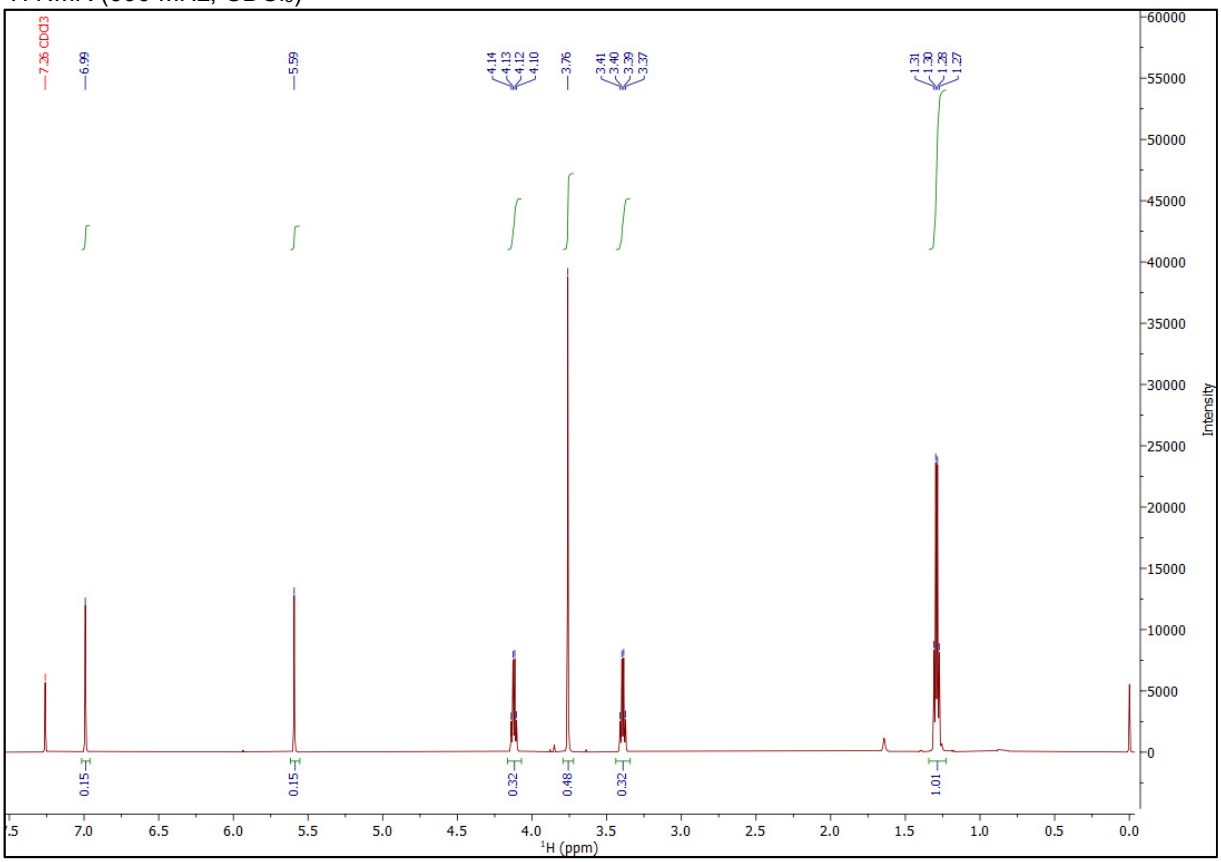


^{13}C NMR (151 MHz, $CDCl_3$)

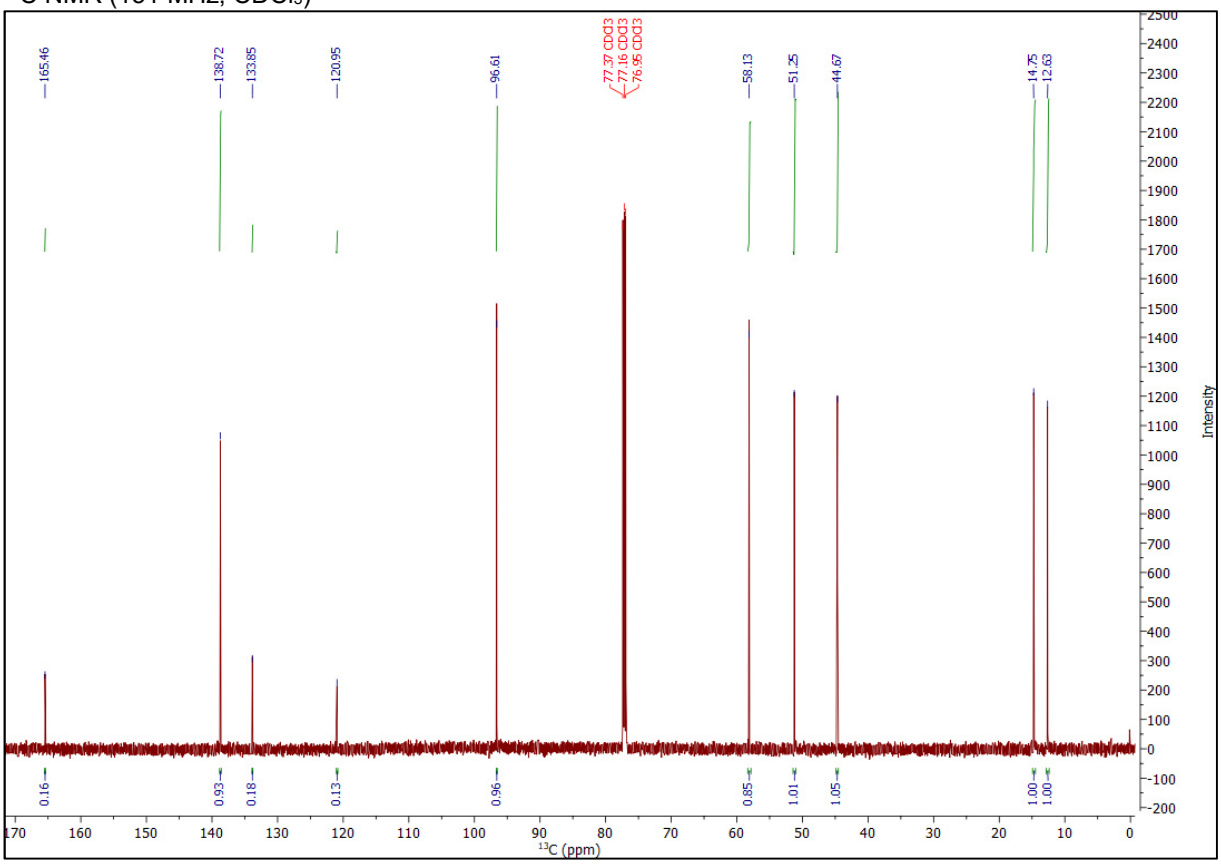


(*Z*)-*N*-[(5-Bromo-3-methoxy-2H-pyrrol-2-ylidene)methyl]-*N*-ethylethanamine (**III-75**)

^{1}H NMR (600 MHz, $CDCl_3$)

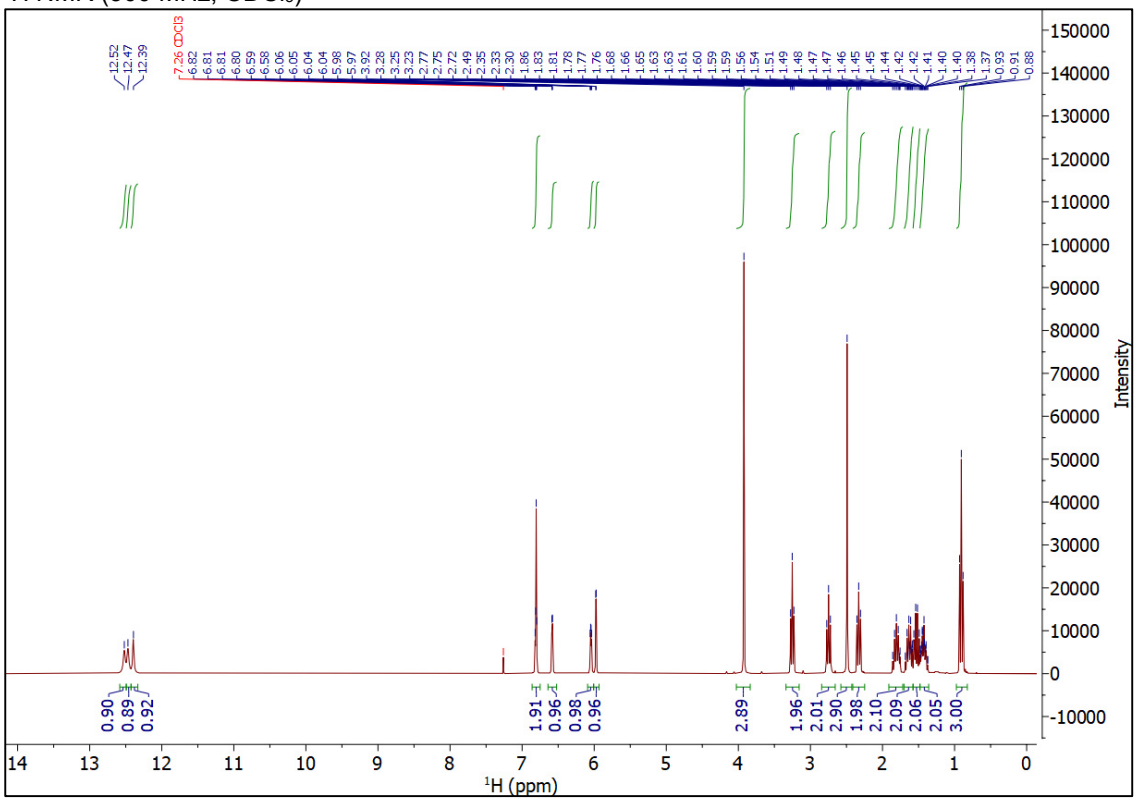


^{13}C NMR (151 MHz, $CDCl_3$)

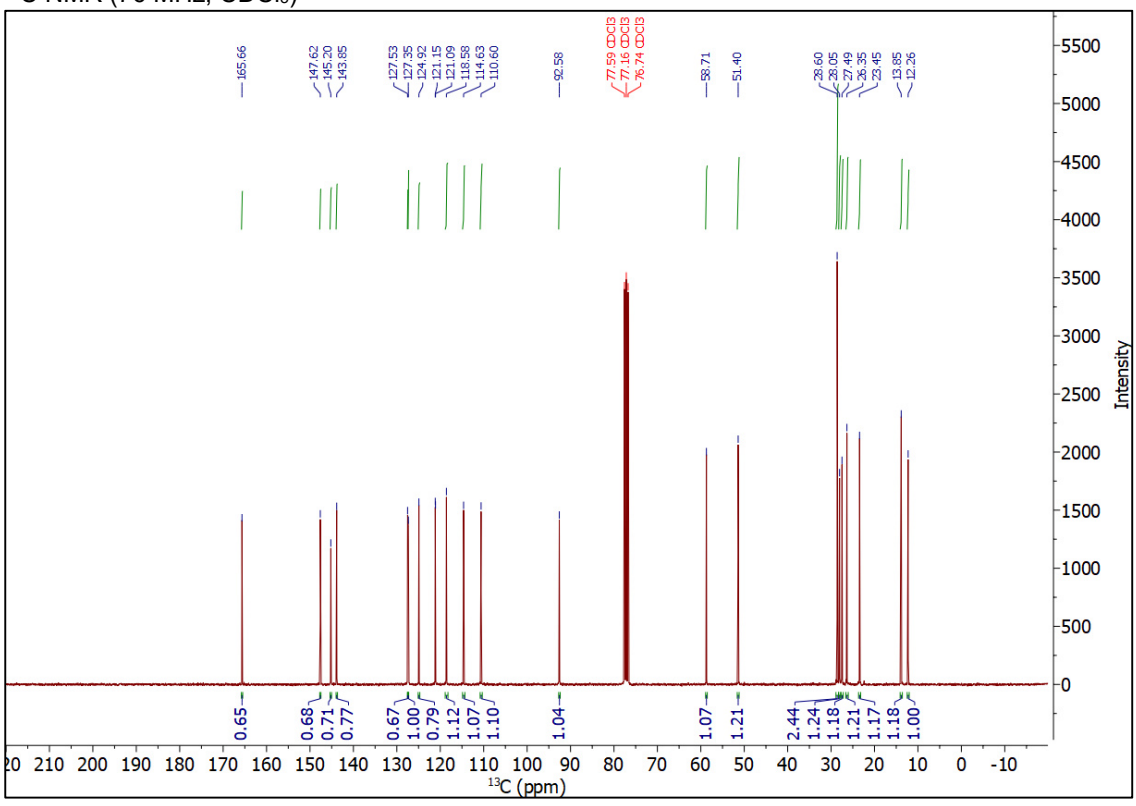


(*Z*)-5-(5-Azidopentyl)-4'-methoxy-5'-((5-methyl-4-propyl-1*H*-pyrrol-2-yl)methylene)-1*H*,5'*H*-[2,2'-bipyrrol]-1'-ium chloride (**III-89·HCl**)

^{1}H NMR (300 MHz, $CDCl_3$)

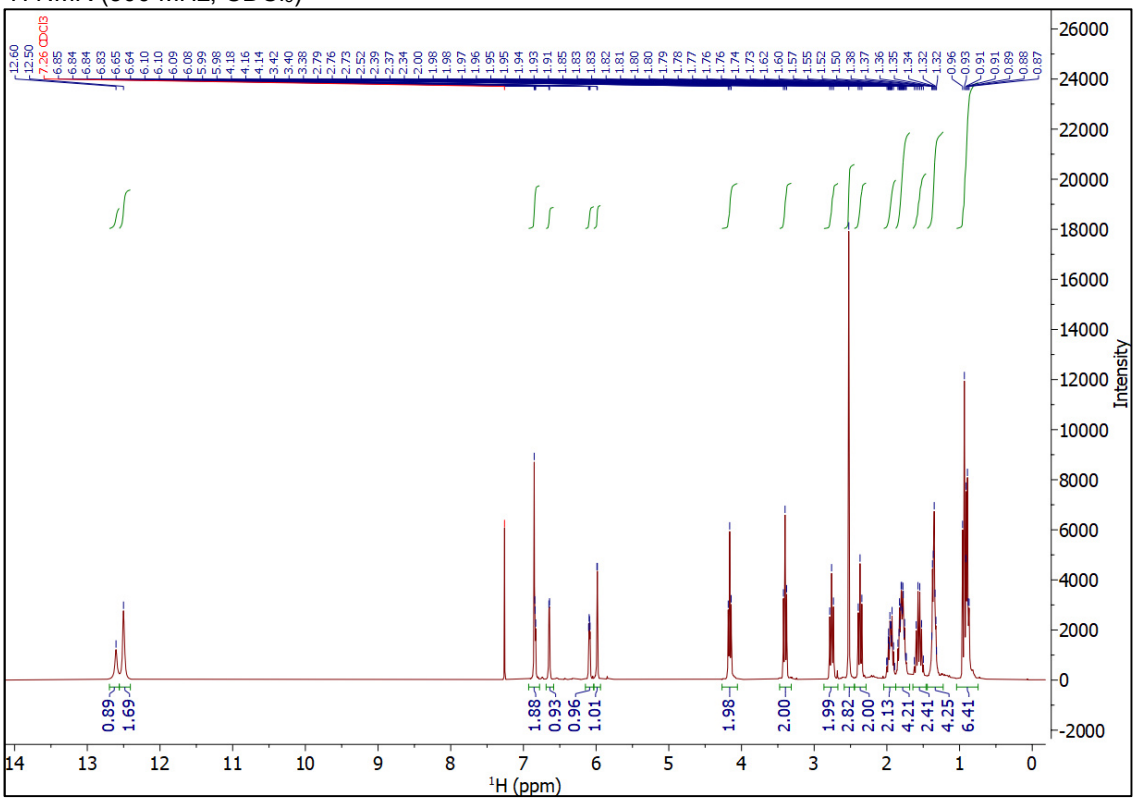


^{13}C NMR (76 MHz, $CDCl_3$)

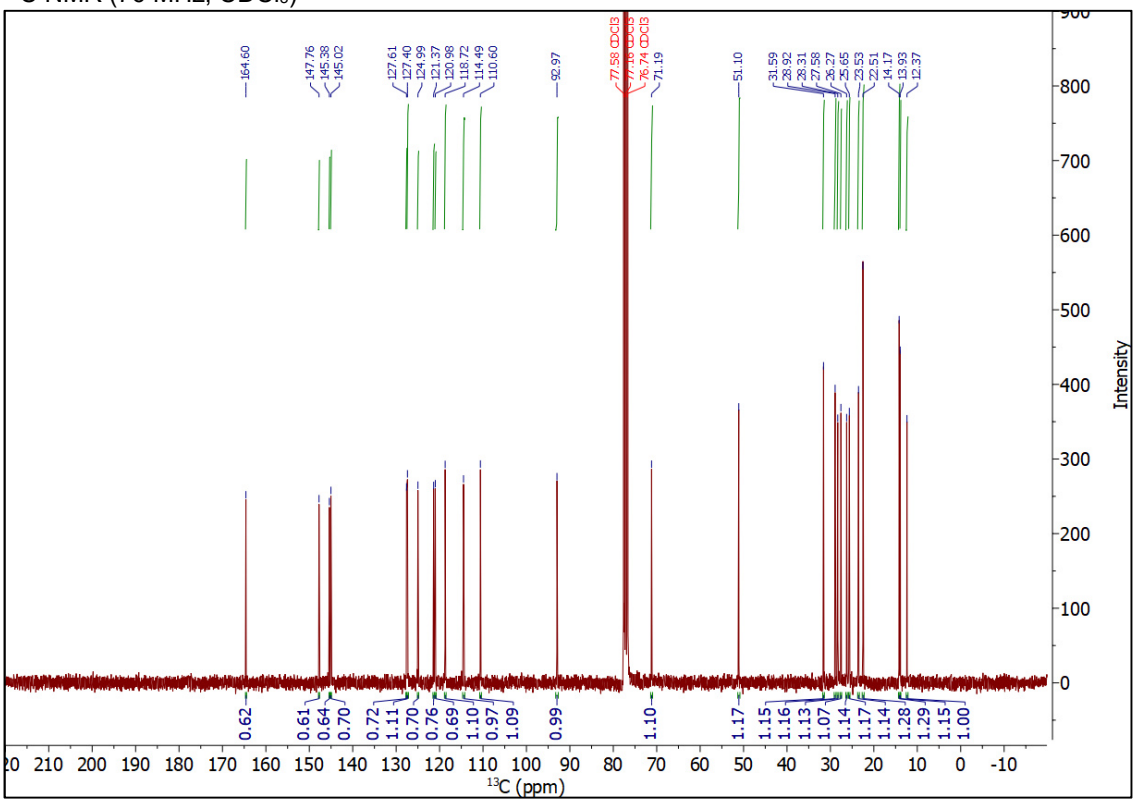


(*Z*)-4'-(4-Azidobutoxy)-5'-((5-methyl-4-propyl-1*H*-pyrrol-2-yl)methylene)-5-pentyl-1*H*,5'*H*-[2,2'-bipyrrol]-1'-ium chloride (**III-90·HCl**)

^{1}H NMR (300 MHz, $CDCl_3$)

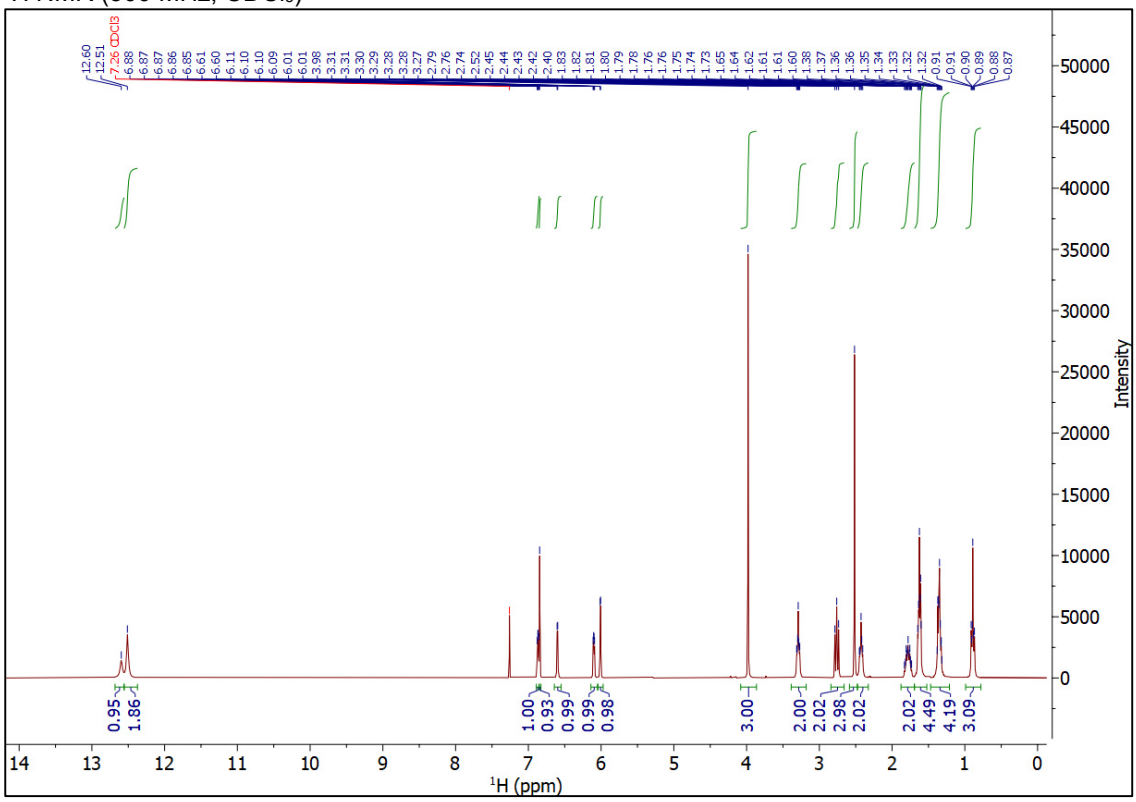


^{13}C NMR (76 MHz, $CDCl_3$)

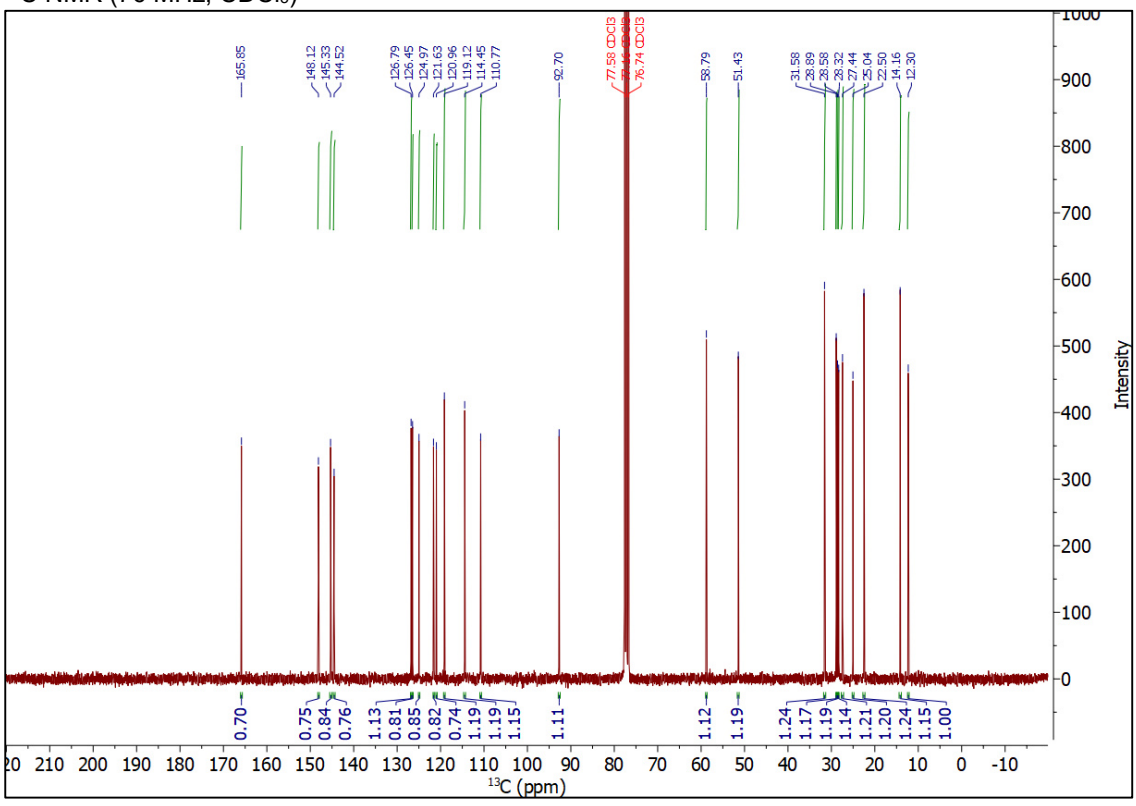


(*Z*)-5'-((4-(4-Azidobutyl)-5-methyl-1*H*-pyrrol-2-yl)methylene)-4'-methoxy-5-pentyl-1*H*,5'*H*-[2,2'-bipyrrol]-1'-ium chloride (**III-91·HCl**)

^{1}H NMR (300 MHz, $CDCl_3$)

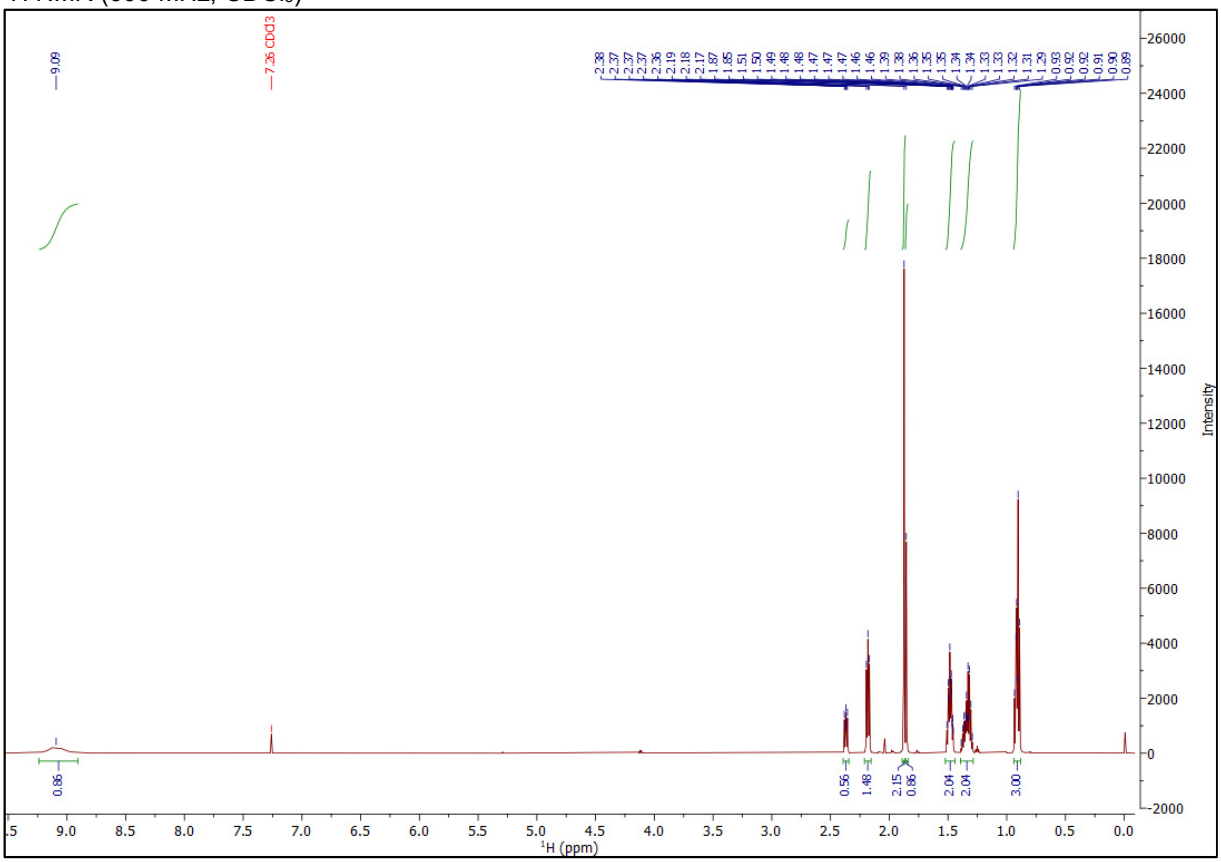


^{13}C NMR (76 MHz, $CDCl_3$)

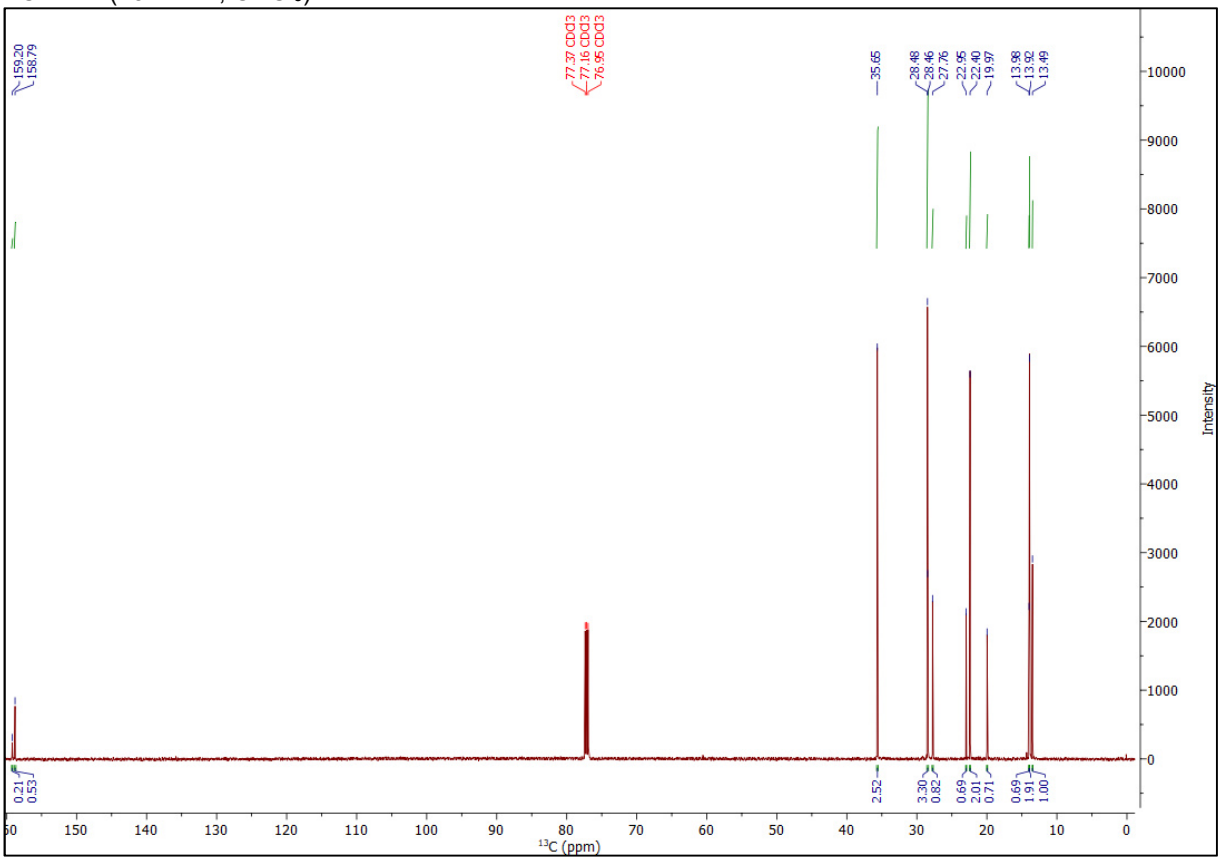


(*E*/*Z*)-Hexan-2-one oxime (**III-93a**)

^{1}H NMR (600 MHz, $CDCl_3$)

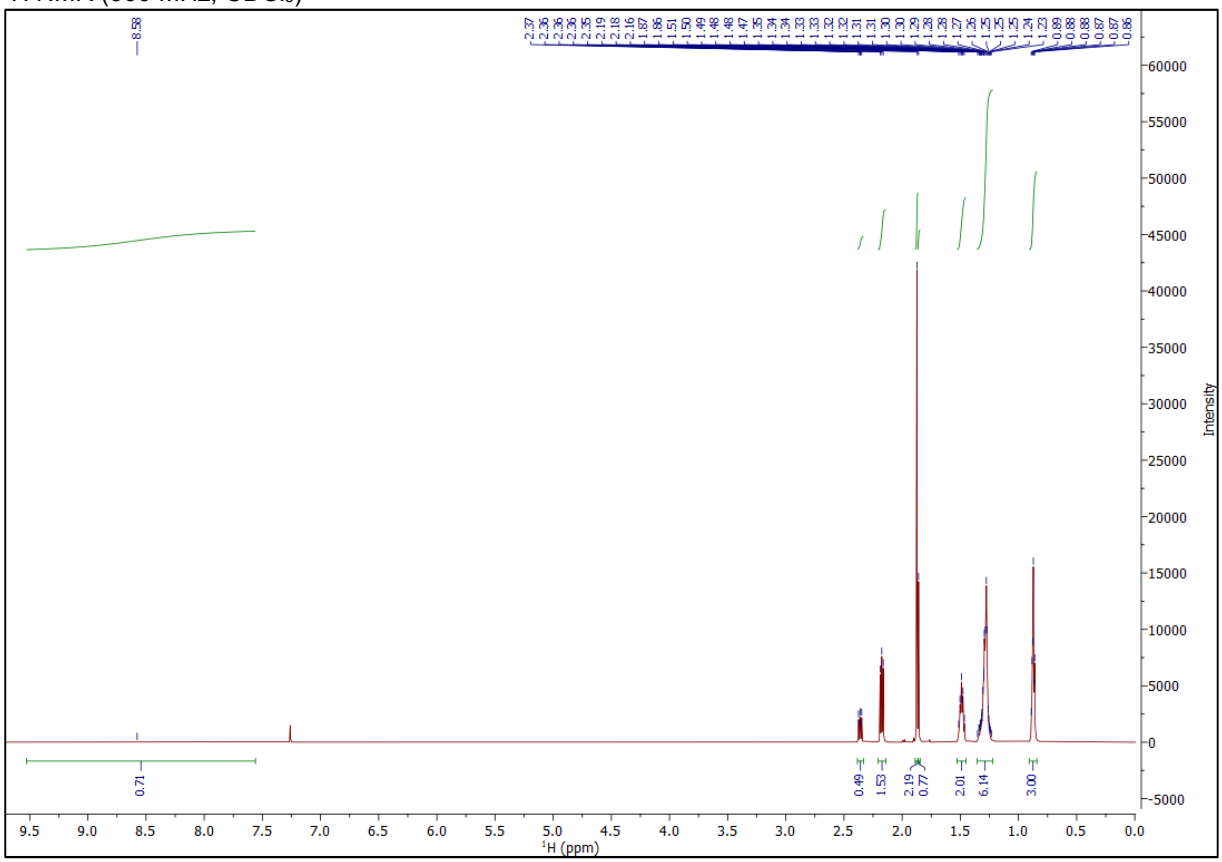


^{13}C NMR (151 MHz, $CDCl_3$)

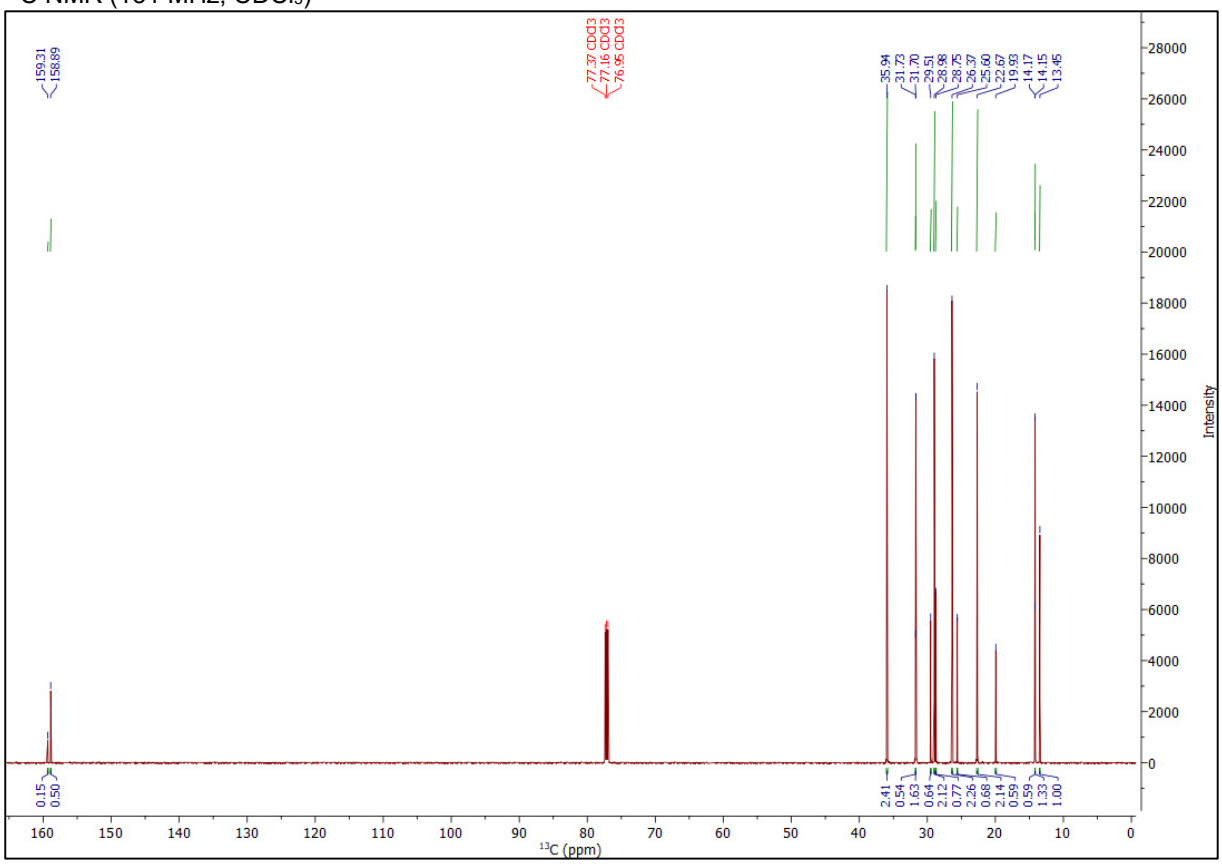


(*E*/*Z*)-Octan-2-one oxime (**III-93b**)

^{1}H NMR (600 MHz, $CDCl_3$)

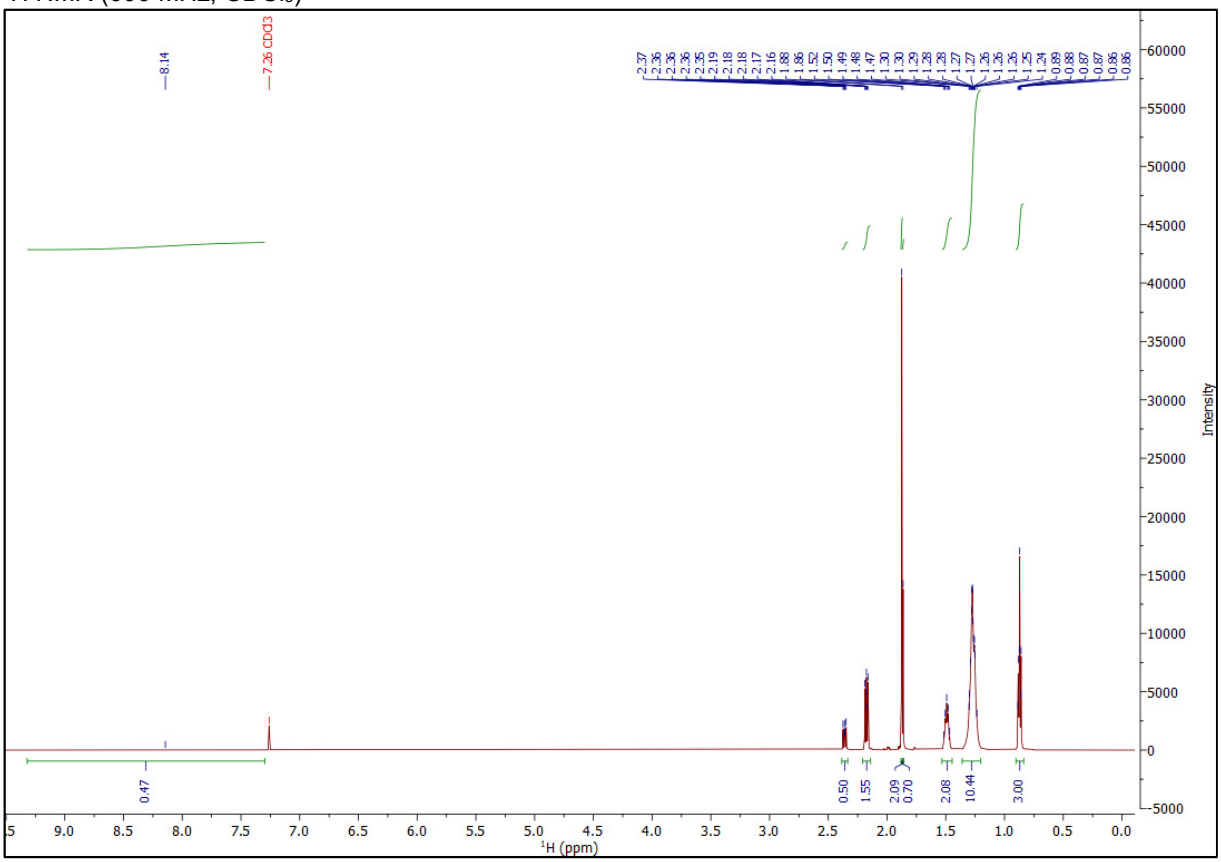


^{13}C NMR (151 MHz, $CDCl_3$)

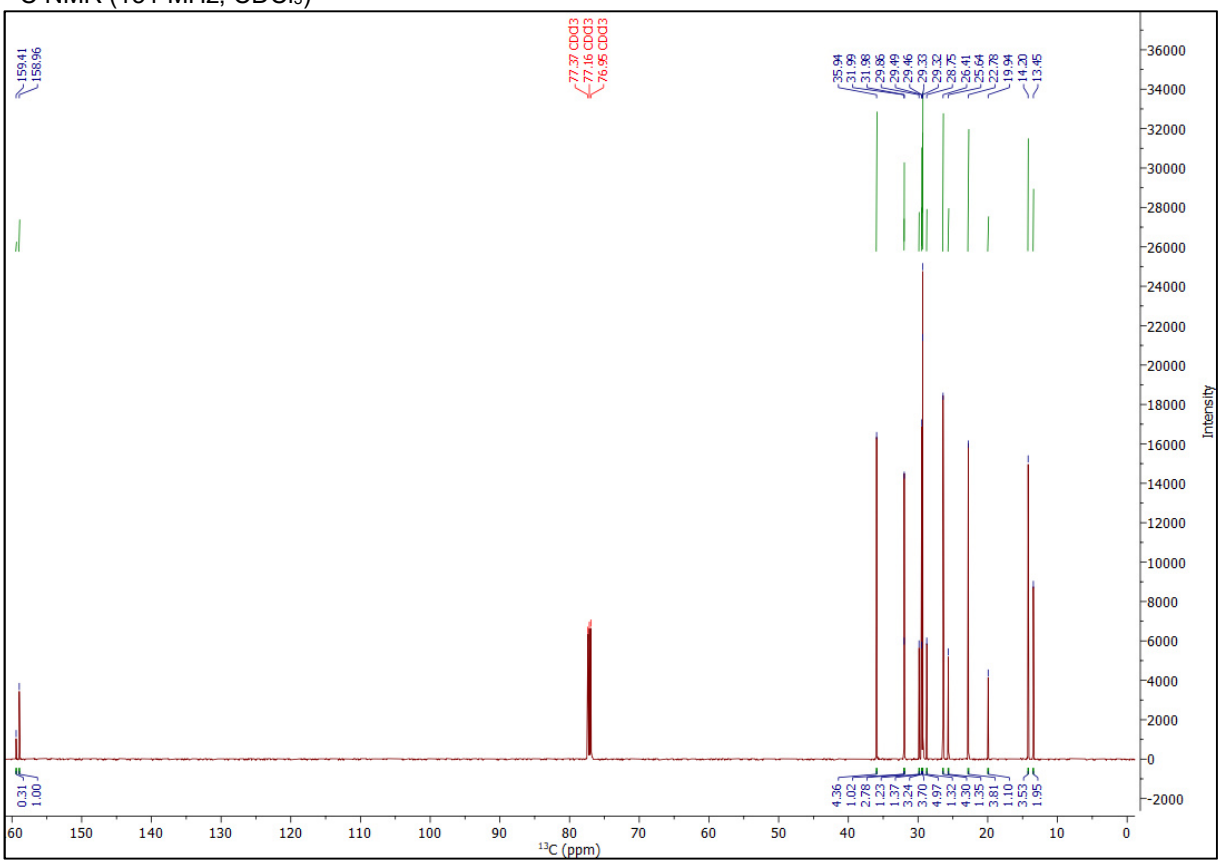


(*E*/*Z*)-Decan-2-one oxime (**III-93c**)

^{1}H NMR (600 MHz, $CDCl_3$)

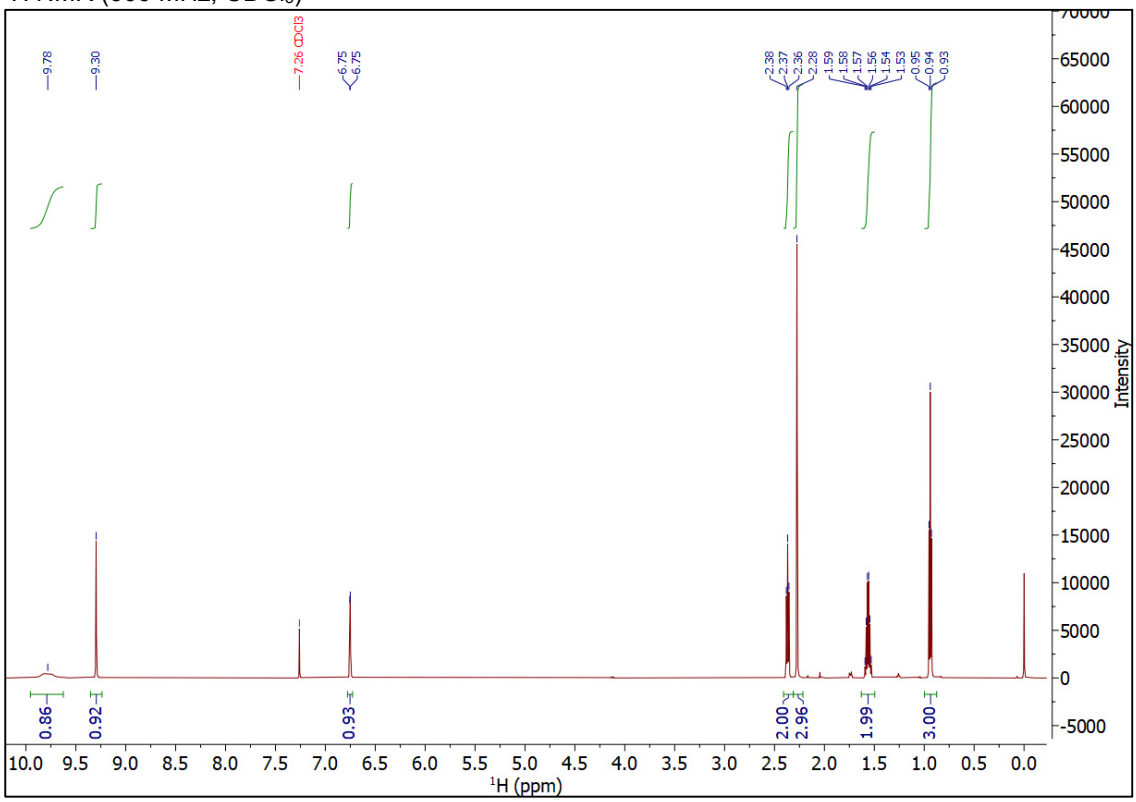


^{13}C NMR (151 MHz, $CDCl_3$)

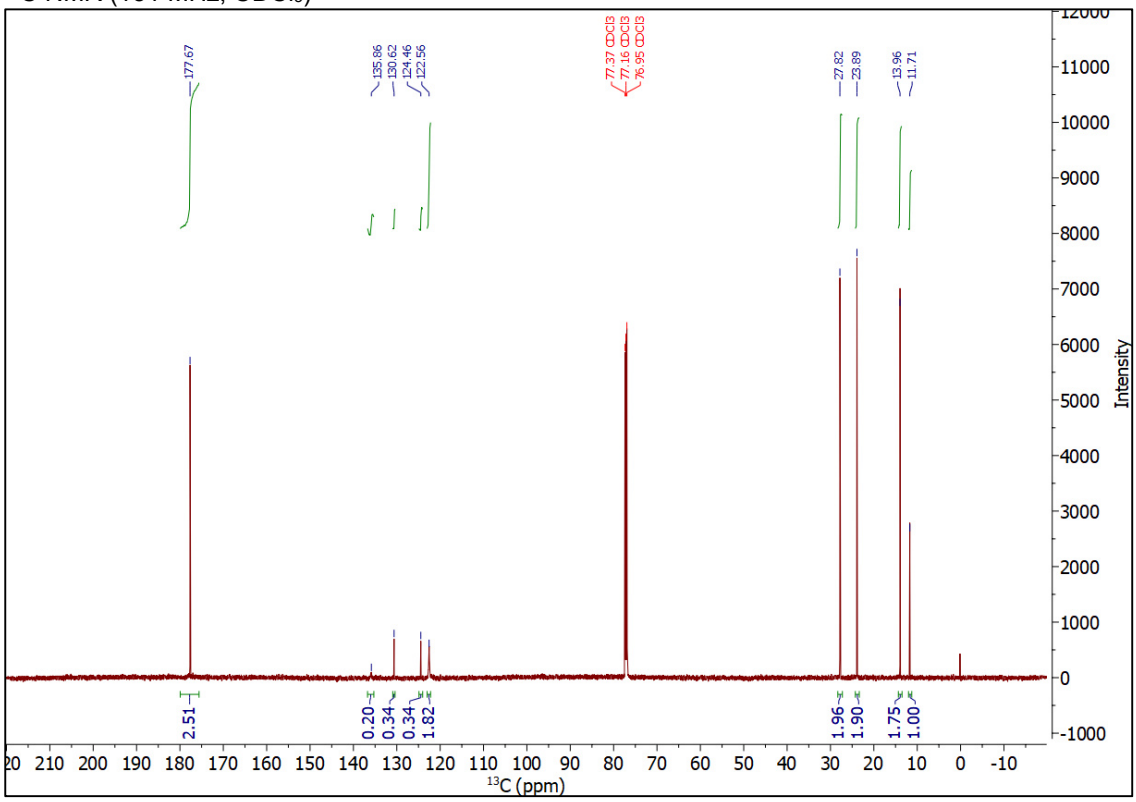


5-Methyl-4-propyl-1*H*-pyrrole-2-carbaldehyde (**III-94**)

^{1}H NMR (600 MHz, $CDCl_3$)

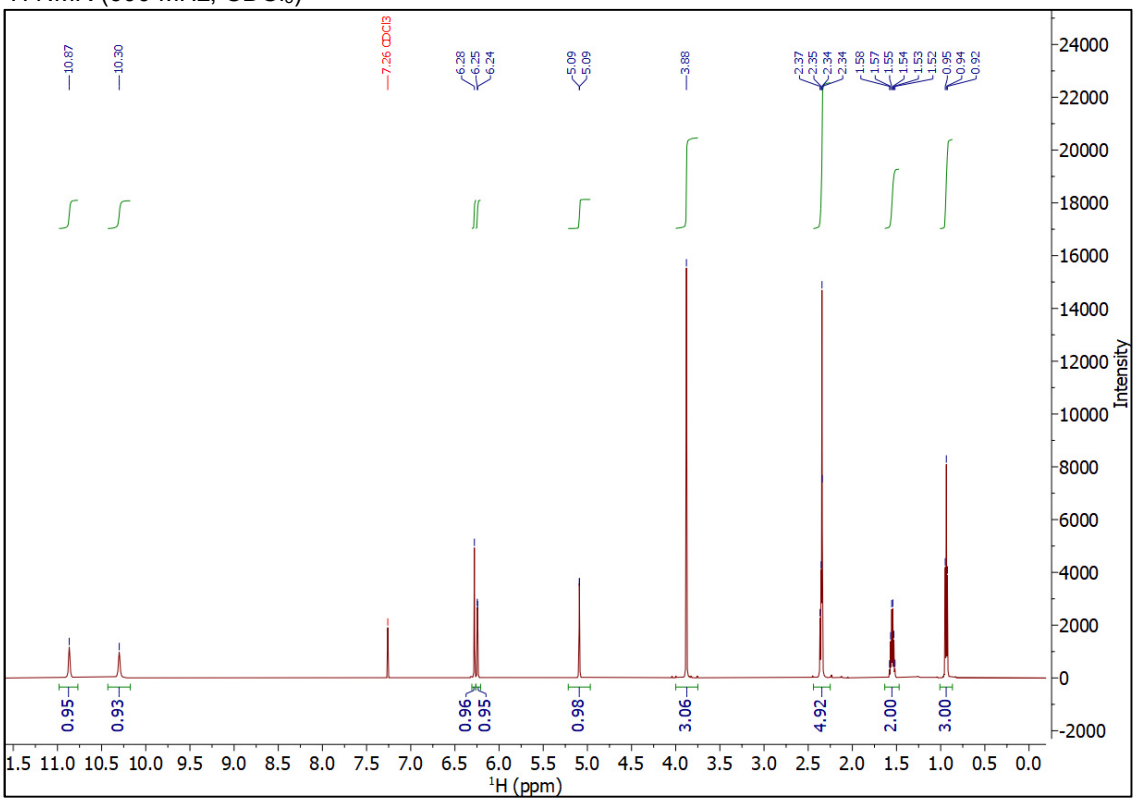


^{13}C NMR (151 MHz, $CDCl_3$)

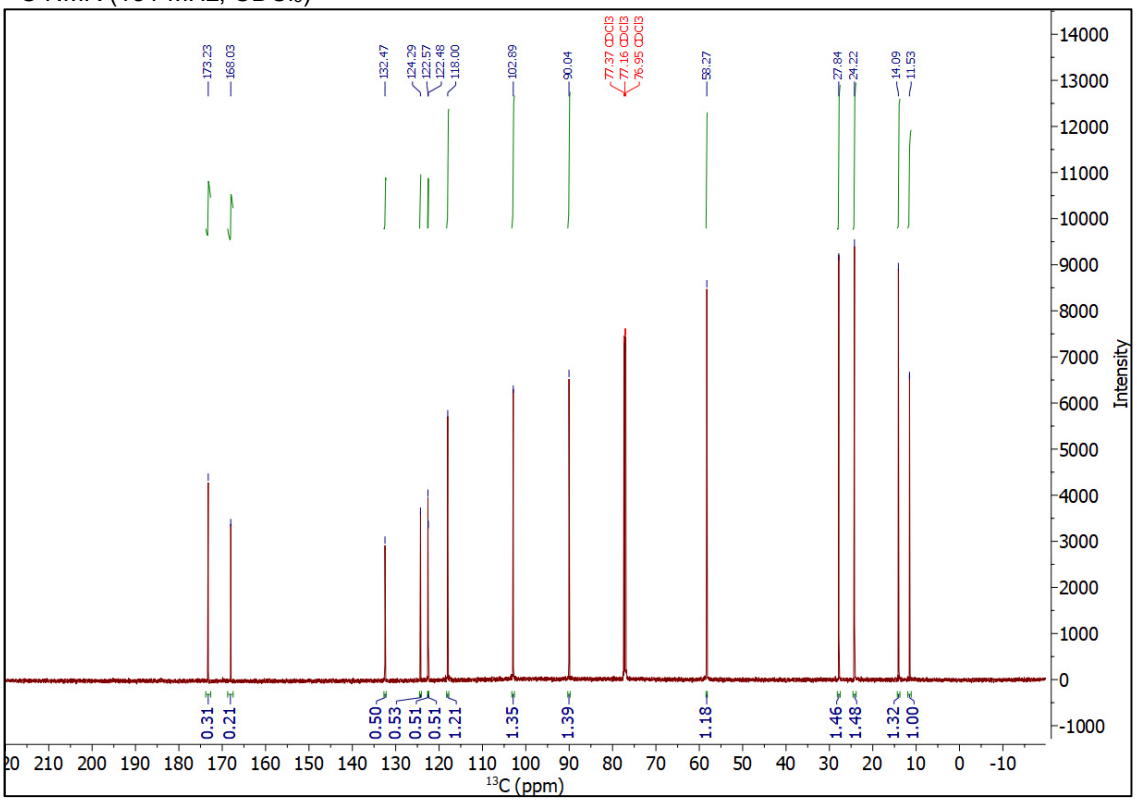


(*Z*)-4-Methoxy-5-((5-methyl-4-propyl-1*H*-pyrrol-2-yl)methylene)-1,5-dihydro-2*H*-pyrrol-2-one (**III-95**)

^{1}H NMR (600 MHz, $CDCl_3$)

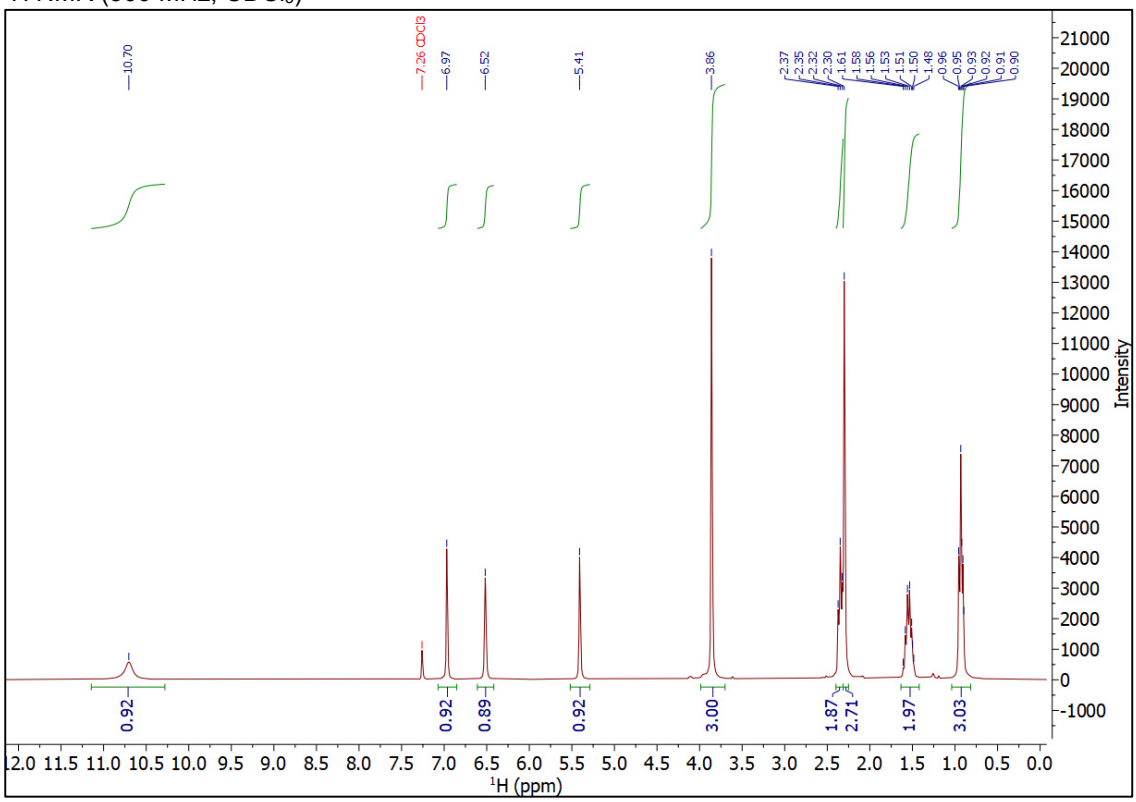


^{13}C NMR (151 MHz, $CDCl_3$)

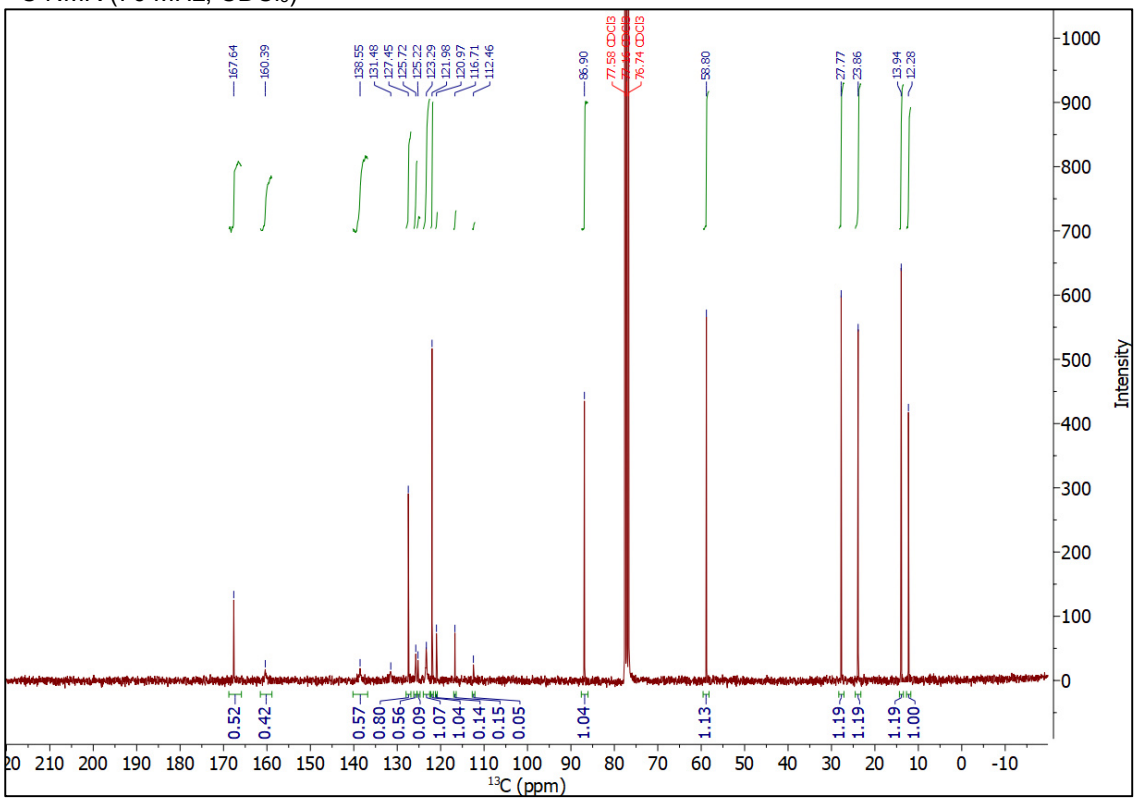


(*Z*)-4-Methoxy-5-((5-methyl-4-propyl-2*H*-pyrrol-2-ylidene)methyl)-1*H*-pyrrol-2-yl trifluoromethanesulfonate (**III-96**)

^{1}H NMR (300 MHz, $CDCl_3$)

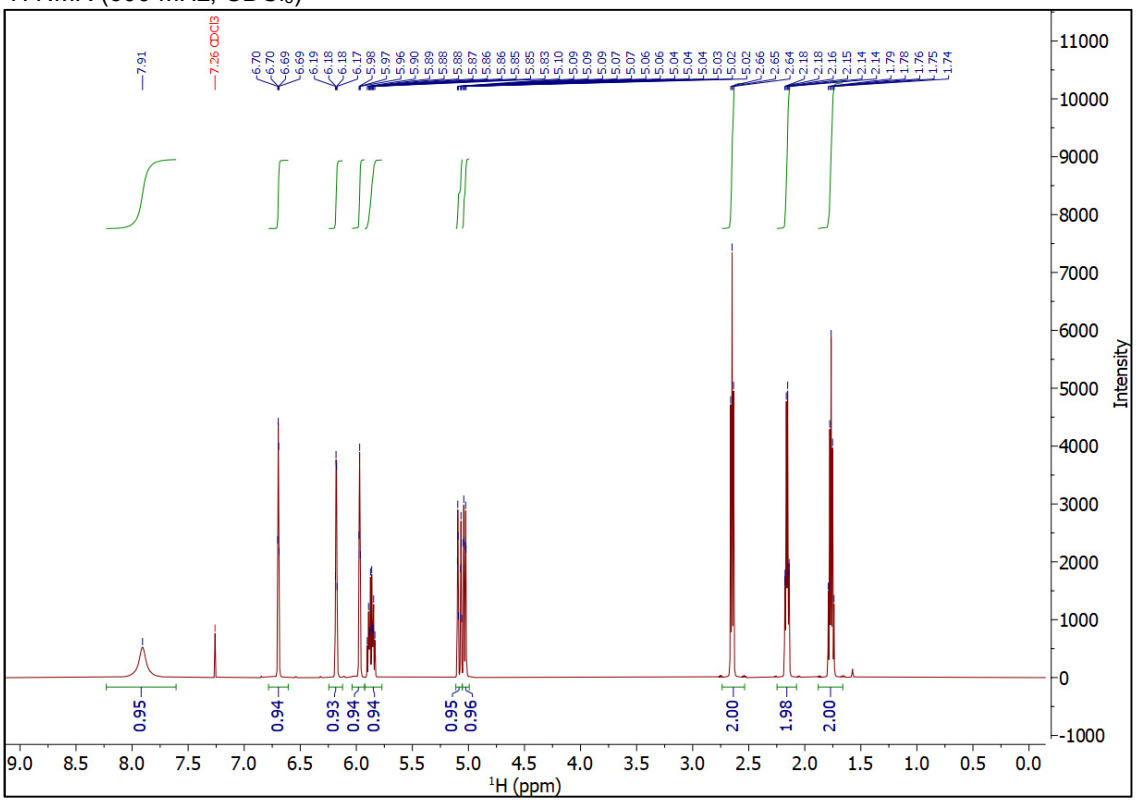


^{13}C NMR (76 MHz, $CDCl_3$)

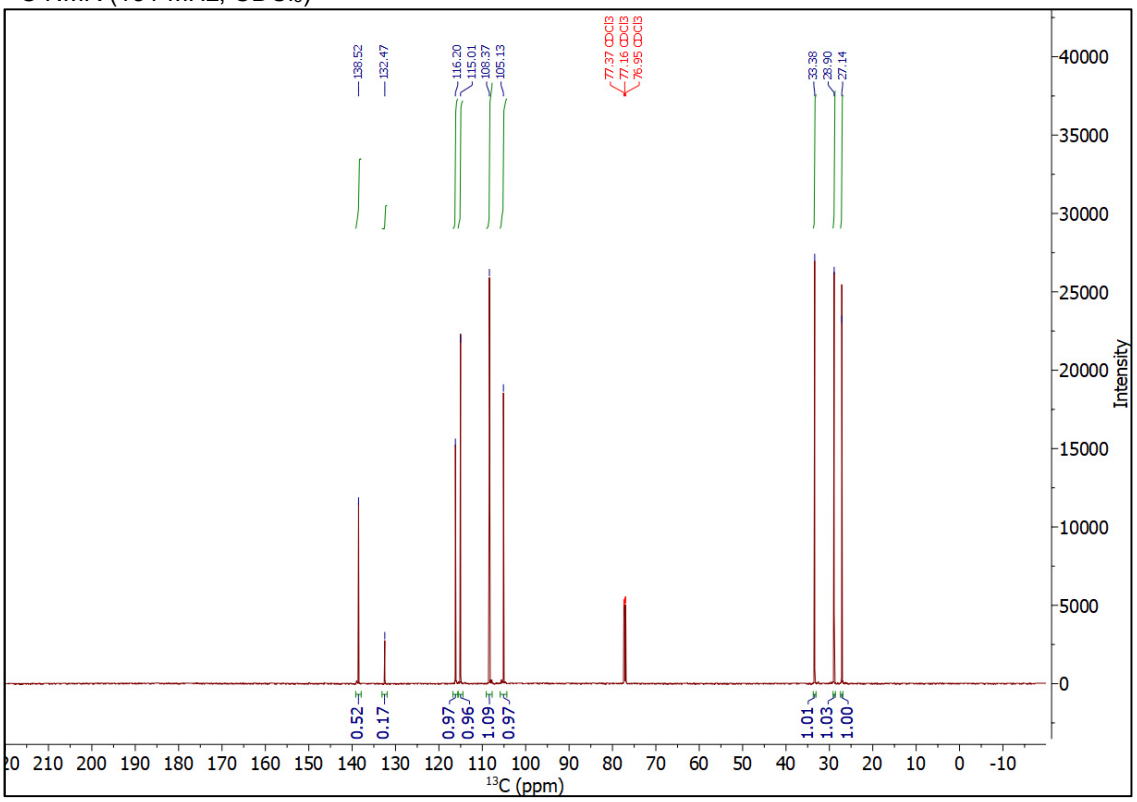


2-(Pent-4-en-1-yl)-1*H*-pyrrole (**III-97**)

^{1}H NMR (600 MHz, $CDCl_3$)

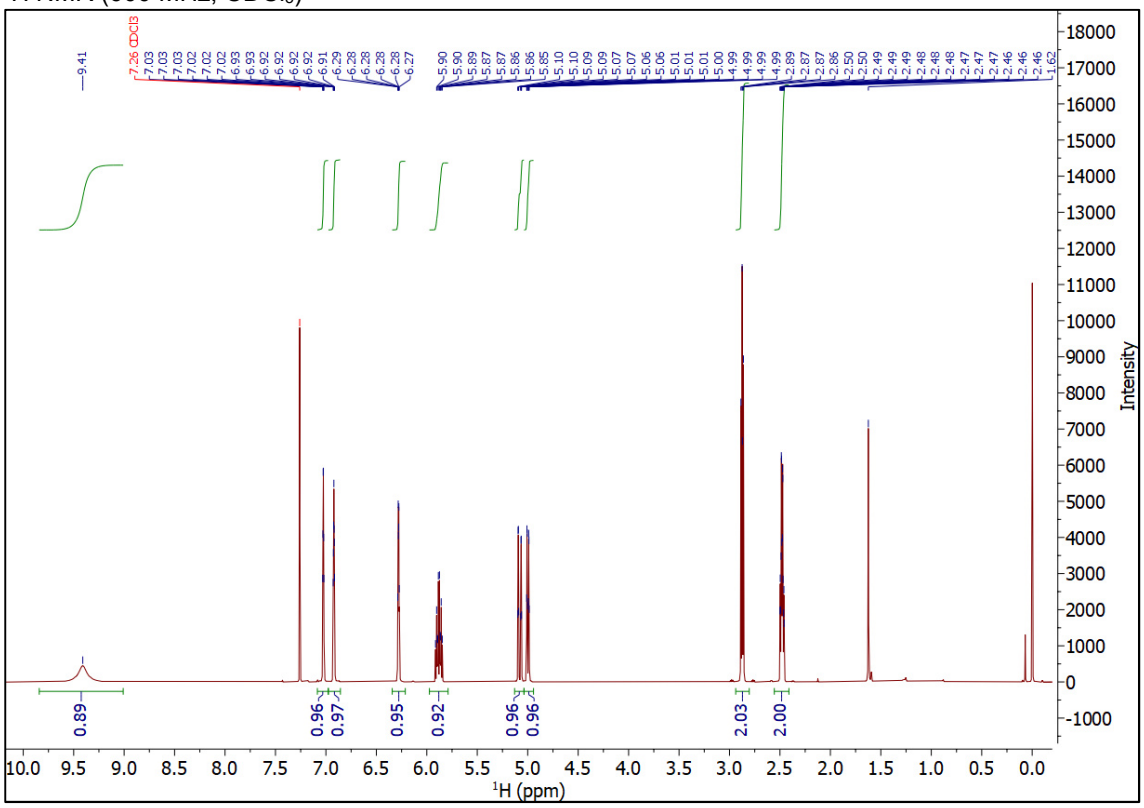


^{13}C NMR (151 MHz, $CDCl_3$)

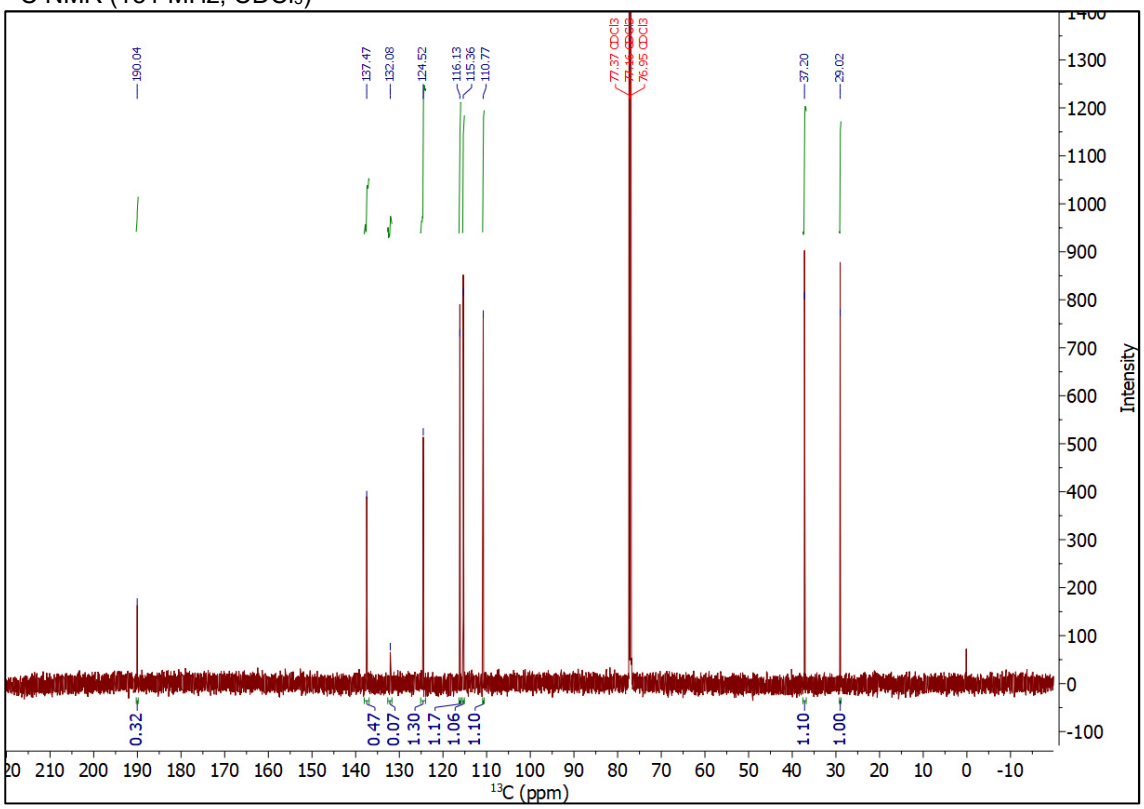


1-(1*H*-Pyrrol-2-yl)pent-4-en-1-one (**III-100**)

^{1}H NMR (600 MHz, $CDCl_3$)

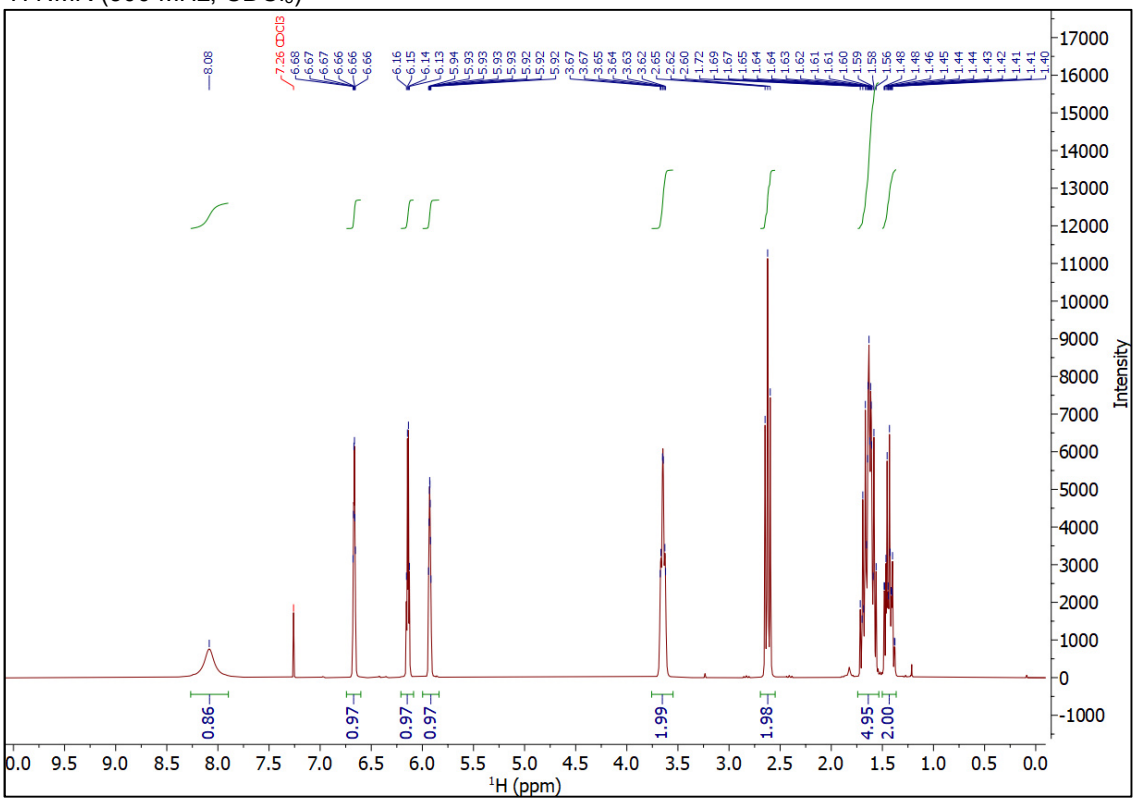


^{13}C NMR (151 MHz, $CDCl_3$)

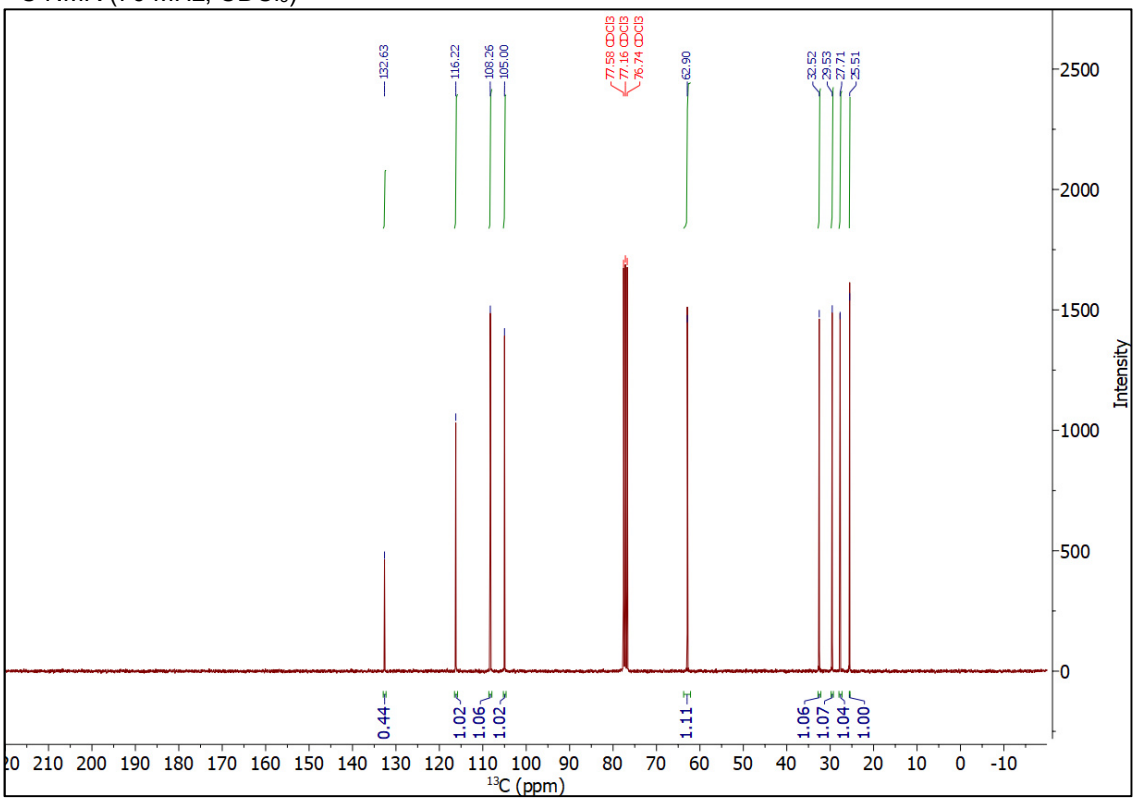


5-(1*H*-Pyrrol-2-yl)pentan-1-ol (**III-101**)

^{1}H NMR (300 MHz, $CDCl_3$)

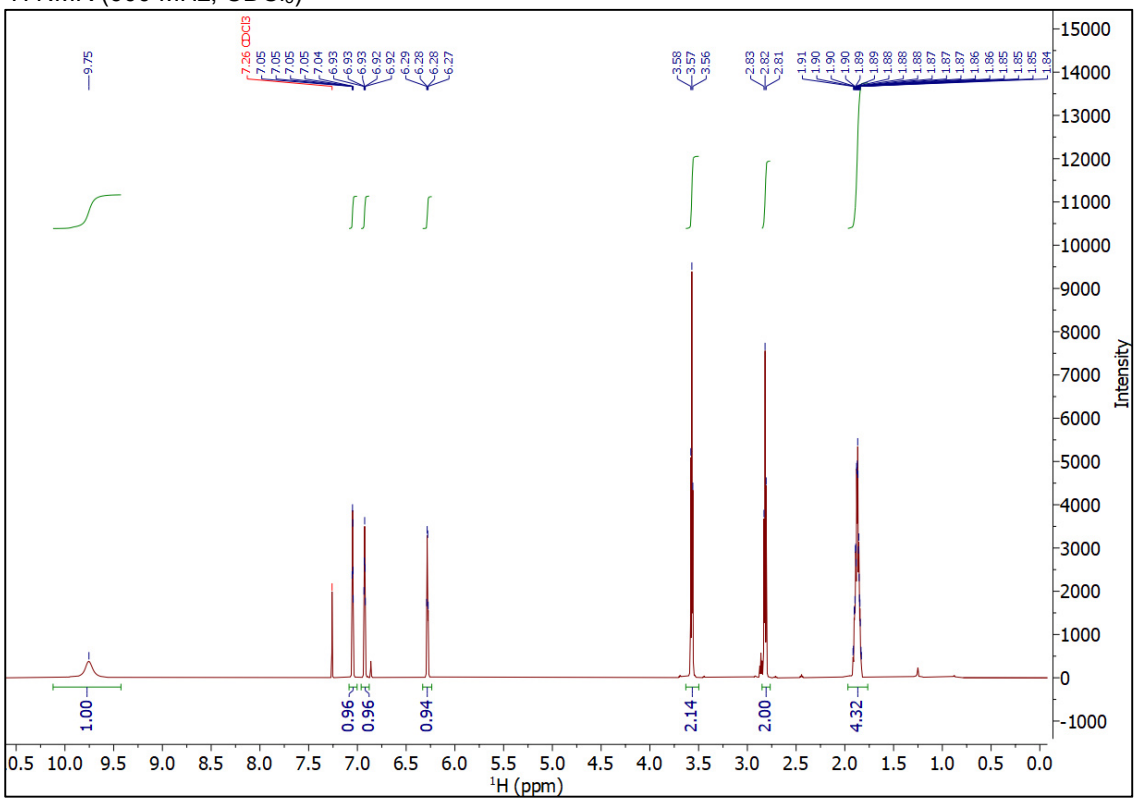


^{13}C NMR (76 MHz, $CDCl_3$)

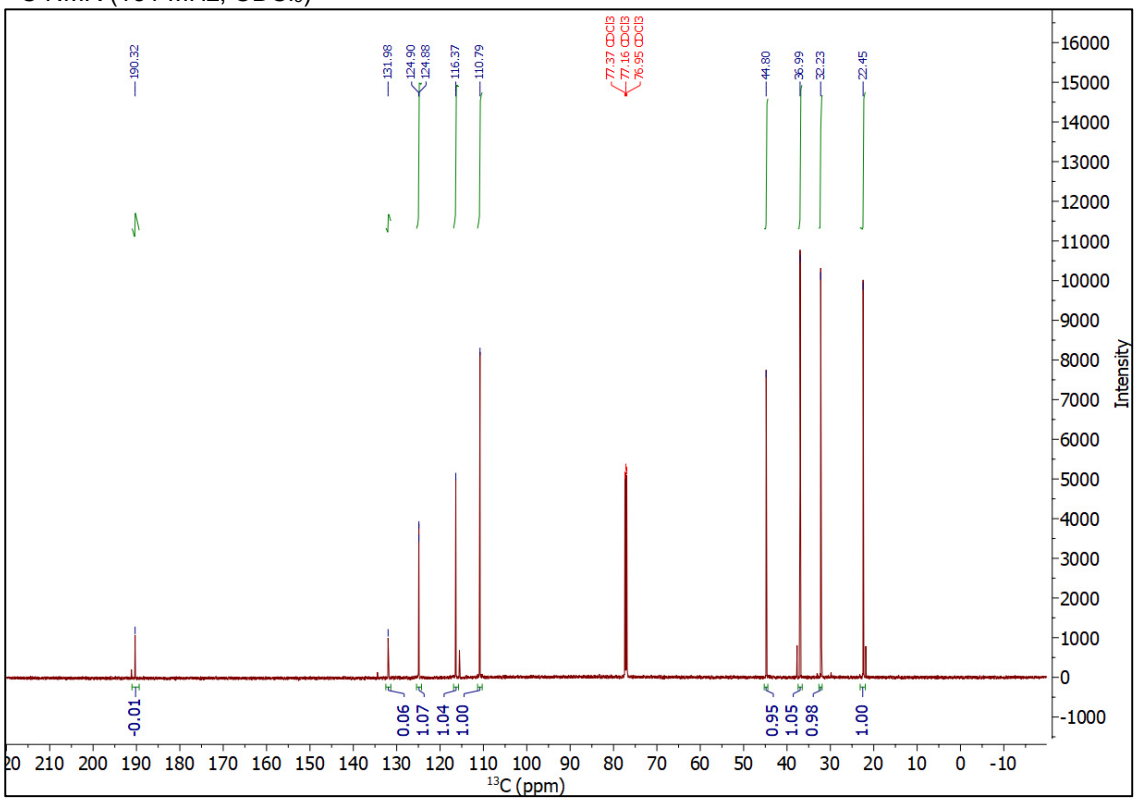


5-Chloro-1-(1*H*-pyrrol-2-yl)pentan-1-one (**III-103**)

^{1}H NMR (600 MHz, $CDCl_3$)

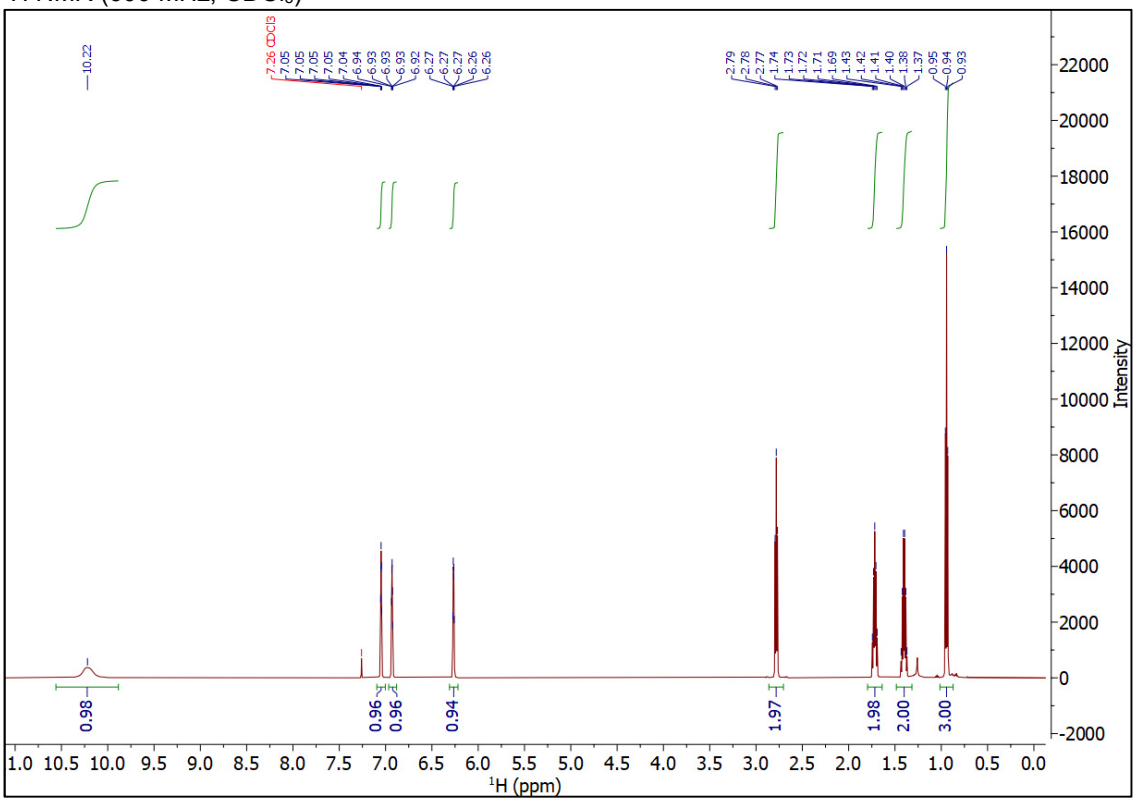


^{13}C NMR (151 MHz, $CDCl_3$)

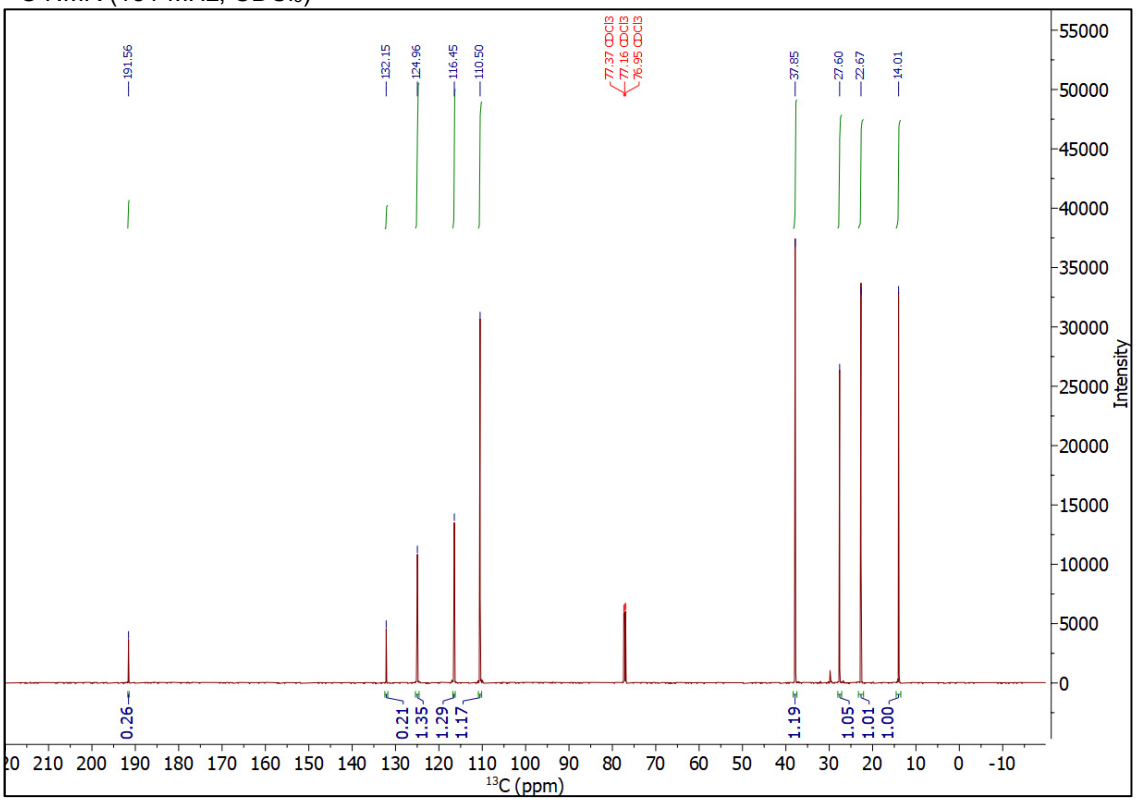


(1*H*-Pyrrol-2-yl)pentan-1-one (**III-105f**)

^{1}H NMR (600 MHz, $CDCl_3$)

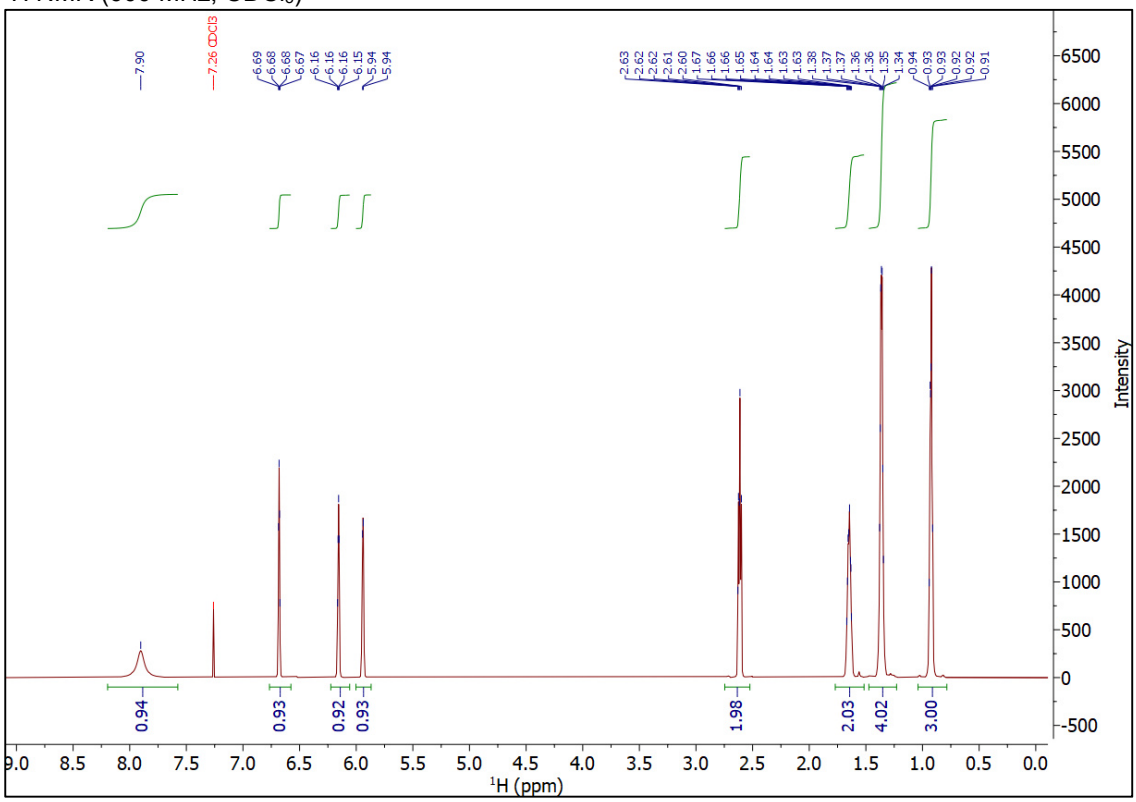


^{13}C NMR (151 MHz, $CDCl_3$)

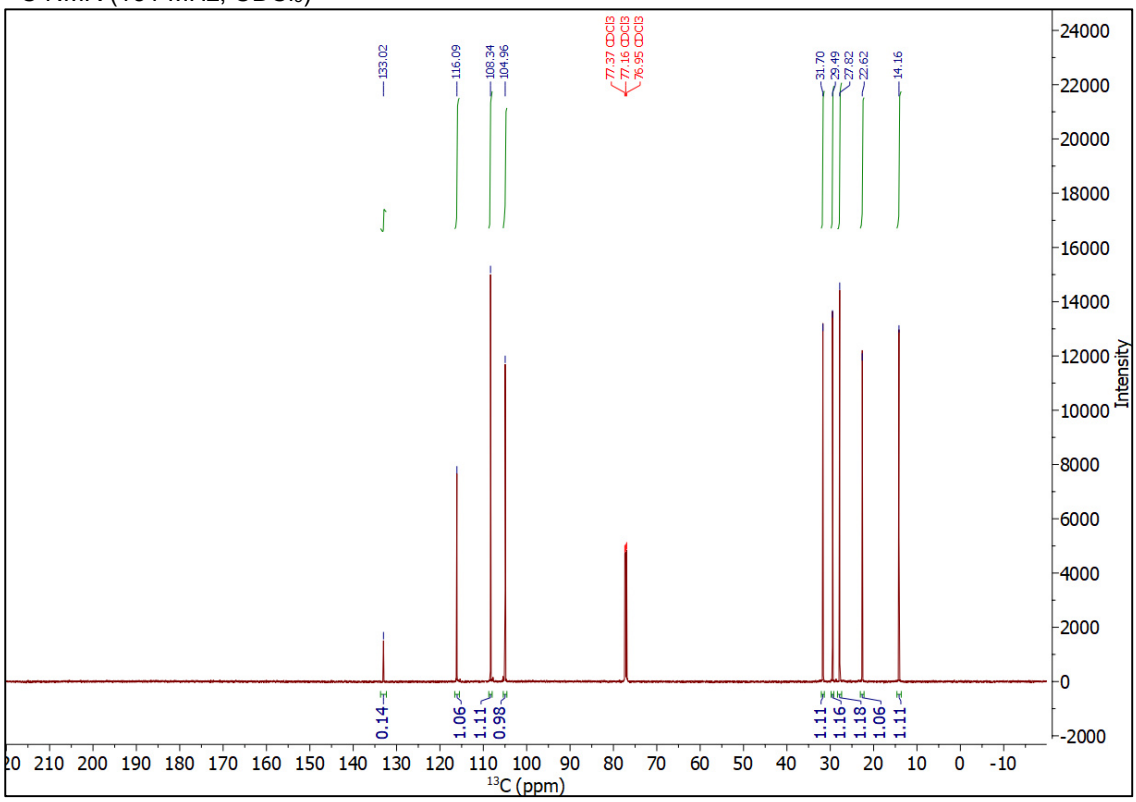


2-Pentyl-1*H*-pyrrole (**III-106f**)

^{1}H NMR (600 MHz, $CDCl_3$)

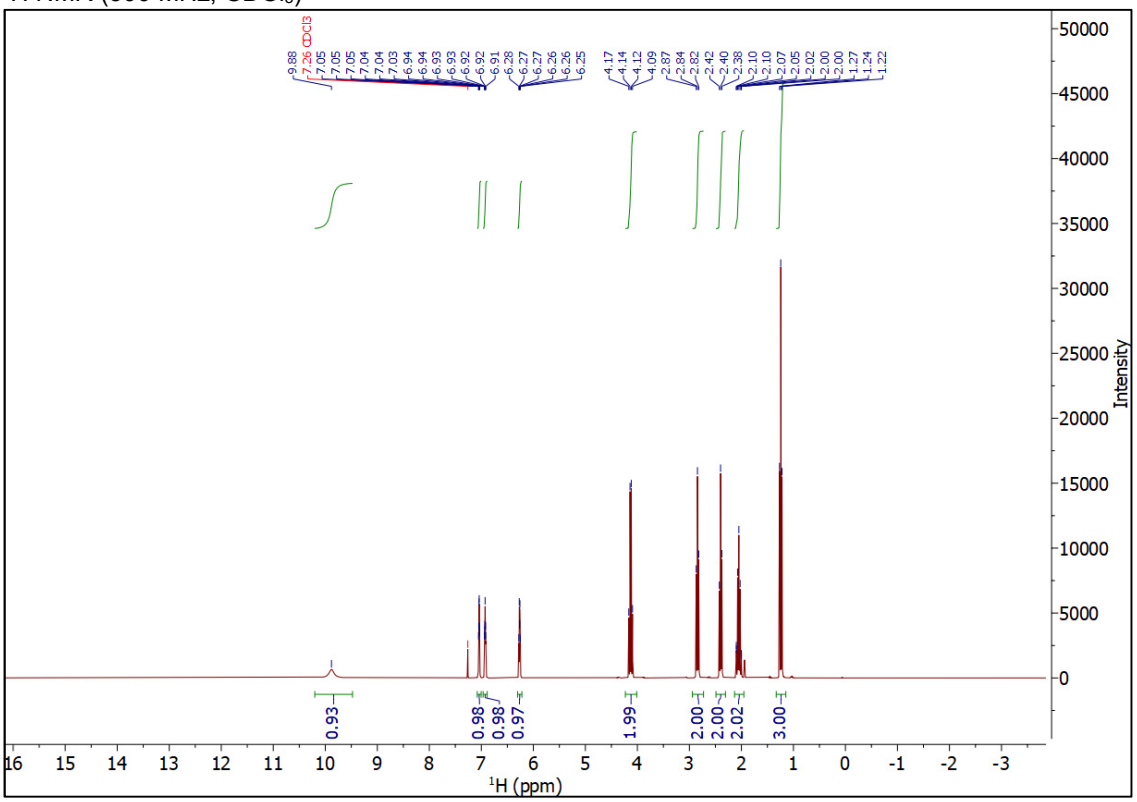


^{13}C NMR (151 MHz, $CDCl_3$)

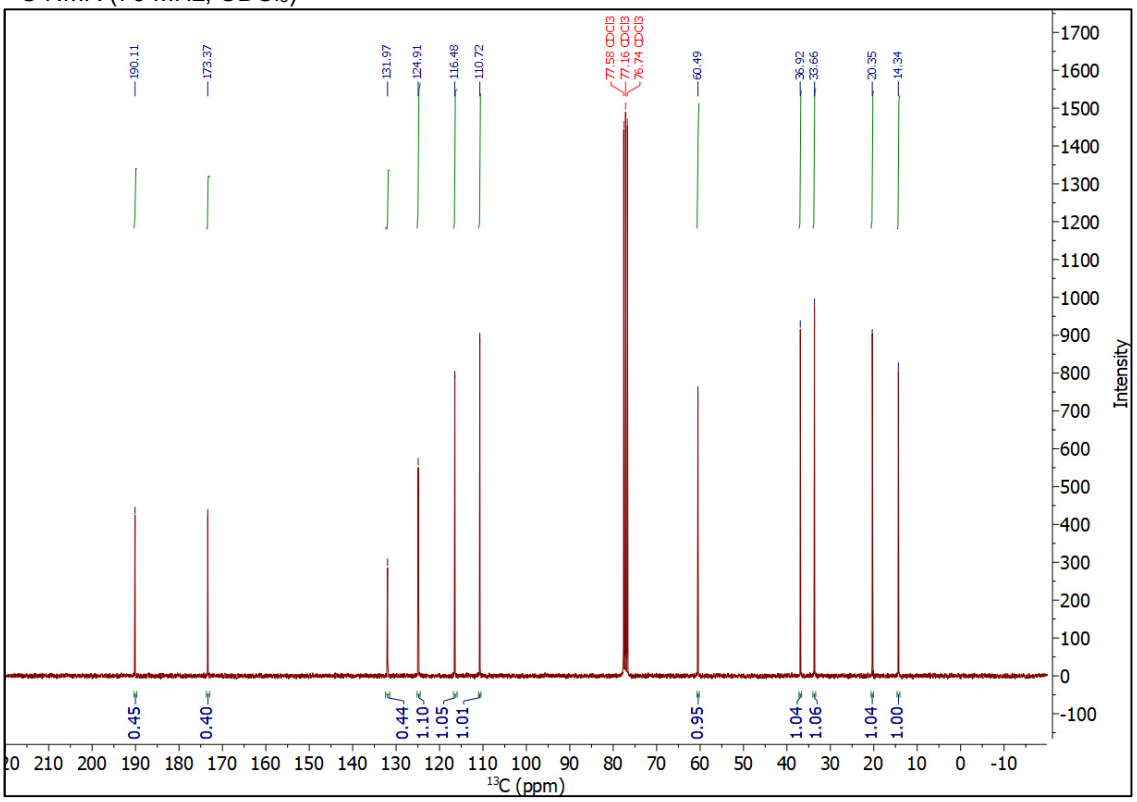


Ethyl 5-oxo-5-(1*H*-pyrrol-2-yl)pentanoate (**III-109**)

^{1}H NMR (300 MHz, $CDCl_3$)

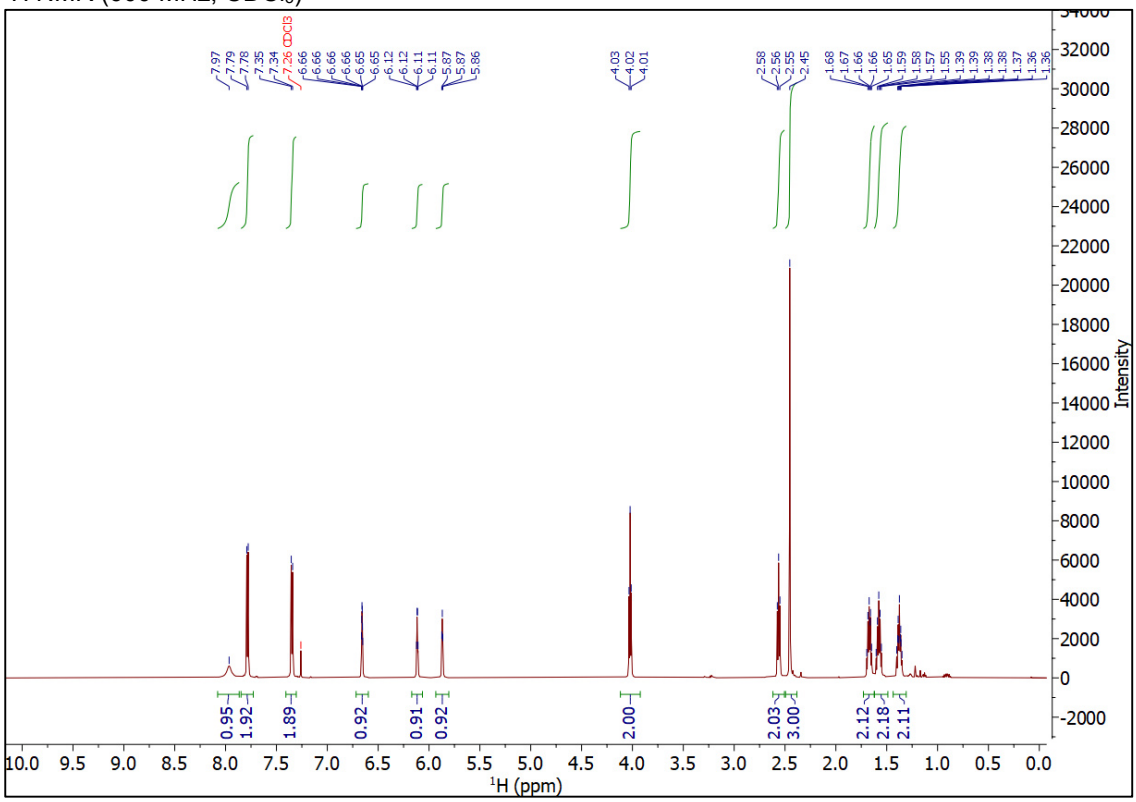


^{13}C NMR (76 MHz, $CDCl_3$)

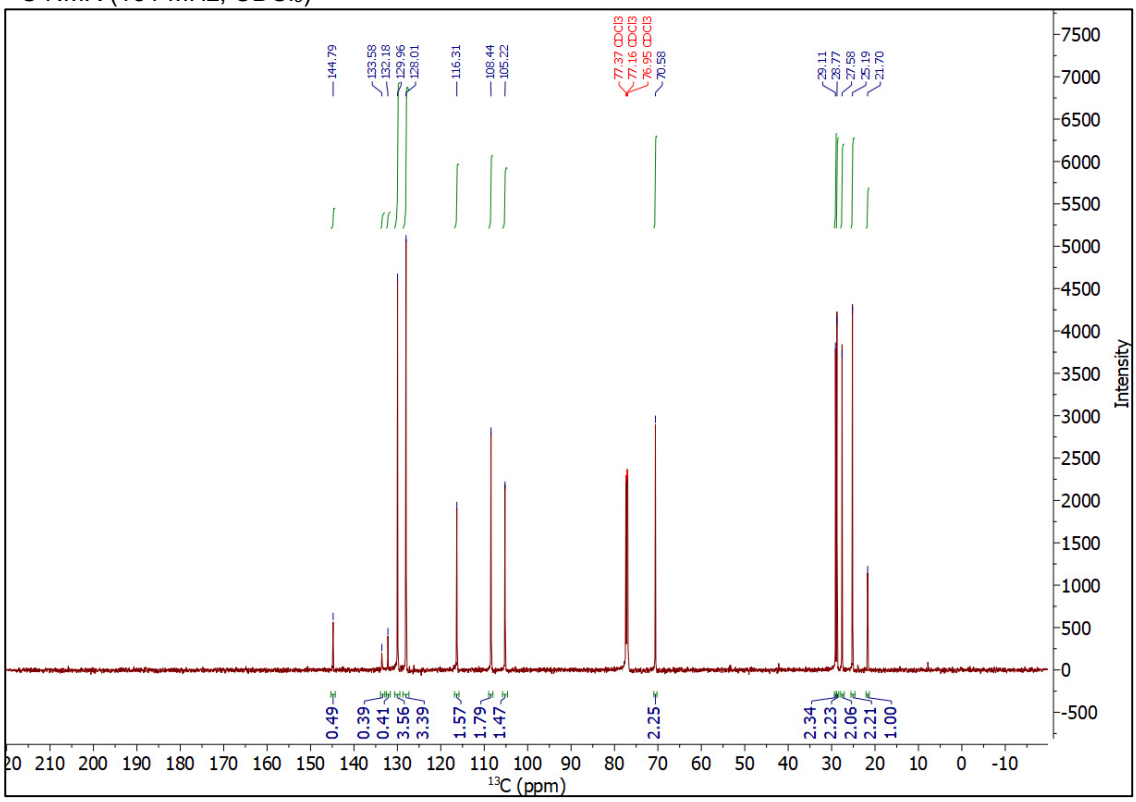


5-(1*H*-Pyrrol-2-yl)pentyl 4-methylbenzenesulfonate (**III-111**)

^{1}H NMR (600 MHz, $CDCl_3$)

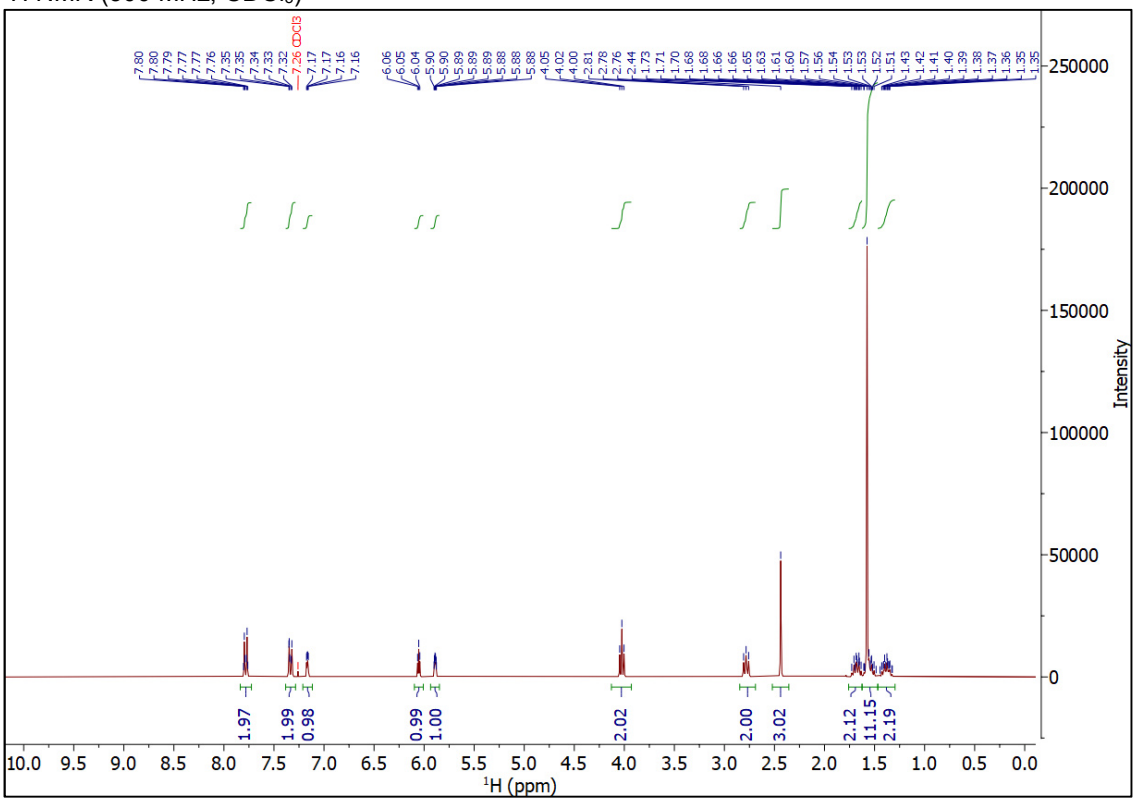


^{13}C NMR (151 MHz, $CDCl_3$)

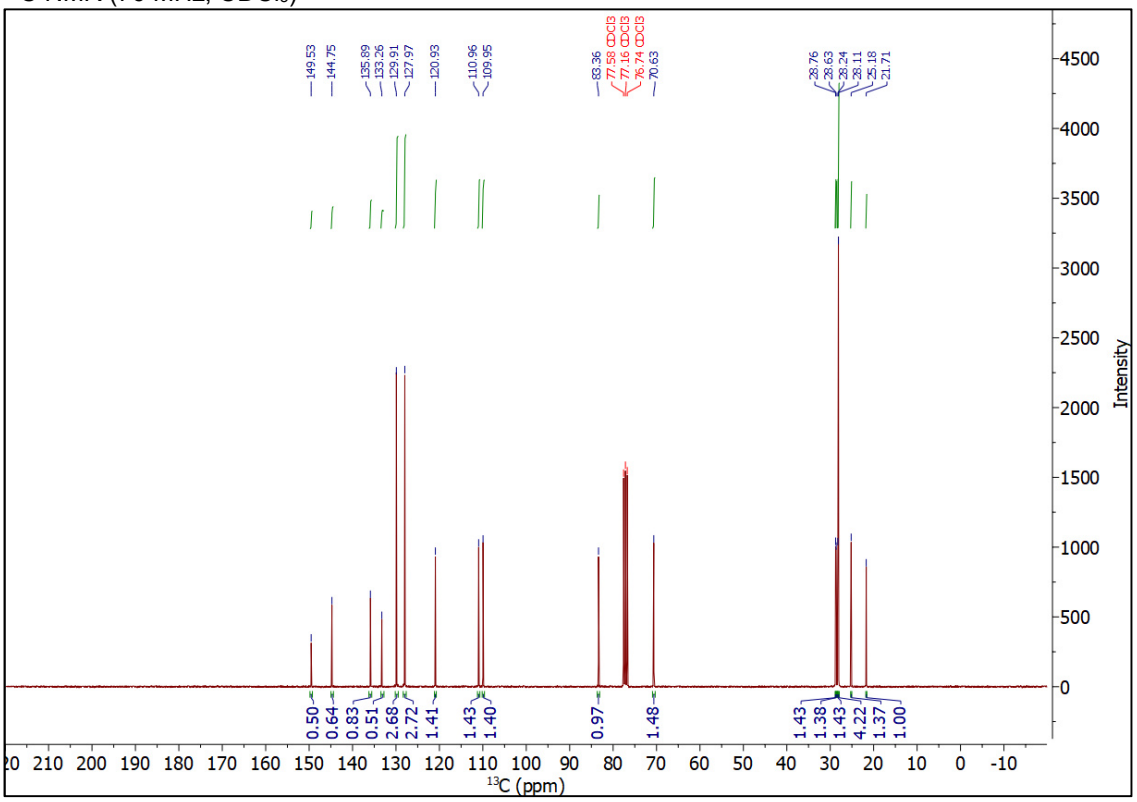


tert-Butyl 2-(5-(tosyloxy)pentyl)-1*H*-pyrrole-1-carboxylate (**III-112**)

^{1}H NMR (300 MHz, $CDCl_3$)

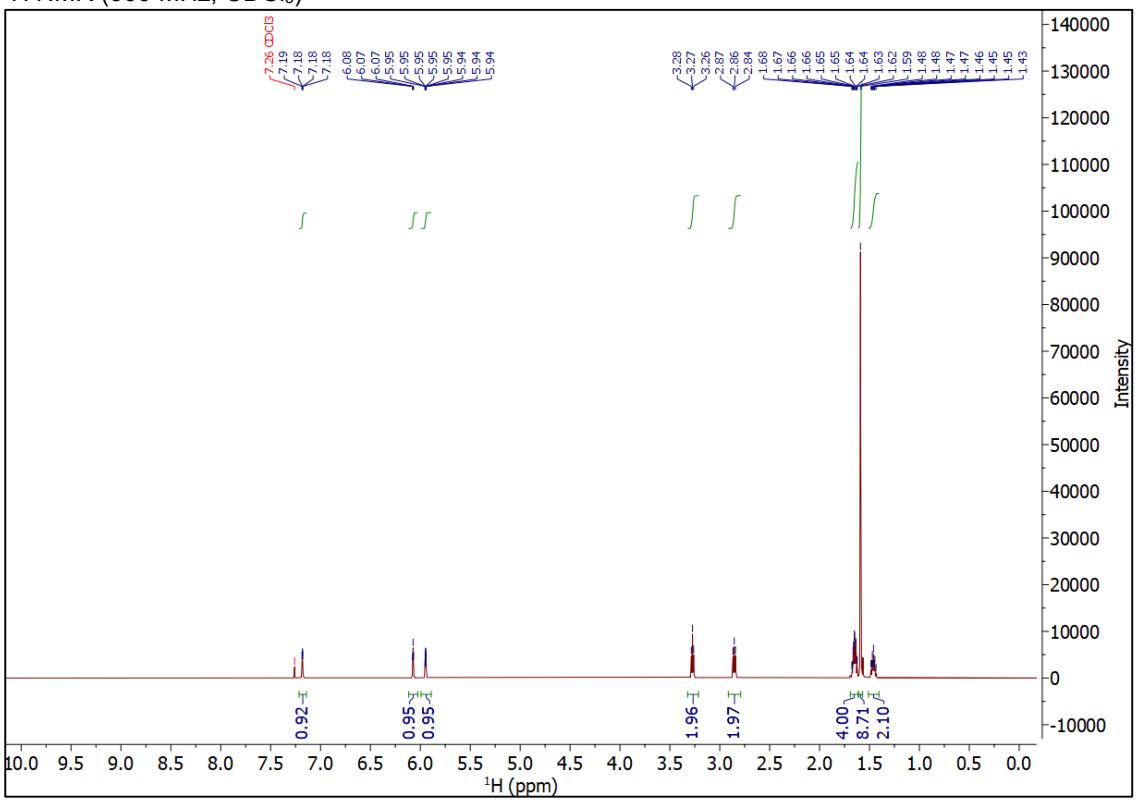


^{13}C NMR (76 MHz, $CDCl_3$)

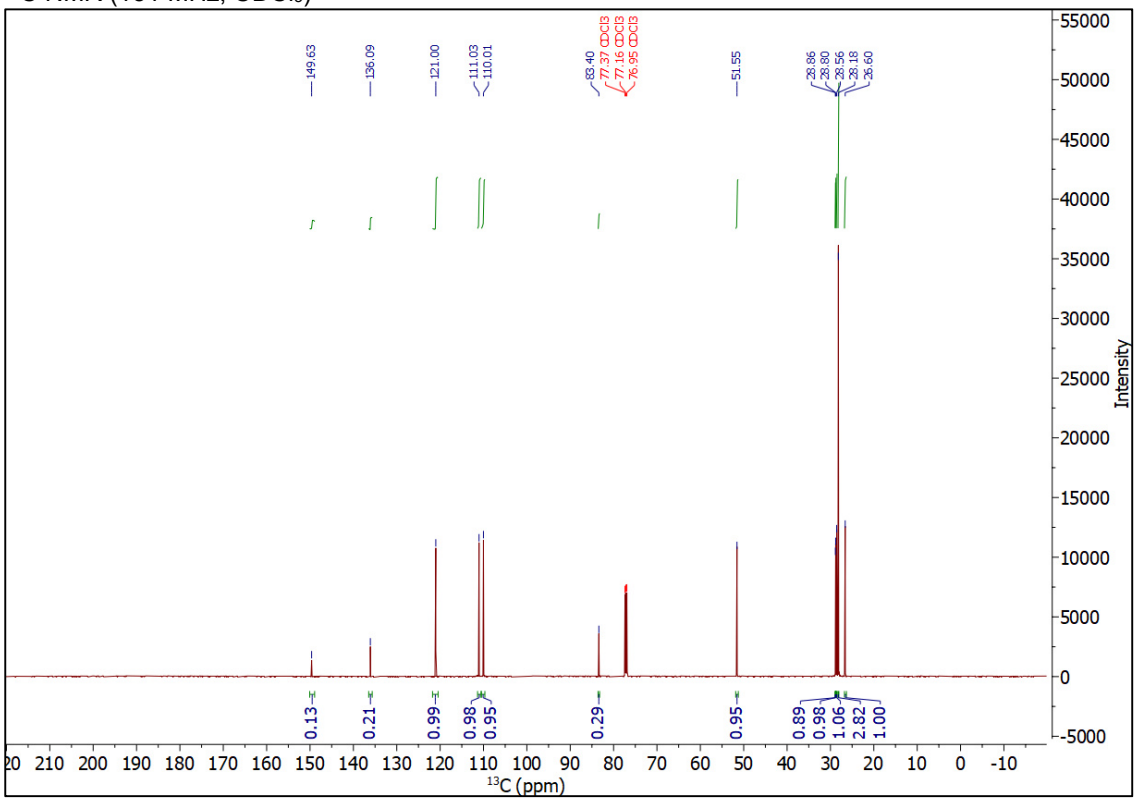


tert-Butyl 2-(5-azidopentyl)-1*H*-pyrrole-1-carboxylate (**III-113**)

^{1}H NMR (600 MHz, $CDCl_3$)

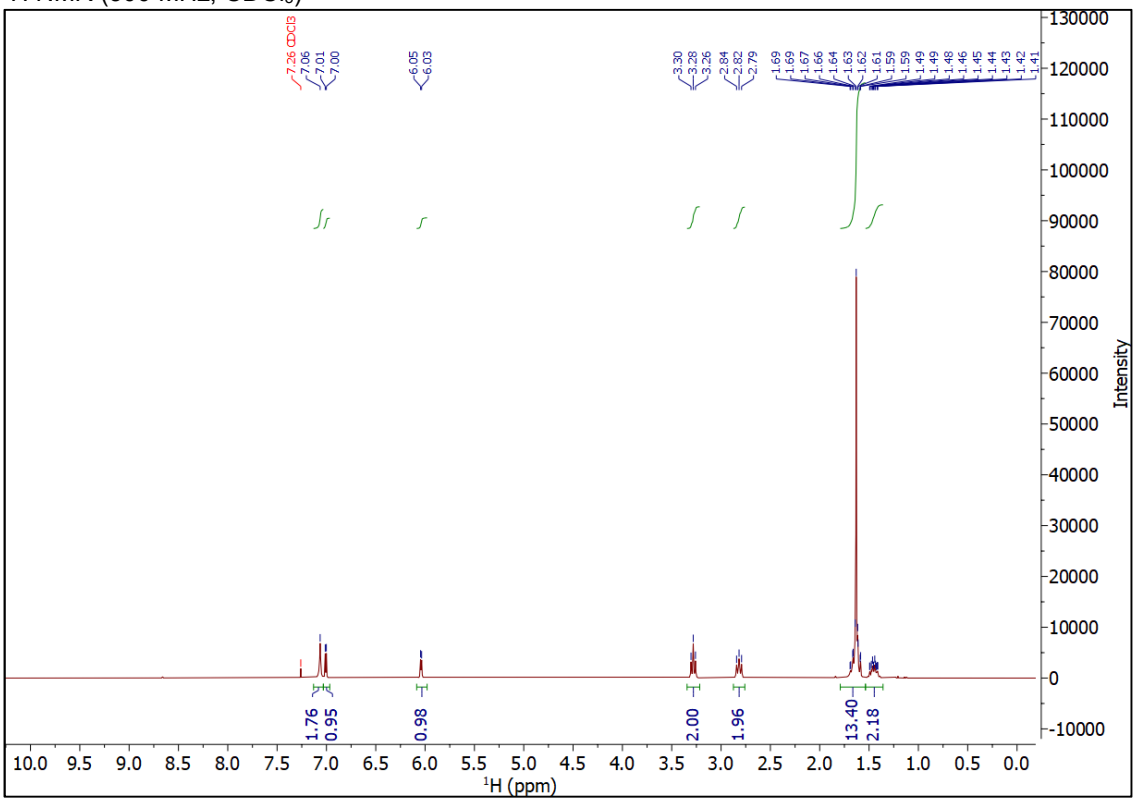


^{13}C NMR (151 MHz, $CDCl_3$)

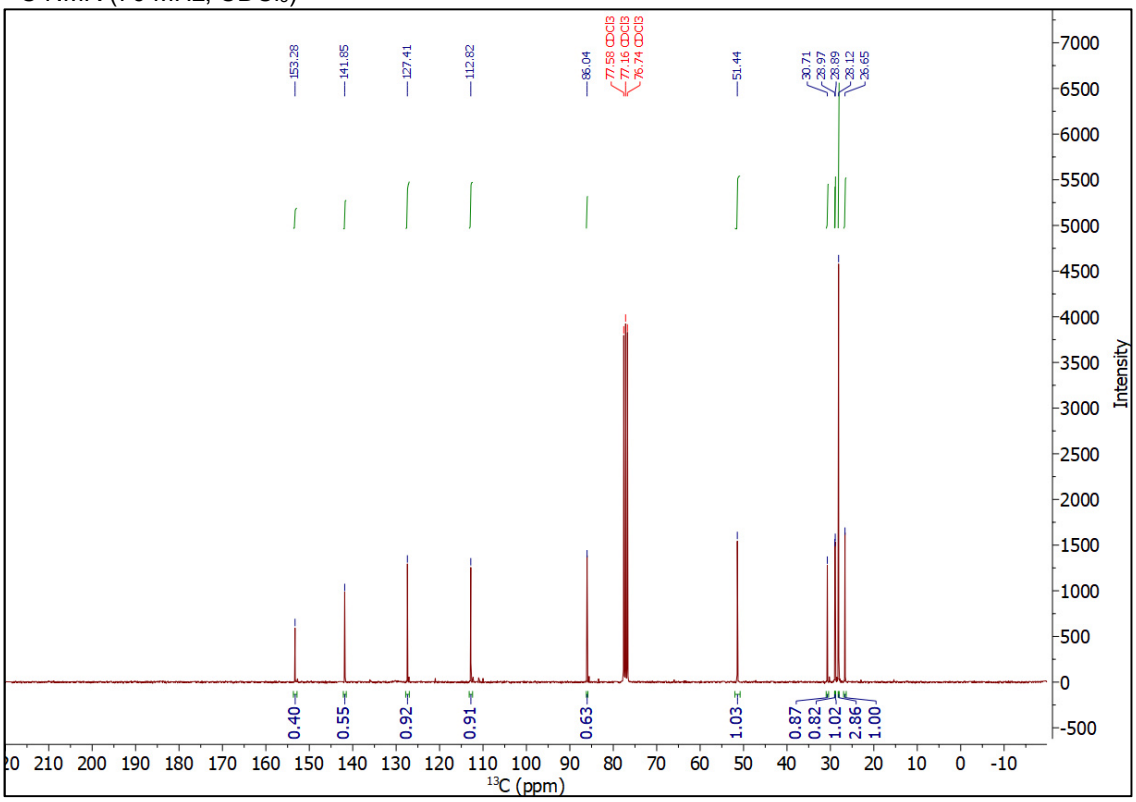


(5-(5-Azidopentyl)-1-(*tert*-butoxycarbonyl)-1*H*-pyrrol-2-yl)boronic acid (**III-114**)

^{1}H NMR (300 MHz, $CDCl_3$)

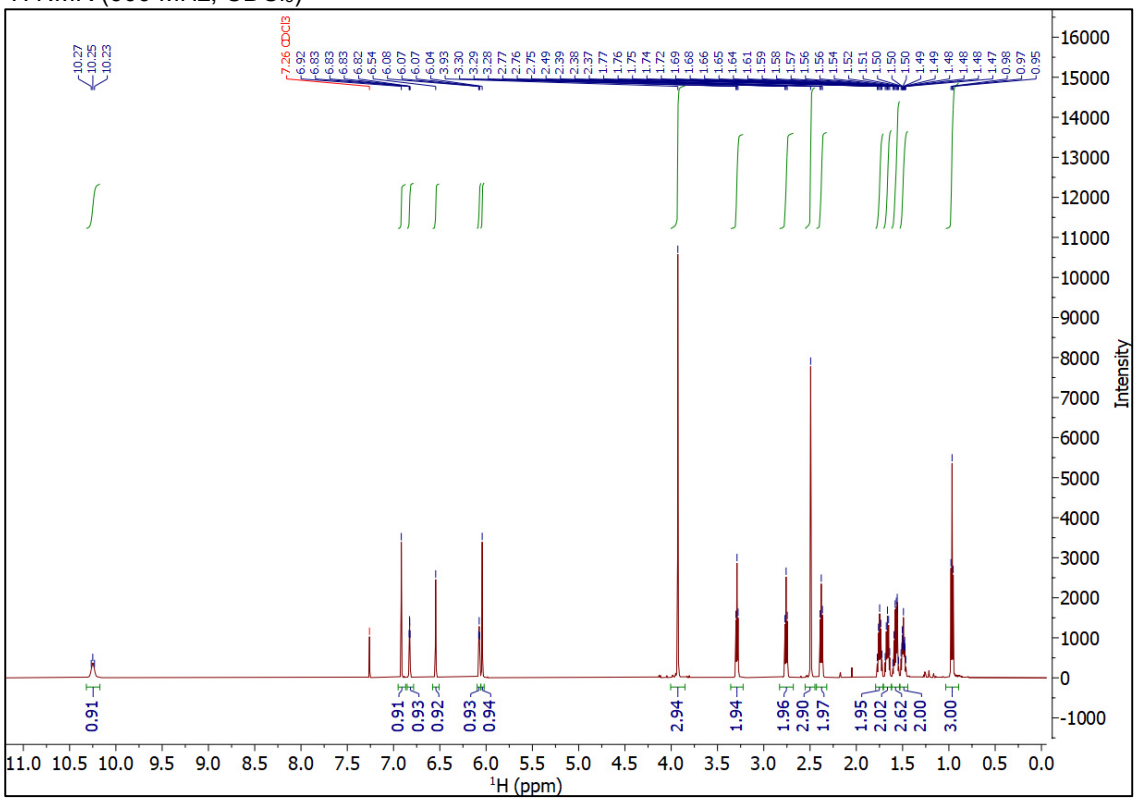


^{13}C NMR (76 MHz, $CDCl_3$)

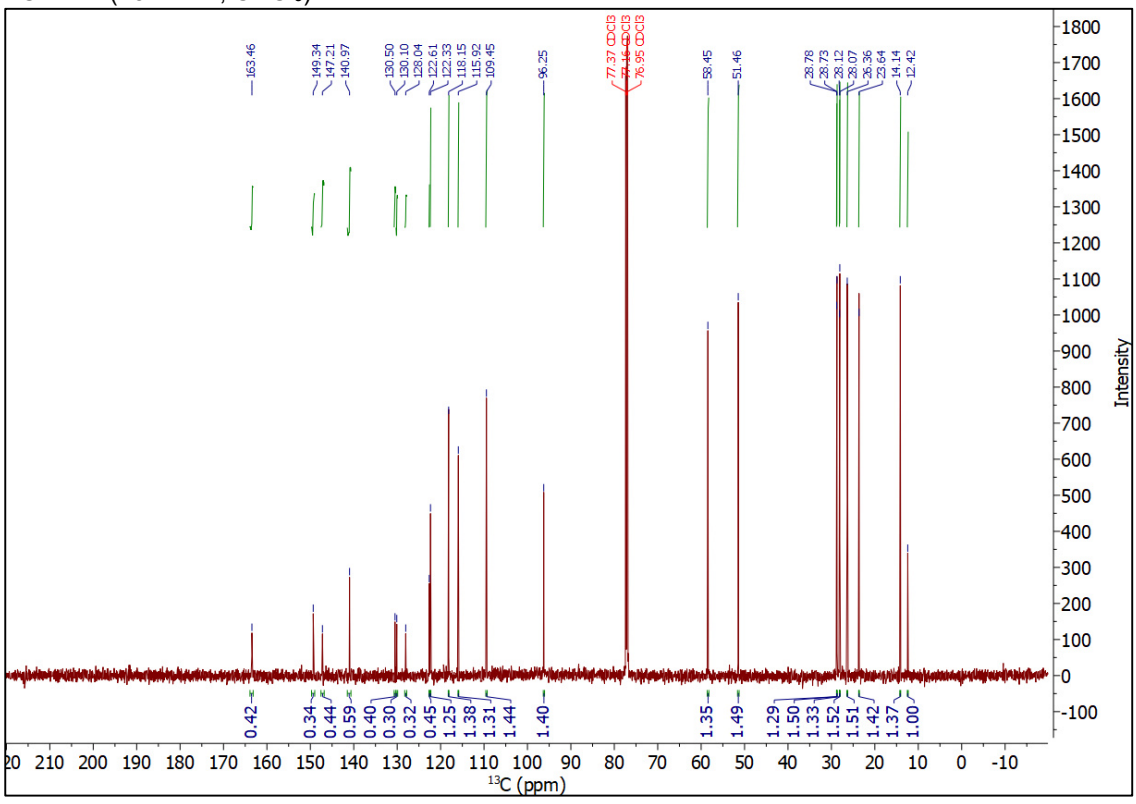


3-(5-(5-Azidopentyl)-1*H*-pyrrol-2-yl)-5,5-difluoro-1-methoxy-7-methyl-8-propyl-5*H*-5λ^4,6λ^4-dipyrrolo[1,2-*c*:2',1'-*f*][1,3,2]diazaborinine (**III-125**)

^{1}H NMR (600 MHz, $CDCl_3$)

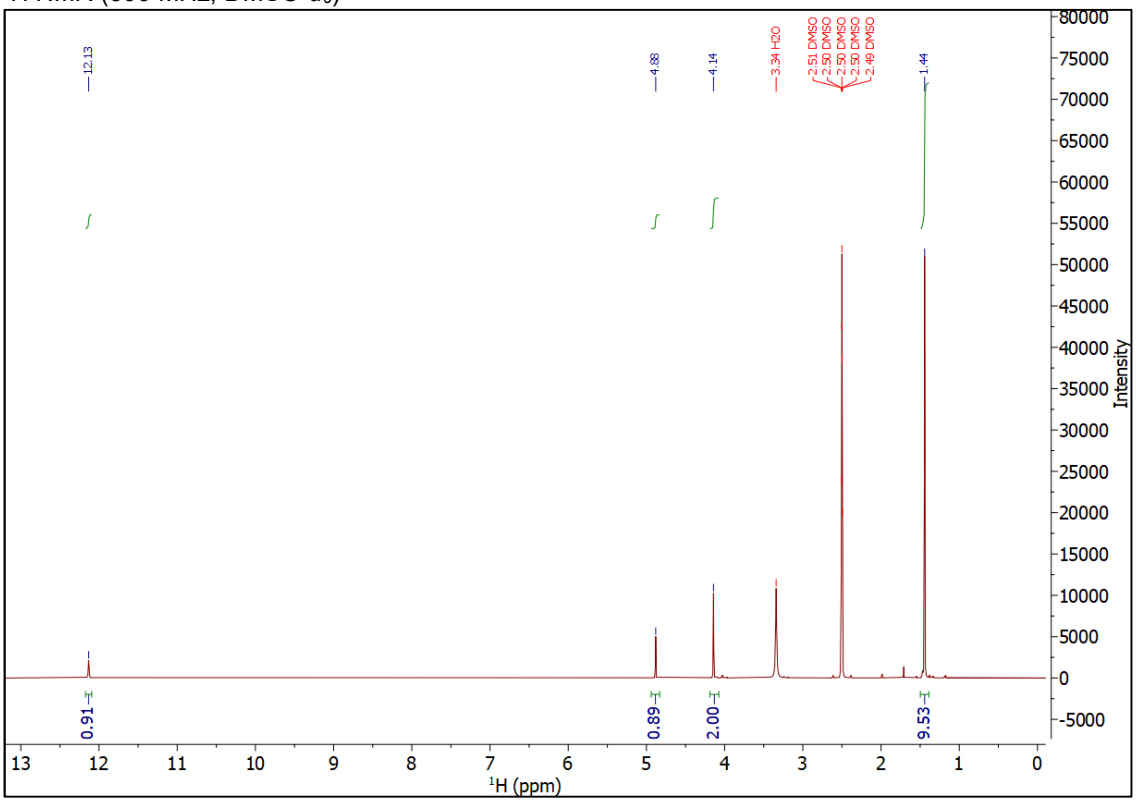


^{13}C NMR (151 MHz, $CDCl_3$)

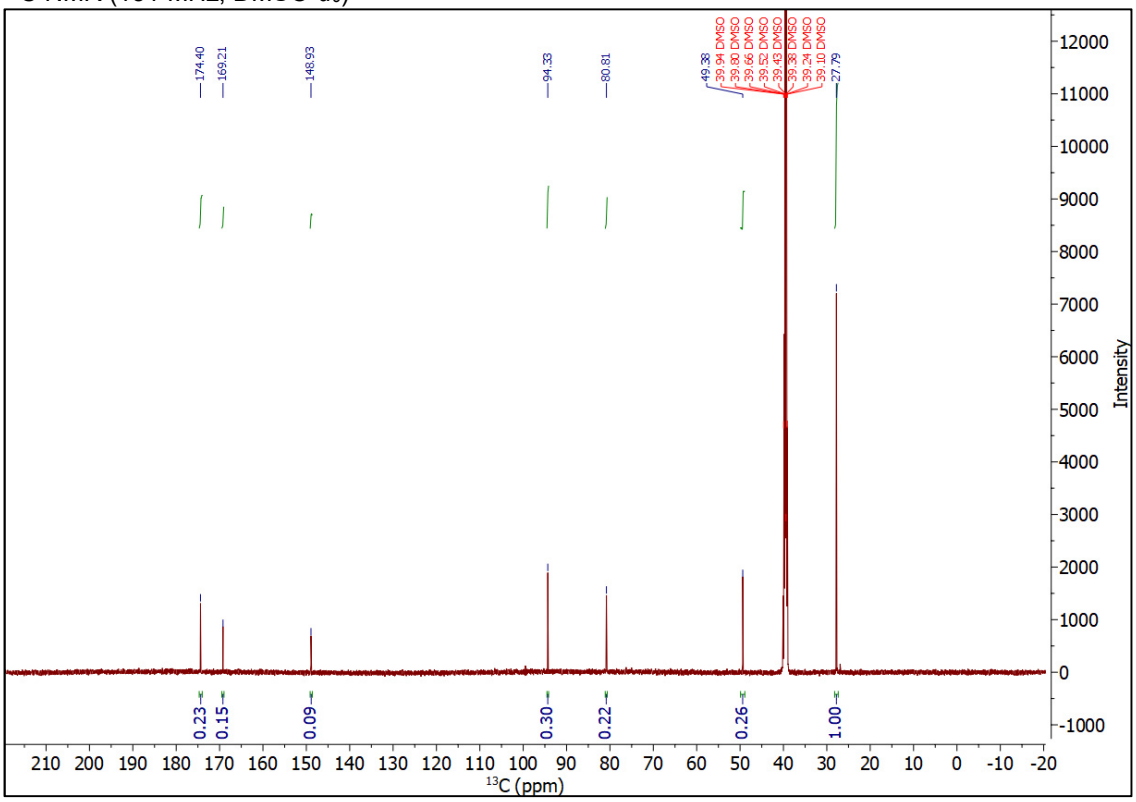


tert-Butyl 4-hydroxy-2-oxo-2,5-dihydro-1*H*-pyrrole-1-carboxylate (**III-126**)

^{1}H NMR (600 MHz, DMSO-d_6)

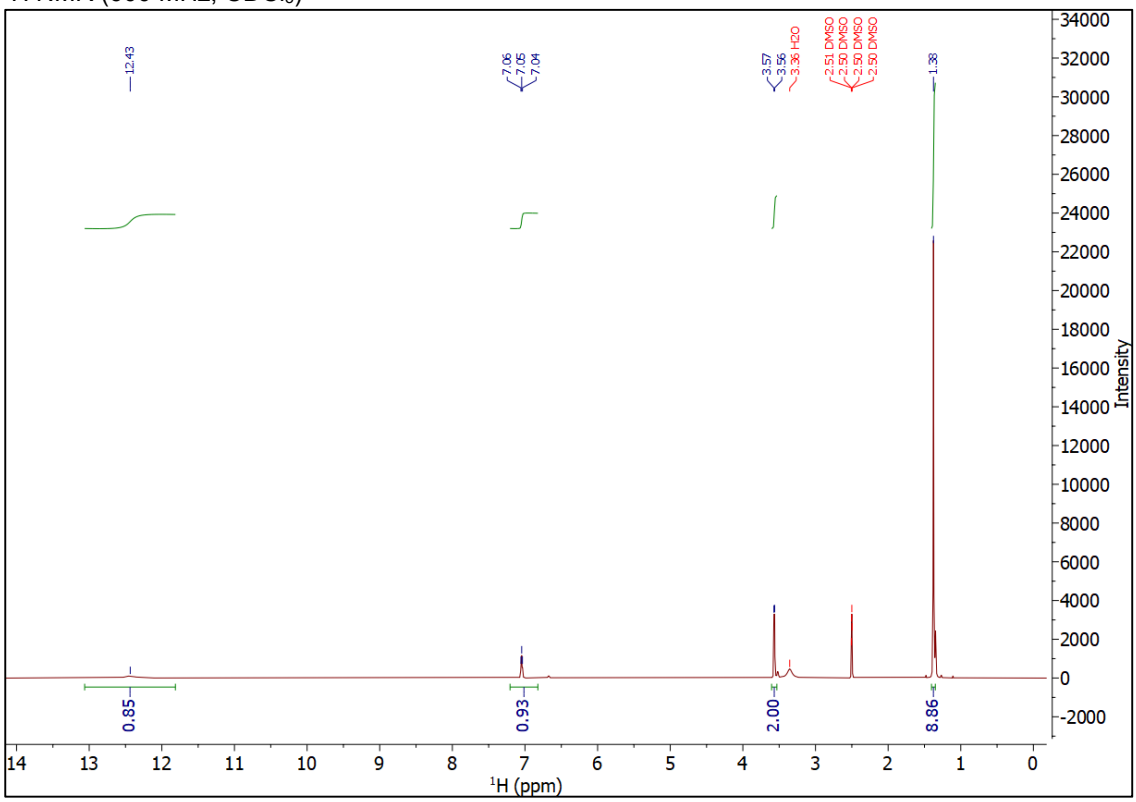


^{13}C NMR (151 MHz, DMSO-d_6)

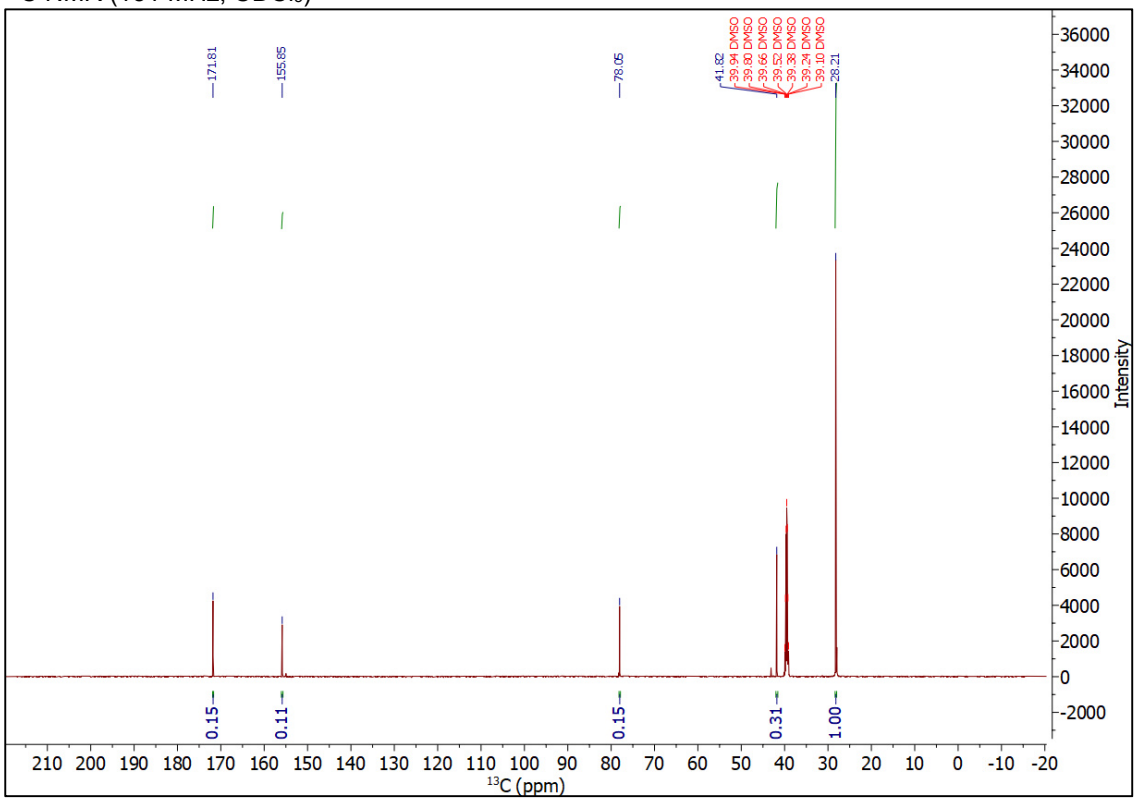


N-Boc-Glycine (**III-128**)

^{1}H NMR (600 MHz, $CDCl_3$)

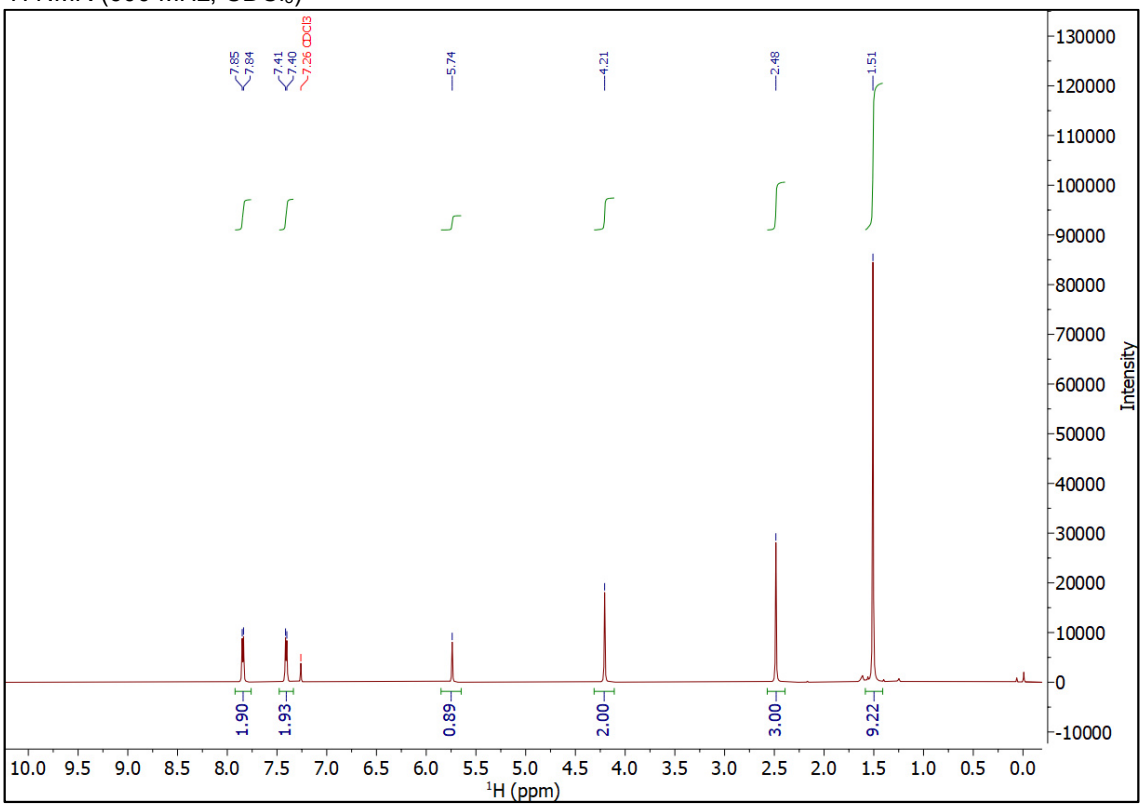


^{13}C NMR (151 MHz, $CDCl_3$)

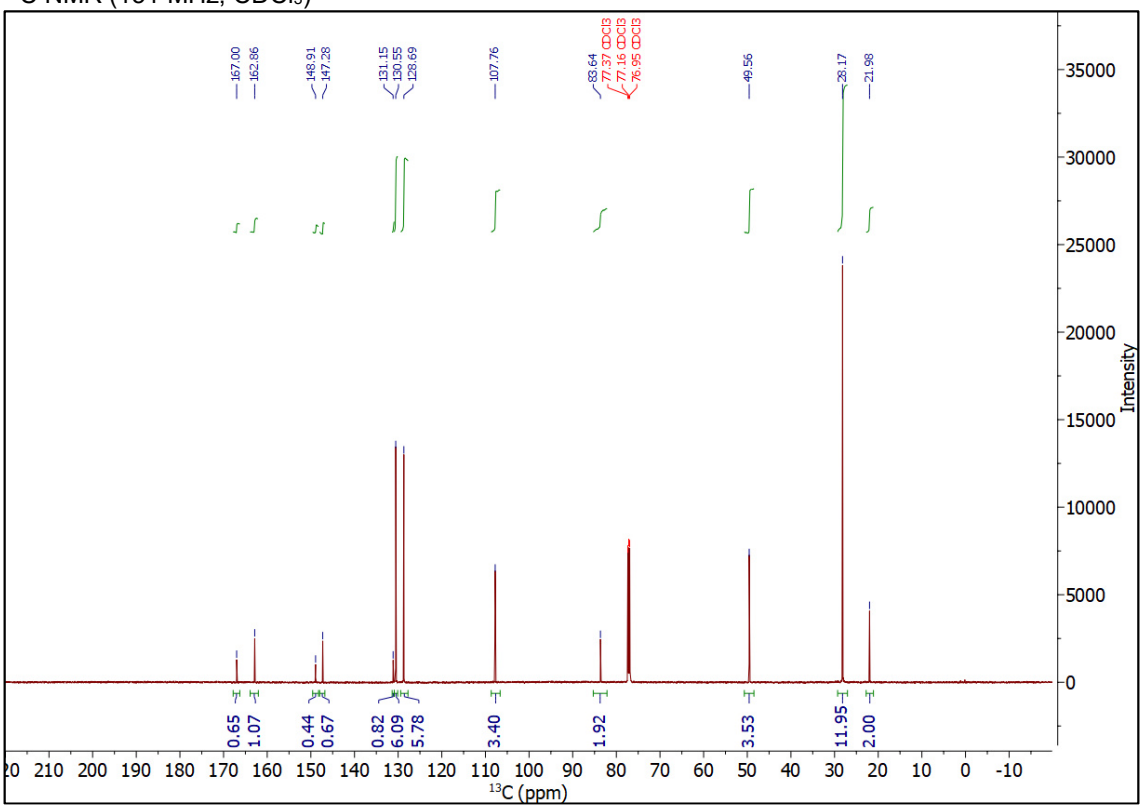


tert-Butyl 2-oxo-4-(tosyloxy)-2,5-dihydro-1*H*-pyrrole-1-carboxylate (**III-130**)

^{1}H NMR (600 MHz, $CDCl_3$)

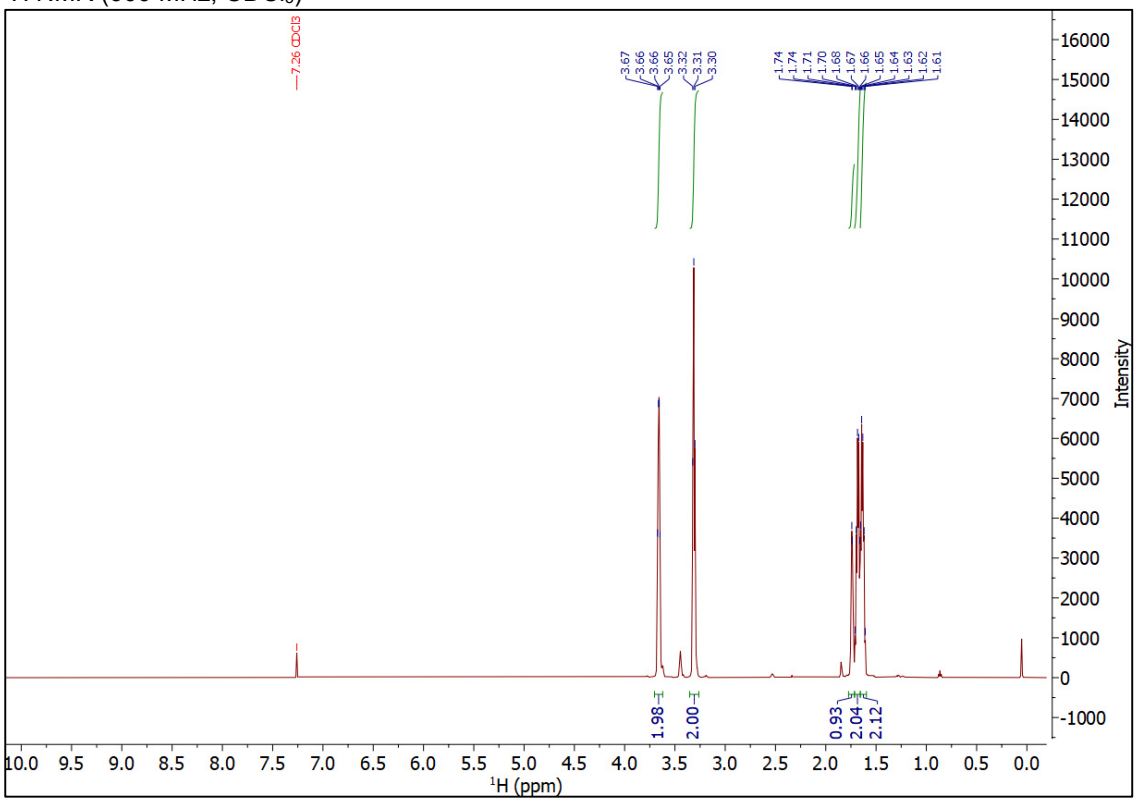


^{13}C NMR (151 MHz, $CDCl_3$)

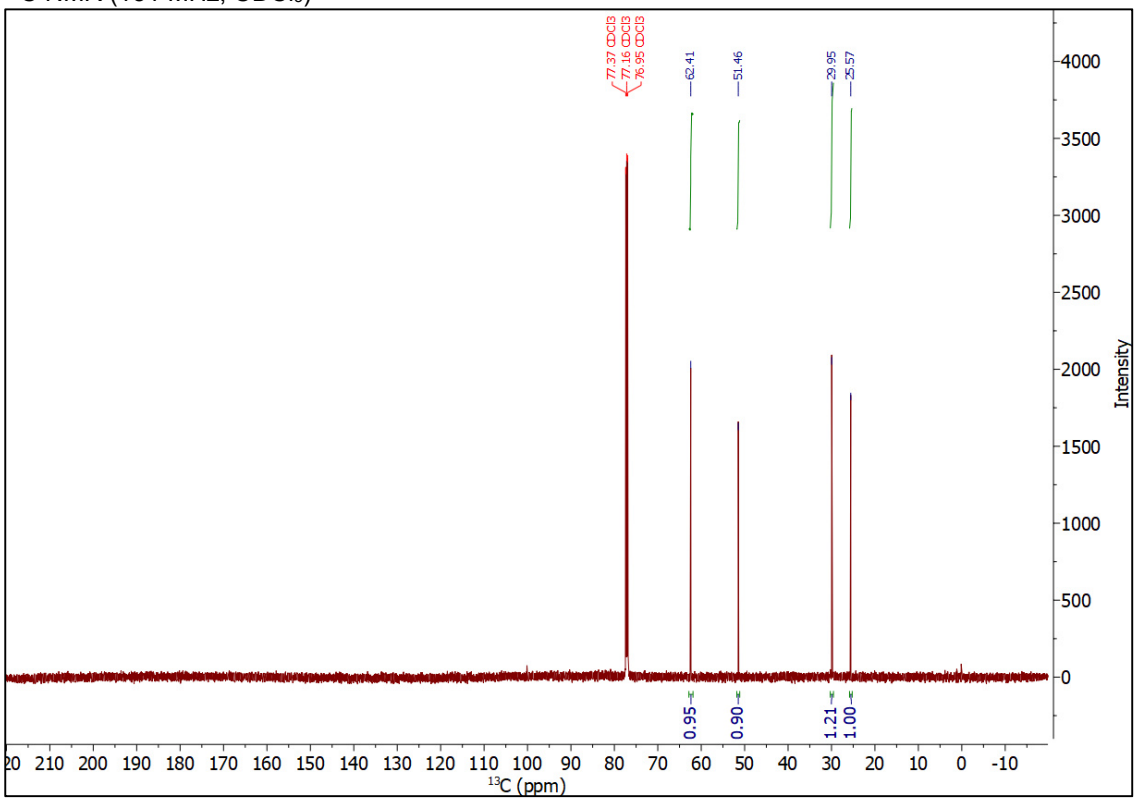


4-Azidobutan-1-ol (**III-132**)

^{1}H NMR (600 MHz, $CDCl_3$)

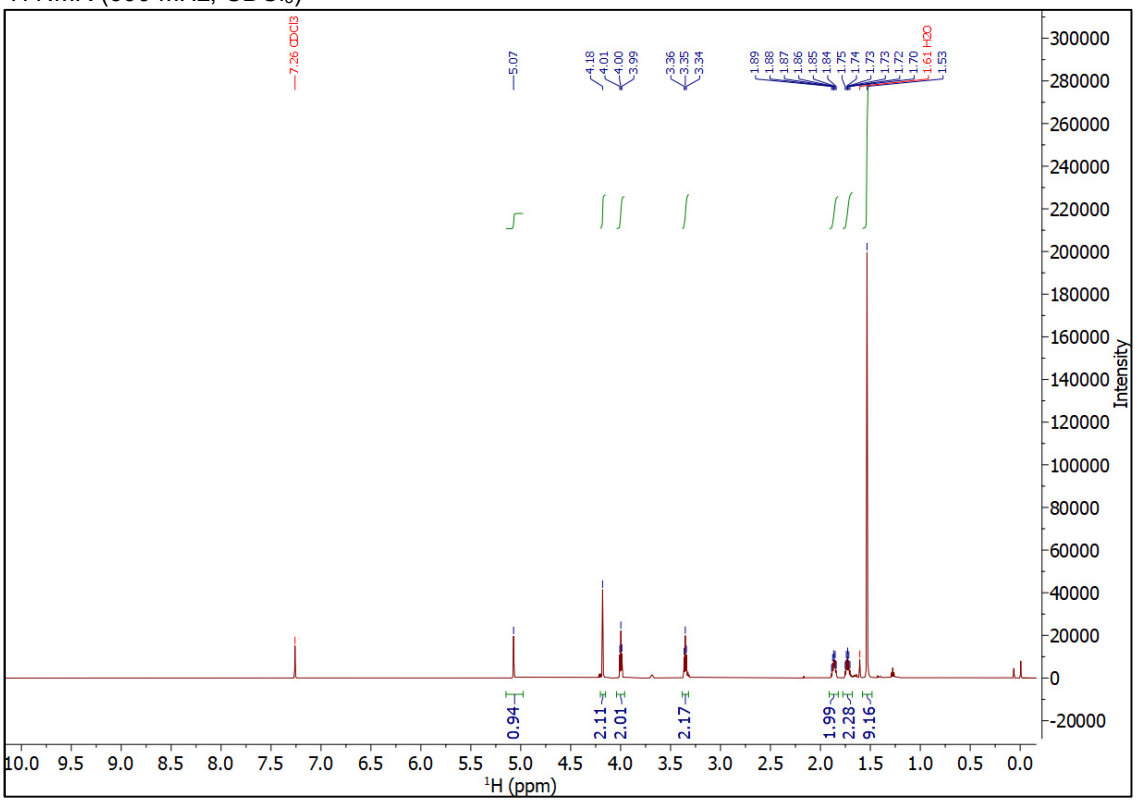


^{13}C NMR (151 MHz, $CDCl_3$)

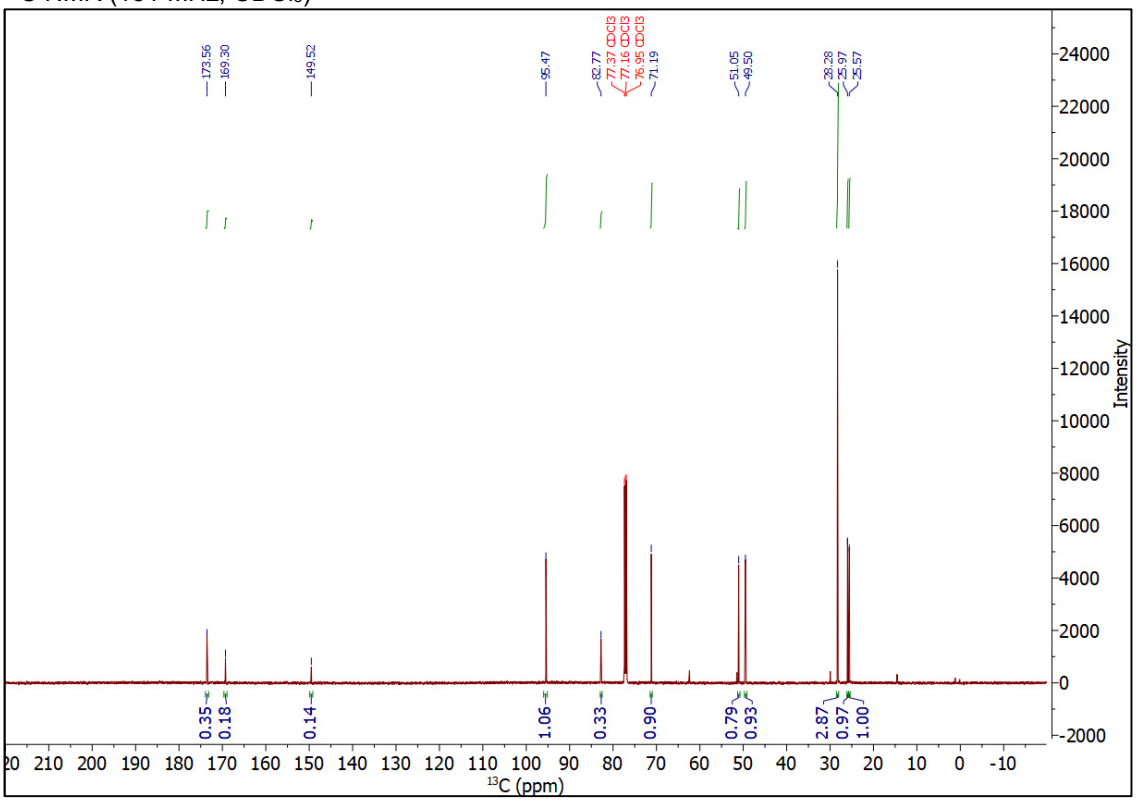


tert-Butyl 4-(4-azidobutoxy)-2-oxo-2,5-dihydro-1*H*-pyrrole-1-carboxylate (**III-134**)

^{1}H NMR (600 MHz, $CDCl_3$)

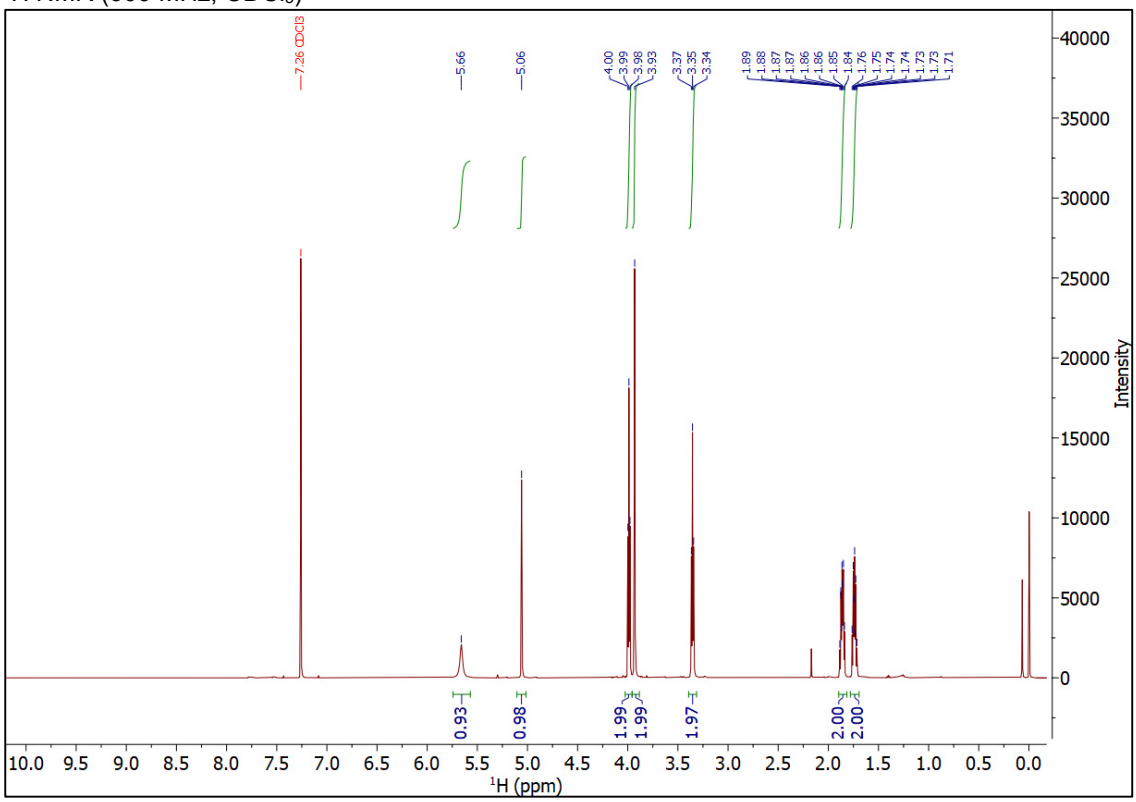


^{13}C NMR (151 MHz, $CDCl_3$)

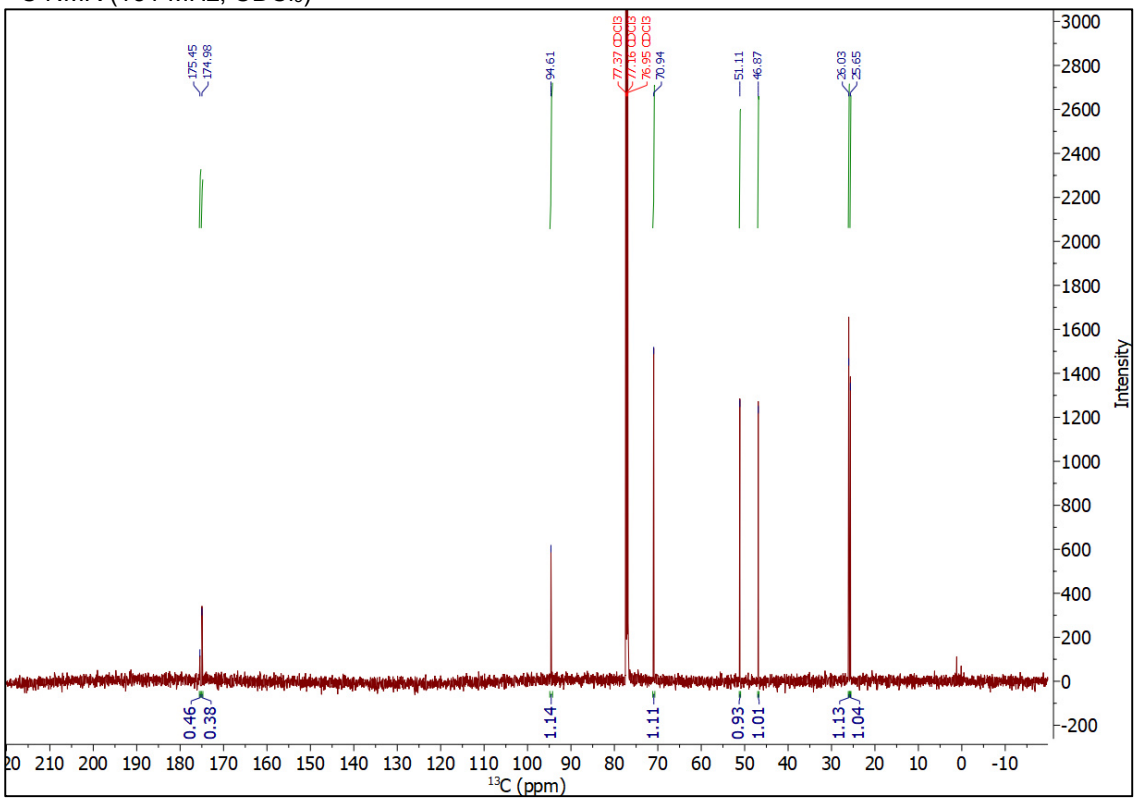


4-(4-Azidobutoxy)-1,5-dihydro-2*H*-pyrrol-2-one (**III-135**)

^{1}H NMR (600 MHz, $CDCl_3$)

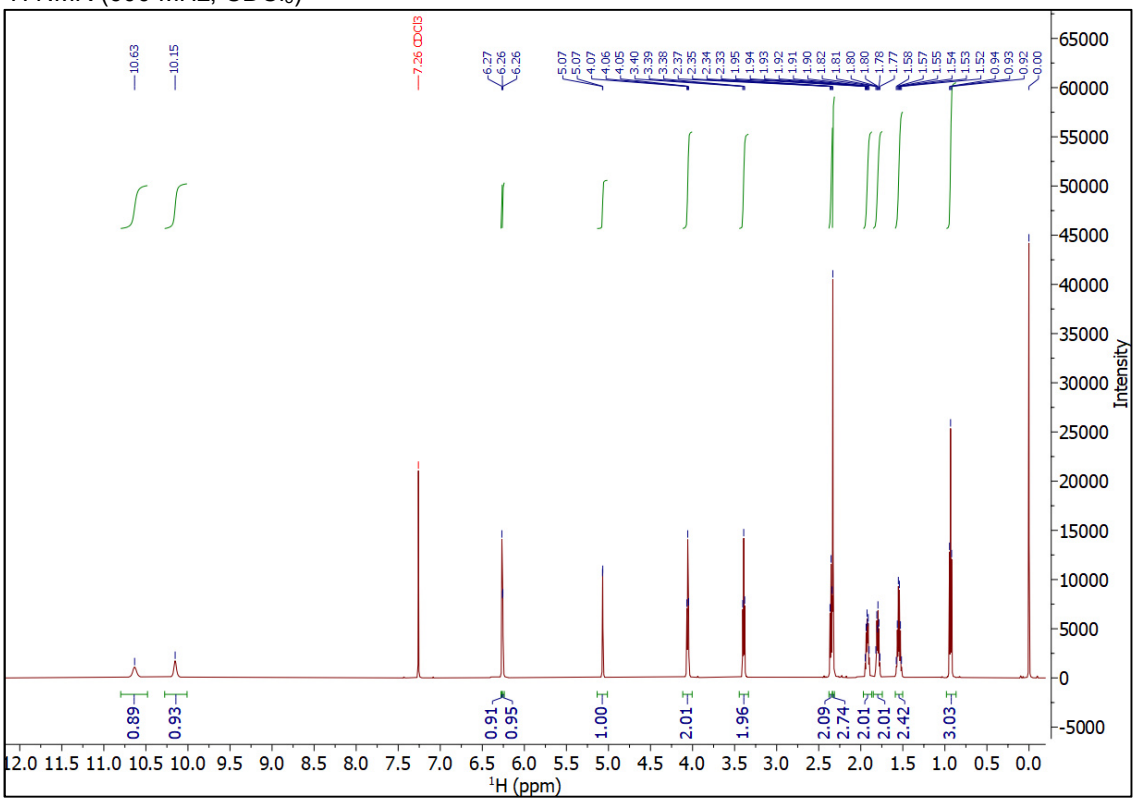


^{13}C NMR (151 MHz, $CDCl_3$)

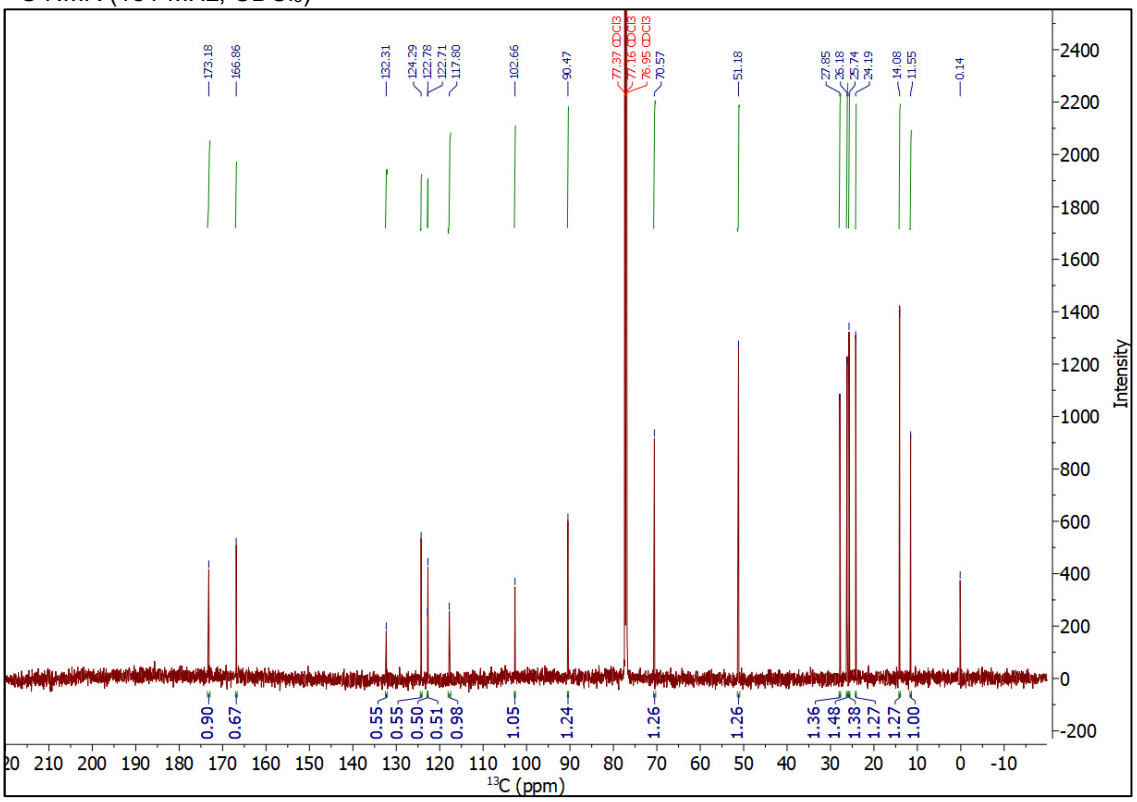


(*Z*)-4-(4-Azidobutoxy)-5-((5-methyl-4-propyl-1*H*-pyrrol-2-yl)methylene)-1,5-dihydro-2*H*-pyrrol-2-one (**III-136**)

^{1}H NMR (600 MHz, $CDCl_3$)

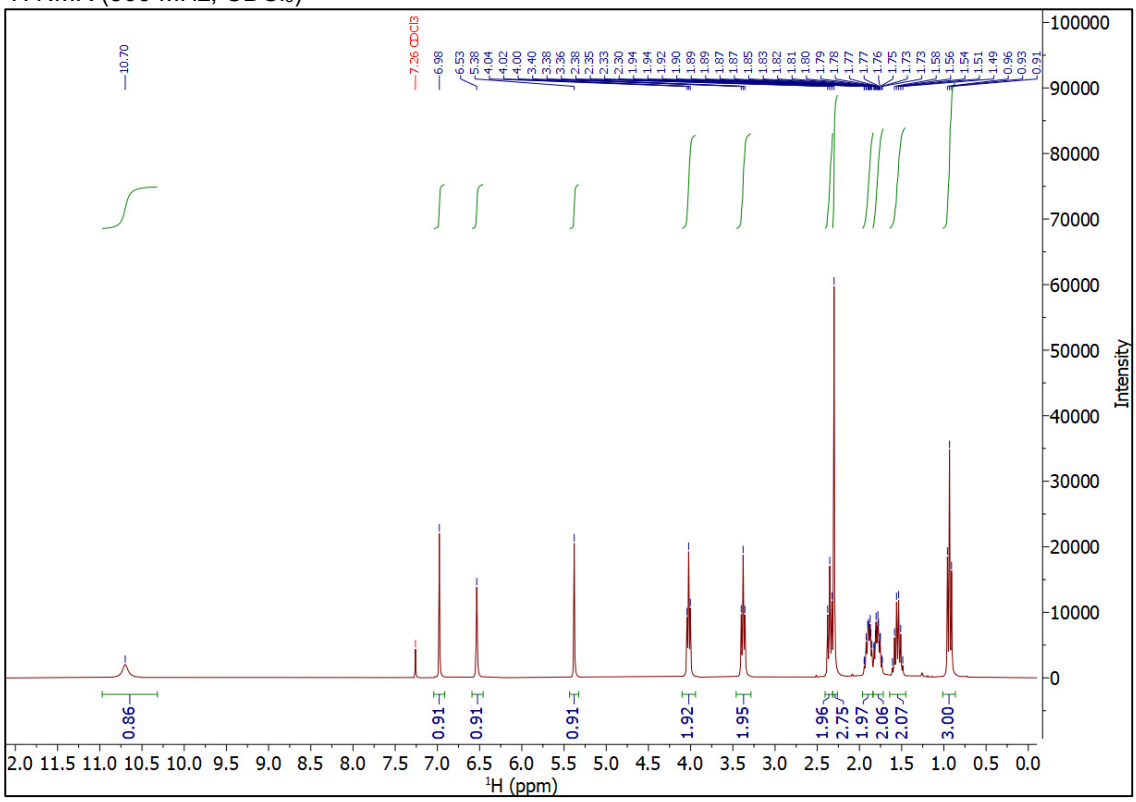


^{13}C NMR (151 MHz, $CDCl_3$)

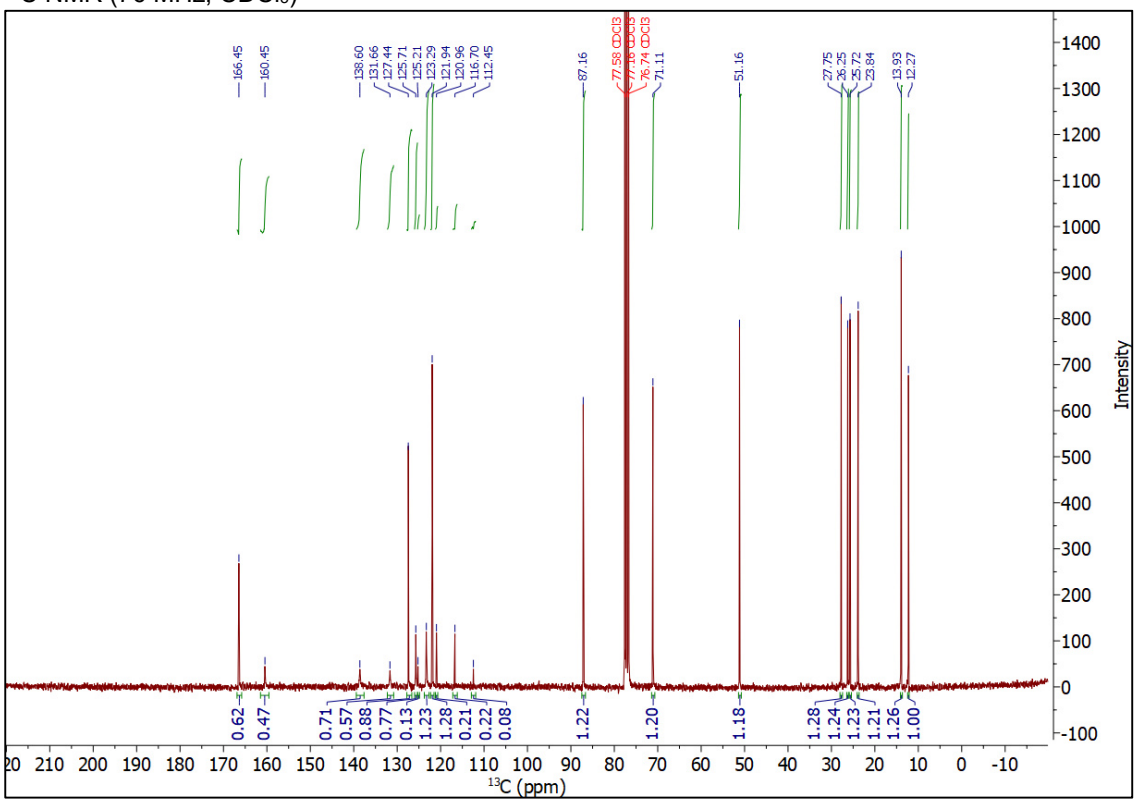


(*Z*)-4-(4-Azidobutoxy)-5-((5-methyl-4-propyl-2*H*-pyrrol-2-ylidene)methyl)-1*H*-pyrrol-2-yl trifluoromethanesulfonate (**III-137**)

^{1}H NMR (300 MHz, $CDCl_3$)

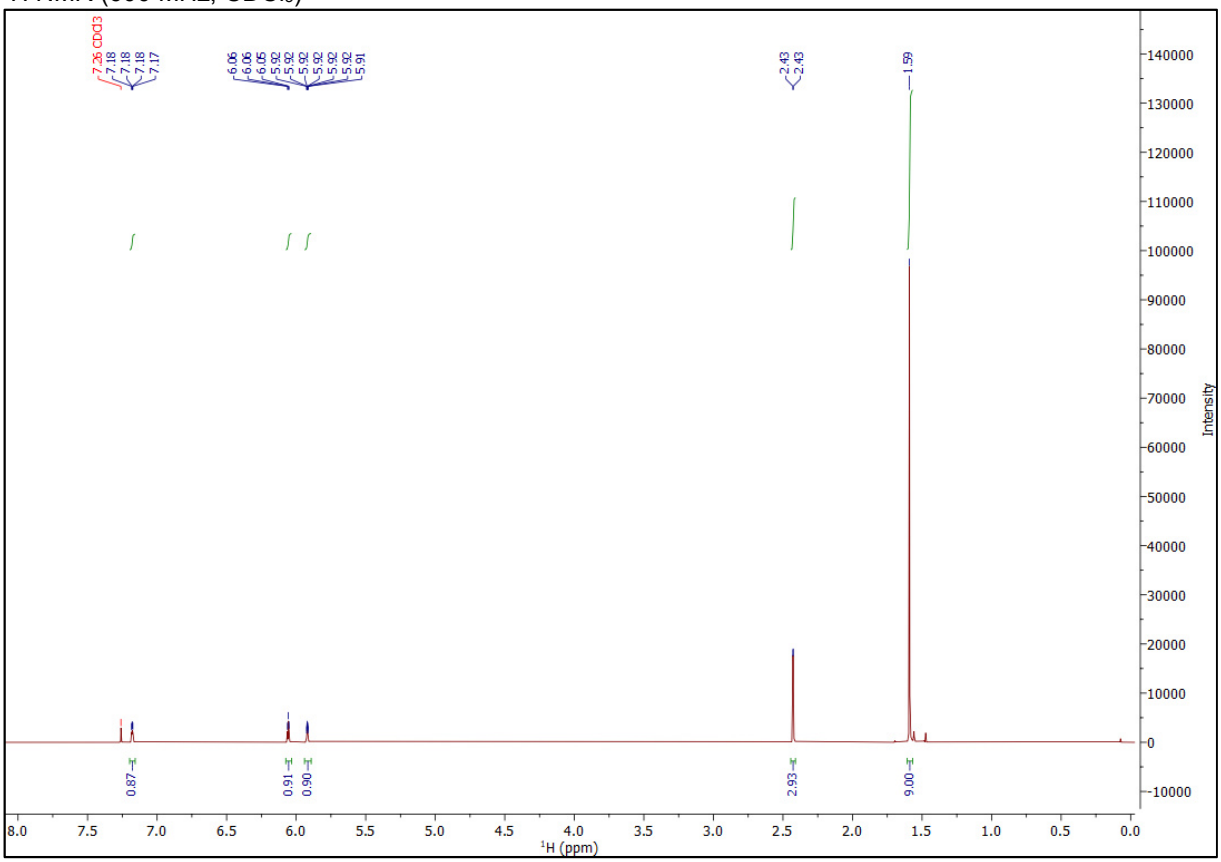


^{13}C NMR (76 MHz, $CDCl_3$)

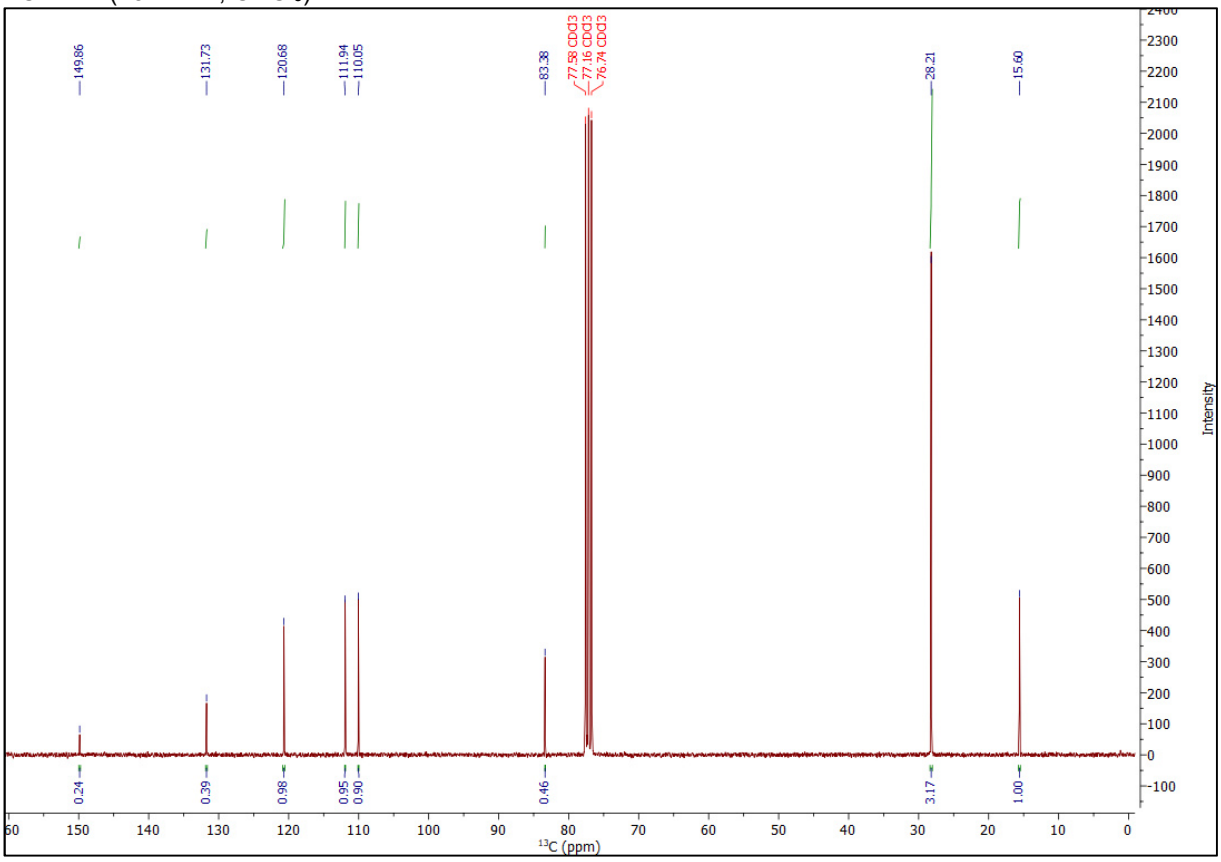


1-*tert*-Butyloxycarbonyl 2-methyl-1*H*-pyrrole (**III-139b**)

^{1}H NMR (600 MHz, $CDCl_3$)

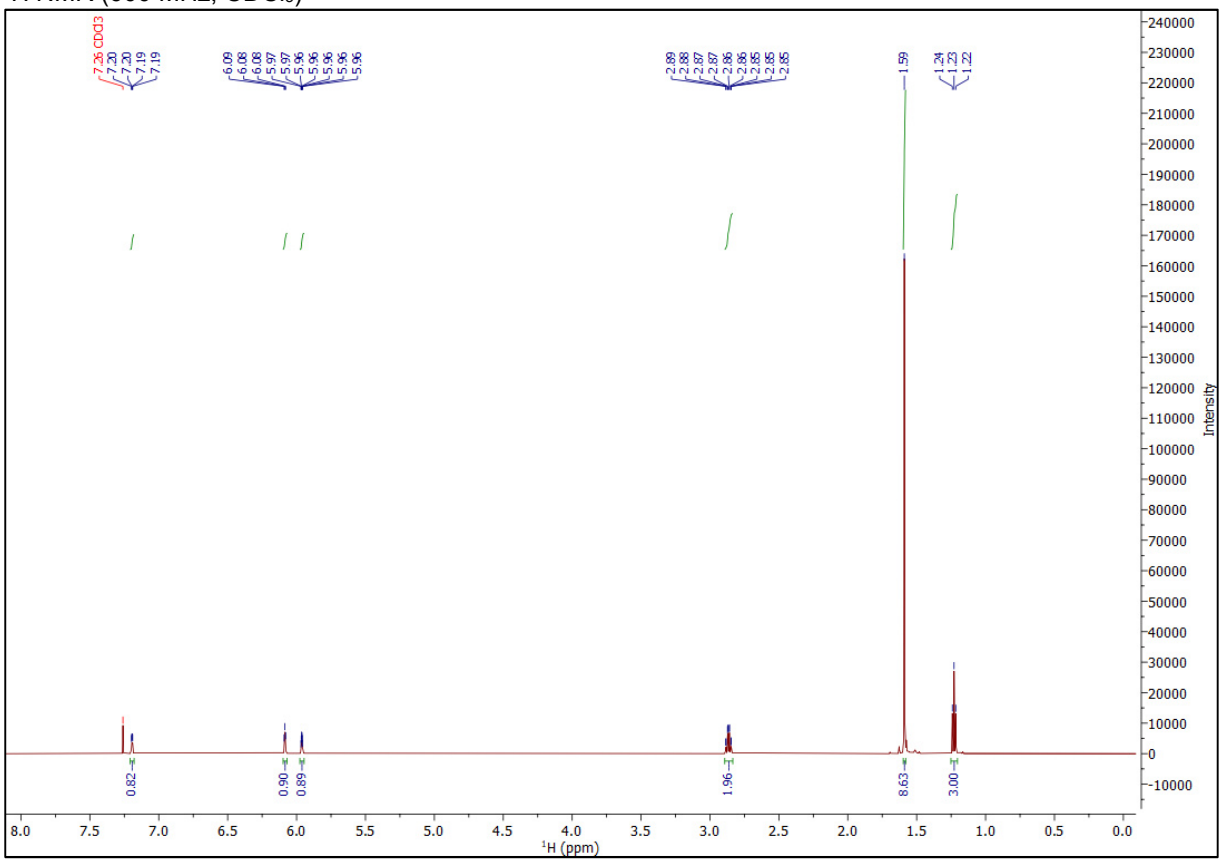


^{13}C NMR (151 MHz, $CDCl_3$)

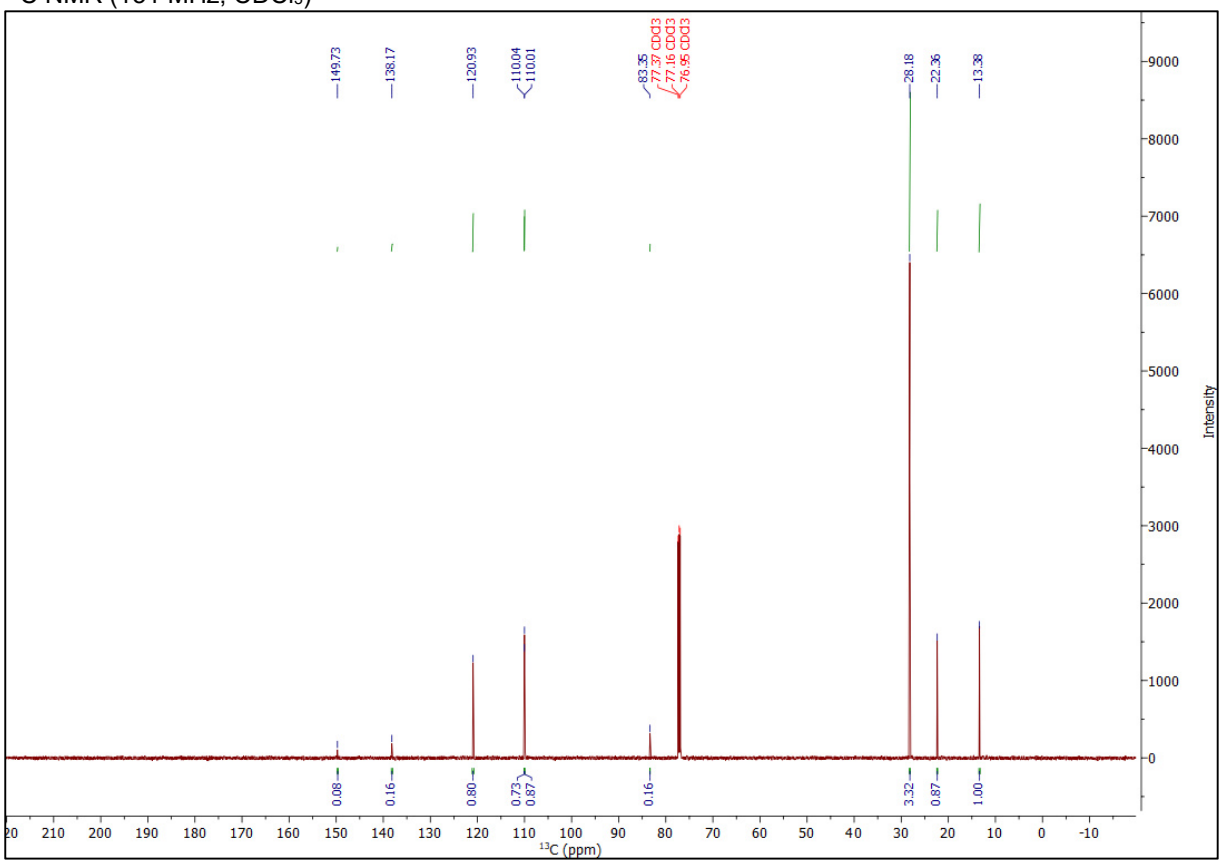


1-*tert*-Butyloxycarbonyl 2-ethyl-1*H*-pyrrole (**III-139c**)

^{1}H NMR (600 MHz, $CDCl_3$)

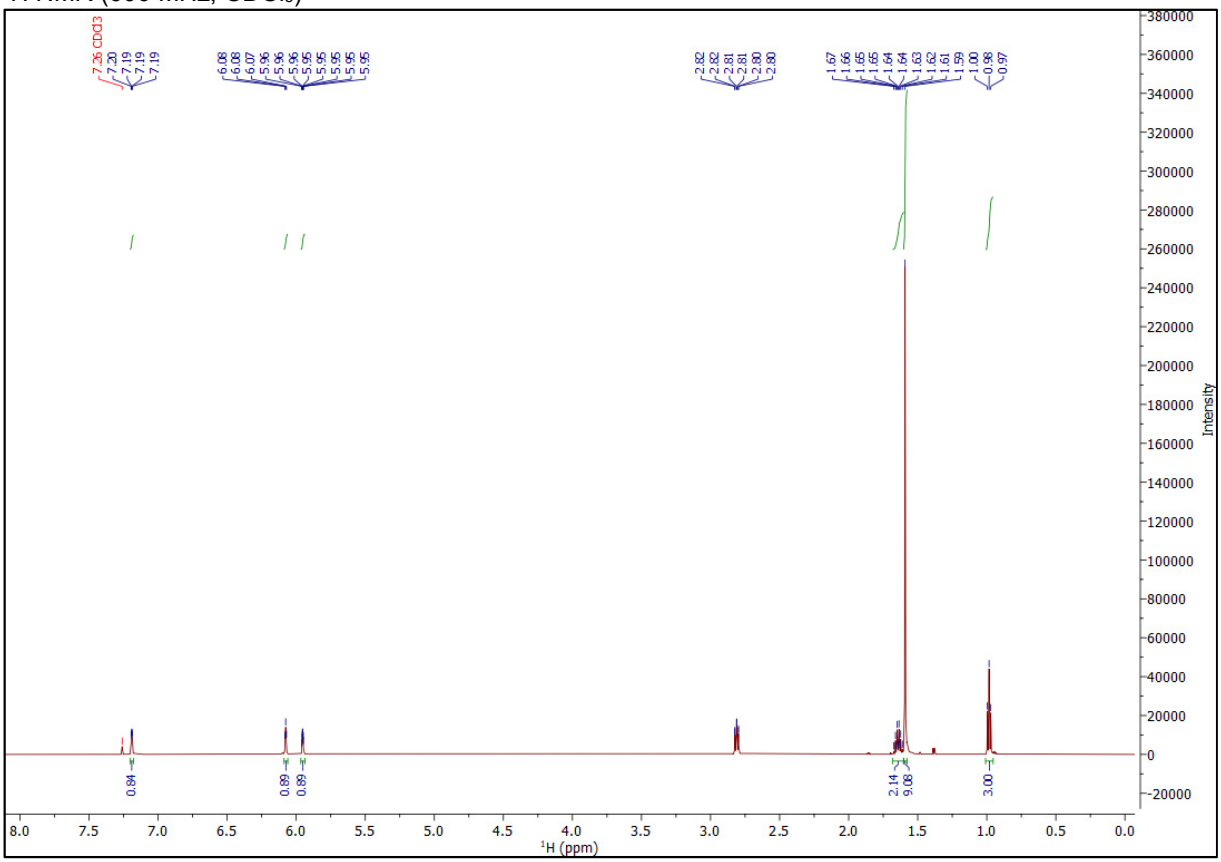


^{13}C NMR (151 MHz, $CDCl_3$)

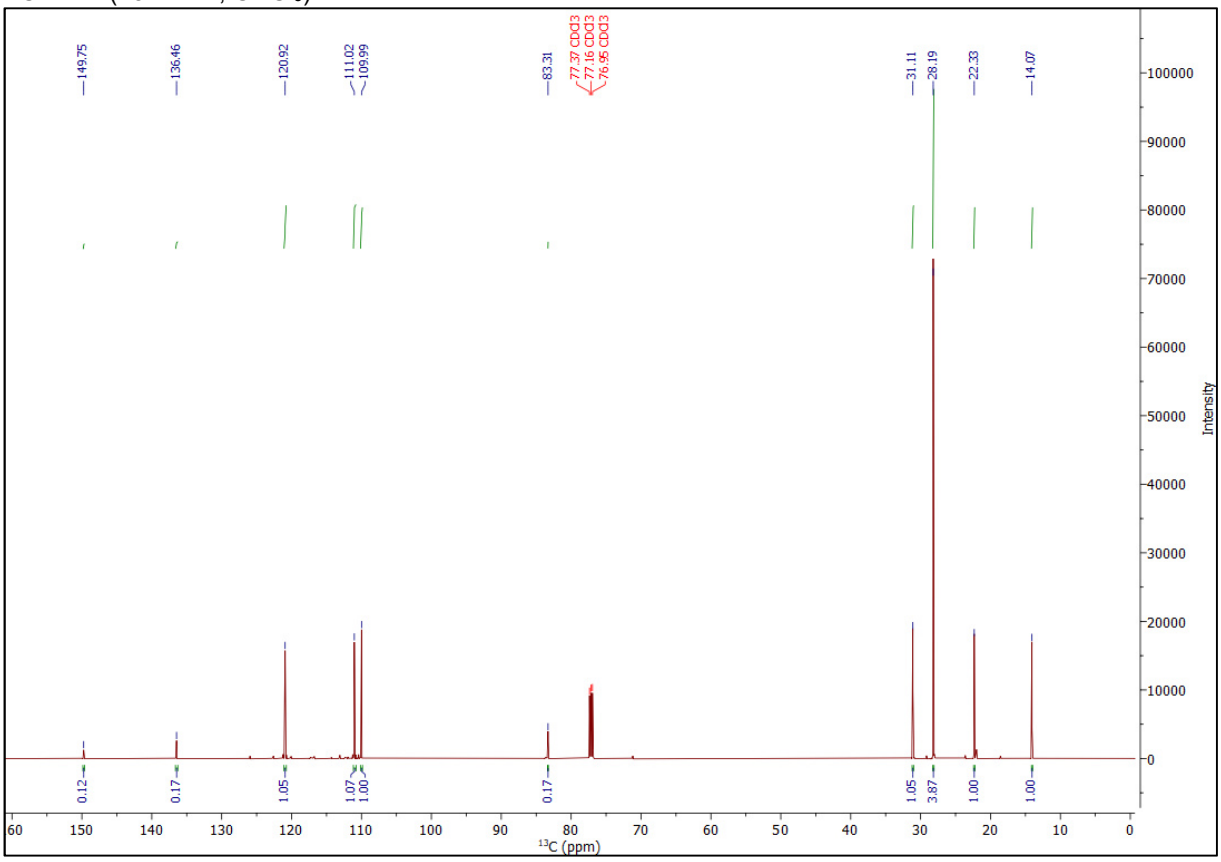


1-*tert*-Butyloxycarbonyl 2-propyl-1*H*-pyrrole (**III-139d**)

^{1}H NMR (600 MHz, $CDCl_3$)

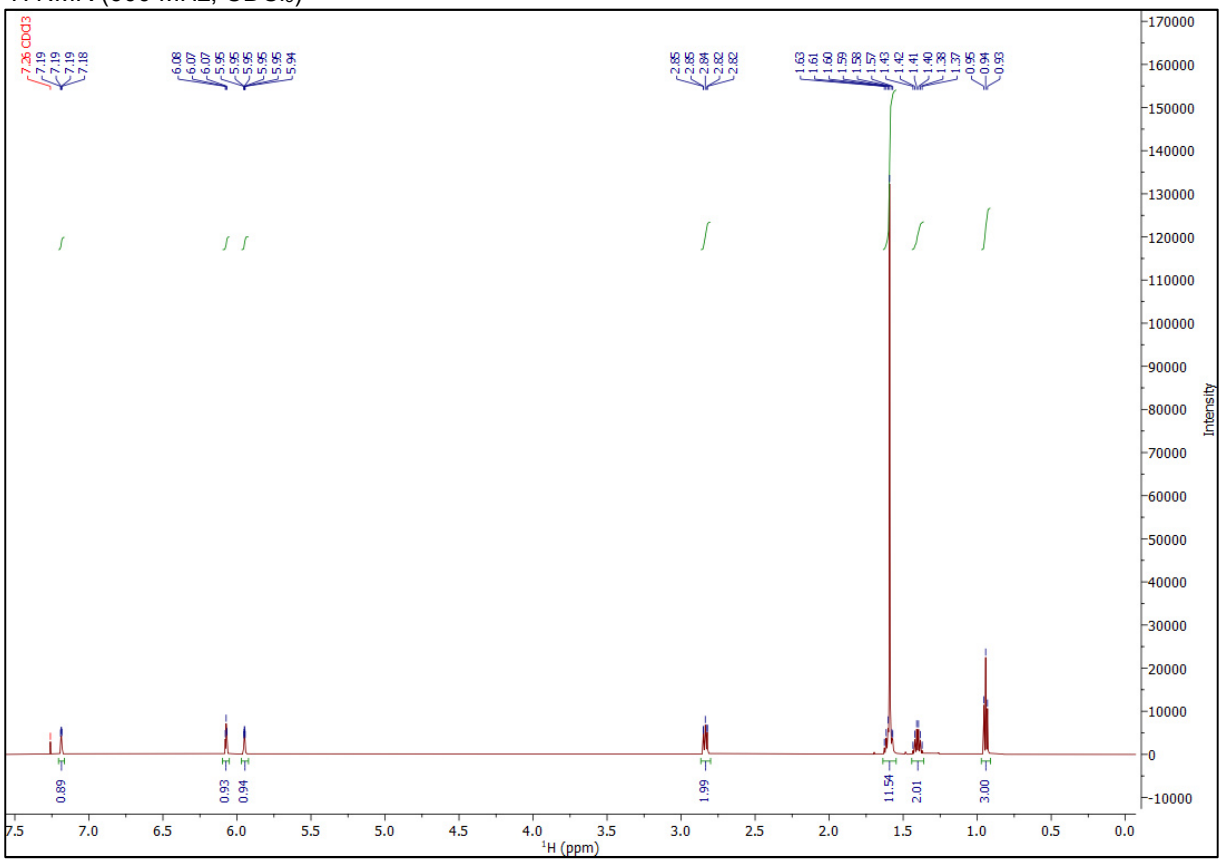


^{13}C NMR (151 MHz, $CDCl_3$)

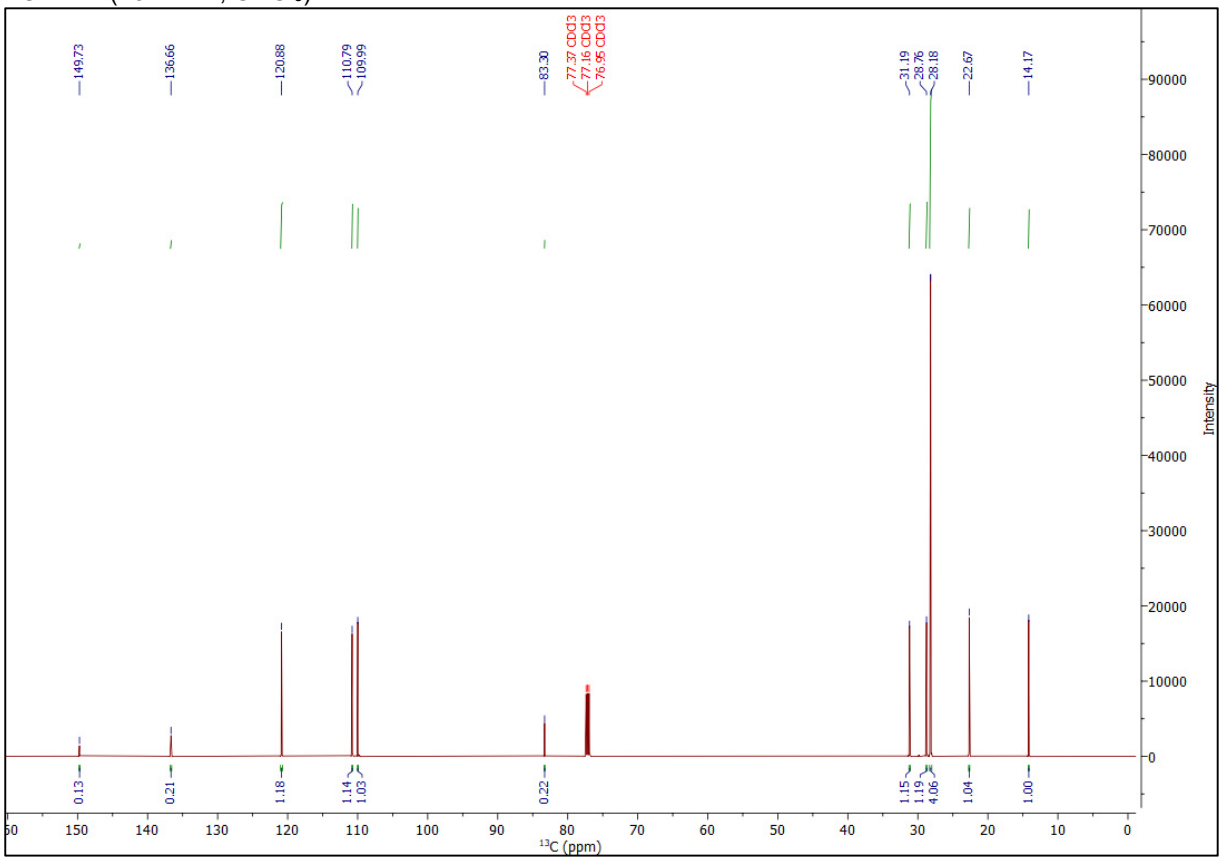


1-*tert*-Butyloxycarbonyl 2-butyl-1*H*-pyrrole (**III-139e**)

^{1}H NMR (600 MHz, $CDCl_3$)

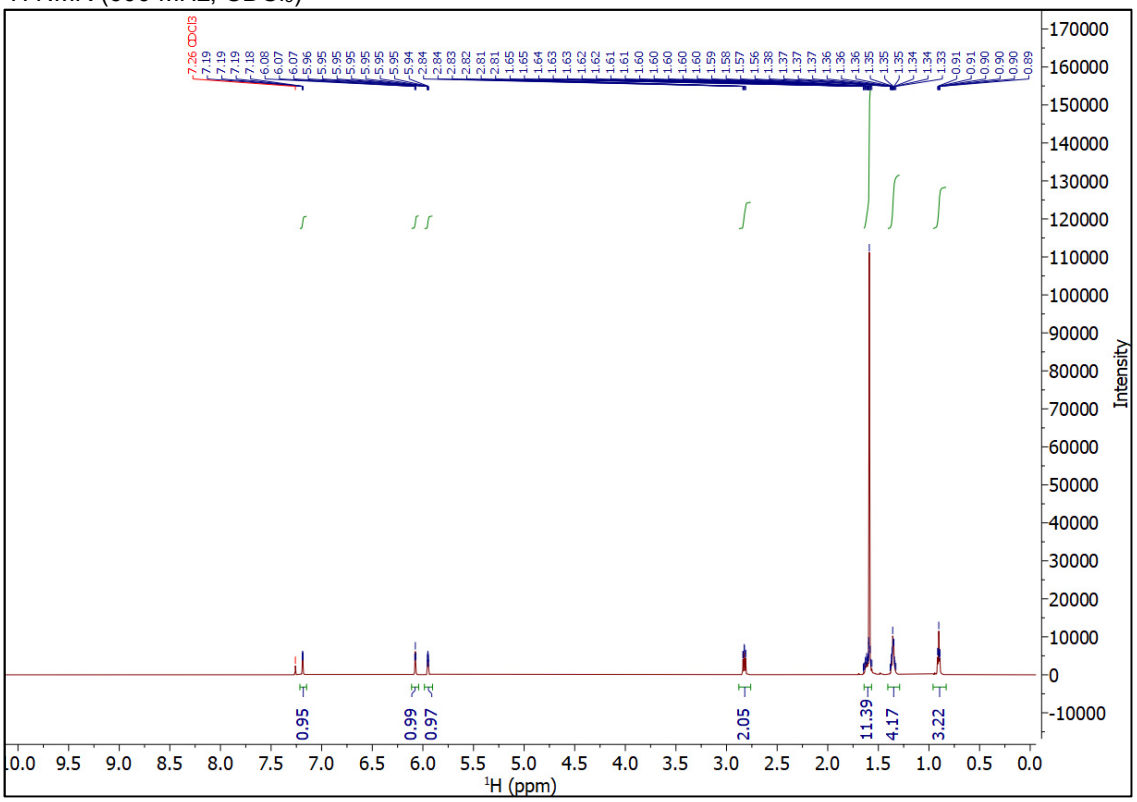


^{13}C NMR (151 MHz, $CDCl_3$)

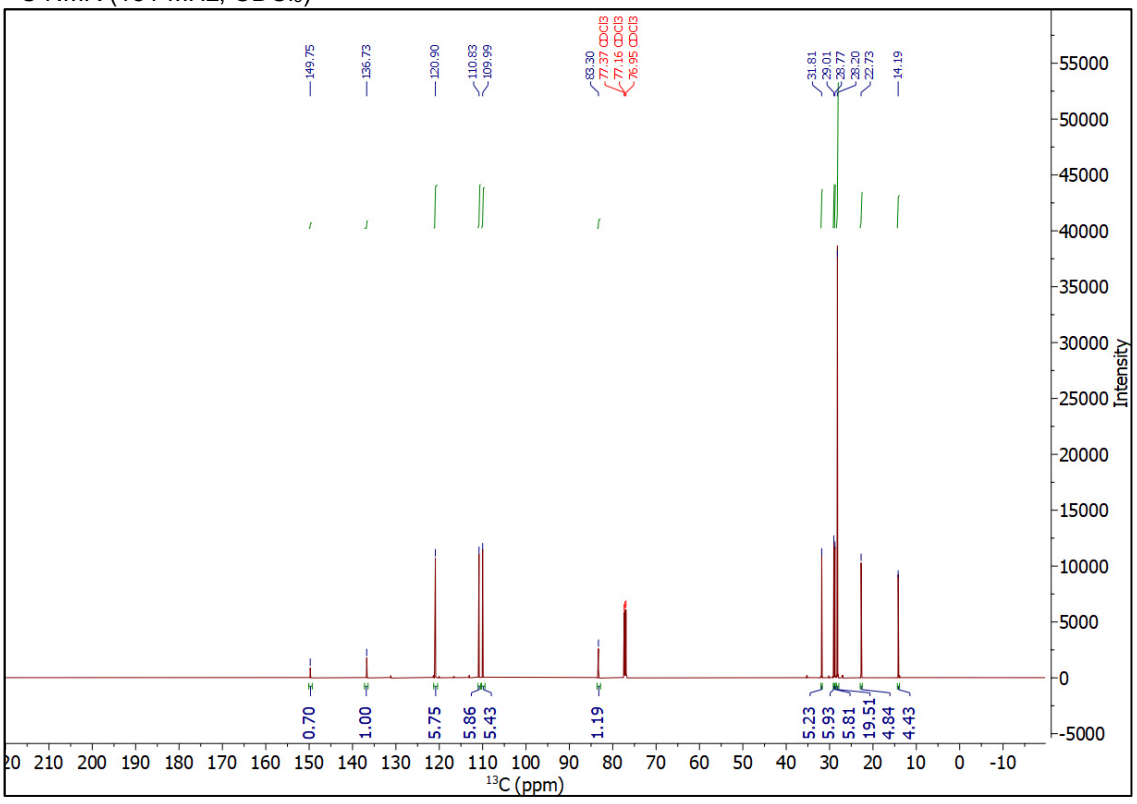


1-*tert*-Butyloxycarbonyl 2-pentyl-1*H*-pyrrole (**III-139f**)

^{1}H NMR (600 MHz, $CDCl_3$)

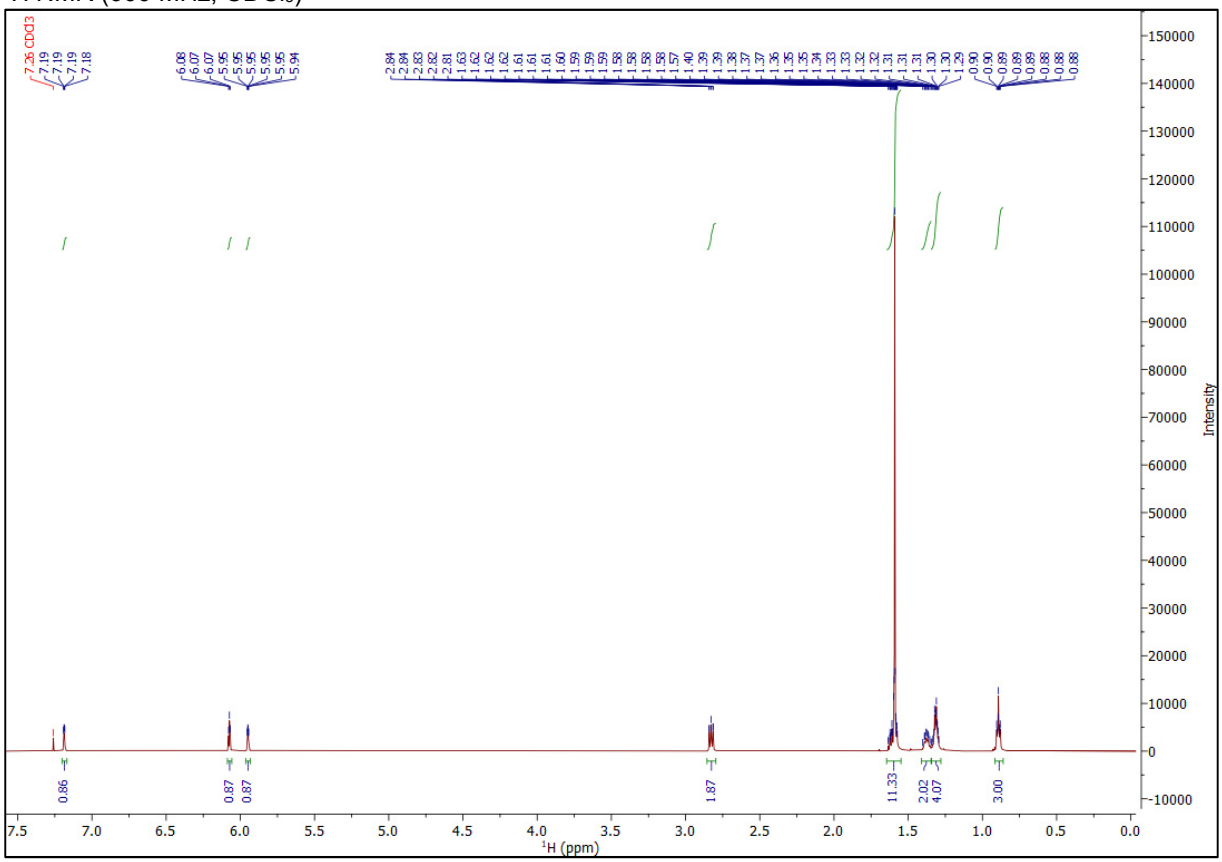


^{13}C NMR (151 MHz, $CDCl_3$)

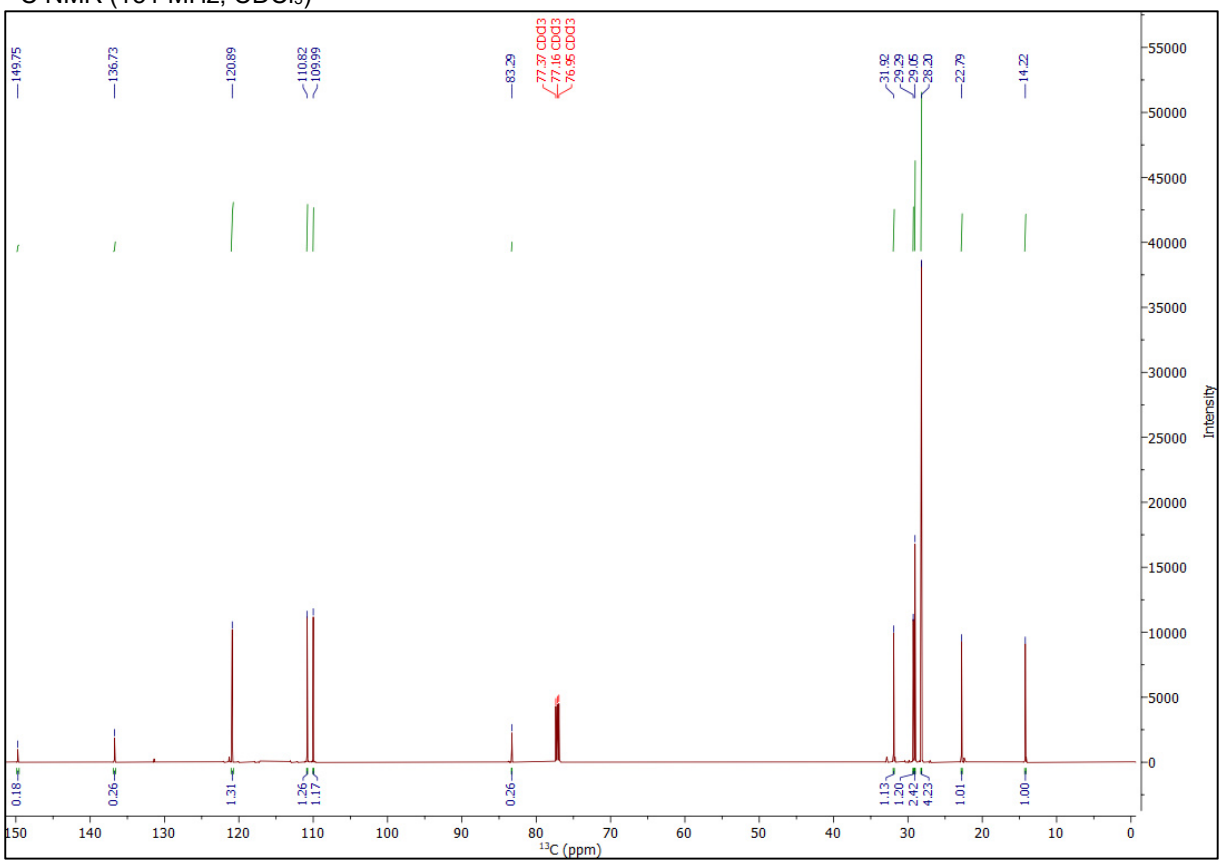


1-*tert*-Butyloxycarbonyl 2-hexyl-1*H*-pyrrole (**III-139g**)

^{1}H NMR (600 MHz, $CDCl_3$)

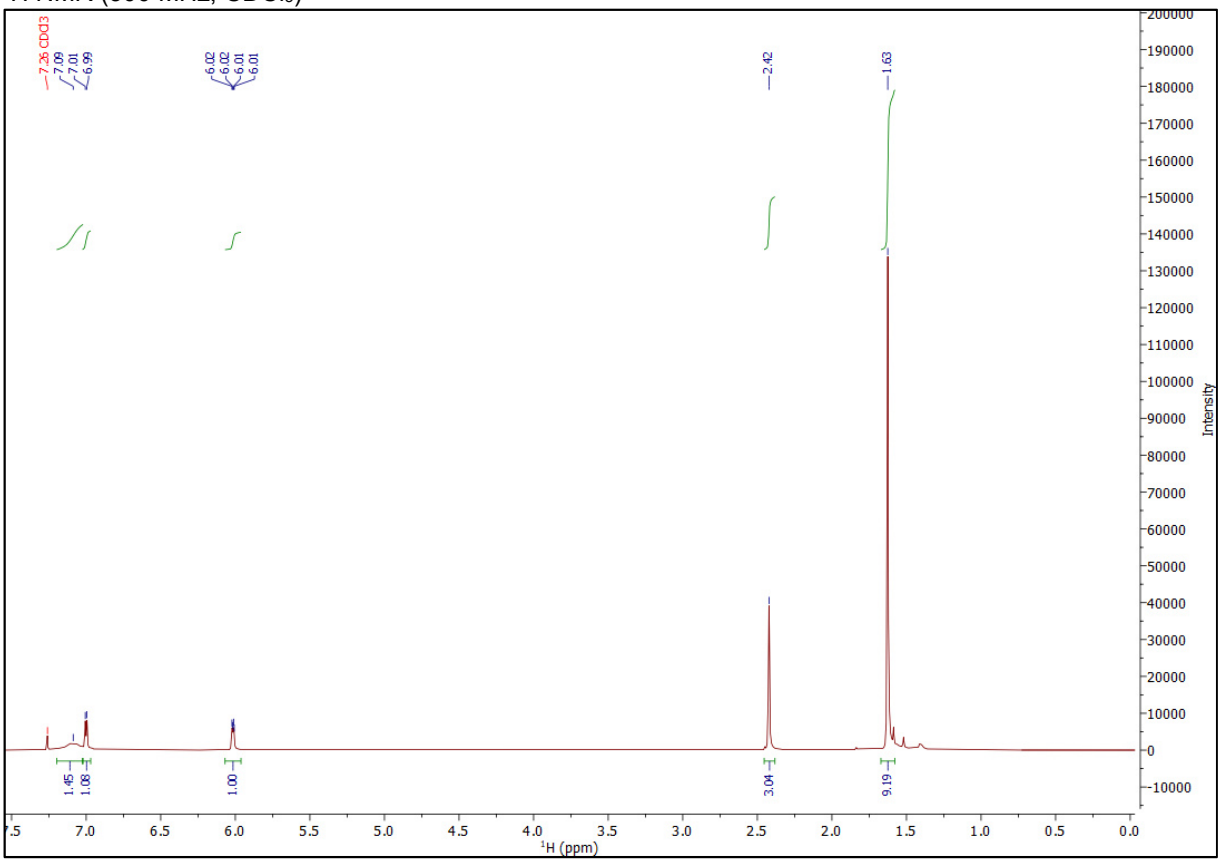


^{13}C NMR (151 MHz, $CDCl_3$)

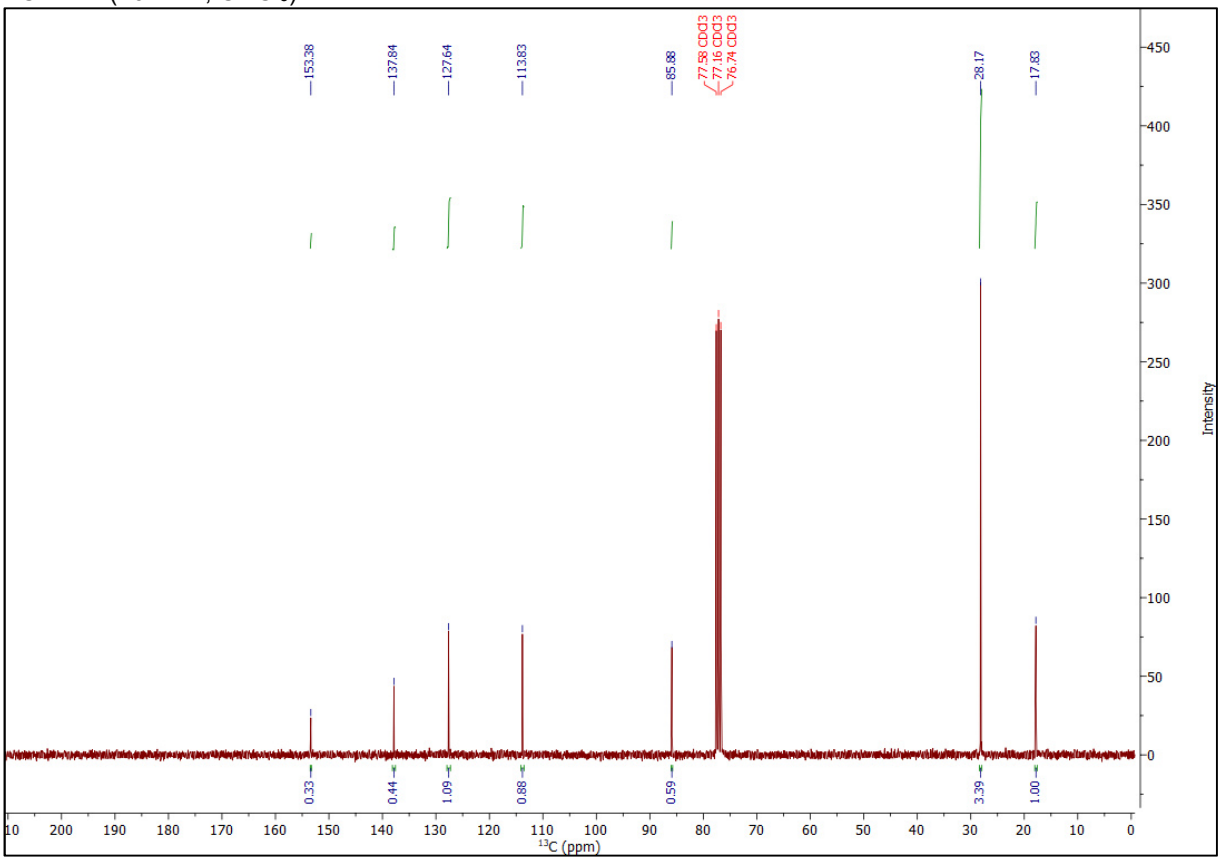


(1-(*tert*-Butoxycarbonyl)-5-methyl-1*H*-pyrrol-2-yl)boronic acid (**III-140b**)

^{1}H NMR (300 MHz, $CDCl_3$)

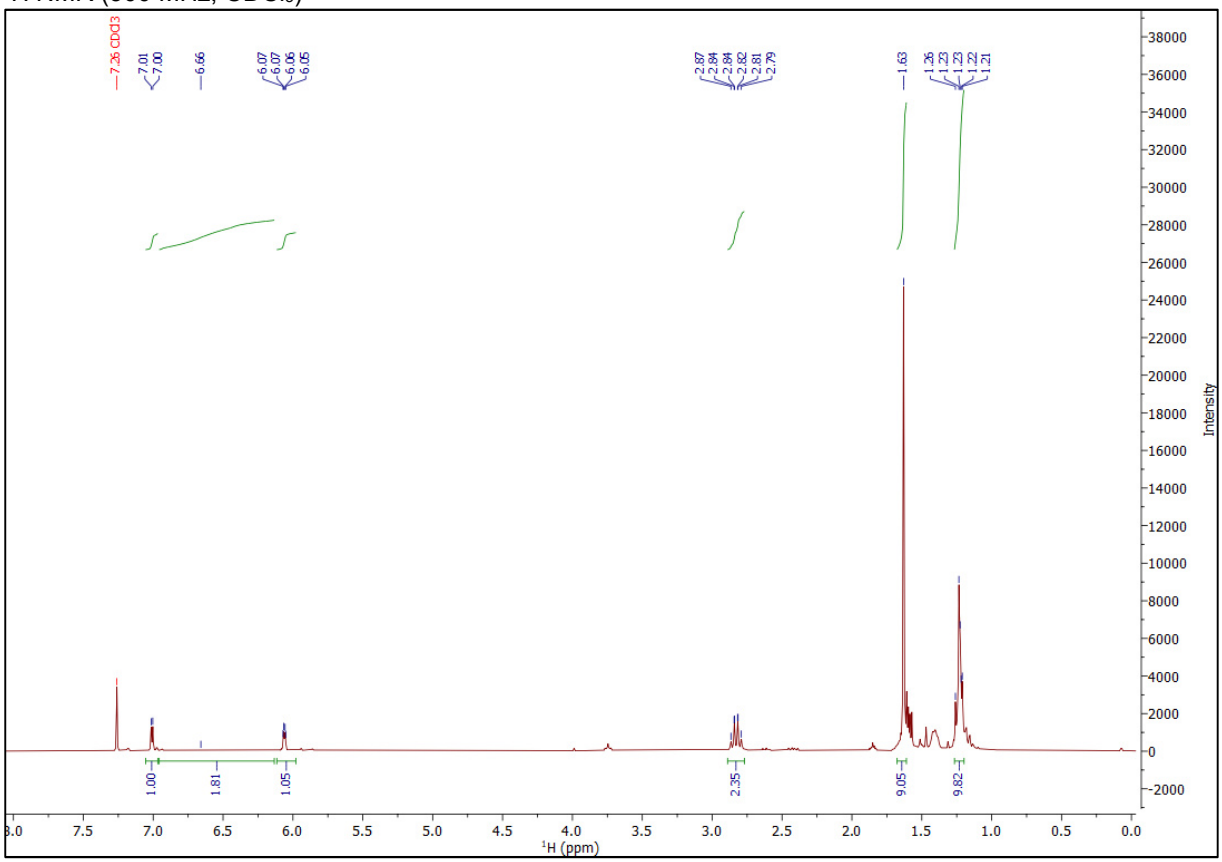


^{13}C NMR (76 MHz, $CDCl_3$)

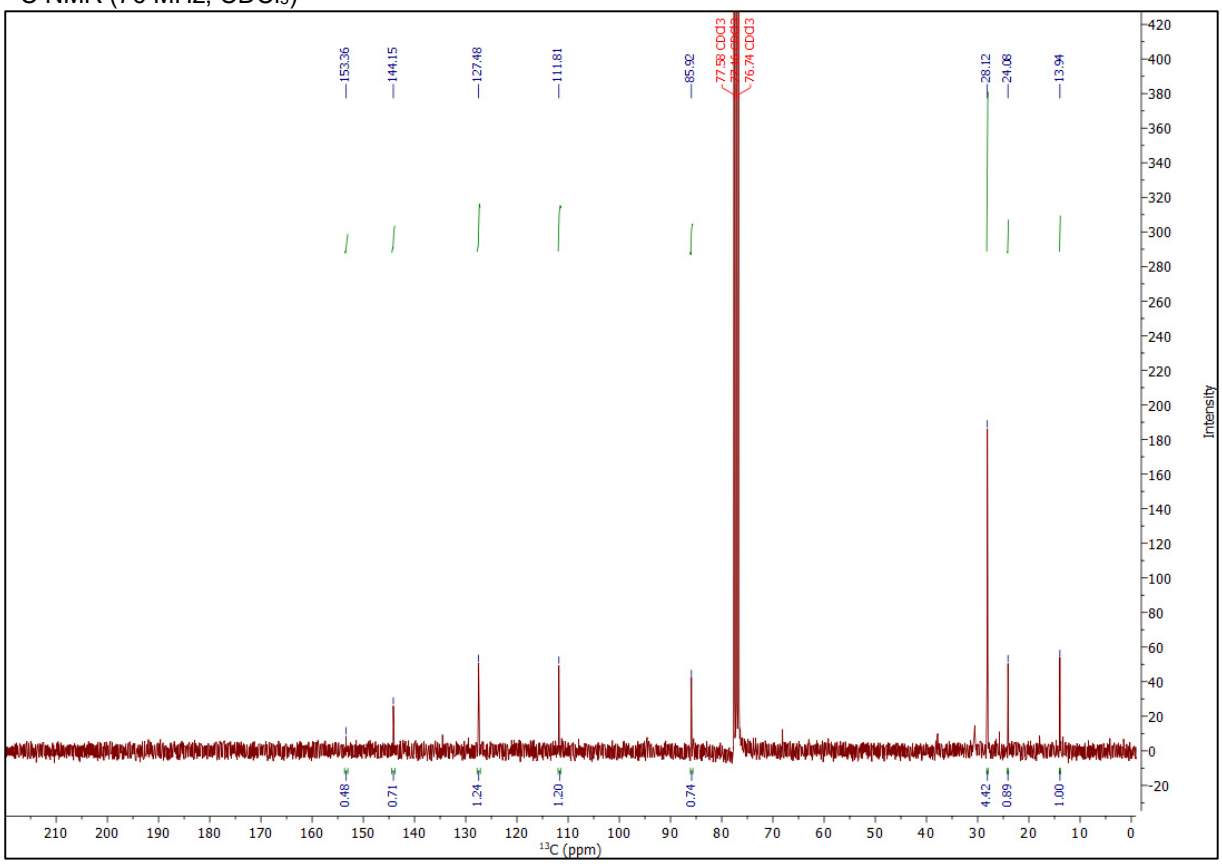


(1-(*tert*-Butoxycarbonyl)-5-ethyl-1*H*-pyrrol-2-yl)boronic acid (**III-140c**)

^{1}H NMR (300 MHz, $CDCl_3$)

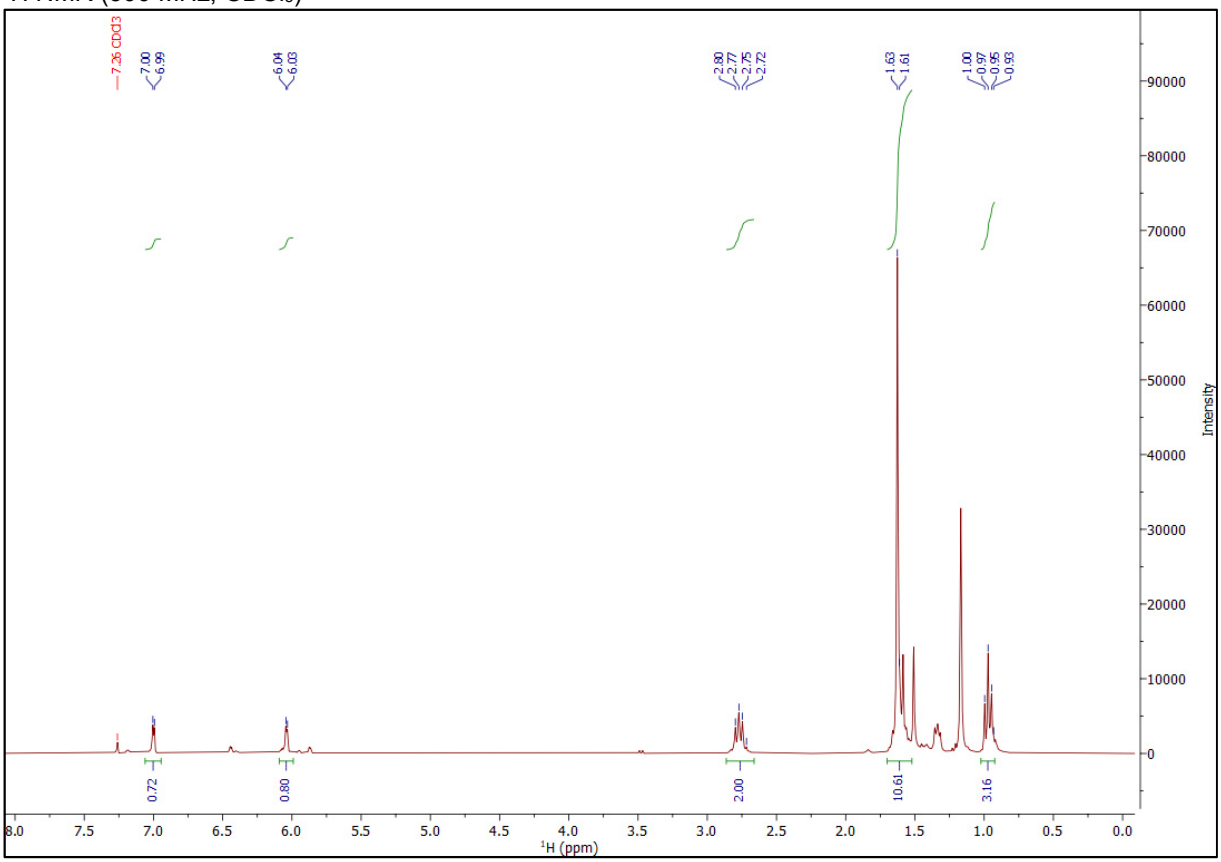


^{13}C NMR (76 MHz, $CDCl_3$)

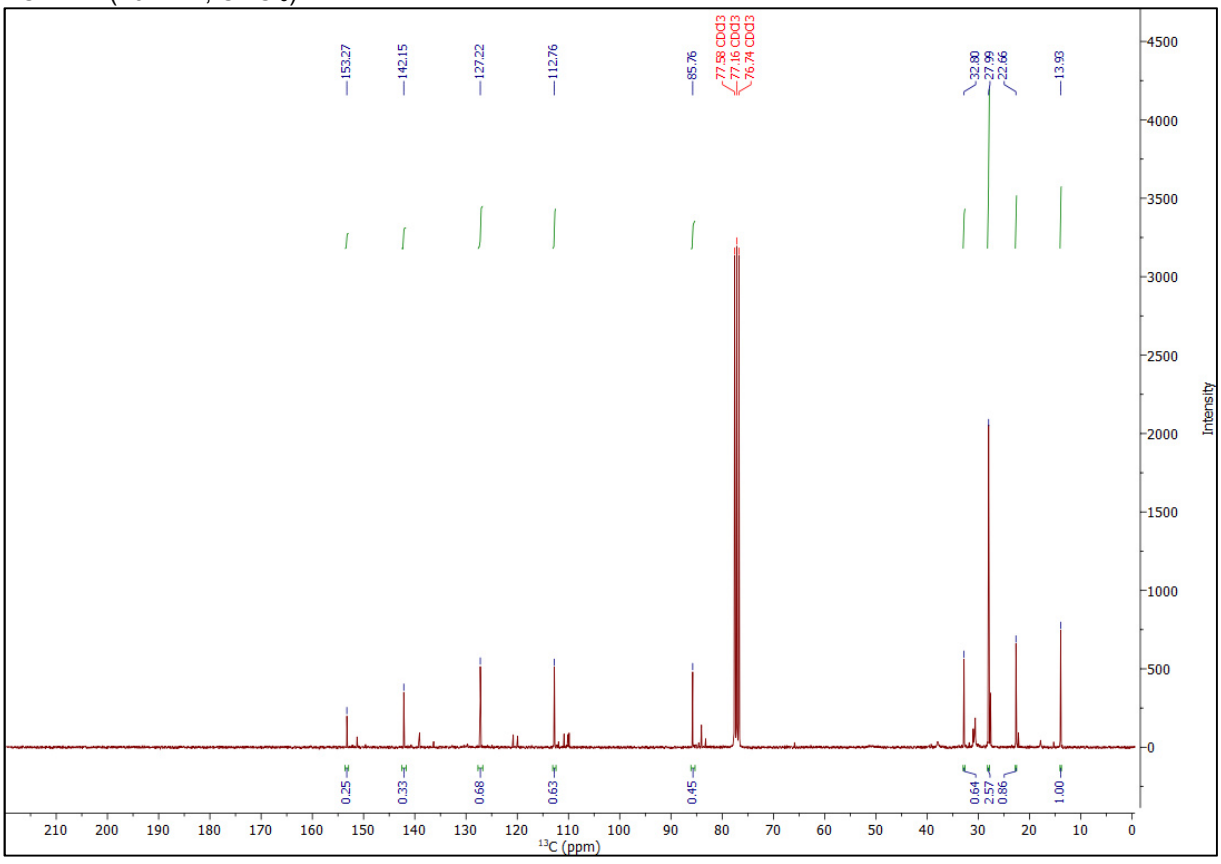


(1-(*tert*-Butoxycarbonyl)-5-propyl-1*H*-pyrrol-2-yl)boronic acid (**III-140d**)

^{1}H NMR (300 MHz, $CDCl_3$)

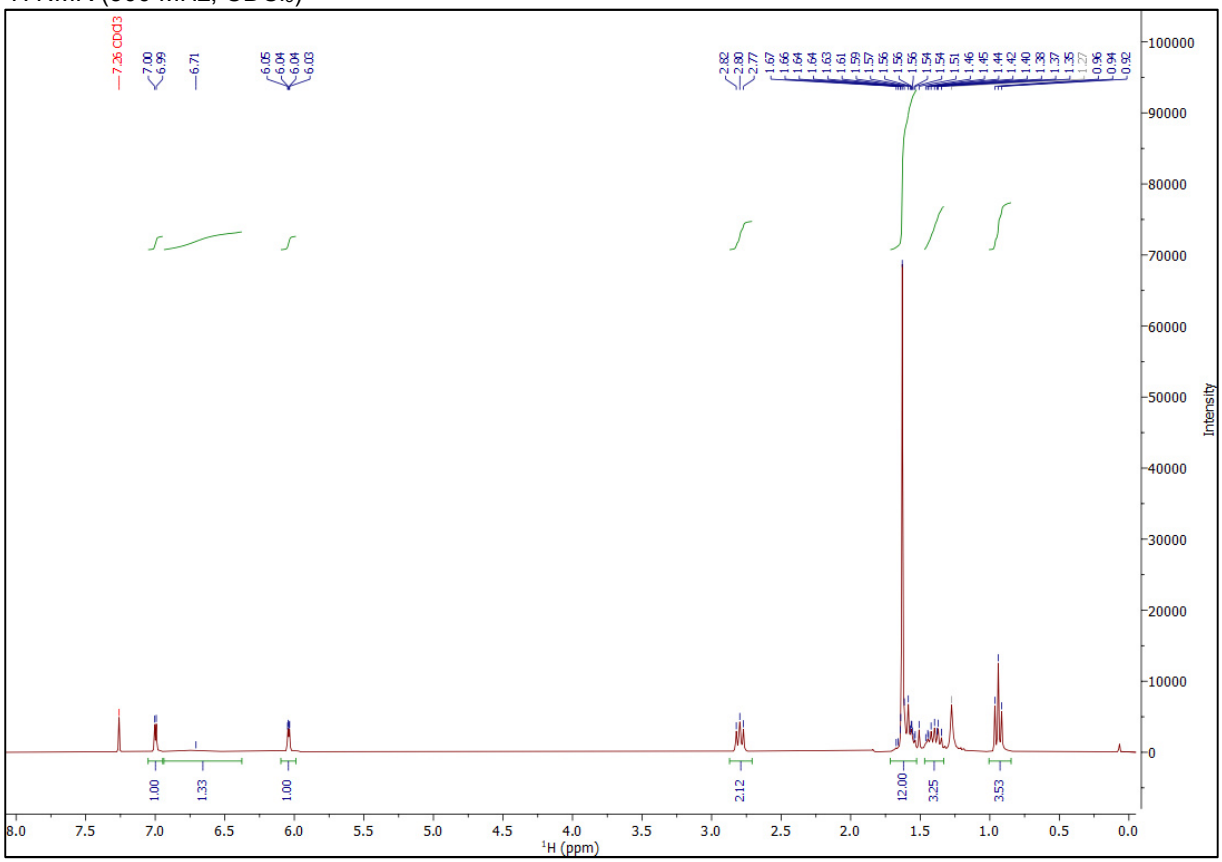


^{13}C NMR (76 MHz, $CDCl_3$)

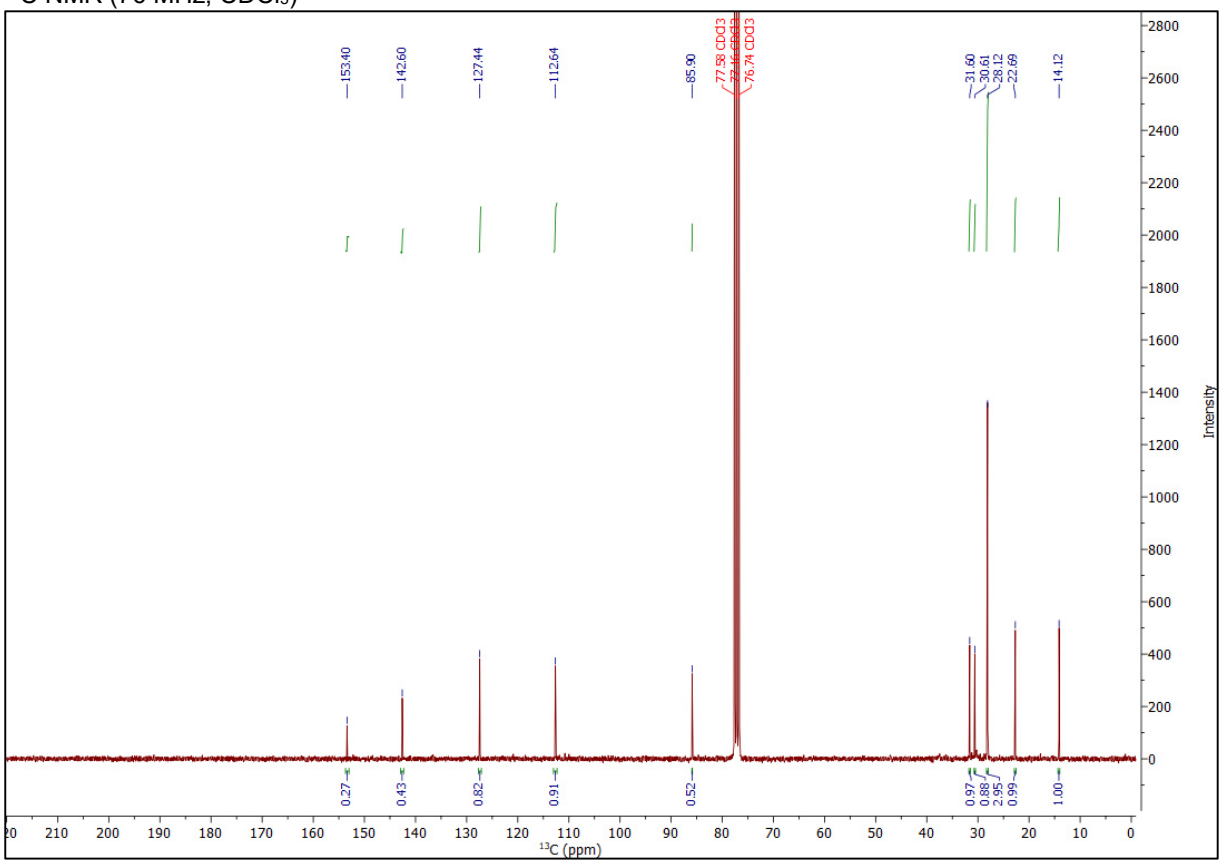


(1-(*tert*-Butoxycarbonyl)-5-butyl-1*H*-pyrrol-2-yl)boronic acid (**III-140e**)

^{1}H NMR (300 MHz, $CDCl_3$)

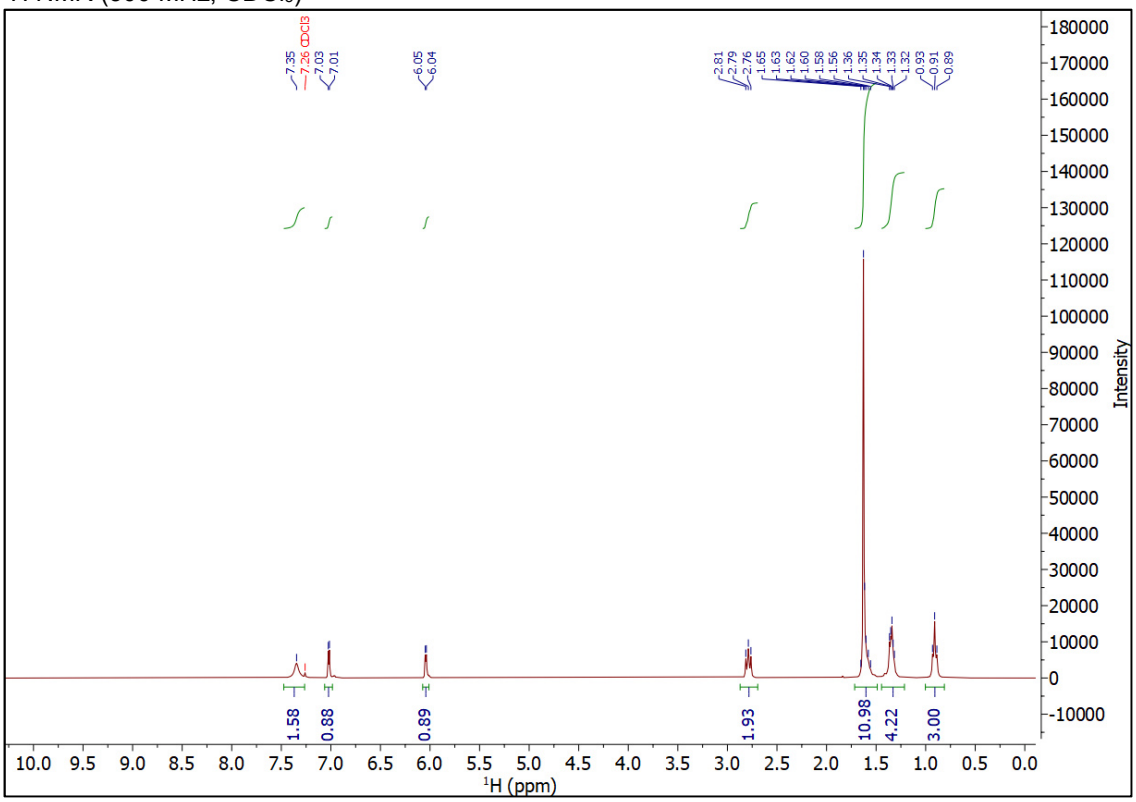


^{13}C NMR (76 MHz, $CDCl_3$)

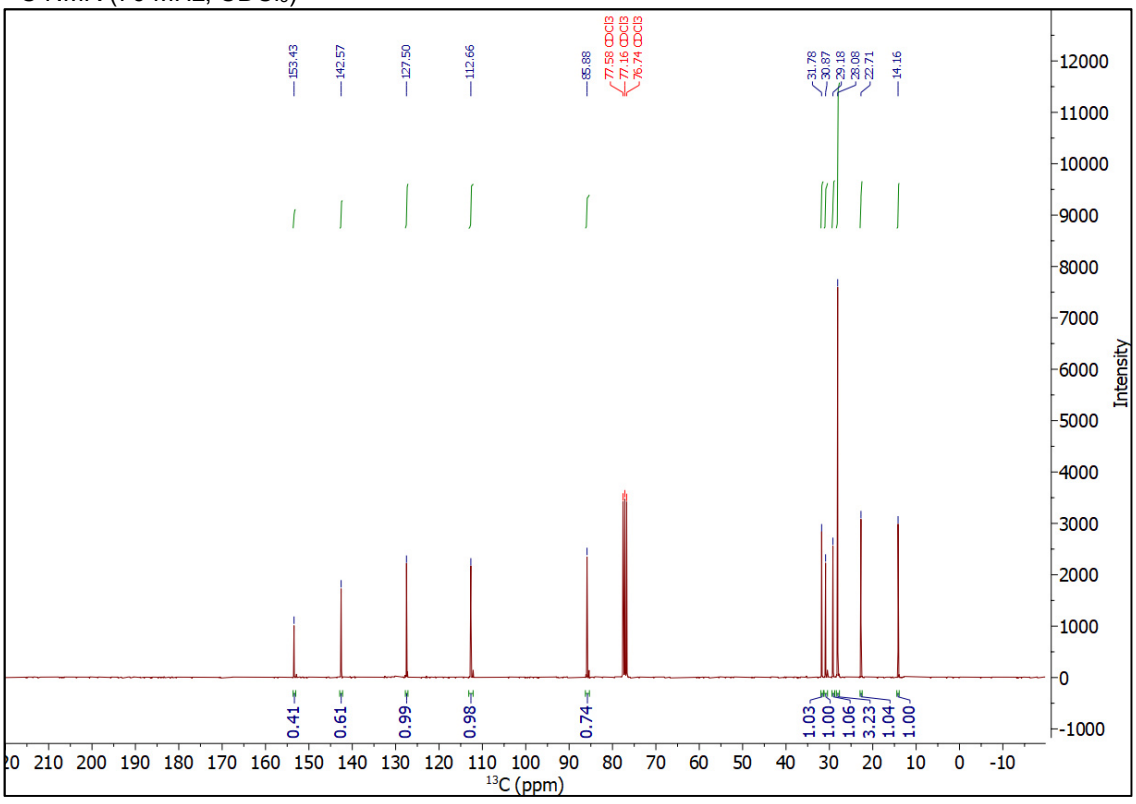


(1-(*tert*-Butoxycarbonyl)-5-pentyl-1*H*-pyrrol-2-yl)boronic acid (**III-140f**)

^{1}H NMR (300 MHz, $CDCl_3$)

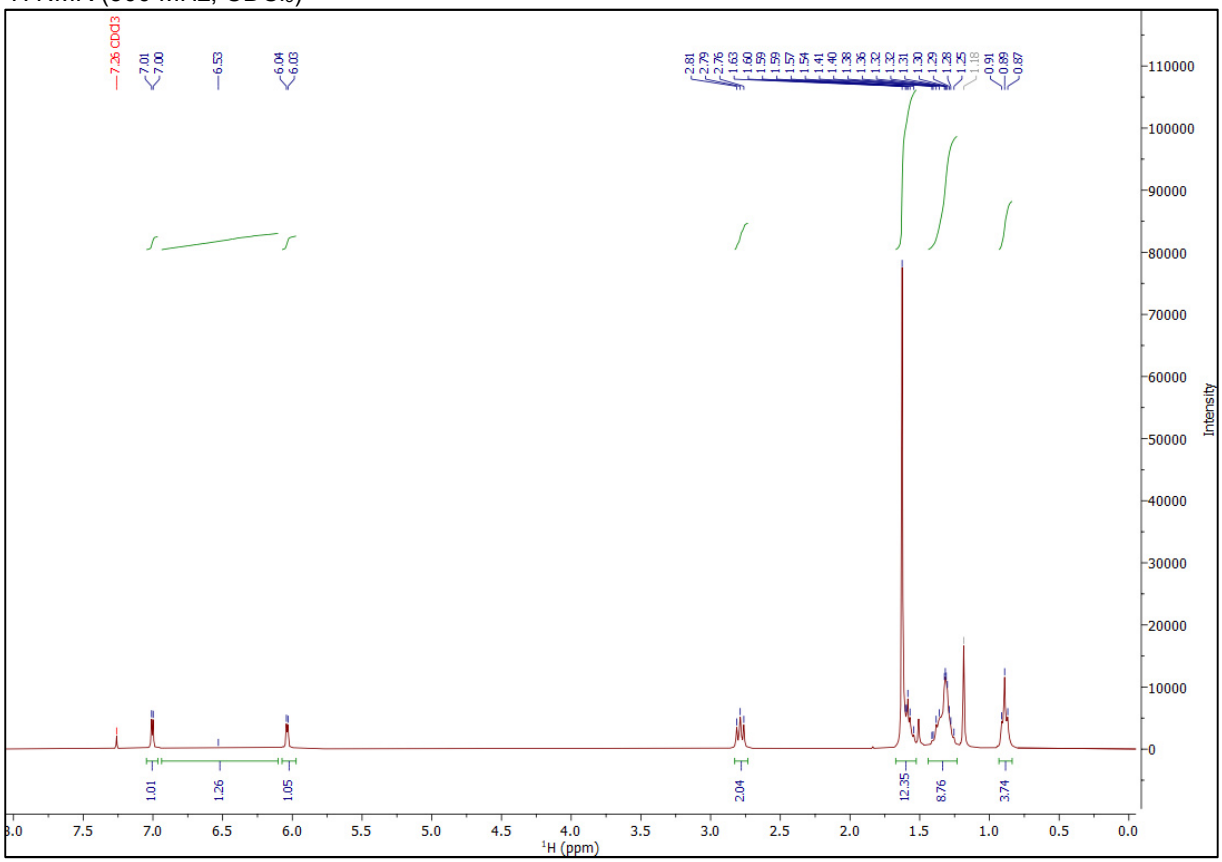


^{13}C NMR (76 MHz, $CDCl_3$)

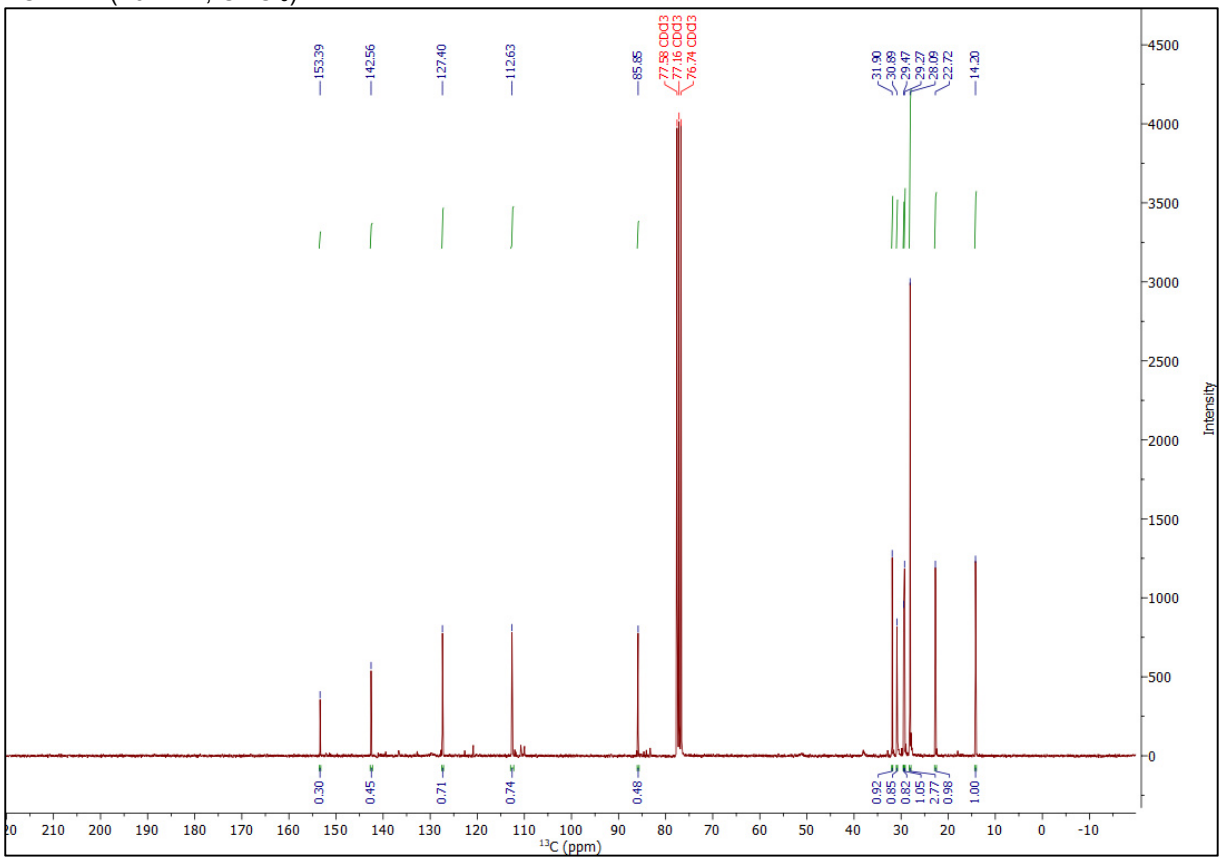


(1-(*tert*-Butoxycarbonyl)-5-hexyl-1*H*-pyrrol-2-yl)boronic acid (**III-140g**)

^{1}H NMR (300 MHz, $CDCl_3$)

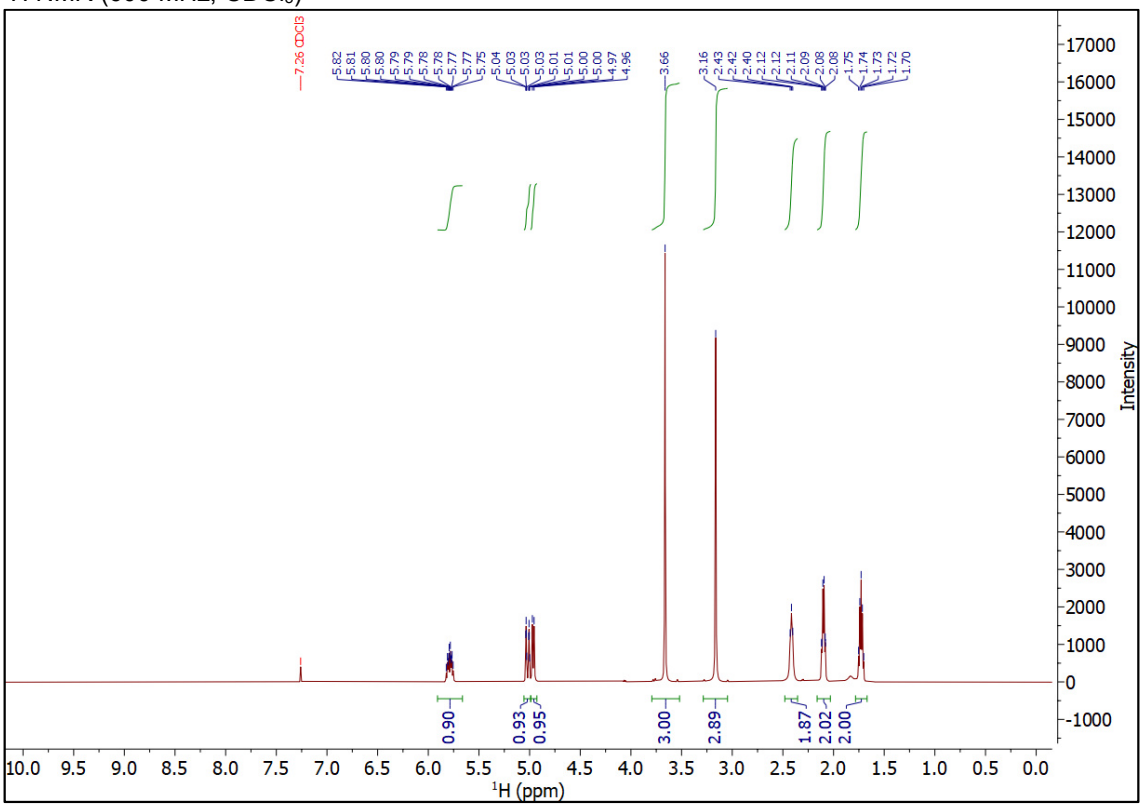


^{13}C NMR (76 MHz, $CDCl_3$)

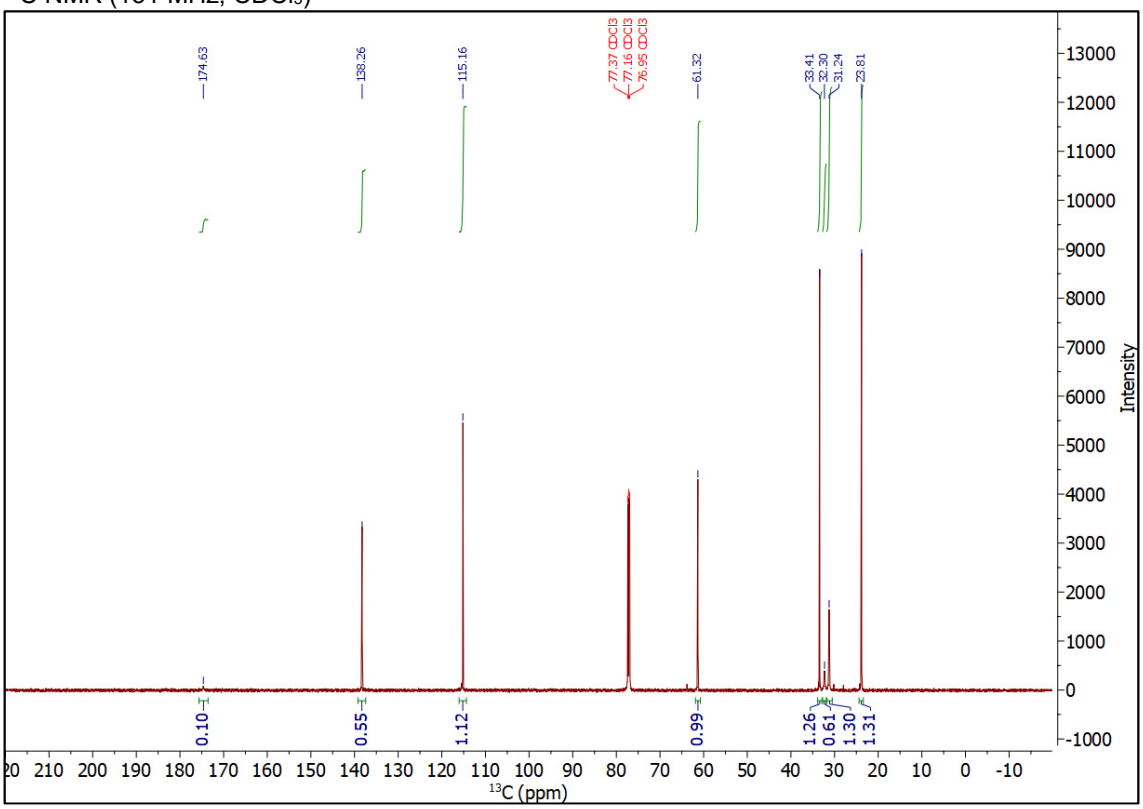


N-Methoxy-*N*-methylhex-5-enamide (**III-142**)

^{1}H NMR (600 MHz, $CDCl_3$)

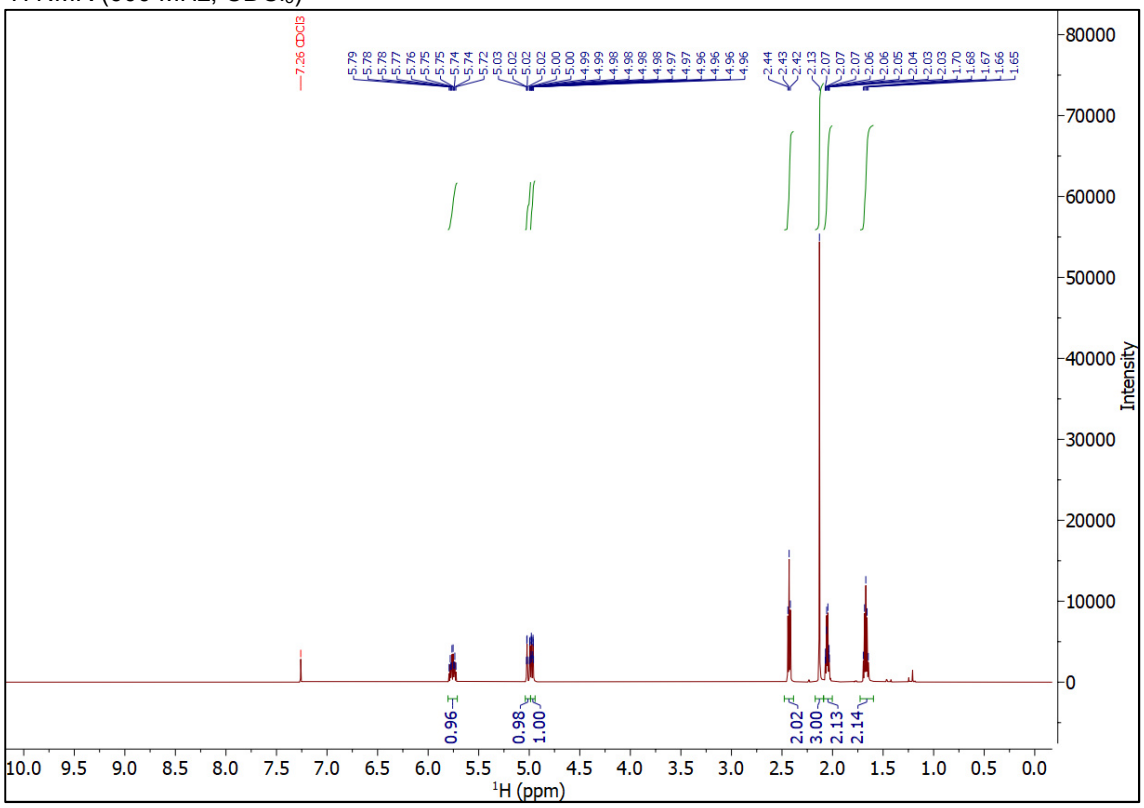


^{13}C NMR (151 MHz, $CDCl_3$)

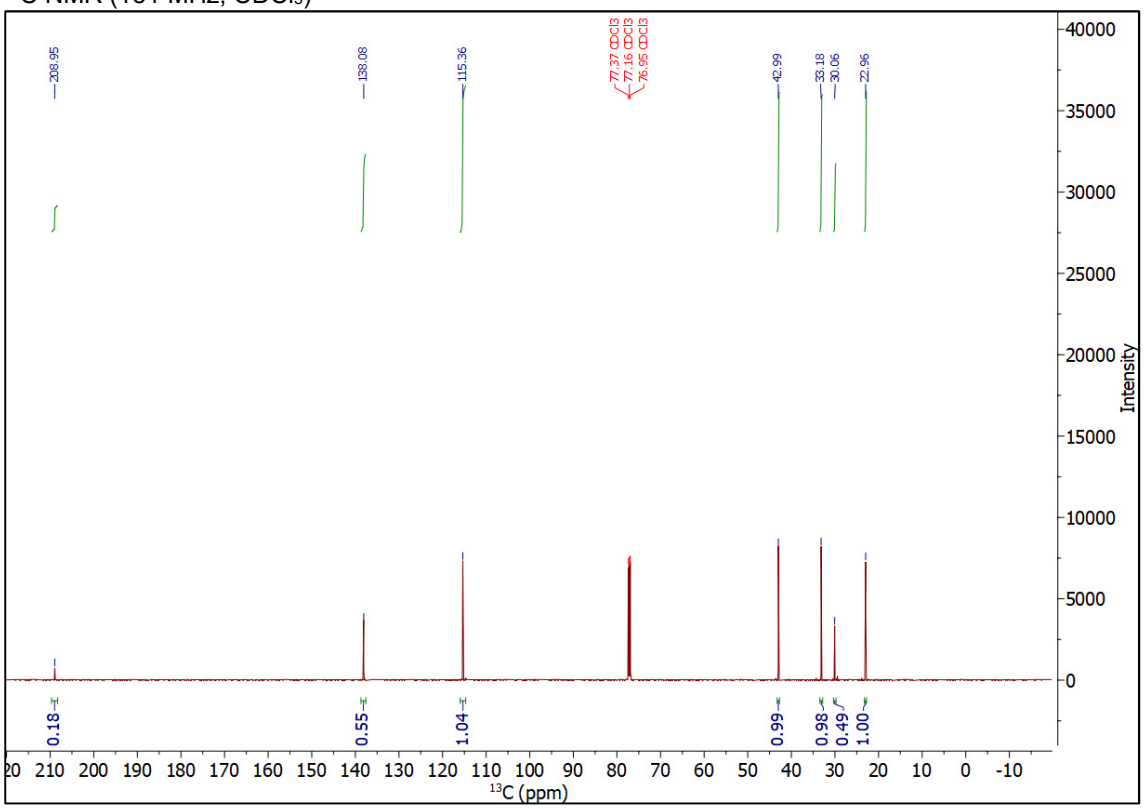


Hept-6-en-2-one (**III-143**)

^{1}H NMR (600 MHz, $CDCl_3$)

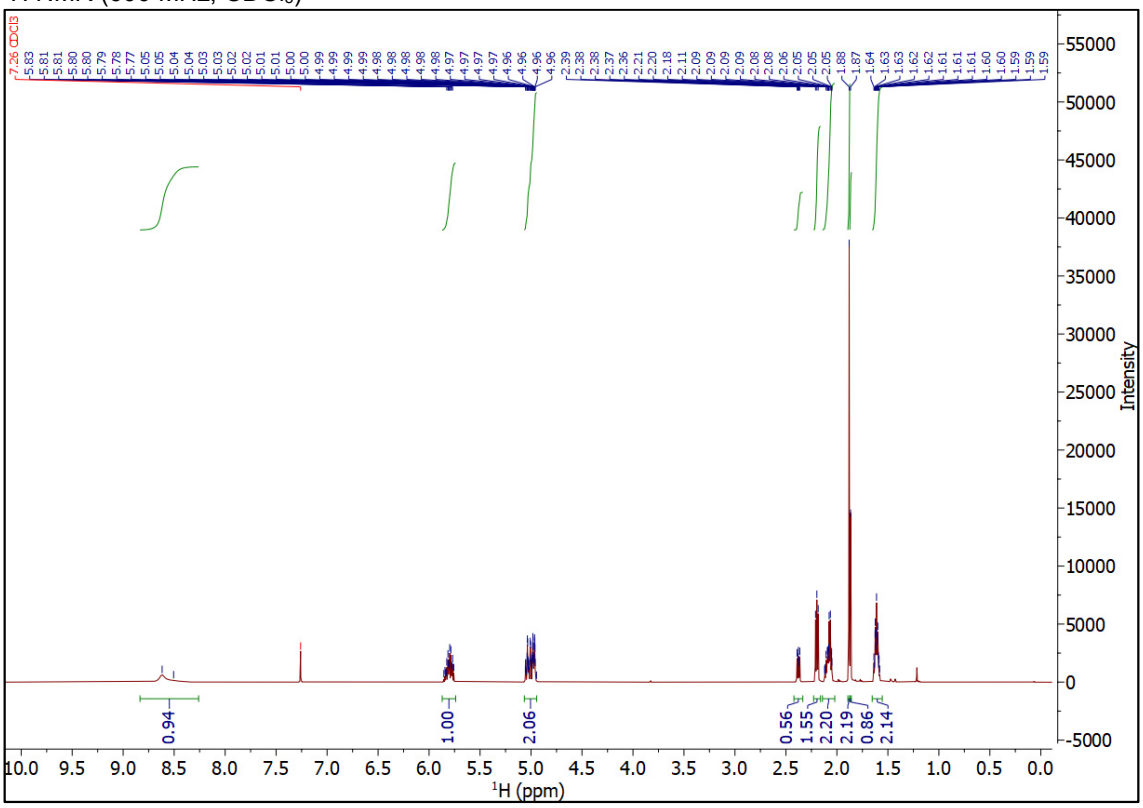


^{13}C NMR (151 MHz, $CDCl_3$)

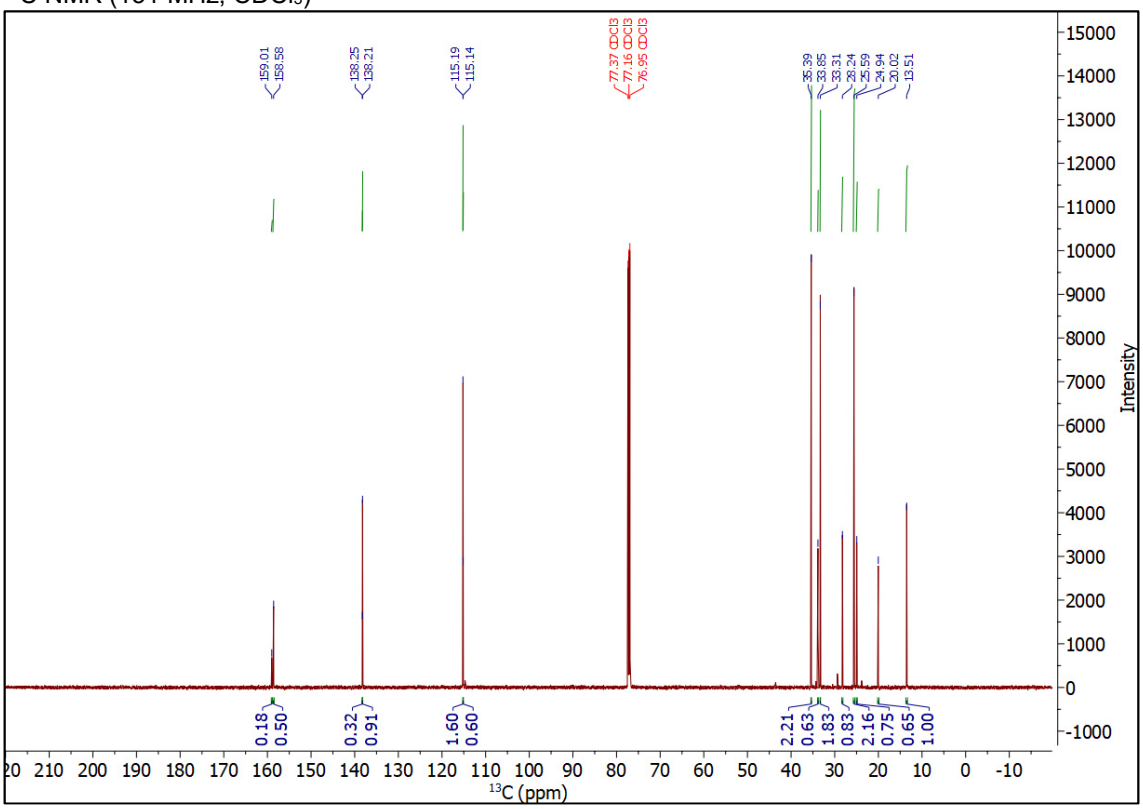


(*E*/*Z*)-Hept-6-en-2-one oxime (**III-144**)

^{1}H NMR (600 MHz, $CDCl_3$)

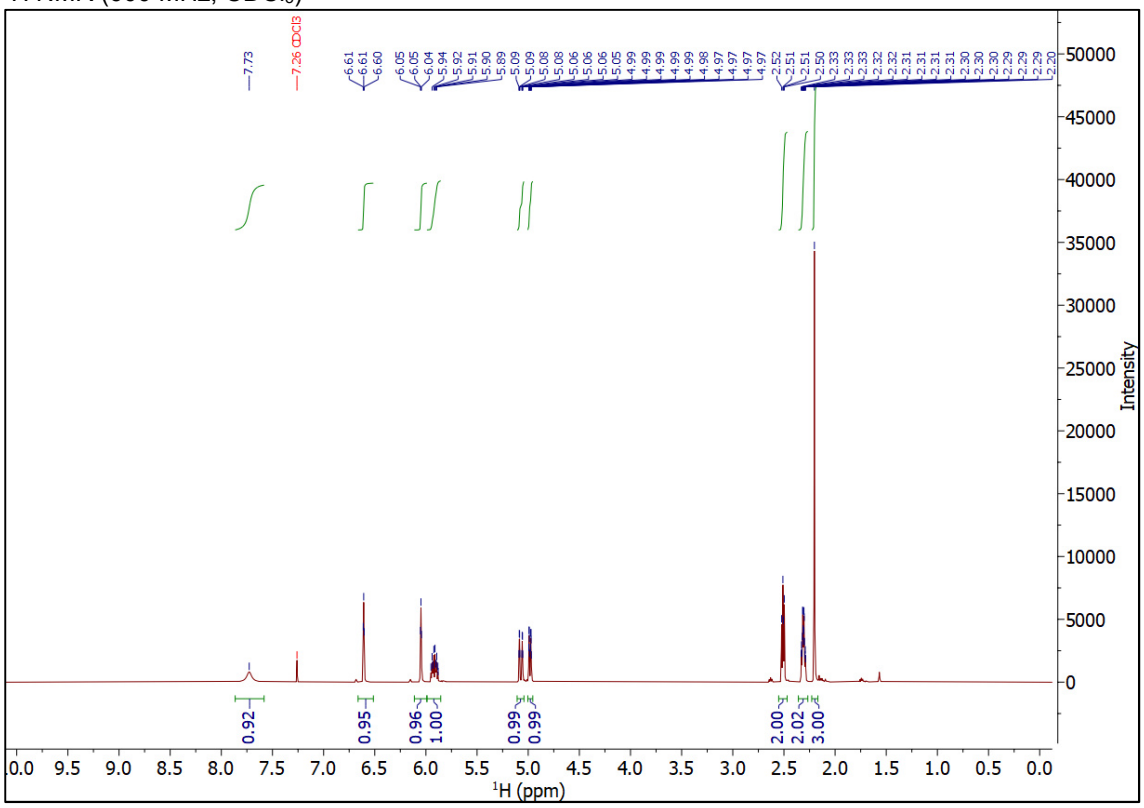


^{13}C NMR (151 MHz, $CDCl_3$)

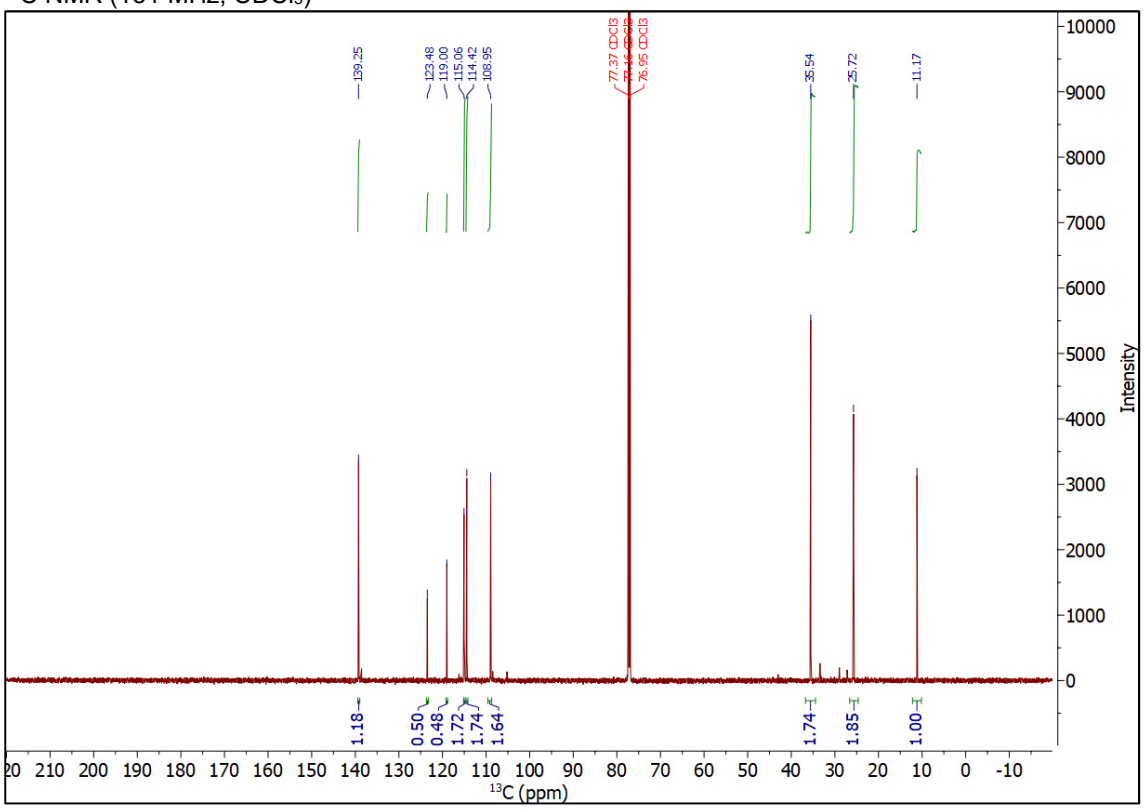


3-(But-3-en-1-yl)-2-methyl-1*H*-pyrrole (**III-145**)

^{1}H NMR (600 MHz, $CDCl_3$)

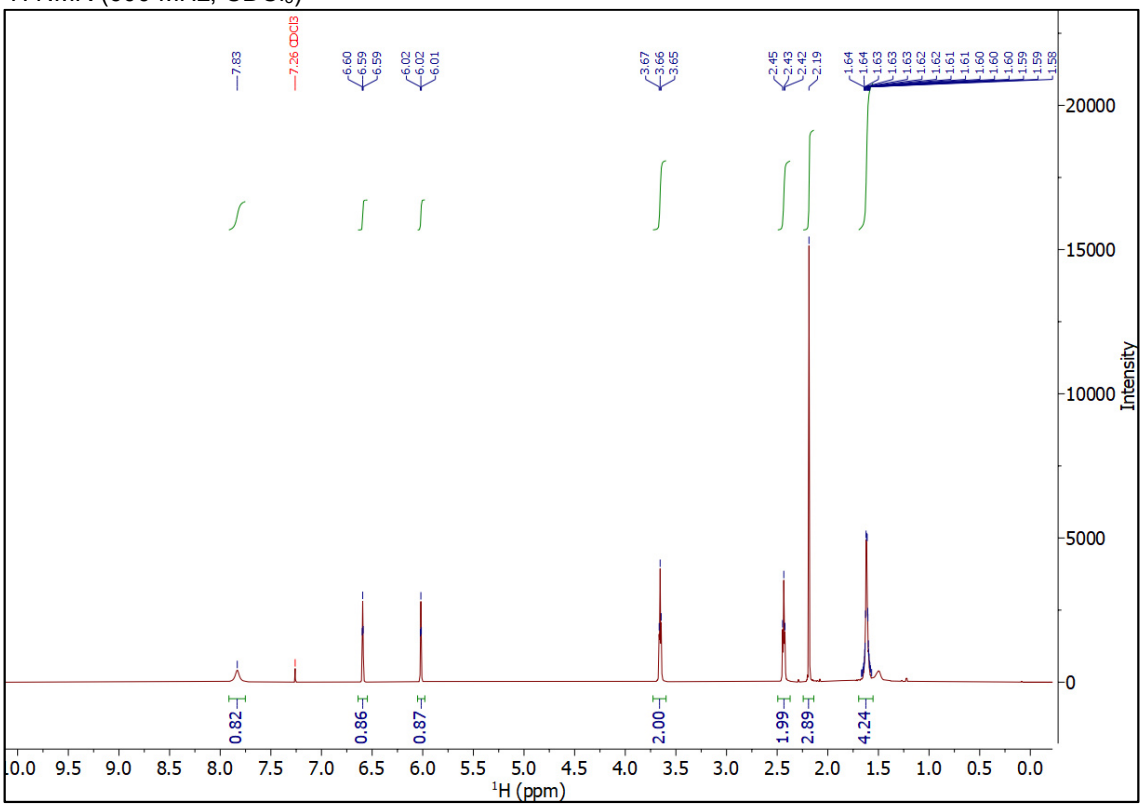


^{13}C NMR (151 MHz, $CDCl_3$)

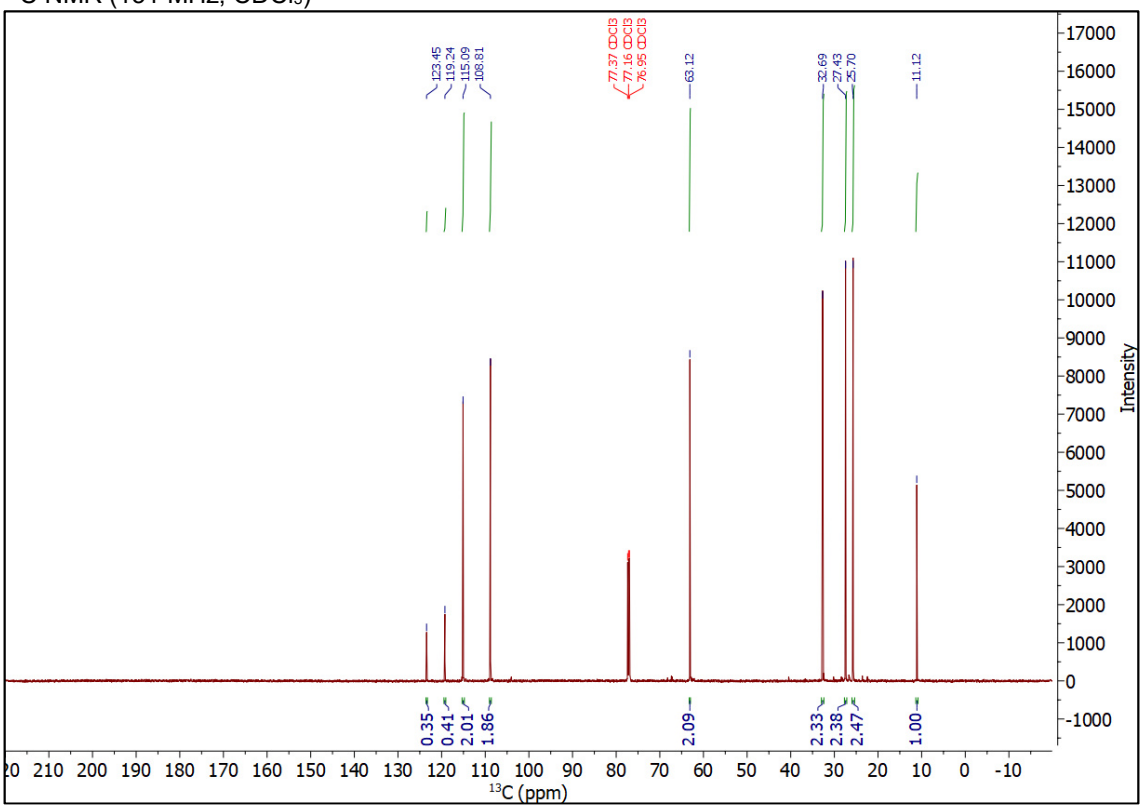


4-(2-Methyl-1*H*-pyrrol-3-yl)butan-1-ol (**III-146**) (from hydroboration-oxidation of alkene pyrrole **III-145**)

^{1}H NMR (600 MHz, $CDCl_3$)

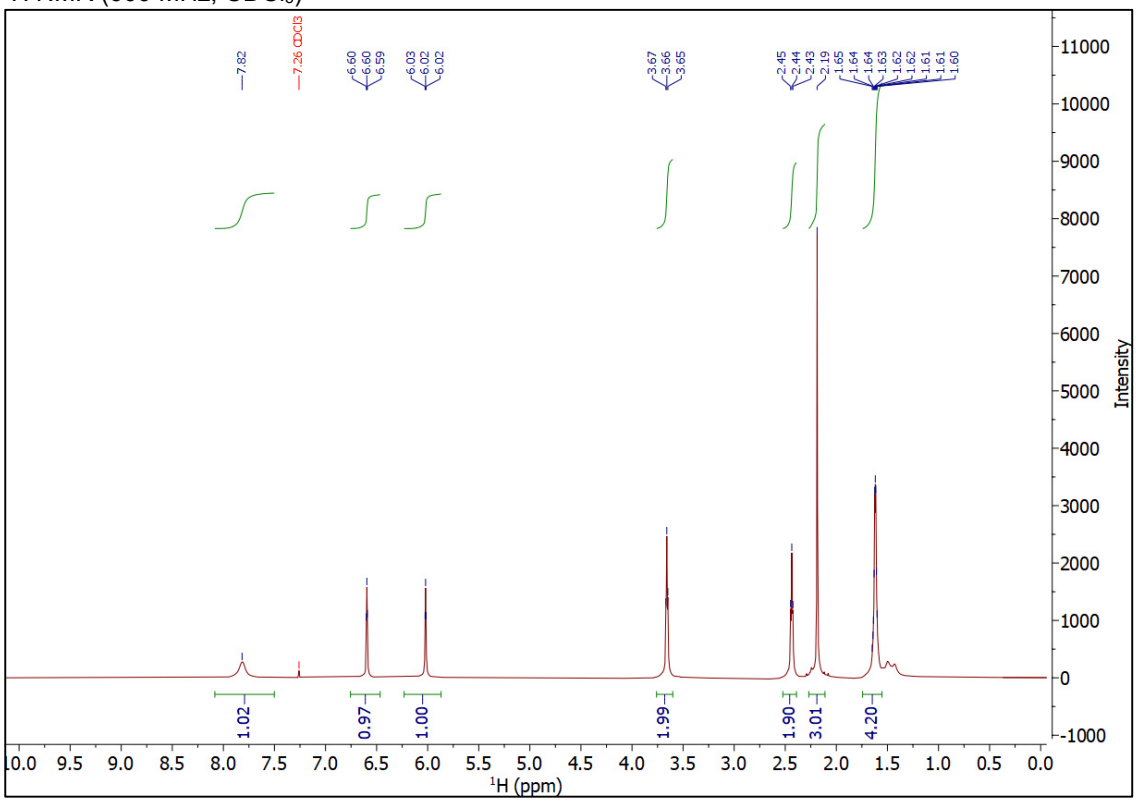


^{13}C NMR (151 MHz, $CDCl_3$)

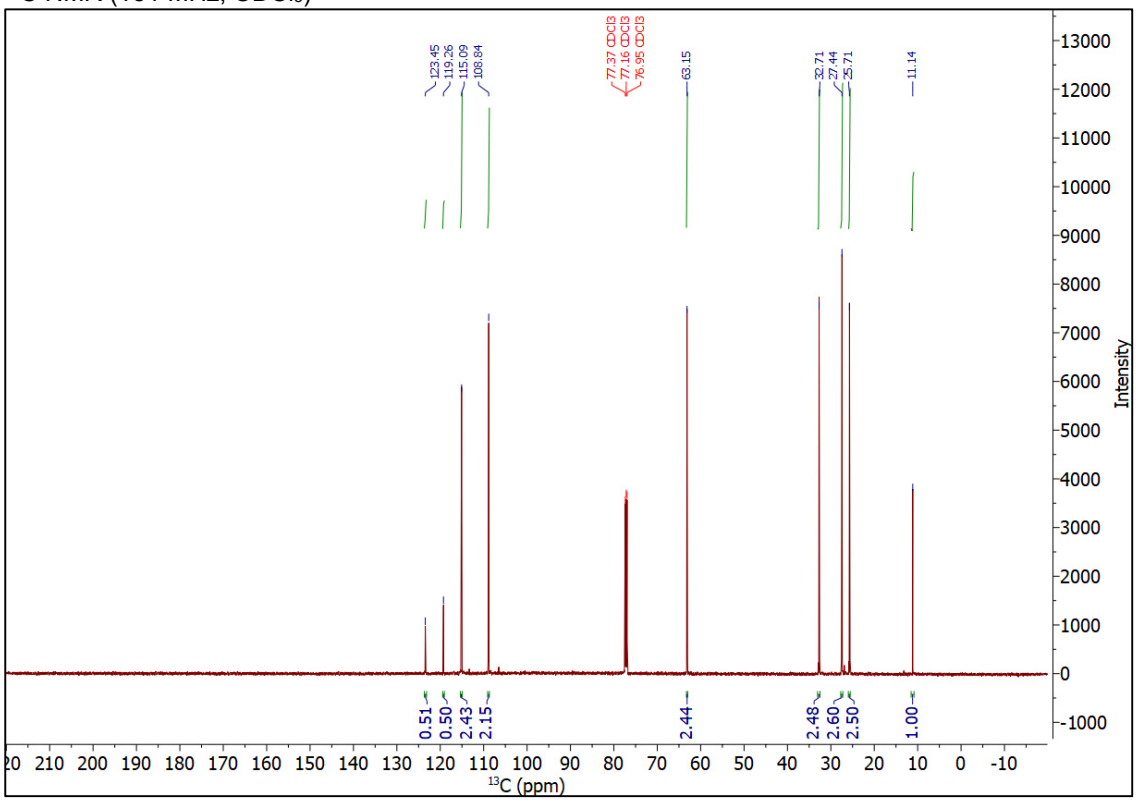


4-(2-Methyl-1*H*-pyrrol-3-yl)butan-1-ol (**III-146**) (from decarboxylation of pyrrole **III-152**)

^{1}H NMR (600 MHz, $CDCl_3$)

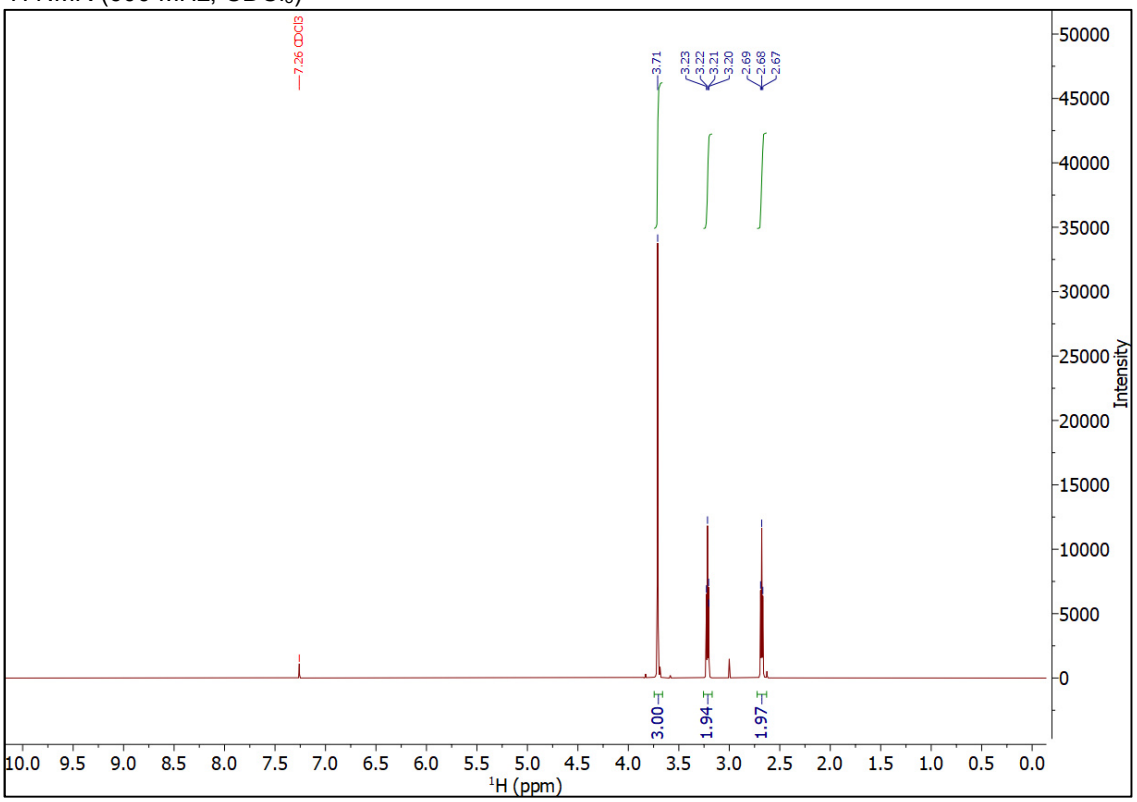


^{13}C NMR (151 MHz, $CDCl_3$)

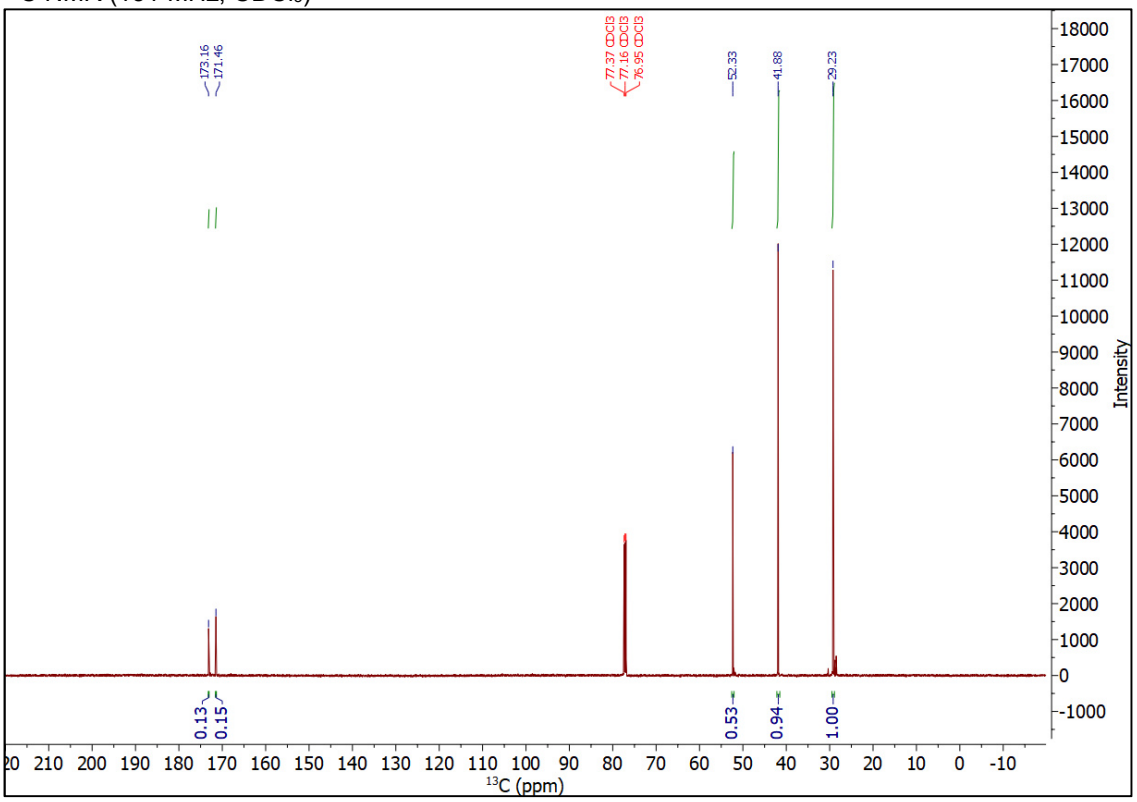


Methyl 4-chloro-4-oxobutanoate (**III-148**)

^{1}H NMR (600 MHz, $CDCl_3$)

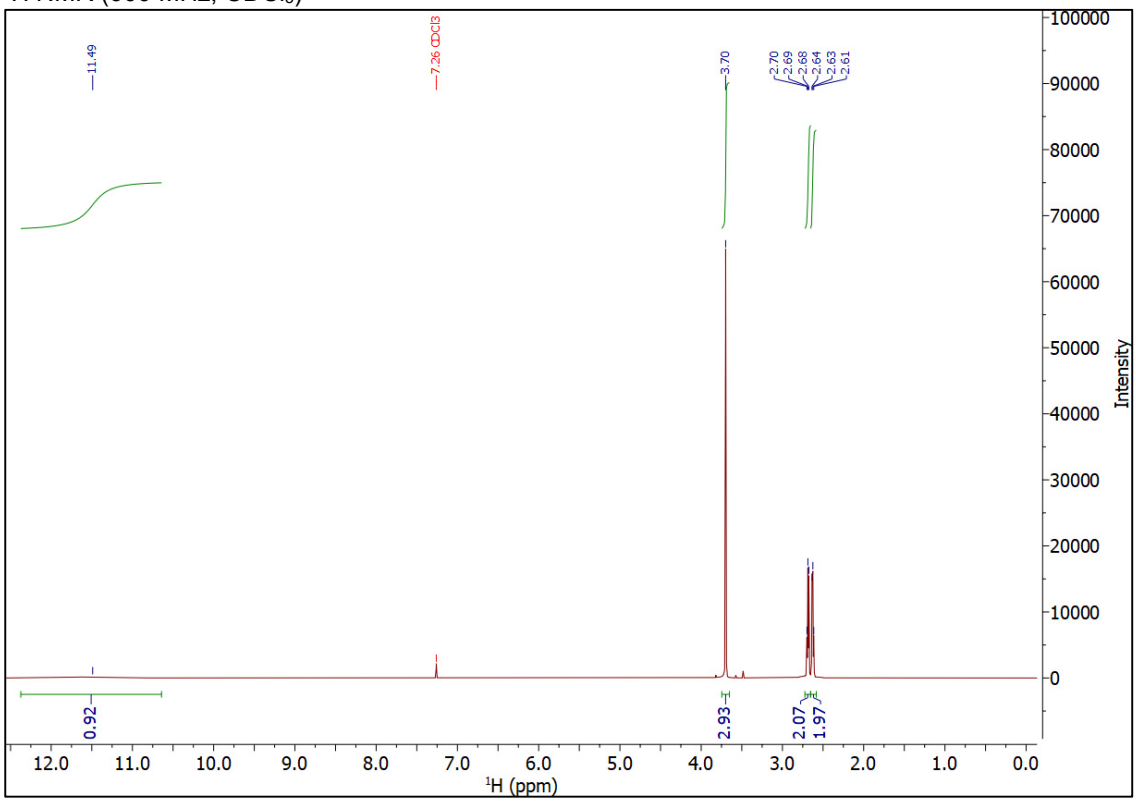


^{13}C NMR (151 MHz, $CDCl_3$)

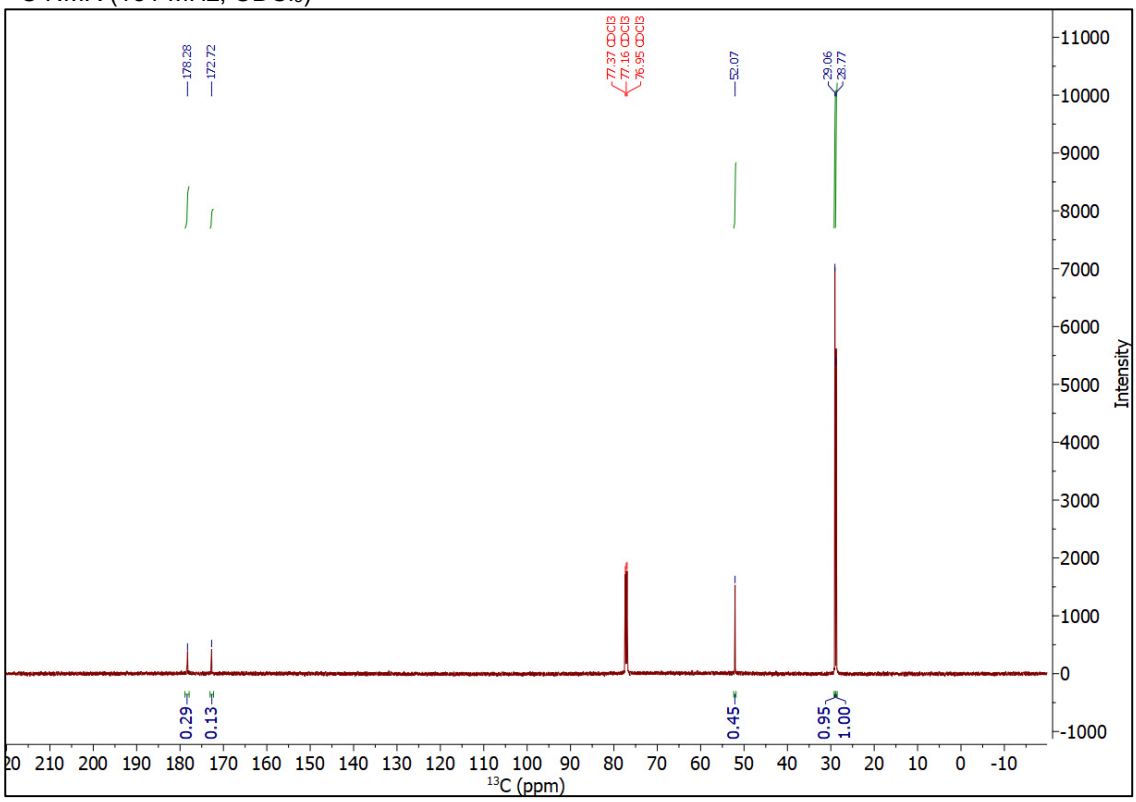


4-Methoxy-4-oxobutanoic acid (**III-150**)

^{1}H NMR (600 MHz, $CDCl_3$)

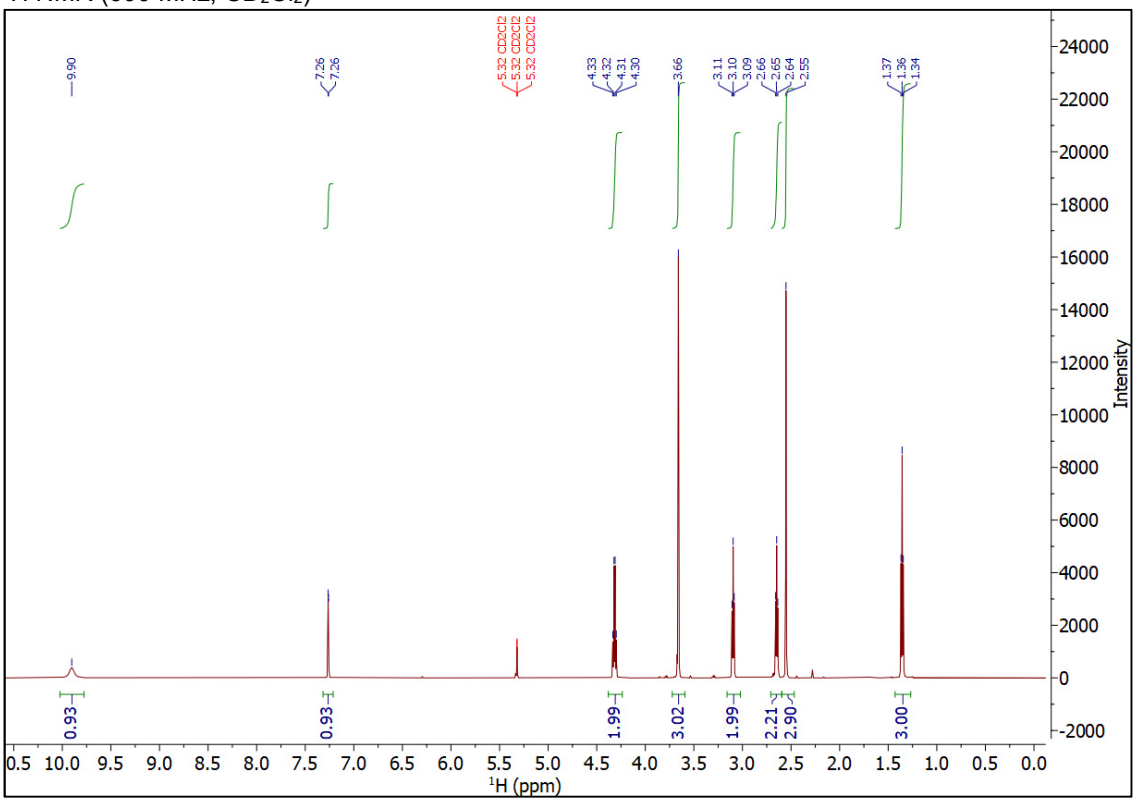


^{13}C NMR (151 MHz, $CDCl_3$)

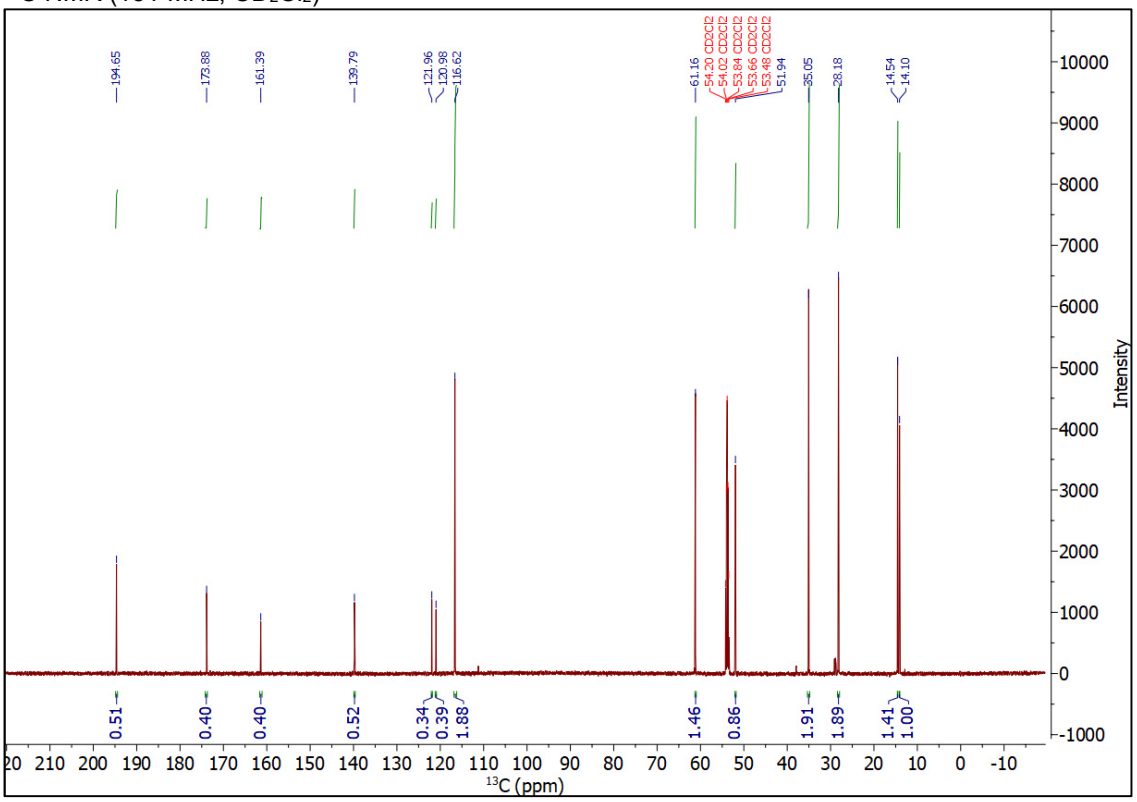


Ethyl 4-(4-methoxy-4-oxobutanoyl)-5-methyl-1*H*-pyrrole-2-carboxylate (**III-151**)

^{1}H NMR (600 MHz, CD_2Cl_2)

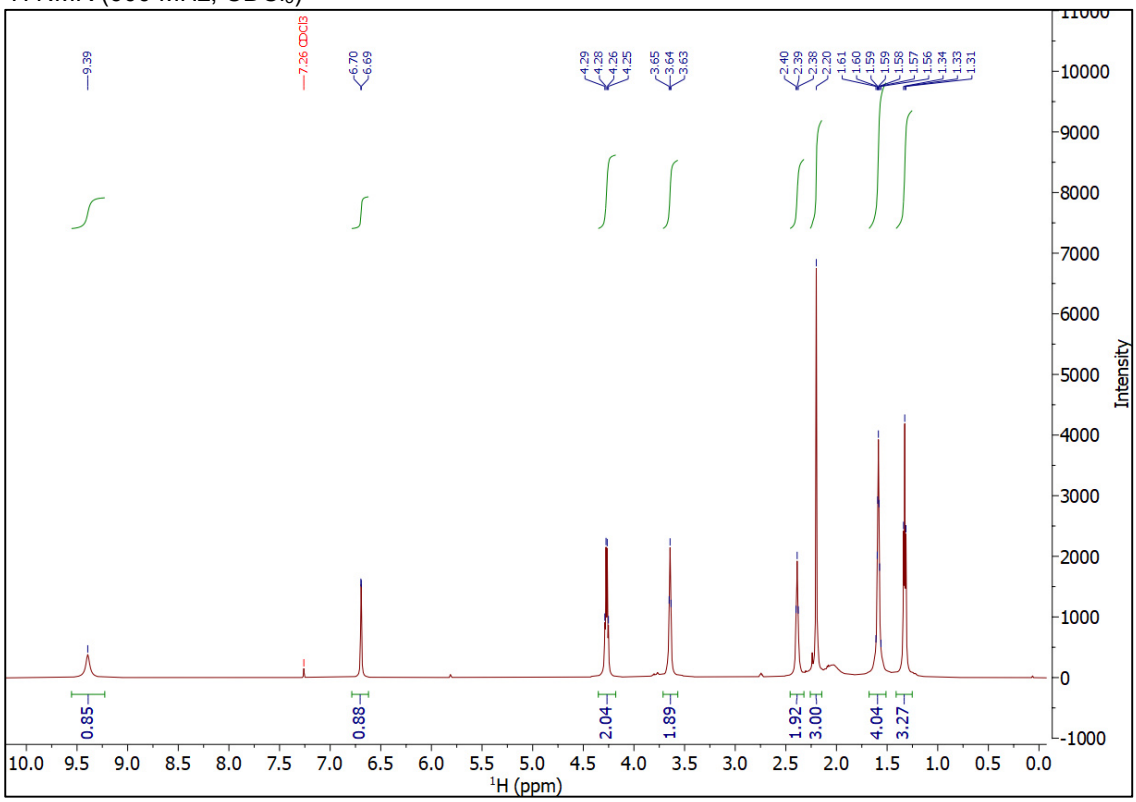


^{13}C NMR (151 MHz, CD_2Cl_2)

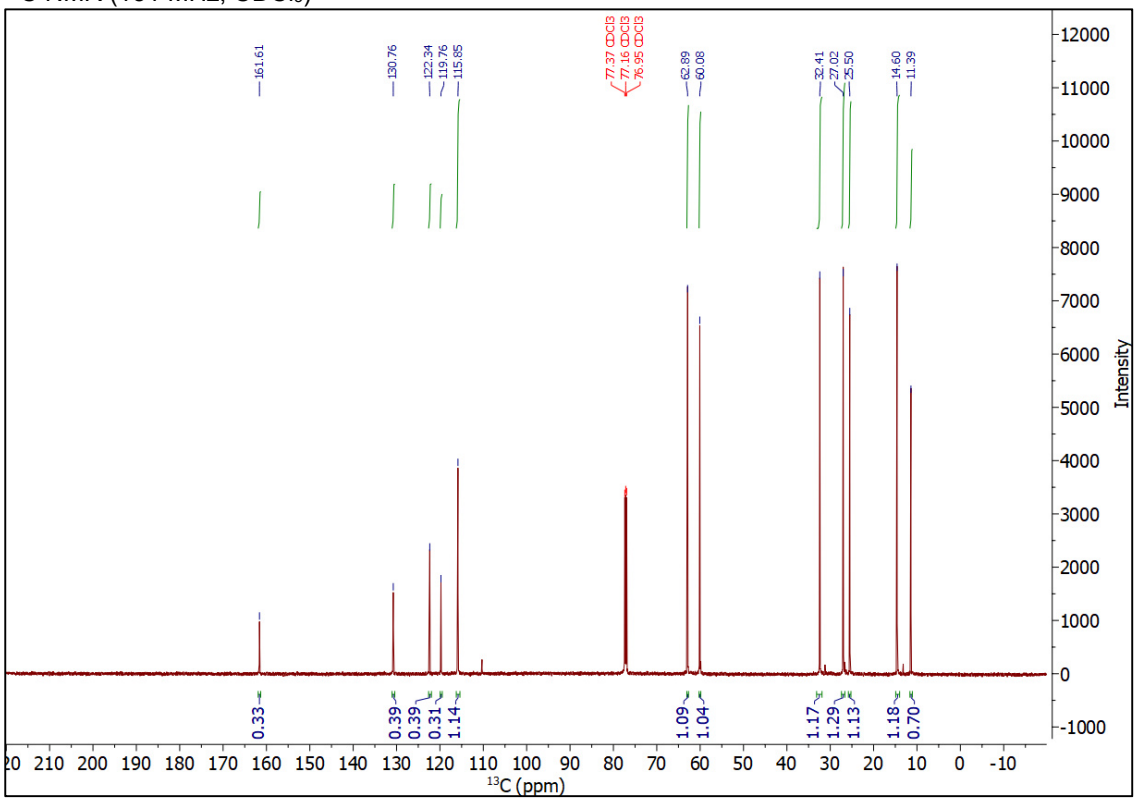


Ethyl 4-(4-hydroxybutyl)-5-methyl-1*H*-pyrrole-2-carboxylate (**III-152**)

^{1}H NMR (600 MHz, $CDCl_3$)

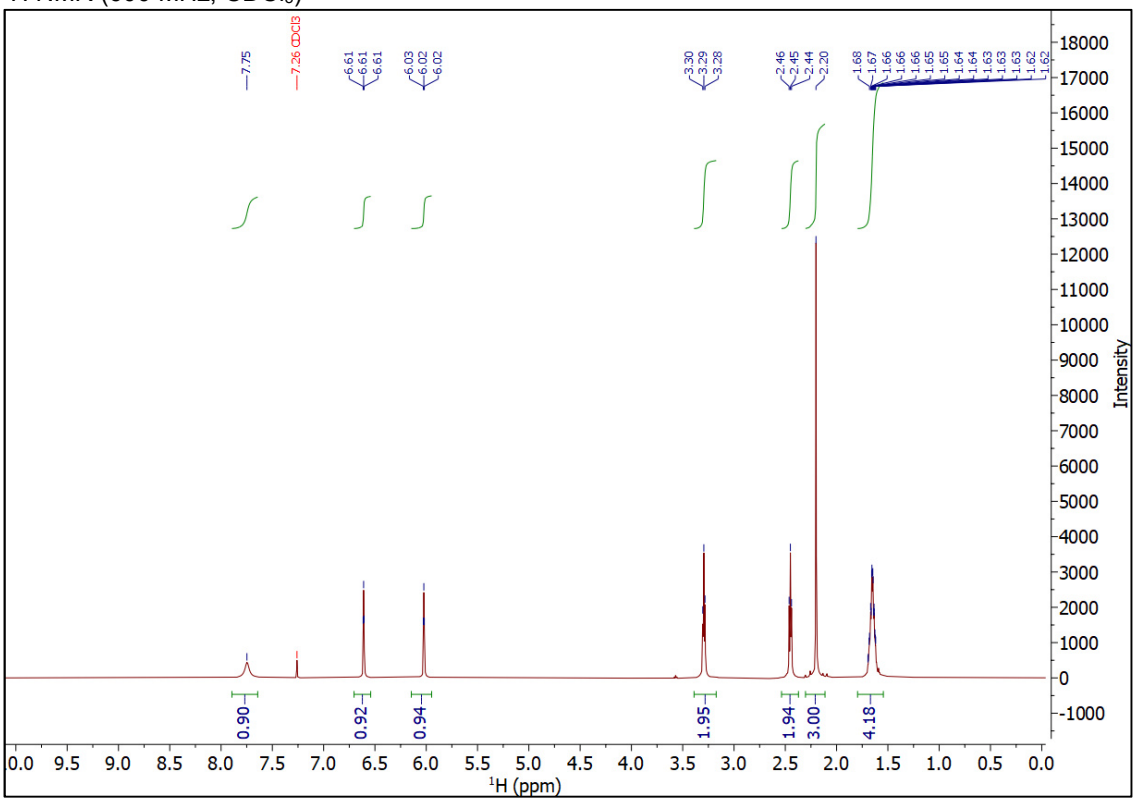


^{13}C NMR (151 MHz, $CDCl_3$)

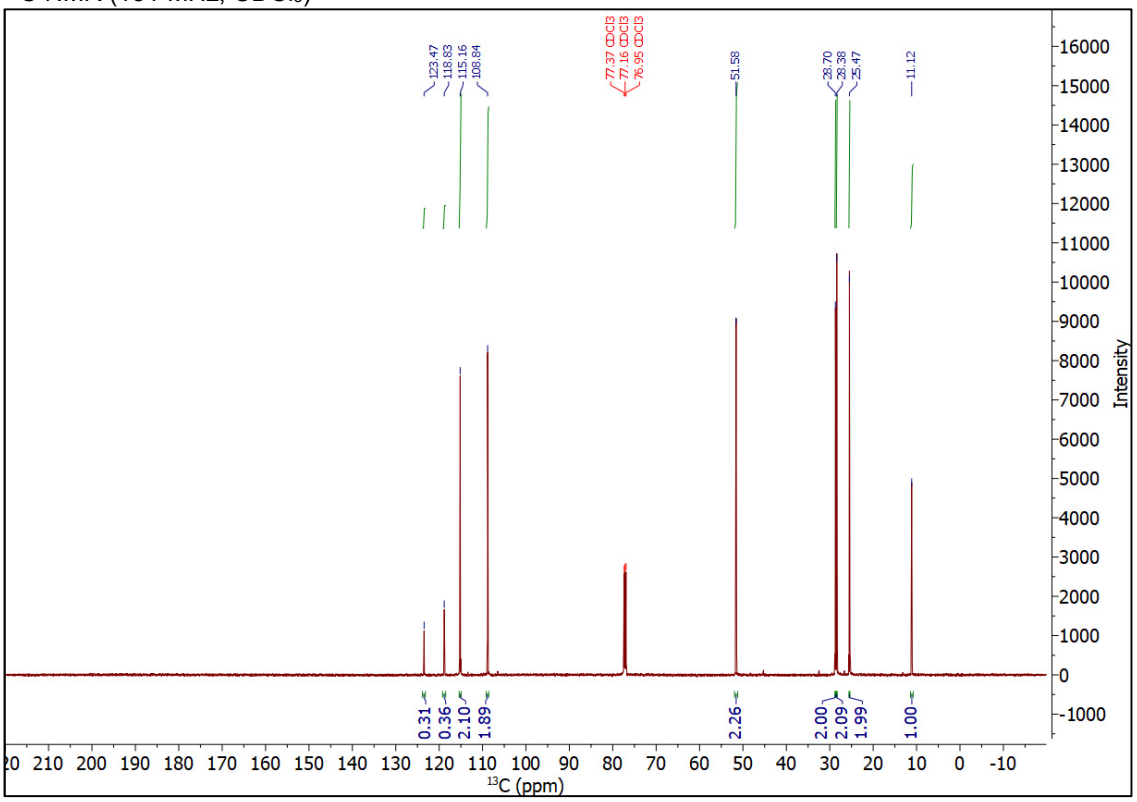


3-(4-Azidobutyl)-2-methyl-1*H*-pyrrole (**III-155**)

^{1}H NMR (600 MHz, $CDCl_3$)

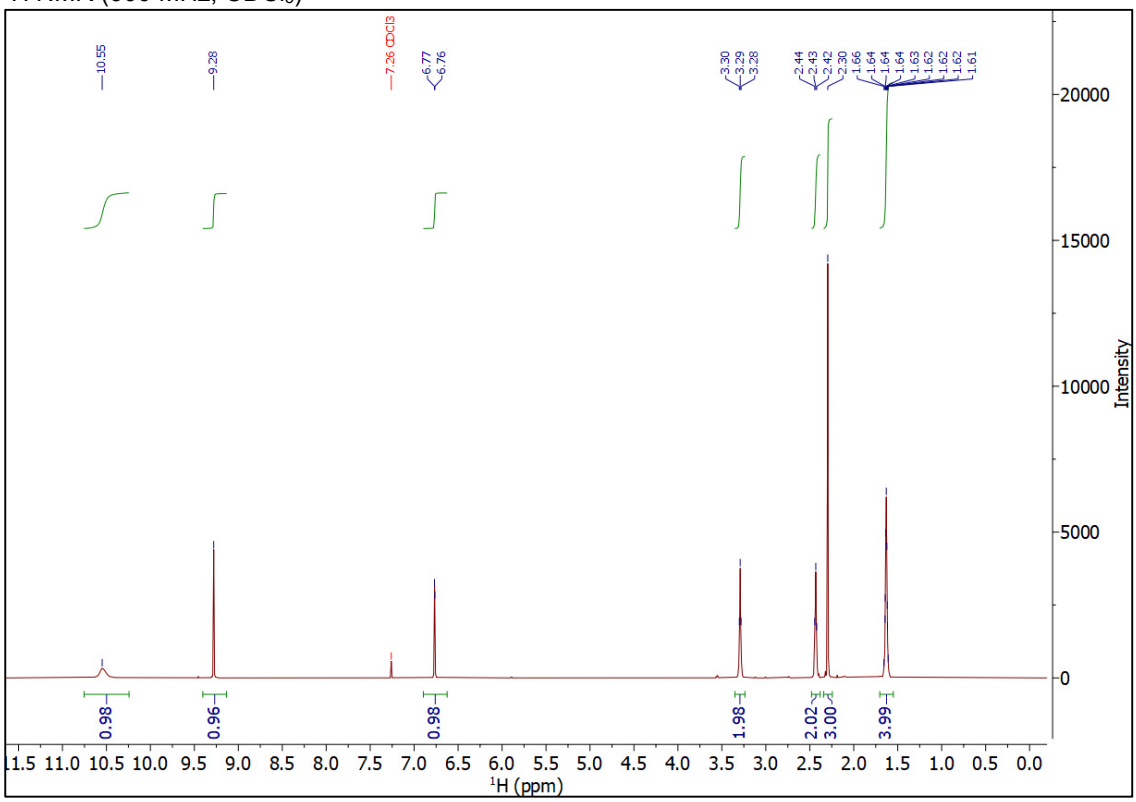


^{13}C NMR (151 MHz, $CDCl_3$)

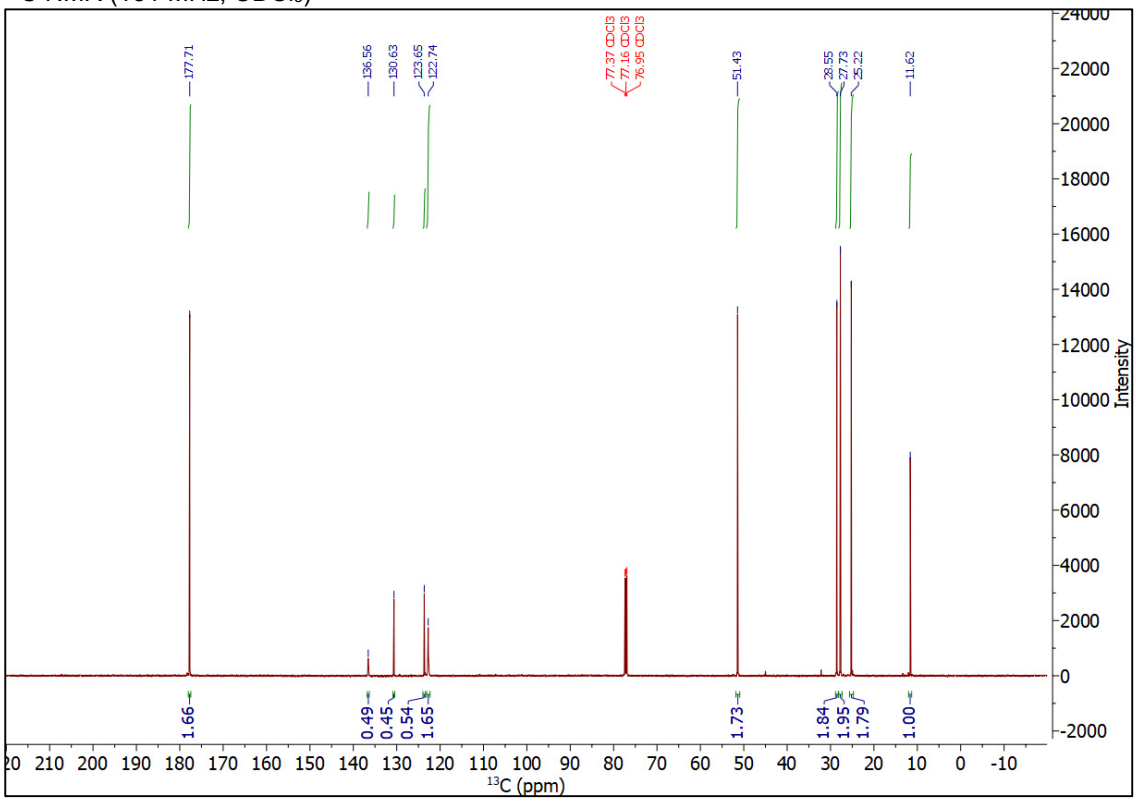


4-(4-Azidobutyl)-5-methyl-1*H*-pyrrole-2-carbaldehyde (**III-156**)

^{1}H NMR (600 MHz, $CDCl_3$)

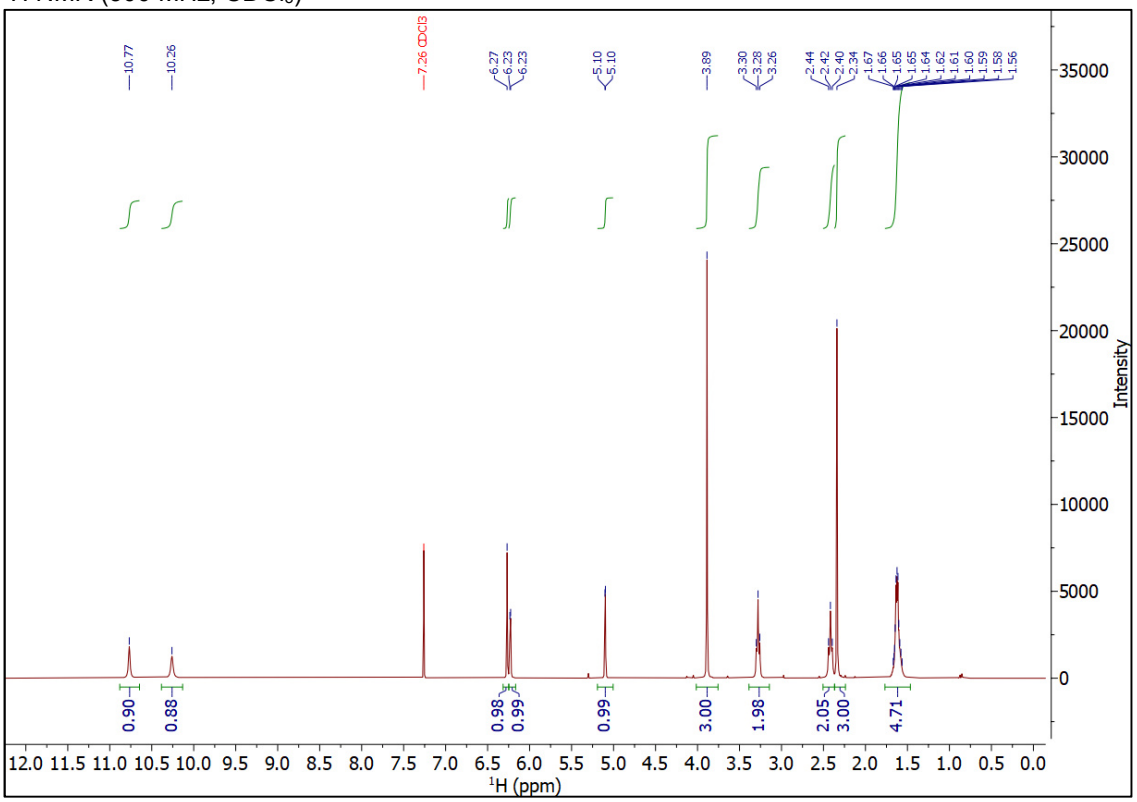


^{13}C NMR (151 MHz, $CDCl_3$)

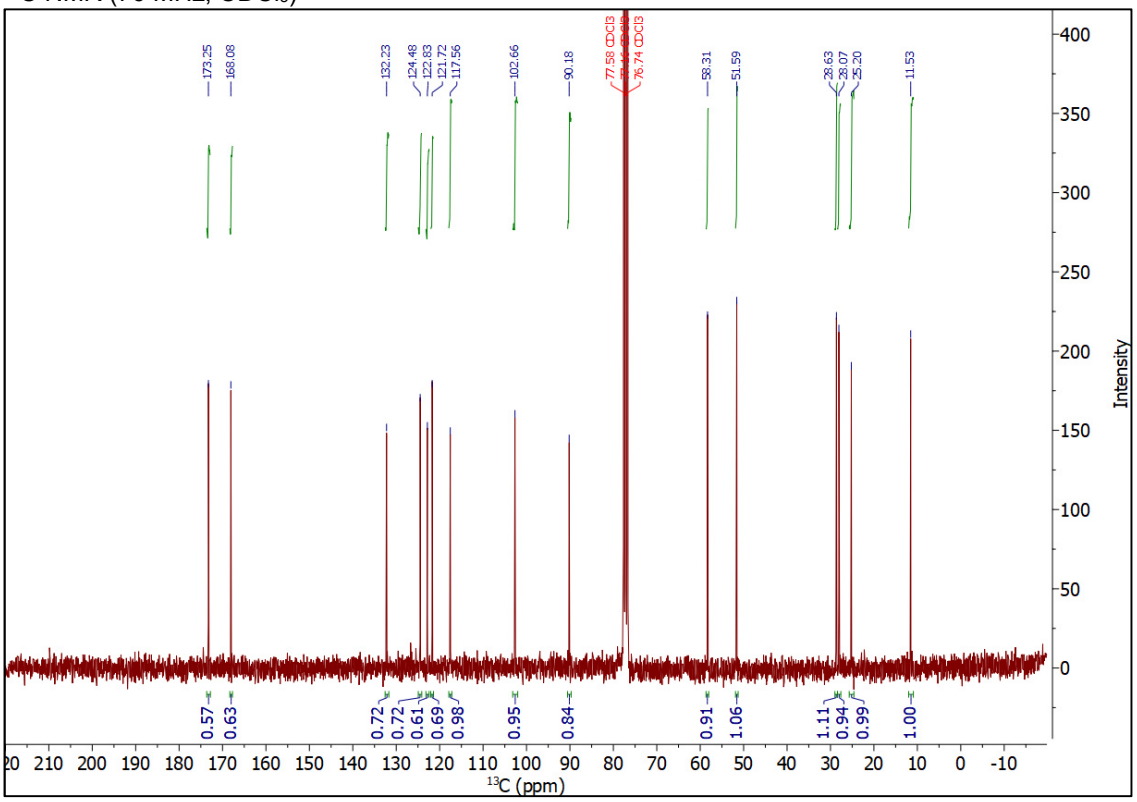


(*Z*)-5-((4-(4-Azidobutyl)-5-methyl-1*H*-pyrrol-2-yl)methylene)-4-methoxy-1,5-dihydro-2*H*-pyrrol-2-one (**III-157**)

^{1}H NMR (300 MHz, $CDCl_3$)

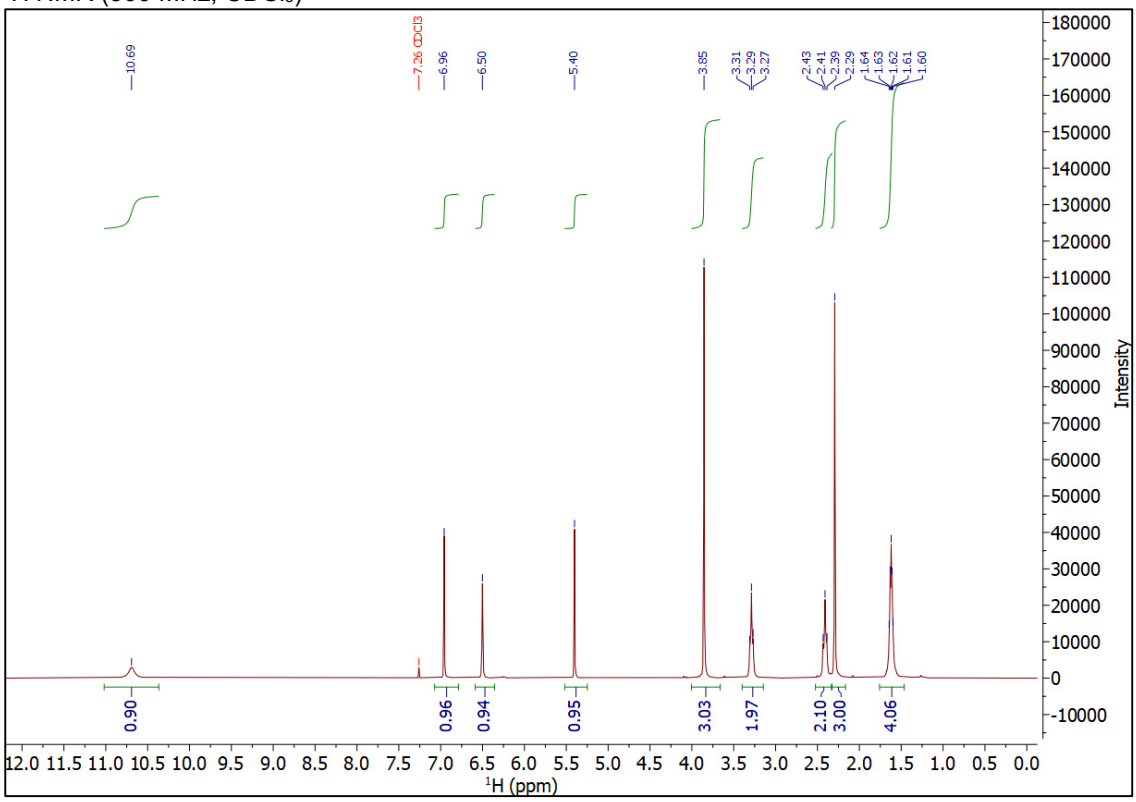


^{13}C NMR (76 MHz, $CDCl_3$)

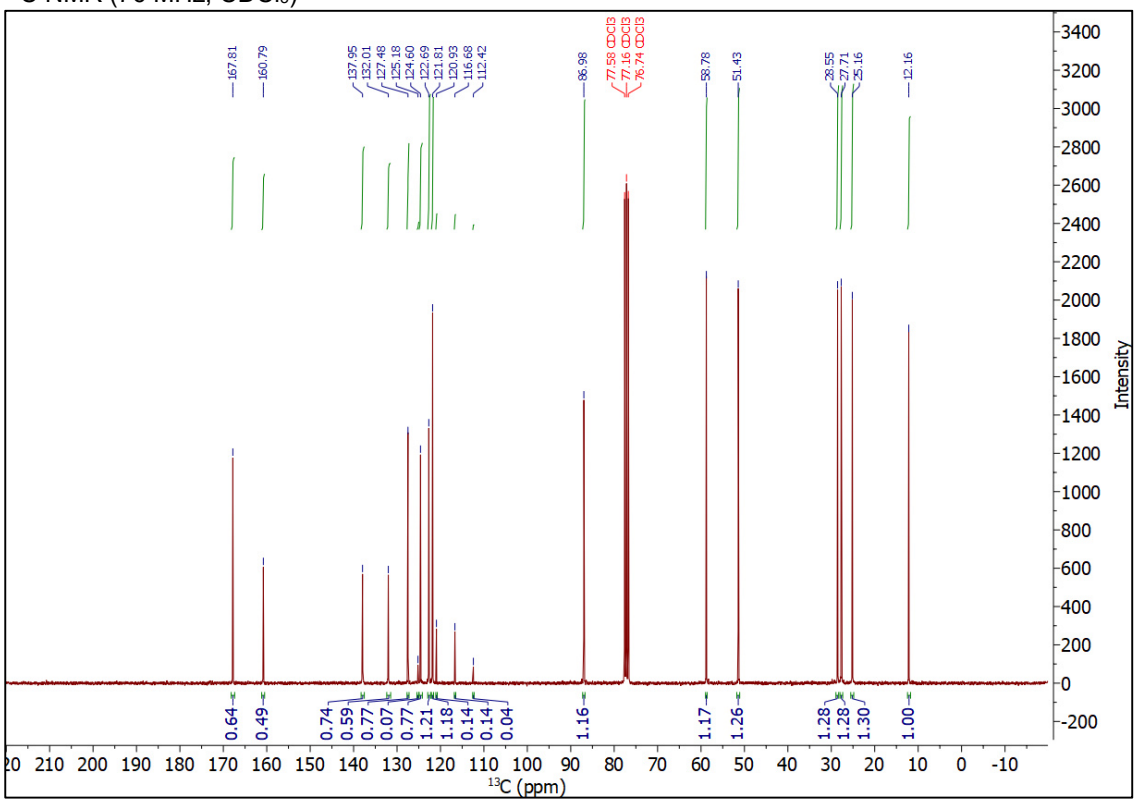


(*Z*)-5-((4-(4-Azidobutyl)-5-methyl-2*H*-pyrrol-2-ylidene)methyl)-4-methoxy-1*H*-pyrrol-2-yl trifluoromethanesulfonate (**III-158**)

^{1}H NMR (300 MHz, $CDCl_3$)

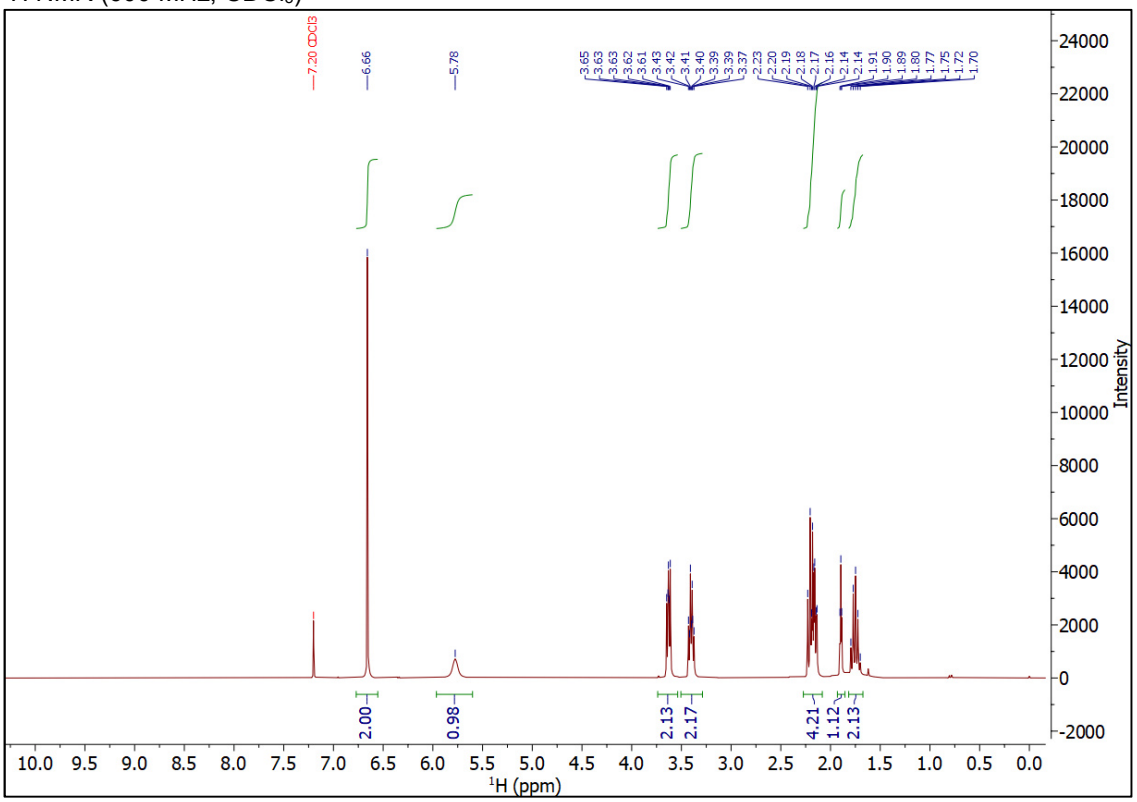


^{13}C NMR (76 MHz, $CDCl_3$)

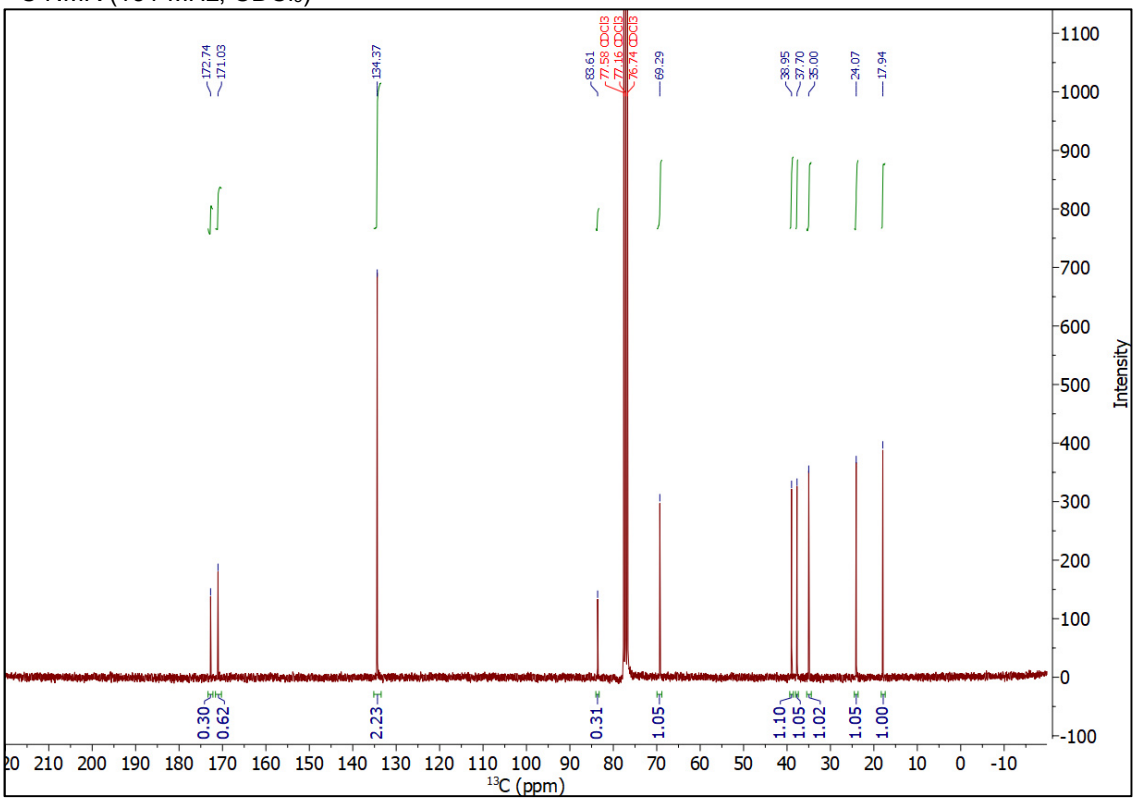


N-(2-(2,5-Dioxo-2,5-dihydro-1*H*-pyrrol-1-yl)ethyl)hex-5-ynamide (**III-159**)

^{1}H NMR (600 MHz, $CDCl_3$)

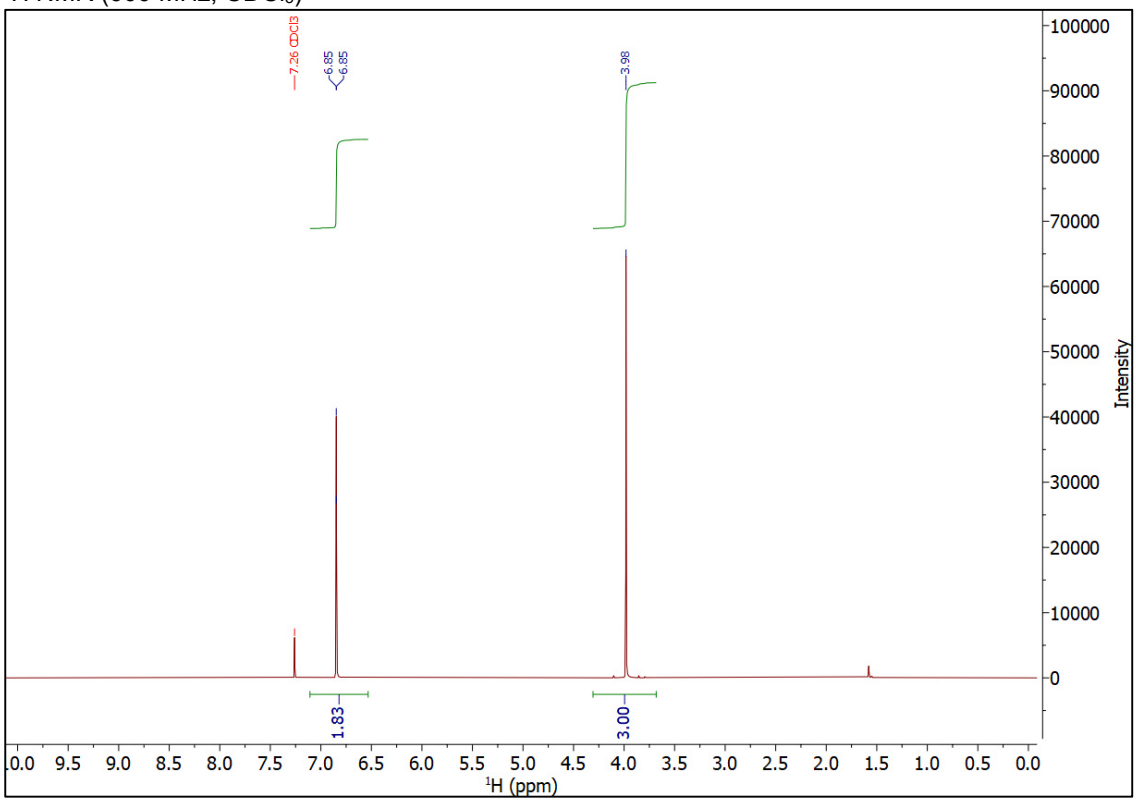


^{13}C NMR (151 MHz, $CDCl_3$)

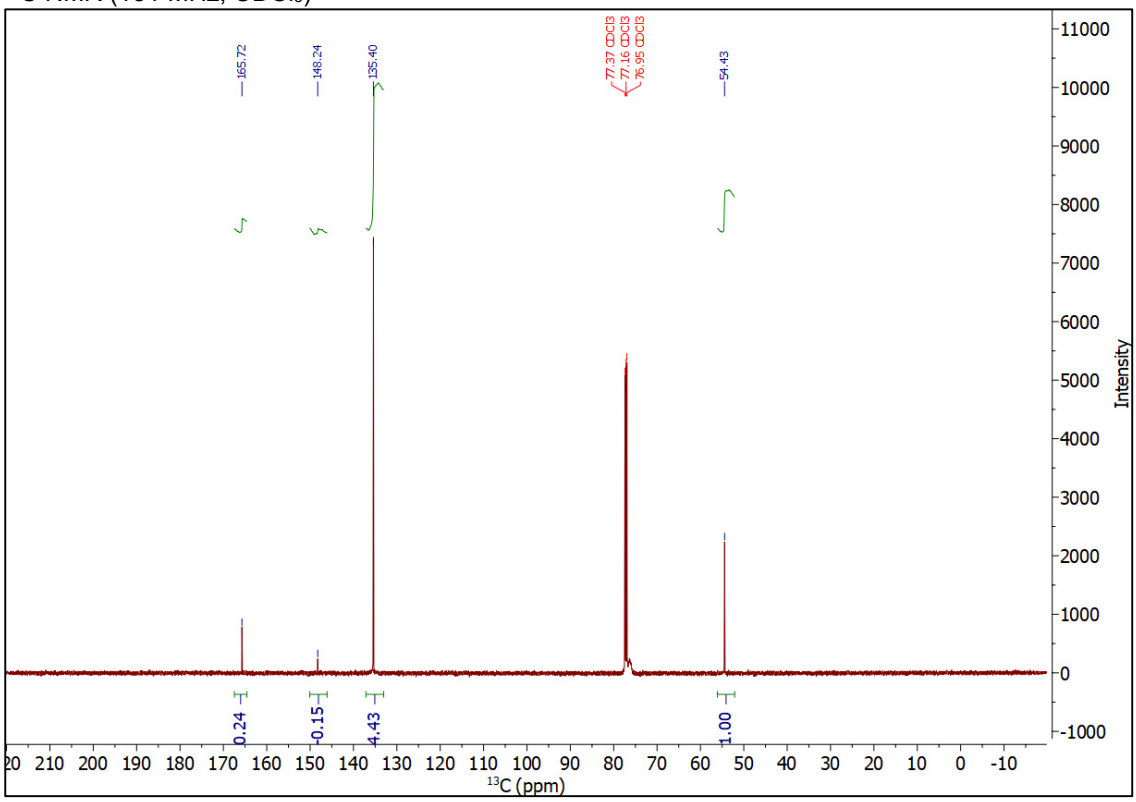


Methyl 2,5-dioxo-2,5-dihydro-1*H*-pyrrole-1-carboxylate (**III-161**)

^{1}H NMR (600 MHz, $CDCl_3$)

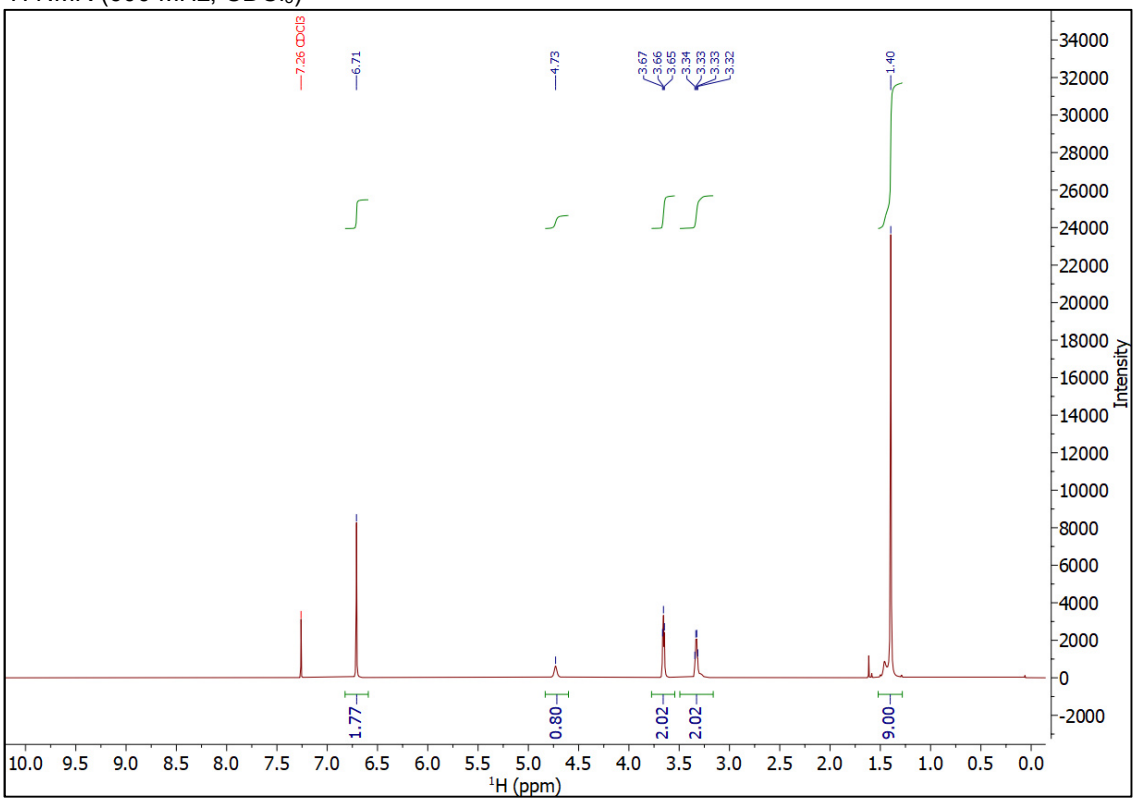


^{13}C NMR (151 MHz, $CDCl_3$)

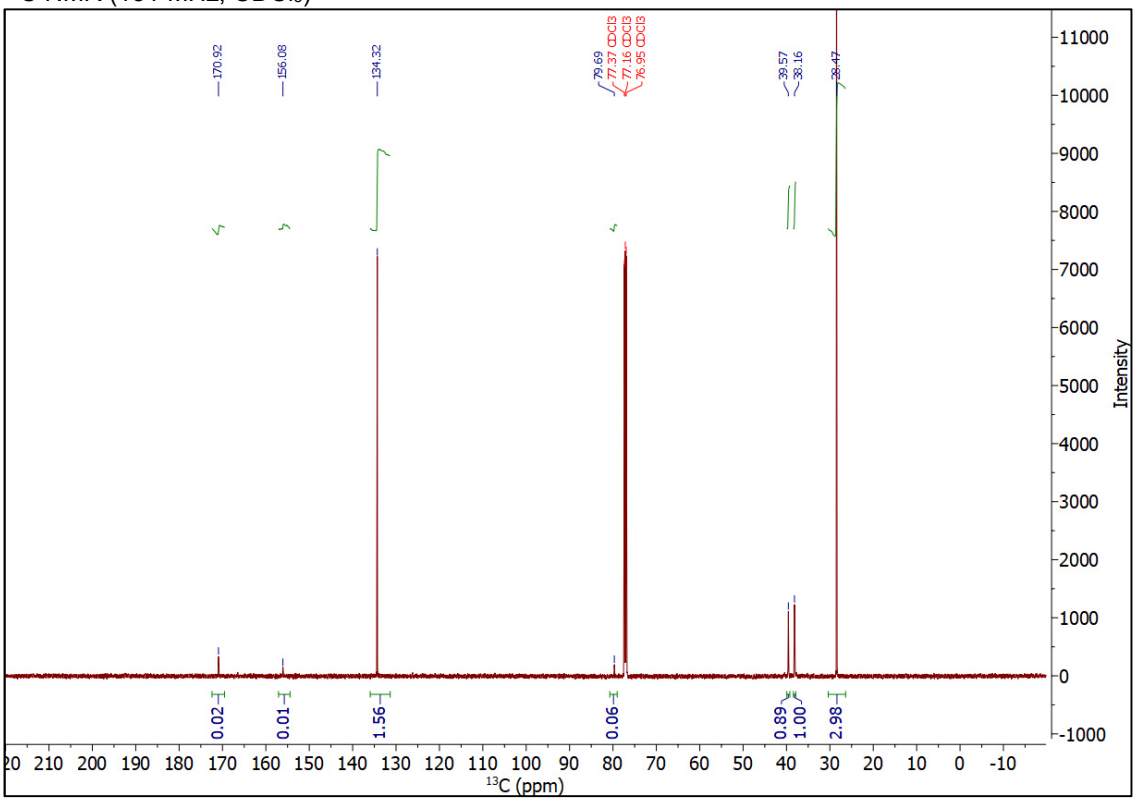


tert-Butyl (2-(2,5-dioxo-2,5-dihydro-1*H*-pyrrol-1-yl)ethyl)carbamate (**III-164**)

^{1}H NMR (600 MHz, $CDCl_3$)

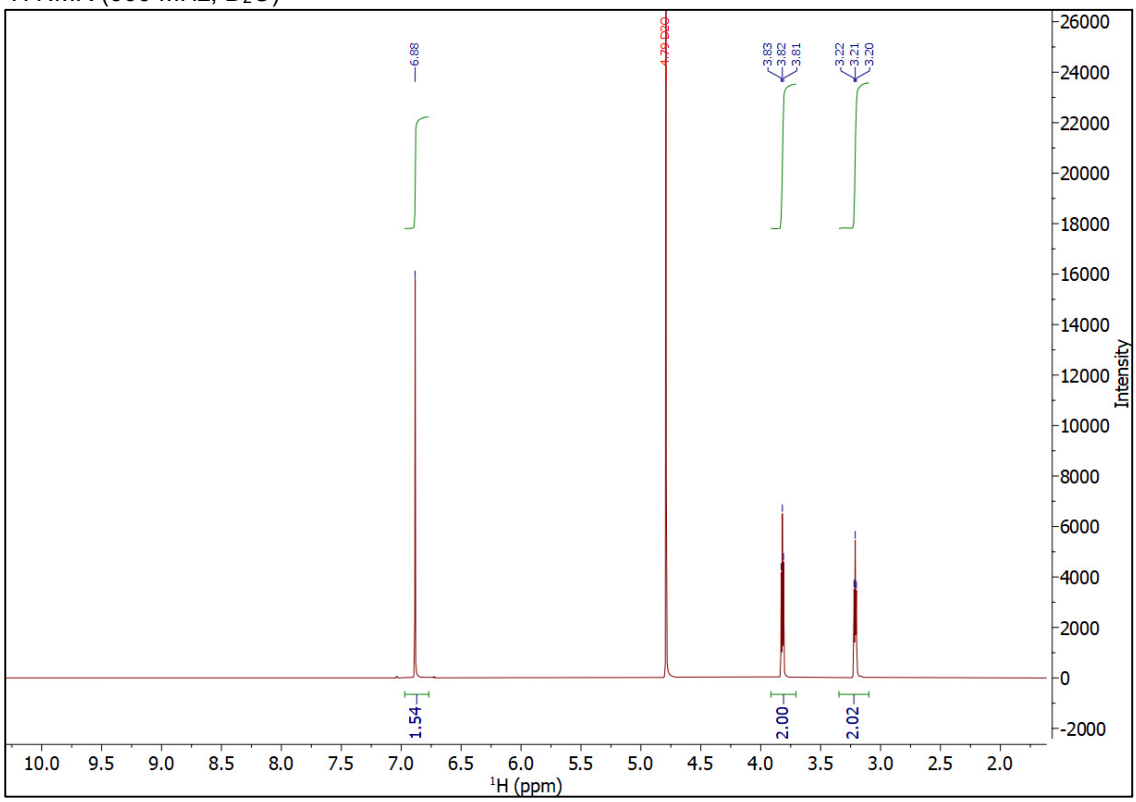


^{13}C NMR (151 MHz, $CDCl_3$)

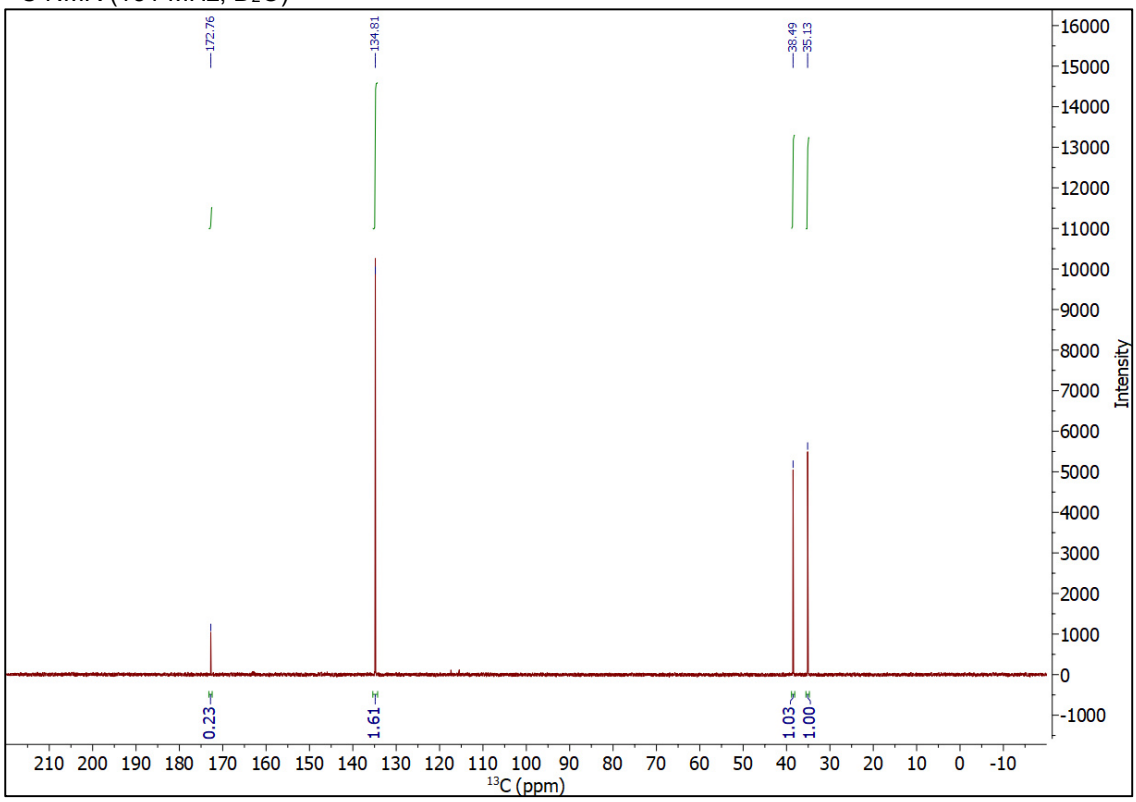


2-(2,5-Dioxo-2,5-dihydro-1*H*-pyrrol-1-yl)ethan-1-aminium 2,2,2-trifluoroacetate (**III-165**)

^{1}H NMR (600 MHz, D_2O)

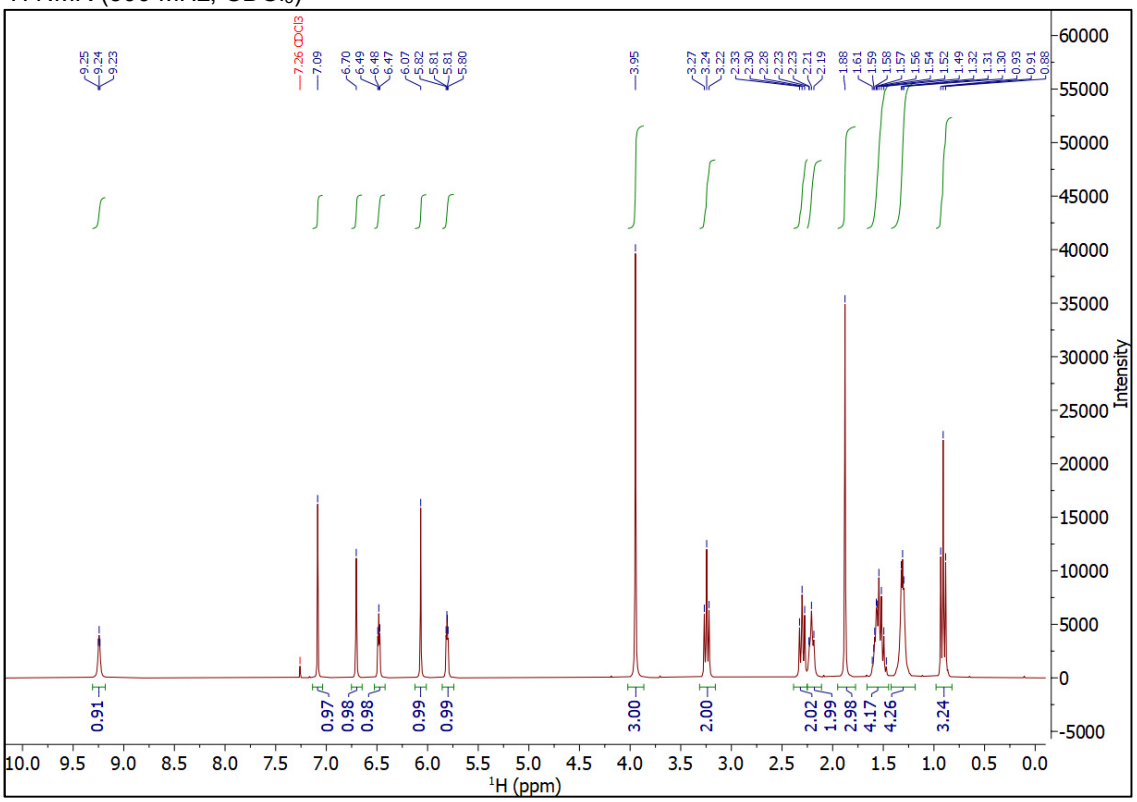


^{13}C NMR (151 MHz, D_2O)

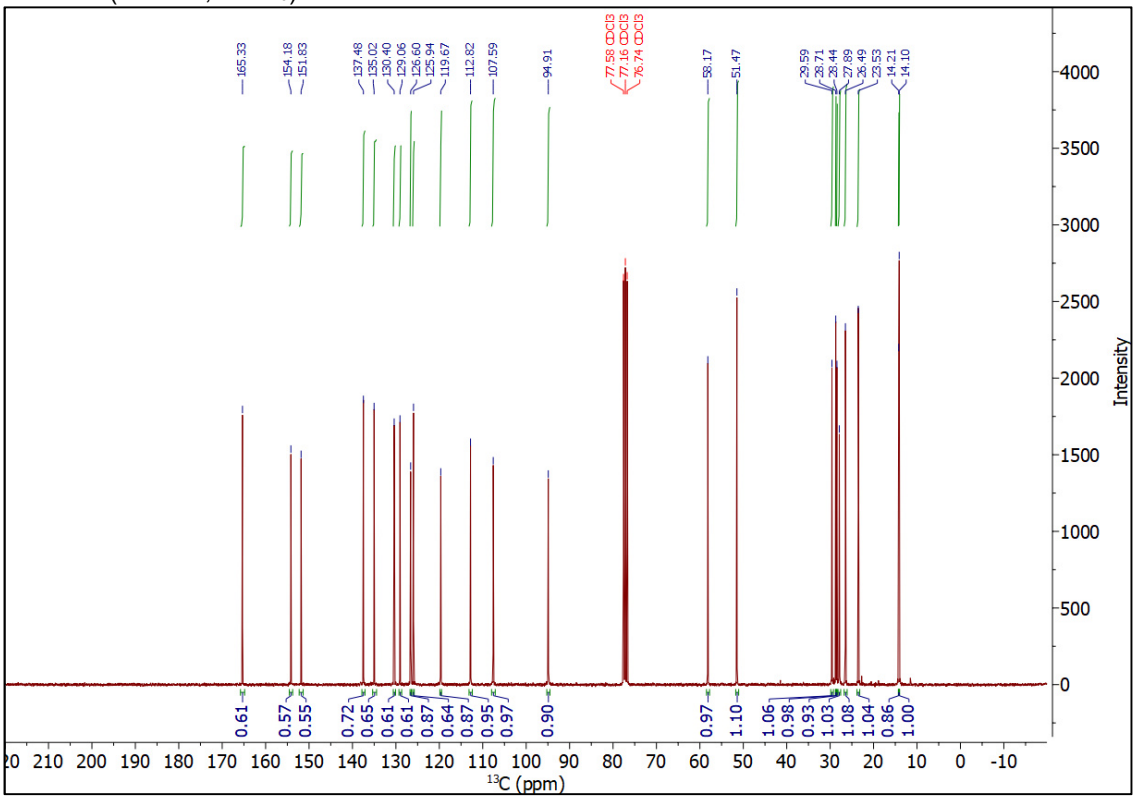


Prodigiosin A-Ring Azide Zinc Complex (**III-166**)

^{1}H NMR (300 MHz, $CDCl_3$)

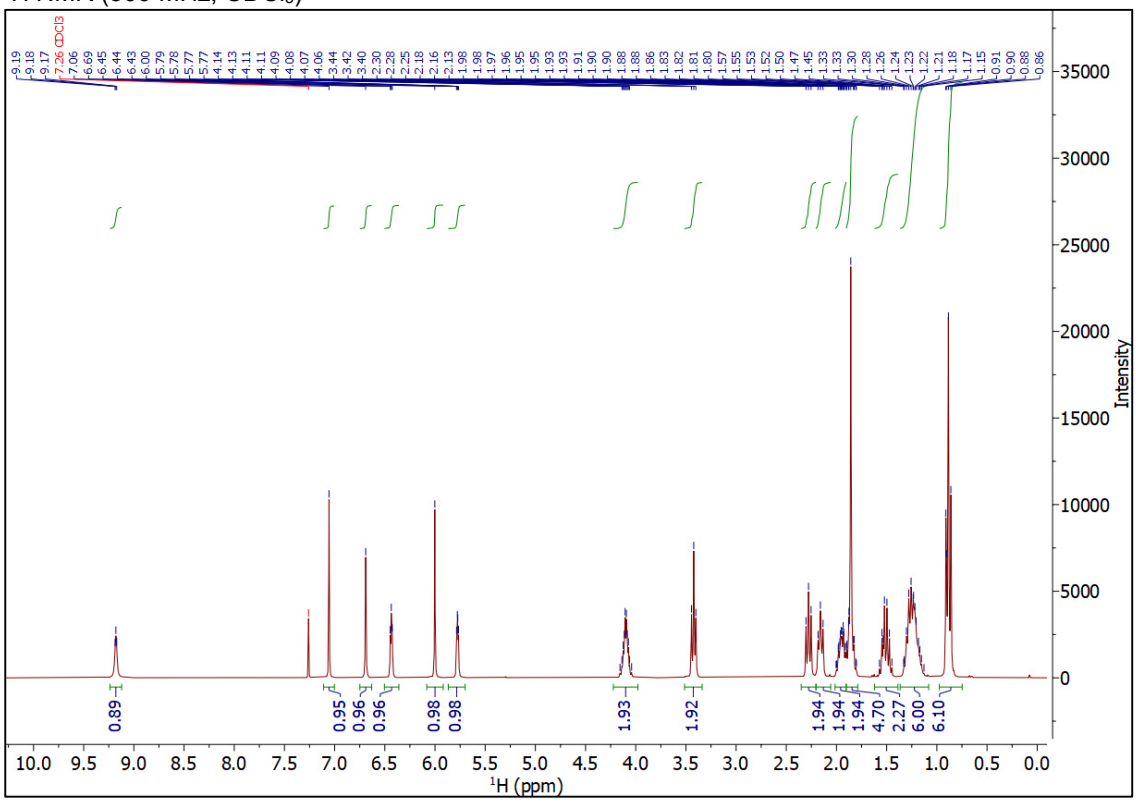


^{13}C NMR (76 MHz, $CDCl_3$)

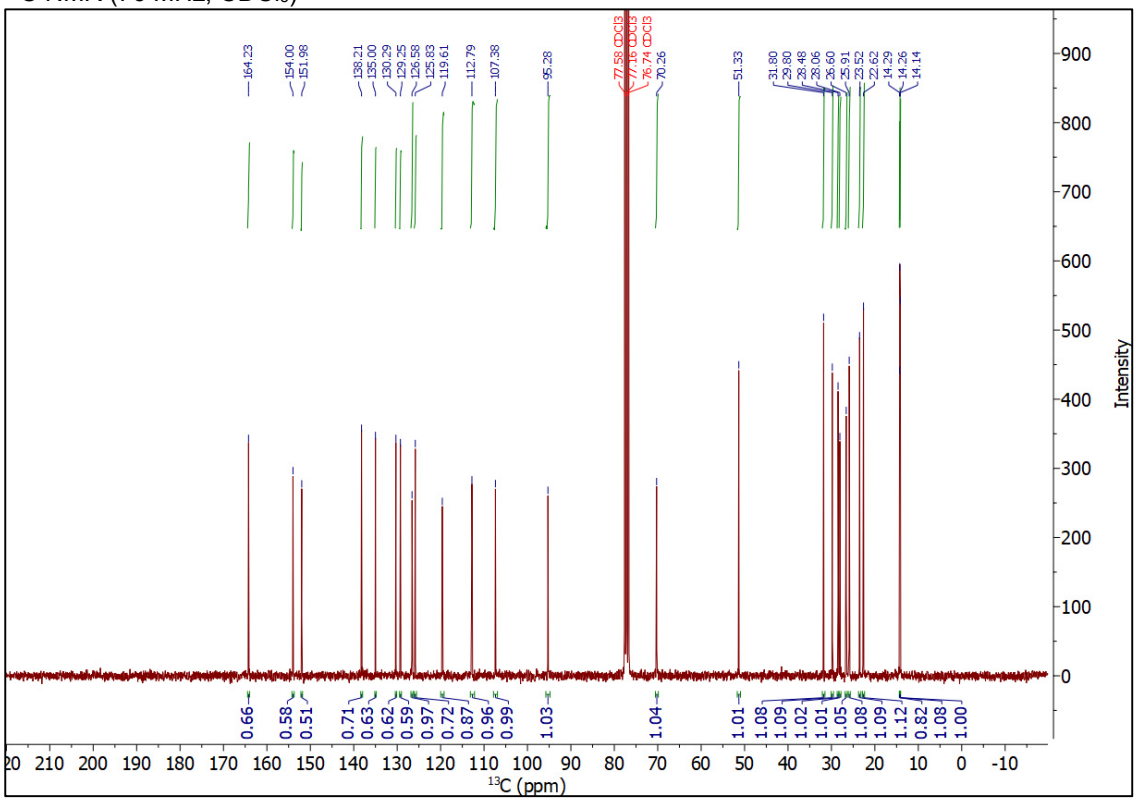


Prodigiosin B-Ring Azide Zinc Complex (**III-167**)

^{1}H NMR (300 MHz, $CDCl_3$)

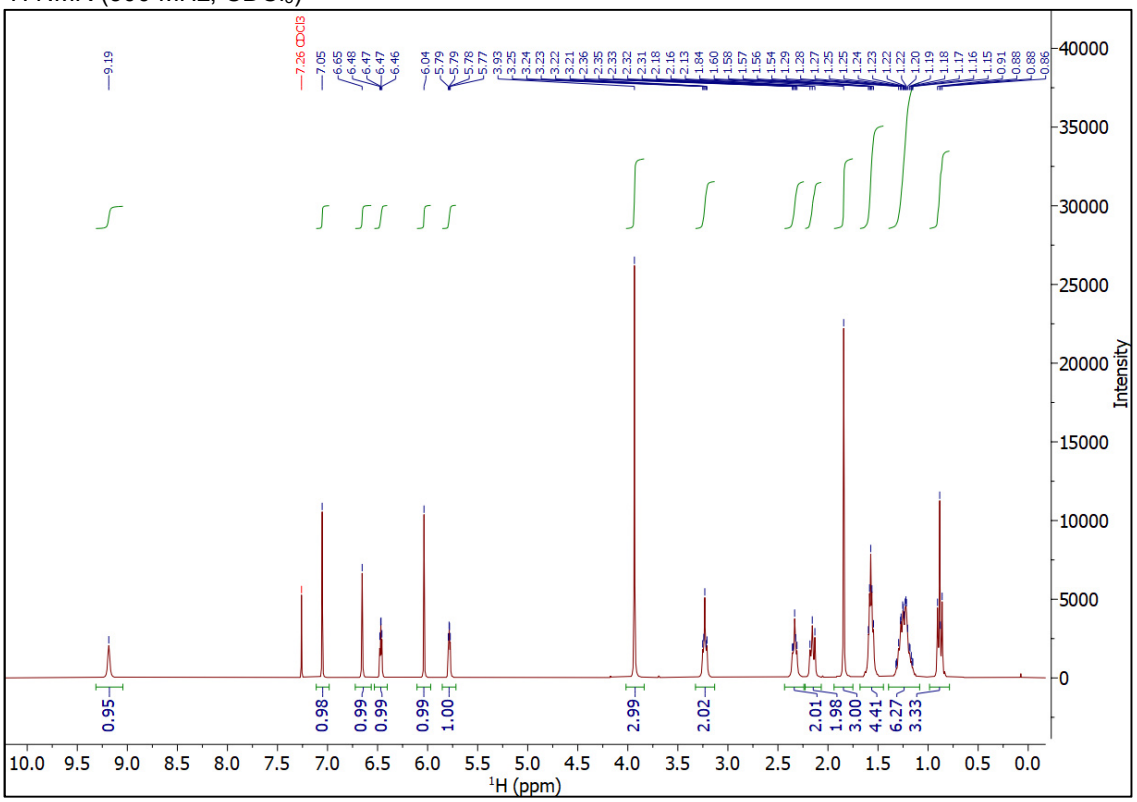


^{13}C NMR (76 MHz, $CDCl_3$)

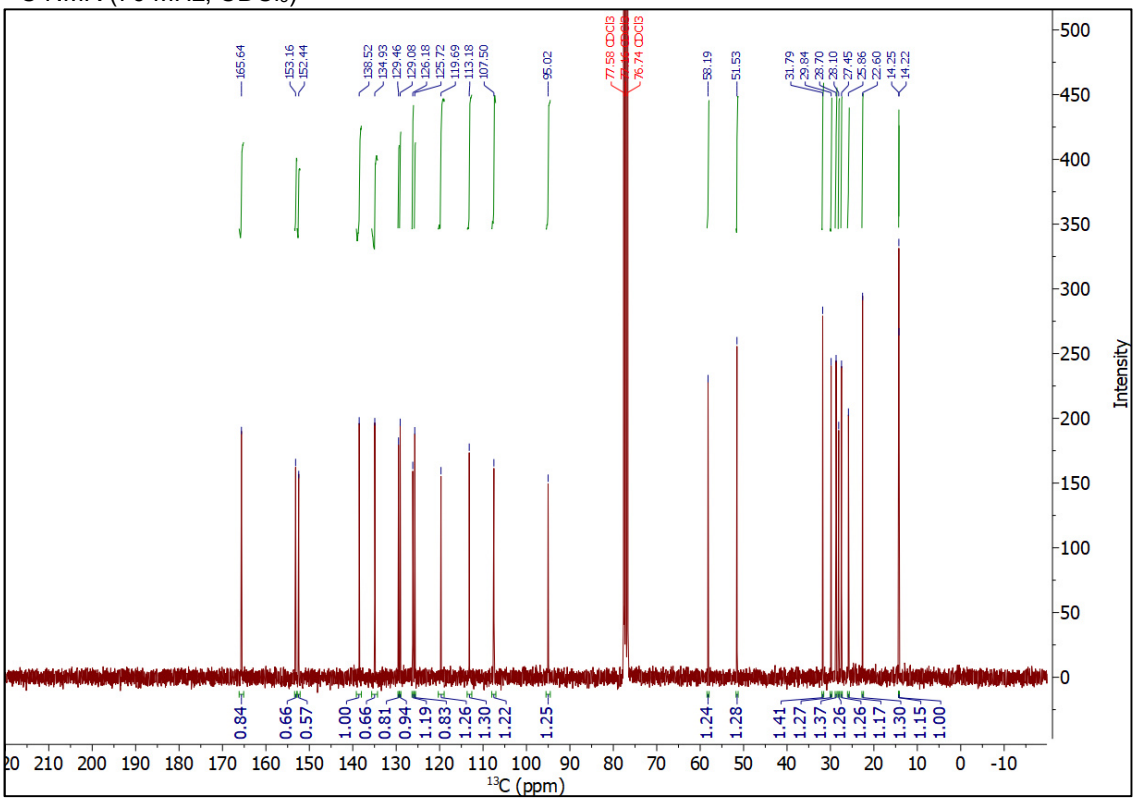


Prodigiosin C-Ring Azide Zinc Complex (**III-168**)

^{1}H NMR (300 MHz, $CDCl_3$)

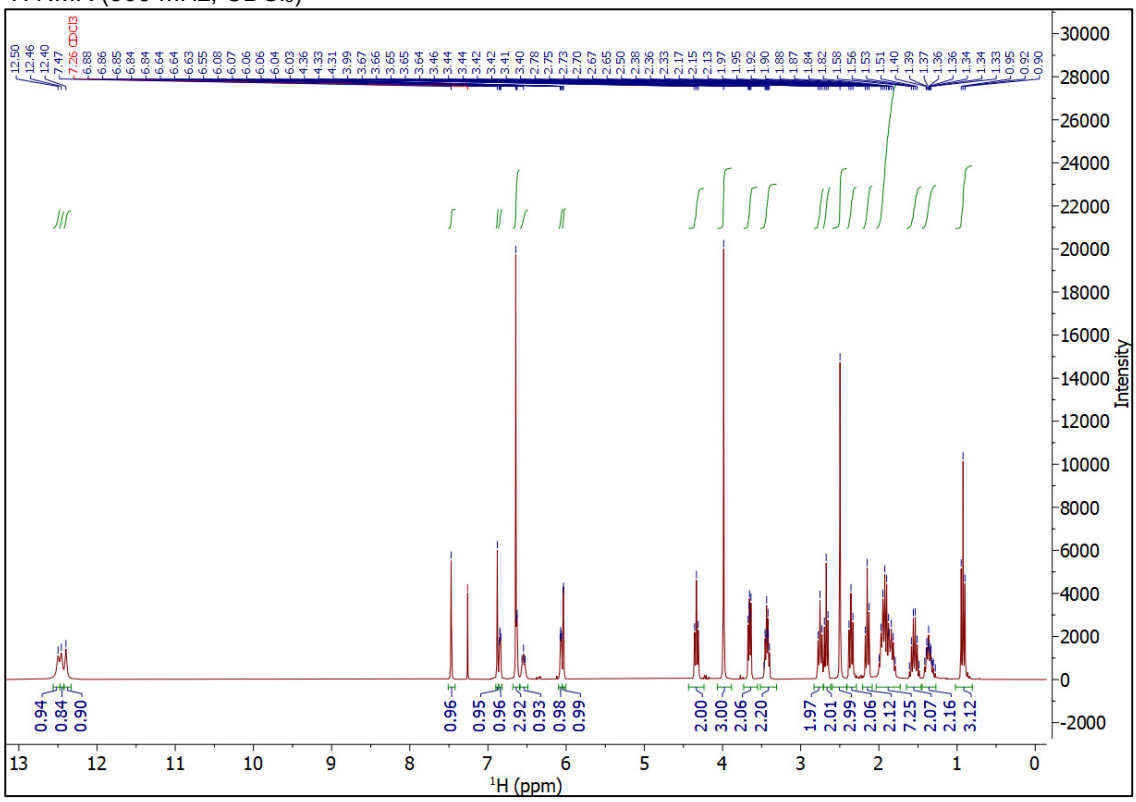


^{13}C NMR (76 MHz, $CDCl_3$)

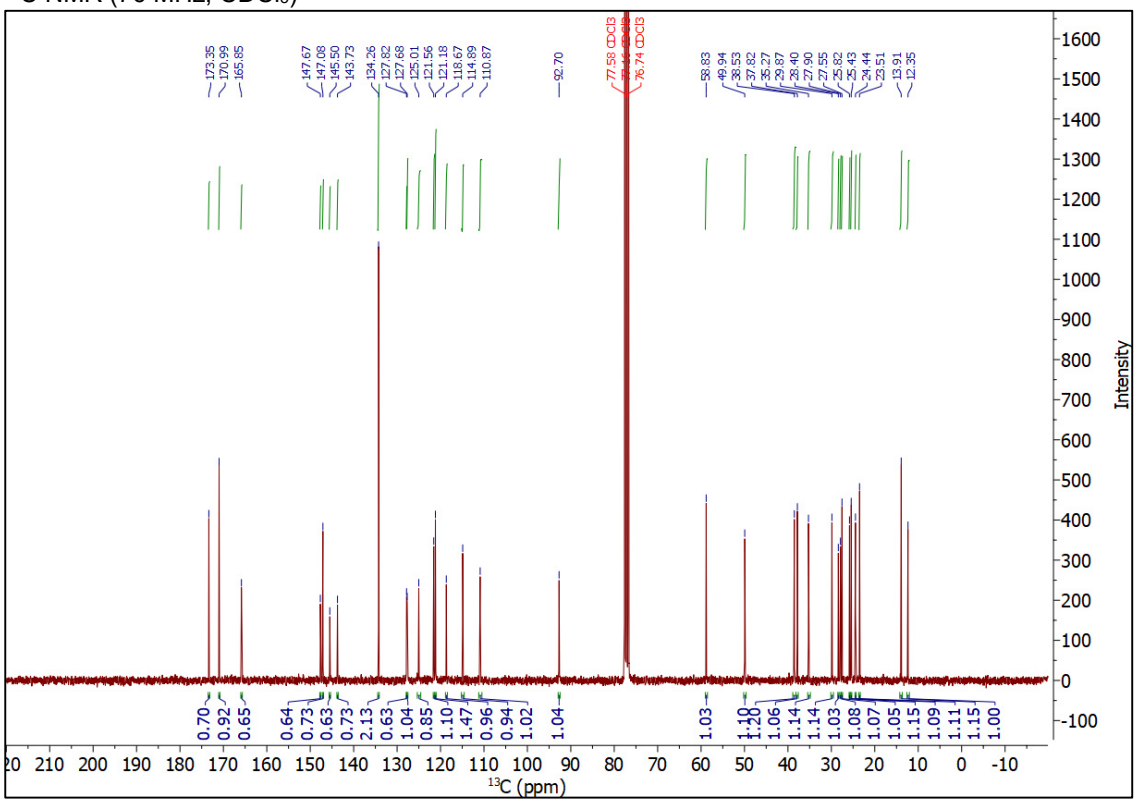


(*Z*)-5-(5-(4-(4-((2-(2,5-Dioxo-2,5-dihydro-1*H*-pyrrol-1-yl)ethyl)amino)-4-oxobutyl)-1*H*-1,2,3-triazol-1-yl)pentyl)-4'-methoxy-5'-((5-methyl-4-propyl-1*H*-pyrrol-2-yl)methylene)-1*H*,5'*H*-[2,2'-bipyrrol]-1'-ium chloride (**III-169·HCl**)

^{1}H NMR (300 MHz, $CDCl_3$)

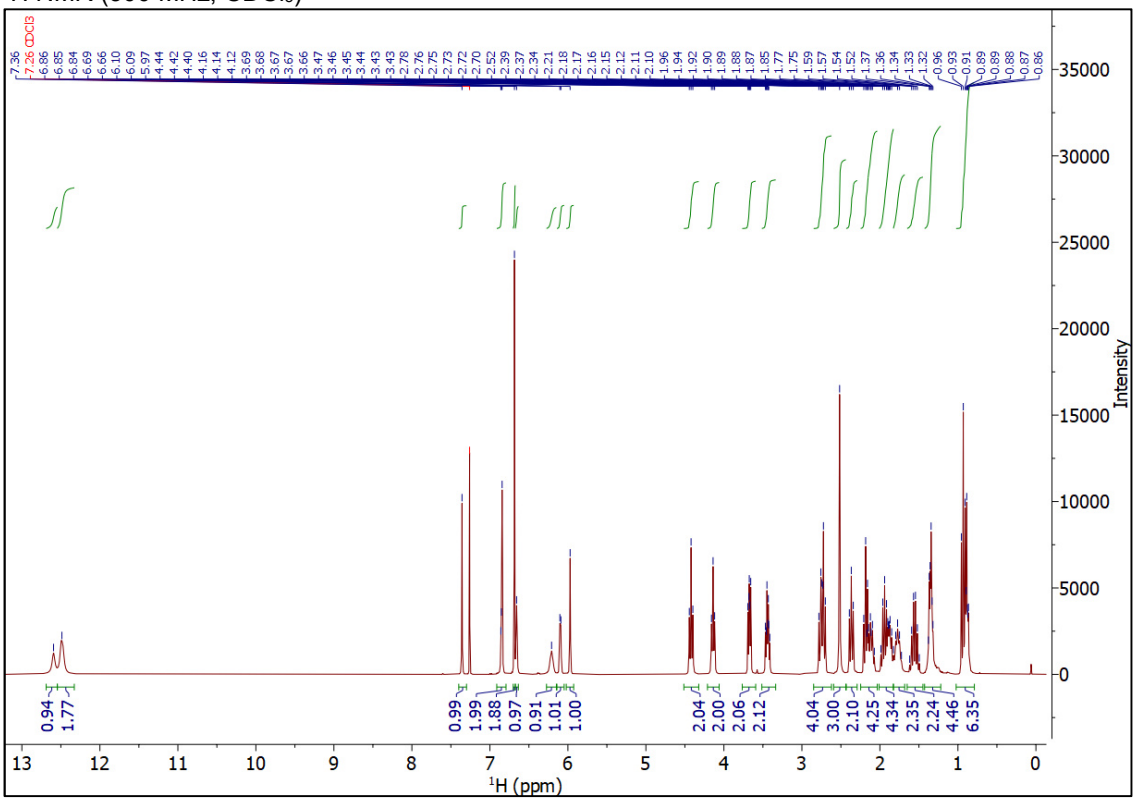


^{13}C NMR (76 MHz, $CDCl_3$)

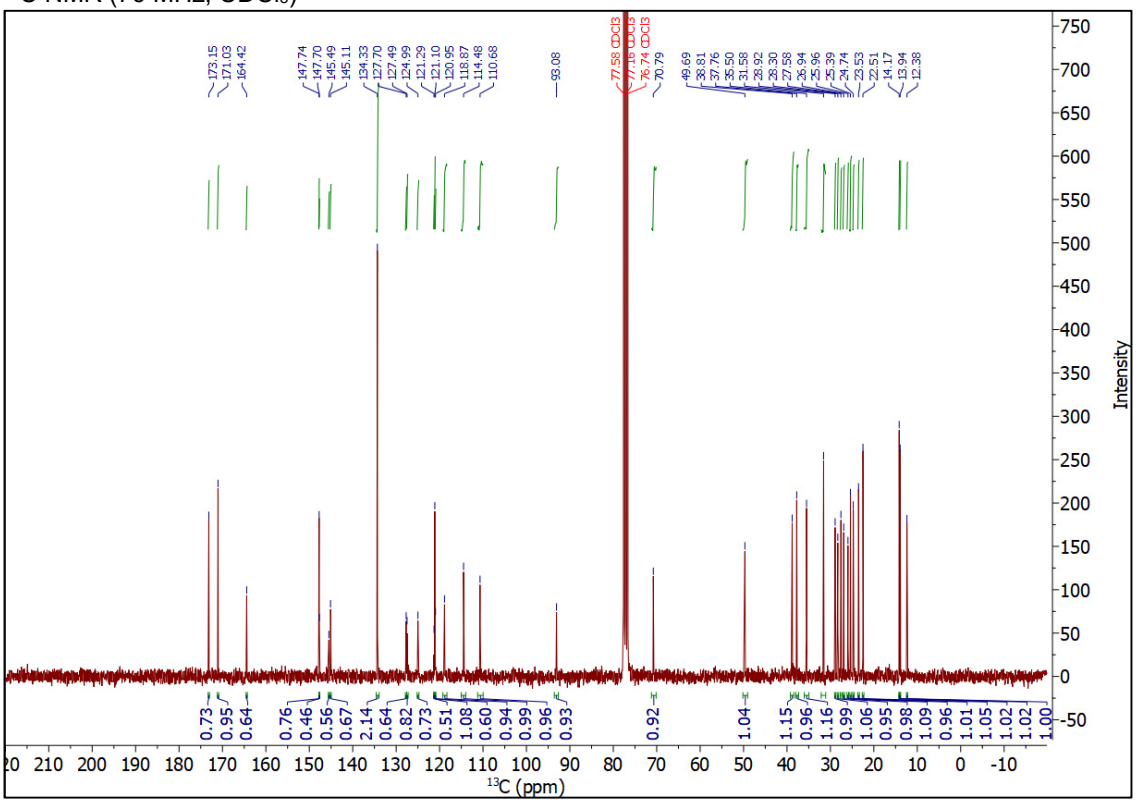


(*Z*)-4'-(4-(4-(4-((2-(2,5-Dioxo-2,5-dihydro-1*H*-pyrrol-1-yl)ethyl)amino)-4-oxobutyl)-1*H*-1,2,3-triazol-1-yl)butoxy)-5'-((5-methyl-4-propyl-1*H*-pyrrol-2-yl)methylene)-5-pentyl-1*H*,5'*H*-[2,2'-bipyrrol]-1'-ium chloride (**III-170·HCl**)

^{1}H NMR (300 MHz, $CDCl_3$)

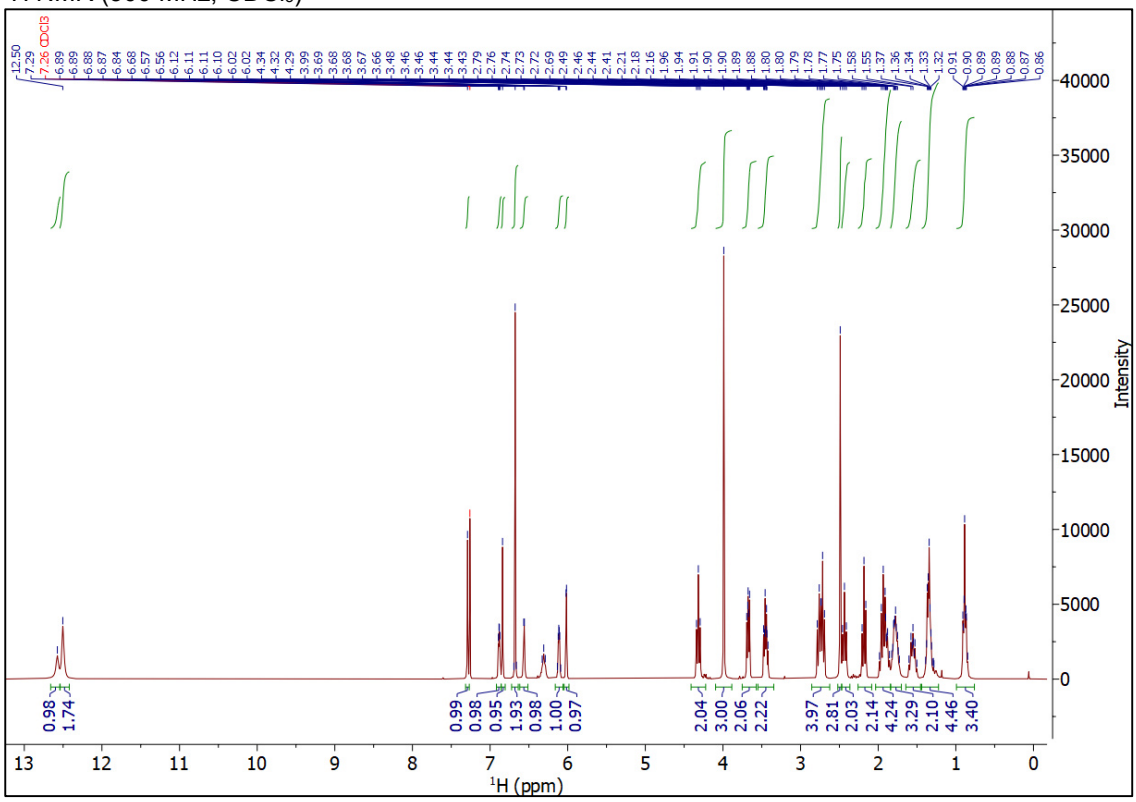


^{13}C NMR (76 MHz, $CDCl_3$)

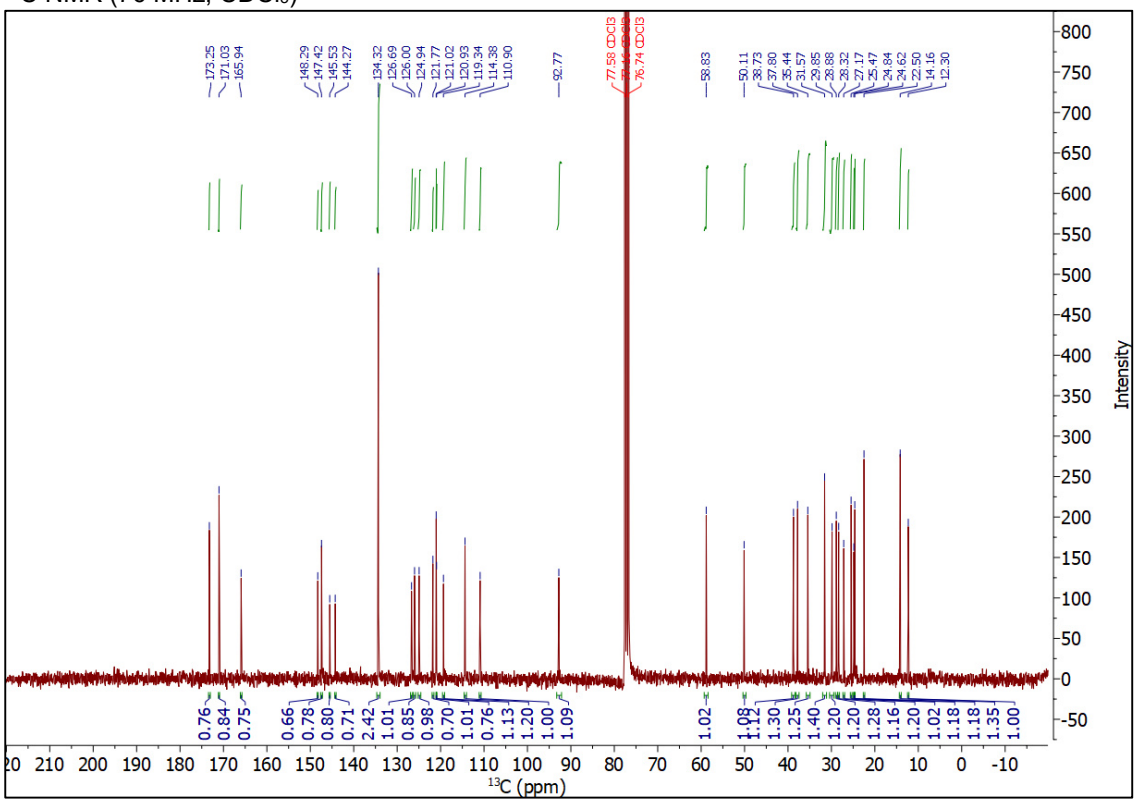


(*Z*)-5'-((4-(4-(4-(4-((2-(2,5-Dioxo-2,5-dihydro-1*H*-pyrrol-1-yl)ethyl)amino)-4-oxobutyl)-1*H*-1,2,3-triazol-1-yl)butyl)-5-methyl-1*H*-pyrrol-2-yl)methylene)-4'-methoxy-5-pentyl-1*H*,5'*H*-[2,2'-bipyrrol]-1'-ium chloride (**III-171·HCl**)

^{1}H NMR (300 MHz, $CDCl_3$)

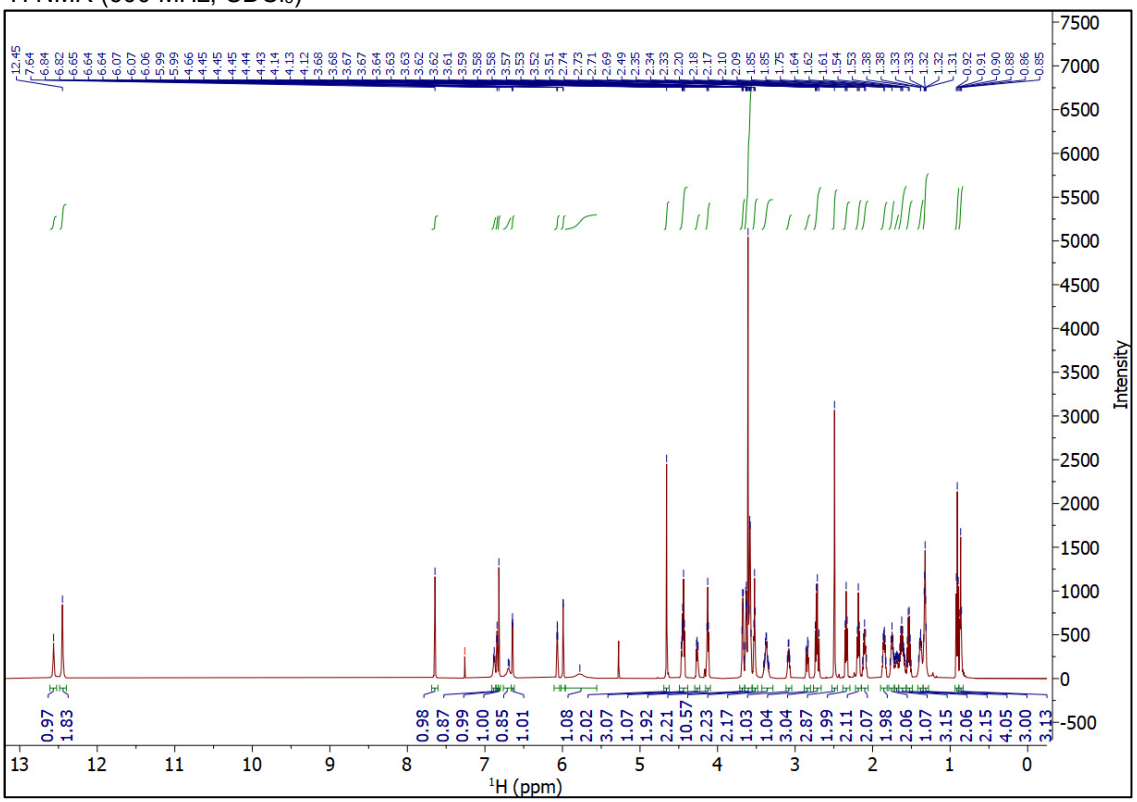


^{13}C NMR (76 MHz, $CDCl_3$)

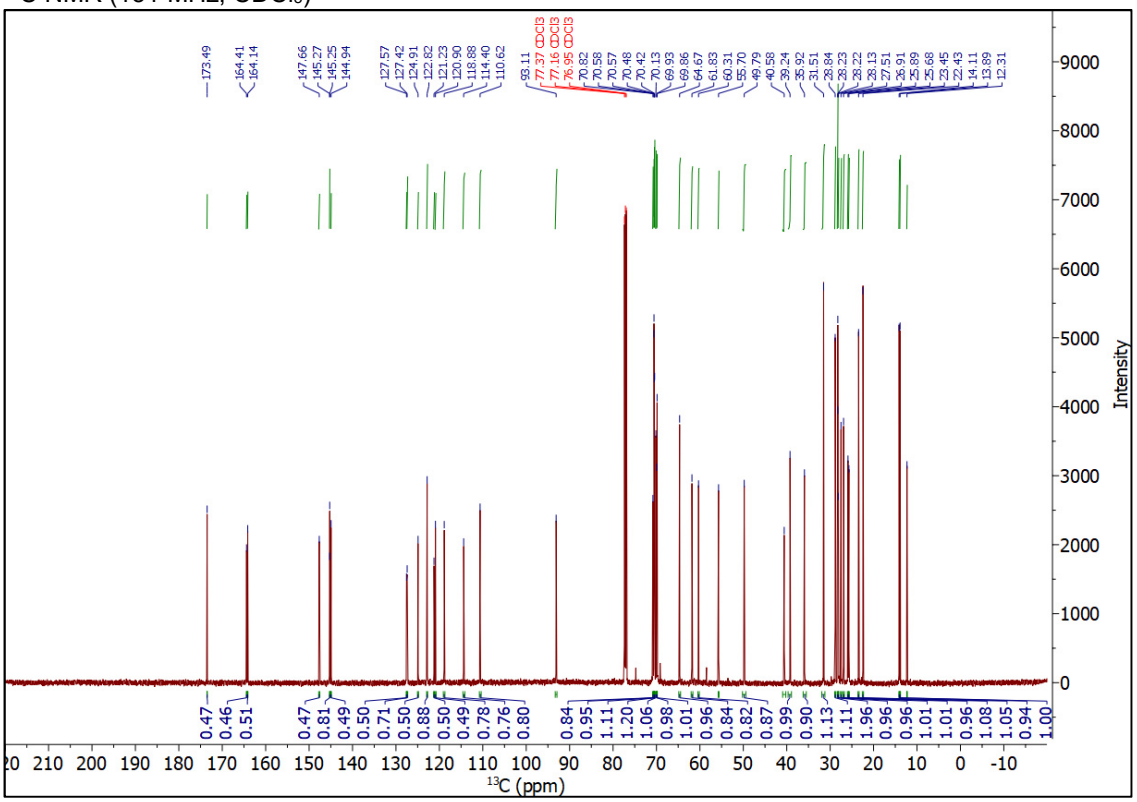


(*Z*)-5'-((5-Methyl-4-propyl-1*H*-pyrrol-2-yl)methylene)-4'-(4-(4-(15-oxo-19-((3a*S*,4*S*,6a*R*)-2-oxohexahydro-1*H*-thieno[3,4-*d*]imidazol-4-yl)-2,5,8,11-tetraoxa-14-azanonadecyl)-1*H*-1,2,3-triazol-1-yl)butoxy)-5-pentyl-1*H*,5'*H*-[2,2'-bipyrrol]-1'-ium chloride (**III-172·HCl**)

^{1}H NMR (600 MHz, $CDCl_3$)

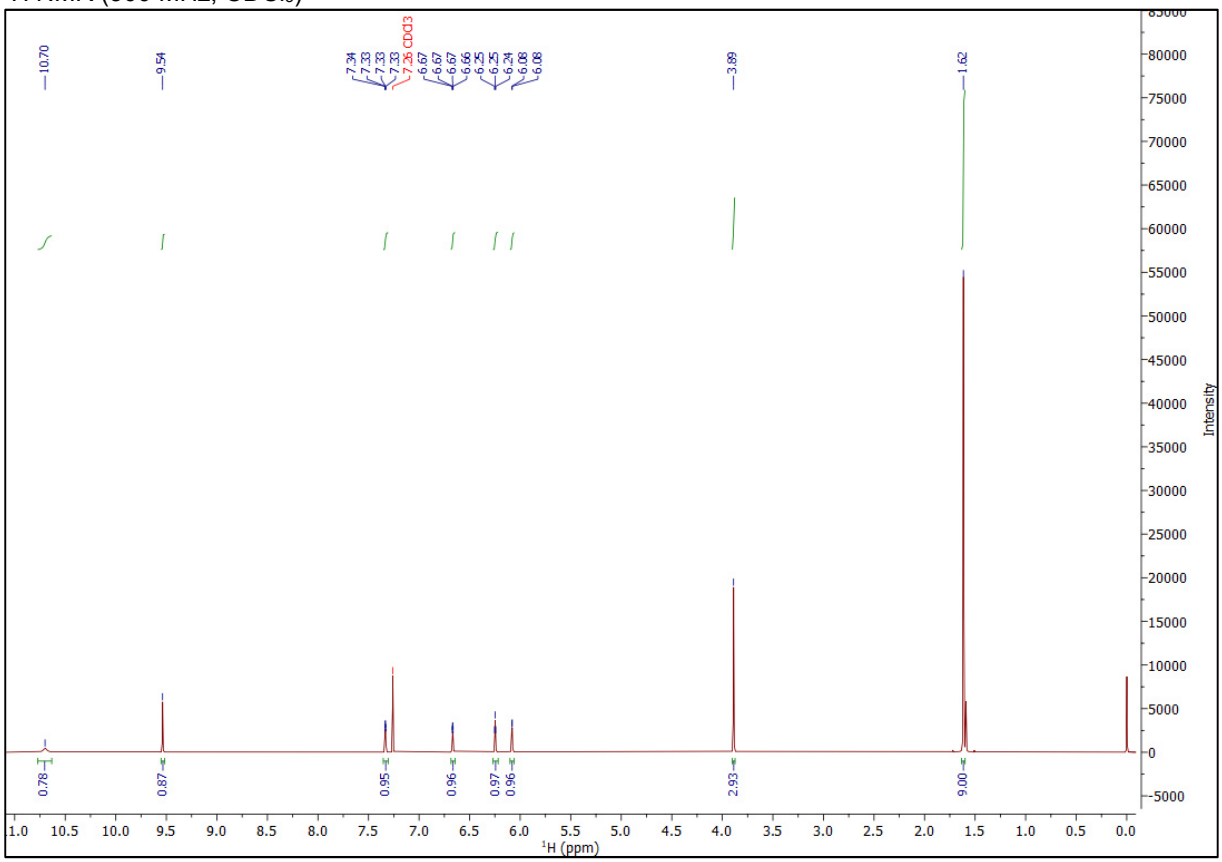


^{13}C NMR (151 MHz, $CDCl_3$)

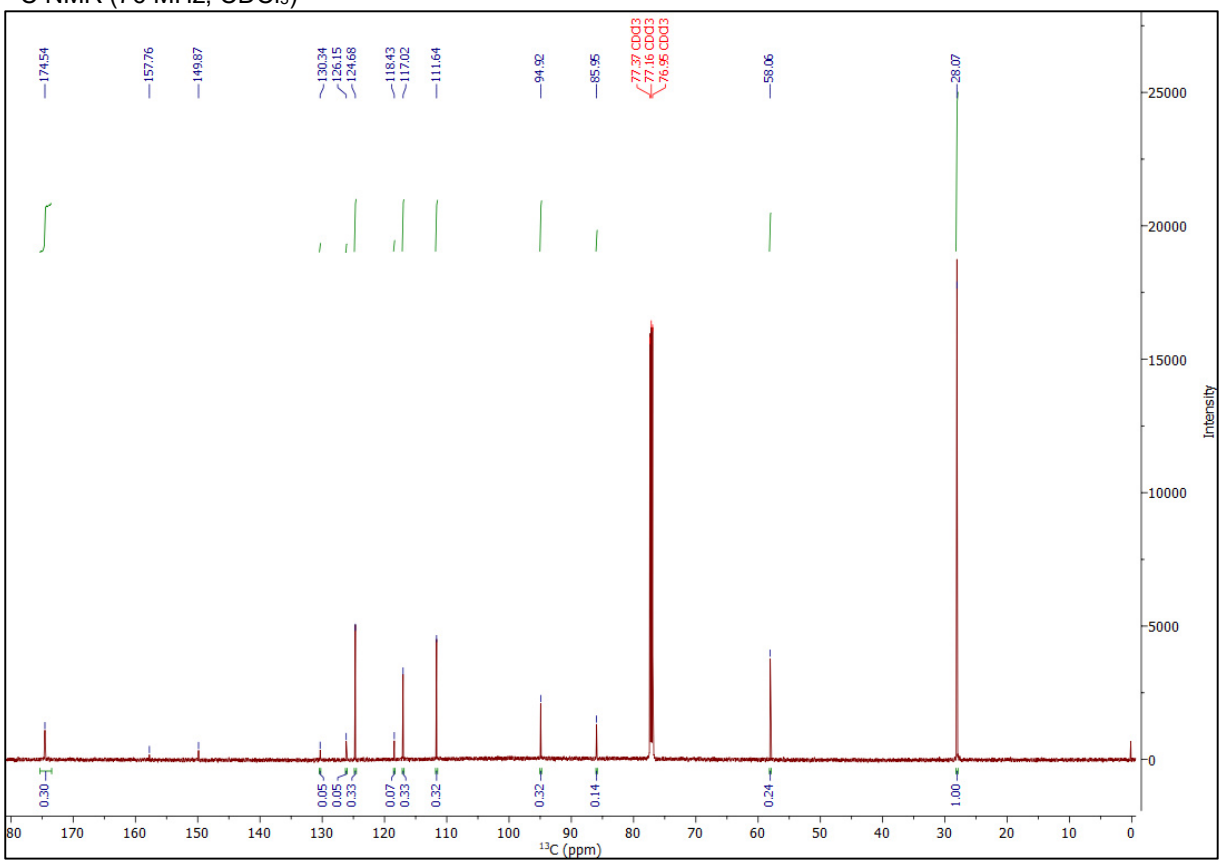


tert-Butyl 5'-formyl-4'-methoxy-1*H*,1'*H*-[2,2'-bipyrrole]-1-carboxylate (**III-174**)

^{1}H NMR (300 MHz, $CDCl_3$)



^{13}C NMR (76 MHz, $CDCl_3$)



IX.18 LC-MS Chromatograms and Spectra – Negative Controls

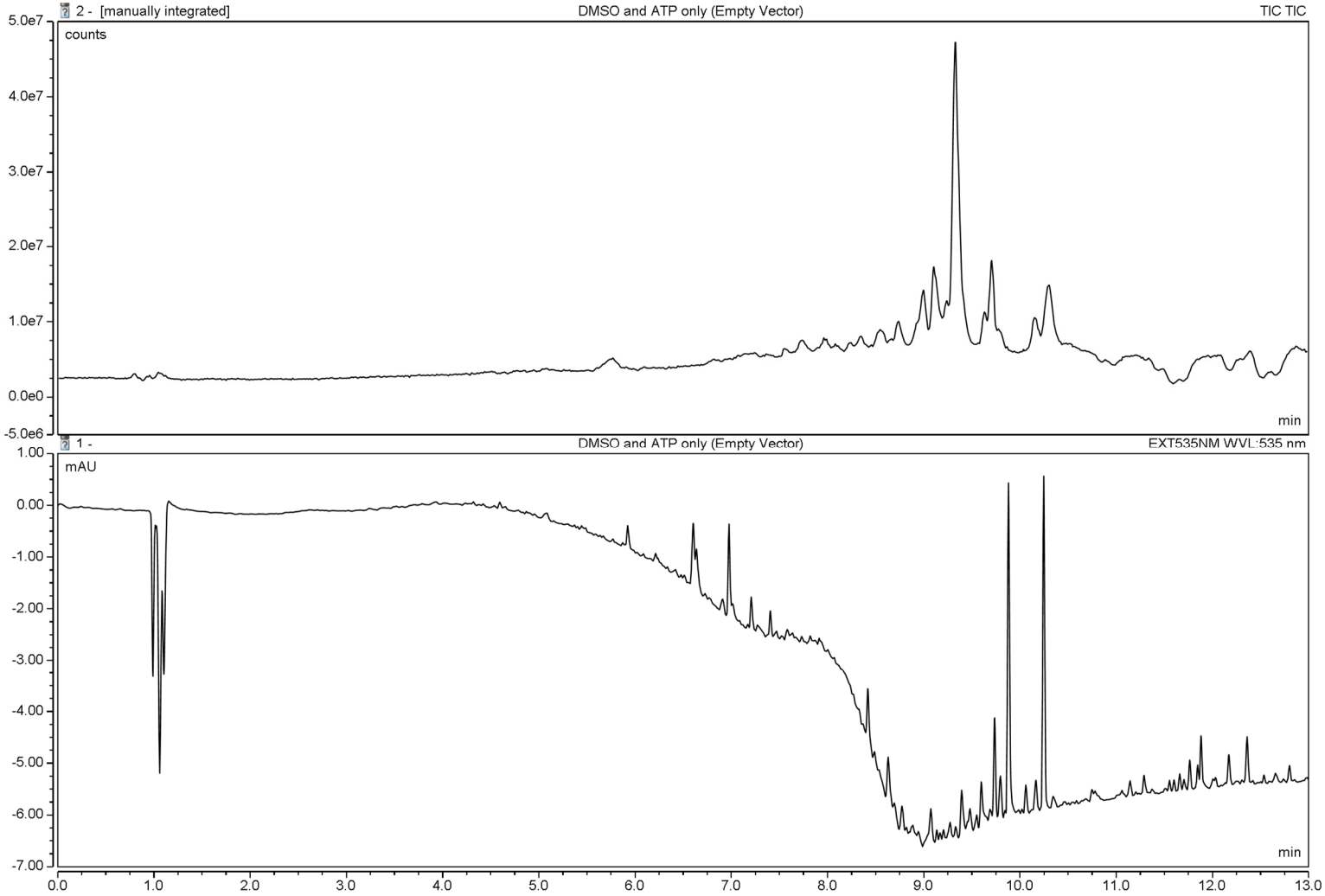


Figure IX.15. LC-MS data (TIC and UV_{535} trace) of the methanolic reaction extract from the empty vector negative control reaction, containing ATP and DMSO only, but no pyrroles or MBC derivatives. The absence of characteristic prodiginine absorption in the UV_{535} trace confirms that no background reaction is taking place. Typical prodiginine elution is expected between 7.56–8.30 min (see experimental section).

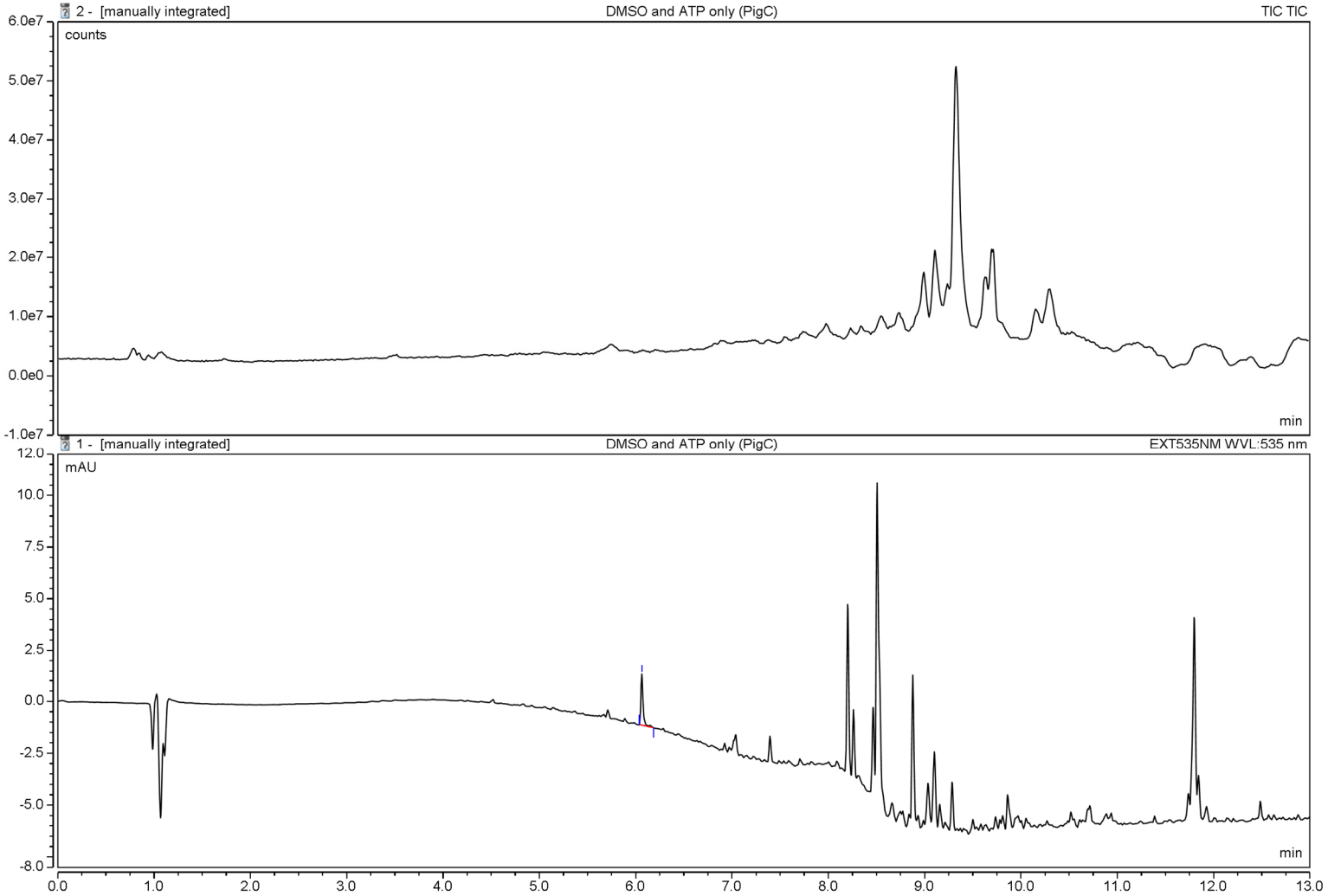


Figure IX.16. LC-MS data (TIC and UV_{535} trace) of the methanolic reaction extract from the PigC negative control reaction, containing ATP and DMSO only, but no pyrroles or MBC derivatives. The absence of characteristic prodiginine absorption in the UV_{535} trace confirms that no background reaction is taking place. Typical prodiginine elution is expected between 7.56–8.30 min (see experimental section).

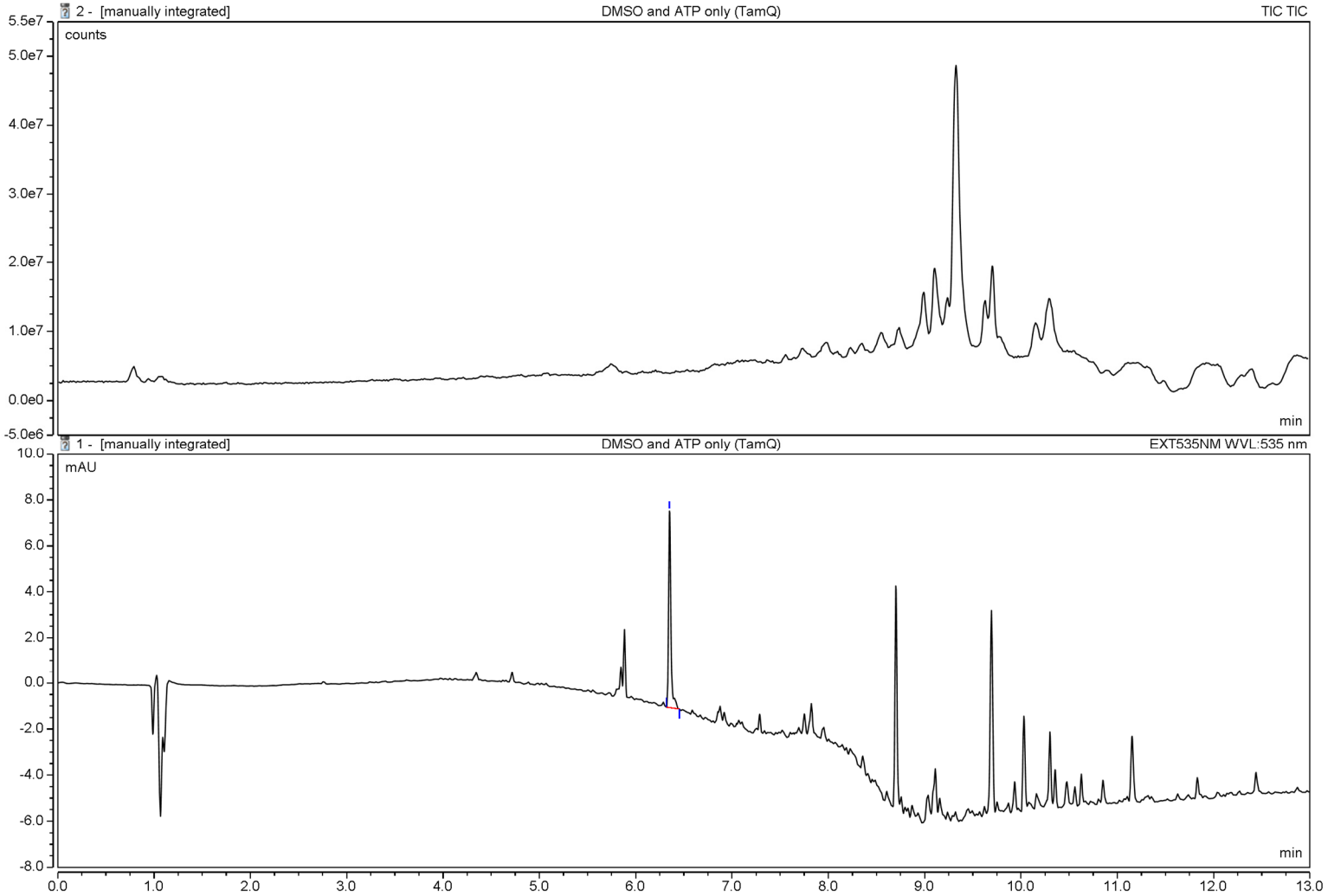


Figure IX.17. LC-MS data (TIC and UV_{535} trace) of the methanolic reaction extract from the TamQ negative control reaction, containing ATP and DMSO only, but no pyrroles or MBC derivatives. The absence of characteristic prodiginine absorption in the UV_{535} trace confirms that no background reaction is taking place. Typical prodiginine elution is expected between 7.56–8.30 min (see experimental section).

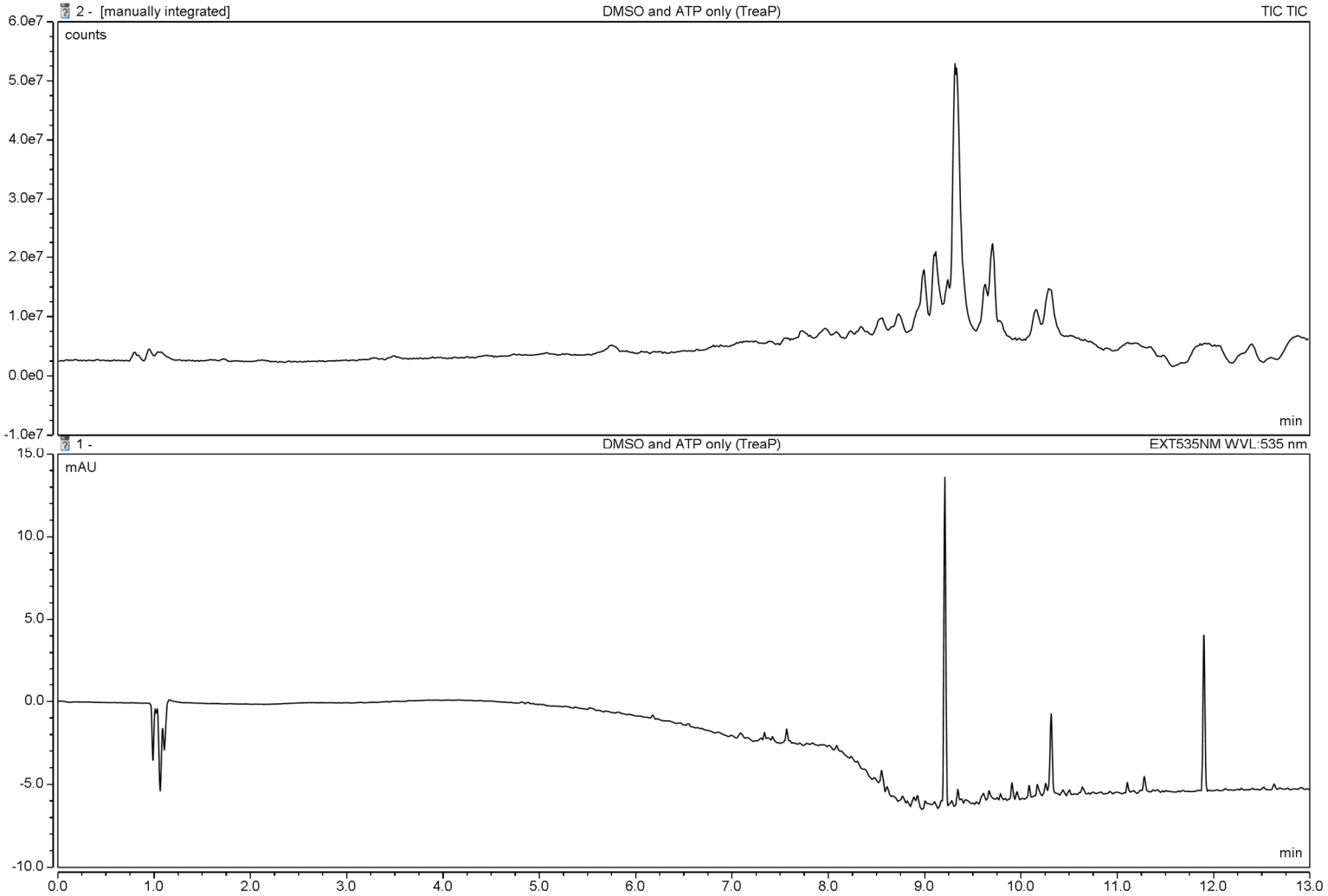


Figure IX.18. LC-MS data (TIC and UV_{535} trace) of the methanolic reaction extract from the TreaP negative control reaction, containing ATP and DMSO only, but no pyrroles or MBC derivatives. The absence of characteristic prodiginine absorption in the UV_{535} trace confirms that no background reaction is taking place. Typical prodiginine elution is expected between 7.56–8.30 min (see experimental section).

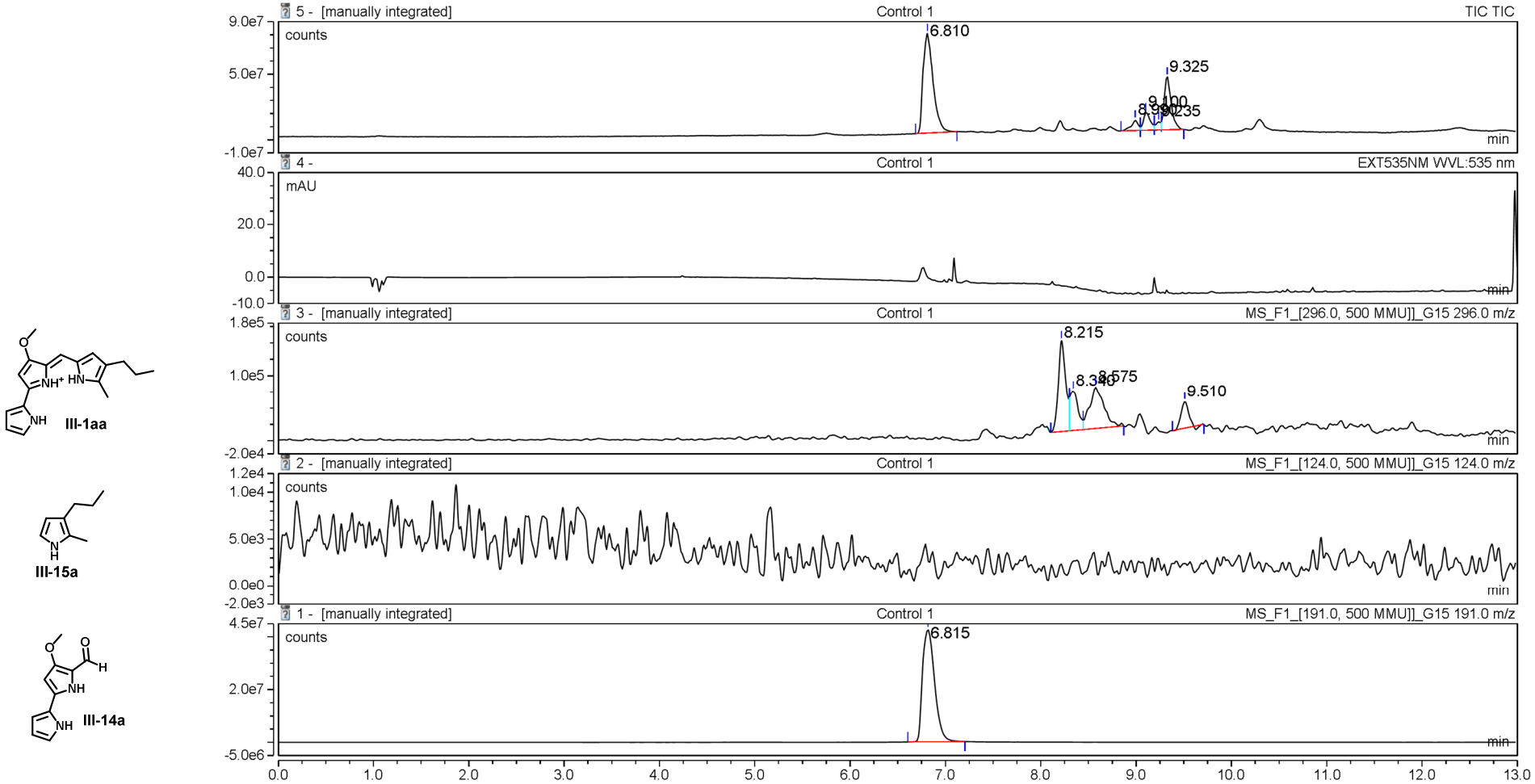


Figure IX.19. LC-MS data (TIC, UV_{535}, and extracted ion chromatograms) of control reaction 1, containing MBC **III-14a** (m/z 191.0) and pyrrole **III-15a** (m/z 124.0), ATP and KP_i buffer, but no enzyme-containing cell lysates. The potential condensation product prodiginine **III-1aa** (m/z 296.0) with a retention time t_R of 7.33 min is not found in the UV trace at 535 nm.

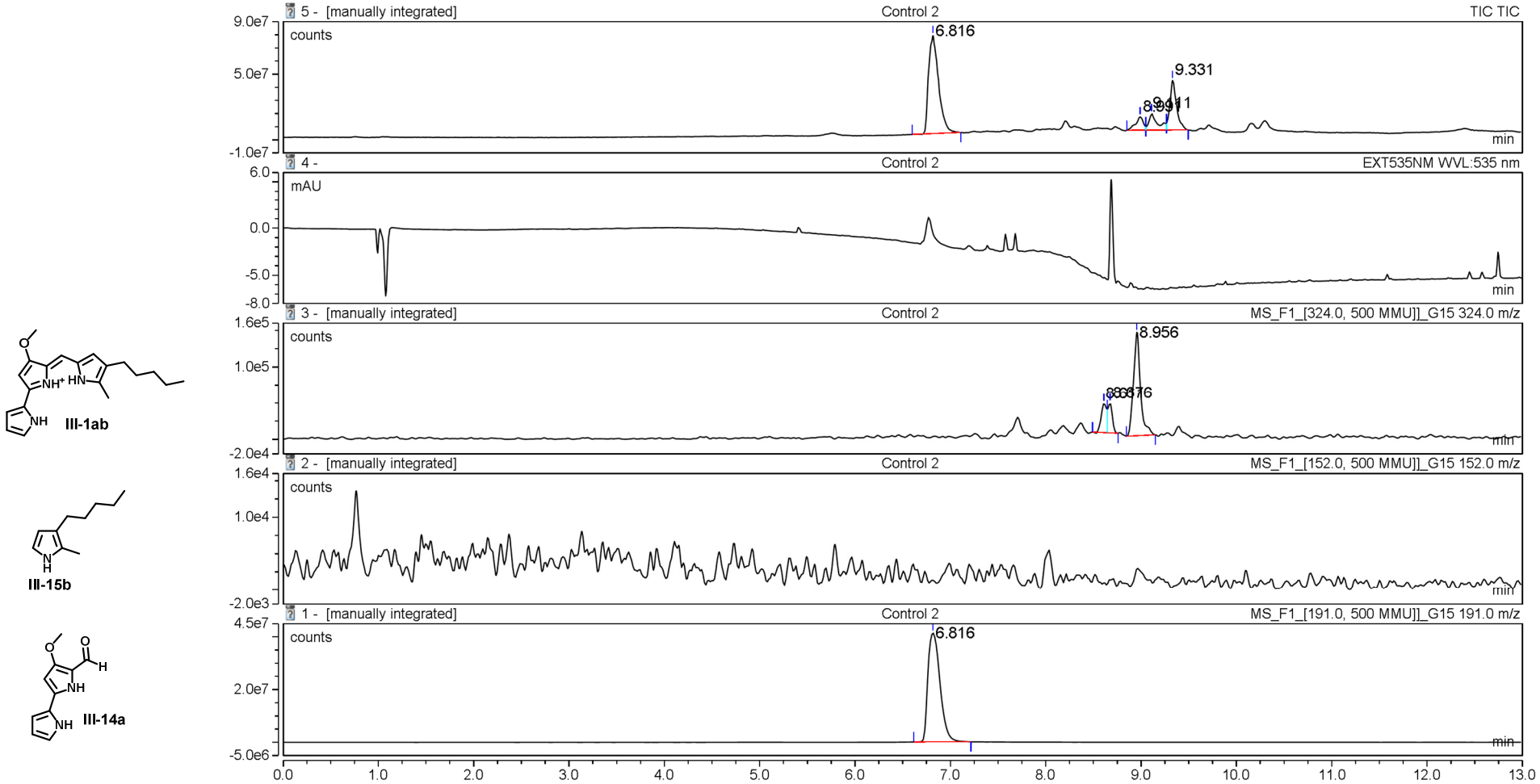


Figure IX.20. LC-MS data (TIC, UV_{535}, and extracted ion chromatograms) of control reaction 2, containing MBC **III-14a** (m/z 191.0) and pyrrole **III-15b** (m/z 152.0), ATP and KP_i buffer, but no enzyme-containing cell lysates. The potential condensation product prodigiosin **III-1ab** (m/z 324.0) with a retention time t_R of 7.62 min is not found in the UV trace at 535 nm.

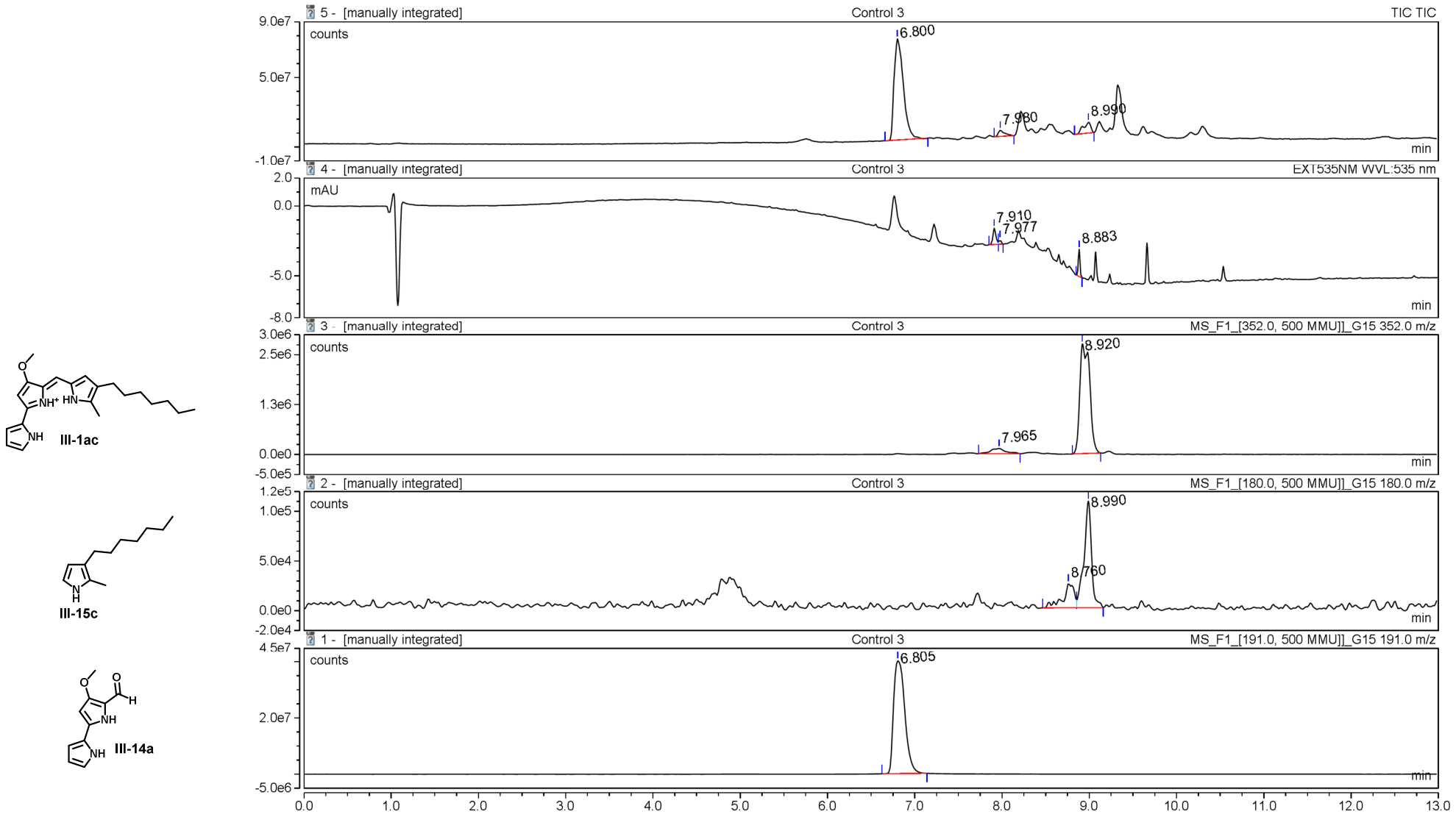


Figure IX.21. LC-MS data (TIC, UV_{535}, and extracted ion chromatograms) of control reaction 3, containing MBC **III-14a** (m/z 191.0) and pyrrole **III-15c** (m/z 180.0), ATP and KP_i buffer, but no enzyme-containing cell lysates. The potential condensation product prodiginine **III-1ac** (m/z 352.0) with a retention time t_R of 7.87 min is not found in the UV trace at 535 nm.

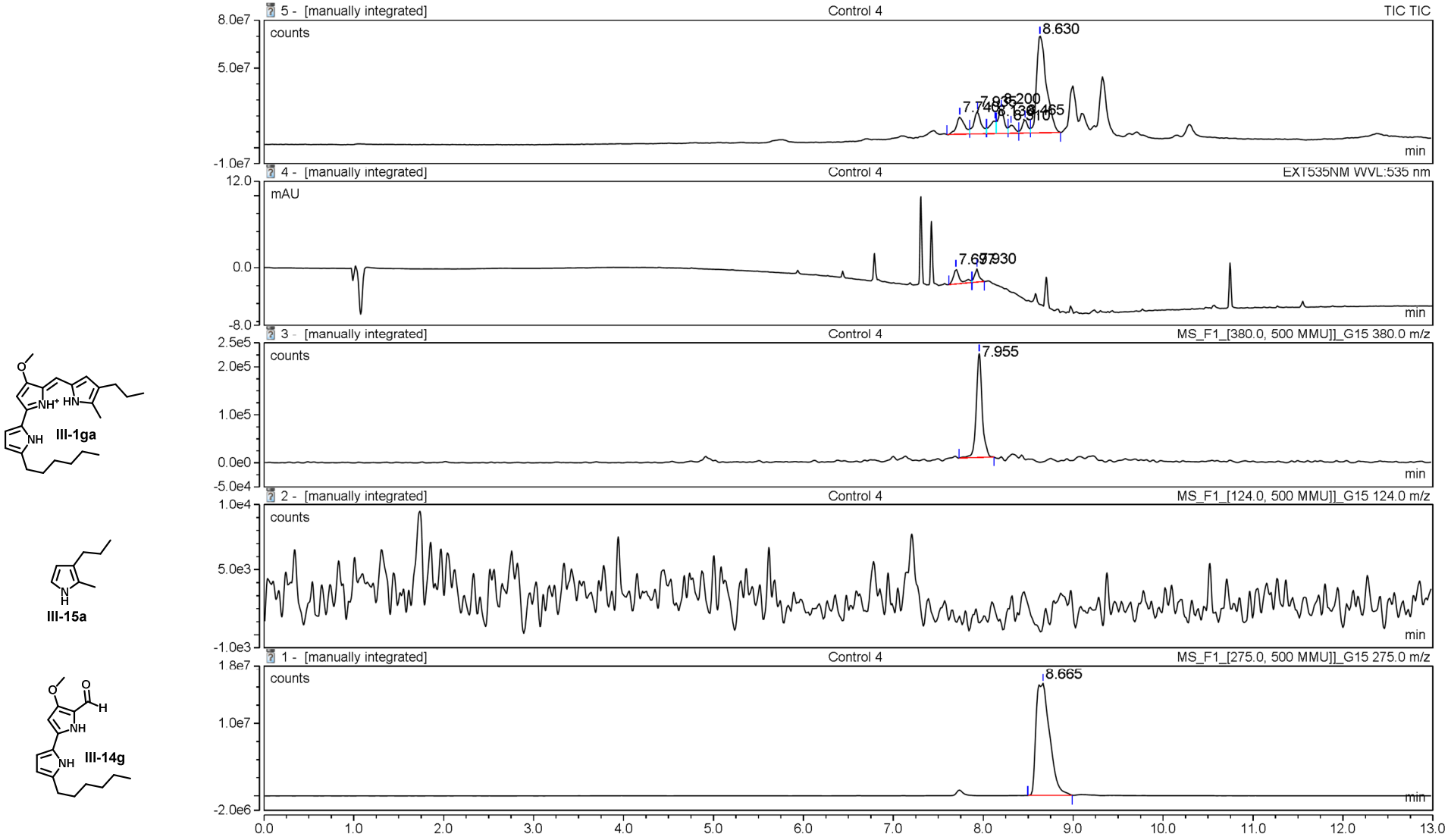


Figure IX.22. LC-MS data (TIC, UV_{535}, and extracted ion chromatograms) of control reaction 4, containing hexyl-MBC **III-14g** (m/z 275.0) and pyrrole **III-15a** (m/z 124.0), ATP and KP_i buffer, but no enzyme-containing cell lysates. The potential condensation product prodiginine **III-1ga** (m/z 380.0) with a retention time t_R of 7.91 min is not found in the UV trace at 535 nm.

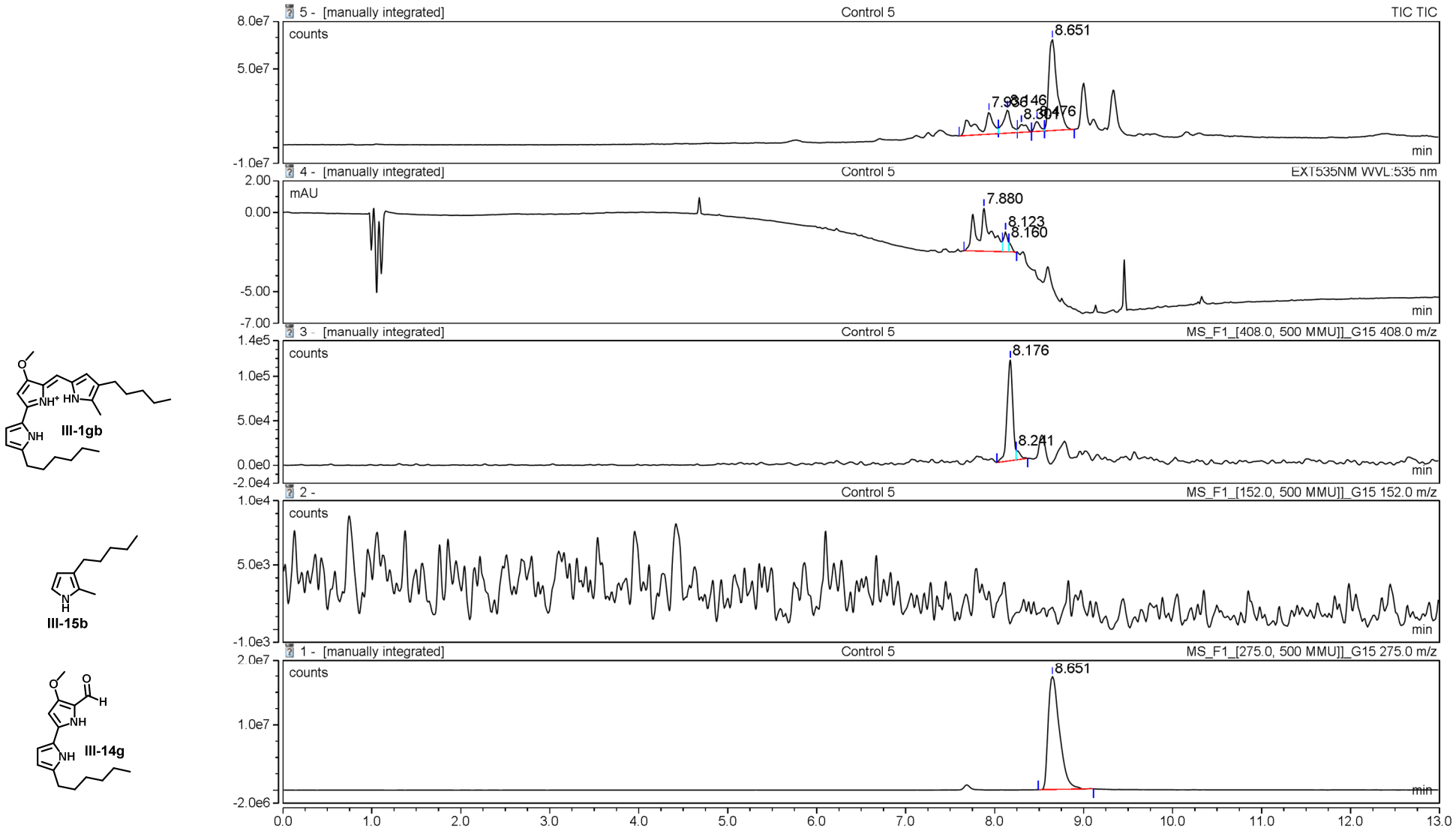


Figure IX.23. LC-MS data (TIC, UV_{535}, and extracted ion chromatograms) of control reaction 5, containing hexyl-MBC **III-14g** (m/z 275.0) and pyrrole **III-15b** (m/z 152.0), ATP and KP_i buffer, but no enzyme-containing cell lysates. The potential condensation product prodiginine **III-1gb** (m/z 408.0) with a retention time t_R of 8.12 min is not found in the UV trace at 535 nm.

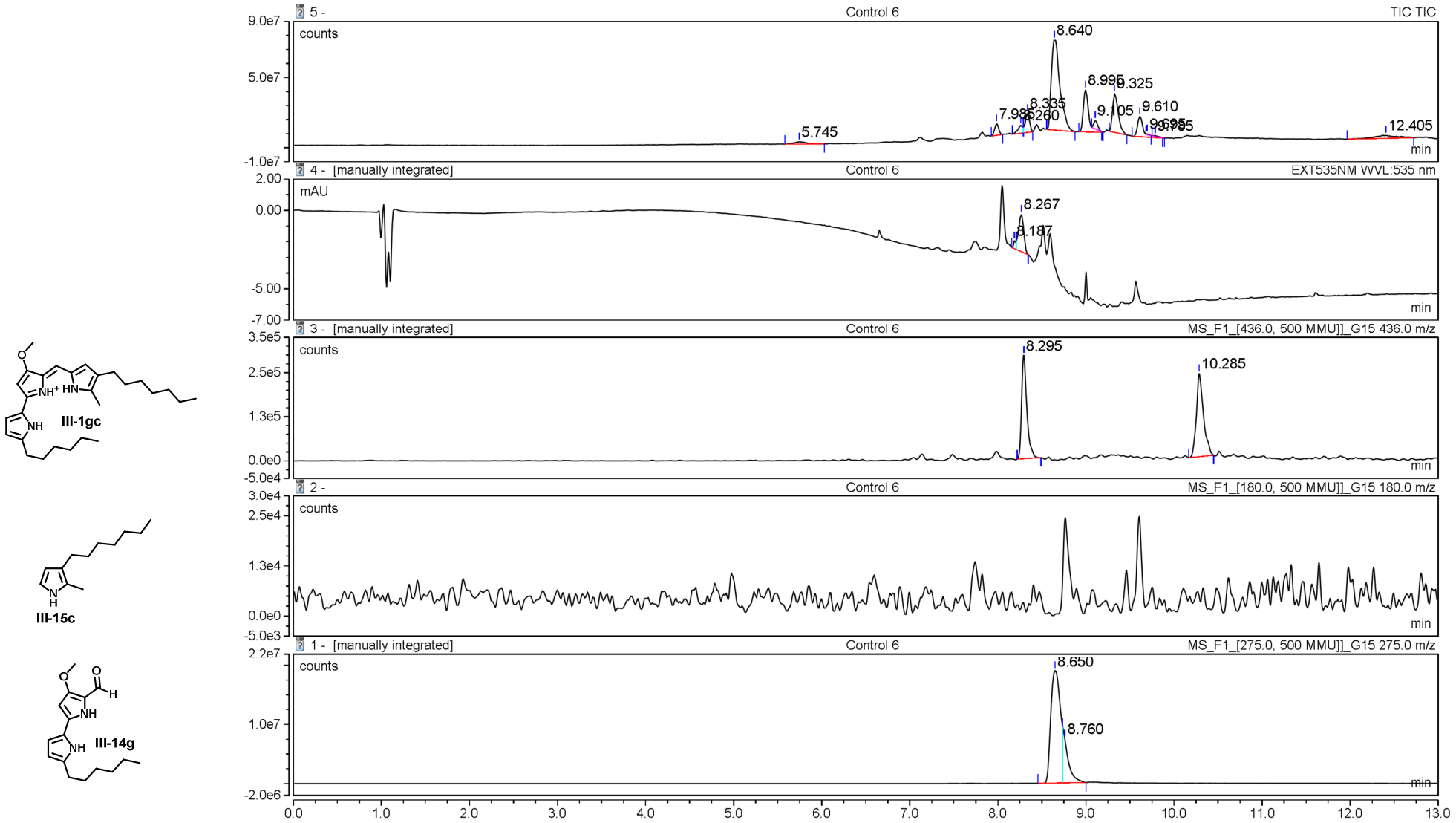


Figure IX.24. LC-MS data (TIC, UV_{535}, and extracted ion chromatograms) of control reaction 6, containing hexyl-MBC **III-14g** (m/z 275.0) and pyrrole **III-14c** (m/z 180.0), ATP and KP_i buffer, but no enzyme-containing cell lysates. The potential condensation product prodiginine **III-1gc** (m/z 436.0) with a retention time t_R of 8.27 min is not found in the UV trace at 535 nm.

X Acknowledgements

An dieser Stelle möchte ich mich aufrichtig bei all den Menschen bedanken, die mich in den vergangenen Jahren begleitet und während der Promotion unterstützt haben.

An erster Stelle steht ein großer Dank *Prof. Dr. Jörg Pietruszka* zu, der mir die freie Ausgestaltung meines Themas am IBOC ermöglicht hat und, trotz der geringen Überschneidung mit dem Fachbereich der organischen Chemie, mein Pyocin „Hobby-Projekt“ unterstützt und mitfinanziert hat. Seine Offenheit für die damit verbundenen Ideen und sein Vertrauen in meine Arbeit haben dieses Projekt erst möglich gemacht. Jörg war über all die Jahre nicht nur ein Mentor und Berater, sondern stets ein verlässlicher Garant von Stabilität und Kontinuität am IBOC.

Bei *Prof. Dr. Julia Frunzke* möchte ich mich herzlich für die Übernahme des Zweitgutachtens bedanken. Die Länge und thematische Vielfalt dieser Arbeit machen die Begutachtung zu einer besonderen Herausforderung, die Offenheit erfordert, sich auf unterschiedliche wissenschaftliche Perspektiven einzulassen und neue Blickwinkel einzunehmen. Da Julia sich ohne Zögern hierzu bereit erklärt hat, gilt ihr mein aufrichtiger Dank und großer Respekt für das engagierte und konstruktive Feedback im Rahmen des Korreferats.

Der *Jürgen Manchot Stiftung* unter Vorsitz von *Dr. Thomas Manchot* und *Thomas Kramer* danke ich für drei Jahre der großzügigen Finanzierung im Rahmen eines Promotionsstipendiums.

Ebenfalls bedanken möchte ich mich bei den zahlreichen Kooperationspartnern, die entscheidend zu den im Rahmen dieser Dissertation entstandenen Publikationen beigetragen haben. Hier zu nennen wären *Dr. Lena Berning* und *Prof. Dr. Björn Stork* (HHU Düsseldorf), *Peter Bitsch* und *Prof. Dr. Peter Kolmar* (TU Darmstadt), sowie *Pelin Özdüzenciler* und *Prof. Dr. Erdem Gültekin Tamgüney* (FZ Jülich). Insbesondere möchte ich an dieser Stelle *Prof. Dr. Stefanie Scheu* nennen, die mich bei dem Verfassen des S2-Antrags in beratender Funktion unterstützt hat. Großer Danke gilt ebenfalls *Raquel Guadarrama-Gonzalez* und *Prof. Dr. Colin MacKenzie*, deren Labore am Universitätsklinikums Düsseldorf ich in Zeiten von Corona uneingeschränkt für meine Studien nutzen durfte. Ebenfalls wären weite Teile dieser Arbeit ohne die von ihnen bereitgestellten klinischen *Pseudomonas aeruginosa* Isolate nicht möglich gewesen.

Im Laufe meiner Promotion wurde ich ebenfalls mit der Betreeung zahlreicher Studenten im Rahmen von Praktika und Bachelorarbeiten betraut. *Annabel Ahrens*, *Stella Pauls* und *Sebastian Sill* möchte ich daher für ihre Unterstützung danken und die tollen Abschlussarbeiten, die in Folge der Zusammenarbeit entstanden sind. Besonders hervorzuheben ist hierbei *Alexandra Leyens*, die mir als Auszubildende am IBOC für gut zwei Jahre unterstützend zur Seite stand. Alexandra war nicht nur hoch motiviert, sondern auch clever und ausgezeichnet organisiert, sodass die Zeit der Zusammenarbeit für uns beide gewinnbringend, produktiv und außerordentlich lehrreich war.

Ebenso zu würdigen ist das gesamte Team des IBOC’s und seine helfenden Hände im Verborgenen. Hier zu nennen sind insbesondere Monika Gehsing, Birgit Henßen, Vera Ophoven und Bea Paschold, die bei Problemen jederzeit zur Stelle waren und durch ihren Einsatz einen reibungslosen Arbeitsalltag ermöglicht haben.

Und natürlich dürfen an dieser Stelle nicht die Menschen fehlen, die auch außerhalb der akademischen Welt einen großen und nicht zu unterschätzenden Beitrag zur Entstehung dieser Arbeit geleistet haben. Aus diesem Grund möchte ich mich bei meinen *Eltern*, *Geschwistern* und *Großeltern* bedanken, die mich von Anbeginn des ersten Semesters im Bachelorstudium unterstützt, motiviert und kritisch hinterfragt haben. Ohne Euch und Euren Support würde ich nicht da stehen wo ich heute bin, wofür ich Euch auf Ewig dankbar sein werde!

Und zu guter letzt gilt ganz besonder Dank *Dr. Nadiia Pozhydaieva*, die sich zahlreiche Male durch diese Arbeit gequält hat und unzählige Tage, wenn nicht sogar Wochen, mit dem Korrigieren und Kommentieren eben dieser verbracht hat. Ohne sie und ihr tiefgreifendes konzeptionelles Feedback wäre diese Arbeit nur ein Bruchteil dessen, was sie nun in der finalen Fassung letztendlich geworden ist. Danke Nadiia, dass Du immer für mich da bist, mich unterstützt, inspirierst und mich über die letzten Jahre begleitet hast. Ich freue mich auf unsere gemeinsame Zukunft – und auf all das, was nach diesem langen Kapitel noch vor uns liegt.